



PHYSICAL CHEMISTRY 2004

Proceedings

*of the 7th International Conference
on Fundamental and Applied Aspects of
Physical Chemistry*

Volume I and II

September 21-23, 2004
Belgrade, Serbia and Montenegro



PHYSICAL CHEMISTRY 2004

Proceedings

*of the 7th International Conference
on Fundamental and Applied Aspects of
Physical Chemistry*

Volume I and II

Editors

A. Antić-Jovanović and S. Anić

ISBN 86-82457-12-x
Title: Physical Chemistry 2004. (Proceedings)
Editors A. Antić-Jovanović and S. Anić
Published by: The Society of Physical Chemists of Serbia, Student-
ski trg 12-16, P.O.Box 137, 11001 Belgrade, Serbia
and Montenegro
Publisher: Society of Physical Chemists of Serbia
Printed by: "Jovan" Printing and Published Comp;
300 Copies; Number of Pages: x + 906; Format B5;
Printing finished in September 2004.
Text and Layout: Aleksandar Nikolić

300 – copy printing

The Conference is organized by
the Society of Physical Chemists of Serbia
in cooperation with
Institute of Catalysis, Bulgarian Academy of Sciences
and
Boreskov Institute of Catalysis,
Siberian Branch of the Russian Academy of Sciences

* * *

The Conference is held under the auspices of the
Ministry of Sciences and Environmental Protection
of the Republic of Serbia

Organizing Committee

Chairman: S. Anić (SCG)
Vice-chairmans: L. Petrov (Bulgaria)
V. N. Parmon (Russia)
B. Adnađević (SCG)

Members:

T. Grozdić (SCG), D. Jovanović (SCG), M. Lalić (BH), D. Marković (SCG),
B. Milosavljević (USA), N. Miljević (SCG), T. Nenadović (SCG), C. Pona (Italy), S.
Stanković (SCG), N. Vukelić (SCG)

Scientific Committee

Chairman: A. Antić-Jovanović (SCG)
Vice-chairmans: D. Mehandjiev (Bulgaria)
O. Nešković (SCG)

Members:

G. Bakalkin, (Sweden), J. Baranac (SCG), J. Gabor (Hungary), V. Gáspár (Hungary),
P. Graae Sørensen (Denmark), V. Dondur (SCG), F. Hynne (Denmark), M. Jeremić
(SCG), J. Kallitsis (Greece), R.M. Leblanc (USA), S. Macura (USA), S. Mentus
(SCG), B. Minčeva-Šukarova (Macedonia), M. Perić (SCG),
N. Petranović (SCG), M. Plavšić (SCG), Y. Quere (France), M. Ristić (SCG),
G. Schmitz (Belgium), A. Terlecki-Baričević (SCG), D. Veselinović (SCG)

Executive Committee

Secretary: B. Adnađević (SCG)

Members:

N. Cvjetičanin (SCG), Z. Čupić (SCG), Lj. Damjanović (SCG),
A. Đerić (SCG), Lj. Ignjatović (SCG), S. Kuprešak (SCG),
M. Micić (USA), B. Simonović (SCG), D. Stanisavljev (SCG),
N. Vukelić (SCG)

SPONSORS

Ministry of Science and Environmental Protection of Republic of Serbia

The Faculty of Physical Chemistry, University of Belgrade

Institute for Chemistry, Technology and Metalurgy, Belgrade

Institute of General and Physical Chemistry, Belgrade

MOL, Belgrade

Hemofarm Group, Vršac

Gradski zavod za zaštitu zdravlja, Beograd

Organisation for the Prohibition of Chemical Weapons

PREFACE

It is a great pleasure for us to welcome all participants to “Physical Chemistry 2004”.

The first Conference on Fundamental and Applied Aspects of Physical Chemistry has been held in Belgrade, 1992. Since then, this biennial international conference has successfully established itself as a forum for presentation and discussion of new results and developments in all branches of physical chemistry.

These Proceedings contain the manuscripts of a total 256 papers. Besides 5 Plenary Lectures, given by internationally recognized scientists, they include 20 Invited Lectures and 231 Contributed Lectures from scientists of over 20 different countries, arranged in section corresponding to their scientific topics.

Those who have been doing research in the field of physical chemistry for a long time are well aware of the usefulness of these proceedings, which have come out every two years since 1992. Those who are new to the field will find these books an excellent source of references for the work in this very active science.

The contributed papers are reviewed but without language revision, for which authors bear responsibility.

We are grateful to the Ministry of Science and Environmental protection of the Republic of Serbia, and to all other sponsors for help to make this conference a success.

Finally, we thank to Plenary and Invited Lecturers for accepting invitation of the Scientific Committee, as well as to all authors of contributing papers for their kind cooperation.

Editors

Contents at a Glance

Volume I

Plenary Lectures (PL)	1
Chemical Thermodynamics (A).....	37
Spectroscopy, Molecular Structures and Physical Chemistry of Plasma (B)	69
Kinetics, Catalysis and Nonlinear Dynamics (C)	177
Electrochemistry (D).....	285
Biophysical Chemistry, Photochemistry and Radiation Chemistry (E).....	329
Radiochemistry and Nuclear Chemistry (F)	417

Volume II

Materials Science (G)	457
Solid State Physical Chemistry (H)	533
Macromolecular Physical Chemistry (I)	575
Environmental Protection (J)	629
Phase Boundaries (K)	719
Complex Compounds (L)	755
General Physical Chemistry (M)	817
Education (N).....	869
Author Index	889
Participating Institutions	897

TABLE OF CONTENTS

Plenary Lectures

R. M. Leblanc, K. M. Gattás-Asfura QUANTUM DOTS: IMMOBILIZATION AND SURFACE CHEMISTRY STUDIES	3
L. A. Petrov APPLICATION OF CHEMICAL KINETICS IN THE HETEROGENEOUS CATALYSIS STUDIES	6
J. Streiff, N. Juranić, D. O. Warner, K. A. Jones, W. J. Perkins, S. Macura STUDY OF PROTEIN-ANESTHETIC INTERACTIONS BY NMR SPECTROSCOPY	14
M. B. Hall, L. M. Pérez THEORETICAL STUDIES ON DIOXOMOLYBDENUM(VI) COMPLEXES AS OXYGEN ATOM TRANSFER (OAT) CATALYSTS	20
A. A. Jensen PERSISTENT ORGANIC POLLUTANTS A THREAT TO THE GLOBAL ENVIRONMENT AND TO HUMAN HEALTH	27

A – Chemical Thermodynamics

N. Begović, Z. Marković, S. Anić, Lj. Kolar-Anić GIBBS FREE ENERGIES AND ENTHALPIES FOR GASEOUS REACTIONS OF OXY-IODINE SPECIES $HxOy$	39
M. Vojić, G. Popović, D. Sladić, L. Pfendt STUDY OF ACID-BASE EQUILIBRIA AND SOLUBILITY OF KETOCONAZOLE	42
G. Popović, M. Čakar THE EFFECT OF ACIDITY ON HYDROSOLUBILITY OF METHYL- AND PROPYLPARABEN	45
L. Gobor, A. D. Nikolić, D. Rikić, D. G. Antonović EXCESS MOLAR VOLUMES FOR BINARY LIQUID MIXTURES OF N-METHYLACETAMIDE WITH CHLOROFORM	48
V. Marjanović, R. Ninković, J. Miladinović, M. Todorović CLEGG-PITZER-BRIMBLECOMBE EQUATION APPLIED TO $Na_2SO_4(aq)$ AT $T = 298.15K$	51
R. Ninković, J. Miladinović, M. Todorović, B. Božović PREDICTED VALUES OF OSMOTIC COEFFICIENT IN $K_2SO_4(aq)$ SUPERSATURATED SOLUTION AT $T = 298.15 K$	54
J. Jovanović TEMPERATURE INFLUENCE ON COURSE OF <i>DDSH</i> SILOXANE REDISTRIBUTION REACTION	57
V. Rakić, I. Cekić, R. Hercigonja THE INTERACTION OF n-HEXANE WITH CATION EXCHANGED Y ZEOLITES	60

J. Savić	63
THERMODYNAMICS OF AZO-DYE IMMOBILIZATION ON ANION-EXCHANGE RESIN	
P. Khazaeli-Parsa, V. Hubscher, F. Arnaud-Neu	66
THERMODYNAMIC STUDIES OF COMPLEXATION OF ALKALI AND ALKALINE EARTH CATIONS BY A DIHOMOOCALIX[4]ARENE TETRAAMIDE	
B – Spectroscopy, Molecular Structures and Physical Chemistry of Plasma	
A. Stamatović	71
LOW ENERGY ELECTRON MOLECULE INTERACTIONS	
S. Todorović, D. Murgida, P. Hildebrandt	74
SURFACE ENHANCED RESONANCE RAMAN SPECTROSCOPY IN THE STUDIES OF IMMOBILIZED REDOX ENZYMES	
O. Nešković	80
MALDI TOF OF CARBON CLUSTERS	
M. Franko	87
DETERMINATION OF OPTO-THERMAL PARAMETERS OF LIQUIDS BY THERMAL LENS SPECTROMETRY –TLS, AND THEIR EFFECTS ON TLS MEASUREMENTS IN CHEMICAL ANALYSIS	
A. R. Tančić	92
<i>AB INITIO</i> CALCULATIONS OF SOME TIME –DEPENDENT PROPERTIES OF ATOMIC SYSTEMS	
A. R. Tančić	95
ON THE SPIN DENSITY WAVE ELECTRON GAS	
A. R. Tančić, M. Nikolić	98
THE INFLUENCE OF THE POLARIZABILITY IN SOME BREMSSTRAHLUNG PROCESSES	
J. J. Savović, M. M. Kuzmanović, M. S. Pavlović, M. Stoiljković, M. Marinković	101
STUDY OF A LONG TERM PROCESSES IN D.C. ARGON ARC PLASMA BY SQUARE POWER MODULATION WITH VARIABLE LOW CURRENT PERIOD	
M. M. Kuzmanović, M. S. Pavlović, J. J. Savović, M. Stoiljković, A. Antić-Jovanović	104
ELECTRON AND GAS TEMPERATURE DIFFERENCE IN LOW CURRENT ARGON D.C. ARC STUDIED BY POWER INTERRUPTION TECHNIQUE	
I. Novović, M. Tripković, I. Holclajtner-Antunović, D. Marković	107
SPECTROCHEMICAL DETERMINATION OF As AND Cd BY U-SHAPED DC ARC	
M. Stoiljković, M. Pavlović, J. Savović, M. Marinković	110
THE STUDY OF THE MAGNETICALLY TAILORED ATMOSPHERIC PRESSURE DC ARC PLASMA WITH AEROSOL SUPPLY FOR ANALYTICAL APPLICATION	
M. Krmar	113
<i>AB INITIO</i> TREATMENT OF THE RENNER-TELLER EFFECT AND SPIN-ORBIT COUPLING IN THE $A^3\Pi_u$ ELECTRONIC STATE OF NCN	

M. Kuzmanović, V. Bojović, A. Antić-Jovanović, D. Pešić VIBRATIONAL ANALYSIS OF THE β SYSTEM OF $^{11}\text{B}^{18}\text{O}$	116
J. Dimitrić-Marković, N. Petranović, J. Baranac, T. Brdarić UV-VISIBLE SPECTROPHOTOMETRIC DETERMINATION OF THE HYDRATATION AND COPIGMENTATION CONSTANTS OF CYANIDIN	119
G. Nikolić, S. Sunarić, R. Pavlović G. Kocić, R. Nikolić SPECTROPHOTOMETRIC STUDY OF THE INFLUENCE OF Mg(II) IONS ON THE HEMATOXYLIN AUTOOXIDATION IN WEAKLY ALKALINE AQUEOUS SOLUTIONS	122
S. Konstantinović, B. Stojčeva-Radovanović, S. Ilić, Z. Todorovi UV/VIS SPECTRA NAD ANTIMICROBIAL ACTIVITY OF Cu(II) AND Zn(II) COMPLEXES ISATIN SCHIFF BASE	125
B. Stojčeva-Radovanović, S. Konstantinović UV/VIS SPECTRA AND ANTIMICROBIAL ACTIVITY OF Co(II) COMPLEXES WITH ISATIN SCHIFF BASES	128
J. Petrović, G. Nikolić, D. Marković COMPLEXES OF CHLOROPHYLL WITH COPPER, ZINC AND LEAD: UV/VIS, FT/IR AND FLUORESCENCE STUDIES	131
G. Petrović, B. Radovanović, O. Jovanović SPECTROSCOPIC CHARACTERIZATION OF SOME PHENYLHYDRAZINE SCHIFF BASES	134
M. Logar, V. Poharc-Logar STRUCTURAL INTERPRETATION OF THE POLARIZED ABSORPTION SPECTRA (400 - 1650 nm) OF ANNABERGITE $\text{Ni}_3(\text{AsO}_4)_2 \cdot 8\text{H}_2\text{O}$	137
G. Bačić, Z. Giba, M. Mojović, D. Grubišić, R. Konjević ELECTRON PARAMAGNETIC RESONANCE SPECTROSCOPY IN THE ANALYSIS OF FREE RADICALS IN SEEDS	140
S. Šašić, M. Jeremić, A. Antić-Jovanović, J. Filipović INFLUENCE OF TEMPERATURE ON RESONANCE RAMAN SPECTRA OF β - CAROTENE IN DIFFERENT MEDIA	143
Z. D. Žujović, Z. Miladinović, C. Mayer, G. A. Bowmaker THE PI TAPF SEQUENCE: CROSS POLARIZATION SPIN DYNAMICS	146
K. P. Bryliakov, E. A. Duban, E. P. Talsi THERMALLY INDUCED SPIN CROSSOVER OF $[\text{Fe}^{\text{II}}(\text{BPMEN})(\text{CH}_3\text{CN})_2](\text{ClO}_4)_2$ IN SOLUTION: PSEUDO SPIN EQUILIBRIUM	149
O. Nešković, M. Veljković, V. Šipka, S. Veličković, A. Đerić TIMS AND MALDI TOF OF ENDOHEDRAL METALLOFULLERENES	152
B. B. Radak, D. S. Maravić, Lj. T. Petkovska, M. N. Damjanović DETECTION OF MALATHION BY THE CO_2 -LASER	155
A. D. Nikolić, L. Gobor, S. Majkić, S. D. Petrović $\text{N} - \text{H} \cdots \text{O}$ HYDROGEN BONDING: FT IR STUDY OF N-BUTYLACETAMIDE - ETHER SYSTEMS	158

D. Minić, M. Baranac, R. Marković CONFIGURATIONAL STUDIES OF 5-ETHOXYCARBONYLMETHYLIDENE-2- ALKYLIDENE-4-OXOTHIAZOLIDINES BY ¹ H NMR	161
B. Radivojević, M. Dašić, S. Petrović VALIDATION OF METHYLPREDNISOLONE HEMISUCCINATE IDENTIFICATION IN LEMOD SOLU 20 mg INJECTIONS	164
Z. Korićanac, T. Jovanović SPECTROPHOTOMETRIC INVESTIGATION ON THE INTERACTION OF FAMOTIDINE WITH COPPER(II)	167
Z. Korićanac, T. Jovanović, J. Petković SPECTROPHOTOMETRIC INVESTIGATION ON REACTION PALLADIUM(II) IONS WITH THREE ANTI-ULCER DRUGS	170
J. S. Nedeljković, A. D. Marinković, S. D. Petrović, D. Ž. Mijin IR STUDY OF CIS/TRANS CONFORMERS OF N-(4-SUBSTITUTED PHENYL)-2- CYANOACETAMIDES	173
Š. S. Miljanić, M. S. Trtica DESIGN AND TEST OF THE GAS-DYNAMIC CARBON DIOXIDE LASER EXPERIMENTAL SETUP	883
C – Kinetics, Catalysis and Nonlinear Dynamics	
V. I. Elokhin SIMULATION OF CATALYTIC PROCESSES OVER SUPPORTED NANOPARTICLES	179
A. Auroux FROM STRONG SOLID ACIDS TO STRONG SOLID BASES: CHARACTERIZATION OF ACID/BASE SITES OF CATALYST SURFACES BY ADSORPTION CALORIMETRY	189
N. M. Ostrovskii NONLINEAR PHENOMENA AND MECHANISMS OF CATALYST DEACTIVATION	195
V. Idakiev, T. Tabakova, P. Konova, A. Naydenov ACTIVITY AND DEACTIVATION OF GOLD CATALYSTS SUPPORTED ON MESOPOROUS TITANIA FOR WATER-GAS SHIFT REACTION	201
D. Paneva, A. Terlecka-Baricević, T. Tsoncheva, M. Jovanović, E. Manova, Lj. Matić, B. Kunev, I. Mitov, Ch. Minchev METHANOL DECOMPOSITION OVER IRON SUPPORTED CATALYSTS – EFFECT OF PHASE COMPOSITION AND OXIDATION STATE OF IRON	204
C. Blanco, V. Krstić, V. Saiz, C. Pesquera, F. González ZEOLITIC STRUCTURES AS SUPPORT OF Rh CATALYSTS	207
V. Krstić, R. Sanz, C. Pesquera, F. González, C. Blanco MESOPOROUS MATERIALS AS SUPPORT OF Pt CATALYSTS	210

C. Blanco, V. Krstić, F. González, C. Pesquera. MCM-41 AS SUPPORT OF Rh- AND Rh-Sn/CATALYSTS. CATALYTIC PROPERTIES	213
F. Papa, D. Berger, G. Dobrescu, N. I. Ionescu METHANE COMBUSTION ON PURE AND DOPED LANTHANUM COBALTITES CATALYSTS	216
M. Stanković, B. Marković, A. Šučurović, D. Jovanović THE EFFECT OF SILVER CONTENT ON THE CIS-TRANS ISOMERIZATION SELECTIVITY DURING HIDROGENATION OF SOYBEAN OIL OVER SILVER-PROMOTED Ni/DIATOMOTE CATALYSTS	219
D. Lončarević, Ž. Čupić TEMPERATURE PROGRAMED PARTIAL OXIDATION OF CYCLOHEXANE ON THE POLYMER SUPPORTED CATALYSTS	222
N. Radić, B. Grbić, A. Terlecki-Baričević DEEP OXIDATION OF N-HEXANE ON ALUMINA SUPPORTED PLATINUM AND MANGANESE OXIDE CATALYSTS	225
V. Parvulescu, S. Somacescu, S. Todorova, K. Tenchev, G. Kadinov, B. L. Su EFFECT OF METAL SUBSTITUTION ON THE PHYSICOCHEMICAL PROPERTIES AND CATALYTIC ACTIVITY IN HYDROCARBON OXIDATION OF Co(VCo)-MCM-41 MOLECULAR SIEVES	228
K. Krinulović EFFECT OF L-CYSTEINE ON THE INHIBITION OF Na,K-ATPase ACTIVITY IN THE PRESENCE OF SOME Pd(II) COMPLEXES	231
D. Kojić, D. Stojić TIME DEPENDENT INHIBITION OF SPMs Na ⁺ /K ⁺ -ATPase INDUCED BY CADMIUM AND LEAD	234
K. Krinulović THE MECHANISM OF INTERFERENCE OF SOME Pd(II) COMPLEXES WITH Na,K-ATPase ACTIVITY - KINETIC ANALYSIS	237
V. Pavelkić, M. Živanović, V. Spasojević-Tišma, M. Ilić KINETICS OF HEAT DENATURATION OF PEPSIN IN A STRONG ACID MEDIA	240
Z. M. Grahovac, S. S. Mitić, E. T. Pecev INFLUENCE OF Co(II) AS THE CATALYST ON KINETICS CHARACTERISTICS OF PONCEAU4R OXIDATION BY HYDROGEN PEROXIDE	243
S. S. Mitić, G. Ž. Miletić, A. N. Pavlović INVESTIGATION OF THE INFLUENCE OF GLYCINE AS THE INHIBITOR ON THE THERMODYNAMIC CHARACTERISTICS OF 1,2,4-TRIHYDROXYANTRAQUINONE OXIDATION WITH HYDROGEN PEROXIDE	246
M. Živanović, V. Vasić, M. Čakar pH DEPENDENT KINETICS OF [PdCl(dien)] ⁺ REACTION WITH SOME AMINO ACIDS IN THE PRESENCE OF SDS	249

E. S. Patmar, N. I. Koltsov THE METHOD OF INVESTIGATION OF STEADY STATES NUMBER IN KINETICS OF CATALYTIC REACTIONS	252
K. P. Bryliakov, E. P. Talsi THE REACTIVE INTERMEDIATES OF CrIII(SALEN) CATALYZED ASYMMETRIC EPOXIDATION OF ALKENES AND FeIII(SALEN) CATALYZED ASYMMETRIC OXIDATION OF SULFIDES	255
M. Stanković, L. Pezo, B. Kovačević, N. Rajić, M. Jovanović, D. Debeljković KINETICS OF SiO ₂ DISSOLUTION IN NaOH AQUEOUS SOLUTION	258
L. Pezo, M. Stanković, B. Kovačević, N. Rajić, M. Jovanović, D. Debeljković KINETICS OF SiO ₂ DISSOLUTION IN NaOH AQUEOUS SOLUTION – MODIFIED SHRINKING CORE MODEL	261
S. S. Mitić, M. V. Obradović, S. B. Tosić A NEW KINETIC METHOD FOR DETERMINATION OF IRON (III)	264
J. Savić KINETIC STUDY OF AZO-DYES IMMOBILIZATION ON ANION-EXCHANGE RESINS	267
M. Grković-Popović, M. Petković, S. Marković DECOMPOSITION OF HYDROGEN PEROXIDE ON Ni (II) EXCHANGED LTA AND FAU _γ ZEOLITES	270
E. N. Efremenko, R. E. Azizov, T. A. Makhlis, S. D. Varfolomeyev, V. M. Abbasov KINETIC PARAMETERS OF BIOLUMINESCENT REACTION FOR SCREENING OF NEW BIOCIDES AMONG CORROSION INHIBITORS	273
V. Rakić, S. Gajinov, V. Rac, R. Hercigonja n-HEXANE INTERACTION WITH TRANSITION-METAL ION EXCHANGED ZEOLITES STUDIED BY TPD	276
M. Gabrovska, R. Edreva-Kardjieva, D. Crisan STRUCTURE AND CATALYTIC PROPERTIES OF Ni-Al AND Ni-Cr METHANATION CATALYSTS	279
V. D. Mitić, S. D. Nikolić, V. P. Stankov-Jovanović DEVELOPMENT OF NEW KINETIC METHOD FOR DETERMINATION OF ULTRAMICRO AMOUNTS OF PHENYLHYDRAZINE	282
 D – Electrochemistry	
M. K. Daletou, N. Gourdoupi, J. K. Kallitsis PROTON CONDUCTING MEMBRANES BASED ON PBI/POLYSULFONE COPOLYMER BLENDS	287
N. Potkonjak, D. Sužnjević ELECTROCHEMICAL INVESTIGATION OF DIFFUSION OF HYDROGEN IN LmNi _{3.55} Co _{0.75} Mn _{0.4} Al _{0.3} ALLOY	290
N. Potkonjak, D. Sužnjević TEMPERATURE DEPENDANCE OF EXCHANGE CURRENT DENSITY OF LmNi _{3.55} Co _{0.75} Mn _{0.4} Al _{0.3} HYDRIDE ELECTRODE IN ALKALINE SOLUTION	293

S. Gorjanović, M. Beljanski DIFFERENTIAL PULSE POLAROGRAPHIC STUDY OF LIPID-TRANSFER PROTEIN	296
D. Lj. Stojić, N. D. Simić, B. Đ. Cekić INTERMETALLICS – ADVANCED CATHODE MATERIALS IN THE ELECTROLYTIC PRODUCTION OF HYDROGEN	299
B. R. Šljukić, C. E. Banks, S. V. Mentus, R. G. Compton MODIFICATION OF CARBON ELECTRODES FOR SONOELECTROCATALYSIS OF OXYGEN REDUCTION AND HYDROGEN PEROXIDE FORMATION	302
S. Mentus OXYGEN REDUCTION ON POTENTIODYNAMICALLY FORMED TiO ₂ IN AQUEOUS SOLUTIONS	305
Š. S. Miljanić, N. D. Simić, M. P. Marčeta Kaninski, A. D. Maksić, D. Lj. Stojić ENERGY CONSUMPTION IN THE ELECTROLYTIC EVOLUTION OF HYDROGEN WITH IRON-NICKEL ELECTRODES	308
A. Kellenberger, W. Brandl, N. Vaszilcsin, N. Plesu POTENTIOMETRIC SENSOR BASED ON POLYANILINE-SKELETON NICKEL ELECTRODE I. ELECTRODE PREPARATION	311
Nicoleta Plesu, Andrea Kellenberger, N. Vaszilcsin, Waltraut Brandl POTENTIOMETRIC SENSOR BASED ON POLYANILINE-SKELETON NICKEL ELECTRODE II. SENSING PROPERTIES	314
G. Popović, M. Aleksić, N. Burić, V. Kapetanović DETERMINATION OF THE IONIZATION CENTERS OF CEFTRIAZONE	317
A. Abu Rabi, D. Sužnjević DETERMINATION OF As (III) IN THE GROUND WATER SPECIES BY DIFFERENTIAL PULSE POLAROGRAPHY	320
J. Savić, V. Vasić, C. Filip Cristea, M. Jitaru ELECTROCHEMICAL INVESTIGATION OF IMIDAZOL AZO CHROMOTROPIC ACID AND ITS Pd(II) COMPLEX	323
D. Tošković, M. B. Rajković, Č. Lačnjevac ELECTRO-CRYSTALLIZATION DURING THE PROCESSES OF TIN ELECTROPLATING FROM SULPHONIC ACIDS	326
 E – Biophysical Chemistry, Photochemistry and Radiation Chemistry	
V. Vukojević, T. Yakovleva, L. Terenius, A. Pramanik, G. Bakalkin DENATURATION OF dsDNA BY p53 STUDIED BY FLUORESCENCE CORRELATION SPECTROSCOPY	331
J. Caldeira, J. L. Figueirinhas, C. Santos, M. H. Godinho EPR SPECTROSCOPY OF ALLIGNED PROTEIN MICROCRYSTALS	338
D. Jakovljević, M. Radulović, A. Nastasović, M. M. Vrvic, M. Hranisavljević-Jakovljević CHEMICAL MODIFICATION OF PARTIALLY HYDROLYZED PULLULAN	341

A. Popović-Bijelić, G. Bijelić, Lj. Kolar-Anić, V. Vukojević pH DEPENDENCE OF THE CATALASE-LIKE ACTIVITY OF HORSERADISH PEROXIDASE	344
D. Đikanović, J. Bogdanović, A. Kalauzi, M. Mičić, M. Jeremić, K. Radotić COMPONENT ANALYSIS OF THE FLUORESCENCE SPECTRA OF LIGNIN ISOLATED FROM OMORIKA (<i>PICEA OMORIKA</i> L.) NEEDLES	347
V. Vukojević, Z. Marinova, S. Surcheva, T. Yakovleva, G. Cebers, L. Hugonin, F. Weijie, J. V. Aldrich, A. Gräslund, L. Terenius, G. Bakalkin. TRANSLOCATION OF DYNORPHINS ACCROSS CELLULAR MEMBRANES	350
V. Dragičević, S. Sredojević, G. Drinić, M. Ivanović, Z. Pajić, M. Vrvic THE CHANGES OF GROWTH IN FUNCTION OF FREE ENERGY INPUT IN MAIZE SEEDLINGS ORIGINATED FROM AGED SEEDS	353
G. Joksić PERSISTENCE OF MICRONUCLEI IN HUMAN LYMPHOCYTES AFTER FRACTIONATED IRRADIATION IN VITRO	356
I. Spasojević, B. Kukavica, J. Zakrzewska, G. Bačić 5-FLUOROURACIL INDUCED CARDIOTOXICITY. Changes in erythrocytes morphology or alternative explanation?	359
N. Mitić, G. Pavlović-Lažetić, M. Beljanski PALINDROME SEQUENCES IN VIRAL GENOMES	362
G. Pavlović-Lažetić, N. Mitić, M. Beljanski ANALYSIS OF SARS CORONAVIRUS GENOME POLYMORPHISM	365
M. Milošević, S. Petrović, A. Horvat EFFECTS OF METAL IONS ON ECTO-ATPase ACTIVITY IN PLASMA MEMBRANE ISOLATED FROM THE RAT OVARY	368
S. Petrović, M. Milošević, A. Horvat FLUX OF Ca ²⁺ IONS IN THE SYNAPTOSOMAL MITOCHONDRIAL MEMBRANE	371
A. Horvat, M. Milošević, S. Petrović, M. Demajo DIFFERENT SENSIBILITY OF ECTO-ATPase FROM BRAIN AND OVARY TO Cu ²⁺ AND Zn ²⁺	374
D. Božin DEHYDRATION: THE STRESS FOR BACTERIOPHAGE λ	377
S. Ostojić, M. Kićanović, M. Živić, S. Gorjanović, M. Pavlović THERMAL ANALYSIS OF WHEY LIPID-PROTEIN FRACTION	380
M. Pavlović EFFECT OF ULTRA-LOW DOSES OF INTERLEUKIN-2 ON HUMORAL IMMUNE RESPONSE ELICITED WITH ANTI-IDIOTYPIC ANTIBODY, MIMICKING COLON CARCINOMA -ASSOCIATED EPIPEPE CO17-1A	383
G. Bačić, R. Srejjć NON-EXCHANGEABLE WATER IN BIOLOGICAL SYSTEMS: AN NMR STUDY	386
S. Ostojić, M. Kićanović, B. R. Simonović Zn(II) BINDING ON BOVINE SERUM ALBUMIN FOLLOWED BY ITC	389

S. Ostojić, V. Dragutinović, B. R. Simonović INFLUENCE OF Zn(II) ON THERMAL UNFOLDING OF BOVINE SERUM ALBUMIN FOLLOWED BY DSC	392
M. Petrović, N. Ilić, Lj. Sofronić-Milosavljević ANTIBODY "OVERCHARGING " BY FLUOROCHROME DYE – FITC.	395
M. S. Jovanović, S. Vranješ, J. Brborić, S. Vladimirov, M. Orlić COMPARISON OF EXPERIMENTAL AND CALCULATION PROCEDURES FOR ESTIMATION OF LIPOPHILICITY: NEW IDA DERIVATIVES	398
D. Filipović, M. B. Radojčić SONOLYTIC DEGRADATION OF OVOMUCIN BASED PROTEIN MATRIX OF HEN EGG WHITE	401
B. M. Kolarić, B. J. Drakulić, I. O. Juranić FLUOROPHORE BASED ON (<i>E</i>)-4-ARYL-4-OXO-2-BUTENOIC ACIDS	404
N. Abazović, J. J. Čomor, M. I. Čomor PHOTOLYTIC DEGRADATION OF CHLORPYRIFOS INDUCED BY AN ARTIFICIAL LIGHT SOURCE	407
A. Leskovac, T. Momić, T. Janković, G. Joksić THE RADIOPROTECTIVE PROPERTIES OF POLYPHENOLS ON HUMAN LYMPHOCYTES	410
L. Korićanac, D. Todorović, N. Popović, A. Ristić-Fira CHANGES OF <i>c-myc</i> EXPRESSION IN B16 MELANOMA CELLS INDUCED BY 8- CHLOROADENOSINE-3', 5'-MONOPHOSPHATE AND TIAZOFURIN	413
F – Radiochemistry and Nuclear Chemistry	
G. Zakrzewska-Trznadel MEMBRANE METHODS FOR PROCESSING OF LIQUID RADIOACTIVE WASTE	419
I. Petrović, D. Todorović, L. Valastro, P. Cirrone, G. Cuttone, A. Ristić-Fira RADIOBIOLOGICAL STUDIES ON THE 62 MeV THERAPEUTIC PROTON BEAM AT LNS CATANIA: I. SURVIVAL OF HTB140 MELANOMA CELLS	426
A. Ristić-Fira, D. Todorović, L. Valastro, P. Cirrone, G. Cuttone, I. Petrović RADIOBIOLOGICAL STUDIES ON THE 62 MeV THERAPEUTIC PROTON BEAM AT LNS CATANIA: II. FACS ANALYSES OF HTB140 MELANOMA CELLS	429
T. Maksin, D. Janković, A. Đorđević HPLC ANALYSIS OF TECHNETIUM(I)-99m LABELLED C ₆₀ (OH) ₂₂	432
D. Đokić, D. Janković THE "ORGANOMETALLIC APPROACH" TO LABELLING OF AMINO ACIDS WITH [^{99m} Tc(CO) ₃ (H ₂ O) ₃] ⁺	435
S. Dragović, S. Stanković, A. Onjia COMPARISON OF TRAINING ALGORITHMS IN NEURAL NETWORK MODELING OF GAMMA SPECTROMETRIC UNCERTAINTY	438

M. Vučković, M. B. Radojčić GAMMA-RADIATION-INDUCED DAMAGE OF PROTEINS IN THE THICK FRACTION OF EGG WHITE	441
A. Nićiforović, M. B. Radojčić GAMMA-RADIATION-INDUCED DAMAGE OF CHICKEN MYOSIN AND ACTIN	444
G. Pantelić, M. B. Rajković, D. Tošković GAMMA SPECTROMETRIC ANALYSIS OF FUR	447
Lj. Lj. Stamenković, D. Đ. Đokić TRICARBONYL TECHNETIUM(I) COMPLEXES WITH DIFFERENT PHOSPHATE LIGANDS	450
M. A. Demajo, D. S. Đorđević, I. S. Đujić CALCIUM (Ca^{2+}) CONTENT IN THE LOWER JAWS OF RATS IRRADIATED IN THE HEAD REGION WITH X-RAYS	453
G – Materials Science	
B. Bonnetot, S. Jacques. CERAMIC MICROSTRUCTURE INDUCED BY MOLECULAR PRECURSORS. THE CASE OF BORON NITRIDE: ADAPTATION OF THE PRECURSOR TO THE BEST PROPERTIES FOR HIGH TECHNOLOGY APPLICATIONS.	459
T. M. Nenadović, M. T. Nenadović THE BASIS OF PHYSICAL CHEMISTRY, PROPERTIES OF TWO-DIMENSIONAL SOLIDS	467
B. Matović, A. Vučković, D. Bucevac, S. Bošković REACTIONS RESPONSIBLE FOR MASS LOSS DURING PRESSURE LESS SINTERING OF Si_3N_4 CERAMICS WITH LiYO_2 ADDITIVE	475
Z. Cherkezova-Zheleva, M. Shopska, B. Kunev, I. Mitov, G. Kadinov, L. Petrov SYNTHESIS AND PROPERTIES OF NANOSIZED Fe/TiO_2 AND FeM/TiO_2 ($\text{M}=\text{Pd}, \text{Pt}$) SYSTEMS. PART 1: PREPARATION AND PHASE ANALYSIS	478
M. Shopska, Z. Cherkezova-Zheleva, I. Shtereva, B. Kunev, G. Kadinov, I. Mitov, L. Petrov SYNTHESIS AND PROPERTIES OF NANOSIZED Fe/TiO_2 AND FeM/TiO_2 ($\text{M}=\text{Pd}, \text{Pt}$) SYSTEMS. PART 2: TEMPERATURE-PROGRAMMED REDUCTION AND CATALYTIC ACTIVITY IN BENZENE OXIDATION	481
J. Kuljanin, M. I. Čomor, V. Đoković SYNTHESIS AND CHARACTERIZATION OF POLYVINYL ALCOHOL / LEAD SULFIDE NANOCOMPOSITE	484
M. Radić, N. Ignjatović, D. Jugović, Z. Nedić, M. Mitrić, M. Miljković SYNTHESIS OF BCP AND BCP/PLGA BIOMATERIALS BY ULTRASONIC SPRAY PYROLYSIS	487
O. Kovačević, B. Kovačević, N. L. Lazić, Z. Filipović-Rojka, K. Andelković, Ž. Lj. Tešić LOW- TEMPERATURE SYNTHESIS OF SILICALITE-1 WITH PRECIPITATED SILICA AS RAW MATERIAL	490

N. Ignjatović, P. Ninkov, D. Krnojelac, D. Uskoković NEW BIOCOMPOSITE FILLER BIPHASIC CALCIUM PHOSPHATE/POLY-DL-LACTIDE-CO-GLYCOLIDE FOR RECONSTRUCTION OF HARD BONE TISSUE	493
A. Milutinović-Nikolić, S. Lukić, J. Krstić, Z. Vuković, M. Stanković COMPOSITES BASED ON BENTONITE CLAYS AND NONWOVEN TEXTILES	496
M. Stanković, B. Marković, A. Šučurović, D. Jovanović THE EFFECT OF SILVER CONTENT ON THE CIS-TRANS ISOMERIZATION SELECTIVITY DURING HYDROGENATION OF SOYBEAN OIL OVER SILVER-PROMOTED Ni/DIATOMOTE CATALYSTS	499
A. Maričić, D. Minić, B. Jordovic, M. M. Ristić THE INFLUENCE OF THE STRUCTURAL RELAXATION ON CHANGE OF FREE ELECTRON DENSITY OF Co ₇₀ Fe ₅ Si ₁₀ B ₁₅ AMORPHOUS ALLOY	502
S. Mentus, Z. Mojović, Z. Tešić ZEOLITE MODIFICATION BY INCORPORATION OF PALLADIUM CLUSTERS	505
M. Vučinić-Vasić, B. Antić, A. S. Nikolić, A. Kremenović, S. Rakić, J. Blanuša, N. Cvjetičanin, A. Kapor <i>IN SITU</i> XRPD AND DSC STUDY OF ORDER-DISORDER PHASE TRANSITION IN NANOSIZE Li-FERRITE	508
S. Zec, S. Bošković MECHANICALLY ACTIVATED CERIA	511
M. B. Tošić, V. D. Živanović, J. D. Nikolić, DTA STUDY OF THE PARTICLE SIZE EFFECT ON THE CRYSTALLIZATION MECHANISM OF SILICATE GLASS POWDER DOPED WITH FLUORINE ANIONS	514
S. Petrović, B. Gaković, M. Radović Z. Rakočević, T. Nenadović STRUCTURAL AND ELECTRICAL PROPERTIES OF TUNGSTEN - TITANIUM SPUTTERED COATINGS	517
Z. Vuković, A. Milutinović-Nikolić, J. Krstić, D. Jovanović, TEXTURAL PROPERTIES AND SURFACE FRACTAL DIMENSION OF ACID-ACTIVATED BENTONITE CLAYS	520
I. Stojković, D. Jugović, M. Mitrić, N. Pavlović, N. Cvjetičanin SYNTHESIS OF LiCr _x Mn _{2-x} O ₄ (x~0.18) BY GLYCINE-NITRATE METHOD	523
S. Marković, N. Cvjetičanin, M. Mitrić, D. Uskoković STRUCTURE AND DIELECTRIC CHARACTERISTICS OF BaTi _{1-x} Sn _x O ₃ CERAMIC POWDERS	526
B. Janković DETERMINATION OF KINETIC PARAMETERS FOR THERMAL DECOMPOSITION OF SODIUM BICARBONATE USING THE SINGLE-HEATING-RATE INTEGRAL METHODS	529
H – Solid State Physical Chemistry	
D. M. Todorović COUPLED PLASMA AND ELASTIC WAVES IN SEMICONDUCTOR	535

G. Postole, M. Caldaranu, M. Carata, C. Hornoiu, C. Munteanu , B. Grzybowska SURFACE CHARACTERISTICS OF OXIDE POWDERS STUDIED BY IN SITU ELECTRICAL CONDUCTIVITY MEASUREMENTS	538
G. A. Bogdanović, V. S. Jevtović, V. M. Leovac CRYSTAL AND ABSOLUTE STRUCTURE OF THE AQUADICHLORO(PYRIDOXAL THIOSEMICARBAZONE) IRON(III) CHLORIDE	541
N. Bošnjaković-Pavlović , N. E. Ghermani , A. Spasojević-de Biré , G. A. Bogdanović, U. Mioč CRYSTAL STRUCTURE REDETERMINATION AND ATOMIC CHARGES OF AMMONIUM DECAVANADATE HEXAHYDRATE BASED ON A LOW TEMPERATURE X-RAY EXPERIMENT	544
S. Marković, V. Dondur, R. Dimitrijević, S. Macura IR, NMR AND XRPD INVESTIGATION OF RINGS EVOLUTION IN ALUMINOSILICATE STRUCTURES	547
Z. Jakšić, M. Maksimović, D. Vasiljević-Radović AN EFFECTIVE MEDIUM APPROACH TO ANALYSIS OF NANOSCALE DISORDER IN PHOTONIC BANDGAP MATERIALS	550
M. Maksimović, Z. Jakšić OPTICAL TRANSMISSION OF PHASE-COMPENSATED 1D PHOTONIC CRYSTALS INCORPORATING NEGATIVE-INDEX MATERIAL AND AMPLIFYING MEDIUM	553
V. Rakić, Lj. Damjanović, V. Dondur, R. Dimitrijević ON THE TREATMENT OF FAU TYPE ZEOLITE BY CITRIC ACID AND AMMONIUM CITRATE	556
Z. Miladinović, J. Zakrzewska INFLUENCE OF SILICA SOURCE ON THE NaA ZEOLITE CRYSTALLIZATION	559
D. Vučinić, I. Miljanović, A. Rosić TWO METHODS FOR FLY ASH CONVERSION INTO NaP1 ZEOLITE	562
Z. S. Nikolić COMPUTER SIMULATION OF LIQUID PHASE SINTERING FOR POROUS STRUCTURE	565
Z. S. Nikolic, M. Yoshimura, S. Araki SIMULATION OF RAPID SOLIDIFICATION OF ALUMINA ON A METALLIC SUBSTRATE	568
Z. S. Nikolić 3-D SIMULATION OF REARRANGEMENT DURING LIQUID PHASE SINTERING	571
 I – Macromolecular Physical Chemistry	
S. I. Kuchanov THEORY OF GELATION IN POLYCONDENSATION PROCESSES	577
B. H. Milosavljević ANALYSIS OF THE SOLUBILITY BEHAVIOR OF IRRADIATED POLY(VINYL ALCOHOL-CO-ETHYLENE)	580

S. Lj. Tomić , T. M. Manić, J. M. Filipović SWELLING BEHAVIOR OF 2-HYDROXYETHYL METHACRYLATE BASED HYDROGELS	583
M. Miljković, M. Purenović, A. Zarubica USE OF REFLECTANCE SPECTROPHOTOMETRIC METHOD FOR THE DETERMINATION OF COLOUR OF ORGANIC COATING WITH TiO ₂ PIGMENT	586
M. B. Plavšić, I. Pajić-Lijaković, B. Bugarski SCALING OF POLYMER NANO -PARTICLE CLUSTERS AND ABILITY FOR HYDRODYNAMIC AGGREGATION	589
M. B. Plavšić, I. Pajić-Lijaković, B. Bugarski FLUCTUATION OF MASS AS MEASURE OF POLYMER CLUSTER LECUNARITY AND HYDRODYNAMIC PERMEABILITY	592
M. B. Plavšić, I. Pajić-Lijaković, Z. Todosijević, B. Bugarski STRUCTURAL FACTOR AND HYDRODYNAMIC PROPERTIES OF POLYMER PARTICLE CLUSTERS	595
S. Blagojević, M. Ilić CATIONIC POLYMERS AS RHEOLOGY MODIFIERS: PROPERTIES OF POLYGEL K-SERIES	598
A. B. Nastasović, Z. Vuković, T. Novaković THE CHARACTERIZATION OF POROUS STRUCTURE OF CHELATING POLY(GMA-CO-EGDMA) COPOLYMER	601
G. Ćirić-Marjanović, B. Marjanović UV-VISIBLE SPECTROSCOPICAL STUDY OF 1-AMINO-2-NAPHTHOL-4- SULFONIC ACID ELECTROPOLYMERIZATION	604
J. Budinski-Simendić, R. Ž. Radičević, M. Špirkova, K. Dušek , M. Ilavsky THE SYNTHESIS AND CHARACTERIZATION OF TELECHELIC DIISOCYANATES AS END-REACTIVE NETWORK PRECURSOR	607
R. Ž. Radičević, D. M. Stojković, J. K. Budinski-Simendić STUDY OF AUTOACCELERATION IN FREE RADICAL POLYMERIZATION OF STYRENE - EFFECT ON THE MOLECULAR WEIGHT DISTRIBUTION OF POLYSTYRENE	610
M. Kalagasidis-Krušić, J. Filipović HYDROGELS OF N-ISOPROPYLACRYLAMIDE, ACRYLAMIDE AND ITACONIC ACID	613
S. J. Veličković, Đ. Anđelkoski, M. Kalagasidis Krušić, I. G. Popović THE VISCOMETRIC INVESTIGATION OF POLY(ITACONIC ACID) IN SOLUTION	616
G. Ćirić-Marjanović, B. Marjanović, P. Holler OXIDATIVE CHEMICAL POLYMERIZATION OF <i>o</i> -TOLIDINE	619
J. Jovanović, B. Adnađević, V. Randelović, D. Uskoković INFLUENCE OF THE CROSS-LINK DENSITY ON THE SWELLING KINETICS OF PAA HYDROGELS IN WATER	622

G. S. Marković, M. Marinović-Cincović, B. Radovanović, H. Valentova, M. Ilavsky, J. Budinski-Simendić	625
PROPERTIES OF ELASTOMERIC MATERIALS BASED ON POLYCHLOROPRENE/ /CHLOROSULFONATED POLYETHYLENE RUBBER BLENDS	
J – Environmental Protection	
I. E. Sitaras, P. A. Siskos	631
PARTITION OF SEMIVOLATILE ORGANIC COMPOUNDS IN THE ATMOSPHERE OF ATHENS, GREECE	
J. Jekić, M. Grbavčić, Z. Stoimirović	637
POWER PLANT FLY ASH-SOURCE OF TRACE ELEMENTS IN AMBIENT AIR	
M. D. Tasić, Z. R. Mijić, S. F. Rajšić, D. S. Đorđević, D. J. Radmanović, V. T. Novaković, M. N. Tomašević	640
ATMOSPHERIC DEPOSITION OF HEAVY METALS IN BELGRADE URBAN AREA	
M. D. Tasić, Z. R. Mijić, S. F. Rajšić, V. T. Novaković, M. N. Tomašević	643
PARTICULATE MATTER MASS CONCENTRATIONS IN THE AMBIENT AIR OF BELGRADE	
P. Gburčik, D. Marković, V. Gburčik	646
ANALYSIS OF AIR POLLUTION AND WIND EPISODIC MEASUREMENTS IN KOSJERIC (Serbia)	
V. Radojčić, M. Nikolić, B. Adnađević, A. Jovanović	649
SELECTIVE REDUCTION OF PAH CONTENT IN CIGARETTE TOBACCO SMOKE BY CATALITIC CRACKING PROCES	
D. S. Đorđević, A. J. Mihajlidi-Zelić, D. J. Radmanović	652
CONTRIBUTION OF EMISSION SOURCES ON METALS CONTENT IN THE AIRBORNE PARTICLES USING PCA	
M. Miljković, M. Purenović, V. Mitić, A. Zarubica	655
NEW METHOD OF CATALYTIC REMOVAL OF ZINC FROM MODEL WATERY SOLUTIONS BY MICRO ALLOYED ALUMINIUM BASED COMPOSITE	
D. Grandić-Aleksić, N. Pavlović, D. Minić	658
CONTENTS DETERMINATION OF METAL IN COMBINED WATER SOLUTIONS USING EDXRF (SOFTWARE PACKAGE ESP)	
D. Grandić-Aleksić, N. Pavlović	661
CONTENTS DETERMINATION OF Mn, Fe, AND Ni IN WATER BY ENERGETIC DISPERSION X-RAY SPECTROMETER	
D. Golobočanin, A. Žujić, N. Miljević	664
CHEMICAL CHARACTERIZATION OF POTABLE MINERAL WATERS	
J. D. Joksić, M. B. Radenković	667
RADIONUCLIDES IN SOME SPRING MINERAL WATERS IN SERBIA	
A. Čučulović, S. Stanković, Š. S. Miljanić, D. Milivojević, D. Veselinović	670
THE EFFECT OF SIMULATED ACID RAIN ON ¹³⁷ Cs DESORPTION IN <i>CETRARIA</i> <i>ISLANDICA</i>	

M. A. Demajo, O. N. Jozanov-Stankov, I. S. Đujić LEVELS OF SELENIUM IN THE RAT PINEAL GLAND: THE EFFECTS OF SELENIUM SUPPLEMENTATION	673
D. Veselinović, D. Marković, A. Savin THE CORRELATION OF THE VALUES OF PLANT-AVAILABLE Cd IN THE SOIL AND AMOUNTS IN THE PLANT PARTS OF WHEAT	676
S. Ražić, S. Đogo, L. Slavković, A. Popović TRACE AND MINOR ELEMENTS DETERMINATION IN SOME HERBAL DRUGS BY FAAS	679
D. Jakovljević, M. M. Vrvic, M. Radulović, M. Hranisavljević-Jakovljević CONVERSION OF PULLULAN INTO KETO-ALDEHYDO POLYMER	682
S. Marinković, B. Simonović, D. Arandelović, A. Kostić-Pulek THE REACTIVITY OF FLY ASH OF INTEREST FOR ITS SOLIDIFICATION	685
T. Jovanović, A. Čosović, V. Adamović COPPER REMOVAL FROM CONTAMINATED WATER USING <i>MEDICAGO SATIVA</i>	688
V. Jovanović, V. Dondur, M. Damjanović, M. Tomašević-Čanović FENITROTHION - ADSORPTION AND DEGRADATION ON SYNTHETIC AND NATURAL ZEOLITE	691
K. Krinulović, V. Vasić, U. Černigoj, M. Franko PHOTOCHEMICAL DEGRADATION OF DIGOXIN TESTED BY NA,K-ATPase ACTIVITY	694
A. Topalov, S. Korom, D. Molnár-Gábor, M. Čomor EFFICIENCY OF IRON(III)OXIDE IN PHOTOCATALYTIC DEGRADATION OF THE FUNGICIDE METALAXYL	697
G. Cvijanović, N. Milošević, D. Cvijanović THE INFLUENCE OF BACTERIZATION OF MAIYE SEEDS IN FUNCTION OF ENVIRONMENT PROTECTION	700
M. B. Rajković, M. Stojanović APPLICATION OF FRACTIONAL EXTRACTION METHOD FOR DETERMINATION OF URANIUM ORIGIN IN BOILER FUR	703
M. D. Pavlović, Z. I. Filipović, S. B. Ostojić, M. Ž. Živić, S. Ž. Gorjanović, S. T. Hranisavljević, M. T. Dojčinović MINERAL CONTENT OF WHEY CONCENTRATES AND ISOLATES	706
Ž. Grbavčić, D. Ranković, Z. Arsenijević LOW CONCENTRATION VOLATILE ORGANIC POLLUTANTS REMOVAL IN COMBINED SORBENT/CATALYTIC REACTOR SYSTEM	709
M. Radenković, D. Todorović, J. Joksić MIGRATION OF DEPLETED URANIUM CONTAMINATION THROUGH THE SOIL	712
J. Krstić, S. Petrović, N. Vukelić INVESTIGATION OF HEAVY METALS IN ROAD DUST AND SOIL SAMPLES IN TOURIST AREA BUDVA	715

M.R. Ilić, S. Miletić SOLIDIFICATION/STABILIZATION AS A METHOD FOR HAZARDOUS WASTE TREATMENT	886
--	-----

K – Phase Boundaries

P. Bankovic, N. R. Demarquette, M. L. P. da Silva CHARACTERIZATION AND EFFICIENCY EVALUATION OF WATER SELECTIVE MEMBRANES WITH HYDROPHOBIC SURFACES	721
A. B. Nastasović, S. K. Milonjić, S. M. Jovanović ADSORPTION ISOTHERMS OF CHLOROFORM ON MACROPOROUS COPOLYMERS DETERMINED BY INVERSE GAS CHROMATOGRAPHY	724
A. Daković, M. Tomašević-Čanović, G. Rottinghaus, S. Matijašević, A. Radosavljević-Mihajlović ADSORPTION OF FUMONISIN B ₁ ON ORGANOZEOLITE	727
B. Adnađević, J. Jovanović INFLUENCE OF THE ENERGETIC HETEROGENEITY OF ADSORBENTS BASED ON SiO ₂ ON CHOLESTEROL ADSORPTION	730
M. Ilic, V. Pavelkić, S. Blagojević, S. Zlatanović, Z. Filipović-Rojka INTERACTION OF SODIUM DODECILSULPHATE (SDS) WITH CALCIUM BENTONITE: ADSORPTION ISOTHERMS	733
T. Stanić, J. Lemic, M. Đuričić INFLUENCE OF HEATING OF KAOLIN, BENTONITE AND ZEOLITE ON ADSORPTION PROPERTIES AND CEC	736
I. Smičiklas, A. Onjia, S. Raičević SORPTION OF Ni ²⁺ BY DIFFERENT SYNTHETIC HYDROXYAPATITE	739
Ž. N. Todorović, S. K. Milonjić DETERMINATION OF THE POINT OF ZERO CHARGE OF ALUMINA BY BATCH EQUILIBRATION METHOD	742
V. Kuntić, N. Pejić, B. Ivković¹, S. Mičić, Z. Vujić, D. Malešev RP-HPLC DETERMINATION OF RUTIN IN SOLID PHARMACEUTICAL DOSAGE FORMS	745
J. Vučina, D. Lukić, M. Stoilković, M. Milošević, M. Orlić SEPARATION OF RHENIUM(VII) FROM TUNGSTEN(VI)	748
M. Tomašević-Čanović, T. Stanić, A. Živanović, J. Lemic REMOVAL OF ARSENATE BY CATIONIC SURFACTANT AND IRON HYDROXIDE-LOADED NATURAL CLINOPTILOLITE	751

L – Complex Compounds

A. Papakyriakou, N. Katsaros STRUCTURAL STUDIES OF METAL ION COMPLEXES OF THE ANTICANCER DRUG BLEOMYCIN USING NMR IN COMBINATION WITH MOLECULAR DYNAMICS SIMULATIONS.	757
---	-----

D. N. Sredojević, M. K. Milčić, N. Juranić, S. D. Zarić, METAL LIGAND AROMATIC CATION- π INTERACTIONS IN CRYSTAL STRUCTURES OF COMPLEXES WITH ACETYLACETONATO LIGAND	760
V. B. Medaković, M. K. Milčić, S. D. Zarić C – H... π INTERACTIONS IN THE METAL-PORPHYRIN COMPLEXES WITH CHELATE RING AS THE H ACCEPTOR	763
M. K. Milčić, V. B. Medaković UNUSUAL CATION- π INTERACTION: CATION- π INTERACTION WITH CHELATE RING AS π -SYSTEM	766
Z. D. Tomić, S. Novaković, S. D. Zarić COMPARISON OF TWO VIEWS REGARDING THE NATURE OF THE X- H...PHENYL INTERACTION	769
A. A. Rakić, V. B. Medaković, Đ. Cvijović, ORIENTATION OF AXIALLY COORDINATED PYRIDINES IN CRYSTAL STRUCTURES OF PORPHYRINATO COMPLEXES	772
G. M. Nikolić, Lj. Ilić, M. Cakić, G. S. Nikolić, R. S. Nikolić, Ž. Mitić COPPER(II) COMPLEXES OF REDUCED LOW-MOLECULAR DEXTRAN: AN ESR STUDY	775
N. Nikolić, D. Veselinović, J. Vučina INFLUENCE OF MAGNETIC FIELD ON THE REDUCTION OF 4,8-DIAZA-3,6,9- TETRAMETHYL UNDECANE-3,8-DIENE-2,10-DIONE DIOXIME	778
S. B. Novaković, G. A. Bogdanović, V. M. Leovac THE SUPRAMOLECULAR ARRANGEMENT IN THE NI(II) COMPLEXES OF ISOTHIOSEMICARBAZIDE	781
G. N. Kaluđerović, V. M. Đinović, Z. Juranić, T. Stanojković, T. J. Sabo ACTIVITY OF SOME PLATINUM(II/IV) COMPLEXES WITH EDDA-TYPE LIGANDS AGAINST HeLa CELL LINE	784
Z. M. Miodragović, B. Krajčinić, S. Anđelić, I. Hodžić, Đ. U. Miodragović SYNTHESIS AND CHARACTERIZATION OF TWO NOVEL MIXED LIGAND COMPLEXES WITH N-CARBOBENZYLOXYGLYCINE AND 2,2'-BIPYRIDINE	787
Đ. U. Miodragović, B. Stojadinović, Z. M. Miodragović, I. Hodžić, M. Vitorović, K. Anđelković THE FIRST COMPLEXES WITH N-CARBOBENZYLOXY-L- PHENYLALANINATO LIGAND	790
D. Janković, D. Đokić HPLC AND SPECTROPHOTOMETRIC INVESTIGATION OF THE FORMATION OF Sn(II)-p-AMINOHIPURIC ACID COMPLEX IN PERCHLORATE MEDIUM	793
M. Cvijović, M. Kićanović, P. Đurđević THERMAL ANALYSIS OF ALUMINIUM-HISTIDINE COMPLEX	796
M. Antonijević-Nikolić, S. B. Tanasković, G. Vučković NEW Cu(II) AND Co(II) COMPLEXES WITH FULLY N-(2-PYRIDYLMETHYL) FUNCTIONALISED CYCLAM (tpmc) AND MULTIDONOR CARBOXYLATO LIGANDS	799

M. J. Lazić, K. K. Anđelković, D. M. Sladić, Ž. Lj. Tešić, S. S. Radulović INADEQUACY OF THE USE OF THE MTT-ASSAY IN THE EXAMINATION OF CYTOTOXIC ACTIVITY OF PLANAR PENTADENTATE LIGAND 2',2'''-(2,6- PYRIDINDIYLDIETHYLIDYNE) DIOXAMOHYDRAZIDE DIHYDRATE (H ₂ L·2H ₂ O) AND ITS COORDINATION METAL COMPLEXES	802
M. Cvijović, V. Pavelkić, N. Miljević, D. Stanisavljev, P. Đurđević SPECTROPHOTOMETRIC STUDY OF SOLUTION EQUILIBRIA BETWEEN Al ³⁺ ION AND L-HISTIDINE	805
S. O. Podunavac-Kuzmanović, G. S. Četković SYNTHESIS AND CHARACTERIZATION OF COBALT(II) AND ZINC(II) COMPLEXES WITH N-1-SUBSTITUTED 2-METHYLBENZIMIDAZOLES	808
S. O. Podunavac-Kuzmanović, Lj. S. Vojinović SYNTHESIS AND PHISICO-CHEMICAL PROPERTIES OF IRON(II), NICKEL(II) AND COPPER(II) COMPLEXES WITH 1-BENZOYL-2-AMINOBENZIMIDAZOLE	811
S. O. Podunavac-Kuzmanović, Lj. S. Vojinović COMPLEXES OF 1-(4-CHLOROBENZOYL)-2-AMINOBENZIMIDAZOLE WITH DIFFERENT METAL IONS	814
M – General Physical Chemistry	
G. Managadze, W. Brinckerhoff, A. Chumikov, N. Managadze THE SYNTHESIS OF ORGANIC MOLECULES IN A LASER PLASMA SIMILAR TO THE PLASMA THAT EMERGES IN HYPERVELOCITY COLLISIONS OF MATTER	819
R. Marković, A. Rašović, S. Jovetić INTRAMOLECULAR INTERACTIONS BETWEEN NON-BONDED ATOMS IN THIAZOLIDINE DERIVATIVES AND CHEMICAL REACTIVITY	826
M. Dugić DECOHERENCE: THE OCCURRENCE AND CONTROL	833
G. M. Nikolić, R. S. Nikolić, J. M. Perović DETERMINATION OF SETSCHENOW SALTING-OUT CON-STANTS OF CATECHOL BY LIQUID-LIQUID EXTRACTION	841
D. Jovanović, Đ. Cvijović SIMPLE UNBIASED ENERGY MINIMIZATION FOR LENNARD-JONES CLUSTERS	844
C. Matei, P. Marote, D. Berger, C. Nitulescu, F. Papa, J. P. Deloume PREDICTION OF MIXED OXIDES FORMATION IN MOLTEN ALKALINE NITRATE EUTECTIC	847
J. Brborić, M. Jovanović, S. Vladimirov DETERMINATION OF THE IONIZATION CONSTANTS OF 2,4-DIODO-6- METHYLPHENYL CARBAMOYLMETHYL IMINODIACETIC ACID	850

O. Čudina, K. Karljiković-Rajić, I. Ruvarac-Bugarčić, I. Janković DERIVATIVE SPECTROPHOTOMETRIC DETERMINATION OF PARTITION COEFFICIENT OF HYDROCHLOROTHIAZIDE BETWEEN CETYLTRIMETHYLAMMONIUM BROMIDE MICELLES AND WATER	853
G. N. Kaluderović, M. Dašić, T. Geđa, Z. Todorović, S. D. Petrović ANALYTICAL METHOD TRANSFER PROCESS IN PHYSICO-CHEMICAL LABORATORIES FOR TRIXIFEN SUGAR COATED TABLETS	856
V. Živković-Radovanović, G. Vučković SALTING-OUT THIN-LAYER CHROMATOGRAPHY (SOTLC) OF SOME AMINOCARBOXYLATO Co(III) COMPLEXES ON MODIFIED SILICA GEL	859
R. M. Jelić, Lj. G. Joksović, P. T. Đurđević POTENTIOMETRIC STUDY OF HYDROLYSIS OF ALUMINIUM(III) ION IN MICELLAR AND MIXED WATER-DIOXANE MEDIA	862
S. Sremac, Ž. Todorović, A. Popović, A. Onjia NEURAL NETWORK PREDICTION OF THE GAS CHROMATOGRAPHIC SEPARATION OF POLYCYCLIC AROMATIC HYDROCARBONS	865

N – Education

V. M. Petruševski, NOVEL EXPERIMENTS IN CHEMISTRY: METHODS TO DEMONSTRATE WHAT CANNOT BE DEMONSTRATED ORDINARILY	871
T. Halasi, R. Halasi ROSALIND E. FRANKLIN IN BELGRADE	878

Plenary Lectures

(PL)

QUANTUM DOTS: IMMOBILIZATION AND SURFACE CHEMISTRY STUDIES

R. M. Leblanc and K. M. Gattás-Asfura

*Department of Chemistry, University of Miami
Coral Gables, FL 33146 USA*

Abstract

Un-catalyzed photopolymerization of polyethylene glycol (PEG)-based hydrogels physically trapped cadmium chalcogenides nanoparticles with size-distribution within the quantum-confined regime. The layer-by-layer (LbL) technique made possible to deposit the quantum dots (QDs) onto solid substrates through electrostatic interaction. This immobilization technique could be utilized to prepare QDs-based platforms for fluorescence microscopy, monitoring systems, and optical sensing. Luminescence properties of the QDs were manipulated through surface chemistry for the fabrication of optical sensors to detect paraoxon, Cu^{2+} , and Ag^+ . Amino acid sequence design facilitated the synthesis of surfactants. Nature of surfactants influenced the organization of the nanocrystals in 2-D Langmuir films and solid substrates. Control over self-assembly of QDs could help to further enhance QDs-based optoelectronic devices.

Introduction

Semiconducting nanocrystals have been an area of intense research for the past few decades. The chemical and physical properties of these so-called quantum dots hold the key behind their success in the fields of chemistry, physics, biology, engineering, and materials science [1]. Significant advances have been made towards the preparation of high quality nanocrystals [2] enhancing their potentiality as photonic materials, dyes, and probes. Particle size, shape, material composition, and surface modification can all be utilized to modify the opto-electronic properties of QDs, which is of crucial importance for most QDs-based applications.

Recently, QDs have been incorporated within inorganic/organic hybrid systems demonstrating optical chemo- and biosensing capabilities including the detection of protein toxins [3], DNA hybridization [4], gases [5], and metallic ions [6] among others. These exciting results have demonstrated the potentiality of QDs within sensing devices. Surface passivation of trap states, inner filter effects, nonradiative recombination pathways, energy transfer, and electron transfer processes have been utilized as mechanisms for analyte-induced opto-electronic changes on QDs for signal transduction.

An eight-branched PEG macromer having a nitrocinnamate (NC) moiety as pendant group was utilized to study physical entrapment of QDs within the hydrogel network upon irradiation with UV-365 nm light [7]. To deposit QDs on solid substrates, electrostatic interactions and the LbL technique was investigated [8]. Surface modification of the QDs and incorporation of the nanocrystals within composite films

were utilized to fabricate optical sensors for the detection of paraoxon, Cu^{2+} , and Ag^+ [9]. Organization of the QDs at the air-water interface was also investigated.

Results and Discussion

Nanocrystalline QDs were effectively immobilized within the photo-cross-linked PEG hydrogel. The immobilization of 3.5-6.0 nm CdTe and 2.0-3.5 nm CdSe QDs within the PEG hydrogel network was shown to be effective through utilization of physical trapping. These QD-immobilized gel systems demonstrated luminescence characteristics unique to semiconductor nanocrystals. Controlled particle extraction from the PEG hydrogel matrix may be possible via a photocleavage process. Minimum by-product formation, hydrophilicity, biocompatibility, and non-toxicity of PEG-NC hydrogels make these systems an ideal medium for applications such as in fluoro-immunoassay, monitoring systems for drug delivery, and signal transducers and platforms for optical sensors.

LbL assembly was utilized to fabricate an ultrathin film of polyelectrolytes. The architecture was composed of chitosan and organophosphorus hydrolase polycations along with thioglycolic acid-capped CdSe QDs as the polyanion. The photoluminescence property of the functionalized QDs improved when sandwiched between the polycation layers. This enhanced optical property of QDs allowed easy monitoring of LbL film growth and detection of paraoxon with high sensitivity, nM levels. Organophosphorus compounds such as paraoxon are of environmental concern because of their related neurotoxicity.

Gly-His-Leu-Leu-Cys coated 2.4 nm CdS QDs detected Cu^{2+} and Ag^+ selectively with high sensitivity, below 0.5 mM. The two Leu residues and the Gly-His sequence imparted the selectivity properties to the QDs against other biological metallic ions. To differentiate between Cu^{2+} and Ag^+ , addition of Cl^- to Ag^+ containing solutions resulted in well-known insoluble and undetected AgCl. Surface loading of the peptide on the QDs was calculated to be 17:1 and when all surface peptides complexed with these ions, full quenching of photoluminescence occurred. Then, system sensitivity demonstrated an inverse relationship with QD concentration.

Trioctylphosphine oxide (TOPO) and 1-octadecanethiol (ODT) were utilized as surfactants to manipulate the 2D packing arrangement of CdSe QDs in Langmuir films. Self-assembly of the QDs at the air-water interface responded to nanocrystal size, mixed monolayers, and surface pressure. Surface pressure-area isotherms revealed that TOPO-capped QDs form close-packed monolayers, and that ODT-capped QDs undergo alkyl chains interdigitation. Corrugated and mixed film topographies were observed. Excess ODT molecules free in solution allowed self-assembly of 2.35 nm ODT-capped QDs into more homogeneous films.

Conclusion

Inorganic/organic hybrid networks and composite films have been successfully synthesized to immobilize QDs and enhance their applications as optical sensors. Surface modifications with peptides and specialized surfactant molecules allowed for selectivity and sensitive detection of bio-analytes as well as to manipulate the solubility prop-

erties of quantum dots for immobilization purposes. Manipulation of the 2D organization of QDs in Langmuir films could further enhance the fabrication of QDs-based optoelectronic devices.

References

- [1] Murphy, C. J. *J. Anal. Chem.*, 2002, 74, 520-526A.
- [2] Qu, L.; Peng, Z. A.; and Peng, X. *Nano Lett.*, 2001, 1(6), 333-337.
- [3] Goldman, E. R.; Balighian, E. D.; Mattoussi, H.; Kuno, M. K.; Mauro, J. M.; Tran, P. T.; and Anderson, G. P. *J. Am. Chem. Soc.*, 2002, 124, 6378-6382.
- [4] Wang, J.; Liu, G.; and Merkoc, A. *J. Am. Chem. Soc.* 2003, 125, 3214-3215.
- [5] Nazzal, A. Y.; Qu, L.; Peng, X.; and Xiao, M. *Nano Lett.*, 2003, 3(6), 819-822.
- [6] Chen, Y.; Rosenzweig, Z. *J. Anal. Chem.*, 2002, 74, 5132-5138.
- [7] Gattás-Asfura, K. M.; Zheng, Y.; Micic, M.; Snedaker, M. J.; Ji, X.; Sui, G.; Orbulescu, J.; Andreopoulos, F. M.; Wang, C.; and Leblanc, R. M. *J. Phys. Chem. B*, 2003, 107, 10464-10469.
- [8] Constantine, C. A.; Gattás-Asfura, K. M.; Mello, S. V.; Crespo, G.; Rastogi, V.; Cheng, T.-C.; DeFrank, J. J.; and Leblanc, R. M. *Langmuir*, 2003, 19, 9863-9867.
- [9] Gattás-Asfura, K. M. and Leblanc, R. M. *Chem. Commun.*, 2003, 2684-2685.

APPLICATION OF CHEMICAL KINETICS IN THE HETEROGENEOUS CATALYSIS STUDIES

L. A. Petrov

*Institute of Catalysis, Bulgarian Academy of Sciences,
acad. G. Bonchev Str. bl. 11, Sofia 1113, Bulgaria*

Introduction

The studies in the field of kinetics of heterogeneous catalytic reactions are an indispensable step of the theoretical and applied investigations on catalysis. They serve as fundamentals upon elucidation of the mechanism of the elementary act of a given heterogeneous reaction and they contribute essentially to the elucidation of the catalyst behavior in the course of its preparation, exploitation, regeneration. Therefore they serve as basis during modeling and selection of optimal catalysts and optimization of catalytic reactors. For these reasons the development of theory and practice in catalysis is inconceivable without unfolding extensive kinetic investigations.

Aims and Purposes of the Kinetics of the Heterogeneous Catalytic Reaction Studies

The tasks that face now the researchers in the field of catalytic reaction kinetics could be formulated as follows:

Kinetics and mechanism of important in theoretical aspect catalytic processes. These studies aim at assisting the development of theory in catalysis, the selection of new catalytic systems and catalysts, elucidation of the intimate mechanism of the catalytic act, the nature of the active site, the behavior of the catalyst - reagent system as a whole.

Creation of kinetic models of industrially important reactions. The kinetic models of catalytic processes are the basis, on which the modeling and the design of catalytic reactors is carried out. The transition from molecular scale to macro - scale during the practical realization of a given catalytic process is accomplished on this basis. That is why it is necessary that the mathematical model be able to reflect all essential aspects of the mechanism of the process.

Development of kinetic models of nonstationary catalytic processes. These models account for the following factors; the rates of the elementary chemical transformations, the rate of changing the composition and the activity of the catalyst, diffusion of the species, dissolved in the catalyst, transfer of reactants from one type of active sites to others. The interconnection between the catalytic properties and the catalytic parameters etc. The investigation of the dynamics of the catalytic process i.e. the evolution of the heterogeneous catalytic reactions is included in this set of tasks. It is on these results that the development of the studies on the dynamics and stability of the catalytic reactors is depending, which in their turn determine the optimal starting and operation conditions.

Development of the theory of kinetics. The investigations in this direction give

impetus to theoretical aspects of the kinetics, the methods of constructing kinetic models, the methods of evaluation of kinetic parameters and the mathematical problems, connected with it.

The elaboration of theoretically grounded methods for testing and controlling the catalytic activity and selectivity of the industrial catalysts. Due to the strongly specific effect of the catalysts it is not possible to propose universal methods for testing and controlling their catalytic activity and selectivity. These methods are individual for each catalytic system. For this reason the elaboration, unification and standardization of these methods has great importance for the correct selection and evaluation of the studied catalysts.

The kinetics of thermochemical processes, occurring during the preparation, exploitation and regeneration of the industrial catalysts. In the course of preparation, operation and regeneration of the catalysts a series of processes are proceeding in them, which lead to alteration of their properties. The good knowledge and control of this type of alteration may bring considerable improvement of the quality of the catalysts and optimization of the regime of their use.

Theory and automation of the experiment. Computer application. The experimental studies in the field of chemical kinetics consume a large volume of research work and they are expensive. They require especially high degree of experience in order to set the task correctly and to select the experimental design. The dynamic development of the industrial catalysis puts on the agenda the problem to increase essentially the rate of kinetic model construction. The solving of this problem is unthinkable without applying the achievements of the optimal experiment theory, the use of automated systems for carrying out the kinetic experiments and data acquisition on the basis of modern computers during all stages of obtaining and processing the experimental data.

Ensuring of laboratory and large scale tests of the catalytic properties of the obtained catalysts.

Industrial catalysts are performance chemicals. It should be offered on the market together with information about:

- (i) reaction kinetics and kinetic model;
- (ii) catalytic activity and selectivity;
- (iii) catalyst pre-treatment regimes;
- (iv) catalyst deactivation kinetics with respect to different catalytic poisons;
- (v) catalyst regeneration regimes;
- (vi) catalyst lifetime: stability, duration of operation, thermal stability;
- (vii) physico-mechanical properties: impact strength, abrasion ability, hardness, surface area;
- (viii) hydrodynamic characteristics of the catalyst grain and of the catalyst bed in the reactor, determined by size, shape, density and porosity of the catalyst grains;
- (ix) safety transition regimes in cases of industrial accident;
- (x) economy of the process.

Most of the data mentioned above can be obtained as a result of kinetic studies.

Steps of the Building of Kinetic Models

1. Formulation of the possible reaction mechanisms based on the information obtained from:

- 1.1. Literature
- 1.2. Adsorption measurements – physical and chemical
- 1.3. Kinetic experimental methods: variations of the reaction parameters must be as wide as possible at steady state and non-steady state conditions. The sequential experimental design may be used for obtaining the best experimental strategy.
- 1.4. Physical methods for catalyst characterization.
- 1.5. Chemical methods for catalyst characterization.

2. Deriving corresponding to the proposed reaction mechanisms kinetic steady state models by using different methods:

- 1.1. Method of Hougen-Watson
- 2.2. Method of Temkin for the Real adsorption layer
- 2.3. Method of Temkin for stationary heterogeneous complex catalytic reactions
- 2.4. Method of graph theory
- 2.5. Method of group theory
- 2.6. Any other available method

3. Estimation of the number of independent parameters for a given kinetic model.

The number of independent parameters in a given kinetic model is equal to the rank of the Jacobi matrix J .

$$J = \begin{vmatrix} \frac{\partial f^{(1)}(k, C)}{\partial k_1} & \dots & \frac{\partial f^{(1)}(k, C)}{\partial k_n} \\ \dots & \dots & \dots \\ \frac{\partial f^{(p)}(k, C)}{\partial k_1} & \dots & \frac{\partial f^{(p)}(k, C)}{\partial k_n} \end{vmatrix}$$

$f^{(p)}(k, C)$ - reaction rate equation for an independent reaction route, p – number of reaction routes, n – number of constants in the kinetic model. If in the kinetic model there are dependent parameters the inverse matrix of the Fisher information matrix

$$\hat{F} = \left\| J^T \cdot J \right\|^{-1}$$

does not exist. In this case it is impossible to perform the sequential experimental design.

4. Calculating the rates along the independent reaction routes.

$$r_i = \sum_{j=1}^{M_T} \left\| \mu_{ij} \right\|^T R_j$$

r_i – experimental reaction rate for the i^{th} reagent

R_j – transposed stoichiometric matrix of the independent reaction routes

5. Kinetic parameters estimation non linear programming methods

$$r_i^{(p)} = f^{(p)}(k_i, P_i)$$

with reparametrization of the rate constants proposed by Frank-Kamenetckii

$$k = k_0 \exp\left(\frac{-E}{RT}\right)$$

$$k = k'_0 \exp\left(\frac{-E}{R} \left(\frac{1}{T} - \frac{1}{T_{average}}\right)\right), \text{ where } k'_0 = k_0 \exp\left(\frac{-E}{RT_{average}}\right)$$

6. Criteria for minimization:

6.1. Sum of the squares of the deviations between experimental rate values and values predicted by a given kinetic model.

$$W_i = (r_i^{\text{exp}} - r_i^{\text{calc}}) \quad E = \sum_{i=1}^N W_i^2$$

N – number of experiments. r_i^{exp} and r_i^{calc} – experimental and calculated by

6.2. Sum of the squares of the relative errors

$$W_i = \left(\frac{r_i^{\text{exp}} - r_i^{\text{calc}}}{r_i^{\text{exp}}}\right) \quad E = \sum_{i=1}^N W_i^2$$

6.3. Sum of the modules of the deviations between experimental rate values and values predicted by a given kinetic model.

$$W_i = \left(\left| r_i^{\text{exp}} \right| - \left| r_i^{\text{calc}} \right| \right) \quad E = \sum_{i=1}^N W_i$$

6.4. Minimization of the maximal deviation between experimental rate values and values predicted by a given kinetic model.

$$W = \min \max \left(\left| r_i^{\text{exp}} \right| - \left| r_i^{\text{calc}} \right| \right) \quad E = W$$

For multiroute reactions we have

$$E = \sum_{q=1}^Q \sum_{i=1}^N (W_i^{(q)})^2$$

Q – number of stoichiometrically independent reaction routes

7. Statistical assessment of the best reaction models

Number of experiments N gives the degree of freedom of the experimental points. Number of constants “p” in the reaction rate model gives the degree of freedom of the model. N-p – residual degree of freedom is a criterion for the exactness of the model. If we repeat the same experiment several times we can established the preciseness of the experiment

$$\sum_{i=1}^M (r_i^{\text{exp}} - r_{\text{average}}^{\text{exp}})^2 \quad M - \text{number of experiments}$$

we can write

$$\sum_{i=1}^N (r_{\text{average}}^{\text{exp}} - r_i^{\text{exp}})^2 = \sum_{i=1}^N (r_i^{\text{calc}} - r_i^{\text{exp}})^2 - \sum_{i=1}^N (r_i^{\text{calc}} - r_{\text{average}}^{\text{exp}})^2$$

which, characterize the discrepancy between the model and experiment.

If we make m repetitions of every experiment at q experimental conditions. Then we will have (m-1)q degrees of freedom and the Lack of fit = N-p-q(m-1)

Elements of Kinetics of Complex Catalytic Reactions

From the point of view complexity of composition of reaction mixture and number of reactions taking place simultaneously, the catalytic processes under study can be divided on two groups:

The single route group consists of single reaction processes such as most of petrochemical processes (hydrogenation processes).

We shall call multiroute (complex) heterogeneous catalytic reaction a reaction system which consist of at least of two independent stoichiometric equations. The multiroute group consists of complex reaction processes such as oil processing processes (cracking, reforming, and hydrotreating), oxidation and isomerization processes.

The maximum number of linearly independent chemical reactions, M_T , in a complex reaction system is given by: $M_T = N - q$,

where N is the total number of reagents in the system, q is the rank of the atomic matrix of the reagents. The linearly independent chemical reactions create the so-called stoichiometric (thermodynamic) basis for the reaction system. All other chemical

processes in the system can be expressed as a linear combination of these basic reactions and do not add any additional information about the reacting system.

For every independent reaction should exist a single reagent named key component. By measuring the concentrations of key reagents we are able to calculate the concentrations of the all reagents present in the reaction mixture. The selection of the key components usually is made by the convenience from the point of view of the experimental measurement.

The set of elementary reactions that allows a qualitative and quantitative description of major characteristics of the process studied to be made, will be named the mechanism of chemical reaction.

The number of independent routes in a given system depends upon our knowledge about the studied process, complexity and structure of the proposed reaction mechanism. According to Horiuty's rule, the number of independent routes M_K in a complex reaction system is given by the expression:

$$M_K = S - L_{\text{tot}} + 1$$

This basis is named kinetic basis. It consists of the routes obtained from proposed reaction mechanism. Their number is different for different mechanisms and depends on the details of the mechanism.

The steady state regime of the proceeding of given chemical process can be realized only in open systems. The steady state regime means that all reaction parameters (concentrations of reagents and ISC, temperatures, partial and total pressure, reagents flow rate) should have constant values which do not change with time. This however does not mean that the parameters should have the same value at different points of the reaction space. At steady state regime we have

$$\sum F(c_j, X_K) = 0$$

which substantially to simplify the problem.

At steady state the reaction rates of all consecutive elementary steps should be approximately equal to each other and equal to the slowest one called limiting reaction step. For the each step we can write

$$r = \frac{r_1^+ - r_1^-}{\sigma_1} = \frac{r_2^+ - r_2^-}{\sigma_2} = \dots = \frac{r_s^+ - r_s^-}{\sigma_s} = \frac{r_L^+ - r_L^-}{\sigma_L}$$

where r_s^+, r_s^- are the reaction rates in the forward and reverse directions of the s^{th} elementary step, σ_s is the stoichiometric number of the s^{th} elementary steps. The stoichiometric numbers vary usually between 1 and 3.

Mass and Heat Transfer in the Kinetics of Heterogeneous Catalytic Reactions

Heterogeneous catalytic reactions are always connected with processes of mass and heat transfer. If these processes are fast enough they do not have any substantial influence on the proceeding of the catalytic processes. When, however, these processes are slow enough the situation becomes different. Under steady state conditions the rates of all consecutive steps should be equal to one another and equal to the slowest one. Since the diffusion steps are the slowest one, the overall reaction rate will be equal to

the rate of the diffusion. In this case, the overall reaction rate will not be connected with the reaction mechanism but will be determined by the rate of physical processes. It is clear that the processes of mass transfer can have a substantial effect on the proceeding of heterogeneous catalytic reactions. The following different regimes for proceeding of heterogeneous catalytic reaction may be observed:

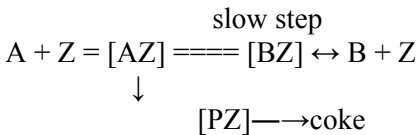
- Kinetic regime in which the intrinsic surface reactions are the slowest and determine the overall reaction rate;
- External diffusion regime in which the processes of mass transfer of the reagents and product of the reaction to and from the external catalyst surface are the slowest and determine the overall reaction rate;
- Internal diffusion regime in which the processes of mass transfer of the reagents and product of the reaction within the pores of catalyst particles are the slowest and determine the overall reaction rate;
- Transition regime in which both the chemical and mass transfer processes have approximately equal rates and the overall reaction rate is determined by the proceeding of the intrinsic surface reactions and diffusion.

Catalyst Deactivation

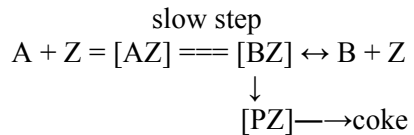
Types of Deactivation

1) Sintering; 2) Poisoning; 3) Changes of catalytic activity due to interactions with reagents: Strong and irreversible adsorption of some reagents; Interaction of reactants with catalytic centers; Induced diffusion of lattice components towards catalyst surface; Formation of coke precursors blocking the catalyst surface. The mechanisms of deactivation are generally two types:

Parallel deactivation



Consecutive deactivation



Kinetic description of deactivation Inseparable deactivation. Coke formation is inseparable part of the reaction mechanism and this process is described by special term in the kinetic equation parafine dehydrogenation

$$r = \frac{kP_1\sigma}{P_1 + k_1P_2 + k^*(c - c_0)}$$

P_1 - parafine; P_2 - reaction product; σ - reaction reversibility; c - coke concentration, c_0 - threshold coke concentration; k - rate constant; k_1 - olefine adsorption constant, k^* - rate constant of coke formation.

Separable deactivation Coke formation is described by rate model which is uncoupled from rate equation describing main reaction.

$$r = r_{kin}(k, P_i, T) \cdot (\phi_d(k_d, P_i, T))_\tau$$

$r_{kin}(k, P_i, T)$ - kinetic model of main reaction at constant catalyst activity;

$\phi_d(k_d, P_i, T)_\tau$ - kinetic model of the reaction of catalyst deactivation.

Diffusion effects in processes accompanied by catalyst deactivation

- (i) Changes in the reaction rate caused by diffusion restrictions;
- (ii) Diffusion modified deactivation caused by diffusion restrictions;
- (iii) Diffusion modified deactivation influence on the main reaction

Conclusions

The catalytic properties of a given catalyst with respect to its application in a certain industrial process are evaluated on the basis of the following criteria: (i) catalytic properties (catalytic activity and selectivity); (ii) chemical properties of the solid catalyst; (iii) surface properties of the solid catalyst; (iv) bulk properties of the solid catalytic material; (v) physical properties of the catalyst grain; (vi) mechanical properties of the catalyst grain, (vii) morphological properties of the catalyst grain. All these factors have strong impact on kinetic behaviour of the catalyst. Due to the complexity of the catalytic phenomena it is impossible to obtain sufficient and reliable information about reaction mechanism or catalyst structure and properties using any single method. In catalyst research practice it is a widely accepted approach that in order to attain deep insight into studied problem one should use as much modern methods as possible. In general the catalyst should be regarded as an inseparable part of the larger system consisting of the reaction medium and the catalyst itself. Heterogeneous catalysts are very complex systems with pre-programmed properties. Some of these properties do not depend very much on the conditions under which they were measured. However, in many cases the situation is different. During the course of catalyst operation in industrial reactors at high temperature and pressure, under the influence of the reaction media and other factors the catalyst structure, composition and properties are changing. In some cases these changes are small, but sometimes they are quite substantial. For this reason it is very important to obtain information about the occurring processes not only from static measurements before and after catalyst use but also to follow all processes in their continuous development in the course of the catalytic process by carrying out 'in situ' studies.

The progress of chemical industry depends on its attitude toward chemical science and interest in research work, while the good shape of science is determined by the fact how far it turns its face to the demand and prospects for developments in industry.

STUDY OF PROTEIN-ANESTHETIC INTERACTIONS BY NMR SPECTROSCOPY

J. Streiff¹, N. Juranić², D. O. Warner¹, K. A. Jones¹, W. J. Perkins¹,
and S. Macura²

*Departments of ¹Anesthesiology and ²Biochemistry and Molecular Biology, Mayo College of
Medicine, Mayo Clinic and Mayo Foundation, Rochester, MN, USA*

Abstract

Binding of volatile anesthetic to proteins is difficult to study because of low affinity and high off rates. We propose to use saturation transfer difference NMR spectroscopy to screen proteins for volatile anesthetic binding. Well-established method will enable the proteome screening on anesthetic binding and will provide detailed knowledge of the protein anesthetic interaction as an important step toward better understanding of anesthetic action.

Volatile Anesthetics and Proteins

Although anesthesia has been studied for more than 150 years, there is no general agreement on the mechanism of action or the putative target of anesthetics. However, there is strong evidence that anesthetics can affect protein function.

Evidence for direct volatile anesthetic interaction with proteins includes stereospecificity of the anesthetic effect [1], reduction of anesthetic effect by GABA receptor subunit knockout [2, 3], domain deletion [4] and site-directed mutagenesis [5-7]. Direct support for anesthetic-protein interactions include inhibition of firefly luciferase by a variety of anesthetic agents [8, 9] and demonstration of anesthetic binding to proteins and polypeptides [10].

Contrary to drugs that bind strongly to their targets, low affinity binding interactions, such as those with volatile anesthetics are difficult to characterize because of the high off rates of the ligands and the short lifetime of the complex. Thus they are challenging to probe with most existing methods.

NMR Methods to Study Weak Interactions

Nuclear magnetic resonance (NMR) spectroscopy is a well-established tool to study molecular structure and dynamics. Many NMR parameters can be used for probing complex formation, which elevates high resolution NMR spectroscopy into one of the most powerful methods in drug design [11].

Particularly useful for the study of weak interactions is the nuclear Overhauser effect (NOE) [12-14], which is the experimental manifestation of cross-relaxation. Cross-relaxation is the incoherent magnetization exchange among nuclear spins due to dipole-dipole interaction [15]. Cross-relaxation rate, σ , like overall relaxation rate, ρ , depends on the inter spin distance, r , correlation time of the motional process that

modulates dipole-dipole interaction, τ_c , and resonance frequency of the observed nuclei, ω_0 . For isolated pair of protons in a rigid body that tumbles isotropically, cross relaxation rates are [12, 14]:

$$\sigma_n = \frac{q}{r^6} \left(\frac{6}{1 + 4\omega_0^2 \tau_c^2} - 1 \right) \tau_c \quad (1)$$

$$\rho_n = \frac{q}{r^6} \left(1 + \frac{3}{1 + \omega_0^2 \tau_c^2} + \frac{6}{1 + 4\omega_0^2 \tau_c^2} \right) \tau_c \quad (2)$$

Subscript n denotes the laboratory frame relaxation rates and q is combination of universal constants: vacuum permittivity, μ_0 , reduced Plank's constant, \hbar , and proton gyromagnetic ratio, γ_H

$$q = \frac{1}{10} \left(\frac{\mu_0}{4\pi} \right)^2 \hbar^2 \gamma_H^4 \quad (3)$$

Cross-relaxation can be investigated either in a transient mode [12, 14] or in steady state mode [13]. Steady state NOE, η , is a ratio between cross-relaxation and overall relaxation rate:

$$\eta = \frac{\sigma_n}{\rho_n} \frac{1}{1 + f_{ex}} = \frac{5 + \omega_0^2 \tau_c^2 - 4\omega_0^4 \tau_c^4}{10 + 23\omega_0^2 \tau_c^2 + 4\omega_0^4 \tau_c^4} \frac{1}{1 + f_{ex}} \quad (4)$$

Parameter f_{ex} represents relative contribution of external relaxation sources. In diamagnetic systems, external relaxation is negligible, $f_{ex} \ll 1$. However, in paramagnetic systems external relaxation may prevail ($f_{ex} \gg 1$) and the steady state NOE can be quenched, $\eta \approx 0$. In double resonance method, NOE between the irradiated (selected) spin and all its neighbors can be probed in a single experiment. In two-dimensional NOE method (NOESY) complete cross-relaxation network can be mapped in a single experiment [14], which provided basis for determination of macromolecular structures in solution [16]. Due to versatility of the effect, many variants of the basic NOE experiment have been developed to probe various aspects of molecular structure and dynamics.

Saturation transfer difference (STD) is a double resonance, NOE based method developed to probe low affinity interactions ($K_d \approx 10^{-8} - 10^{-3}$ M) between small molecules and proteins [17] for the purpose of lead generation in drug discovery [18, 19]. In the STD technique, saturation transfer from the protein protons to the ligand protons identifies ligand binding to a protein. The saturation transfer takes place only to molecules bound to the protein with a rate that depends on the protein mobility, ligand/protein complex lifetime and geometry, and, when calibrated and repeated with different ligand concentrations, could be related to the binding constant. Because in high resolution spectroscopy the chemical shifts of small molecules are distinctive, several molecules can be screened for binding to a single protein simultaneously [17].

The goal of this work is to validate STD as a technique to study weak binding, i.e., to screen soluble proteins for binding interactions with anesthetics. We believe that the proteome screening on anesthetic binding is important step toward better understanding of anesthetic action.

Saturation Transfer Difference Spectroscopy

The STD NMR spectroscopy technique involves the comparison of the ^1H NMR spectra of a solution of protein and anesthetic(s) measured under on-resonance (I_{on}) and off-resonance (I_{off}) irradiation. In on-resonance irradiation only the magnetization of selected protons is affected (partially or completely saturated) but not the anesthetics or water. If the protein protons are irradiated on-resonance, their fast cross-relaxation with other protein protons (spin diffusion) [14] rapidly distributes spin saturation throughout the network of protein protons. Saturation further transfers to any bound molecule (anesthetics) that satisfies the condition that the effective correlation time (τ_{eff}), which is the combined complex lifetime (τ_B) and the protein tumbling correlation time (τ_C), is longer than the period of proton resonance frequency (ω_0):

$$\frac{1}{\tau_B} + \frac{1}{\tau_C} < \omega_0 \quad \text{or} \quad \frac{1}{\tau_{eff}} < \omega_0 \quad (5)$$

Off-resonance irradiation denotes that the sample is irradiated, with the same rf power and duration, far from resonance for the protein, anesthetic, or water protons. Selecting off-resonance frequency symmetrically with respect to the target resonance (free anesthetic) ensures that all other potential ways of saturating free anesthetic resonance without NOE (for example partial saturation by direct influence of the off-resonance rf power) are eliminated in a difference spectrum.

A difference spectrum (ΔI) is generated by subtracting the ^1H NMR spectra, on-resonance from off-resonance ($\Delta I = I_{off} - I_{on}$). Nuclear magnetization of the anesthetics that do not interact with the protein is unaffected by protein pre-irradiation ($\Delta I = 0$). Conversely, the nuclear magnetization of anesthetics that interact with the protein is partly saturated, which results in a reduction of peak integral intensity in on-resonance irradiation ($I_{off} > I_{on}$). The relative amount of saturation transferred to the anesthetic $\Delta I/I_{off}$, is the measure of the NOE on the anesthetic. The sign and the magnitude of the steady state NOE depend on the overall mobility and the structure of the complex. Models for analyzing cross-relaxation when motion is more complex have been in use [20] but for the screening purposes, a model of isotropic rigid body motion (Eqs 1-4) is adequate. Then, it is sufficient to substitute tumbling correlation time τ_C , in Eqs. 1-4 by effective correlation time τ_{eff} , from Eq.5. This model assumes that the mobility of the free ligand is much higher than the mobility of the complex ($\tau_{free} \ll \tau_C$) and that the complex is rigid, with life time τ_B .

The rotational correlation time of the protein anesthetic complex, τ_c , increases with the size of the protein. For complexes with either short rotational correlation times or

lifetimes, such that $\omega\tau_{eff} \ll 1$, the NOE will result in an increase in the area of NMR peaks of saturated molecules (positive NOE $I_{off} < I_{on}$). For complexes with long correlation times, such that $\omega_0\tau_{eff} \gg 1$, the NOE will result in a decrease in the area of NMR peaks of saturated molecules (negative NOE, $I_{off} > I_{on}$). In between, the NOE is a continuous function that passes through zero when $\tau_{eff} \approx \sqrt{5}/2\omega_0$. This occurs at τ_{eff} of approximately 360 ps for a Larmor frequency of 500 MHz Eqs. 1,4. Folded proteins have $\tau_c > 1$ ns so it is the direct transfer of saturation from a protein to an anesthetic through a binding interaction which leads to a decrease in the area of anesthetic NMR peaks. For example, bovine serum albumin (BSA) has $\tau_c = 42$ ns [21]. Thus, the interaction of anesthetics with proteins result in a decrease in the areas of the anesthetic NMR peaks in the on-resonance spectra ($I_{off} > I_{on}$) only when $\omega_0\tau_B > 1$. This means that at resonance frequency of 500 MHz the life time limit of the anesthetic/protein complex is around 300 ps; shorter living complexes will not be detected by the STD method. Thus, the only criterion on anesthetic binding in the NOE type experiments is an effective correlation time, i.e., average lifetime of the complex.

Results

Figure 1 shows representative set of STD spectra on BSA with 1.4 mM halothane recorded at 22°C. Panel A shows a series of ^1H NMR spectra collected at t_{sat} between 0.1 – 12 s with rf radiation tuned off-resonance (15 ppm). Panel B shows the spectra recorded at the same power level and t_{sat} , but with rf on-resonance for the protein, but not the anesthetic (0.4 ppm). The difference spectra (A-B) are shown in panel C. Obviously, in the difference spectra the intensity (more exactly the integral) of the anesthetic line increases with the irradiation time, approaching the steady state value for longest times. The steady state NOE (NOE at $t_{sat} \rightarrow \infty$) is proportional to the lifetime of the complex and the number of bound anesthetic molecules. Assuming that all bound molecules have the same average residence time on the protein, the steady state NOE can be used to estimate the binding constant.

Discussion

The STD finding that volatile anesthetics bind to BSA agrees with other methods [10, 22]. The STD technique could prove to be a robust method to screen for anesthetic-protein interactions. Nonexchangeable protons are abundant in proteins some being always nearby anesthetic binding site. In proteins, the saturation of one set of protons rapidly spreads to all the protons through spin diffusion. The spin diffusion is general phenomenon in macromolecules, which ensures that the saturation spreads among all macromolecule protons including temporarily bound ligand protons. Thus, STD should be able to identify anesthetic binding to protein sites, regardless of the local sequence or structure. Though this study is confined to soluble proteins, STD could be

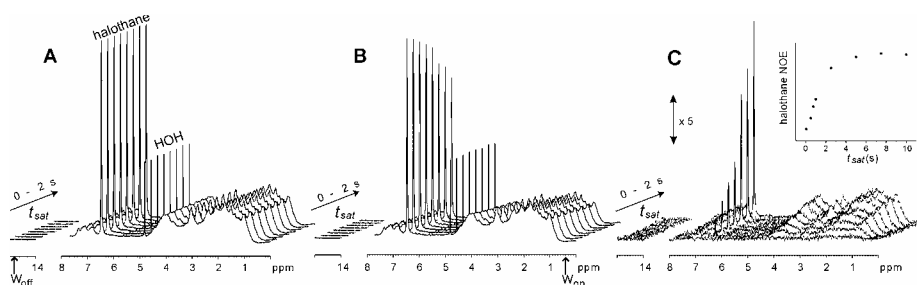


Figure 1. Generation of STD spectra in a solution of BSA and 1.4 mM halothane: **A** Spectra collected with off-resonance irradiation with t_{sat} 0.1-12 s. Constant peak area indicates that the system is not affected by irradiation. **B** Spectra of the same sample with rf irradiation on-resonance to BSA. The area of the halothane and BSA, peaks decreases with increasing t_{sat} due to increasing saturation transfer. **C** Difference of the spectra in panels A and B generates STD spectrum. Insert in panel C shows STD build-up curve.

even more efficient to screen for anesthetic interactions with proteins in lipid environments. Namely, spin-diffusion rate increases with the size of the complex.

In this work we are focused on using STD as fast and direct method for screening proteins for anesthetics binding. We have shown that STD has a potential to screen proteins for anesthetic interaction. A detailed account on the application of the STD spectroscopy to different anesthetic/protein combinations will be published elsewhere [23].

References

- [1] B. Harris, E. Moody, P. Skolnick, *European Journal of Pharmacology*. 1992, 217, 215.
- [2] J. J. Quinlan, G. E. Homanics, L. L. Firestone, *Anesthesiology*. 1998, 88, 775.
- [3] S. D. Ugarte, G. E. Homanics, L. L. Firestone, D. L. Hammond, *Neuroscience*. 2000, 95, 795.
- [4] J. J. Quinlan, L. L. Firestone, G. E. Homanics, *Pharmacology, Biochemistry & Behavior*. 2000, 66, 371.
- [5] D. Belelli, M. Pistis, J. A. Peters, J. J. Lambert, *Neurochemistry International*. 1999, 34, 447.
- [6] B. X. Carlson, A. C. Engblom, U. Kristiansen, A. Schousboe, R. W. Olsen, *Mol. Pharmacol*. 2000, 57, 474.
- [7] Q. L. Zhou, Q. Zhou, S. A. Forman, *Biochemistry*. 2000, 39, 14920.
- [8] S. Curry, W. R. Lieb, N. P. Franks, *Biochemistry* 1990, 29, 4641.
- [9] G. W. Moss, S. Curry, N. P. Franks, W. R. Lieb, *Biochemistry* 1991, 30, 10551.
- [10] R. G. Eckenhoff, H. Shuman, *Anesthesiology* 1993, 79, 96.
- [11] O. Zerbe, *BioNMR in Drug Research*, Wiley-VCH, Weinheim, 2003.
- [12] I. Solomon, *Phys.Rev.* 1955, 99, 559.
- [13] J. H. Noggle, R. E. Schirmer, *The nuclear overhauser effect Chemical applications*, Academic Press, New York, 1971.
- [14] S. Macura, R. R. Ernst, *Mol. Phys.* 1980, 41, 95.
- [15] S. Macura, Y. Huang, D. Suter, R. R. Ernst, *J. Magn. Reson.* 1981, 43, 259.

-
- [16] K. Wüthrich, *NMR of Proteins and Nucleic Acids*, 1 ed., John Wiley & Sons, New York, 1986.
- [17] M. Mayer, B. Meyer, *Angew. Chem. Int. Ed. Engl.* 1999, 38, 1784.
- [18] J. W. Peng, C. A. Lepre, J. Fejzo, N. Abdul-Manan, J. M. Moore, *Methods Enzymol.*, 2001, 338, 202.
- [19] B. J. Stockman, C. Dalvit, *Prog. NMR. Spec.*, 2002, 41, 187.
- [20] B. T. Farmer, II, S. Macura, L. R. Brown, *J. Magn. Reson.*, 1988, 80, 1.
- [21] S. Kiihne, R. G. Bryant, *Biophys. J.* 2000, 78, 2163.
- [22] B. W. Dubois, A. S. Evers, *Biochemistry*, 1992, 31, 7069.
- [23] J. H. Streiff, N. Juranic, S. Macura, D. O. Warner, W. J. Perkins, *Mol. Pharmacol.*, 2004, in press.

THEORETICAL STUDIES ON DIOXOMOLYBDENUM(VI) COMPLEXES AS OXYGEN ATOM TRANSFER (OAT) CATALYSTS

M. B. Hall and L. M. Pérez

Department of Chemistry, Texas A&M University, College Station, TX 77843-3255, U. S. A.

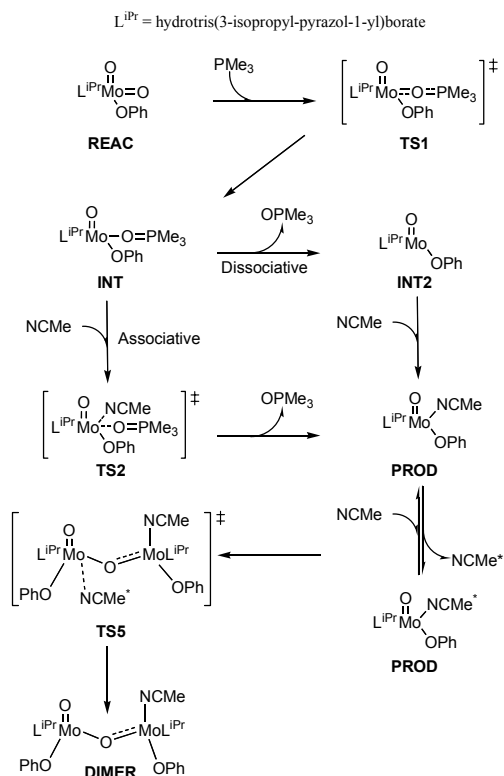
Introduction

Molybdenum oxotransferase enzymes catalyze the transfer of an oxygen atom to and from a biological substrate [1]. These enzymes contain a similar molybdenum center and it has been found that in the active site molybdenum is surrounded by one or two dithiolene-pterin derivatives called molybdopterin, zero, one or two terminal oxo groups, and/or a terminal sulfur group. Studies of the enzymatic reaction show that in the catalytic cycle molybdenum cycles among VI, IV and V oxidation states [1-2].

Analog reaction systems can be used to verify experimental data on the structure and reaction mechanism of complex molybdenum enzyme system. There have been several model systems that have been studied both experimentally and theoretically [3-7].

With the use of the bulky ligand, hydrotris(3,5-dimethyl-1-pyrazolyl)borate anion, Xiao *et al.* was able to synthesize a model system that can complete the catalytic cycle of an oxotransferase [8-9]. Simple model systems were studied theoretically to characterize the catalytic cycle of the experimental model [6-7]. These calculations show that there is an associative mechanism for the oxo transfer step, and that the calculated energies for the complete catalytic cycle are progressively exothermic.

In another molybdoenzyme model system, an intermediate, $[\text{MoO}(\text{OPh})(\text{OPET}_3)\text{L}^{\text{iPr}}]$ ($\text{L}^{\text{iPr}} = \text{hydrotris}(3\text{-isopropylpyrazol-1-yl})\text{borate}$), in the oxygen atom transfer reaction was isolated [10] and structurally characterized with x-ray crystallography, in agreement with the theoretically predicted intermediate [6-7]. Interestingly it was found that the O-Mo-O-P torsion angle was 57.5° , while in the calculation of the model systems



it was calculated to be close to 0° . In order to resolve this calculations on an improved model system, $[\text{MoO}(\text{OPh})(\text{OPMe}_3)\text{L}]$ ($\text{L} = \text{hydrotris}(1\text{-pylpyrazol})\text{borate}$), were performed [11]. In the improved model, the calculated O-Mo-O-P torsion angle was calculated to be 71.0° , in much better agreement with the experimental value. In this work, we describe a theoretical investigation of the formation and the decomposition of the intermediate ($[\text{MoO}(\text{OPh})(\text{OPEt}_3)\text{L}^{\text{iPr}}]$) via an associative or dissociative path as shown in Scheme 1.

Theoretical Details

The theoretical model system used in this work consists of the full $\text{L}^{\text{iPr}}\text{MoO}_2(\text{OPh})$ reactant and PMe_3 as a model substrate rather than PEt_3 as used in the experiments. The geometries of all structures for the theoretical model system were fully optimized by the B3LYP [12] DFT [13] method as implemented in Gaussian 98 or Gaussian 03 [14]. Analytical harmonic frequencies have been calculated for all stationary points to confirm the nature of these points, for the zero point energies, and for the thermodynamic properties. Solvation corrections in acetonitrile were performed by the Polarizable Continuum Model (PCM) method [15] as implemented in Gaussian 03. The results reported in this work have been obtained with a standard valence double- ζ quality basis set (D95V) [16] for B, C, N, O, and H. A small core ECP [17] was used for Mo (1s2s2p3s3d) with a double- ζ quality basis set that includes the outer 5p function developed by Couty and Hall [18]. An ECP (1s2s2p) with a double- ζ quality basis set (LANL2DZ) [19] was used for P, and to properly describe the hypervalent character of P, a polarization function with an exponent of 0.340 was added [20].

Results and Discussion

Calculated structures. Calculations have been performed on stable species and transition states that are involved in the oxygen atom transfer (OAT) reaction and in the replacement of the phosphine oxide by the acetonitrile solvent. The optimized geometries of the species in this reaction are shown in Figure 1.

The comparison of the geometrical data of the calculated $\text{L}^{\text{iPr}}\text{MoO}_2(\text{OPh})$ reactant (REAC, Figure 1), with crystallographic data [21] for $[\text{L}_a\text{MoO}_2(\text{SPh})]$, where L_a is hydrotris(3,5-dimethylpyrazol-1-yl)-borate anion are in good agreement. The optimized Mo-O bond lengths (1.75 Å) are slightly longer than the experimental values (1.70 Å). The optimized Mo-N bond lengths (2.34 Å, 2.21 Å) are also slightly longer than the experimental ones (2.30 Å, 2.17 Å), while the optimized O-Mo-O angle (103.7°) is similar to the experimental angle (102.6°). In agreement with the experimental results, the Mo-N bonds trans to the strongly bonded oxo groups are longer by 0.13 Å, than the Mo-N bond trans to the more weakly bound OPh group.

The optimized geometry of the transition state (TS1, Figure 1), for the attack of PMe_3 on the reactant $\text{L}^{\text{iPr}}\text{MoO}_2(\text{OPh})$ shows bond lengths that are intermediate between those in reactant (REAC) and those in the $\text{L}^{\text{iPr}}\text{MoO}(\text{OPMe}_3)(\text{OPh})$ intermediate (INT). The Mo-O bond under attack (1.83 Å) is slightly longer than that in the reactant (1.75 Å) but shorter than that in the intermediate (2.21 Å). The O2-P bond is beginning

to form in the transition state but is significant longer in the transition state (2.15 Å) than it is in the intermediate (1.58 Å). In terms of these distances, TS1 would be an early transition state. In our optimized structure for TS1, the torsion angle O-Mo-O-P is -79.6°. This value is in good agreement with previous theoretical work, [22] that suggested an angle near $\pm 90^\circ$ was necessary in order to occupy the correct Mo d orbital in the $2e^-$ reduction from the Mo(VI) to Mo(IV) that occurs on OAT. The calculated vibrational frequencies of the completely optimized transition-state geometry show one imaginary frequency ($194i \text{ cm}^{-1}$) with a motion appropriate for this transition state.

Usually, the attack of the M=O bond by a substrate is thought of as the attack of a nucleophile (the substrate) on the π^* M-O orbital forcing a $2e^-$ reduction of the metal center. Ultimately, of course, this is the result; however, the metal based oxygen may also act as a nucleophile and attack an empty orbital on the substrate. The surprisingly large O-P-C_{Me} angle (153°) suggest that some of this "role reversal" is taking place in TS1. If the attack of OPMe₃ on the Mo=O bond only involved the P lone pair attacking the Mo-O π^* , one would expect the 3-fold axis of OPMe₃ to be aligned with the axis of attack, P→O. This alignment would produce an O-P-C_{Me} angle of $\sim 115^\circ$. On the other hand, if the O were the nucleophile and it attacked the P through the P-C_{Me} σ^* orbital, the P would become a hypervalent trigonal bipyramid (surrounded by 5 electron pairs) with its own lone pair in an equatorial TBP site. In this alternative extreme the O-P-C_{Me} angle would be 180° . Thus, the calculated angle of 153° , which is nearly halfway between the two extremes, suggests an intermediate situation with nearly equal mixtures of the two types of nucleophile attack. As the system proceeds to the intermediate, the O-P-C_{Me} angle decreases to that expected for OPMe₃.

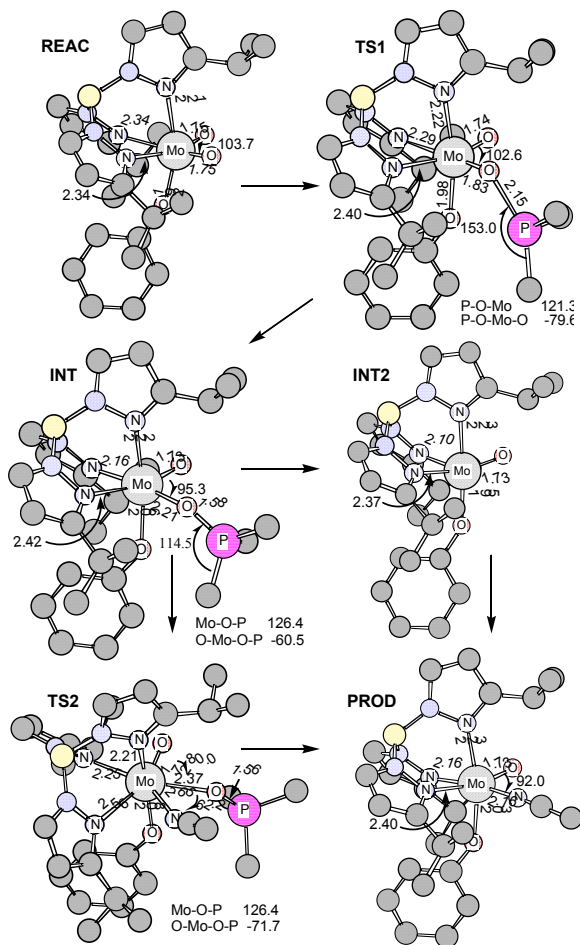


Figure 1

Our calculated $L^{iPr}MoO(OPMe_3)(OPh)$ intermediate structure (INT, Figure 1), has a fully formed O-P bond and a weak Mo-OPMe₃ dative bond (2.21 Å). In this structure the differences in the strength of the three Mo-O bonds can be seen in the trans influence on the Mo-N bonds. The calculated bond lengths are in good agreement with the experimental values [23] for the $L^{iPr}MoO(OPEt_3)(OPh)$ structure, the "spectator" Mo-O bond has the largest error, but the shortening from that in REAC is correctly predicted. The Mo-O-P angle (126.4°) is similar to the experimental value of 132.4°. The calculated O-Mo-O-P dihedral angle is -60.5°, in good agreement the observed values of -57.5°.

The next step in the oxo-transfer reaction, after the formation of the intermediate, is the substitution of phosphine oxide with a molecule of solvent (acetonitrile in this case). There are two possible "ideal" mechanisms: a dissociative mechanism where OPMe₃ leaves before acetonitrile (MeCN) enters; and an associative mechanism where acetonitrile binds to the intermediate (INT) before OPMe₃ leaves. For the former one expects a 5-coordinate intermediate while for the latter one expects a 7-coordinate intermediate. Of course, exchange pathways which are intermediate between these "ideal" situation are common. In an exchange pathway the 7-coordinate species would be expected to be a transition state with the degree of attachment of the exchanging ligands being a measure of the associative or dissociative character. In order to examine both possible pathways, we calculated the five coordinate $L^{iPr}MoO(OPh)$ intermediate (INT2), that one expects in the dissociative mechanism and a 7-coordinate species (TS2) corresponding to an associative exchange mechanism. The structures are shown in Figure 1. The square pyramidal, five-coordinated $L^{iPr}MoO(OPh)$ intermediate (INT2) has a vacant coordination site trans to one of pyrazol nitrogens, and this Mo-N bond is now even shorter (2.10 Å) than it was in the intermediate.

In the pathway for the associative mechanism no 7-coordinate intermediate was found but a 7-coordinate transition state (TS2) for exchange of OPMe₃ with MeCN was found. In the optimized geometry of TS2 there is one imaginary frequency (64i cm⁻¹) corresponding to the vibration that breaks (makes) the Mo-OP bond and makes (breaks) the Mo-NC bond. The Mo-OP bond is longer (2.37 Å) and the O-P bond is shorter (1.56 Å) than those in the intermediate. The Mo-NC bond is longer (2.65 Å) than that of the product (PROD) where MeCN is fully coordinated. In this 7-coordinate TS2 the weakest Mo-N (pyrazol) bond, trans to oxo ligand becomes even longer (2.56 Å).

In the structure of the acetonitrile substituted product (PROD, Figure 1), the Mo-NC bond is completely formed with a Mo-NC bond length of 2.16 Å. The Mo-N bond length trans to MeCN is similar to that in the intermediate. This similarity in trans influence of OPMe₃ and MeCN suggest similarities in their Mo-ligand bond strength.

Calculated Energies. The reaction energies in Table 1 and Figure 2 are all relative to the energy of the reactant (REAC) plus the energy of both PMe₃ and MeCN. Gas phase enthalpies and free-energies, and solvation corrected free-energies

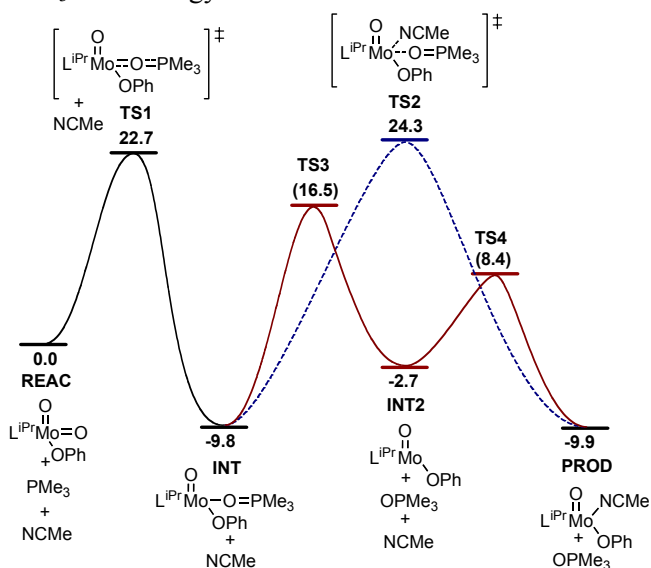
for acetonitrile are given in Table 1. Figure 2 shows the free-energy profile for the predictions in acetonitrile. The PMe_3 substrate reacts by crossing the transition state, TS1, to form the intermediate, INT. For TS1, the B3LYP gas-phase enthalpic barrier (ΔH^\ddagger) is 9.0 kcal/mol. Gas-phase corrections for the loss in entropy on forming this transition state produce a free-energy barrier (ΔG^\ddagger) of 20.4 kcal/mol. Solvation corrections increase the free-energy barrier ($\Delta G^\ddagger_{\text{solv}}(\text{MeCN})$) to 22.7 kcal/mol. Additional corrections for the reduction in entropy due to restricted motion of the separated species in solution were not made. The enthalpy of formation (ΔH°) of INT is -21.6 kcal/mol [24]. Even the free-energy, $\Delta G^\ddagger_{\text{solv}}(\text{MeCN})$, where entropy disfavors its formation, is favorable at -9.8 kcal/mol. Thus, the intermediate (INT) is quite stable.

Table 1

	ΔH°	ΔG°	$\Delta G^\circ_{\text{solv}}(\text{NCMe})$
REAC	0.00	0.00	0.00
TS1	8.98	20.43	22.71
INT	-21.57	-9.08	-9.80
TS2	-3.07	20.25	24.26
(TS3)		(17.20)	(16.47)
INT2	4.70	3.21	-2.73
(TS4)		(14.71)	(8.40)
PROD	-13.59	-3.58	-9.89

Energies for the replacement of the OPMe_3 ligand in INT by acetonitrile were determined for both a dissociative and associative path. The barrier for the dissociative path was taken to be the dissociation energy of the OPMe_3 . The enthalpic differences corresponds to a Mo- OPMe_3 bond energy of 26.3 kcal/mol. In this dissociative

reaction there is a gain in the free energy from the increased entropy of having two species. However, this increase in entropy only occurs after most of the enthalpic barrier is achieved. Thus, in comparing the free-energy barriers for the associative and dissociative mechanisms, the free-energy of the dissociative intermediate species (INT2) cannot be used. Thus, the maximum free-energy barrier for the dissociative route corresponds to the en-

**Figure 2**

thalpic barrier of 26.3 kcal/mol. After formation of INT2, acetonitrile must overcome an entropic barrier to coordinate to INT2 and form the product (PROD). In this “forward” reaction we assume that the full entropic barrier is encountered before the enthalpic stabilization from the formation of the new Mo-NCMe bond reduces the energy to that of the product. For these estimated dissociative transition states, TS3 and TS4, the solvation corrections corresponds to that for INT and PROD, respectively.

On the associative path, TS2 has an enthalpic barrier (from the intermediate, INT) of 24.6 kcal/mol. Gas-phase entropic corrections and solvent corrections produce a free-energy barrier ($\Delta G_{\text{solv}}^{\ddagger}(\text{MeCN})$) of 24.3 kcal/mol, a barrier that is ~ 7 kcal/mol higher than that for the dissociative path.

The enthalpic data (uncorrected for solvent) suggest that the Mo-OPMe₃ bond is ~ 8 kcal/mol stronger than the Mo-NCMe bond. However, the large dipole moment of OPMe₃ leads to a large solvation correction favoring the replacement of the phosphine oxide by acetonitrile, an overall reaction which is now favored by 0.1 kcal/mol. The high concentration of acetonitrile further favors formation of this substituted product (PROD).

Conclusion

The calculations predict the structure of an intermediate in good agreement with experiments. For the replacement of the phosphine oxide by solvent (acetonitrile) the calculations predict that the dissociative path will be favored over the associative one by ~ 7 kcal/mol in acetonitrile. The free-energy barrier for the reaction of phosphine to form the phosphine oxide complex (INT) is ~ 4 kcal/mol smaller than the barrier for the replacement of the phosphine oxide by acetonitrile. Thus, the latter step should be rate determining.

References

- [1] a) R. H. Holm, *Coord. Chem. Rev.* 1990, 110, 183. b) J. H. Enemark, C. G. Young, *Adv. Inorg. Chem.* 1993, 40, 1. c) R. Hille, *Chem. Rev.* 1996, 96, 2757.
- [2] H.-K. Li, C. Temple, K. V. Rajagopalan, H. Schindelin, *J. Am. Chem. Soc.* 2000, 122, 7673.
- [3] M. L. Thomson, M. B. Hall, *J. Am. Chem. Soc.* 2001, 123, 3995.
- [4] A. Thapper, R. J. Deeth, E. Nordlander, *Inorg. Chem.* 1999, 38, 1015.
- [5] C. E. Webster, M. B. Hall, *J. Am. Chem. Soc.* 2001, 123, 5820.
- [6] M. A. Pietsch, M. B. Hall, *Inorg. Chem.* 1996, 35, 1273.
- [7] S. Zaric, M. B. Hall, “Molecular Modeling and Dynamics of Bioinorganic Systems”, Kluwer Academic Publishers, 1997, 255.
- [8] Z. Xiao, C. G. Young, J. H. Enemark, A. G. Wedd, *J. Am. Chem. Soc.* 1992, 114, 9194.
- [9] Z. Xiao, A. M. Bruck, J. H. Enemark, C. G. Young, A. G. Wedd, *Inorg. Chem.* 1996, 35, 7508.
- [10] P. D. Smith, A. J. Millar, C. G. Young, A. Ghosh, P. Basu, *J. Am. Chem. Soc.* 2000, 122, 9298.
- [11] A. Zmiric, S. D. Zaric, *Inorg. Chem. Commun.* 2002, 5, 446.
- [12] A. D. Becke, *J. Chem. Phys.* 98, 5648 (1993). C. Lee, W. Yang, and R. G. Parr, *Phys. Rev. B*, 1988, 37, 785.

- [13] R.G. Parr and W. Yang Density-functional theory of atoms and molecules Oxford Univ. Press, Oxford, 1989.
- [14] Gaussian 98 Revision A11 Gaussian 03, Revision B5, M. J. Frisch, G. W. Trucks, H. B. Schlegel, G. E. Scuseria, M. A. Robb, J. R. Cheeseman, J. A. Montgomery, Jr., T. Vreven, K. N. Kudin, J. C. Burant, J. M. Millam, S. S. Iyengar, J. Tomasi, V. Barone, B. Mennucci, M. Cossi, G. Scalmani, N. Rega, G. A. Petersson, H. Nakatsuji, M. Hada, M. Ehara, K. Toyota, R. Fukuda, J. Hasegawa, M. Ishida, T. Nakajima, Y. Honda, O. Kitao, H. Nakai, M. Klene, X. Li, J. E. Knox, H. P. Hratchian, J. B. Cross, C. Adamo, J. Jaramillo, R. Gomperts, R. E. Stratmann, O. Yazyev, A. J. Austin, R. Cammi, C. Pomelli, J. W. Ochterski, P. Y. Ayala, K. Morokuma, G. A. Voth, P. Salvador, J. J. Dannenberg, V. G. Zakrzewski, S. Dapprich, A. D. Daniels, M. C. Strain, O. Farkas, D. K. Malick, A. D. Rabuck, K. Raghavachari, J. B. Foresman, J. V. Ortiz, Q. Cui, A. G. Baboul, S. Clifford, J. Cioslowski, B. B. Stefanov, G. Liu, A. Liashenko, P. Piskorz, I. Komaromi, R. L. Martin, D. J. Fox, T. Keith, M. A. Al-Laham, C. Y. Peng, A. Nanayakkara, M. Challacombe, P. M. W. Gill, B. Johnson, W. Chen, M. W. Wong, C. Gonzalez, and J. A. Pople, Gaussian, Inc., Pittsburgh PA, 2003.
- [15] M. Cossi, N. Rega, G. Scalmani, and V. Barone, *J. Chem. Phys.*, 2002, 117, 43.
- [16] T. H. Dunning Jr. and P. J. Hay, in *Modern Theoretical Chemistry*, Ed. H. F. Schaefer III, Vol. 3, Plenum, New York, 1976, 1-28.
- [17] P. J. Hay and W. R. Wadt, *J. Chem. Phys.*, 1985, 82, 299.
- [18] M. Couty and M.B. Hall, *J. Comp. Chem.*, 1996, 17, 1359.
- [19] P. J. Hay and W. R. Wadt, *J. Chem. Phys.*, 1985, 82, 270.
- [20] S. Huzinaga, *Gaussian Basis Sets for Molecular Calculations*, Elsevier, Amsterdam, 1984.
- [21] Z. Xiao, M. A. Bruck, C. Doyle, J. H. Enemark, C. Grittini, R. W. Gable, A. G. Wedd, and C. G. Young, *Inorg. Chem.*, 1995, 34, 5950.
- [22] M.A. Pietsch and M.B. Hall, *Inorg. Chem.*, 1996, 35, 1273.
- [23] P.D. Smith, A.J. Millar, C.G. Young, A. Ghosh, P.J. Basu, *J. Am. Chem. Soc.*, 2000, 122, 9298.
- [24] We also calculated triplet state for five-coordinated intermediate in the dissociative path. The geometry of this state is trigonal bipyramidal. The calculations predict this structure to be a few kcal/mol more stable than singlet. However, it is known that B3LYP method overestimates the stability of triplet states). Furthermore, no indication of any contribution by a triplet state was observed in the experiments. Thus, we believe that triplet is less stable than singlet and hence, it is not important in this reaction.

PERSISTENT ORGANIC POLLUTANTS A THREAT TO THE GLOBAL ENVIRONMENT AND TO HUMAN HEALTH

A. A. Jensen

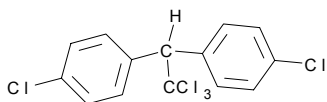
Force Technology, Søborg Gladsaxe Møllevej 15, DK-2860 Søborg, Denmark

Introduction

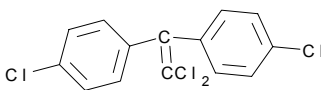
Persistent organic pollutants (POPs) are lipophilic chemical substances that persist long in the environment and in living organisms, bioaccumulate and biomagnify through the food webs, and pose a risk of causing adverse effects to human health and the environment. With the evidence of long-range transport of these substances to regions, where they have never been used or produced, and the consequent threats they pose to the environment of the whole globe, the international community has called for urgent global actions to reduce and eliminate releases of these chemicals. On May 23 2001 92 countries and the European Union signed the Stockholm Convention on Persistent Organic Pollutants. The Convention entered into force officially on May 17 2004, after 50 states had ratified. UNEP Chemicals in Geneva is the secretariat. Website: www.pops.int.

Persistent Organic Pollutants

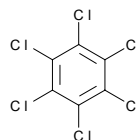
In the UNEP POP Convention 12 chemicals/chemical groups are on the list of POPs, which need immediate global action, a virtual phase-out. These are 9 chlorinated pesticides: *Aldrin*, *Chlordane*, *Dieldrin*, *DDT*, *Endrin*, *Hexachlorobenzene*, *Mirex*, *Toxaphene* and *Heptachlor*. Some formulas:



DDT

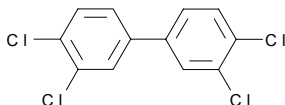


DDE

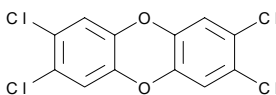


Hexachlorobenzene

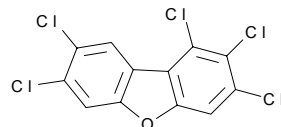
In addition, the phase-out list consists of the industrial chemical *PCBs* and the unintended pollutants *chlorinated dibenzo-p-dioxins* and *dibenzofurans* (*PCDD/F*) called “dioxins”



3,3',4,4'-Tetrachlorobiphenyl



2,3,7,8-Tetrachlorodibenzo-p-dioxin



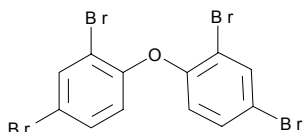
1,2,3,7,8-Pentachlorodibenzofuran

There are in total 210 different members of the dioxin family called congeners. Specifically the 17 dioxins with 2,3,7,8-chlorine substitution are the most toxic and bioac-

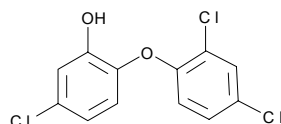
cumulating and most abundant in animal and humans. The most toxic is 2,3,7,8-tetrachlorodibenzo-*p*-dioxin (TCDD) or the Seveso-dioxin. In order to aggregate the results for the various congeners in a sample and get a total dioxin content, some international systems for calculating dioxin toxicity equivalence (TEQ) have been developed. All these systems are based on a relative ranking system giving the congeners toxicity equivalence factors (TEF) with TCDD assigned the factor 1. The newest system (WHO-TEF) was recommended by a WHO Working Group.

More chemicals and chemical families are candidates for the UNEP list, for instances polybrominated diphenyl ethers (PBDEs) and perfluorooctane sulfonate (PFOS).

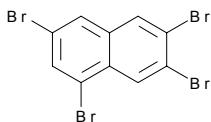
Some selected chemical formulas:



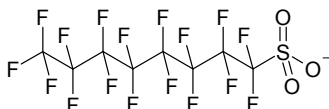
2,2',4,4'-Tetrabromodiphenyl ether (PBDE-47)



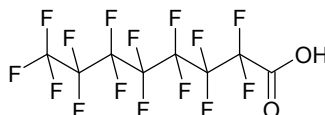
Triclosan



1,3,6,7-Tetrabromonaphthalene



Perfluorooctane sulfonate, PFOS



Perfluorooctanoic acid, PFOA

Criteria for POPs

UNEP expert groups have developed various criteria for persistent organic pollutants:

(a) *Potential for long-range transboundary atmospheric transport:*

There is evidence for that, if the substance has a vapour pressure below 1,000 Pa and an atmospheric half-life greater than two days. Alternatively, monitoring data showing that the substance is found in remote regions can be used; and

(b) *Toxicity:*

Potential to adversely affect human health and/or the environment; and

(c) *Persistence:*

If there is evidence that the substance's half-life in water is greater than two months, or that its half-life in soils is greater than six months, or that its half-life in sediments is greater than six months. Alternatively, evidence that the substance is otherwise sufficiently persistent to be of concern within the scope of the protocol; and

(d) *Bioaccumulation:*

- (i) Evidence that the bioconcentration factor (BCF) or the bioaccumulation factor (BAF) for the substance is greater than 5,000, or the octanol-water partition coefficient ($\text{Log}K_{ow}$) is greater than 5; or
- (ii) Alternatively, if the bioaccumulative potential is significantly lower than (i) above, and other factors, such as the high toxicity of the substance, that make it of concern within the scope of the protocol.

Global Distribution

These persistent organic pollutants are all chemicals, which commercial usage has lasted less than about 50 years. The long environmental residence time means a potential for global distribution by sea currents, contaminated fishes and long-range air transportation to areas where these chemicals have never been used.

A possible mechanism is the so-called “grass-hopping”, where in the northern hemisphere POPs are transported from warmer south to the colder north in “jumps” – evaporation/transport/deposition.

The situation is that POPs are now widespread globally and even contaminate remote arctic environments and populations. The levels are generally low but the consequences unclear. In some instances health impacts have been discovered.

Accumulation of POPs in Human Tissues

Nowadays, everybody has POPs in their body from birth and will keep that contamination their whole life. This was not well known and was probably difficult to realise for common people, before it in November 2003 was announced by the European Commission that an investigation had shown that 77 persistent chemicals contaminated the blood of Environment Commissioner Margot Wallström.¹ This was further underlined in April 2004, when it was announced by WWF that the blood of 39 members of the European Parliament was contaminated by 76 similar chemicals.²

The situation has arisen gradually in the last 50 years. In the beginning we were not aware of the problem, it was first when the analytical methods became sensitive enough. For instance, dioxin congeners were not possible to determine 25 years ago. Regulations have restricted some of the well-known POPs, for instance PCB, and the contamination by them has topped and is slowly decreasing. However, the contamination by other chemicals continues to rise.

POPs are lipophilic and accumulate mainly in body fats. At constant exposure “steady state” equilibrium will develop in the body resulting in about the same concentration of the POPs in all tissues calculated on lipid weight. It is illustrated in Figure 1:

¹ Press release, EU Commission 6 November 2003. Presence of persistent chemicals in the human body results of Commissioner Wallstrom’s blood test. <http://europa.eu.int>

² Press Release, WWF Newsroom 21 April 2004. European parliamentarians contaminated by 76 chemicals. <http://www.panda.org>

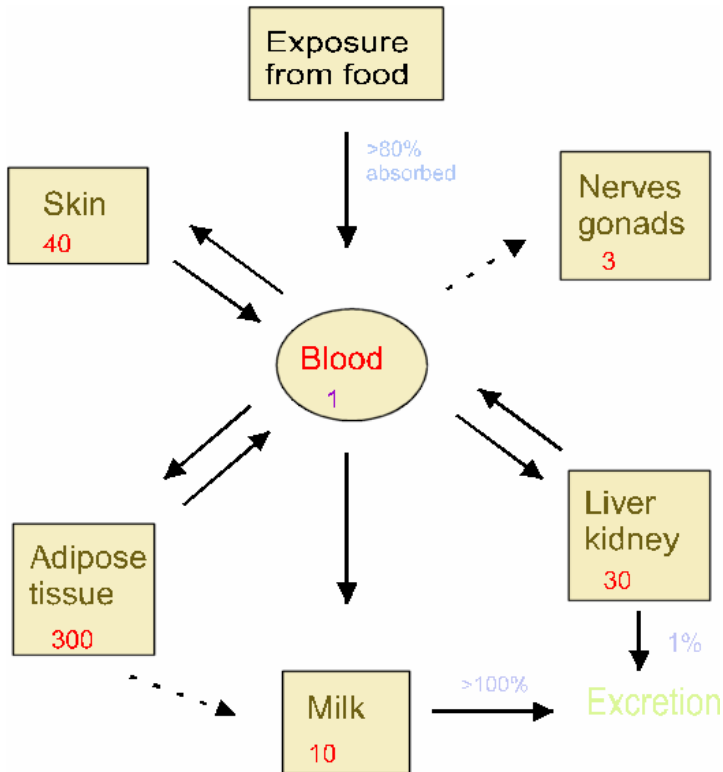


Figure 1. Simplified model of pathways of POPs in lactating women (after Jensen and Slorach 1991).

The human exposure to POPs is mainly from fatty food intake. The chemicals are well absorbed in the gut and distributed to the blood, where the chemicals are bound to lipoproteins. The blood delivers chemicals to the various organs and adipose tissue. The approx 300 times higher fat content of the latter means high potential for storage away a large amount of POPs and in that way decrease the concentrations in the blood and in important internal organs. Monkeys do have less fat deposits than humans and are more susceptible to the adverse effects of POPs.

Pregnancy will redistribute body fats and food deprivation and lactation will mobilize the fat depots and the contaminants herein and because the fats are degraded/consumed rapidly the concentration of POPS in the blood will increase. The metabolism and excretion of POPs with the faeces and urine are very insignificant but during lactation parts of the body accumulated in the previous years will be released and excreted with the breast milk. That is the explanation why POP levels in adipose tissues from adult females in general are lower than in adult males.

Human Milk Studies

Human milk studies can be used as a monitoring instrument/indicator of the general pollution level, geographical differences and trends of POPs. It may help discovering new pollution sources and high-exposure risk groups. Breast milk is a biological monitoring item with many advantages. The sampling is rather easy compared with e.g. adipose tissue. Not but not last human milk studies are essential for evaluating infant intake of POPs and possible adverse effects.

There are many factors to consider, when assessing human milk studies. The levels may depend on the mothers' age, parity, origin, residence, food habits, occupation etc. Further, the levels depend on the sampling time in lactation and sampling time during the day. Milk from milk banks are often lower in fat and in contaminants therein but that pooled milk from many individual mothers may be more useful for studying time trends and geographical differences. The analytical methods applied may also be important to consider, when comparing result from different laboratories. Differences in extraction solvents and in fat determination and quantification methods may result in very different results.

Trends in Human Milk Levels

For more than 30 years a Swedish research group has analysed DDT, DDE and PCB in human milk from a milk bank in Stockholm. These unique results are shown in Figure 2 (after: Norén and Meironyte 2000):

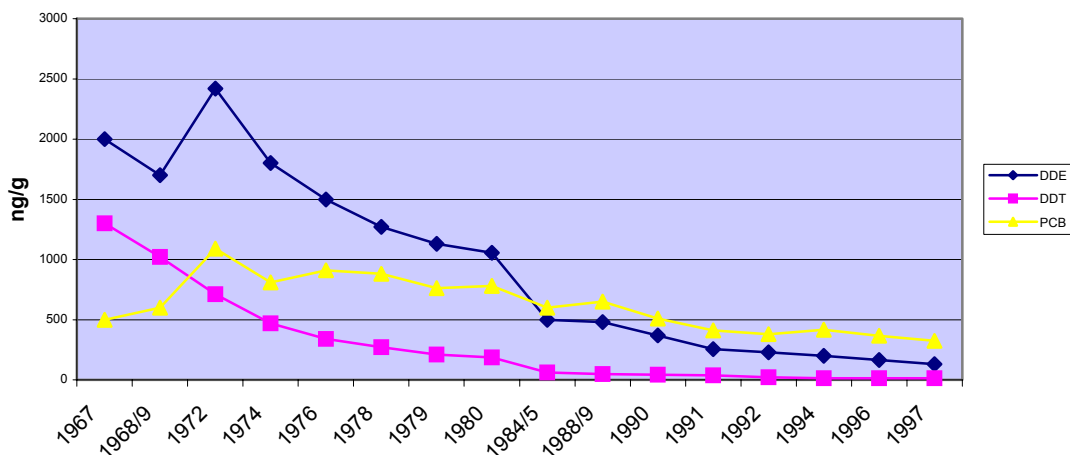


Figure 2. Thirty Years trends of DDE, DDT and PCB in human milk from a milk bank in Stockholm

The common use of DDT was banned in Sweden in the sixties, and the levels of DDT and DDE in human milk have declined dramatically during the years, while the decrease of PCB has only been moderate. There are still many diffuse pollution sources although the PCB use has stopped. The situation concerning DDT will be different in

the many developing countries, where DDT is still in use for fighting malaria, and for PCB in the Arctic, where highly contaminated sea mammals are major food sources.

The situation concerning dioxin levels in Sweden is quite similar as for PCB. A small decrease in concentration is seen. Unfortunately, levels of some brominated flame-retardants, another type of POPs used for instance in electronics, show the opposite trend. Figure 3 shows the sharp increase of polybrominated diphenylethers (PBDEs) in human milk with a doubling in 5 years until recently. A decrease is now seen because of the early restrictions in Sweden. The levels in humans in the USA, UK and other countries continue to increase.

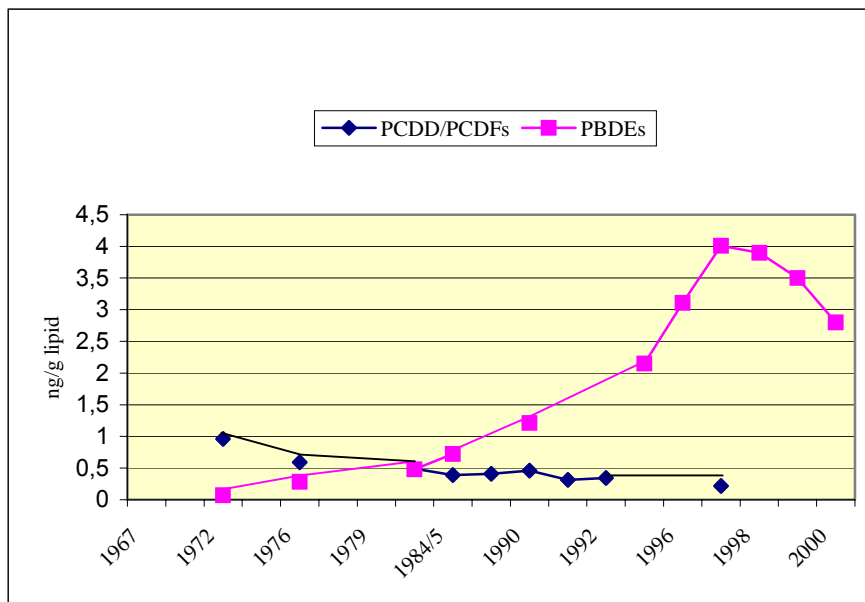


Figure 3: Trend of dioxins and PBDEs in human milk from Stockholm (after: Norén and Meironyte 2000)

Human Intakes of PCB and Dioxins

The typical daily adult intake of PCB in industrialised countries can be estimated to 0.1-0.2 $\mu\text{g}/\text{kg}$ body weights. This is much less than the tolerable daily intake (TDI) of 3 μg PCB/kg body weight. However, the typical daily infant intakes by breast-feeding are 2-4 $\mu\text{g}/\text{kg}$ body weight or around the TDI for adults but higher than the in-official TDI for infants of 1 $\mu\text{g}/\text{kg}$ body weight.

For dioxins and furans the adult daily intake is typical around 0.6 pg I-TEQ /kg body weight without fish eating, 1 pg/kg body weight with normal fish intake and 15 pg/kg body weight with a heavy fish intake. If co-planar-PCBs are included the daily intake without fish could be as high as 2-6 pg I-TEQ/kg body weight. This is more than the tolerable daily intake of 1 pg WHO-TEQ/kg body weight. Breast-fed infants have a 20-50 times higher intake or 70 pg/kg body weight without and 150 pg/kg body

weight with co-planar PCBs. Thus, if any group in our society is at risk from the adverse effects of dioxins, it has to be breast-fed infants. There are also investigations from the US, Canada, Germany, Slovakia and the Netherlands, which indicate subtle adverse effects on the development.

Dioxin in the Baltic Sea

The Baltic Sea is the largest brackish sea area in the World and has great variations in salinity, climate, flora and fauna from The Bothnian Bay and Bothnian Sea in North, The Gulf of Finland, Baltic Proper and the southern part of the Baltic Sea. Some large rivers flow into the shallow Baltic Sea with an average depth of 60 m and maximal depth of 459 m. The narrow Danish sounds and belts limit the water exchange, and a total exchange is estimated to take 20-25 years.

Dioxins have a very low solubility in water. The average level in the Baltic Sea water was 2,8 fg/L (ng/m^3) with 2,3,4,7,8-PeCDD as the most WHO-TEQ contributing congener. Thus dioxins (and PCBs) will concentrate in the sediments, where half-lives of dioxin congeners have been estimated to between 20 and 275 years in the Baltic. Nevertheless, by time some small amounts of dioxin will be released from these enormous reservoirs and be biological available in the food webs.

Investigations of dioxin in surface sediments are available from Danish, Swedish, Finnish and German areas. The concentrations of dioxins are typically 500-1500 ng (PCDD+PCDF)/kg dry weight. The highly chlorinated congeners and less water soluble, including OCDD and OCDF, dominate, and most dioxin in sediment samples are not 2,3,7,8-substituted, thus as toxic equivalents levels only correspond to 10-30 ng TEQ/kg dry weight. In the neighbourhood of point sources such as pulp industries and vinyl chloride plants dioxin concentrations in sediments may be ten to hundred times higher. In addition, coplanar PCBs contribute with 1-2 ng TEQ dry weight, or 3-20% of the total TEQ. Figure 4 shows an overview of the sediment dioxin data from the Baltic Sea.

Dioxin Levels in Baltic Fish

The biodiversity of the Baltic Sea is relatively low. There is only a limited number of fish species. Most abundant and economically important is Baltic herring and salmon. Herring and salmon are fatty fish, which also contains most dioxin. The degree of contamination varies geographically, yearly and with the season (highest in the spring), fat content, size and age. The main WHO-TEQ contributing congener of dioxin in Baltic herring is 2,3,4,7,8-PeCDF.

If the purpose of a study is environmental monitoring, results are mostly given on fat basis, and if the purpose is food control, results are given as fresh weight data. When applying risk assessment of dioxin it is necessary to include the contribution from coplanar PCBs. Regards herrings from Baltic Proper dioxin contributes to a little more 50% of the TEQ.

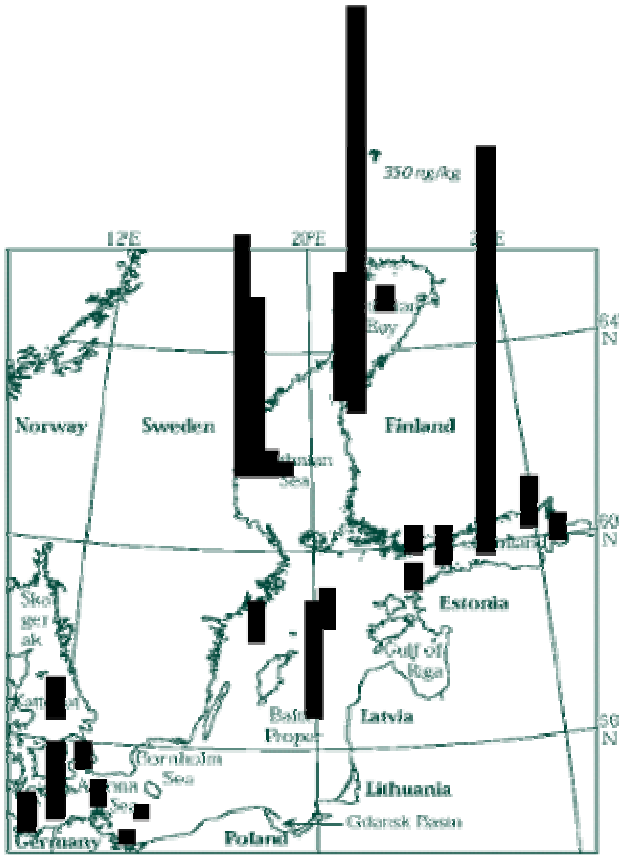


Figure 4. Dioxin (7-350 ng TEQ/kg dry matter) in sediments from the Baltic Sea

Most Baltic dioxin fish data are concerning herring. In the south-western part of the Baltic and in Danish waters the average dioxin content in herrings is now 2-2,5 ng WHO-PCDD/F-TEQ/kg fresh weight. In comparison, levels are about the double in Baltic Proper and the Gulf of Finland and four times higher in the Bothnian Sea and in the southern part of the Bothnian Bay - far exceeding the EU limit value of 4 ng WHO-PCDD/F-TEQ/kg fresh weight. Sweden and Finland have until 2006 got a temporary exception from the regulation to sell the polluted fish in their own countries.

The exceeding levels are particularly in the areas, where the paper and pulp industries for many years' emitted large amounts of dioxins. Figure 5 shows an

overview of dioxin in herrings.

A decrease in levels by time has sometimes been demonstrated. Typical dioxin levels in Baltic wild salmon are presently 2-8 ng WHO-TEQ/kg fresh weight or comparable with herrings. Twenty years ago ten times higher dioxin levels were measured in wild salmon from the Umeå area. Farmed or lake salmon have normally ten times lower dioxin levels. This is opposite what it is for salmon from less polluted waters (Hites et al. 2004).

Most other Baltic fish do have less fat content and lower dioxin levels on fresh weight basis than herrings and salmon but rather similar levels calculated on lipid weight. Only in the case of fish caught close to a point source, there will be a risk to exceed the EU limit value concerning dioxins - but only if the contribution from coplanar PCB is included. That is especially relevant for eels for which the TEQ-contribution from PCB is much more important (85% of WHO-TEQ) than the dioxin contribution.

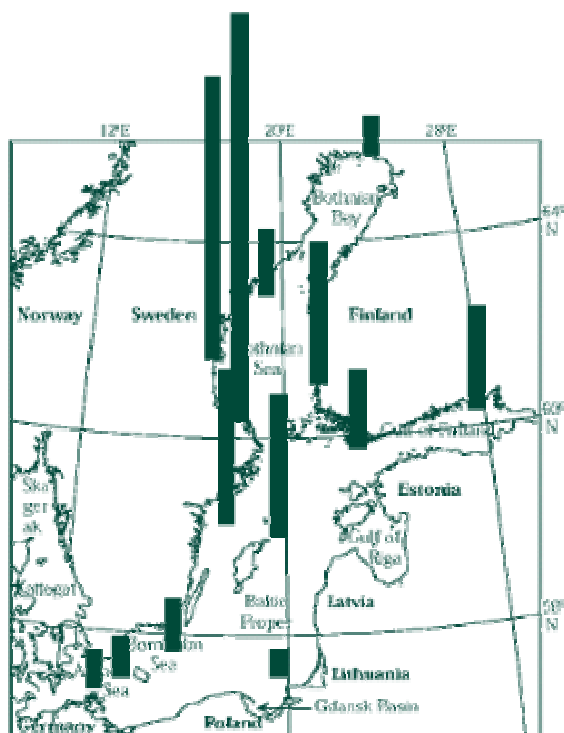


Figure 5: Recent data on dioxin (1.5-20 ng TEQ/kg fresh weight) in herrings from the Baltic Sea.

Conclusions

Presently, more than 100 different persistent environmental chemicals have been found in human blood and breast milk and more will be discovered in the future. In the last 25 years restrictions and bans have been introduced for most of the POPs, and the levels of these chemicals in human milk are now slowly declining in many countries, however, breast-fed infants still get more than the tolerable daily intake of PCB and dioxins.

Unfortunately, levels of some brominated flame-retardants used e.g. electronics show the opposite trend with a doubling in 5 years. The levels of these POP chemicals also increase in various aquatic environments around the globe. It looks like mankind will not learn from the history. Restrictions and bans of

some of these chemicals have recently been introduced in some countries. However, we react generally too slow on the signals, and not before the chemicals are widespread in the nature and in human tissues. Now, the brominated flame-retardants do have an even more widespread diffuse usage, than PCB had 25 years ago, and are already a real challenge for the waste handling system.

The large amounts of dioxin previously released from the large Swedish and Finnish pulp industries seem to be the explanation, why the dioxin levels in fish still are especially high in the northern part of the Baltic Sea, and regards herring and salmon exceed the EU limit value of 4 ng WHO-TEQ/kg fresh weight.

Present and future regulations of dioxin emissions will not be able to remedy and clean the Baltic Sea for dioxin already emitted. These chemicals will stay in the bottom sediments and pollute the Baltic for centuries. Never the less, further regulation limiting the future dioxin input to the Baltic is useful and necessary, because it will decrease further build-up of the most biological available dioxin, and thus slowly decrease the burden on the organisms living in the Baltic Sea and on the populations in surrounding countries.

The morale is: “Never release any man-made persistent and lipophilic chemicals to the environment or expose any individual to the such chemicals”. Use the precautionary principle and don’t wait for a final proof of adverse effects. Then it will be too late to call the chemicals back, they will continue to expose natural organisms and humans for decades or centuries.

References

- [1] Jensen, A.A., and Slorach, S.A., eds. Chemical contaminants in human milk. Boca Raton, FL, CRC Press Inc. 1991, 298 pp.
- [2] Norén, K., and Meironyte, D. Certain organochlorine and organobromine contaminants in Swedish human milk in perspective of past 20-30 years. *Chemosphere*. 2000, 40, 1111-1123.
- [3] Jensen A.A. Kortlægning af dioxinforurening samt kilder til dioxinforurening i Østersøen. Research Report No. 796. Copenhagen: Danish EPA, 2003. (and references herein) The report is freely available from: www.mst.dk.
- [4] Hites R. A. Foran J.A. Carpenter D.O. et al. Global assessment of organic contaminants in farmed salmon. *Science* 2004, 303, 226-229.

Chemical Thermodynamics

(A)

GIBBS FREE ENERGIES AND ENTHALPIES FOR GASEOUS REACTIONS OF OXY-IODINE SPECIES HIXOY

N. Begović¹, Z. Marković², S. Anić³ and Lj. Kolar-Anić³

¹*Institute of General and Physical Chemistry, Studenski trg 12-16, 11000 Beograd*

²*Faculty of Science, Department of Chemistry, Radoja Domanovica 12, 34000 Kragujevac*

³*Faculty of Physical Chemistry, University of Belgrade, Studenski trg 12-16, 11000 Beograd*

Abstracts

Taking into account in literature determined values of enthalpies and Gibbs free energies of formation for the species HI_xO_y ($x = 0, 1, 2$; $y = 0, 1, 2$) at 0 and 298 K, the enthalpies $\Delta_r H_{298}$ and Gibbs free energies $\Delta_r G_{298}$, for the numerous reactions in the gaseous phase are calculated. It has been found that the most of them have $\Delta_r G < 0$, and that they are thermodynamically possible in the considered system. For these theoretical investigations, the density functional method is used.

Introduction

The experimental and the theoretical investigation of the oxy-iodine species and the reactions between them are of great importance for the investigations of the complex reaction systems containing iodine species, such as the aerosol formation in the marine boundary layer is [1]. Here, the enthalpies $\Delta_r H_{298}$ and Gibbs free energies $\Delta_r G_{298}$, for the numerous reactions in the gaseous phase are calculated by means of already determined values of enthalpies and Gibbs free energies of formation for the species HI_xO_y ($x = 0, 1, 2$; $y = 0, 1, 2$) at 0 and 298 K [2-6].

Results

Taking into account the obtained values for enthalpies and Gibbs free energies of formation for the species with the common formula HI_xO_y ($x = 0, 1, 2$; $y = 0, 1, 2$) at 0 and 298 K (**Table I**), the thermochemical characteristics for the following gaseous reactions are analyzed. Particularly, the enthalpies of reactions at 0 and 298 K ($\Delta_r H_0$ and $\Delta_r H_{298}$), and the corresponding Gibbs free energies at 298 K ($\Delta_r G_{298}$) are calculated (**Table II**).

Discussion

Analyzing the results, given in **Table II**, one can see that first fifteen reactions ((1)-(15)) have negative values for $\Delta_r H_0$, $\Delta_r H_{298}$ and $\Delta_r G_{298}$, whereas this is not the case for last three reactions ((16)-(18)). Therefore, the first fifteen reactions with $\Delta_r G < 0$ are thermodynamically possible. For the kinetic justification of the same reactions, the corresponding energies of activation would be calculated.

Conclusion

From the thermodynamic results presented here follow that first fifteen reactions in Table II would be considered in the modeling of complex gaseous processes having oxy-iodine species.

Table I. Enthalpy of formation at 0 and 298 K and corresponding Gibbs free energies of formation at 298 K in gas phase

Species	$\Delta_f H_0$ (kJ mol ⁻¹)	$\Delta_f H_{298}$ (kJ mol ⁻¹)	$\Delta_f G_{298}$ (kJ mol ⁻¹)
HOI	-68.4 ^a	-73.1 ^a	-81.8 ^a
HOIO	-22.4 ^a	-28.8 ^a	-17.2 ^a
OIO	93.3 ^a	89.6 ^a	84.7 ^a
IOI	115.8 ^a	111.2 ^a	84.9 ^a
OI(O)I	87.0 ^a	81.5 ^a	75.8 ^{af}
IO	117.8 ^b	115.9 ^b	92.4 ^f
HOO	12.6 ^c	9.7 ^c	22.00 ^f
HOOH	-129.9 ^c	-135.9 ^c	-103.6 ^f
HI	27.1 ^d	26.5 ^d	1.7 ^f
OH	37.0 ^e	37.2 ^e	34.2 ^f
HOH	-238.9 ^d	-241.8 ^d	-228.6 ^f
I ₂	65.5 ^d	62.4 ^d	19.30 ^f
I	107.2 ^d	106.8 ^d	70.2 ^f
O	246.8 ^d	249.2 ^d	231.7 ^f
O ₂ (g)	0 ^d	0 ^d	0 ^f

^a-[2]; ^b-[3]; ^c-[4]; ^d-[5]; ^e-[6], ^f-calculated here.

Table II. Thermochemical characteristics of the reactions at 298 K, in gas phase

Reaction	$\Delta_r G_{298}$ in kJ mol ⁻¹	$\Delta_r H_{298}$ in kJ mol ⁻¹	
HO• + IO• → HOIO	-143.8	-181.9 kJ	(1)
HOO• + I• → HOIO	-109.4	-145.2	(2)
HOO• + OIO• → HOIO + O ₂	-123.8	-128.1	(3)
HOO• + I ₂ O ₂ → HOIO + OIO•	-30.3	-30.4	(4)
IOI + HOOH → HOI + HOIO	-80.3	-77.2	(5)
HOIO + HI → IOI + HOH	-128.1	-128.3	(6)
HOIO + HO• → HOH + OIO•	-160.9	-160.7	(7)
HOIO + HOO• → HOOH + OIO•	-23.8	-27.2	(8)
IOI + HOH → 2 HOI	-20.0	-15.6	(9)
HO• + OIO• → HOI + O ₂	-200.6	-199.9	(10)
HOO• + IOI → HOI + OIO•	-104.1	-104.4	(11)
HO• + I ₂ O ₂ → HOI + OIO•	-107.1	-102.2	(12)
HO• + HOI → HOH + IO•	-88.6	-90.1	(13)
HOO• + HI → HOI + HO•	-71.3	-72.1	(14)
HOI + HI → I ₂ + HOH	-129.2	-132.8	(15)
I ₂ O ₂ +HIO→ HIO+HOIO	53.8	58.4	(16)
IO+HOH→ HOIO+H	322.2	315.1	(17)
OIO+HOH→ HOIO+OH	160.9	160.7	(18)

Acknowledgements

The present investigations, are partially supported by Ministry of Sciences, Technologies and Development of Serbia, grant no. 1448.

Reference

- [1] J. L. Jimenez, D. R. Cocker, R. Bahreini, H. Zhuang, V. Varutbangkul, R. C. Flagan, J. H. Seinfeld, C. O'Dowd, T. Hoffmann, *Journal of Geophysical Research – Atmospheres*, 2003, 108 4318; J. M. Mäkelä, T. Hoffmann, C. Holzke, M. Väkevä, T. Suni, T. Mattila, P. P. Aalto, U. Tapper, E. Kaupinen, C. O'Dowd, *J. Geophys. Res.*, 2002, 107, 8110; C. D. O'Dowd, J. L. Jimenez, R. Bahreini, C. R. Flagan, H. J. Seinfeld, K. Hämeri, L. Pirjola, M. Kulmala, S. G. Jennings, T. Hoffmann, *Nature*, 2002, 417 632.
- [2] N. Begović, Z. Marković, S. Anić, Lj. Kolar-Anić, Computational investigations of stability of HIO₂ isomers, in S. Anić (Ed.), *Physical Chemistry 2002*, SPCS, Belgrade 2002, 102; *J.Phys.Chem.A*, 2004, 108, 651; *Environ.Chem.Lett.*, 2004, 2(2), 65.
- [3] Y Bedjanian, G Le Bras, G Poulet *Kinetics and Mechanism of the IO + ClO Reaction. J. Phys. Chem. A*, 1997 101 4088.
- [4] L. V. Gurvich, I. V. Veyts, C. B. Alcock, *Thermodynamic Properties of Individual Substances. Fourth Edition*, Hemisphere Pub. Co., New York, 1989.
- [5] J D Cox, , D D Wagman, V A Medvedev, *CODATA Key Values for Thermodynamics. Hemisphere Publishing Corp. New York*, 1989.
- [6] B. Ruscic, A. F. Wagner, L. B. Harding, R. L. Asher, D. Feller, D. A. Dixon, K. A. Peterson, Y. Song, X. Qian, C-Y Ng, J. Liu, W. Chen, D. W. Schwenke, On the Enthalpy of Formation of Hydroxyl Radical and Gas-Phase Bond dissociation Energies of Water and Hydroxyl. *J. Phys. Chem. A*, 2002, 106 2727.

STUDY OF ACID-BASE EQUILIBRIA AND SOLUBILITY OF KETOCONAZOLE

M. Vojić¹, G. Popović², D. Sladić¹ and L. Pfenđt¹

*1*Faculty of Chemistry, P.O.Box 158, 11000 Belgrade, *2*Faculty of Pharmacy, P.O.Box 146, 11000 Belgrade, Serbia and Montenegro

Abstract

Acid-base equilibria in homogeneous and heterogeneous aqueous system of a diprotic, slightly hydrosoluble base ketoconazole was studied. Determinations were performed at 25 °C and constant ionic strength of 0.1 M (NaCl). Acidity constant pK_{a1} 3.20 was determined by a potentiometric method. The pK_{a2} constant of 6.10 was obtained based on equilibrium constants $pK_{s0} = 4.84$ and $pK_{s1} = -1.26$, determined in heterogeneous ketoconazole system.

Introduction

Ketoconazole is an orally active agent from the class of antimycotics, derivatives of imidazole. Ketoconazole is the only member of the imidazole derivatives currently used for the treatment of systemic infections.

As to its chemical characteristics, ketoconazole represents a diprotic base and its molecular form is slightly hydrosoluble. Knowledge on the distribution of the equilibrium species and ketoconazole solubility within physiological range of pH could help to understand better the details on the mechanism underlying this drug action. However, there are no data in the available literature on ketoconazole protolytic equilibria in homogeneous and heterogeneous water system and the aim of this work was devoted to these studies.

Results and Discussion

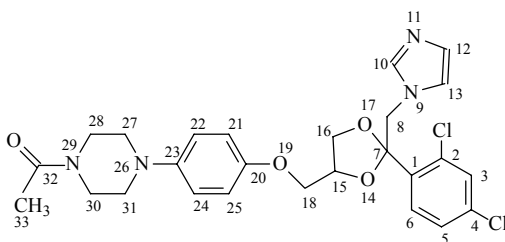
Piperazine nitrogen atom N-26 and imidazole nitrogen atom N-11 represent two basic centers of ketoconazole molecule (B) which participate in protolytic reactions within the pH range from 0 to 14. Based on the comparison with aniline (pK_a 4.6) and imidazole (pK_a 6.9) as model compounds [1], it can be

concluded that imidazole nitrogen atom expressed a higher affinity for proton. The corresponding acidity constants are defined as:

$$K_{a1} = \frac{[H_3O^+][BH^+]}{[BH_2^{2+}]} \quad (1)$$

$$K_{a2} = \frac{[H_3O^+][B]}{[BH^+]} \quad (2)$$

Since ketoconazole in molecular form is slightly hydrosoluble, in heterogeneous system between the solid base (B_s) and saturated water solution the following equilibria get established:





There is the following relation between the acidity constants and the constants in heterogeneous system:

$$K_{a1} = \frac{K_{s1}}{K_{s2}} \quad (6) \quad K_{a2} = \frac{K_{s0}}{K_{s1}} \quad (7)$$

Since ketoconazole is stable in acidic medium and its protonated forms BH_2^{2+} and BH^+ are soluble, it was possible to determine acidity constant K_{a1} by potentiometric method. Determination was performed by method of bound protons [2] within the pH range from 3.0-4.0 where acid-base pair BH_2^{2+} - BH^+ is dominant.

Formation function (\bar{n}), i.e. average number of protons bound to the base can be expressed by the following equation:

$$\bar{n} = \frac{2 [BH_2^{2+}] + [BH^+]}{[BH_2^{2+}] + [BH^+]} \quad (8)$$

Linear plot was obtained by combining equations (1) and (8):

$$\frac{2 - \bar{n}}{\bar{n} - 1} = K_{a1} \frac{1}{[H_3O^+]} \quad (9)$$

Experimentally \bar{n} was determined from pH-metric titration of acidic ketoconazole solution with standard sodium hydroxide solution, and calculated by the following equation:

$$\bar{n} = \frac{c_{HCl} - c_{NaOH} - [H_3O^+]}{c_{KC}} \quad (10)$$

where c_{KC} , c_{HCl} and c_{NaOH} represent ketoconazole, HCl and NaOH concentrations in the solution, respectively; $[H_3O^+]$ is equilibrium concentration of hydronium ion obtained from measured pH values [3]: $pH = -\log[H_3O^+] = pH - 0.12$. On the basis of determined \bar{n} at different pH and eqn. (10), K_{a1} constant was calculated by regression analysis from the slope of the corresponding line (eqn. (9)).

Acidity constant K_{a2} of ketoconazole was impossible to determine spectrophotometrically (low differences between the absorption spectra which follow the protonation of imidazole nitrogen atom) and potentiometrically (slight hydrosolubility of molecular ketoconazole form). Thus, pK_{a2} was indirectly determined based on the equilibria in heterogeneous system.

Equilibrium constants in heterogeneous system were estimated applying a solubility method [3]. The determination was performed within two different pH ranges from 5.5-6.5 (BH^+ and B ketoconazole forms are present in saturated solution) and at $pH > 8.5$ (molecular ketoconazole form B is dominant in saturated solution):

$$S = [\text{BH}^+] + [\text{B}] = K_{s0} + K_{s1}[\text{H}_3\text{O}^+] \quad (\text{pH } 5.5\text{-}6.5) \quad (11)$$

$$S = [\text{B}] = K_{s0} \quad (\text{pH} > 8.5) \quad (12)$$

On the basis of spectrophotometrically determined solubility (S) within the pH range from 5.5 to 6.5 and the application of eqn. (11), K_{s0} and K_{s1} constants were determined from the intercept and the slope of the corresponding line. Equation (12) shows that ketoconazole solubility in an alkaline medium was constant (equal to K_{s0} constant). Equilibrium constants K_{s0} and K_{s1} determined in heterogeneous system and the eqn. (7) served to calculate acidity constant K_{a2} .

The equilibrium constants determined in homogeneous and heterogeneous ketoconazole system are summarized in Table I. On the basis obtained value for equilibrium constants mole fraction (χ) of the equilibrium particles and solubility of ketoconazole can be calculated by following equations:

$$\chi_{\text{BH}_2^{2+}} = \frac{[\text{H}_3\text{O}^+]^2}{[\text{H}_3\text{O}^+]^2 + K_{a1}[\text{H}_3\text{O}^+] + K_{a1}K_{a2}} \quad (13)$$

$$\chi_{\text{BH}^+} = \frac{K_{a1}[\text{H}_3\text{O}^+]}{[\text{H}_3\text{O}^+]^2 + K_{a1}[\text{H}_3\text{O}^+] + K_{a1}K_{a2}} \quad (14)$$

$$\chi_{\text{B}} = \frac{K_{a1}K_{a2}}{[\text{H}_3\text{O}^+]^2 + K_{a1}[\text{H}_3\text{O}^+] + K_{a1}K_{a2}} \quad (15)$$

$$S = [\text{B}] + [\text{BH}^+] + [\text{BH}_2^{2+}] = K_{s0} + K_{s1}[\text{H}_3\text{O}^+] + K_{s2}[\text{H}_3\text{O}^+]^2 \quad (16)$$

Table I. The concentration equilibrium constants in homogeneous and heterogeneous system of ketoconazole. $t=25$ oC; $I=0.1$ M (NaCl).

Constant	$\text{p}K_{a1}$	$\text{p}K_{a2}$	$\text{p}K_{s0}$	$\text{p}K_{s1}$	$\text{p}K_{s2}$	
Value	3.20	6.10	4.84	4.5	-1.26	-4.46
\pm sd	± 0.01	± 0.07	± 0.06	± 0.2	± 0.03	± 0.03
Equation applied	(9)	(7)	(12)	(11)	(11)	(6)

Acknowledgements.

This work was supported by the Ministry for Science, Technology and Development of Serbia, Grant #1713.

References

- [1] D. Perrin, B. Dempsey, Buffers for pH and Metal Ion Control, Chapman and Hall, London, 1974.
- [2] H. Rossotti, The Study of Ionic Equilibria, Longman, New York, 1978.
- [3] L.B. Pfendt, D.M. Sladić, T.J. Janjić, G.V. Popović, Analyst 1990, 115, 383-387.

THE EFFECT OF ACIDITY ON HYDROSOLUBILITY OF METHYL- AND PROPYLPARABEN

G. Popović and M. Čakar

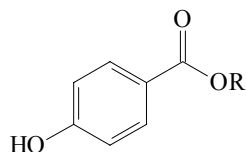
*Faculty of Pharmacy, University of Belgrade, P.O. Box 146, Vojvode Stepe 450,
11000 Belgrade, Serbia and Montenegro*

Abstract

Acidity constants (pK_a) and intrinsic hydrosolubility (K_{s0}) of two parabens, methyl-*p*-hydroxybenzoate and propyl-*p*-hydroxybenzoate, were spectrophotometrically determined at 25 °C and a constant ionic strength of $I=0.1 \text{ mol/dm}^3$ (NaCl). The determined equilibrium constants served for calculation of solubility of the parabens as a function of solution acidity. In addition, the effects of varying β -cyclodextrin concentrations on pK_a values of the two parabens were examined. The results showed that β -CD influenced absorption spectra of the parabens, but their pK_a values remained almost unchanged.

Introduction

Due to their antimicrobial and antifungal action, alkyl esters of *p*-hydroxybenzoic acid (parabens) are widely applied as preservatives in numerous pharmaceutical preparations (oral solutions, creams and lotions), cosmetics and food industry.



R = -CH₃, -C₂H₅, -C₃H₇, -C₄H₉

Parallel to the increase of the chain length of alkyl substituent, paraben activity is also increasing, accompanied by a decrease of their hydrosolubility. Since hydroxyl group in the molecule of parabens is a subject to protolysis (pK_a 8.4) [1], acidity of the medium also affects the solubility of parabens, but there is no data on this phenomenon in the available literature.

The aim of the present study was to examine the effect of pH on hydrosolubility of two most frequently applied parabens, methyl-*p*-hydroxybenzoate (methylparaben, MP) and propyl-*p*-hydroxybenzoate (propylparaben, PP). Matsuda et al. [2] demonstrated an increased paraben solubility in the presence of β -cyclodextrin (β -CD) and a part of this work was focused on the examinations of the influence of β -CD on pK_a values of methyl- and propylparaben.

Results and Discussion

Within the pH range from 0-14.0, both methyl- and propylparaben are the subjects to protolysis of the hydroxyl group, i.e. they behave as acids (HA):



Because both parabens in molecular form are slightly soluble in water, the following equilibria between the solid phase (HA_s) and saturated aqueous solution of these compounds get established:



There is the following relationship between the constant of acidity equilibrium and the equilibrium constants in the heterogeneous system :

$$K_a = \frac{K_{s1}}{K_{s0}} \quad (4)$$

Acidity constants (pK_a) determined spectrophotometrically [3] at 295 nm were 8.03 and 8.00 for methyl and propylparaben, respectively.

The constant K_{s0} was determined in a heterogeneous system within the pH interval from 3.0-4.0, in which the molecular form of the parabens is dominant. Under these conditions, the solubility (S) is independent on pH value and represents the intrinsic solubility:

$$S = [HA] = K_{s0} \quad (5)$$

Based on the obtained K_a and K_{s0} values, the constant K_{s1} was calculated applying the equation (4). The values of equilibrium constants are listed in Table I. By comparing the pK_a values, it can be concluded that the alkyl radical in alcoxy carbonyl group does not effect the acidity of the examined parabens. However, the intrinsic solubility of propylparaben (1.80×10^{-3} M) is approximately 8-fold lower than that of methylparaben (1.42×10^{-2} M).

Table I. Equilibrium constants in homogeneous and heterogeneous system of methyl- and propylparaben. $t=25$ °C; $I=0.1$ M (NaCl).

Paraben	$pK_a \pm sd$	$pK_{s0} \pm sd$	$pK_{s1} \pm sd$
Methylparaben	8.03 ± 0.01	1.85 ± 0.01	9.88 ± 0.01
Propylparaben	8.00 ± 0.03	2.74 ± 0.01	10.74 ± 0.03

Knowledge on equilibrium constants in a heterogeneous system enables the calculations of paraben solubility as a function of acidity of a solution:

$$S = [HA] + [A^-] = K_{s0} + \frac{K_{s1}}{[H_3O^+]} \quad (6)$$

The equation (6) can be applied within the pH range from 6.0-10.0, in which molecular and anionic paraben forms are in equilibrium. At $pH < 6.0$, paraben solubility is constant and equal to the K_{s0} value.

Absorption spectra of molecular (pH 2.0) and anionic (pH 11.0) forms of methyl- and propylparaben in the absence and in the presence of different β -CD concentrations (10^{-4} , 10^{-3} and 10^{-2} M) are depicted in Fig. 1. Although it is evident that β -

CD influenced absorption spectra of the parabens (a decreased absorptivity and a bathochromic shift of the absorption maxima), their pK_a values remained almost unchanged (Table II).

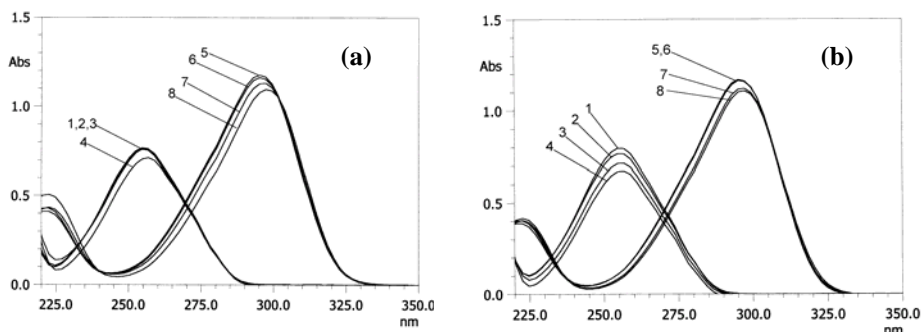


Figure 1. Absorption spectra of molecular (pH 2.0) and anionic (pH 11.0) form of parabens (5×10^{-5} M) in the absence and in the presence of β -cyclodextrin. **(a)** 1 - MP (molecular form); 2, 3 and 4 - MP in the presence of 10^{-4} , 10^{-3} and 10^{-2} M β -CD (molecular form), respectively; 5, MP (anionic form); 6, 7 and 8 - MP in the presence of 10^{-4} , 10^{-3} and 10^{-2} M β -CD (anionic form), respectively; **(b)** 1 - PP (molecular form); 2, 3 and 4 - PP in the presence of 10^{-4} , 10^{-3} and 10^{-2} M β -CD (molecular form), respectively; 5 - PP (anionic form); 6, 7 and 8 - PP in the presence of 10^{-4} , 10^{-3} and 10^{-2} M β -CD (anionic form), respectively.

Table II. The effect of varying β -cyclodextrin concentrations of pK_a values of methyl- and propylparaben. $t=25$ °C; $I=0.1$ M (NaCl).

Paraben	$pK_a \pm sd$		
	10^{-4} M β -CD	10^{-3} M β -CD	10^{-2} M β -CD
Methylparaben	8.00 ± 0.01	8.01 ± 0.01	8.02 ± 0.01
Propylparaben	8.01 ± 0.02	8.00 ± 0.02	8.02 ± 0.01

Acknowledgements

This work was supported by the Ministry for Science, Technology and Development of Serbia, Grant #1458.

References

- [1] Martindale, The Extra Pharmacopoeia, 29th ed. London: The Pharmaceutical Press, 1989.
- [2] H. Matsuda, K. Ito, Y. Sato, D. Yoshizawa, M. Tanaka, A. Taki, Chemical & Pharmaceutical Bulletin, 1993, 41, 1448.
- [3] A. Albert, E.P. Serjeant, The determination of ionization constants, 2nd ed., Chapman and Hall, London, 1971, p 44.

EXCESS MOLAR VOLUMES FOR BINARY LIQUID MIXTURES OF N-METHYLACETAMIDE WITH CHLOROFORM

L. Gobor¹, A.D. Nikolić¹, D. Rikić¹ and D.G. Antonović²

¹*Department of Chemistry, Faculty of Sciences, Trg D. Obradovića 3
21000 Novi Sad, Serbia and Montenegro*

²*Faculty of Technology and Metallurgy, Karnegijeva 4,
11000 Belgrade, Serbia and Montenegro*

Abstract

Excess molar volumes, V_m^E , for binary liquid mixtures of N-methylacetamide and chloroform have been determined at temperatures between 303.15 K and 318.15 K. V_m^E values are negative over whole concentration region and at all temperatures. Experimental excess volumes have been fitted using Redlich-Kister equation.

Introduction

This paper is a part of our continuous study of N-substituted amides in solutions by both, spectroscopic [1-3] and thermodynamic [4,5] point of view. The present work involves N-methylacetamide and chloroform. The excess molar volumes, V_m^E , have been determined at four temperatures in the range 303.15 to 318.15 K, on the basis of the measured densities. V_m^E values have been fitted to the Redlich-Kister [6] equation.

Experimental

N-methylacetamide (NMA), Fluka, p.a., was dried over freshly ignited quicklime and then vacuum distilled. Chloroform (Aldrich) was better than 99.5% pure and have been used without further purification. Excess molar volumes have been obtained from the density measurements at 303.15, 308.15, 313.15 and 318.15. Densities of the liquids were measured using a Mettler-Toledo DE 40 vibrating tube density meter. Calibration of the apparatus was performed using ambient air and specially prepared pure water for calibration delivered by the manufacturer. The densimeter was automatically thermostated (Peltier) at ± 0.05 K. The uncertainty of the densities was less than 2×10^{-4} g cm⁻³. The mixtures were prepared by mass using a Mettler balance. The possible error in the mole fractions is estimated to be less than 1×10^{-4} .

Results and Discussion

Excess molar volume, V_m^E , was computed using the following expression:

$$V_m^E = x_1 M_1 \left(\frac{1}{\rho} - \frac{1}{\rho_1} \right) + x_2 M_2 \left(\frac{1}{\rho} - \frac{1}{\rho_2} \right) \quad (0.1)$$

where M_i , x_i and ρ_i are the molar mass, mole fraction and density of the pure liquid i , respectively, ρ stands for the density of the mixture.

V_m^E values for NMA-chloroform mixtures are given in Table 1. The investigated mixtures have negative excess molar volumes, for the entire concentration range and for all temperatures. The excess molar volumes decrease with increase of the temperature.

Table 1. Excess molar volumes for the binary mixtures NMA + chloroform.

	x_{NMFA}	$V^E \cdot 10^6$ (m ³ /mol)			
		303.15 K	308.15 K	313.15 K	318.15 K
1	0	0	0	0	0
2	0.051	-0.082	-0.091	-0.100	-0.108
3	0.115	-0.136	-0.150	-0.164	-0.257
4	0.161	-0.250	-0.270	-0.284	-0.310
5	0.218	-0.433	-0.455	-0.479	-0.505
6	0.320	-0.437	-0.465	-0.486	-0.521
7	0.424	-0.448	-0.483	-0.513	-0.545
8	0.540	-0.324	-0.349	-0.384	-0.414
9	0.617	-0.184	-0.218	-0.248	-0.278
10	0.719	-0.132	-0.163	-0.186	-0.216
11	0.811	-0.066	-0.089	-0.097	-0.117
12	1	0	0	0	0

The values of excess molar volume are the result of several energetic and structural effects that act in a different way both in pure liquids and the mixtures. Negative values for V_m^E indicate better packing in the mixture. It should be kept in mind that NMA is highly self-associated in liquid state through hydrogen bonding. Presence of the second component disrupts some of the hydrogen bonds in liquid NMA. Chloroform has possibility to form hydrogen bond with NMA. Excess molar volumes were fitted to a Redlich-Kister type equation:

$$V_m^E = x_1 x_2 \sum_{i=0}^n A_i (1 - 2x_2)^i \quad (0.2)$$

where A_i are adjustable parameters, and n is number of coefficients in the equation. The standard deviation of the fit is given as

$$\sigma V_m^E = \left[\sum_{1}^m (V_{\text{exp}}^E - V_{\text{calc}}^E)^2 / m - n \right]^{1/2} \quad (0.3)$$

where m denotes number of experimental data points, and n is number of coefficients in the equation. The coefficients in Redlich-Kister equation as well as the standard deviation of the fit are summarized in Table 2. Correlation coefficients are better than 0.98, for all mixtures and temperatures.

Table 2. The coefficients in Redlich-Kister equation and the standard deviation of the fit.

T (K)	A ₀	A ₁	A ₂	A ₃	σV^E
303,15	-1.451	2.511	0.385	-3.154	0.033
308,15	-1.577	2.505	0.331	-3.180	0.033
313,15	-1.709	2.450	0.444	-2.905	0.035
318,15	-1.823	2.344	0.218	-2.284	0.030

References

- [1] A.D. Nikolić, N.L. Kobilarov, A.N. Brzić, J. Mol. Struct., 1983, 99, 179.
[2] A.D. Nikolić, M. Tarjani, N.U. Perišić-Janjić, S.D. Petrović, J. Mol. Struct., 1988, 174, 129.
[3] A.D. Nikolić, S. Petrović, D. Antonović, L. Gobor, J. Mol. Struct., 1997, 408/409, 355.
[4] A.D. Nikolić, N.U. Perišić-Janjić, N.L. Kobilarov, J. Chem. Thermodyn., 1985, 17, 859.
[5] A. Nikolić, Đ. Vaštag, M. Rozsa-Tarjani, S. Petrović, J. Chem. Eng. Data, 1994, 39, 618.
[6] O. Redlich, A. Kister, Ind. Eng. Chem., 1948, 40, 345.

CLEGG-PITZER-BRIMBLECOMBE EQUATION APPLIED TO $\text{Na}_2\text{SO}_4(\text{aq})$ AT $T = 298.15\text{K}$

V. Marjanović*, R. Ninković, J. Miladinović and M. Todorović

**High Technical School, 34 St. Sava square, 31000 Užice, SCG*

Department of Inorganic Chemical Technology, Faculty of Technology and Metallurgy, Universitet of Belgrade, Karnegijeva 4, 11120 Belgrade, SCG

Abstract

The osmotic coefficient of $\text{Na}_2\text{SO}_4(\text{aq})$ has been measured at $T = 298.15\text{K}$ by the isopiestic method, in the ionic strength range from 1.2 to 2.0 $\text{mol}\cdot\text{kg}^{-1}$, using $\text{KCl}(\text{aq})$ as the reference solution. The results are compared to the osmotic coefficient values calculated by Clegg-Pitzer-Brimblecombe's equation.

Introduction

Research on aqueous solution of Na_2SO_4 has practical and theoretical significance in industrial and chemical applications. Osmotic and activity coefficients are important properties of $\text{Na}_2\text{SO}_4(\text{aq})$ solution. A certain number of isopiestic vapor-pressure studies have been reported for $\text{Na}_2\text{SO}_4(\text{aq})$ [1-3]. In this work isopiestic measurements were performed on $\text{Na}_2\text{SO}_4(\text{aq})$ at $T = 298.15\text{K}$ in the ionic strength range from 1.2 to 2.0 $\text{mol}\cdot\text{kg}^{-1}$ with $\text{KCl}(\text{aq})$ as the reference solution. The experimentally determined values of the osmotic coefficient were compared to that calculated by the Clegg-Pitzer-Brimblecombe's[4] equation developed for single electrolyte solution.

Experimental

The isopiestic apparatus and experimental procedure used in this work were the same as those previously described[3]. The reference solution of $\text{KCl}(\text{aq})$ was prepared from KCl ("Sigma-Aldrich" suprapur-grade chemicals) and double distilled, deionized water. The molality of $\text{KCl}(\text{aq})$ was checked by dehydration on three samples, by heating between $T = 523\text{K}$ and $T = 573\text{K}$. The average molality was $(0.9532 \pm 0.0027)\text{mol}\cdot\text{kg}^{-1}$. The stock solution of $\text{Na}_2\text{SO}_4(\text{aq})$ was prepared from $\text{Na}_2\text{SO}_4 \cdot 10\text{H}_2\text{O}$ ("Merck" suprapur-grade chemicals) and double distilled, deionized water. The molality of $\text{Na}_2\text{SO}_4(\text{aq})$ was determined also on three samples, gravimetrically[5], through $\text{BaSO}_4(\text{s})$ precipitation, by adding $\text{BaCl}_2(\text{aq})$ solution. The molality of the $\text{Na}_2\text{SO}_4(\text{aq})$ stock solution was $(0.3157 \pm 0.0004)\text{mol}\cdot\text{kg}^{-1}$.

The equilibrium periods at $298 \pm 0.01\text{K}$ lasted from 2 to 15 days. The molalities of the investigated solution at isopiestic equilibrium agreed to within $\pm 0.001\text{mol}\cdot\text{kg}^{-1}$ with the average value used for duplicate samples of the solutions.

Results and Discussion

The osmotic coefficient of the $\text{Na}_2\text{SO}_4(\text{aq})$ was determined from the following equation, which is valid only at isopiestic equilibrium:

$$\phi = 2 m_R \phi_R / (3 m_A), \quad (1)$$

where m_R is the molality of the KCl(aq) reference solution, ϕ_R is the osmotic coefficient of the reference solution, m_A is the isopiestic molality of the Na₂SO₄(aq) and ϕ osmotic coefficient of the investigated solution. The osmotic coefficient of the referent solution was calculated using Pitzer's equation and parameters determined by Archer for the KCl(aq) at $T = 298.15$ K[6]. The experimental results of the isopiestic measurements performed on Na₂SO₄(aq) are given in Table 1.

According to Clegg-Pitzer-Brimblecombe[4], the equation for the osmotic coefficient, $\phi(CPB)$, of Na₂SO₄(aq) solution, can be written as:

$$\phi(CPB) = - \left[\left(\frac{1000}{M_{H_2O}} \right) / (3 m_A) \right] \left\{ 2 A_x^\phi I_x^{3/2} / (1 + \rho I_x^{1/2}) - x_{Na} x_{SO_4} B_A \exp(-\alpha I_x^{1/2}) + x_1^2 W_A + x_1^2 (x_1 - x_{H_2O}) U_A + \ln x_{H_2O} \right\} \quad (2)$$

In equation (2) M_{H_2O} is the molar mass of water in $\text{g}\cdot\text{mol}^{-1}$; A_x^ϕ is the Debye-Hückel parameter on a mole fraction scale having value 2.917 for water at $T = 298.15$ K; I_x is ionic strength of the solution on a mole fraction scale; x_{H_2O} , x_{Na} and x_{SO_4} are mole fractions of water and ionic species present in Na₂SO₄(aq); B_A , W_A and U_A are parameters related to short-range forces.

Mole fractions x_{H_2O} , x_{Na} and x_{SO_4} together with solution ionic strength, I_x were calculated by the equations:

$$x_{Na} = 2 m_A / (3 m_A + 1000/M_{H_2O})$$

$$x_{SO_4} = m_A / (3 m_A + 1000/M_{H_2O})$$

$$x_1 = x_{Na} + x_{SO_4} = 3 m_A / (3 m_A + 1000/M_{H_2O})$$

$$x_{H_2O} = (1000/M_{H_2O}) / (3 m_A + 1000/M_{H_2O})$$

$$I_x = 3 m_A / [3 m_A + (1000/M_{H_2O})].$$

In Table 1 are given the molalities m_R of the KCl(aq) reference solution, the ionic strengths I_A ($I_A = 3 m_A$) of the Na₂SO₄(aq) investigated solution, together with experimental and calculated values of the osmotic coefficient of Na₂SO₄(aq) solution at the temperature $T = 298.15$ K.

Table 1. Isopiestic molalities m_R of the KCl(aq) referent solution, ionic strength I_A of the Na₂SO₄(aq), the experimental osmotic coefficient ϕ_e of Na₂SO₄(aq), and calculated osmotic coefficient ϕ (CPB) by Clegg-Pitzer-Brimblecombe equation at $T = 298.15$ K

m_R [mol·kg ⁻¹]	I_A [mol·kg ⁻¹]	ϕ_e	ϕ (CPB)
0.7182	1.9433	0.6641	0.6743
0.7049	1.8852	0.6720	0.6765
0.6811	1.8144	0.6746	0.6792
0.6617	1.7565	0.6771	0.6815
0.6213	1.6386	0.6817	0.6863
0.6064	1.5935	0.6843	0.6883
0.5814	1.5207	0.6875	0.6915
0.5701	1.4869	0.6896	0.6931
0.5453	1.4181	0.6918	0.6963
0.5180	1.3386	0.6964	0.7002
0.4968	1.2692	0.7047	0.7038

Conclusion

Application of Clegg-Pitzer-Brimblecombe equation to osmotic coefficient values of Na₂SO₄(aq) at $T = 298.15$ K and comparing the results of calculation to experimentally determined values are showing good mutual agreement with standard deviation of the fit having value $s = 0.0049$.

References

- [1] R. A. Robinson, R. H. Stokes, Electrolyte Solutions, Butterworth, London, 1955.
- [2] J. A. Rard, D. G. Miller, J. Chem. Eng. Data, 1981, 26, 33.
- [3] V. Pavičević, R. Ninković, M. Todorović, J. Miladinović, Fluid Phase Equilibria, 1999, 164, 275.
- [4] S. L. Clegg, K. S. Pitzer, P. Brimblecombe, J. Phys. Chem., 1992, 96, 9470.
- [5] L. M. Kolthoff, E. B. Sandell, Textbook of Quantitative Inorganic Analysis, Macmillan, New York, 1952.
- [6] D. G. Archer, J. Phys. Chem. Ref. Data, 1999, 28, 1.

PREDICTED VALUES OF OSMOTIC COEFFICIENT IN $K_2SO_4(aq)$ SUPERSATURATED SOLUTION AT $T = 298.15\text{ K}$

R. Ninković, J. Miladinović, M. Todorović and B. Božović

*Faculty of Technology and Metallurgy, University of Belgrade,
Karnegijeva 4, 11 120 Belgrade, Serbia and Montenegro*

Abstract

Zdanovskii rule was applied in prediction of osmotic coefficient values of $K_2SO_4(aq)$ in supersaturated solution by treatment of isopiestic data of mixed electrolyte solutions containing K_2SO_4 , at $T = 298.15\text{ K}$. Systems treated were: $K_2SO_4-Li_2SO_4-H_2O$, $K_2SO_4-Rb_2SO_4-H_2O$ and $K_2SO_4-Cs_2SO_4-H_2O$. The results of prediction show different general trend of osmotic coefficient behaviour in function of molality for supersaturated region of $K_2SO_4(aq)$.

Introduction

Very often, the ionic strength of the mixed electrolyte solution exceeds the ionic strength of the pure solution of electrolyte, as part of the mixture. Therefore, it is necessary to predict the thermodynamic properties of the pure electrolyte solution in supersaturated region.

Zdanovskii rule[1] can be used for estimation of osmotic coefficients of multi-component mixtures based on properties of pure solutions and vice versa. The rule is based on the experimental fact that a linear or approximately linear relation exists between the molalities of the pure and mixed isopiestic solutions in equilibrium.

Results and Discussion

The Zdanovskii rule[1], applied to a mixed solution of electrolytes A and B is given by:

$$m_A/m_{A0} + m_B/m_{B0} = 1, \quad (1)$$

where m_A and m_B are the molalities of electrolytes A and B in mixed solution at isopiestic equilibrium (e.g. the same solvent activity a_w) with the pure electrolyte solutions having molalities m_{A0} and m_{B0} , respectively. Equation (1) for a constant solvent activity, a_w , represents a straight line in diagram m_A against m_B . When a_w exceeds the solubility limit of electrolyte A, the molality m_{A0} in supersaturated solution of pure electrolyte A is obtainable by linear extrapolation of straight lines in diagram m_A against m_B , as illustrated in Figure 1., where the rule is applied to the system $K_2SO_4-Rb_2SO_4-H_2O$. Once the molality, m_{A0} , of supersaturated solution of A is determined, the appropriate osmotic coefficient, ϕ , is given by fundamental equation for isopiestic equilibrium:

$$\phi = \nu_R m_R \phi_R / \nu_A m_{A0}, \quad (2)$$

where M_W is the molar mass of solvent in $\text{g}\cdot\text{mol}^{-1}$, ν_A is the stoichiometric ionization number of electrolyte A, and ν_R , m_R and ϕ_R denote the corresponding quantities for the isopiestic reference standard.

Zdanovskii rule[1] was used in treatment of literature isopiestic data for the systems: $\text{K}_2\text{SO}_4\text{-Li}_2\text{SO}_4\text{-H}_2\text{O}$ [2], $\text{K}_2\text{SO}_4\text{-Rb}_2\text{SO}_4\text{-H}_2\text{O}$ [3] and $\text{K}_2\text{SO}_4\text{-Cs}_2\text{SO}_4\text{-H}_2\text{O}$ [4] at $T = 298.15$ K. Predicted values of $\text{K}_2\text{SO}_4(\text{aq})$ osmotic coefficient in function of molality for the concentrations above solubility limit ($m = 0.7$ $\text{mol}\cdot\text{kg}^{-1}$) are given in Figure 2.

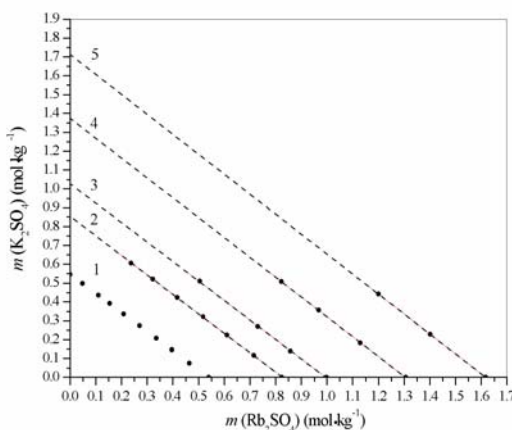


Figure 1. Zdanovskii rule applied to the system $\text{K}_2\text{SO}_4\text{-Rb}_2\text{SO}_4\text{-H}_2\text{O}$ [3]:
1- $a_w = 0.9800$; 2- $a_w = 0.9706$; 3- $a_w = 0.9643$; 4- $a_w = 0.9535$; 5- $a_w = 0.9428$.

Depending on the system data treated, there are different results of prediction of the osmotic coefficient values for $\text{K}_2\text{SO}_4(\text{aq})$. Figure 2. contains also the experimental data for the osmotic coefficient, up to saturation limit, originating from the paper of Palmer-Archer-Rard[5]. General trend obtained by treatment of isopiestic data for the systems $\text{K}_2\text{SO}_4\text{-Rb}_2\text{SO}_4\text{-H}_2\text{O}$ and $\text{K}_2\text{SO}_4\text{-Cs}_2\text{SO}_4\text{-H}_2\text{O}$ is that values of the osmotic coefficient of $\text{K}_2\text{SO}_4(\text{aq})$ are increasing with solution molality, while the treatment of $\text{K}_2\text{SO}_4\text{-Li}_2\text{SO}_4\text{-H}_2\text{O}$ data gives decreasing tendency of the osmotic coefficient values. All the systems do not show larger departures from Zdanovskii rule.

Chen et al.[6] observed that, although most of the largely deviating systems are known to form complexes, many other complex forming systems obey the rule exactly or at least as well. Chen et al., attributed this fact to the cancellation of opposite effects caused by formation of solvent separated (outer-sphere) complexes and ion pair (inner-sphere) complexes, on solvent activity. The complex formation in $\text{Li}_2\text{SO}_4(\text{aq})$ exists according to certain literature data[7,8] to much higher extent than in $\text{Rb}_2\text{SO}_4(\text{aq})$ and $\text{Cs}_2\text{SO}_4(\text{aq})$. This explains differing in the prediction results obtained from the $\text{K}_2\text{SO}_4\text{-Li}_2\text{SO}_4\text{-H}_2\text{O}$ comparing to the $\text{K}_2\text{SO}_4\text{-Rb}_2\text{SO}_4\text{-H}_2\text{O}$ and $\text{K}_2\text{SO}_4\text{-Cs}_2\text{SO}_4\text{-H}_2\text{O}$ data.

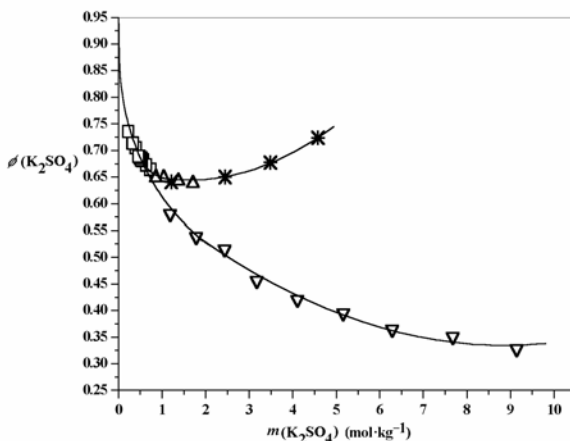


Figure 2. Predicted values of the osmotic coefficient for supersaturated $\text{K}_2\text{SO}_4(\text{aq})$ at $T = 298.15$ K by Zdanovskii rule applied to different systems: \square - experimental data of Palmer-Archer-Rard[5]; $*$ -system $\text{K}_2\text{SO}_4\text{-Cs}_2\text{SO}_4\text{-H}_2\text{O}$; ∇ - system $\text{K}_2\text{SO}_4\text{-Li}_2\text{SO}_4\text{-H}_2\text{O}$; \triangle - system $\text{K}_2\text{SO}_4\text{-Rb}_2\text{SO}_4\text{-H}_2\text{O}$

Conclusion

Prediction of the osmotic coefficient of $\text{K}_2\text{SO}_4(\text{aq})$ in supersaturated solution, by Zdanovskii rule, gives different results depending on the system data treated. If the system was $\text{K}_2\text{SO}_4\text{-Li}_2\text{SO}_4\text{-H}_2\text{O}$, the osmotic coefficient shows decreasing tendency with solution molality, and increasing tendency if the systems were: $\text{K}_2\text{SO}_4\text{-Rb}_2\text{SO}_4\text{-H}_2\text{O}$ and $\text{K}_2\text{SO}_4\text{-Cs}_2\text{SO}_4\text{-H}_2\text{O}$. Explanation for this is the formation of complexes to much higher extent in $\text{Li}_2\text{SO}_4(\text{aq})$ comparing to $\text{Rb}_2\text{SO}_4(\text{aq})$ and $\text{Cs}_2\text{SO}_4(\text{aq})$.

Literature:

- [1] A. B. Zdanovskii, Trudy Solyanoi Laboratorii Akad. Nauk SSSR, No.2., 1936.
- [2] V. K. Filippov, A. M. Kalinkin, S. K. Vasin, J. Chem. Thermodynamics, 1989, 21, 935.
- [3] A. M. Kalinkin, A. V. Rumyantsev, J. Solution Chem., 1996, 25, 695.
- [4] V. K. Filippov, A. M. Kalinkin, S. K. Vasin, J. Chem. Thermodynamics, 1987, 19, 185.
- [5] D. A. Palmer, D. G. Archer, J. A. Rard, J. Chem. Eng. Data, 2002, 47, 1425.
- [6] H. Chen, I. Sangster, T. T. Teng, F. Lenzi, Can. J. of Chem. Eng., 1973, 51, 234.
- [7] F. Rull, H. Ohtaki, Spectrochimica Acta, 1997, 53, 643.
- [8] D. G. Leaist, J. Goldik, J. Solution Chem., 2001, 30, 103.

TEMPERATURE INFLUENCE ON COURSE OF *DDSH* SILOXANE REDISTRIBUTION REACTION

J. Jovanović¹

¹*Institute of Technical Science of the Serbian Academy of Science and Arts, Knez Mihailova 35,
11000 Beograd, Serbia and Montenegro,*

Abstract

The heterogeneously catalyzed siloxane redistribution reactions of dimethyldichlorsilan-hydrolyzate, *DDSH*, without addition of any disiloxane, at temperatures 25°, 50°, 75°, 95° and 120 °C, with constant concentration of catalyst, Duolite C26, were investigated. The obtained results imply that the entire *DDSH* redistribution process consist of two main stages. Within the first stage, linear polymer products with high molar mass and bimodal molar mass distribution were formed. In the latter stage, the main process was some kind of “transformation” within the linear polymers, and uniformity of polymers molar mass fraction occurred, so that bimodal molar mass distribution transformed to a normal Gauss distribution. The temperature increase accelerates the reaction and makes narrower molar mass distribution.

Introduction

Siloxane redistribution reaction is one of the most characteristic polysiloxanes chemical reactions. With the exception of some anionic cyclosiloxanes polymerizations, siloxane redistribution reaction occurs in the all proceses for polysiloxanes synthesys. Siloxane bond, $\equiv\text{Si-O}$, due to its partly ionic nature, easy undergoes to ionic agents attack, and under their catalitic action come to characteristic proces redistribution proces, which consist of continual successively broken and re-forming of siloxane bonds, untill the most stable thermodynamic state of molecular equilibrium is formed, and that state is called equilibration [1]. State of equilibrium is independant on catalyst type and practically is predetrmined with nature of the substituents on silicon atoms, temperature and concentrations of siloxane units. In the equilibrium state reaction mixture consist of linear polymrs molecules and some amounts of cyclic siloxanes [2, 3]. This paper investigates temperature influence on siloxane redistribution reaction of dimethyldichlorsilan hydrolyzate (*DDSH*) taking place in the presence of sulfonated crosslinked polystyrene as reaction catalyst.

Experimental

Materials: *Dimethyldichlorsilan hydrolyzate(DDSH)* used in this work was “Dow corning Fluid 2,0176” produced by Dow Corning, USA. A detailed analysis of used *DDSH* was done and presented in Table 1. *Cation exchange resin* “Duolite C26”, was obtained from Diamond Shamrock, USA and used as the reaction catalyst. *Choloroform* was p.a., Merck, Germany.

Table 1. DDSH analysis: refractive index (n_D^{25}), viscosity (η_o), and compounds content cyclosiloxanes (CS) and polymer component

DDSH total	
n_D^{25}	1.4000
η_o , P	0.5
Cyclosiloxanes (CS)	
total	47.5
Octamethylcyclotetrasiloxane (D ₄)	35.4
Decamethylcyclopentasiloxane (D ₅)	9.1
Dodecamethylcyclohexasiloxane (D ₆)	1.9
other	2.1
Polymer component	
n_D^{25}	1.4040
η_o , P	2
M_{HPLC} , g/mol	13000
Molar mass polydispersity, P (M_w/M_n)	1.53

Polymerization procedure: A typical redistribution reaction was performed as follows. A measured quantity of DDSH was warmed up to the desired temperature with stirring and the weighed amount of catalyst was added to start the reaction. Experimental details of these reactions are described elsewhere [3].

Monitoring methods: *Refractometry:* Refractometer type "Abbe" was used for refractive index determination at 25°C. *Rheometry:* Rheological flow curves were determined by using Feranty-Shirley, cone-and-plate rotational viscometer at 25°C. *High performance liquid chromatography:* A Varian liquid chromatograph model 1250 with Supelco Pl-Gel columns and RI detector was used at 25°C with chloroform as the mobile phase. *Gas chromatography (GC):* A Varian 3400 gas chromatograph with DB-wax column and a FI detector was used.

Content of volatile and non-volatile products, i.e. CS and polymer product (PP) was determined gravimetrically. CS were analyzed by GC and PP by rheometry and HPLC.

Results and Discussion

Table 2 presents values of physico-chemical properties of reaction mixture: refractive index (n_D^{25}), viscosity (η_o) and CS content and polymer products (PP): η_o and M_{HPLC} , during the times of siloxane redistribution reaction of DDSH at 50°C.

Table 2. Changes of physico-chemical properties of reaction mixture (n_D^{25} , η_o , CS) and PP (η_o , M_{HPLC}) during times of DDSH redistribution at 50°C

Time, h	Reaction mixture			Polymer product		
	n_D^{25}	η_o , P	CS total, %	D ₄	η_o , P	M_{HPLC}
5	1.4018	10	20.4	14.2	42	40000
10	1.4027	30	13.9	8.8	77	49000
14	1.4029	45	8.5	5.5	165	51000
20	1.4030	100	7.4	4.9	210	65000
48	1.4031	380	5.8	4.2	480	83000

Based on the results presented at Table 2, it can be concluded that during the investigated siloxane redistribution reaction, n_D^{25} and η_o of the reaction mixture, as

well as η_0 and M_{HPLC} of the PP increased, while amount of CS in reaction mixture, both total and particular (given example of D_4) decreased. Table 3 shows influence of the reaction temperature on the characteristic physico-chemical properties of reaction mixture and PP of the investigated siloxane redistribution reaction for equal reaction time of 5 hours.

Table 3. Changes in physical-chemical properties of reaction mixture (n_D^{25} , η_0 , CS) and PP (η_0 , M_{HPLC}) after 5 hours redistribution reaction at different temperature

Temperature, °C	Reaction mixture				Polymer product	
	n_D^{25}	η_0 , P	CS, %	D_4 , %	η_0 , P	M_{HPLC}
25	1.4008	8.5	37	29.3	18	22000
50	1.4018	10	20.4	14.2	42	40000
75	1.4028	23	8.5	5.4	44	41600
95	1.4030	20	8.2	4.9	31	38000
120	1.4030	15	7	3.9	25.7	34000

Based on the obtained results, it can be seen that n_D^{25} of the reaction mixture increased with reaction temperature increase, while CS content decreased. Reaction mixture η_0 and PP η_0 , M_{HPLC} exhibited complex relationship on reaction temperature. At low temperatures, temperature increase leads to the increase of the reaction mixture η_0 , PP η_0 and M_{HPLC} . At 75 °C these values have reached maximums. HPLC analysis revealed that entire DDSH redistribution process consists of two main stages. Within the first stage, PP with high molar mass and bimodal molar mass distribution were formed. In the latter stage, the main process was some kind of transformation within the PP and uniformity of polymers molar mass fraction occurred, so that bimodal molar mass distribution transformed to a normal Gauss distribution. The temperature increase accelerates the reaction and makes narrower molar mass distribution.

Literature

- [1] W.Noll, Chemie und Technologie der Silikone, Verlag Chemie, GmbH, Weinheim, 1968, p.188.
- [2] P.W.Wright, Cyclic Siloxanes in Ring Opening Polymerization, Elsevier Applied Science, London, 1976, 2, 1055.
- [3] J.D. Jovanovic, PhD Thesis, Faculty of Chemistry, Belgrade, 1993.

THE INTERACTION OF n-HEXANE WITH CATION EXCHANGED Y ZEOLITES

V. Rakić¹, I. Cekić², and R. Hercigonja²

¹Faculty of Agriculture, Nemanjina 6 Zemun, ²Faculty of Physical Chemistry, Studentski trg 12, Beograd, University of Belgrade, Serbia and Montenegro

Abstract

Temperature-programmed desorption (TPD) and infrared (IR) spectroscopy were performed in order to study the room temperature interaction of n-hexane with cation-exchanged Y zeolites. It has been shown that the adsorption of n-hexane depends on the charge balancing cations in the zeolite structure (Zn^{2+} or Cu^{2+}), and competes with the H_2O adsorption.

Introduction

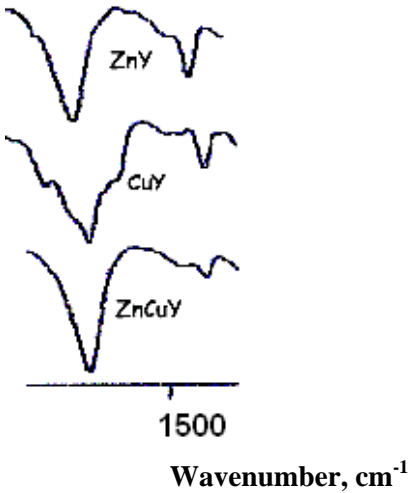
Zeolites are three-dimensional, interconnected channel systems with known diameters of pores. Adsorption of many different gases is a method used to characterize either the pore system (adsorption of N_2 or Ar) or the nature and strength of their active sites (adsorption of NH_3 or pyridine). Catalytic behaviour of these materials have been widely studied by so-called test reactions, among them, catalytic cracking of n-hexane at high temperatures (≈ 450 °C) is commonly used method, both in the past [1] and nowadays [2]. However, in the case of room temperature interaction of n-hexane with zeolite systems, only the results obtained on HY and N-ZSM-5 zeolites are reported in the newest literature [3].

In this work, we investigated the room temperature adsorption of n-hexane on Y zeolites ion-exchanged with Zn and Cu(II) ions. Zeolite systems with Cu(II) as a charge-balancing cation are very interesting catalysts for conversion of NO_x [4], while Zn^{2+} ion is known to create very strong Lewis acidity in zeolite systems [5].

Experimental

The samples used in this work were prepared from synthetic FAU (SK-40, Union Carbide). The investigated samples were obtained by conventional ion-exchanged procedures from acetate solutions. The following formulae were derived: $H_{56}(AlO_2)_{56}(SiO_2)_{56}$; $H_{40}Cu_8(AlO_2)_{56}(SiO_2)_{56}$; $H_{38}Zn_9(AlO_2)_{56}(SiO_2)_{56}$; $H_{34}Cu_4Zn_7(AlO_2)_{56}(SiO_2)_{56}$. As-prepared samples were placed in a closed vessel containing n-hexane, for 24 hours. The adsorption of n-hexane was confirmed by IR spectroscopy, done at Perkin-Elmer 1760 FTIR, using KBr technique. A series of TPD experiments was performed using differential scanning calorimeter Setaram DSC 111 coupled with a mass spectrometer (Baltzers Thermostar), in a helium flow (≈ 10 cm³/min), in a temperature region 25 – 300 °C. Masses corresponding to water and n-hexane were recorded.

Results



As a result of room-temperature adsorption, n-hexane interacts with zeolite framework. Bands at 1380 cm^{-1} and 1460 cm^{-1} , assigned to C-H bending in n-hexane molecule [6], are found during the adsorption of n-hexane on various zeolite structures [7]. However, the positions of these bands are influenced by the presence of charge-balancing cation, as shown in Figure 1.

Figure 1 IR spectra of n-hexane adsorbed on the samples of cation-exchanged Y zeolite

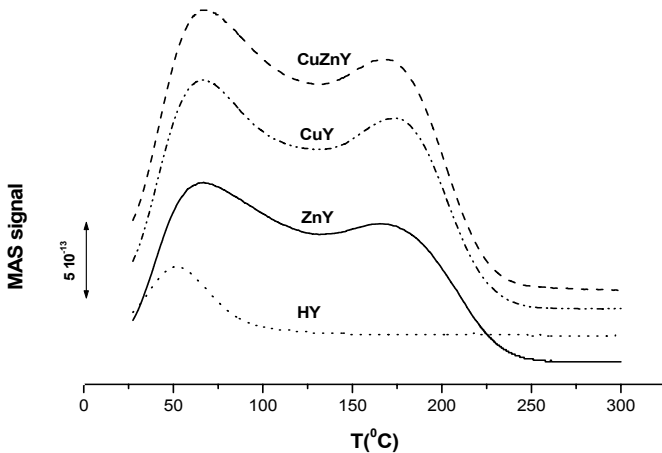


Figure 2 TPD spectra of n-hexane ($m/e = 41$) recorded from the samples of Y zeolite. For all experiments, the same masses of the samples (20 mg) were applied.

The profiles of TPD spectra - two well separate peaks with temperature of maxima only slightly dependent on the type of cation, indicate desorption of n-hexane from two different places in the structure of Y zeolite. However, the areas under the TPD curves are evidently dependent on the cation present in the structure.

It is worth noticing that n-hexane was adsorbed on the samples saturated with water. In spite of this, the adsorption evidently happened at room temperature. In addition, it can be concluded that adsorption of n-hexane caused the migration of water molecules in the structure, what can be inferred from the results shown in Figure 3. Evidently, n-hexane adsorption shifts the desorption of water to a higher temperature region, compared with that one obtained from as-synthesized sample.

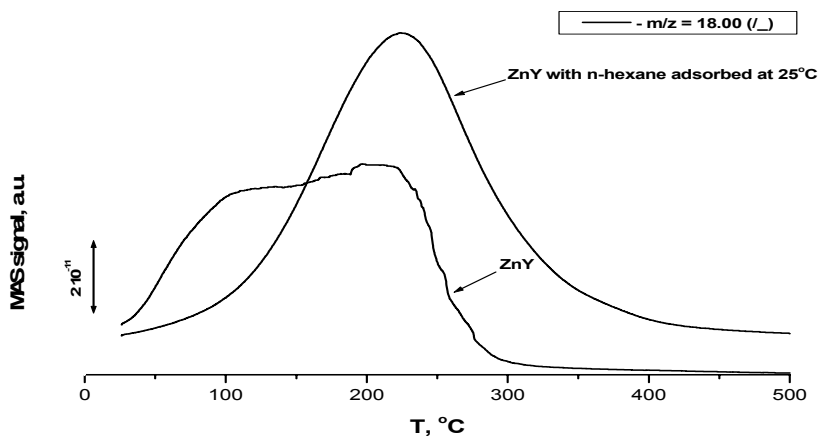


Figure 3 TPD profiles of water ($m/e = 18$) from ZnY

Conclusions

In this work, the room temperature interaction of n-hexane with active sites of cation-exchanged Y zeolite saturated with water was investigated by the use of temperature programmed desorption (TPD) and infrared (IR) spectroscopy. The adsorption of n-hexane was found to be dependent on the nature and amount of charge-balancing cation.

References

- [1] A.P. Bolton and R.L. Bujalski, *J. Catal.*, 1971, 23, 331.
- [2] A. Smiešková, E. Rojasová, P. Hudec and L. Šabo, *in press* in: *Applied Catalysis A: General*, for 2004, www.sciencedirect.com
- [3] W. Makowski and D. Majda, *Thermochim. Acta*, 2004, 412, 131.
- [4] J.Despers, M.Koebel, O.Krocker, M.Elsener and A.Wokann, *Micropor.Mesopor.Mater.* 2003, 58, 175.
- [5] L. A.M.M. Barbosa and R. A. Van Santen, *Catal. Lett.*, 1999, 63, 97.
- [6] C.J. Pouchert, *The Aldrich Library of FT-IR Spectra*, vol.1, Aldrich Chem. Co., Milwaukee, WI, 1985.
- [7] Y.S. Lin, N. Yamamoto, Y. Choi, T. Yamaguchi, T. Okubo, S.-I. Nakao, *Micropor. Mesopor. Mater.* 2000, 38, 207.

THERMODYNAMICS OF AZO-DYE IMMOBILIZATION ON ANION-EXCHANGE RESIN

J. Savić

*Department of Physical Chemistry, VINČA Institute of Nuclear Sciences,
POB 522, 11001 Belgrade, Serbia and Montenegro*

Abstract

Sorption thermodynamics of pyrazol (PACA) and imidazol-azo chromotropic acid (IACA) onto anion exchange resin Dowex 1-X8, 20-50 mesh at pH 4.5 was investigated. It was found that obtained experimental results obeyed Langmuir isotherm model. The values of Gibbs free energy ΔG for azo-dye sorption onto Dowex resin were $-30,6$ kJ/mol for PACA and $-28,8$ kJ/mol for IACA.

Introduction

Azo-dyes sorbed onto the solid support play the great role in the sorption-spectroscopic test methods and development of chemical sensors for determination of low concentration of metal ions [1]. Consequently, the investigation of the equilibrium sorption isotherm is important in the design of sorption systems. This work deals with the investigations of sorption isotherm of 1,8-dihydroxy-2-(pyrazol-5-ylazo)-naphthalene-3,6-disulphonic acid (PACA) and 1,8-dihydroxy-2-(imidazol-5-ylazo)-naphthalene-3,6-disulphonic acid (IACA) on anion exchange resin.

Experimental

Chemicals. The investigated azo-dyes (PACA and IACA) in the form of the disodium salt were synthesized as described previously [2]. The acidity of the solutions was adjusted by addition of Britton–Robinson buffer. The anion-exchange resin Dowex 1-X8 (50-100 mesh) was used as a carrier for dye sorption [3,4]. The sorption of reagents was investigated by mixing 0.5 g of exchanger with 10 ml of dye solution of the desired concentration and shaken for the time necessary to achieve the equilibrium. *Apparatus.* Absorbance of solutions and resin phase spectra was measured in 1.0 and 0.2 cm quartz cells with Beckman 5260 UV VIS recording spectrophotometer. The resin prepared without dye was used as the reference.

Results

The dye sorption was investigated in the PACA and IACA solutions containing 5×10^{-6} to 7×10^{-4} M dye at the media acidity between pH 1 and pH 10, since in this acidity range the change of the molecule charge occurs due to the protonation and dissociation equilibria. The mean values of (0.80 ± 0.06) μmol PACA and (0.82 ± 0.06) μmol IACA per g of resin Dowex 1-X8, 50-100 mesh, at temperature 20°C were obtained after 25-minute contact between solution and solid phase at pH 4.4 were sorbed. At pH 2.5, the mean values were (0.75 ± 0.06) μmol PACA and (0.76 ± 0.06) μmol IACA per g of resin.

In order to obtain the sorption isotherms, amount of sorbed dye was followed depending on dye concentration in solution after equilibration (Fig. 1). The initial dye concentrations in contact solution were in the range from 5×10^{-5} M to 5×10^{-3} M, and the remained concentrations, in solution, after the equilibration were from 1.5×10^{-6} M to 8.6×10^{-5} M.

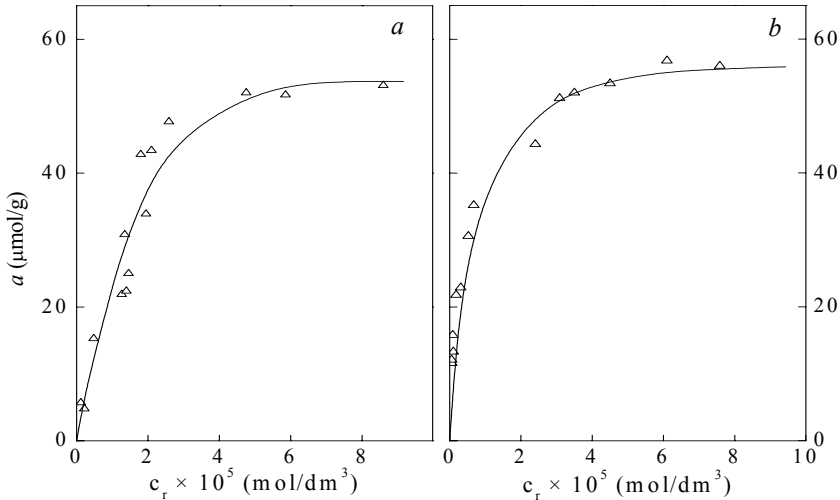


Fig.1 Dependence of the amount of sorbed dye per g of resin (a) on reagent equilibrium concentration in solution (c_r) for PACA (a) and IACA (b); resin Dowex 1-X8, 50-100 mesh, Cl⁻ form; pH 4.2; $t = 18^\circ\text{C}$

The Langmuir adsorption model was applied to describe the equilibrium isotherms. The experimental data were fitted to linearized form of the Langmuir equation:

$$\frac{c_r}{a} = \frac{I}{a_m(K-1)} + \frac{c_r}{a_m} \quad (1)$$

where c_r is the reagent concentration in the solution (in mol/dm^3); a – amount of reagent sorbed on the resin (in mol/g); a_m – monolayer capacity (in mol/g); K - sorption constant.

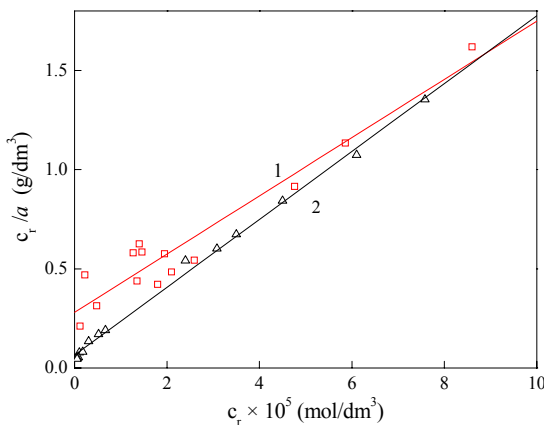


Fig.2 Graphic determination of monolayer capacity a_m and sorption constant K according to Eq. 1 for PACA (1) and IACA (2); resin Dowex 1-X8; pH 4.2; $t = 18^\circ\text{C}$

The dependence of the left hand side of Eq. 1 on reagent equilibrium concentration (c_r) was linear, as represented on Fig.2. Values of the slope and intersection on ordinate, obtained from the dependences presented on Fig. 2, are given in Table 1. The thermodynamic parameters (a_m, K) for PACA and IACA sorption onto Dowex resin, were calculated from the intercept and the slope according to Eq. 1.

The change of Gibbs free energy ΔG during the azo-dye sorption, was determined according to the equation 2:

$$\Delta G = - RT \ln K \quad (2)$$

The thermodynamic parameters for the sorption of PACA and IACA onto Dowex 1-X8 resin are given in Table 1.

Table 1. Thermodynamic parameters of azo-dyes PACA and IACA for sorption onto Dowex 1-X8 resin, at 18°C ($m_{\text{resin}} = 0.5 \text{ g}$; $V = 10 \text{ ml}$; pH 4,2)

reagent	a_m ($\mu\text{mol/g}$)	K $\times 10^{-5}$	$-\Delta G$ (kJ/mol)
PACA	6.67	2.87	30.6
IACA	5.88	1.35	28.8

As can be seen from Table 1, the similar results were obtained for both dyes. This finding can be explained by their similar structure, i.e. PACA and IACA are structure isomers with the same functional groups acting in sorption process.

Conclusion

The results gained from the study of sorption of pyrazol (PACA) and imidazol-azo chromotropic acid (IACA) onto anion exchange resin Dowex 1-X8, 20-50 mesh at pH 4.5 were described by the Langmuir isotherm. The thermodynamics of the investigated system pointed out that sorption was spontaneous.

Acknowledgement

Financial support was provided by the MSTD of the Republic of Serbia, Grant No. 1991. This work has been partly supported by AUF project "Pôle d'excellence régionale"; Référence: 2700PL309/2003.

References

- [1] K. Yoshimura, H. Waki, *Talanta*, 1985, 32, 345.
- [2] V. Vasić, A. Muk, T. Petrova, V. Nikolić, *Zh Anal Khim*, 1988, 43, 793.
- [3] V. Vasić, J. Savić, V. Pavelkić, S. Milonjić, *Colloid Surface A*, 2003, 215, 277.
- [4] V. Vasić, J. Savić, N. Vukelić, *J Serb Chem Soc*, 2004, 69, 309.

THERMODYNAMIC STUDIES OF COMPLEXATION OF ALKALI AND ALKALINE EARTH CATIONS BY A DIHOMOOXACALIX[4]ARENE TETRAAMIDE

P. Khazaeli-Parsa^a, V. Hubscher^b and F. Arnaud-Neu^b

^aChemistry Department, Islamic Azad University-North Tehran Branch, N°9, Darab-nia b.alley, Daftari-Sharghi alley, Shariati St., Tehran-IRAN., ^bLaboratoire de Chimie-Physique, UMR 7512 (CNRS-ULP), 25, rue Becquerel 67087 Strasbourg Cedex 02, France

Abstract

The complexation abilities of a new *p-tert*-butyldihomooxcalix[4]arene tetra-diethylamide towards alkali and alkaline earth metal ions in methanol have been evaluated by UV/Vis spectroscopy or competitive potentiometry. The results reveal that the ligand is capable to complex alkali and alkaline earth cations with a 1 : 1 metal to ligand ratio. The results will be compared to those obtained with the reference compound *p-tert*-butylcalix[4]arene tetra-diethylamide in order to stress the role of the oxygen heteroatom present in the macrocyclic ring.

Introduction

Dihomooxcalix[4]arenes are cyclic tetramers where a $-\text{CH}_2\text{OCH}_2-$ group replaces one of the methylene bridges. They have a cavity size that stands between the respective calix[4]- and calix[5]arenes and a conformational mobility somewhat higher than that of conventional tetramers. These characteristics make these molecules suitable for inclusion studies. With appropriate lower rim substitution, dihomooxcalix[4]arenes with binding properties can be obtained [1].

For a few years dihomooxcalix[4]arene derivatives with carbonyl group containing substituents on the lower rim have been synthesized. The binding properties of such compounds bearing ketone and ester groups towards alkali, alkaline earth and some transition and heavy metal cations have been reported [2].

We reported here the complexing properties of *p-tert*-butyldihomooxcalix[4]arene tetra(diethyl)amide [3] (figure 1) towards alkali and alkaline earth cations in methanol. The results are compared with those obtained with the reference compound *p-tert*-butylcalix[4]arene tetra(diethyl)amide [4] in order to stress the role of the oxygen heteroatom present in the macrocyclic ring.

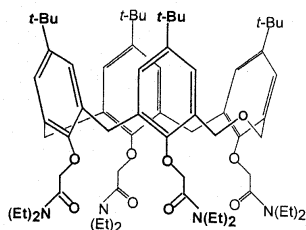


Figure 1:

Structure of *p-tert*-butyldihomooxcalix[4]arene tetra(diethyl)amide.

Results and Discussion

Assuming 1:1 stoichiometry for the complexes formed between metal cations and *p*-*tert*-butyldihomooxalix[4]arene tetra(diethyl)amide, the equation describing the complexation equilibrium of the cations is as follow:



The corresponding stability constant β is then defined as:

$$\beta = \frac{[ML^{n+}]}{[M^{n+}][L]}$$

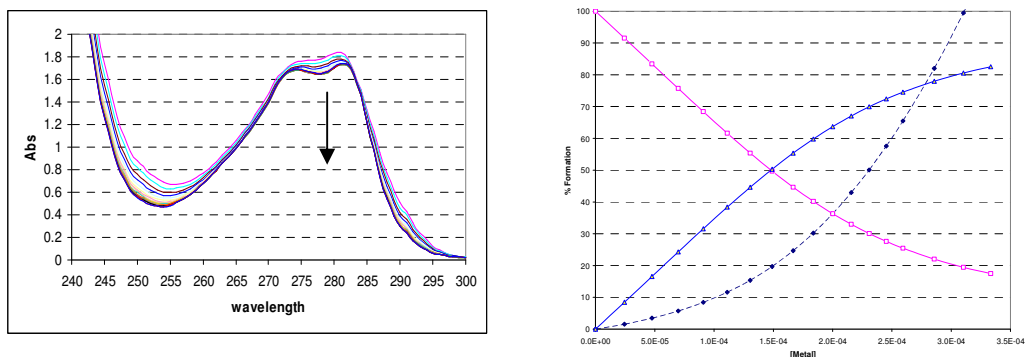


Figure 2 Changes in absorption spectrum (after correction for dilution effects) and percent of formation of different species of a 5×10^{-4} M solution of *p*-*tert*-butyldihomooxalix[4]arene tetra(diethyl)amide in methanol upon addition of CsCl ($I = 0.01\text{M}(\text{Et}_4\text{NCl})$, $T = 25^\circ\text{C}$)

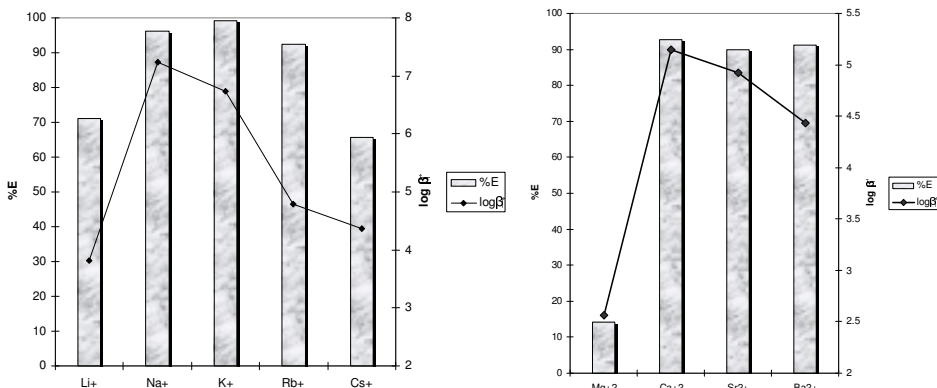


Figure 3 Percent cation extracted (%E) from water to dichloromethane of alkali and alkaline earth picrates and logarithm of stability constants ($\log \beta$) in methanol vs. cations for the complexation of alkali and alkaline earth cations by *p*-*tert*-butyldihomooxalix[4]arene tetra(diethyl)amide ($I=0.01\text{M}(\text{Et}_4\text{NCl})$, $T=25^\circ\text{C}$).

The potentiometric measurements with Ag^+ as an auxiliary cation were performed with the following electrochemical cell:

Ag(s)|| AgBF₄, C_{Ag}⁺, C_{Mn}⁺, EtNClO₄ 10⁻²M || EtNClO₄ 10⁻²M || AgBF₄10⁻²M |Ag(s)
 The reference and measurement cells were thermoregulated at 25.00±0.01 °C.

The stability constants of the formed complexes with Li⁺, Rb⁺, Cs⁺ Mg²⁺, Ca²⁺, Sr²⁺, Ba²⁺, cations, were determined by UV/Vis spectrophotometry in methanol. The cation solution has been stepwise added in the spectrophotometric cell to a volume of *p-tert*-butyldihomooxalix[4]arene tetra(diethyl)amide solution (figure 2). The results have been shown in figure 3.

Conclusion

The percent cation extracted (%E) and the stability constants β in methanol for the complexation of alkali cations by *p-tert*-butyldihomooxalix[4]arene tetra(diethyl)amide⁽²⁵⁾ and *p-tert*-butylcalix[4]arene tetra(diethyl)amide show the more stable complex formation for bigger cations (K⁺, Rb⁺ and Cs⁺) with dihomooxalix[4]arene, that is in acceptance with the effect of hole size of calixarenes.

Also comparing stability constants β in methanol for the complexation of alkaline-earth cations, shows the less stable complex formation for *p-tert*-butyldihomooxalix[4]arene tetra(diethyl)amide (figure 4).

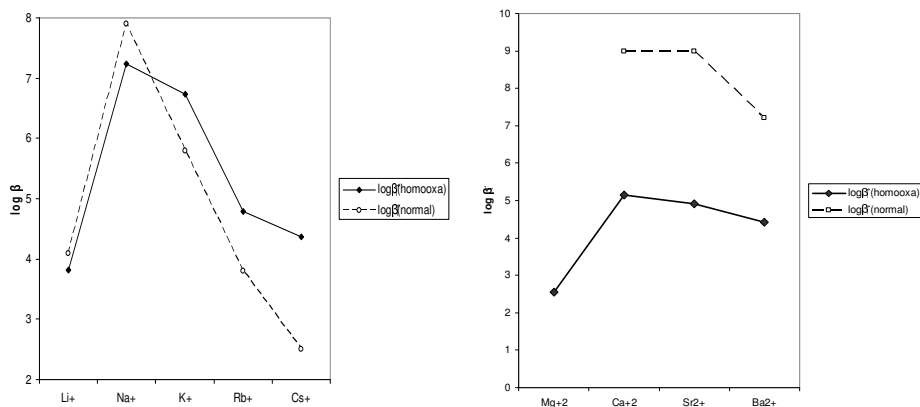


Figure 4 Logarithm of stability constants ($\log \beta$) in methanol vs. cations for the Complexation of alkaline and alkaline-earth cations by *p-tert*-butyldihomooxalix[4]arene tetra(diethyl)amide and *p-tert*-butylcalix[4]arene tetra(diethyl)amide.

References

- [1] C.D.Gutsche, Calixarenes, The royal Society of Chemistry. Cambridge, England, 1989.
- [2] P.M.Marcos, J.R.Ascenso, M.A.P.Ssegurado, J.L.C.Pereira, J. Incl. Phenom. Macrocyclus. Chem. 2002, 42, 281.
- [3] S. Félix, J. R. Ascenso, R. Lamartine, J. L. C. Pereira, Tetrahedron, 1999, 55, 8539.
- [4] F.Arnaud-Neu, G.Barret, S.Fanni, D.Marrs, W.McGregor, M.A.McKervey, M.J.Schwing-Weill, V.Vetrogon and S.Wechsler, J. Chem. Soc. Perkin Trans., 1995, 2, 453.

Spectroscopy
Molecular Structures
Physical Chemistry of Plasma

(B)

LOW ENERGY ELECTRON MOLECULE INTERACTIONS

A. Stamatović

Fizički fakultet, 11001 Beograd, P.O.Box 368, SCG

Abstract

The references to the basic literature and the newest publications in the field of Low Energy Electron Molecule Interactions have been given along the review of the basic classifications of the processes involved.

Introduction

Interaction of electron with a matter in a wide range of energies, from subthermal to relativistic, has revealed a lot of knowledge that opened new fields of Science and found numerous applications. The Low Energy Electron Molecule Interactions (LEEMI) [1] are particularly interesting because they cover the energy range of the living matter, i.e. Biology, Chemistry, Physics and Physical Chemistry of it. The importance of scientific research in this field has been confirmed by the fact that it is "active" for more than one century giving new results and applications. The energy range meant under "Low Energy" in this case, expressed in temperature, starts just above the liquid helium temperature and ends approximately at the values characteristic for combustion flames and low temperature plasmas.

Classification of the processes involved

One could classify the LEEMI according to the scheme used in scattering classification to elastic and inelastic interaction [2,3]. Although the elastic scattering is giving very valuable information about the scattering potential of a target, a multitude of processes encompassed by inelastic scattering make it very attractive and dominant field of research. Taking in account the energy of interaction in a growing order one could talk about interaction with the following targets: **Agregates of molecules** [4] giving information about: relative abundances (neutrals, ions); magic numbers (neutrals, ions); binding energies [5]; excitation [6]. **Biological targets** giving information about: pos. & neg. MS of biomolecules & derivatives [7]; structures & rearrangement; dissociative attachment (radiation damage); **Gaseous and ionic targets from non-thermal plasma** [8] giving, through different spectral analysis, information on target and processes involved: optical spectroscopy; pos. & neg. Mass Spectrometry; binding energies; fragmentation patterns; structures & rearrangement; dissociative attachment, all types of excitation; reactivity of excited species; forbidden transitions (optically inactive, not allowed); translational/internal energy transfer.

Theory

The classical theory of scattering does not describe correctly the interaction in the lower part of the mentioned energy range. Great effort has been and continues to be

invested in creating an adequate theory [2,3,9,10]. The agreement with the experimental results, and the energy range in which it exists, are getting better, but satisfying results are available only for the targets of modest complexity.

Experiments

Rather wide range of the experimental geometries have been used in this field [3]. Two of them, a swarm and a crossed beam experiments, have been mostly used [7,8]. The swarm experiments are less complicated and closer to the processes in Nature on the Earth, but it is not always easy to interpret correctly the results of measurements. The single collision, crossed beam experiments are straightforward in principle but very complex and demanding in practice.

Conclusion

Theoretical and experimental research in the field of LEEMI have given a rich contribution to basic understanding of the Nature and a valuable test of the Quantum Chemistry and Quantum Physics premises.

Acknowledgment

Partial financing of the research in this field by The Ministry of Science and the Environmental Protection of Republic Serbia and by WUS Austria, Office Belgrade are gratefully acknowledged.

References

- [1] Int.J. Mass Spectrom. 2001, 205, Nos.1-3, Special issue: Low Energy Electron-Molecule Interactions, and 2004, 233, Nos. 1-3, Special issue in honor of Tilmann D. Märk
- [2] H.S.W. Massey, E.H.S. Burhop, H.B. Gilbody, *Electronic and Ionic Impact Phenomena, Vol. II: Electron Collisions with Molecules and Photoionization*, Clarendon Press, Oxford, 1969.
- [3] L.G. Christophorou (Ed.), *Electron-Molecule Interactions and Their Applications*, Vol. 1 and 2, Academic Press, Orlando, FL, 1984.
- [4] M.A. Johnson, T.D. Märk, Van der Waals cluster and mass spectrometry: meeting the challenge of size-dependence in the nanosolvation regime, *Int. J. Mass Spectrom.* 220 (2002) 97.; A. Stamatovic, T.D. Märk, Study of clusters by mass spectrometry, *Rapid Commun. Mass Spectrom.*, 1991, 5, 51; O. Echt, T.D. Märk, Clusters and cluster ions, in: J. London, G. Trautner, J. Holmes (Eds.), *Encyclopedia of Spectroscopy*, Academic Press, London, 1999, p. 327.
- [5] R. Parajuli, S. Matt, O. Echt, A. Stamatovic, P. Scheier, T.D. Märk, Binding energies of neon and krypton clusters, *Chem. Phys. Lett.*, 2002, 352, 288; K. Gluch, S. Matt-Leubner, L. Michalak, O. Echt, A. Stamatovic, P. Scheier, T.D. Märk, High resolution measurements of kinetic energy release distributions of neon, argon, and krypton cluster ions using a three sector field mass spectrometer, *J. Chem. Phys.*, 2004, 120, 2686; R. Parajuli, S. Matt, A. Stamatovic, T.D. Märk, P. Scheier, Unimolecular dissociation of nonstoichiometric oxygen cluster ions On^+ . ($n = 5, 7, 9, 11$): a switch from O3 to O2 loss above size $n = 5$, *Int. J. Mass Spectrom.*, 2002, 220, 221

- [6] O. Echt, R. Parajuli, S. Matt, A. Stamatovic, P. Scheier, T.D. Märk, Kinetic energy release in exciton-driven metastable decay of neon cluster ions, *Chem. Phys. Lett.* 2002, 61, 511.
- [7] S. Denifl, S. Ptasinska, P. Scheier, T.D. Märk, Electron impact ionization of 5- and 6-chlorouracil: appearance energies, *Int. J. Mass Spectrom.* 2004, 232, 99; R. Balog, J. Langer, S. Gohlke, M. Stano, H. Abdoul-Carime, E. Illenberger, Low energy electron driven reactions in free and bound molecules: from unimolecular processes in the gas phase to complex reactions in a condensed environment, *Int. J. Mass Spectrom.* 2004, 233, 267; S. Denifl, S. Matejcik, S. Ptasinska, B. Gstir, M. Probst, P. Scheier, E. Illenberger, T.D. Märk, Electron attachment to chlorouracil: a comparison between 6-CIU and 5-CIU, *J. Chem. Phys.* 2004, 120, 704.
- [8] E. Illenberger, J. Momigny, *Gaseous Molecular Ions. An Introduction to Elementary Processes Induced by Ionization*, Steinkopff Verlag, Darmstadt/Springer-Verlag, New York, 1992.; T.D. Märk, Free electron attachment to van der Waals clusters, *Int. J. Mass Spectrom. Ion Proc.* 1991, 107, 143; W. Lindinger, T.D. Märk, F. Howorka (Eds.), *Swarms of Ions and Electrons in Gases*, Springer Verlag, Wien, New York, 1984, ISBN 3-211-81823-5, 1-311; C.A. Mayhew, R. Peverall, C.M. Timperley, P. Watts, A selected ion flow tube study of the reactions of OH. with a number of fully and partially halogenated methanes, *Int. J. Mass Spectrom.* 2004, 233, 155; T. Wang, D. Smith, P. Španel, Selected ion flow tube, SIFT, studies of the reactions of H_3O^+ , NO^+ and O^{2+} with compounds released by *Pseudomonas* and related bacteria *Int. J. Mass Spectrom.* 2004, 233, 245; E. Illenberger, Electron attachment reactions to free and bound molecules, in: C.Y. Ng (Ed.), *Photoionization and Photodetachment, Part I and II*, World Scientific, Singapore, 2000.
- [9] P. Scheier, H. Deutsch, K. Becker, T.D. Märk, Calculations of electron-impact cross sections for the fragmentation and dissociative ionization of fullerenes using a semi-empirical method, *Int. J. Mass Spectrom.* 2004, 233, 293; H. Deutsch, P. Scheier, K. Becker, T.D. Märk, Calculated cross sections for the electron impact detachment from negative ions using the Deutsch-Märk (DM) formalism, *Chem. Phys. Lett.* 2003, 382, 26./10/ M. Allan and I.I. Fabrikant, Threshold peaks and structures in vibrational excitation of CH₃I by electron impact, *J. Phys. B* 2002, 35, 1025.

SURFACE ENHANCED RESONANCE RAMAN SPECTROSCOPY IN THE STUDIES OF IMMOBILIZED REDOX ENZYMES

S. Todorović¹, D. Murgida² and P. Hildebrant²

¹Laboratory for Raman Spectroscopy, Instituto de Tecnologia Química e Biológica - Universidade Nova de Lisboa, Apartado 127, 2781-901, Oeiras, Portugal, ²Max-Volmer-Laboratorium für Biophysikalische Chemie Institut für Chemie, Technische Universität Berlin Strasse des 17. Juni 135, D-10623 Berlin, Germany.

Abstract

In order to develop a general methodology for analysing active site structure and reaction dynamics of immobilized redox enzymes, and therefore elucidate the molecular basis of their functioning in bioelectronic devices, we have studied different redox proteins. The cytochrome P450 (Cyt-P450) was electrostatically bound to the self-assembled monolayers of ω -carboxylalkanethiols that were covalently attached to Ag electrodes. The redox reaction of the immobilized enzyme was followed by Surface Enhanced Resonance Raman Spectroscopy (SERRS). In the presence of Cyt-P450 in the bulk solution, SERR spectra of adsorbed Cyt-P450 display characteristic vibrational band pattern found in heme *b* proteins. Potential dependent SERR experiments revealed Nernstian behaviour.

Introduction

Enzymes immobilised on electrodes represent key elements for bioelectronic devices that can be applied as biocatalysts, biosensors, or nanostructured electronic switches [1]. The most versatile approach to immobilise enzymes on a conducting support, such as Ag electrode, is based on coatings of bifunctional thiols that form self-assembled monolayer (SAM) [2]. By choosing appropriate headgroups, proteins can be adsorbed on these biocompatible layers via different types of intermolecular interactions (electrostatic, hydrophobic, hydrogen-bonding, or covalent attachment). SAMs may also be used as building blocks for lipid-bilayer-type coatings, offering thereby the possibility for immobilising even membrane proteins.

Resonance Raman (RR) techniques have the advantage of selective enhancement of the vibrational bands of cofactors in chromoproteins when excited in resonance with an electronic transition of the chromophore. Thus, it is possible to study the active site structure of enzymes without interference of Raman bands originating from apoprotein. This molecular RR effect can be combined with the surface enhanced Raman effect, resulting in surface enhanced resonance Raman – SERR spectroscopy. SERRS is based on the enhancement of the Raman scattering for molecules in the proximity of (sub-) microscopically roughened Ag surfaces when the excitation line is in resonance with the surface plasmons of the metal. Consequently, appropriate choice of the excitation conditions allows probing the cofactors solely of the adsorbed enzymes [3-6]. Using an electrode as SERR-active material, variations of the electrode potential can be used to monitor potential-dependent processes, *i. e.*, redox processes of enzymes.

Cytochromes P450 constitute a superfamily of *b*-type heme proteins that catalyse the monooxygenation of a wide variety of apolar compounds by molecular oxygen, through the insertion of one oxygen atom. They metabolize hydrophobic compounds of endogenous origin such as cholesterol, lipids and steroids as well as a numerous exogenous compounds like drugs and pollutants. It is known that human liver cytochrome P450, CYP3A4, metabolizes over 50% of all the drugs with known metabolic pathways. All cytochrome P450 enzymes share a common active site structure and reaction cycle. Members of this superfamily have been isolated from plants, bacteria and yeast, as well as from mammals where they play a major role in determining the response of the organism to exogenous chemicals [7]. Moreover, cytochrome P450 offers the advantage that three-dimensional structures are available for the enzymes from various organisms. Furthermore, the mechanism of the reaction cycle in solution is largely understood and the various states have been characterized by different techniques including RR spectroscopy. Availability of structural and spectroscopic reference data for cytochrome P450 facilitates the development of correlations between molecular structure and dynamics of the active site with the biological function. So far no bioelectronic devices based on cytochrome P450 were reported although they can be of great importance in synthetic chemistry [8; 9]. The presented work is devoted to research, design, development and application of cytochrome P450 based biosensors and bioelectronics.

Experimental part

SERR set-up. A Raman microscope (Jobin Yvon XY) equipped with nitrogen cooled CCD detector was adapted for vertical sample arrangement by incorporating a mirror and a long working distance objective (20x; N.A. 0.25) to the microscope revolving nose. All measurements were performed with the 413 nm excitation line of a krypton ion laser (Coherent Innova 302), which is well in resonance with the Soret electronic transition of heme prosthetic groups of the proteins and with the surface plasmons of the Ag electrodes. The spectral resolution was ca. 2 cm^{-1} and the increment per data point ca. 0.25 cm^{-1} . The laser power at sample was varied between 0.5 and 5 mW.

Band fitting and global component analysis of the SERR spectra were performed with a Linux based homemade software.

SERR spectra were measured in the high frequency region ($1100\text{-}1700\text{ cm}^{-1}$), where the highly specific marker bands for redox, ligation and spin state of the heme groups are localized.

Electrochemical cell. The three-electrode electrochemical cell, designed and constructed for this particular application, consists of a Delrin body with two quartz windows for measurement and visual inspection, a loop and sensor for temperature control and septa for sample injection and purging. As counter and reference electrodes a platinum wire and a miniature dry Ag/AgCl system were used. The working electrode consists of a silver ring mounted on a rotating shaft to avoid laser induced degradation of the sample. The whole electrochemical cell was mounted on an XYZ micrometric stage for final positioning and optical alignment in front of the microscope objective.

Electrode preparation. After mechanical polishing, the Ag ring electrode was mounted into the cell for electrochemical cleaning and subsequent electrochemical microscopic roughening in order to create the SERR active surface. The surface of the Ag ring was then modified by dipping it into ethanolic solutions of ω -functionalized alkanethiols for 24 hs. After careful rinsing and drying, the modified electrode was mounted into the electrochemical cell containing ca. 0.5 μ M solution of the enzyme in a 12.5:12.5 mM mixture of phosphate buffer (pH 6.5- 7.5) and K_2SO_4 . Prior to the addition of the protein, the electrolyte solution was flushed with Ar for at least 1 hour, and kept under Ar overpressure during the experiments.

Results and Discussion

The present studies were performed with bacterial Cyt-P450cam from *Pseudomonas putida*, obtained by overexpression of the enzyme in *E.coli*. The natural function of this enzyme is catalyzing the stereospecific hydroxylation of camphor to form 5-*exo*-hydroxycamphor.

The development of bioelectronic devices based on redox enzymes requires the immobilization of the proteins on electro-active surfaces in a well defined manner. This implies that the electrodes have to be chemically modified to provide a biocompatible surface where the protein can be fixed in a uniform orientation, while keeping good accessibility for the substrate, maintaining the native active site structure and ensuring good electrochemical communication. Fulfilling these conditions requires a systematic study of the immobilization procedures as well as a powerful analytical method able to probe the enzyme structure.

Our strategy for the enzyme immobilization is based on the modification of Ag electrodes with self-assembled monolayers (SAMs) of ω -functionalized alkanethiols (Figure 1).

The immobilization of the enzymes was followed by SERR spectroscopy at 413 nm, i.e. in resonance with the Soret electronic transition of the heme group and with the surface plasmons of the metal. Under these conditions, the vibrational modes of the heme group are enhanced up to six orders of magnitude, allowing a selective detection of the redox active centers without interference of the protein matrix. However, surface enhancement effect is strongly dependent on the distance, such that only those molecules in close contact with the modified electrode will be enhanced. Thus, the adsorbed molecules can be detected without interference of species in the bulk solution, which are nevertheless in a fairly low concentration (ca. 0.5 μ M) and out of focus.

The SERR technique allows not only detecting protein adsorption but, due to its high sensitivity towards redox, spin and ligation states, provides direct information about the heme pocket structure. SERR spectra were measured in the high frequency region (1100-1700 cm^{-1}), where the majority of the bands originates from heme in-plane skeletal vibrations. Furthermore, potential-dependent SERR measurements yield a detailed description of the redox equilibria and dynamics. The component analysis of the data revealed that in the reduced state Cyt-P450 is in the ferrous low spin state while the ferric state has to be characterized as a mixture of a high spin ($S=5/2$) and low spin ($S=1/2$) components.

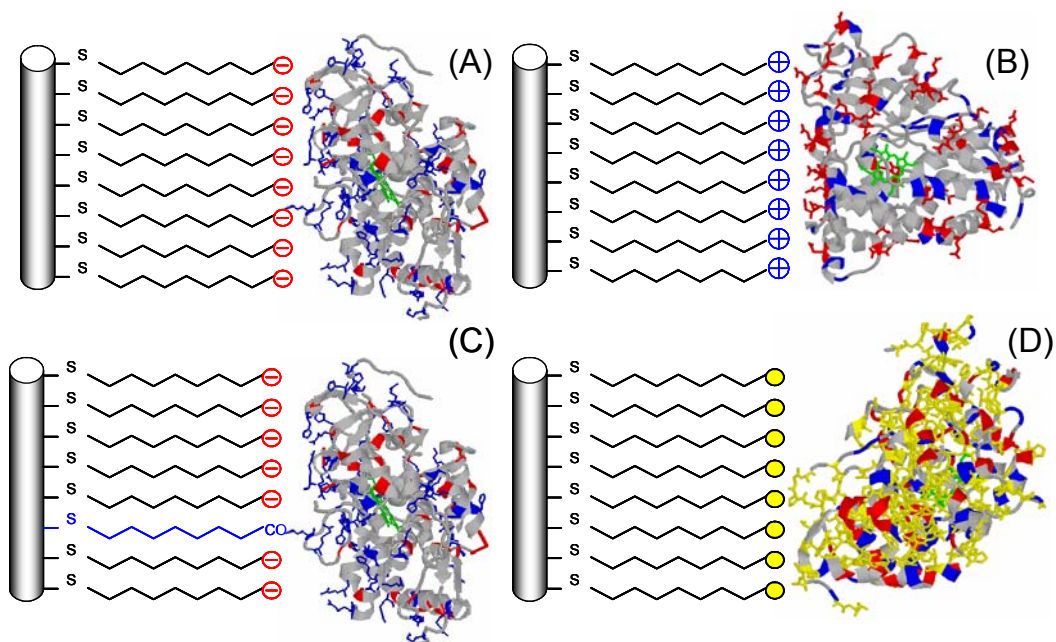


Figure 1. Cytochrome P450cam immobilized on Ag electrodes coated with SAMs of ω -functionalized alkenethiols via electrostatic interactions (A and B), covalent attachment (C) and hydrophobic interactions (D). The color code for the protein is: green for heme; blue for basic residues, red for acidic residues and yellow for hydrophobic residues. For the SAMs, red denotes carboxyl, blue amino and yellow methyl groups.

The surface of Cyt-P450cam exhibits a very heterogeneous charge distribution which includes positive, negative and hydrophobic patches. It could be immobilized on carboxyl-, amino- and methyl-terminated SAM-modified electrodes of different chain lengths (Figure 1), as shown by SERR. Electrostatic adsorption gives rise to SERR signals which are significantly larger than for the hydrophobic case, in which the immobilization is only entropically driven. Among the two types of SAMs used for electrostatic immobilization, carboxyl-terminated alkanethiols showed a larger affinity than amino-terminated ones. Most likely this is due to a better alignment of the protein dipole moment with the electric field, rather than to specific interactions. Covalent attachment via cross-linking reactions resulted in a non-specific immobilization of the enzyme.

For both electrostatic and hydrophobic adsorption, stationary potential dependent SERR measurements show that the protein can efficiently communicate with the electrode. As shown in Figure 2, at negative potentials the most prominent marker band (ν_4) appears at 1361 cm^{-1} , which is a typical position for a reduced heme, and upshifts to 1373 cm^{-1} at 150 mV indicating an oxidized protein. As expected, interme-

diate potentials show both contributions. This is in agreement with earlier works on cytochrome *c* and some model compounds, in which it was observed that the most of the marker bands are shifted upfield upon oxidation, reflecting changes in the electron density and the porphyrin structure upon oxidation [3-6].

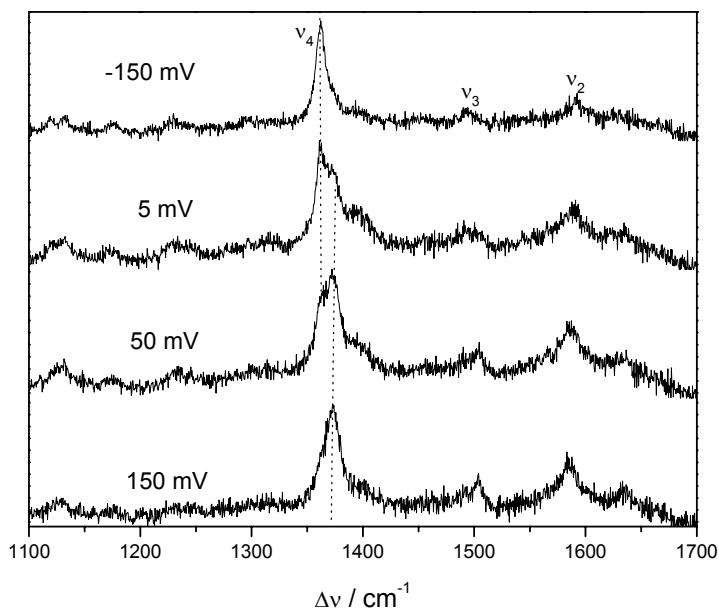


Figure 2. SERR spectra of Cyt-P450_{cam} adsorbed on Ag electrodes modified with 11-carboxyl undecanethiol SAMs as a function of the applied potential (*vs.* Ag/AgCl).

The RR spectrum of ferrous Cyt-P450_{cam} in solution indicates a native five coordinated high spin heme configuration [10]. Upon adsorption, the positions and relative intensities of the heme bands are modified such that, for example, the ν_4 band is shifted from 1351 cm^{-1} in solution to 1361 cm^{-1} in the adsorbed state. These changes strongly suggest that a substantial fraction of the adsorbed protein undergoes a conformational transition which implies the removal of the cystein-357 axial ligand to form the so-called P420 form of the enzyme, in which the axial ligands are most likely a histidine residue and a water molecule [10].

For determination of the redox potentials, SERR spectra were measured as a function of potential applied to the Ag electrode. Employing the component analysis, the potential dependent equilibrium of the reduced and oxidized forms of the enzyme was determined quantitatively. The corresponding Nernstian plots are linear and allow the determination of the number of electrons taking place in the electron transfer process.

References

- [1] Willner, I. and Katz, E., *Angew.Chem.Int.Ed.* 2000, 39, 1180;
- [2] Ferreti, S., Paynter, S., Russell, D.A., and Spasford, K.E., *Trends.Anal.Chem.* 2000, 19, 530;
- [3] D.H. Murgida, P. Hildebrant, *J.Phys.Chem.B.* 2001, 105, 1578;
- [4] D.H. Murgida, P. Hildebrant, *J.Mol.Struct.* 2001, 565-566, 97;
- [5] D.H. Murgida, P. Hildebrant, P., *J.Am.Chem.Soc.* 2001, 123, 4062;
- [6] D.H. Murgida, P. Hildebrant, *Angew.Chem.Int.Ed.* 2001, 40, 728;
- [7] P. Anzenbacher, E. Anzenbacherova, , *Cell. Mol. Life Sci.*, 2001, 58, 737;
- [8] K.M. Koeller, C.H. Wong, *Nature* 2001, 409, 232;
- [9] Fang, J.M., Lin, C.H., Bradshaw, C.W., and Wong, C.H., *J.Chem. Soc. Perkin Trans.* 1995, 1, 967;
- [10] A.V. Wells, P. Li, P.M. Champion, S.A. Martinis, S.G. Sligar, *Biochemistry*, 1992, 31, 4384.

MALDI TOF OF CARBON CLUSTERS

O. Nešković

Vinča Institute of Nuclear Sciences, P.O. Box 522, 11000 Belgrade, SCG

Abstract

Some of the most significant discoveries and achievements concerning the MALDI TOF mass spectra and gas phase ion chemistry of carbon clusters are reviewed. These include endohedral fullerenes comprising recent data on ion beam implantation and fullerene derivatives. Matrix assisted laser desorption/ionization (MALDI) coupled with reflectron time-of-flight (TOF) mass spectrometry has been applied to the analysis of such clusters. Using a structurally similar model analyte, this investigation includes the screening of two different compounds regarding their suitability as MALDI matrices. The appearance of positive- and negative-ion mass spectra has been detailed, and the analysis has been supported by delayed extraction experiments.

Introduction

Carbon clusters, in general, and fullerenes, in particular, owe their discovery to mass spectrometry [1,2]. This article does not attempt to give a comprehensive review on carbon clusters and not even a complete review of their mass spectrometry and gas phase ion chemistry. Rather a more personal review is planned covering, out of necessity, a rather limited range of topics that have interested our laboratory in the past years. Within these topics an attempt will be made to cover the most important work done worldwide.

MALDI TOF Mass Spectrometry

Matrix assisted laser desorption/ionization coupled with reflectron time-of-flight mass spectrometer is an extremely powerful tool for the analysis of derivatized fullerenes in very low quantities, although proper choice of matrix is essential. The matrix is typically an organic molecule that absorbs light strongly at the wavelength of the laser being used. It must be capable of incorporating and isolating the analyte in a solid matrix (usually crystalline), and it must facilitate analyte ionization. In a particular sense, the matrix and the analyte should both be soluble in the same solvent or mixture of solvents. The ideal matrix produces strong, symmetrical peaks showing a minimum of unimolecular decay. It is thought that gas-phase proton transfer reactions are responsible for the formation of analyte ions, so the gas-phase acidity of the matrix must play an important role. The prominent use of MALDI as a mean to analyze fullerene based materials is most evident from the frequent quotations in the synthetic literature. The variety of different fullerene derivatives makes it rather unlikely that one particular matrix compound is of universal applicability. The present investigation is concerned with analysis of fullerenes (Figures 1 and 2), endohedral metallofullere-

nes: $\text{Li}@C_{60}$, $\text{Li}@C_{70}$ and $\text{Li}_2@C_{70}$, fulleranol $C_{60}(\text{OH})_{16}$ and derivatized fullerene $C_{60}C_{15}H_{29}N_3O_4$. However, the best results for the analytes investigated here have been obtained employing α -cyano-4-hydroxycinnamic acid (CHCA) and 2-[(2E)-3-(4-*tert*-butylphenyl)-2-methylprop-2-enylidene]malononitrile (DCTB).

All MALDI mass spectrometer experiments have been accomplished by the use of a commercial reflectron-time-of-flight Voyager de Pro (AB Applied Biosystem, UK). The sample activation has been achieved applying a nitrogen laser providing ultraviolet light of 337 nm with a pulse width of 3 ns and a pulse frequency of 1.5 Hz. The instrument operates on a continuous acceleration voltage of 20 kV. The drift region preceding the reflectron houses a deflection electrode (the ion gate), which allows the selection of ions as a function of their arrival times at the gate and has been utilized here for delayed extraction experiments. Each individual TOF mass spectrum shown represents the accumulation of 200 single-laser-shot spectra. The resolution remained insufficient to resolve the isotopic pattern of the ions in the mass range of interest.

Endohedral Fullerenes

One of the fascinating properties of fullerenes is their ability to trap atoms and small molecules inside the cage. A wide variety of metal atoms may reside in this space and form endohedral fullerenes. The first evidence for endohedral metallofullerenes was reported soon after discovery of C_{60} in 1985. However, only in 1991 could endohedral metallofullerenes be isolated in macroscopic amounts. This was achieved by using laser- or arc-vaporization [3] of graphite-metal composites in helium. Endohedral fullerenes are prepared by the arc discharge method by adding the appropriate materials during the formation of the fullerenes. High temperature and high pressures are employed for the encapsulation of noble gas atoms into C_{60} . Endohedral compounds can also be prepared by ion implantation. This technique has been applied to lithium and other alkali atom fullerenes [4,5]. We have ionized a mixture of the lithium compounds $\text{Li}@C_{60}$, $\text{Li}@C_{70}$ and $\text{Li}_2@C_{70}$ by MALDI TOF and characteristic mass spectrum with its isotope pattern is clearly observed. Singly charged cations of the metallofullerenes were completely unreactive in the gas phase with oxygenated compounds such as ethylene oxide; however, the corresponding neutral species appear to react readily with oxygenated species. Collisional dissociation of the ionized endohedral fullerenes listed above revealed multiple C2 loss (either as sequential C2 loss or larger C2n eliminations) to generate similar terminal fragmentation products which might be predicted due to the similar ionic radii of the encapsulated metals.

Fullerenol $C_{60}(\text{OH})_{16}$

Since the discovery of fullerenes, C_{60} has elicited intense interest and recent intensive chemical studies have revealed the diverse reactivity of C_{60} . Application in biomedical research is quite limited because native C_{60} is soluble only in polar organic solvent. One of the first chemical methods for polyfunctionalization of molecule C_{60} with the aim to obtain water-soluble derivative was starting from $C_{60}\text{Br}_{24}$ [6]. Two-step synthesis yielded fulleranol $C_{60}(\text{OH})_{16}$. The MALDI mass spectrum of a

$C_{60}(OH)_{16}$ is displayed in Figure 3. In both experiments (CHCA and DCTB) signal at $m/z = 993.20$ is clearly detected.

MALDI TOF of novel fullerene bisadduct derivative $C_{60}C_{15}H_{29}N_3O_4$

The 1,3-dipolar cycloaddition reaction was used to synthesis of bisadduct were detected in the MALDI TOF mass spectrum (Figure 4). derivative of C_{60} [7]. M^+ and $[M-H]^+$ positive ions, $m/z = 1035.56$ and 1036.48 , were detected in the MALDI TOF using CHCA and DTCB matrices.

Conclusion

A MALDI TOF mass spectrometry with matrices CHCA and DCTB has provided us with a new method for detecting fullerene and fullerene derivatives. It should be possible to apply this method to other fragile fullerene derivatives or biomolecules.

Acknowledgments

This work was financially supported by the Ministry of Science and Environmental Protection, Republic of Serbia, under Project No. 1995.

References

- [1] J. Berkowitz, W.A. Chupka, J. Chem. Phys., 1964, 40, 2735.
- [2] H.W. Kroto, J.R. Heath, S.C. O'Brien, R.F. Curl, R.E. Smalley, Nature, 1985, 318, 162.
- [3] Y. Chai, T. Guo, C. Jin, R.E. Haufler, L.P.F. Chibante, J. Fure, L. Wang, J.M. Alford, R.E. Smalley, J. Phys. Chem., 1991, 95, 7564.
- [4] R. Tellmann, N. Krawez, S-H. Lin, I-V. Hertel, E.E.B. Campbell, Nature, 1996, 382, 407.
- [5] A. Đerić, M. Veljković, O. Nešković, M. Miletić and K. Zmbov,
- [6] Full. Sci. Tech., 2000, 8(6), 461.
- [7] A. Đorđević, O. Nešković, M. Veljković, J. Čanadi, M. Vojinović-Miloradov, V. Đorđević-Milić, Tetrahedron, 2004, in press.
- [8] S. Bosi, L. Feruglio, D. Milic and M. Prato, Eur. J. Org. Chem., 2003, 24, 4741.

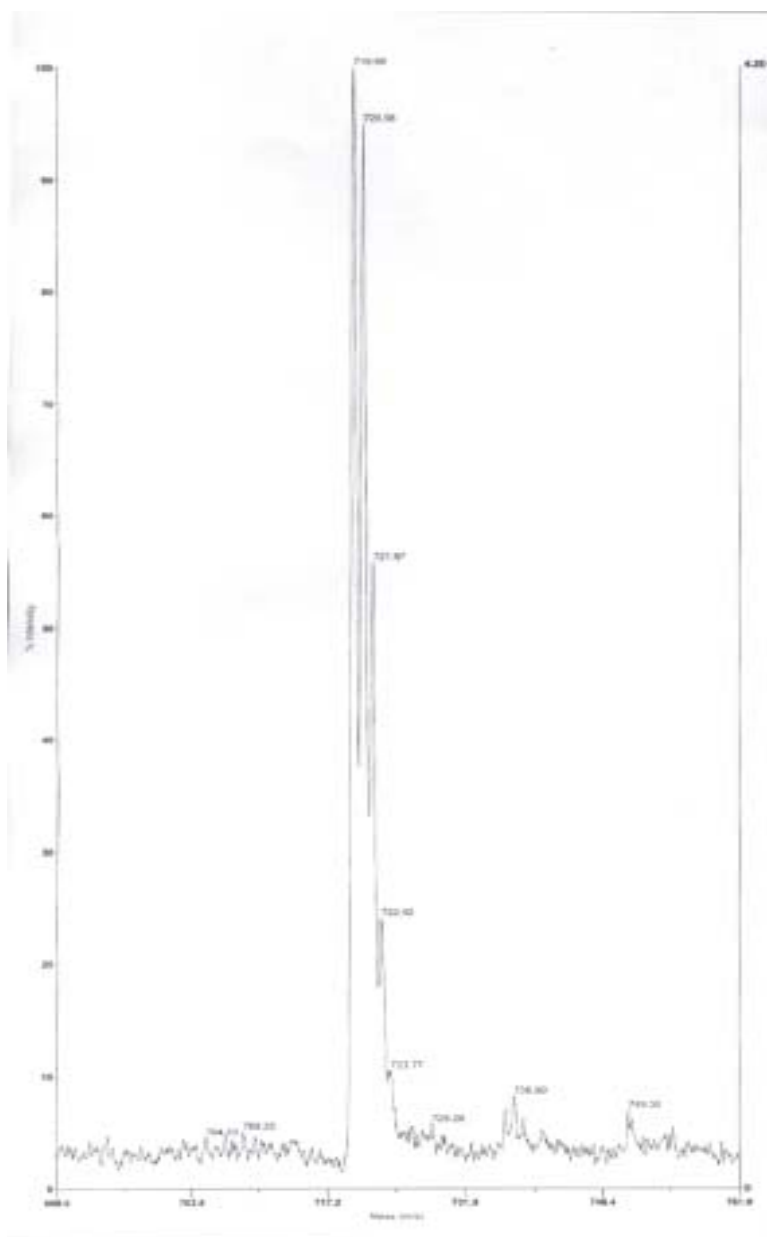


Figure 1. Partial positive-ion MALDI mass spectra of the C_{60} using CHCA as the matrix.

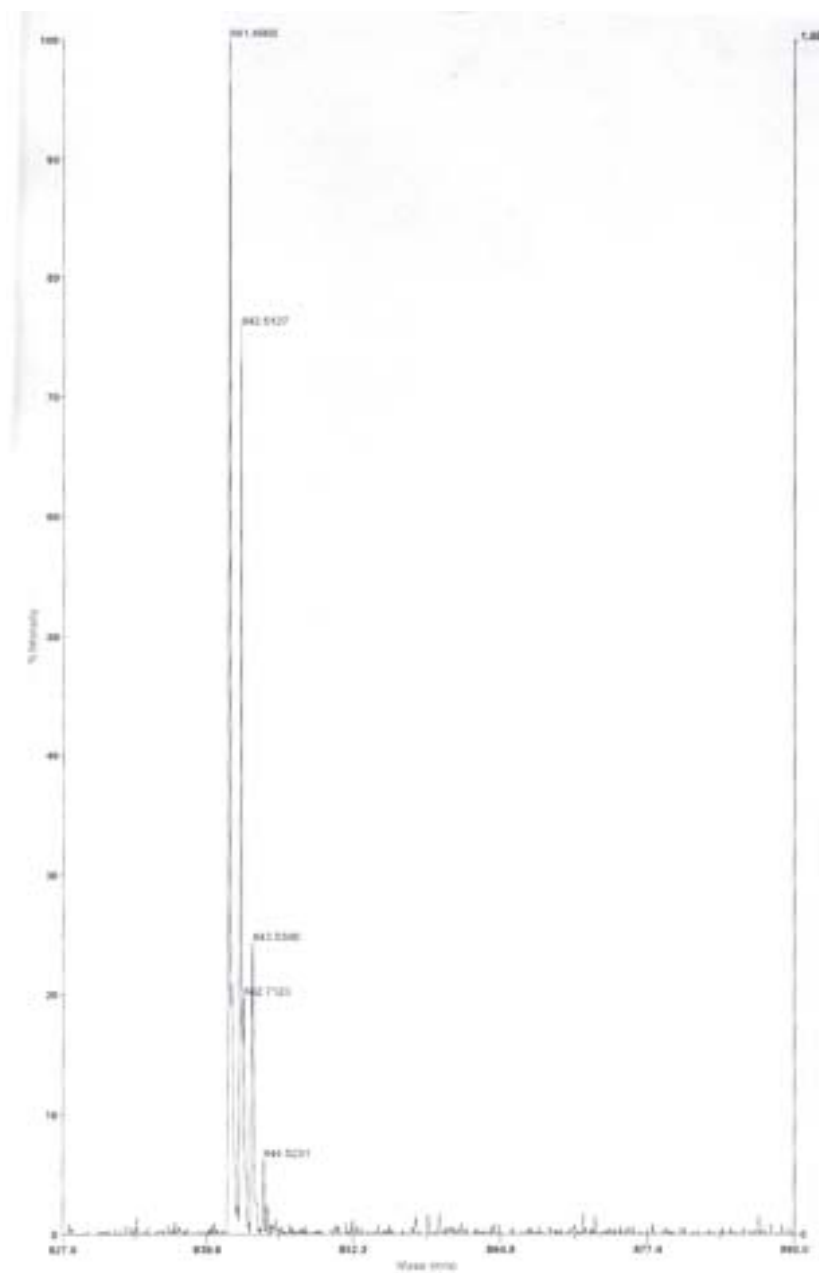


Figure 2. Partial positive-ion MALDI mass spectra of the C_{70} using CHCA as the matrix.

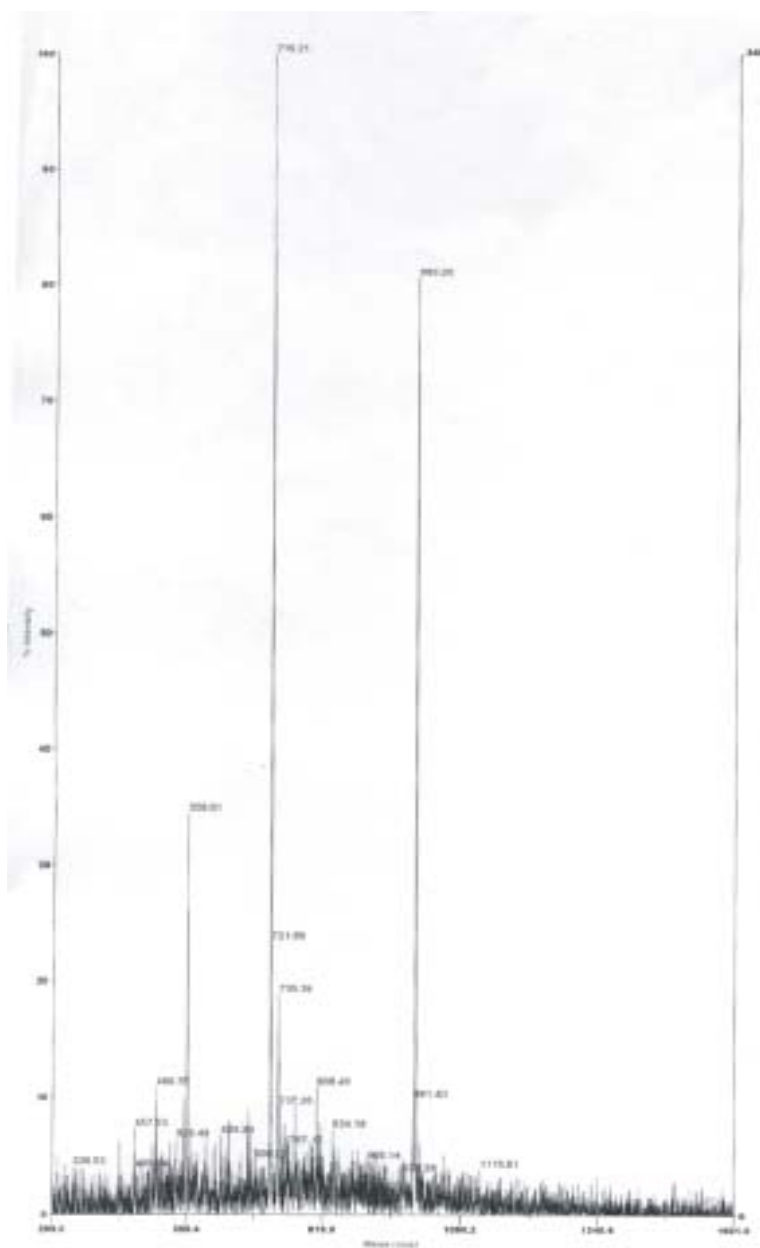


Figure 3. MALDI TOF mass spectrum of the fullereneol $C_{60}(OH)_{16}$ containing sample using DCTB as a matrix and the corresponding negative-ion results.

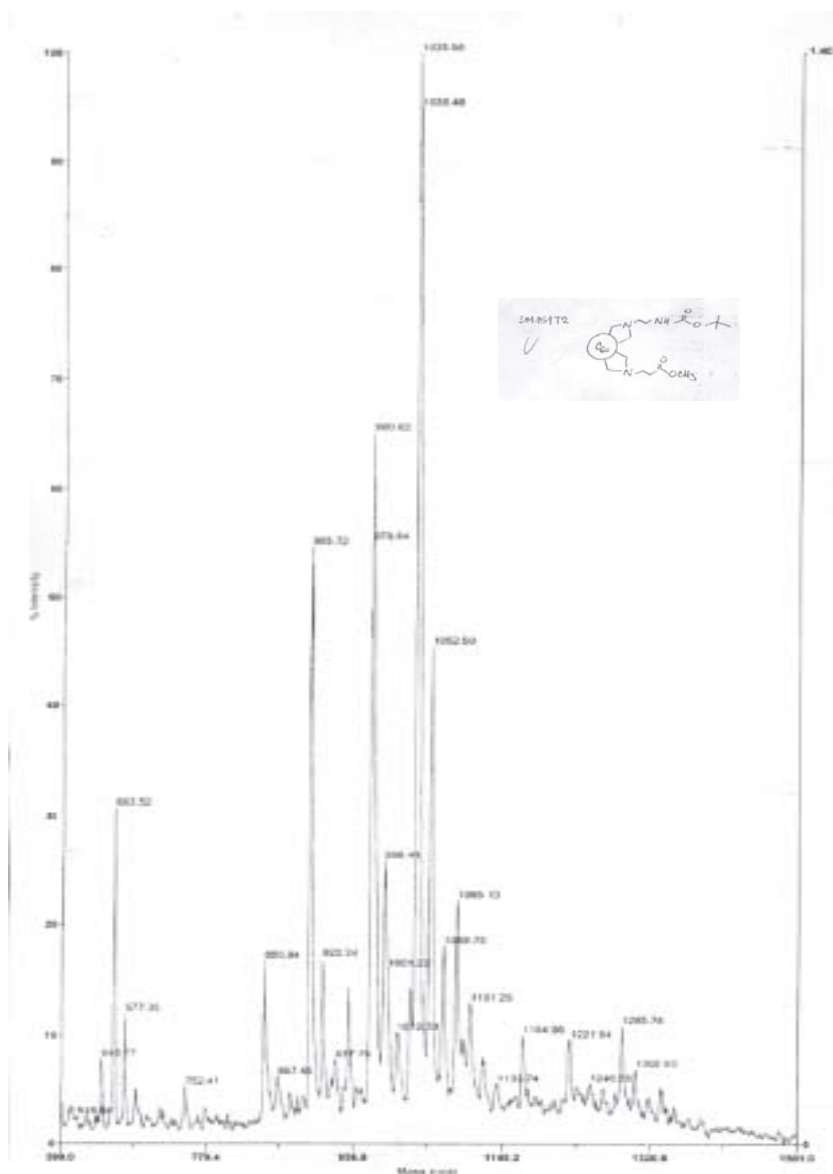


Figure 4. MALDI TOF mass spectrum of the novel fullerene bisadduct derivative $C_{60}C_{15}H_{29}N_3O_4$. M^+ and $[M-H]^+$ positive ions, $m/z=1035.56$ and 1036.48 , were detected using CHCA and DCTB matrices.

DETERMINATION OF OPTO-THERMAL PARAMETERS OF LIQUIDS BY THERMAL LENS SPECTROMETRY –TLS, AND THEIR EFFECTS ON TLS MEASUREMENTS IN CHEMICAL ANALYSIS

M. Franko

*Nova Gorica Polytechnic, Laboratory of Environmental Research,
P.O.B. 301, SI-5001 Nova Gorica, Slovenia*

Introduction

In thermal lens spectrometry (TLS) the absorbance is measured indirectly via the so-called thermal lens effect, which was described for the first time by Gordon et al [1]. Optical absorption and subsequent heating of the sample in regions confined by the dimensions of the excitation laser beam (Fig. 1) changes the temperature distribution across the irradiated sample positioned usually in the focal point of excitation beam. A lens-like element is created within the sample through the temperature dependence of refractive index of the sample, which influences the radial intensity distribution of the beam used to probe the effect. The probe beam intensity changes with a characteristic time constant t_c , and the change of light intensity on the axis of the probe beam can be described by different theoretical models such as the one given in Eq. 1 for a dual beam (pump/probe) configuration [2].

$$I(t) = I(0) \left[1 - \frac{\theta}{2} \tan^{-1} \left(\frac{2mV}{\left((1+2m)^2 + V^2 \right) (t_c/2t) + 1 + 2m + V^2} \right) \right]^2 \quad (1)$$

In Eq. (1) $I(t)$ is the temporal dependence of the probe laser beam intensity at the detector, $I(0)$ is the initial value of $I(t)$ at time $t = 0$, and θ is the thermally induced phase shift of the probe beam after its passing through the sample, which is described in more detail by Eq.2, where the meanings of parameters m and V are also given.

$$\theta = - \frac{P_e A_e l_0}{K \lambda_p} \left(\frac{dn}{dT} \right)_p \quad ; \quad V = \frac{Z_1}{Z_c} \quad ; \quad m = \left(\frac{\omega_p}{\omega_e} \right)^2 \quad (2)$$

P_e is the excitation beam power, A_e is the absorption coefficient at the excitation beam wavelength, λ_p is the probe beam wavelength, l_0 is the sample thickness, $(dn/dT)_p$ is the temperature dependence of the refractive index of the sample, and k its thermal conductivity. ω_p is the probe beam spot size at the sample, ω_e is the excitation beam waist at the sample position, Z_c is the confocal distance of the probe beam, and Z_l is the distance from the probe beam waist to the sample.

Since the characteristic thermal lens time constant t_c is defined as by Eq.3:

$$t_c = \frac{\omega_e^2}{4D} \quad \text{with} \quad D = \frac{K}{\rho c} \quad (3)$$

in which ρ is the density, c is the specific heat, and D the thermal diffusivity of the sample, it is obvious that one can deduce the thermal parameters of the sample such as thermal diffusivity and thermal conductivity if the time constant is obtained from curve fitting of time dependent experimental values of $I(t)$ to Eq. 1. From the same fit the parameter θ and consequently the temperature coefficient of sample's refractive index (dn/dT) can be obtained, provided that other experimental ($P_e, A_e, l_0, \lambda_p, \omega_p, \omega_e, Z_l$) and physical parameters (ρ, c) are known and kept constant during the measurement. An important advantage of using TLS for determination of opto-thermal parameters is the fact that the thermal lens effect can be accurately measured at temperature changes as low as 10^{-3} K. This enables measurements at well defined sample temperature and significantly eliminates the contribution of convection to the measured D or k , which is frequently the main problem for accurate determination of thermal conductivity of some liquids. TLS has been so far successfully applied to measurement of optothermal parameters of samples such as liquid crystals [3], polymers [4, 5] and glasses [6], as well as organic solvents [7], water [8] and different aqueous solutions [7], and even fatty acids [9].

In analytical applications of TLS the just described inherent characteristics of the thermal lens must be taken into account, because they not only contribute to the extremely high sensitivity of TLS technique, but can also hinder the performance of TLS if changing during the measurement like for example in a gradient elution HPLC. The TLS is more sensitive than conventional transmission spectrometry because the photothermal effect amplifies the measured optical signal (relative change in the beam intensity) [10]. This amplification, referred to as the enhancement factor [11], is the ratio of the signal obtained using photothermal spectrometry to that of conventional transmission spectrometry. Enhancement factor depends on the thermal and optical properties of the sample and the properties of the pump and probe laser beam, what can be seen from the equation 4, which is a simplified form of Eq. 1 for a steady state condition ($t \gg t_c$), equal pump and probe beam sizes, and for the sample positioned in the optimal position ($Z_l = Z_c\sqrt{3}$):

$$\frac{\Delta I}{I} = \left(-\frac{dn}{dT} \right) \frac{PA}{\lambda k} = EA, \quad \text{where} \quad (4)$$

$$E = \left(-\frac{dn}{dT} \right) \frac{P}{\lambda k}$$

with $\Delta I/I$ being the relative change of the probe beam intensity, A the absorbance, and E the enhancement factor.

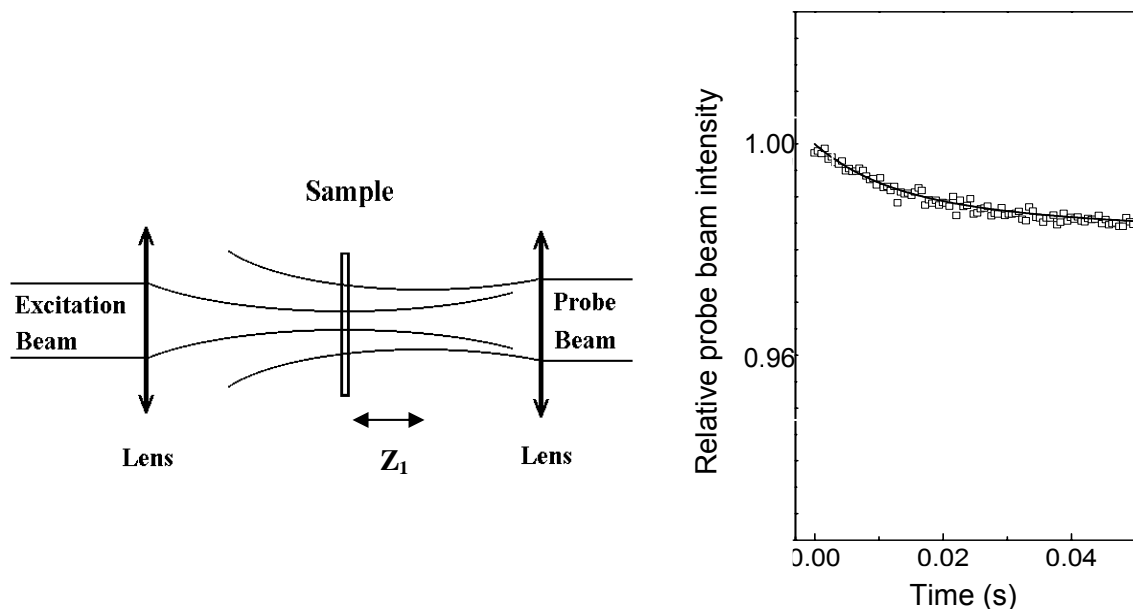


Fig. 1: Schematic representation of a possible beam geometry in a dual beam TLS measurement with indicated position of the sample with respect to the focal points of two beams (left). Probe beam intensity change during a thermal lens measurement (squares), and the curve fit of experimental data to Eq. 1 (solid line) (right).

Measurements of Opto-Thermal Properties of Liquids by TLS

One of the first applications of TLS to measurements of optothermal properties of liquids was the determination of the temperature of the maximum of refractive index of water, which was a subject of dispute for quite some time, with the reported values ranging from 270 K to 275.3 K [8]. The determination of the temperature in question was performed by measuring the TLS signal at different temperatures from supercooled water at 267 K to 293 K, and by observing the point at which the signal was equal to zero. A close inspection of equations 1 and 2 or 4 reveals that the TLS signal equals zero when $(dn/dT) = 0$, which is true at the maximum of refractive index. By using this procedure the temperature of the maximum of refractive index of water was determined to be at -0.01 ± 0.04 °C [8].

Differently from the zero point measurement such as described above, the determination of (dn/dT) and k values requires time resolved measurements and curve fitting of experimental data as described in the introduction. Experimental parameters must however be known with sufficient accuracy, which is often not the case. Therefore, TLS measurements of (dn/dT) and k values for liquids were made in a relative mode, by determining the cumulative experimental constant for the TLS set-up from the θ and t_c values obtained from curve fitting of experimental data for pure water at 25 °C. Experimental parameters were subsequently determined from θ and t_c values by

using known values of physical parameters of water at 25 °C from literature, and unknown (dn/dT) and k values for samples measured under identical experimental conditions were obtained after curve fitting of experimental TLS data for liquids to equation 1, as already described. It is also important to note, that some absorbing compound such as azulene or Ni-phtalocyanine were needed as additives to transparent liquids including water, to induce sufficient TLS signal. Their concentration was however very low (10^{-8} M or less) and did not affect the determined optothermal parameters, as it has been confirmed by measuring the known (dn/dT) and k values for some liquids such as D₂O and some organic solvents [7]. The (dn/dT) and k values for some liquids such as highly volatile hexane, solutions of electrolytes at various concentrations, surfactants and fatty acids were obtained and reported for the first time [7, 9], and the validity of the method was further confirmed by good agreement of the determined values compared to other measurements such as those with photopyroelectric technique [12].

The Effects of Opto-Thermal Parameters on TLS Measurements in Chemical Analysis

The fact that the enhancement factor in TLS is dependent on opto-thermal properties of the measured solution implies that TLS measurements in organic solvents, which are characterised by high absolute value of (dn/dT) and low k , are more sensitive than measurements in liquids with low (dn/dT) and high k . Unfortunately, water which is the most common solvent exhibits over 20 times lower enhancement factor compared to most organic solvents. This deficiency was however successfully circumvented by addition of water-mixable organic solvents such as for example demonstrated for determination of Cr(VI) by ionic chromatography with TLS detection. By adding 30% of acetonitrile to the eluent the enhancement factor was improved by over 3 times and an LOD for Cr(VI) in water on the order of 100 ppt was achieved. This competes well with ET-AAS and in addition enables on-line determination of Cr(VI) as well as Cr(III) [13].

A different approach, exploiting primarily the temperature of (dn/dT) of water and the position dependence of TLS signal [10], was proposed to improve the sensitivity of TLS measurements in water [14]. It was demonstrated, that by placing two identical samples symmetrically with respect to the waist of the probe beam, and by cooling one to - 8 °C and the second one to 12 °C an improvement in sensitivity by a factor of almost 2 can be achieved since at these temperatures the absolute values of (dn/dT) are equal but opposite in sign, while the two samples at room temperature would also show an equal signal but opposite in sign, and would thus cancel out as known from theory [10].

References:

1. J.P. Gordon, R.C.C. Leite, R.S. Moore, S.P.S. Porto, J.R. Whinnerz, *Bull. Am. Phys. Soc.* 1964, 9, 501.
2. J. Shen, R.D. Lowe, R.D. Snook, *Chem. Phys.* 1992, 165, 385.
3. J. Mura, J.H. Rohling, A.N. Medina, A.J. Palangana, A.C. Bento, J.R.D. Pereira, M.L. Baesso, L.C.M. Miranda, *Braz. J. Phys.* 2002, 32, 575.
4. J.H. Rohling, A.M.F. Caldeira, J.R.D. Pereira, A.N. Medina, A.C. Bento, M.L. Baesso, L.C.M. Miranda, *J. Appl. Phys.* 2001, 89, 2220.
5. J.H. Rohling, A.N. Medina, A.C. Bento, J.R.D. Pereira, M.L. Baesso, L.C.M. Miranda, *J. Phys. D: Appl. Phys.* 2001, 34, 407.
6. S.M. Lima, T. Catunda, R. Lebullenger, A.C. Hernandez, M.L. Baesso, A.C. Bento, L.C.M. Miranda, *Phys. Rev. B*, 1999, 6, 1517.
7. M. Franko C.D. Tran, *J. Phys. Chem.* 1991, 95, 6688.
8. M. Franko C.D. Tran, *Phys. Chem. Lett.* 1989, 158, 31.
9. M. Franko, D. Bicanic, J. Gibkes, M. Bremer, E. Akkermans, *Food Technol Biotechnol.* 1997, 35, 39.
10. S.E. Bialkowski, *Photothermal Spectroscopy Methods for Chemical Analysis*, In: J.D. Winefordner (ed.) *Chemical Analysis 134.*, John Wiley&Sons Inc., New York, 1996.
11. N.J. Dovichi, J.M. Harris, *Anal. Chem.* 1979, 51, 728.
12. N. Dadarlat, D. Bicanic, H. Visser, F. Mercuri, A. Frandas, *JAOCS*, 1995, 72, 281.
13. M. Šikovec, M. Franko, Mi. Novič, M. Veber, *J Chromatogr A*, 2001, 920, 119.
14. M. Franko, C.D. Tran, *Anal. Chem.*, 1989, 61, 1660.

AB INITIO CALCULATIONS OF SOME TIME –DEPENDENT PROPERTIES OF ATOMIC SYSTEMS

A. R. Tančić

VINČA Institute for Nuclear Sciences, 11001 Beograd, Serbia and Montenegro

Abstract

Within the framework of the many-body theory by using the method of Random Phase Approximation with Exchange we calculated the polarizabilities, the refractive index and Verdet of Ar and Be atoms.

Introduction

Up to day, the interest for the theoretical prediction of the time-dependent properties of atomic systems such as the polarizabilities, the refractive index, the Verdet coefficients and so on, is not decreased. The most notable methods for *ab initio* calculations are the oscillator sum rules [1], the variation-perturbation approach [2] and the many-body theory [3,4]. In this paper the improved random phase approximation with exchange (RPAE) calculations of the polarizabilities, the Verdet coefficient and refractive index for Ar and Be atoms, are presented. All notations follow those in refs. [3,4].

Results and Discussion

The polarizabilities of arbitrary multipolarity are defined as [1]

$$\alpha^{(L)}(\omega) = 2 \sum_{n,n'} \omega_{nn'}^2 \left| \langle n' | M^L | n \rangle \right|^2 (\omega_{nn'}^2 - \omega^2)^{-1}, \quad (1)$$

where M^L is an operator for L -pole momentum of system; ω is the photon energy, and $\omega_{nn'}^2$ is the excitation energy. They can be expressed in length (L) or in velocity form (V) [2]. In the RPAE approximation the dipole dynamic polarizability is given by the expression [4]:

$$\alpha^{(RPAE)}(\omega) = 2 \sum_{\substack{n \leq F \\ n' > F}} \omega_{nn'}^2 \left| \langle n' | D | n \rangle \right|^2 (\omega_{nn'}^2 - \omega^2)^{-1} \quad (2)$$

The knowledge of polarizability makes possible to find the refractive index, the Verdet coefficients, and other atomic properties [5]. The refractive index n , which is the mean refractive index for the right and left circularly polarized light in optically active media, in dilute gas can be commonly written: $n^2 - 1 = 4\pi N \alpha^{(1)}(\omega)$; N is the number of atom per centimeter cubic at STP (standard temperature and pressure).

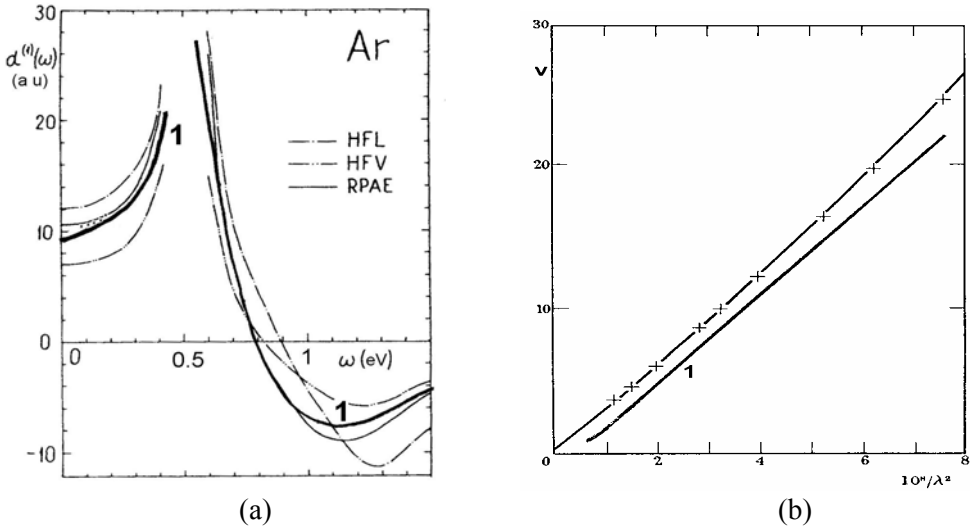


Fig.1(a). The dipole dynamic polarizabilities for Ar. The curve 1 present our improved RPAE calculations; other curves are earlier results [3]; the experiment: x [5]. The right **fig. 1(b)** show the Verdet constant V of Ar as function of wavelength λ : the full line- [7]; the crosses (experiment)-[6] and the line 1 is our RPAE result.

In the case when the magnetic field H is parallel to the direction of linearly polarized radiation, the plane of polarization is rotated and this rotation is proportional to the H . The factor of proportionality is the Verdet coefficient $V = k\lambda\partial n / \partial\lambda$ in rad/(Oe cm) units; λ is the wavelength of the incident radiation, and the value of the constant k is given in refs.[2,5]. Using the improved calculations of the $\alpha(\omega)$ [4] we obtained the values of the Verdet coefficient and refractive index. As an example we present in fig.1(a) our improved RPAE results (curve 1) of $\alpha^{(1)}(\omega)$ for Ar atom. This results are compared with our earlier results in the Hartree-Fock (L, V) and RPAE approximation. In fig.1(b) we show the results of the Verdet coefficient V for Ar. The Verdet constants are expressed in [μ min/ Oe cm] and λ in [\AA]. Using our recently obtained results for $\alpha(\omega)$ for Be atom, in fig.2 we show the results for refractive index n . We compare our RPAE values (2) with the results of fully coupled HF calculations [5]. Our results are close with the experimental and theoretical results [6, 7]. The theoretical predictions [5] contain the adjustable parameters which are connected with the experimental data and are fitted to polynomial in even power of $1/\lambda$. The principal contribution to the obtained values of RPAE calculations of $\alpha(\omega)$, V and n comes from the transition of the outer subshell. For noble gas atoms the role of the discrete excitations is negligible in low energy region. In fig.3. we present the result for the refractive index for Be atom.

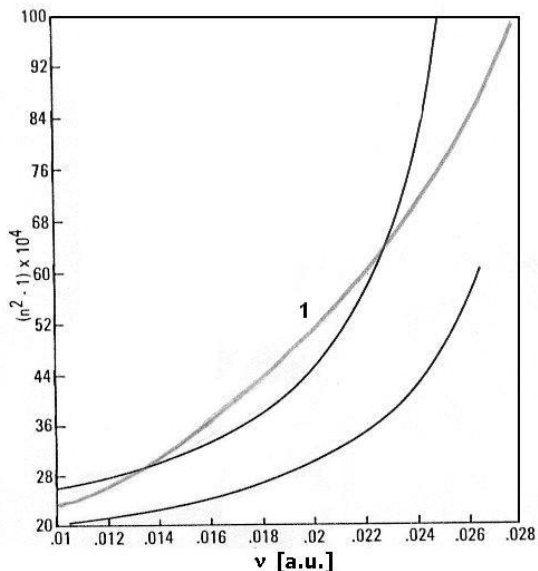


Fig. 2 The refractive index of Be as a function of the frequency. The curve 1 is the RPAE results, and other curves (HF) are from ref.[5].

Conclusion

In this paper we presented some results of the RPAE calculations of $\alpha(\omega)$, V and n for Ar and Be atoms. The presented results are in agreement with the known experimental values. The influence of many-electron correlations is important.

References

- [1] A. Dalgarno, Perturbation Theory and its Applications in Quantum Mechanics, J.W., N.Y., 1966., p. 145
- [2] M. Karplus and H. J. Kolker, J. Chem. Phys., 1963, 38, 1493.
- [3] M. Amusia and N. Cherepkov, Case Studies in Atomic Physics, 1975, 5, 47.
- [4] A. R. Tancic, NTB, 2002, 2, 63.
- [5] V. Kaveeshvar and R. Hurst, Phys. Rev., 1968, 172, 35.
- [6] C. Cuthberston and M. Cuthberston, Proc. Roy. Soc., London, A135, 40.
- [7] A. Dalgarno and A. Kingston, Proc. Roy. Soc., London, A259, 424.

ON THE SPIN DENSITY WAVE ELECTRON GAS

A. R. Tančić

The "Vinča" Institute of Nuclear Sciences, Belgrade, Yugoslavia

Abstract

The possibility of a non-trivial ground state of an electron gas in metal featuring a spin density wave (SDW) was widely discussed. We investigated the collective spectrum (CS) of a spin density wave electron gas using the many-body theory.

1. Introduction

The problems which are connected with the ground and excitations states of the interacting electrons has been the subject of much theoretical study up to days. One of the methods of treating of this problem is based upon the idea which origin is the microscopic theory of superconductivity. Namely, for the ground state in the Hartree-Fock (HF) approximation one use the so called state of the spin density waves (SDW). This method is usually considered in the limits of the high and low electron density [1, 2].

2. Results and Discussion. Spin Density Waves (SDW)

For the uniformly infinite system of electrons in the HF approximation one electron wave function satisfies the equation:

$$H' \varphi_k(r) - \int \frac{d\vec{l}}{(2\pi)^3} \int \varphi_l^*(r') \frac{e^2}{|\vec{r} - \vec{r}'|} \varphi_k(r') d\vec{r}' \varphi_l(r) = \varepsilon_k \varphi_k(r). \quad (1)$$

Here $H' = [-\nabla^2/2 + U_H(r) + U_+(r)]$. U_H is the Hartree potential; U_+ is the potential of positive distributed charges, and ρ is the electron density. One of the solutions of the equation (1) is SDW. The ground state with SDW may be constructed with the one-electron wave functions which are the superposition of the states with different spin projections:

$$\varphi_p^Q = \begin{pmatrix} \cos \theta_p \exp(i\vec{p}\vec{r}) \\ \sin \theta_p \exp[i(\vec{p} + \vec{Q})\vec{r}] \end{pmatrix} \quad (2)$$

Here the wave vector Q characterizes direction and the wavelength of the spin density. The angle is $\theta_p \in [0, \pi/2]$. For one-electron excitations we have:

$$E_p = (1/2)(\varepsilon_p + \varepsilon_{\vec{p}+\vec{Q}}) \pm \sqrt{(1/4)(\varepsilon_p - \varepsilon_{\vec{p}+\vec{Q}})^2 + g^2(p)}, \quad (3)$$

where ε_p , $\varepsilon_{\vec{p}+\vec{Q}}$, $g(p)$ are defined in ref. [2]. When $|\varepsilon_{\vec{p}} - \varepsilon_{\vec{p}+\vec{Q}}| \sim 0$ the expression (3) give the spectrum with the gap which is equal $2g$, and for

$|\varepsilon_{\vec{p}} - \varepsilon_{\vec{p}+\vec{Q}}| \gg g$ the E_p is equal ε_p or $\varepsilon_{\vec{p}+\vec{Q}}$ which means that no the gap in the one-electron excitations spectrum. The equation for $g(p)$ has the trivial solution ($g(p) = 0$, if $\theta_p = 0$ or $\pi/2$). The energies of states with φ_p^Q corresponding to the nontrivial solutions are lowest to that corresponding to trivial solutions. In the investigations of “nontrivial” states one can use the method [2]. This method is used when the symmetry of the wave functions of the ground states is lower than the symmetry of Hamiltonian H. In our case, in the SDW states, the complete translation invariant of H is absent and therefore the averages values

$$f_{p\uparrow\uparrow} = \langle a_{p\uparrow}^+ a_{p\uparrow} \rangle; \quad f_{\vec{p}+\vec{Q}\downarrow\downarrow} = \langle a_{\vec{p}+\vec{Q}\downarrow}^+ a_{\vec{p}+\vec{Q}\downarrow} \rangle; \quad f_{p\downarrow\uparrow} = \langle a_{\vec{p}+\vec{Q}\downarrow}^+ a_{p\uparrow} \rangle \quad (4)$$

which vanish in the ordinary paramagnetic phase are different from zero (and its complex conjugates). The averages values (4) in the ground state define the amplitude of the SDW, a^+, a are the Fermi creation and annihilation operators, respectively. The exact Green function is connected with free Green function and self-energy Σ via Dyson equation. The self-energy is connected with the effective interaction Γ of the pair of electrons, also. In the HF approximation $\Gamma(p, p') = 4\pi e^2 |\vec{p} - \vec{p}'|^{-2}$. In the simple case when Γ is diagonal on the spin index α, β and depend on the $|\vec{p} - \vec{p}'|$, only, Σ attains the following form:

$$\sum_{\alpha\beta} \Sigma(p) = - \int \frac{d\vec{p}'}{(2\pi)^3} \Gamma(\vec{p} - \vec{p}') f_{\alpha\beta}(p') \quad (5)$$

Now we can find the spectrum of one-electronic excitations (the poles of $G(p)$). The off diagonal matrix elements of G give the mixed states with the spin projections \uparrow, \downarrow (in the coordinate space they are not translationly invariant). By this many body method we can investigate the structure of the SDW collective excitations spectrum. It was done in the random phase approximation –RPA [3]. As a result we obtained that the spectrum of collective excitations has more than two branches. In the fig.1 we present the spin state structure of the SDW. The direction of the polarization vector \vec{P} is arbitrary. The rotation of the \vec{P} is equivalent to the collective oscillation with the infinitive wavelength with zero energy. For the oscillations with finite wavelength the energy must be $\omega \sim q$ (that is because the wave functions of the SDW has the low symmetry as compared to the symmetry of H. These branches of spectrum correspond to the so-called Goldstone (G) boson [4, 5]. In the SDW state the symmetry invariant in the Q direction is broken. It is not necessary for the energy of the translation of the system in this direction - that means that exist the special branches of the collective spectrum.

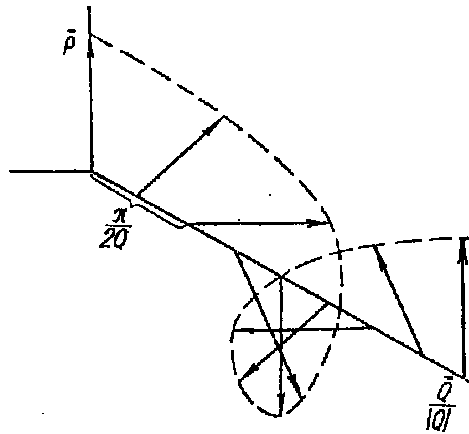


Fig.1. The spin structure of the SDW state

In the ground SDW state the lengths of Q and P has the particular values, which correspond to the minimum energy. The dispersion from the equilibrium values give rise to the oppose force. Consequently the new branches in collective spectrum appears which are connected with the oscillations of P, Q . The analysis of the SDW states may be done on the basis of the general symmetry considerations. There is the three gapless branches in the SDW electron gas collective spectrum (three G-bosons). If we explicitly write the current in terms of creation and annihilations operators, the results of averages on the ground state are different from zero. Therefore, since the generators of translation S^i commute with the excitation operators it follows that the number of G-bosons in the system is equal to the number of "broken symmetries". Furthermore, some of the other branches in collective spectrum correspond to the oscillations of the dynamic variables $|\vec{P}|, |\vec{Q}|$.

3. Conclusion

Thus, applying the RPA [3] method, or the G - theorem [2, 5] to the system with ground states of complex structure, one can obtain valuable information about the collective excitation spectrum.

References

- [1] A.W. Overhauser, Phys. Rev. 1962, **128**,1437
- [2] M.Ya. Amusia, Phys. Lett. 1966, **20**, 596
- [3] A.R. Tancic, Jpn. J. App. Phys. 1977, **36**, 4737
- [4] A.K. Rajagopal, Phys. Rev. 1965, **137**, A 1429
- [5] R.V. Lange, Phys. Rev. 1966, **146**, 301

THE INFLUENCE OF THE POLARIZABILITY IN SOME BREMSSTRAHLUNG PROCESSES

A. R. Tančić and M. Nikolić*

The VINČA Institute for Nuclear Sciences, Beograd, Serbia and Montenegro

**The Faculty of Natural Sciences, Niš, Serbia and Montenegro*

Abstract

We consider the general results of the theory of the polarizational bremsstrahlung (BrS) and we present the results of recent calculations of the cross sections in the conditions when the radiation of atomic electrons dominates in the total spectrum. For example, we investigated the case when the frequency of the emitted photon is comparable with the energy of the great dipole or plasmon resonance in a cluster (fullerene).

Introduction

An electron undergoing scattering with some targets absorbs or emits radiations as a result of its acceleration in the target field. A photon is emitted (BrS) or absorbed (inverse BrS). The incident electron gains or loses the corresponding amount of kinetic energy.

In this paper we present recent results of the theory of the polarizational bremsstrahlung PB [1] of clusters and fullerenes. We considered the photon emission in the collisions of electrons with targets under the special conditions. We concentrate our interest on the spectrum of photon emission in the region of frequencies where the polarizability is very large. In this case most of the radiation is formed by the PB. There are two mechanisms of photon radiation during a collision: the ordinary electron BrS (OB) (the photon is emitted by electron decelerating in the static field of the target) and PB (the photon is emitted by the target as a results of its virtual excitations-polarization of target electrons). In the polarizational BrS process the cluster (target) is polarized by a distant collision with the electron. In this case dipole moment is induced in the cluster during the collision process, which is directed along a center-of-mass line of the colliding particles. Since that line rotates in space, the motion of an induced dipole moment is accelerated with a deformed radiating target even it is neutral.

We considered the PB process in collisions of electrons with clusters [1,2] and fullerenes [2,3] because these kind of targets have some features in common with a single atomic system. In the "cluster (fullerene) case" the specific feature of PB process consists in fact that the dominance of the polarization mechanism in the great resonance frequency range is much more pronounced than for atoms. The photon emission spectrum generated in electron-fullerene collisions was described in the main logarithmic approach [1,2]. Recently, experiments of the electron – clusters, and electron-fullerenes [4] have been performed.

We set $\hbar = m_e = c = 1$.

Results and Discussions

To handle theoretically the metal clusters and fullerenes we can apply the method, which is known for description of atoms [1]. We calculated the PB in the process of the collision of electrons with the clusters (fullerenes). All notations follow those in [2, 3].

The total amplitude of Bs (including OB and PB) radiative mechanisms are [2, 3]:

$$A^{tot} = \langle \Psi_2 | \vec{e} \vec{r} | \Psi_1 \rangle + \int \frac{d^3 q}{(2\pi)^3} \frac{4\pi}{q^2} \langle \Psi_2 | e^{i\vec{q}\vec{r}} | \Psi_1 \rangle \vec{e} \vec{q} \alpha(\omega, \vec{q}) \quad (1)$$

Ψ_1, Ψ_2 are the initial or final wave functions of the electron (respectively), q is the momentum transfer, \vec{e} is the photon polarization vector and $\alpha(\omega, \vec{q})$ is the generalized dynamic polarizability of the target:

$$\vec{e} \alpha(\omega, \vec{q}) = i \sum_n 2\omega_{n0} (\omega_{n0}^2 - \omega^2 - i\delta)^{-1} \langle 0 | \sum_j \exp(i\vec{q}_j \vec{r}_j) | n \rangle D_{n0}(\omega) \quad (2)$$

where $\omega_{n0} = \varepsilon_n - \varepsilon_0$ is the transition energy between the ground and excited state of the cluster. The delocalized electrons in the cluster are denoted by index j . D_{n0} describes the interaction of the cluster with the radiation field. This interaction we describe in the framework of the Random Phase Approximation with Exchange (RPAE) [1]. Treating the a/R (where R is the radius of the cluster and a characterizes the depth of the surface layer on cluster (or the thickness of the fullerene depth) as a small parameter, we can obtain the expression for $\alpha(\omega, \vec{q})$ which is applicable near a plasmon resonance ω_p . Using the alteration of the electron density of a cluster (fullerene) $\delta\rho(\vec{r})$ under the action of an external field in the RPAE [1, 3], we can obtain the generalized dipole polarizability α for the cluster or fullerene. As an example we calculated the PB spectra for electron- C_{60} collision using the expression [2]:

$$\omega \frac{d\sigma}{d\omega} = \frac{16e^2 \omega^4}{3c^3 v^2} |\alpha(\omega)|^2 [S_1(q_{\min} R) - S_1(q_{\max} R)] \quad (3)$$

where the functions S_1 are defined in [2]. In fig. 1 we plotted the PB spectra. Our results are presented as a full curve 1 and correspond to the calculations of $\alpha(\omega)$ in the simplified version of the RPAE [3]. The polarizational mechanism manifests itself in the resonance behavior of the spectrum at $\omega \approx \omega_p$.

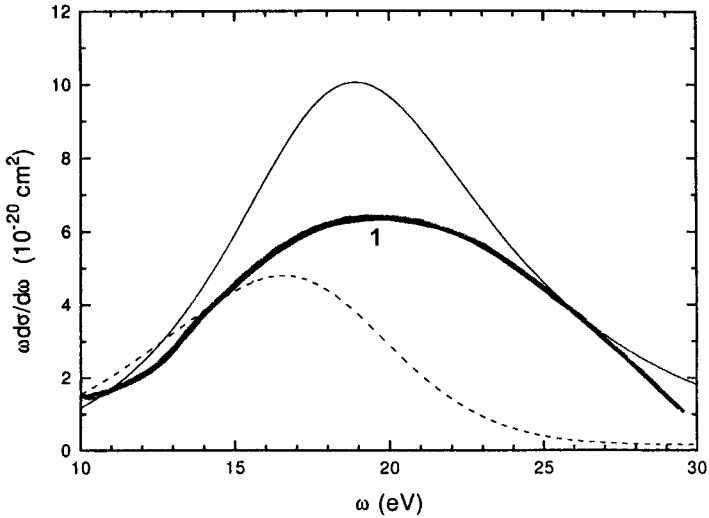


Fig.1. PB cross section for $e^- - C_{60}$ collision as a function of emitted photon energy for projectile electron velocities: $v = 3,5$ (full curve), $v = 2$ (broken curve) [2], and for $v = 4$ (full curve 1, our result).

Conclusion

Our results are close to the other calculations [2]. In ref. [2] $\alpha(\omega)$ was partially derived from the empirical data and by applying the dispersion relations. The correct description of PB, in the vicinity of the great plasmon resonance is only possible by accounting the many-electron correlation effects.

References

- [1] M. Ya. Amusia, *Tormoznoe izluchenie*, Moscow (in Russian), 1990.
M. Ya. Amusia, *Atomic Bremsstrahlung*, Phys. Rep., 1988, 162, 249.
- [2] A. V. Korol and A. Solovy`ov, *J. Phys. B.*, 1997, 30, 1105.
N. Avdonina and R. Pratt, *J. Phys. B*, 1999, 32, 4261.
- [3] A. R. Tancic, *NTB*, 2001, 1, 149.
- [4] V. Kresin, A. Scheidemann and W. Knight, *Proc. Int. Symp. on Elec. Collis. with Molec., Clusters and Surfaces*, 1993, London
J. Keller and M. Kaplan, *Chem. Phys. Lett.*, 1992, 193, 89.

STUDY OF A LONG TERM PROCESSES IN D.C. ARGON ARC PLASMA BY SQUARE POWER MODULATION WITH VARIABLE LOW CURRENT PERIOD

J.J. Savović¹, M.M. Kuzmanović², M.S. Pavlović¹, and M. Marinković¹

¹Laboratory of Physical Chemistry, The Vinča Institute, P.O. Box 522, 11001 Belgrade,

²Faculty of Physical Chemistry, University of Belgrade,

P.O. Box 137, 11000 Belgrade, Serbia and Montenegro

Abstract

U-shaped d.c. argon stabilized arc with aerosol supply was investigated by current modulation between 9 and 3 A level and low current period lasting from 0.05 to 40 ms. The variable low current period has great influence on delayed line intensity response that provides information about a recombination and transport processes in plasma. The obtained results indicate that plasma slowly reaches stationary state and that processes related to changes in atom concentration play important role. Character of temporal responses strongly depends on first ionization energy of analyte.

Introduction

The method of power modulation is a useful tool for studying processes in plasma [1]. At a moment of a sudden current drop various processes starts. Thermalization processes, in which plasma particles reach new stationary temperature, has time constant with order of magnitude of few microseconds. On the other hand, ionization-recombination balance takes place on a time scale ranging from few hundred microseconds to several milliseconds or even more depending on ionization energy of analyte and radial distance of the observed part of plasma. Analyte atom concentration increases due to recombination and diffusion from plasma periphery. This type of diffusion is caused by decreasing of the demixing effect as a consequence of radial field declining [2]. The diffusion process is usually slower than recombination process.

In the moment of sharp current jump the reverse processes take place. The time evolution of these processes strongly depends on the plasma state reached during the low current period. In other words temporally response of line intensities accompanying the current jump depend on the extent transport processes have reached in evolution to stationary state. If the low current period lasted long enough and plasma reached stationary state further increase of the low period has no effect. Interruption of intensity evolution at different temporally points give insight into processes that govern reestablishment of a stationary state.

Experimental

This study is performed with U-shaped d.c. argon arc operating at atmospheric pressure, construction details described elsewhere [3]. The analyte water solutions were introduced into plasma as aerosol obtained with glass concentric nebulizer and double-pass cloud chamber.

The arc current was square modulated (sharply changed between 9 and 3 A) by electronic switch circuit based on fast MOS-FET transistors connected in parallel with the arc gap. The arc current circuit was optimized in such a way as to minimize the current transition rise time (less than 2 μs). In order to monitor the power evolution the oscilloscope current probe was used. Repetition period was 100 and 200 ms, with low period lasting from 0.05 to 40 ms.

The photomultiplier current was amplified by a factor of 50 with a fast pre-amplifier, and fed into a digital storage oscilloscope. The oscilloscope is PC controlled via GPIB interface. The oscilloscope traces are averaged 32 times, and subsequently transferred to the PC. The whole measurement process was governed by PC program specially developed for this purpose.

Results and Discussion

Figure 1. illustrates typical responses of line intensity for high ionization energy elements in a submillisecond time domain. The intensity responses are normalized to stationary state and vertically shifted for the clearness of presentation.

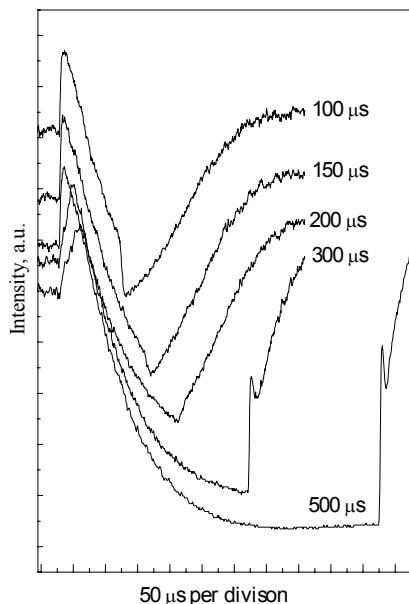


Figure 1. Intensity responses of Ar I 696.54 nm line for short low current period.

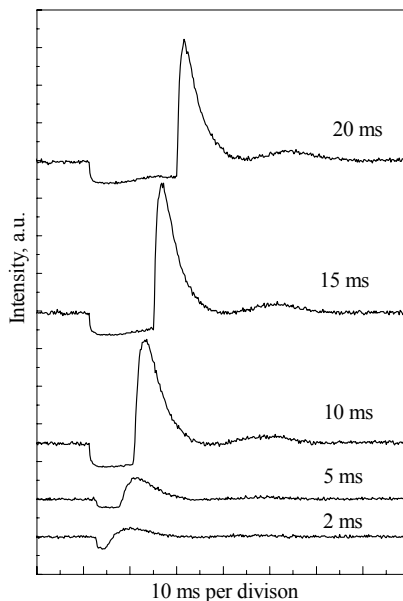


Figure 2. Intensity responses of Be II 313.04 nm line for low current period longer than 1ms.

It is evident that the behavior of responses drastically changes with prolonged low current period. Such behavior is related to decreasing electron number density i.e. with change in excitation mechanisms [3]. Elements with lower ionization energy shows even more pronounced intensity peak that is connected with a current jump (order of magnitude of the time constant several microseconds). This intensity peak first

shows increase with increasing low period time and then starts to decrease thus indicating connection with recombination processes. The appearance of this intensity peak is probably related to fast changes in excitation balances. Spatially resolved intensity measurements demonstrate that appearance of this peak is connected with the arc core because at larger radial distances peak disappears.

Influence of the millisecond low period duration on intensity responses is illustrated in Figure 2. As a representative example results for Be II are shown. As it can be seen, at the moment of a current jump, a large peak appears. The shape and intensity of this peak are strongly determined by a low period duration, ionization energy of analyte and radial position of the observed part of plasma. Influence of a low period duration on peak intensity and its relaxation time indicates that this process is connected with diffusion of analyte atoms. Among previously mentioned factors, the time length of disturbances has major influence on the time needed for plasma to reach stationary state. A care was taken that the influences of two subsequent perturbations do not overlap.

Conclusion

The obtained results have shown that time evolution of intensity responses on a sub millisecond scale are preferably induced by processes connected with electrons (excitation, ionization-recombination and transport) while for responses on a millisecond scale the dominant role has diffusion of analyte.

Acknowledgments

This work has been financially supported by Ministry of Science and Environmental Protection, Republic of Serbia, under Project No. 1995 and No. 1928.

References

- [1] J. W. Olesik, K.R. Bradley, *Spectrochim. Acta*, 1987, 42B, 377.
- [2] M. S. Pavlovic, M. Marinkovic, *Spectrochim. Acta*, 1998, 53B, 81.
- [3] M. M. Kuzmanovic, M. S. Pavlovic, J. Savovic, M. Marinkovic, *Spectrochim. Acta*, 2003, 58B, 239.

ELECTRON AND GAS TEMPERATURE DIFFERENCE IN LOW CURRENT ARGON D.C. ARC STUDIED BY POWER INTERRUPTION TECHNIQUE

M.M. Kuzmanović¹, M.S. Pavlović², J.J. Savović², M. Stoiljković²
and A. Antić-Jovanović²

¹*Faculty of Physical Chemistry, University of Belgrade, P.O. Box 137, 11000 Belgrade,*

²*Laboratory of Physical Chemistry, The Vinča Institute,
P.O. Box 522, 11001 Belgrade, Serbia and Montenegro*

Abstract

Atmospheric pure argon plasma without analyte water solution injection has been exposed to power interruption experiments in order to study the difference between electron and gas temperature. The arc plasma was studied in low currents range, between 3 and 10 A. Obtained temperature difference ranges from 3000 to 1500 K, from low to high current. A comparison with previous results, for argon plasma with water aerosol supply, have shown that introduction of water reduces temperature difference.

Introduction

In plasmas with lower electron number densities deviations from local thermodynamical equilibrium occurs. The deviations become more pronounced as the concentration of electrons decreases. The disturbance of plasma equilibrium is especially reflected in electron (T_e) and heavy particle (T_h) temperature difference. In arc plasmas that difference increases when current decrease.

Power interruption technique is convenient diagnostic method for investigation of thermal disequilibrium in low electron density plasmas [1]. At the moment of power interruption T_e becomes equal to the T_h while electron-ion recombination requires longer time. If the population of the level is determined by the electron-ion interaction electron temperature drop will cause increase of excited atoms concentration (in contrast to recombination ionization strongly depends on temperature). As a consequence the line intensity sharply increases at the moment of a sudden current interruption. This intensity increase is related to T_e - T_h .

The object of this work was U-shaped d.c. argon stabilized arc which is suitable for spectrochemical analysis of water solutions [2]. In literature there is a lack of precision data for temperature equilibrium in low current argon plasmas. This arc device is very stable for low current burning and thus convenient for this kind of measurements. The aim of this work was to get more insight into analyte excitation conditions by comparing with previously obtained results [3,4] for the same device but with introduction of aerosol.

Experimental

The U-shaped arc column is burning in a channel of 16 mm diameter formed by water-cooled electrically insulated brass segments. The argon gas was introduced

into the cavity of the central segment providing additional vortex stabilization. Geometrical features of the plasma make possible “end-on” observation without the use of Abel inversion.

The power interruption was accomplished by fast electronic switch circuit. On the trigger signal, the switch short-circuits the arc column that extinguishes discharge. The anode current of the photomultiplier tube was amplified 50 times with a wide band d.c. amplifier and then recorded by a digital storage oscilloscope. The oscilloscope and switch circuit was controlled by external trigger signal. Data acquisition was controlled by a PC computer.

Results and Discussion

In order to use power interruption technique to obtain T_e - T_h difference it is necessary to measure electron temperature first. In this work electron temperature was approximated with excitation temperature, which was determined from absolute integral emissivities of the argon line at 430.01 nm. Absolute emissivities of the argon line were determined with a carbon arc anode as a radiation standard. A value of $0.00394 \cdot 10^{-8} \text{ s}^{-1}$ was taken as the probability of the transition of this spectral line.

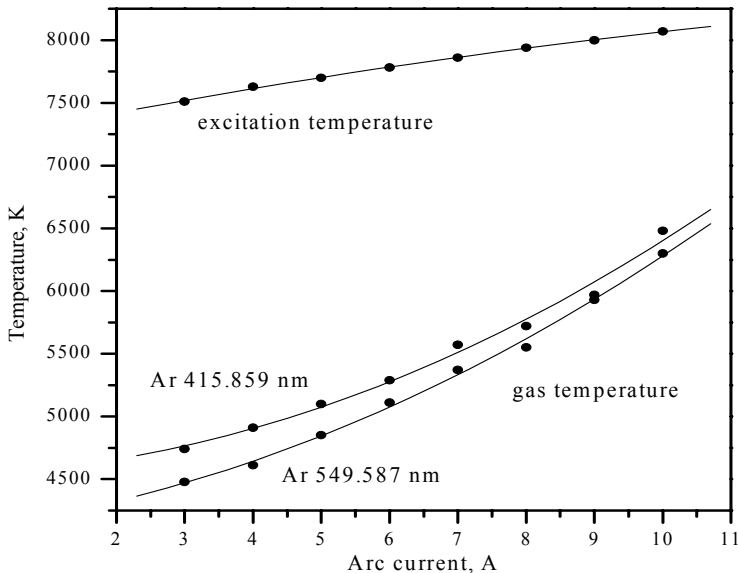


Figure 1. Dependence of excitation and gas temperature on arc current.

Intensity jumps were measured as the difference between intensity at maximum and in stationary state. In order to determine the intensity jump accurately the continuum evolution beside the line was taken into account. The time needed for spectral line intensity to reach the maximum is around $5 \mu\text{s}$. Two argon lines with different first ionization energies (14.53 and 15.33 eV) were used for evaluation of gas tempera-

ture. Results for the line with lower ionization energy are more reliable because of smaller deviation from partial local thermodynamic equilibrium (p-LTE) but the intensity jump is larger for the line with higher ionization energy and the measurements are more precise. With current increase intensity jump of a spectral line decrease. Also intensity jumps exponentially decrease with the increase of line excitation energy.

For higher arc currents results obtained for two different spectral lines come close to each other because lower excited level approach p-LTE, as it can be seen from Figure 1. In the measured current range (3-10 A) obtained temperature difference ranges from 3000 to 1500 K with the tendency for equalization at higher currents.

Conclusion

Argon d.c. arc plasma burning at atmospheric pressure is two temperature plasma where electron temperature determines excitation and ionization processes, i.e. the plasma is in p-LTE. The obtained temperature difference reaches as much as 30%. Previous results [4] for the same plasma device, but with water aerosol introduction, have shown smaller temperature difference. In other words introduction of water causes more efficient electron energy transfer to heavy particles.

Acknowledgments

This work is supported by the Ministry of Science and Environmental Protection, Republic of Serbia, Project No. 1928.

References

- [1] D. B. Gurevich, I. V. Podmoshenskii, *Opt. Spectrosc.*, 1963, 15, 319.
- [2] M. Marinkovic, V. G. Antonijevic, *Spectrochim. Acta*, 1980, 35B, 129.
- [3] M. M. Kuzmanovic, M. S. Pavlovic, J. J. Savovic, M. Marinkovic, *Spectrochim. Acta*, 2003, 58B, 239.
- [4] M. M. Kuzmanovic, A. Antic-Jovanovic, M. Stoiljkovic, M. S. Pavlovic, M. Marinkovic, *Spectrosc. Lett.*, 2003, 36(4), 303.

SPECTROCHEMICAL DETERMINATION OF As AND Cd BY U-SHAPED DC ARC

I. Novović,¹ M. Tripković,¹ I. Holclajtner-Antunović² and D. Marković¹

¹*Institute of Physics, P.O.Box 57, Pregrevica 118, and* ²*Faculty of Physical Chemistry, P.O.Box 137, YU-11001 Belgrade, Serbia and Montenegro*

Abstract

The U-shaped dc arc with aerosol supply was applied for determination of As and Cd in aqueous solutions. By optimization of the operating parameters and by selection of the most appropriate signal integration time, the obtained limits of detection are comparable with those obtained by ICP-MS and ICP-OES, for the elements studied.

Introduction

Arsenic and cadmium are considered as a major toxic metals with multiple effects. Therefore the very sensitive methods should be applied for their determinations. In this paper a simple method for determination of these elements is suggested. By optimization of the operating parameters of U-shaped argon DC arc plasma and spectrometer parameters, the satisfactory low detection limits can be achieved for the analytes mentioned. It is worth mentioning that the main characteristics of this plasma source are its high emission stability, very simple construction and low running cost.

Experimental

An U-shaped low current argon DC arc with aerosol supply was applied as excitation source. The essential parts of the arc device are given in detail elsewhere [1]. The emission was axially viewed from the horizontal part of arc column in the direction parallel to the arc axis. A laboratory modified 2-meter spectrograph PGS-2 with holographic grating (2100 grooves/mm) was used as spectrometer. The analyte spectral line intensities were photoelectrically recorded (Hamammatsu R 3788) and *via* an AD conversion card (ED-300) connected to PC. The recorded signal intensities were accumulated during the varied integration times, by application of the appropriate computer program. The slit width was 0.2 mm.

A series of reference solutions were prepared in the range from 1 to 1000 ng/ml, by appropriate dilution of the stock solutions. Each reference solution contained 0.5% potassium chloride as spectroscopic buffer. The measurements were performed for standard and blank solutions. The nebulization of the solution was performed by a Meinhard concentric glass nebulizer (type C) connected with a double-pass spray chamber.

From the lateral relative emission intensity distribution, recorded for each analyte, the peak position (relative to the arc axis) was determined and applied in all the measurements. Spectral line intensities were measured for Cd I 228.8 nm at 2.5 mm from arc axis and for As I 234.98 nm at 2.0 mm from arc axis.

Results and Discussion

At the radius of the peak emission, for each element, calibration curves were determined for the varied integration (exposure) times. The obtained results are given for Cd, as an example, in Fig. 1.

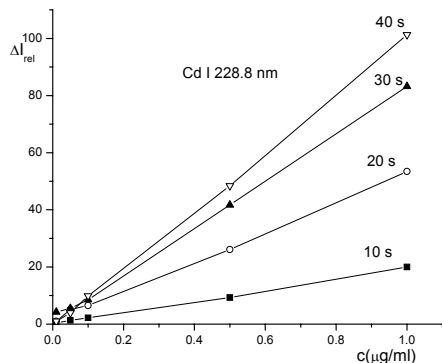


Fig. 1 Calibration curves for Cd I 228.8 nm line

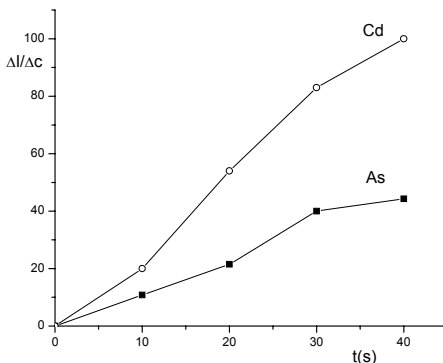


Fig. 2 Dependence of the concentration sensitivity on the integration time

It is obvious that the concentration sensitivity ($\Delta I/\Delta c$) increases with the integration time, thus indicating the increased precision of the analyte determination. The dependence of the concentration sensitivity, normalized to unity for integration time of one second, is presented in Fig. 2.

The detection limit (c_L) was determined for each integration time from the standard deviation of the blank and sensitivity obtained under the optimum operating conditions. It was found that the limit of detection is decreased with increasing integration time. The dependence of the detection limit on integration time can be applied for the estimation of the optimum integration time for the applied experimental set up. In the case of Cd the detection limit of 4 ng/ml is attained for optimum integration time of 30 s. In the case of As, the obtained detection limit is 4 ng/ml for integration time of 40 s. The detection limits estimated from measurements with optimum integration time are comparable to those obtained with ICP-OES and DCP-OES for Cd and with ICP-MS for As [2].

Conclusion

From the results obtained in this report, it can be concluded that with optimum integration time and experimental set up used, the obtained detection limits for Cd and As compare favorably to those of ICP-OES, DCP-OES and ICP-MS. Thus, a simple method for determination of these toxic elements, with low detection limit is suggested.

References

- [1] M. Marinković, V.G. Antonijević, *Spectrochim. Acta*, 1980, 35B, 129.
- [2] L. H. J. Lajunen, *Spectrochemical Analysis by Atomic Absorption and Emission*, Royal Society of Chemistry, Cambridge, 1992.

THE STUDY OF THE MAGNETICALLY TAILORED ATMOSPHERIC PRESSURE DC ARC PLASMA WITH AEROSOL SUPPLY FOR ANALYTICAL APPLICATION

M. Stoiljković, M. Pavlović, J. Savović and M. Marinković

VINČA Institute, Department of Physical Chemistry, P. O. Box 522, 11001 Belgrade, Serbia and Montenegro, ¹Faculty of Physical Chemistry, P. O. Box 137, 11001 Belgrade, Serbia and Montenegro

Abstract

Preliminary studies have shown that external oscillatory magnetic fields of a few mT imposed to the atmospheric pressure DC argon arc plasma with aerosol supply, can produce significant favourable changes of its spatial and spectral characteristic. These changes are promising for improvement the analytical performance of such treated plasma. In this work, the applied magnetic fields strengths were in the range of 29-23 mT and frequencies of 300-900 Hz. Spatial emission intensities of several element lines have been investigated in such magnetic field-plasma configuration with various plasma operating conditions and arc device construction modifications. Applied magnetic field induces lines emission intensity enhancements of the most elements observed. Enhancements (up to 20 times) depend on arc current, magnetic field strength and frequency applied, composition of sprayed solution, spatial plasma zone observed and construction details.

Introduction

Direct current arc plasma with aerosol supply still attracts considerable attention as excitation source for atomic spectroscopy in routine analytical work. Beside such application, a large number of arc constructions are improved and used in wide areas of technology (material processing-welding, cutting, plasma spraying; development of new materials-semiconductors, nano-material synthesis, etc).

In analytical application, one of the limiting factors for improvement of arc analytical capabilities is demixing effect existence caused by presence of radial electric field inside the plasma volume [1, 2]. In steady state this effect hinders sample vapor penetration the hottest plasma zones and consequently limits the analyte spectral emission. The introduction of potassium as an easily ionizable element (EIE) in the arc plasma reduces demixing effect and produces enhancement of the analyte emission [2].

If the DC arc plasma is imposed to a fast oscillating transverse magnetic field of sufficiently strength, the ionized plasma core will be oscillatory driven and penetrates the immovable surrounding gas mantle abundant with analyte vapour. If such penetrating is fast enough (comparable to the velocity of analyte species diffusion) emission intensity enhancement should be expected.

This is our idea in the most extensive experiments how to reduce existing demixing effect in DC arc plasma and improve its analytical capabilities. Preliminary results are presented in this work.

Experiment and Discussion

The device for stabilized DC arc plasma generation is described elsewhere [3]. A single magnet coil was positioned 18 mm away from the arc axis and collinearly to the optical axis of monochromator. Sinusoidal wave current powered magnet coil. Such plasma - magnetic coil configuration induces plasma core oscillations perpendicular to the optical axis, according to $\vec{E} \times \vec{B}$ coupling. Solutions that contain elements of interest are introduced into the plasma as aerosol, generated by pneumatic nebulizer.

When the whole plasma volume was focused onto the collimator, the applied magnetic fields of 23 mT and 800 Hz produces strong emission enhancement for the several elements measured, while the background stays nearly unchanged. It is also noticed that enhancement increase with ascending the arc current, but this increase is smaller if nebulized solutions contains EIE.

For more detail picture about the changes induced by imposed magnetic fields, lateral plasma scans were performed at YII 566.292 nm line for different fields strengths and frequencies, Fig. 1. Signal-to-background ratio (SBR) was used as a measure of effect. The plasma zone, 1 mm high, above the central segment was observed. Obviously, the strongest field (lower frequency) produces the biggest SBR net grow, but under such conditions plasma is less usable because it is wide stretched surrounded by flame-like tufts and spatially unstable because of swinging. When the frequency of applied field is much higher (780 Hz), there is no appreciable movement of the plasma core, Fig. 2., but there is still strong SBR peak, about six times higher in comparison when no magnetic field applied, Fig 1.

Conclusion

The data presented suggest that DC arc plasma can be effectively modeled by external magnetic field to improve its analytical characteristics. Basic assumption is qualitatively indicated, but further analysis of spatial and temporal behavior of the effect will provide details about its mechanism.

Acknowledgments

This work has been financially supported by Ministry of Science and Environmental Protection, Republic of Serbia, under Project No. 1995.

References

- [1] M. S. Pavlović, M. Marinković, *Spectrochim. Acta*, 1998, B53, 81.
- [2] M. S. Pavlović, M. M. Kuzmanović, V. M. Pavelkić, M. Marinković *Spectrochim. Acta*, 2000, B55, 1373.
- [3] M. M. Stoiljković, I. Holclajtner-Antunović, *Contrib. Plasma Phys.* 1997, 37(5), 459.

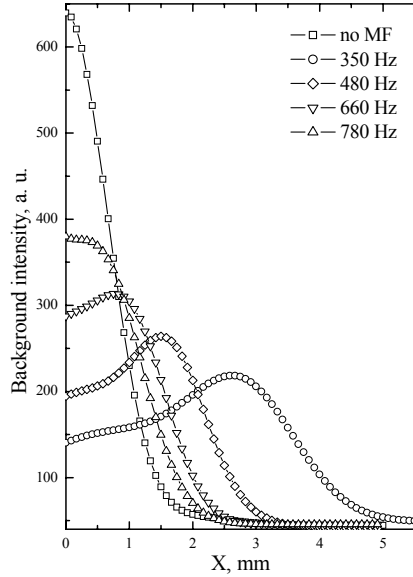
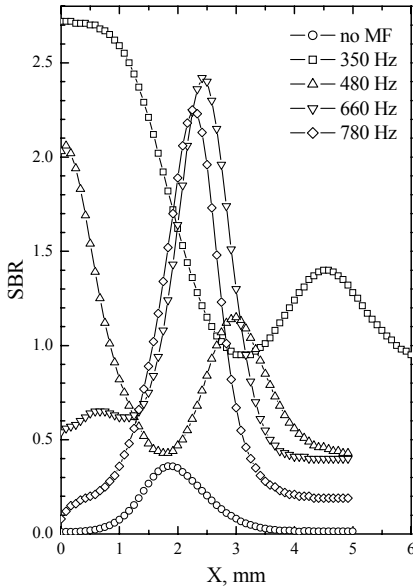


Figure 1. Lateral distribution of signal-to-background ratio (SBR) for line YII 566.292 nm for different magnetic field strengths and frequencies. Arc current 8A.

Figure 2. Lateral background intensity for different magnetic field strengths and frequencies. Arc current 8A.

AB INITIO TREATMENT OF THE RENNER-TELLER EFFECT AND SPIN-ORBIT COUPLING IN THE $A^3\Pi_u$ ELECTRONIC STATE OF NCN

M. Krmar

Institute Goša, Milana Rakića 35, 11000 Beograd

Abstract

Ab initio calculation are carried in order to compute vibronic and spin-orbit structure in the $A^3\Pi_u$ electronic state of the NCN radical.

Introduction

The first observed spectrum of NCN, corresponding to the $A^3\Pi_u - X^3\Sigma_g^-$ electronic transition, was detected in emission by Jennings and Linnet [1]. A detailed analysis of this electronic transition in absorption was carried out by Herzberg and Travis [2]. The evidence of the Renner – Teller interaction in the upper state was stated, but none of the vibrational frequencies could be determined. Recent spectroscopic studies in the gas phase performed by Mc Naughton et al. [3] and by Brown et al. [4-7] have provided precise values for the rotational constants and bending vibrational frequencies in the $X^3\Sigma_g^-$ and $A^3\Pi_u$ electronic states. An extensive theoretical study of the $^3\Pi_u$ state was carried out by Rajendra and Chandra [8].

Handling of the Renner-Teller Effect and Spin-Orbit Coupling

Variational treatment of the Renner-Teller effect in the $^3\Pi_u$ state of NCN is explained in detail in our previous study [9,10]. Briefly, it consists of diagonalization of a model Hamiltonian in the basis formed by products of linear combinations of electronic and vibrational wave functions. We have used diabatic electronic basis functions, linear combinations of the electronic wave functions calculated in the Born-Oppenheimer approximation. Vibrational wave functions were the eigenfunctions of a two-dimensional harmonic oscillator. A model Hamiltonian involves the electronic part, the kinetic energy operator for the bending vibrations, the operator for rotations around the z axis, corresponding to the smallest moment of inertia, and the spin-orbit Hamiltonian in the phenomenological form. It is assumed that the terms describing the stretching vibrations and x,y -rotations can be separated from those contributing directly to the Renner-Teller effect and spin-orbit coupling. Molecular potentials functions, calculated by means of the DIESEL MR-CI [11] method, are assumed in the form of polynomial expansion in the coordinate ρ .

Results and Discussion

In Figure 1 the bending potential curves for the low-lying electronic states of NCN, are presented computed at bond lengths kept fixed at 2.328 bohr. The potential curves for the $1^1\Delta_g$ and $1^1\Sigma_g^+$ species are taken from our previous study [11]. In the same figure (top) are given the electronic moments for transitions between the ground state and the components of the $A^3\Pi_u$ state. The value for the electronic transition moment between the $X^3\Sigma_g^-$ and the components of the $A^3\Pi_u$ state computed at equilibrium geometry of the latter species is 0.334 a.u. The results of calculated spin-orbit splitting for the $K=1$ and $K=2$ vibronic levels are presented in Fig.2. *Ab initio* results are compared with experimentally obtained results.

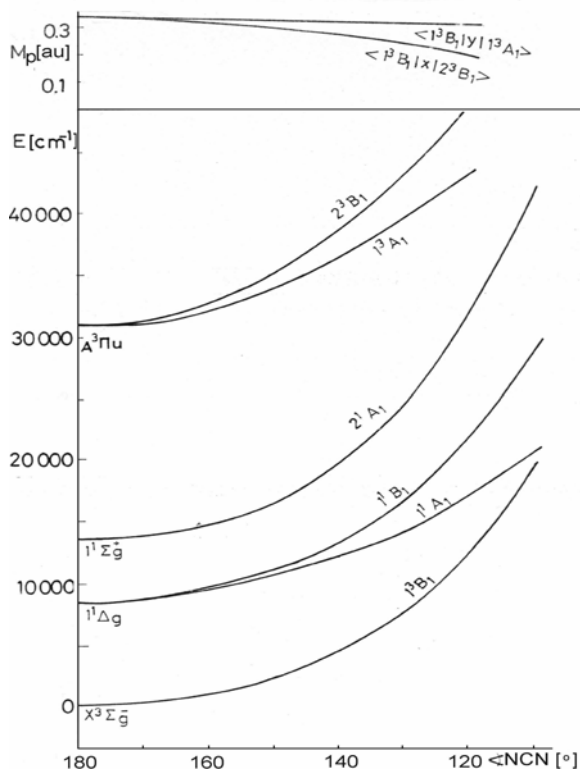


Fig.1. Bottom: Bending potential energy curves for the low-lying triplet and singlet electronic states of NCN, computed at the bond lengths kept fixed at 1.232 Å. Zero point at the energy scale corresponds to the minimum of the potential curve for the ground state, $X^3\Sigma_g^-$. Top: Electronic moments for transitions between the $1^3B_1(X^3\Sigma_g^-)$ state and the components of the $A^3\Pi_u$ state.

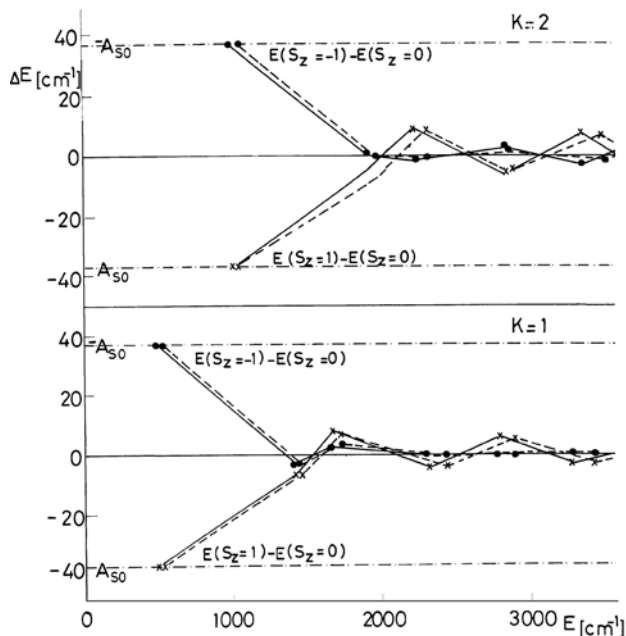


Fig.2. Spin-orbit splitting in $K=1$ and 2 vibronic levels of the $A^3\Pi_u$ state of NCN .

Solid line connects the results of calculations which employ *ab initio* potential curves, dashed line the results obtained using the experimentally derived potentials.

The results of this study are in good agreement with the corresponding experimental findings. They also could help the interpretation of future experiments.

References

- [1] K.R. Jennings and J.W. Linnett, *Trans. Faraday Soc.*, 1960, 56, 1737.
- [2] G. Herzberg and D.N. Travis, *Can. J. Phys.*, 1964, 42, 1658.
- [3] D. Mc. Naughton, G. F. Metha and R. Tay, *Chem. Phys.*, 1995, 198, 107.
- [4] K.D. Hensel and J. M. Brown, *J. Mol. Spectrosc.*, 1996, 180, 170.
- [5] M. Wienkoop, W. Urban and J. M. Brown, *J. Mol. Spectrosc.*, 1997, 185, 185.
- [6] S.A.Beaton, Y.Ito and J.M.Brown, *J. Mol. Spectrosc.*, 1996, 178, 99.
- [7] S. A. Beaton and J.M.Brown, *J. Mol. Spectrosc.*, 1997, 183, 347.
- [8] P. Rajendra and P. Chandra, *J. Chem. Phys.*, 2000, 114, 1589.
- [9] M. Perić, M. Krmar, J. Radić-Perić and Lj. Stevanović, *J. Mol. Spectrosc.*, 2001, 208, 271;
M. Krmar and M. Perić, *J. Serb. Chem. Soc.*, 2001, 66, 613.
- [10] M. Perić, M. Krmar, J. Radić-Perić and M. Hanrath, *J. Mol. Spectrosc.*, 2000, 204, 226.
- [11] M. Hanrath and B. Engels, *Chem. Phys.*, 1997, 225, 197.

VIBRATIONAL ANALYSIS OF THE β SYSTEM OF $^{11}\text{B}^{18}\text{O}$

M. Kuzmanović, V. Bojović, A. Antić-Jovanović and D. Pešić

*Faculty of Physical Chemistry, University of Belgrade,
P.O. Box 137, 11001 Belgrade, SCG*

Abstract

Twelve bands of the β system of $^{11}\text{B}^{18}\text{O}$ with $v' \leq 5$ and $v'' \leq 3$ have been recorded in emission between 230 and 300 nm and vibrationally analysed. The assignments have been confirmed by the isotope shift measurements. Vibrational constants have been determined for two electronic states involved.

Introduction

The first observation of the electronic spectrum of isotopic boron monoxide, including oxygen 18, has been done recently [1, 2]. Ten bands of the β system of $^{10}\text{B}^{18}\text{O}$, which is the $B^2\Sigma^+ - X^2\Sigma^+$ transition, have been vibrationally assigned and the rotational structure of the 0-0 and 0-1 bands, obtained at high resolution, has been analysed. Both analysis gave a set of the corresponding spectroscopic constants for two electronic states involved in transition.

No other data concerning the spectra of the isotopomers of BO containing the oxygen 18 could be found in the literature. Because this molecule is of astrophysical interest, as well as a candidate for chemical laser emission, it is important to assemble as much spectroscopic information as possible and to obtain the isotopic ratios allowing accurate predictions to be made. In the present paper the results of the vibrational analysis of the $^{11}\text{B}^{18}\text{O}$ molecule are presented.

Experimental

The source of the emission spectrum of $^{11}\text{B}^{18}\text{O}$ has been a low-pressure arc with the water cooled copper electrodes. The lower positive electrode contained amorphous boron with natural abundance of ^{11}B (~81%) and ^{10}B (~19%). The arc was run at the current of 6 A in an atmosphere of 4:1 mixture of argon and oxygen enriched up to 90 atome %, at about 2 kPa of total pressure. This conditions have been chosen as a result of tests with other ratios and other total pressures, considering the best spectrum/background ratio and appropriate intensity ratio of the bands of two isotopes. Favorable exiting conditions made it possible to record ten heads of the $^{11}\text{B}^{18}\text{O}$ with good intensity.

Exposures were taken on a 2m Ebert spectrograph (PGS-2, VIB Varl Zeiss) equipped with a 600 lines/mm grating giving a reciprocal linear dispersion of 0,37 nm/mm in the first order with double pass. The exposure time, using a HP5 spectral emulsion, varied from 30-60 minutes. The Fe standard lines have been used as a calibration spectrum. The wavenumber uncertainty of the band head positions is estimated to be better than 0,5 cm^{-1} .

Vibrational Analysis

Twelve bands in the spectrum recorded between 230 and 300 nm have been identified and vibrationally assigned. All the bands have a single headed structure because the R_1 and R_2 branches, which form the heads, are not resolved at low J values under dispersion used. Figure 1 show, as an example, the isotope shifts of the 0,1 and 0,2 bands of $^{10}\text{B}^{18}\text{O}$ and $^{11}\text{B}^{18}\text{O}$ molecules.

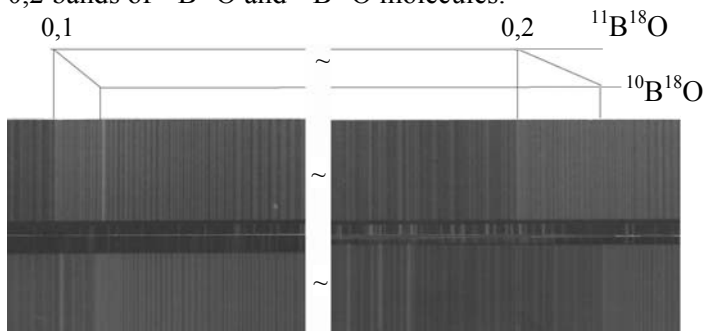


Figure 1. The isotope shifts of the 0,1 and 0,2 bands of the $^{10}\text{B}^{18}\text{O}$ and $^{11}\text{B}^{18}\text{O}$ molecules

The vibrational assignments, wavenumbers of measured band heads, experimental and calculated band head isotope displacements are given in the first, second, third and fourth columns of Table 1, respectively.

Table 1. Band heads of $^{11}\text{B}^{18}\text{O}$ and vibrational isotope shifts (cm^{-1})

ν', ν''	ν_h	$\Delta \nu^i = \nu(^{11}\text{B}^{18}\text{O}) - \nu(^{10}\text{B}^{18}\text{O})^*$	
		$\Delta \nu^i(\text{exp})$	$\Delta \nu^i(\text{cal})$
1,0	44120.2 (4)	-27.7	-27.8
0,0	42888.6(-2)	9.3	9.0
1,1	42300.9 (3)	27.0	26.9
2,2	41715.4(-7)	45.1	44.8
0,1	41069.1 (0)	63.5	63.6
2,3	39941.8 (1)		96.7
0,2	39272.5(-2)	115.7	116.8
0,3	37498.8(-6)	167.1	168.6
1,3	38731.0 (4)	132.1	131.9
1,4	36979.5 (1)	182.7	182.3
1,5	35249.7(-3)		231.4
1,6	33543.9 (3)	278.4	279.1

*Data used from ref.[2]

The spectrum of $^{11}\text{B}^{18}\text{O}$ is related to that of $^{10}\text{B}^{18}\text{O}$ by the constant $\rho = (\mu/\mu^i)^{1/2} = 0,9704877$, where μ^i denotes the reduced mass of the heavier isotope molecule.

The vibrational isotope effect Δv_i have been calculated within framework of the Born-Oppenheimer approximation according to the second order equation:

$$\Delta v_i = (1 - \rho)[\omega_e'(v'+1/2) - \omega_e''(v''+1/2)] - (1 - \rho^2)[\omega_e'x_e'(v'+1/2) - \omega_e''x_e''(v''+1/2)]$$

In this calculation, the equilibrium constants of the $^{10}\text{B}^{18}\text{O}$ for both *B* and *X* states have been used from ref [2]. The small differences between experimental and calculated values listed in the third and fourth columns arise as a consequence of disregarding the contribution of the rotational isotope effect at the heads. From the rotational analysis of the 0,0 and 0,1 bands of $^{10}\text{B}^{18}\text{O}$ [1] it was found that the latter is not more than half unit in the last digit. Hence it was neglected and the electronic isotope shift was assumed to be zero.

Determination of the Constants

Evaluation of the vibrational constants for the $^{11}\text{B}^{18}\text{O}$ isotope species has been done using the measured band heads given in Table 1 and the usual second order relation [3]. The results are given in Table 2.

Table 2. Vibrational constants of $^{11}\text{B}^{18}\text{O}$ molecule

State	ω_e	$\omega_e x_e$	T_e
$B^2\Sigma^+$	1253,00	10,96	43173,6
$X^2\Sigma^+$	1842,06	11,20	0

The wavenumbers of the band heads calculated with derived constants agree well with those given in the second column of Table 1. Numbers in parentheses denote differences $\nu_h(\text{exp}) - \nu_h(\text{cal})$ in the units of 10^{-1}cm^{-1} and all of these are free from any systematic deviation.

Conclusion

The present work gives the first vibrational constants for the electronic states $X^2\Sigma^+$ and $B^2\Sigma^+$ of isotopic molecule $^{11}\text{B}^{18}\text{O}$. The results confirm the vibrational assignments of the bands for all boron monoxide isotopomers including oxygen 18 as well as oxygen 16.

Acknowledgment

This work was supported by the Ministry of Science and Environmental Protection, RS, Grant no. 1928.

References

- [1] V. Bojović, A. Antić-Jovanović, D.S. Pešić and D. Isailović, Proceedings of the 6th International Conference "Physical Chemistry 2002". Beograd, 2002, 96.
- [2] V. Bojović, A. Antić-Jovanović, D. S. Pešić, D. Isailović and M. Kuzmanović, Spectrosc. Letters, 2003, 36, 531.
- [3] G. Herzberg, *Spectra of Diatomic Molecules*, 2nd ed., Van Nostrand, New York, 1950, p. 151.

UV-VISIBLE SPECTROPHOTOMETRIC DETERMINATION OF THE HYDRATATION AND COPIGMENTATION CONSTANTS OF CYANIDIN

J. Dimitrić-Marković*, N. Petranović, J. Baranac and T. Brdarić

*Faculty of Physical Chemistry, University of Belgrade,
Studentski trg 12-16, 11000 Belgrade*

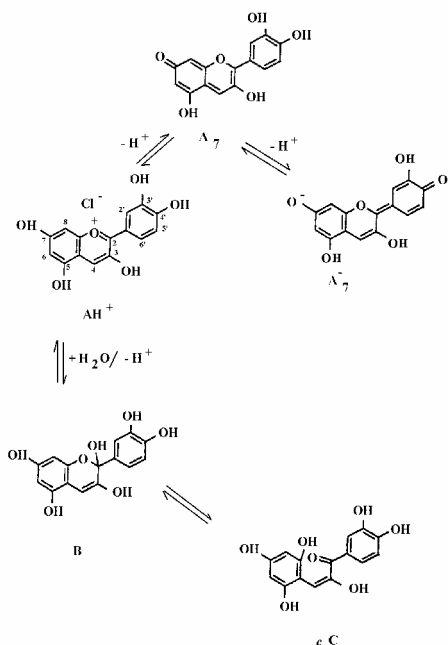
Abstract

The present paper reports on spectroscopic investigation of copigmentation effect of quercetin on cyanidin molecule. It was found that the association of cyanidin with the copigment molecule, namely quercetin, occurred for flavylium ion (pH 3.0) as well as for its pseudobase transformation form (pH 5.0). The hydration konstant pK_h value was found to be 2.43 and the copigmentation reaction constants: $K = 2332.1 \text{ mol}^{-1} \text{ dm}^3$ (pH 3.0) and $K = 1462.0 \text{ mol}^{-1} \text{ dm}^3$ (pH 5.0).

Introduction

The great variety of red, blue and purple tones of the flowers and fruits in nature come from anthocyanins, hydroxylated and metoxylated flavylium compounds, important plant pigments of the flavonoid class. In addition to their metabolic function in the pigmentation of many flowers, fruits, vegetables and grains anthocyanins are constantly gaining increasing interest because of their great ability against oxidative stress [1-3].

In vitro studies have shown that flavylium chromophore, upon dissolution in model buffered aqueous solutions, undergo complex equilibrium very sensitive to pH value and also to structural features of the investigated molecules [1]. An average pH value of natural media is moderately acidic [3] causing decolourisation of the most of flavylium molecules. It is therefore assumed that the color of anthocyanin molecules *in vivo* is influenced, besides by the pH value of the environment, their and concentration also by the composition of the media. The copigmentation is one of the possible reactions and is generally considered to be one of the most important factors influencing plant pigmentation *in vivo* [1-3]. It causes stabilization of the colored anthocyanin struc-



tural forms and consequently enhances their color. The present paper reports on spectroscopic determination of the hydration constant of cyanidin as well as on the *in vitro* investigation of copigmentation effect of quercetin on the cyanidin molecule structure.

Results and Discussion

Thermodynamic measurements: Hydration equilibrium.

The first step in experimental measurements was hydration constant determination. The K_h value gives access to the relative amounts of flavylium ion and pseudobase form at equilibrium at a given pH value and can be considered as a static measure of the pigment resistance to hydration process which always occurs in moderately acidic aqueous solutions. Since the copigmentation of cyanidin occurred at pH 3.0, involving the flavylium ion copigmentation, it was necessary to determine hydration constant and establish its influence on the copigmentation constant. The smaller K_h value (the larger pK_h value), the more resistant the pigment to hydration. Recording the visible absorbance of equilibrated cyanidin solutions at different pH values, the concentration of the pigment and the wavelength being held constant, allows the determination of the hydration thermodynamic constant according to the eq $A_0/(A_0 - A) = (K_h + K_a)/[K_h + K_a(1 - r_A)] + 10^{-pH}/[K_h + K_a(1 - r_A)]$ [4]. Obtained value for cyanidin pK_h 2.43 indicates little more pronounced susceptibility of cyanidin to hydration comparing to some of its glycosidized and acylated analogs [5].

Copigmentation

A reaction of copigmentation was investigated by the use of UV-vis absorption spectra in the whole range of acidic, moderately acidic and neutral buffered aqueous solutions (pH range 1.0 – 7.0). It was observed that the ratio $(A - A_0)/A_0$ (Fig. 1), as a good measure of the copigment effect, has two maxima, at pH 3.0 and pH 5.0 indicating the association of cyanidin with quercetin in its flavylium as well as in its anhydrobase form which was not the case with malvin, showing the affinity to association with quercetin only in its flavylium form [6]. At constant cyanidin concentration ($8 \times 10^{-5} \text{ mol dm}^{-3}$) adding of different aliquots of quercetin caused a bathochromic and a hyperchromic effect of the fundamental absorption maximum of cyanidin which were the main evidence of the copigment formation at the given pH values (Fig. 2). The copigmentation constant has been determined from equations $K = (A - A_0)/c[rA - A_0/(1 + K_h 10^{pH})]$ and $K = (A - A_0)/r'cA_0$ valid at different pH ranges, referring to flavylium ion and anhydrobase copigmentation. Obtained equilibrium constant values are: $K = 2332.1 \text{ mol}^{-1} \text{ dm}^3$ at pH 3.0 and $K = 1462.0 \text{ mol}^{-1} \text{ dm}^3$ at pH 5.0. Corresponding Gibbs function values are: and $\Delta G^0 = -19.2 \text{ kJ mol}^{-1}$ (pH 3.0) and $\Delta G^0 = -18.06 \text{ kJ mol}^{-1}$ (pH 5.0), indicating the spontaneous course of the reaction.

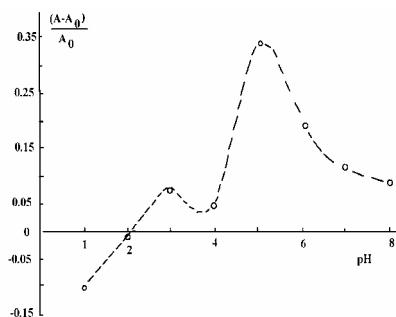


Fig. 1. Plot of $(A - A_0)/A_0$ vs. pH for $8 \times 10^{-5} \text{ mol dm}^{-3}$ cyanidin solutions in copigmentation with quercetin (mole ratio 1:1)

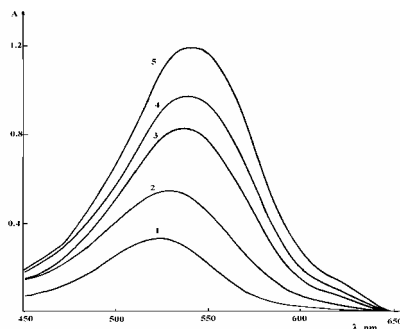


Fig. 2. UV-vis absorption spectra of cyanidin (1) and copigmentation complex with quercetin at pH 5.0. Mole ratios 1:0.5 (2); 1:1 (3), 1:1.5 (4) and 1:3 (5)

Conclusion

The obtained results confirm the copigmentation reaction between cyanidin, in its cationic and anhydrobase forms, and quercetin at pH values investigated. The copigmentation constant values indicate good copigmentation ability of quercetin molecule as was also the case with malvin copigmentation [6]. The negative values of ΔG^0 function generally indicate that copigmentation proceeds spontaneously. Concerning the Gibbs's function values, ΔG^0 , it can be said that the thermodynamic conditions for the reaction are more favorable at pH 3.0 than at pH 5.0. Relatively smaller pK_h value of the cyanidin aglycone form, comparing to the pK_h values of some acylated and glycosidized cyanidin analogs [5], indicate a less pronounced resistance of the pigment to hydration as a consequence of the substitution pattern of the pyrilium ring, namely position C3.

References

- [1] J. Harborne, C. Williams, *Natural Product Reports*, 1998, 15, 631.
- [2] J. Harborne, *Handbook of Natural Flavonoids*, Wiley, Chichester, 1999.
- [3] J. Harborne, *Chemistry and Biochemistry of Plant Pigments* (T.W. Goodwin) Academic Press, 1976, p 736.
- [4] O. Dangles, N. Saito, R. Brouillard, *J. Am. Chem. Soc.*, 1993, 115, 3125.
- [5] F. Stintzing, A. Stintzing, R. Carle, B. Frei, R. Wrolstad, *J. Agric. Food. Chem.*, 2002, 50, 6172.
- [6] J. Dimitric Markovic, PhD Thesis, Fac. of Physical Chemistry, Belgrade, 2001.

SPECTROPHOTOMETRIC STUDY OF THE INFLUENCE OF Mg(II) IONS ON THE HEMATOXYLIN AUTOOXIDATION IN WEAKLY ALKALINE AQUEOUS SOLUTIONS

G. Nikolić¹, S. Sunarić¹, R. Pavlović¹, G. Kocić² and R. Nikolić³

¹ Department of Chemistry, Faculty of Medicine, Bulevar dr Zorana Đinđića 81, 18000 Niš, Serbia and Montenegro, ² Department of Biochemistry, Faculty of Medicine, Bulevar dr Zorana Đinđića 81, 18000 Niš, Serbia and Montenegro, ³ Department of Chemistry, Faculty of Science, Višegradska 33, 18000 Niš, Serbia and Montenegro

Abstract

The influence of Mg(II) ions on the autooxidation of hematoxylin in weakly alkaline aqueous solutions was investigated. Based on the results of spectrophotometric measurements we concluded that hematein was the first product of the hematoxylin autooxidation in weakly alkaline aqueous solutions. In the presence of Mg(II) ions the spin stabilized *ortho*-semiquinone radical was probably the first autooxidation product of hematoxylin. Autooxidation at later stages proceeded via the breakage of extended double bond conjugation as evidenced by the absorbance decrease at higher wavelengths and slow, but steady, increase of absorbance at lower wavelengths.

Introduction

Hematoxylin is a natural polyphenolic compound with many applications in dyeing and histochemical staining [1]. These applications are largely dependent on its ease of oxidation and ability of complex formation with various metal ions for both hematoxylin and its oxidation product hematein [2-4]. Recent research pointed out that due to its specific structure with two *ortho*-dihydroxy groups at two separated benzene rings hematoxylin might act as a very efficient antioxidant and superoxide anion radical scavenger [5].

In this paper we studied the influence of Mg(II) ions on the hematoxylin autooxidation in weakly alkaline aqueous solutions by using UV/VIS spectrophotometry.

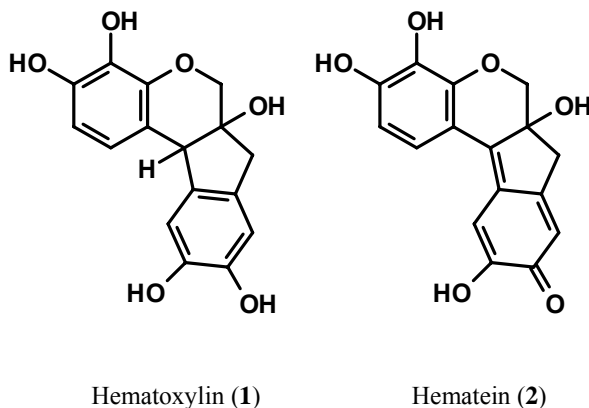


Figure 1. Chemical structures of hematoxylin (1) and its oxidation product hematein (2)

Experimental

All the chemicals used in this study were of reagent grade purity and hematoxylin (Merck, Germany) was used without additional purification. Solutions were prepared just prior the use by dissolving exactly weighted amount of hematoxylin in distilled water saturated with ambient air. Hematoxylin autooxidation was stimulated by mixing hematoxylin solution ($5 \times 10^{-5} \text{ mol dm}^{-3}$) with equal volume of either Tris or Tris-Mg buffer in an open glass cup. Tris-Mg buffer was prepared by dissolving magnesium chloride in Tris buffer (100 mmol, pH 8.4) up to the final concentration of $0.2 \text{ mol dm}^{-3} \text{ Mg(II)}$ ions.

A Beckman DU530 spectrophotometer with 1 cm quartz cuvettes was employed for recording UV/VIS spectra.

Results and Discussion

The UV/VIS spectra of hematoxylin solution in Tris and Tris-Mg buffer after various time intervals are presented in Figure 2.

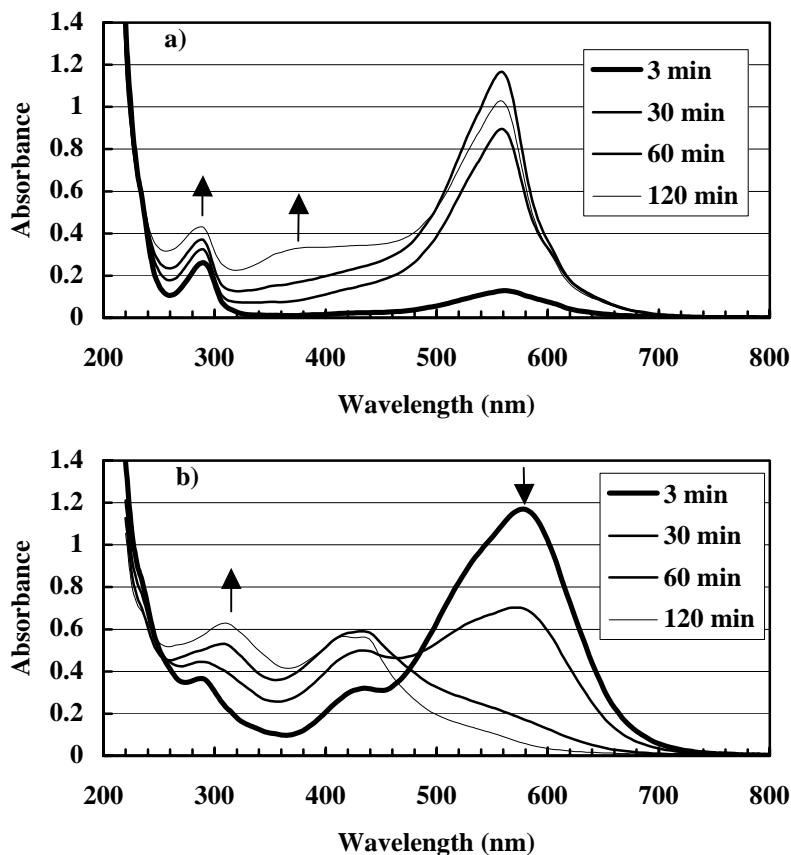


Figure 2. UV/VIS spectra of hematoxylin solution in Tris (a) and Tris-Mg buffer (b) after various time intervals.

Spectrophotometric data for both hematoxylin/Tris buffer and hematoxylin/Tris-Mg buffer solution indicate that complex transformations of hematoxylin took place during the autooxidation in weakly alkaline aqueous solutions. In the case of hematoxylin/Tris buffer solution we suppose that the first step during the autooxidation was slow formation of hematein as evidenced by the absorbance increase at 560 nm [3].

As for the hematoxylin/Tris-Mg buffer solution the quick appearance of the large absorption maximum at 575 nm may be explained by the formation of the Mg(II) ion spin stabilized *ortho*-semiquinone type radical. Similar changes, although at slower rates, have already been observed during the autooxidation of catechol (1,2-benzenediol) in the presence of Mg(II) ions [6]. Also, some preliminary electron spin resonance (ESR) measurements confirmed the formation of stable free radical(s) only in the presence of Mg(II) ions.

Autooxidation at later stages proceeded via the breakage of extended double bond conjugation as evidenced by the absorbance decrease at higher wavelengths and slow, but steady, increase of absorbance at lower wavelengths. It is clear, however, that additional experiments and use of other spectroscopic and/or chromatographic techniques are necessary for more detailed conclusions.

References

- [1] H. Puchtler, S.N. Meloan, F.S. Waldrop, *Histochemistry*, 1986, 85, 353.
- [2] K. Shirai, M. Matsuoka, *Dyes Pigm.*, 1996, 32, 159.
- [3] Ch. Bettinger, H.W. Zimmermann, *Histochemistry*, 1991, 95, 279.
- [4] F. Roubani-Kalantzopoulou, N.A. Katsanos, *Z. Phys. Chem. (Munich)*, 1986, 149S, 165.
- [5] S. Kitagawa, H. Fujisawa, H. Sakurai, *Chem. Pharm. Bull.* 1992, 40, 304.
- [6] G.M. Nikolić, P.I. Premović, R.S. Nikolić, *Spec. Lett.*, 1998, 31, 327.

UV/VIS SPECTRA NAD ANTIMICROBIAL ACTIVITY OF Cu(II) AND Zn(II) COMPLEXES ISATIN SCHIFF BASE

S. Konstantinović¹, B. Stojčeva-Radovanović², S. Ilić¹ and Z. Todorović¹

¹Faculty of Technology, Bulevar Oslobođenja 124, 16000, Leskovac

²Department of Chemistry, Faculty of Science, Cirila i Metodija 2, 18000, Nis, Serbia and Montenegro

Abstract

Coordination compounds of Cu(II) and Zn (II) with Schiff base β -phenylhydrazone of isatin were prepared. Their structure was established to be MeLCl_2 using elemental analysis, atomic absorption (AA), molar conductivity, magnetic susceptibility measurements, Fourier transform infrared (FTIR), electron absorption (UV/VIS) spectroscopic methods. The results indicate complexation through the nitrogen and the oxygen atom of the isatin part of the ligand. The central ion is in an tetrahedral environment. The complexes were tested for an antibacterial activity against *Staphylococcus aureus* ATTC 6538, *Pseudomonas aeruginosa*, *Proteus vulgaris*, *Escherichia coli* 95 and *Candida albicans* ATTC 10231 by the disc method.

Introduction

A large number of isatin products have great activity against some microorganisms. Also, many thiosemicarbazone products find wide application in medicine as active physiological preparations, due to their activities against tuberculosis, certain types of cancers and microorganisms. Also, many hydrazine products find wide application in medicine as active physiological preparations, due to their activities against tuberculosis, certain types of cancers and microorganisms [1]. It has been established that many coordination compounds of transition metals with some Schiff base as ligands have selective activities and it has been established that complexes have greater activity than the ligands [2-5].

Experimental

All chemicals used for the preparation of the compounds were of AR grade. The electronic absorption spectrum was recorded on a Varian GBC UV/VIS 911 A Spectrophotometer, using $1 \cdot 10^{-3} \text{ mol} \cdot \text{dm}^{-3}$ solutions in DMF of complexes. For the disc method [9], stock solutions of $15 \text{ mg} \cdot \text{cm}^{-3}$ concentration were made with a solvent mixture of 50% DMF and 50% $0.1 \text{ mol} \cdot \text{dm}^{-3}$ NaOH. Onto disks, $2 \cdot 10^{-6} \text{ mol} \cdot \text{dm}^{-3}$ of stock solution was dropped, and then dried at room temperature. Suspensions were made from the 24-hour blood agar culture of the bacteria incubated at 310 K for 3 h. The microbial suspension was transferred to the antimicrobial test medium and the disk was placed on it. After the incubation at 310 k for 178 h, the incubation zones were measured (mm).

Synthesis of Ligand and Complexes

Ligand was obtained by reacting isatin and phenylhydrazine in 1:1 ratio in ethanol solution following the procedure previously reported [4,5].

A hot solution of ligand was added to an ethanol solution of metal(II) chloride. The solution was refluxed for 2 h and stirred for 1 day. After slow evaporation of the solvent a solid was isolated.

[CuLCl₂].H₂O

Yield: 64.15%

Found: 43.40%C, 2.95%H, 10.96%N, 18.19%Cl, 16.29%Co

Calcd: 43.24%C, 2.83%H, 10.81%N, 18.27%Cl, 16.34%Cu.

Mp: 255⁰C

[ZnLCl₂].H₂O

Yield: 60.15%

Found: 43.11%C, 2.79%H, 11.59%N, 18.05%Cl, 16.92%Co

Calcd: 43.03%C, 2.81%H, 10.75%N, 18.18%Cl, 16.75%Zn.

Mp: 254⁰C

Results and Discussion

The coordination compound of Cu(II) and Zn(II) were synthesized by the direct reaction of the Schiff base in the presence of the MeCl₂ in 95% ethanol, using 1:1 mole ratio of all reactants.

Electronic Spectra

The electronic spectra of the investigated complexes and ligand were recorded in DMF (Table I). The copper (II) coordination compound retained their brown color in solution. The electronic absorption spectra of the Cu(II) complex exhibit bands (bands II and III) which can be assigned to an ²E→²T₂ transition, which is consistent with tetrahedral geometry around the metal ion. The I band in the electronic spectra of the copper and I and II bands in the electronic spectra of the zinc ion, are assigned to charge transfer transitions. [6-8].

Table I Electronic spectral data of the investigated complexes recorded in DMF

Compound.	Band position (cm ⁻¹)/ε _{max} × 10 ³ (mol ⁻¹ dm ³ cm ⁻¹)	Bands	Geometry
CuLCl ₂	21.5/0.942	I	<i>Td</i>
	19.7/0.405	II	
	15.01/0.201	III	
ZnLCl ₂	26.9/1.345	I	<i>Td</i>
	20.4/0.450	II	

Antimicrobial Activity

All tested compounds have antimicrobial activity against selected microorganisms (Table II). The results show that the coordination compounds have enhanced activity compared to the ligands, which indicates that the coordinated metal(II)ion have an influence on the antibacterial effects.

Table II The range of inhibition zones (mm) of the investigated compounds

Compound	<i>E. coli</i>	<i>P.vulgaris</i>	<i>S. aureus</i> (mm)	<i>P. aeruginosa</i>	<i>C. albicans</i>
L	20	20	8	28	28
CuLCl ₂	24	28	15	30	31
ZnLCl ₂	25	28	16	35	35

The best activity show ZnLCl₂ complex. All complexes show the best activity against bacteria *Pseudomonas aeruginosa* and yeast *Candida albicans*.

Acknowledgment

The authors gratefully acknowledge the financial support of the Ministry of Science and Technology of the Republic of Serbia.

References

- [1] N. M. Samus, T. A. Burdenko, V. V. Gylka, V. J. Tsapkov, J. Chem. Pharma., 1994, 12, 40.
- [2] E. M. Jouad, G. Larcher, M. Allain, A. Riou, G. M. Bouet, M. A. Khan, X. D. Thanh, J. Inorg. Biochem., 2001, 86, 565.
- [3] P. Tarsconi, S. Capacchi, G. Pelosi, M. Cornia, R. Albertini, A. Bonati, P. P. Dall'Aglio, P. Lunghi, S. Pinelli, Bioorg. Med. Chem., 2000, 8, 157.
- [4] B.C. Stojceva Radovanović, S. S. Anđelković, J. Serb. Chem. Soc., 1998, 63, 379.
- [5] B.C. Stojceva Radovanović, S. S. Anđelković, Analytical Lab., 1997, 6, 90.
- [6] J. Csaszar, J. Moway, O. Herceczeg, Acta Phys. et Chem., 1988, 31, 717.
- [7] A. Z. El-Sonbati, Spectroscopy Lett., 1998, 30, 459.
- [8] A. B. P. Lever, Inorganic Electronic Spectroscopy, 2nd Edn., Toronto, 1987, pp. 147-216.
- [9] N. M. Samus, E. N. Shlyahov, T. A. Burdenko, L. L. Simonova, V. J. Tsapkov, J. Chem. Pharma, 1985, 20, 705.

UV/VIS SPECTRA AND ANTIMICROBIAL ACTIVITY OF Co(II) COMPLEXES WITH ISATIN SCHIFF BASES

B. Stojčeva-Radovanović¹ and S. Konstantinović²

¹Department of Chemistry, Faculty of Science, Cirila i Metodija 2, YU-18000, Nis

²Faculty of Technology, Bulevar Oslobođenja 124, YU-16000, Leskovac

Abstract

Coordination compounds of Co (II) with Schiff bases such as β -semicarbazone of isatin (L_1) and β -thiosemicarbazone of isatin (L_2) were prepared. Their structure was established to be CoL_2Cl_2 by using elemental analysis, as well as molar conductivity, FTIR, UV/VIS and 1H NMR spectroscopic methods. This paper presents the results gained from the UV/VIS spectra. The results indicate complexation through the nitrogen and the oxygen atom of the isatin part of the ligand. The central ion is in an octahedral environment. The complexes were tested for an antibacterial activity against *Staphylococcus aureus* ATTC 6538, *Enterococcus D*, *Proteus mirabilis*, *Escherichia coli* 95 and *Candida albicans* ATTC 10231 in a standard minimum inhibitory concentration (MIC) of serial dilution test.

Introduction

A large number of isatin products have great activity against some microorganisms. Also, many thiosemicarbazone products find wide application in medicine as active physiological preparations, due to their activities against tuberculosis, certain types of cancers and microorganisms [1]. The heterocyclic thiosemicarbazones and their metal complexes are among the most widely studied compounds for their potential therapeutic uses, such as antitumoral, fungicidal, bactericidal or antiviral activity [2,3].

Experimental

All chemicals used for the preparation of the compounds were of AR grade. The electronic absorption spectrum was recorded on a Varian GBC UV/VIS 911 A Spectrophotometer, using $1 \cdot 10^{-3}$ mol·dm⁻³ solutions in DMF of complexes. Bacteria and yeast was inoculated into 5 cm³ of a liquid medium. Antimicrobial activity of the ligands and their metal complexes was determined by following the bacterial growth for 24 h at 35⁰C, and yeast growth for 48 h at 30⁰C in the nutrition medium. The different concentration of the tested compounds in DMF as solvent at which no increase in the optical density was observed after incubation of 24 h and 48 h, were accepted as the minimal inhibitory concentration (MIC, $\mu\text{g} \cdot \text{cm}^{-3}$) [9]. The presented results present average values gained from three measured.

Synthesis of Ligands and Complexes

Ligands were obtained by reacting isatin and semicarbazide (thiosemicarbazide) in 1:1 ratio in ethanol solution following the procedure previously reported [4,5].

A hot solution of ligand was added to an ethanol solution of cobalt(II) chloride. The solution was refluxed for 2 h and stirred for 1 day. After slow evaporation of the solvent a dark red solid was isolated.

Results and Discussion

The coordination compound of Co(II) were synthesized by the direct reaction of the Schiff base in the presence of the $\text{CoCl}_2 \cdot 6\text{H}_2\text{O}$ in methanol, using 1:1 mole ratio of all reactants.

$\text{Co}(\text{L}^1_2)\text{Cl}_2$

Yield: 45.20%

Found: 39.68%C, 3.65%H, 17.86%N, 14.68%Cl, 12.41%Co

Calcd: 39.51%C, 3.29%H, 17.28%N, 14.61%Cl, 12.12%Co.

Mp: 258⁰C

$\text{Co}(\text{L}^2_2)\text{Cl}_2$

Yield: 61.12%

Found: 41.8%C, 2.8%H, 15.86%N, 20.05%Cl, 16.92%Co

Calcd: 30.69%C, 2.84%H, 15.91%N, 20.17%Cl, 16.73%Co.

Mp: 264⁰C

Electronic Spectra

The electronic spectra of the investigated complexes and ligand were recorded in DMF (Table I). The spectra of the ligand show intense bands in the UV region around 30000 cm^{-1} and 36000 cm^{-1} . None of the observed bands can be assigned to an $n - \pi^*$ transition, since any such transition would be completely overlapped by $\pi - \pi^*$ bands of much higher intensity [6]. The cobalt (II) coordination compounds retained their dark red color in solution. The electronic absorption spectra of the Co(II) complexes exhibit bands, which are assigned to ${}^4\text{T}_{1g} \rightarrow {}^4\text{T}_{2g}(\text{F})$ and ${}^4\text{T}_{1g} \rightarrow {}^4\text{T}_{1g}(\text{P})$ transitions, typical for octahedral geometry [7,8].

Table I Electronic spectral data of the investigated complexes recorded in DMF

Compound.	Band position (cm^{-1})/ $\epsilon_{\text{max}} \times 10^3 (\text{mol}^{-1} \text{dm}^3 \text{cm}^{-1})$	Assignments	Geometry
$\text{Co}(\text{L}^1_2)\text{Cl}_2$	8798/0.45	${}^4\text{T}_{1g} \rightarrow {}^4\text{T}_{2g}(\text{F})$	<i>Oh</i>
	22000/0.92	${}^4\text{T}_{1g} \rightarrow {}^4\text{T}_{1g}(\text{P})$	
$\text{Co}(\text{L}^2_2)\text{Cl}_2$	8699/0.0.62	${}^4\text{T}_{1g} \rightarrow {}^4\text{T}_{2g}(\text{F})$	<i>Oh</i>
	21910/0.95	${}^4\text{T}_{1g} \rightarrow {}^4\text{T}_{1g}(\text{P})$	

Antimicrobial activity

The Schiff bases as ligands possess different antimicrobial activity against selected microorganisms which decreases in order $\text{L}_2 > \text{L}_1$, probably due to the presence of an C=S group present in β -thiosemicarbazone of isatin.

The results show that the coordination compounds have enhanced activity compared to the ligands, which indicates that the coordinated cobalt(II) ion has an influence on the antibacterial effects.

The best activity shows $\text{Co}(\text{L}^2)_2\text{Cl}_2$.

All complexes show the best activity against gram-positive bacteria *Staphylococcus aureus* and yeast *Candida albicans*.

Table II MIC values ($\mu\text{g}\cdot\text{cm}^{-3}$) of the investigated compounds

Compound	<i>E. coli</i>	<i>P. mirabilis</i>	<i>S. aureus</i>	<i>E. grupa D</i>	<i>C. albicans</i>
	MIC (μgcm^{-3})				
L^1	>1000	>1000	>1000	>1000	>1000
$\text{Co}(\text{L}^1)_2\text{Cl}_2$	200-500	50-200	50-200	200-500	<50
L^2	>500	>500	>500	>500	>500
$\text{Co}(\text{L}^2)_2\text{Cl}_2$	50-200	50-200	<50	50-200	<50

Acknowledgment

The authors gratefully acknowledge the financial support of the Ministry of Science and Technology of the Republic of Serbia.

Reference

- [1] N. M. Samus, T. A. Burdenko, V. V. Gylka, V. J. Tsapkov, *J. Chem. Pharma.*, 1994, 12, 40.
- [2] E. M. Jouad, G. Larcher, M. Allain, A. Riou, G. M. Bouet, M. A. Khan, X. D. Thanh, *J. Inorg. Biochem.*, 2001, 86, 565.
- [3] P. Tarsconi, S. Capacchi, G. Pelosi, M. Cornia, R. Albertini, A. Bonati, P. P. Dall'Aglio, P. Lunghi, S. Pinelli, *Bioorg. Med. Chem.*, 2000, 8, 157.
- [4] B.C. Stojceva Radovanovic, S. S. Andjelkovic, *J. Serb. Chem. Soc.*, 1998, 63, 379.
- [5] Sandra S. Konstantinovic, Blaga C. Radovanovic, Zivojin Cakic, Vesna Vasic, *J. Serb. Chem. Soc.*, 2003, 68, 641.
- [6] J. Csaszar, J. Moway, O. Hercezeg, *Acta Phys. et Chem.*, 1988, 31, 717.
- [7] A. Z. El-Sonbati, *Spectroscopy Lett.*, 1998, 30, 459.
- [8] A. B. P. Lever, *Inorganic Electronic Spectroscopy*, 2nd Edn., Toronto, 1987, pp. 147-216
- [9] N. M. Samus, E. N. Shlyahov, T. A. Burdenko, L. L. Simonova, V. J. Tsapkov, *J. Chem. Pharma.*, 1985, 20, 705.

COMPLEXES OF CHLOROPHYLL WITH COPPER, ZINC AND LEAD: UV/VIS, FT/IR AND FLUORESCENCE STUDIES

J. Petrović, G. Nikolić and D. Marković

University of Nish, Faculty of Technology, 16000, Leskovac, Serbia

Abstract

Several toxic heavy metals like zinc (Zn), lead (Pb) and copper (Cu), are easily absorbed by plants. Once absorbed, they penetrate to plant tissues (including leaves) and in higher concentrations, they may inhibit photosynthesis by replacing labile bonded central magnesium atom (Mg), forming chlorophyll-heavy metal complexes (Chl-HMS). The Chl-HMS complexes may cause an impairment of photosynthetic function, and this, as a final consequence, may lead to plants' fatal end. That is why is so important to note difference between the Chl-HMS complexes and unsubstituted chlorophylls; for this purpose UV/VIS, FT/IR and fluorescence spectroscopies have been employed in this work. The Chl-HMS complexes are prepared *in vitro* by using several heavy metals with different affinities toward central Mg-position in chlorophyll molecule. However they have affinity toward other position, too: between C-13³ keto (C=O) group and the enolic form of C-13¹ keto group they can make peripheral chelat complexes (Fig.1b). The chosen heavy metals (Cu, Zn and Pb) are well known pollutants.

Introduction

Chlorophyll (Chl) has a major function in photosynthesis. In chemical terms, Chl is a chlorin, porphyrin derivate (cyclic tetrapyrrol with isocyclic cyclopentanone ring, fused to pyrrole ring between C-13 and C-15), where central metal Mg-atom coordinates four symmetric pyrrole rings (Fig.1a).

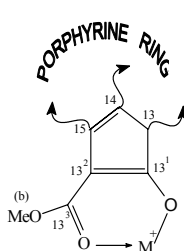
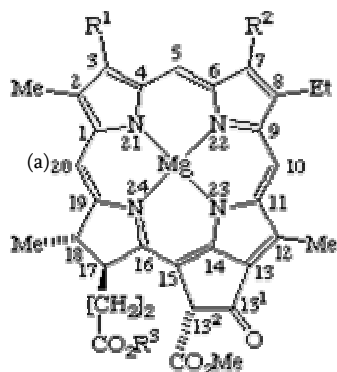


Fig.1: (a) Structure of Chl_a molecule (R¹= vinyl, R², Me= methyl, R³= phytyl, Et= ethyl)

(b) Peripheral chelat Chl-HMS complex (M=Zn, Cu, Pb).

A substitution of central Mg-atom by three chosen metals (Cu, Zn, Pb) in isolated Chl-fractions (from spinach leaves) has been examined in this work, by investigating stability of Chl-HMS complexes, as well as a

change in their spectral behavior following an increase of metals concentration: UV/VIS, FT/IR and fluorescent spectra have been employed for such a purpose.

Materials and Methods

Plant pigments were extracted from spinach leaves by using method proposed by Swec [1]. The pigments mixture contains large amounts of various Chl-forms (with predominant

contribution of Chlorophyll *a* - Chl*a*) as well as accessory pigments, carotenoids. The Chl-fractions were isolated using a modified procedure of Swec [2] – column chromatography with silica gel as the adsorbent and benzene/acetone mixture as the eluent. High percentage of Chl*a* in the separated Chl-fractions has been proved by HPLC (modified method by Scholz and Ballschmiter [3]), by using the appropriate standards. Chl-HMS were prepared according to a modified method proposed by Kupper [4-5], by using aqueous Cu^{2+} , Zn^{2+} and Pb^{2+} solutions, varying their concentrations (0.025M and 0.05M), as well as time periods following the complexes formation (t_c). Visible and fluorescence spectra of Chl-HMS were recorded (a) with constant heavy metal concentration but after different t_c periods and, (b) with different, increasing heavy metal concentrations, for the same t_c value (Figs.2-4). In FT/IR spectra new bands emerged, indicating structural differences between the Chls and Chl-HMS.

Results and Discussion

Chlorophylls have two major absorption regions in visible range: “red” (Q) band and “blue” (Soret or *B*) band [6] (Fig.2). The changes were detected in Chl-HMS both with B and Q-bands.

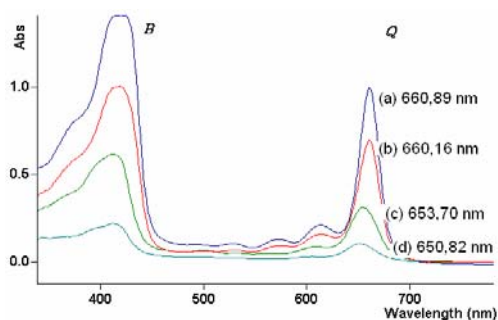


Fig.2. UV/VIS spectra:

- (a) Chl-fraction
- (b) Cu-Chl complex (105 min)
- (c) Cu-Chl complex (5 days)
- (d) Cu-Chl complex (19 days)
- (in acetone)

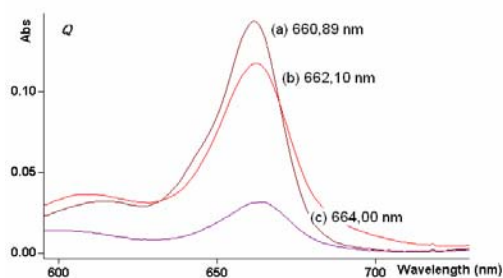


Fig.3. UV/VIS spectra:

- (a) Chl-fraction
- (b) Pb-Chl complex (4 days)
- (c) Pb-Chl complex (5 days)
- (in acetone)

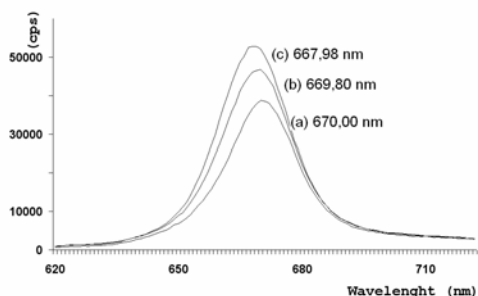


Fig.4. Fluorescent spectra:

- (a) Chl-fraction
- (b) Zn-Chl complex ($C_{\text{Zn}^{2+}}=0,025\text{M}$)
- (c) Zn-Chl complex ($C_{\text{Zn}^{2+}}=0,05\text{M}$)
- (in acetone, $\lambda_{\text{ex}}=430\text{ nm}$)

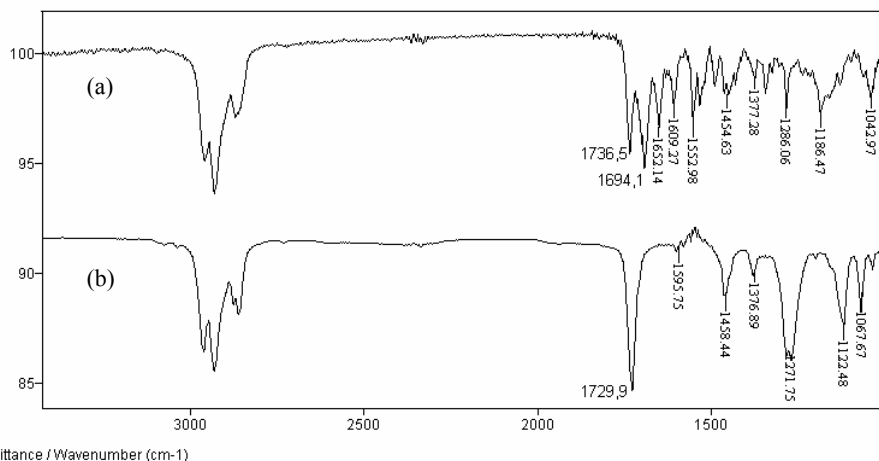


Fig.5. FT/IR spectra: (a) Chl-fraction; (b) Zn-Chl-complex (in CCl_4)

A hypsochromic shift has been observed for Q-band of Cu-Chl complexes - relative to t_c time (Fig. 2) - and a bathochromic shift (Q-band, too) for the Pb-Chl complexes (Fig.3). The fluorescence spectrum of Chl (obtained by using 430 nm excitation beam) obeys a mirror-image relationship between absorption and fluorescence spectra [7]. The spectra suffer “blue” shift and increasing intensity of Zn-Chl complexes relative to increasing concentration of Zn^{2+} (Fig. 4). The FT/IR spectrum of unsubstituted Chl shows expected band at 1694.1 cm^{-1} assigned to the free $\text{C}-13^1\text{C}=\text{O}$ group and a band at 1736.5 cm^{-1} assigned to the ester $\text{C}-17^3$, $\text{C}-13^3\text{C}=\text{O}$ groups [8]. In FT/IR spectrum of Zn-Chl the 1694.1 cm^{-1} band has disappeared, but the latter one is shifted to 1729.9 cm^{-1} (Fig.5). An interaction between Chl molecule and Zn^{2+} ion to form peripheral chelat metal-Chl complex [9] (Fig.1b) has been suggested (band at 1122.48 cm^{-1} in FT/IR spectrum of Zn-Chl complex is assigned to the $\text{C}-13^1\text{C}-\text{O}$ enolic group).

Conclusion

Complexes of chlorophyll with Cu, Zn and Pb appeared to be promising, potential probe to detect presence of toxic metals in polluted environment. Clear differences in UV/VIS, FT/IR and fluorescent spectra have been noted between unsubstituted chlorophylls and Chl-HMS complexes. Stability of the complexes appeared to be time-dependent. They are also sensitive to the metals concentration.

References

- [1] W. A. Svec, Chlorophylls, CRC Press, Boca Raton, Fl., 1991.
- [2] W. A. Swec, The Porphyrins, Academic Press, New York, 1978.
- [3] B. Scholz, K. Ballschmiter, J. Chromatogr., 1981, 208, 148.
- [4] H. Kupper, F. Kupper, M. Spiller, J. Exp. Botany, 1996, 47, 259.
- [5] H. Kupper, M. Spiller, F. Kupper, Anal. Biochem., 2000, 286, 247.
- [6] J. Hoff, J. Amesz, Chlorophylls, CRC Press, Boca Raton, Fl., 1991.
- [7] K. K. Karukstis, Chlorophylls, CVRC Press, Boca Raton, Fl., 1991.
- [8] K. Ballschmiter, J. J. Katz, Nature, 1968, 220, 1231.
- [9] H. Scheer, J. Am. Chem. Soc., 1975, 97, 3273.

SPECTROSCOPIC CHARACTERIZATION OF SOME PHENYL-HYDRAZINE SCHIFF BASES

G. Petrović, B. Radovanović and O. Jovanović

Faculty of Natural Sciences Niš, Višegradska33, 18 000 Niš, SCG

Abstract

A certain number of Schiff bases were synthesised, by condensation reaction of different substituted benzaldehydes as carbonyl component with various phenylhydrazines. Each compound was observed through its spectral characteristics, established by FT IR and UV/VIS spectroscopies, in aim to prove its' chemical structure. Analysis which were undertaken for these compounds, results in some specific conclusions for every of these Schiff bases, mostly in domain of electron density transition.

Introduction

A large number of Schiff bases were investigated by the different authors in the aim to examine their significant biological and pharmacological activity^[1]. It is known that many of Schiff bases find wide chemotherapeutic applications in clinical and veterinary medicine. It has also been found that that derivatives of benzilidene can be very useful, not only because of their strong activity against some micro organisms, but also because they can act as scavengers of free radicals. The phenylhydrazines itself find wide application in medicine as active physiological preparations, due to their activities against tuberculosis, certain types of cancers and micro organisms^[2,3]. The electron pair on the nitrogen atom and the electron-donor characteristic of the double bond enable Schiff bases to behave as bases. As the activity of Schiff bases is derived from the C=N group, the presence of the different substituents in their molecules can strongly effect the electron density and change their properties at all^[4-6].

Considering all of this, it was interesting to synthesize compounds of this nature with potential biological activity and examine their spectral characteristics. Four phenylhydrazine Schiff bases were prepared and examined by FT IR and UV/VIS spectroscopy.

Experimental

The four Schiff bases were prepared by refluxing equimolar amounts of 3,4-dihydroxy-benzaldehyde and 3,4-dimethoxy-benzaldehyde with phenylhydrazine and 2,4-dinitro-phenylhydrazine in 95% ethanol at pH 4,5 for about 0,5h. The products were filtered off, washed, recrystallized from absolute ethanol and finally dried. The yield of all products was over 80%.

All the chemicals and solvents used were of AR grade.

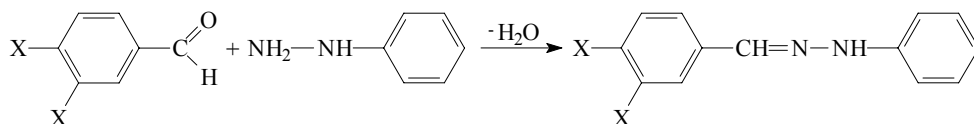


Figure 1. Simple reaction scheme

The Fourier transformation infrared spectra (FT-IR) were recorded with a Michaelson Bomen MB-series spectrophotometer, using the potassium bromide pellet (1mg/100mg KBr) technique.

The electronic (UV) spectra were recorded between 450nm and 190nm on a Perkin Elmer Lambda 15 UV/VIS spectrophotometer. The absorbances were measured in 1cm long quartz cell using 10^{-4} M solutions in absolute ethanol.

Results and Discussion

The synthesised Schiff bases were: *N*-(3,4-dihydroxy-bezilidene)-*N'*-phenyl-hydrazine (HBPH); *N*-(3,4-dimethoxy-bezilidene)-*N'*-phenyl-hydrazine (MBPH); *N*-(3,4-dihydroxy-bezilidene)-*N'*-(2,4-dinitro-phenyl)-hydrazine (HBNPH) and *N*-(3,4-dimethoxy-bezilidene)-*N'*-(2,4-dinitro-phenyl)-hydrazine (MBNPH).

It was observed by the analysis of FT IR spectra of prepared compounds (Table I.) that there are no more characteristic aldehyde C=O stretching absorption bands around 1660cm^{-1} . This fact and the presence of the new band in the region of $1611\text{-}1620\text{cm}^{-1}$ of C=N stretching vibrations, confirms the formation of Schiff bases. Valence vibrations of azomethine group are shifted to the lower frequencies. Explanation of such behaviour can be found in the effect of *para*-substituents and their electron influence on the rest of the molecule. The conjugation in the hydrazine part of molecule produce the absorption bands at 2359cm^{-1} and 1419cm^{-1} related to the contributions of the resonance forms.

Table I. FT IR spectral data of investigated compounds

Compound	Assignment of bands				
	$\nu(\text{C}=\overset{\oplus}{\text{N}}=\overset{\ominus}{\text{N}})$	$\nu(\text{C}=\text{N})$	$\nu(\text{C}=\text{N})$	$\nu(\text{C}-\text{O})$	$\nu(\text{C}-\text{NO}_2)$
HBPH	2359w	1611m	1419m	1264,1233s	-
MBPH	2359w	1611m	1419m	1264,1234s	-
HBNPH	2359w	1620s	1418m	1275,1250s	1330s
MBNPH	2359w	1617s	1420m	1267,1241s	1321s

Relative intensity: s – strong, m – medium, w – weak.

The precise explanation of the UV spectra of the obtained Schiff bases is very difficult because of the presence of the two similar benzene rings (Table II). Absorption bands of the benzene ring from the aldehyde part of molecule and the ring from the hydrazine part of molecule covered each other and make spectra very complicated. Gener-

ally, both rings are substituted with the unsaturated and saturated groups in para position to one another (complementary substitution). It produces a hyperchromic effect and strong bathochromic shift of the E_1 , E_2 and B band. The overlap of absorption positions of the E_2 and K bands may lead to confusion in the interpretation of spectra and the only way to solve this problem was to compare it with the spectra of reactants.

Table II. Electronic spectral data of investigated compounds
[wavelength (nm) and $\epsilon_{\max} \times 10^3$ ($\text{mol}^{-1}\text{dm}^3\text{cm}^{-1}$)]

Compound	E_1	R_1	R_2	$E_2(K)$	B
HBPH	216/3,929	257/2,438*	310/2,326	353/3,386	covered
MBPH	209/3,602	260/1,770*	318/1,750*	352/2,492	covered
HBNPH	214/3,071	245/2,233*	308/1,482*	387/3,124	404/2,815
MBNPH	214/2,985	264/2,003*	306/1,850*	389/3,192	391/2,100

* - ridge

R_1 and R_2 bands originated from the absorption of the azomethine group in conjugation with the both benzene rings. The lower wavelength band (R_1) is assigned to the $\text{Ar} \rightarrow \text{CH}=\text{N}-\text{NH}-\text{Ar}$ conjugated system and band R_2 to the $\text{Ar}-\text{CH}=\text{N}-\text{NH} \leftarrow \text{Ar}$ conjugation.

Reference:

- [1] B. Bartel, Annu. Rev. Plant Physiol. Plant Mol. Biol. 1997, 48, 49.
- [2] B. Andonovski, I. Spirevska, A. Nikolovski, Croat. Chem. Acta 1996, 69, 1201.
- [3] M. Kawaguchi, K. Syono, Plant Cell Physiol. 1996, 37, 1043.
- [4] P.A. Cohen, L.A. Cohen, Can. J. Chem. 1992, 70, 282.
- [5] E. Epstein, J. Ludwigmiller, Physiol. Plant. 1993, 88, 382.
- [6] N.M. Samus, T.A. Burdenko, V.V. Gylka, V.J. Tsapkov, J. Chem. Pharm. 1991, 12, 40.

STRUCTURAL INTERPRETATION OF THE POLARIZED ABSORPTION SPECTRA (400 - 1650 nm) OF ANNABERGITE $\text{Ni}_3(\text{AsO}_4)_2 \cdot 8\text{H}_2\text{O}$

M. Logar and V. Poharc-Logar

Faculty of Mining and Geology, Belgrade, Dušina 7

Abstract

Annabergite, $(\text{Ni}_{2.50}\text{Mg}_{0.42}\text{Fe}_{0.05})_{2.97}(\text{AsO}_4)_2 \cdot 8\text{H}_2\text{O}$, from Marušići, Kopaonik Mt. (South Serbia), crystallizes in space group C2/m, with $a=10.185(3)$, $b = 13.323(3)$, $c = 4.730(1)$ Å, $\beta = 105,00(2)^\circ$, $V = 620,0(2)$ Å³, $Z = 2$. Polarized absorption spectra (400 - 1650 nm) were measured on the 0.3x0.5 mm crystal mounted on the microscope included in the optical path of the system consisted of computer controlled monochromator, chopped source, lock-in amplifier and three detectors. Due to perfect cleavage the exposed crystal face was (010) so the measurement was possible in two vibration directions, β and γ . Two spectra approved enhanced differences as the consequence of ${}^3\text{T}_{2g}$ (F) level splitting by ligand field of lower symmetry. Ni ions in the structure of annabergite are distributed over two sites: single *trans*-octahedra M (1) of C_{2h} and double *cis* octahedral groups M (2) of C_2 ligand field symmetry. Both are mutually rotated for 90° so that z-axis of their ligand field coincides with different vibrational directions. Therefore, the excitations of the electron transition $\text{B}_g \leftarrow \text{B}_g$ M (1) and $\text{A} \leftarrow \text{B}$ M (2) has polarization dependence according to the given selection rules.

Introduction

Annabergite, $(\text{Ni}_{2.50}\text{Mg}_{0.42}\text{Fe}_{0.05})_{2.97}(\text{AsO}_4)_2 \cdot 8\text{H}_2\text{O}$, from Marušići, Kopaonik Mt. (South Serbia), [1] crystallizes in space group C2/m, with $a = 10.185(3)$, $b = 13.323(3)$, $c = 4.730(1)$ Å, $\beta = 105,00(2)^\circ$, $V = 620,0(2)$ Å³, $Z = 2$. The mineral having a characteristic apple green color, occurs as radial on the surface and in the cavities of the matrix rock composed calcite and dolomite with irregularly dispersed sulphides. The structure of annabergite [2] consists of isolated AsO_4 tetrahedra connected with two non-equivalents octahedral M^{2+} sites. Single octahedral site, M(1), is built by four water molecules and two *trans* oxygen atoms, while M(2) site is surrounded by two water ones in *cis* configuration and four oxygen atoms. Two M(2), constitute double octahedral group, held together by O - O sharing edges, lying in the (010) mirror plane. Both sites, are occupied by Ni^{2+} which can be partially replaced by Mg^{2+} .

Experimental

Polarized spectra was obtained by placing the polarizing microscope (Leitz with Nicol prism) in the optical path of the computer controlled monochromator (Beckman DU). The chopped signal, synchronized and amplified by lock-in amplifier (LIA100 Thorlab), was recorded to the computer. Between 26000 and 6000 cm^{-1} 1321 points were measured with the photomultiplier tube, Si and InGaAs photo-diode respectively, using 0.06 mm slit. Due to perfect cleavage, observed face of the selected crystal is (010) and the 2-fold axis coincide with microscope optical axis. This orientation permitted measurements to be made parallel to the two principal directions, β and γ , lying in the (010) plane.

Discussion

Fife of six prominent absorption bands (Fig. 1) are due to d-d transition of Ni^{2+} in an octahedral environment. Sharp, narrow peak at 7140 cm^{-1} represent first overtone of (OH) stretching vibrations.

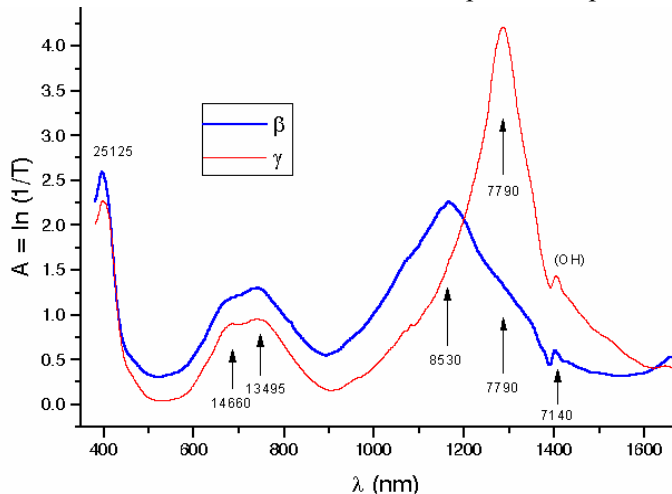


Fig. 1. Polarized spectra of annabergite. Peaks pos. are in cm^{-1} .

${}^3T_{1g}$ (F) appears as a well defined doublet. Accepting O_h ligand field symmetry the spectrum could be very well fit to using Tanabe-Sugano [3] matrices (Fig. 2). Polarized spectra, however, exhibits apparent separation of the ${}^3T_{2g}$ (F) level, depending of the vibrational direction. The ligand field environment of M(1) site has the form of an deformed *trans* octahedra. Unequal O - H_2O distances produce lowering the symmetry to C_{2h} [5]. The axis of 2-fold symmetry emerge between H_2O ligands lying on the x and y axes of the ligand field.

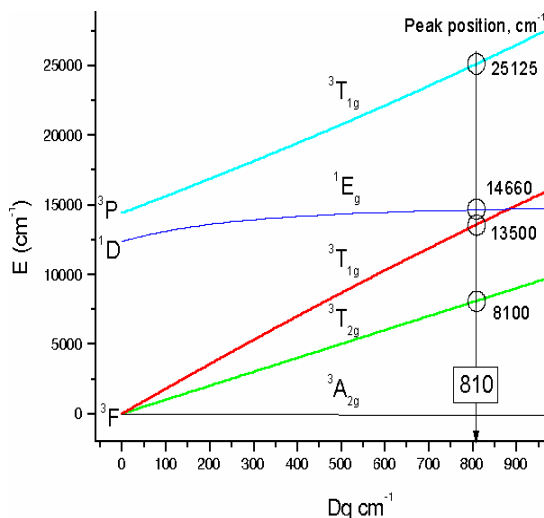


Fig. 2. $Ni^{2+}(d^8)$ energy levels diagram in O_h ligand field. $B = 960, C = 3803\text{ cm}^{-1}$

Unpolarized spectrum of annabergite exhibit a three spin allowed transition bands usual for octahedral Ni^{2+} (d^8) involving transition between spin triplet terms ${}^3A_{1g}$ (F) (ground state) and ${}^3T_{2g}$ (8100), ${}^3T_{1g}$ (F) (13500) and ${}^3T_{1g}$ (P) (25125) levels. Additionally, the spin forbidden band 1E_g (D) (14660) is also observed so the transition to the

trans axes coincide with z-axis (Fig. 3). In the C_{2h} group the ground state ${}^3A_{1g}$ (F) change to B_g and ${}^3T_{2g}$ (F) split into three levels ($2A_g + B_g$). The components of a dipole moment operator transforms as: $P_z = B_u$ and $P_{x,y} = A_u + B_u$ so that all transitions are orbitally forbidden. Nevertheless the absorption does occur as the consequence of the temporary removal of the center of symmetry by an odd vibration, which can be found among the normal modes [4] of group C_{2h} : $4A_g + 2B_g + 4A_u + 5B_u$. Ligand field around M(2) belongs to the symmetry group C_2 . The ground state ${}^3A_{1g}$ (F) change to B and ${}^3T_{2g}$ (F) split

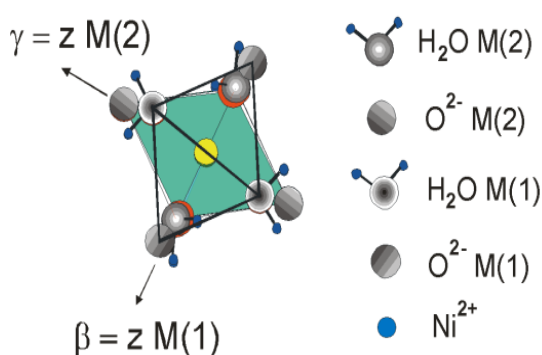


Fig. 3. Octahedral sites in the annabergite structure. Projection to (010).

planation that two in-plane transitions in M(2) can produce such differences in intensities, as it was experimentally observed. Also, the transition ($\parallel z$) must be of a higher intensity, comparing with in-plane transition (\perp), where vibrational direction lays between ligands making both transitions possible, but low in intensity. In vibrational direction γ just one, very strong transition $A \leftarrow B$ of (M2) occurs at 7790 cm^{-1} . Band due to second transition can not be observed as a consequence of the fact that in-plane M(1) site transitions are orbitally forbidden and thus of a low intensity.

Table 1: Selection rules for ${}^3T_{2g}(F)$ splitting in M(1) and M(2) Ni^{2+} sites

Vib. dir.	M(1) vibronic		M(2)		Transition energy, cm^{-1}
	Polarization	Transition	Polarization	Transition	
β	$\parallel (z)$	-	$\perp (x, y)$	$A \leftarrow B$	7790
		$B_g \leftarrow B_g$		$B \leftarrow B$	8530
γ	$\perp (x, y)$	$A_g \leftarrow B_g$	$\parallel (z)$	$A \leftarrow B$	7790
		$B_g \leftarrow B_g$		-	8530

References

- [1] V.Poharc- Logar, A.Rosić, S.Jelić, Mineralogija, Godiš. JAM, 2000, 3, 9.
- [2] Wildner M., Giester. G., Lengauer C., McCammon C., Eur. J. Mineral., 1996, 8, 187.
- [3] Tanabe Y. & Sugano S. (Journ. Phys. Soc. Japan, 1954, 9, 753.
- [4] Nacamoto K., Wiley & Sons, 1970, USA, p.338.
- [5] Cotton A., Wiley&Sons, sec. ed., 1971

ELECTRON PARAMAGNETIC RESONANCE SPECTROSCOPY IN THE ANALYSIS OF FREE RADICALS IN SEEDS

G. Bačić¹, Z. Giba², M. Mojović¹, D. Grubišić² and R. Konjević²

¹ Faculty of Physical Chemistry, University of Belgrade, ² Institute of Biological Research "Siniša Stanković", Belgrade and Faculty of Biology, University of Belgrade

Abstract

EPR spectroscopy of unimbibed (dry) seeds of *Paulownia tomentosa* was used to detect which EPR active species (free radicals and/or paramagnetic metal ions) could be detected by this technique and to determine their relation with the physiological status of seeds. In natural seed samples the presence of a delocalized electron in polycondensed benzene rings within cell walls of the seed coat was detected as well as the signal of manganese (Mn²⁺). Unfortunately, none of these signals could be correlated to the seed age and/or their seed viability. On the other hand, using the DTSC spin trap we showed that the NO production is a bioactive component which mediates the action of nitrogenous stimulators of seed germination.

Introduction

The germination of *Paulownia tomentosa* seeds is phytochrome-controlled probably involving transplasmamembrane electron transport. The light requirement for maximum germination may vary from very brief exposure to several hours of red light. In seeds otherwise requiring long periods of light exposure (in some cases up to 18 hours), it can be reduced to a single pulse of 5 min red light by the application of substances with redox potential equal or higher than $E_0' = 360$ mV such as inorganic nitrates (1). Other, very different nitrogenous compounds (such as organic nitrates), all of which can act as donors of nitric oxide (NO) donors, could provoke the same effect in this experimental system (2). Electron paramagnetic resonance spectroscopy (EPR) is the only technique that can non destructively detect free radicals and/or paramagnetic metal ions (Fe, Mn, Cu) which participate in redox reactions in biological systems. We therefore conducted a series of EPR measurements to evaluate the potential of this method and compare the status of the *in situ* free radicals and other components of the redox system with the physiology of the signal transduction in the germination.

Materials and Methods

Plant material. Empress tree (*Paulownia tomentosa*) seeds were collected in the Botanical Garden of the University of Belgrade. Seed wings were separated from seeds in some experiments.

Chemicals. N-(dithiocarboxy)sarcosine (DTCS), a component of the spin-trap specific for nitric oxide radical, was synthesized from sarcosine and carbon disulfide according to the modified literature procedure as described for N-methyl-D-glucamine dithiocarbamate (MGD) and it was used as ammonium salt (3).

Spin-trapping EPR measurements. For all measurements deionized water was used: conductivity was not higher than 0.8 μ S. Reaction mixtures containing chemical

NO generating system consisting of egg albumin, $\text{Fe}(\text{DTCS})_2$, sodium nitroprusside as NO source, and reducing agent ($\text{Na}_2\text{S}_2\text{O}_4$) or system including biological material were introduced in 4 mm diameter EPR tube. After 5 min of reaction time, the mixture was frozen in liquid nitrogen and transferred into the EPR cavity. During EPR measurements low temperature was maintained by blowing N_2 gas, previously cooled down by liquid nitrogen, around a sample tube in the EPR cavity. All measurements were performed using a Varian EPR spectrometer, model E 104A, operating at X-band frequency (9.5 GHz).

Results

Pivotal EPR signal in *P. tomentosa* seeds. Figure 1 shows the EPR spectrum of unimbibed (dry) seeds. A strong signal found at $g = 2.003$ can be attributed to the delocalized electron in polycondensed benzene rings within cell walls of the seed coat. The EPR measurements were made on several species from the genus *Paulownia* and for *P. tomentosa* seeds of different age ranging from zero (freshly harvested seeds) to thirteen years. Although intensities of EPR signals were slightly different from sample to sample, no correlation between spectral characteristics and seed age was found. Obviously, this EPR signal originates from structures that are extremely stable in time. Interestingly, it also was found in wheat kernels originating from an ancient Syrian tomb (Ain Dare, Siria) estimated to be 3300 years old (data not shown).

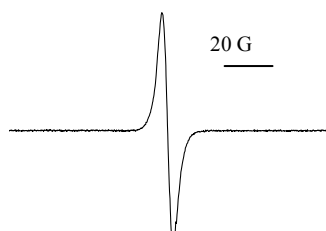


Fig 1. EPR signal of *P. tomentosa* seeds at room temperature. Modulation amplitude 2G, microwave power 5 mW

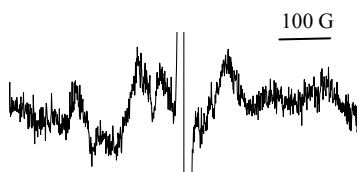


Fig 2. EPR signal of *P. tomentosa* seeds at room temperature. Modulation amplitude 5G, microwave power 20m W

Determination of Mn content in P. tomentosa seeds. The other less prominent spectral feature, detectable only under different experimental settings (Fig 2), is an indication of a six-line spectrum of manganese, showing that a small amount of Mn^{2+} ions are mobile enough to produce such a spectral feature even in dry seeds. Manganese bound to macromolecules is certainly more abundant, however it exhibits a very wide line that cannot be readily detected. The presence of Mn^{2+} ions in these seeds was subsequently measured by using atomic absorption spectrometry. After separation of seed components, manganese was observed in embryonic tissues, but not in a seed envelope including seed wings. No correlation between seed age and manganese content in *P. tomentosa* seeds was found (Table I).

Seed age (years)	Manganese content ($\mu\text{g/g}$)
28	27.0
14	19.0
13	18.8
10	19.0
6	20.2
5	21.3

Detection of nitric oxide in P. tomentosa seeds. Although it possesses an unpaired electron, NO is by itself EPR silent, which necessitates the use of spin traps. The EPR spectrum obtained in an NO generating system with DTCS spin-trap (Fig. 3A) shows a hyperfine structure with two characteristic g-values ($g_{\perp} - 2.035$, and $g_{\parallel} - 2.02$) attributable to the formed spin-trap/NO adduct, i.e. $[(\text{Fe}^{\text{II}}(\text{DTCS})_2(\text{NO}))^2\text{-complex}]$ (4). Figure 3B shows a profound production of NO by seeds in the presence of nitroglycerin indicating that NO is the bioactive compound which mediates the of action of nitrogenous stimulators of seed germination



Fig. 3 EPR spectra at 177 K obtained in spin-trapping experiments (microwave power 20 mW, modulation amplitude 6.3 gauss). A. Egg albumin [33mg/l] + $\text{Fe}(\text{DTCS})_2$ [3.3 mM] + sodium nitroprusside [0.3 mM] + reductant $\text{Na}_2\text{S}_2\text{O}_4$ [2M]. B. Whole seeds imbibed in darkness in 33 mM solution of DTCS for 24h. Solution was decanted and replaced by 1mM nitroglycerin solution supplemented with 33 mM FeSO_4 . Three hours later the seeds were introduced in EPR tube and frozen.

Conclusions

We showed that it is possible to detect a number of EPR active species in intact seeds. Unfortunately, evaluation of the readily accessible species cannot be used as a noninvasive method for the estimation of seed age, or for prediction of seed viability and/or quality. On the other hand, the ability of EPR technique to in vivo detect NO production in seeds opens the possibility of using this technique in studying the action of different nitrogenous stimulators of seed germination.

Acknowledgements

This work was supported by the grant 1928 from the Ministry of Science and Environmental Protection of Republic of Serbia.

References

- [1] D. Grubišić, R. Konjević, *Planta*, 1990, 181, 239.
- [2] D. Grubišić, Z. Giba, R. Konjević, *Photochem. Photobiol.*, 1992, 56, 629.
- [3] L.A. Shinobu, S.G. Jones, M.M Jones, *Acta Pharmacol. Toxicol.* 1984, 54, 189.
- [4] T. Yoshimura, *et al.*, *Nature Biotechnology*, 1996, 14, 992.

INFLUENCE OF TEMPERATURE ON RESONANCE RAMAN SPECTRA OF β -CAROTENE IN DIFFERENT MEDIA

S. Šašić, M. Jeremić, A. Antić-Jovanović and J. Filipović

*Faculty of Physical Chemistry, University of Belgrade,
Studentski trg 16, Belgrade, Serbia and Montenegro*

Abstract

Resonance Raman (RR) spectra of β -carotene in solution of DMSO, H₂O-DMSO mixtures, and incorporated in oleic acid micelles have been recorded at different temperatures. Observed intensity changes of the ν_1 (C=C) and ν_3 (C-C) bands have been explained in terms of β -carotene aggregation influenced by intermolecular interaction, changing with temperature.

Introduction

Resonance Raman (RR) spectroscopy is a unique tool for the study biologically relevant molecules in their natural state. If exciting radiation is in resonance with electronic transition of the molecule, the intensity of a few lines is selectively enhanced producing very simple RR spectrum with extremely small number of lines. Contrary to RR, IR spectra of the same molecule have very complex structure usually overlapped with spectra of surrounding media. The class of carotenoid molecules has received great attention because of its relevance in biochemistry, biophysics and particularly in photochemistry[1,2]. Many practical applications of carotenoids in food and pharmaceutical industry is known. The existence of a chain of polyconjugated π bonds with highly polarizable electrons in the backbone of carotenoid molecules is a basis for fundamental photochemical phenomena of biological relevance. As a representative large class of carotenoids, we studied β -carotene in different media at various temperatures. In this study β -carotene has been dissolved in the DMSO and H₂O-DMSO mixture, and incorporated in oleic acid micelles.

Experimental

The solutions investigated have been prepared by dissolving of commercial crystalline β -carotene (purchased from Fluka) in spectroquality DMSO. Solution in neat solvent and its 10%, 20% and 39% aqueous mixtures have been prepared immediately before measurements.

Micelles of oleic acid, containing β -carotene in the same concentration as in solutions ($5 \cdot 10^{-5}$ mol dm⁻³), have been prepared in phosphate buffer solution. Raman spectra have been excited by means of the 514 nm line of a Spectra Physics argon ion laser Model 2000 at an effective power of 50 mW at the sample and recorded at different temperatures by a Spex 1401 Spectrometer interfaced to a Aple IIe computer. Experiments have been carried out with 90 geometry. Temperature of the

sample has been controlled by means of a home designed thermostat. The uncertainty of the measured band positions has been estimated to be 1 cm^{-1} .

Results and Discussion

The molecule is planar and belongs to the symmetry point group C_{2h} , and has 282 normal modes of vibration, of which 141 are Raman active. Due to RR enhancement, only two bands at 1523 cm^{-1} and 1158 cm^{-1} are observed, which are assigned to $\nu_1(\text{C}=\text{C})$ and $\nu_3(\text{C}-\text{C})$ stretching vibrations, respectively.

The band positions remained the same in both, solutions and the micelles, within the limits of experimental error, suggesting that ground electronic state of β -carotene is not perturbed by intermolecular interaction in solutions and in micelles, and by temperature. However, a considerable intensity changes on both RR bands have been observed.

Fig. 1 shows the spectrum of β -carotene in 10% H_2O -90%DMSO solution at different temperatures, while the Fig. 2 shows the spectrum of β -carotene incorporated in oleic acid micelles.

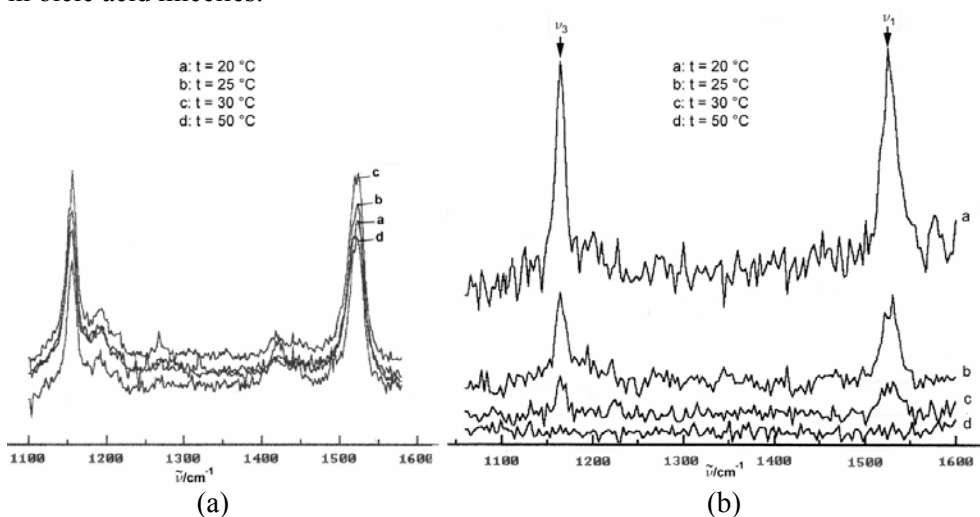


Figure 1. RR spectra of β -carotene at different temperatures in: 10% H_2O – 90% DMSO mixture (a) and in micelles (b).

As seen, the spectra are changed in different ways. In the solutions, the intensity of both bands increases with temperature reaching maximal value at about 35°C , and thereafter slowly decreases even below room temperature level. The same trend is observed in all solutions. In the micellar system, however, the intensity of both bands steadily decrease from room temperature vanishing completely at 50°C . Contrary to band positions, which depend only on ground electronic state, intensity of RR bands depends on both, ground and excited electronic states. Observed variations of band intensity with temperature indicate perturbation of excited electronic state, which is temperature dependent. It shows that interaction of β -carotene molecules is not only a

consequence of solvent polarizability, as proposed previously [3], but that also depends on the structure of β -carotene molecule aggregates. These results are in good agreement with absorption electronic spectral study [4]. Decrease of band intensity observed in micelles is attributed to collapse of micellar system and precipitation of β -carotene since it is insoluble in aqueous media.

Conclusion

RR spectroscopy revealed that ground state of β -carotene remains the same in different media and at different temperatures since both, $\nu_1(\text{C}=\text{C})$ and $\nu_3(\text{C}-\text{C})$ vibrations remained at the same position. Intensity variation of these bands with variation of temperature and environment, however, shows that excited electronic state of β -carotene molecule is significantly perturbed. It is explained in terms of formation of β -carotene aggregates with head to tail structure. This study demonstrates that combined Raman and absorption spectroscopy can provide information about energy states of this important molecule in living system.

Acknowledgement

This work is supported by the Ministry of Science and Environmental Protection, RS, Grant no. 1928.

References

- [1] J. C. Merlin, *Pure & Appl. Chem.*, 1985, 57, 785.
- [2] R. Withnall, B. Z. Chowdhry, J. Silver, H.G.M. Edwards and L. F.C de Oliveira, *Spectrochimica Acta, Part A: Molecular and Biomolecular Spectroscopy*, 2003, 59, 2207.
- [3] A.B. Mayers and R.R. Birge, *J. Chem. Phys.* 1980, 73, 5314.
- [4] M. Jeremic, A. Antic-Jovanovic, S. Sasic, C. Radenovic, M. Lalic, *Proc. 4th Inter. Conf. Fundamental Appl. Phys. Chem. »Physical Chemistry 1998«* Belgrade, 1998, pp. 146.

THE PI TAPF SEQUENCE: CROSS POLARIZATION SPIN DYNAMICS

Z. D. Žujović, Z. Miladinović*, C. Mayer** and G. A. Bowmaker

Department of Chemistry, The University of Auckland, Private Bag 92019, Auckland, New Zealand,

**Institute of General and Physical Chemistry, Studentski Trg 12-18, Belgrade, Serbia and Montenegro,*

***Institut für Physikalische und Theoretische Chemie, Universität Duisburg, 47048 Duisburg, Germany,*

Abstract

The effect on the static ^{13}C powder spectrum of increasing the time interval between phase alternation in the Polarization Inversion Time Averaged Precession Frequency, (PI-TAPF), pulse sequence is studied. The proton-carbon dipolar interaction is partially averaged due to the fast phase alternation, resulting in a significant narrowing of the lineshape singularities in the powder pattern. The frequency scaling of the transient oscillations observed in the PI-TAPF experiment with $\tau_1 = 4 \mu\text{s}$ and $\tau_2 = 16 \mu\text{s}$ is due to the fact that the relation $\tau_c \ll \tau_d$ is no longer valid for $1/R_{\text{dp}} = \tau_d = 80 \mu\text{s}$ and $\tau_c = 20 \mu\text{s}$.

Introduction

The phenomenon of transient oscillations (TO) was initially observed by Müller et al. [1] in Hartmann-Hahn $^{13}\text{C}/^1\text{H}$ CP experiments on a single crystal of ferrocene and has been attributed to the coherence energy transfer caused by the dipolar coupling of the ^{13}C (*S*) to the directly coupled proton (*I*). Since then, TO have been used in a number of investigations for the study of spin dynamics, or as a basis for creating new pulse sequences for use in structural investigations [2, and reference therein].

The aim of the present work is to investigate CP spin dynamics in the PI-TAPF pulse experiment [2], which is designed to produce transient oscillations under significantly reduced RF power in the *S* channel. In particular the effect of increasing the time interval between phase alternation in the TAPF [3] pulse sequence for the same scaling factor (0.6) of the RF field strength.

Experimental

The experiments were performed at ambient temperature on a static powder sample of ferrocene. All spectra are obtained on a Bruker Avance spectrometer equipped with a 7-mm MAS probe operated in the static mode at 75.468 MHz ^{13}C frequency.

Results and Discussion

The PI-TAPF experiment uses the segmentation applied in the standard TAPF sequence during the depolarization (or evolution) period. Alternating the phase of the *I* spin-locking field with different periods τ_1 and τ_2 allows a significant reduction of the RF field strength in the *S* channel by a scaling factor *SC*. This scaling factor is limited

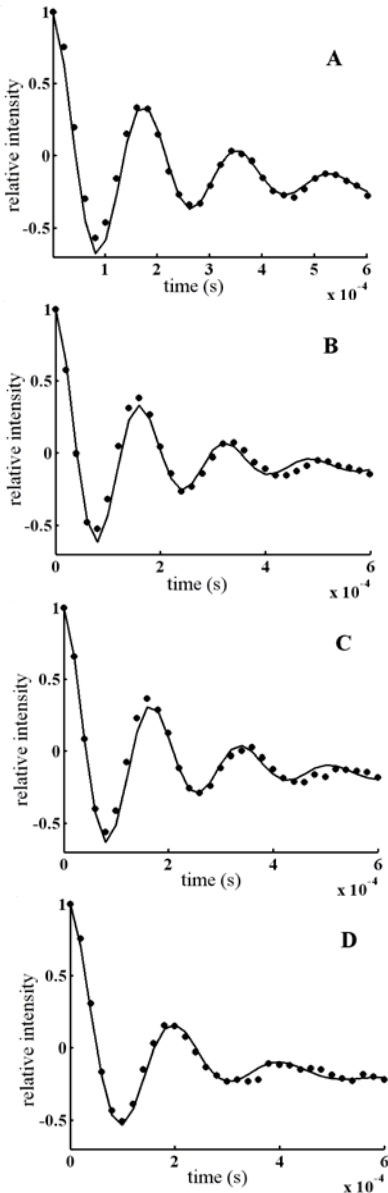


Figure 1. For the standard PI experiment (see Fig. 1 (A)), ^1H and ^{13}C rf fields, $\gamma B_{1f}/2\pi$ and $\gamma B_{1s}/2\pi$, were set to 59.524 kHz. B, C, D are obtained from the PI-TAPF experiments with time intervals τ_1 and τ_2 of 1 μs and 4 μs and 2 μs and 8 μs and 4 μs and 16 μs , respectively. The scaling factor for all PI TAPF experiments is 0.6. ^1H and ^{13}C rf fields, $\gamma B_{1f}/2\pi$ and $\gamma B_{1s}/2\pi$, were set to 59.524 kHz during the cross-polarization interval. During the PI-TAPF-depolarization period, according to the relative ratio of time intervals τ_1 and τ_2 , the ^{13}C rf fields were reduced to 35.714 kHz, while $\gamma B_{1f}/2\pi$ was kept at 59.514 kHz.

by the correlation time of the dipolar fluctuation in the rotating frame, τ_d , and can take any value between 0 and 1 as long as $\tau_c \ll \tau_d$ i.e.:

$$SC = \left| \frac{\tau_1 - \tau_2}{\tau_c} \right| \leq 1$$

where $\tau_c = \tau_1 + \tau_2$.

Due to the fast rotation of the C_5H_5 ring about the C5 axis, the heteronuclear I-S interactions in ferrocene exceed the vicinal H-H interactions by a factor 3.7. This results in a virtually isolated two-spin system with an oscillatory dependence of the S magnetization on contact time characterized by:

$$S(t_1) = -1 + \exp(-R_{df}t_1) + \exp[-0.5(R_{dp} + 2R_{df})t_1] \times \cos\left(\frac{\gamma_H\gamma_C\hbar}{8\pi r_{IS}^3}(3\cos^2\theta^{IS} - 1)t_1\right) \quad \text{Eq.1.}$$

where R_{dp} and R_{df} are orientation dependent spin-diffusion rates of a particular spin I , and θ^{IS} is the angle between the internuclear vector of the I - S spin pair and the static magnetic field. The TO obtained from the peak at 94 ppm in the powder spectrum of ferrocene and fitted by Eq. 1 are shown in Fig. 1. Cheung and Yarris [4] have shown that $T_{dp} = 1/R_{dp}$ and $T_{df} = 1/R_{df}$ may be related to the correlation time of the dipolar fluctuations τ_d and the spin diffusion time constant $T_s = 1/W$, respectively. An estimation of T_{dp} is given by the relation:

$$T_{dp} = \tau_d = 3\sqrt{\frac{8}{5M_2^H}} \quad \text{Eq.2.}$$

where M_2^H is the second moment of the neighbouring proton-proton interactions which usually also represents the major contribution to the second moment of the proton resonance line shape.

$$2\pi \Delta\nu_{1/2} = 1.18\sqrt{M_2^H} \quad \text{Eq.3.}$$

The proton linewidth which we obtained for powder ferrocene is $\Delta\nu_{1/2} = 6500 \text{ Hz}$ and

the dipolar correlation time (Eq. 2) could be easily obtained: $T_{dp} = \tau_d = 110 \mu\text{s}$

This is in good agreement with fitting results (Eq. 1) for standard PI experiment ($115 \mu\text{s}$, see Table 1). The local field in the proton reservoir is given by following ex-

pression $\omega_{loc} = \sqrt{\frac{M_2''}{12}} = 1590 \text{ Hz}$, and this is also in accordance with the results reported

elsewhere [5]. As can be seen from Table 1., implementation of the TAPF segment leads to the shortening of $\tau_d = 1/R_{dp}$. At the same time spin diffusion for time intervals τ_1 and τ_2 of $1 \mu\text{s}$ and $4 \mu\text{s}$ (1_4) is significantly longer (5.0 ms) than in the case of standard PI (2.1 ms) and PI-TAPF with $2 \mu\text{s}$ and $8 \mu\text{s}$ i.e. 2_8, (2.9 ms) and $4 \mu\text{s}$ and $16 \mu\text{s}$ i.e. 4_16, (2.2 ms).

It is known that the rate of a spin diffusion process is directly related to the strength of the local dipolar field of the protons. Thus, the longer spin diffusion in the case of 1_4 is probably due to the fast phase alternation, which averages dipolar interactions in spin space, (like MAS), and leads to partial homonuclear decoupling. This is consistent with the narrowing effect in ferrocene spectra that we observed. There are four full 1_4 intervals during the incrementing time of $20 \mu\text{s}$. However in the case of 2_8 and 4_16 there are two and one intervals, respectively. Decreasing the number of time intervals from four to one reduces the effect of homonuclear decoupling and leads to the spin diffusion rate obtained in the standard PI experiment.

On the other hand $\tau_d = 1/R_{dp}$ is smaller for all three values of $\tau_c = \tau_1 + \tau_2$, which implies faster damping of the oscillations, probably due to the phase transient effects and RF field inhomogeneity [6]. The frequency scaling obtained in 4_16 experiment (4700 Hz) is due to the fact that the relation $\tau_c \ll \tau_d$ is no longer valid for $1/R_{dp} = \tau_d = 80 \mu\text{s}$ and $\tau_c = 20 \mu\text{s}$.

Table 1. The results obtained from the fitting of TO.

Experiment	TO frequency (Hz)	$1/R_{dp}$ (μs)	$1/R_{df}$ (μs)
PI	5700	115	2100
1_4	6000	80	5000
2_8	5700	90	2900
4_16	4700	80	2200

References

- [1] L. Müller, A. Kumar, T. Baumann, R. R. Ernst, Phys. Rev. Lett., 1974, 32, 1402.
- [2] Z. D. Zujovic, G. A. Bowmaker, and C. Mayer, J. Magn. Reson., 2003, 164, 358.
- [3] K. Takegoshi, C. A. McDowell, J. Magn. Reson., 1986, 67, 356.
- [4] S. Zhang, B. H. Meier and R. R. Ernst, Solid State NMR, 1992, 1, 313.
- [5] T. T. P. Cheung and R. Yaris, J. Chem. Phys., 1980, 72, 3604.
- [6] J. Hirschinger and M. Herve, Solid State NMR, 1994, 3, 121.

THERMALLY INDUCED SPIN CROSSOVER OF $[\text{Fe}^{\text{II}}(\text{BPMEN})(\text{CH}_3\text{CN})_2](\text{ClO}_4)_2$ IN SOLUTION: PSEUDO SPIN EQUILIBRIUM

K. P. Bryliakov, E. A. Duban and E. P. Talsi

*G. K. Boreskov Institute of Catalysis, Siberian Branch of the Russian Academy of Sciences,
630090 Novosibirsk, Russian Federation.*

Abstract

Thermally induced spin crossover behavior of $[\text{Fe}^{\text{II}}(\text{BPMEN})(\text{CH}_3\text{CN})_2](\text{ClO}_4)_2$ in CD_3CN solution (low spin (LS) – high spin (HS)) was investigated. Variable temperature solution magnetic susceptibility measurements gave $\Delta H^\circ_{\text{LS-HS}} = 39.7 \pm 2.0 \text{ kJ mol}^{-1}$ and $\Delta S^\circ_{\text{LS-HS}} = 135 \pm 9 \text{ J mol}^{-1} \text{ K}^{-1}$ values. These values are too high for a purely spin transition reaction and reflect determinative contribution of chemical processes into spin transition, namely, the detected dissociation of one bound CH_3CN molecule. Thus, the LS-HS conversion should be regarded as a chemical rather than conventional spin equilibrium. The thermodynamic parameters estimated from NMR shifts with temperature are in perfect agreement with those obtained by magnetic susceptibility measurements in CD_3CN : $\Delta H^\circ = 40 \pm 3 \text{ kJ mol}^{-1}$, $\Delta S^\circ = 137 \pm 10 \text{ J mol}^{-1} \text{ K}^{-1}$.

Introduction

In recent years, Que. et al. reported a series of non-heme Fe(II)(BPMEN)- and Fe(II)(TPA)-type catalysts of stereospecific oxidation of hydrocarbons with H_2O_2 (TPA is tris(2-pyridylmethyl)amine ligand and BPMEN is tetradentate N,N' -dimethyl- N,N' -bis(2-pyridylmethyl)-1,2-diaminoethane ligand) [1]. These catalysts can be functional models for non-heme iron oxygenases, such as Rieske dioxygenases capable of olefin cis-dihydroxylation. Interestingly, the parent $[\text{Fe}^{\text{II}}(\text{BPMEN})(\text{CH}_3\text{CN})_2](\text{ClO}_4)_2$ (**I**) complex displayed solution spin transition behavior in the temperature range -40 to $+30$ °C. However, the spin transition was not studied experimentally in detail, although this could be of help in understanding of reactivity of these systems.

The temperature-induced LS-HS transitions in Fe(II) complexes have been extensively studied over the last years, mostly in the solid state; some variable-temperature studies in solution also appeared [2-4]. In this work, we present a detailed solution magnetic susceptibility and ^1H NMR study of $[\text{Fe}^{\text{II}}(\text{BPMEN})(\text{CH}_3\text{CN})_2](\text{ClO}_4)_2$ spin transition in acetone- d_6 and the thermodynamic parameters of this reaction. The results of solution magnetic susceptibility measurements are compared with those obtained by paramagnetic ^1H NMR study.

Results and Discussion

At room temperature, complex **I** exhibited a magnetic moment of $4.1 \mu_{\text{B}}$ in acetonitrile solutions that is indicative of a spin-crossover system. Temperature dependent magnetic susceptibility measurements were carried out to explore the equilibria that occur in acetonitrile solutions of complex **I** (Figure 1, trace I). Fitting the observed magnetic moment dependencies μ_{eff} vs. T to eq 1 gave the limiting magnetic

moment values $\mu_{LS} = 1.30 \pm 0.1 \mu_B$ and $\mu_{HS} = 5.45 \pm 0.1 \mu_B$, that are higher than the spin-only values 0 and $4.90 \mu_B$, thus suggesting significant orbital contributions to the observed magnetic moments. The μ_{LS} value is in good agreement with the solid-state magnetic moment $1.40 \mu_B$ ($T = 294$ K).

$$\mu_{\text{eff}}(T) = \{\mu_{LS}^2 + \mu_{HS}^2 [\exp(\Delta S^\circ/R) \exp(-\Delta H^\circ/RT)]\}^{1/2} \{1 + \exp(\Delta S^\circ/R) \exp(-\Delta H^\circ/RT)\}^{-1/2}, \quad (1)$$

where μ_{LS} and μ_{HS} are the limiting magnetic moments of the low-spin and high-spin states and $\exp(\Delta S^\circ/R) \exp(-\Delta H^\circ/R)$ is the observed equilibrium constant $K_{\text{obs}} = [\text{HS-Fe(II)}]/[\text{LS-Fe(II)}]$.

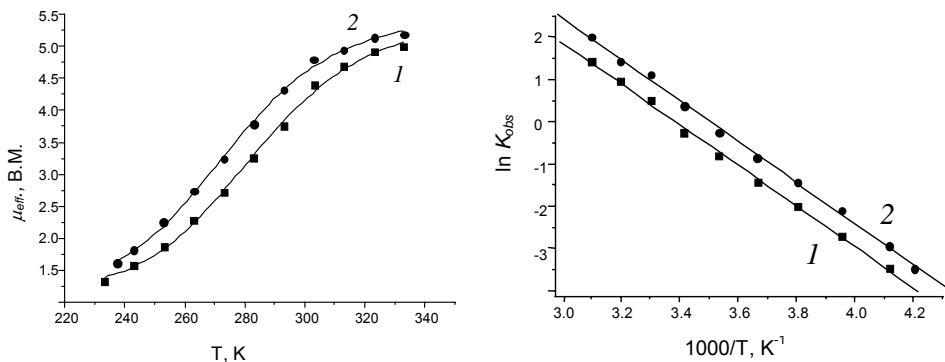
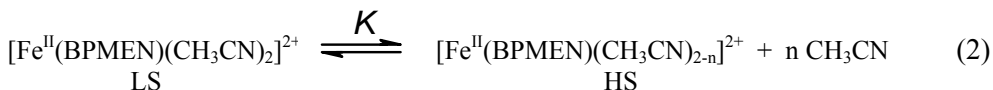


Figure 1. Fits of $\mu_{\text{eff}}(T)$ to eq 2 for complex **I** (a) and linear fits of $\ln K_{\text{obs}}$ versus $1000/T$ (b) in acetonitrile- d_3 – trace (■), in acetonitrile- d_3 /acetone- $d_6 = 1:1.65$ – (●).

The equilibrium parameters ΔS° and ΔH° (Figure 1, trace *I*) measured in acetonitrile- d_3 as in Ref. [5] gave $\Delta S^\circ = 135 \text{ J mol}^{-1} \text{ K}^{-1}$ (in which contribution of $R \ln 5$ arises from spin degeneracy of the HS state) and $\Delta H^\circ = 39.7 \text{ KJ mol}^{-1}$, $T_{1/2} = 284$ K. Both values are substantially higher than those reported in the literature for solutions spin crossover systems. Addition of acetone- d_6 to the mixture to obtain acetonitrile- d_3 /acetone- d_6 ratio of 1:1.65 lead to $T_{1/2}$ shift to 275 K. This lead us to a suggestion that spin crossover in this system could be a consequence of other (chemical) processes. The fact that in other solvents (e.g. acetone- d_6) a conventional Curie dependence of ^1H paramagnetic shifts is observed is in favor of dissociation of bound acetonitrile molecules at elevated temperatures:



A similar behavior was proposed previously to described spin-state variation of $[\text{Fe}(\text{Me}_3\text{tacn})(\text{MeCN})_3]$ in solution [3]. The question what is n in eq 2 could be answered as follows: if both acetonitrile molecules dissociated at high temperatures, we should observe similar high temperature spectra in acetone- d_6 and in acetonitrile- d_6 /acetone- d_6

combined solvent. However, the spectra were substantially different, indicating the existence of $[\text{Fe}^{\text{II}}(\text{BPMEN})]^{2+}$ in the first case $[\text{Fe}^{\text{II}}(\text{BPMEN})(\text{CD}_3\text{CN})]^{2+}$ in the second one. We conclude that the experimentally observed picture is consistent with dissociation of one acetonitrile molecule, leading to a weaker ligand field. The thermodynamic parameters estimated from NMR shifts as described in Ref. [6]: $\Delta S^\circ = 137 \pm 10 \text{ J mol}^{-1} \text{ K}^{-1}$ and $\Delta H^\circ = 40 \pm 2 \text{ KJ mol}^{-1}$ do not differ from those obtained by magnetic measurements.

In a few cases, dramatic solvent effects have been reported for spin crossover systems, in which substitution or dissociation of coordinated ligands lead to the change of spin state. Phenomenologically, such effects could be erroneously regarded as spin equilibrium, but the detailed physico-chemical consideration of these phenomena reveals their different nature. Particularly, 1) they can take place only in solutions containing molecules the same as those coordinated to the metal ion, via replacement or dissociation of some ligands; 2) spin transition is governed by weakening of the crystal field and 3) characterized by extraordinary high ΔS° and ΔH° values. Toftlund mentions that phenomena like these should not be considered as true spin crossover interconversions [7]; however, they have not been particularly named so far. Thus, in distinction to conventional spin equilibria, we propose a specific term for its unequivocal denomination: *solution pseudo spin equilibrium*.

Acknowledgments

This work was supported by the Russian Foundation for Basic Research, grant 03-03-32009.

References

- [1] K. Chen, M. Costas, J. Kim, A. Tipton, L. Que, J. Am. Chem. Soc., 2002, 124, 3026.
- [2] J. W. Turner, F. A. Schultz, Coord. Chem. Rev., 2001, 219-221, 81.
- [3] D. W. Blakesley, S. C. Payne, K. S. Hagen, Inorg. Chem., 2000, 39, 1979.
- [4] J. W. Turner, F. A. Schultz, Inorg. Chem., 2001, 40, 5296.
- [5] T. H. Crawford, J. Swanson, J. Chem. Educ., 1971, 48, 382.
- [6] K. P. Bryliakov, E. A. Duban, E. P. Talsi, Inorg. Chem., submitted.
- [7] H. Toftlund, Monatsh. Chem., 2001, 132, 1269.

TIMS AND MALDI TOF OF ENDOHEDRAL METALLOFULLERENES

O. Nešković¹, M. Veljković¹, V. Šipka¹, S. Veličković¹ and A. Đerić²

¹*Vinča Institute of Nuclear Sciences, P.O. Box 522, 11000 Belgrade, SCG*

²*Faculty of Physical Chemistry, 11000 Belgrade, SCG*

Abstract

Mass spectral studies (both TIMS – thermal ionization and MALDI TOF – matrix-assisted laser desorption time-of-flight mass spectrometry) of the endohedral metallofullerenes, Li@C₆₀, Li₂C₇₀ and ^{99m}Tc@C₇₀, provided detailed structural and reactivity information about these unusual species. MS experiment revealed that both fullerenes and endohedral metallofullerenes fragment by multiple C₂ loss. However, a difference in the terminal fragmentation products was observed for metallofullerene relative to C₆₀, suggesting that the encapsulation metal strongly impacts the fragmentation product. Singly charged cations of the metallofullerenes (M@C_n⁺) were completely unreactive in the gas phase with oxygenated compounds such as ethylene oxide: however, the corresponding neutral species appear to react readily with oxygenated species. Collisional dissociation of the ionized endohedral fullerenes listed above revealed multiple C₂ loss (either as sequential C₂ loss or larger C_{2n} eliminations) to generate similar terminal fragmentation products, which might be predicted due to the similar ionic radii of the encapsulated metals. The observed ionization energies of endohedral molecules were 5.9 ± 0.1 eV, 5.3 ± 0.1 eV and 5.7 ± 0.1 eV, respectively.

Introduction

During the last few years, considerable progress has been made in the exploration of metallofullerene chemistry especially that endohedral [1-3]. As is well known, fullerenes have a unique type of inner empty space with their unusual cage-like structures. A wide variety of metal atoms may reside in this space and form endohedral metallofullerenes. These new series of materials with novel physical and chemical properties are very important for their potential application as new types of superconductors, organic ferromagnets, nonlinear optical materials, functional molecular devices, magnetic resonance imaging agents, biological tracing agents, etc., which will have great influence over electronics, optics, electromagnetics and medicine. Up to now, many metals including Group 3 metals (Sc, Y, La), Group 2 metals (Ca, Sr, Ba), alkali metals (Li, Na, K, Cs) and some tetravalent metals (U, Zr, Hf) have been successfully encapsulated into a fullerene cage to form mono-, di-, and trimetallofullerenes. Especially, the important progress has been marked by the successful isolation and purification of many metallofullerenes, which has led to further investigation of their molecular structures, physical and chemical properties as well as electronic states by a variety of experiment means, particularly that of spectroscopy. Subsequently, an active search for new of the selective synthesis of individual metallofullerenes was performed *in situ* in a mass spectrometer with the aim of exercising mass spectrometric monitoring of gas phase reaction products. In favourable cases, small amounts of

TIMS reaction products could be collected directly from the mass spectrometer on a cold plate for additional MALDI TOF characterization, even before macroscopic amounts were available.

Experimental

The mass spectrometers used in this investigation were a 12-inch radius, 90° sector, magnetic instrument of local design and MALDI TOF Voyager De Pro (AB Applied Biosystem, UK). Thermal ionization instrument was equipped with a combined electron impact Nier-type and surface ionization source. The beam of the molecules to be investigated was produced by heating the C₇₀, LiI sample in a Re canoe in the vicinity of a Re ionizing filament, where a certain fraction of the neutrals are ionized (for Li₂@C₇₀, C₆₀ and LiI for Li@C₆₀ and carbonyl Tc and C₇₀ for ^{99m}Tc@C₇₀). The biological behaviour of fullerene derivatives shows their considerable potential for medical applications. We have produced, characterized and purified (in milligram quantities) endofullerenes containing Li or gamma-ray emitting ^{99m}Tc by the metal ion implantation technique (by introducing negatively charged C₆₀ or C₇₀ into a low-temperature Tc plasma column by a strong axial magnetic field). Identification of and ^{99m}Tc@C₇₀ has been accomplished by application of ultra-low level radiation detection methods and mass spectrometry. Appropriately derivatized endofullerenes could be used as a pharmaceutical for medical imaging. Such encapsulation of Li and radionuclides in a carbon cage could facilitate their inert transport through biological systems and await further studies.

Results

Li@C₆₀, and Li₂C₇₀: LiI was the first Li reagent used successfully for the *in situ* thermal ionization incorporation Li into C₆₀ and C₇₀ in a mass spectrometer [4]. A series of experiments performed at 400-800°C with various C₆₀ or C₇₀/LiI ratios showed that endohedral fullerenes were the main products (Figure 1) without impurities. Observed ionization energies for Li@C₆₀ and Li₂@C₇₀ were 5.9 eV and 5.3 eV respectively. The following crucial information about behaviour of these species were: (a) they are thermally stable, since vacuum resublimation did not result in a change in composition of the mixture. Subsequent MALDI TOF mass spectral analysis of the powdered material collected from the cold parts of the ion source after completion of the reaction precisely reproduced the results obtained during the *in situ* experiments (Figure 3). Singly charged cations of the metallofullerenes (M@C_n⁺) were completely unreactive in the gas phase with oxygenated compounds such as ethylene oxide: however, the corresponding neutral species appear to react readily with oxygenated species. Collisional dissociation of the ionized endohedral fullerenes listed above revealed multiple C₂ loss (either as sequential C₂ loss or larger C_{2n} eliminations) to generate similar terminal fragmentation products, which might be predicted due to the similar ionic radii of the encapsulated metals (Figure 2).

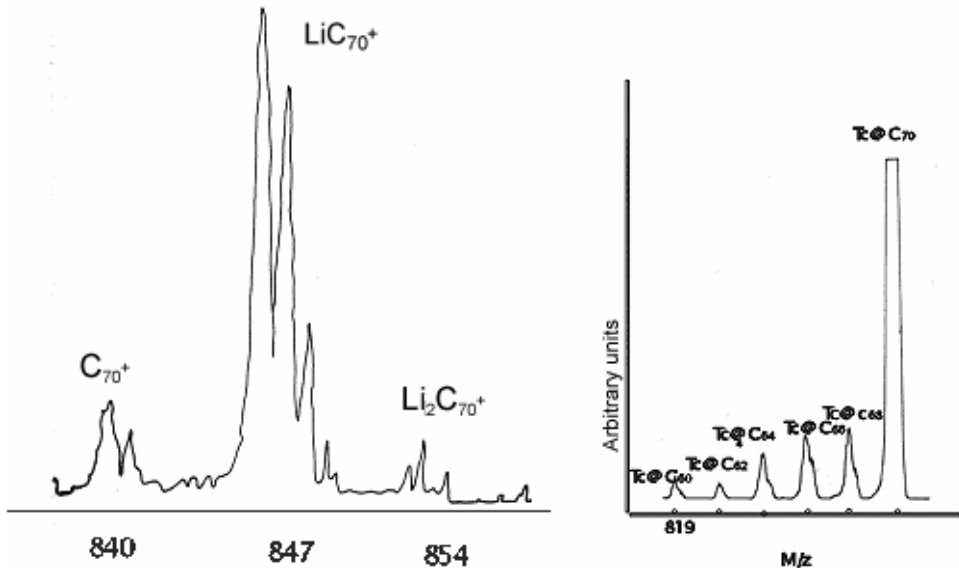


Figure 1. Mass spectrum for a C_{70} /LiI sample containing C_{70}^+ , $Li@C_{70}^+$ and $Li_2@C_{70}^+$ species.

The ratio of the filled to the empty fullerene is seen to be about 1.5: 8: 1. In addition, one observes the isotopic composition of Li and C.

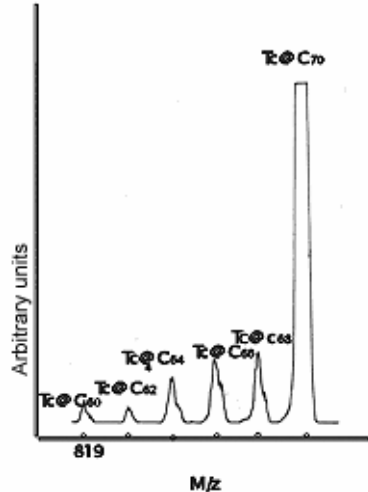
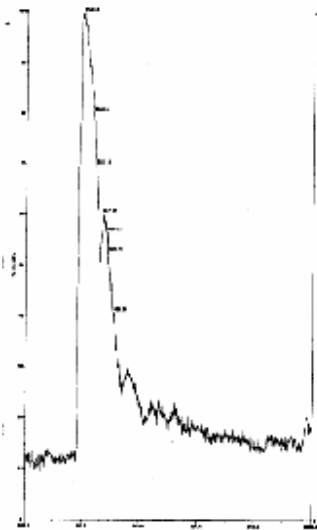


Figure 2. Electron impact fragmentation mass spectrum of $^{99m}Tc@C_{70}$.

Figure 3. MALDI mass spectra (linear mode) of $Li_2@C_{70}$.



Acknowledgments

This work was financially supported by the Ministry of Science and Environmental Protection, Republic of Serbia, under Project No. 1995.

References

- [1] D.S. Bethune, R.D. Johnson, J.R. Salem, M.S. de Vries, S.C. Yannoni, *Nature*, 1993, 36, 123.
- [2] S. Nagase, K. Kobayashi, T. Akasaka, *Bull. Shem. Soc. Jpn.*, 1996, 69, 2131.
- [3] S. Nagase, K. Kobayashi, T. Akasaka, *J. Mol. Struc. Theochem.*, 1997, 398-399, 221.
- [4] A. Djeric, M. Veljkovic, O. Neskovic, M. Miletic and K. Zmbov, *Full. Sci. Tech.*, 2000, 8(6), 461.

DETECTION OF MALATHION BY THE CO₂-LASER

B.B. Radak, D.S. Maravić, Lj.T. Petkovska and M.N. Damjanović*

Vinča Institute of Nuclear Sciences, POB 522, 11001 Belgrade, Serbia & Montenegro;

**Galenika Fitofarmacija, Batajnički drum b.b., Zemun, Serbia & Montenegro*

Abstract

Possibilities of detecting the vapour of the pesticide malathion by a CO₂-laser, using a photoacoustic technique developed in our laboratory were investigated. A set of vapor photoacoustic spectra of coincidence with this laser were obtained, the samples being: the commercial product available on the market, solvent, emulsifiers, and neat malathion. Relative contributions of the components in the product are discussed.

Introduction

Detecting pesticides and measuring their concentration is a regular concern and objective of analytical chemistry [1]. The usual way would be to take a solid sample (of ground, plant, fruit, etc.) and analyse it by any suitable conventional method - gas/liquid chromatography, or similar. However, a fast and real-time assessment should be done nondestructively, in the field. Atmospheric measurements would be ideal [2]. On the other hand, malathion does not have significant vapour pressures at ordinary temperatures. But, it is never alone in a commercial mixture available on the market. Other components of the mixture have measurable vapour pressures.

We investigated the possibilities of detecting malathion vapor by a CO₂-laser, using a photoacoustic technique developed in our laboratory [3]. The experiments include recording of laser/vapour spectral coincidences in the usual range of CO₂-laser wavelengths, the vapour being: the commercial pesticide product found on the market, neat pesticide (at the commercial purity of the raw component), additives (emulsifiers and the solvent), all with and without air added to a mid-pressure of about 100 mbar.

Results and Discussion

The commercial product found on the market usually consists of neat malathion (at 95% purity), solvent (xylol), and emulsifiers (geronol ff4 and geronol ff6). We found that all the components can give rise to a laser coincidence spectrum, and participate in the spectrum of the product. The spectra of the commercial product and of each of the components are presented in Fig. 1. Since the formulation of the product cannot be published, the discussion is restricted here to quantitative considerations.

It can be assessed that the main contributions to the spectrum of the commercial product come from the emulsifiers and from neat malathion component. This is because of the following. The coincidences of the product are substantially higher at the 9 μ band of the laser, whereas xylol does not show such a pronounced difference between the two CO₂-laser bands. Hence, it apparently does not contribute significantly to the

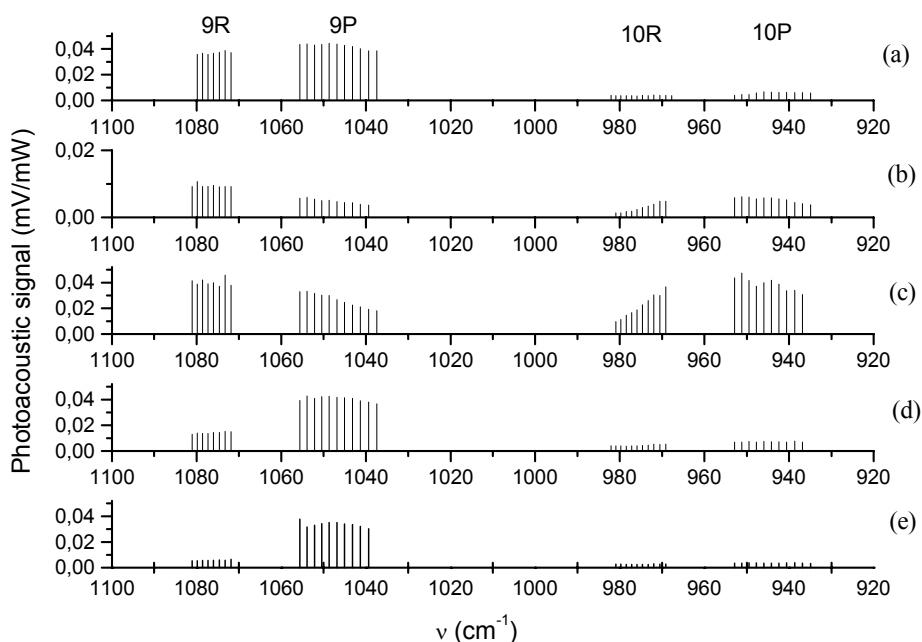


Fig. 1. Laser coincidence spectra of (a) 14.4 mbar commercial malathion product + air to 101 mbar, (b) 3 mbar neat malathion + air to 91.6 mbar, (c) 12.7 mbar xylol + air to 103 mbar, (d) 4.64 mbar geronol ff4 + air to 98.6 mbar, (e) 4.6 mbar geronol ff6 + air to 104 mbar.

spectrum of the product. In the 9μ region, both branches of the laser band are absorbed to a similar extent. This is probably due to the combined contributions of the emulsifiers and malathion. The emulsifiers absorb more in the 9P branch and malathion in the 9R branch.

Overall, the spectrum of the commercial product has fingerprinting potential in the fact that 9μ laser transition gives rise to significantly stronger coincidences than the 10μ one.

The question remains, however, how does malathion show measurable vapour pressure and, consequently, a measurable spectrum, if it nominally has a vapour pressure of only 0.5×10^{-9} bar at $30\text{ }^\circ\text{C}$? We suspect the vapour pressure is created by the impurities present in the malathion component of technical purity. This purity is declared at 95%, which leaves 5% for the impurities, consisting mainly of isomalathion, malaaxon, and analogues of trimethylphosphate. It is possible that some of these impurities gives rise to the actual spectrum measured. That can be a subject of further investigations, but is irrelevant to the present practical consideration.

Conclusion

Possibilities of detecting the vapor of the pesticide malathion by a CO₂-laser, using the photoacoustic technique developed in our laboratory were investigated. A set of vapor photoacoustic spectra of coincidence with this laser showed that most significant contributions to the spectrum of the commercially available product come from the emulsifiers used in the commercial mixture and neat malathion of the available purity of 95%. The fact that measurable vapor pressure (several mbar) was obtained from the neat substance and that nominally malathion does not possess it, points to a conclusion that it comes from the impurities, i.e. 5% of the contents of the neat substance. Whatever the source of the spectrum, it is measurable by the photoacoustic laser technique, and shows some fingerprinting potential in the pronounced difference between the two laser transitions, such that the 9 μm transition has significantly stronger coincidences.

References

- [1] F. A. Tarbah, H. Mahler, O. Temme, T. Daldrup, *Forensic Sci Int.*, 2001, 121, 126.
- [2] M. W. Sigrist, A. Bohren, T. Lerber, M. Nagele, A. Romann, *Analytical Sci* 2001, 17, 511.
- [3] B.B. Radak, M.T. Petkovska, M.S. Trtica, S.S. Miljanic, Lj.T. Petkovska, *Anal. Chim. Acta*, 2004, 505, 67.

N - H...O HYDROGEN BONDING: FT IR STUDY OF N-BUTYLACETAMIDE - ETHER SYSTEMS

A.D. Nikolić¹, L. Gobor¹, S. Majkić¹ and S.D. Petrović²

¹Department of Chemistry, Faculty of Sciences, Trg D. Obradovića 3, 21000 Novi Sad,

²Faculty of Technology and Metallurgy, Karnegijeva 4, 11000 Belgrade, Serbia and Montenegro

Abstract

N – H...O hydrogen bonding of N-n-butylacetamide and N-tert-butylacetamide with diethylether and tetrahydrofuran have been investigated FT IR spectroscopy, in fundamental stretching vibration region, was used. The spectroscopic parameters for hydrogen bonded complexes as well as the equilibrium constants at 298 K have been determined.

Introduction

N-substituted amides and their hydrogen bonds deserve great scientific attention since this class of compounds can be regarded as a simple model for biological systems with peptide groups. This study is a part of our continuous interest in amide behaviour in solutions [1-4] and involves N-n-butylacetamide and N-tert-butylacetamide and two ethers: diethylether and tetrahydrofurane.

Experimental

N-n-butylacetamide (NnBA) and N-tert-butylacetamide (NtBA) have been synthesized. NnBA was redistilled under reduced pressure. NtBA was recrystallized. Diethylether (DEE) and tetrahydrofurane (THF), Fluka, p.a., were freed from peroxydes by shaking with acidified aqueous iron (II) sulphate. They were distilled and collected over sodium.

IR spectra, in the NH fundamental stretching vibration region, were recorded on a Thermo-Nicolet Nexus 640 FT IR spectrometer, at 25°C. UVIRSIL (1-5 cm) cells have been employed. The concentration of the amides was kept below 0.005 mol dm⁻³, in order to eliminate amide selfassociation. The concentration of the ethers varied between 0.5 and 1.5 mol dm⁻³.

Results and Discussion

Spectroscopic characteristics for the monomer (free) $\nu(NH)$ band of the amides are given in Table 1. Also, a characteristic IR spectra for the systems in this study is given in Figure 1.

Spectroscopic parameters and the equilibrium constants for N - H...O complexes of NnBA and NtBA with the ethers are summarized in Table 2. Also, a characteristic IR spectrum for the systems in this study is given in Figure 1.

Table 1. Spectroscopic characteristics for the monomer $\nu(NH)$ band of NnBA and NtBA obtained for diluted CCl_4 solutions at 298 K

Amide	$\frac{\nu(NH)}{cm^{-1}}$	$\frac{\nu_{1/2}}{cm^{-1}}$	$\frac{\varepsilon}{cm^2 mol^{-1}}$	$\frac{10^6 B^0}{cmmol^{-1}}$
NnBA	3461	22	130	4.49
NtBA	3450	13	194	4.11

The spectroscopic parameters: frequency shift ($\Delta\nu$), band halfwidth ($\nu_{1/2}$), molar absorptivity (ε) and molar integrated absorption coefficient (B^0) clearly show the presence of $N-H\cdots O$ hydrogen bonding between N-H proton and ether oxygen. It is evident that NnBA forms more stable complexes than NtBA, due to the steric hindrance of tert-butyl group. Similar effect of the tert-butyl substituent has been already recorded [4]. Also, the $N-H\cdots O$ complexes with THF are more stable than ones with DEE.

Table 2. Spectroscopic parameters and the equilibrium constants for N - $H\cdots O$ complexes between N-butylacetamides and ethers at 298 K

Complex	$\frac{\Delta\nu}{cm^{-1}}$	$\frac{\nu_{1/2}}{cm^{-1}}$	$\frac{\varepsilon}{cm^2 mol^{-1}}$	$\frac{10^{-6} B^0}{cm \cdot mol^{-1}}$	$\frac{K_c}{dm^3 mol^{-1}}$
NnBA-DEE	94	55	230	19.1	0.43
NnBA-THF	96	60	240	22.6	0.99
NtBA- DEE	84	44	246	16.6	0.38
NtBA- THF	87	50	300	23.6	0.55

For N-methylacetamide - diethylether system, Luckii and Gončarova [5] have obtained $0.37 dm^3 mol^{-1}$ for the equilibrium constant. Also, their spectroscopic data are similar to those in Table2.

Comparison of the data from this study with the results obtained for $N-H\cdots\pi$ hydrogen bonding [1, 3, 4] indicates that $N-H\cdots O$ hydrogen bond is significantly stronger (based on the frequency shifts) and more stable (based on the equilibrium constants).

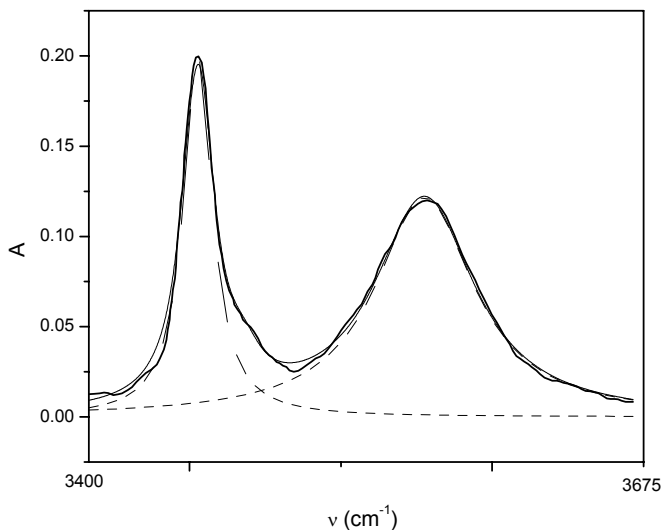


Figure 1. Infrared spectrum in the region of NH fundamental vibration for NtBA - DEE system.

References

- [1] A.D. Nikolić, N.L. Kobilarov, A.N. Brzić, *J. Mol. Struct.*, 1983, 99, 179.
- [2] A.D. Nikolić, N.U. Perišić-Janjić, N.L. Kobilarov, *J. Chem. Thermodyn.*, 1985, 17, 859.
- [3] Nikolić, S. Petrović, D. Antonović, L. Gobor, *J. Mol. Struct.*, 1997, 408/409, 355.
- [4] A.D. Nikolić, M.M. Mladenović, L. Gobor, D.G. Antonović, S.D. Petrović, *J. Serb. Chem. Soc.*, 2003, 68, 715.
- [5] A.E. Luckii, E.I. Gončarova, *Spektroskopia-Metodi i primeneniye*, izd. Nauka, Moskva, 1969, p 39.

(2*E*,5*Z*) Ethyl (5-ethoxycarbonylmethylidene-4-oxothiazolidin-2-ylidene)ethanoate (1b**):** $^1\text{H NMR}$ (CDCl_3): 1.30 (t, 3H, CH_3 , $J = 7.1$ Hz), 1.35 (t, 3H, CH_3 , $J = 7.1$ Hz), 4.22 (q, 2H, CH_2O , $J = 7.1$ Hz), 4.31 (q, 2H, CH_2O , $J = 7.1$ Hz), 5.35 [s, 1H, =CH (C2)], 6.88 [s, 1H, =CH (C5)], 10.82 (s, 1H, NH).

(2*Z*,5*Z*) Ethyl (5-ethoxycarbonylmethylidene-4-oxothiazolidin-2-ylidene)ethanoate (1b**):** $^1\text{H NMR}$ (CDCl_3): 1.32 (t, 3H, CH_3 , $J = 7.0$ Hz), 1.35 (s, 3H, CH_3 , $J = 7.0$ Hz), 4.25 (q, 2H, CH_2O , $J = 7.0$ Hz), 4.32 (q, 2H, CH_2O , $J = 7.0$ Hz), 5.83 [s, 1H, =CH (C2)], 6.80 [s, 1H, =CH (C5)], 10.54 (s, 1H, NH).

Results and Discussion

An analysis of the diagnostic chemical shifts in the $^1\text{H NMR}$ spectra of the configurational isomers of ethyl (5-ethoxycarbonylmethylidene-4-oxothiazolidin-2-ylidene)ethanoate **1b**, compiled in Table 1, provides a fairly complete picture of the 2*E*,5*Z*-**1b** / 2*Z*,5*Z*-**1b** equilibrium (Scheme).

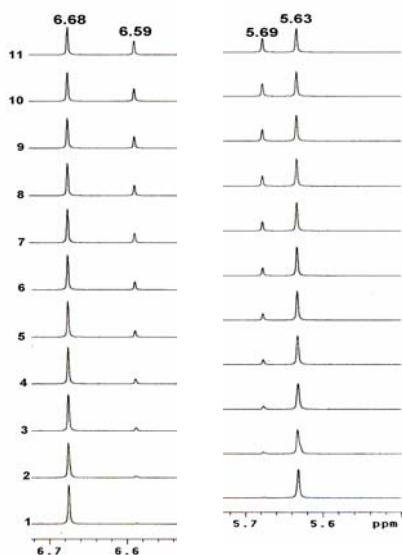


Figure 1. Spectral evidence for the presence of the starting 2*E*,5*Z*-**1b** isomer, based on the observation of the olefinic signals at σ 5.63 and 6.68 ppm, and 2*Z*,5*Z*-**1b** isomer (olefinic signals at σ 5.69 and 6.59 ppm) in $\text{DMSO}-d_6$ at room temperature.

Thus, Figure 1. depicts series of partial $^1\text{H NMR}$ spectra of diastereomers 2*E*,5*Z*-**1b** and 2*Z*,5*Z*-**1b** (only the resonances of the olefinic protons are shown; see also Table 1) recorded in $\text{DMSO}-d_6$ during the isomerization process at 25 °C. The same time-dependent process was similarly followed at four different temperatures). The diastereomer ratios of 2*E*,5*Z*-**1b** versus 2*Z*,5*Z*-**1b** in regular time interval (30 min at rt) were calculated by the integration of the well-resolved signals at σ 5.63 and 5.69 ppm corresponding to the C(2')-vinyl protons of the 2*E*,5*Z*-**1b** and 2*Z*,5*Z*-**1b** isomers, respectively. Alternatively, the kinetics of the isomerization at different temperatures can be studied by the determination of the configurational ratio via integration of the C(5')-H signals at σ 6.68 ppm (the 2*E*,5*Z*-**1b** isomer) and 6.59 ppm (the 2*Z*,5*Z*-**1b** isomer).

Table 1. Selected $^1\text{H NMR}$ chemical shifts (σ in ppm) of configurational isomers of compound **1b**

(2*Z*,5*Z*)-**1b**: (H-2') **5.69** and (H-5') **6.59**
 (2*E*,5*Z*)-**1b**: (H-2') **5.63** and (H-5') **6.68**

It is noteworthy that the lower double bond polarization of the (*Z*)-configured C(5)=C(5') bond, combined with the unfavorable steric and dipole-dipole interactions

of the *E*-configured C(5)-double bond, make the configuration of this bond in **1a-d** derivatives stable and not prone to the *Z/E* isomerization. The main factor dictating the direction of the isomeric equilibrium (Scheme), i.e. the contribution of the configurational isomers, is the polarity of the solvent used in the isomerization process [3]. In the case of polar solvent, such as DMSO-*d*₆, the prevailing species in the equilibrated configurational mixture is the *2Z,5Z*-isomer **1b**. The variable-temperature ¹H NMR data for the isomerization of ethyl (5-ethoxycarbonylmethylidene-4-oxothiazolidin-2-ylidene)ethanoate (**1b**) in DMSO-*d*₆, possessing the two exocyclic C=C bonds at the C(2)- and C(5)-positions, indicate that the rotational barrier ΔG^\ddagger separating the *2E,5Z-1b* and *2Z,5Z-1b* isomers, is 100.20 kJ/mol (at 298 K). In a polar solvent-dependent equilibrium the major *2Z,5Z*-form (>90%) is stabilized by the intermolecular resonance-assisted hydrogen bonding and strong 1,5-type S...O interactions within the -S-C=C-C=O entity, implying the *s-cis* conformation around the C=C-C=O single bond. In addition, the ¹³C NMR $\Delta\delta_{C(2)C(2')}$ values which indicate the importance of electron withdrawal at C(2') position of the polarized thiazolidines **1a-d** nicely correlate with the degree of the push-pull character of the exocyclic C(2)=C(2') bond.

References

- [1] J. Sandström, Top. Stereochem., 1983, 14, 83 and references cited therein.
- [2] R. Marković, M. Baranac, Z. Džambaski, M. Stojanović and P. Steel, Tetrahedron, 2003, 59, 7803.
- [3] R. Marković, A. Shirazi, Z. Džambaski, M. Baranac and D. Minić, J. Phys. Org. Chem., 2004, 17, 118.

VALIDATION OF METHYLPREDNISOLONE HEMISUCCINATE IDENTIFICATION IN LEMOD SOLU 20 mg INJECTIONS

B. Radivojev¹, M. Dašić¹ and S. Petrović^{1,2}

¹*Hemofarm koncern, Vršac, Serbia and Montenegro*

²*Faculty of Technology, University of Belgrade, Serbia and Montenegro*

Abstract

This paper explains the approach to the method validation for active substance identification which is in compliance with the ICH (International Conference on Harmonisation of technical requirements for registration of pharmaceuticals for human use) regulations, on the example of methylprednisolone hemisuccinate identification in Lemod solu 20 mg injections, using the transmission technique of IR spectroscopy.

Introduction

The identification of methylprednisolone hemisuccinate in Lemod solu 20 mg injections is performed by the transmission technique of infrared spectroscopy [1]. Validity of the identification method is established by testing its specificity [2,3]. The specificity of the active substance identification method implies that the tested sample provides a positive result, while the related substances and substances with similar structure provide a negative result when compared with the reference substance. Likewise, it is necessary that the matrix and sample preparation have no impact on the identification. The validity of the above mentioned method was tested by multiple preparation of Lemod solu 20 mg injections sample and identification, then by the identification of the related substances [4] (methylprednisolone and methylprednisolone acetate) and substances with similar structure (hydrocortisone hydrogen succinate) to methylprednisolone hemisuccinate and by recording IR spectrum of matrix.

Experimental

The IR spectra of the samples as KBr pellets have been recorded on a Thermo Nicolet FTIR spectrophotometer AVATAR 370 in the range from 4000 to 400 cm^{-1} . The KBr pellets, of 13 mm diameter, were prepared as 1% sample triturate in KBr powder. Certified reference substances were used for recording reference spectra of methylprednisolone hemisuccinate, methylprednisolone, methylprednisolone acetate and hydrocortisone hydrogen succinate. Identification was performed through automatic search of the reference spectra library using the OMNIC software [5], in the range from 2600 to 450 cm^{-1} .

Results and Discussions

The figure 1. a) shows the reference spectrum of methylprednisolone hemisuccinate, and the figure 1. b) matrix spectrum

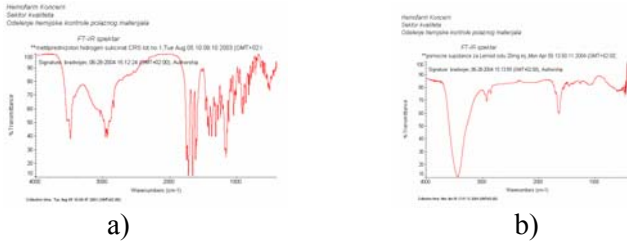


Figure 1. a) Reference spectrum of methylprednisolone hemisuccinate; b) matrix spectrum.

Based on the comparison of spectra, one can see that the matrix of Lemod solu 20 mg injections does not interfere with the identification of methylprednisolone hemisuccinate.

The identification of the sample Lemod solu 20 mg injections is shown on Figure 2.



Figure 2. Identifikacija of Lemod solu 20 mg injections

The table 1. illustrates the identification results of five samples of Lemod solu 20 mg injections.

Table 1.

Sample Ord. No.	Matching (%)	Result
1	86.15	very good
2	89.21	very good
3	94.86	very good
4	93.36	very good
5	89.01	very good

It is obvious that sample preparation has no major impact on the identification result.

The figures 3. and 4. obviously show that the related substances spectra (methylprednisolone and methylprednisolone acetate) do not match the spectrum of methylprednisolone hemisuccinate.

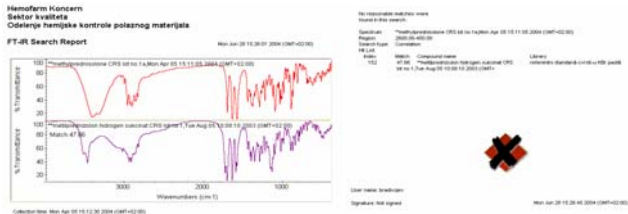


Figure 3. Methylprednisolone spectrum

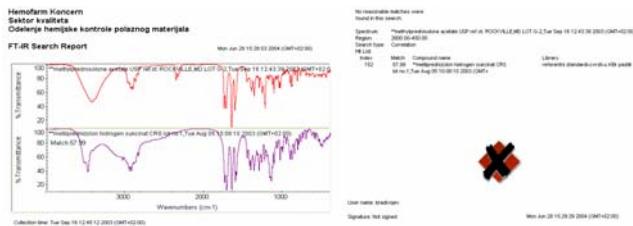


Figure 4. Methylprednisolone acetate spectrum

On the figure 5. it is obviously that the spectrum of substance with similar structure (hydrocortisone hydrogen succinate) does not match the spectrum of methylprednisolone hemisuccinate.

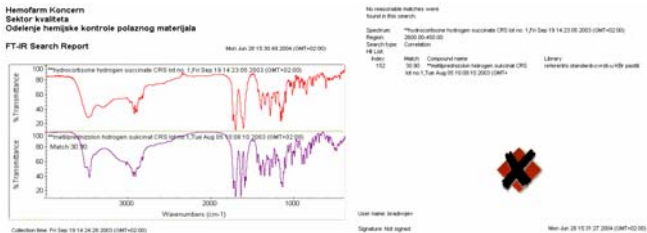


Figure 5. Hydrocortisone hydrogen succinate spectrum

Conclusion

The method of methylprednisolone hemisuccinate identification in Lemod solu 20 mg injections by means of the transmission technique of IR spectroscopy meets all discussed specificity aspects and can be considered as valid.

References

- [1] ANALITIČKI POSTUPAK, Lemod solu 20 mg iv./im. injekcije, Hemofarm koncern AD, Januar 2003, HFG 0083-01.
- [2] ICH Harmonised Tripartite Guideline, Text on Validation of Analytical Procedures Q2A, ICH Steering Committee, October 1994.
- [3] ICH Harmonised Tripartite Guideline, Validation of Analytical Procedures: Methodology Q2B, ICH Steering Committee, November 1996.
- [4] European Pharmacopeia 4th Edition 2002, pages 1569,1570.
- [5] OMNIC Software Version 6.1a, Thermo Nicolet

SPECTROPHOTOMETRIC INVESTIGATION ON THE INTERACTION OF FAMOTIDINE WITH COPPER(II)

Z. Korićanac and T. Jovanović

Faculty of Pharmacy, University of Belgrade, Vojvode Stepe 450, 11000 Belgrade, SCG

Abstract

The formation of the complex between famotidine and copper(II) ions in Britton Robinson buffer solutions was studied. It has been established that in pH range 2.23-4.30 famotidine forms with copper(II) ions blue water-soluble complex with maximum absorbance at 318.5 nm. It was found that the composition of the complex of famotidine : Cu(II) was 2 : 1, and the conditional stability constant of the complex, $\log K'$, was 7.65 ± 0.05 . The molar absorptivity for the complex was $1.067 \times 10^3 \text{ L mol}^{-1} \text{ cm}^{-1}$ at pH 2.62.

Introduction

Famotidine, [3-[[[2-[(aminoiminomethyl)amino]-4-thiazolyl]methyl]thio]-N-(aminosulfonyl)propanimidamide], is an antagonist of histamine at H_2 -receptor sites and effective inhibitor of gastric secretion. It is widely used in the treatment of gastrointestinal disorders, such as aspiration syndrome, dyspepsia, gastro-esophageal reflux disease and peptic ulcer [1].

Molecule of famotidine should act as effective ligands towards metal ions, because it is composed of several groups provided with very strong coordinating ability.

The present communication reports the results obtained during a study of the reaction of metal ions with H_2 -antagonists [2-4].

Results and Discussion

The reaction between famotidine and Cu(II) ions in Britton-Robinson buffer solutions was studied. It was found that at pH range 2.23-4.30 famotidine (FAM) reacts with copper(II) to forming aquasoluble, blue coloured complex. Absorption spectra were recorded over the wavelength range 250-400 nm. The complex gave a sharp absorption peak at 318.5 nm. Since neither Cu(II) nor famotidine absorb at 325 nm all measurements were performed using water as a blank.

The pH of the reaction mixture had a considerable influence on the absorbance and solubility of the complex. The position of the maximum absorbance changes with pH, except in the pH range 2.23-4.30, where the λ_{max} stays constant; this fact indicates that in this pH range one type of the complex was formed (Fig. 1). Absorption curves show that the absorbance of the complex increases from pH 2.23-4.30, therefore, at pH 4.50 solution becomes turbid. A Britton-Robinson buffer of pH 2.60 was used to provide the working pH. At this pH at least a five-fold molar ratio of reagent to analyte is necessary for maximum complex formation. No influence of ionic strength (KCl, NaClO₄) on the course of the reaction was observed.

Under these conditions the color takes 15 min for full development, and then was stable for at least 24h.

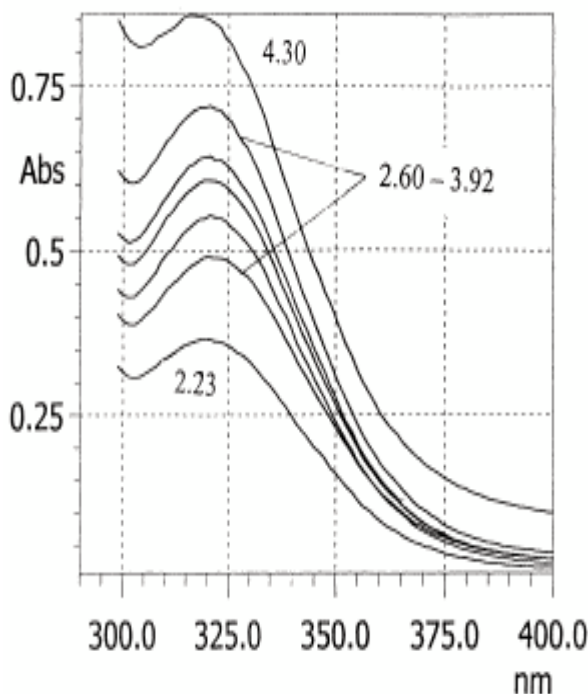


Fig. 1. The effect of pH on the complex formation
 $c_{\text{FAM}}=2.5 \times 10^{-4} \text{M}$; $c_{\text{Cu(II)}}= 2. \times 10^{-3} \text{M}$; $\mu=0.2 \text{ M}$

For the complex formation a linear relationship between absorbance and concentration of famotidine was established over the range 3×10^{-5} - $3.6 \times 10^{-4} \text{M}$, at $\mu=0.2$ and $\text{pH}=2.60$. The molar absorptivity at 325 nm for the complex was $1.067 \times 10^3 \text{Lmol}^{-1} \text{cm}^{-1}$.

The composition of the complex was established by the continuous-variation method [5,6]. The plot reached a maximum at a fraction x_{max} 0.33 which indicates the formation of 2 : 1 famotidine-copper(II) complex. The comparison with the results obtained by the molar-ratio [7], Bent-French [8] and conductivity [9] methods definitely proves that a famotidine : Cu(II) = 2 : 1 complex was formed.

To determine the conditional stability constant (K') the Job's method of non-equimolar solutions [5, 6] was used. In this purposes the curve for five-fold excess of reagent ($p = 5$, $x_{\text{max}} = 0.175$) was obtained and the conditional stability constant calculate. The mean value of $\log K'$ obtained by this method was 7.65.

Acknowledgements

Financial support for this research (Project 1458) was provided by the Ministry of Science and Technology of the Republic of Serbia.

References

- [1] Goodman and Gilman's, in *The Pharmacological Basis of Therapeutics*, 9th ed., 1996, McGraw Hill, New York, 904.
- [2] J.Petković, D.Minić, Z.Korićanac, T.Jovanović, *Pharmazie*, 1998, 53, 163.
- [3] Z.Korićanac, T.Jovanović, B.Stanković, *Pharmazie*, 1995, 50, 151.
- [4] D.Minić, J.Petković, Z.Korićanac, T.Jovanović, *J.Pharm. Biomed. Anal.*, 1996, 14, 1355.
- [5] P.Job, *Ann. Chim. Phys.*, 1928, 9, 113.
- [6] W.C. Vosburg, G.R. Copper, *J. Am. Chem. Soc.*, 1941, 63, 437.
- [7] J. Yoe, A.Jones, *Ind. Eng. Chem. Soc.* 1944, 16, 111.
- [8] H.Bent, C.French, *J. Am. Chem. Soc.*, 1941, 63, 568.
- [9] W.J. Geary, *Coord. Chem. Rev.*, 1971, 7, 81.

SPECTROPHOTOMETRIC INVESTIGATION ON REACTION PALLADIUM(II) IONS WITH THREE ANTI-ULCER DRUGS

Z. Korićanac^a, T. Jovanović^a and J. Petković^b

^a Faculty of Pharmacy, University of Belgrade, Vojvode Stepe 450, 11000 Belgrade, SCG

^b Faculty of Physical Chemistry, University of Belgrade, Studentski Trg 12-16, 11000 Belgrade, SCG

Abstract

It has been established that famotidine, nizatidine and ranitidine react with palladium(II) chloride in Britton-Robinson buffer solution in the pH range 2.25-7.98 to form yellow coloured water soluble complexes. The optimum conditions for reaction of complexation were determined.

It was found by using different spectrophotometric methods that these compounds form with Pd(II) ions complexes, which stoichiometric ratios are 1:1. The conditioned stability constants of formed complexes were found as: $\log K' = 3.74 \pm 0.02$ (pH = 2.62) for famotidine; $\log K' = 4.72 \pm 0.02$ (pH = 3.50) for nizatidine and 4.85 ± 0.02 (pH = 3.35) for ranitidine. Calibration graphs for the three complexes are linear over the concentration ranges 10^{-5} - 10^{-4} M, with correlation coefficients > 0.999 . The proposed method was successfully applied to the determination of famotidine, nizatidine and ranitidine in pharmaceuticals dosage forms.

Introduction

Famotidine, (N'-[aminosulfonyl]-3-[(2-[diaminomethyl]eneamino)-4-thiazolyl)methylthio]-propamidine), nizatidine, (N-[2-[[[2-(dimethylamino)methyl]-4-thiazolil]methyl]thio]ethyl]-N'-methyl-2-nitro-1,1-etheneamine), and ranitidine, (N-[[2-(5-dimethylaminomethyl-2-furanyl)-methyl-thio]ethyl]-N'-methyl-2-nitro-1,1-ethene-diamine) are the antagonists of histamine at H₂-receptor sites and effective inhibitors of gastric acid secretion introduced for the treatment of peptic ulcers and related disorders [1,2]. Methods for the quantitative analysis of these drugs in biological fluids and in pharmaceutical formulations include HPLC [3, 4], UV spectrophotometry [5,6] potentiometry [7], and many others methods.

The present work reports results obtained during spectrophotometric studies of the colour reaction of famotidine, nizatidine and ranitidine with bivalent palladium(II) ions, as well as to apply this complexation reaction to the assay of these antiulcer drugs in pharmaceutical preparations by simple spectrophotometric method.

Experimental

Spectrophotometric measurements were performed on a Pye Unicam SP-6-500 spectrophotometer with matched 10 mm quartz cells and a Radiometer PHM 62 pH meter calibrated with standard buffer solutions were used.

Standard substance famotidine (Alkaloid, Skopje), nizatidine (Eli Lilly and Co.), ranitidine (Zdravlje, Leskovac) and palladium(II) chloride (p.a., Merck) were used.

Pharmaceutical preparations: Famosan[®] tablets, Lacidil[®] tablets, Galitidine[®] capsules and ampoules, Ranisan[®] tablets and ampoules.

Results and Discussion

The reaction between palladium(II) ions with famotidine, nizatidine and ranitidine were investigated in Britton-Robinson buffer solutions over the pH range 2.25-7.98. Full colour development were observed after five minutes and the absorbance remained unchanged up to 60 minutes, at pH 2.25-4.50. All measurements were performed against a reagent blank, palladium(II) chloride.

Absorption curves show that absorption maximum of the complexes shifted slightly from 325 nm for nizatidine, over 327 nm for ranitidine to 345 nm for famotidine, at pH 3.20. Investigation of the effect of reagent concentration showed that a two-fold molar ratio of palladium(II) to analytes are necessary for maximum complexes formation. Little influence of ionic strength on the course of the reactions were observed.

The composition of the complexes formed were established by the continuous variation method of Job and the molar ratio method. It was found that the 1 : 1 complexes were formed for all three compounds.

To determine the stability constants, the methods of Sommer et al., Asmus and the Job method of non-equimolar solutions were used. The mean values of log K' are: 3.74 ± 0.02 (pH = 2.62) for famotidine-Pd (II), 4.72 ± 0.02 (pH = 3.50) for nizatidine-Pd(II) and 4.85 ± 0.02 (pH = 3.35) for ranitidine-Pd(II).

Under the optimum conditions, the linear relationship between absorbance and anti-ulcer drugs concentration were investigated. The Beer's law were verified over the concentration range: 5×10^{-5} - 6.4×10^{-4} M for famotidine; 1×10^{-5} - 9×10^{-5} for nizatidine and 10^{-5} - 1.2×10^{-4} M for ranitidine. The reability of the method were checked at three different concentrations. The relative standard deviation varied from 1.02 to 1.8 % for famotidine, 1.27-3.28 % for nizatidine and 1.00-2.28 % for ranitidine.

The complexes compound formed between palladium(II) and famotidine, nizatidine and ranitidine can be applied for the determination of these drugs in different pharmaceutical dosage forms. High recovery values and low values for standard deviations and relative error demonstrate the suitability for routine analysis of pharmaceutical preparations. The analysis of commercial dosage forms by the method explained above concluded that excipients do not interfere in the analysis, and the results meet the tolerance limits of USP XXIII.

In conclusion, it may be considered that proposed method, using palladium(III) chloride as an analytical reagent, is suitable for accurate and sensitive analysis of famotidine, nizatidine and ranitidine both as the substance and their dosage forms.

Acknowledgements

Financial support for this research (Project 1458) was provided by the Ministry of Science and Technology of the Republic of Serbia.

References

- [1] R.N. Brogden, A.A. Carmine, R.C. Heel, T.M. Speight, G.S. Avery, *Drugs*, 1982, 24, 267.
- [2] J. Dawson, R. Cockel, G.T. Dixon, D.A. Richards, R. Stables, *J. Clin. Hosp. Pharm.*, 1983, 8, 1.
- [3] D. Zendelovska, T. Stafilov, *J. Pharm. Biomed. Anal.*, 2003, 33, 165.
- [4] B. V. Kamath, S. Vangini, *Anal. Lett.*, 1992, 25, 2239.
- [5] E.M. Hassan, F.Belal, *J. Pharm. Biomed. Anal.*, 2002, 27, 31.
- [6] D. Minić, J. Petković, Z. Korićanac, T. Jovanović, *J. Pharm. Biomed. Anal.*, 1996, 14, 1355.
- [7] Z. Korićanac, T. Jovanović, B. Stanković, *Pharmazie*, 1995, 50, 151.

IR STUDY OF CIS/TRANS CONFORMERS OF N-(4-SUBSTITUTED PHENYL)-2-CYANOACETAMIDES

J. S. Nedeljković¹, A. D. Marinković¹, S. D. Petrović^{1,2} and D. Ž. Mijin¹

¹Faculty of Technology and Metallurgy, University of Belgrade, Karnegijeva 4, P.O. Box. 3503,
11000 Belgrade, ²Hemofarm group, Beogradski put b.b., 16300 Vršac

Abstract

The cis/trans isomer ratios of the amide bond for the N-(4-substituted phenyl)-2-cyanoacetamides were studied on the basis of ν^{NH} frequency in the infrared spectra. It could be assumed that the ratio of cis/trans isomers is controlled by resonance effect as well as by secondary bond interactions.

Introduction

The conformations of various N-substituted-2-phenylacetamides have been extensively studied in our previous works [1-4]. As a continuation of the cis/trans conformational study of amides, in this work a study of N-(4-substituted phenyl)-2-cyanoacetamides has been performed.

In order to examine the effects on barrier heights to rotation, we wish to report the results of a spectroscopic study of N-(4-substituted phenyl)-2-cyanoacetamides. In general, it can be expected that N-(4-substituted phenyl)-2-cyanoacetamides may exist as cis- or trans-isomers. These two possible conformational isomers are presented in Figure 1.

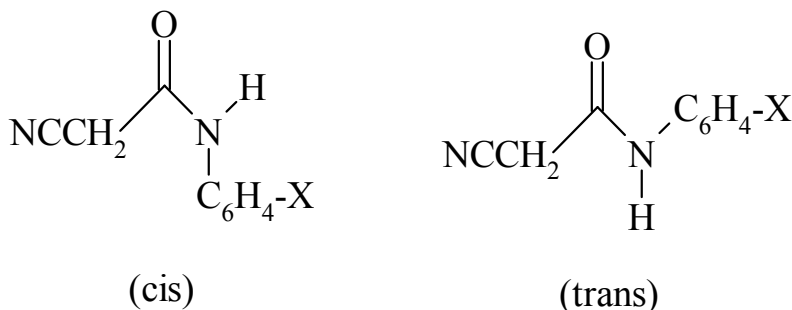


Figure 1. Two possible conformational isomers of
N-(4-substituted phenyl)-2-cyanoacetamides

Experimental Part

N-(4-substituted phenyl)-2-cyanoacetamides were synthesized using two different procedures. The first procedure was the acylation of amines by chloro acetyl chloride following with the substitution of potassium cyanide [5, 6]. The reactions were carried out in the presence of pyridine which were added to take up the hydrochloric acid. The second procedure was the acylation of corresponding substituted anilines, by previously synthesized cyanoacetyl chloride [7] in the presence of trimethyl-

amine as acid acceptor. Obtained amides were characterized by m.p., FT-IR, and ^1H NMR spectra.

IR spectra were recorded on Bomem MB-series FT-IR spectrophotometer in the form in the diluted solutions (10^{-3} mol dm^{-3}) of N-(4-substituted phenyl)-2-cyanoacetamides in carbontetrachloride.

Results and Discussion

The structures of the synthesized N-(4-substituted phenyl)-2-cyanoacetamides were defined using FT-IR and ^1H NMR. The cis/trans isomer ratios of the amide bond for the synthesized amides were studied on the basis of ν^{NH} frequency in the infrared spectra, particularly $\nu^{\text{N-H}}$ stretching vibrations for the amide monomers in carbontetrachloride (concentrations 10^{-3} mol dm^{-3}) at ambient temperature.

On the basis of FT-IR data for diluted solutions of N-(4-substituted phenyl)-2-cyanoacetamides in carbontetrachloride the exact positions of N-H stretching bond were established. It can be seen that all of the investigated amides show characteristics for trans and cis forms (Table 1.).

Table 1. Cis/trans isomer ratio in the N-(4-substituted phenyl)-2-cyanoacetamides

X	trans		cis	
	$\nu^{\text{N-H}}$ (cm^{-1})	%	$\nu^{\text{N-H}}$ (cm^{-1})	%
H	3445.24	2.8	3421.69	97.2
4-methyl	3443.72	2.5	3422.33	97.5
4-methoxy	3446.7	4.2	3422.58	95.8
4-iodo	3446.76	3.2	3419.85	96.8
4-bromo	3445.24	2.9	3420.55	97.1
4-chloro	3445.24	15.9	3421.32	84.1
4-nitro	3446.56	22.3	3419.54	77.7
4-hydroxy	3445.24	53.0	3419.85	47.0
4-carboxy	3446.75	2.2	3411.38	97.8
4-sulfonyl	3446.54	61.4	3421.39	38.6
4-acetyl	3447.47	26.0	3420.41	74.0

Although we have shown earlier that the trans-conformation of N-mono-substituted amides often predominates over cis-conformation [1], it seems that in the studies amides, when substituent as H, CH_3 , OCH_3 , Br and I is present, the amides exist almost as cis isomer. On the other hand the amides with a substituent present on phenyl ring like NO_2 , Cl, OH, COOH, SO_3H and CH_3CO exist as a mixture of cis/trans isomers, as it has been shown earlier for N-(4-substituted phenyl)-2,3-diphenylpropanamides [4, 8]. It could be assumed that the ratio of cis/trans isomers is controlled by resonance effect as well as by secondary bond interactions.

Conclusion

Eleven N-(4-substituted phenyl)-2,3-diphenylpropanamides with H, CH₃, OCH₃, Br, I, Cl, NO₂, OH, COOH, SO₃H and CH₃CO as substituents were synthesized. On the basis of FT-IR data for diluted solutions of N-(4-substituted phenyl)-2-cyanoacetamides in carbontetrachloride the exact positions of N-H stretching bond were established. All of the investigated amides show characteristics for trans and cis forms. Resonance effect as well as secondary bond interactions influence the ratio of cis/trans isomers in the studied N-(4-substituted phenyl)-2,3-diphenylpropanamides.

References

- [1] D.G.Antonović, A.D.Nikolić, S.D.Petrović, *J. Mol. Struct.*, 1988, 174, 255.
- [2] S.D.Petrović, N.D.Stojanović, D.G.Antonović, D.Ž.Mijin, A.D.Nikolić, *J. Mol. Struct.*, 1997, 410-411, 35.
- [3] D.Ž.Mijin, B.M.Božić, S.D.Petrović, *Facta Universitatis, Series: Physics, Chemistry and Technology*, 2000, 2 (2), 109.
- [4] V.D.Janković, D.Ž.Mijin, S.D.Petrović, *Physical Chemistry 2002, 6th International Conference on Fundamental and Applied Aspects of Physical Chemistry*, book of abstracts, Vol. I, Belgrade, 2002, p.117.
- [5] T. Dahlbom, *Acta Chem. Scand.*, 1959, 13, 6.
- [6] T. Weston, J. Taylor, *J. Chem. Soc.*, 1930, 12, 2739.
- [7] I. Kandror, *Zh. Obsch. Khim.*, 1990, 60 (9), 2160.
- [8] V.D.Janković, D.Ž.Mijin, S.D.Petrović, *2nd International Conference of the Chemical Societies of the South-East European Countries - Chemical Sciences and Industry*, book of abstracts Vol. II, Greece, 2000, p.162.

DESIGN AND TEST OF THE GAS-DYNAMIC CARBON DIOXIDE LASER EXPERIMENTAL SETUP

Š. S. Miljanić^{a)} and M. S. Trtica^{b)}

^{a)}University of Belgrade, Faculty of Physical Chemistry,
11001 Belgrade, P.O.B. 137

^{b)}Vinča Institute of Nuclear Sciences, Department of Physical Chemistry,
11001 Belgrade, P.O.B. 522
Serbia & Montenegro

Abstract

An experimental gas-dynamic laser apparatus based on acetylene-in-oxygen combustion has been designed and tested. Main setup volume was designed as a modular type for flexibility. A vacuum system, electrical and measuring elements were attached to the volume. Tests of the gas supply, vacuum system, electronics and lasing have been performed. They have shown reliable functionality and durability of all units.

Introduction

In principal, the gas-dynamic laser (GDL) is based on rapid cooling of a hot gas by expanding it through a supersonic nozzle to obtain the *gas-dynamic* flow. The gas must be previously heated in the *stagnation* chamber in front of the nozzle using a suitable method. While its translational temperature significantly drops, it remains the vibrational temperature at a sufficiently high level to reach population inversion and to lase. The gas-dynamic flow of the escaping gas can be controlled by the combustion parameters and slit dimensions.

Although the first GDL laser was built more than thirty years ago [1] it still retain significant interest between researchers and especially in practice. These are typical high power lasers operating in either cw or (long) pulse regime. In the case of the CO₂ laser, as here, they do not need electricity for operation because they are *fuel powered*, thus very convenient for mobile units. Beside military interest great practical importance can be found in the material processing [2].

The main purpose of this work is to present the design and testing of an apparatus, built for the gas-dynamic CO₂ laser, based on the acetylene combustion in oxygen. Thus, carbon dioxide and water are formed in that reaction. A certain fraction of nitrogen is added to the mixture to control the explosion and improve the laser emission. We want to use this apparatus rather to investigate physico-chemical processes and mechanisms in the gas than only to measure pure laser effects, since a variety of non-solved physico-chemical problems still remain in this area [3].

Setup Design

The experimental setup consists of two main parts:

a) The *process volume* with attached gas mixture supply, vacuum equipments and gas exhausts, to make a unique system, all shown in Figure 1. This system was assembled from many segments for several reasons: (i) The modular unit offers flexibility in op-

eration; (ii) It is easier for manufacturing and more convenient when making inspection, repairing or cleaning the apparatus. Disadvantages are vacuum problems due to many points to seal.

Central part of the apparatus is the supersonic two-dimensional slit nozzle separating *high pressure/high temperature* combustion (stagnation) chamber from the expansion volume, in which the gas-dynamic flow is established due to the transfer of thermal energy of molecules into the energy of the directional beam. The nozzle slit height was typically 0.35 mm and the *cavity-to-slit* ratio above 50. The expansion to the combustion volume ratio was about 187. First part of that volume consists of four two-centimeter thick segments with side holes to attach laser mirrors, in order to investigate the distance dependence of the laser action. The role of the diffuser is to shock down the supersonic flow to subsonic speeds before exhausting gaseous products to the atmosphere. All heated parts of the system are water cooled.

b) Driving electronics: (i) The stagnation chamber shutter. It controls the moment and duration of opening the door to the nozzle. It consists of an electromagnet pushing the rods carrying the shutter plate. This unit can be programmed to trigger a defined period before or after the spark firing. (ii) Spark firing takes place at a programmable moment in regards to the shutter opening. It starts ignition of the fuel (acetylene) by the same type of plug as those used in automobiles. (iii) A pyroelectric detector (Gen-tech, ED200) along with a digital oscilloscope (Gould 4050) are used to monitor the optical signal from the laser cavity. Copper made mirrors, the output one having a hole covered with the NaCl window, were used to form the laser resonator.

Test Measurements

Firstly, the vacuum pumps and accompanied units were adjusted to work properly and reach pressure below 1 mbar at the low-pressure side.

Typical gas mixture contained acetylene, oxygen and nitrogen. The mole ratio was varied around the stoichiometric one, $C_2H_2/O_2/N_2 = 2/5/5$, to get as stronger explosion as possible for the given amount of nitrogen. The apparatus behaved as a good and safe machine under all experimental conditions. The supply system, opening mechanisms, pumps etc. responded in a proper way. After about one thousand or more pulses the apparatus had to be opened for cleaning.

We looked at the optical signal through the output mirror and saw some good indications of the lasing.

References

- [1] E.T. Gerry, IEEE Spectrum, 1970, 7, 51.
- [2] V.T. Karpukhin et al., 100-kW Power Range Mobile Railway CO₂ GDL Facility for Civil Engineering, Int. Forum on Advanced High-Power Lasers and Applications AH-PLA 99, 1-5 November, 1999, Osaka (Japan). p. 110.
- [3] A.M. Ghorbanzadeh et al., Atmos. Oceanic Opt., 2001, 14, 926.

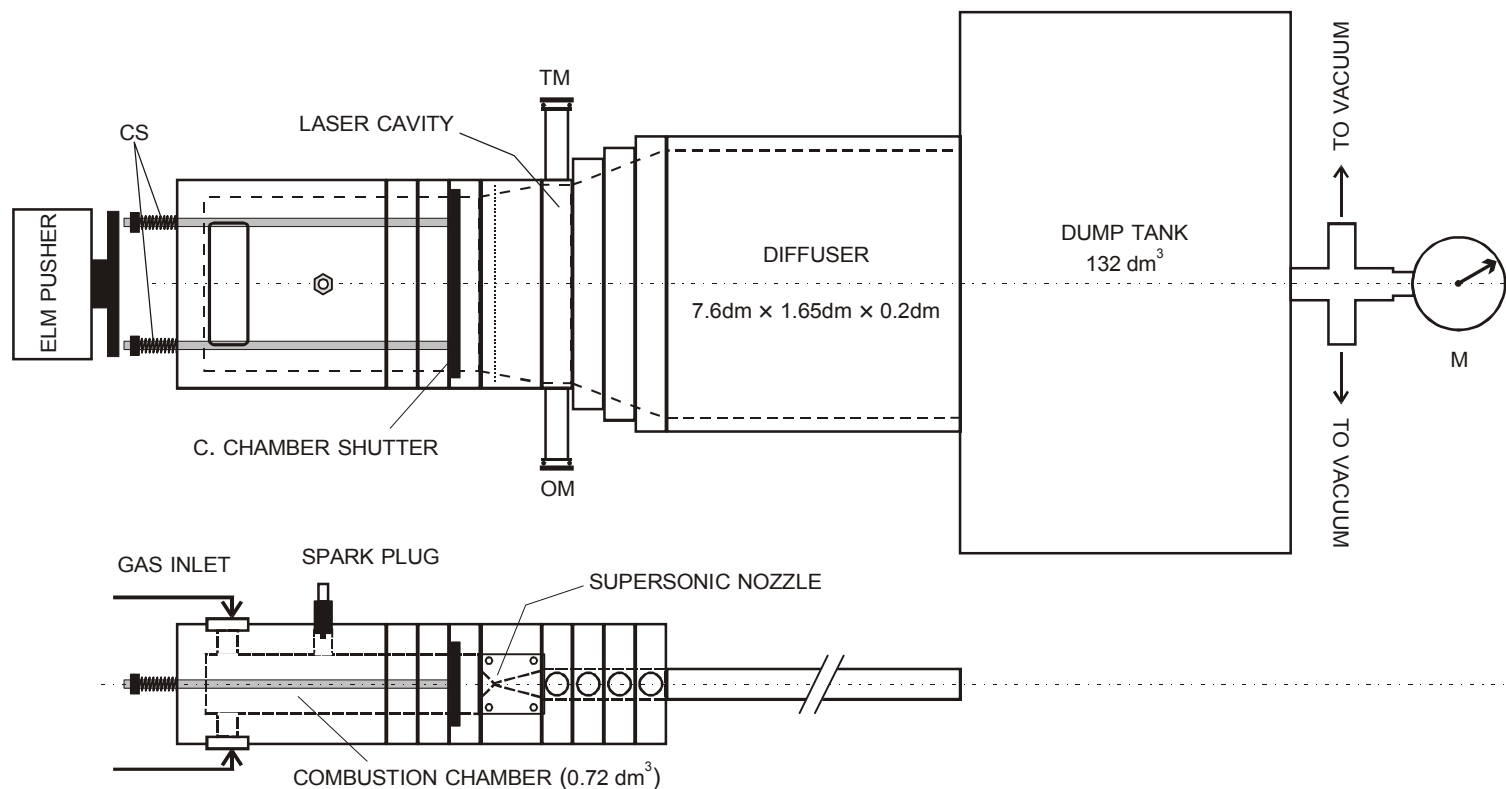


Figure 1. Schematic diagram of the experimental setup for the gas-dynamic laser, top view (upper) and side view (lower): CS – Counter-recoil springs, ELM PUSHER – Electromagnet for the combustion chamber shutter, TM – Total reflector (back laser mirror), OM – Output mirror, M – Vacuum meter. Electrics and electronics not included.

Kinetics
Catalysis
Nonlinear Dynamics

(C)

SIMULATION OF CATALYTIC PROCESSES OVER SUPPORTED NANOPARTICLES

V.I. Elokhin

Boriskov Institute of Catalysis SB RAS

Prosp. Akad. Lavrentieva, 5, 630090, Novosibirsk, Russia

Introduction

In heterogeneous catalysis, adsorption and reaction processes usually occur on supported metal nanoparticles. To study such processes experimentally, a vast variety of surface-science techniques came into the use in the last decades of the 20th century [1,2]. Along with the appearance of high-precision techniques for surface characterisation, considerable progress in manufacturing of model catalysts with well-defined properties like particle size, shape and separation has been achieved. Despite this progress, the cognitive potential of the experimental studies in this field is still limited because the measurements are usually indirect and the information derived demands quantitative processing and interpretation. This can be done only with the use of mathematical models. Successful interpretation of the results requires constructing mathematical models providing accurate description of systems under consideration. Application of the conventional mean-field models is often limited here due to the peculiarities of the reaction performance on the nanometer scale, including the inherent heterogeneity of metal crystallites as well as spontaneous and adsorbate-induced changes of the shape and degree of dispersion of supported catalysts. Under such circumstances, the use of stochastic simulations based, e.g., on the Monte Carlo technique, is almost inevitable.

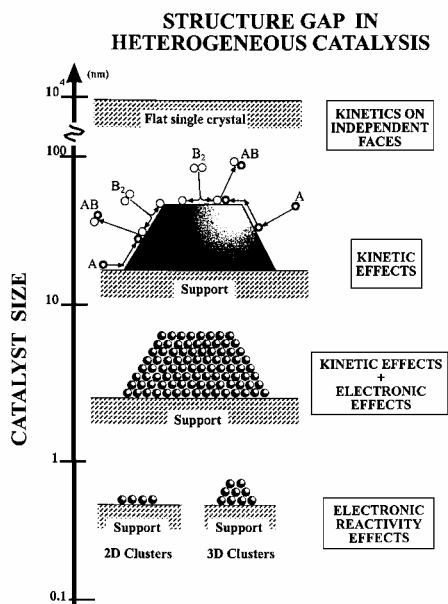
Specifics of Catalytic Reactions on nm Particles

It is well known that the overwhelming majority of the real commercial catalysts consist of the particles of nanometer size deposited on the porous support with a high surface area. These objects attract attention both from applied and theoretical points of view because their properties differ significantly from those of similar systems with large dimensions. Particularly the surface morphology of supported nanoparticles is not fixed and can appreciably change in the course of reaction. At the same time the specific catalytic activity (the rate per surface metal atom or per adsorption site) can substantially depend upon the size of the active particle [3].

The fact that the turnover rate of catalytic reactions often depends on the diameter of the particle, d , indicates that the relationship between the reaction kinetics on nanoparticles and those measured on single crystal surfaces is not straightforward. This structure gap between the kinetics may have different origins as indicated schematically in Fig. 1. The geometric shapes, exposed crystal planes, of nm crystallites depend in general on their size, properties of the support (including the metal-support interaction), temperature, and the method of fabrication. For clusters or very small metal particles with $d < 4$ nm the electron structure is significantly different from that of bulk metals and their catalytic activities are also different. This factor may be crucial for understanding catalytic activity of such small particles. The metal-support interaction may

modify the catalytic properties and this effect may be important for particles up to $d \sim 4$ nm. For crystallites with $4 < d < 10$ nm, the role of edges is usually believed to be

appreciable. For $d > 10$ nm, the particles are electronically identical to bulk metal but may still exhibit remarkably different kinetics compared to single crystals. In this case, reactions may occur primarily on facets although the edges may of course be important as well. From the theoretical point of view, the latter size range is especially interesting because on this scale there is hope to understand the special features of the size-dependent reaction kinetics on the basis of kinetic data obtained for single-crystal surfaces.



The possible difference between single crystals and supported catalysts could result

from the following [4,5]: (i) the different catalytic activities on different facets of a small supported crystalline particle become coupled in a strongly non-linear (synergistic) fashion due to diffusion occurring over facet boundaries, (ii) equilibrium-shape changes of small particles and their surface morphology, caused by adsorbates, induce changes in catalytic behaviour, (iii) the chemical modification of dispersed particles due to metal-support interaction, especially important in the case of the small (< 3 nm) particles, (iv) different kinetic rate constants at the facet boundaries of a supported particle compared to those for the perfect facets give rise to new kinetics, and (v) spillover by diffusion of reactants between the particle and its support, also create new kinetics. These peculiarities of the supported nanosystems dictate the special requirements to the theoretical models aimed at the simulating of catalytic properties of nanoparticles.

Possible Approaches to Simulations

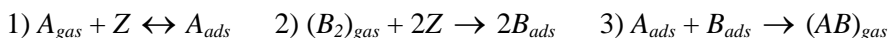
The theoretical study of supported catalysts is a rather complicated problem and an analysis of reaction performance on the small particles almost inevitably requires use of atomic-scale computer simulations taking into account the intrinsic heterogeneity of nanoparticles.

There are three main classes of atomic-scale computer techniques: molecular dynamics, Monte-Carlo algorithms based on Metropolis-like procedures, and so-called kinetic (or dynamic) Monte-Carlo. Despite the potential power of molecular dynamics, the use of this technique for the analysis of the physicochemical processes over supported particles is rather limited due to the short length and time scales typical for this

approach. The most effective tool for the simulation of the spatiotemporal dynamics of adsorbed species on the real catalytic surfaces which structure and properties can change under the influence of the reaction are now the stochastic methods based on the Monte-Carlo technique permitting one to obtain qualitatively new results. The Monte-Carlo method [6] considers the dynamics of the processes occurring on the catalytic surface as a random Markovian chain of elementary events (adsorption, desorption reaction, diffusion, local surface reconstruction, etc.) on the active sites of the catalysts, represented as the cells of a lattice with the preliminary determined rigid or dynamically changed structure. An obvious disadvantage of stochastic methods is the large body of calculations, whereas their main advantage is the possibility of precise control over the local environment and state of each active site on the surface of the catalyst. The other attractive advantage of the Monte-Carlo technique is the possibility of including in the simulation all relevant physical and chemical processes (specifically those which can hardly be described analytically) with the rate constants obtained from experimental data or from molecular dynamics simulations. Active use of the Monte-Carlo technique for the simulation of the heterogeneous catalytic reaction kinetics (see, e.g., [7-8]) started after the pioneering paper [9].

At present, the theoretical study of the adsorption and reaction processes over supported catalysts is at the very beginning. A comprehensive and careful review of simulations of the reaction kinetics on the supported nanoparticles has been published recently by Zhdanov and Kasemo [5]. The details of simulations of reaction kinetics on supported nm catalyst particles depend on the particle structure, reaction mechanism, and ratio between the rates of elementary reaction steps (like adsorption, desorption, reaction steps, and surface diffusion). Thereupon one more shortcoming of the kinetic Monte Carlo algorithms should be mentioned – it is difficult to take into account real ratios between the rates of elementary steps.

In most publications the $2A + B_2 = 2AB$ reaction is used to compare the reaction performance on the flat homogeneous surfaces of single crystals and small supported particles. It occurs via the standard Langmuir-Hinshelwood (LH) mechanism:



As stated in [5,10], the following relationships should be fulfilled between the rate constants for diffusion jumps of A and B particles to nearest-neighbour vacant sites and for the reaction between two nearest-neighbour reactants: the rate of A diffusion is usually rapid compared to the LH step, while the rate constant for the LH step might be higher than that for B diffusion. This practically important limit, ($k_{dif}^B \ll k_r \ll k_{dif}^A$) is far from the mean-field (MF) approximation and also far from the case when the LH step is considered to be instantaneous [9] (the latter assumption is widely used in MC simulations of reaction kinetics on single-crystal surfaces, but often does not correspond to reality).

Often as a model of the supported particle a top projection of the truncated pyramid has been considered, i.e., the pyramid is represented by a $N \times N$ square lattice, where

the central MxM array of sites mimics the top facet (active surface of the particle) and the periphery corresponds to the support (or to the side facets with different catalytic properties, depending on the aim of the study). Despite of the simplicity of such models, both predictable and unexpected result has been obtained by modelling of different peculiarities of the reaction performance over the supported particles. Such factors as reactant supply due to the diffusion over the support (spillover) [10-12], interplay of the reaction kinetics on the different facets of the supported particle due to the adsorbed species diffusion between the facets [13], the jump-wise reshaping of the active particle under the influence of the adlayer composition [14-16], oscillations and chaos in the catalytic reactions proceeding on the supported catalysts [15, 17-20], the influence of geometric parameters of the supported particles on the reactivity and selectivity of the multi-route catalytic reactions [21], reciprocal effect of the surface morphology and adsorption-reaction processes over the catalytic particle [24-25] were examined in various studies.

Brief Review of some Results

Reactant Supply via the Support (Spillover)

A factor of both fundamental and practical importance in catalysis, which might change the reaction kinetics on supported systems [5], is the possibility of adsorption of reactants on the support followed by diffusion to the catalyst and vice versa. In [10] this effect was analysed on the example of CO oxidation reaction occurring via LH mechanism by solving the MF equations for the reaction kinetics on the catalyst particle self-consistently with the diffusion equation describing the net flux of *A* particles from the support to the catalysts. The model used includes circularly shaped catalyst particles regularly distributed on the support. Typical results obtained in the limit when the *A* diffusion zones around different catalytic particles are not overlapping (i.e. the particles are sufficiently far apart) are shown in Fig. 2 together with the results corresponding to the case when there is no *A* supply via the support. Due to the *A* supply from the support, the position of the maximum reaction rate shifted to a lower value of the $P_A/(P_A + P_{B_2})$ ratio. This intuitively expected result could be expressed in terms of an increased "effective pressure" the reactant(s) supplied to the

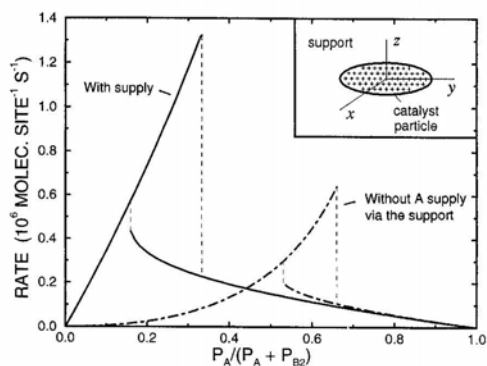


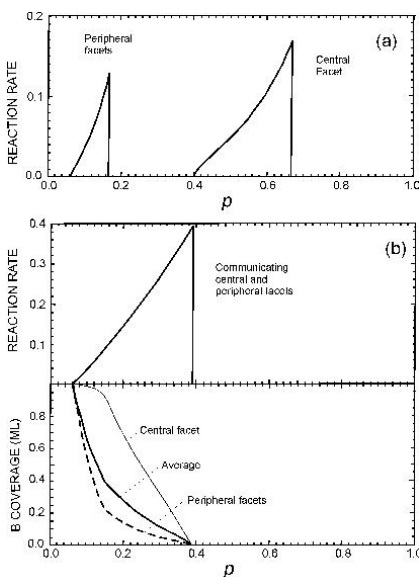
Fig. 2. Reaction rate for the $2A + B_2 \rightarrow 2AB$ reaction under steady-state conditions. The solid and dashed lines show the kinetics with and without *A* supply via the support. The insert exhibits the model used in calculations (Reprinted from [10], with permission from Elsevier).

catalyst via adsorption on the support and diffusion to the catalyst. Note also

that with the action of the support to trap reactant particles, a much higher (by a factor of two) maximum rate becomes possible, compared with an inert support. Similar effects were revealed by means of MC simulation [11] considering the same LH reaction mechanism, but with irreversible A adsorption. Another aspect of the spillover phenomena has been studied by means of scanning tunnelling microscopy (STM) [12]. It has been shown that Pd nanoparticles enhance the rate of re-oxidation of a substoichiometric $TiO_2(110)$ surface. Employed Monte-Carlo model, in which mobile oxygen, dissociatively adsorbed on Pd, spillover from the metal particle and performs a random walk until it reached a step edge where it may react to form TiO_2 , has been found to be in good agreement with STM images.

Interplay of Kinetics on Different Adjacent Facets

During catalytic reactions on nm crystallites, adjacent crystal facets can communicate with each other by reactant diffusion. The effect of this factor on the reaction kinetics has been simulated [5,13] by using the same $2A + B_2 \rightarrow 2AB$ catalytic reaction (with irreversible A adsorption) on the catalyst particle shaped into a truncated pyramid with top and bottom (100) faces and (111) side faces, with the largest (100) facet attached to the substrate. In kinetic simulations [13] the pyramidal particle was represented by a 100×100 square lattice, where the central 50×50 array of sites mimics the top (100)-(1x1) facet, and the periphery corresponds to the side (111) facets. In the framework of this model, one can use different values of the B_2 (and/or A) sticking coefficient for adsorption on the top (central) facet and side (peripheral) facets. The A and/or B binding energies and the LH-reaction rate constants for the different facets may be different as well. Many other effects can also be easily incorporated into the model, but *even the simplest case*, when the central part and the periphery of the lattice differ only in the sticking coefficients for B_2 adsorption (differing by a factor 10), can provide the unexpected results. Usually, it is assumed that the geometry of the nanoparticles surface area introduces no additional complications. Small particles exposing different



crystal faces are then simply regarded as presenting a superposition of the contributions from different structural elements. This statement is illustrated in Fig. 3a where the total reaction rate for a finite catalyst particle is given simply by

Fig. 3. Modelling the influence of adsorbate diffusion on the overall kinetics of reaction on a nanoparticle exposing two different kinds of planes: (a) without diffusion; (b) with diffusion across the facet boundaries (Reprinted from [13], with permission from Elsevier).

a superposition of the rates corresponding to two infinite faces (without communication be-

tween the facets). However, if there is diffusion-mediated coupling of the reaction on the different crystal planes, the distinctly new kinetics appear (Fig. 3b), compared to those for the infinite surfaces, and completely different compared to that predicted by employing the conventional superposition prescription. Specifically, a single new reaction window appears, very different from those on either facet. Compared to the isolated facets, the communicating facets provide new channels for A particles. The central facet, which in isolation can resist the self-poisoning by A particles up to high values of p (here p is $P_A/(P_A + P_{B_2})$), will in communicating system receive an additional supply of A particles from the adjacent peripheral area, which is less resistant to A poisoning since the B_2 sticking coefficient is ten times smaller there. This latter net flow of A particles from the peripheral to the central area facilitates A poisoning of the central facet at high values of p and prevents A poisoning from occurring on the peripheral area at low values of p . The most important result of these studies is that it has been explicitly shown that the kinetics on nm-sized particles, exposing different facets, can be dramatically different from the mere superposition of the kinetics on the individual facets due to the combined effect of the difference in the sticking coefficients and the diffusion transport of reactants over the facet boundaries.

Adsorbate-induced reshaping of crystallites.

Crystallite shape transformations, due to adsorbed reactants, may affect the steady-state kinetics of catalytic reactions. In particular, adsorbates can change the surface energy situation of a crystallite, so that it transforms into a new shape with new kinetic conditions. To study such transformations, MC simulations of the $A + B_2 = 2AB$ reaction kinetics combined with the use of the Wulff rule has been employed [14, 15]. It has been shown that adsorbate-induced reshaping of nm-sized catalyst particles may result in dramatic changes in the steady-state reaction kinetics.

In [14], in the absence of adsorbates, the equilibrium shape was assumed to be a truncated pyramid with the (111) and (100) faces. During the reaction the particle shape and reaction kinetics were calculated self-consistently by assuming a linear dependence of the surface tension of the (100) facet on B coverage. If this dependence is sufficiently strong, the pyramid-shaped catalyst particles become unstable with respect to reconfiguration to the parallelepiped shape with (100) facets. Such reconfiguration results in shifting the reaction window to higher values of p . If the adsorbate-induced transition from one shape to another is energetically impossible, the adsorbate-induced changes in the relative areas of different facets may still take place and influence the reaction kinetics. An example illustrating this case has recently been given in [16]. The kinetics of methanol synthesis on nm Cu particles supported by ZnO has been analysed. The generalised surface tension for the substrate-particle interface was assumed to be dependent on the reduction potential of the gas-phase. The latter resulted in the dependence of the areas of the (111), (100) and (110) facets on the gas-phase concentrations (such changes were observed by using EXAFS). This dynamic model is able to describe the change in particle morphology with change in feed gas composition as well as the reaction rate over the three basal Cu surface planes. The total reaction rate was found to be strongly affected by the changes in particle morphology.

Oscillations and chaos.

In the models, constructed for CO oxidation reaction over Pt(100) [15, 17-19], adsorbate-induced surface restructuring, treated as a first-order phase transition, occurs only on the central (100) facet. That means that the active centres of the central facet could exist in two different states: active Z_{1x1} and inactive Z_{hex} . The reaction under consideration is run via the conventional LH mechanism ($CO = A$, $O_2 = B_2$). The peripheral (111) facets are considered to be stable. In this case the interplay of the reaction kinetics on different facets may weaken or even suppress oscillations on the central facet. The simulations show however that the amplitude of oscillations may still be large and in addition may exhibit qualitatively new features [5, 17]. These features taken as a whole result in chaotic oscillations. Such chaos seems to be inherent for reactions on nm particles and can hardly be observed in reactions on single-crystal surfaces.

The algorithm constructed on the prescriptions of statistical physics [15, 17-18] makes it possible to take into account substrate-substrate, substrate-adsorbate and adsorbate-adsorbate lateral interactions. The MC algorithm combine the kinetic Monte-Carlo procedures for the calculation of probabilities of elementary steps (1)-(3) of LH mechanism and Metropolis rules for attempts of surface restructuring and A_{ads} particles diffusion, i.e., the latter events, as well as A_{ads} desorption, depend on local environment of the lattice sites and their respective states. It has been shown [18], using the restricted set of lateral interactions, that the model predicts the formation of well-developed restructured islands with a size of 5-10 nm, in agreement with experimental data.

An alternative version for oscillatory behaviour of catalytic reaction, such as formation of subsurface oxygen, has been considered in [19]. The model includes the conventional LH-mechanism and the stages of subsurface oxygen formation and removal. It has been shown [19], that (i) CO supply via the support shifts the oscillatory windows, as was shown above [10], and may also result in non-uniform oxide distribution on the catalyst particle; (ii) with physically reasonable model parameters, synchronisation of oscillations on the adjacent catalyst particles due to the CO supply via the support seems to be unlikely; (iii) heterogeneous nucleation and cooperative effects in the subsurface oxygen formation may worsen oscillations. But in combination with CO adsorption via precursor states, oscillations may be well-developed [19].

The results presented illustrate that catalytic reactions occurring on a single nm particle may exhibit oscillatory regimes [5]. Oscillations may be more or less regular or chaotic. On the macroscopic scale, observation of such oscillations may be hampered if synchronisation of oscillations on different particles is not effective. Practically, synchronisation is expected to occur via the gas-phase or, in exothermic reactions, due to thermal conductivity via the support. Simulations describing the latter aspect of the reaction kinetics on nm particles are just beginning and not numerous. One of the first studies in this field [20] uses the Monte-Carlo method for simulation of CO oxidation over a non-isothermal supported catalysts. It has been shown that thermal communications among active particles affect the shape of global oscillations: regular, irregular and chaotic oscillations were observed depending on crystallite size, activity and dis-

tribution of the particles on the support.

Reaction selectivity and particles size

An increase of selectivity of catalytic reactions toward desirable products is often the main goal of applied catalytic chemistry. For this reason, the understanding of factors influencing selectivity of catalytic reactions is an important and challenging problem. The purpose of the simulations [21] was to determine the extent to which simple geometrical parameters, such as the average size of catalyst particles and the spatial distribution of active sites, determine the selectivity of complex catalytic reactions. The main qualitative conclusion in [21] that the influence of the catalyst particle size on the reaction activity and selectivity becomes significant below a particle size of ~10-20 nm is expected to be robust [5]. This conclusion is in agreement with experimental observations for a range of hydrocarbon reactions over supported catalysts [3].

Reaction kinetics and particles surface morphology.

As follows from the experimental data, the influence of the various surface defects appearing under the action of the reaction media, as well as the change of the shape and size of deposited particles, can significantly determine the catalyst performance. For example, it was shown recently that, in some cases, the nanoparticles undergo the reversible adsorbate-induced shape changes (H_2+H_2O and $CO+H_2$ over Cu/ZnO system studied by *in situ* transmission electron microscopy [22]) and even disintegrate into atoms (effects of CO and NO adsorption on the morphological changes of Rh/TiO₂ studied by scanning tunnelling microscopy [23]). For better understanding of the reaction kinetics one should take into account these processes and the inherent heterogeneity of supported particles.

The attempt to distinguish the active centres according their coordination on the surface was undertaken in [24] where the influence of crystallite size on the activity of a supported catalyst in the case of the LH reaction mechanism has been investigated. Catalytic centres with different configuration have the differing activity with respect to the elementary reaction steps. These activities were calculated as a product of specific process rates for adsorption, desorption and reaction and of some additional weight coefficients, that account for enhancement or reduction of these rates on each type of centres. The ratio between the number of different active centres depends, of course, on the size of the crystallites (the relative concentration of surface defects increase with decreasing particle size). The important result of simulations [24] is that the structural features affect the production rate in ways that depend on which of the elementary steps in the reaction mechanism is altered by the presence of different types of sites.

Recently [11,25] a statistical lattice model has been proposed which imitates the physicochemical processes that proceed on the supported particle. To simulate the active metal particle the finite Kossel crystal [26] located on the inert support has been chosen. The surface morphology of the particle is defined by distribution of heights of the metal atom columns. The metal atoms attract the nearest neighbours and the atoms of the support. The change of morphology is caused by the thermal diffusion of the surface atoms. To model diffusion of metal atoms on the metal and support surfaces the

Metropolis algorithm has been used (similar algorithm had been employed in [27] for the modelling of catalyst sintering behaviour). Although this model is two-dimensional, it permits to model adsorption, diffusion and reaction events on the dynamically changed surface of the particle taking into account various lateral metal-adsorbate and adsorbate-adsorbate interactions. It has been shown [11] that the reaction kinetics on such particles can be qualitatively and quantitatively different from those corresponding to the flat surface only due to the change of the shape and surface morphology of nanoparticles and spillover phenomena. The simulations show that the nanoparticles undergoes reversible adsorbate-induced reshaping [25], and that the particles size determines the degree of reshaping as in experiments [22]. The proposed approach offers the new routes to model the catalytic reactions closer to reality.

Conclusions

The results of the simulations reviewed have far-reaching consequences both for the interpretation of kinetics data and for the design of catalysts. In particular, one should in analysis of experimental data consider the special kinetics *inherently* associated with nanoparticles, before more complex explanations are tried, such as size-related electron-structure effects, support-related effects, special active sites, etc. With respect to catalyst design, it is evident that the kinetics on supported catalysts may be manipulated by influencing the relative amounts of different facets, the size of the nanoparticles, and the adsorption properties of the support. The mutual influence of the reaction media on the particle shape and surface morphology and, vice versa, of nanoparticles characteristics on the reaction kinetics is one of the fundamental problems in heterogeneous catalysis

References

- [1] Henry C.R. Surf. Sci. Rep., 1998, 31, 231.
- [2] Gunter P.L.J., Niemantsverdriet J.W., Ribeiro F.H., Somorjai G.A. Cat. Rev.-Sci. Eng., 1997, 39, 77.
- [3] Che M., Bennett C.O. Adv. Catal., 1989, 36, 55.
- [4] Zhdanov V.P. Surf. Sci., 2002, 500, 966.
- [5] Zhdanov V.P., Kasemo B.. Surf. Sci. Rep., 2000, 39, 25.
- [6] Landau D.P., Binder K. A Guide to Monte-Carlo Simulation in Statistical Physics. Cambridge University Press, Cambridge, 2000.
- [7] Zhdanov V.P., Kasemo B. Surf. Sci. Rep., 1994, 20, 111.
- [8] Albano E.V. Heter. Chem. Rev., 1996, 3, 389.
- [9] Ziff R.M., Gulari E., Barshad Y. Phys. Rev. Lett., 1986, 56, 2553.
- [10] Zhdanov V.P., Kasemo B. J. Catal., 1997, 170, 377.
- [11] Kovalyov E.V., Resnyanskii E.D., Elokhin V.I., Bal'zhinimaev B.S., Myshlyavtsev A.V. Phys. Chem. Chem. Phys., 2003, 5, 784.
- [12] Ramires-Cuesta A.J., Bennet R.A., Stone P., Mitchell P.C.H., Bowker M. J. Mol. Catal. A: Chem., 2001, 167, 171.
- [13] Zhdanov V.P., Kasemo B.. Surf. Sci., 1998, 405, 27.
- [14] Zhdanov V.P., Kasemo B. Phys. Rev. Lett., 1998, 81, 2482.
- [15] Persson H., Thormählen P., Zhdanov V.P., Kasemo B. Catal. Today, 1999, 53, 273.
- [16] Ovesen C.V., Clausen B.S., Schiøtz J., Stoltze P., Topsøe H., Nørskov J.K. J. Catal.,

- 1997, 168, 133.
- [17] Zhdanov V.P., Kasemo B. *Phys. Rev. E*, 2000, 61, R2184.
- [18] Zhdanov V.P. *Surf. Sci.*, 1999, 426, 345.
- [19] Zhdanov V.P., Kasemo B. *Surf. Sci.*, 2002, 511, 23.
- [20] Qin Feng, Tagliabue L., Piovesan L., Wolf E.E. *Chem. Eng. Sci.*, 1998, 53, 911.
- [21] McLeod A.S., Gladden L.F. *J. Catal.*, 1998, 173, 43.
- [22] Hansen P.L., Wagner J.B., Helveg S., Rostrup-Nielsen J.R., Clausen B.S., Topsøe H. *Science*, 2002, 295, 2053.
- [23] Berko A., Solymosi F. *J. Catal.*, 1999, 183, 91.
- [24] Gracia F., Wolf E.E. *Chem. Eng. Jour.*, 2001, 82, 291.
- [25] Kovalyov E.V., Elokhin V.I., Myshlyavtsev A.V., Bal'zhinimaev B.S. *Dokl. Phys. Chem.*, 2001, 381, 309.
- [26] Lapujoulade J. *Surf. Sci. Rep.*, 1994, 20, 191.
- [27] Sault A.G., Tikare V. *J. Catal.*, 2002, 211, 19.

FROM STRONG SOLID ACIDS TO STRONG SOLID BASES: CHARACTERIZATION OF ACID/BASE SITES OF CATALYST SURFACES BY ADSORPTION CALORIMETRY

A. Auroux

*Institut de Recherches sur la Catalyse, CNRS
2 avenue Einstein, 69626 Villeurbanne Cedex, France*

Abstract

Most of the applications of solids such as zeolites, mesoporous materials, bulk and supported oxides, heteropolyanions, hydrotalcites, ... in heterogeneous catalysis are based on their acid/base properties.

Though no single method provides complete information about the nature, number and strength of the active sites, adsorption microcalorimetry of acidic or basic probe molecules is one of the best methods available to determine the distribution and strength of acid/base sites. Ammonia and pyridine are commonly used as probe molecules in the study of acidic sites. Carbon dioxide and sulfur dioxide are less commonly used for the determination of basic sites.

The aim of the present work is to assign a scale of strength to different kinds of acid sites and to evaluate the energy distribution functions of the acid/base sites of a wide range of catalysts varying from superbases to superacids.

Introduction

The importance of reactions initiated by solid acid catalysts (dehydration, alkylation, isomerization, cracking) or solid base catalysts (aldolisation, transesterification, Michael and Knoevenagel reactions) provides motivation for the development of theories and techniques that can be used to characterize the acidity or basicity of solids.

Acidity and basicity are general terms referring to the properties that determine the effectiveness of an acid or a base for reaction with a base or an acid respectively [1]. However, there is a lack of a precise scale of strength for the acidity/basicity of solids analogous to the pK_a and pH values available for aqueous solutions. An attempt was made with the Hammett acidity function (H₀) based on amine titration in the presence of organic indicators [2,3], but the equilibrium is not easily determined and this method is limited to protonic acids.

The techniques involving the adsorption of probe molecules are the most commonly used for the investigation of acid-base interactions. Ammonia and pyridine are routinely used as probe molecules in order to study surface acidic sites. Carbon dioxide and sulfur dioxide are less commonly used for the determination of surface basic sites. From the analysis of NMR and IR spectroscopic data, conclusions can be drawn about the nature of the acidity (Brønsted or Lewis) and the concentrations of the different sites. But only adsorption microcalorimetry and to a lesser extent temperature-programmed desorption (TPD) can be employed to determine simultaneously the number, strength and strength distribution of the various acid/base sites [4-8].

In this study, adsorption microcalorimetry of acidic or basic probe molecules has been used to determine the number, strength and strength distribution of basic or acidic sites of a wide range of catalysts varying from superbases to superacids. Using these data, we attempt to assign a scale of strength to different kinds of acid/base sites and to evaluate the energy distribution functions of the acid/base sites.

Experimental

The various catalysts were investigated by means of adsorption microcalorimetry linked to volumetry. Prior to adsorption, the catalysts were outgassed at the desired temperature (400°C in most cases) and under high vacuum (~ 0.1 mPa) in the calorimetric cell. After cooling to the adsorption temperature (150°C or 80°C for ammonia adsorption on zeolites or oxides respectively, 30°C for CO₂ adsorption, and 80°C for SO₂ adsorption) and establishing the thermal equilibrium of the calorimeter (C80 from Setaram), a dose of gaseous probe molecules was brought into contact with the catalyst sample, and both the pressure and heat signal were monitored until equilibrium was reached. Then successive new doses were added and the new equilibrium pressures were recorded together with the corresponding evolved heats. The collected data made it possible to plot the adsorption isotherm and the curve of the differential heat of adsorption as a function of the coverage.

After an equilibrium pressure of about 66 Pa was reached, the sample was evacuated for 1 h at the same temperature and a second adsorption was performed in order to allow the determination of chemisorption uptakes.

Results and Discussion

In order to provide a thermodynamic scale of surface acidity and basicity, we explored the acid-base properties of numerous solids by measuring the heats of adsorption and the adsorption uptakes of gas-phase probe molecules (NH₃, CO₂, SO₂). The investigated solids, varying in their physical and chemical properties, have been selected in order to cover a wide range of acid-base behaviors representative of acidic, amphoteric and basic solids. The samples have been divided into three main groups according to their adsorption capacities towards acidic probes (basic solids) or basic probe molecules (acidic solids). The amphoteric solids display an adsorption capacity towards both the acidic and basic probe molecules.

The investigated materials include supported catalysts, in which the role of the support is to disperse the active phase and to create new active surface species by host (active phase) – guest (support) interaction. The dispersion of the active phase plays a fundamental role, and very often a maximum of strength of the active sites is observed when the monolayer coverage is reached.

The most frequently used catalyst supports (Al₂O₃, ZrO₂, TiO₂) carry both basic and acidic Lewis sites on their surface; depending on the reactant (CO₂ or NH₃) these pure oxides can exhibit either acidic or basic character. Excess negative or positive charges can be induced and subsequently acidity (Brönsted or Lewis) can be generated by mixing oxides. Modifying the surface with a minor anionic, cationic or metallic component enhances or decreases the acidic strength of the sites. For example,

the incorporation of chloride, fluoride or sulfate ions increases the acidity of carrier oxides (Al_2O_3 , ZrO_2 , TiO_2), while alkali cations enhance the basic strength of alumina, silica or zeolites.

The curves showing the differential heat variations in relation to the adsorbed amounts generally present the following features : 1) an initial region of high heats of adsorption, representing adsorption on the strongest sites, which are usually thought to be of Lewis type. The initial drop in the curve of Q_{diff} vs coverage can be observed even in the case of adsorption on apparently homogeneous surfaces, where it could be ascribed to residual surface heterogeneities. 2) one or more regions of intermediate strength. A region of constant heat in this domain is characteristic of a set of acid sites of homogeneous strength, such as e.g. Brönsted acid sites in the case of zeolites. 3) a region where heats decrease more or less steeply depending on the heterogeneity of the sites. 4) a region at high coverage where the heat of adsorption approaches a nearly constant value characteristic of hydrogen bonding between the probe and the sample or physisorption of the probe. This constant value depends on the nature of the probe.

Acidic solids can be divided into the following main families: 1) bulk oxides [9], 2) doped oxides (chlorinated alumina, doped silica, ...) [10], 3) supported oxides [11], 4) mixed oxides such as silica-alumina, silica-titania or silica-zirconia, zeolites and clays [4], 5) heteropolyanions such as $\text{H}_3\text{PW}_{12}\text{O}_{40}$, $\text{H}_4\text{SiW}_{12}\text{O}_{40}$ and $\text{H}_5\text{BW}_{12}\text{O}_{40}$, 6) phosphates (Zr, Al, V, Ti, B, Sn), 7) superacids such as sulfated oxides or Nafion H (perfluororesin sulfonic polymeric acid).

Amphoteric solids can be divided into the following main families: 1) bulk oxides (such as $\gamma\text{-Al}_2\text{O}_3$, ZrO_2 , TiO_2 , Ga_2O_3 , ...), 2) alkali-exchanged zeolites (Li, Na, K, Rb, Cs-X or Y zeolites, ...), 3) doped and supported oxides (V-MgO), 4) oxynitrides (ZrPON, AlPON, AlVON).

Basic solids can be classified into: 1) bulk oxides (CaO , La_2O_3 , ZnO , MgO , ThO_2), 2) doped oxides (Ca^{2+} -doped MgO), 3) hydrotalcites ($\text{MgO-Al}_2\text{O}_3$).

For each of the listed solids, the differential heat of adsorption of the probe molecule was plotted as a function of the coverage. This has allowed us to obtain scales of acidic and basic strength for the studied solids, based on the average heat at the plateau of the differential heat curve or at half coverage (Figures 1 and 2). This scale for acid-base strength of solid surfaces can be compared with the " $\text{H}_{0,\text{max}}$ " scale proposed by Yamanaka and Tanabe [2,3], relying on titration using colorimetric indicators.

Finally, we can also compare our scale of gas-phase acidity/basicity to a similar scale developed in liquid phase (for a limited number of samples). A large variety of solvents (n-decane, isopropanol, cyclohexane, toluene, 1,4-dioxane, ...), presenting different polarities, were tested in order to study the specific donor-acceptor interactions. Moreover the influence of the acid/base strength of the probe molecule was also studied by using probes presenting various pK_a such as aniline, 2-phenylethylamine, phenol, ...

For a given probe molecule, the influence of the solvent on the surface reactivity of the solid, was found to be primordial. The solvent polarity plays a fundamental role in discriminating selectively the acid site strength. A very polar solvent (isopropanol)

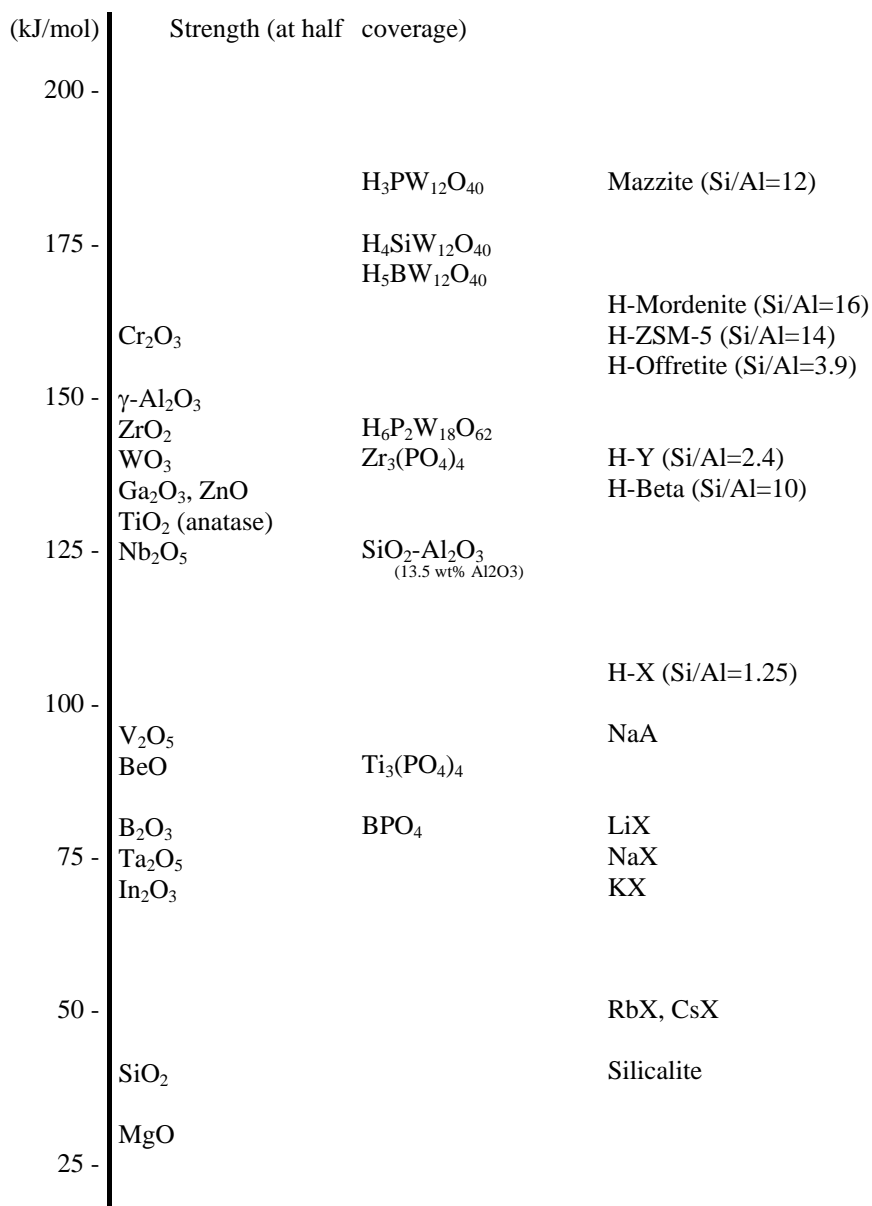
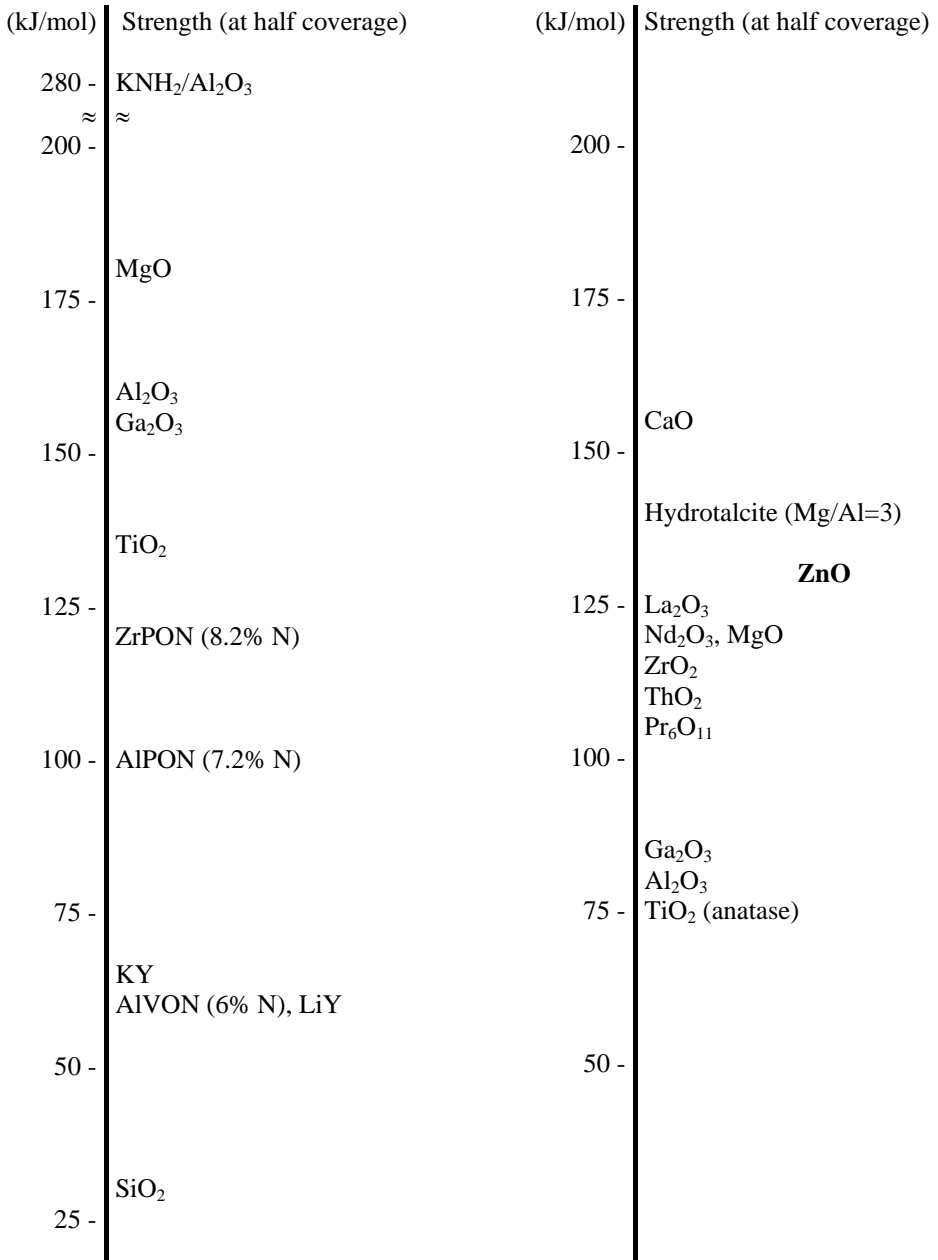
Figure 1 Acidity (NH_3) at 80°C or 150°C

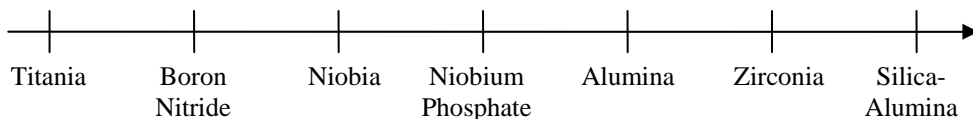
Figure 2 Basicity (SO₂, at 80°C)

Basicity (CO₂, at 30°C)



cannot be displaced by the probe while a weakly polar solvent (cyclohexane) helps for the selective titration of very strong acid/base sites. In an apolar solvent (n-decane), all sites are titrated but the measured heats are averaged [12].

These results have allowed us to compare the acidities of various catalytic solids in liquid phase, based on aniline adsorption experiments carried out in cyclohexane solution (which seemed to be the best solvent to discriminate the strength of the sites), giving rise to the following scale of acidity:



Acknowledgements

The author thanks Dr. Antonella Gervasini (Universita di Milano) and all the coworkers and students who participated in the experimental studies reported here.

Conclusion

Adsorption calorimetry is ideally suited to determine the number, strength and strength distribution of the active sites of catalysts.

The average differential heat of adsorption determined by this method can be regarded as a practical parameter to describe the acid-base properties of solids in a manner sensitive to the surface structure. For example, solids presenting high heats of NH_3 adsorption have strong acidic sites and weak basic sites, and thus are able to play an important role in reactions requiring strong acidity, such as e.g. cracking of paraffins. On the other hand, solids with high heats of CO_2 or SO_2 adsorption have strong basic sites and can be active in reactions such as aldolisation or Knoevenagel reactions.

References

- [1] J. Valyon, Gy. Onyestyak, L.V.C. Rees, *Langmuir*, 2000, 16, 1331.
- [2] T. Yamanaka, K. Tanabe, *J. Phys. Chem.*, 1975, 79, 2409.
- [3] T. Yamanaka, K. Tanabe, *J. Phys. Chem.*, 1976, 80, 1723.
- [4] A. Auroux, *Topics in Catalysis*, 1997, 4, 71 and 2002, 19, 205.
- [5] N. Cardona-Martinez, J.A Dumesic, *Adv. Catal.*, 1992, 38, 149.
- [6] W.E. Farneth, R.J. Gorte, *Chem. Rev.*, 1995, 95, 615.
- [7] P.J. Andersen, H.H. Kung, *Catalysis*, 1995, 11, 441.
- [8] V. Solinas, I. Ferino, *Catal. Today*, 1998, 41, 179.
- [9] A. Auroux, A. Gervasini, *J. Phys. Chem.*, 1990, 194, 6371.
- [10] A. Gervasini, G. Bellussi, J. Fenyvesi, A. Auroux, *J. Phys. Chem.*, 1995, 99, 5117.
- [11] A. Gervasini, J. Fenyvesi, A. Auroux, *Langmuir*, 1996, 12, 5356.
- [12] A. Auroux, A. Gervasini, in preparation.

NONLINEAR PHENOMENA AND MECHANISMS OF CATALYST DEACTIVATION

N. M. Ostrovskii

AD Chemical Industry HIPOL, Odžaci, Serbia & Montenegro

Some phenomena in catalyst deactivation are called nonlinear ones. Those are the volcano-shape of catalyst activity vs. time, the changing of selectivity during deactivation, the drastic drop of catalyst activity after long stable work, etc.

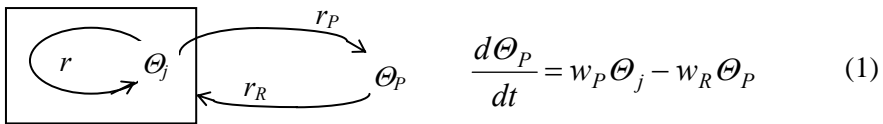
As a matter of fact, only some of them are caused by nonlinear kinetics of deactivation. The others are related to the simultaneous action of several linear processes, or to the influence of mass transfer in catalyst pores, or in solid bulk of the catalyst.

Three types of nonlinear deactivation kinetics will be analyzed in this report:

- 1 – caused by combined effect of deactivation and self-regeneration;
- 2 – caused by interactions in adsorbed layer;
- 3 – caused by ions diffusion in catalyst bulk.

Deactivation and Self-Regeneration

Let us consider some catalytic reaction proceeding in accordance with a linear mechanism: $\Theta_0 \leftrightarrow \Theta_1 \leftrightarrow \dots \leftrightarrow \Theta_j \leftrightarrow \Theta_{j+1} \leftrightarrow \dots \leftrightarrow \Theta_n \leftrightarrow \Theta_0$. It may be presented as a catalytic cycle with reaction rate r . Deactivation and self-regeneration are assumed to be slow steps external to catalytic cycle:



where r, r_P, r_R are the rates of reaction, deactivation and self-regeneration (for example by H_2 in naphtha reforming or by H_2O in CH_4 conversion); $w_j = r_j / \Theta_j$ are the weight of steps, which are the functions of concentration and temperature;

Θ_j are concentrations of intermediates (coverage), participating in the catalytic cycle; Θ_P refers to coverage excluded from the catalytic cycle due to deactivation.

According to [1,2] the general equation for such a reversible deactivation has a form in terms of relative activity $a = r / r^0 = 1 - \Theta_P$:

$$-\frac{da}{dt} = \frac{r^0}{w_j} w_P \frac{a - a_S}{1 - a_S} \quad (2)$$

where r^0 is the reaction rate on fresh catalyst ($t = 0$); a_S is the stationary level of activity, which is attained at $t > t_S$, when deactivation rate r_P becomes equal to the rate of self-regeneration r_R .

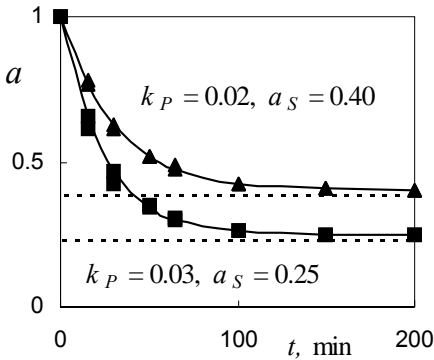


Figure 1. Deactivation of Pt/Al₂O₃ during dehydrogenation of cyclohexane .

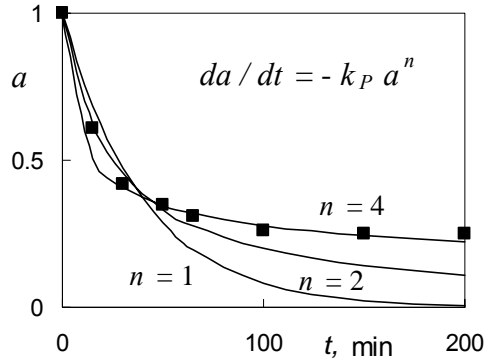


Figure 2. Formal description of data of Fig 1.

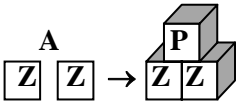
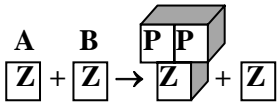
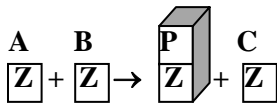
In the case of Pt/Al₂O₃ deactivation during cyclohexane dehydrogenation in presence of methylcyclopentane (MCP) (Fig. 1), the equation has a form:

$$\frac{da}{dt} = -k_P \frac{P_{MCP}}{P_{H_2}} \frac{a - a_S}{1 - a_S} \quad (3)$$

At a formal fitting of experimental data the nonlinear deactivation kinetics is required $da / dt = -k_P a^n$, at $n = 4$ (Fig. 2). Therefore, the apparent nonlinear kinetics of deactivation can be caused by self-regeneration phenomenon at linear intrinsic kinetics of reaction and deactivation.

Interactions in Adsorbed Layer

Because of a very low probability for more than two species to interact on the surface, most nonlinear mechanisms can be reduced to binary interactions in the adsorbed layer. In this case, only three types of nonlinear binary interactions can be formulated:

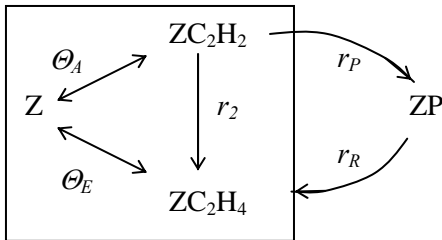
Double-center adsorption	Surface dimerization	Surface disproportionation
		
1 molecule of precursor poisons 2 active centers	2 molecules of precurs. poisons 1 active center	1 molecule of precursor poisons 1 active center
$2 Z \rightarrow 2 PZ$	$2 Z \rightarrow 1 PZ$	$2 Z \rightarrow 1 PZ$

Z – active center, AZ, BZ – precursors of poison or coke, PZ – blocked center.

It was shown in previous publications [2,3] that general equation of deactivation kinetics for these schemes depends on the mechanism of main reaction:

$$-\frac{da}{dt} = w_P (\Theta_i^o \Theta_j^o) a^2, \quad -\frac{da}{dt} = 2 w_P (\Theta_i^o \Theta_j^o) a \sqrt{a} \quad (4a,b)$$

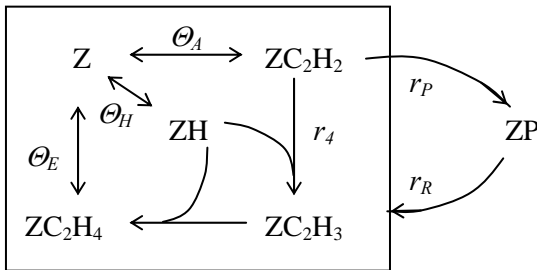
The first equation is valid for the linear mechanism of main reaction, where $a = 1 - \Theta_P$, and the second for nonlinear one, where $a = (1 - \Theta_P)^2$. For example, in the reaction of alkynes hydrogenation ($A + H_2 = E$), the mechanism changes together with temperature and catalyst modification [4,5]:



$$\Theta_A = b_A P_A \Theta_O \quad \Theta_E = b_E P_E \Theta_O$$

$$r = r_2 = k_2 P_{H_2} \Theta_A \quad (\text{linear})$$

$$r_P = k_P \Theta_A^2 \quad r_R = k_R P_{H_2} \Theta_P$$



$$\Theta_H = (b_H P_{H_2})^{0.5} \Theta_O$$

$$\Theta_A = b_A P_A \Theta_O \quad \Theta_E = b_E P_E \Theta_O$$

$$r = r_4 = k_4 \Theta_A \Theta_H \quad (\text{nonlinear})$$

$$r_P = k_P \Theta_A^2 \quad r_R = k_R P_{H_2} \Theta_P$$

The stage of deactivation is the same for both mechanisms and corresponds to surface dimerization ($2 ZA \rightarrow ZP$, i.e. $2 ZC_2H_2 \rightarrow ZC_4H_4$ [4]).

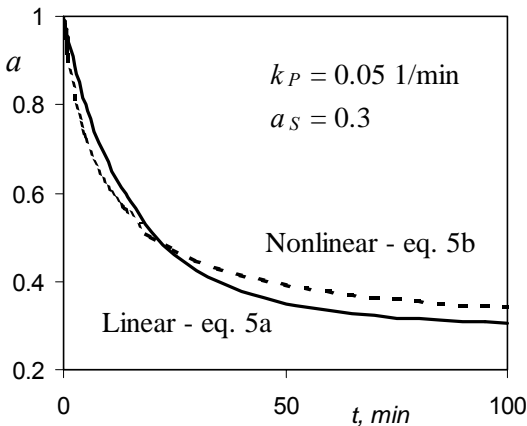


Figure 3. Nonlinear deactivation kinetics for linear and nonlinear mechanisms of main reaction.

Then corresponding equations (4a,b) become:

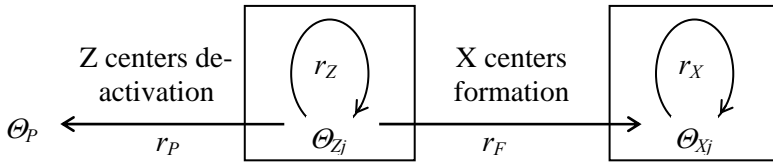
$$-\frac{da}{dt} = \frac{k_P}{1-a_S} (a^2(1-a_S) - a_S^2(1-a)), \quad -\frac{da}{dt} = \frac{2k_P}{1-a_S^2} (a^2 - a_S^2)a\sqrt{a} \quad (5a,b)$$

The graphics of these equations are presented in Fig. 3 and illustrate real nonlinear deactivation kinetics. They indicate that it is practically impossible to identify the actual mechanism using only deactivation kinetic curve.

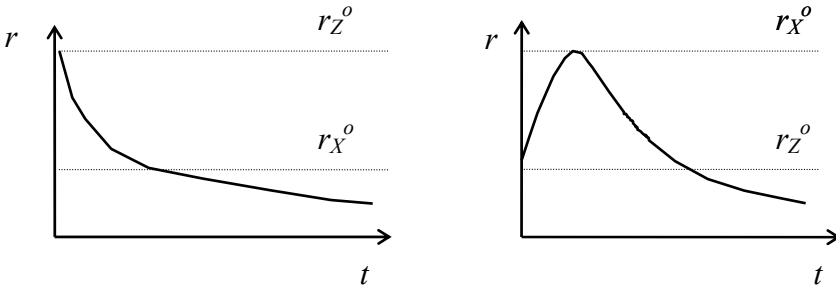
“Qualitative” Deactivation

In some catalytic processes, the active centers are forming during the reaction. Then active centers of deactivation and transformation into another type occur simultaneously. The reaction rates on “new” and “old” centers usually differ.

Schematically it can be presented as some catalytic cycle on Z - type centers (reaction rate r_Z) with slow deactivation (r_P) and slow transformation (r_F) of Z to X - type centers (reaction rate r_X):



If the reaction rate on Z centers is higher than on the new centers ($r_Z > r_X$), the activity declines gradually. In the opposite case ($r_Z < r_X$) the activity initially grows and then decreases due to deactivation:



Using the approach described above it is possible to derive a general equation for “qualitative deactivation” phenomena.

$$-\frac{da}{dt} = r_Z^o \left(\frac{w_P}{w_{ZP}} + \frac{w_F}{w_{ZF}} \right) \left(a - \frac{\gamma}{1+\gamma} a_m \right), \quad (6)$$

where $\gamma = w_F w_{ZP} / w_P w_{ZF}$; w_j are weights of corresponding steps; $a_m = r_X^o / r_Z^o$.

An example of such a nonlinear reaction dynamics is presented in Fig. 4 for alkyl-aromatics oxidation on oxide catalyst.

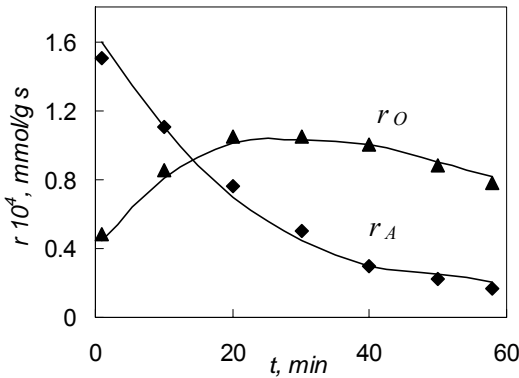
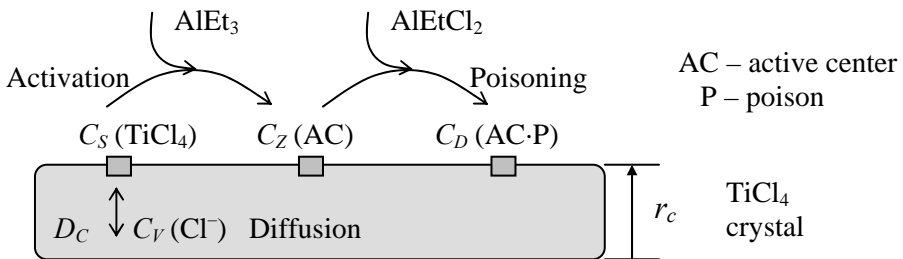


Figure 4. Alkyl-aromatics oxidation on oxide Cu-Cr-Al catalyst [6]. Rates of adsorption (r_A) and deep oxidation (r_O). Points – experiment, lines – calculation using model like (6).

Diffusion of Ions in Catalyst Bulk

The diffusion of ions and atoms in solid catalyst can affect significantly on a catalytic reaction dynamics [2]. First of all, it concerns with the diffusion of oxygen in metal oxides [7,8]. Similarly, the model based on Cl⁻ ions mobility in polymerization catalyst can explain the reaction dynamics in these processes [9].

The rate of polymerization is usually expressed as $R_p = k_p C_Z C_m$, where C_Z and C_m are concentrations of active centers and of monomer. The mechanism of active centers transformation can be presented by the following scheme:



Here C_S and C_V are concentrations of potential active centers on the surface and in catalyst bulk. The equation for chlorine mobility may have a diffusion form:

$$\frac{\partial C_V}{\partial t} = D_C \frac{\partial^2 C_V}{\partial r^2}, \quad (7)$$

with boundaries conditions:

$$r = 0: \frac{dC_V}{dr} = 0, \quad r = r_c: D_C S \frac{dC_V}{dr} = -k_A^1 C_S C_A. \quad (8)$$

The equation for active centers concentration includes its activation and deactivation stages. Their rates are proportional to activator concentration $AlEt_3$ (C_A), assuming that poison ($AlEtCl_2$) is in adsorption equilibrium with $AlEt_3$:

$$\frac{dC_Z}{dt} = k_A^1 C_S C_A - k_d^1 C_Z C_A, \quad C_S = C_V \Big|_{r=r_c} \quad (9)$$

The system (7-9), together with the reaction rate equation $R_p = k_p C_Z C_m$, provides the qualitative and quantitative simulation of typical dynamics of polymerization rate (Fig. 5). The chlorine diffusivity $D_c = 10^{-17} \div 10^{-15} \text{ cm}^2/\text{s}$, obtained from simulation, is typical for diffusion in solids.

If the transient regime of polymerization is controlled by such a diffusion, then corresponding characteristic time ($\tau_D = r_c^2 / D_c$) is about 1÷3 hours, that is comparable with the residence time in slurry reactor.

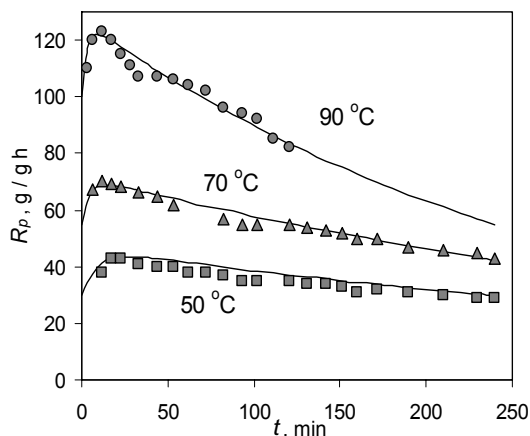


Fig. 5. Dynamics of propylene polymerization rate on catalyst $\text{TiCl}_3 + \text{AlEt}_2\text{Cl}$. Points – experiments of [10]; lines – model prediction.

References

- [1] N.M.Ostrovskii, G.S.Yablonskii, *React. Kinet. Catal. Lett.*, 1989, 39, 287.
- [2] N.M. Ostrovskii, *Catalyst deactivation kinetics*. Moskva: Nauka, 2001, 334 p.
- [3] N.M. Ostrovskii, *Proc. Int. Seminar "New Challenges in Catalysis II"*, Ed. by Paula Putanov. Novi Sad, 1999, p. 99.
- [4] C.J.Baddeley, R.M.Ormerod, R.M.Lambert, *Proc. 10-th Int. Congr. Catal.*, Budapest, 1992, p. 43.
- [5] Li Zon Gva, Kim En Ho, *Kinetika i Kataliz*, 1988, 29, 381.
- [6] N.M.Ostrovskii, Yu.A.Kachurovskii, O.A.Reutova, *Proc. Int. Conf. "Unsteady-State Processes in Catalysis"*, Novosibirsk, 1990, p. 63.
- [7] O.A.Makhotkin, N.M.Ostrovskii, Yu.I.Kuznetsov, M.G.Slin'ko, *Dokladi Akademii nauk SSSR*, 1979, 249, 403.
- [8] N.M.Ostrovskii, S.I.Reshetnikov, *Proc. Int. Conf. Chemreactor-16*, Berlin, 2003, p. 82.
- [9] N.M.Ostrovskii, F.Kenig, *Proc. Int. Conf. "Chemreactor-16"*, Berlin, 2003, p. 62.
- [10] K.Y.Choi, W.H.Ray, *J. Appl. Polymer Sci.*, 1985, 30, 1065.

ACTIVITY AND DEACTIVATION OF GOLD CATALYSTS SUPPORTED ON MESOPOROUS TITANIA FOR WATER-GAS SHIFT REACTION

V. Idakiev^a, T. Tabakova^a, P. Konova^b and A. Naydenov^b

^a *Institute of Catalysis, Bulgarian Academy of Sciences, 1113 Sofia, Bulgaria*

^b *Institute of General and Inorganic Chemistry, Bulgarian Academy of Sciences, 1113 Sofia, Bulgaria*

Abstract

Au/mesoporous titania catalysts were prepared and characterized by X-ray diffraction, TEM, N₂ adsorption analysis and TPD. The WGS activity was tested at a wide temperature range (140-300 °C). The slow deactivation of the catalysts was attributed to their ability to adsorb CO and accumulate it as carbonates. This deactivation is reversible and after heating in air the activity was restored.

Introduction

Gold has historically been considered to be ineffective for catalytic applications. However, the work by Haruta and co-workers [1] on supported nano-gold catalysts has changed the traditional view about gold. Their work showed an exceptionally high CO oxidation activity when gold is supported on different metal oxides. The mesoporous materials with different composition, new pore system and novel properties have attracted considerable attention because of their remarkably large surface area and narrow pore size distribution. The structure of mesoporous oxide supports facilitates the formation of well-dispersed and stable gold particles on the surface upon calcinations and reduction and thus strongly improves the catalytic performances.

Water-gas shift reaction (WGS) has recently been attracting rapidly growing interest due to development of fuel cell power systems and need of pure hydrogen production. The aim of this study was to investigate the catalytic behaviour and the reasons for deactivation of Au/mesoporous titania catalysts.

Experimental

Mesoporous titania with high surface area and uniform pore size distribution was synthesized using surfactant templating method through a neutral [C₁₃(EO)₆-Ti(OC₃H₇)₄] assembly pathway [2]. Different gold content was loaded on mesoporous titania by deposition-precipitation (DP) method. The XRD patterns were obtained with a Philips PW 170 diffractometer. The transmission electron micrographs were taken using a 100 kV Philips Tecnai microscope. The gold content in catalysts was analyzed by Atomic absorption method. Nitrogen adsorption-desorption isotherms and specific surface areas were measured at -196 °C on a Micromeritics TRISTAR 3000 volumetric adsorption analyzer. Temperature programmed desorption of the catalysts was performed in an argon (99.999%) flow with a gas flow rate of 4.4 l/h and a pressure of 0.101 MPa in temperature range from 20 to 300 °C with a heating rate of 4 °C/min. The mass of the catalysts was 0.2 g. Catalytic activity test was performed in a flow

reactor at atmospheric pressure and temperature range from 140 to 300 °C. The following conditions were applied: catalyst bed volume 0.5 cm³, space velocity 4000 h⁻¹, partial pressure of water vapor 31.1 kPa and the reactant gas mixture contained 4.494 vol.% CO, the rest being argon. The catalytic activity was expressed by degree of CO conversion.

Results and Discussion

The characteristics of the samples are listed in Table 1.

Table 1.

Sample	S _{BET} (m ² /g)	Pore diameter (nm)	Au content (wt. %)	Au particle size (nm)
T	125	11.0	-	-
2.5 AT	133	9.0	1.63	4.1
5 AT	134	8.0	4.73	6.2

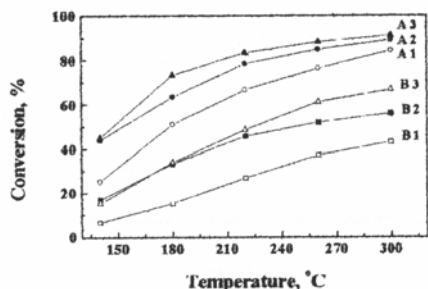


Fig. 1. Catalytic activity of the catalysts.

catalysts is their lack of stability. Generally, two reasons for deactivation are under discussion: i) the agglomeration of gold particles during catalytic test and ii) ability of the catalysts to form surface carbonate species. Schubert et al. registered the existence of a carbonate phase formed on the support as a thin surface layer [4]. This carbonate layer on the oxide surface leads to the blocking of the active sites.

WGS activity was measured at different temperatures in steady-state conditions Fig. 1 (curves A2 and B2). After the test the catalysts are kept at room temperature in reactant gas mixture for about 12 hours. The catalysts show activity change during a second catalytic test (curves A1 and B1). We propose that the deactivation of Au/mesoporous titania is caused by poisoning of the active sites by carbonates. TPD experiments were carried out in order to confirm this hypothesis. The results obtained are presented in Fig. 2. It was found that during desorption 5 AT evolved CO₂, producing two peaks: at 158 and 238 °C (Fig.2b). The total amount of CO₂ liberated during the TPD experiment was calculated to be 1.26 mg. Desorption of small amount CO (0.24 mg) was also registered. Higher amount of CO₂ (3.38 mg) was detected during TPD of 2.5 AT (Fig.2a). It is reasonable to suppose that there are more free support sites on the surface of 2.5 AT, able to adsorb carbonates, because of the lower gold content and smaller gold particle size.

The variation of catalytic activity of the catalysts with different content of gold as a function of reaction temperature is plotted in Fig.1 (curves A and B). The higher activity of the sample with lower gold loading (A1, A2 and A3) was related to the size of Au particles and the contact structure of Au nanoparticles with the support [3]. One of the most important problems with nano-gold

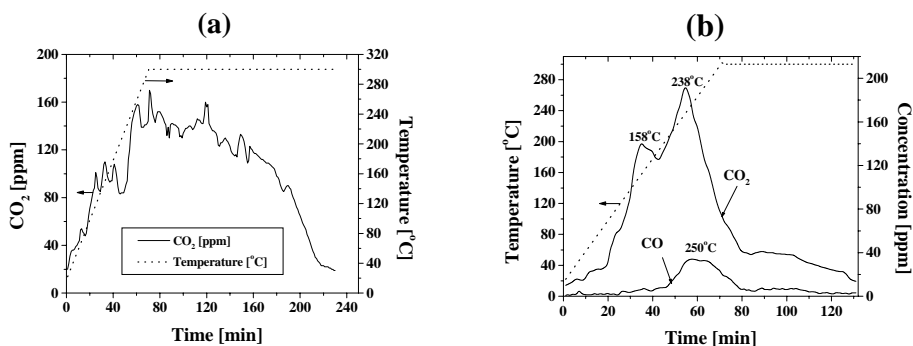


Fig. 2. TPD spectra of the samples: (a)-2.5 AT and (b)-5 AT.

The results allow us to conclude that the change in WGS activity of the catalysts is probably due to their tendency to adsorb CO and accumulate it as carbonates under temperature conditions above or near ambient. If the carbonates deactivate the surface, oxidation treatment should regenerate the activity. Indeed, activation with air at 200 °C for 1 h restored the CO conversion. Moreover, after oxidation the activity is higher than the initial one (Fig. 1, curves A3 and B3).

Conclusions

Au/mesoporous titania catalysts show high activity that could be related to the high stability of the gold dispersion. The different loading, average particle size and dispersion of the gold strongly influence the catalytic activity. The slow deactivation of the catalysts is due to their ability to adsorb CO and accumulate it as carbonates. This deactivation is reversible and after heating in air the activity was restored.

Acknowledgement

V.I. and T.T. gratefully acknowledge financial support from the Bulgarian National Science Fund (Project X-1320).

References

- [1] M. Haruta, S. Tsubota, T. Kobayashi, H. Kageyama, M. J. Genet, B. Delmon, *J. Catal.*, 1993, 144, 175.
- [2] V. Idakiev, L. Ilieva, D. Andreeva, J.L. Blin, L. Gigot, B.L. Su, *Appl. Catal. A: Gen.*, 2003, 243, 25.
- [3] V. Idakiev, T. Tabakova, J.L. Blin, B.L. Su, *Appl. Catal. A: Gen.*, 2004, in press.
- [4] M. Schubert, V. Plzak, J. Garche, R. Behm, *Catal. Lett.*, 2001, 76, 143.

METHANOL DECOMPOSITION OVER IRON SUPPORTED CATALYSTS – EFFECT OF PHASE COMPOSITION AND OXIDATION STATE OF IRON

D. Paneva¹, A. Terlecka-Baricević², T. Tsoncheva³, M. Jovanović⁴, E. Manova¹, Lj. Matić⁵, B. Kunev¹, I. Mitov¹ and Ch. Minchev³

¹*Institute of Catalysis, Bulgarian Academy of Sciences, 1113 Sofia, Bulgaria,* ²*IchTM-Centre of Catalysis and Chemical Engineering, Njegoseva 12, 11000 Belgrade, Serbia and Montenegro*

³*Institute of Organic Chemistry, Bulgarian Academy of Sciences, 1113 Sofia, Bulgaria*

⁴*Scientific Research Centre at the Oil Refinery Panchevo, Serbia and Montenegro*

⁵*Trayal Corporation, Krusevac, Serbia and Montenegro*

Abstract

Transmission, conversion Mössbauer spectroscopy and XPS measurements were used to characterize iron catalysts (in oxidized and reduced state), supported on activated carbon in reaction of methanol decomposition.

Introduction

The information about phase composition of the surface or of subsurface layers is of importance for both identification of the catalytically active component and for elucidation of the mechanism of the catalytic reaction. Our previous study revealed that iron catalysts supported on activated carbon, in oxidized and in partially reduced state, are relatively active in catalytic decomposition of methanol [1, 2].

The main objective of this study was to identify the phase composition of the surface and in the bulk of iron catalysts supported on activated carbon (in oxidized and in reduced state) in methanol decomposition prior and after catalytic test.

Experimental

Granulated activated carbon (AC) from Trayal Corporation, Krushevac ($S = 545 \text{ m}^2/\text{g}$, $V_p = 0.55 \text{ cm}^3/\text{g}$) was used as support. The oxidized $\text{Fe}_2\text{O}_3/\text{AC}$ sample was prepared through impregnation and subsequent heating under conditions described in ref. [1]. The Fe/AC sample was obtained through reduction of the $\text{Fe}_2\text{O}_3/\text{AC}$ sample with hydrogen at 573K and 773K (2 h) [2]. Both samples contained 10 mass % Fe.

The phase composition was obtained by Mössbauer spectroscopy (transmission – TMS and conversion – CMS mode), XRD and XPS method. Processing of the spectra was carried out analogously to the way described in [2].

Catalytic experiments were performed in a fixed-bed reactor with methanol partial pressure of 1.57 kPa and WHSV of 1.5 h^{-1} at 450-670K [2].

Results and Discussion

The initial $\text{Fe}_2\text{O}_3/\text{AC}$ sample is an amorphous one. Its composition was determined by means of TMS and XPS. The particle size of the active phase was evaluated as well [3]. The active phase comprised hematite-like ultra disperse oxide particles in superparamagnetic state (SPM Fe_2O_3), formed by Fe^{3+} -ions with octahedral co-

ordination and a size of $D \leq 4.0$ nm [1,2]. The reduced Fe/AC sample involved α -Fe, $D=40$ nm (62 %), SPM nanoparticles of Fe_2O_3 (33 %) and cluster structures of Fe^{2+} -ions (5%) [2].

The plots of conversion of methanol and selectivity in respect to CH_4 formation vs. temperature for oxidized and reduced samples are presented in fig. 1.

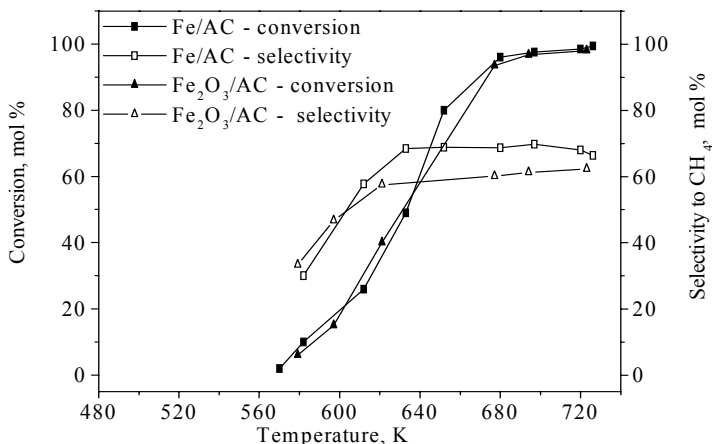


Figure 1. Catalytic activity and selectivity to CH_4 of investigated samples

Almost identical dependence of catalytic activity and close values of selectivity on temperature obtained over $\text{Fe}_2\text{O}_3/\text{AC}$ and Fe/AC in decomposition of methanol could be ascribed to the formation of similar composition of surface layer of catalysts under reaction conditions. XPS and juxtaposition of date of TMS and CMS at samples after catalytic test (figs. 2, 3) reveal the presence on the surface of both studied samples layer of ultra disperse magnetite (SPM Fe_3O_4). The formation of such a layered structure is more probable for the reduced Fe/AC sample with larger effective particle size. In oxidized $\text{Fe}_2\text{O}_3/\text{AC}$ sample, with smaller effective particle size, the ultra disperse magnetite can exist as independent non-layered micro crystallites, whose development is limited by the reactant access to the nano-sized particles of the initial iron oxide.

The present study reveal that the iron-containing phases with different initial oxidation state of iron ions, structure of main phases and particle size in the course of the catalytic decomposition of methanol form at surface of catalyst working layer that comprises similar structural units incorporated into a phase of identical chemical nature.

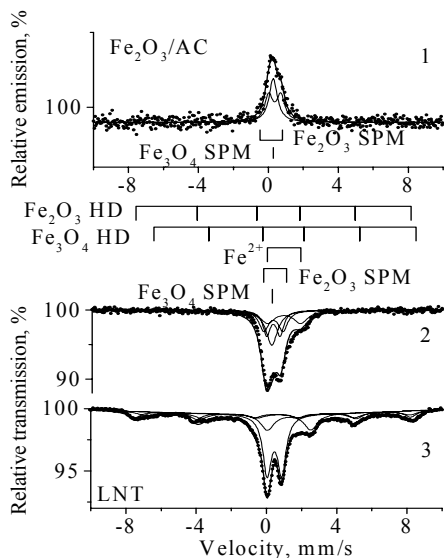


Figure 2. CMS (1) and TMS (2) at room temperature and (3) at liquid nitrogen temperature (LNT) of $\text{Fe}_2\text{O}_3/\text{AC}$ after catalytic test

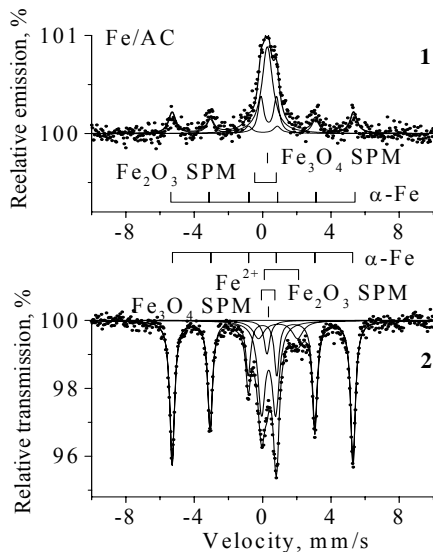


Figure 3. CMS (1) and TMS (2) of Fe/AC after catalytic test

Acknowledgement

Financial support by the Bulgarian National Scientific Fund (X-1208) is gratefully acknowledged.

References

- [1] D. Paneva, M. Jovanovic, T. Tzoncheva, Lj. Matic, B. Kunev, A. Terlecki-Baricevic, I. Mitov, C. Minchev, *Bulg. Chem. Commun.*, 2002, 34(3/4), 384.
- [2] D. Paneva, T. Tzoncheva, G. Tyuliev, E. Manova, I. Mitov, *Nanoscience and Nanotechnology*, (Eds. E. Balabanova, I. Dragieva), Heron press Ltd, Issue 2003, 3, 60.
- [3] V. Leon, *Surf. Sci.*, 1995, 339, 931.

ZEOLITIC STRUCTURES AS SUPPORT OF Rh CATALYSTS

C. Blanco, V. Krstic, V. Saiz, C. Pesquera and F. González

*Grupo de Química Inorgánica. Dept. de Ingeniería Química y Química Inorgánica,
E.T.S.I.I. y T., Universidad de Cantabria, E- 39005 Santander, Spain*

Abstract

Zeolitic structures prepared from a Spanish clay minerals have been used as support of Rh catalysts and Rh promoted with Sn. Catalysts have been prepared by using the organometallic complex $[\text{Rh}(\text{Me}_2\text{CO})_x(\text{NBD})]\text{-ClO}_4$, in which NBD is 2,5-norbornadiene in acetone medium as a metal precursor. The tin (II) acetate in water medium is used as a metal promoter. The supports have been characterised by different techniques: X-ray diffraction (XRD), infrared spectroscopy (IR), thermo-gravimetric analysis (TG). Catalytic behaviour has been studied for the hydrogenation of crotonaldehyde (But-2-enal) in the vapour phase in gas chromatography (GC). Results show that the introduction of Sn on the zeolitic supports in the Sn/Rh atomic ratio 1.7 greatly modifies the catalytic behaviour of Rh alone and enhances the selective hydrogenation of the carbonyl bond.

Introduction

The hydrogenation of α,β -unsaturated carbonyl compounds on single metal catalysts, mainly conducted in vapour-phase hydrogenation (acrolein and crotonaldehyde) usually leads to the reduction of the conjugated C=C double. Different efforts have been made to improve the selectivity to the corresponding unsaturated alcohol [1–5]. Catalysts based on noble metals deposited on an inert support display a very low selectivity towards the unsaturated alcohol. An important enhancement in selectivity may be obtained by using reducible supports; the addition of promoters (second metal, oxides or cationic species); modifying the metal particle size, etc. [6, 7]. It has also been demonstrated [8] that the addition of Sn to Rh, Pt or Ru catalysts produces also an increase in the selectivity to crotyl alcohol.

This communication reports the beneficial effect of Rh (1%) promoted with Sn (1,7%) in the vapour-phase hydrogenation of crotonaldehyde to the formation of crotyl alcohol. For this end, zeolitic structures formed from a Spanish bentonite as support have been prepared and characterized. The homogenised bentonite was used as a support of the catalyst too and has been studied for comparative effects.

The supports were prepared from a bentonite supplied by GADOR [9], homogenised with NaCl and designated as BENa. This material was used to synthesize zeolitic products. The zeolitic materials were obtained through alkaline treatment of the bentonite and structural characterization by XRD. The conditions of treatment were varied. The media used as solvent was seawater and the sample is called ZESE. To designate the two conditions tested, a final - P is added when the reacting mixtures were

kept in an autoclave at 160°C at autoclave pressure for 24h without stirring; and a final – X, when the treatment took place at boiling point using a reflux system with continuous stirring for 24h. The samples were washed in dialysis membranes; oven dried at 105 °C, powdered and kept in desiccators. The final products were denoted: ZESEP and ZESEX. More details about preparation and characterisation of support are in other publications [10, 11].

Results and Discussion

The specific surface area, (S_{BET}), was determined from N_2 adsorption at 77 K, using Micrometrics ASAP-2000 equipment. The results are shown in table 1. The support of zeolitic structure prepared by reflux system (**ZESEX**) presents the highest specific surface area ($90 \text{ m}^2/\text{g}$).

Table 1: The specific surface area of supports.

Support	BENT	BENa	ZESEP	ZESEX
$S_{\text{BET}} (\text{m}^2/\text{g})$	64	87	70	90

Table 2 shows the resulting metal load (theoretical charge 1%Rh) and dispersion D(%). When the catalysts are Rh alone supported, the incorporation of Rh is higher than when the catalysts are with Rh-Sn.

Table 2: Metal dispersion, D(%), and real charge of rhodium catalysts.

	Rh/BENa	Rh Sn/BENa	Rh/ZESEP	Rh-Sn/ZESEP	Rh/ZESEX	Rh-Sn/ ZESEX
D(%)	40	25	27	47	25	9
Rh	0.90	0.68	0.97	0.61	0.92	0.74

Table 3 demonstrates the conversion of crotonaldehyde and selectivity to crotyl alcohol. The results show the different reaction temperatures for the Rh and the Sn promoted Rh catalysts. The behaviour of the Rh catalysts in the hydrogenation of crotonaldehyde shows that all catalysts have a high activity at all temperatures tested and that the main product obtained from crotonaldehyde hydrogenation is saturated aldehyde (butanal). The catalyst with minor dispersion, Rh-Sn/ZESEX, shows a better selectivity towards crotyl alcohol in all ranges of the reaction temperature (table 2).

Conclusion

The zeolitic structures formed from a Spanish bentonite have been useful supports of Rh and Rh-Sn catalysts. When the catalysts are Rh-supported, the activity increases and the main product obtained from crotonaldehyde hydrogenation, is saturated aldehyde (butanal). On the other hand, when the Rh – supported promoted with Sn, the conversion of crotonaldehyde decreases drastically and increases the selectivity towards crotyl alcohol.

Table 3: Catalytic behaviour in the reaction of hydrogenation of crotonaldehyde in the reaction temperature range 180-280 °C.

Catalyst	180		200		220		240		260		280	
	C%	S%	C%	S%	C%	S%	C%	S%	C%	S%	C%	S%
Rh / BENa	97	0.1	100	-	100	-	100	-	100	-	100	-
Rh -Sn /BENa	20	12	21	10	22	8	23	0.1	30	0.0	36	0.0
Rh /ZESEP	99	-	100	-	100	-	100	-	100	-	100	-
Rh -Sn /ZESEP	18	3	19	4	28	7	35	9	35	7	38	3
Rh /ZESEX	98	-	100	-	100	-	100	-	100	-	100	-
Rh -Sn/ ZESEX	5	35	6	31	7	23	7	17	11	15	14	11

C(%) = total conversion and S(%) = selectivity of the catalyst at the reduction temperature of Rh at 500 °C.

References:

- [1] M.A. Vannice, *J. Mol. Catal.*, 1990, 59, 165.
- [2] C. Mohr and P. Claus, *Science Progress*, 2001, 84 (4), 311.
- [3] V. Ponc, *Appl. Catal. A: Gen.*, 1997, 149, 27.
- [4] A. Huidobro, A. Sepúlveda-Escribano and F. Rodríguez-Reinoso, *J. Catal.*, 2002, 121, 94.
- [5] P. Gallezot and D. Richard, *Catal. Rev. Sci. Eng.*, 1998, 40(1&2), 81.
- [6] A. Guerrero Ruiz, A. Sepúlveda-Escribano, I. Rodríguez-Ramos, *Appl. Catal. A: Gen.*, 1994, 120, 71.
- [7] A. Sepúlveda-Escribano, F. Coloma and F. Rodríguez-Reinoso, *J. Catal.*, 1998, 178, 649.
- [8] M. del C. Aguirre, P. Reyes, M. Oportus, J.L.G. Fierro, *Appl. Catal. A: Gen.*, 2002, 233, 183.
- [9] R. Ruiz, C. Blanco, C. Pesquera, F. González, I. Benito, J.L. López, *Appl. Clay Sci.*, 1997, 12, 73.
- [10] C. Blanco, R. Ruiz, C. Pesquera, F. González, *Appl. Org.-Met. Chem.*, 2002, 16, 84.
- [11] R. Ruiz, C. Pesquera, F. González, C. Blanco, *Appl. Catal. A: Gen.*, 2004, 257, 165.

MESOPOROUS MATERIALS AS SUPPORT OF Pt CATALYSTS

V. Krstic, R. Sanz, C. Pesquera, F. González and C. Blanco

*Grupo de Química Inorgánica. Dept. de Ingeniería Química y Química Inorgánica,
E.T.S.I.I. y T., Universidad de Cantabria, E- 39005 Santander, Spain*

Abstract

The mesoporous Al-MCM-41 was synthesised, characterized and used as support of Pt catalyst. Other catalyst supported over commercial manufactured silica (silica "fumed") has been studied for comparative effects. The Pt catalysts were prepared by the impregnation method from $\text{Pt}(\text{NH}_3)_4\text{Cl}_2$ complex. Hydrogenation of crotonaldehyde was studied in the gas phase, at atmospheric pressure and reduction temperature of 773 K over 1%Pt and 2%Pt / Al-MCM-41 catalysts. The reaction temperatures were from 393 to 493K. The X-ray diffraction (XRD) and BET surface area (N_2 77K) shows the mesoporous nature of the support. The results show that the selectivity towards crotyl alcohol increased with increasing wt. % of Pt in the catalysts. The 1%Pt containing Al-MCM-41 material shows a small activity and selectivity. The catalytic behaviour of the Pt/Silica catalyst has been catalytic active, but not selective towards crotyl alcohol in the reaction.

Introduction

Selective catalytic hydrogenation of organic substrates containing a number of unsaturated functional groups is an important step in the industrial preparation of fine chemicals and has been attracting much interest for fundamental research in catalysis. For example, crotyl alcohols obtained by preferred hydrogenation of the C=O group of crotonaldehyde are valuable intermediates for the production of perfumes, flavouring and pharmaceuticals. In the presence of most of the conventional group VIII metal hydrogenation catalysts, crotonaldehyde is hydrogenated predominantly to butanal by reduction of the C=C group or to crotyl alcohols, C=O group. Therefore, it is desirable to find catalysts which will control the intermolecular selectivity by hydrogenation preferentially the C=O group while keeping the olefinic double bond intact [1-5].

Mesoporous materials such as MCM-41 [6] and SBA-15 [7] are very interesting due to their potential use as adsorbent and catalyst support.

The aim of this paper is to show the application of Al-MCM-41 as support of Pt catalyst and study the influence in the selectivity catalytic of metallic charge incorporated on this support. Also, the catalytic behaviour was compared to Pt over commercial silica.

The reagents that were used for the preparation of the Al-MCM-41 support were silica (silica fumed), Na silicate, NaAlO_2 anhydrous, TMAOH, CTABr and deionised water. In this case the molar composition was the following one: 1 SiO_2 / 0.25 Na_2SiO_3 / 0.1 TMAOH / 0.25 CTABr / 100 H_2O ; Si/Al=25.

The specific surface area, (S_{BET}), was determined from N_2 adsorption at 77 K, using Micrometrics ASAP-2000 equipment. The monometallic Pt/Al-MCM-41 catalyst was prepared by incipient humidity impregnation using $\text{Pt}(\text{NH}_3)_4\text{Cl}_2$. The catalytic behavior of the samples in the vapor-phase hydrogenation of crotonaldehyde (2-butenal) was tested by on-line gas chromatography (GC) in a Perkin Elmer equipped with a FID detector and a 15% DEGS-PS WHP-80/100 column.

Results and Discussion

Table 1 shows the textural parameters of the supports. Al-MCM-41 has high surface area.

Table 1: Textural parameters of silica and MCM-41 supports.

Support	Silica	Al-MCM-41
S_{BET} (m^2/g)	486	1131
Rp (nm)	-	1.60

The Pt/Al-MCM-41 catalyst also shows high activity (table 2) such as mesoporous SBA-15, microporous H-ZSM-5 and HY zeolites, amorphous silica–alumina, amberlist 15, active alumina and silica gel [7]. Moreover, the Pt/Al-MCM-41 catalysts are promising candidates for the synthesis of large organic products whose sizes are too large to enter into the pores of the microporous zeolites.

Table 2 present the results of active phase (Pt) incorporated on different kind of support, in different charge and in different range of reaction temperature. The catalyst of 1%Pt over Al-MCM-41 support shows a small activity and selectivity. When the charge of Pt over Al-MCM-41 support was 2% the activity and selectivity increased and the best results were on temperatures 413 and 433 K with conversion 12-17% and selectivity 23-14%, respectively. On the other hand, the catalyst of 2% of Pt over silica commercial, shows a selectivity minor of 0.3% on the same temperatures. The 2Pt/Silica catalyst has high activity and practically zero selectivity in all of reaction temperatures.

Table 2: Catalytic behaviour of the catalysts in the reaction of hydrogenation of crotonaldehyde in the reaction temperature range 393-493 K.

T(K)	2Pt/Silica		1Pt /Al-MCM-41		2Pt /Al-MCM-41	
	C (%)	S (%)	C (%)	S (%)	C (%)	S (%)
393	12	0.04	0.41	0.01	8	19
413	24	0.26	0.66	0.01	12	23
433	42	0.05	2.49	0.12	17	14
453	72	0.01	2.67	0.01	27	2.0
473	98	0.01	3.78	0.01	45	0.1
493	100	0.01	4.89	0.01	66	0.0
D(%)	13.4		10.4		10.9	

C(%) = total conversion and S(%) = selectivity towards crotyl alcohol of the catalyst at the reduction temperature of Pt at 773 K.

Conclusion

Results of this work have demonstrated the potential use of Al-MCM-41 in reaction of α,β -unsaturated aldehyde hydrogenation. The selectivity of the Al-MCM-41 catalysts was increased with increase wt.% of Pt introduction into the framework of support. The increase in the selectivity up, show the catalyst of 2Pt/Al-MCM-41, to an optimum level increased the catalytic activity in all of the reaction temperatures.

References

- [1] F. Ammari, J. Lamotte and R. Touroude *J. Catal.* 2004, 221, 32.
- [2] P. Claus, S. Schimpf, R. Schödel, P. Kraak, W. Mörke and D. Hönicke, *Appl. Catal. A: Gen.*, 1997, 165, 429.
- [3] V. Ponec, *Appl. Catal. A: Gen.*, 1997, 149, 27.
- [4] Z. M. Michalska, B. Ostaszewski, J. Zientarska and J. M. Rynkowski; *J. Mol. Cat. A: Gen.* 2002, 185, 279.
- [5] A. Sepúlveda-Escribano, F. Coloma and F. Rodríguez-Reinoso, *J. Catal.*, 1998, 178, 649.
- [6] J.S. Beck, J.C. Vartuli, W.J. Roth, M.E. Leonowicz, C.T. Kresge, K.D. Schmitt, C.T-W Chu, D.H. Olson, E.W. Sheppard, S.B. McCullen, J.B. Higgins, J.L. Schlenker, *J. Am. Chem. Soc.*, 1992, 114, 19834.
- [7] T. Kugita, S. K. Jana, T. Owada, N. Hashimoto, M. Onaka, S. Namb, *Appl. Catal. A: Gen.* 2003, 245, 353.

MCM-41 AS SUPPORT OF Rh- AND Rh-Sn/CATALYSTS. CATALYTIC PROPERTIES

C. Blanco, V. Krstić, F. González and C. Pesquera.

*Grupo de Química Inorgánica. Dept. de Ingeniería Química y Química Inorgánica,
E.T.S.I.I. y T., Universidad de Cantabria, E- 39005 Santander, Spain*

Abstract

The MCM-41 materials have been attracted much attention because of their potential use as adsorbents and catalyst supports. This paper presents preliminary results of the study of the selective hydrogenation of crotonaldehyde using Rh-catalysts, or Rh promoted with Sn supported. For this end, new supports as MCM-41 have been prepared and characterised. The effect of the support on the incorporation of the active phase and the activity and selectivity of the above-mentioned reaction has been studied. Another catalysts supported over silica have been studied for comparative effects. Results show that catalysts containing Rh promoted with Sn and MCM-41 as supports are, in general, more selective and active towards crotyl alcohol than the silica-supported ones.

Introduction

Mesoporous molecular sieves such as hexagonally ordered MCM-41 have been attracted much attention because of their potential use as adsorbents and catalyst supports. They are characterized by uniform structure, high pore volume and high specific surface area. They are materials where a metallic phase can be incorporated within their framework or as catalytic support in metal support catalysts [1].

The unsaturated alcohols preparation by selective hydrogenation of α - β -unsaturated aldehydes is a great important reaction in the production of many pharmaceutical, agrochemical and fragrances compounds. One important step is the selective hydrogenation of the carbonyl bond, the olefinic bond remaining unaffected. Although, this hydrogenation reaction is almost quantitatively selective to the saturated aldehyde because the hydrogenation of the olefinic double bond is favoured by both kinetic and thermodynamic considerations, it would be desirable to find catalysts which may control the intermolecular selectivity by preferential hydrogenation of C=O bond while the olefinic bond, is kept intact. Monometallic Rh or Pt catalysts usually produce the saturated aldehyde, and it is necessary to modify them either by support effects or by addition of a second metal –as bimetallic or promoter- (for instead Sn, Fe o Ni) in order to improve the selectivity towards crotyl alcohol [2-9].

This paper presents preliminary results of the study of the selective hydrogenation of crotonaldehyde using Rh-catalysts, or Rh promoted with Sn supported. For this end, new supports as MCM-41 have been prepared and characterized. The effect of the support on the incorporation of the active phase and the activity and selectivity of the above-mentioned reaction has been studied. Another catalysts supported over silica have been studied for comparative effects.

Commercially silica and MCM-41 synthesized in the laboratory with one or two silicon sources were used as supports, MCM-41(1) and MCM-41(2) respectively.

The incorporation of the metallic phase (1% Rh) in the supports was performed in acetone medium by immobilizing of a cationic organometallic rhodium compound at room temperature. When Sn (1%) has been added as promoter in the supports the source was tin acetate.

Supports and catalysts were characterized by different physicochemical techniques: X-ray diffractometry, IR spectroscopy, nitrogen adsorption-desorption, ammonium adsorption-desorption, thermal analysis, UV-Visible spectroscopy and oxygen-hydrogen chemisorptions.

The catalytic activity analysis was done in gaseous phase (atmospheric pressure and temperature reaction between 180 and 280°C), in a fixed-bed reactor. All the catalysts were reduced in situ at 500°C under a flow of hydrogen. The products of the hydrogenation of crotonaldehyde reaction were analyzed in a gas chromatograph equipped with a FID.

Results and Discussion

The MCM-41 materials have been result useful supports for preparing Rh-catalysts and Rh- promoter with Sn. The characteristics of the supports in the presence of Sn as promoter had an influence on the capacity of the incorporation of the metal load and on the Rh dispersion (Table 1).

Moreover, the behaviour of the Rh-catalysts on the hydrogenation of crotonaldehyde shows that all the catalysts have a high activity at all the temperatures tested and the activity remaining steady during all time tested (500min). The main product obtained on crotonaldehyde hydrogenation is saturated aldehyde (butanal). However, when the catalysts are Sn-Rh/supports there is a big increase of the selectivity to crotyl alcohol. Moreover, when the materials MCM-41 are used as supports, the main product obtained on crotonaldehyde hydrogenation is crotyl alcohol. This may be due to the effect of the physicochemical support properties (Table). The apparent activation energy (26-34 kJ/mol) is within the range of data reported by other authors [10].

Conclusions

The MCM-41 materials have been useful supports for preparing Rh promoters with Sn catalyst, achieving high load values of incorporated Rh close to the theoretical value with good dispersions. When the MCM-41 materials are used as supports, the main product obtained on crotonaldehyde hydrogenation is crotyl alcohol.

Table 1

T°C	Catalyst	RhSn/Silica	RhSn/MCM-4(1)	RhSn/MCM-4(2)
180	C% Crotyl Aldehyde	14.16	7.75	3.89
	S% Crotyl Alcohol	0.02	39.41	41.25
200	C% Crotyl Aldehyde	24.02	10.13	6.86
	S% Crotyl Alcohol	1.46	38.40	46.75
220	C% Crotyl Aldehyde	40.18	19.12	13.98
	S% Crotyl Alcohol	9.87	27.83	38.60
240	C% Crotyl Aldehyde	49.08	28.76	26.18
	S% Crotyl Alcohol	5.10	24.17	31.05
260	C% Crotyl Aldehyde	72.01	58.05	39.97
	S% Crotyl Alcohol	5.11	3.84	20.51
280	C% Crotyl Aldehyde	79.82	-	52.83
	S% Crotyl Alcohol	4.26	-	12.21
% Real Charge rhodium		0.77	0.77	0.86
% Dispersion		36	31	52

Note: C% = % total conversion; S% = % Selectivity to crotyl alcohol.

References

- [1] J.S. Beck, J.C. Vartuli, W.J. Roth, M.E. Leonowicz, C.T. Kresge, K.D. Schmitt, C.T.-W. Chu, D.H. Olson, E.W. Sheppard, S.B. McCullen, J.B. Higgins and J.L. Schlenker, *J. Am. Chem. Soc.*, 1992, 114, 19834.
- [2] P. Claus, *Topics in Catalysis*, 1998, 5, 51.
- [3] F. Coloma, J. Llorca, N. Homs, P. Ramirez de la Piscina, F. Rodriguez-Reinoso, A. Sepúlveda-Escribano, *Phys. Chem. Chem. Phys.*, 2000, 2, 3063.
- [4] P. Gallezot and D. Richard, *Catal. Rev. Sci. Eng.*, 1998, 40(1&2), 81.
- [5] A. Guerrero Ruiz, A. Sepúlveda-Escribano, I. Rodríguez-Ramos, *Appl. Catal. A: General*, 1994, 120, 71.
- [6] N. Homs, J. Llorca, P. Ramirez de la Piscina, F. Rodríguez-Reinoso, A. Sepúlveda-Escribano; J. Silvestre-Alvero, *Phys. Chem. Chem. Phys.*, 2001, 3, 1782.
- [7] P. Reyes, M. del C. Aguirre, J.L.G. Fierro, G. Santori, O. Ferreti, *J. Mol. Catal.*, 2002, 184, 431.
- [8] V. Ponec, *Appl. Catal. A: Gen.*, 1997, 149, 27.
- [9] T.B.L.W. Marinelli, V. Ponec, *J. Catal.*, 1995, 156, 51.
- [10] M.A. Vannice, *J. Mol. Catal.*, 1990, 59, 165.

METHANE COMBUSTION ON PURE AND DOPED LANTHANUM COBALTITES CATALYSTS

F. Papa^a, D. Berger^b, G. Dobrescu^a and N. I. Ionescu^a

^aRomanian Academy, Institute of Physical Chemistry, 202 Splaiul Independentei, 77208 Bucharest,

^b“Politehnica” University Bucharest, Department of Inorganic Chemistry, 1 Polizu street, 011061, Bucharest, Romania

Abstract

The catalytic behavior of $\text{La}_{1-x}\text{A}_x\text{CoO}_3$ (A=Sr, Ag; $x=0-0.2$) in the methane combustion was investigated. The catalysts were characterized by X-ray diffraction (XRD), scanning electron microscopy – energy dispersive X-ray spectroscopy (SEM-EDX), as well as specific surface area measurements. The catalytic activity measurements on pure and doped lanthanum cobaltite samples in the methane combustion were carried out in a fixed-bed quartz reactor at atmospheric pressure.

Introduction

During the past decade many efforts have been focus in investigation of carbon monoxide (CO) and light hydrocarbons ($\text{C}_n\text{H}_{2n+2}$) oxidation on perovskite-type, LaMO_3 (M=Mn, Co, Fe, Ni) [1]. It has been demonstrate that the performance of the catalysts depend not only on their composition, but also the preparation method, which might determine their physical state, especially the surface composition. To improve the catalytic activity of $\text{La}_{1-x}\text{Sr}_x\text{CoO}_3$, the powders must by synthesized with a good surface crystalline and large surface area [2]. The present study deals with the investigation of $\text{La}_{1-x}\text{A}_x\text{CoO}_3$ (M=Sr, Ag; $x=0-0.2$) catalytic properties in the methane combustion.

Experimental

$\text{La}_{1-x}\text{A}_x\text{CoO}_3$ (A=Sr, Ag; $x=0-0.2$) catalysts were obtained by thermal decomposition of the maleate-based precursors [3]. The $\text{La}_{1-x}\text{A}_x\text{CoO}_3$ ($x=0-0.2$) catalysts were prepared by calcining the isolated precursors at 800°C, 3h for LaCoO_3 and at 1000°C, 4-6h for $\text{La}_{1-x}\text{A}_x\text{CoO}_3$ (A=Sr, Ag; $x=0.1-0.2$). The catalysts were characterized by X-ray diffraction (XRD) patterns, scanning electron microscopy – energy dispersive X-ray spectroscopy (SEM-EDX), as well as specific surface area measurements. XRD patterns were obtained using a Bruker AXS D8 Advance diffractometer with $\text{CuK}\alpha$ radiation at a step of 0.02°/s in the range $2\theta = 10$ to 90°. SEM-EDX analysis of the pure and doped lanthanum cobaltite catalyts were obtained using a JEOL JSM-5800 scanning electron microscope. BET specific surface areas were measured by nitrogen adsorption at liquid nitrogen temperature in a volumetric, apparatus.

Activity tests of catalysts for methane oxidation reaction were carried out at atmospheric pressure, in a fix bed reactor with 20 mm diameter which contained 0.5 g catalyst. The reactor was heated by a furnace connected to a temperature controller. The gas flows (5% CH_4 balanced with air) were controlled by the mass flow controllers.

The corresponding gas hour space velocity of reactant mixture was $10000 \text{ cm}^3 \text{ h}^{-1} / \text{g}$ catalyst. In all experiments, the catalysts were first pretreated in argon at 500°C for 2 h. The analysis of the effluent gas was performed by gas chromatography (Hewlett Packard 5480A) equipped with a TCD detector. The reaction products were analyzed by using Porapaq Q column for CO_2 , CH_4 and a 5\AA molecular sieve column for CO , O_2 , N_2 . The temperature range for catalytic tests was $200^\circ\text{-}850^\circ\text{C}$.

Results and Discussion

The XRD data for $\text{La}_{1-x}\text{Sr}_x\text{CoO}_3$ ($x = 0\text{-}0.2$) obtained by both methods show that all the samples are single phases with rhombohedral distorted perovskite structure. The XRD pattern of $\text{La}_{0.9}\text{Ag}_{0.1}\text{CoO}_3$ presents the characteristic peaks of perovskite phase and an additional peak at $2\theta = 38.146$ specific for Ag_2O (Fig. 1).

Table 1 lists the crystallite sizes, (D_{110}), determined from full width at half-maximum of the the (110) X-ray reflection (FWHM) using Scherrer's equation and the specific surface area values of $\text{La}_{1-x}\text{A}_x\text{CoO}_3$ (A=Sr, Ag; $x=0\text{-}0.2$) determined by BET method.

Table 1. Crystallite size and specific surface area values of $\text{La}_{1-x}\text{A}_x\text{CoO}_3$ catalysts

Compound	D_{110} (nm)	S (m^2/g)
LaCoO_3	46	34.6
$\text{La}_{0.9}\text{Sr}_{0.1}\text{CoO}_3$	38	37.9
$\text{La}_{0.8}\text{Sr}_{0.2}\text{CoO}_3$	46	38.5
$\text{La}_{0.9}\text{Ag}_{0.1}\text{CoO}_3$	48	35.4

The specific surface area values increase with the increasing of strontium content. The elemental analysis results by EDX for lanthanum cobaltite catalysts show a homogenous distribution of metallic cations. SEM examination of the powder surfaces of $\text{La}_{1-x}\text{Sr}_x\text{CoO}_3$ catalysts showed that all the samples obtained from both methods have primary fine particles with a small tendency of agglomerates formation and high porosity (Fig. 2).

Figure 3 shows the catalytic behavior of the $\text{La}_{1-x}\text{Sr}_x\text{CoO}_3$ catalysts in the methane combustion. It can be noticed that the methane conversion increases with the increasing of strontium content. These results could be correlated with the light increase of specific surface area and the presence of Co^{4+} and /or oxygen vacancies as results of the charge compensation when some La^{3+} were replaced with Sr^{2+} . The $\text{La}_{0.9}\text{Sr}_{0.1}\text{CoO}_3$ has shown a higher activity than $\text{La}_{0.9}\text{Ag}_{0.1}\text{CoO}_3$ (Fig. 4).

Conclusions

Catalytic tests on methane combustion were performed in the $200^\circ\text{-}850^\circ\text{C}$ temperature range over pure and doped lanthanum cobaltite catalysts. The catalytic tests indicated that all the catalysts show 100% selectivity for CO_2 in the $200^\circ\text{-}850^\circ\text{C}$ temperature range. The conversion of methane increases noticeably with the strontium content. $\text{La}_{0.9}\text{Sr}_{0.1}\text{CoO}_3$ presents better activity than $\text{La}_{0.9}\text{Ag}_{0.1}\text{CoO}_3$ in the methane combustion.

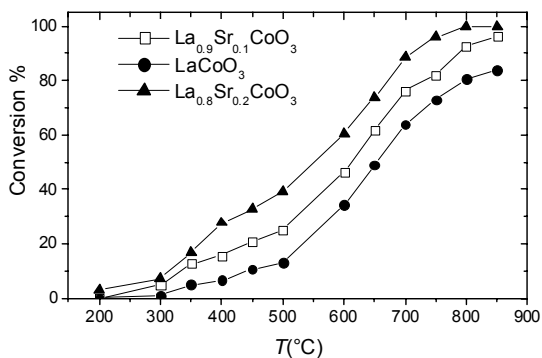


Fig. 3. Catalytic activity of $\text{La}_{1-x}\text{Sr}_x\text{CoO}_3$

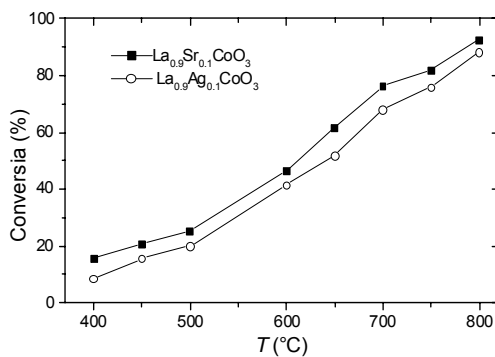


Fig. 4. Catalytic activity of $\text{La}_{1-x}\text{A}_x\text{CoO}_3$

References

- [1] M. A. Pena, J.L.G. Fierro, Chem. Rev. 2001, 101, 1981.
- [2] H. Taguchi, S. Yamada, M. Nagao, Y. Ichikawa, K. Tabata, Mater. Res. Bull., 2002, 37, 69.
- [3] D. Berger, V. Fruth, I. Jitaru, J. Schoonman, Mater. Lett. (in press)

THE EFFECT OF SILVER CONTENT ON THE CIS-TRANS ISOMERIZATION SELECTIVITY DURING HYDROGENATION OF SOYBEAN OIL OVER SILVER-PROMOTED Ni/DIATOMITE CATALYSTS

M. V. Stanković, B. Marković, A. Šućurović and D. Jovanović

*IChTM Department of Catalysis and Chemical Engineering,
Njegoševa 12, 11000, Belgrade, Serbia and Montenegro*

Abstract

The effect of silver content in silver-promoted Ni/Diatomite catalyst on the cis-trans isomerization selectivity in the process of soybean oil hydrogenation was studied. Precursors of silver-promoted Ni/Diatomite catalyst were prepared by coprecipitation. The silver content in obtained catalyst varied in the range from 0.1 to 4.0 wt %. Catalytic test was performed in a three-phase semi batch reactor at 160 °C and pressure of hydrogen 0.16 MPa. Samples were characterized by atomic absorption spectrometry (AAS), nitrogen adsorption at -196 °C (BET), mercury porosimetry, and FT-IR spectrometry. The results obtained suggest that formation of trans fatty acids (TFA) during soybean oil hydrogenation depend on the silver content. A correlation between the silver content and the cis-trans isomerization selectivity was established. The results also reveal that, this effect was in a good correlation with the textural characteristics of the prepared samples.

Introduction

Reduced Ni/Diatomite is a classic vegetable oil hydrogenation catalyst used in industrial conditions at $393 < T < 453$ K and $0.1 < P_{H_2} < 1.0$ MPa [1]. In these conditions, polyunsaturated fatty acids are hydrogenated preferentially compared to monounsaturated species. This selectivity increases with the increase of temperature and decreases with hydrogen pressure; unfortunately, this also applies to the production of TFA. The selectivity in hydrogenation could be greatly improved by using a promoted nickel catalysts [2, 3], with aim to suppress cis-trans isomerization reaction during hydrogenation vegetable oils. If the factor contributing to this complex hydrogenation process can be understood, then the industry would benefit because margarine and vegetable shortening would contain less undesired TFA.

In the present paper, the silver promotion of Ni/Diatomite was performed in order to improve cis-trans isomerization selectivity during hydrogenation of soybean oil. The research was focused on the effect of silver content in promoted catalyst samples on the cis-trans isomerization selectivity.

Experimental

Precursors of silver-promoted Ni/Diatomite catalysts have been prepared by coprecipitation from mixed solution of $Ni(NO_3)_2 \cdot 6H_2O$ and $AgNO_3$ using solution of Na_2CO_3 . The amount of mixed salt solution of nickel and silver were chosen in order

to achieve desired composition of silver in the final catalyst (0.1-4.0 wt %), while the Diatomite/Ni weight ratio was 1.17. The co-precipitation was performed at 90 °C with stirring and controlled pH at pH 9.2±0.05. After the co-precipitation was completed, the resultant precipitates were filtered, washed, and reduced at 430 °C in a stream of gas mixture (50% H₂/50% N₂). In order to reduce pyrophority of the reduced metal nickel, passivation was performed with the mixture of 350 ppm O₂ in nitrogen at ambient temperature. Impregnation of passivated catalyst samples were made with pure paraffin oil.

Catalyst samples were tested in the process of soybean oil hydrogenation using a three-phase semi batch reactor operating under 0.16 MPa P_{H₂} and 160 °C. Each experiment was performed with 5 dm³ of soybean oil, 0.1 wt% of catalyst, and stirring rate of 750 r.p.m. The change in the TFA composition of the soybean oil during hydrogenation with a certain catalyst sample was determined by means of a series of hydrogenations, interrupted at various intervals of time. After each interval, the content of TFA was determined by IR [4].

The nickel and silver content of the catalyst samples were determined on a Varian AA1275 atomic absorption spectrophotometer. Adsorption and desorption isotherms for nitrogen were obtained at -196 °C using a Thermo Finnigan Sorptomatic 1990. Specific surface (S_{BET}) values were obtained using the Brunauer-Emmet-Teller (BET) equation [5]; mean pore size distributions were those of the Barrett-Joyner-Halenda (BJH) method [6], with the desorption branch being analyzed. Pore volume was determined by mercury porosimetry (Carlo Erba Porosimeter 2000 series). The IR spectra were obtained on a Perkin Elmer FT-IR spectrometer 1725 X.

Results and Discussion

Textural characteristics of the prepared silver-promoted Ni/Diatomite catalyst samples are summarized in Table 1.

Table 1. Textural characteristics of the prepared Ag-Ni/Diatomite catalyst samples

Sample	Silver wt %	S _{BET} m ² /g	Pore volume cm ³ /g	B.J.H. Pore size median pore diameter/nm
0.1Ag-Ni/Diatomite	0.1	41.4	0.630	71
1.0Ag-Ni/Diatomite	1.0	60.4	0.539	30
4.0Ag-Ni/Diatomite	4.0	109.9	0.455	11

From data presented in Table 1, it can be observed that the specific surface area (S_{BET}) is affected by the silver content. The increase in S_{BET} with the increase of silver content can be explained by the development of surface of silver within the diatomite support and possible metal-support interaction [7]. On the other hand, pore volume and median pore diameter decreased with the increase of silver content.

Results of the catalytic test are shown in Table 2. The formation of TFA is controlled by the silver content; increased amount of silver promoter decrease the cis-trans selectivity. The explanation that selectivity and cis-trans isomerisation are controlled by the silver content may be results of several factors among the most important are:

(i) surface reaction of hydrogenation of oil are favoured on the samples with better textural performances (Table 1); (ii) hydrogen spillover mechanism in the presence of silver particles [8].

The data obtained for refractive index and solid fat content are in accordance with the TFA content (Table 2).

Table 2. Characteristics of hydrogenated soybean oil vs x%Ag-Ni/Diatomite catalyst

Sample	Time min	Refractive index ^a	SFC ^b (AOCS)			Total TFA %
		n_D^{20}	20 °C	30 °C	35 °C	
0.1Ag-Ni/Diatomite	55	1.4620	0.75	0.78	0.55	45.2
	115	1.4612	1.45	0.93	0.55	70.5
	155	1.4608	2.07	1.12	0.59	79.2
	195	1.4606	2.53	1.17	0.61	81.1
1.0Ag-Ni/Diatomite	55	1.4615	0.70	0.63	0.22	12.9
	115	1.4613	1.32	0.53	0.77	41.2
	155	1.4609	2.01	0.93	0.71	60.9
	195	1.4605	2.94	0.54	0.74	66.4
4.0Ag-Ni/Diatomite	55	1.4609	2.67	0.60	0.71	5.0
	115	1.4590	21.17	1.91	0.46	20.0
	155	1.4578	32.99	5.13	0.67	33.8
	195	1.4573	36.32	6.37	0.96	39.5

^aRefractive index determined by Abbe refract meter; ^bSolid Fat Content determined by NMR

Conclusion

The whole set of measurement carried out has shown that silver content in silver-promoted Ni/Diatomite catalyst could control product distribution in the process of soybean oil hydrogenation.

Selectivity of silver-promoted Ni/Diatomite catalyst samples to the formation of TFA decrease in the in the following order:

4.0 Ag-Ni/Diatomite < 1.0 Ag-Ni/Diatomite < 0.1 Ag-Ni/Diatomite.

Acknowledgement.

This work was supported by the Ministry of Science and Environmental Protection of Republic of Serbia (Project-MHT.2.09.0022.B).

References

- [1] J. W. E. Coenen, J. Am. Oil Chem. Soc., 1976, 53, 382.
- [2] H. Li, H. Li, J. F. Deng, Catal. Today, 2002, 74, 53.
- [3] M. P. Gonzales-Markos, J. I. Gutiérrez-Ortiz, C. Conzález-Ortiz de Elguea, J. I. Alvarez, J. R. González-Velasko, Canadian J. Chem. Eng. 1998, 76, 927.
- [4] R. R. Allen, J. Am. Oil Chem. Soc., 1969, 46, 552.
- [5] S. Brunauer, P. H. Emmett, E. Teller, J. Am. Chem. Soc. 1938, 60, 309.
- [6] E. P Barrett, L. G. Joyner, P. P. Halenda, J. Am. Chem. Soc. 1951, 73, 373.
- [7] R. Lamber, N. Jaeger, G. Schulz-Ejkloff, Surf. Sci. 1990, 227, 268.
- [8] G. M. Pajonk, S.J. Teichner in Catalytic Hydrogenation, L. Červený (ed.), Elsevier, Amsterdam, 1986, 284.

TEMPERATURE PROGRAMED PARTIAL OXIDATION OF CYCLOHEXANE ON THE POLYMER SUPPORTED CATALYSTS

D. Lončarević and Ž. Čupić

Institute of Chemistry, Technology and Metallurgy, Department of Catalysis and Chemical Engineering, Njegoševa 12, 11000 Belgrade, Serbia and Montenegro

Abstract

Several polymer-supported Co(II) catalysts with different promoters were prepared and their activity and selectivity in the partial oxidation of cyclohexane were determined. Results indicate possibility to decrease reaction temperature without significant loss in cyclohexane conversion.

Introduction

Partial oxidation of cyclohexane to the mixture of cyclohexyl hydroperoxide (Chhp), cyclohexanol (Chl) and cyclohexanone (Chn) is the first step in an important industrial process for production of adipic acid [1]. The system, currently in use, employs 0.3-3 ppm of a soluble cobalt catalyst, at temperature value of 150-175 °C and pressure value of 0.8-1.0 MPa.

According to the literature data, investigations are focused to the heterogenization of batch reactions, which should afford the easily recoverable catalyst [2]. Among the solid supports used (inorganic oxides, zeolites *etc.*) [3], polymeric materials [2] are of particular interest due to the possible synergetic effect of polymer matrix and supported transition metal, which can lead to the better catalyst performances. Metal ion acts as an initiator of free radical autoxidation which proceeds further via radical chain reaction [3]. Our previous results show that polymer-supported Co(II) catalyst, catalyze cyclohexane partial oxidation at 170 °C and 2.8 MPa, with high conversion and good selectivity towards desired products [4]. The goal of present work was to prepare several modifications of the polymer-supported Co(II) catalysts with different promoters, and to determine their activity and selectivity in the temperature programmed partial oxidation of cyclohexane.

Experimental

The support used was macroreticular copolymer of poly-4-vinylpyridine with divinylbenzene (REILLEX-425), produced by Reilly Tarr & Chemical Corporation. Catalysts, listed in Tab. 1, were prepared from the ethanol solutions of the Co (A0 and A1), Co and Cr (AB1 and AB2), Co and Fe (AE1 and AE2), Co complex with EDTA and Fe complex with ascorbic acid. All of the metal salts were nitrates dissolved in absolute ethanol before addition of the polymer support.

Activity tests were performed in stainless steel, laboratory scale (100 cm³), stirred autoclave. In all catalytic runs the following conditions were used: polymer fraction in reaction mixture equal to wt. 2.5 % with respect to cyclohexane, air pressure 2.8 MPa, stirrer speed 350 rpm. Air-flow rate was maintained at about 100 cm³ min⁻¹. Gas and

liquid samples were analyzed by gas chromatography.

The activity tests were performed under the temperature programmed conditions: after an initial fast heating up to 110 °C, a constant heating rate of 0.3 degree/min was used in the range between 110 °C and 170 °C, and the system was kept at 170 °C for 10 min before the reaction was stopped. In each experiment, the fresh charge of the catalyst was used.

Composition of the liquid samples was analyzed by gas chromatography using stainless steel column packed with 10% Carbowax 20M on Chromosorb WAW, coupled to a flame ionisation detector, isothermally at 150 °C. The Chhp concentration was determined by iodometric titration and indirectly by reduction with triphenylphosphine [5].

Results and Discussion

The final yields of the Chhp, Chl and Chn mixture, and Chn/Chl ratio are presented in the Tab. 1, with composition of the used catalysts. The higher yields were obtained for lower content of the supported metal, in accordance to catalyst-inhibitor effect of the metal. On the other side, for the samples with higher metal content, both promoters, Fe and Cr were active in increasing yield of the products. The Chn/Chl ratio was increasing with decreasing of the conversion, and reached highest value for the sample EK.

Tab. 1 The composition of the catalysts, yield equal to $(\text{Chhp} + \text{Chl} + \text{Chn})/\text{Ch}_0$ ratio (where Ch_0 is initial concentration of Ch), and Chn/Chl ratio in the temperature programmed oxidation of the cyclohexane.

	<i>Co</i> (mas %)	<i>Cr</i> (mas %)	<i>Fe</i> (mas %)	<i>Yield</i> (%)	<i>Chn/Chl</i>
A0	0.11	-	-	4.14	1.2
A1	0.52	-	-	2.94	1.6
AB1	0.10	0.10	-	4.24	1.2
AB2	0.44	0.38	-	3.69	1.4
AE1	0.10	-	0.09	4.18	1.2
AE2	0.44	-	0.40	3.70	1.3
AK ¹	0.44	-	-	3.00	1.5
EK ²	-	-	0.56	2.00	2.1

¹Co-EDTA (1:1)

²Fe-ascorbic acid (1:1).

Samples with higher content of the supported metal resulted in significant decrease of the Chhp concentration during the process, Fig. 1, and in decreasing autoxidation.

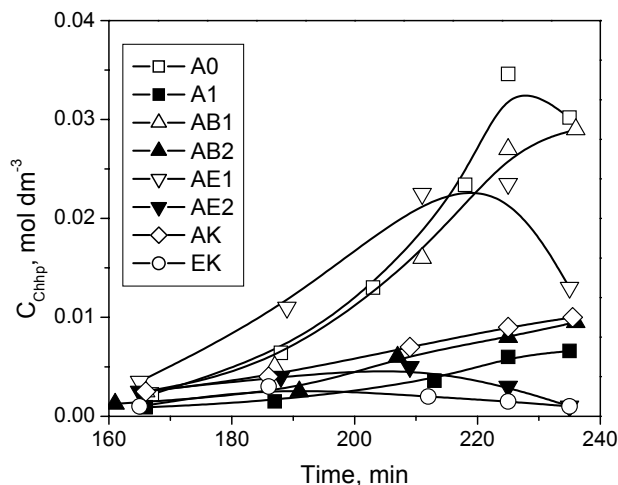


Fig. 1 The Chhp concentration during cyclohexane oxidation, for all tested catalysts.

Conclusions

Results obtained in cyclohexane partial oxidation over the macroporous polymer supported Co catalysts, indicate possibility to decrease reaction temperature without significant loss in conversion.

Reaction proceeds selectively to Chn and Chl, with very low extent of deep oxidation. Influence of the promoters on the conversion were more favorite in catalysts with higher Co contents, while in the reaction with catalysts of the lower Co contents, autoxidation reaction initiated with Chhp was dominant.

The influence of the iron ions seem to be favorable when it was combined with Co, but iron compound alone was less active.

Acknowledgement:

The authors gratefully acknowledge the partial support of the Fund for Science and Technologies and Development of Serbia. Proj. 1807

References:

- [1] D. E. Danley, C. R. Campbell, in Kirk Othmer Encyclopedia of Chemical Technology, (3rd Ed.) John Wiley & Sons; New York, 1978, 1, 514.
- [2] G. L. Goe, C. R. Marston, E. F. V. Scriven, E. E. Sowers in 'Catalysis of Organic Reactions', Ed. D. W. Blackburn, Marcel Dekker, Inc., New York, 1989, p. 275.
- [3] I. W. C. E. Arends, R. A. Sheldon, Appl. Catal., 2001, A 212, 175.
- [4] Ž. Čupić, A. Terlecki-Baričević, M. Stanković, Activity of the Polymer Catalyst for the partial oxidation of Cyclohexane, 4th World Congress on Oxidation Catalysis, Berlin, 2001, Extended Abstracts, p.p.155.
- [5] G. B. Shul'pin, J. Mol. Cat. A: Chemical, 2002, 189, 36.

DEEP OXIDATION OF N-HEXANE ON ALUMINA SUPPORTED PLATINUM AND MANGANESE OXIDE CATALYSTS

N. Radić, B. Grbić and A. Terlecki-Baričević

Institute of Chemistry, Technology, and Metallurgy - Department of Catalysis and Chemical Engineering, Njegoseva 12, 11000 Belgrade, Serbia and Montenegro.

Abstract

The oxidation of n-hexane in air over Pt/Al₂O₃, Pt/Mn/Al₂O₃, and Mn/Al₂O₃ catalysts with different content of Mn has been studied. The measurements were performed in an fixed bed catalytic reactor in temperature range 100 – 500 °C, with space velocity of 17 500 h⁻¹. The addition of Mn to the Pt/Al₂O₃ catalysts improves catalytic activity. The conversion of n-hexane over Pt/Mn/Al₂O₃ catalysts is not affected by the content of Mn.

Introduction

Deep catalytic oxidation of volatile organic compounds (VOCs) on noble metals is a widely used method to remove VOCs from industrial waste gases [1]. Typical combustion catalysts are based on noble metals, platinum and palladium. Metal oxides are a cheaper substitutions to noble metals as combustion catalysts, although they are less active than noble metal. It is known that deep oxidation of VOCs can be catalyzed by compositions involving manganese oxides [2,3].

The aim of this work is to clarify the influence of the addition of Mn on catalytic activities of Pt/Al₂O₃ catalyst. Thus we investigated the complete oxidation of n-hexane in air as a function of temperature over Pt/Al₂O₃, Pt/Mn/Al₂O₃, and Mn/Al₂O₃ catalysts.

Experimental

Catalyst preparation

Pt/Al₂O₃ catalysts were synthesized by impregnation of a (γ+θ)Al₂O₃ support (Rhone-Poulenc) by an aqueous solution of chloroplatinic acid. A detailed description of the synthesis, subsequent processing and characterization of the catalyst was presented in previous paper [4]. The preparation of Pt/Mn/Al₂O₃ and Mn/Al₂O₃ catalysts was carried out using the deposition – precipitation method. The Al₂O₃ support and Pt/Al₂O₃ catalyst were impregnated by the adequate amount of water solution of NH₄OH (about 5 cm³ g⁻¹ support) during 10 min. After filtration and rinsing with distilled water Al₂O₃ support and Pt/Al₂O₃ catalyst were brought into the contact with the water solution of MnCl₂. The concentration of MnCl₂ was estimated in the range of 0.025-0.1 M in order to obtain manganese loading of 0.1 and 0.4 wt.%. After the precipitation of manganese the catalyst was filtered, rinsed with distilled water, air-dried at 110 °C for 2 h and finally calcinated at 500 °C for 4 h in air. The content of the active components in the catalysts are presented in Table 1.

Table 1. Composition of the active components in the catalysts

Sample	Pt (wt.%)	Mn(wt.%)
0.12Pt/Al ₂ O ₃	0.12	-
0.12Pt/0.1Mn/Al ₂ O ₃	0.12	0.1
0.12Pt/0.4Mn/Al ₂ O ₃	0.12	0.4
0.1Mn/Al ₂ O ₃	-	0.1
0.4Mn/Al ₂ O ₃	-	0.4

All the catalysts had an egg-shell distribution, with almost all active components content deposited in the outer shell of the support to a depth of 100 μm , S_{BET} of 110 m^2g^{-1} , and a pore volume of 0.68 cm^3g^{-1} .

Catalytic activity

The experiments were performed in a fixed bed catalytic reactor, made of a stainless steel tube having a diameter of 16 mm. All measurements were done with 2 g of catalyst, which is near to a volume of 4 cm^3 . The activity of the catalysts was investigated in temperature range 100 – 500 $^{\circ}\text{C}$, with space velocity of 17 500 h^{-1} . The inlet and the outlet concentrations of n-hexane were analyzed by an FID detector using stainless-steel column, 6.5 ft. long and 1/8" in diameter, containing 23 % SP 1700 on chromosorb PAW.

Results and Discussion

The temperature dependence of conversion was determined for each catalyst and presented in Fig. 1. Measurements are performed at constant inlet concentrations of n-hexane of 1500 ppm in air.

The oxidation of n-hexane starts at about 120 $^{\circ}\text{C}$ on all samples that contains platinum. Samples containing only manganese are found to be less active and oxidation of n-hexane starts at about 175 $^{\circ}\text{C}$. It is evident that the two Pt/Mn/Al₂O₃ samples are more active than Pt/Al₂O₃. The n-hexane conversions for both Pt/Mn/Al₂O₃ catalysts are almost identical, while, the slight improvement for conversion is observed at a higher temperatures ($>200^{\circ}\text{C}$) for sample with 0.4 wt.% of Mn. The conversion of n-hexane over Pt/Mn/Al₂O₃ catalysts is not significantly affected by the content of Mn. The activity of Mn/Al₂O₃ catalyst with 0.4 wt.% Mn is higher than that of the Mn/Al₂O₃ catalyst with 0.1 wt.% of Mn. This results point out that Pt/Mn/Al₂O₃ catalytic system require further investigation to clarify the influence of the addition of Mn to the Pt/Al₂O₃ catalysts.

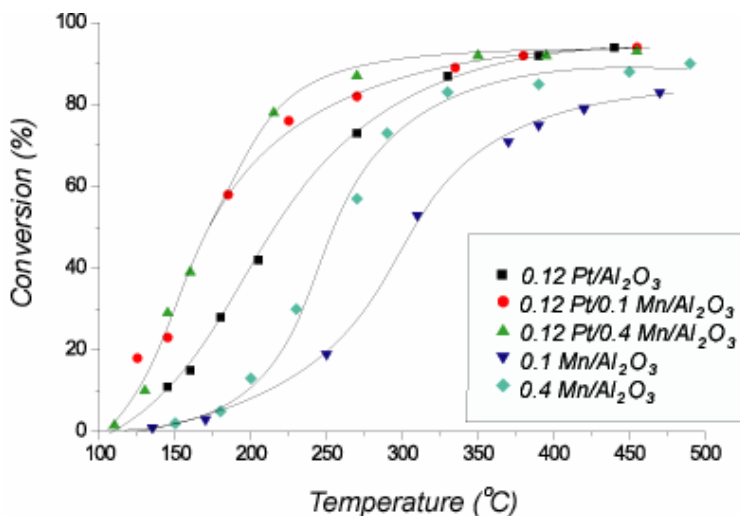


Fig 1 Conversion of n-hexane as a function of temperature for Pt/Al₂O₃, Pt/Mn/Al₂O₃, and Mn/Al₂O₃ catalysts

Acknowledgements:

This research is financed by the Ministry of Science and Technology of Serbia, through the Grant number 1807.

References:

- [1] J.J. Spivey, *Ind. Eng. Chem. Res.*, 1987, 26, 2165.
- [2] M. Baldi, E. Finocchio, F. Milella, G. Busca, *Appl. Catal. B:Env.*, 1998, 16, 43.
- [3] M. Ferrandon, J. Carno, S. Jaras, E. Bjornbom, *Appl. Catal. A:Gen.*, 1999, 180, 153.
- [4] B. Grbic, N. Radic, A. Terlecki-Baricevic, *Appl. Catal. B:Env.*, 2004, 50, 161.

EFFECT OF METAL SUBSTITUTION ON THE PHYSICOCHEMICAL PROPERTIES AND CATALYTIC ACTIVITY IN HYDROCARBON OXIDATION OF Co(VCo)-MCM-41 MOLECULAR SIEVES

V. Parvulescu¹, S. Somacescu¹, S. Todorova², K. Tenchev², G. Kadinov²
and B. L. Su³

¹ *Institute of Physical Chemistry, 202 Independentei Blvd., Bucharest, Romania*

² *Institute of Catalysis, Bulgarian Academy of Sciences,
Acad. G. Bonchev St., Block 11, 1113 Sofia, Bulgaria*

³ *Laboratoire de Chimie des Matériaux Inorganiques, ISIS,
The University of Namur (FUNDP), 61 rue de Bruxelles, B-50 Namur, Belgium*

Abstract

Co- and CoV-modified MCM-41 molecular sieves are prepared by direct synthesis and hydrothermal treatment. Their physicochemical properties are characterized by XRD, N₂ adsorption-desorption, SEM, TEM, TPR, XPS and IRS study of ammonia adsorption. The catalytic activity is tested in liquid phase oxidation of hydrocarbons.

Introduction

Co-containing MCM-41 mesoporous molecular sieves are used as catalysts for selective oxidation of the organic compounds [1, 2]. Their activity and selectivity depend on the localisation of Co species and their surroundings. Incorporation of second metal might therefore create catalysts with new redox and acid properties. In the present study, Co-MCM-41 and VCo-MCM-41 catalysts with various metal loading and V/Co ratio are synthesized directly or by hydrothermal treatment. The obtained materials are characterized by XRD, N₂ adsorption-desorption, SEM, TEM, TPR, XPS and IRS study of ammonia adsorption. The catalytic activity is tested in liquid phase oxidation of cyclohexene, styrene and benzene with hydrogen peroxide.

Results and Discussion

TEM pictures of calcined samples show regular array of mesoporous channels in a hexagonal arrangement (Fig. 1). Well-defined channels with pore diameter of about 3.0 nm and good contrast are observed, differentiating the walls and the internal pores. The morphology of Co-MCM-41 and VCo-MCM-41 samples was studied by SEM, too. After calcination, the materials consist of globular particles of 0.25–0.50 μm in diameter. Both SEM and TEM images show less ordered structure and larger amount of amorphous phase for the samples with high metal content (Co4 -7.4% Co, Co5- 9.2 % Co).

These results are confirmed by XRD and N₂ adsorption. XRD patterns of Co- and VCo-MCM-41 molecular sieves (Fig. 2) show well resolved diffraction lines, characteristic of mesoporous materials with hexagonal channel array, thus indicating a highly ordered pore system of the prepared samples. Variation of Co/Si ratio between 0.02 and 0.1 results in changes of the ordered hexagonal structure of the molecular

sieve and in the surface area. XRD study revealed less ordered hexagonal structure for samples with $M/Si > 0.06$. The surface area and the cell parameter decrease with the increase of the Co/Si ratio.

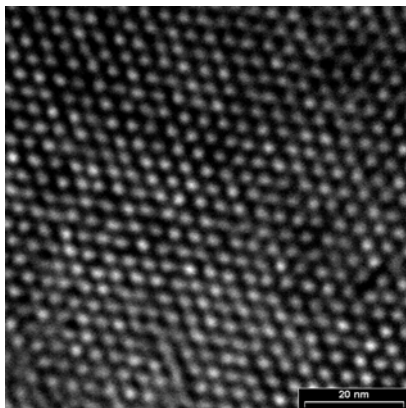


Figure 1. TEM images of VCo₂-MCM-41

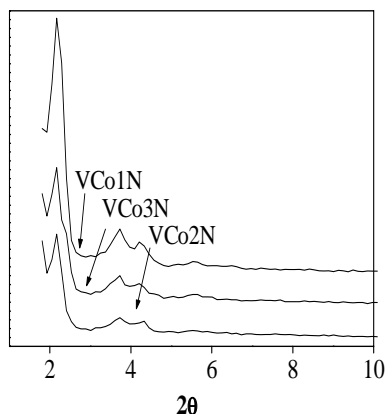


Figure 2. XRD patterns of CoV samples

In the IR spectra of the samples obtained after adsorption of ammonia a sharp negative peak and two bands appear at 3740, 3410 and 3320 cm^{-1} , respectively. A broad band in the range of 2500-3300 cm^{-1} is also registered at about 2970 cm^{-1} for Si-MCM-41 and at 3020 cm^{-1} for metal incorporated samples. The negative peak arises from interaction of weak acid Si-OH group of MCM-41 with ammonia. This interaction shifts the band of the silanol groups towards lower wavenumbers and generate a new broad band. The band shift registered for all mono- or bimetallic incorporated samples is similar ($\Delta\nu = 720 \text{ cm}^{-1}$) but it is smaller than that for MCM-41 ($\Delta\nu = 770 \text{ cm}^{-1}$). The results of IRS study prove the substitution of Si by metal atoms in the MCM-41 framework. They indicate also that the substituting transition metal atoms can modify (weaken) the activity of the silanol groups.

TPR profiles of samples with different metal loading are shown in Fig. 3. The reduction behavior of the catalyst with lowest Co content (1.8% for Co1) exhibits one peak at high temperature 795 K (HT peak). The increase in Co loading up to 7.4% (Co4) results in the appearance of another peak at lower temperature 660 K (LT peak). The HT peak shifts to lower temperature on increase in Co content. The occurrence of several reduction peaks indicates the presence of a number of cobalt species in the catalysts. We suggest that, depending on cobalt loading, two CoO phases differing in interaction with the MCM-41 material could be formed in the samples.

Two reduction zones are seen in the TPR spectra for the bimetal samples show two reduction zones: in the range 600-800K (for CoO phase) and above 900K (reduction of VO_x species). The decrease in the reduction temperature of CoO phase with about 100 K comparing with monometal sample of the same Co content (Fig 3a and 3d), is, most probably, result of lower interaction between CoO phases and the support after incorporation of vanadium. High reduction temperature for VO_x species led us to

the conclusion that V strongly interacts with MCM-41 and is, most probably, incorporated in the framework. Diffuse reflection spectroscopy data confirm this suggestion. The DR spectra exhibit two broad bands at 260 nm and 330 nm associated to oxygen-to-tetrahedral V^{5+} charge transfer transitions, involving oxygen in bridging V–O–Si and terminal V=O position respectively [3].

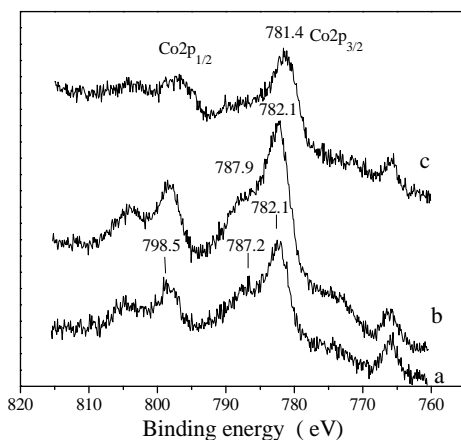
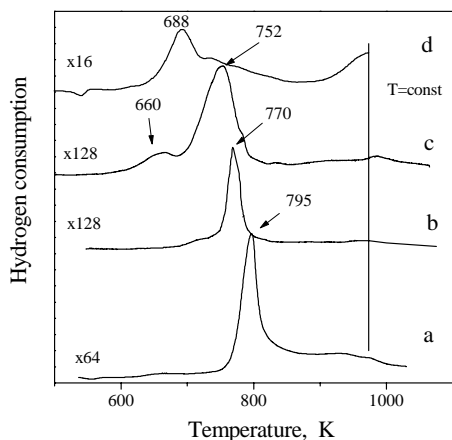


Figure 3. TPR profiles of Co(VCo)–MCM-41:

a. Co1 (1.8% Co); b. Co2 (3.6% Co);
c. Co4 (7.4% Co); d. VCo2 (1.6% V+1.8% Co).

Figure 4. Co 2p XPS spectra of Co–MCM-41 samples: a. Co1; b. Co2; c. Co4.

Fig. 4 shows XPS spectra of the catalysts in the Co 2p region. The presence of Co^{2+} in the Co–MCM-41 samples is confirmed by the Co 2p_{3/2} peak at 782.1 eV, accompanied by relatively intense 3d→4s shake-up satellite peak at 787.5 eV. On increase of the metal loading in the catalyst, the Co 2p_{3/2} peak is shifted to lower binding energy and the satellite peak registered as a shoulder decreases in intensity. DRS study showed a broad band at around 520 nm for all samples with low Co content that is consistent with the presence of Co^{2+} in Td coordination.

Co- and VCo–MCM41 molecular sieves are active in the liquid phase oxidation of cyclohexene, styrene and benzene by H_2O_2 . The selectivity to epoxide, benzaldehyde and phenol, respectively, is very high for all the samples. The catalysts with ordered structure in which cobalt forms a CoO phase strongly interacting with mesoporous silicas are more active in styrene oxidation.

References

- [1] M. Dusi, T. Mallat, A. Baiker, *Catal. Rev. Sci. Eng.*, 2000, 42, 231.
- [2] V. Parvulescu, B. L. Su, *Catal. Today*, 2000, 61, 19.
- [3] St. Dzwigaj, M. Matsuoka, M. Anpo, M. Che, *Catal. Lett.*, 2001, 72, 211.

EFFECT OF L-CYSTEINE ON THE INHIBITION OF Na,K-ATPase ACTIVITY IN THE PRESENCE OF SOME Pd(II) COMPLEXES

K. Krinulović

*Vinča Institute of Nuclear Sciences, P.O.Box 522, 11001 Belgrade,
Serbia & Montenegro*

Abstract

The effects of some Pd(II) complexes on Na,K-ATPase activity in the presence and absence of L-cysteine were studied. The aim of the study was to examine the ability of sulphur-donor ligand (L-cysteine) to prevent and recover the Pd(II) complexes-induced inhibition of Na,K-ATPase. The dose-dependent inhibition of Na,K-ATPase activity was induced in all cases. The addition of 1 mM L-cysteine to the reaction mixture prevented the inhibition. Moreover, the inhibited enzymatic activity was reversed by L-cysteine in concentration-dependent manner.

Introduction

Na,K-ATPase is membrane bound enzyme, which catalyze ATP hydrolysis and plays a key role in the active transport of monovalent cations across the membranes [1]. The activity of this enzyme is very sensitive to the action of various bioregulators. Metal ions binding to enzyme sulfhydryl groups have often been implicated in Na,K-ATPase inhibition [2,3]. It is well known that platinum group elements (Pt, Pd) have great affinity to form complexes with -SH containing ligands. There is lack of data concerning the interaction of Pd(II) complexes with Na,K-ATPase, but literature reference indicate that their Pt(II) analogues inhibit Na,K-ATPase activity [4]. Various palladium complexes are often used as model compounds for their platinum analogues with antitumor activity, since they exhibit about 10^4 - 10^5 times higher reactivates, while their structural and equilibrium behavior is similar [5]. The aim of this work was to study the effects of Pd(II) complexes on Na,K-ATPase activity. In addition, the ability of sulphur-donor ligand (L-cysteine) to prevent and recover the Na,K-ATPase activity inhibition was investigated.

Experimental

Chemicals: All chemicals were of analytical grade. Na,K-ATPase from porcine cerebral cortex was purchased from Sigma Co. Pd(II) complexes, $[\text{Pd}(\text{dien})\text{Cl}]^+$ and $[\text{Pd}(\text{Me}_4\text{dien})\text{Cl}]^+$, were prepared according to the standard procedure[6].

ATPase assay: Na,K-ATPase activity was determined in a standard incubation medium (200 μl), containing 50 mM Tris - HCl (pH 7.4), 100 mM NaCl, 20 mM KCl, 5 mM MgCl_2 and 2 mM ATP and protein (2 mg/ml) in the presence or absence (control) of the desired concentration of Pd(II) complexes. Incubation mixtures were preincubated for 15 min at 37°C. The reaction was started by the addition of ATP, allowed to proceed for 15 min, and interrupted by the addition of the ice cold HClO_4 and imme-

diate cooling on ice. The inorganic orthophosphate (P_i) liberated from the hydrolysis of ATP was measured using modified spectrophotometric procedure [2].

Results and Discussion

Inhibition of Na,K-ATPase activity by Pd(II) complexes

To investigate the interference of $[PdCl_4]^{2-}$, $[Pd(dien)Cl]^+$ and $[Pd(Me_4dien)Cl]^+$ with the activity of Na,K-ATPase, the Pd(II) complexes were added to the reaction mixture in the concentration range from 1×10^{-9} to 1×10^{-2} M. The increasing concentration of complex ions induced inhibition of the enzyme activity relative to the control samples (without Pd(II) complexes). In all cases sigmoid shaped inhibition curves were obtained (Fig. 1.). The half-maximum inhibitory activities (IC_{50}) determined by Hill analysis of the experimental curves were 2.25×10^{-5} M, 1.21×10^{-4} M and 2.73×10^{-4} M, respectively.

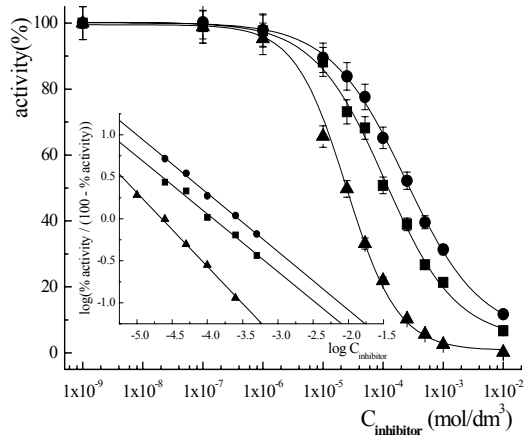


Figure 1. Inhibition of Na,K -ATPase activity by $[PdCl_4]^{2-}$ (▲), $[Pd(dien)Cl]^+$ (■) and $[Pd(Me_4dien)Cl]^+$ (●). Inset: The Hill transformation of the experimental curves.

Prevention and recovery Na,K-ATPase inhibition by L-cysteine

The presence of 1 mM L-cysteine in the reaction mixture prevented enzyme inhibition at Pd(II) complexes concentrations below 1 mM and reduced inhibition at higher concentrations of inhibitors. The IC_{50} values in presence of 1 mM L-cysteine were 1.94×10^{-4} M for $[PdCl_4]^{2-}$, 6.84×10^{-4} M for $[Pd(dien)Cl]^+$ and 1.39×10^{-3} M for $[Pd(Me_4dien)Cl]^+$.

The recovery of the enzyme activities inhibited by Pd(II) complexes was investigated by varying L-cysteine concentrations in the range of 1×10^{-6} - 1×10^{-2} M. The results presented in Fig. 2. show that L-cysteine had a dose-dependent recovery effect on Na,K-ATPase activity exposed to 5×10^{-5} M $[PdCl_4]^{2-}$, 1×10^{-4} M $[Pd(dien)Cl]^+$ or 1×10^{-4} M $[Pd(Me_4dien)Cl]^+$. Full recovery was achieved when concentration of L-cysteine was equal or higher than the Pd(II) complex concentration.

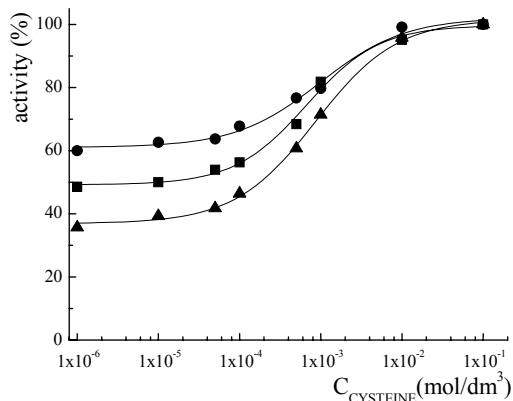


Figure 2. Recovery effect of L-cysteine on the Na,K-ATPase activity in the presence of $5 \times 10^{-5} \text{ M } [\text{PdCl}_4]^{2-}$ (▲), $1 \times 10^{-4} \text{ M } [\text{Pd}(\text{dien})\text{Cl}]^+$ (■) and $1 \times 10^{-4} \text{ M } [\text{Pd}(\text{Me}_4\text{dien})\text{Cl}]^+$ (●).

Conclusion

Comparison of the IC_{50} values for various Pd(II) complexes indicated that their potency to inhibit the enzyme activity depended strongly on ligand of the related compound, as follows $[\text{PdCl}_4]^{2-} > [\text{Pd}(\text{dien})\text{Cl}]^+ > [\text{Pd}(\text{Me}_4\text{dien})\text{Cl}]^+$. Most likely, the reason for such sequence of Na,K-ATPase sensitivity to Pd(II) complexes is steric bulk of the later two complexes that hindered contact of these complexes with enzyme.

The inhibition of Na,K-ATPase by Pd(II) complexes can be prevented or recovered by the addition of L-cysteine. Its potency to reverse Pd(II) complexes induced inhibition of Na,K-ATPase can be attributed to very high affinity of Pd^{2+} for binding to sulphur-donor ligands and formation of stable Pd(II)-cysteine complexes that can't affect Na,K-ATPase activity.

References

- [1] L.A. Vasilites, W. Schwartz, *Biochim. Biophys. Acta*, 1993, 1154, 201.
- [2] V. Vasić, D. Jovanović, D. Krstić, G. Nikezić, A. Horvat, Lj. Vujisić, N. Nedeljković, *Toxicol.Let.*, 1999, 110, 95.
- [3] V. Vasić, K. Krinulović, D. Krstić, T. Momić, A. Horvat, *Monats. Chem.*, 2004, 135, 605.
- [4] B.R. Nechay, S.L. Neldon, *Cancer Treat Rep.*, 1984, 68, 1135.
- [5] T. Rau, R. van Eldik, in *Metal Ions in Biological Systems*, eds. A. Sigel and H. Sigel, Marcel Dekker, New York, 1996, 32, 339-378.
- [6] E.L.J. Breet, R. van Eldik, *Inorg. Chim. Acta*, 1983, 76, L301.

TIME DEPENDENT INHIBITION OF SPMs Na^+/K^+ -ATPase INDUCED BY CADMIUM AND LEAD

D. Kojić and D. Stojić

*Department of Physical Chemistry Institute of Nuclear Sciences "Vinča",
11001 Belgrade, Serbia and Montenegro*

Abstract

In this work, time depended interaction of SPMs Na^+/K^+ -ATPase with Cd^{2+} and Pb^{2+} by single exposure and in the mixture, was investigated. The possibility to selectively detect these ions on the basis on the rate of their interaction with the protein was studied. The decreasing protein concentration increased the sensibility of Na^+/K^+ -ATPase towards both metals. The selectivity was obtained by variation of metal-enzyme contact time.

Introduction

The enzyme Na^+/K^+ -ATPase is integral part of plasma membranes of all higher organisms, especially in synaptic plasma membranes (SPM), and transfer chemical energy of hydrolysis of ATP to potential energy of electrochemical ion gradients [1]. Because heavy metals and many organic compounds inhibit the activity of this enzyme in concentration dependent manner [2], development of respective biosensing system, using this enzymatic system, for selective detection of toxic agents becomes interesting. The measure of ATPase activity is temporal change of the concentration of inorganic ortho-phosphate (P_i) and is usually determined by spectrophotometric methods [3]. Development of test method for inhibitors detection based on the colour reaction for orthophosphate determination seems reasonable. The aim of this work was to investigate the possibility for selective recognition of inhibitors of Na^+/K^+ -ATPase activity by Cd^{2+} and Pb^{2+} based on influence of time on the inhibition of the enzymatic activity.

Experimental

The SPM were isolated from the whole brain of 3-month-old male Wistar albino rats as described previously [4]. Total ATPase activity was determined in a standard incubation medium [2] containing $125\mu\text{g}/\text{ml}$ protein concentration, and final volume of 2 ml containing $12.5\mu\text{g}/\text{ml}$ protein. Incubation mixtures were incubated before enzymatic reaction for different incubation time and metal-enzyme contact time, at 37°C . The enzymatic reaction started with addition of ATP. The concentration of inorganic orthophosphate was determined using the modified spectrophotometric procedure based on the modified stannous chloride method [3]. Na^+/K^+ -ATPase activity was calculated as a difference between the total ATPase and Mg^{2+} -ATPase activities, obtained without NaCl and KCl.

Results and Discussion

The activity of Na^+/K^+ -ATPase was investigated by varying the concentrations of $\text{Pb}(\text{NO}_3)_2$ and $\text{Cd}(\text{NO}_3)_2$ from 1×10^{-9} to 1×10^{-3} M in the reaction mixture containing 125 $\mu\text{g}/\text{ml}$ or 12.5 $\mu\text{g}/\text{ml}$ protein. The tubes were incubated for 10 minutes at 37°C before starting enzymatic reaction. In all cases concentration dependent sigmoidal inhibition curves were obtained. The IC_{50} values (metal ion concentration which produced 50% inhibition of the enzymatic activity) were calculated from experimental results. As the results indicate, in the presence of 125 $\mu\text{g}/\text{ml}$ protein concentration, IC_{50} value was $(2.0 \pm 0.1) \times 10^{-5}$ M for Cd^{2+} and $(1.0 \pm 0.1) \times 10^{-4}$ M for Pb^{2+} . By lowering protein concentration to 12.5 $\mu\text{g}/\text{ml}$ IC_{50} value was also ten fold lower, for Cd^{2+} was $(2.0 \pm 0.2) \times 10^{-6}$ M and $(7.0 \pm 0.3) \times 10^{-6}$ M for Pb^{2+} . However, in the presence of 12.5 $\mu\text{g}/\text{ml}$ protein the metal concentration which produced 50% of enzyme activity inhibition was lower than the maximal allowed concentration of this metal in water [3].

Inhibition of Na^+/K^+ -ATPase activity in the presence of low protein concentration (12.5 $\mu\text{g}/\text{ml}$) was investigated in the presence of 1×10^{-4} M Pb^{2+} , 2×10^{-6} M Cd^{2+} and combination of these metals as a function of the metal-enzyme contact time. Results are present in Fig. 1. The results show that the variation of the contact time (time before starting of enzyme reaction) between the enzyme and metal ions produced the various effects on the enzyme activity. As can be seen from Fig. 1 (curve 1), Cd^{2+} induced about 35% inhibition during the first 5 minutes, by single exposure. The prolonged contact time did not influence the change of the enzyme inhibition. On contrary, in the first five minutes the change of the enzyme activity by single exposure to Pb^{2+} remained in the range of the experimental error (Fig. 1. curve 2). Prolonged contact time caused that inhibition of activity, that continually decreased to 100% after 40 min. Various effects of contact time on the inhibition of Na^+/K^+ -ATPase activity by Cd^{2+} and Pb^{2+} could be explained by the difference in the reaction rate of solvent exchange (water) in coordination sphere of the metal ion during the ligand-protein interaction. Namely, the rate of binding of Cd^{2+} ions to inhibitory sites of enzyme was faster compared to Pb^{2+} ions, and the results show that the equilibration was achieved in the first five minutes. On contrary, the reaction of Pb^{2+} ions with enzyme inhibitory sites was much slower, but this metal exerted more toxic effect, since it inhibited the enzyme activity completely after 40 min exposure. Simultaneous exposure of Na^+/K^+ -ATPase to $\text{Pb}^{2+}/\text{Cd}^{2+}$ showed that both salts induced an additive effect (Fig. 1., curve 3). Experimental data (Fig. 1. open triangle) fit with calculated data (fig. 1. dash line). The results show that the both metals induced the inhibition of the enzyme activity that depended on the metal-enzyme contact time.

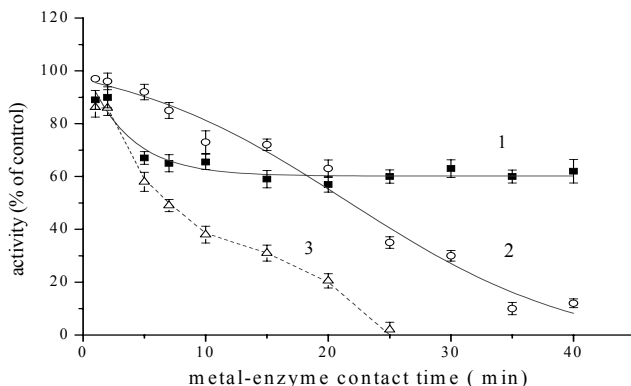


Fig.1 Effect of metal-enzyme contact time on Na^+/K^+ -ATPase activity in presence of $2 \times 10^{-6} \text{M Cd}^{2+}$ (curve 1), $1 \times 10^{-6} \text{M Pb}^{2+}$ (curve 2) and simultaneous exposure $2 \times 10^{-6} \text{M Cd}^{2+}/1 \times 10^{-6} \text{M Pb}^{2+}$ (curve 3-experimental data open triangle and calculated data dash line)

Conclusion

By decreasing protein concentration from $125 \mu\text{g/ml}$ to $12.5 \mu\text{g/ml}$ in standard medium mixture, IC_{50} values of Cd^{2+} and Pb^{2+} induced inhibition of Na^+/K^+ -ATPase decreased ten fold. The variation of metal-enzyme contact time by simultaneous exposure enabled the selective recognition of inhibition induced by these ions. Keeping the short contact time between the mixture of these ions and protein, the inhibition is mainly due to Cd^{2+} ions. The increasing of the inhibition by prolonged contact time under the same experimental conditions can probably be induced by the presence of Pb^{2+} ions.

References:

- [1] G.Rodríguez de Lores Arnaiz, C. Pena, *Neurochim Int*, 1995, 27, 319.
- [2] V.Vasić, K. Krinulović, D. Krstić, T. Momić, A. Horvat, *Monats.Chem.*, 2004, 135, 605.
- [3] Standard Metodes for Examination of Water and Wastwater, 13th ed., American Public Health Association, Washington, 1971.
- [4] A.Horvat, G.Nikezić, J.Martinović, *Experientia*, 1995, 51, 11.

THE MECHANISM OF INTERFERENCE OF SOME Pd(II) COMPLEXES WITH Na,K-ATPase ACTIVITY - KINETIC ANALYSIS

K. Krinulović

*Vinča Institute of Nuclear Sciences, P.O.Box 522, 11001 Belgrade,
Serbia & Montenegro*

Abstract

The effects of some Pd(II) complexes on Na,K-ATPase were studied by kinetic analysis. Na,K-ATPase obeyed Michaelis-Menten kinetics in the absence and presence of $[\text{PdCl}_4]^{2-}$, $[\text{Pd}(\text{dien})\text{Cl}]^+$ and $[\text{Pd}(\text{Me}_4\text{dien})\text{Cl}]^+$. The kinetic parameters (K_m and V_{\max}) showed that Pd(II) complexes are noncompetitive inhibitors of Na,K-ATPase. Based on the values of inhibitor constants (K_i) determined from Dixon plots, we concluded that Pd(II) complex potency to inhibit the Na,K-ATPase activity depends on steric bulkness of its ligands.

Introduction

Na,K-ATPase is transmembrane enzyme that transfers chemical energy of ATP hydrolysis to potential energy for elektrochemical Na^+ and K^+ gradients across the cell membrane [1]. Various metal ions binding to enzyme sulfhydryl groups have often been implicated in inhibition of Na,K-ATPase activity [2]. It is well known that the platinum group compounds inhibit Na,K-ATPase activity due to the interaction with –SH group of proteins [3]. The aim of this work was to investigate the mechanism and kinetic of inhibition of Na,K-ATPase induced by some Pd(II) complexes with various ligands. For this purpose, the influence of MgATP^{2-} , the real substrate for Na,K-ATPase activity in the presence of $[\text{PdCl}_4]^{2-}$, $[\text{Pd}(\text{dien})\text{Cl}]^+$ and $[\text{Pd}(\text{Me}_4\text{dien})\text{Cl}]^+$ complex ions was followed.

Experimental

Chemicals: All chemicals were of analytical grade. Na,K-ATPase from porcine cerebral cortex was purchased from Sigma Co. Pd(II) complexes, $[\text{Pd}(\text{dien})\text{Cl}]^+$ and $[\text{Pd}(\text{Me}_4\text{dien})\text{Cl}]^+$, were prepared according to the standard procedure [4].

Kinetic analysis: Kinetic experiments were carried out according to slightly modified method *Philips et al* [5]. Na,K-ATPase activity, apropos the initial velocity, was determined in a standard incubation medium (200 μl), containing 50 mM Tris – HCl (pH 7.4), 100 mM NaCl, 20 mM KCl, protein (2 mg/ml) in presence or absence (control) of the desired concentration of Pd(II) complexes, as the function of rising substrate (MgATP^{2-}) concentrations (0.15–4.00 mM). Incubation mixtures were preincubated for 5 min. at 37° C. The enzymatic reaction was started by the addition of sub-

strate, allowed to proceed for 2 min, and interrupted by the addition of the ice cold HClO_4 and immediate cooling on ice. The inorganic orthophosphate (P_i) liberated from the hydrolysis of ATP was measured using modified spectrophotometric procedure [2].

Results and Discussion

The kinetic properties of Na,K-ATPase were determined in absence and presence of $5 \times 10^{-5} \text{ M}$ $[\text{PdCl}_4]^{2-}$, $1 \times 10^{-4} \text{ M}$ $[\text{Pd}(\text{dien})\text{Cl}]^+$ and $1 \times 10^{-4} \text{ M}$ $[\text{Pd}(\text{Me}_4\text{dien})\text{Cl}]^+$. The dependence of the initial velocities (v) vs. MgATP^{2-} concentration in the absence and the presence of investigated Pd(II) complexes exhibited typical Michaelis-Menten kinetics which is presented in Fig. 1. Kinetic parameters (V_{\max} and K_m) were derived using Eadie-Hofstee transformation of the experimental data (Fig. 1.inset). As it is shown in Table 1. V_{\max} value in the presence of investigated Pd(II) complexes decreased, while K_m value remained the same compared to the control sample (without Pd(II) complexes). This kind of enzyme behavior in presence of Pd(II) complexes indicated the noncompetitive type of inhibition.

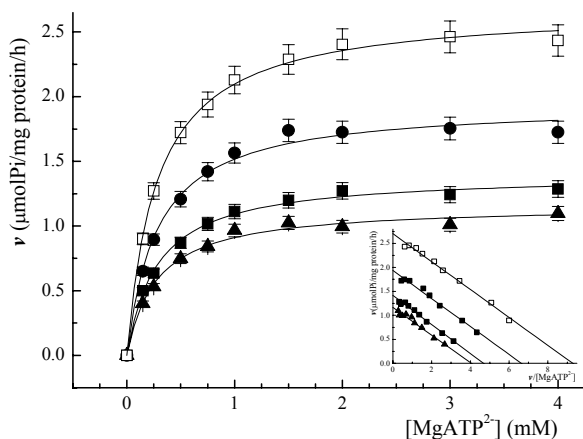


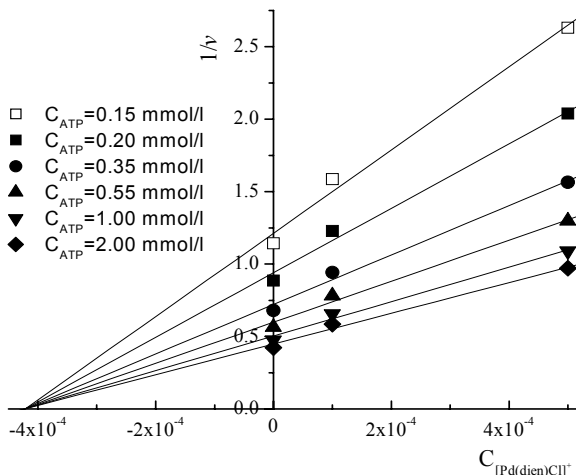
Fig. 1 Na,K-ATPase activity (v) dependence of MgATP^{2-} concentration in the absence (\square) and presence of $5 \times 10^{-5} \text{ M}$ $[\text{PdCl}_4]^{2-}$ (\blacktriangle), $1 \times 10^{-4} \text{ M}$ $[\text{Pd}(\text{dien})\text{Cl}]^+$ (\blacksquare) and $1 \times 10^{-4} \text{ M}$ $[\text{Pd}(\text{Me}_4\text{dien})\text{Cl}]^+$ (\bullet). Inset: The Eadie-Hofstee transformation of the experimental data.

Table 1. Kinetic analysis of Na,K-ATPase activity in the absence (control) and presence of inhibitor

inhibitor	C (M)	K_m (mM)	V_{\max} ($\mu\text{M P}_i/\text{h}/\text{mg}$)	K_i (M)
control	0	0.291 ± 0.010	2.70 ± 0.03	/
$[\text{PdCl}_4]^{2-}$	5×10^{-5}	0.290 ± 0.019	1.17 ± 0.03	3.97×10^{-5}
$[\text{Pd}(\text{dien})\text{Cl}]^+$	1×10^{-4}	0.292 ± 0.011	1.39 ± 0.02	1.04×10^{-4}
$[\text{Pd}(\text{Me}_4\text{dien})\text{Cl}]^+$	1×10^{-4}	0.291 ± 0.015	1.94 ± 0.03	4.19×10^{-4}

To determine Pd(II) complexes potency to inhibit Na,K-ATPase activity the Dixon plots were created (Fig.2.). The reaction velocity was measured at six fixed concentrations of substrate (MgATP^{2-}) in the presence of various inhibitor concentrations in range $0\text{-}5 \times 10^{-4}$. Graphs of the reciprocal velocity against inhibitor concentration were plotted. The inhibitor constants (K_i) of the Pd(II) complexes were read off directly from intersections of lines with x-axis on Dixon plots. The order of K_i values (Table 1.) was $K_i([\text{PdCl}_4]^{2-}) < K_i([\text{Pd}(\text{dien})\text{Cl}]^+) < K_i([\text{Pd}(\text{Me}_4\text{dien})\text{Cl}]^+)$. Apropos, complex potency to inhibit the enzyme activity was $[\text{PdCl}_4]^{2-} > [\text{Pd}(\text{dien})\text{Cl}]^+ > [\text{Pd}(\text{Me}_4\text{dien})\text{Cl}]^+$.

Fig. 2. The Dixon Plot for $[\text{Pd}(\text{dien})\text{Cl}]^+$. The symbols representing MgATP^{2-} concentrations are shown in the inset.



Conclusion

The values of Na,K-ATPase kinetic parameters (V_{\max} and K_m) in absence and presence of some Pd(II) complexes indicated that these complexes were noncompetitive inhibitors of Na,K-ATPase activity. The order of complex potency to inhibit the enzyme activity, deduced from K_i values, was $[\text{PdCl}_4]^{2-} > [\text{Pd}(\text{dien})\text{Cl}]^+ > [\text{Pd}(\text{Me}_4\text{dien})\text{Cl}]^+$. This indicated that Pd(II) complex potency to inhibit the Na,K-ATPase activity depended strongly on ligand of the related compound. Most likely, the reason for such sequence of Pd(II) complexes potency to inhibit Na,K-ATPase activity is steric bulk of the later two complexes that hinder contact of these complexes with enzyme.

References

- [1] L.A. Vasilites, W. Schwartz, *Biochim. Biophys. Acta*, 1993, 1154, 201.
- [2] V. Vasić, D. Jovanović, D. Krstić, G. Nikezić, A. Horvat, Lj. Vujisić, N. Nedeljković, *Toxicol. Let.*, 1999, 110, 95.
- [3] B.R. Nechay, S.L. Neldon, *Cancer Treat Rep.*, 1984, 68, 1135.
- [4] E.L.J. Breet, R. van Eldik, *Inorg. Chim. Acta*, 1983, 76, L301.
- [5] T.D. Philips, A. W.Hayes, I.K. Ho, D. Desiah, *J.Biol.Chem.*, 1978, 253, 3487.

KINETICS OF HEAT DENATURATION OF PEPSIN IN A STRONG ACID MEDIA

V. Pavelkić¹, M. Živanović¹, V. Spasojević – Tišma¹ and M. Ilić²

¹*Vinča Institute of Nuclear Sciences, Department of Physical Chemistry,
POBox 522, 11001 Belgrade,*

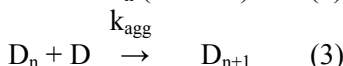
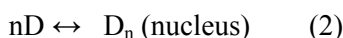
²*Institute of General and Physical Chemistry, Studentski trg 12-16, 11000 Belgrade*

Abstract

Heat aggregation of pepsin, in a strong acid media; involve the stage of nucleation, and the stage of growth of aggregates. The initial parts of the kinetic curves of aggregation were followed via monitoring the increase of absorbance (A) and were linearized as $\{dA/dt; t\}$ and $\{A; t^2\}$ functions. The slope of these curves is proportional to the product rate constant of reversible denaturation and the rate constant of growth of aggregates. Addition of Al^{3+} ions display a lag period whose appearance is caused by intramolecular predenaturational changes in the pepsin molecule.

Introduction

Heat denaturation of proteins is often accompanied by aggregation of denatured protein molecules [1]. Accumulation of aggregates may be easily registered via monitoring the increase of absorbance. According the theory proposed by Patro and Przybycien [2], the initial stage of reversible protein aggregation involves the reaction of nucleation and the reaction of growth of aggregates. Mechanism can be schematically presented as:



where: N and D are the native and denatured states of a protein, respectively.

k_{den} – is the rate constant of denaturation.

N – is the number of "monomer" D participating in the formation of the nucleus.

k_{agg} – is the rate constant of the stage of growth of aggregates.

In this paper we presented the kinetic parameters that follow heat aggregation of pepsin in a strong acid media (pH 2), at 37 °C, and the influence of Al^{3+} on kinetic aggregation of pepsin at the same experimental condition.

Experimental

Porcine pepsin was purchased from Sigma Chem. Co. and used without further purification. Other chemicals were of reagent grade and were prepared prior to use.

UV absorbance measurements were carried out Perkin Elmer, Lambda 35 UV-VIS spectrophotometer with temperature control cell units. The change in absorbance was measured at 280 nm and 37 °C.

Results and Discussion

The kinetic curve of heat aggregation of pepsin at 37 °C and pH 2 is presented in Figure 1A. At sufficiently low values of time (t) the accumulation of denatured form D proceeds linearly in time: $[D] = k_{\text{den}} [N_0] t$, where $[N_0]$ is initial concentration of pepsin (0.015 mM). For initial parts of the kinetic curves registered value of absorbance A is proportional to the amount of aggregates formed and the rate of the change in the A value, dA_{280} / dt is proportional to the product $k_{\text{agg}} [D]$ (Figure 1B.). According to Patro and Przybycien theory [2], and taking into account the linear character of accumulation of the form D, change dA/dt will be proportional to $k_{\text{agg}} k_{\text{den}} [N_0] t$. Integration of this equation shows that at sufficiently low values of time value A become proportional to t^2 (Figure 1C.).

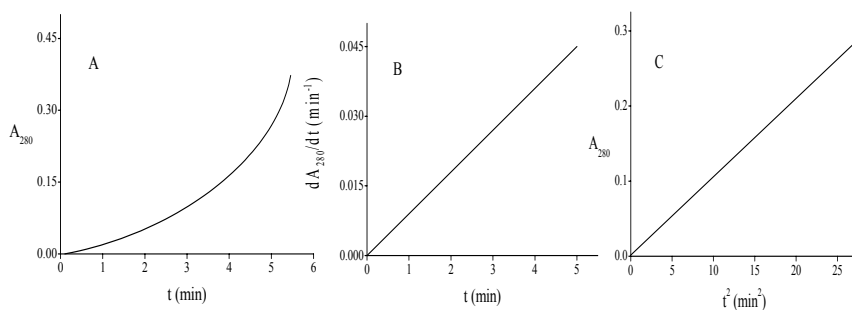


Figure 1. Heat aggregation of pepsin: A. Time dependence of the increase in absorbance of pepsin at 280 nm (pH 2; 37 °C); B and C linearisation in the coordinate $\{dA_{280}/dt; t\}$ and $\{A_{280}; t^2\}$, respectively.

The assumption was that the nuclei concentration remain constant. Calculated values of k_{den} and k_{agg} for pepsin at pH 2 were $(0.0092 \pm 0.0004) \text{ min}^{-1}$ and $(0.0101 \pm 0.0004) \text{ min}^{-1}$ respectively.

Addition of Al^{3+} (0.015 mM) causes a delayed character of the kinetic curve. The appearance of a lag period on the dA/dt versus t curve means that the formation of the denatured form is preceded by the pre-denatural changes in the pepsin molecule [3]. The slope of the linear part of the $(dA/dt) = f(t)$ curve after passing a lag period is proportional to the rate of accumulation of the D form (Figure 2 A and B).

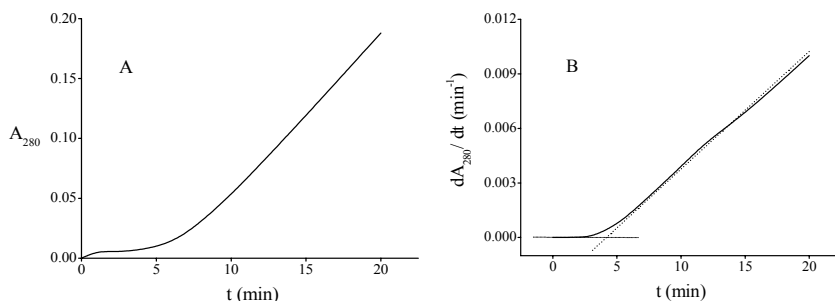


Figure 2. Heat aggregation of pepsin in a presence of Al^{3+} ions; A. Dependence of absorbance at 280 nm on time; B. Linearisation in coordinates $\{dA/dt; t\}$ at $[\text{Pepsin}] = 0.015 \text{ mM}$, and $[\text{Al}^{3+}] = 0.015 \text{ mM}$.

Calculated value of k_{den} of pepsin in a presence of Al^{3+} ions, after 5 min of lag period is (0.00068 ± 0.00005) , i.e. bound Al^{3+} on pepsin slow down the aggregation and lead to stabilization of pepsin molecule.

Conclusion

Heat aggregation of pepsin, in a strong acid media involves the stage of nucleation, and the stage of growth of aggregates. Addition of Al^{3+} causes a delayed character of the kinetic curve and also slow down the aggregation and lead to stabilization of pepsin molecule.

Acknowledgement

Financial support was provided by the MSTD of the Republic of Serbia, Proj. No. 1991.

References

- [1] B.A. Kornialev, B.I. Kurganov, T.B. Eronina, N.A. Chebotareva, N.B. Livanova, V.N. Orlov, V.Y. Chernyak, *Mol. Biol. (Moscow)*, 1997, 31, 82.
- [2] S.Y. Patro, T.M. Przybycien, *Biophysical Journal*, 1996, 2888.
- [3] U. Jakob, H. Lilie, I. Meyer, J. Buchner, *J.Biol.Chem.*, 1995, 270, 7288.

INFLUENCE OF Co(II) AS THE CATALYST ON KINETICS CHARACTERISTICS OF PONCEAU4R OXIDATION BY HYDROGEN PEROXIDE

Z. M. Grahovac, S. S. Mitić and E. T. Pecev

*Faculty of Mathematics and Natural Sciences, Department of Chemistry,
University of Niš, Višegradska 33, 18000 Niš*

Abstract

The paper described the characteristics of the new kinetic method for determination of Co(II), based on its catalytic effect on the oxidation of trisodium-2-hydroxy-1-(4-sulphonato-1-naphthylazo)naphthalene-6,8-disulphonato (Ponceau4R) by hydrogen peroxide in borate buffer. Ponceau 4R(P4R) is food red artificial color which is used like indicatory substance in this investigation, chemical family is mono-azo dye. Under the optimum conditions for the determination of Co(II), kinetic equations for non-catalysed and catalysed reaction were derived. On the basis of these equations, the rate constants for both reactions on three different temperatures calculated. The thermodynamic parameters also were calculated.

Introduction

Cobalt is one of the more important microelement in human body. It is essential element for the function of many vital processes. It has very important influence for the function of enzymes, vitamins and hormones. It is significant in the metabolism of proteins, minerals, and it is important in function of growth and development of cells. Cobalt takes part in the structure of vitamine B₁₂, and function of many enzymes depends on vitamin B₁₂. Therefore it is necessary to control its concentration in food and pharmaceutical samples. [1,2]

There are indicatory reactions which are based on reaction of some organic compounds by H₂O₂ in presence of Co(II) ions like catalyst. [3,4]

Results and Discussion

The investigated reaction rate was followed spectrophotometrically. The absorbance of the solution was measured at the wavelength of 478,4 nm which corresponds to the maximum absorption of P4R in borate buffer at pH 10,50. The dependence of the absorbance (A) on time (t) was measured by Perkin-Elmer Lambda 15 spectrophotometer, connected to a thermochirculating bath. The reaction was carried out in the following way: in first compartment of the special vessel (Budarin vessel) solution of borate buffer was placed, H₂O₂ solution was placed in the second, P4R in the third, and the Co(II) and water (total volume 10 cm³) in the fourth compartment. The vessel was thermostated at 295 K and reaction was initiated by vigorous mixing. During the reaction the initial red color of the reaction mixture disappears. A integral variant of the tangent method was used for the processing of the kinetic data, because of the existing linear correlation between the logA=f(t) (Fig 1.). [5]

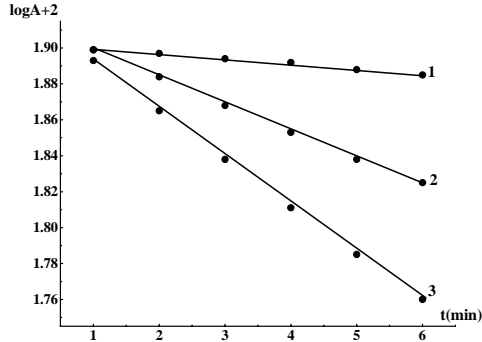


Fig. 1. Dependence of the logarithm of the absorbance of the solution in time.

Initial conditions: $c_{P4R} = 8 \cdot 10^{-6} \text{ mol/dm}^3$; $c_{H_2O_2} = 3 \cdot 10^{-2} \text{ mol/dm}^3$;
 $\text{pH} = 10,50$; $c_{Co(II)} \text{ ng/cm}^3$: 1) 0,00; 2) 11,70; 3) 23,57.

Under the optimal reaction condition: $\text{pH} = 10,50$; $c_{H_2O_2} = 3 \cdot 10^{-2} \text{ mol/dm}^3$;
 $c_{P4R} = 8 \cdot 10^{-6} \text{ mol/dm}^3$; $T = 295 \text{ K}$, the influence of Co(II) ion, as the catalyst, on the kinetics characteristics of the mentioned reaction was investigated. On the basis of the dependence of reaction rate ($\Delta \log A / \Delta t$) of concentration of each reactant, kinetic equations for both process were deduced. [6,7]

For the noncatalyzed reaction (1), and for catalyzed reaction (2):

$$-\frac{dc}{dt} = k_0 \cdot c_{H_2O_2} \cdot c_{H^+}^{-1} \quad (1)$$

$$-\frac{dc}{dt} = k_1 \cdot c_{H_2O_2}^0 \cdot c_{P4R} \cdot c_{H^+}^{-0,65} \cdot c_{Co(II)} \quad (2)$$

k_0 – constant proportional to the rate constant of the noncatalyzed reaction

k_1 – constant proportional to the rate constant of the catalyzed reaction

On the basis of these equations, the rate constants for the noncatalyzed and catalyzed reaction were calculated. (Table 1.)

A linear relationship between the logarithm of the rate constant and the reciprocal of the absolute temperature was found for both reactions. On the basis the slope of this plot in the coordinates $\log k - (1/T)$, the activation energies were calculated. The other thermodynamic parameters at 295 K for both reactions were calculated (Table 2.). [8]

Table 1. The rate constants for the noncatalyzed and catalyzed reaction on the different temperatures

$k_0 \cdot 10^{-7}$	$k_1 \cdot 10^{-2}$	T(K)
4,6	2,31	291
6,57	2,82	295
8,90	3,66	298

Table 2. Thermodynamic characteristics for noncatalysed and catalysed reaction

Reaction	T(K)	E_a^* (kJmol ⁻¹)	ΔH^* (kJmol ⁻¹)	ΔS^* (JKmol ⁻¹)	ΔG^* (kJmol ⁻¹)	pK [*]
P4R-H ₂ O ₂	295	71,77	69,32	-130,93	107,94	19,11
P4R-H ₂ O ₂ -Co(II)	295	33,26	30,80	16,97	28,25	5,00

According to the experimental results, the reaction can be spontaneous even when $\Delta H > 0$, $\Delta S > 0$. Under those conditions, the direction of the reaction will be spontaneous within certain limits of the temperature. Decreasing of E_a^* in catalysed reaction indicate that Co(II) has catalytic effect in this reaction.

Conclusion

In this work the kinetics characteristic of the new kinetic method for determination nanogram amounts of Co(II), which is based on its catalytic effect, are examined. Under the optimal condition of reaction the kinetic equations for catalysed and noncatalysed reaction are calculated. Rate constants for catalysed and noncatalysed reaction are calculated. Other thermodynamic parameters are calculated too, at temperature of 295 K.

References

- [1] J.I. Vučetić, Lj.T. Krstić, Mineralne supstance u ishrani i njihov biološki značaj, Beograd, 2000.
- [2] R.S. Nikolić, Hemija prelaznih metala, PMF, Niš, 2002.
- [3] M. G. Angelova, A. A. Alexiev, Anal. Chim. Acta, 1994, 290, 363.
- [4] G. Zhang, S. Feng, D. Cheng, Microchem. J., 1996, 53, 308.
- [5] H. Müller, M. Otto, G. Werner, Katalytische methoden in der spuren analyse, Leipzig, 1980.
- [6] D. Perez-Bendito, S. Silva, Kinetic Methods in Analytical Chemistry, Ellis Horwood, Chichester, 1998, 261.
- [7] K. B. Yatsimirskii, Kinetic Methods of Analysis, Pergamon press, Oxford, 1966.
- [8] H. Avery, Basic reaction kinetics and mechanisms, Macmillan, 1974.

INVESTIGATION OF THE INFLUENCE OF GLYCINE AS THE INHIBITOR ON THE THERMODYNAMIC CHARACTERISTICS OF 1,2,4-TRIHIDROXYANTRA-QUINONE OXIDATION WITH HYDROGEN PEROXIDE

S. S. Mitić, G. Ž. Miletić and A. N. Pavlović

Faculty of Mathematics and Natural Sciences, Department of Chemistry, University of Niš, Višegradska 33, 18000 Niš, Serbia and Montenegro

Abstract

The paper describes the characteristics of the kinetic method for the determination of trace amounts of amino acid glycine (Gly), based on its inhibiting effect. The catalytic activity of copper in the reaction of oxidation of purpurin (1,2,4-trihydroxy-antraquinone, PP) by hydrogen peroxide in alkaline buffer solution decreases in the presence of micro quantities of glycine, because of the formation of the complex. Under the optimum conditions for the determination of glycine, kinetic equations are proposed for the investigated process. On the basis of these equations, the rate constants for both reactions on three different temperatures were calculated. The thermodynamic parameters also were calculated.

Introduction

In a continuation of our studies of the effect of amino acids on the catalytic oxidation of purpurin [1] this paper describes the influence of glycine as the inhibitor on the thermodynamic characteristics of purpurin oxidation with hydrogen peroxide.

Experimental

The reaction rate was monitored spectrophotometrically by measuring the decrease in absorbance of purpurin at 540 nm. The readings were done on a Perkin-Elmer Lambda 15 UV/VIS spectrophotometer, connected to a thermo-circulating bath. pH measurements were carried out using Hanna instruments pH meter. The reaction was carried out in the following way: In the reaction-mixture vessel with four compartments, the solution of purpurin and buffer was placed in one compartment, hydrogen peroxide in the second, cobalt (II) in the third, and glycine and water (total volume 10 cm^3) in the fourth compartment. The solutions were thermostated at $22 \pm 0.1\text{ }^\circ\text{C}$ before the beginning of the reaction.

A tangent method [2] was used for the processing of the kinetic data. The reaction rate was followed by changing the absorbance vs. time with slope = dA/dt .

Results and Discussion

Under the optimal reaction conditions ($c_{pp} = 1 \times 10^{-5}\text{ mol dm}^{-3}$, $c_{buffer} = 0.13\text{ mol dm}^{-3}$, $c_{H_2O_2} = 1.2 \times 10^{-3}\text{ mol dm}^{-3}$, $c_{Co(II)} = 15\text{ ng cm}^{-3}$, $pH = 10.25$, $t = 22 \pm 0.1\text{ }^\circ\text{C}$), the influence of glycine as the inhibitor on the thermodynamic characteristics of the mentioned reaction was investigated. The following kinetic equations for the investigated process were deduced on the basis of the graphic correlations obtained.

For the catalytic reaction :

$$-dc_{PP} / dt = k_1 \cdot c_{PP} \cdot c_{buff} \cdot c_{H_2O_2} \cdot c_{H_3O^+}^{-0.4} \cdot c_{Co^{2+}}$$

For the inhibited reaction :

$$-dc_{PP} / dt = k_2 \cdot c_{PP} \cdot c_{buff}^{-1} \cdot c_{H_2O_2} \cdot c_{H_3O^+}^{-0.1} \cdot c_{Co^{2+}} \cdot c_{Gly}^{-1}$$

k_1 - rate constant of the catalytic reaction

k_2 - rate constant of the inhibited reaction

On the basis of these equations, the rate constants for the inhibited and catalytic reactions were calculated. (Table 1)

Table 1. The rate constants for the catalytic (1) and inhibited (2) reaction on the three temperatures

$k_1 \times 10^{-3} (mol dm^{-3})^{1-n} s^{-1}$	$k_2 (mol dm^{-3})^{1-n} s^{-1}$	T (K)
1.09	0.67	292
1.52	1.0	295
2.04	1.32	298

n -order of the reaction

The activation energies were calculated from linear regression analysis of Arrhenius plots. The other thermodynamic parameters for the conversion of reactants into activated complex at 22 °C (295 K) for both reactions also were calculated. [3] (Table 2)

Table 2. Thermodynamic characteristics for the conversion of reactants into activated complex for catalytic and inhibited reaction

Reaction	T (K)	E_a (kJ mol ⁻¹)	ΔH^* (kJ mol ⁻¹)	ΔS^* (J mol ⁻¹ K ⁻¹)	ΔG^* (kJ mol ⁻¹)	pK [*]
PP-H ₂ O ₂ -Co(II)	295	86.1	83.7	99.7	54.3	9.6
PP-H ₂ O ₂ -Co(II)-Gly	295	91.9	89.4	22.2	82.9	14.7

Conclusion

The inhibitory effect of glycine is the results of the complexation with Co(II) ions, which decreases the amount of Co(II) available for the reaction with PP-H₂O₂.

The concept of entropy of activation (ΔS^*) is of utmost importance for an understanding of reactivity. The entropy of activation corresponds to the difference in entropy between the ground and transition states of the reactants. Positive ΔS^* suggests that the transition state is more disordered (more translational, vibrational and rotational degrees of freedom) than the ground state. When more molecules interact at the onset of a chemical reaction and pass into a more structured transition state, some of these degrees of freedom will be lost. For this reason entropy of activation for inhibited reaction is less positive. The reduction of the entropy also can be explained by the formation of the activated complex which is charged [PP-H₂O₂-Co²⁺-Gly]^{*}. The solution molecules, that is the water, surrounding this particle showing the strong interaction with it, and in that way reduce the movement possibility. This effect, known as "tight solvent", leads to the reduction of entropy, which will be less positive if the charge of the complex is higher.

Acknowledgment

This research was supported by grant number 1211 from the Ministry of Sciences and Technology of Serbia.

References

- [1] S. S. Mitić, G. Ž. Miletić, A. N. Pavlović, S. B. Tošić, J.Serb.Chem.Soc., 2002, 67, 783.
- [2] D. Perez-Bendito, M. Silva, Kinetic Methods in Analytical Chemistry, Ellis Horwood, 1988.
- [3] P.W. Atkins, The Elements of Physical Chemistry, Oxford Univer. Press, 1996.

pH DEPENDENT KINETICS OF [PdCl(dien)]⁺ REACTION WITH SOME AMINO ACIDS IN THE PRESENCE OF SDS

M. Živanović¹, V. Vasić¹ and M. Čakar²

¹*Vinča Institute of Nuclear Sciences, POB 522, 11001 Belgrade*

²*Faculty of Pharmacy, POB 146, 11001 Belgrade, Serbia & Montenegro*

Abstract

We examined the micellar effects on the mechanisms of complex formation between [PdCl(dien)]Cl and amino acids L-cysteine and Gluthathione in the pH range from 0.5 to 3.5. In the presence 1×10^{-2} M sodium dodecyl sulphate micelles (SDS) the strongest effect on the reaction rate around pH 2 was observed.

Introduction

Gluthathione (GSH) and amino acid L-cysteine are sulfur containing ligands that belong to the group of biomolecules exerting the great role in thiol dependent biochemical reactions. The both are highly reactive towards platinum complexes revealing the effective antitumor activity [1]. The Pd(II) complexes with various tridentate ligands are suitable model systems for the investigations of the reaction mechanism of Pt(II) anticancer drugs with amino acids, since they exhibit about $10^4 - 10^5$ times higher reactivity, while their structural and equilibrium behavior is similar [2]. So far, kinetics of the reactions of several Pt(II) and Pd(II) complexes with sulfur bonding molecules have been reported [3-4]. We focussed on the investigation of the effects of micellar systems on the reactions of Pd(II) and Pt(II) coordination compounds with thiols [5]. Although the micelles do not influence the stoichiometry and mechanism of the complex formation [5-9], the reaction rate was found to be strongly dependent on the presence of the surfactant. These studies are important for better understanding of exchange reactions on the surface of biomembrane or at the interface of a globular protein.

Experimental

The complex [PdCl(dien)]Cl was prepared according to standard procedure [10]. Ligand stock solutions (1×10^{-2} M GSH and L-cysteine) were prepared in 0.1 M HClO₄ shortly before use. The acidity was controlled by addition of Britton-Robinson buffer. The ionic strength was kept constant using NaClO₄.

All measurements were performed on Beckman 5260 UV VIS spectrophotometer. pH values of the solutions were measured by a Metrohm pH - meter, Model 713. For the stopped-flow experiments, the universal rapid kinetic accessory HI-TECH model SFA 12 was fitted to a spectrophotometer. Kinetic experiments were performed by mixing equal volumes of the [PdCl(dien)]⁺ complex and thiol solutions. The rate of the complex formation was followed by monitoring the increase of the absorbance at 250 nm, for L-cysteine and 260 nm for GSH as a function of time for at

least eight half-lives. Values of k_{obs} were determined by fitting the experimental trace (A vs. t) to the function $(A_f - A)/(A_f - A_0) = \exp(-k_{\text{obs}}t)$ (A_0 and A_f were the initial and final absorbancies, respectively).

Results and Discussion

The kinetics of the formation of the $[\text{Pd}(\text{dien})(\text{thiols})]^+$ in the presence and in the absence of 1×10^{-2} M micelle forming surfactant SDS was followed at different acidities (pH range from 0.5 to 3.5) in the temperature range from 276 to 298 K under pseudo-first-order conditions ($[\text{thiols}] \gg [\text{PdCl}(\text{dien})]^+$). The experimentally determined rate constants (k_{obs}), calculated from the exponential kinetic curves, followed the simple rate expression common for the substitution reactions of square-planar complexes, according to the eq. 1:

$$k_{\text{obs}} = k_f [\text{L}_f] + k_b \quad (1)$$

where k_f and k_b are the forward and reverse pH dependent rate constants, respectively.

The bell shaped pH profile of the forward rate constants (k_{obs}) was obtained for the reaction of thiols with $[\text{PdCl}(\text{dien})]^+$ in the presence of SDS micelles over the investigated temperature range (Fig. 1).

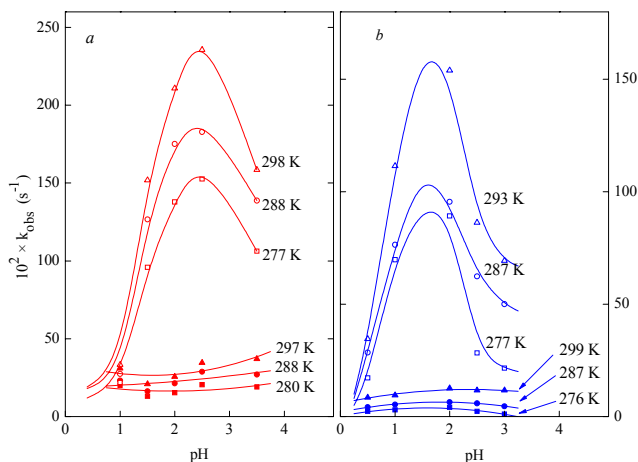


Fig. 1 pH profiles of the observed rate constant (k_{obs}) for the formation of the (a) $[\text{PdCl}(\text{dien})]^+$ -L-cysteine complex, $c_{\text{thiol}}=5 \times 10^{-4}$ M, $c_{\text{Pd}}=1 \times 10^{-5}$ M; (b) $[\text{PdCl}(\text{dien})]^+$ -GSH complex, $c_{\text{thiol}}=5 \times 10^{-5}$ M, $c_{\text{Pd}}=1 \times 10^{-6}$ M in the presence (solid symbols) and in the absence (open symbols) of 1×10^{-2} M SDS at various temperatures.

On the contrary, the reaction rates do not significantly depend on pH in the absence of SDS. The obtained results indicated that the SDS micelles have the strongest effect on the reaction rate around pH 2, *i.e.* at the acidity corresponding to the pK_a

values of the dissociation of -COOH groups. Also, acceleration of complex formation up to one order of magnitude can be observed in the presence of the SDS micelles compared to results obtained in aqueous medium. Acceleration of the complex formation between $[\text{PdCl}(\text{dien})]^+$ and L-cysteine or GSH can be explained as a result of the increased concentration of the reactants in the vicinity of the anionic micelles. The anionic micelles provide a dispersed negatively charged surface in solution.

Conclusion

The positively charged $[\text{PdCl}(\text{dien})]^+$ ions will partition out of the bulk aqueous phase into the surface region of the micelles. On the other hand, both ligands are protonated below pH 2 because the dissociation of the -COOH group occurs above pH 2 where formation of zwitterions takes place.

Acknowledgement

Financial support was provided by the MSTD of the Republic of Serbia, Proj. No. 1991.

References

- [1] Cisplatin. Chemistry and Biochemistry of a leading Anticancer Drug, Ed. B. Lippert, Verlag Helvetica Chimica Acta/Wiley-VCH, Zürich/Weinheim, 1999.
- [2] T. Rau and R. van Eldik, Metal Ions in Biological Systems, eds. A. Sigel, H. Sigel, Marcel Dekker, New York, 1996, 32, 339.
- [3] Ž. D. Bugarčić, M. Shoukry and R. van Eldik, J. Chem. Soc. Dalton Trans., 2002, 3945.
- [4] Ž. D. Bugarčić, F. W. Heinemann and R. van Eldik, J. Chem. Soc. Dalton Trans., 2004, 279.
- [5] V. Vasić, M. Čakar, J. Savić, B. Petrović, J. Nedeljković, Ž. Bugarčić, Polyhedron, 2003, 22, 279.
- [6] V. M. Vasić, M. S. Tošić, J. M. Nedeljković, J.Phys.Org.Chem., 1996, 9, 398.
- [7] M. S. Tošić, V. M. Vasić, J. M. Nedeljković, Lj. Ilić, Polyhedron, 1997, 16, 1157.
- [8] V. M. Vasić, M. S. Tošić, T. Jovanović, Lj. Vujisić, J. M. Nedeljković, Polyhedron, 1998, 17, 399.
- [9] V. M. Vasić, J. M. Nedeljković, J.Serb.Chem.Soc., 1994, 59, 157.
- [10] E. L. J. Breet and R. van Eldik, Inorg. Chim. Acta, 1983, 76, L301.

THE METHOD OF INVESTIGATION OF STEADY STATES NUMBER IN KINETICS OF CATALYTIC REACTIONS

E. S. Patmar and N. I. Koltsov

*Department of Physical Chemistry, Chuvash State University,
Moskovskii prospect 15, 428015 Cheboksary, Russia*

Abstract

The method of the estimation of internal steady states number both upper and lower is described in this paper. This method helps to determine the real number of internal steady states for concrete catalytic reactions.

Introduction

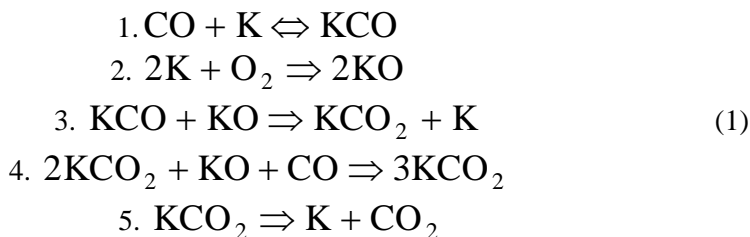
One of the important problems of reaction kinetics of catalytic reactions characterised by critical phenomena is the investigation of their internal steady states (ISS) – steady states having no zero coordinates. The wide-spread way of investigating ISS is constructing kinetic curves in the coordinates - rate (r) to one of reagents (C_A) concentration. The kinetic curves can, have complex form of S - hysteresis, isola, self-crossing and mushroom. The characteristic peculiarity of these curves is the possibility of existing not less than three ISS, two of them are stable and one is unstable. Besides the above- mentioned curves there can exist kinetic curves of more complex form. This proves that more than three ISS can appear.

Results and Discussion

Below the method of the estimation of ISS number both upper and lower is described. The lower bound is based on the action that at first an arbitrary stage complex of the investigated scheme is taken, the boundary steady stages (BSS) number is analysed, SS have at least one zero coordinate. Then the types (zero coordinates number) of these BSS are determined. After that the investigated mechanism stages (not included into the initial stage complex) are added in succession. The appearing of new BSS and the motion direction of the obtained at the previous stage BSS in a reaction simplex are fixed. There are some cases. If a BSS type does not decrease, then ISS formation does not take place. If the type decrease, then the possibility of BSS converting into ISS arises. Sometimes it converts into the non-physical region (one of the coordinates becomes negative). It is worth noting that BSS can disappear, that is it transfers into a complex plane. This happens, however, if BSS is multiple. This is a rare case because multiple roots are degeneration ones. The previous ISS can disappear but we are able to avoid it if to take small values of rate constants of added stages. Thus, adding stages in succession we get a mechanism at each step which approaches to the initial one. The number at some steps can increase, this helps to estimate the lower bound of the ISS number for the reaction initial mechanism.

The ISS upper bound estimation is the following. For example, there is an algebraic equation system which describes the stationary behaviour of a concrete catalytic reaction. At first this equation system is brought to a trinomial form. Let some equation has more than three terms (monomials). Let's choose any two terms and take a new variable which is equal to these monomials sum. Then in the initial equation the term number decreases by unity because instead of two terms a new one equal to their sum appears. Having done this action several times, we get a system in which every equation has not more than three members. Then the base variable and equation are selected, the differentiation of the base equation via the base variable take place. We get an equation of, the initial system variables and their derivatives. To find these derivatives the equation system which is obtained from the initial one by excluding the base equation is differentiated. The number of solutions of the initial system is not more than by unity surpasses the number of solutions of the obtained system. Consequently, the analysis of the obtained system decision shows if this system can have two solutions. If the obtained system is unsolvable, then the research work is over. If it is solvable, then with the new system (after some steps of the above-mentioned procedure) we learn if the initial system has tree solutions.

Let's analyse the application of this method for a reaction of carbon monoxide catalytic oxidation proceeding via the following scheme:



where K are active centres on the catalyst surface. Having applied the above described methods to scheme (1), we get the data that the ISS lower bound is equal to six and upper bound is equal six too. This results in the fact that the maximal possible ISS number for an experimental reaction is equal to six. Fig. 1 illustrates this fact.

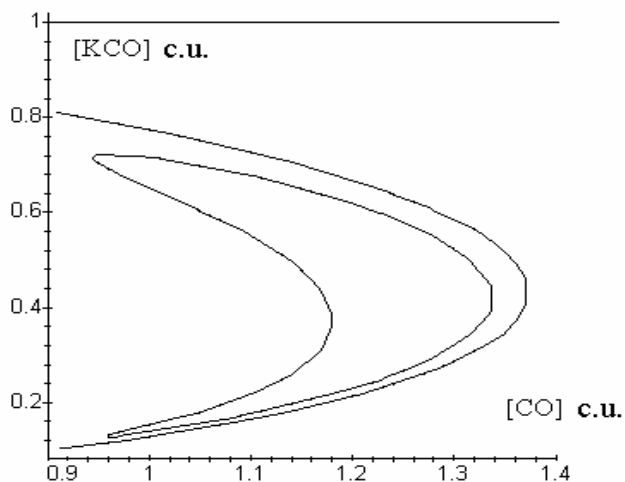


Fig. 1 The dependence of the concentration of adsorbed carbon monoxide on the catalyst surface on the concentration of gas CO

Thus, we have developed the method which can be used for ISS number estimation of catalytic reactions. With its help stage schemes describing $r(C_A)$ kinetic dependencies are established.

THE REACTIVE INTERMEDIATES OF Cr^{III}(SALEN) CATALYZED ASYMMETRIC EPOXIDATION OF ALKENES AND Fe^{III}(SALEN) CATALYZED ASYMMETRIC OXIDATION OF SULFIDES

K.P. Bryliakov and E.P. Talsi

*G. K. Boreskov Institute of Catalysis, Siberian Branch of the Russian Academy of Sciences,
630090 Novosibirsk, Russian Federation.*

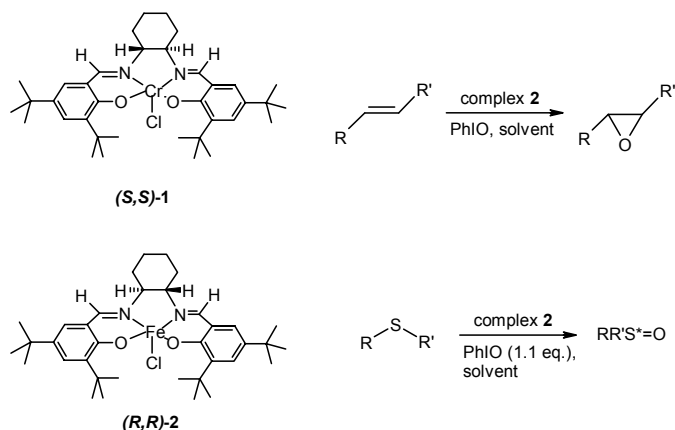
Abstract

In this work, the active intermediates of two catalytic systems for asymmetric oxidation of organic substrates by iodossylbenzene (PhIO) were studied by ¹H NMR and EPR spectroscopy. In the system for enantioselective epoxidation of alkenes, catalyzed by Cr^{III}(salen)Cl, high-valence chromium intermediates of epoxidation reactions were detected and characterized by EPR and NMR. They are the reactive mononuclear oxochromium(V) intermediate (**A**) Cr^VO(salen)L (where L= Cl or a solvent molecule) and inactive chromium-salen binuclear complex (**B**) which acts as a reservoir of the active species. As the second part of the work, a new catalytic system for enantioselective oxidation of sulfides was proposed (catalyzed by Fe^{III}(salen)Cl) and oxidation of several sulfides carried out with high conversion and selectivity (up to 99%) and moderate to good enantioselectivity (*ee* up to 62%). The active intermediate was detected and shown to be a iodossylbenzene-iron(III)(salen) complex.

Introduction

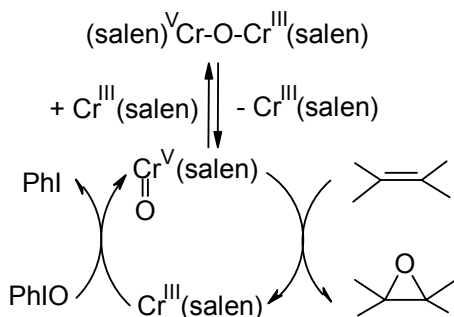
Metal-salen complexes (metals are Mn^{III}, Cr^{III}, Co^{II} etc.) are widely used in catalytic asymmetric synthesis. Chromium-salen complexes are well-known catalysts of stereoselective alkene epoxidations [1], [2], to give enantiomeric excess (*ee*) up to 92 % in epoxidation of *E*-β-methylstyrene. However, except the works of Kochi [3-4] there have not been mechanistic studies of its catalytic action. As distinct from the manganese-salen alkene epoxidations, the established oxygen transferring Cr^V=O species is relatively stable and EPR active [3]. These facts, as well as our previous experience in EPR and ¹H investigation of Cr^{III}(salen) catalysts [5] stimulated mechanistic investigations by EPR and ¹H NMR.

In recent years, growing interest in iron-catalyzed asymmetric sulfide oxidation appears, due to availability and non-toxicity of these catalysts [6]. Recently, a mechanistic study of non-stereoselective [(salen)Fe^{III}Cl] catalyzed oxidation of sulfides with iodossylbenzene has been published [7]. In our group, asymmetric version of this system was developed and studied, and the mechanism of its catalytic action was clarified by using ¹H NMR and EPR spectroscopy. Some of the complexes studied are presented below.



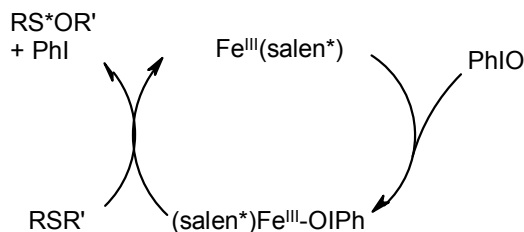
Results and Discussion

In $\text{Cr}^{\text{III}}(\text{salen})$ system, two EPR active high valence chromium species are formed upon stirring of complex **1** with PhIO in dry acetonitrile. The first one denoted as **A** (green solution, $g = 1.970$, $a_{\text{Cr}} = 19.3$ G, natural abundance of ^{53}Cr 9.55%, $I = 3/2$) is unstable and almost completely decays within 3h at room temperature. The other complex denoted as **B** (brown solution) is more stable ($g = 1.976$, $a_{\text{N}} = 2.1$ G, $a_{\text{Cr}} = 19.3$ G, natural abundance of ^{53}Cr 9.55%, $I = 3/2$). By using ^1H NMR, EPR and UV-Vis/NIR spectroscopy they have been characterized and identified as $\text{Cr}^{\text{V}}\text{O}(\text{salen})\text{L}$ (**A**, where $\text{L} = \text{Cl}^-$ or a solvent molecule) and inactive chromium-salen binuclear complex $\text{L}_1(\text{salen})\text{Cr}^{\text{III}}\text{OCr}^{\text{V}}(\text{salen})\text{L}_2$ (**B**, $\text{L}_1, \text{L}_2 = \text{Cl}^-$ or solvent molecules). The latter mixed-valence binuclear species acts as a reservoir of the active species. Reactivity of the $\text{Cr}^{\text{V}}\text{O}(\text{salen})\text{L}$ complex towards *E*- β -methylstyrene was measured in DMF at 290 K to give the second-order rate constant $1.3 \pm 0.3 \cdot 10^{-4} \text{ l} \cdot \text{mol}^{-1} \cdot \text{s}^{-1}$. Based on the results obtained, the catalytic cycle for this process was proposed:



In the second system, the catalysts proposed demonstrated high activity towards alkylarylsulfides (at least 200 turnovers within 2h without loss of enantioselectivity). Complex *(R,R)*-**2** affords *S*-sulfoxides; the highest enantioselectivity was achieved in CH_3CN at 0°C (with benzylphenylsulfide). Further ligand adjustment

seems to be possible for improving *ee*. The active species was detected and characterized by ^1H NMR at low temperature (-20 to 0 °C). After shaking of complex **2** with PhIO in CDCl_3 upon cooling, formation of a new Fe(III) complex is observed, although no PhI can be detected by ^1H NMR. The new Fe(III) complex is unstable: if the substrate (*p*-BrPhSMe) was added, the corresponding sulfoxide and PhI formed, and concentration of the intermediate decreased. Thus, the intermediate is a iodosylbenzene-iron(III)(salen) complex. Recently, similar iodosylbenzene-iron(III) porphyrin intermediates have been discussed in the literature [8]. The catalytic cycle for $\text{Fe}^{\text{III}}(\text{salen})$ catalyzed sulfide oxidation was proposed.



Acknowledgment

This work was supported by the Russian Foundation for Basic Research, grant 03-03-32009.

References

- [1] C. T. Dalton, K. M. Ryan, V. M. Wall, C. Bousquet, G. G. Gilheany, *Topics in catalysis*, 1998, 5, 75.
- [2] H. Imanishi, T. Katsuki, *Tetrahedron Lett.*, 1997, 38, 251.
- [3] E. G. Samsel, K. Srinivasan, J.K. Kochi, *J. Am. Chem. Soc.*, 1985, 107, 7606.
- [4] K. Srinivasan, J. K. Kochi, *Inorg. Chem.*, 1985, 24, 4671.
- [5] K. P. Bryliakov, M. V. Lobanova, E. P. Talsi, *J. Chem. Soc. Dalton Trans.*, 2002, 2263.
- [6] J. Legros, C. Bolm, *Angew. Chem. Int. Ed. Engl.* 2003, 115, 5645, and references therein.
- [7] V. K. Sivasubramanian, M. Ganesan, S. Rajagopal, R. Ramaraj, *J. Org. Chem.*, 2002, 67, 1506.
- [8] J. P. Collman, A. S. Chien, T. A. Eberspacher, J. I. Brauman, *J. Am. Chem. Soc.*, 2000, 122, 11098, and references therein.

KINETICS OF SiO₂ DISSOLUTION IN NaOH AQUEOUS SOLUTION

M. Stanković, L. Pezo, B. Kovačević¹, N. Rajić, M. Jovanović²
and D. Debeljković³

¹Eng. Dept. Holding Institute of General and Physical Chemistry, Studentski trg 12/V, Belgrade,

²Faculty of Technology and Metallurgy, Karnegijeva 4, Belgrade,

³Faculty of Mechanical Eng., 27. marta 80, Belgrade, Serbia and Montenegro

Abstract

Silica dissolution in aqueous NaOH, corresponding to the ratio SiO₂/Na₂O=2, is a complex process at elevated temperatures and high pressure. However, it is desirable to have a simple model for predictive purposes. In this study several kinetics models were developed, and compared with experimental results. As a first approximation, the silica was assumed to be smooth spheres, which decreased in size, as dissolution proceeds. The influence of the particle size, the operating temperature and the hydroxide ion molality on the kinetic rate were studied. It is certain that these models can be used to correlate the experimental data on dissolution.

Introduction

Production of sodium silicate in a pressure reactor, i. e. wet process, according to the following reaction: $y\text{SiO}_{2(\text{sd})} + \text{NaOH} \rightarrow \text{Na}_2\text{Si}_y\text{O}_{3+y}$, has increased over the last ten years, /1,2,3/. The compound corresponding to $y=2$, i. e. SiO₂/Na₂O=2 (silicate module), is used as a supplement in detergent manufacture, because of the good buffering action of silicates, and raw material for detergent zeolite 4A production. For the optimization of the process, kinetic data obtained from experimental data are of great importance, as well as reaction temperature and the size of sand particles. Chemical process model of SiO₂ dissolution in NaOH aqueous solution, is used for better understanding of steps by which process is been carried out, which parameters are more important, and how many parameters are present in the system. Confirmation of the model, as well as the mechanism should be done by experimental results. Within this article a few kinetics models should be presented: one empirical model, and four shrinking core models.

Experimental

Experiments were carried out with sand (average particle size 250 μm), and minimum SiO₂ content of 97%. The sodium hydroxide solution of 12.5 mol/kg were used, prepared from pure reagent – grade sodium hydroxide dissolved into distilled water. For the sand used in this work, the specific surface area was evaluated at approximately 200 cm²/g, which indicate low porosity. Amounts of sand (m_0), and NaOH solution, corresponding to the molar ratio SiO₂/Na₂O=2 were introduced into a 2l autoclave (Parr). The temperature was regulated at 220 °C, and checked with thermocouple. The autoclave is equipped with agitator. At the end of each experiment, the autoclave was quenched into water. The mixture was filtered and the un-reacted sand was washed with hot water until the filtrate became non – basic. The remaining solid (m) was dried and weighed. Measured parameters (m_0 , m , T , R) are used for evaluation of calculated parameters ($\alpha(t)$, $r(t)$, S).

Mathematical model

In the case of mathematical modeling of SiO₂ dissolving in NaOH solution, under high pressure and temperature, a few different approach can be presented: empirical model, shrinking core model using diffusion expression of kinetics, shrinking core model using assumption that

at the beginning of reaction the system is controlled by chemical reaction, modified shrinking core model and variable activation energy shrinking core model.

The experimental results can be described by different empirical functions. Using the mean standard deviation between model predictions and experimental data as test, the following expression can be used to predict kinetic data, [1,2]:

$$\alpha = a \cdot [1 - \exp(-b \cdot t)] + c, \quad (1)$$

where: a , b , c are adjustable parameters, which are calculated from experimental values, and

$\alpha = \frac{m_0 - m}{m_0}$ - degree of conversion, m_0 - initial mass of silica, m is the mass of un-reacted silica

at time t . Using experimental results, diagram on Fig. 1, continuous line, was plotted, and adjustable parameters were found.

Using geometrical equation for particle radius in time t :

$$r(t) = R \cdot \sqrt[3]{1 - \alpha}, \quad (2)$$

it is possible to plot the radius change diagram, Fig. 2, continuous line. This diagram shows that a large radius of particle remains even when degree of conversion reaches 99%, which does not represent the real nature of this process. That is why some shrinking core approach is used later on.

In shrinking core model using diffusion expression of kinetics, the mole variation of SiO_2 with time is, [1,2]:

$$\frac{dn}{dt} = \frac{D \cdot (C_m - C_s)}{\delta} \cdot \frac{4\pi r^2}{\sigma}, \quad (3)$$

where D is the diffusion coefficient of OH^- , C_m is the OH^- concentration in the bulk of solution, and C_s is the OH^- concentration on the particle surface.

By combining equation (3) with equation for degree of conversion α it is possible to plot a diagram of degree of conversion, shown on Fig. 1, with dashed line.

In shrinking core model using assumption that at the beginning of reaction the system is controlled by chemical reaction, it is possible to write, [1,2]:

$$\frac{d\alpha}{dt} = k \cdot S \cdot [\text{OH}^-]^\gamma, \quad (4)$$

where k is the kinetic constant, γ - the reaction order, with respect to OH^- . Using this equation, it is possible to plot a diagram shown on Fig. 1, with dashed - dotted line.

Modified shrinking core model has been proposed to describe the kinetic of dissolution of sand into sodium hydroxide solutions, under experimental conditions (220°C, 27.5 bar), close to those in the industry of the wet - process sodium silicate production. The attention was directed to the effect of particle size on the reaction rate. The experimental kinetic data were analyzed to determine the controlling mechanisms.

When the rate - limiting step is a surface reaction, the reaction rate can be expressed by the following equation, [3]:

$$m_0 \cdot \frac{d\alpha}{dt} = y \cdot k^0 \cdot S \cdot C_{\text{OH}^-}^b \cdot \exp\left(-\frac{E_a}{R \cdot T}\right), \quad (5)$$

where: y - stoichiometric coefficient, k^0 - a constant factor, S - surface area, E_a - activation energy, C_{OH^-} - hydroxide ion molality, b - reaction order with respect to ion hydroxide, R - universal gas constant, T - absolute temperature, t - reaction time. Using equation (5) diagram of degree of conversion can be plotted, Fig. 1, dotted line.

Considering the variable activation energy term the kinetic expression of the sand dissolution can be written as, [3]:

$$\frac{d\alpha}{dt} = \frac{a_1}{R_p} \cdot \exp \left[- \left(\frac{E_a}{R} \cdot \left(\frac{1}{T} - \frac{1}{T'} \right) + \frac{a_2 \cdot \alpha^{a_3}}{R \cdot T} \right) \right] \cdot (C_{OH^-}^0 - \alpha \cdot C_{OH^-}^{st})^b (1-\alpha)^{2/3}, \quad (6)$$

where: a_1 , – constant, a_2 , a_3 – are parameters related to the change of activation energy, $C_{OH^-}^{st}$ – the stoichiometric hydroxide molality, $C_{OH^-}^0$ – initial hydroxide molality, R_p is the mean particle radius and T' – absolute reference temperature.

Variable activation energy shrinking core model take into account the change of the activation energy as the reaction proceeds.

Using experimental results, diagram shown on Fig. 1, thick continuous line was plotted, and adjustable parameters were found. Using equations (2) and (6) it is possible to plot the radius change diagram, Fig. 2, dashed line. This diagram shows that after approx. 70 minute dissolution process ends, and diameter of sand particles becomes zero, which represents the real nature of this process.

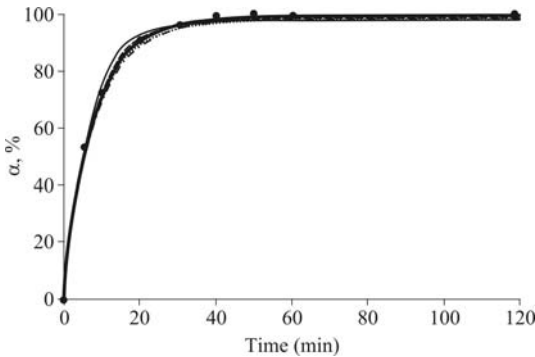


Fig. 1. Degree of conversion

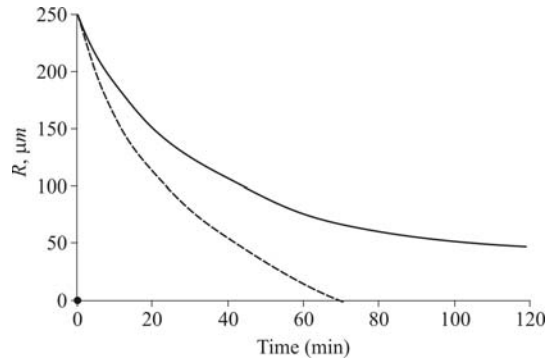


Fig. 2. Mean particle size decreasing during the dissolution process

Conclusion

Here presented study shows that silica and sodium hydroxide react rapidly at high pressure and temperature. Obtained curves seem to be a good representation of dissolution process. On the basis of acquired data, using geometrical resembles, an analytical expressions of kinetic model for shrinking core models was written, which describes the system well enough.

Reference

- [1] F. Jendoubi, A. Mgaidi, M. El Maaoui, The Canadian Journal of Chemical Engineering, 1998, 76, 233.
- [2] F. Jendoubi, A. Mgaidi, M. El Maaoui, The Canadian Journal of Chemical Engineering, 1997, 75, 721.
- [3] A. Mgaidi, F. Jendoubi, D. Oulahna, M. El Maaoui, J. A. Dodds, Hydrometallurgy, 2004, 71, 435.

KINETICS OF SiO₂ DISSOLUTION IN NaOH AQUEOUS SOLUTION – MODIFIED SHRINKING CORE MODEL

L. Pezo, M. Stanković, B. Kovačević¹, N. Rajić, M. Jovanović², D. Debeljković³

¹ Eng. Dept. Holding Institute of General and Physical Chemistry, Studentski trg 12/V, Belgrade,

² Faculty of Technology and Metallurgy, Karnegijeva 4, Belgrade,

³ Faculty of Mechanical Eng., 27. marta 80, Belgrade, Serbia and Montenegro

Abstract

The batch dissolution kinetics of SiO₂ particles in aqueous NaOH, corresponding to the ratio SiO₂/Na₂O=2, was investigated at elevated temperatures and high pressure. As a first approximation, the silica was assumed to be smooth spheres, which decreased in size, as dissolution proceeds. The influence of the particle size, the operating temperature and the hydroxide ion molality on the kinetic rate were studied. Two mathematical models are developed, both of them shows well correlation with experimental data.

Introduction

Dissolution of sand into sodium hydroxide solutions (for the production of sodium silicate) according to the following reaction: $y\text{SiO}_{2(\text{sd})} + \text{NaOH} \rightarrow \text{Na}_2\text{Si}_y\text{O}_{3+y}$ corresponding to $y=2$, i. e. SiO₂/Na₂O=2 (silicate module), have been extensively studied establishing kinetic curves, /1,2,3/. Obtained sodium silicate is used as a supplement in detergent manufacture, because of the good buffering action of silicates, and as raw material for detergent zeolite 4A production. In this paper the modified shrinking core model and the variable activation energy shrinking core model were developed.

Experimental

Experiments were carried out with sand (average particle size 250 μm), and minimum SiO₂ content of 97%. The sodium hydroxide solution of 12.5 mol/kg were used, prepared from pure reagent – grade sodium hydroxide dissolved into distilled water. For the sand used in this work, the specific surface area was evaluated at approximately 200 cm²/g, which indicate low porosity. Amounts of sand and NaOH solution, corresponding to the molar ratio SiO₂/Na₂O=2 were introduced into a 2l autoclave (Parr). The temperature was regulated at 220 °C, and checked with thermocouple. The autoclave is equipped with agitator. At the end of each experiment, the autoclave was quenched into water. The mixture was filtered and the un-reacted sand was washed with hot water until the filtrate became non – basic. The remaining solid was dried and weighed.

Mathematical model

Modified shrinking core model has been proposed to describe the kinetic of dissolution of sand into sodium hydroxide solutions, under experimental conditions (220°C, 27.5 bar), close to those in the industry of the wet – process sodium silicate produc-

tion. The attention was directed to the effect of particle size on the reaction rate. The experimental kinetic data were analyzed to determine the controlling mechanisms. When the rate – limiting step is a surface reaction, the reaction rate can be expressed by the following equation, /3/:

$$m_0 \cdot \frac{d\alpha}{dt} = y \cdot k^0 \cdot S \cdot C_{OH^-}^b \cdot \exp\left(-\frac{E_a}{R \cdot T}\right), \quad (1)$$

where: $\alpha = \frac{m_0 - m}{m_0}$ - degree of conversion, m_0 – initial mass of silica, m is the mass of un-reacted silica at time t , y - stoichiometric coefficient, k^0 – a constant factor, S – surface area, E_a – activation energy, C_{OH^-} – hydroxide ion molality, b – reaction order with respect to ion hydroxide, R – universal gas constant, T – absolute temperature, t – reaction time.

Using equation (1) diagram of degree of conversion can be plotted.

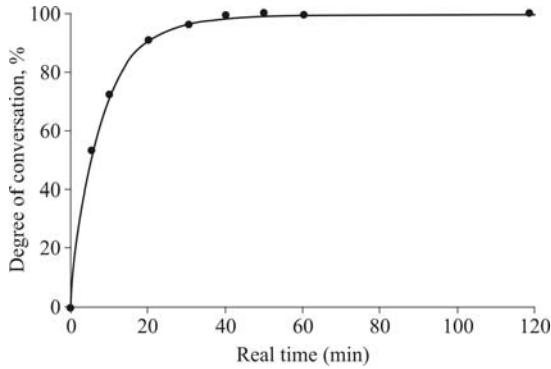


Fig. 1. Degree of conversion for modified shrinking core model

Considering the variable activation energy term the kinetic expression of the sand dissolution can be written as, /3/:

$$\frac{d\alpha}{dt} = \frac{a_1}{R_p} \cdot \exp\left[-\left(\frac{E_a}{R} \cdot \left(\frac{1}{T} - \frac{1}{T'}\right) + \frac{a_2 \cdot \alpha^{a_3}}{R \cdot T}\right)\right] \cdot (C_{OH^-}^0 - \alpha \cdot C_{OH^-}^{st})^b (1-\alpha)^{2/3}, \quad (2)$$

where: a_1 , – constant, a_2 , a_3 - are parameters related to the change of activation energy, $C_{OH^-}^{st}$ - the stoichiometric hydroxide molality, $C_{OH^-}^0$ - initial hydroxide molality, R_p is the mean particle radius and T' – absolute reference temperature.

Variable activation energy shrinking core model take into account the change of the activation energy as the reaction proceeds.

Using experimental results, diagram shown on Fig. 2 was plotted, and adjustable parameters were found.

Using geometrical equation for particle radius in time t :

$$r(t) = R \cdot \sqrt[3]{1-\alpha}, \quad (3)$$

it is possible to plot the radius change diagram. This diagram shows that after approx. 70 minute dissolution process ends, and diameter of sand particles becomes zero, which represents the real nature of this process.

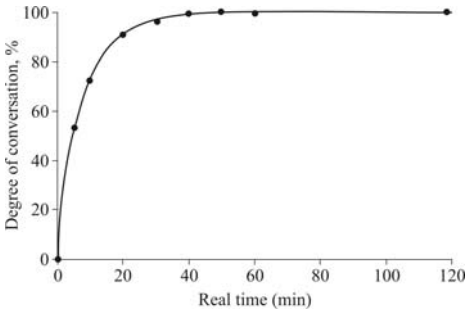


Fig. 2. Degree of variable activation energy shrinking core model

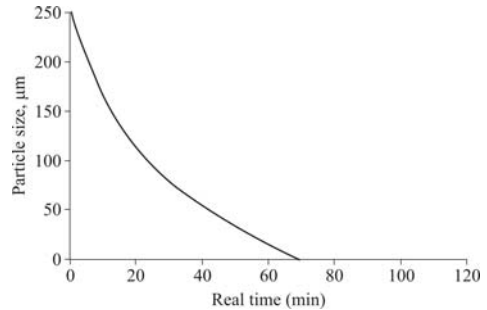


Fig. 3. Mean particle size decreasing during the dissolution process

Conclusion

The dissolution of silica into sodium hydroxide solution at high T and p was investigated by taking into consideration the parameters of temperature, particle size and hydroxide ion molality. The kinetic data fit very well to both modified shrinking core model and variable energy shrinking core model. These models represent the real nature of dissolving process, especially near the end of dissolving process, when the mean diameter of particles becomes zero, comparing to empirical and shrinking core models, where the mean particles becomes zero in infinity (not in real reaction time).

Reference

- [1] F. Jendoubi, A. Mgaidi, M. El Maaoui, The Dissolution Kinetics of Sand as Function of Particle Size, *The Canadian Journal of Chemical Engineering*, 1998, 76, 233.
- [2] F. Jendoubi, A. Mgaidi, M. El Maaoui, Kinetics of the Dissolution of Silica in Aqueous Sodium Hydroxide Solution at High Pressure and Temperature, *The Canadian Journal of Chemical Engineering*, 1997, 75, 721.
- [3] A. Mgaidi, F. Jendoubi, D. Oulahna, M. El Maaoui, J. A. Dodds, Kinetics of the Dissolution of Sand into Alkaline Solutions: Application of a Modified Shrinking Core Model, *Hydrometallurgy*, 2003, Article in press.

A NEW KINETIC METHOD FOR DETERMINATION OF IRON (III)

S. S. Mitić, M. V. Obradović and S. B. Tosić

Faculty of Sciences and Mathematics, Department of Chemistry, University of Nis, Visegradska 33, P. O. Box 224, Serbia and Montenegro

Abstract

A new kinetic method for the determination of Fe(III) based on its catalytic effect on reaction of oxidation of disulphonated hydroquinone by hydrogen peroxide in acid media at constant ionic strength is described. The experimental conditions were optimized. The calibration line is linear in the concentration range of Fe(III) from 1.12 to 18.7 ng cm⁻³. Kinetic equations are proposed for investigated reaction. The effect of certain foreign ions on the reaction rate were determined

Introduction

Many kinetic methods are based on redox reactions involving the oxidation of organic compounds such as phenols and their sulphonated products. The oxidation of these compounds leads to the formation of coloured products. One of the sulphonated products of phenols, pyrogallol-5-sulphonate behave as a indicator substance in reaction of oxidation by hydrogen peroxide in presence of Fe(III) as a catalyst. The calibration graph is linear in the range 2.0-75.0 ng cm⁻³[1]. In a works reported previously, the oxidation of monosulphonated product of hydroquinone by hydrogen peroxide was used for the determination of Cu(II) (0.2-7.33 µg cm⁻³)[2] and Fe(III) (6.66-66.6 ng cm⁻³)[3]. The aim of this work is to develop the new kinetic method for determination of Fe(III) using its catalytic effect on reaction of oxidation of disulphonated product of hydroquinone by hydrogen peroxide.

Experimental

A Perkin Elmer Lambda 15 UV/VIS Spectrophotometer, connected to a thermocirculating bath was used for the absorbance measurements.

All reagents used were p.a. grade: potassium salt of hydroquinone disulfonic acid, FeCl₃·6H₂O, H₂O₂, HClO₄, NaClO₄ (Merck).

Selected volumes of the reagents were put into a reaction mixture vessel with four compartments and water was added to give the volume of 15 cm³. The vessel was thermostated for a few minutes at working temperature and vigorously shaken. The absorbance at 450 nm was measured every 30s for 6min. Differential variante of tangents method was applied. The slope of the linear section of the absorbance-time curve was used as a measure of the reaction rate[4].

Results and Discussion

The oxidation of disulphonated hydroquinone by hydrogen peroxide gives a coloured product. The fact that this reaction is catalysed by trace amounts of iron (III) is used for its kinetic-catalytic determination.

In order to determine the lowest possible determinable concentration of iron (III), the conditions needed to be optimized. The optimum reaction concentrations were determined by estimating the concentration effects of reactants in the mixture where the concentration of one of reactants was varied and concentration of others kept constant. The influence of pH, hydrogen peroxide, potassium salt of disulphonic hydroquinone concentration was studied for both catalytic and non-catalytic reactions in the aim to determine the orders of both reactions.

The kinetic equation for the non-catalytic and catalytic reaction:

$$\frac{dx}{dt} = k_0 c_{H_3O^+}^{-1} c_{H_2O_2} c_{K_2S_2Hy}$$

for interval of concentrations: $c_{H_3O^+}$ ($1.82-5.50 \cdot 10^{-4}$ moldm⁻³), $c_{H_2O_2}$ ($2.67-6.66 \cdot 10^{-2}$ moldm⁻³), $c_{K_2S_2Hy}$ ($2.67-26.7 \cdot 10^{-4}$ moldm⁻³)

$$\frac{dx}{dt} = k_1 c_{H_3O^+}^{-1} c_{Fe(III)}$$

for interval of concentrations: $c_{H_3O^+}$ ($1.82-5.50 \cdot 10^{-4}$ moldm⁻³), $c_{H_2O_2}$ ($5.60-6.66 \cdot 10^{-2}$ moldm⁻³), $c_{K_2S_2Hy}$ ($13.3-26.7 \cdot 10^{-4}$ moldm⁻³), where are $\frac{dx}{dt}$ is change of absorbance in

function of time (reaction rate), k_0 and k_1 conditional rate constants for non-catalytic and catalytic reaction.

Under the optimal conditions of reaction :

$$c_{H_3O^+} = 4.07 \cdot 10^{-4} \text{ moldm}^{-3}, c_{H_2O_2} = 6 \cdot 10^{-2} \text{ moldm}^{-3}, c_{K_2S_2Hy} = 2 \cdot 10^{-3} \text{ moldm}^{-3},$$

$I=0.1$ the iron concentration was varied from 1.12 to 18.7 ng cm⁻³ and calibration curve was linear in this interval of concentrations (Fig. 1). The equation of the dependence of slope of the linear section of the absorbance-time curve, as a measure of the reaction rate, on the iron concentration:

$$\text{slope} = 0.0132 + 0.00168 \cdot c_{Fe(III)} (\text{ng cm}^{-3})$$

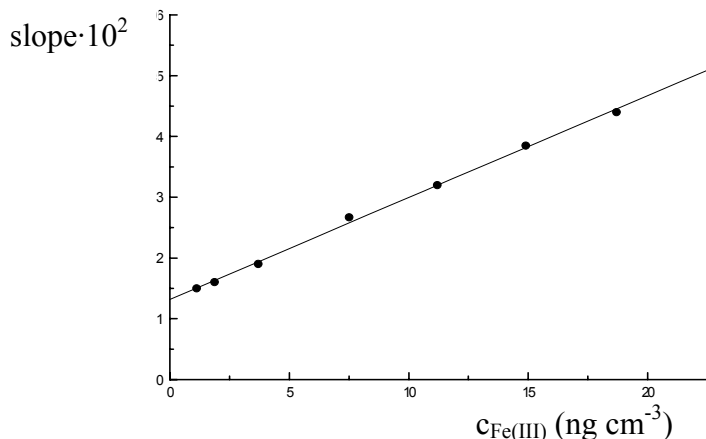


Fig.1 Dependence of the rate of the catalytic reaction on the iron (III) concentration under the optimal conditions. $t=20 \pm 0.1^\circ\text{C}$

The influence of foreign ions on the accuracy of the results was investigated and there are few interferences. Oxalate and citrate in a 1:1 ratio and Ni^{2+} and Hg^{2+} in a 10:1 ratio with Fe(III) interfered with the reaction.

Acknowledgement:

This research was supported by grant number 1211 from the Ministry of Science Serbia. The authors are grateful for the financial support provided by the Ministry of Science.

References

- [1] S. S. Mitić, G. Ž. Miletić, M. V. Obradović, *Talanta*, 1995, **42**, 1273.
- [2] S. S. Mitić, M. V. Obradović, S. B. Tošić, *Oxidation communication*, 2004, **27**.
- [3] S. S. Mitić, M. V. Obradović, S. B. Tošić, *IV Jugoslovenski simpozijum Hemija i zaštita životne sredine*, Zrenjanin 2001, 148.
- [4] D. Perez-Bendito, M. Silva, *Kinetic Methods in Analytical Chemistry*, Ellis Horwood, 1988, 46.

KINETIC STUDY OF AZO-DYES IMMOBILIZATION ON ANION-EXCHANGE RESINS

J. Savić

*Department of Physical Chemistry, VINČA Institute of Nuclear Sciences,
POB 522, 11001 Belgrade, Serbia and Montenegro*

Abstract

Adsorption kinetics of pyrazol (PACA) and imidazol-azo chromotropic acid (IACA) from water solutions on anion exchange resins Dowex 1-X8 and Dowex 2-X8 was investigated at pH 4.5. Kinetics of adsorption was studied in static conditions at the temperature range from 0 to 25 °C, by following the amount of adsorbed dye vs. contact time. In all cases, adsorption was first order process. PACA and IACA diffusion coefficient values were from 4.6×10^{-9} to 7.0×10^{-9} cm²/s for Dowex 1-X8 and from 3.5×10^{-9} to 5.8×10^{-9} cm²/s for Dowex 2-X8. Activation energy values for adsorption of investigated azo-dyes onto Dowex 1-X8 resin were 9.89 and 24.52 kJ/mol, and for Dowex 2-X8 11.22 and 25.44 kJ/mol, for PACA and IACA respectively.

Introduction

Azo dyes are among the compounds with continually increasing application in analytical chemistry. Many organic reagents immobilized on ion-exchange resins are usually used in adsorption-spectroscopic test methods for sensitive determination of many metal ions [1]. A great number of publications on the immobilized reagents deals with heterocyclic azo dyes [2]. This work deals with the investigations of kinetics of azo-dye immobilization on anion exchange resins Dowex 1-X8 and Dowex 2-X8.

Experimental

Chemicals. Investigated azo-dyes (PACA and IACA) in the form of the disodium salt were synthesized as described previously [3]. The acidity of the solutions was adjusted by addition of Britton–Robinson buffer. The anion-exchange resins Dowex 1-X8 and Dowex 2-X8 (both 20-50 mesh) were used as a carrier for dye adsorption. The amount of the adsorbed dye was determined spectrophotometrically as the difference of reagent concentration before and after the adsorption.

Apparatus. Absorbance of solutions and resin phase spectra was measured in 1.0 and 0.2 cm quartz cells with Beckman 5260 UV VIS recording spectrophotometer. The resin prepared without dye was used as the reference.

Results

The adsorption kinetics of PACA (5×10^{-5} M) and IACA (7.1×10^{-5} M) was investigated under static conditions in the temperature range from 0 to 25°C. The experiments were performed at pH 4.5. The dependence of the amount of adsorbed dye on resin vs. contact time is presented by the Eq. 1:

$$a_t = a_e(1 - e^{-k_s t}) \quad (1)$$

where a_e and a_t are the amounts of dye adsorbed on resin at equilibrium and at time t , respectively, k_s is the rate constant of adsorption. It was evident that adsorption rate increased with temperature and the adsorption was a first order process. Dependence $\ln(a_e - a_t)$ vs. t for adsorption of PACA (a) and IACA (b) on anion-exchange resin Dowex 1-X8, 20-50 mesh, is represented on Fig. 1a. Values for k_s and a_e were attained from slope and intersection on ordinate. Similar results were obtained for Dowex 2-X8 resin (Fig. 2). The values of k_s , obtained from the slope of the dependence of $\ln(a_e - a_t)$ vs. t at various temperatures, are given in Table 1.

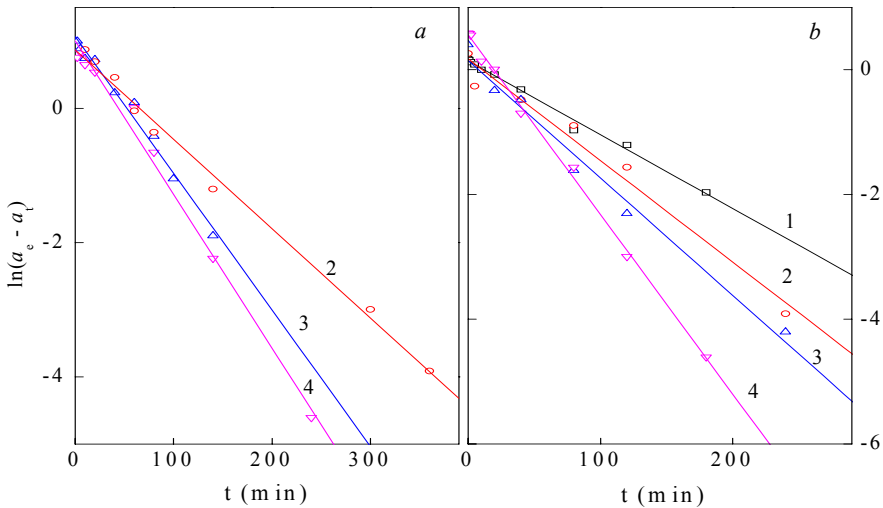


Fig. 1. The time dependence of $\ln(a_e - a_t)$ for PACA (a) and IACA (b) adsorption onto Dowex 1-X8 resin, 20-50 mesh at different temperatures; 0.5 g of resin

a) $C_{\text{PACA}} = 5 \times 10^{-5}$ M (2 - 6°C; 3 - 16°C; 4 - 25°C)

b) $C_{\text{IACA}} = 7.1 \times 10^{-5}$ M (1 - 0°C; 2 - 8°C; 3 - 16°C; 4 - 25°C)

In the course of adsorption, the molecule migrate across the liquid film around the resin particle and through the interior of the particle. Since the sufficient mixing of aqueous solution containing PACA or IACA and porous resins was provided, the pore diffusion was rate limiting step. The mechanism of adsorption process can be determined by plotting the fractional attainment of equilibrium a_t/a_e against $t^{1/2}$ according to Fick's second law relationship:

$$\frac{a_t}{a_e} = \frac{6}{r} \sqrt{\frac{Dt}{\pi}} \quad (2)$$

where r is the radius of the resin particle and D is the diffusion coefficient. Diffusion coefficients D calculated from the slope of the plot a_t/a_e vs. $t^{1/2}$ are also listed in Table 1 and are in good agreement with literature data.

The Arrhenius relationship was used for calculation of the activation energy of azo-dye adsorption:

$$\ln k_s = -\frac{E}{RT} + \ln k_o \quad (3)$$

k_o is a constant, E is the activation energy, R is the ideal gas law constant, and T is the adsorption temperature. A plot of $\ln k_s$ versus $1/T$ resulted in a straight line with a slope of $-E/R$ and an intercept of $\ln k_o$. The values of activation energy for adsorption of investigated azo-dyes (PACA and IACA) onto Dowex 1-X8 resin were 9.89 and 24.52 kJ/mol, and for Dowex 2-X8 11.22 and 25.44 kJ/mol.

Table 1. The values of rate constants and diffusion coefficients for PACA and IACA adsorption onto Dowex 1-X8 and Dowex 2-X8 resins

Reagent	T (°C)	Resin			
		Dowex 1-X8		Dowex 2-X8	
		k_s (min ⁻¹)	$D \times 10^9$ (cm ² /s)	k_s (min ⁻¹)	$D \times 10^9$ (cm ² /s)
PACA	0	-	-	0.014	3.6
	6	0.019	5.0	-	-
	16	0.021	5.1	0.018	4.0
	25	0.025	5.3	0.021	4.2
IACA	0	0.012	4.6	0.011	3.5
	8	0.013	5.1	0.017	4.1
	16	0.022	5.6	0.021	4.9
	25	0.029	7.0	0.029	5.8

Conclusion

Adsorption of PACA and IACA onto Dowex 1-X8 and Dowex 2-X8 resins is an effective, reproducible method for the immobilization of these dyes. Electrostatic interactions with the resin skeleton were found to be a predominant factor in the dye adsorption. Obtained results are in good agreement with literature data.

Acknowledgement

Financial support was provided by the MSTD of the Republic of Serbia, Grant No. 1991. This work has been partly supported by AUF project "Pôle d'excellence régionale"; Référence: 2700PL309/2003.

References

- [1] K. Yoshimura, H. Waki, *Talanta*, 1985, **32**, 345.
- [2] V. Vasić, J. Savić, V. Pavelkić, S. Milonjić, *Colloid Surface A*, 2003, **215**, 277.
- [3] V. Vasić, A. Muk, T. Petrova, V. Nikolić, *Zh Anal Khim*, 1988, **43**, 793.

DECOMPOSITION OF HYDROGEN PEROXIDE ON Ni (II) EXCHANGED LTA AND FAU_y ZEOLITES

M. Grković-Popović¹, M. Petković² and S. Marković³

¹*Faculty of Physical Chemistry, University of Belgrade, Studentski trg 12-16*

²*Institut für Chemie-Physikalische und Theoretische Chemie Freie Universität Berlin*

³*Institute of Technical Sciences of the Serbian Academy of Sciences and Arts*

Abstract

Ni (II) exchanged zeolites LTA and FAU_y was synthesized and used as catalysts for the decomposition of hydrogen peroxide. Parameters such as concentration of H₂O₂ and concentration of substrates were varied. It was shown that catalytic decomposition of H₂O₂ depends on Ni/H₂O₂ ratio. Concentrations of hydrogen peroxide were measured by UV/VIS technique and permanganate titration.

Introduction

The study of the catalytic properties of transition metal exchanged zeolites is of great importance due to their industrial applications [1], especially as heterogeneous catalysts. Transition metal complexes are known to effect the decomposition of hydrogen peroxide either by a free radical mechanism [2] or through the formation of active peroxy species in the coordination sphere [3]. Hydrogen peroxide can be catalytically decomposed on transition metals exchanged zeolite. Decomposition of hydrogen peroxide on Ni (II) exchanged zeolites LTA and FAU_y was investigated in this paper.

Experimental

Materials

Initial sodium form of zeolite LTA (Si/Al=1) and FAU_y (Si/Al=2.5) were supplied by Union Carbide Co.

Almost completely exchanged Ni (II) forms of the LTA zeolite were prepared after eight successive cycles of cation exchanges using 0.1 M water solution of NiCl₂·6H₂O and 0.1 M water solution of Ni(CH₃COO)₂·4H₂O. Ni (II) exchanged FAU_y form were prepared after three successive cation exchanges using 0.04 M water solution of NiCl₂·6H₂O at 85 °C.

Decomposition of H₂O₂

The catalytic activities of both exchanged zeolites were tested for the decomposition of H₂O₂ at two different contact times (8 and 30 h). Known quantity of Ni (II) exchanged zeolites was recast by given volume of hydrogen peroxide of known concentration and mixed on a magnetic stirrer. The change of concentration of hydrogen peroxide during decomposition was measured by UV/VIS technique and permanganate titration. Absorption measurements were carried out by UV/VIS-CINTRA spectrophotometer at λ_{\max} =390 nm.

Results and Discussion

In the case of NiA zeolites concentration of H_2O_2 decrease in first 30-40 minutes, after that slightly oscillate between 0.3 and 0.4 mol dm^{-3} (when starting concentration was 0.506 mol dm^{-3} , Fig. 1a) i.e. between 0.6 and 0.9 mol dm^{-3} (when starting concentration was 0.825 mol dm^{-3} , Fig. 1b). In the case of NiY zeolites concentration of H_2O_2 decrease in first 30-40 minutes, after that concentration increase and slightly oscillate around 0.35 mol dm^{-3} (Fig. 2).

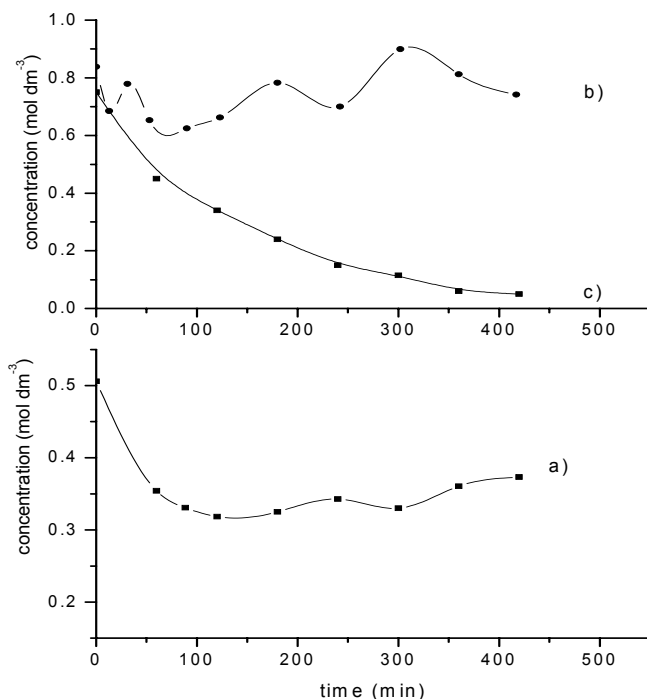


Fig. 1 Kinetic curves for NiA zeolite: a) $c_{0,\text{perox}}=0.506$, b) $c_{0,\text{perox}}=0.825$ mol dm^{-3} and c) spontaneous decomposition of H_2O_2 in water solution, $c_{0,\text{perox}}=0.7$ mol dm^{-3} .

Although both, zeolites in general and cation-exchanged zeolites, are good catalysts for decomposition of hydrogen peroxide, Ni-exchanged zeolites exhibit unexpected behavior. Both chosen methods yielded similar results which indicate oscillatory nature of the process and a complex mechanism.

An analogy could be made between transition metal exchanged zeolites and transition metal complexes. Transition metal complexes are known to effect the decomposition of hydrogen peroxide either by a free radical mechanism, or through the formation of active peroxy species in the coordination sphere. While the electronic state of the metal site is important in the free radical mechanism, the latter is strongly influenced by the steric environment of the active site [5].

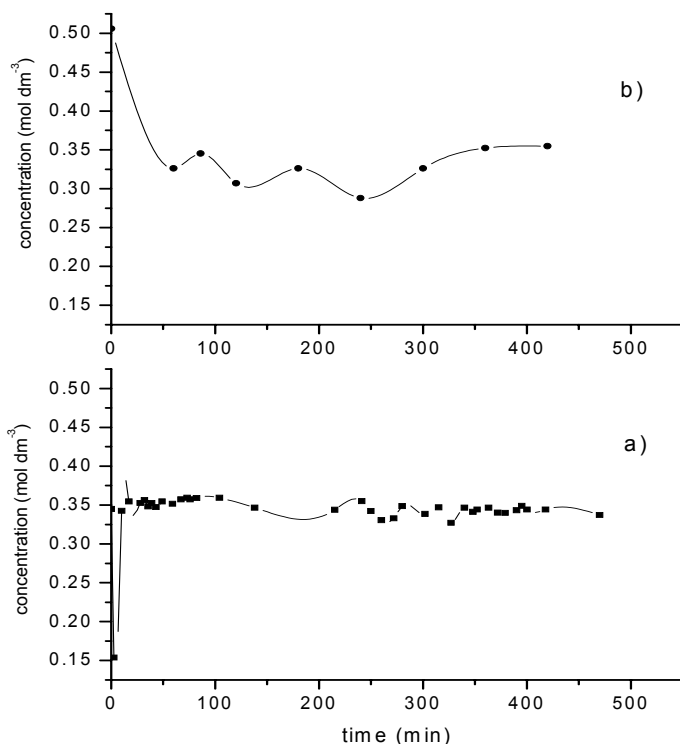


Fig. 2 Kinetic curves for NiY zeolite: a) $c_{0,perox}=0.345$ and b) $c_{0,perox}=0.506$ mol dm⁻³.

Conclusion

The obtained results show that Ni (II) exchanged zeolites are weakly active catalysts for decomposition of hydrogen peroxide, but they could be used almost like buffers and maintain certain range of hydrogen peroxide concentration. On the other side a reliable assessment of the mechanism, free radical or formation of active peroxo species, has remained uncertain.

Acknowledgment

This work was supported by the Serbian Ministry of Science and Technology, under grant no. 1243.

References

- [1] M.R. Mayria, S.J.J. Titinchi, S. Chand, J. Mol. Cat. A, 2003, 201, 119.
- [2] I. Mochida, K. Takeshita, J. Phys. Chem., 1974, 78, 1655.
- [3] V.S. Sharma, J. Schubert, J. Am. Chem. Soc., 1969, 91, 6291.
- [4] G. Schmitz, J. Chim. Phys., 1987, 84, 957,
- [5] K.O. Xavier, J. Chacko, K.K. Mohammed Yusuff, Appl. Cat. A, 2004, 258, 251.

KINETIC PARAMETERS OF BIOLUMINESCENT REACTION FOR SCREENING OF NEW BIOCIDES AMONG CORROSION INHIBITORS

E.N. Efremenko¹, R.E. Azizov¹, T.A. Makhlis¹, S.D. Varfolomeyev¹,
and V.M. Abbasov²

¹Chemical Faculty, The M.V. Lomonosov Moscow State University, Moscow, 119992, Russia,

²Azerbaijan NAS the Y.H. Mamedaliyev Institute of Petrochemical Processes, Baku, Azerbaijan

Abstract

Highly sensitive and express method for screening of corrosion inhibitors (CI) was offered. New method is based on the detection of intracellular ATP concentration by bioluminescent method. The influence of inhibitor nature on the bioluminescent reaction was studied and kinetic parameters of catalytic reaction going on in the presence of CI were defined. The Minimal Inhibitory Concentrations of several CI completely killing living cells were estimated.

Introduction

The analysis of recent results of multiple investigations of different corrosion objects [1-2] revealed that various microorganisms (MO) provoke 50% of all corrosive situations, therefore it is necessary to undertake simultaneous counteraction against the chemical corrosion as well as destruction of MO promoting biocorrosion processes. To achieve this goal, corrosion inhibitors (CI) having biocide activity are preferred [3,4]. Minimal Inhibitory Concentrations (MIC) causing the death of all cells of certain type of MO usually are defined by microbiological method, whereas the last one is time and labor consuming [5,6].

This work is devoted to the development of express method for the screening of new CI by determination of MIC in relation to different biocorrosive MO. Investigation demonstrates the influence of various CI on the kinetic parameters of luciferase reaction being main part of bioluminescent assay.

Materials and Methods

The following strains were used as representatives of MO widely spread in the biocorrosive objects: *Desulfovibrio vulgaris* B-1388, *Pseudomonas putida* B-1091 and *Acidithiobacillus ferrooxidans* B-458. All strains were taken from the VKM (All-Russian Collection of MO). Cells were cultivated as previously described [7].

There were several CI under investigation: Kathon-893 (Russia); SXT 1003 (Nalco, USA); VFIKS-82, Khazar, Nitro-1, Nitro-2, Caspii-2 and Caspii-4 (INKOR, Azerbaijan) [3,4].

Intracellular ATP concentration and MIC determination were conducted as previously described [7].

To investigate the kinetic parameters of luciferase reaction in the presence of CI, solutions containing the standard concentrations of ATP (0.05 - 0.2 mM) and various CI concentrations (0.1 - 3 g/l) were prepared on the base of physiological solution

(PS). Calculation of kinetic parameters (K_m and K_i) was carried out by Dickson's method, in coordinates $1/v - 1/[S]$ for K_m and $1/v - [I]$ for K_i , where $[S]$ and $[I]$ are concentrations of ATP and Inhibitors, respectively.

Results and Discussions

The luciferine-luciferase reaction is the main part of suggested method [8], therefore the influence of CI on bioluminescent reaction is very important. It appeared that such CI as Kathon-893, Khazar, Nitro-2, Caspii-4 and SXT-1003 inhibited the luciferase reaction, whereas Nitro-1, Caspii-2 and VFIKS-82 slightly activated or did not effect luciferase reaction. Kinetic parameters (K_i , inhibition constant and K_m , Michaelis constant for luciferase and ATP interaction) were calculated for CI inhibited luciferase reaction (Figs.1, 2).

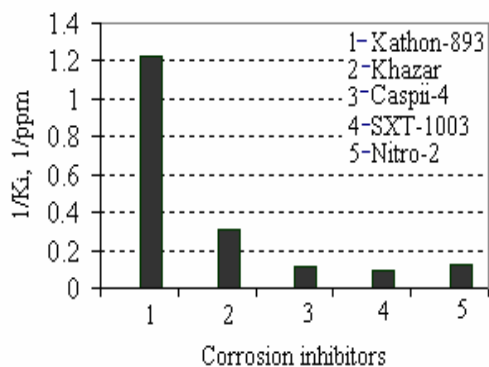


Fig.1. Inhibition constants of luciferase reaction

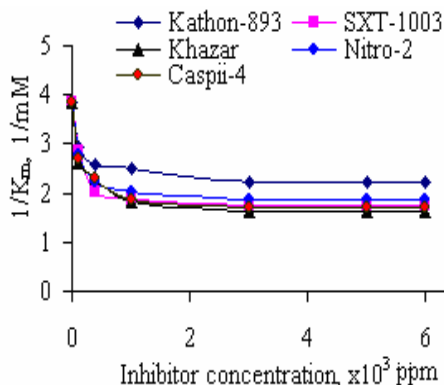


Fig.2. Observed Michaelis constants for luciferase reaction

It was shown that, K_m characterizing of ATP-luciferase interaction slightly increased in the presence of CI (Fig.2). The values of inhibition constants for investigated compounds appeared to be 100-300 times higher than the maximal concentrations of CI used in practice [3,4]. It means that possible inhibition of luciferase reaction by the actual concentrations of CI present in the real samples of waste waters can have neglected influence on the final results of probe analysis.

Mechanisms of cell death provoked by compounds with biocide activity can be different, but in all cases MIC is the most important parameter. So, MIC was determined for six CI, namely, Kathon-893, Khazar, Nitro-1, Caspii-4, VFIKS-82 and Caspii-2, in relation to three groups of MO being main participants of biocorrosion processes. The minimal concentrations of CI causing the decrease of cell biomass down to the non-detectable level were considered as MIC of corresponding compounds. MIC values reflecting the biocide efficacy of CI were revealed (Fig.3).

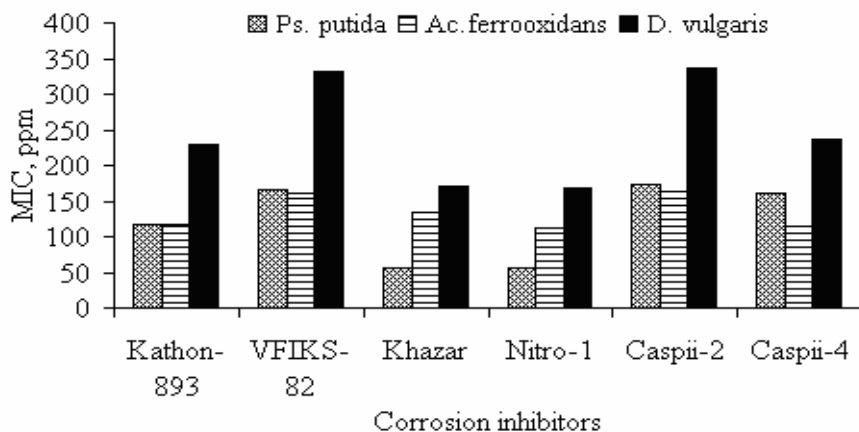


Fig.3. Minimal Inhibition Concentration of CI.

Various CI have biocide influence on the different MO in non-equal concentrations. Khazar and Nitro-1 appeared to be the most effective biocides for *Ps. putida* and *D. vulgaris* cells, whereas there was no big difference among the MIC values of various CI determined for the *Ac. ferrooxidans* cells. The 2-3 fold increase MIC values defined for *D. vulgaris* cells in comparison with the other types of bacteria deals with the use of nutrient medium instead of PS. The results testify to the higher tolerance of sulphate-reducing cells to the biocide action of CI in the presence of organic substrate. That fact should be taken into account in practice when CI are used as biocides.

Conclusion

It should be noted that bioluminescent method is enough convenient and highly sensitive for screening of new corrosion inhibitors with biocide activity.

Acknowledgements

This work had financial support from ISTC (Grant No. 2245p).

References

- [1] L.-C. Xu, K.-Y. Chan, *Materials charact.*, 2002, **48**, 195.
- [2] S. Da Silva, R. Basseguy, *bioelectrochem.*, 2002, **56**, 77.
- [3] A.M. Samedov, *Proc. Petrochem. Oil ref.*, 2000, **2**, 35.
- [4] E.S. Abdullayev, *Proc. Petrochem. Oil ref.*, 2000, **3**, 18.
- [5] S.K. Jigletsova, *Appl. Biochem. Microbiol.*, 2000, **36**(6), 694.
- [6] L.V. Piddock, *J. Appl. Bacteriol.*, 1990, **68**, 307.
- [7] E.N. Efremenko, R.E. Azizov et al., *Proc. Petrochem. Oil ref.*, 2003, **4**, 70.
- [8] E.N. Efremenko, R.E. Azizov et al., *Proc. Petrochem. Oil ref.*, 2002, **4**, 79.

n-HEXANE INTERACTION WITH TRANSITION-METAL ION EXCHANGED ZEOLITES STUDIED BY TPD

V. Rakić¹, S. Gajinov², V. Rac¹ and R. Hercigonja³

¹Faculty of Agriculture, Nemanjina 6 Zemun, ²Institute of General and Physical Chemistry, ³Faculty of Physical Chemistry, Studentski trg 12, Beograd, Serbia and Montenegro

Abstract

In this work, room-temperature n-hexane adsorption on transition metal (iron-, cobalt- and nickel-) ion-exchanged zeolites (faujasites and silicalites) was studied by means of temperature programmed desorption (TPD) and infrared (IR) spectroscopy. It is shown that extra-framework cations are active sites for n-hexane adsorption. The profiles of TPD spectra indicate that the adsorption of n-hexane is influenced not only by the nature of active sites, but also by the type of aluminosilicate framework.

Introduction

Transition-metals as charge-balancing cations incorporated in zeolites provide a wide variety of catalytic reactions. In our previous work, we showed that, in spite of very small dipole moment of carbon monoxide molecule, during its room temperature adsorption on transition-metal exchanged FAU type zeolite, the disproportionation of CO happened [1]. Recent literature data indicate a particular interest of numerous investigators about iron-exchanged zeolites because they are recognized as promising catalysts in the processes of selective catalytic reduction of nitrogen oxides [2]. It was shown that, among the others, over-exchanged Fe/ZSM-5 and ZSM-5 with aluminium isomorphously substituted with Fe³⁺ exhibit higher catalytic activities [3].

n-Hexane cracking is known as a test catalytic reaction very often applied for estimation of catalytic activity of different solid catalysts [4]. In this work, we investigated the room temperature interaction of n-hexane with transition metal (iron-, cobalt- and nickel-) ion-exchanged zeolites: X, Y and ZSM-5 types.

Experimental

The samples of FAU type zeolites used in this work were prepared from synthetic NaY and NaX (SK-40 and 13X, Union Carbide). The cation exchanged (Fe²⁺, Fe³⁺, Ni²⁺ and Co²⁺) X and Y zeolite samples were obtained by conventional ion-exchanged procedure and denoted according to the compensating cation. ZSM-5 (Si/Al = 40) samples isomorphously substituted with Fe³⁺ with different weight percentage (from 0.03 to 0.1) were home synthesized.

As-prepared samples were placed in a desiccator containing n-hexane, for 24 hours. The adsorption of n-hexane was investigated by IR spectroscopy, done at Perkin-Elmer 983 spectrophotometer, using KBr technique. TPD experiments were performed using differential scanning calorimeter Setaram DSC 111 coupled with a mass spectrometer (Baltzers Thermostar), in a helium flow ($\approx 10 \text{ cm}^3/\text{min}$), in a temperature region 25 - 300°C. Masses corresponding to n-hexane were recorded.

Results and Discussions

In this work, n-hexane was adsorbed on: Co(II)Y and Co(II)X, Ni(II)Y and Ni(II)X, Fe(II)X and Fe(III)X, Fe(II)Y and Fe(III)Y and on the samples of ZSM-5 zeolite isomorphously substituted with Fe(III) (samples denoted as FeZ). The interaction of n-hexane with investigated structures was not found only in the case of Fe(III)X and Fe(II)Y zeolites. Figure 1 presents the TPD spectra of n-hexane obtained for Co(II)Y, Co(II)X, Ni(II)Y, Fe(II)X and Fe(III)Y in the temperature range from 25°C up to 300°C. It is worth noticing that profiles of TPD spectra are strongly dependent on both the type of charge-balancing cation and on the type of zeolite framework.

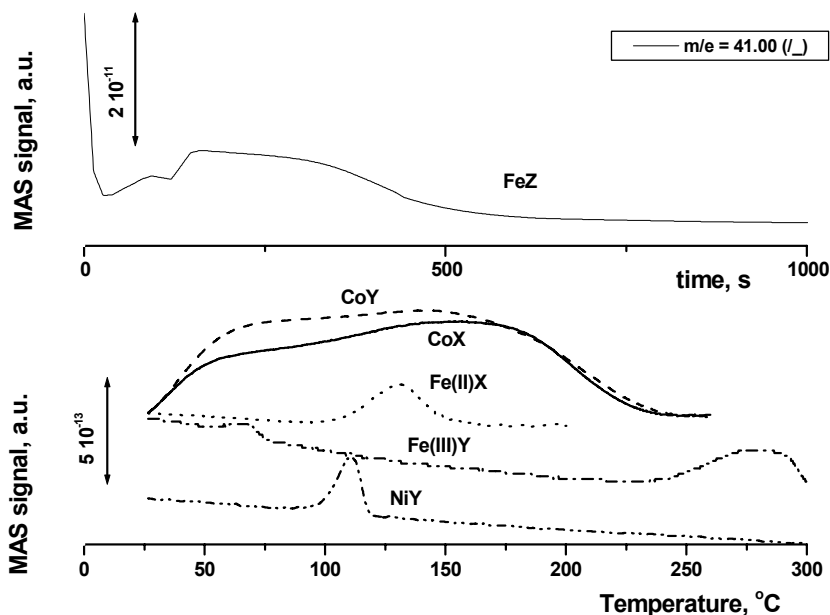


Figure 1 TPD spectra of n-hexane recorded from the samples of Y, X and ZSM-5 zeolite. The most intensive signal ($m/e = 41$) is presented.

In the case of FeZ zeolites, n-hexane was desorbed isothermally, at 25°C (Figure 1, upper spectrum), indicating the adsorption of n-hexane on weak active sites. Among other zeolites investigated in this work, n-hexane was not adsorbed on Fe(III)X and Fe(II)Y zeolites. A band at 1480 cm^{-1} which is found in the IR spectra of n-hexane adsorption on Fe(III)Y zeolite confirm its interaction with the active sites, while its absence is a clear indication that n-hexane was not adsorbed on Fe(II)X (Figure 2).

The results presented so far indicate the influence of zeolite lattice, which is negatively charged, on the interaction of n-hexane with the investigated modified zeolites.

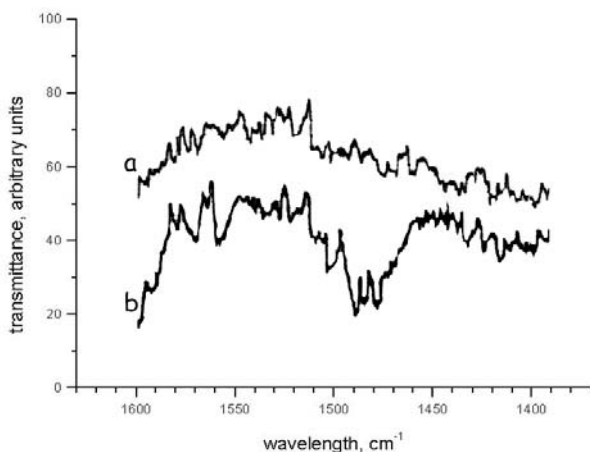


Figure 2 IR spectra of n-hexane adsorption on Fe(II)X (a) and Fe(III)Y (spectrum b).

Conclusions

The results obtained in this work show that the profiles of n-hexane desorption exhibit not only the dependence on the nature of extra-framework cation but also on the type of zeolite lattice, and thus can be a tool for their characterization.

References

- [1] V.M.Rakić, R.V.Hercigonja and V.T.Dondur, *Micropor. Mesopor. Mater.* 1999, 27, 27.
- [2] Q.Zhu, B.L. Mojet, R.A.J. Janssen, E.J.M.Hensen, J. van Grondelle, P.C.M.M. Magusin and R.A. van Santen, *Catal. Lett.*, 2002, 81, 205.
- [3] H. Liu, G. H. Kuehl, I. Halasz and D. H. Olson, *J. Catal.* 2003, 218, 155.
- [4] A. Smiešková, E. Rojasová, P. Hudec and L. Šabo, *in press* in: *Applied Catalysis A: General*, for 2004, www.sciencedirect.com

STRUCTURE AND CATALYTIC PROPERTIES OF Ni-Al AND Ni-Cr METHANATION CATALYSTS

M. Gabrovska*, R. Edreva-Kardjieva and D. Crisan¹

Institute of Catalysis, Bulgarian Academy of Sciences, Acad. G. Bonchev str. 11, Sofia 1113, Bulgaria, ¹Institute of Physical Chemistry, Romanian Academy, Bucharest 77208, Romania

Abstract

The structure and the catalytic properties of the Ni-Al and Ni-Cr hydrotalcite-like samples ($\text{Ni}^{2+}/\text{M}^{3+} = 3.0/1$, $\text{M}^{3+} = \text{Al}^{3+}$ or Cr^{3+}) are compared in order to establish the effect of the trivalent cation M^{3+} on the phase composition and the crystal size of the Ni-containing particles in the primary layered structure and in the tested materials. The catalytic activity of the uncalcined samples, preliminary reduced with hydrogen, are checked in the methanation reaction. The presence of Al^{3+} ions in the primary Ni-Al sample favors the formation of crystalline takovite phase of nanosized particles, while the presence of Cr^{3+} in the Ni-Cr one leads to a quasi-amorphous compound. The low activity of the NiCr sample is attributed to the spinel NiCr_2O_4 formation and the big Ni^0 crystallites appearance. The higher catalytic activity of the NiAl sample is related to the presence of the un-bonded in the spinel-like phase, more easily reducible, Ni^{2+} ions.

Introduction

The hydrotalcites belong to a great group of compounds, with homogeneous distribution of the ions, named layered double hydroxides or anionic clays. These compounds have the general formula $[\text{M}^{2+}_{1-x}\text{M}^{3+}(\text{OH})_2]^{x+}[\text{A}^{n-}_{x/n}]_x \cdot m\text{H}_2\text{O}$, where M = metal and A = anion and may be modified during preparation in order to produce materials with specific structures and properties. Their thermal decomposition in air results in the formation of stoichiometric spinels and free oxides. The spinel formation depends considerably on the nature of the cations. For example, NiCr_2O_4 is formed at a lower temperature (600°C) than NiAl_2O_4 (900°C) [1–4]. A member of the hydrotalcite group is the mineral *takovite*, $\text{Ni}_6\text{Al}_2\text{CO}_3(\text{OH})_{16} \cdot 4\text{H}_2\text{O}$. The Ni-Al mixed oxides, obtained from coprecipitated takovite-like compounds ($\text{Ni}^{2+}/\text{Al}^{3+} = 3/1$), are used as the catalyst precursors for the hydrogenation of CO-rich mixture to methane at high temperatures [2].

The interest in the catalytic hydrogenation of carbon oxides to methane is determined by the fact that the methanation reaction can be used both to obtain synthesis gas from gaseous mixtures rich in CO and CO_2 and for the fine purification of the hydrogen-rich gases from the CO and CO_2 impurities. The commercial catalysts used in the process are commonly based on nickel dispersed on oxide supports such as Al_2O_3 , SiO_2 , MgO , Cr_2O_3 , etc. [5]. The efforts to improve their catalytic activity and stability are still in progress.

The structure, thermal evolution and reactivity of the Ni-Cr hydrotalcite-like system before and after calcination (450–900°C) are investigated in details [1-4]. However, there is scanty information about the catalytic applications of the system. These facts directed us to study the Ni-Cr hydrotalcite-like material, as methanation catalyst.

The aim of this work is to compare the structure and the catalytic properties of the Ni-Al and Ni-Cr hydrotalcite-like samples ($\text{Ni}^{2+}/\text{M}^{3+} = 3.0/1$, where $\text{M}^{3+} = \text{Al}^{3+}$ or Cr^{3+}), in order to establish the effect of the trivalent cation (M^{3+}) on the phase composition and the crystal size of the Ni-containing particles in the primary layered structure and the tested materials. The unreduced Cr^{3+} and Al^{3+} ions are supposed to ensure a high dispersion of the Ni^{2+} ions leading to the high and stable dispersion of the active phase of the Ni^0 crystallites.

Results and Discussion

The samples are prepared by coprecipitation at constant pH value. The primary materials are characterized by BET and XRD measurements (Tables 1). According to the BET analysis of the samples, Al gives rise to a higher surface area in comparison to Cr.

Table 1. The BET area and the structural characteristics of the primary samples

Samples	BET ($\text{m}^2 \text{g}^{-1}$)	Structural characteristics			
		a (nm)	c (nm)	V_t (nm^3)	$L_{(006)}$ (nm)
NiAl	71	0.3043(2)	2.328(2)	0.186(7)	7
NiCr	48	amorphous			
takovite	-	0.3027	2.262	0.179	-

The XRD patterns of the primary sample NiAl (Fig. 1) indicated that a single takovite-like phase with nanosized particles is present. The structural characteristics of this sample (Table 1) are similar to these for mineral takovite (+) (JCPDS file 15-0087). The sample NiCr (Fig. 2) shows XRD powder patterns of a quasi-amorphous compound.

The uncalcined samples, preliminary reduced (pre-reduction) with pure hydrogen at 400, 450, 530 and 600°C, are tested in the methanation reaction in the temperature interval 240–400°C. The methanation activity is represented by the gas hourly space velocity (GHSV) at which the concentration of CO_2 at the reactor outlet is 10 ppm (0.0010 vol % CO_2).

Table 2. The BET area and the structural characteristics of the tested (T) samples

Tested samples	BET ($\text{m}^2 \text{g}^{-1}$)	Structural characteristics		
		a_{Ni^0} (nm)	V_{Ni^0} (nm^3)	$L_{(111)\text{Ni}^0}$ (nm)
NiAl-T	92	0.3532(3)	0.0441(4)	13
NiCr-T	6	0.3521(2)	0.0436(5)	39
Ni⁰	-	0.35238	0.04375	-

The catalytic activity tests (Fig. 2) show that the sample NiCr exhibits the lowest methanation activity, almost independent of the pre-reduction temperatures. The sample NiAl demonstrates the higher activity at all GHSV and all pre-reduction temperatures. The obtained XRD data show that catalytic test provokes formation of mainly Ni^0 phase (x) (JCPDS file 4-850) and small quantities of NiO (o) (JCPDS file 4-835) in the sample NiAl-T (Fig. 3) and Ni^0 phase (x) and NiCr_2O_4 phases (*) (JCPDS file 23-0432) in the tested sample NiCr-T (Fig. 3). The low catalytic activity of the NiCr sample may be correlated with the spinel NiCr_2O_4 formation and corresponding increase of the

Ni^0 crystal size and decrease of the sample surface area (Table 2). The higher catalytic activity of the NiAl sample is related to the presence of the un-bonded in the spinel-like phase, more easily reducible, Ni^{2+} ions. It may be concluded that Al^{3+} ions in contrast to the Cr^{3+} ones stabilized the Ni^{2+} ions at higher temperatures.

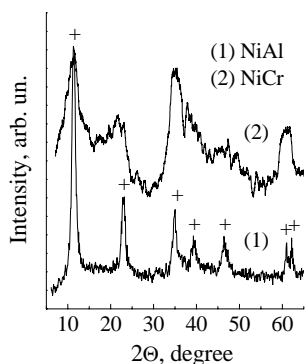


Figure 1. XRD patterns of the primary samples

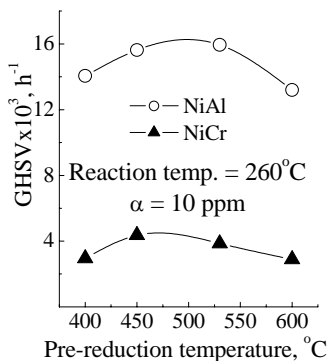


Figure 2. Catalytic activity test

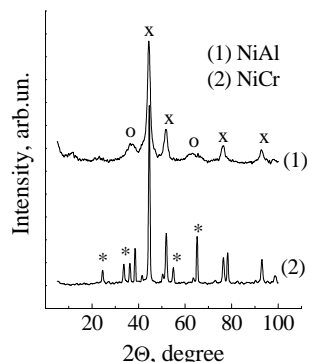


Figure 3. XRD patterns of the tested samples

Conclusions

The structure, properties and reactivity of the Ni-containing samples are strongly influenced by the nature of the trivalent cation.

The presence of the Al^{3+} ions in the primary sample favors the formation of the single crystalline takovite phase of nanosized particles that reflect in higher surface area, while the presence of the Cr^{3+} ions leads to a quasi-amorphous compound with lower surface area.

The formation of the spinel-type phases take place at different temperatures as a function of the M^{3+} presence and provoke considerable modification in the catalytic properties of the sample under study. The higher catalytic activity of the NiAl sample is related to the NiAl_2O_4 spinel formation at temperatures higher than the pre-reduction and reaction temperatures.

Acknowledgements

The authors are grateful to the Bulgarian National Science Fundation of for the partial financial support (Project X-1217).

References

- [1] O. Clause, *Catal. Today*, 1994, 21, 185.
- [2] A. Vaccari, *Catal. Today*, 1998, 41, 53.
- [3] O. Clause, M. Gazzano, F. Trifiro, A. Vaccari, L. Zatorski, *Appl. Catal.*, 1991, 73, 217.
- [4] O. Clause, M. Coelho, M. Gazzano, D. Matteuzzi, F. Trifiro, A. Vaccari, *Appl. Clay Sci.*, 1993, 8, 169.
- [5] G. Mills and F. Steffgen, *Catal. Rev.*, 1973, 8, 159.

DEVELOPMENT OF NEW KINETIC METHOD FOR DETERMINATION OF ULTRAMICRO AMOUNTS OF PHENYLHYDRAZINE

V. D. Mitić¹, S. D. Nikolić² and V. P. Stankov-Jovanović¹

¹*Faculty of Natural Science and Mathematics, Department of Chemistry, University of Nis,
Visegradaska 33, 18000 Nis, Serbia & Montenegro*

²*Faculty of Chemistry, University of Belgrade, P.O. Box 550 11001 Belgrade, Serbia & Montenegro*

Abstract

A new sensitive kinetic method has been developed for the determination of trace amounts of phenylhydrazine. The method was based on the inhibitory effect of phenylhydrazine on the oxidation of Victoria Blue 4-R by KBrO_3 . The reaction is monitored spectrophotometrically at 596.3 nm. Method development includes optimization of reagent concentration: $\text{HCl} = 2.0 \times 10^{-2} \text{ mol/dm}^3$; $\text{KBrO}_3 = 2.0 \times 10^{-4} \text{ mol/dm}^3$, $\text{KCl} = 0.1 \text{ mol/dm}^3$, $\text{VB} = 2.0 \times 10^{-6} \text{ mol/dm}^3$ $t = 22 \pm 0.1^\circ\text{C}$. Under optimal conditions it could be determine phenylhydrazine over the range of $1.08 \times 10^{-7} \text{ g/cm}^3$ to $1.08 \times 10^{-6} \text{ g/cm}^3$.

Introduction

Phenylhydrazine is a strong reducing agent used as oxygen scavenger for corrosion control in boilers and hot-water heating systems [1]. It is also employed as starting material for many derivatives such as foaming agents for plastics, antioxidants, polymers, pesticides, plant-growth regulators and pharmaceuticals. Phenylhydrazine is volatile and toxic, and is readily absorbed by oral, dermal or inhalation routes of exposure. Adverse health effects on people living near hazardous waste sites caused by hydrazine and its derivatives (such as phenylhydrazine) have been described [2]. Contact with phenylhydrazine irritates the skin, eyes, and respiratory track. Thus, there has been an increasing demand for a highly sensitive method for determination of phenylhydrazine in various samples, such as water and industrial or environmental materials. The paper describe the new sensitive kinetic method has been developed for the determination of trace amounts of phenylhydrazine, based on their inhibitory effect on the oxidation of Victoria Blue 4-R by KBrO_3 . The reaction is monitored spectrophotometrically at 596.3 nm. Method development includes optimization of reagent concentration and temperature.

Experimental

At room temperature, Victoria Blue 4-R can be oxidized rapidly in presence of trace amounts of KBrO_3 in acidic media. When the oxidation goes on, the initial blue color of solution disappears and the colorless reaction product is forming. On the other hand, when trace amounts of phenylhydrazine are added to the mixture of the reaction, the reaction rate strongly decreases. The differential variant of the tangent method [3] was used for processing the kinetic data. The reaction rate was followed by the change

in the values of the tangent of the angle ($\tan \alpha$) of the slope of the linear part of the kinetic curve to the abscissa in the coordinates A-t, because $\tan \alpha = dA/dt$.

Recommended Procedure

A UV-VIS Perkin-Elmer-Lambda 15 spectrophotometer with 10 cm cylindrical cells connected to the thermocirculating bath, was used for the absorbance measurements. The pH-values of solutions were determined by a Radiometer PHM 29 b pH-meter. The selected volumes of VB, $KBrO_3$, and phenylhydrazine were separately measured in a Budarin vessel [4], until solutions of KCl, HCl and deionized water (total volume 10 cm^3) were measured into one compartment of vessel. The vessel was thermostated for ten minutes of $22 \pm 0.1^\circ\text{C}$, than the solution was stirred and the chromometer was simultaneously turned on. The cell of the spectrophotometer was rinsed well and filled with corresponding solution. The absorbance, A, at 596.3 nm, was measured every 30 s over a period of 5 min after mixing. Between the measurements the vessels were washed properly using HCl (1:1), and then rinsed with tap, distilled and deionized water. The glassware was dried out at 50°C and stored under clean air conditions. All chemicals were of analytical reagent grade, and were provided by Merck.

Effect of Reaction Parameters

To take full advantages of the procedure, the reagent concentrations and reaction conditions must be optimized. Various experimental parameters were studied in order to obtain optimized systems. The parameters were optimized by setting all parameters to be constant and optimizing one each time.

Keeping all other experimental parameters constant, we studied the dependence of hydrochloric acid concentration on the system in the range $1.6 \times 10^{-2} - 2.8 \times 10^{-2} \text{ mol/dm}^3$. There is a linear relationship between the pH and the indicating and inhibiting reaction rate in the range of concentrations studied. The greatest difference between the rates of indicating and inhibiting reactions occurs at $2.0 \times 10^{-2} \text{ mol/dm}^3$, when phenylhydrazine maximally decrease the reaction rate. For further work, a hydrochloric acid concentration of $2.0 \times 10^{-2} \text{ mol/dm}^3$ was selected.

The indicating and the inhibiting reaction reaction were first order with respect to the VB concentration. With increasing VB concentrations, the difference between the rates of the indicating and inhibiting reactions increases. For further work, a VB concentration of $2.0 \times 10^{-6} \text{ mol/dm}^3$ was selected.

The dependence of the reaction rates on the $KBrO_3$ concentration was also studied. It could be seen that both reactions are first order with respect to the $KBrO_3$ concentration. For further work, the $KBrO_3$ concentration of $2 \times 10^{-4} \text{ mol/dm}^3$ was selected as optimal.

A calibration graph was prepared for the optimal conditions described above at $22 \pm 0.1^\circ\text{C}$. There is a linear relationship between $\tan \alpha$ and phenylhydrazine concentration from 0.1×10^{-6} to $1.0 \times 10^{-5} \text{ mol/dm}^3$ ($1.08 \times 10^{-7} \text{ g/cm}^3$ to $1.08 \times 10^{-6} \text{ g/cm}^3$).

Acknowledgements

The financial support of the Ministry of Science Serbia Project 1727, is gratefully acknowledged.

References:

- [1] H. W. Schessl, in: K. Othmer (Ed.), Encyclopedia of Chemical Technology, 4th Edition, Vol. 13, Wiley/Interscience, New York, 1995, 560.
- [2] G. Choudhary, H. Hansen, Chemosphere 1998, 37, 801.
- [3] K. B. Yatisimirskii, Kineticheskie metody analiza, Khimiya, Moskva, 1967.
- [4] L. J. Budarin, K. E. Prik, Zavodskaya laboratoriya, 1960, 26, 1018.

Electrochemistry

(D)

PROTON CONDUCTING MEMBRANES BASED ON PBI/POLYSULFONE COPOLYMER BLENDS

M. K. Daletou, N. Gourdoupi and J. K. Kallitsis

Department of Chemistry, University of Patras, 26500 Patras, Greece, and Institute of Chemical Engineering and High Temperature Chemical Processes, ICE/HT-FORTH, P.O.Box 1414, 26500 Patras, Greece.

Abstract

Blends of a new polysulfone copolymer (PPy(50)coPSF) with polybenzimidazole were prepared at different compositions. Depending on the composition, phase separated or miscible pairs were obtained as was found based on the single glass transition criterion. The thermal and oxidative stability of these blends were also tested. Even the membranes with high PBI content retained their flexibility and good thermomechanical properties after the treatment with H₂O₂, indicating the high oxidative stability of the system. Doping with phosphoric acid resulted in ionically conducting membranes, with conductivity in the range of 10⁻² S/cm, a prerequisite for use of these materials in fuel cells operating above 100 °C.

Introduction

Polymer electrolyte membrane fuel cell (PEMFC) is one of the most promising candidates and has been receiving increased attention due to its certain advantages [1]. Operation of PEMFCs at elevated temperatures (150 °C) increases the kinetic reaction rate, which would give higher efficiency and reduces the temperature dependent catalyst poisoning, resulting thus in flexibility to use not so pure hydrogen or other types of fuels and even lower loading of the expensive Pt on the electrode.

Up to now the perfluorinated polymers, mainly Nafion[®] [2], which is produced by DuPont, have been applied almost exclusively as polymer electrolytes. In general, proton conductivity increases as the hydration level of the polymer increases and conductivities at about 10⁻¹ S/cm are obtained. Since, though, conductivity is dependent on the presence of water, the currently possible operational temperature is limited to be below 100 °C. Above that temperature the membrane dehydrates and the proton conductivity decays.

As noted before, it is important to increase the operation temperature above 100 °C. Research is underway to optimize the performance of the high temperature PEM fuel cells by finding the electrolyte material that combines certain prerequisites. The ideal polymer electrolyte for this type of cell, should exhibit high proton conductivity, long term durability, good mechanical properties and high thermal and oxidative stability in order to be applicable in the particular conditions under which the cell operates. A degradation in properties of the membrane such as the oxidative or long term stability, may occur due to the presence of different radical

species in the cell. More specifically, species such as HO• and HO₂• originate from oxygen diffusion through the membrane and incomplete reduction at the fuel cell anode [3].

Polymer electrolytes in this type of cells must be able to be doped with a strong acid in order to assure conductivity. Poly(benzimidazole) (PBI) [4] is widely studied with various strong acids. It has a vitreous transition temperature of 420 °C, exhibits high thermal stability even when it is doped, high acid uptake and high ionic conductivities when doped with phosphoric acid and has been applied in fuel cells [5]. Blends of PBI with sulfonated polysulfone (SPSF) with different sulfonation degrees have been also studied in regards to their miscibility, mechanical properties [6] and doping behavior. PBI/SPSF showed conductivities higher than acid doped PBI while they have been tested in fuel cell showing high performance with both pure hydrogen and hydrogen containing carbon monoxide [7].

In this work we report on characterization of blends of polysulfone copolymers with polybenzimidazole.

Results and Discussion

It is well known that polymer blends are generally not miscible. There are, however, polymer pairs that do exhibit miscibility due to some type of specific interactions between the two components. This possibility was tested in the system PBI/PPy(50)coPSF. Thus, solution casted films at the compositions 75/25, 50/50 and 25/75, were prepared. The 25/75 blend composition appears to be phase separated since a phase with glass transition close to that of PPy(50)coPSF (200 °C) is obtained. The other two blend compositions show one T_g at 325°C, showing the potential of these blends to be used as polymer electrolytes in high temperature PEM fuel cells.

It is well known that PBI shows low oxidative stability. This could negatively affect the properties of the blends, especially the one rich in PBI. Using the Fenton's test, membrane samples of the PBI/PPy(50)coPSF 75/25 and 50/50 blends were treated with H₂O₂/Fe⁺². Thermogravimetric analysis in N₂ atmosphere and dynamic mechanical analysis were carried out for both samples before and after the treatment. The mechanical properties were not affected notably. The film remained flexible and it could be tilted to 180° angle. Moreover the TGA showed that the treatment did not degrade the thermal properties of the membranes, since almost the same thermal stability was obtained.

Furthermore, a study of the membrane ability to be doped with phosphoric acid has been performed. It was found that the maximum acid uptake increases with the percentage of PBI in the blend. The maximum doping level was high, above 300 %wt for 75/25 and 50/50 blend compositions and it is worth mentioning that even the blend poor in PBI reaches a satisfying doping level, about 150%wt. The electrochemical characterization of the acid doped membranes was carried out using the 4-probe current interruption techniques. Measurements showed ionic conductivity of all the blends over 10⁻² S/cm at room temperature.

The dependence of the conductivity on doping level was also examined. The ionic conductivity for PBI/PPy(50)coPSF 50/50 blend with doping levels ranging from 40 to 220 wt% at room temperature is presented in **Figure 1**. Conductivity increases upon increasing the doping level and values over 10^{-2} S/cm were obtained for doping levels above 180 wt%.

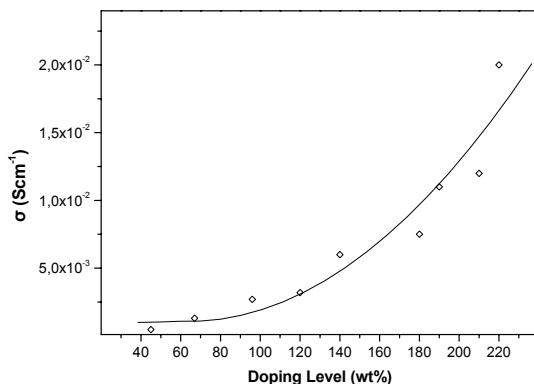


Figure 1: Doping level dependence of ionic conductivity of the blend PBI/PPy(50)coPSF 50/50.

Conclusion

Blends of a polysulfone type copolymer with PBI were prepared and studied in respect to their miscibility, their mechanical behavior and their thermal and oxidative stability. The studied materials possess high glass transition temperatures, good mechanical properties and high thermal and oxidative stability. Doping of the membranes prepared from these blends, showed high acid uptake resulting thus in materials with high ionic conductivity which can eventually be used as polymer electrolytes in PEM fuel cells operating above 100°C.

References:

- [1] B. C. H Steele, A. Heinzl, *Nature* 2001, 414, 345.
- [2] M. Rikukawa, K. Sanui, *Prog. Polym. Sci.* 2000, 25, 1463.
- [3] G. Hubner, E. Roduner, *J. Mater. Chem.* 1999, 9, 409.
- [4] Y.-L. Ma, J. S. Wainright, M. H. Litt, R. F. Savinell, *J. Electrochem. Soc.* 2004, 151, A8.
- [5] J.-T. Wang, R.F. Savinell, J. Wainright, M. Litt, H. Yu, *Electrochim. Acta* 1996, 41(2), 193.
- [6] V. Deimede, G.A. Voyiatzis, J.K. Kallitsis, L. Qingfeng, N.J. Bjerrum, *Macromolecules* 2000, 33, 7609.
- [7] Q. Li, H. A. Hjuler, C. Hasiotis, J. K. Kallitsis, C. G. Kontoyannis, N. J. Bjerrum, *Electrochim. Solid-State Lett.* 2002, 5, A125.

ELECTROCHEMICAL INVESTIGATION OF DIFFUSION OF HYDROGEN IN $\text{LmNi}_{3.55}\text{Co}_{0.75}\text{Mn}_{0.4}\text{Al}_{0.3}$ ALLOY

N. Potkonjak and D. Sužnjević

Institute of General and Physical Chemistry, Studentski trg 12-16, 11000 Belgrade, SCG,

Abstract

Hydrogen storage alloy electrode having composition $\text{LmNi}_{3.55}\text{Co}_{0.75}\text{Mn}_{0.4}\text{Al}_{0.3}$ was used for the evaluation of diffusion coefficient parameter of hydrogen by potential-step method. The values obtained depend in linearly fashion on hydrogen concentrations in the bulk of the alloy. An obtained phenomenon was discussed based on the electrostatic interaction between constituent metal of alloy and hydrogen.

Introduction

Hydrogen storage alloys are used as negative electrode in nickel/metal-hydride (Ni/MH) batteries because of their better environmental desirability over conventional anode materials [1, 2]. During charging and discharging processes, diffusion of hydrogen atoms within the bulk of alloy accompanies the charge-transfer reactions on the alloy/electrolyte interface. Both of these processes for LaNi_5 -based alloy have been studied extensively, but the knowledge about them is not complete and still presents the subject of numerous papers [3, 4].

As regards to the hydrogen diffusion, disagreements of reported diffusion coefficient of hydrogen values (D_H), vary over the three orders of magnitude (10^{-8} - 10^{-11} $\text{cm}^2 \text{s}^{-1}$) [4-6].

In the present work, the diffusion parameter of hydrogen in a commercial LaNi_5 -based hydrogen storage alloy was evaluated by using potential-step method.

Experimental

The electrochemical measurements were performed in a thermostated three electrode electrolytic cell. The working electrode was $\text{LmNi}_{3.55}\text{Co}_{0.75}\text{Mn}_{0.4}\text{Al}_{0.3}$ (Lm: 50%La, 30%Ce, 15%Pr and 5%Nd). A $(\text{Ni}(\text{OH})_2/\text{NiOOH})$ pressed in the nickel sponge, placed in a separated compartment, served as the counter electrode. The reference electrode was a Hg/HgO/1M KOH electrode, equipped with Luggin capillary. The electrolyte was an aqueous 1M KOH solution, deaerated by pure nitrogen and thermostated on 30°C.

The working electrode was galvanostatically charged to achieve a determined hydrogen concentration (charge depth, Q_c), using the current density of 60 mA g^{-1} . The open circuit potential (equilibrium potential) of charged electrode amounted to -0.91 V vs. Hg/HgO/1M KOH electrode. An overvoltage of 0 V was applied steeply, and the current-time transient curve was recorded immediately using an I-t plotter (time rate was $v = 1 \text{ sec cm}^{-1}$).

Results and Discussion

In Fig 1, the anodic discharge current densities (j), for several initial hydrogen concentrations, as the functions of time (t), are given in the semilogarithmic form. From these curves at least two separate regions were noticed. The first one, in which $\log j$ does not decrease linearly with t , represents the region where the charge transfer kinetics or mixed charge transfer and diffusion kinetics, are rate determining steps for hydrogen electrode reaction (HER). The second one, in which $\log j$ decreased linearly with t ; the region in which surely the hydrogen diffusion is the rate determining step.

According to the model of G.Zang et al. [6], the diffusion coefficient parameter of hydrogen, D_H/δ^2 , (D_H is Fick's diffusion coefficient, δ is thickness of diffusion layer) can be estimated from the slope of the linear part of the $\log j$ versus t plots.

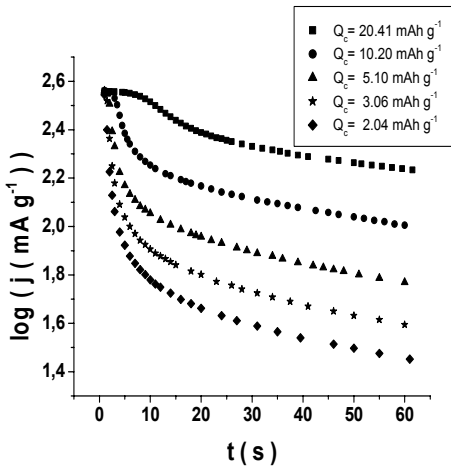


Figure 1. Semilogarithmic plots of anodic current vs. time for a $\text{LmNi}_{3.55}\text{Co}_{0.75}\text{Mn}_{0.4}\text{Al}_{0.3}$ alloy electrode in 1 M KOH at 30°C.

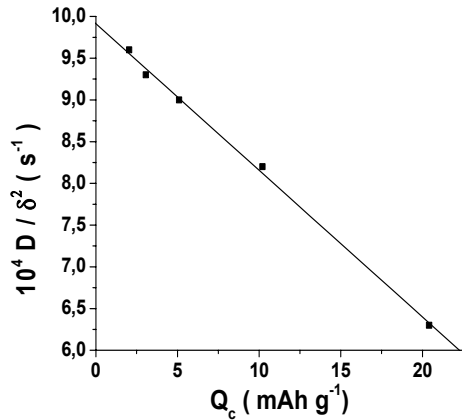


Figure 2. Hydrogen diffusion coefficient parameter, D/δ^2 , as function of hydrogen concentration (Q_c) for a $\text{LmNi}_{3.55}\text{Co}_{0.75}\text{Mn}_{0.4}\text{Al}_{0.3}$ alloy electrode in 1 M KOH at 30°C.

Values D_H/δ^2 for the investigated $\text{LmNi}_{3.55}\text{Co}_{0.75}\text{Mn}_{0.4}\text{Al}_{0.3}$ alloy electrode are shown in Fig.2 as a function of initial hydrogen concentration, expressed in terms of charge depth Q_c .

The obvious decrease of D_H/δ^2 with the increase of Q_c , points to the possible interaction between the absorbed hydrogen atoms and the constituent metals of alloy. As per Fig. 2, the interaction forces cause the decrease of hydrogen diffusion coefficient parameter with the increase in hydrogen concentration, likely as found in ref. [4].

Conclusion

Electrochemical investigation of hydrogen evolution/dissolution on $\text{LmNi}_{3.55}\text{Co}_{0.75}\text{Mn}_{0.4}\text{Al}_{0.3}$ alloy in 1M KOH solution evidenced the change of rate determining step with increasing hydrogen concentration in alloy. Also the linear decrease of hydrogen diffusion parameter with the increase in hydrogen concentration was observed. Further investigations will be focused on the behavior of studied system at higher temperatures.

Acknowledgement

This work is carried out within the project No. 1399, supported by the Ministry of Science and Environmental Protection of Republic Serbia. One of the authors (S.M.) participates also in the EU Project "Prometeas", Contract No. ICA2-CT-2001-10037, relating to the hydrogen energetics.

References

- [1] P.J. Sebastian, S.A. Gamboa, *Chem. Ind.*, 2001, 55, 541.
- [2] J.J. Reilly, G.D. Adzic, J.R. Johnson, T. Vogt, S. Mukerjee, J. McBreen, *J. Alloys Comp.*, 1999, 293-295, 569.
- [3] A. Zuttel, V. Guther, A. Otto, M. Bartsch, R. Kotz, D. Chartouni, Ch. Nutzenadel, L. Schlapbach, *J. Alloys Comp.*, 1999, 293-295, 663.
- [4] C. Iwakura, T. Oura, H. Inoue, M. Matsuoka, Y. Yamamoto, *J. Electroanal. Chem.*, 1995, 398, 37.
- [5] H. Pan, Y. Liu, M. Gao, Y. Zhu, Y. Lei, Q. Wang, *J. Alloys Comp.*, 2003, 351, 228.
- [6] G. Zheng, B.N. Popov, R.E. White, *J. Electrochem. Soc.*, 1995, 142, 2695.

TEMPERATURE DEPENDANCE OF EXCHANGE CURRENT DENSITY OF $\text{LmNi}_{3.55}\text{Co}_{0.75}\text{Mn}_{0.4}\text{Al}_{0.3}$ HYDRIDE ELECTRODE IN ALKALINE SOLUTION

N. Potkonjak and D. Sužnjević

Institute of General and Physical Chemistry, Studentski trg 12-16, 11000 Belgrade, SCG,

Introduction

Metal hydride electrodes are an attractive substitute for the cadmium electrode in Cd-Ni batteries. Currently, there are two types of alloy stoichiometric composition useful as metal hydride (MH) electrodes classified as AB_5 and AB_2 classes of intermetallic compounds.

The member of AB_5 class of alloys is, LaNi_5 , has been extensively investigated because of its high adsorption/desorption hydrogen capacity, easy electrochemical activation and good charge/discharge kinetics. For economical reasons unrefined natural rare earth mixture, mischmetal (Mm =Ce, Pr, Nd ...), or lanthanum-rich mischmetal (Lm) has been used as substitute for La in LaNi_5 to reduced material cost. On the other hand, late transition, or p-shell elements, (Co, Mn, Al Cu, Fe, Si est.) can be used as partial substitutes of Ni in LaNi_5 alloys. These substitutes stabilize crystal structure, increase thermodynamic stability and corrosion resistance, and improve charging reversibility [1, 2].

The electrocatalytic investigations of the hydrogen evolution reaction (HER) on MH electrodes are one of the fundamentals of the electrode kinetics. The exchange current density (j_0) and the activation energy (E_a) are important parameters of (MH) electrodes, when the charge transfer step presents the rate determining step for the HER [3]. In the present work, the temperature dependence of exchange current density for the HER on LmB_5 type alloy was investigated by potentiodynamic method.

Experimental

The crystal structure of hydrogen storage alloy with composition $\text{LmNi}_{3.55}\text{Co}_{0.75}\text{Mn}_{0.4}\text{Al}_{0.3}$ (Lm: 50%La, 30%Ce, 15%Pr and 5%Nd) was proved by X-ray diffraction (XAD) using Cu $K\alpha$ radiation ($\lambda_1 = 1,54060 \text{ \AA}$, $\lambda_2 = 1,54438 \text{ \AA}$). The electrolytic cell for electrochemical measurements consisted of a working electrode (investigated MH alloy), a counter electrode ($\text{Ni}(\text{OH})_2/\text{NiOOH}$ plate electrode), held in a glass separator and a reference electrode (Hg/HgO/1M KOH electrode). The reference electrode was equipped with Luggin capillary. The electrolyte was 1M KOH aqueous solution, deaerated by pure nitrogen. Before electrochemical measurements, the working electrode was stored in electrolyte solution during 24 h, in order to wet it completely. The working electrode was activated by five galvanostatic charge-discharge cycles.

Activated electrode was charged galvanostatically at 60 mA g^{-1} for 2,5 h under various temperatures (30, 40, 50 and 60 °C). Upon a rest period of 20 min, required for electrode potential to reach steady state value, $E_{\text{eq}} \approx -0.91 \text{ V}$, a linear polarization

test was carried out in the vicinity of the equilibrium potential (i.e. $E = E_{eq.} \pm 10$ mV) at scan rate of 1 mV sec^{-1} . Such a small scan rate ensured to record polarization curve in a steady state regime.

Results and Discussion

The X-ray diffraction lines of the investigated alloy corresponding to the hexagonal structure of CaCu_5 type, with lattice parameters $a = 5.012 \pm 0.028 \text{ \AA}$, $c = 4.0430 \pm 0.019 \text{ \AA}$, $V = 88.21 \text{ \AA}^3$ [4, 5]. An apparent charge transfer resistance (R_{ct}) and exchange current density (j_0) were calculated from the slope of the polarization curves according to zero voltage approximation equation [6]. The Table 1. contains the data for the temperature dependence of R_{ct} and j_0 .

Since the investigated electrode was in completely charged state and the investigations were performed in vicinity of E_{eq} it was really to suppose that charge the transfer step of hydrogen electrode reaction (HER) is the one which exclusively determines the slope of the polarization curve (i.e. that the diffusion of hydrogen through the alloy is fast enough to be negelegated as the rate determining process in this case).

Table 1. Kinetic parameters in function of temperature for HER on $\text{LmNi}_{3.55}\text{Co}_{0.75}\text{Mn}_{0.4}\text{Al}_{0.3}$

T / K	R_{ct} / $\text{m}\Omega \text{ g}$	j_0 / mA g^{-1}	E_a / kJ mol^{-1}
303	683.7	38.2	29.9
313	482.0	55.9	
323	326.7	85.2	
333	261.3	109.8	

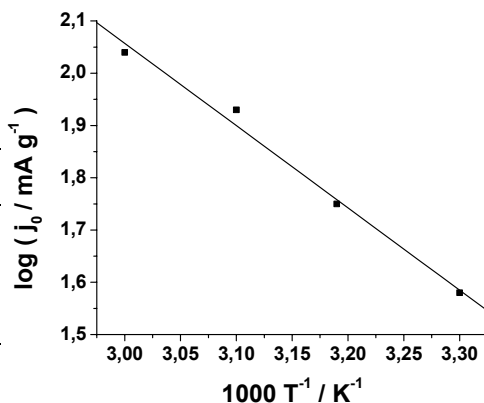


Figure 1. Arrhenius plot of the j_0 for the $\text{LmNi}_{3.55}\text{Co}_{0.75}\text{Mn}_{0.4}\text{Al}_{0.3}$ electrode

The measurements showed clearly, that the kinetic parameters under consideration are temperature dependent. From the slope of $\log j_0$ vs. T^{-1} plot (i.e. Arrhenius plot), it was possible to calculate the activation energy (E_a) of the hydride electrode [6]. The calculated E_a value was 29.9 kJ mol^{-1} .

This value is similar to the one reported for a LaNi_5 based alloy electrodes of similar composition [6, 7], and significantly lower than the one for nickel hydride electrode [6].

Conclusion

On the basis of exchange current density measurements for hydrogen electrode reaction involving $\text{LaNi}_{3.55}\text{Co}_{0.75}\text{Mn}_{0.4}\text{Al}_{0.3}$ alloy hydride in 1 M KOH, at different temperatures, the activation energy was determined to amount to 29.9 kJ mol^{-1} .

Acknowledgement

This work is carried out within the project No. 1399, supported by the Ministry of Science and Environmental Protection of Republic Serbia. One of the authors (S.M.) participates also in the EU Project "Prometeas", Contract No. ICA2-CT-2001-10037, relating to the hydrogen energetics.

References

- [1] C. Iwakura, K. Fukuda, H. Senoh, H. Inoue, M. Matsuoka, Y. Yamamoto, *Electrochim. Acta*, 1998, 42, 2041.
- [2] J.J. Reilly, G.D. Adzic, J.R. Johnson, T. Vogt, S. Mukerjee, J. McBreen, *J. Alloys Comp.*, 1999, 293-295, 569.
- [3] H. Pan, J. Ma, C. Wang, S. Chen, X. Wang, C. Chen, Q. Wang, *J. Alloys Comp.*, 1999, 293-295, 648.
- [4] J.K.Chang, D.N. Simon Shong, W.T.Tsai, *Mat. Chem. Phys.*, 2004, 83, 361.
- [5] Y. Fukumoto, M. Miyamoto, M. Matsuoka, C. Iwakura, *Electrochim. Acta*, 1995, 40, 845.
- [6] G. Wu, N. Li, C.S. Dai, D.R. Zhou, *Mat. Chem. Phys.*, 2004, 83, 307.
- [7] H. Inoue, M. Miyamoto, M. Matsuoka, Y. Fukumoto, C. Iwakura, *Electrochim. Acta*, 1997, 42, 1087.

DIFFERENTIAL PULSE POLAROGRAPHIC STUDY OF LIPID-TRANSFER PROTEIN

S. Gorjanović and M. Beljanski

*Institute of General and Physical Chemistry,
P.O. Box 551, Belgrade, Yugoslavia*

Abstract

Electrochemical study of lipid-transfer protein from domestic cultivar of barley grain revealed presence of metal ions in its structure and also its ability to bind some metal ions. Using differential pulse polarography presence of Cu (II) and Zn (II) ions was revealed and affinity of LTP towards Cu (II), Pb (II), Zn (II), Cd (II), Cr (II), Co (II) and Ni (II) was investigated. It was found that LTP could bind Co (II), Ni (II) and Pb (II), but has no affinity towards other investigated metal ions.

Introduction

Lipid-transfer proteins (LTP) transport phospholipids, glycolipids and fatty acids between membranes. They are small proteins of about 90 residues with high pI values. The three dimensional structure of barley LTP is known, it consists of four α -helices held together with four disulphide bridges. A large hydrophobic cavity within the protein can adapt its volume to bind a variety of lipids and hydrophobic molecules¹. They are involved in the formation of cuticle by transporting the hydrophobic cutin monomers to the apoplast². Also, LTP has been suggested to be important in several types of plant stress responses towards pathogens, drought, salt and temperature changes. Barley LTPs are active *in vitro* against a number of bacteria and fungi; however, the mechanism of its action is still not known³.

The aim of the present work was to investigate metal ion presence in LTP structure using differential pulse polarography (dpp). Also, we were interested if LTP could bind other metal ions, particularly toxic ones. LTP was isolated from barley grain extract by means of fractional precipitation with ammonium sulphate, followed by anion exchange, gel-permeation and cation exchange chromatography without addition of metal ions investigated⁴.

Results and Discussion

The presence of metal ions in LTP and its binding affinity towards some toxic metal ions were estimated by dpp using a dropping mercury electrode (DME) as working electrode, a saturated calomel electrode (SCE) as reference and a Pt-foil as auxiliary one. The polarographic curves, as it is seen from Fig. 1, show the peak currents of Cu (II) (A) and Zn (II) (D), existing in LTP, which was established by the analysis of the corresponding metal-ion buffered solution without protein. Another peaks at -0.25V (B) and C at -0.6V (C) *vs* SCE, probably arose from disulphide bonds reduction, occurring at the same reduction potential as Pb (II) and Cd (II) ion respectively.

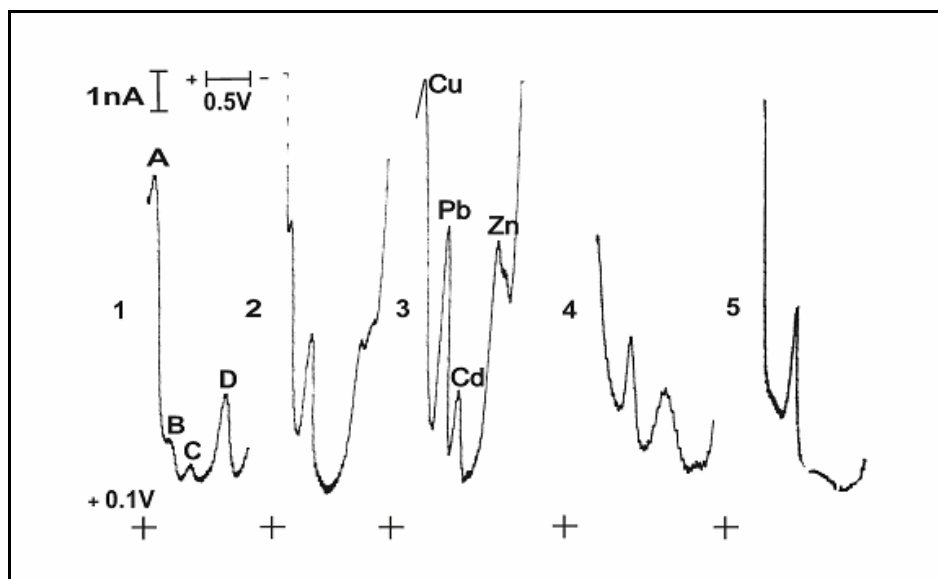


Fig. 1. Differential pulse polarographic curves of:

1. LTP in 50 mM Tris-HCl buffer (pH 7.8);
2. After addition of HClO_4 to the pH \approx 2;
3. After addition of the corresponding metal ions (1 μM);
4. Cystine in 50 mM Tris-HCl (pH 7.8) buffer;
5. Cystine in the same buffer after addition of HClO_4 to the pH \approx 2;

When HClO_4 is added in the examined solution to achieve pH about 2, the peak potentials of disulphide bond reduction changed, but peak which may belong to Cd (II) ion reduction was not observed. However, the current signals resulted from disulphide bonds reduction must be more intensive than peaks which arise from Pb (II) and Cd (II) ion reduction. For that, the presence of these two ions in LTP structure was established by applying the more sensitive voltammetric technique as it is anodic stripping voltammetry.

The ability of LTP for binding metal ions such as Cu (II), Pb (II), Co (II), Cr (III), Zn (II) and Cd (II), was followed for each element separately, by dpp, from buffered solution having a constant concentration of the corresponding metal ions and raised LTP concentration. The peak currents were measured in the determined time interval, until approximately constant peak current of metal-ion reduction was reached. It was found that LTP have affinity for binding Pb (II), Co (II) and Ni (II) ions, because in the presence of LTP the current of the mentioned metal-ions decrease, as it was seen from Fig. 2, in case of Pb (II).

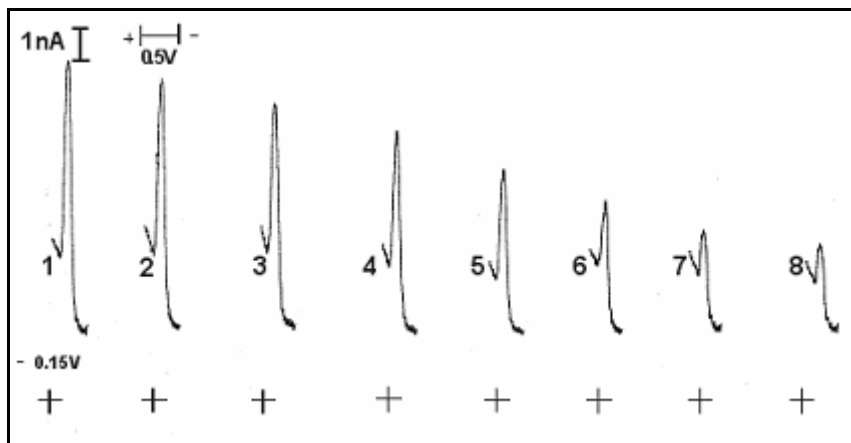


Fig. 2. Dpp curves of Pb (II) ion after gradual addition of LTP:

1. 0.1 μmol $\text{Pb}(\text{NO}_3)_2$ in Tris-HCl buffer pH 7.8;
- 2-7. after gradual addition of LTP to the final concentration 0.1 μmol

The other investigated ions Cu (II), Cr (III), Cd (II) and Zn (II), do not show any interaction with LTP. In these cases, after gradual addition of LTP into the buffered metal ion solution, there was no change in the current peak height of the corresponding metal-ion reduction process.

Conclusion

Presence of Cu (II) and Pb (II) ions in LTP structure was established using dpp. Applying this method it was revealed that LTP could bind Pb (II), Ni (II) and Co (II) but has no affinity towards Cd (II), Cu (II), Zn (II) and Cr (III) ions.

Literature

- [1] J. P. Douliez, T. Michon, K. Elmorjani, D. Marion, J. Cereal Sci., 2000, 32, 1.
- [2] Sterk P., Booij H., Schellekens G.A., Van Kammen A., De Vries S.C., The Plant Cell 1991, 3, 907.
- [3] Garcia-Olmedo F. Molina A., Sequra A., Moreno M., Trends Microbiol. 1995, 72-74.
- [4] Gorjanović S., Sužnjević D., Beljanski M., Hranisavljević J., Environ. Chem. Lett. 2004 (in press)

INTERMETALLICS – ADVANCED CATHODE MATERIALS IN THE ELECTROLYTIC PRODUCTION OF HYDROGEN

D. Lj. Stojić^a, N. D. Simić^a and B. Đ. Cekić^b

^a*Vinča Institute of Nuclear Sciences, Laboratory of Physical Chemistry,* ^b*Laboratory of Physics
11001-Belgrade, P.O. Box 522, Serbia & Montenegro*

Abstract

The intermetallics, Ti-Pt, Nb-Pd (80%Nb), Pd-Ta, Nb-Pd (65% Nb), Zr-Pt, Hf₂Fe and PtMo₃, of transition metals have been investigated as cathode materials for the electrolytic hydrogen evolution in an attempt to increase the electrolytic process efficiency. These materials were compared with conventional cathode, Ni. An significant upgrade of the electrolytic efficiency using intermetallics was achieved.

The effects of those cathode materials on the process efficiency were discussed in the context of transition metal features that issue from their d-electronic configuration.

Introduction

Hydrogen is a very convenient secondary energy source at the end of the oil era. As recent technology progress makes hydrogen a realistic long-term energy option with little or no pollution, development of new methods and improvement of conventional technology for its production is important. The limiting factor for use the electrolytic method on the large scale is well known high energy consumption. In spite of this, hydrogen production *via* water electrolysis promises to be of great future importance. So, the development of high-efficiency electrolytic method represents a step towards the improvement of the hydrogen economy with the idea to adjust all aspects of “hydrogen philosophy” with sustainable development.

The main idea of this work was to investigate the water electrolysis efficiency using different intermetallic phases of transition metals as cathodes. This specific combination of transition metals (hypo d- electronic and hyper d-electronic) demonstrates a well-pronounced electrocatalytic effect. Also, some of high electrocatalytic activities could be explained on the basis of three-dimensional hydridic features of composite electrocatalysts and their ability to absorb certain amount of hydrogen [1, 2].

Experimental

The electrolytic cell was made of plexiglass, having the cathode made of intermetallic materials attached on one side, and the round shaped anode (nickel) on the other. The amount of gases evolved during certain time was determined using a water filled U-manometer. The standard electrolyte was 30 wt.% KOH water solution. The experimental conditions were as follows: Current density ranges from 15 to 700 mA/cm². The applied temperatures were from 256 K to 348 K (from -17 °C to +75 °C).

The intermetallics used as cathodes were as follows: 1. Ti-Pt, 2. Nb-Pd (80%Nb) 3. Pd-Ta, 4. Nb-Pd (65% Nb), 5. Zr-Pt, 6. Hf₂Fe and 7. PtMo₃, while nickel was used as the anode material in all investigated systems. Thus, the anode contribution was always the same. In this way we were able to see the role of cathode materials in energy consumption, as a function of the overall current density and voltage.

Results and Discussion

The hydrogen electrode reaction, $2\text{H}^+ + 2\text{e}^- = \text{H}_2$, is a heterogeneous reaction where an electrode material acts as the catalyst. The activity is closely related to its electronic configuration.

The energy consumption was determined using the relation: $Q = I U t$, where I (A) and U (V) are overall current and voltage through the cell, while t (s) is the time of evolution of a certain volume of hydrogen. The results obtained for Ti-Pt and PtMo₃ were compared with those for Ni in Fig. 1, also obtained in our laboratory by the same method [3]. It might be concluded that the intermetallics are more efficient than Ni as it was expected, and PtMo₃ is the best electrocatalyst among them.

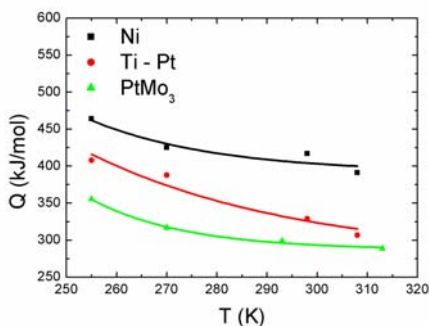


Fig. 1. Comparison of the Ti-Pt and PtMo₃ cathodes to Ni cathode at current density of 30 mA/cm².

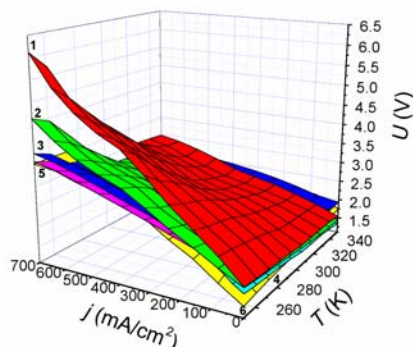
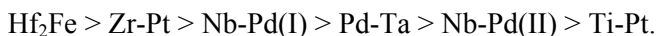


Fig. 2. Cell voltage as a function of current density at different temperatures for investigated intermetallics.

The overall voltages through the cell, U (V), as a relative measure of the energy consumption, at different current densities and temperatures for investigated intermetallics: 1) Ti-Pt, 2) Nb-Pd(II), 3) Pd-Ta, 4) Nb-Pd(I), 5) Zr-Pt, 6) Hf₂Fe, are presented in three-dimensional diagram (Fig. 2). On the basis of these data the intermetallics used could be ordered as follows, according to their electrocatalytic activity (the energy requirement is in the inverse order):



The use of vacant d-orbitals of Zr, Nb or Hf by the nonbonding electrons of Pd and Pt could optimize the employment of available orbitals and electrons in the hydrogen evolution reaction. In the case of Zr-Pt intermetallic the expected transfer of

d- electrons is from platinum (d^7sp^2) to low-lying vacant orbitals of zirconium and these intermetallics should be unusually stable. Further, since the strength of d-electron bonding increases quite markedly from 3d to 4d, and substantially from 4d to 5d levels, the stability of intermetallics and consequently electrocatalytic activity, could be rather low when only 3d-orbitals are involved, being higher when 4d orbitals and highest when 5d orbitals are employed [4]. This can explain why the Zr-Pt combination is better than the Ti-Pt one. This explanation and the fact that Hf_2Fe intermetallic absorbs large amounts of hydrogen [2], could further explain the better electrocatalytic activity of this material.

Conclusion

Several intermetallic combinations of transition metals were used as cathode materials in the electrolytic evolution of hydrogen from alkaline aqueous solutions. In comparison with the conventional cathode; Ni, an upgrade of the electrolytic effect using these intermetallics has been achieved. These intermetallics have shown significant electrocatalytic effects.

The pronounced electrocatalytic effects of these intermetallics were discussed in the context of the mutual interaction of their d-orbitals. Generally, all those effects connected with the electrocatalytic activity, are in close correlation with d-electronic configuration of single transition metals and/or their mutual combinations.

Acknowledgments

The financial support for this study was provided by the Ministry of Science, Technologies and Development of the Republic of Serbia, Project No. 1995.

References

- [1] B.E.Conway, L.Bai and M.A.Sattar, *Int. J. Hydrogen Energy*, 1987, 12, 607.
- [2] X.G.Li, A.Chiba, S.Takahashi, K.Aoki and T.Masumoto, *Intermetallics*, 1999, 7, 207.
- [3] D.Lj.Stojić, M.P.Marčeta, S.P.Sovilj, Š.S.Miljanić, *J.Power Sources*, 2003, 118, 315.
- [4] L.Brewer and P.R.Wengert, *Metall. Trans.*, 1973, 4, 83.

MODIFICATION OF CARBON ELECTRODES FOR SONOELECTROCATALYSIS OF OXYGEN REDUCTION AND HYDROGEN PEROXIDE FORMATION

B. R. Šljukić[†], C. E. Banks^{*}, S. V. Mentus[†] and R. G. Compton^{*}

^{}Physical and Theoretical Chemistry Laboratory, Oxford University,
South Parks Road, Oxford OX1 3QZ, UK,*

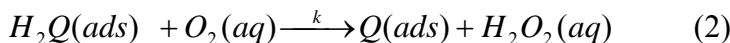
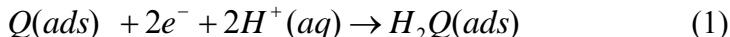
*[†]Faculty of Physical Chemistry Belgrade University,
Studentski trg 12-16, 11000 Belgrade, Serbia and Montenegro*

Abstract

Glassy carbon electrode was modified with 1,2-naphthoquinone for their applicability as catalytic materials for oxygen reduction and hydrogen peroxide production. The modified electrode was found to be suitable for use under ultrasound, so providing a basis for the green electrochemical production of hydrogen peroxide.

Introduction

The catalysis of electrochemical reduction of oxygen continues to attract attention especially because of its importance for electrochemical energy conversion, industrial electrolysis and hydrogen peroxide formation [1, 2, 3]. The immobilization of quinone species onto the surface of electrodes is becoming a common approach for hydrogen peroxide production via the following mechanism [3, 4]:



where Q (ads) is the adsorbed anthraquinone moiety.

In this paper glassy carbon electrode, modified with 1,2-naphthoquinone was investigated for their applicability as catalytic materials for oxygen reduction and hydrogen peroxide generation mediators using cyclic, rotating disc and sono voltammetry. The stability of the modified electrode under ultrasound is assessed.

Experimental

Voltammetric measurements were carried out on a μ -Autolab (ECO-Chemie, Utrecht, The Netherlands) potentiostat. All measurements were conducted in a thermostatted (22 °C) three-electrode cell. The working electrode made of glassy-carbon (3mm diameter, BAS, Indiana, USA). The counter electrode was a bright platinum wire, with a saturated calomel electrode (Radiometer, Copenhagen, Denmark) completing the circuit.

Glassy-carbon electrodes were polished using diamond-lapping compounds (Kelmet, UK) and then rinsed to remove any surface residue. These were then pre-treated before modification by cycling between -0.5 V and +2.0 V (vs SCE) at a scan rate of 100 mVs⁻¹ in 0.1 M H₂SO₄ for 10 min. Following that, the electrodes were held at +1.8 V (vs SCE) in the same solution for 3 minutes. The pre-treated GC electrodes were modified with 1,2 naphthoquinone (NQ), 20 μ L of 1.5 mM solution of NQ in

acetonitrile was pipetted on the pre-treated electrode and allowed to evaporate at room-temperature.

An ultrasonic horn, model CV 26 (Sonics and Materials Inc. USA), operating at a frequency of 20 kHz and fitted with a 3 mm diameter titanium alloy microtip (Jencons, Leyton Buzzard, UK) was used for sonovoltammetry studies. The intensity of the ultrasound was determined calorimetrically and it was found that a 20% amplitude corresponded to 87 W cm^{-2} . The working electrode was placed in a face-on arrangement to the ultrasonic horn. The horn was immersed beyond the shoulder of the stepped tip to ensure that ultrasound is efficiently applied into the solution. The horn to electrode distance was 10 mm throughout all measurements.

Results and Discussion

The regular cyclic voltammogram of 1,2-naphthoquinone modified GC electrode is shown in Fig. 1 **a**, where the reduction waves at ca. -0.2 V (vs. SCE) are consistent with the expected 2-electron, 2-proton process. When the solution was saturated with oxygen, as one can see in figure 1 **b**, the reverse peak (anodic) peak almost vanishes on the reverse scan whilst the forward peak is considerably increased indicating excellent electroactivity.

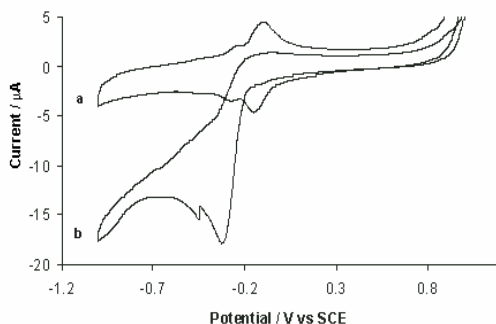


Figure 1. Comparison of cyclic voltammograms for GC electrode modified by 1,2-naphthoquinone in pH 8 phosphate buffer in the absence (a) and in the presence of oxygen (b)

effects of ultrasound on removing oxygen from a solution have already been examined [6] where it was found that the kinetic parameter of the oxygen reduction reaction *via* sonovoltammetry was possible using a modified Koutecky – Levich equation. First, the surface coverage of NQ on GC electrode was calculated from cyclic voltammetry data [5] and found to be $22 (\pm 0.4) \times 10^{-9} \text{ mol cm}^{-2}$. Fig. 2 illustrates effects of ultrasound of different intensities in oxygen saturated solution; there is considerable increase in magnitude of the current with increasing ultrasound intensity in accordance with amplified mass transport, *via* thinning the diffusion layer thickness [6, 7]. The rate constant of reduction of oxygen was determined in this case from the intercept of the sono Koutecky – Levich plot [6]. If a value for the coverage after insonation was used, the rate constant was found to be $9.9 \times 10^2 \text{ M}^{-1} \text{ s}^{-1}$ (for a coverage of $13.4 \times$

excellent electroactivity. By Andrieux and Savéant [5] method, the rate constant was found to be $5.6 \times 10^2 \text{ M}^{-1} \text{ s}^{-1}$ for a surface coverage of $16.5 \times 10^{-9} \text{ mol cm}^{-2}$. For this purpose, surface concentration, Γ , was calculated from the following equation:

$$\Gamma = \frac{Q}{nFA}$$

The electro - catalytic reduction of oxygen at a glassy carbon electrode modified by 1,2-naphthoquinone was explored also using sonovoltammetry. The

10^{-9} mol cm^{-2}). The coverage before ultrasound was found to be 24.8×10^{-9} mol cm^{-2} , while after insonation this was 18.2×10^{-9} mol cm^{-2} ; the average of these was used to calculate the rate constant. This was found to be 5.3×10^2 $\text{M}^{-1}\text{s}^{-1}$ and is in good agreement with that obtained from cyclic voltammetry. The combined chemical rate constant, $k\Gamma$ obtained from cyclic voltammetry and sonovoltammetry differ slightly: 93×10^{-5} $\text{dm}^3 \text{s}^{-1}$ for cyclic voltammetry comparing to 114×10^{-5} $\text{dm}^3 \text{s}^{-1}$ for sonovoltammetry.

Conclusions

Glassy carbon electrodes modified with 1,2-naphthoquinone for their applicability as catalytic materials for oxygen reduction and hydrogen peroxide mediators under ultrasound have been explored. The results encourage the investigation of sonoelectrochemistry with modified electrodes for producing large amounts of hydrogen peroxide quickly and efficiently.

Acknowledgements

B.Š. thanks the OSI / FCO Chevening Scholarship Scheme for funding. C.E.B. thanks the EPSRC for support via a project studentship (Grant GR/R14392/01). B.Š. and S.M. participate in the project No 1399 funded by the Ministry of Science and Environmental Protection of Republic Serbia.

References:

- [1] H. Inoue, S. R. Branković, J. X. Wang and R. R. Adžić. *Electrochim. Acta*, 2002, 47, 3777.
- [2] Y. Zhang, S. Asahina, S. Yoshihara and S. Shirakashi. *Electrochim. Acta*, 2003, 48, 741.
- [3] S. M. Golabi and J. B. Raouf. *J. Electroanal. Chem.*, 1996, 416, 75.
- [4] K. Vaik, D. J. Schiffrin and K. Tammeveski. *Electrochem. Commun.*, 2004, 6, 1.
- [5] C. P. Andrieux and J. M. Savéant. *J. Electroanal. Chem.*, 1978, 93, 168.
- [6] A. Salimi, C.E.Banks, and R.G.Compton, *Phys.Chem.Chem.Phys.*, 2003, 5, 3988
- [7] B.Šljukić, C.E.Banks, S.Mentus and R.G.Compton, *Phys.Chem.Chem.Phys.*, 2004, 6, 992

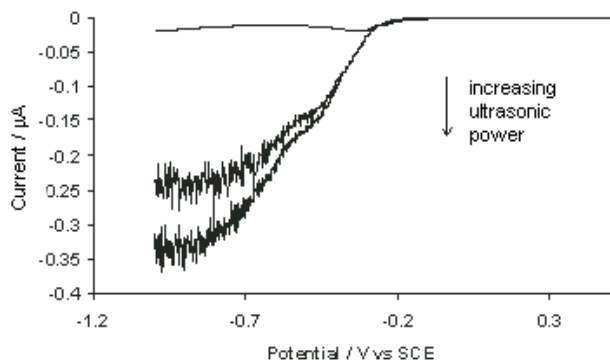


Figure 2. Cyclic voltammograms for GC electrode modified by 1,2-naphthoquinone in oxygen saturated pH 8 phosphate buffer for increasing ultrasound intensity at a fixed horn – to – electrode distance of 10 mm

OXYGEN REDUCTION ON POTENTIODYNAMICALLY FORMED TiO₂ IN AQUEOUS SOLUTIONS

S. Mentus

Faculty of Physical Chemistry, Belgrade University, Studentski Trg 12, 11000 Belgrade

Abstract

Oxygen reduction on anodically formed TiO₂ was studied in both alkaline and acidic water solutions, using *dc* voltammetry and rotating disc electrode. With the transition from acidic to alkaline media, a gradual transition from preferably two-electron reduction to a four-electron one was observed.

Introduction

Oxygen reduction reaction (ORR) is a very sluggish electrochemical reaction, characteristic of several different reaction paths, directed primarily by the catalytic action of metal support [1,2]. Nowadays this reaction is especially interesting as being a main cathodic reaction in fuel cells. Its kinetics and mechanism was widely investigated primarily on platinum surface, since platinum is the best electrocatalyst for this reaction [1,2]. There are few papers which deal with ORR on TiO₂ [3,4], both in acidic [3] and alkaline solutions [3,4]. The ORR was found to proceed on TiO₂ surface at very pronounced overvoltages, i.e. more cathodically than -1 V vs. SCE [3,4]. Nowadays, TiO₂ is an attractive compound in electrocatalysis, since, if used as a support of metallic catalysts or electrocatalysts, it may enhance their catalytic activity on the basis of Strong Metal Support Interaction (SMSI) effect, as reported for Pt/TiO₂ [5,6].

In this work, oxygen reduction was studied in aqueous media on anodically formed TiO₂, and a new insight into its mechanism was achieved upon a systematic variation of pH.

Experimental

A rod of titanium, 3 mm in diameter, within a teflon cylinder, served as the working electrode. Its surface was dry-cleaned by emery paperd No 1000, and oxidized immediately in 0.2 M KClO₄ aqueous solution by a potentiodynamic cycle from -1 up to 1.4 V vs. SCE, as described elsewhere [7]. By this procedure the surface was covered by an approx. 3 nm thick oxide film. Further potentiodynamic cycles within the same limiting anodic potential did not increase the film thickness, but only slightly improved its compactness.

The solution used were aqueous perchlorate solution, in which pH was adjusted either by HClO₄ or NaOH. The solutions were either argon or oxygen saturated. The voltammetric curves were recorded by a PAR Model 273 Potentiostat/Galvanostat. The rotation speed of working electrode was controlled by a Beckman rotating electrode device.

Results and Discussion

In oxygen saturated solutions, the current waves appear, preceding the background current of hydrogen evolution, which may be nothing other than the currents of oxygen reduction. In Fig 1, the plateau currents were plotted against the square root of rotation frequency according to Levich equation. For comparison, the line related to the $4e^-$ oxygen reduction on platinum in 0.1 M HClO_4 solution, based on the reference [9], is plotted too. The plots for TiO_2 make positive intercepts on the current axis, which is caused most probably by the high background current in the region of diffusion limitation of oxygen reduction. It is easily to note that the slopes of these plots are grouped around two different values. The higher slopes overlap with that found in ref. [9] for a $4e^-$ reduction path. The lower slope is factor 0.59 that of higher one. Therefore, one may conclude that in the studied case, with the transition from acidic to alkaline solutions, one deals with the transition from preferably $2e^-$ to a $4e^-$ oxygen reduction.

It is known that the direct, 4-e path, of oxygen reduction is favored on such surfaces which enable the dissociation of adsorbed O_2 , i.e., in the cases when adsorption forces are uniformly distributed to both oxygen atoms. If one atom of is more strongly bonded than the other, the dissociation is aggravated and the indirect, 2-electron reduction path is favored. On a non-polarized TiO_2 / aqueous solution interface, surface species are either H^+ , adsorbed on O^{2-} ions, or OH^- , adsorbed on Ti^{4+} ions [8]. On cathodically polarized interface, reduced species, Ti^{3+} ions, on the surface of TiO_2 layer are produced, which manifest itself in cyclovoltammetry as a cyclovoltammetric curve symmetric toward potential axis [4], characteristic otherwise of the surface processes.

On the basis of existing knowledge, as well as on the basis of the experimental results in this study, the following simplified model of oxygen reduction on TiO_2 surface may be proposed:

Most probably, O_2 reduction proceeds through the interaction of oxygen with Ti^{3+} ions, which become sufficiently numerous at a sufficiently large cathodic poten-

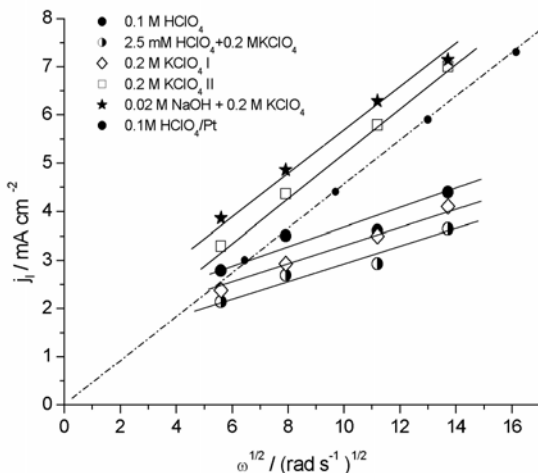


Fig. 4. The limiting currents of oxygen reduction plotted versus square root of angular rotating frequency, for the solutions assigned in the legend. The dashed line is constructed from the data in ref.[9].

tials. Within a Ti^{4+} matrix of TiO_2 , these ions act as the electron excess sites, and thus in acidic solution they are blocked by adsorbed protons. Thus, in acidic solutions, the oxygen molecules compete for rare free Ti^{3+} sites, and the molecules may be adsorbed unsymmetrically, with only one O atom bonded to the surface. In alkaline solutions, the free protons are practically absent, OH^- ions are unable to adsorb on Ti^{3+} sites which thus remain free, and there is high probability that the O_2 molecule may be distorted between the two closely distributed Ti^{3+} sites.

Conclusion

It was found that oxygen reduction proceeds at anodized titanium surface, opposite to the existing literature data that this reaction may proceed at only porous, thermally applied TiO_2 . The voltammograms on rotating TiO_2 disc, recorded in acidic, neutral and alkaline solution indicate a transition from $2e^-$ path, in acidic solution, toward $4e^-$ path, in alkaline one. Under a reasonable assumption that the reduction proceeds on Ti^{3+} ion sites, using the recent models of TiO_2 /aqueous solution surface, a self-consistent explanation of the transition from $2e^-$ to $4e^-$ reduction path was proposed.

Acknowledgement

The study has been supported by and carried out within the EU Project "Prometeas", Contract No ICA2-CT-2001-10037. The Ministry of Science and Environmental Protection of Republic Serbia supported also the work through the contract No 1399.

References

- [1] H.S.Wroblowa, Y.C.Pan, G.Razumney, J.Electroanal.Chem., 1976, 69, 195.
- [3] M.R.Tarasevich, A.Sadkowski, E.Yeager, Comprehensive Treatise in Electrochemistry, Plenum Press:New York, Chapter 6, 1983, 301-398.
- [3] P.Clechet, C.Martelet, J.R.Martin, and R.Olier, Electrochim.Acta, 1979, 24, 457.
- [4] V.B.Baez, J.E.Graves, D.Pletcher, J.Electroanal. Chem., 1992, 340, 273.
- [5] B.C.Bead, P.N.Ross, J.Electrochem.Soc., 1986, 133, 1839.
- [6] S. G. Neophytides, S. H. Zafeiratos, M. M. Jakšić, J. Electrochem. Soc., 2003, 150, E512.
- [7] J.Pješčić, S.Mentus, N.Bлагоjević, Mater. Corros., 2002, 53, 44.
- [8] U.Diebold, Appl.Phys., 2002, A76, 1.
- [9] U.A.Paulus, A.Wokaun, G.E.Scherer, T.J.Schmidt, V.Stamenkovic, N.N.Markovic, P.N.Ross., Electrochim.Acta, 2002, 47, 3738.

ENERGY CONSUMPTION IN THE ELECTROLYTIC EVOLUTION OF HYDROGEN WITH IRON-NICKEL ELECTRODES

Š.S. Miljanić^a, N.D. Simić^b, M.P. Marčeta Kaninski^b, A.D. Maksić^b
and D.Lj. Stojić^b

^aUniversity of Belgrade, Faculty of Physical Chemistry
11001-Belgrade, P.O. Box 137,

^bVinča Institute of Nuclear Sciences, Laboratory of Physical Chemistry
11001-Belgrade, P.O. Box 522, Serbia & Montenegro

Abstract

The possibilities to reduce energy consumption in the electrolytic hydrogen production using ionic activators added into an alkaline electrolyte have been investigated. Two cathode/anode systems, Fe/Ni and Ni/Fe were investigated. We have found that some activators, like *tris-(ethylenediamine)Co(III) chloride* complex in combination with the sodium molybdate can reduce energy needs per mass unit of hydrogen produced for more than ten percent in all investigated systems compared to those of non-activated electrolytes. Additionally, iron exhibits some special properties in this view.

Introduction

Hydrogen is becoming increasingly important as an energy medium for the 21st century. It ensures an energy storage function, easy distribution *via* gas lines and direct conversion to electricity. Fossil fuels especially oil, approach the exhausting world's supplies, as well as cause pollution generating greenhouse gases cited in the Kyoto agreements. As hydrogen does not exist on the Earth it must be produced. It will be necessarily obtained from water as the main raw material, but that requires energy. There are a large variety of production approaches. The most attractive method, in regard to greenhouse gas emissions, appears to be water electrolysis, using electric power sources that do not themselves produce greenhouse gases.

Among overall world technologies for hydrogen production today about 10% belong to the electrolysis. Use of this technology on the large scale is limited because of high-energy consumption. Thus, development of new methods and improvement of the existing ones is extremely important, especially in countries where electricity is relatively cheap or great excesses are available in some periods of the day or year.

Possible mechanism through which ionic activators increases electrolytic efficiency is the electrocatalytic effect of two, so called d-metals, deposited on the electrode surface, in the form of powder, providing at the same time very large surface area of active centers.

Experimental

Iron-nickel and nickel-iron combinations of electrodes were used in experiments to compare efficiencies of activated and non-activated systems in order to see the effect of iron as a cheap commercial material.

Similar investigations we have performed in our previous work to find out the efficiency of nickel in the same context. Also, further details about the experiment can be found in [1]. Additionally, a rough estimation of the economy of the activation oriented process is presented here. It is based on the life time and stability investigation of activators added [2].

Measurements were done both with the ‘standard electrolyte’ (30 wt% KOH) and ‘activated electrolyte’ (1×10^{-3} mol dm⁻³ of *tris-(ethylenediamine)Co(III) chloride* complex and 1×10^{-2} mol dm⁻³ of Na₂MoO₄, both laboratory made from p.a. chemicals, in the standard electrolyte. Cobalt [3] or molybdenum [4] deposited on the electrode surfaces during electrolysis have been known to increase the efficiency of the process. In this work we tried these elements together.

Results and Discussion

The energy requirement for the electrolytic process run was calculated using the relation: $Q = I \times U \times t$, where I and U are overall current and voltage through the cell, and t is the time of evolution of a certain volume of hydrogen. It was calculated as two thirds of the entire volume evolved in the cell.

The data were collected in a wide temperature range from -17 to about $+75^\circ\text{C}$, and arranged to show dependence of energy consumption (Q) as a function of current densities and temperatures.

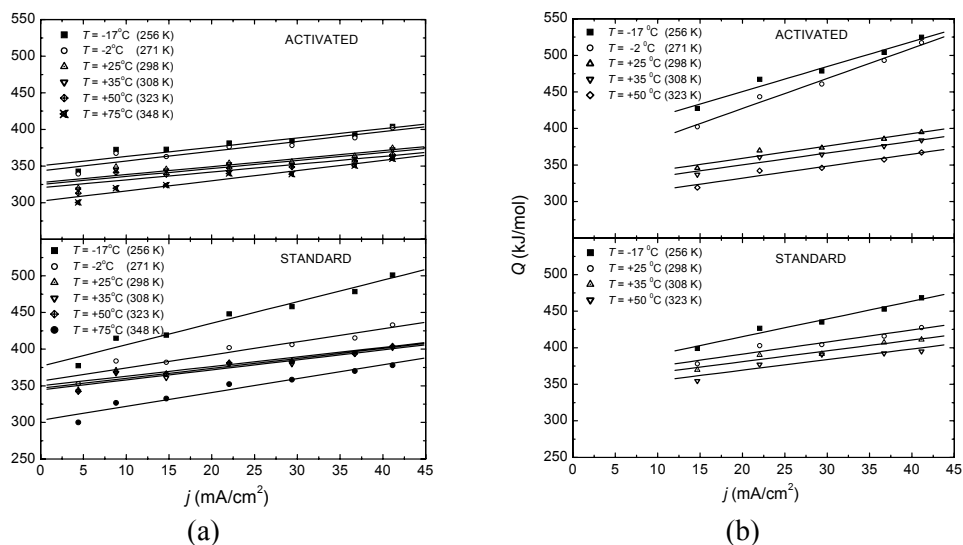
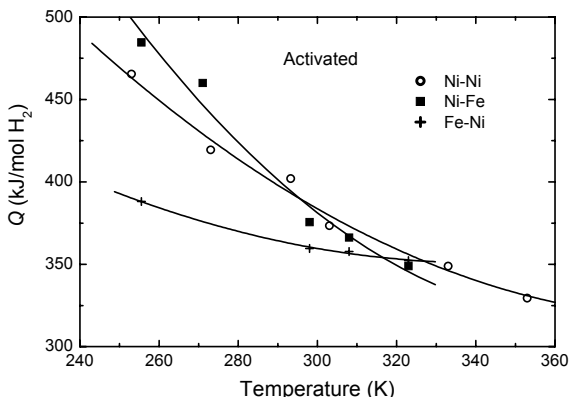


Fig. 1 Energy consumed to evolve one mol of hydrogen as a function of the current density at different temperatures for two *cathode-anode* combinations: Fe-Ni (a); Ni-Fe (b).

As shown in these figures, both the temperature and activation significantly reduce energy consumption. It is expected since both factors have catalytic effects on the hydrogen evolution reaction. However, at sufficiently high temperatures, activators influence becomes dominant.

There are some indications [3] that iron, if used as a cathode, is a specific material in this view. Our measurements also show that, especially at lower temperatures, iron is more efficient than nickel. Figure 2 illustrate this statement in regard to the nickel-cathode. This practically offers a possibility to optimize the process at another position on the temperature scale.

Fig. 2. Comparison of the activation effects for different combinations of electrode materials (cathode-anode) at a current density of 30 mA/cm^2 .



Conclusion

Nickel-iron combinations of electrodes were used as electrode materials in the electrolytic evolution of hydrogen from alkaline solutions. Behavior that iron exhibits, regarding activation with ionic activators, was shown in our experiments. On the basis of the obtained diagrams we estimated an average energy saving to be around 10 percent. That is advantageous since in practice, it should be more attractive electrode material due to lower price compared to that for nickel.

Acknowledgment

The financial support for this study was provided by the Ministry of Science, Technologies and Development of the Republic of Serbia, Project No. 1995.

References

- [1] D.Lj. Stojić, M.P. Marčeta, S.P. Sovilj and Š.S. Miljanić, *J. Power Sources*, 2003, 118, 315.
- [2] M.P. Marčeta Kaninski, A.D. Maksić, D.Lj. Stojić and Š.S. Miljanić, *J. Power Sources*, 2004, 131, 107.
- [3] L. Brossard, *Mater. Chem. Phys.*, 1991, 30, 61.
- [4] J.Y. Huot, L. Brossard, *Surf. Coat. Techn.*, 1988, 34, 373.

POTENTIOMETRIC SENSOR BASED ON POLYANILINE-SKELETON NICKEL ELECTRODE I. ELECTRODE PREPARATION

A. Kellenberger^a, W. Brandl^b, N. Vaszilcsin^a and N. Plesu^c

^aUniversity "Politehnica" of Timisoara, Piata Victoriei 2, 1900 Timisoara, Romania,

^bFachhochschule Gelsenkirchen, Neidenburger Strasse 10, 45877 Gelsenkirchen, Germany,

^cRomanian Academy-Institute of Chemistry, Bd.Mihai Viteazul 24, 1900 Timisoara, Romania

Abstract

A conducting polymer polyaniline (PANI)-selective electrode has been prepared by electropolymerization of aniline in sulphuric acid solution on skeleton nickel electrode. The results indicate a granular, highly crystalline structure, similar to the polyaniline films deposited on conventional substrates, like smooth nickel or platinum. The major advantage conferred by the skeleton substrate consists in improved adherence and stability of the polyaniline coating.

Introduction

In the recent years several studies were dedicated to the deposition of polyaniline on various substrates, such as platinum, graphite, glassy carbon, gold or ITO. The aim of our paper is to extend the applicability field of this type of conductive polymer, by deposition of polyaniline on original substrates (skeleton nickel).

Experimental

In all experiments, freshly distilled aniline (MERCK) and sulphuric acid (MERCK) were used. The skeleton nickel electrode was prepared according to the thermal arc spraying technique [1], using Praxair Ni and Al wires. The electrode was activated by dissolving the aluminium for 4 h in 1 mol L⁻¹ NaOH solution at 80°C.

For the PANI deposition a conventional three-electrode cell was used. The working electrode was skeleton nickel (S=1 cm²), the reference electrode - saturated calomel electrode and the counterelectrode graphite rods. The electrochemical deposition was performed from an aqueous solution of 0.027 mol L⁻¹ aniline in 1 mol L⁻¹ H₂SO₄, by sweeping the potential between -0.2 V/SCE and 1.2 V/SCE, using a PAR Potentiostat 273. The polymerization was finished after 30 cycles. The deposited polymer was rinsed with 1 mol L⁻¹ H₂SO₄ and finally with bidistilled water. The morphology of the PANI coating was studied by scanning electron microscopy (Philips XL 30 ESEM), coupled with energy-dispersive X-Ray analysis (EDX). X-Ray diffraction patterns of the polyaniline coating were registered with a Philips Xpert Diffractometer using the Cu-K α radiation ($\lambda = 1.54$). The working temperature was 25 \pm 1°C in all cases.

Results and Discussion

The principle of arc spraying implies the formation of an electric arc at the convergence point of two wire electrodes which moves with a constant velocity. A

high velocity gas atomizes the molten metal and accelerates the particles towards the substrate. Depending on the spray parameters a rough, porous deposit can be obtained.

The dissolution of the aluminium from the coating leads to the increase of the real surface area of the skeleton electrodes. The EDX analysis indicates a decrease of the Al content from 24.97 to 1.54 wt% after 4 hours of activation [2]. The structure of the skeleton nickel electrode obtained by arc spraying, before and after activation is presented in Fig. 1. (a) before activation and (b) after activation.

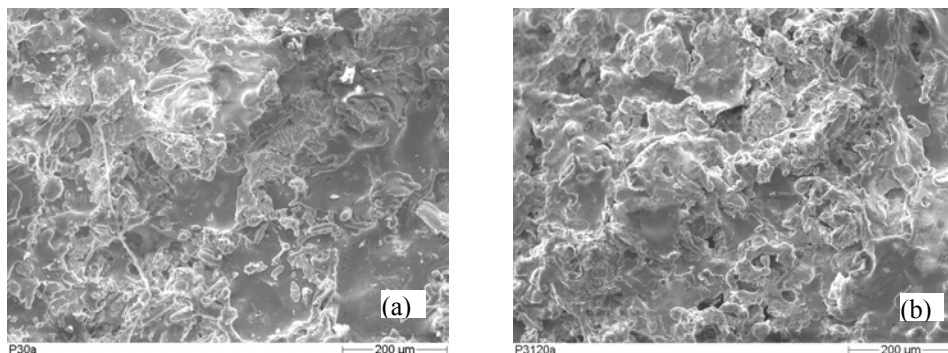


Fig. 1. SEM micrographs of the skeleton nickel electrodes. Magnitude 100x.

For the electrochemical polymerization of aniline cyclic voltammograms were recorded between -0.2 and 1.2 V/SCE, with a scan rate of 100 mV s^{-1} , shown in Fig. 2.

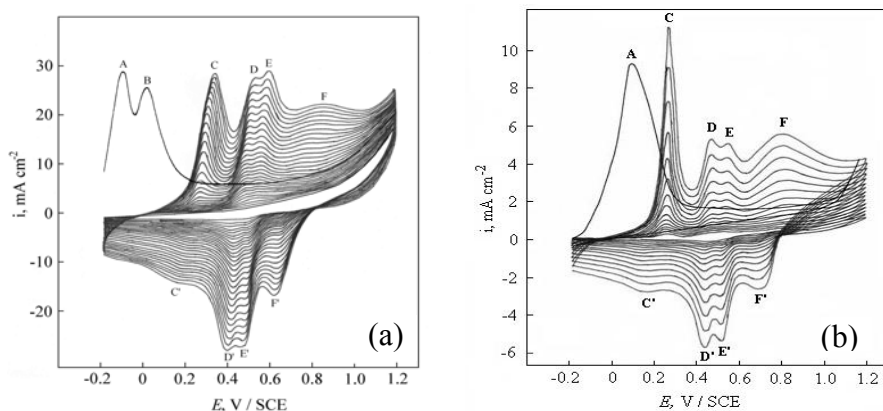


Fig. 2. Cyclic voltammogram recorded in 0.027 mol L^{-1} aniline in $1 \text{ mol L}^{-1} \text{ H}_2\text{SO}_4$. (a) skeleton nickel electrode; (b) smooth nickel electrode.

The peaks appearing on the voltammogram were attributed to different steps of the mechanism [3] and correspond to the literature data.

PANI film was deposited in the same conditions on a smooth nickel electrode. The morphology of the PANI deposit on smooth and skeleton nickel electrodes was compared by SEM. The corresponding micrographs are presented in Figure 3.

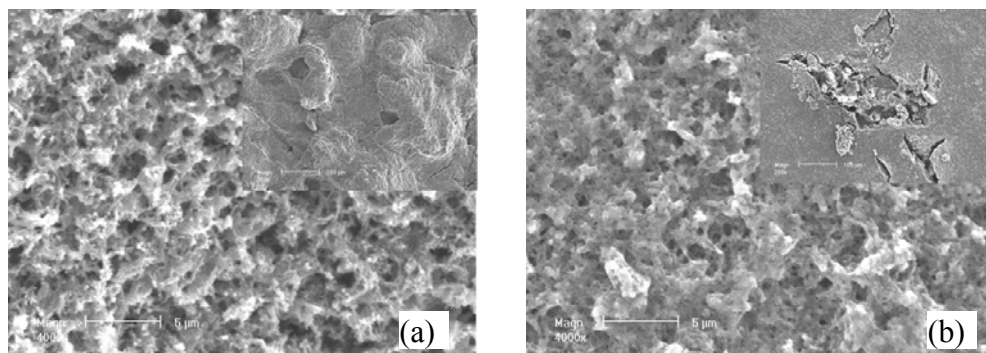


Fig. 3. SEM micrographs of the PANI film. Magnitude 4000x. Inserts: magnitude 200x. (a) skeleton nickel; (b) smooth nickel.

The PANI deposited on smooth nickel was not adherent and presented numerous defects and cracks. On the skeleton nickel a continuous, adherent PANI film was obtained, with only very few micro-cracks. Increasing the magnitude, a porous, granular structure of PANI was observed on both substrates.

The S/N ratio determined from EDX analysis for the PANI-skeleton nickel electrode gives information about the doping level of polyaniline. The values between 0.53 – 0.62 demonstrates that polyaniline was obtained in the form of emeraldine salt. The C/N ratio approximates the theoretic value (6).

Conclusions

The skeleton nickel substrate is suitable for obtaining PANI in an easy and reproducible manner. On skeleton nickel the PANI film reveals a continuous structure with improved adherence and stability in time, compared to the PANI deposit obtained on smooth nickel.

References

- [1] J. Fournier, D. Miousse, J.G. Legoux, *Int. J. Hydrogen Energy*, 1999, 24, 519.
- [2] N. Vaszilcsin, W. Brandl, A. Kellenberger, D. Toma, *Chem. Bull. "Politehnica" Univ. (Timisoara)* 1998, 43, 330.
- [3] A. Kellenberger, N. Vaszilcsin, N. Plesu, I. Manovicu, *Annals of West University Timisoara*, 2003, 12, 575.

POTENTIOMETRIC SENSOR BASED ON POLYANILINE-SKELETON NICKEL ELECTRODE II. SENSING PROPERTIES

Nicoleta Plesu^a, Andrea Kellenberger^b, N.Vaszilcsin^b, Waltraut Brandl^c

^aRomanian Academy-Institute of Chemistry, Bd.Mihai Viteazul 24, 1900 Timisoara, Romania,

^bUniversity "Politehnica" of Timisoara, Piata Victoriei 2, 1900 Timisoara, Romania,

^cFachhochschule Gelsenkirchen, Neidenburger Strasse 10, 45877 Gelsenkirchen, Germany

Abstract

The sensing properties of the Ni-polyaniline (PANI)-selective electrode were determined for Cl⁻, I⁻ and SO₄²⁻. The modified electrode presents short response time and Nernstian behaviour in the concentration range of 10⁻¹ to 10⁻⁵ mol L⁻¹.

Introduction

It is well known that during the synthesis of polyaniline the anions present in the reaction media are included in the polyaniline matrix as dopant anions. By immersing polyaniline in solutions containing other types of anions an exchange equilibrium process occurs, and the dopant anions are replaced [1-3]. As a result of this behaviour it is possible to use polyaniline as anion sensor.

In this paper our results concerning the utilization of PANI-skeleton nickel electrode as potentiometric anion sensor are presented. An unconventional substrate was selected for the deposition of PANI, namely skeleton nickel [4]. This kind of substrate solves the problems related to the adherence of the polyaniline film. The substrate doesn't influence the sensing properties of the modified electrode, thus, the potentiometric response is the same as in case of conventional substrates.

Experimental

In all experiments, freshly distilled aniline (MERCK) and sulphuric acid (MERCK) were used. The skeleton nickel electrode was prepared according to the thermal arc spraying technique [5].

The PANI-skeleton nickel electrode was prepared by electrochemical deposition of PANI on a substrate made of skeleton nickel. The PANI was deposited from an aqueous solution of 0.027 mol L⁻¹ aniline in 1 mol L⁻¹ sulphuric acid, by sweeping the potential between -0.2 V/SCE and 1.2 V/SCE, at 100 mV s⁻¹ scan rate, 30 cycles.

The potentiometric response of the PANI-skeleton nickel electrodes was measured (digital voltmeter E 0302) in solutions with different concentration of Cl⁻, I⁻ and SO₄²⁻. A saturated calomel electrode (SCE) was used as reference. In all experiments the temperature was 25° ± 1°C.

Results and Discussion

Before measurements the modified electrode was conditioned in 10^{-4} mol L^{-1} solution of anions, in order to reduce the response time. Prior to each experiment the electrode was rinsed with bidistilled water.

In order to obtain the calibration curves (figure 1 and 2), KCl, KI and K_2SO_4 solution were prepared, with different concentrations, ranging from 10^{-1} to 10^{-5} mol L^{-1} (pH = 7.05).

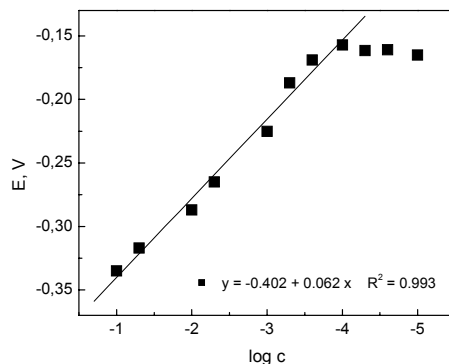
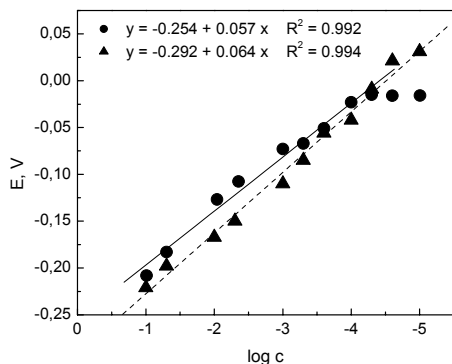


Figure 1. Potentiometric calibration curves for chloride (●) and iodide (▲) anions. **Figure 2.** Potentiometric calibration curves for sulphate anions.

The electrodes give Nernstian potentiometric responses in the concentration range of 10^{-1} to $5 \cdot 10^{-5}$ mol L^{-1} , equation (1) and (2).

$$E = E^{o'} - 2.303 \frac{RT}{F} \lg a_{X^-} \quad (1); \quad E = E^{o''} - 2.303 \frac{RT}{F} \lg a_{SO_4^{2-}} \quad (2)$$

Equations (1) and (2) correspond to a linear variation of the potential with the anion activity in the solution, with the general form $y = a + bx$, where $a =$ ordinate (E_o' or E_o'') and $b =$ slope (0.059 V decade $^{-1}$).

The slope of the calibration curves approaches the theoretical value of 0.059 V decade $^{-1}$ for each anion. The detection range was between 10^{-1} and $5 \cdot 10^{-5}$ mol L^{-1} for chloride anions, 10^{-1} to 10^{-5} mol L^{-1} for iodide and 10^{-1} to 10^{-4} for sulphate anions.

To confirm the stability of the modified electrode, the calibration curves were recorded during a period of three month. The detection range was preserved and the electrode can be used for 12 weeks without any major deviations (figure 3 and 4).

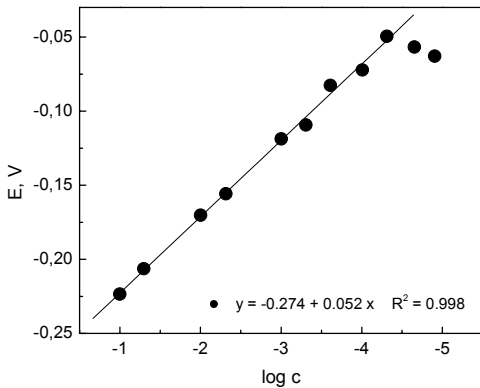


Figure 3. Potentiometric calibration curves for chloride anions after 3 month.

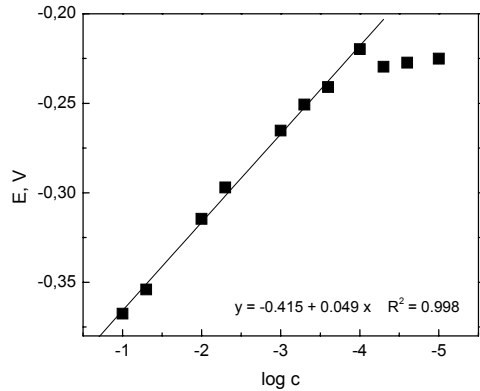


Figure 4. Potentiometric calibration curves for sulphate anions after 3 month.

In order to investigate the selectivity of the modified electrode for Cl^- anions, with respect to I^- interfering ions, the potentiometric selectivity coefficient ($K_{\text{Cl-I}}$) was evaluated by the separate solution method, according to equations (3) and (4).

$$-\log K_{\text{Cl-I}} = \frac{E_2 - E_1}{2,303(RT/F)} \quad (3); \quad K_{\text{Cl-I}} = \frac{a_{\text{Cl}^-}}{a_{\text{I}^-}} \quad (4)$$

The value of the calculated selectivity coefficient ranges between 1.66-3.09. The selectivity of the PANI-skeleton nickel electrode is relatively low, but the main advantages of rapid response and stability in time, ease of preparation and insolubility of PANI in organic solvents make the electrode attractive.

Conclusions

The PANI-skeleton nickel electrode reveals a good sensitivity for chloride, iodide and sulphate anions. The best detection limit is $10^{-5} \text{ mol L}^{-1}$ and the electrode is stable in time. The equilibrium installs quickly and the electrode is facile to handle.

The skeleton substrate confers improved adherence of the polymeric film and is economically more attractive than conventional substrates (Pt, Au).

References

- [1] C.R. Martin, H. Freiser, *Anal Chem.*, 1981, 53, 902.
- [2] Z.Lu, Z.Sun, S. Dong, *Electroanalysis*, 1989, 1, 271.
- [3] J.Wang, *Synthetic Metals*, 2002, 132, 49.
- [4] N.Plesu, A.Kellenberger, N.Vaszilcsin, I. Manovicu, *Chem. Bull. Politehnica Univ. (Timisoara)*, 2000, 45 (59), 198.
- [5] N.Vaszilcsin, W.Brandl, A.Kellenberger, D.Toma, *Chem. Bull. Politehnica Univ. (Timisoara)*, 1998, 43, 330.

DETERMINATION OF THE IONIZATION CENTERS OF CEFTRIAXONE

G. Popović¹, M. Aleksić², N. Burić³ and V. Kapetanović⁴

¹*Institute of Inorganic Chemistry*, ²*Institute of Physical Chemistry*, ³*Institute of Physics and Mathematics*, and ⁴*Institute of Analytical Chemistry, Faculty of Pharmacy, Vojvode Stepe 450, P.O.Box 146, 11000 Belgrade*

Abstract

Ionization constants of cephalosporin antibiotic ceftriaxone are determined using pH-potentiometric titrations at $I=0,1M$ (NaCl) and $t=25\text{ }^{\circ}\text{C}$, and the obtained values are attributed to the corresponding ionization centers: $pK_1=2.37$ (COOH), $pK_2=3.03$ (N aminothiazole), $pK_3=4.21$ (enol) and $pK_4=10.73$ (NH - amide).

Introduction

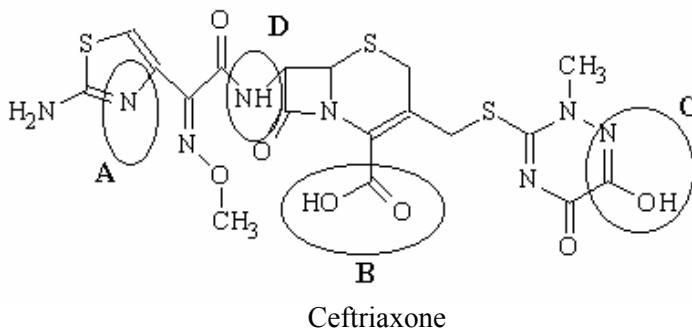
This paper deals with pH potentiometric determination and characterization of the ionization constants of ceftriaxone (CFRX) in water solution. An effort has been made for the correct characterization of the three overlapping ionization constants since, only two ionization constants are reported in acid medium up to now. Besides, in alkaline medium, the ionization constant of amide group in position 7 of the Δ -cephem ring has been evaluated too.

Experimental

Potentiometric measurements were performed on TIM900 Titration Manager-TitraLab (Radiometer Copenhagen) equipped with a combined pH electrode (GK2401B), and ABU901 autoburette (Radiometer Copenhagen). Investigated drug CFRX is produced by SIGMA. Other reagents were of analytical-reagent grade. The solutions were prepared in doubly distilled water. All the investigations were performed in solutions of constant ionic strength, $I=0.1\text{ M}$ (NaCl), at 25°C .

Results and Discussion

In the interval of pH from 0 to 14 CFRX (H_3C) is involved in four acid-base processes.



Three of them: protonation of nitrogen in amino-thiazole ring (**A**), and protolysis of carboxyl (**B**) and enol (**C**) groups happens in acid medium and they overlap. In acid medium CFRX is dominantly present in four forms: H_4C^+ , H_3C , H_2C^- and HC^{2-} . The fourth acid-base process corresponding to the protonated amide group (**D**) occurs in alkaline medium, where CFRX is dominantly present as HC^{2-} and C^{3-} . The corresponding ionization equilibrium constants are defined as:

$$K_1 = \frac{[H_3C][H^+]}{[H_4C^+]} \quad (1) \qquad K_2 = \frac{[H_2C^-][H^+]}{[H_3C]} \quad (2)$$

$$K_3 = \frac{[HC^{2-}][H^+]}{[H_2C^-]} \quad (3) \qquad K_4 = \frac{[C^{3-}][H^+]}{[HC^{2-}]} \quad (4)$$

Ionization constants were determined potentiometrically, by using the formation function method [1]:

$$\bar{n} = \frac{\sum_1^n n[H_nC]}{\sum_0^n [H_nC]} \quad (5)$$

Equation (5) allows determination of the experimental value for \bar{n} at each data point using pH-metric titration of the acid solution of CFRX ($c_{CFRX} = 1 \times 10^{-3}$ M; $c_{HCl} = 2.12 \times 10^{-3}$ M) with standard solution of NaOH ($c_{NaOH} = 0.10023$ M):

$$\bar{n} = \frac{3c_{CFRX} + c_{HCl} - c_{NaOH} - [H^+] + [OH^-]}{c_{cef}} \quad (6)$$

In Equation (6) c_{CFRX} , c_{HCl} and c_{NaOH} represents ceftriaxone, HCl, and NaOH concentration in the solution, while $[H^+]$ and $[OH^-]$ are equilibrium concentrations of hydrogen and hydroxyd ions obtained from the measured pH values [2]. Constants K_1 , K_2 and K_3 are determined in the pH range 2-7 where the concentration of the anionic form $[C^{3-}] \rightarrow 0$ using the expression:

$$\bar{n} = \frac{4[H^+]^3 + 3K_1[H^+]^2 + 2K_1K_2[H^+] + K_1K_2K_3}{[H^+]^3 + K_1[H^+]^2 + K_1K_2[H^+] + K_1K_2K_3} \quad (7)$$

According to the experimental results obtained for $\bar{n} - [H^+]$ pairs using non-linear curve-fitting analysis the corresponding constants were evaluated.

At $\text{pH} > 8$ the ionization constant K_4 was evaluated regardless to the process occurring in the acid medium. Since, only one acid – base pair (HC^{2-} - C^{3-}) exists at $\text{pH} > 8$, the formation function is given by:

$$\bar{n} = \frac{[\text{HC}^{2-}]}{[\text{HC}^{2-}] + [\text{C}^{3-}]} \quad (8)$$

By combination of eqs. (4) and (8) the linear dependence is obtained, as follows:

$$\frac{1 - \bar{n}}{\bar{n}} = K_4 \frac{1}{[\text{H}^+]} \quad (9)$$

By applying the linear regression analysis the ionization constant K_4 is calculated.

The obtained pK values for CFRX and the corresponding ionization centers are shown in Table 1.

Table 1. Ionization constants of CFRX; $t=25$ °C, $I=0.1$ M(NaCl)

Constant	pK_1	pK_2	pK_3	pK_4
Value	2.37	3.03	4.21	10.73
Ionization center	-COOH	N (amino-thiazole)	-N=COH (enol)	-NH-(amide)

Ionization centers are predicted related to the structurally similar compounds [3].

Acknowledgments

This work was supported by the Ministry for Science, Technology and Development of Serbia, Grant #1458.

References

- [1] H. Rossotti, The Study of Ionic Equilibria, Longman, New York, 1978.
- [2] L.B. Pfenđt, D.M. Sladić, T.J. Janjić, G.V. Popović, Analyst, 1990, 115, 383.
- [3] V. Evagelou, A. Tsantili-Kakoulidou, M. Koupparis, J. Pharm. Biomed. Anal., 2003, 31, 1119.

DETERMINATION OF As (III) IN THE GROUND WATER SPECIES BY DIFFERENTIAL PULSE POLAROGRAPHY

A. Abu Rabi¹ and D. Sužnjević²

¹*ICTM-Department of Catalysis, P.O. Box 815, Belgrade, SCG*

²*Institute of General and Physical Chemistry, P.O. Box 551, Belgrade, SCG*

Abstract

The few ground water species from south Serbia were analyzed by differential pulse polarography (DPP) from 1 M HCl without any other water pretreatments. Based on concentration dependence of two As (III) reduction peaks at -0.50 and at -0.65 V, the quantitative determination of As (III) concentration in water species on the level of 55 and 75 $\mu\text{g l}^{-1}$ was obtained. The possibility of Sn (IV) determination besides As (III) was also proved.

Introduction

In case of arsenic determinations in different environmental samples a various analytical methods were applied. Between them there are a lot of electroanalytical ones, such as voltammetric, which are rather simple and sensitive enough to directly determine As (V) and As (III), lack of their different behavior in reduction processes. Opposite to As (III), As (V) is electroinactive, in most situations which is useful for electrochemical determinations. Arsenic determination can be realized mainly by a well known voltammetric techniques such as differential pulse polarography (DPP) [1,2], anodic stripping voltammetry (ASV) [3,4] and cathodic stripping voltammetry (CSV) [5,6]. The purpose of this work is to develop a common and versatile method for direct As(III) determination in natural waters without any sample pretreatments, using DPP with dropping mercury electrode (DME), and also to find the possibility for determination of Sn (IV) in the presence of As (III).

Experimental

The whole experiments were performed using the polarographic analyzer PA3 Czech production (Laboratorný přístroje) with three electrode system. Besides the working electrode, saturated calomel electrode (SCE) as reference, and Pt-foil as auxiliary electrode were immersed in the electrolytic cell. The concentrated HCl is added to the natural ground water species, in which As (III) is not present, into electrolytic cell to the concentration of 1M playing role of a supporting electrolyte. Before DPP curve recording, the pure nitrogen was passed 5 min through the experimental solution.

Results and Discussion

After recording DPP curve of the supporting electrolyte, a standard solution of As (III) was added to the desired concentrations from $1.2 \cdot 10^{-5}$ to $1.1 \cdot 10^{-4}$ M. In the beginning

of the mentioned interval only one reduction peak of As (III) at -0.5V was developed (Fig.1). With increasing As (III) concentration, besides this peak (a) in Fig.1, a second reduction peak, very sharp and narrow, was observed at -0.65V , (Fig.1, peak b), followed by another peak at -0.85V , which is not suitable for analytical purposes and was not presented in Fig.1. The nature of all As (III) reduction peaks which arise from inorganic acids, including HCl, is already known in the literature [7]. It was proved also, that peaks at -0.5 and -0.65V are concentration dependant, showing a good linearity of peak current intensity with As (III) concentration, as it is shown in Fig.1. Having in mind such behavior of As (III), upon reduction from HCl as supporting electrolyte, the three ground water species from south Serbia were analyzed. It was found that two of them contained As (III) on the level of $55\ \mu\text{gl}^{-1}$ and $75\ \mu\text{gl}^{-1}$, established from analysis of peak (a) which is characteristic for low As (III) concentration. However, if small amount of Sn (IV), which is most common interferences in quantitative arsenic determinations, is added into As (III) solution, the second peak decreased significantly (Fig.1, curve6). As it was known that reduction current of Sn (IV), under applied conditions, interferes with first peak of As (III), it gives an opportunity for using this peak in the quantitative determination of Sn (IV) when As (III) is present. The method for quantitative determination of Sn (IV) besides As(III), based on this finding statement is in progress.

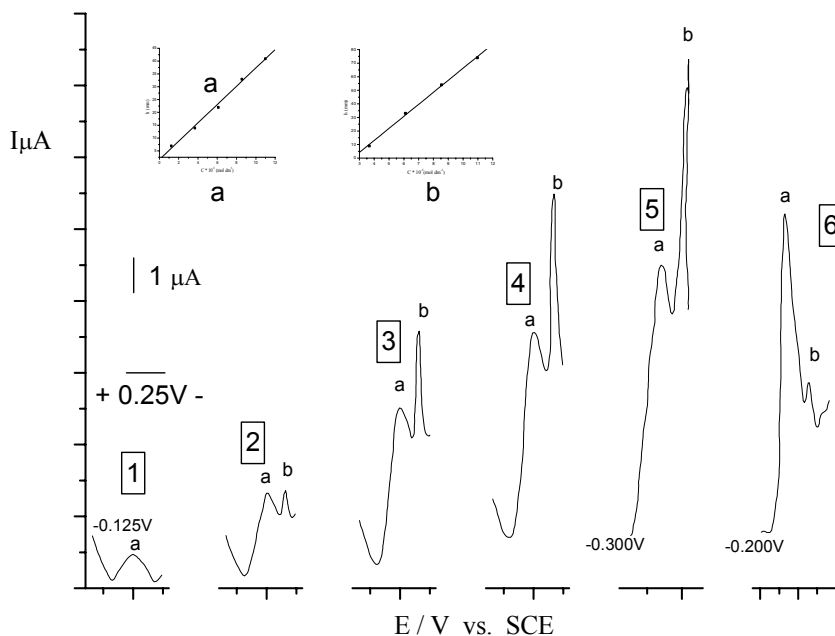


Fig.1 Dpp curves of As (III) reduction from 1 M HCl as supporting electrolyte: 1) supporting electrolyte, (2-5) upon addition of different As (III) concentration, 6) 5+standard solution of Sn (IV) on the level of $20\ \mu\text{gl}^{-1}$

Conclusion

Differential pulse polarography was applied to the quantitative determination of As(III) in three ground water species without any simple pretreatments. Based on the results obtained with acidified (with concentrated HCl) water species without and with different concentration of As (III), it was found that both of As(III) in two from three ground water species was found to be on the level of 55 and 75 $\mu\text{g l}^{-1}$. Also, the possible quantitative determination of Sn (IV) besides As (III) was proved.

References

- [1] D.J. Myers, J. Osteryoung, *Anal. Chem.* 1973, 45, 267.
- [2] F.T. Henry, T.M. Thorpe, *Anal. Chem.* 1980, 52, 80.
- [3] F.G. Bodewig, P. Valenta, H.W. Nirnberg, *Fres. Z. Anal.Chim.*, 1982, 311, 187.
- [4] M. Kopanica, L.Novotny, *Anal. Chim. Acta*, 1998, 368, 211.
- [5] W. Holak, *Anal. Chem.* 1980, 52, 2189.
- [6] H. Li, R.B. Smart, *Anal. Chim. Acta*, 1996, 325, 25.
- [7] J.P. Arnold, J.M. Johnston, *Talanta*, 1969, 16, 1191.

ELECTROCHEMICAL INVESTIGATION OF IMIDAZOL AZO CHROMOTROPIC ACID AND ITS Pd(II) COMPLEX

J. Savić, V. Vasić, C. Filip Cristea¹ and M. Jitaru¹

*Department of Physical Chemistry, Vinča Institute of Nuclear Sciences,
PO Box 522, 11001 Belgrade, Serbia and Montenegro,*

¹*Associated Francophone Laboratory, Faculty of Chemistry and Chemical Engineering,
Babes-Bolyai University, 11 Arany Janos, 3400 Cluj-Napoca, Romania*

Abstract

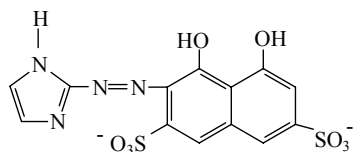
The electrochemical behaviour of 1,8-dihydroxy-2-(imidazol-2-ylazo)-naphthalene-3,6-disulphonic acid (IACA) and its complex with Pd(II) was investigated using cyclic voltammetry. Experiments were performed in the concentration range from $5 \times 10^{-6} \text{M}$ to $4.8 \times 10^{-4} \text{M}$ of IACA. Linear dependence of current intensity vs. IACA concentration was obtained in the investigated concentration range. According to the obtained results, process is controlled by diffusion.

Introduction

Azo compounds are among the most profoundly explored classes of organic compounds both from theoretical and practical viewpoints [1]. The power of cyclic voltammetry results from its ability to rapidly provide considerable information of redox processes, the kinetics of heterogeneous electron transfer reactions or adsorption processes [2]. The aim of this study was to investigate the electrochemical behaviour of IACA and its complex with Pd(II) using different electrochemical conditions. It is presented here the preliminary results obtained with glassy carbon (GCE) and carbon paste electrodes (CPE). Pd(II)-IACA complex was investigated beforehand by using of spectrophotometric methods [3].

Experimental

IACA (Scheme 1) was synthesized as described previously [4]. Cyclic voltammetry experiments were performed using a modular electrochemical system (BAS 100). A GCE was used as a working electrode; with an Ag/AgCl and a Pt coil as the reference and auxiliary electrodes, respectively. Before each electrochemical step, the solutions were deoxygenated by purging with pure nitrogen. GCE and blank electrode for the CPE



Scheme 1.

were supplied by BAS Inc. CPE was prepared by mixing of IACA and carbon powder with paraffin oil in an 80:20 (m/m) mass ratio until a homogeneous paste was obtained. The pastes were packed into the electrode and smoothed until a shiny, smooth surface was obtained. The blank CPE was prepared in the similar way without adding the modifier.

Results and Discussion

All experiments were carried out in quasi-isothermal conditions, at room temperature. Scan rates in the range from 25 to 200 mV/s were used. The potential range in which voltammograms were recorded was between 0 and -1.2 V. The supporting electrolyte was Britton–Robinson buffer (pH 4). Cyclic voltammograms, recorded for IACA concentrations in the range from $5 \times 10^{-6} \text{ M}$ to $4.8 \times 10^{-4} \text{ M}$, with GCE as a working electrode at scan rate 100 mV/s are presented on Fig. 1.

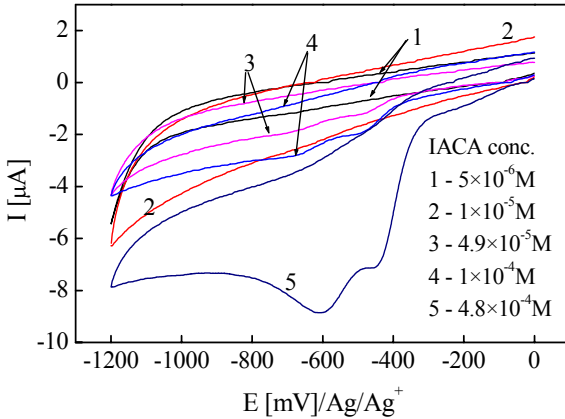
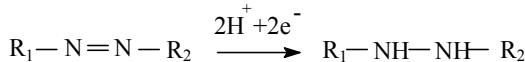


Figure 1. Cyclic voltammograms of IACA obtained at scan rate 100 mV/s on CPE.

As expected, the reduction curves confirmed the linear relationship between the current intensity and IACA concentrations. Two reduction peaks have been observed in this potential range at -600 and -450 mV for IACA concentration $4.8 \times 10^{-4} \text{ M}$. According to Refs. [5,6] these peaks could be attributed to the following processes on the level of azo group:



and further, two electrons participate in the reduction to the corresponding amines.

Table 1. Electroanalytical data regarding the electrochemical behaviour of investigated substances (scan rate 50 mV/s)

Substance	E_{red}^1 [V/Ag/Ag ⁺]	I_{red}^1 [µA]	E_{red}^2 [V/Ag/Ag ⁺]	I_{red}^2 [µA]
IACA	-0.51	-0.86	-0.86	-3.85
Pd(II)	-1.10	-371.29	-0.85	-259.00
IACA : Pd	-1.05	-429.82	-0.90	-158.65

¹ glassy carbon electrode

² carbon paste electrode (unmodified)

The regression equation line for the IACA concentration range from $5 \times 10^{-6} \text{ M}$ to $4.8 \times 10^{-4} \text{ M}$ was $I = (0.01 \times C_{IACA} + 0.36)$ where I is in µA and C_{IACA} is in $\mu\text{mol}/\text{dm}^3$ ($r^2 = 0,99$) and allow the determination of IACA with good results. The reduction potentials for IACA, Pd and their complex are given in Table 1.

Cyclic voltammograms obtained for electrochemical system with GCE as working electrode for $4.9 \times 10^{-5} \text{M}$ Pd-IACA complex at different scan rates is presented on Fig. 2.

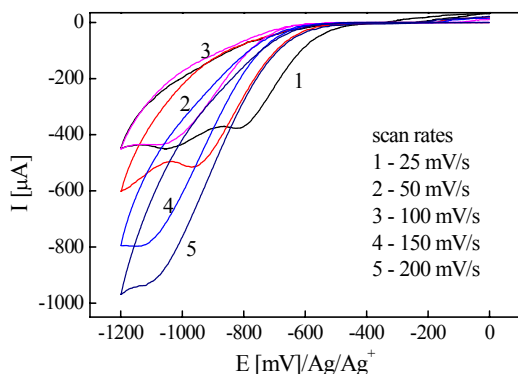


Figure 2. Cyclic voltammograms obtained for $4.9 \times 10^{-5} \text{M}$ Pd-IACA complex at different scan rates, on GCE.

As we see from Fig.2 the peak potentials shift toward negative values with increasing sweep rate, which indicates that at lower overvoltages the reduction is controlled by electron transfer process. Consequently, the second cathodic peak shifts out of range of potential axis at sweep rates higher than 150 mV/s. For the first cathodic peak, linear dependence of peak current on square root of sweep rate was evidenced, which indicates that at high overvoltages the reduction process becomes diffusion controlled.

Conclusion

IACA and its Pd(II) complex may be reduced on glassy carbon and carbon paste electrodes, respectively. The reduction is two-step quasireversible process. The peak current was found to depend linearly on concentration, for IACA/CPE, and on square root of sweep rate, for IACA-Pd(II)/GCE.

Acknowledgement

Financial support was provided by the AUF project “Pôle d’excellence régionale”; Référence: 2700PL309/2003.

References

- [1] U.Eisner and E.K.Eisner, Encyclopedia of Electrochemistry of the Elements, A. J.Bard (Ed.), Marcel Dekker, 1979, NY.
- [2] J.Wang, Analytical Electrochemistry, II edition, Wiley-VCH, 2000, 28.
- [3] V.Vasić, A. Muk, Polyhedron, 1992, 11, 1597.
- [4] V.Vasić, A.Muk, T.Petrova, V.Nikolić, Zh Anal Khim, 1988, 43, 793.
- [5] M.Jitaru, C.Cirtiu, M.Stan, M.Schiopu, G.Petrica, Journés d’Electrochimie, JE’03, 3-6 June 2003, Poitiers, France.
- [6] N.Goyal, S.Verma, K.Singhal, Croatica Chemica Acta, 1998, 71, 715.

ELECTRO-CRYSTALLIZATION DURING THE PROCESSES OF TIN ELECTROPLATING FROM SULPHONIC ACIDS

D. Tošković¹, M.B. Rajković² and Č. Lačnjevac²

¹ Faculty of Technology, University of Serbian Sarajevo, Bosnia & Herzegovina and ² Faculty of Agriculture, Zemun, University of Belgrade, Serbia & Montenegro

Abstract

In this paper nucleation phenomenon of tin electro-crystallization on iron from acid sulphate and sulphonic baths is followed by using potentiostatic and galvanostatic pulsing voltmeters. Obtained results show that the type of sulphonic acid conditions the nucleation process during electrolytic tin-electroplating. The consequences, observed in the behaviour of deposit tin coating, are possible to explain by the surface adsorption and the presence of the aromatic ring and heteroatoms.

Introduction

The mechanism of tin electrodeposition from acid baths in similar conditions that are used in industrial lines of electrolytic tin electroplating and electro-crystallization are priceless for the producers of white tin.

In this paper nucleation phenomenon of tin electro-crystallization on iron from acid sulphate and sulphonic baths is followed by using electrochemical methods: potentiostatic and galvanostatic pulsing voltmmetry.

The influence of sulphur acid and some sulphonic acids are analysed: toluene-sulfonic, β -naphthol sulphonic and p-phenol sulphonic, with different substituents in an aromatic ring in order to make difference between the influence of every single quick nucleation and the process of seed growth. Because of that, the aim of this paper is to analyse the influence of aromatic sulfonic acid on nucleation and growth of tin crystal on (steel) iron base under strictly controlled conditions.

Experimental

In order to analyse the influence of sulphonic acid on the quality of the formed coating (MR cold roll tape Č O148) on iron of high quality degree is used for the support, during which the polycrystallinity of the support emerged as the only unhomogeneity.

Small characteristic peak at the beginning of a curve shows certain overstrain during deposition, indicating processes that emerge during nucleation. The constant potential during the deposition of tin coating for given value of current density is then restored, that in the end it rises to some amounts on which begins the separation - the creation of free hydrogen. The equipment was used for potentiodynamic measurement potentiostat-galvanostat (PAR 373, USA) and HP 8046A X-Y recorder. Saturated calomel electrode was used as reference electrode.

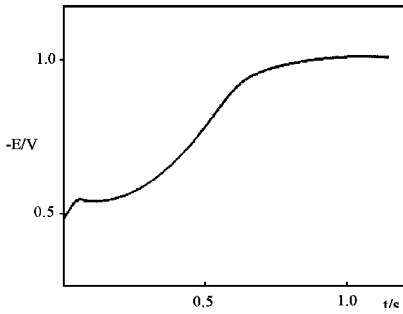


Figure 1. Potential transient for tin electrodeposition on iron from Sn^{2+} ($5 \cdot 10^{-3}$ M) in phenol-sulphonic acid solution 0.6 M. Applied current density 5 mA/cm^2

Fig.2. shows the line loop of voltammogram that characterizes the deposition of metals – a balanced potential $E_{\text{Sn}7\text{Sn}^{2+}}$ under the said conditions is shown on vertical part of the loop.

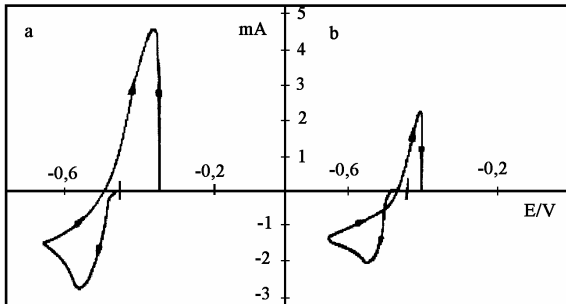


Figure 2. Voltammogram of tin deposition on iron. Sweep rate 100 mV/s .

- (a) sulphuric acid 0.6 M
($\text{Sn}^{2+} 1.8 \cdot 10^{-3}$ M);
(b) p-phenolsulphonic acid
($\text{Sn}^{2+} 5.0 \cdot 10^{-3}$ M).

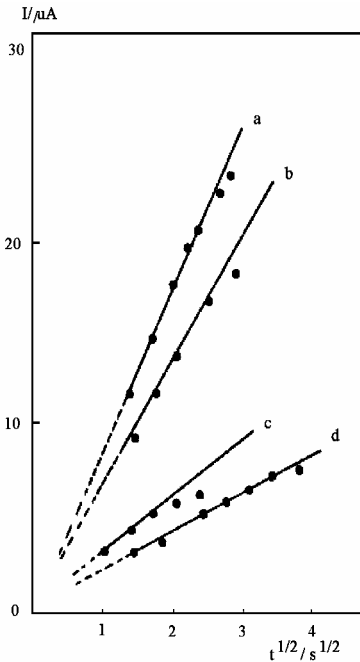
The existence of cathodic hydrating and sudden growth of current density again confirms that it is necessary for system to reach the critical over intensity to come to nucleation.

Tin layer 11.2 g/m^2 – deposition of tin is followed periodically, during which is observed the growth of cathodic peak that also depends of concentration. The sharp anodic peak indicates the beginning of dissolution and exhaustion of the solution. It is obvious that the behaviour of p-phenol sulphonic acid (Fig. 2b) is such that it rises critical intensity which is visible in the relation to the previous example with H_2SO_4 (Fig. 2a) where the inhibition of electro-crystallization process is clear. The process of nucleation highly depends of electrolyte content. In diluted solutions of tin the sudden nucleation on iron is observed and further growth of nucleus in hemispheric diffusion filed. Variations in the structure of the sulphonic acid aromatic ring also enable access in the reasons of observed inhibitions.

Three-dimensional sudden nucleation and the diffuse growth after that, is ideal extreme description that is reachable by the usage of lower concentrations and lower overstrains. Three conditions define this process: 1. all the nuclei N , emerged simultaneously, 2. all the nuclei N grow with the same speed and 3. in given time t , all the nuclei N have the same size.

Cathodic electricity for the growth of nucleus N in time t could be shown in following equation, where K – a constant of the system, c – concentration of Sn(II) , N – the thickness of nucleation, F – Faraday constant, R – universal constant, T – temperature, η – overvoltage. Due to interlace of neighbouring diffusion fields it leads to situation that the system does not behave anymore as in previous case and with increasing

$$I_{N,t} = K \cdot c^{3/2} \cdot N \cdot \left(1 - \exp\left(\frac{2F}{RT} \cdot \eta\right)\right)^{3/2} \cdot t^{1/2}$$



of time of the action the surface will be identified with linear on the rust coating. In this case, the growth of electricity over time can be described in the following equation,

where is

$$I_{N,t} = K' \cdot c^{3/2} \cdot A \cdot (1 - \exp(-\frac{2F}{RT} \cdot \eta)) \cdot t^{1/2}$$

geometrical surface of electrode and K' a constant of the system. So, the growth of electricity should be expected at the beginning, but then it reaches the maximum and then slowly falls.

Figure 3. $I-t^{1/2}$ plots corresponding to the rising part of current transients for tin electrodeposition at fixed overpotential (-28 mV) from Sn^{2+} solution in 0.3 M acids: H_2SO_4 (a); toluenesulphonic (b); β -naphthalensulphonic (c) and p-phenolsulphonic (d).

Fig.3. shows that nucleation decreases in the following order: in H_2SO_4 , toluene-sulphonic, β -naphtol sulphonic, and p-phenol sulphonic acids. The graph shown in Fig.3. is same as the growth of electricity of the transitional regime during the tin electrodeposition for chosen overstrain (-28 mV) from 0.3 M acid solutions and the concentration Sn(II) from 10^{-3} M.

The increasing of sulphonic acid concentration from 10^{-6} to 10^{-3} M results with the decreasing of nucleation thickness, while the constant value of nucleation is reachable above the given values of acid concentration.

Adsorption of aromatic sulphonic molecules is highly believable which leads to inhibition of electro-crystalization process. As the result, it comes to increasing of crystallisation overstrain values and decreasing of the numbers of nuclei during the constant overstrain values. Maximal influence is observed for the values of acid concentration that are lower from industrially applicable (approximate 0.3 M). According to this, the sulphonic acid in baths for tin-electroplating is not only in function of inhibitor of oxidation Sn(II) into Sn(IV) , but also to enable higher electro conduction of baths and is very involved in the first – the beginning degree of tin deposition.

Conclusion

The type of sulphonic acid conditions the nucleation process during electrolytic tin-electroplating. Under well conducting processes the inhibiting effect of sulphonic acid which is in direct correlation with the structure of molecules of that acid is observed. The thickness of nucleation decreases with the acid concentration and for adopted industrial conditions shows the constant value. The consequences, observed in the behaviour of deposit tin coating, are possible to explain by the surface adsorption and the presence of the aromatic ring and heteroatoms.

**Biophysical Chemistry
Photochemistry
Radiation Chemistry**

(E)

DENATURATION OF dsDNA BY p53 STUDIED BY FLUORESCENCE CORRELATION SPECTROSCOPY

V. Vukojević, T. Yakovleva, L. Terenius, A. Pramanik¹ and G. Bakalkin

*Department of Clinical Neuroscience and ¹Department of Medical Biochemistry and Biophysics,
Karolinska Institute, Stockholm, Sweden*

Abstract

We report a novel activity of p53, its ability to denature double stranded DNA molecules aggregated by basic peptides. Stable complexes of coiled single-stranded DNA molecules with basic peptides are formed in this reaction. Thus, complementary to the ability to catalyze DNA renaturation, p53 denatures double-stranded DNA when the latter reaction is thermodynamically favorable.

Introduction

The tumor suppressor p53, a sequence-specific transcription factor that plays a central role in cancer surveillance, exerts its main functions by activating or repressing transcription of its target genes [1]- [5]. Protein products of several genes activated by p53, including p21, Bax, GADD45, Mdm2, and Cyclin G, are required to regulate cell cycle progression and apoptosis. In “normal”, *i.e.* non-stressed cells, p53 is present at low levels and is latent. Genotoxic stress, or oncogene activation, activate p53-mediated gene transcription, and stabilize its concentration by disrupting the p53-MDM2 interactions that are targeting p53 to degradation by the ubiquitin-proteasome system. Both activation and stabilization (accumulation) of p53 appear to be essential responses to cellular stress.

We demonstrated previously that p53 binding to specific DNA target sites is activated by basic fragments of the CTD and by other basic peptides including poly-L-Lysine, and that activating peptides do not interact with p53 but rather aggregate the target DNA molecules [6], [7]. In the course of these studies we observed that p53 dissociates the dsDNA aggregates formed in the presence of basic peptides [6], [7]. We demonstrate here that p53 not only dissociates the dsDNA aggregates, but also denatures dsDNA into single-stranded molecules. We identified the ssDNA molecules, which in the presence of basic peptides are stable in a coiled form [8] by Fluorescence Correlation Spectroscopy (FCS) [9].

Fluorescence correlation spectroscopy (FCS)

Principles of Fluorescence correlation spectroscopy (FCS) were formulated about thirty years ago in the frame of a physical method called fluctuation correlation analysis [9]. In this method statistical analysis of the time course and the amplitudes of spontaneous fluctuations in the number of particles occurring in a very small volume of a system is performed to derive conventional diffusion transport and chemical rate coefficients. Building on advantages of fluctuation correlation analysis FCS benefits

additionally from the high sensitivity and spectroscopic selectivity of fluorescence measurements. A schematic presentation of a typical FCS setup is given in Figure 1.

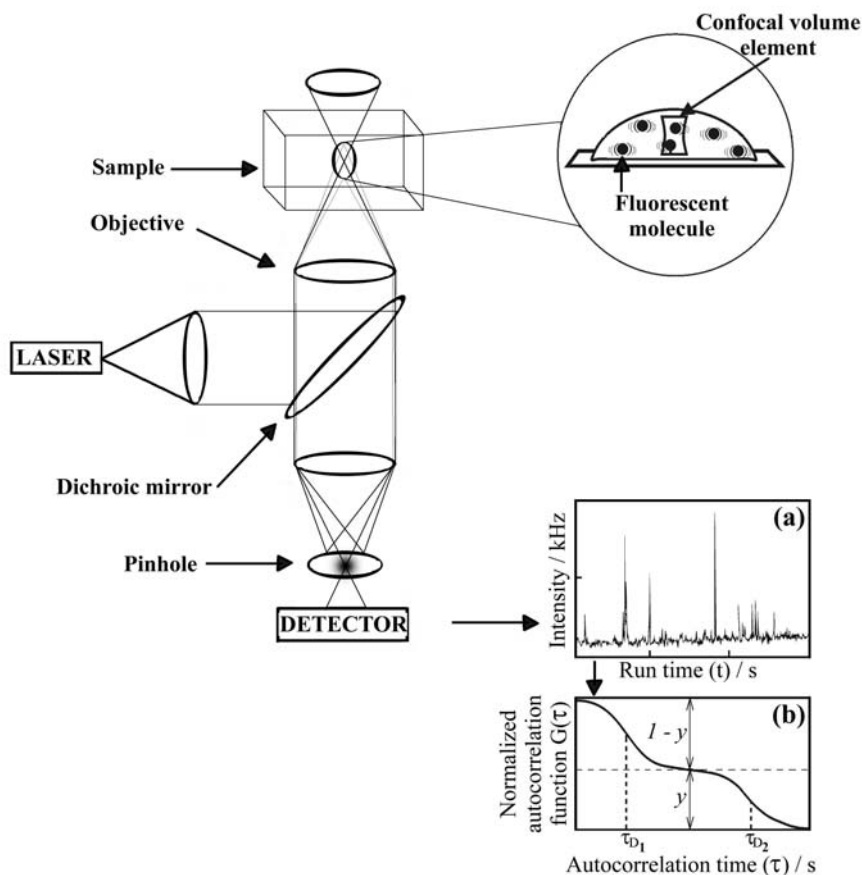


Figure 1. Schematic presentation of the instrumentation for fluorescence correlation spectroscopy (FCS). **a)** The number of pulses originating from the detected photons, recorded during a specific time interval, corresponds to the measured light intensity. Thus, in one experimental run we monitor how the intensity of fluorescence changes in time. **b)** The electrical signal is gathered in regular time intervals, transferred to a digital signal correlation unit, and the corresponding normalized autocorrelation function $G(\tau)$ is calculated on line.

To induce fluorescence, the sample is illuminated by incident light of a certain wavelength delivered by a laser. The laser beam is reflected by a dichroic mirror and sharply focused by the objective to form a miniature, yet very well defined volume element in the sample. The volume from which fluorescence is detected is further reduced by a confocal aperture (pinhole) in the image plane, to reject out-of-focus light

and provide an elliptical volume element. This is crucial for providing a very small volume element (in today's equipment the observation volume from which fluorescence is detected is typically about 2×10^{-16} liters), and enables a submicrometer resolution facilitating detection at defined loci, as well as quantitative and background-free analysis. Following the absorption of energy, fluorescent molecules lose energy through photon emission. The light emitted by fluorescing molecules passing through the confocal volume element is separated from the exciting radiation and scattered light by a dichroic mirror and barrier filter, and transmitted to the detector, which responds with an electrical pulse to each detected photon. The number of pulses originating from the detected photons, recorded during a specific time interval, corresponds to the measured light intensity. Thus, in one experimental run we register changes in fluorescence intensity in time (Fig. 1 (a)).

To evaluate the gathered data, i.e. to analyze time series sampled at regular intervals during one run, temporal autocorrelation analysis is performed to detect non-randomness in the data, and to identify an appropriate time series model if the data are not random (Fig. 1(b), Fig. 2). In temporal autocorrelation analysis we first derive the intensity autocorrelation function $G(t)$. $G(t)$ gives the correlation between the intensity of light, $I(t)$, measured at a certain time, t , and its intensity measured at a later time $t + \tau$, $I(t + \tau)$. The intensity autocorrelation function may be defined as an ensemble average:

$$G(\tau) = \langle I(t)I(t + \tau) \rangle \quad (1a)$$

or, alternatively, as a time average of the product $I(t)I(t + \tau)$ measured over a certain accumulation time T :

$$G(\tau) = \lim_{T \rightarrow \infty} \frac{1}{T} \int_0^T I(t)I(t + \tau) dt \quad (1b)$$

Since the unprocessed data in FCS are essentially fluorescence fluctuations over the mean fluorescence intensity $\langle I \rangle$, it is also possible to express the autocorrelation function through fluctuations of light intensities $\partial I(t) = I(t) - \langle I \rangle$ and $\partial I(t + \tau) = I(t + \tau) - \langle I \rangle$, at times t and $t + \tau$, respectively. In this way, the intensity autocorrelation function is defined as:

$$G(\tau) = \langle I \rangle^2 + \langle \partial I(t) \partial I(t + \tau) \rangle \quad (1c)$$

Regardless of the form of expression (1a) – (1c), as they are all equivalent, it is not convenient to use the intensity correlation function in practice because its value depends on properties of the applied experimental setup. Therefore, instead of using the intensity autocorrelation function, it is more convenient to use the so-called normalized autocorrelation function, $G(\tau)$, defined as:

$$G(\tau) = 1 + \frac{\langle \partial I(t) \partial I(t + \tau) \rangle}{\langle I \rangle^2} \quad (2)$$

which is independent of properties as laser intensity, detection efficiency and fluorescence quantum yield.

Thereafter, the experimentally obtained autocorrelation curve has to be compared to autocorrelation functions derived for different model systems. For example, if one fluorescent species is present in the sample and there are no intramolecular changes affecting the fluorescence of the observing molecules, the intensity fluctuations will reflect the passage of fluorescent particles through the observation volume. Since the passage of fluorescent particles is governed solely by diffusion, the best fitting of the autocorrelation curve will be obtained by an autocorrelation function describing free diffusion of fluorescent particles [9],[10]:

$$G(\tau) = \frac{1}{N} \cdot \frac{1}{\left(1 + \frac{\tau}{\tau_D}\right) \sqrt{1 + \frac{w_{xy}^2}{w_z^2} \frac{\tau}{\tau_D}}} \quad , \quad (3)$$

where τ_D is a characteristic decay time. Its value is calculated from the autocorrelation function (3) that matches best the actual, experimentally determined, autocorrelation curve. This parameter, derived directly from FCS measurements, is related to the translation diffusion coefficient D :

$$\tau_D = \frac{w_{xy}^2}{4D} \quad , \quad (4)$$

which is related to the size of the fluorescent molecules *via* the Stokes-Einstein equation:

$$D = \frac{kT}{6\pi\eta R} \quad . \quad (5)$$

In equation (5) k is the Boltzmann constant, T is absolute temperature, η is the solvent viscosity, and R is the hydrodynamic radius of a hypothetical compact sphere in a viscous medium. Furthermore, as can be seen from equation (3), the limiting value of $G(\tau)$ as $\tau \rightarrow 0$ is related to the average number of molecules in the observation volume (N), i.e. it can be used to determine the absolute concentration (c) of the fluorescing molecules.

Results and Discussions

Our previous FCS studies demonstrated that large aggregates of DNA with basic peptides are dissociated into smaller nano-scale particles when incubated with p53 [6], [7]. To investigate further this novel p53 activity by FCS we first incubated fluorescently labeled ds-Rh-SO or ds-Rh-NO containing the wild type and mutant p53 binding sites, respectively, alone (Fig. 2 a) and b)), with basic peptides (Fig. 2 c) and d)), and in the presence of p53 (Fig. 2 e) and f)) and recorded changes in fluorescence intensities. As previously observed, 2 nM solution of ds-Rh-SO exhibits fluorescence

fluctuations typical for a single fluorescent species (Fig. 2 a) with a single diffusion time $\tau_D = (0.60 \pm 0.05)$ ms. Addition of GST-p53, in particular the following concentrations were tested 3.7 nM, 7.0 nM, 12 nM, 37 nM and 74 nM, to the ds-Rh-SO solution does not alter the diffusion time of ds-Rh-SO. Thus, at nanomolar concentrations of ds-Rh-SO and p53, protein-dsDNA complexes do not form.

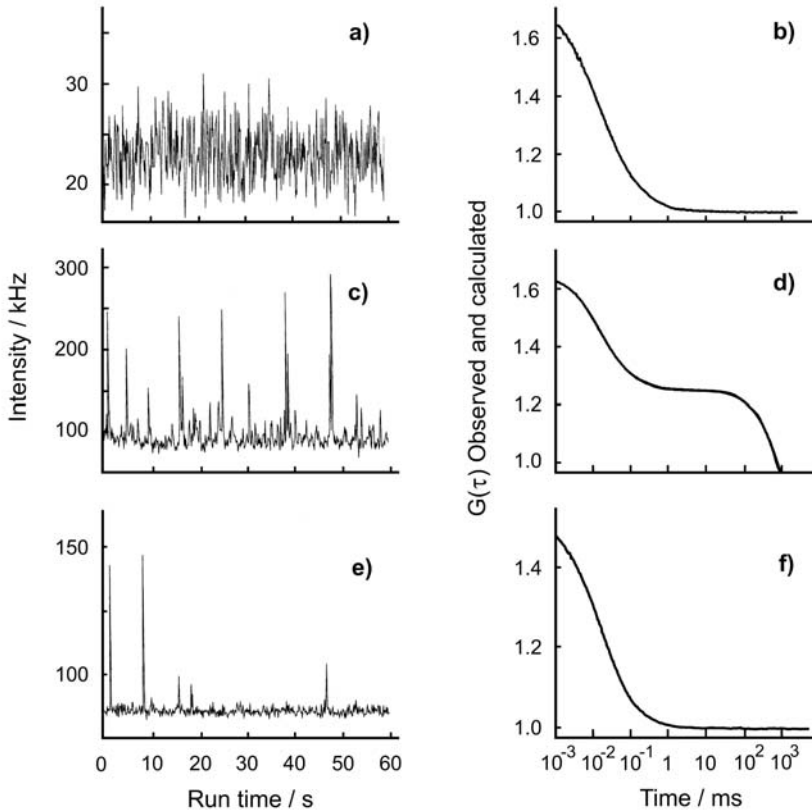


Fig. 2. FCS measurements of the p53 mediated denaturation of dsDNA aggregates formed in interaction with basic peptide big dynorphin. (a, c, d) Fluorescence intensity fluctuations. (b, d, f) Observed and calculated autocorrelation functions $G(\tau)$. Data were recorded 10-20 min after the initiation of the reaction. Observed and calculated data points are completely overlapping. (a, b) 2 nM 5-carboxytetramethylrhodamine-labeled 50mer oligonucleotide SO in the double stranded form (ds-Rh-SO) incubated alone. (c, d) 2 nM ds-Rh-SO incubated with 3 μ M BD. (e, f) 2nM ds-Rh-SO incubated with 3 μ M BD and 37 nM GST-p53. The equipment and experimental setup are described in [6], [8]. FCS data are evaluated by temporal autocorrelation analysis. Experimentally obtained intensity autocorrelation functions are best fitted with the autocorrelation function for free 3D diffusion (3).

When basic peptides BD (Fig. 2 c) and d)) or poly-L-Lysine are added to the reaction mixture with ds-Rh-SO, increased fluorescence intensity and broadening of fluctuation peaks are observed (Fig. 2 c)). Autocorrelation analysis of the intensity fluctuations (Fig. 2 d)) shows that two distinct fluorescent components characterized by diffusion times $\tau_{D1} = (0.60 \pm 0.05)$ ms and $\tau_{D2} = (3400 \pm 300)$ ms are present in the reaction mixture. Diffusion time of the first component coincides with the diffusion time for free ds-Rh-SO, while appearance of the second component with a considerably longer diffusion time reflects the formation of large ds-Rh-SO-peptide aggregates. The same behavior was observed with ds-Rh-NO.

Whereas GST-p53 did not alter fluorescence intensity fluctuations of 2 nM dsRh-SO and dsRh-NO alone, it inhibited DNA aggregation induced by BD. Autocorrelation analysis (Fig. 2 f)) of the fluorescence intensity fluctuations (Fig. 2 e)) showed that particles characterized by diffusion times $\tau_{D1} = (0.20 \pm 0.07)$ ms in equilibrium with small aggregates characterized by $\tau_{D2} = (2.0 \pm 0.5)$ ms are formed. Thus, the products of dsDNA disaggregation are particles that are much smaller in size than the dsDNA molecules alone. These nano-scale particles are present in excess ($y = 0.70$) along with residues of the large dsDNA aggregates that are not yet totally resolved.

In experiments with single-stranded oligonucleotides we determined that diffusion times of ssRh-SO and ssRh-NO are practically the same as for double-stranded oligonucleotides. However, incubation of ss-Rh-SO and ss-Rh-NO with BD and poly-L-Lysine leads to formation of particles with diffusion times $\tau_D = (0.20 \pm 0.07)$ ms that are substantially shorter than those of ss-oligonucleotides alone. Particles characterized with these rather short diffusion times appear to represent single ssDNA molecules in a compact coiled conformation stabilized by one or several molecules of basic peptides [3]. Somewhat larger and heterogeneous in size ssDNA-peptide complexes characterized by diffusion times ranging from 2.4 ms to 4.8 ms were also observed. About 30% of ssDNA molecules are engaged in these aggregates, as compared to 70% of the aggregated ds-oligonucleotides, confirming that complexes of ssDNA with basic peptides are significantly smaller and demonstrate lesser aggregative behavior than those of dsDNA [3]. Addition of p53 does not modify diffusion properties of the ssDNA-BD complexes. Based on these results we conclude that final product of the p53 mediated dissociation of dsDNA aggregates are ssDNA molecules in coiled conformation stabilized by basic peptides present in excess in the reaction mixture.

Conclusion

dsDNA aggregates are not only dissociated by p53, but dsDNA is also denatured and compact coiled ssDNA – peptide polycation complexes are formed.

Acknowledgements

This work was supported by grants from The Swedish Cancer Society, The Swedish Research Council and AFA to GB, and The Wenner-Gren Foundations to VV.

References

- [1] L.J. Ko, C. Prives, *Genes Dev.*, 1996, 10, 1054.
- [2] D.W. Meek, *Oncogene*, 1999, 18, 7666.
- [3] M. Oren, *J. Biol. Chem.*, 1999, 274, 36031.
- [4] N. Albrechtsen, I. Dornreiter, F. Grosse, E. Kim, L. Wiesmüller, W. Deppert, *Oncogene*, 1999, 18, 7706.
- [5] V. Vukojević, T. Yakovleva, G. Bakalkin, *The p53 pathway*, Ed. Ted Hupp, Publisher: Landes Biosciences, 2004, in press.
- [6] T. Yakovleva, A. Pramanik, T. Kawasaki, K. Tan-No, I. Gileva, H. Lindegren, Ü. Langel, T.J. Ekström, R. Rigler, L. Terenius, G. Bakalkin, *Sequences. J. Biol. Chem.*, 2001, 276, 15650.
- [7] T. Yakovleva, A. Pramanik, L. Terenius, T.J. Ekström, G. Bakalkin, *Trends Biochem. Sci.*, 2002, 27, 612.
- [8] V. Vukojević, T. Yakovleva, L. Terenius, A. Pramanik, G. Bakalkin, *Biochem. Biophys. Res. Commun.*, 2004, 316, 1150.
- [9] V. Vukojević, A. Pramanik, T. Yakovleva, R. Rigler, L. Terenius, G. Bakalkin, *Cell Mol. Life Sci.* submitted.
- [10] R. Rigler, Ü. Mets, J. Widengren, P. Kask, *Eur. Biophys. J.* 1993, 22, 169.

EPR SPECTROSCOPY OF ALLIGNED PROTEIN MICROCRYSTALS

J. Caldeira^{a,b,*}, J.L. Figueirinhas^c, C. Santos^a and M.H. Godinho^d

^a *Requimte / Centro de Química Fina e Biotecnologia, Faculdade de Ciências e Tecnologia, Universidade Nova de Lisboa, 2829-516 Caparica, Portugal,*

^b *Instituto Superior de Ciências da Saúde – Sul, 2829-516 Caparica, Portugal*

^c *Departamento de Física, Instituto Superior Técnico, 1049-001 Lisboa, and Centro de Física da Matéria Condensada, Universidade de Lisboa, Av. Professor Gama Pinto 2, 1649-003 Lisboa, Portugal.*

^d *Departamento de Ciência dos Materiais, and CENIMAT, Faculdade de Ciências e Tecnologia, Universidade Nova de Lisboa, 2829-516 Caparica, Portugal.*

Abstract

Correlation of the g -tensor of a paramagnetic active centre of a protein with its structure provides a unique experimental information on the electronic structure of the metal site. To address this problem, we made solid films containing metalloprotein (*D.gigas* cytochrome c_3) microcrystals. The microcrystals in a liquid crystalline polymer medium (water/hydroxypropylcellulose) were partially aligned by a shear flow. A strong orientation effect of the metalloprotein was observed by EPR spectroscopy and polarizing optical microscopy. The proposed method enhances sensitivity and resolution and provides a general tool for correlating spectroscopic data, obtained by EPR or some other technique, with the three dimensional structure of a protein or a model compound.

Introduction

It is known that the study of oriented molecules by EPR or other techniques can reveal information valuable for molecular orbital calculations[1-3], spin-spin interactions[4,5], ENDOR simulations[6] and NMR studies of paramagnetic proteins[7,8]. In order to relate spectroscopic data with a molecular structure, a sample has to possess a macroscopic structural feature which can be related with its microscopic order. Protein crystals can provide the direct link between molecular structure and macroscopic sample. EPR single crystal studies were done on some systems[9-11] and the further advances are expected with the use of high frequency spectrometers. Unfortunately, the protein crystals are often of a small size, failing to meet common demands for sensitivity of different spectroscopic techniques. Moreover, it was reported, that membrane proteins deposited on a flat surface[12,13] or paramagnetic molecules linked to DNA oriented fibres[14,15] yield a one-dimensional oriented systems that provide the correlation of the g -tensor with the structural features of the material. A very small degree of protein orientation induced by magnetically aligned liquid crystalline bicells[16] or by strain induced alignment of polyacrilamide gels[17] was reported and used for calculation of residual dipolar couplings by NMR.

Results and Discussions

Significant angular dependence of the resonances upon the sample tube rotation can be observed. Enhancement or decrease of the intensity of different resonances is caused

by a non-random molecular distribution in the sample. This effect resulted in: *i*- additional resolution of the heam resonances by direct spectral deconvolution of the present paramagnetic species which appear overlapped in a spectrum of an isotropic sample which is especially important for protein molecules where quantity available is scarce. *ii*- increased sensitivity in different regions of the spectra due to alignment of the “spin-packets”. This feature is of great utility for multi center protein molecules. To simulate the EPR spectra of partially oriented samples we developed a theoretical model that uses an orientation distribution function (*odf*). The *odf* accounts for the average orientation of the microcrystals in the solid films. The *odf* was parameterized by square of the modulus of a series expansion of Wigner D[18,19] functions.

$$odf(\phi, \theta, \psi) = \left| \sum_{j=0}^{j_{\max}} \sum_{m=-j}^j \sum_{m'=-j}^j C^j_{m, n_1} D_{mm'}^j(\phi, \theta, \psi) \right|^2 \quad (1)$$

The EPR spectra were calculated according to a $S = 1/2$ spin Hamiltonian with resonances of gaussian line shape[20]. Calculations of the EPR spectra were performed for each sample orientation in the laboratory frame (X_L, Y_L, Z_L) with $Z_L \parallel \mathbf{h}_0$ and $X_L \parallel \mathbf{h}_I$, where \mathbf{h}_0 and \mathbf{h}_I are the unit vectors along the static and radio frequency magnetic field, respectively. Simulated spectra represent the sum of resonances originating from 16 paramagnetic species coming from 4 different haems present in the *D.g. cyt c₃* molecule, with 4 molecules present in the crystal unit cell, conveniently weighted by the *odf*, as given by equation (2).

$$G(H) = \int_0^{2\pi} d\phi \int_0^{\pi} \sin\theta d\theta \int_0^{2\pi} d\varphi odf(\phi, \theta, \varphi) g(\phi, \theta, \varphi, H) \quad (2)$$

Numerical simulations imply the use of six reference frames, from the Lab frame to the *g*-tensor principal frame of each unpaired electron, according to the scheme given below.

[*Lab frame*] – *i* ($\alpha_L, \beta_L, \gamma_L$) – [*Solid Film frame*] – *ii* (ϕ, θ, ψ) – [*Crystal frame*] – *iii* ($\alpha_C, \beta_C, \gamma_C$) – [*Molecule_n frame*] – *iv* ($\alpha_M, \beta_M, \gamma_M$) – [*Heam_m frame*] – *v* ($\alpha_H, \beta_H, \gamma_H$) – [*g-tensor principal_m frame*].

Euler angles (*i*) are experimentally set and their variation results in different EPR spectra; Euler angles (*ii*) are distributed according to the *odf*; Euler angles (*iii*) describe the spatial relationships between 4 *n* molecules in the crystal unit cell; Euler angles (*iv*) define 4 *m* heam molecular axis (defined by the atomic positions of the iron coordinating ligands from the 3D protein structure (1wad.pdb)), and Euler angles (*v*) were obtained from NMR evaluation of the empirical magnetic susceptibility tensor[21].

Conclusions

The availability of a solid material with many oriented microcrystals overcomes the current size limitation of the single crystal spectroscopic studies. The data obtained from partially aligned systems require a complex analysis compared to single crystal studies. However, since the concentration of the oriented sample is no longer a limitation, a wide range of biomolecules can now be studied. Therefore this new method

enables the determination of the *g*-tensor orientation of the paramagnetic center in respect to the molecular structure.

References

- [1] A. Aizman, D.A. Case, *J. Am. Chem. Soc.*, 1982, 104, 3269.
- [2] L. Noodlman, *Inorg. Chem.*, 1991, 30, 256.
- [3] F. Neese, E.I. Solomon *Inorg. Chem.*, 1998, 37, 6568.
- [4] P. Bertrand, P. Camensuli, C. More and B. Guigliarelli, *J. Am. Chem. Soc.*, 1996, 118, 1426.
- [5] J. Caldeira, M. Asso, V. Belle, B. Guigliarelli, C. More, I. Moura, J. Moura, P. Bertrand, *Biochemistry*, 2000, 39, 2700.
- [6] R. Kappl, S. Ciurli, C. Luchinat, J. Huttermann. *J. Am. Chem. Soc.*, 1999, 121, 1925.
- [7] N. V. Shokhirev, F. A. Walker, *J. Biol. Inorg. Chem.*, 1988, 3, 581.
- [8] R.O. Louro, I.J. Correia, L. Brennan, I.B. Coutinho, A.V. Xavier and D.L. Turner, *J. Am. Chem. Soc.*, 1998, 120, 13240.
- [9] B. Guigliarelli, P. Bertrand, C. More, R. Haser, J.P. Gayda, *J. Mol. Biol.*, 1990, 216, 161.
- [10] O. Trofanchuk, M. Stein, C. Gessner, F. Lenzian, Y. Higuchi, W. Lubitz, *Single crystal, J. Biol. Inorg. Chem.*, 2000, 5, 36.
- [11] W. Hofbauer, A. Zouni, R. Bittl, J. Kern, P. Orth, F. Lenzian, P. Fromme, H. T. Witt, W. Lubitz, *Proc. Natl. Acad. Sci. U.S.A.*, 2001, 98, 6623.
- [12] M. Brugna, S. Rodgers, A. Schricker, G. Montoya, M. Kazmeier, W. Nitschke, I. Sinning, *Proc. Natl. Acad. Sci. U.S.A.*, 2000, 97, 2069.
- [13] J.K. Blaise, M. Erecinska, S. Samuels and J.S. Leigh, *Biochim. Biophys. Acta*, 1978, 501, 53.
- [14] W. Gatzweiler, J. Huttermann, A. Rupprecht. *Radiat Res.*, 1994, 138, 151.
- [15] M. Chikira, W.E. Antholine, D.H. Petering, *J. Biol. Chem.*, 1989, 264, 21478.
- [16] N. Tjandra and A. Bax, *Science*, 1997, 278, 1111.
- [17] Y. Ishii, M.A. Markus, R. Tycko. *J. Biomol. NMR*, 2001, 21, 141.
- [18] P.M. Matias, J., Morais, R. Coelho, M.A. Carrondo, K. Wilson, Z. Dauter, L. Sieker, *Protein Sci.*, 1996, 5, 1342.
- [19] D.A. Varshalovich, A.N. Moskalev, V. K. Khersonskii, World Scientific Publishing, London, (1989).
- [20] A. Abragam, B. Bleaney, Clarendon Press, Oxford, (1970).
- [21] D.L. Turner, L. Brennan, A.C. Messias, M.L. Teodoro, A.V. Xavier, *Eur. Biophys J.*, 2000, 29, 104.

CHEMICAL MODIFICATION OF PARTIALLY HYDROLYZED PULLULAN

D. Jakovljević¹, M. Radulović¹, A. Nastasović¹, M. M. Vrvic^{1,2}
and M. Hranisavljević-Jakovljević²

¹Department of Chemistry, Institute of Chemistry, Technology and Metallurgy, 11001 Belgrade, Njegoševa 12, ²Faculty of Chemistry, University of Belgrade, 11001 Belgrade, Studentski trg 16, P.O. Box 158, Serbia and Montenegro

Abstract

Pullulan was subjected to the partial hydrolysis with low concentration of trifluoroacetic acid and successfully selectively functionalized at its reducing terminus via reductive amination of the terminal aldehyde with some amino compounds.

Introduction

Hydrophilic polymers having a reactive end group are of interest for the modification of proteins, biomaterial surfaces and for the preparation of prodrug derivatives. In that respect extensive work has been devoted to the use of end group functionalized polyoxyethylens [1]. Recently the end group modification of dextrans has been reported as a tool for coupling with bioactive molecules [2]. For a number of biomedical applications there is an interest in pullulan. This polymer contains α -1,6-linked maltotriosyl repeating units. Pullulan is a water-soluble polysaccharide with many advantageous properties [3]. Especially the properties as nontoxicity, plasticity, lower permeability of oxygen gas, and so on make it widely used in food packaging, pharmacy, and other industries. The selection of pullulan in the preparation of drug derivatives is justified on the basis of its water solubility, biocompatibility, biodegradability, and in the case of chemical modification in aqueous media, makes it an attractive polymer for the synthesis in medicine, biotechnology, and food and cosmetic industry, in particular, to develop new and improve the existing drugs. This polysaccharide contains one reducing end group which can be used to introduce end group functionalities.

In this work we reported preliminary results on the activation of end group of partially hydrolyzed pullulan with some amines (L-lysine, ethylenediamine) by reductive amination to give alkyl amines as coupling occurs in the presence of a reducing agent sodium cyanoborohydride.

Results and Discussion

Pullulan used in this work was produced by the fungus *Aureobasidium pullulans*, strain CH-1 (IChTM, Collection of Microorganisms). It consists of α -1,6-linked maltotriosyl units having about 7% of maltotetraosyl units randomly distributed in the polysaccharide chain [4].

Pullulan has a high molecular weight ($M \sim 198100$, gel filtration data) [4]. In order to study the end group modification of pullulan low molecular weight pullulan is preferred. Therefore, pullulan was hydrolyzed in 0.1 M TFA at 80°C. The mixture of

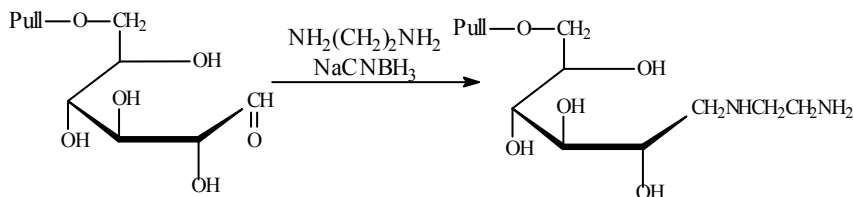
polysaccharides lower molecular mass was resolved by gel-permeation chromatography and on hypiodite oxidation the degree of polymerization (DP) investigated components was determined. Three main fractions obtained with DP about 115, 64 and 47.

More structural information about the chemical shifts of the reducing end group was obtained by $^1\text{H-NMR}$ analysis. Two signals were observed from the anomeric proton of the reducing end group: an α -linked proton at 5.22 ppm and a β -linked proton at 4.63 ppm. Similar values have been reported for dextran [5]. In Table 1. the signals in the $^1\text{H-NMR}$ spectrum of pullulan are given.

Table 1. $^1\text{H-NMR}$ data of pullulan CH-1

Typ of linkage	δ (ppm)
(1 \rightarrow 4)-(1 \rightarrow 6)-(1 \rightarrow 4)-Glc	4,96
(1 \rightarrow 4)-(1 \rightarrow 4)-(1 \rightarrow 6)-Glc	5,37
(1 \rightarrow 6)-(1 \rightarrow 4)-(1 \rightarrow 4)-Glc	5,39

Functionalization end group of pullulan can be performed with reductive coupling with ethylenediamine and L-lysine. As reducing agent NaCNBH_3 was used (Scheme 1). It has been reported that NaCNBH_3 is a selective reductant for Schiff bases. Aldehydes react reversibly with primary amines to form aldimines which can be reduced to secondary amines with sodium cyanoborohydride. The optimum pH for imine formation is 6-8; in this pH range, the rate of carbonyl reduction is low compared to that of imine reduction. Hence, despite the unfavourable equilibrium for imine formation in aqueous solutions, a good yield of amine can be obtained [6].



Scheme 1. Reaction of the reducing end group of pullulan with ethylenediamine

Coupling of the reducing end group of pullulan with ethylenediamine and L-lysine. Polysaccharide derivatives with free amino functions or free carboxylic groups are interesting materials for further coupling, e.g. with bioactive agents. For the introduction of amino end groups ethylenediamine was used whereas L-lysine was used for the introduction of a carboxylic and amino groups. The degree of substitution after coupling of the reducing end group of pullulan with ethylenediamine and L-lysine was calculated from the nitrogen content. It has been found that the degree of substitution was 714 meqv per D-glucose residue for ethylenediamine and 652 meqv per D-glucose residue for L-lysine.

Conclusion

In this paper has been report method for the modification of the reducing end group of the partially hydrolyzed polysaccharide pullulan. This method is direct coupling of amines with reducing end group of pullulan via reductive amination in presence of sodium cyanoborohydride.

References

- [1] P. Lisli, A. Abuchowski and T. J. Davis, *Appl. Biochem.* 1982, 4, 19.
- [2] K.Hashimoto, S. Imanashi, M. Okada, *J. Polym. Sci., Polym. Chem. Edn.* 2001, 29, 1271.
- [3] J. W. Saterlend, *TIBTECH*, 1998, 16, 41.
- [4] D. M. Jakovljević, M. M. Vrvić, M. Dj. Radulović, M.S. Hranisavljević-Jakovljević, *J. Serb. Chem. Soc.* 2001, 66, 377.
- [5] N.W.H. Cheetram and E. Fiala-Beer, *Carbohydr. Polym.* 1991, 14, 149.
- [6] M. Yalpani and D. E. Brooks, *J. Polym. Sci. Polym. Chem. Ed.* 1985, 23, 1395.

pH DEPENDENCE OF THE CATALASE-LIKE ACTIVITY OF HORSERADISH PEROXIDASE

A. Popović-Bijelić¹, G. Bijelić², Lj. Kolar-Anić¹ and V. Vukojević^{1,3}

¹ Faculty of Physical Chemistry, Belgrade, SCG, ² Institute for General and Physical Chemistry, Belgrade, SCG, ³ Department of Clinical Neuroscience, Karolinska Institute, Stockholm, Sweden

Abstract

pH dependence of the catalase-like activity of horseradish peroxidase was investigated. A model mechanism that can account for the observed pH dependence is proposed.

Introduction

Horseradish peroxidase (HRP; donor: hydrogen peroxide oxidoreductase, EC 1.11.1.7) is an extracellular plant enzyme involved in the formation of free radical intermediates necessary for polymerization and cross-linking of cell wall components, oxidation of secondary metabolites, regulation of cell growth and differentiation *etc.* [1]. In absence of the usual reducing substrates, H₂O₂ can perform a dual role, as an oxidant in the formation of compound I and as a typical one-electron donor (reducing) substrate for peroxidase. Such enzymatic activity of HRP is usually referred to as catalase-like activity and the following reaction scheme for this reaction has been proposed [2]:

1. $\text{HRP} + \text{H}_2\text{O}_2 \rightarrow \text{comp I} + \text{H}_2\text{O}$
2. $\text{comp I} + \text{H}_2\text{O}_2 \rightleftharpoons \text{comp I} \cdot \text{H}_2\text{O}_2$
3. $\text{comp I} \cdot \text{H}_2\text{O}_2 \rightarrow \text{HRP} + \text{O}_2 + \text{H}_2\text{O}$
4. $\text{comp I} \cdot \text{H}_2\text{O}_2 \rightarrow \text{comp II} + \text{H}^+ + \text{HO}_2^\cdot$
5. $\text{comp II} + \text{H}_2\text{O}_2 \rightleftharpoons \text{comp II} \cdot \text{H}_2\text{O}_2$
6. $\text{comp II} \cdot \text{H}_2\text{O}_2 \rightarrow \text{comp III} + \text{H}_2\text{O}$
7. $\text{comp III} \rightarrow \text{O}_2^- + \text{HRP}$
8. $\text{comp I} \cdot \text{H}_2\text{O}_2 \rightarrow \text{P}(670)$

In this paper we investigated the pH dependence of the catalase-like activity of HRP. Based on the results obtained in our own study, we propose a model that can account for the observed pH dependence of the catalase-like activity of HRP.

Methods

The reaction was commenced by addition of different concentrations of HRP to the reaction medium containing 5 mM H₂O₂ in 50 mM sodium phosphate buffer. The pH of the reaction medium was adjusted to the required values by sodium citrate (pH 2.0-5.5) and sodium phosphate (pH 6.0-8.5) buffers. During the course of the reaction the concentration of H₂O₂ was determined by measuring the absorbance at 240 nm,

taking $\varepsilon_{240\text{nm}} = 41.25 \text{ mM}^{-1}\text{cm}^{-1}$, which was obtained from a calibration curve, $A=f(c)$ (Fig 1 a, curve *a*); the intermediate compound III was monitored at 417 nm, taking $\varepsilon_{417\text{nm}} = 108 \text{ mM}^{-1}\text{cm}^{-1}$ [3] (Fig 1 a, curve *b*); the enzyme concentration was estimated using the Soret extinction coefficient, $\varepsilon_{403\text{nm}} = 102 \text{ mM}^{-1}\text{cm}^{-1}$ [3] (Fig 1 a, curve *c*). Oxygen production was measured with an oxygen electrode (Fig 1 b).

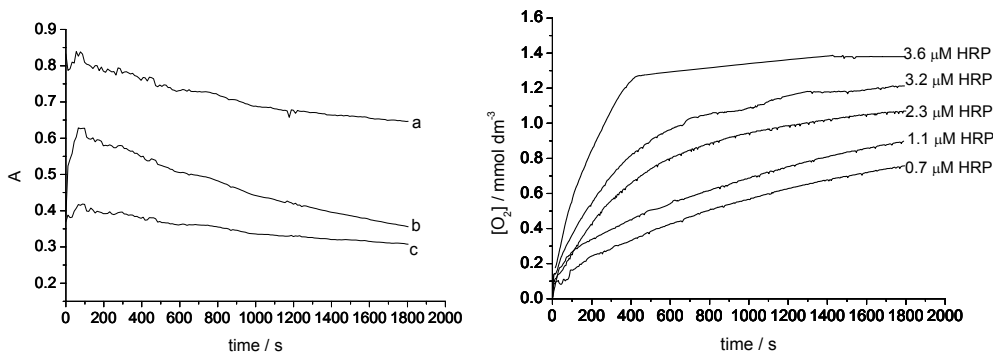


Figure 1. a. Spectrophotometric monitoring of the concentrations of H_2O_2 (curve *a*), HRP (curve *c*) and compound III (curve *b*); initial concentration of HRP was $3.6 \mu\text{M}$. **b.** Oxygen production for different initial concentrations of HRP. The reactions were started by the addition of 100-800 μl HRP to the reaction medium containing 5 mM H_2O_2 in 50 mM sodium phosphate buffer, pH 7, at 25°C .

Results and Discussion

The oxygen production curves (Figure 1 b) exhibit a short initial linear phase allowing the calculation of initial rates of oxygen formation (v_0). These initial rates exhibit a linear dependence on enzyme concentration across a certain concentration range of HRP (Figure 2 a) and depend considerably on the pH (Figure 2 b).

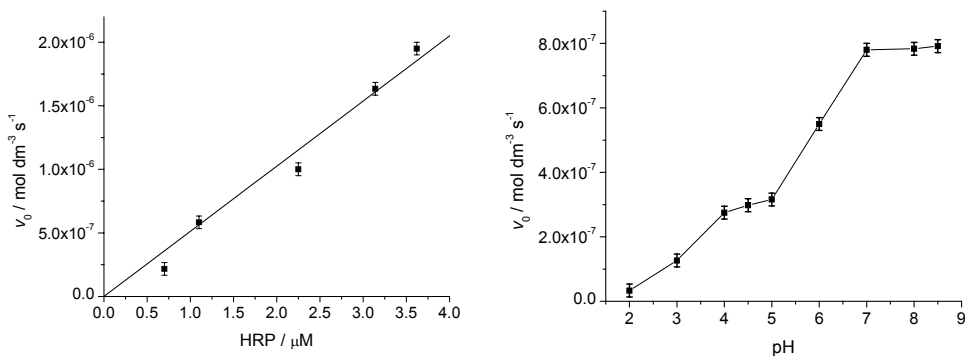


Figure 2. a. Initial rate of oxygen production at pH = 7 in the concentration range $0.7 \mu\text{M} < [\text{HRP}] < 3.6 \mu\text{M}$. **b.** pH dependence of the initial rates of oxygen production. The reactions were started by the addition of $0.5 \mu\text{M}$ HRP to the reaction medium containing 10 mM H_2O_2 in 50 mM citric and phosphate buffers.

The experimentally observed pH dependence of the initial rates of oxygen production cannot be accounted for by the reaction scheme proposed in reference [2]. Therefore, as a first step in deriving a model that can reproduce in numerical simulations the actual pH dependence, we enlarged the suggested reaction scheme by an enzyme protonation reaction. The numerically simulated pH dependence of initial rates of oxygen production is shown in Figure 3.

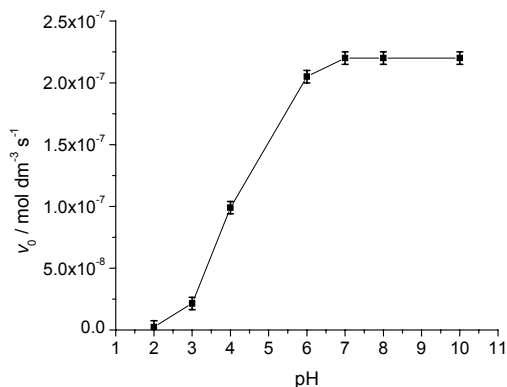


Figure 3. Numerically simulated pH dependence of the initial rates of oxygen production.

Conclusion

Initial rates of oxygen formation during the catalase-like activity of HRP show a linear dependence on enzyme concentration across a certain concentration range of HRP. The actual value of the initial rate of oxygen production is pH dependent. To account for these experimental observations we proposed an enlarged reaction scheme. We verified experimentally and numerically the previously determined value of K_m . This confirms that the kinetic constants used in the numerical simulation are correctly chosen and that the model can be used to emulate the reaction between HRP and H_2O_2 in a wide range of concentrations. Also, we have shown that HRP type II, a mixture of 5 isoenzymes, exhibits same kinetic properties (catalase-like activity) as the purified, basic isoenzyme HRP-C.

Acknowledgment: This study was supported in part by The Ministry of Science and Environmental Protection, Project no. 1448 – Physical chemistry of dynamic states and structures of non - equilibrium systems - selforganization, multistability and oscillatory.

References

- [1] C. Penel, T.H. Gaspar, H. Greppin, (eds) Plant Peroxidases: 1980-1990, University of Geneva, Geneva, 1992.
- [2] J. Hernandez-Ruiz, M.B. Arnao, A.N.P. Hiner, F. Garcia-Canovas, M. Acosta, *Biochem. J.*, 2001, 354, 107.
- [3] H.B. Dunford, *Heme Peroxidases*, J.Wiley and Sons Inc., New York, 1999.
- [4] S.A. Adediran, A. Lambeir, *Eur. J. Biochem.*, 1989, 186, 571.

COMPONENT ANALYSIS OF THE FLUORESCENCE SPECTRA OF LIGNIN ISOLATED FROM OMORIKA (*PICEA OMORIKA* L.) NEEDLES

D. Đikanović¹, J. Bogdanović¹, A. Kalauzi¹, M. Mičić², M. Jeremić³, K. Radotić¹

¹Centre for Multidisciplinary Studies, University of Belgrade, 29. Novembra 142, 11000 Beograd, Serbia; ²MP Biomedicals, Inc., 15 Morgan, Irvine CA 92618-2005; ³Faculty of Physical Chemistry, University of Belgrade, Studentski Trg 12-16, Beograd

Abstract

We analyzed fluorescence emission spectra of lignin isolated from *P. omorika* needles, using multicomponent decomposition of lignin emission band in blue-green part of the spectrum. Decomposition of a family of fluorescence spectra, obtained by lignin excitation at different wavelengths, starting from excitation maximum at 365 nm, with 5 nm-step, resulted in five band components. We concluded that distinct fluorophores in lignin structure are responsible for fluorescence.

Introduction

Lignin is one of the main constitutive polymers of the plant cell wall, which protects plant cell from different kinds of stress (chemical, biological, physical). It consists of various types of substructures bound into branched polymeric network assemblies. Due to disorder at the molecular level the electronic properties of lignin are difficult to predict.

Fluorescence spectroscopy is a sensitive and selective technique suitable for both structural and kinetic studies. There are only a few incomplete studies of fluorescence spectra and lifetimes of lignin precursors, isolated lignins and lignin-like polymers.

We report here fluorescence emission spectra of lignin isolated from *P. omorika* needles, using multicomponent decomposition of lignin emission band in blue-green part of the spectrum.

Materials and Methods

Lignin was isolated from purified cell wall of omorika needles using thioglycolic acid [1]. As an example, we present a study of one of the genetic lines of omorika. Fluorescence spectra were collected using Fluorolog-3 (Jobin Yvon Horiba, Paris, France). We used front-face illumination-detection geometry.

Nonlinear fitting was performed using the Nead-Melder algorithm implemented in Matlab, version 6p5. Spectra were decomposed into gaussian components:

$$I(\lambda) = \sum_i A_i \frac{1}{\sqrt{2\pi}\sigma_i} \exp \frac{-(\lambda - \lambda_{0i})^2}{2\sigma_i^2},$$

where $I(\lambda)$ stands for relative spectral intensity at wavelength λ , A_i for component surface, σ_i for component standard deviation, λ_{0i} wavelength of component maximum. For each component, all three parameters A_i , σ_i and λ_{0i} were fitted.

Results and Discussion

We performed decomposition of a family of fluorescence spectra, obtained by lignin excitation at different wavelengths, starting from excitation maximum at 365 nm, with 5 nm-step, shown in Figure 1. Analysis shows that each spectrum from the family is complex and consists from four components. An attempt to decompose any spectrum into more than four components resulted in duplication of their positions. Decomposition of all of the spectra analyzed resulted around the following component wavelength positions: 445, 478, 503, 535, 580 nm. A typical result of four-component gaussian decomposition of the lignin fluorescence spectrum obtained by excitation at 390 nm is shown in Figure 2.

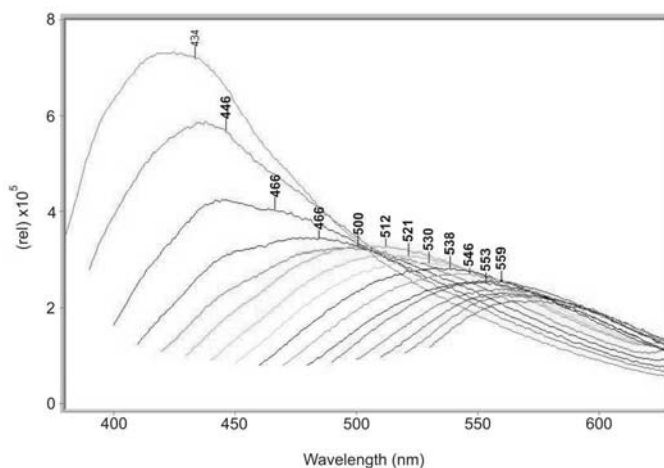


Figure 1. Family of fluorescence spectra, obtained by lignin excitation at different wavelengths. Excitation wave lengths are given in the graph

Some of the authors state that lignin fluorescence is produced by charge-transfer mechanism, without existing defined fluorophores within the polymer [2]. The others propose that distinct molecular species within lignin polymer (such as phenylcoumarone and stilbene structures) may be source of the lignin fluorescence [3]. The performed spectral decomposition shows that fluorescence of isolated lignin originates from at least five fluorophores, which may be different molecular species, or similar species in different molecular environment. Stepwise increase of wavelength excitation brings one by one fluorophore in excited state; four fluorophores are excited at the same time since their absorption spectra overlap.

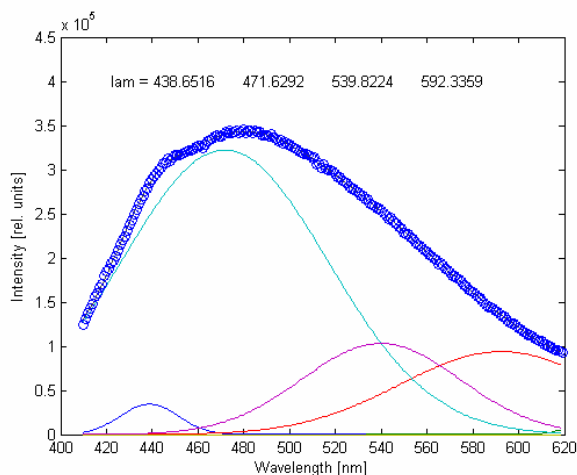


Figure 2. Four-component gaussian decomposition of the lignin fluorescence spectrum, obtained by excitation at 390 nm

Conclusion

Results of the analysis using multicomponent decomposition of lignin fluorescence emission band in blue-green spectral region show that at least five distinct fluorophores in lignin structure are responsible for fluorescence.

References

- [1] M. Chen, A.J. Sommer, J.W. McClure, *Phytochem. Anal.*, 2000, 11, 153.
- [2] S. Barsberg, T. Elder, C. Felby, *Chem Mater.*, 2003, 15, 649.
- [3] B. Albinson, S. Li, K. Lundquist, R. Stomberg, *J. Mol. Struc.*, 1999, 508, 19.

TRANSLOCATION OF DYNORPHINS ACROSS CELLULAR MEMBRANES

V. Vukojević, Z. Marinova, S. Surcheva, T. Yakovleva, G. Cebers, L. Hugonin¹,
F. Weijie², J.V. Aldrich², A. Gräslund¹, L. Terenius and G. Bakalkin.

Department of Clinical Neuroscience, Karolinska Institute, Stockholm, Sweden;

¹*Department of Biochemistry and Biophysics, Stockholm University, Stockholm, Sweden;*

²*Department of Medicinal Chemistry, School of Pharmacy, The University of Kansas, Lawrence,
USA*

Abstract

We report confocal fluorescence microscopy studies on live and fixed cells showing that big dynorphin and dynorphin A can gain access to their cytoplasm, whereas dynorphin B and the central fragment of big dynorphin cannot. Results obtained by fluorescence spectroscopy and Circular Dichroism (CD) on artificial membrane systems indicate that structure induction is relevant for dynorphin translocation across cellular membranes.

Introduction

Dynorphins are endogenous opioid peptides widely distributed in the central nervous system. Along with other endogenous opioid peptides in the opioid system, they regulate the reward and reinforcement system, response to painful stimuli and stressors, homeostatic adaptive functions, motor control and memory acquisition [1], [2], [3]. Overwhelmingly, opioid peptides perform their physiological functions by acting selectively on specific (μ -, δ - and κ -) opioid receptors [4], however there is increasing biochemical and pharmacological evidence of non-opioid effects of various opioid neuropeptides [5]. Non-opioid activity of dynorphins is mainly attributed to direct interactions with NMDA-receptors, but other mechanisms that are not yet identified may also be implicated [5]. We hypothesized that dynorphins, being arginine rich and most basic naturally occurring peptides, which are common properties of cell penetrating peptides (CPP), may also be able to translocate across plasma membranes, and that some non-opioid actions may be due to this property of dynorphins.

Results and Discussion

To study the cellular uptake (translocation) of dynorphins, HeLa, PC12 and COS-1 cells were incubated with peptides for 1 hour, whereas cerebellar cells were incubated for 2 hours. The concentration of the peptides: dynorphin A, dynorphin B, big dynorphin (a 32 amino acid prodynorphin fragment, consisting of dynorphin A and dynorphin B) and the 22 aa central fragment of big dynorphin was 10 μ M. After fixation cells incubated with dynorphin A were stained with rabbit anti-dynorphin A antibody and cells incubated with dynorphin B or big dynorphin with rabbit anti-dynorphin B antibody. In experiments on live cells, HeLa cells were incubated with 10 μ M and 250 μ M solution of fluorescently labelled dynorphin A (5-carboxytetramethylrhodamine-dynorphin A) for 15 minutes. Confocal laser scanning microscopy

showed that in all cell types studied big dynorphin and dynorphin A were taken up efficiently by cells and were localized throughout the cytoplasm. Under the same conditions dynorphin B and the central fragment of big dynorphin do not translocate at all.

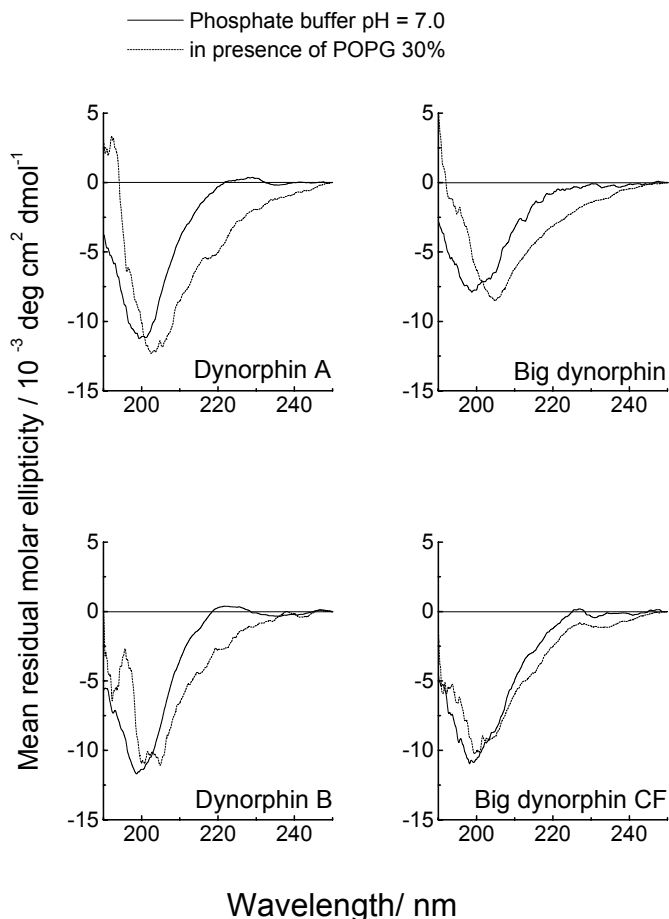


Figure 1. Circular dichroism spectra of dynorphins. Concentration of peptides is 10 μM , and the lipid/peptide ratio is 100. In the case of dynorphin B, peptide concentration is 20 μM , and the lipid/peptide ratio is 50. 10 mM phosphate buffer pH = 7.0 is used throughout.

To determine whether internalization into cells occurs via endocytosis or a non-endocytotic pathway, we used several assays. First, we performed co-localization studies of big dynorphin and transferrin, a marker of receptor-mediated endocytosis. No colocalization between big dynorphin and transferrin was detected. Thereafter, endocytosis was blocked using three different approaches: incubation of cells with big dynorphin and transferrin at 4 $^{\circ}\text{C}$, in the presence of 0.45 M sucrose or preincubation with metabolic inhibitors (10 mM sodium azide and 50 mM deoxyglucose) in glucose free medium for 1 hour. Confocal microscopy showed that internalization of transfer-

rin was apparently abolished under all these conditions, whereas big dynorphin was still present in the cells. The lack of colocalization between big dynorphin and transferrin and the ability of big dynorphin to translocate into cells in conditions when endocytosis is blocked, demonstrate that big dynorphin, at least partially, enters cells via a non-endocytotic pathway.

As we observed that big dynorphin and dynorphin A can be internalized via pathways that are not mediated through opioid and NMDA receptors, and apparently in temperature- and energy-independent ways, we used fluorescence spectroscopy and circular dichroism (CD) spectroscopy to characterize the peptide-lipid interactions in more detail. As a model system, we used small unilamellar partially charged 1-palmitoyl-2-oleoyl-phosphoglycerol (POPG 30%) vesicles (diameter < 100 nm). We observed that translocation properties of dynorphins can be correlated to the induction of secondary structure. As can be seen in Fig. 1, upon interaction with lipids the CD spectra show that α -helical structure is induced in dynorphin A and big dynorphin, and the content of helical structure increases from residual values of about 7% in a buffer solution, to a value of about 40% when the lipid/peptide ratio is 100. At the same time, a smaller degree of secondary structure is induced in dynorphin B and in the central fragment of big dynorphin, even with lipid/peptide ratios of 300.

Conclusion

Translocation of dynorphin A and big dynorphin into cells occurs rapidly and appears to be temperature- and energy-independent, suggesting direct penetration across the lipid bilayer. Results obtained by fluorescence spectroscopy and circular dichroism spectroscopy indicate that induction of secondary structure upon interaction with lipids, rather than electrostatic charge of the peptide, is relevant for dynorphins translocation properties.

Acknowledgements

This work was supported by grants from The Swedish Research Council and AFA to GB, the European Commission (contract HPRN-CT-2001-00242) to AG, and The Wenner-Gren Foundations to VV.

References

- [1] B. A. Jordan, L. A. Devi, *Nature*, 1999, 399, 697.
- [2] C.J. Woolf, M.W. Salter, *Science*, 2000, 288, 1765.
- [3] R. Przewlocki, B. Przewlocka, *Eur. J. Pharmacol.*, 2001, 429, 79.
- [4] A. Janecka, J. Fichna, T. Janecki, *Curr. Top. Med. Chem.*, 2004, 4, 1.
- [5] M. Wollemann, S. Benyhe, *Life Sci.*, 2004, 75, 257.

THE CHANGES OF GROWTH IN FUNCTION OF FREE ENERGY INPUT IN MAIZE SEEDLINGS ORIGINATED FROM AGED SEEDS

V. Dragičević¹, S. Sredojević¹, G. Drinić¹, M. Ivanović², Z. Pajić¹ and M. Vrvic³

¹*Maize Research Institute, Slobodana Bajića 1, 11185 Zemun Polje, SCG*

²*Institute of Field and Vegetable Crops, Maksima Gorkog 30, 21000 Novi Sad, SCG*

³*Faculty of Chemistry, 11001 Belgrade, Studentski trg 16, SCG*

Abstract

The ageing process as silent is visible only by germination drop and suppression of seedling growth. The aim of experiment was to study the growth of maize seedlings originated from accelerate aged seeds in function of free energy input, reflecting on the entropy of system. The lower water intake means lower differential free energy in the seedling originated from aged seed, reflects on the water distribution in it, shifts differential entropy to equilibrium. The consequence is lagged growth.

Introduction

The seed ageing is deteriorative process, includes damaging of membrane and enzymes [1]. This manifestation appears only during germination, through its lowering, lagging of seedling growth, lowering of water input in plant [2]. The aim of experiment was to explain the growth of maize seedlings originated from accelerate aged seeds in function of free energy input and changes of entropy.

Material and Methods

The seeds of two maize hybrids: H1 and H2 were exposed to the accelerated ageing (AA) treatment [3] during 3, 6, 9 and 12 days according to the ISTA Rules [4]. The uniformly grown seedlings were fractioned in the plant (root+shoot) and the seed rest, then weight (fresh mass- M_f determination) and dried together with initial seeds, at 130°C [5] to calculate the water content (W_c). The measurements were used to calculate: water distribution by relative water content (W_{p1}/W_{tot}), differential free energy (ΔG) and differential entropy (ΔS), according to Clausius-Clapeyron equation for heat of vaporization [6]:

$$\Delta G = R \times T \times \ln(W_{c1}/W_{c2})$$

$$\Delta S = \{[(R \times T1 \times T2)/(T2 - T1) \times \ln(W_{c1}/W_{c2})] - \Delta G\}/T$$

where R is gas constant; W_{c1} and W_{c2} are water contents in seed and seedling; T1 and T2 are temperatures of seed storage (4°C) and germination (25°C).

Results and Discussion

The moderate germination drop occurs until 9-th day of AA for H1 and 6-th day for H2: 5% and 10%, then rapid to 12-th day: 53.2 and 47.1% (Tab. 1). At the same time, the M_f declined in plant [3]: 32.2 % averagely for both hybrids, but in the seed rest it fluctuated only to $\pm 7\%$.

Table 1 The changes of germination percentage, M_f , C_m and W_c of maize seedlings

		H1					H2				
Days of AA	\emptyset	3	6	9	12	\emptyset	3	6	9	12	
Germ. (%)		98.0	97.7	96.0	87.7	41.0	95.5	95.0	83.0	77.5	41.0
M_f (mg)	Plant	765	715	710	558	517	760	653	623	603	517
	S. rest	425	405	428	405	417	325	300	343	333	333
ΔG (KJ sdl. ⁻¹)		-29,6	-29,8	-30,1	-31,9	-32,6	-29,6	-30,9	-31,0	-31,3	-32,6

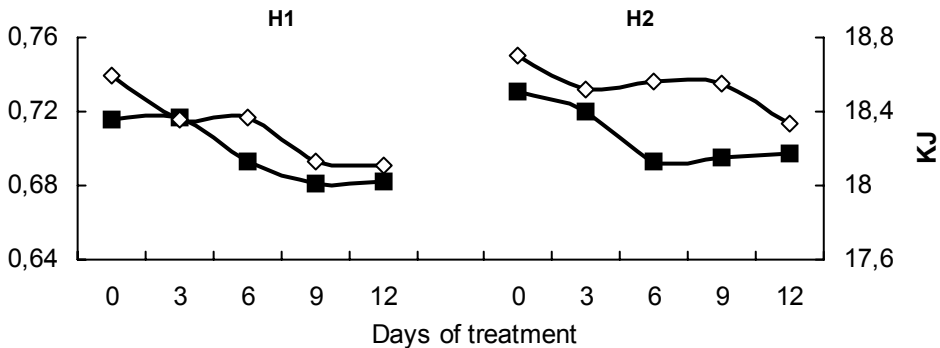


Fig. 1: The changes of relative water content and entropy (■- W_{pl}/W_{tot} , ◇- ΔS) in maize seedlings

The differences of ΔG in seedlings induced by treatment were 9.2% for both hybrids (Tab. 1). At the same time the decrease of W_{pl}/W_{tot} expressed unequal water distribution and the decrease of ΔS directed the seedling system to approach equilibrium (Fig. 1) [6,7].

Conclusion

The seed is system of relative stable state. The AA pushes system silently out of balance, so the change manifests through germination obstruction and legged growth of seedlings. The lower water intake means lower ΔG in the AA seedling, reflects on the water distribution in it, shifts ΔS to equilibrium. The consequence is lagged growth.

References

- [1] E. A. Golovina, A. N. Tikhonov, F. A. Hoekstra, *Plant Physiol.*, 1997, 114, 383.
- [2] V. Dragičević, S. Sredojević, M. Vrvić, L. Djukanović, M. Todorović, *Fresen. Environ. Bull.*, 2004, 13, 336.
- [3] J. M. Woltz, D. M. TeKrony, *Seed Technol.*, 2001, 23, 21.
- [4] *ISTA Seed Sci. Technol.*, 27 Suppl., 1999, 155-199
- [5] *ISTA, Seed Sci. Technol.*, 1999, 27, Suppl., 47-59 & Annexe, 271.
- [6] C. W. Vertucci, A. C. Leopold, *Plant Physiol.*, 1984, 75, 114.
- [7] D. D. Davies, *Experimental Biology*, Cambridge University Press, 1961, 35.

PERSISTENCE OF MICRONUCLEI IN HUMAN LYMPHOCYTES AFTER FRACTIONATED IRRADIATION IN VITRO

G. Joksić

Vinča Institute of Nuclear Sciences, POB 522 11001 Belgrade, Serbia and Montenegro

Abstract

The study evaluate relationship between incidence of micronuclei and chromosomal aberrations after fractionated irradiation of human lymphocytes in vitro. Obtained results have shown that incidence of chromosome aberrations declined faster than micronuclei at all given doses if the time between two irradiations is longer than 2 hours. The study confirmed that CBMN test is very sensitive assay for estimation of effects of ionizing radiation in the case of fractionated irradiation. This observation could be of interest for radiotherapy, particularly for applying micronucleus test as predictive test for hypersensitivity to ionizing radiation.

Introduction

The two most common in vivo cytogenetic assays, the micronucleus (MN) and metaphase aberration assays (CA) are inconsistent among countries worldwide [2]. Since there is a mechanistic link between chromosome breaks and micronuclei, it is generally agreed that these two endpoints detect similar types of chromosomal damage. Micronuclei are chromatin-containing structures in cytoplasm surrounded by a membrane without any detectable link to the cell nucleus. Micronuclei originate from chromosome fragments or whole chromosomes that lag at anaphase because they lack a centromere, or centromere is defective, or there is a defect in mechanism that enables the chromosome to distribute correctly to the poles of the cell at anaphase. Despite the increased popularity and use of the micronucleus test little has been reported on the comparative outcomes of the CA and MN tests, particularly in the cases of fractionated or prolonged conditions of irradiation. The aim of this study is to establish persistence of micronuclei in circulating human lymphocytes after fractionated irradiation in vitro and compare it with incidence of chromosomal aberrations.

Methods

Subjects: blood samples were taken from three donors of mean age 38 and were irradiated using X-rays 300 kVp, 10mA, 2.7mm CuHVT. The radiation dose employed were 1-4 Gy. Each dose was given in two equal fractions with four different time intervals between two irradiations: 30 minutes, 1 hour, 2 and 3 hours.
Blood culture and micronuclei analysis: The micronuclei analysis was carried out according to method of Fenech et al [1].

Results and Discussion

The results of the study are presented in Figure 1.

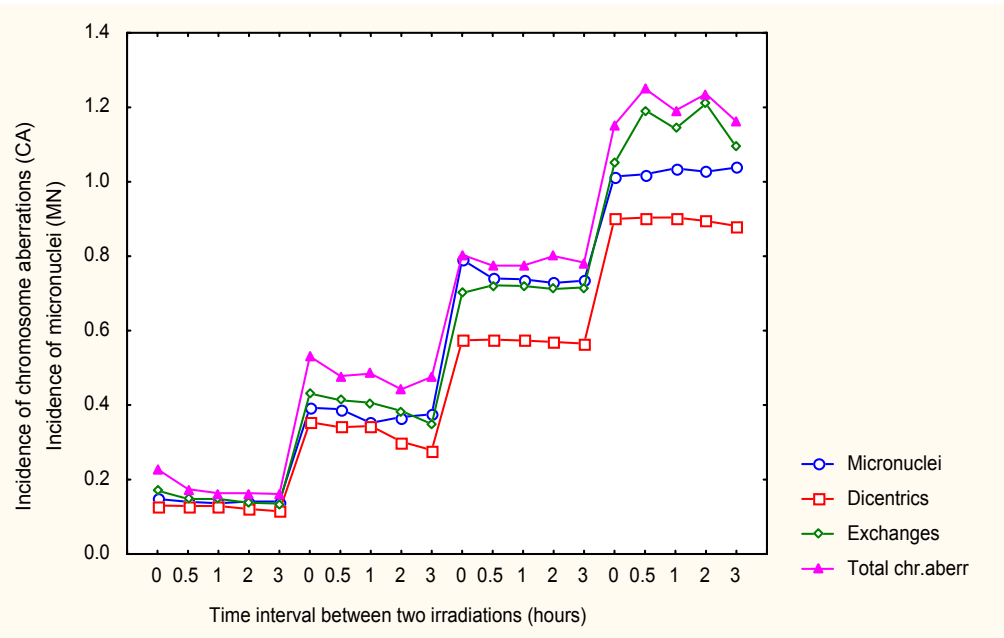


Figure 1: Incidence of chromosome aberrations and micronuclei in human lymphocytes after acute and fractionated irradiation employing doses of 1,2,3 and 4 Gy (X-rays)

Dose fractionated experiments for studying the interaction of lesions are based on the premise that the breaks induced by the first dose remain open to interact with the breaks induced by the second dose and the kinetics of disappearance of this possible interaction are similar to the repair kinetics of DSBs. Dose-fractionated experiments have indicated that the time during which the lesions are available for further interactions.

The comparison of the yields of chromosome aberrations and micronuclei in our previous investigation has shown that the best correlation is between the incidence of exchange aberrations and micronuclei [2]. At dose of 1 Gy incidence of chromosome aberrations decline slowly as a function of time interval between two irradiations. At the longest time interval between two irradiations (3 hours) incidence of dicentric is lowered for 8%. The same tendency of declining aberrations is observed at dose of 2 Gy, where percent of dicentric is lowered for 17%. In contrast to findings at doses of 1 and 2 Gy, incidence of dicentric radiation doses of 3 and 4 Gy is almost the same to the incidence found in samples acute irradiated with the same doses. Considering incidence of total chromosome aberrations, at doses of that decline significantly and reach 70.6% of the value found in acute irradiated samples. At dose of 4 Gy incidence of exchanges is slightly higher compared with acute irradiated sample.

Total incidence of chromosomal aberrations declined significantly at dose of 1 Gy, particularly at the longest time interval between two irradiations. At dose of 2 Gy they decline much slowly, whereas at dose of 3 Gy they reach the incidence found in acute irradiated sample. At dose of 4 Gy the incidence of aberrations are higher than found in acute irradiated sample. Micronuclei findings are following: at dose of 1 and 2 Gy the incidence of micronuclei decline slowly, as dicentrics, while at dose of 3 and 4 Gy their incidence is almost constant as to those values counted in acute irradiated samples. Mainly types of lesions that are induced in the DNA by ionizing radiation are single- and double strand breaks (DSBs), base damages (BDs) and DNA-protein cross-links. DSBs and BDs are considered to be the most possible lesions. The yield of exchange type of aberrations after low LET radiation follows a linear-quadratic model ($y = \alpha D + \beta D^2$) + C. The α component is contributed from lesions probably DSBs, occurring close together arising from a single track and increasing linearly with the dose. The repair of these lesions is very fast (less than 20 minutes). The β component comes from two independently induced lesions interacting with each other from an exchange aberration and therefore follows two-hit kinetics. The presence of micronuclei indicates that a cell has suffered chromosome damage. Micronucleus arise after cell division when a chromosome or chromatid fragment is lost from the nucleus but retained by the cytoplasm. Although it is clear that relation between micronucleus yield and yield of chromosomal damage (as measure as number of dicentrics) is complex, the present investigation support the CBMN test as simple and sensitive method for monitoring the sensitivity of persons undergoing radiotherapy.

References

- [1] M. Fenech, *Mutat Res.*, 1993, 285, 35.
- [2] C.M.L. West, *Advanced Radiation Biology*, 1994, 18, 148.
- [3] G. Joksić G, M. Nikolić, V. Spasojević-Tišma, *Neoplasma*, 1997, 44(2), 117.

5-FLUOROURACIL INDUCED CARDIOTOXICITY. Changes in erythrocytes morphology or alternative explanation?

I. Spasojević^{1,2}, B. Kukavica², J. Zakrzewska³ and G. Bačić¹

¹Faculty of Physical Chemistry, University of Belgrade, ²Center for Multidisciplinary Studies, University of Belgrade, ³Institute of General and Physical Chemistry, Belgrade

Abstract

The objective of our study was to investigate effects of antineoplastic drug 5-fluorouracil (5-FU) on constituents of the oxygen delivery system in erythrocytes. We determined, using SDS electrophoresis, that 5-FU induces release of glyceraldehyde-3-phosphate dehydrogenase (GAPDH) an enzyme involved in the production of 2,3-biphosphoglycerate (2,3-BPG). Also, we observed increased binding of deoxy-hemoglobin (deoxyHb) on erythrocyte membrane band 3 macrocomplex, which is involved in erythrocyte CO₂/O₂ gas exchange. ³¹P NMR spectroscopy of erythrocytes treated with 5-FU showed an increase in intracellular level of 2,3-BPG, a regulator of the release of oxygen from oxyHb. These results indicate that 5-FU provokes disfunction of the erythrocyte oxygen delivery system, which could be an alternative explanation for 5-FU induced cardiotoxicity.

Introduction

Antineoplastic drug 5-FU is widely used in treatment of breast, abdomen, head and neck cancers. Besides the "usual" negative effects of citostatic drugs, like myelosuppression, mucositis, diarrhea and vomiting, it has been reported that 5-FU also shows cardiotoxic effects which may end with myocardial infarction [1,2]. Although reported occurrence of the 5-FU cardiotoxicity exceeds 10% [1], very little effort has been put into elucidating the biophysical mechanisms behind these effects. It appears, however, that direct effects of 5-FU on myocardial cells can be excluded [2]. As an alternative, it has been reported that 5-FU induced *in vitro* changes in erythrocyte morphology and rheology [2], which in turn could lead to an increase in blood viscosity and due to that, to inadequate oxygen supply to the heart. Since *in vivo* studies report moderate decrease in blood viscosity after 5-FU application [1], changes in the shape of erythrocytes are not likely to be the only explanation for 5-FU cardiotoxicity. In this *in vitro* study we tried to examine whether effects of 5-FU on the erythrocyte oxygen delivery system could be an additional explanation for 5-FU induced cardiotoxicity.

Materials and Methods

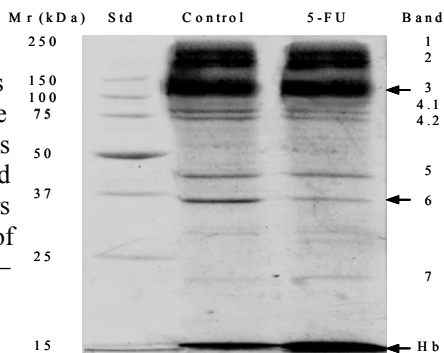
Fresh blood was drawn from four healthy volunteers, using vacutainer tubes preloaded with K3EDTA as the anticoagulant. **SDS-polyacrylamide gel electrophoresis.** Erythrocytes were washed with the 0,9% NaCl solution (3000 rpm/10 minutes) and then resuspended in hypotonic PBS solution, (Na₂HPO₄ 1,2 g/l, NaH₂PO₄ 0,43 g/l, pH 7.4, hematocrit 0,33%). 5-FU was added (final concentration was 10 mg/ml), and control samples were also taken. During the incubation (37°C/1hour), erythrocytes were fully lysed [3]. Membranes were separated by centrifugation at 15000 rpm/20

minutes/4°C, and washed twice with 20 ml of hypotonic PBS at 19000 rpm/20 minutes/4°C. Protein concentration of erythrocyte membranes was estimated using the Bradford assay, and equal amounts (20 µg) of proteins were loaded per track of SDS-polyacrylamide gel prepared according to the procedure of Laemmli [4] (with 5% stacking gel and 12% separating gel). Gels were stained with CBB. **³¹P NMR spectroscopy.** NMR measurements were performed at 37°C using a Bruker MSL 400 NMR spectrometer. Blood was incubated immediately after collection, at 37°C with 10 mg of 5-FU/ml of blood for 30, 60 and 120 minutes (hematocrit 40%). Following incubation, erythrocytes were packed by centrifugation at 3000 rpm/10 minutes and placed in a 10-mm quartz tube. A capillary containing 25 mM methylenediphosphonate (MDP) was placed in the center of the NMR tube as an external chemical shift reference (17.05 ppm) and peak intensity standard [5]. Repetition was 250 ms and pulse angle ≈ 40°. 2,3-BPG concentrations were determined from 3P/MDP area ratio. All experiments were done at least in triplicate.

Results and Discussion

Figure 1 shows SDS-PAGE of the erythrocyte membrane proteins isolated from untreated and 5-FU treated erythrocytes. The electrophoretic profile shows no new bands in the treated sample relative to control, suggesting that 5-FU does not induce polymerization or fragmentation of membrane proteins. Additionally, the relative amounts of the band 3 membrane protein are similar in the absence and presence of 5-FU. However 5-FU decreased the intensity of band 6 representing GAPDH, while the intensity of the hemoglobin (Hb) monomer band is significantly increased relative to the control.

Figure 1. SDS-PAGE of erythrocyte membrane proteins isolated from 0.33% cell suspensions incubated in the absence (Control) or in the presence of 10 mg/ml 5-FU. Nomenclature of the bands is given according to the classification of Fairbanks and using the molecular relative weight (Mr) of markers used as standards (Std). Arrows indicate bands of interest for this study: band 3; band 6 – GAPDH; Hb – hemoglobin monomer.



These two proteins are components of the band 3 macrocomplex, which is thought to have a central role in erythrocyte CO₂/O₂ gas exchange [6]. Since GAPDH is inactive when bound to band 3, its enhanced release and subsequent activation could lead to an enhanced rate of production of 1,3-biphosphoglycerate; a precursor for the production of 2,3-BPG, a modulator of Hb oxygen affinity [7]. Free GAPDH is also known to be directly involved in regulation of 2,3-BPG production [7]. Simultaneously, 5-FU induced increase of the intensity of the Hb monomer band indicates an increased amount of Hb bound to band 3. Since it is known that band 3 preferentially binds deoxyHb over oxyHb [8], our results indicate that 5-FU induces deoxygenation of the oxyHb, by increasing the level of 2,3-BPG in erythrocytes and/or through some other mechanism.

Figure 2 shows a characteristic ^{31}P NMR spectrum of packed erythrocytes. Spectrum contains three peaks, characteristic of ATP and well resolved peaks of ^{31}P on second and third carbon atom in 2,3-BPG. The inorganic phosphate signal is obliterated by the 2P peak of the 2,3-BPG signal broadened due to magnetic field gradients across the erythrocyte membrane [5].

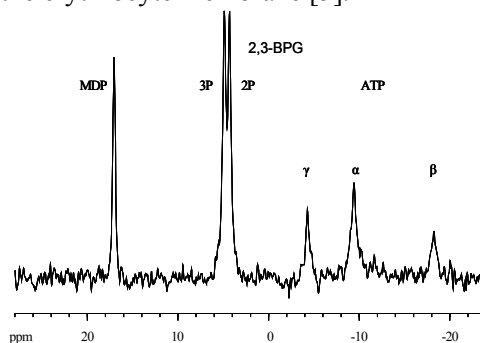


Figure 2. ^{31}P NMR spectrum of the packed erythrocytes incubated with 5-FU (10 mg/ml erythrocytes) for 30 minutes. Accumulation time was 16 minutes.

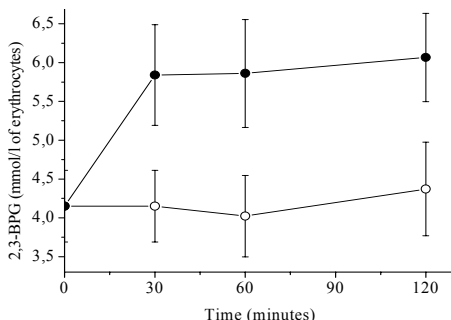


Figure 3. Effects of 5-FU on 2,3-BPG level in erythrocytes. ● - 5-FU 10 mg/ml of cells; ○ - control sample. The data are presented as means \pm S.D.

During the incubation, qualitative changes in the spectra of treated or untreated erythrocytes did not take place. However, quantitative changes in peak areas relative to MDP peak area were observed (Fig. 3). Figure 3 shows that 5-FU provoked a rapid and significant (Student's t-test $P < 0.05$) increase in the concentration of 2,3-BPG; the molecule that regulates O_2 level in blood by binding preferentially to deoxyHb, thus decreasing the total Hb affinity for oxygen and inducing its release. We also observed 5-FU induced slight decrease in the level of ATP (data not shown). Increased level of free and active GAPDH (Fig. 1), could be the ground for increment in intracellular 2,3-BPG concentration (Fig. 3). High 2,3-BPG level could further lead to the increase in Hb membrane binding though deoxygenation of oxyHb, and. The consequence of these effects could be uncontrolled oxygen release from erythrocytes, regardless of the level of metabolic activity of the nearby tissue. As a result, the myocardium as highly active tissue, could be inadequately oxygenated. These preliminary results are providing an alternative explanation for 5-FU induced cardiotoxicity

Acknowledgement This work was supported by grant 1928. from the Ministry of Science and Environmental Protection of the Republic of Serbia.

References

- [1] M. Cwikiel *et al.*, Acta Oncologica, 1995, 34, 83.
- [2] G.M. Baerlocher *et al.*, Br. J. Haematol., 1997, 99, 426.
- [3] M.M. Cruz Silva *et al.*, Biocim. Biophys. Acta, 2000, 1464, 49.
- [4] U.K. Laemmli., Nature, 1970, 227, 680.
- [5] R.J. Labotka., Biochemistry, 1984, 23, 5549.
- [6] L.J. Bruce *et al.*, Blood, 2003, 101, 4180.
- [7] K.V. Fokina *et al.*, Biochemistry (Moscow), 2000, 65, 547.
- [8] J.A. Walder *et al.*, J. Biol. Chem., 1984, 259, 10238.

PALINDROME SEQUENCES IN VIRAL GENOMES

N. Mitić¹, G. Pavlović-Lažetić¹ and M. Beljanski²

¹*Faculty of Mathematics, 11000, Belgrade*

²*Institute of General and Physical Chemistry, 11000 Belgrade*

Abstract

Palindrome sequences may contribute in RNA virus genome secondary structure formation. We investigated their number and clustering within SARS CoV and Ebola virus genomes as a model system.

Introduction

RNA secondary structure in RNA viruses may be important for RNA – protein interaction, taking part in packing of viral genome in viral particle and also in regulation of viral gene expression and replication. Since complementary palindrome sequences are responsible for formation the most abundant RNA secondary structures [1] in this paper we analyzed some palindrome characteristics on SARS CoV and Ebola virus as a model systems. Sequences were taken from the PubMed NCBI Entrez site [2] in fasta format. Palindrome program [3] was used for palindrome sequences determination which were stored in IBM RDBMS DB2 [4] and further processed.

Results and Discussion

The genome of SARS-CoV consists of a single non-segmented positive RNA strand approximately 30Kb in length, consisting of about 10 open reading frames (ORF), and about 10 intergenic regions (IGRs) [5]. The average number of palindromes (length 7 or more) is 28253. The longest palindrome consists of 30 (times 2, for both strands) nucleotides and is found in only one isolate, while the longest palindrome represented in all isolates is 16 (times 2) nucleotides long.

The genome of Ebola virus consists of a single non-segmented negative RNA strand approximately of 19Kb consisting of seven ORFs [1]. The average number of palindromes (length 7 or more) is 1157. The longest palindrome consists of 15 (times 2, for both strands) nucleotides represented in three isolates, while the longest palindrome represented in all isolates is 9 (times 2) nucleotides long

Average distance between palindrome (outer) ends related to palindrome length is shown on Figure 1.

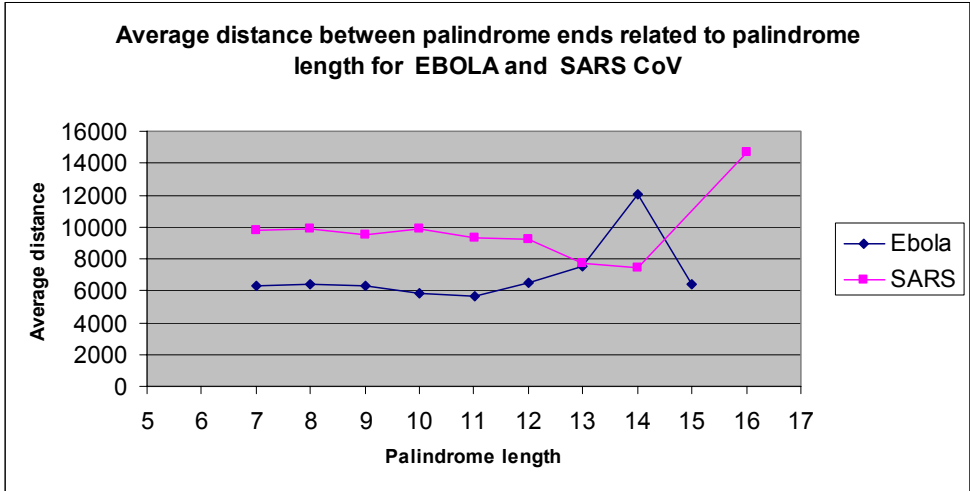


Figure 1.

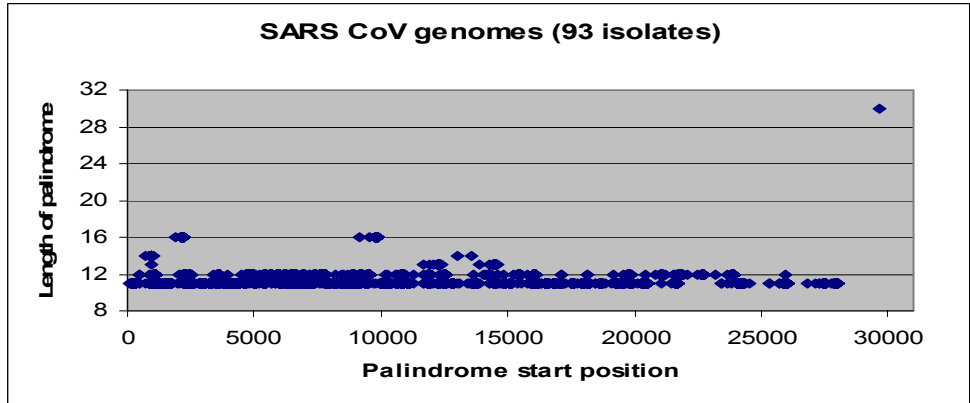


Figure 2a.

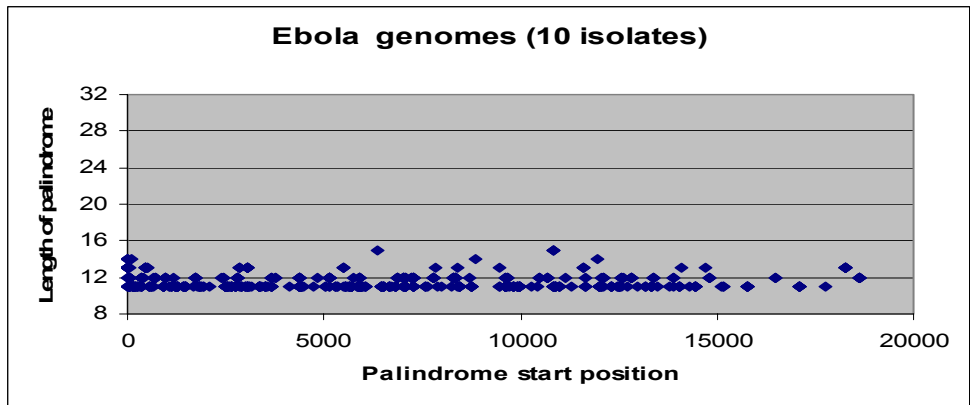


Figure 2b.

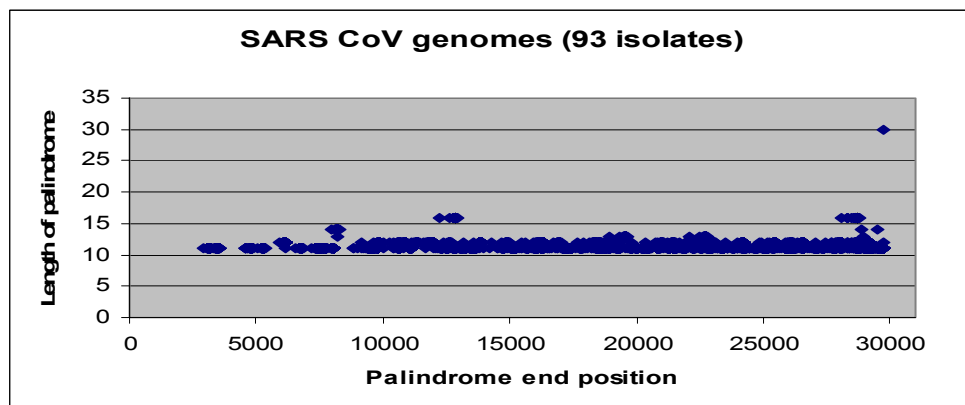


Figure 2c.

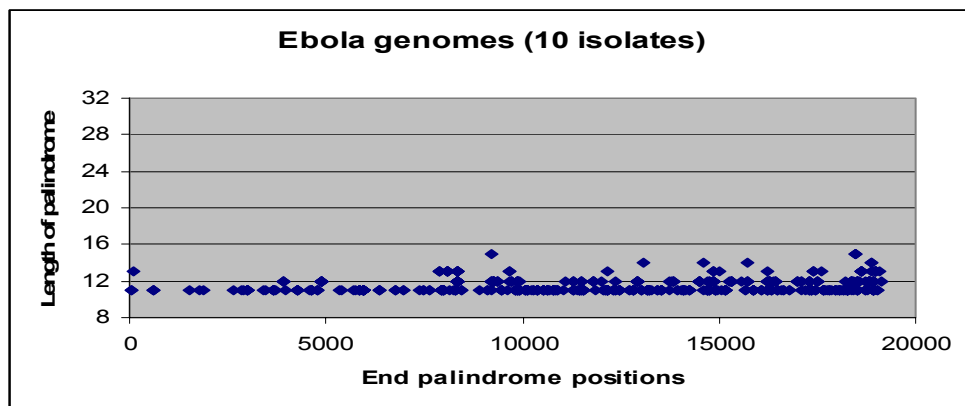


Figure 2d.

Start and end positions of left and right halves of palindromes (5' and 3' ends for SARS CoV and 5' and 3' ends for Ebola) are shown in Figure 2 reveal that start positions of longer palindromes are clustered in the left part of SARS genomes (Figure 2a) as opposed to clustering (mainly) the central part of Ebola genomes (figure 2b). End parts of palindromes are clustered mainly in the last two third of genome (SARS, Figure 2c) or in the second half of genome (Ebola, Figure 2d).

Literature

- [1] Crary S. M., et al., *Virology*, 2003, 306, 210.
- [3] <http://www.ncbi.nlm.nih.gov/entrez/>
- [4] <http://www.emboss.org/>
- [5] <http://www.ibm.com/software/data/db2/>
- [6] Zhi-gang W., et al. *Chin. Med. J.*, 2004, 117(1), 42.

ANALYSIS OF SARS CORONAVIRUS GENOME POLYMORPHISM

G. Pavlović-Lažetić¹, N. Mitić¹ and M. Beljanski²

¹*Faculty of Mathematics, 11000, Belgrade*

²*Institute of General and Physical Chemistry, 11000 Belgrade*

Abstract

We have compared 38 isolates of the SARS-CoV complete genome. The main goal was twofold: first to compare and analyze nucleotide sequences and to identify positions of single nucleotide polymorphism (SNP), insertions and deletions and, second, to group them according to sequence similarity, eventually pointing to phylogeny of SARS-CoV isolates. The comparison is based on genome polymorphism such as number and positions of SNPs and insertions or deletions.

Introduction

Severe Acute Respiratory Syndrome (SARS) is a new infectious disease reported first in the autumn of 2002. New member of Coronaviridae, SARS coronavirus (CoV) has been associated with the pathogenesis of SARS according to Kochs postulate [1]. The genome of SARS CoV consists of a single positive RNA strand (~30Kb in length), consisting of about 10 open reading frames (ORF) and about 10 intergenic regions (IGR). The first two overlapping ORFs at 5' end encompass two thirds of the genome, while the rest of ORFs at 3' end encompass the remaining third of it [2].

Results and Discussion

Nucleotide sequences are taken from PubMed NCBI Entrez database (38 complete genomes published by October 31, 2003.), [3]. For similarity analysis original program has been developed. ClustalW [4] for multialignment and phylogenetic tree construction (drown by PhyloDraw program [5]), were also used.

Based on dissimilarity due to SNPs and insertions and deletions, the dataset of all the isolates has been qualitatively classified into three groups having their own subgroups. Those are: **A**-group with "regular" isolates (No insertions / deletions except for 5' and 3' ends), **B**-group of isolates with "long insertions", and **C**-group of isolates with "many individual" insertions and deletions. Further, SNPs properties and positions may divide A and C group into A1 and A2 and C1 and C2 subgroups giving the final grouping of isolates that may be presented as a structural tree:

A1: TWH, TWC3, TWK, TWS, TWY, Urbani, TWJ, TWC, TW1, Tor2, HSR1, CUHK-Su10, AS, Sin2500, Sin2679, Sin2774, Sin2748, Taiwan TC1, TC2, TC3, Frankfurt1, FRA, HKU and WHU;

A2: CUHK-W1, GY50, and BJ01 to BJ04;

B: GD01, SZ3 and SZ16;

C1: ZJ01;

C2: ZMY 1.

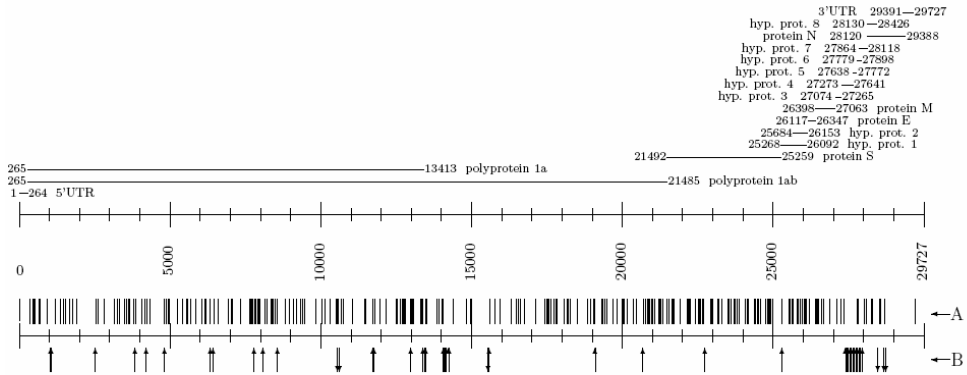


Figure 1. Gene map of SARS CoV with the overall density distribution of (A) SNPs and (B) insertions (↑) and deletions (↓) along with the gene map for TWH.

The isolate with the smallest average number of SNPs, compared to other isolates, has been identified (TWH). Cumulative density distribution of all SNPs, insertions and deletions, for all of the isolates is presented, along with gene map for TWH (Fig. 1). Since individual SNPs may have occurred at random, positions corresponding to multiple SNPs (occurring in two or more isolates) are identified and presented (Fig. 1). This result revises some previous results of a similar type [2].

Amino acid changes caused by multiple SNPs are also identified (for annotated sequences, as well as presupposed amino acid changes for non-annotated ones). Exact SNP positions for the isolates in each group or subgroup are identified.

Finally, a phylogenetic tree for the SARS CoV isolates has been produced using ClustalW program, showing high compatibility with former qualitative classification (Fig. 2.).

Conclusions

The comparative study of SARS-CoV isolates provides essential information for genome polymorphism, indication of strain differences and variants evolution. It may help in development of an effective treatment.

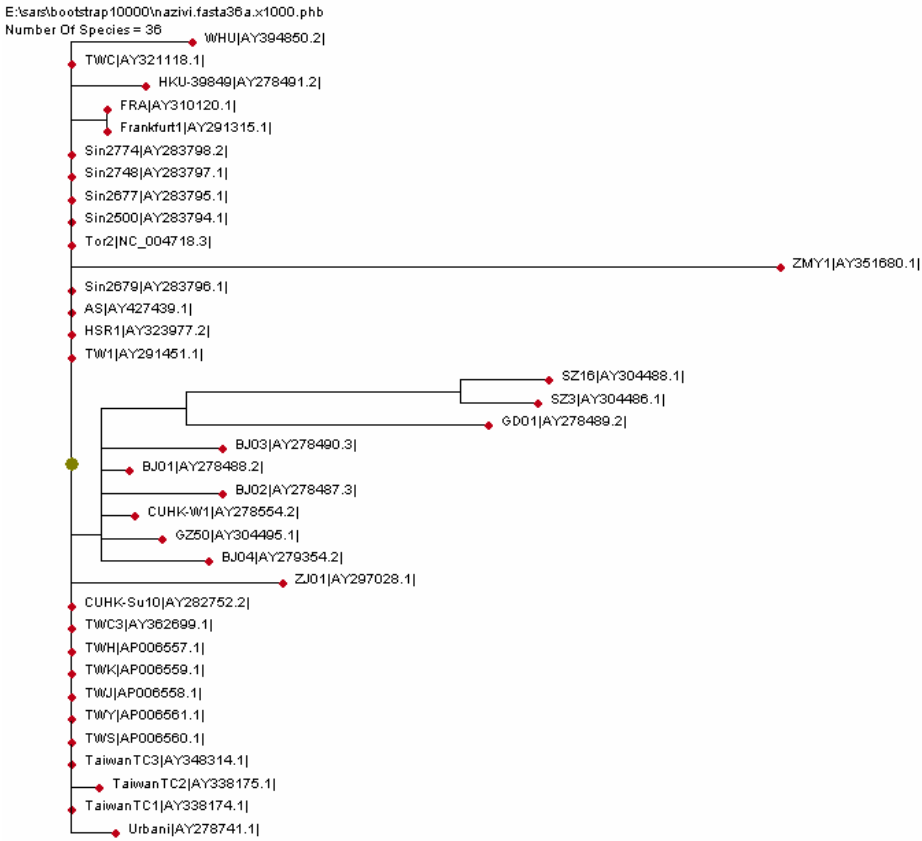


Figure 2. Phylogenetic tree of 38 SARS-CoV complete genome isolates produced with ClustalW and Phylodraw programs.

Literature

- [1] Fouchier R. A. M., et al. *Nat.*, 2003, 423(6937), 240.
- [2] Ruan Y. J., et al., *Lancet*, 2003, 9(9), 1163.
- [3] <http://www.ncbi.nlm.nih.gov/entrez/>
- [4] <ftp://ftp.ebi.ac.uk/software/dos/clustalw/>
- [5] <http://pearl.cs.pusan.ac.kr/phyldraw/>

EFFECTS OF METAL IONS ON ECTO-ATPase ACTIVITY IN PLASMA MEMBRANE ISOLATED FROM THE RAT OVARY

M.Milošević, S.Petrović and A.Horvat

*Laboratory of Molecular Biology and Endocrinology, "Vinča" Institute of Nuclear Sciences,
P.O. Box 522, 11001 Belgrade, Serbia and Montenegro*

Abstract

Effects of increasing concentrations of metal salts SrCl_2 , CsCl , CrCl_3 , CdCl_2 , and HgCl_2 on rat ovarian plasma membrane ecto-ATPase activity were investigated. CrCl_3 , CdCl_2 , and HgCl_2 exert total inhibition of enzyme activity in the presence of 0.01 M and 0.1 M respectively. SrCl_2 and CsCl exhibit up to 25% of inhibition. According to the IC_{50} , ecto-ATPase possesses greater sensibility to Cd^{2+} (IC_{50} is 0.887 mM) > Cr^{3+} (IC_{50} is 1.936 mM) > Hg^{2+} (IC_{50} is 4.39 mM). All investigated ions exert negative cooperativity ($n < 1$). Physico-chemical properties of the metal are of importance in metal toxicity. Cr^{3+} and Cd^{2+} ions, with lower radius may inhibit ecto-ATPase activity by binding to hydrolytic site or by replacing Mg^{2+} in Mg-ATP , a substrate of the enzyme. Hg^{2+} , as a larger ion probably inhibits the enzyme activity through conformational changing the enzyme by binding to S-S or -SH groups on the site distinct to hydrolytic one. By inhibiting the enzyme activity these metals may affect maturation and release of oocytes as well as synthesis and release of gonadal hormones and decrease the fertility of mammals.

Introduction

Metals are widely dispersed throughout the environment. Environmental pollution by metals increase the exposure of organisms, which results in their accumulation in various tissues, including the ovary [1]. Metals have a number of toxic mechanisms including interference with enzyme function either by binding competitively with binding sites or by modifying metal-binding proteins. A plenitude of evidence indicates that heavy metals such as lead, mercury, cadmium, arsenic, chromium, nickel and several others, are developmental and reproductive toxicants acting on DNA transcription and production of reactive oxygen species [1]. The ecto-adenosine triphosphatase (ecto-ATPase, EC 3.6.1.3) is a membrane-bound enzyme, which in the presence of divalent cations (Ca^{2+} or Mg^{2+}) plays a role in the extra cellular metabolism of ATP. By controlling the concentration of the extra cellular ATP, it influences a large variety of P2 receptor-mediated processes [2]. ATP may influence maturation of ovarian cells and synthesis of gonadal hormones. The specific inhibitor(s) of ecto-ATPase has not been found up to now. In this work, we investigated possible metal toxicity on the reproductive system of mammals. With this aim we examined the effects of CrCl_3 , SrCl_2 , CsCl , CdCl_2 , and HgCl_2 , on plasma membrane ecto-ATPase activity from the rat ovary, as a model system.

Experimental Procedure

Experiments were performed on 3-month-old female Wistar albino rats obtained from a local colony. Ovarian plasma membranes (OPM) were isolated as described previously [3]. The activity of ecto-ATPase was determined by the spectrophotometric method by measuring the inorganic phosphate liberated from hydrolysis of ATP. OPM (70 μ g) were preincubated at 37 $^{\circ}$ C without or in the presence of increasing concentrations of CrCl₃, SrCl₂, CsCl, CdCl₂, and HgCl₂, for 20 min in an enzyme assay medium containing (in mM) 50 Tris-HCl, pH 7.4; 1 EDTA; 5 MgCl₂. After incubation, the enzyme reaction was started by the addition of 2 mM ATP, allowed to proceed for 15 min and stopped by the addition of 3 mol/l perchloric acid. All measurements were performed in triplicate. The results are expressed as the mean percentage of enzyme activity compared to the corresponding control.

Results and Discussion

Chloride salts of the investigated metals were added to the reaction mixture in the concentration range from 1x10⁻⁷ to 0.1 M. The effects of increasing concentrations of metal salts CrCl₃, CdCl₂, and HgCl₂ on OPM ecto-ATPase activity shows total inhibition relative to the control samples while, SrCl₂ and CsCl exhibits up to 25% of inhibition. Concentrations of metals for 50% of enzyme activity inhibition (IC₅₀) were calculated from the Hill analysis of the experimental results.

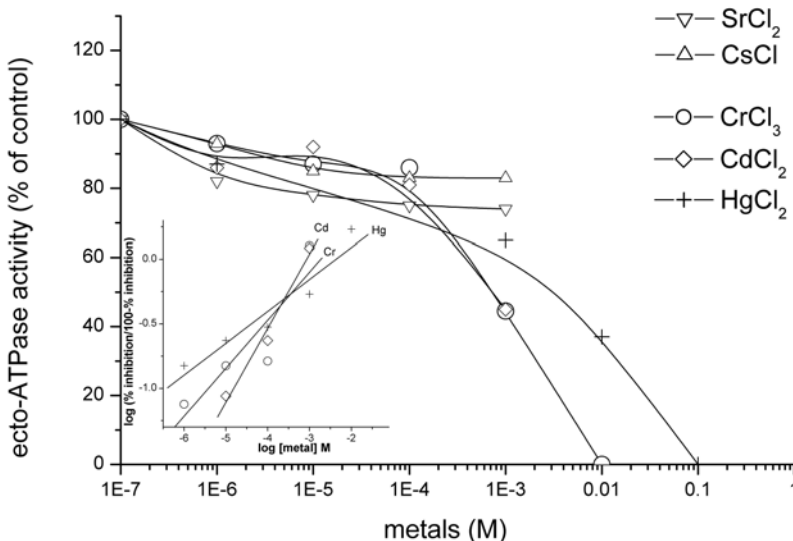


Figure 1. Effects of CrCl₃, SrCl₂, CsCl, CdCl₂, and HgCl₂ on ecto-ATPase activity. Hill graph presented as inset.

Cr^{3+} , Cd^{2+} and Hg^{2+} ions exert total inhibition of control enzyme activity (0.130 $\mu\text{mol Pi/mg/min}$) in the presence of 0.01 M and 0.1 M respectively (Fig. 1.). According to the IC_{50} , ecto-ATPase possesses greater sensibility to Cd^{2+} (IC_{50} is 0.887 mM) followed by Cr^{3+} (IC_{50} is 1.936 mM), and Hg^{2+} (IC_{50} is 4.39 mM). According to the Hill coefficient, n , all investigated ions exert negative cooperativity ($n < 1$). When dealing with defining the metal toxicity, particular attention should be focused on metal chemical specificity in the physico-chemical properties of the metal coordination sphere. The absence of ecto-ATPase inhibition by Cs and Sr may be explained by large ionic radius, compared to Mg^{2+} , so they probably cannot substitute Mg^{2+} in the Mg-ATP complex. Also they lack the ability to form complexes with $-\text{SH}$, $-\text{NH}_2$, $-\text{OH}$ or other groups in protein. Transition metals may modify the secondary structure of the protein, compete with free Mg^{2+} or bind to functional catalytic groups, such as SH-groups and exert the inhibition of enzyme activity. Due to similarity in ionic radius, Cd^{2+} and Cr^{3+} can probably substitute Mg^{2+} ions in Mg-ATP, which is the substrate for ecto-ATPase, or binding to the hydrolytic site. Hg^{2+} , possessing high radius may form complexes with $-\text{SH}$ or $-\text{S-S-}$ residues, out of active center of enzyme, affecting protein conformation and inhibition of hydrolytic activity.

Conclusion

When dealing with metal ion toxicology, particular attention should be focused on metal chemical speciation in that the physico-chemical properties of the metal coordination sphere are of importance in defining the metal toxicity. Metals, Cd^{2+} and Cr^{3+} , with lower a radius may inhibit ecto-ATPase activity by binding to hydrolytic site or replacing Mg^{2+} in Mg-ATP, a substrate of the enzyme. Hg^{2+} , as the larger ion probably inhibits enzyme activity by conformational changing the enzyme protein by binding to S-S or -SH groups on the site distinct to the hydrolytic one. By inhibiting the enzyme activity, these metals may affect maturation and release of oocytes as well as synthesis and release of gonadal hormones and consequently decrease the fertility of mammals. Further investigations will be undertaken with the aim to define inhibition mechanisms of the studied metals.

Acknowledgements

This study was supported by the Ministry of Science and Environmental Protection of the Republic of Serbia, Grant No. 1956

References

- [1] P. Kovacic, J.D. Jacintho, *Curr. Med. Chem.*, 2001, 8, 863.
- [2] H. Zimmermann, N. Braun, B. Kegel, P. Heine, *Neurochem. Intern.*, 1998, 32, 421.
- [3] A. Horvat, G. Nikezić, J. Martinović, *Experientia* 1995, 51, 11.

FLUX OF Ca^{2+} IONS IN THE SYNAPTOSOMAL MITOCHONDRIAL MEMBRANE

S. Petrović, M. Milošević and A. Horvat

Laboratory of Molecular Biology and Endocrinology

VINČA Institute of Nuclear Sciences, P.O.Box 522, 11001 Belgrade, Serbia and Montenegro

Abstract

In the present study, the flux of Ca^{2+} ions in the synaptosomal mitochondrial membrane isolated from the whole brain and hippocampus of chronically ovariectomized female rats was examined. Under basal conditions no significant difference was found. Addition of estradiol (0.5 nmol/l) in the preincubation mixture decreased significantly (25%) Na-dependent Ca^{2+} efflux in mitochondria from both sources which may be the way that it exerts its role in nerve cell homeostasis.

Introduction

The maintaining Ca^{2+} homeostasis is of great importance for the normal functioning of cells, especially the excitable ones. In neurons, neurotransmitter release and other specialized cell functions are associated with changes in free cytosolic Ca^{2+} concentration [1]. Beside two membrane mechanisms for Ca^{2+} extrusion, $\text{Na}^+/\text{Ca}^{2+}$ exchange and ATP-driven Ca^{2+} efflux, the role of mitochondria in Ca^{2+} buffering has been suggested [2]. The influx of Ca^{2+} in mitochondria, which occurs through ruthenium red sensitive channels, is an electrogenic process driven by the large electrical gradient across the inner mitochondrial membrane, set up through the proton extrusion by the electron transport chain [3]. The efflux of calcium from brain mitochondria is an Na-dependent, electroneutral process mediated by antiporter, $\text{Na}^+/\text{Ca}^{2+}$ exchanger [4]. In order to compare the influx and efflux of Ca^{2+} in mitochondria isolated from synaptosomes of the whole female rat brain and hippocampus were investigated. The effect of estradiol *in vitro* was found.

Experimental

Synaptosomal mitochondria used for Ca^{2+} transport measurements were isolated from the whole brain and hippocampus of chronically (3 weeks prior to use) ovariectomized (OVX) female rats as described previously [5]. Isolated synaptosomal mitochondrial pellets were suspended in 0.3 mannitol and kept at -20°C until use. For Ca^{2+} transport monitoring mitochondria were preincubated at 22°C for 10 min in medium containing (in mM): 300 mannitol, 10 KCl, 1 maleate, 5 glutamate, 10 Tris-HCl, pH 7.4. The influx of Ca^{2+} to synaptosomal mitochondria was initiated by adding 0.2 mM CaCl_2 (0.6 μCi $^{45}\text{CaCl}_2$), lasted 5 min and stopped by ruthenium red (17.5 $\mu\text{g}/\text{mg}$ protein), a specific inhibitor for Ca^{2+} uniporter. For Ca^{2+} efflux monitoring, mitochondria were loaded with calcium in the same way and after adding ruthenium red the efflux of Ca^{2+} was initiated by adding NaCl (20mM) and 0.2mM EDTA and lasted 5 min. Aliquots of 1ml, before and after addition of Na/EDTA, were vacuum-filtered and

washed on cellulose-nitrate filters. The influx of Ca^{2+} (pmol/mg protein) in mitochondria was calculated from radioactivity counting in samples just after addition of ruthenium red. The Na-dependent Ca^{2+} efflux was calculated by subtracting Ca^{2+} concentration retained in mitochondria after addition of Na/EDTA from Ca^{2+} concentration in mitochondria after addition of ruthenium red (no EDTA). The effect of estradiol on Na-dependent Ca^{2+} efflux was measured by incubating Ca^{2+} -preloaded mitochondria with estradiol 5pM and 0.5nM for 10 min and initiating efflux by NaCl and EDTA for 5 min.

Results and Discussion

In this study, the movement of calcium ions through the mitochondrial membrane was monitored. Mitochondria were isolated from synaptosomes of the whole brain and hippocampus of OVX female rats with the aim to explore the *in vitro* effect of estradiol on Ca^{2+} flux. The hippocampus is the structure of interest since it is filogenetically an old cortical structure, directly involved in memory functions and therefore the brain region with extremely high neuronal activity which could be the reason for intensive movements of ions, especially Ca^{2+} movements.

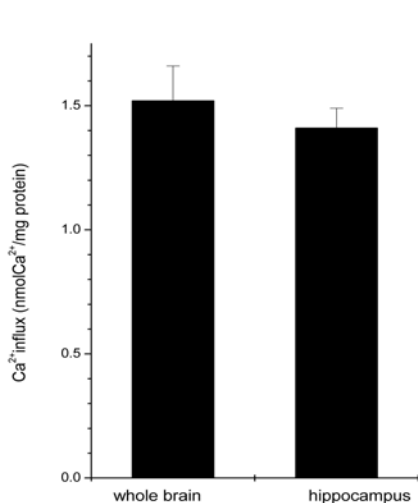


Figure 1. Influx of Ca^{2+} in synaptosomal mitochondria.

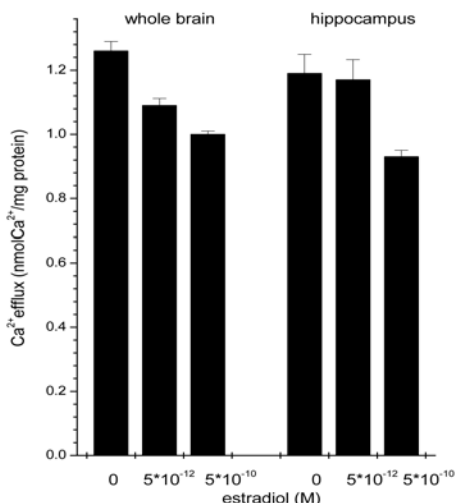


Figure 2. Na-dependent Ca^{2+} efflux from synaptosomal mitochondria.

As presented in Fig. 1, the influx of Ca^{2+} ions in mitochondria from hippocampus (1.41 nmol Ca^{2+} /mg protein) is pretty similar to the one measured in mitochondria from the whole brain (1.52 nmol Ca^{2+} /mg protein). These results may be expected and compared with our previous results on mitochondria from synaptosomes of the whole brain of intact female rats (1.1 nmol Ca^{2+} /mg protein) [6] where a certain decrease in

influx activity is noticeable. Estradiol *in vitro* did not affect the influx of investigated ions (data not shown).

Na-dependent Ca^{2+} efflux was measured in $^{45}\text{Ca}^{2+}$ preloaded synaptosomal mitochondria isolated from the whole brain and hippocampus in the presence and absence of estradiol *in vitro*. As shown in Fig. 2. in the absence of estradiol, there was no significant difference in released calcium, 1.26 nmol Ca^{2+} /mg protein for whole brain and 1.19 nmol Ca^{2+} /mg protein for hippocampus, which is in both cases about 85% of preloaded Ca^{2+} content. Estradiol had a different effect on ion efflux depending on its concentration. While the concentration of 5 pmol/l decreased Ca^{2+} efflux in the whole brain mitochondria about 15%, there was no effect in the case of the hippocampus. At 100x higher concentration (0.5 nmol/l) estradiol decreased Ca^{2+} efflux in mitochondria from both sources about 25%.

Conclusion

These results suggesting that the transport of Ca^{2+} ions through ruthenium red sensitive channels and by antiporter, $\text{Na}^+/\text{Ca}^{2+}$ exchanger, in synaptosomal mitochondria isolated from the whole brain and hippocampus are nearly the same under basal conditions (absence of estradiol). Na-dependent Ca^{2+} efflux in hippocampus are probably less sensitive to estradiol when presented in small concentrations. The inhibition of $\text{Na}^+/\text{Ca}^{2+}$ exchanger by 0.5 nmol/l concentration of estradiol can be expected to increase ability of mitochondria to buffer changes in cellular Ca^{2+} .

Acknowledgements. This study was supported by the Ministry of Science and Environmental Protection of the Republic of Serbia, Grant No. 1956

References

- [1] S.J. Smith, G.J. Augustine, Trends Neurosci. 1988, 11, 458.
- [2] M.R. Duchen, M. Valdeolmillos, S.C. O'Neill, D.A. Eisner, J. Physiol. (London) 1990, 424, 411.
- [3] H. Rottenberg, M. Marbach, Biochim. Biophys. Acta 1990, 1016, 77.
- [4] T.E. Gunter, D.R. Pfeiffer, Amer. J. Physiol. 1990, 258, C755.
- [5] J.C.K. Lai, J.B. Clark, Methods Enzymol. 1970, 55, 51.
- [6] A. Horvat, S. Petrović, N. Nedeljković, J. Martinović, Gen. Physiol. Biophys 2000, 19, 59.

DIFFERENT SENSIBILITY OF ECTO-ATPase FROM BRAIN AND OVARY TO Cu^{2+} AND Zn^{2+}

A.Horvat, M.Milošević, S. Petrović and M.Demajo

Laboratory of Molecular Biology and Endocrinology, "Vinča" Institute of Nuclear Sciences, P.O.B. 522, 11001 Belgrade, Serbia and Montenegro

Abstract

Ions of zinc and copper represents micro elements present in all organisms but they can be accumulated in various tissues from the environment by food or pollution. In this work we examined the effects of chloride salts of Cu^{2+} and Zn^{2+} on the activity of ecto-ATPase, integral plasma membrane protein, in brain and ovarian cells. Both ions exhibit similar effects on brain or ovarian enzyme activity. Copper in brain and ovary totally inhibits enzyme activity at the concentration of 1 mM and 0.1 M respectively. IC₅₀ for brain is 36 μM while in ovary it is 192 μM . Zinc inhibits in both tissues 50% of the control enzyme activity at concentrations of 1 mM in brain and 0.1 M in ovary with IC₅₀ of 1mM and 14 mM respectively. These metals possess an affinity for -SH groups in the enzyme protein, may replace Mg^{2+} in enzyme substrate, MgATP or to bind for enzyme substrate site. According to the total inhibition of ecto-ATPase activity by Cu^{2+} , it may be proposed that its site of action is on the substrate or substrate binding site, while Zn^{2+} modulates enzyme activity by acting on the -SH or S-S groups of the enzyme. Inhibiting or decreasing ecto-ATPase activity in brain and ovary, these two metal ions may be toxic and seriously disturb the proper functioning of the investigated tissues.

Introduction

The ecto adenosine triphosphatase (ecto-ATPase, EC 3.6.1.3) is an integral membrane protein that, in the presence of divalent cations (Ca^{2+} or Mg^{2+}), hydrolyses extra cellular nucleosides, since the nucleotide-hydrolysing site is outwardly orientated. By hydrolysing ATP, this enzyme is the major inactivating agent in purine triphosphate signalling. In the central nervous system, as in other tissues, these enzymes have multiple roles. By controlling the concentration of the extra cellular ATP and adenosine, along with 5'-nucleotidase, it influences a large variety of P1 and P2 receptor-mediated processes [1]. In brain as well as ovarian cells, the existence of P2X and P2Y purinoceptors were detected. ATP, as a neurotransmitter and neuromodulator, is stored within vesicles and co-released with neurotransmitters. When released, ATP may modulate the release and influence other neurotransmitters in the brain or influence maturation of ovarian cells and synthesis of gonadal hormones. The specific inhibitor(s) of ecto-ATPase has not been found up to now. In numerous tissues, the activities of ecto-ATPase may be influenced by different endogenous modulators [1] and may be modulated by a variety of agents such are detergents, lectins, ATP-

analogues and drugs [2]. In order to determine if this enzyme may be modulated by micro elements, we tested the effects of Cu^{2+} and Zn^{2+} ions in the rat brain and ovary.

Experimental Procedure

Experiments were performed on 3-month-old (300-350 g) female Wistar albino rats obtained from the local colony. Synaptosomal plasma membranes (SPM) and ovarian plasma membranes (OPM) were isolated from the rat brain and ovary as described previously [3]. The activity of ecto-ATPase was determined by the spectrophotometric method by measuring the inorganic phosphate liberated from the hydrolysis of ATP. SPM (20 μg) or OPM (70 μg) were preincubated at 37° C without or in the presence of increasing concentrations of CuCl_2 and ZnCl_2 for 20 min in an enzyme assay medium containing (in mM) 50 Tris-HCl, pH 7.4; 5 MgCl_2 and 1 EDTA. After incubation, the enzyme reaction was started by the addition of 2 mM ATP, allowed to proceed for 15 min and stopped by the addition of 3 mol/l perchloric acid. The results are expressed as the mean percent of enzyme activity compared to the corresponding control performed in triplicate.

Results and Discussion

Chloride salts of metals were added to the reaction mixture in the concentration range from 1×10^{-7} to 1 M. Effects of increasing concentrations of metal salts on SPM as well as on OPM ecto-ATPase activity shows inhibition activity relative to the control samples. Concentrations of metals for 50% of enzyme activity inhibition (IC50) were calculated from the Hill analysis of the experimental results. Cu^{2+} ions exert sigmoidal inhibition of enzyme activity for both membrane preparations (Fig. 1.). According to the IC50, brain ecto-ATPase possesses greater sensibility to this ion than ovarian enzyme (36 μM for brain, 192 μM for ovary). These results imply tissue specificity in abundance of the enzyme, which confirms specific activity of ecto-ATPase in SPM and OPM under control conditions (0.253 $\mu\text{mol Pi/mg/min}$ and 0.130 $\mu\text{mol Pi/mg/min}$ respectively).

Inhibition of ecto-ATPase by Zn^{2+} ions is maximum about 55% in both preparations. In the case of Zn^{2+} inhibition, brain ecto-ATPase possess higher sensibility, like as for Cu^{2+} , with IC50 of 1 mM in comparison to OPM enzyme inhibition with IC50 of 14 mM. According to the Hill coefficient, n , Cu^{2+} exerts no cooperativity ($n=1$) in binding to the enzyme, while Zn^{2+} ($n<1$) exerts negative cooperativity.

Conclusion

Cu^{2+} and Zn^{2+} are metals from first transition group, they exert similar inhibition in ovarian and brain ecto-ATPase activity, but there is distinction between the action of copper and zinc in the same tissue. Therefore, we may assume that their sites of action are different. These metals possess affinity for $-\text{SH}$ is on the substrate or substrate binding site, while Zn^{2+} modulates the enzyme activity by acting on $-\text{SH}$

and/or S-S groups of the enzyme. Inhibiting or decreasing ecto-ATPase activity in the brain and ovary, these two metal ions increase extra cellular ATP, which may seriously disturb proper functioning of the investigated tissues.

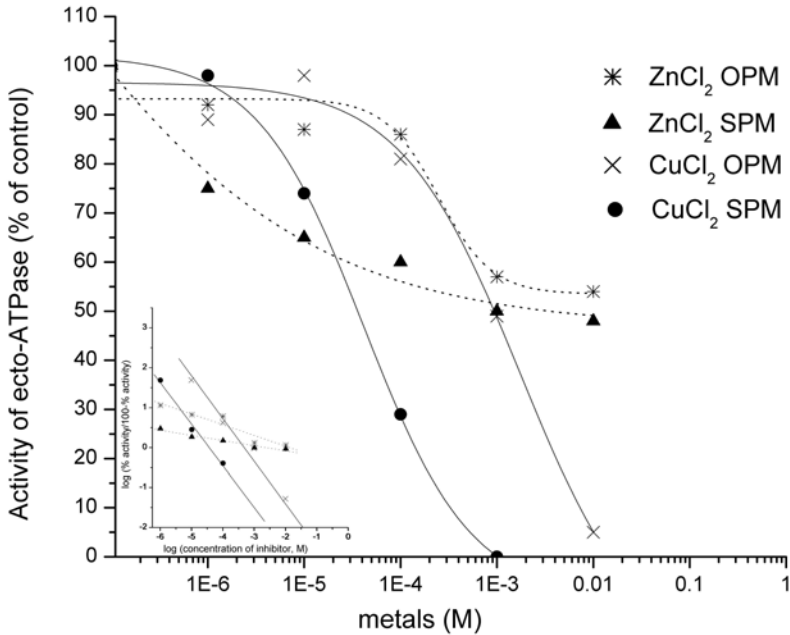


Fig. 1. Inhibition of ecto-ATPase activity from SPM by CuCl₂ (●) and ZnCl₂ (▲) as well as from OPM by CuCl₂ (×) and ZnCl₂ (*) ions. Hill graph presented as inset.

Acknowledgements

This study was supported by the Ministry of Science and Environmental Protection of the Republic of Serbia, Grant No. 1956

References

- [1] H. Zimmermann, N. Braun, B. Kegel, P. Heine, *Neurochem. International*, 1998, 32, 421.
- [2] A.K. Nagy, In *Ecto-ATPase Recent progress on structure and function*. (L. Plesner, T.L. Kirley, A.F. Knovles, Eds.) Plenum Press, New York and London, 1997, 1-13.
- [3] A. Horvat, G. Nikezić, J. Martinović, *Experientia*, 1995, 51, 11.

DEHYDRATION: THE STRESS FOR BACTERIOPHAGE λ

D. Božin

Institute for nuclear sciences Vinča, P. O. Box 522, 11001 Belgrade, SCG

Abstract

The effect of dehydration of different duration on air or in high vacuum was investigated. Under the tested conditions, it caused inactivation in 95%, but did not DNA damage λ 1390 bacteriophage. Neither, DNA strand break nor DNA mutation were detected, but capsid proteins were destabilized.

Introduction

Viruses are the smallest, simplest form of life on earth - they are just an assembly of nucleic acids wrapped by a protein coat (or 'capsid'). Viruses are not cells, but they cannot reproduce itself outside another cell. Their small size and simple biological construction, make them useful laboratory model systems for different kind of tests, particularly in studies of effects of extreme conditions of environment like dehydration, temperature changes, pressure, pH or different kind of chemicals. The stress during dehydration of viruses may be particularly important. The literature notes a few data of inactivation of the bacteriophage (a true parasite in bacteria) mainly as a collateral data in other studies. So, whereas T1 bacteriophage remained not more than 20% inactivated [1] or was unaffected by dehydration in vacuum, 40 to 80% of the plaque-forming units of ϕ X174 bacteriophage [2], 25-50% of λ bacteriophage [3], and 60% of T7 [4] were inactivated. We report here the results of the preliminary experiments on the response of bacteriophage λ 1390, deficient in their own recombination repair system, to dehydration on air or in high vacuum conditions. The following effects have been analyzed: surviving of bacteriophage λ and the amount of damages in bacteriophage λ DNA or capsid proteins after dehydration.

Experimental Procedure

Phage and Host Stocks. The bacteriophage λ 1390 strain and different *E. coli* bacterial strains used in this study were from Radman's laboratory (M. Radman, France). Stock of λ 1390 (Red Gam⁺) bacteriophage was prepared by confluent lysis on a plate and stored at 4 °C [5]. As host for propagation of phage strain *E. coli* P2 lysogen was used. λ 1390 strain give transparent plaques on a lawn of *E. coli* plating bacteria. Counting of plaques was performed after 18 hours. Plating *E. coli* bacteria were: P2 lysogen for surviving, recA⁻ for frequency of DNA recombination and recA⁻uvrA⁻ double mutant - for bacteriophage DNA mutations.

Dehydration. For dehydration, 30 μ l of λ 1390 stock have been applied directly at full concentration on still surfaces prepared by TritoneX-100 detergent. The samples were dried for 30 min at 37 °C, put to sterile Petri dishes and the dehydration

was continued in room conditions or in vacuum chamber at room temperature and pressure of 10^{-5} mbar for 7 or 120 hours. After appropriate time, dehydrated phages were resuspended in 10 mM MgSO_4 and stored at 4°C .

Surviving and DNA test. Surviving fraction of dehydrated phages was measured by titration on layer of *E. coli* P2 lysogen strain. Possible bacteriophage DNA breaks were tested on recA^- mutant of *E. coli*, and mutations in bacteriophage DNA were tested on $\text{recA}^- \text{uvrA}^-$ double mutant of *E. coli*.

Capside proteins test. Temperature sensitive test at 37°C and 50°C was performed for 10 days.

Measurement of phage survival and DNA damage rate. Survivors λ were scored by plating dehydrated bacteriophages on a lawn of P2 lysogenic bacteria. The counting of plaques was performed after 18 h. The relative number of surviving bacteriophage was the ratio of both titers measured for non-dehydrated control bacteriophage and dehydrated λ . DNA damage rate was counted in the same manner but on another bacteria lawn. DNA breaks were scored by plating non-dehydrated control bacteriophage and dehydrated λ on a lawn of recA^- bacteria. DNA mutations were scored by plating non-dehydrated control bacteriophage and dehydrated λ on a lawn of $\text{recA}^- \text{uvrA}^-$ double mutant bacteria.

Results and Discussion

To provide experimental evidence that dehydration is stress, bacteriophage λ 1390 strain has been exposed to dehydration on air and in high vacuum for 7h or 120h. After drying bacteriophages were rehydrated in 10mM MgSO_4 , and the following effects have been analyzed: surviving of rehydrated bacteriophage λ and the amount of damages in rehydrated λ DNA or λ capsid proteins. Surviving test was performed by titration on *E. coli* P2 lysogen bacteria strain and surviving was similar for all tested samples: 1.3 – 4.6%. In the same time, rehydrated bacteriophage λ has been tested for possible DNA damages by titration on recA^- (for DNA breaks) and $\text{recA}^- \text{uvrA}^-$ double mutant of *E. coli* (for DNA mutations). Neither, DNA strand break nor DNA mutation, were detected. These data allow us to conclude: dehydration, in oxygen and oxygen-free conditions, caused inactivation of 95%, but had not DNA damaging effect on λ 1390 bacteriophage.

To test the stability of λ capsid

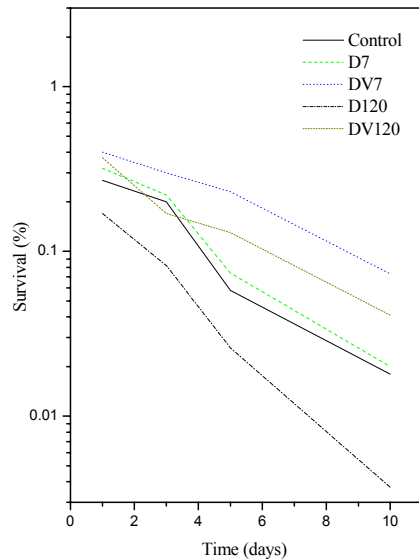


Figure1. λ capsid protein destabilization.

proteins, each sample of resuspended dry λ aliquot were transferred to 37 °C or 50 °C. Number of survivors was screened every day for 10 days. At 37 °C we have not noted significant differences between samples, but at higher temperature (50 °C) differences were significant (Figure 1). The best surviving at high temperature was for samples dehydrated in vacuum and 7h on air. These three groups were more stable than non-dehydrated control group. The worst survival was of sample dehydrated for 120h on air. Also, neither DNA strand break nor DNA mutation were caused by the high temperature in all samples.

Acknowledgements

The technical expertise in vacuum chamber dehydration of Dr J. Comor and Mr M. Siljegovic (of Vinca Institute, Belgrade, SCG) is greatly appreciated. This work was supported by the grant of Ministry of science technologies and development of the government of Serbia (BOI1953) and financial equal of Prof. Radman's laboratory.

References

- [1] D.J. Fluke and F.Jr. Forro, *Radiat. Res.*, 1960, 13, 305.
- [2] P.E. Schambra and F. Hutchinson, *Radiat. Res.*, 1964, 23, 514.
- [3] S.E. Bresler, V.L. Kalinin, I. Yu, A.S. Kopylova, V.N. Krivisky, Rybchin and V. N. Shelegedin, *Mut. Res.*, 1975, 29, 1.
- [4] A., Fekete, Gy. Rondo, M. Hegedus, K. Modos, A. Berces, G. Kovacs, H. Lammer and C. Panitz, *Adv. Space Res.*, 2004, (in press).
- [5] R.W. Hendrix, J.W. Roberts and F.W. Stahl, In: *Lambda II*, Cold Spring Harbor Laboratory, 1983, 440.

THERMAL ANALYSIS OF WHEY LIPID-PROTEIN FRACTION

S. Ostojić, M. Kićanović, M. Živić, S. Gorjanović and M. Pavlović

*Holding Institute of General and Physical Chemistry,
Studentski trg 12/V, Belgrade, Serbia & Montenegro*

Abstract

Thermal stability of obtained whey fraction has been analyzed by Differential Scanning Calorimetry (DSC), sensitive DSC and thermogravimetric analysis (TGA). Partial characterization of prepared fraction and information on thermal stability of sample, valuable for technological process, were obtained. Temperatures of transitions for whey fraction in solution were: $T_{m1}=302.8$ K, lipid thermo tropic transition, $T_{m2}=345.7$ K and $T_{m3}=356.7$ K, protein unfolding and for dry whey fraction: $T_{m1}=373.3$ K, water evaporation, $T_{m2}=421.9$ K, lipid melting and $T_{m3}=476.5$ K, protein degradation.

Introduction

Whey is valuable by-product of dairy industry. Usage of whey products is common in food industry. Production of whey components (proteins, lipids, lactose) could transform these by-products into products with high nutritional and technological values. There are many facts about biological activity of whey proteins [1,2]. Lipids from whey are potential anticancerogen agents [3,4] and bactericides [5]. In our country, in spite of knowledge about whey protein benefits to the human health and known improvements of technological properties of different products by addition of whey proteins, whey is treated like waist and simply disposed.

Experimental

Sample preparation: Whey, from IMLEK-PKB, Belgrade, was concentrated by vacuum evaporation at 328 K. After concentration to 55% DM (dry matter), crystallized lactose was separated by centrifugation. Supernatant was filtered and sediment with 45.46% DM, lipid-protein fraction, was separated. Concentration of lipid (of 19.4% in DM) in obtained lipid-protein fraction was determined by gravimetry and protein concentration (of 6.6% in DM) was determined by Lowry method.

Sample preparation for thermal analysis: The lipid-protein fraction (45.46% DM) was diluted with deionised water to protein concentration of 1.7 mg/ml, lipid concentration of 5.1mg/ml and used as sample for sensitive DSC analysis. Lipid-protein fraction (45.46 DM) was dried under the vacuum at room temperature and obtained powder (73% DM) was used as sample for DSC and TGA analysis. DSC scans of lipid-protein fraction water solution were performed by MicroCal MC-2 Scanning Calorimeter, MicroCal Inc. Northampton, MA, USA. Origin software was used for DSC data analysis (non two-state curve fitting model, for estimating thermodynamical parameters: T_m -temperature of transition midpoint, ΔH^{cal} - calorimetric enthalpy. The scan rate was 1.5 K/min, in temperature range from 293 K to 373 K. Thermal analysis

of dry lipid-protein fraction was performed by Du Pont Instruments 910 Differential Scanning Calorimeter and Du Pont Instruments 951 Thermogravimetric Analyzer. Scans were performed in the inert atmosphere (N_2), in temperature range from 293 K to 573 K, scan rate 10 K/min. TA Universal Analysis: TA2000, TA Instruments, software was used for DSC and TGA data analysis.

Results and Discussion

Obtained DSC curves of whey lipid-protein fraction are shown on Fig. 1. From Fig. 1A (first scan) it can be seen that there are three endothermic peaks with temperature midpoints at $T_{m1}=302.8$ K, $T_{m2}=345.7$ K and $T_{m3}=356.7$ K. Transition occurred at lower temperature ($T_{m1}=202.8$ K) corresponds to thermotropic transition of lipid components, while transitions at higher temperatures $T_{m2}=345.7$ K and $T_{m3}=356.3$ K represent the protein unfolding (denaturation).

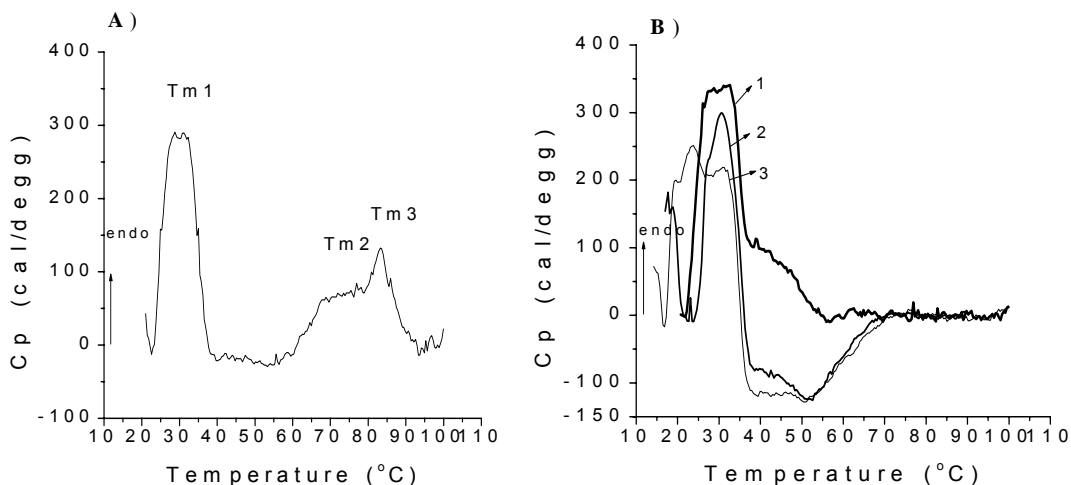


Figure 1. DSC curves of whey lipid-protein fraction **A)** first scan and **B):** 1-second scan; 2-third scan; 3-fourth scan

After first scan, the same sample was cooled and rescanned three more times, under the same experimental conditions (Fig. 1B). It can be seen that lower temperature transition (T_{m1}) for repeated scans was approximately the same as in the first scan. The higher thermal transitions disappeared after the second scan due to irreversible denaturation of proteins. DSC curve of fourth scan (Fig. 2), shows that lipid thermotropic transition becomes complex (divided into two peaks with $T_m=295.0$ K and $T_m=301.0$ K). Figures 2A and B present DSC and TGA curves for dried lipid-protein whey fraction. Three endothermic peaks can be seen on DSC thermogram (Fig. 2A): the first one with $\Delta H^{cal} = 100.9$ J/g at 373.3 K, the second with $\Delta H^{cal} = 7.82$ J/g at 421.9 K and

the third with $\Delta H^{\text{cal}} = 4.71 \text{ J/g}$ at 476.5K. The first endothermic peak corresponds to water evaporation, as can be seen from TGA curves shown in Fig. 2B.

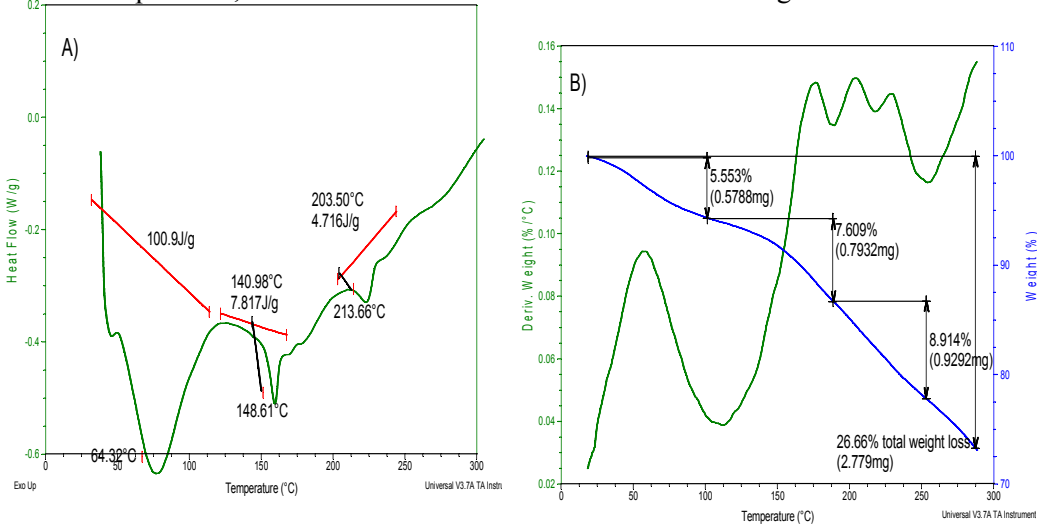


Figure 2. A) DSC curve of dried lipid protein whey fraction, B) TGA curves of dried lipid-protein whey fraction

It has been found that second broad endothermic transition between 398 K and 446 K, characteristic for whey protein isolate, was similar to the melting transition of semicrystalline polymers [6]. Our results suggest that second endothermic transition of lipid-protein whey fraction mainly represents melting of lipid component. The third endothermic transition represents thermal degradation of proteins [6].

Conclusion

During the whey processing, it is crucial to maintain the low temperature regime, to preserve biological activity of whey components.

References

- [1] Burington K. J., Dairy Pipeline, 2002, 14, 1.
- [2] www.wheyliife.org
- [3] Parodi P.W., The Journal of Nutrition, 1997, 12, 6 1055.
- [4] Vesper H., et al., J. Nutrition, 2000, 130, 522.
- [5] Sprong R.C., Hulisten M.F.E., Van der Meer R., Antimicrobial Agents and Chemistry, 2001, 45, 1298.
- [6] Kim S.J., Ustunol Z., J. Food Sci., 2001, 66, 7, 985.

EFFECT OF ULTRA-LOW DOSES OF INTERLEUKIN-2 ON HUMORAL IMMUNE RESPONSE ELICITED WITH ANTI-IDIOTYPIC ANTIBODY, MIMICKING COLON CARCINOMA -ASSOCIATED EPITOPE CO17-1A

M. Pavlović

*Institute for General and Physical Chemistry,
P.O. Bo 551, Studentski trg 12-16, Belgrade, Serbia and Montenegro*

Abstract

Anti-idiotypic rat monoclonal antibody BR3E4, mimicking the CO17-1A epitop of CO17-1A/GA733 antigen (Ag), associated with colorectal carcinoma, is a candidate for tumor vaccine. Ultra-low doses of interleukin-2 (IL-2) enhance idiotype-specific response in all and Ag-specific response in one rabbit, which, previously were immunized with Ab2 alone and developed both idiotype-specific and Ag-specific response. This data suggest the importance of timing of IL-2 treatment with immunization with BR3E4. It was, also, noted that anti-rat immunoglobulin antibodies, elicited by BR3E4, cross-react with extracellular matrix proteins: tenascin-C and laminin-nidogen complex, which may influence the anti-tumor response to anti-idiotypic tumor vaccine.

Introduction

Anti-idiotypic antibodies (Ab2), binding to the antigen-combining site of anti-tumor antibodies (Ab1), can functionally or structurally mimic tumor antigens. Ab2 have induced Ag-specific humoral (Ab3) and cellular (T3), but rarely protective immunity against tumors in experimental animals and patients. The CO17-1A/GA733 Ag (further GA733 Ag), associated with colorectal carcinoma was the target of numerous studies in experimental animals and phase-I clinical trials with polyclonal and monoclonal rat-derived Ab2 and monoclonal human Ab2 (reviewed in [1, 2]). The effects of Ab2 tumor vaccines depend on the dose and form of Ab2 (whole molecule or Fab2), the carrier or the adjuvant used [1]. Recombinant IL-2, as the adjuvant, was shown to improve the protective effect of several viral vaccines [3]. Ultra-low doses of IL-2 are supposed to improve the Ag-specific response, stimulating Ag-activated T and B lymphocytes and were found to modulate immune response in tumor patients [4]. In order to increase the Ag-specific immunity to Ab2 BR3E4, mimicking the CO17-1A epitop of colorectal carcinoma-associated Ag, the investigations have been conducted, using Ab2 as the substitute for Ag and ultra-low doses of IL-2 as the adjuvant.

Experimental

Eight rabbits (R1-8) were immunized intradermaly with 200 µg of Ab2 and given a dose of 15×10^3 IU/12 h of recombinant human IL-2 for 5 days after immunization, in a two different regimes, groups 1. and 2., Table 1. The idiotype-specific response was demonstrated by binding of Ab3 from sera to BR3E4 antibody, compared to binding

to rat Ig and the inhibition of binding of Ab2 BR3E4 to Ab1 CO17-1A in indirect radio immuno assay (RIA). The Ag-specific response was demonstrated by binding of Ab3 from sera to recombinant GA733 Ag in enzyme-linked immunosorbed assay (ELISA) and binding to colon-carcinoma cell line Colo 201 in RIA. Specificity of binding of Ab3 to GA733 Ag was tested by several control antigens: bovine and human serum albumin, human recombinant fibronectin and tenascin-C and mouse EHS (a complex of mouse laminin and nidogen) in ELISA, after purification of immunoglobulin G (IgG) from preimmune and immune rabbit sera by caprylic acid and ammonium sulfate precipitation and further purification of Ab3 on rat Ig and BR3E4 affinity columns. Methods described in detail in [2, 5].

Results and Discussion

The study was designed to determine the effect of ultra-low doses of IL-2, given in a multiple injection regime, on immunization with Ab2 BR3E4, as a substitute of tumor-associated antigen GA733.

Table 1. Rabbits (R), were immunized with Ab2 BR3E4 and treated with ultra-low doses of IL-2. ^aThe highest reciprocal serum dilution (titer) showing activity of Ab3 in each assay that differ significantly from values obtained with the preimmune sera and corresponding control sera from rabbits immunized with normal rat Ig ($p < 0.05$, Students t-test). ^bThe highest titer of each sera showing difference in binding to Ab2 BR3E4 vs normal rat Ig ($p < 0.01$, Students t-test).

R	Treatment Ab2 BR3E4 or Ab2/IL-2	Immun. No.	Time: week	Ab3 serum titer		Binding to GA733 Ag ^a	Binding to Ab2 vs rat Ig ^b	Inhibit. of bind- ing of Ab2 to Ab1 CO17- 1A ^a
				Sera not absorbed	Sera absorbed with melanoma cells			
I group								
1	Ab2	5	13	120	120	243	6250	40
	Ab2/IL-2	7	21	120		81	31250	1280
2	Ab2	5	13	30		243	31250	320
	Ab2/IL-2	7	21	30		243	31250	2560
7	Ab2	5	13	30		243	31250	1280
	Ab2/IL-2	7	21	30		243	31250	5120
8	Ab2	5	13	30		0	31250	1280
	Ab2/IL-2	7	21	30		243	31250	640

II group								
3	Ab2/IL-2	5	13	60	120	27	31250	1280
	Ab2	7	21	60		27	6250	640
4	Ab2/IL-2	5	13	30		27	31250	5120
	Ab2	7	21	30		27	31250	1280

The idiotype-specific response, the GA733 Ag-response and colon carcinoma cell-response were evident in unprocessed sera of six out of eight animals immunized with Ab2, with or without IL-2 as the adjuvant, Table 1., When administered to the animals, that were previously immunized 5 times with Ab2 alone, and developed idiotype-specific and Ag-specific response, IL-2 augments the idiotype specific response (sera titer) in all and Ag specific response in one animal, which did not responded to previous treatment with Ab2, Table 1.

The response to recombinant CO17-1A Ag was found in low titers (27-243) in the sera of immunized animals. In the same titers, the cross-reaction with extracellular matrix proteins: tenascin-C and EHS (a complex of laminin and nidogen), was observed. It was demonstrated that cross-reaction of immune sera with these proteins depends on anti-rat Ig antibodies, because it was almost eliminated by extensive purification of anti-rat Ig antibodies (data not shown)

Ab2, as tumor vaccines, can provoke unspecific responses, which could be even beneficial for the diseases, eg. the response to tyrosinase in melanoma patients, immunized against High Molecular Weight Melanoma Associated Antigen, which was found to correlate with the best clinical outcome [5]. It was, also, found that the response to mouse Ig improve clinical response in colon carcinoma patients treated with monoclonal mouse Ab1 CO17-1A [6]. We can speculate that anti-rat Ig response, cross-reactive with some extracellular matrix proteins could participate in the immune response to Ab2, mimicking tumor antigens.

Conclusion

The timing of administration of ultra-low doses of IL-2 during immunization with anti-idiotypic antibody BR3E4, mimicking the colorectal carcinoma associated Ag CO17-1A/GA733, was shown to influence the idiotype-specific response to this Ab2, but the effect on Ag-specific response could not be proven.

References

- [1] D.Herlyn, R. Somasundram, W. Lee, H. Marujama, *Cancer Immunol. Immunother.*, 1996, 43, 65.
- [2] B. Birebent, E. Mitchell, N. Akis, W. Li, R. Somasundram, E. Purev, D. Hoey, M. Mas-trangelo, H. Maguire, D.T. Harris, S. Nair, D. Cai, T., Zhang, D.M. Herlyn, *Vaccine*, 2003, 21, 1601.
- [3] S.C. Meuer, H. Dumann, K.H. Meyer zum Buchenfelde, H. Kohler, *Lancet*, 1989, 7, 15.
- [4] A. Lindemann, P. Brossart, K. Hoffken, M. Flashove, D. Voliotis, V. Dichl, G. Hecker, H. Wagner, R. Mertelsmann, *Cancer Immunol. Immunother.* 1993, 37, 307.
- [5] E. Baharav, O. Merimsky, M. Altomonte, Y. Shoenfeld. M. Pavlovic, M. Maio, *Melanoma Res.*, 1995, 5, 337.
- [6] G. Reithmuller, E. Holz, G. Schlimok, *J. Clin. Oncol.*, 1998, 16, 1788.

NON-EXCHANGEABLE WATER IN BIOLOGICAL SYSTEMS: AN NMR STUDY

G.Bačić and R. Srejić

Faculty of Physical Chemistry, University of Belgrade, Belgrade, Yugoslavia.

Abstract

In this work we investigated whether the type of water which cannot be exchanged by deuterated water exists in biological systems. Using proton NMR spectroscopy and several types of cells and tissues, we demonstrated the existence of such water and showed that its amount positively correlates with the amount of dry matter in the system. It was also found that the fraction of unfreezable water is higher for non-exchangeable water than for the bulk water. Taken together these findings argue that non-exchangeable water is entrapped within some macromolecular structures.

Introduction

A great deal of scientific research has been devoted to the structure of water in biological systems and its classification into different types. It has been investigated by numerous experimental techniques and most notably by ^1H NMR spectroscopy. A complementary approach to the same problem is an isotope (D_2O or HTO) exchange method, exploited both *in vivo* and *in vitro*. Here, the exchange kinetics has been analyzed for classifying different types of water and/or compartments. In all but a few cases, it has been taken as a matter of course that the entire amount of cellular or tissue water is available for exchange. However, our previous studies (1-3), as well as results of some other researchers (4-6), indicated the existence of a non-exchangeable fraction of water in biological systems. Here we focused on the nature of this water fraction, showing that its origin is not connected with some specific organization of certain tissues, since its presence was detected in a variety of systems.

Materials and Methods

Material. Investigated biological samples are listed in Table I. However, the majority of measurement were performed on primary maize roots and isolated nerves (*nervus ishiadicus*) obtained from adult frogs. The samples were soaked in 99.8% D_2O (roots) or deuterated Ringer solution (nerves). The ratio of external D_2O to sample volume was around 20:1. Soaking time was 1 h, after which samples were soaked once more for 1 h in fresh D_2O , which is sufficient for the complete exchange (1-3). Samples were then blotted and measured in an NMR tube previously saturated with N_2 to prevent atmospheric moisture to interfere with measurements.

NMR measurements. All proton relaxation measurements were made on a Bruker SXP-100 spectrometer operating at 90 MHz. The FID signal amplitude of protons from samples was measured 250 ms after the 90° pulse in order to eliminate the contribution from protein protons and the amount of non-exchangeable (NEX) water was determined from the ratio of proton signals in normal and deuterated samples. Water proton relaxation times were measured inversion inversion recovery pulsed sequence (T_1) and

CPMG sequence (T₂), with the spacing between 180° pulses varying from 0.2 to 150 ms. High-resolution proton NMR spectra were recorded at ambient temperature with a Bruker MSL 400 spectrometer.

Results and Discussion

Table I show that that the amount of NEX water is not negligible and that is inversely correlated with the water content of the sample as shown in Fig. 1. This in turn can raise suspicion that the proton signal detected by NMR is due to some other protons (proteins and/or lipids) and not to water protons. However, a body of evidence confirms the existence of NEX water: a) High resolution ¹H NMR results clearly showed a single line with the chemical shift of water and b) Values of relaxation times (Table 1) are typical for water protons, and c) Freezing pattern of the NMR signal is the same as for bulk water (Fig. 2).

Table 1 The amount of non-exchangeable and unfreezable water in some biological systems as measured by proton NMR. Proton relaxation times of H₂O in normal and deuterated samples measured at 22°C. *CPMG with = 0.2 ms pulse spacing. **Expressed as a percentage of non-exchangeable water.**

Sample	g H ₂ O per g dry weight	NEX water %	T ₁ (ms)	T ₂ (ms)*	Unfreezable water (%)**
Maize root	13.4± 1.3	13±2	1350±100	120±10 410±50	11.4
deuterated	na	na	1450±100	140±10 450±50	26*
Maize cortex	14.2± 1.4	9±1	/	/	/
Maize steel	8.8± 0.9	/	/	/	/
Frog nerve	3.1± 0.2	20±2	1000±100	80±10 230±35	17
deuterated	na	na	1000±100	90±10 250±40	22*
Nitella cells	~ 39	~ 5	T ₁ (ms)	T ₂ (ms)	/
Leech ganglion	~ 28	~ 6	1350±100	120±10 410±50	/

A possible source of error in our estimate of the amount of NEX water is the light water already present in D₂O, which amount inevitably increases during the sample manipulation due to atmospheric moisture. This water also equilibrates between the sample and external solution and can mimic incomplete exchange. Therefore, the amount of H₂O in the sample of D₂O, handled in the same manner as in exchange measurements, was determined by measuring its peak area and it was found that this might introduce an error of less than 10% in our estimate of the amount of non-exchangeable water.

The existence of NEX water is certainly not dependent on some structures specific to a particular biological system, since it was found in a variety of systems (Table I, 4-6). Figure 2 shows the temperature dependence of the FID amplitudes of water protons for maize roots (similar results were obtained for nerves). A slow increase of

signal amplitude in the region room temperature - 0°C, is due to the well-known increase of the NMR sensitivity with the decrease of temperature. Sharp decrease of signal amplitude around -2°C represents freezing of the major portion of tissue water, which T_2 is now too short ($< 15 \mu\text{s}$) to be detected. The signal amplitude of unfrozen water further decreases with the decrease of temperature because of the shortening of T_2 .

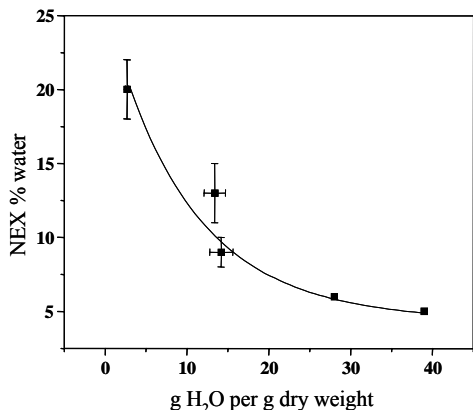


Figure 1. The amount of non-exchangeable water in various biological samples vs. their water content.

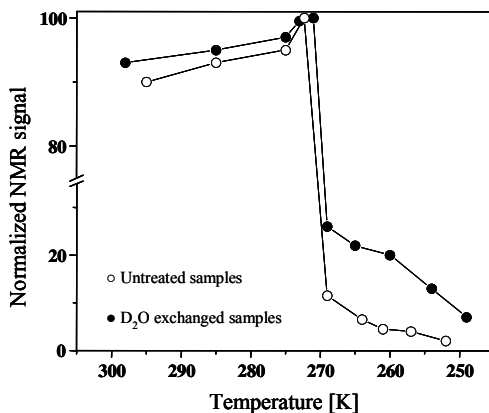


Figure 2. The amplitude of the proton free induction decay (FID) signals from maize root as a function of temperature. Signal amplitudes are plotted relative to the amplitude at 0 °C to bring them onto a common scale.

The existence of unfreezable water (referred to as water that does not freeze at around 0°C) is a common finding in biological systems and its amount is correlated to the amount of dry matter (consistent with results in Table I). However, the percentage of unfreezable water is higher in NEX water than in bulk water indicating closer contact with solid surfaces. The dependence of T_2 on the pulse spacing in CPMG sequence (data not shown) also indicated diffusional restrictions of NEX water. Both findings are consistent with the encasement of NEX water within macromolecular structures.

Acknowledgement. This work was supported by grant 1928 from the Ministry of Science and Environmental Protection of the Republic of Serbia.

References

- [1] G. Bačić and S. Ratković, *J. Exp. Bot.*, 1987, 38, 1284.
- [2] G. Bačić, and S. Ratković, *Period. Biol.*, 1982, 84, 111.
- [3] R. Srejić, et al., *Period. Biol.*, 1988, 90, 175.
- [4] V. Vasilescu and E. Katona. In *Methods in Enzymology*, Vol. 127. L.Packer, editor. Academic Press, New York. 1986, 662.
- [5] G. Pifat, In *Biophysics of Water*, F.Franks and S.Mathews, editors. John Wiley & Sons, Chicester, 170.
- [6] K. Ruckpaul, et al., *Croat. Chem. Acta*, 1976, 48, 69.

Zn(II) BINDING ON BOVINE SERUM ALBUMIN FOLLOWED BY ITC

S. Ostojić, M. Kićanović and B. R. Simonović

*Holding Institute of General and Physical Chemistry
Studentski trg 12/VP.O.Box 551 11000 Belgrade, Serbia&Montenegro*

Abstract

Interaction between bovine serum albumin (BSA) and Zn(II) was studied by isothermal titration calorimetry (ITC). Obtained thermodynamical parameters for interaction on temperature $T=293$ K were: number of binding sites, $N=5.5$, binding constant, $K=1.494 \times 10^2$ M and the heat of binding, $\Delta H = 20.59$ kJ and on temperature $T=310$ K were: number of binding sites, $N=7.32$, binding constant, $K=1.675 \times 10^2$ M and the heat of binding, $\Delta H = 54.59$ kJ respectively. We found that binding affinity of Zn(II) on protein was higher at physiological temperature, 310 K.

Introduction

Zinc is essential element in the body, critical for the development and function of all cells, for the immune system and for transmission of genetic information. It has catalytic or structural roles in wide range of proteins [1]. Albumin is the major soluble protein constituent of circulatory system and has many physiological functions as transport and distribution of various ligands. [1-4]. Albumin is a single chain protein of 585 amino acids, it consists three structurally homologous, largely helical domains: I, II and III. Serum albumin has a variety of metal sites with different specificities, best characterized are those for Cu^{+2} and Ni^{+2} .

Albumin is the major transport protein in blood for Zn^{+2} . It modulates zinc uptake by endothelial cells, facilitates uptake of Zn^{+2} by erythrocytes and increases its oxygen affinity [1].

In this work we studied the Zn^{+2} binding on bovine serum albumin in the aim of better understanding albumin zinc interaction. The isothermal titration calorimetry (ITC) method for studying of Zn^{+2} /protein interaction was used.

Experimental

Bovine serum albumin (BSA) was purchased from Boehringer Mannheim (Fraction V) and used without further purification. ZnCl_2 and other chemicals were of p.a. grade and freshly prepared. All protein solutions were degassed before loaded into the calorimeter to prevent bubble entrapment in the cells. Calorimetric titration were made using the MicroCal "OMEGA" titration microcalorimeter: details of instrumental design and data analysis ("Origin" software) are described previous [5]. BSA (concentration 0.050 mM in deionised water) was placed in the cell and titrated with 20mM ZnCl_2 deionised water solution. Typically, 20 injections of 5 μ l 20mM ZnCl_2 each were made with 10 min intervals between two injections. The data were integrated to provide a titration curve and by use of nonlinear last squares fit number of

binding sites N , binding constant K and the heat of binding ΔH were calculated from the curve by using “single set of identical sites” curve fitting model. Non-negligible heat of dilution was subtracted prior to data fitting.

Results and Discussion

Obtained titration curves, of Zn^{+2} /BSA interaction, at temperature 293 K and 310 K (physiological temperature) are presented on Figure1.

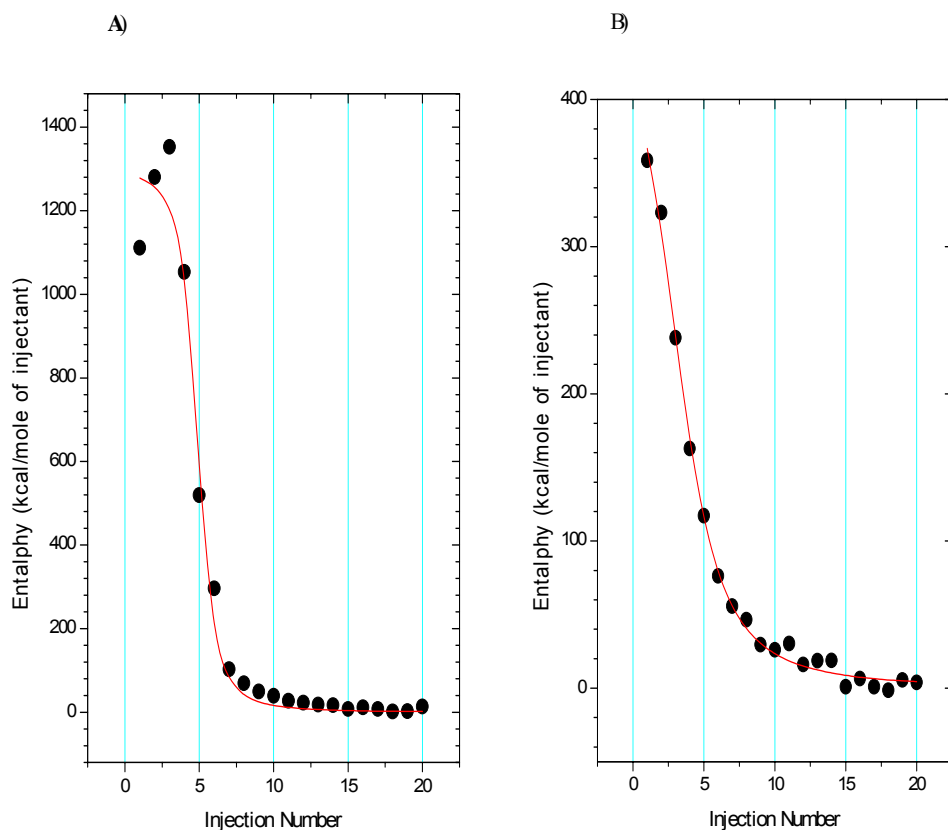


Figure 1: Titration curve of BSA with 20mM $ZnCl_2$ at $T=310K$ (A), and at $T=293K$ (B): integrated curve showing experimental points (\bullet) and (- -) least squares fit to the integrated data.

Stewart et al. [1] identified a potential five coordinate Zn site at the interface of domains I and II consisting of N ligands from his-67 and His-247 and O ligands from Asn-99, Asp-249 which are the same amino acid ligands as those in zinc enzymes calcineurin, endonucleotidase and purple acid phosphatase [1].

Obtained thermodynamical parameters of interaction at 293K were: number of binding sites, $N=5.5$, binding constant, $K=1.494 \times 10^2 \text{M}$ and the heat of binding, $\Delta H = 20.59 \text{ kJ}$ and for interaction at 310 K number of binding sites, $N=7.32$, binding constant, $K=1.675 \times 10^2 \text{ M}$ and the heat of binding, $\Delta H = 54.59 \text{ kJ}$ respectively.

Conclusion

It can be assumed, from obtained thermodynamical parameters of binding, that binding affinity of Zn(II) on protein is higher at physiological temperature 310K. Thermodynamical parameters of binding are mainly in agreement with known results, but cannot be directly compared because slight differences regarding experimental conditions (pH, temperature) [1, 6].

Acknowledgment

The present investigations are partially supported by Ministry of Science Technologies and development of Serbia.

References

- [1] A.J. Stewart, C.A. Blindauer, S. Berezenko, D. Sleep, P. Sadler, PANAS, 2003, 100(7) 3701.
- [2] M. X. He, C. D. Carter, Nature, 1992, 385, 209.
- [3] M. Sokolowska, A. Krezel, M. Dyba, Z. Szewczuk, W. Bal, Eur. J. Biochem., 2002, 269, 1323.
- [4] M. Dockal, D.C. Carter, F. Ruker, JBC, 1999, 274, 41 19303.
- [5] T. Wiseman, S. Williston, J. F. Brandts, and L. N. Lin, Anal., Biochem., 1989, 179, 131.
- [6] J. Masouka, J. Hegenauer, B.R. VanDike, P. Saltman, the Journal of Biological Chemistry, 1993, 268(29), 21533.

INFLUENCE OF Zn(II) ON THERMAL UNFOLDING OF BOVINE SERUM ALBUMIN FOLLOWED BY DSC

S. Ostojić, V. Dragutinović and B. R. Simonović

*Holding Institute of General and Physical Chemistry
Studentski trg 12/VP.O.Box 551 11000 Belgrade, Serbia&Montenegro*

Abstract

The differential scanning calorimetry method (DSC) was used for studying the influence of different concentration Zn(II) (0.050mM, 0.150mM, 0.300mM, 0.450mM, and 20mM ZnCl₂) on thermal unfolding of bovine serum albumin (BSA), in the aim of better understanding albumin/zinc interaction. From obtained thermodynamical parameters of protein unfolding: temperature midpoint (T_m), calorimetric enthalpy (ΔH^{cal}) and Van't Hoff enthalpy (ΔH^{VH}), it can be assumed that obtained differences in stability of protein structure were consequence of zinc presence during the process of thermal unfolding.

Introduction

Zinc is essential element in the body, critical for the development and function of all cells, for the immune system and for transmission of genetic information. It has catalytic or structural roles in wide range of proteins [1]. Albumin is the major soluble protein constituent of circulatory system, which accounts for about 60% of total protein in blood. Albumin has many physiological functions as transport and distribution of various ligands, chemically diverse molecules like fatty acids, amino acids, steroids, metals and pharmaceuticals. [1- 4].

Albumin is the major transport protein in blood for Zn⁺². Albumin modulates zinc uptake by endothelial cells, facilitates uptake of Zn⁺² by erythrocytes and increases its oxygen affinity [1].

Experimental

Bovine serum albumin (BSA) was purchased from Boehringer Mannheim (Fraction V) and used without further purification. ZnCl₂ and other chemicals were of p.a. grade and freshly prepared. All protein solutions were degassed before loaded into the calorimeter to prevent bubble entrapment in the cells. Calorimetric measurement were carried out on a MicroCal MC -2 sensitive differential scanning calorimeter (DSC) using a standard DA - 2 software package for data acquisition and Origin software for DSC data analysis (non two -state curve fitting model, for estimating thermodynamical parameters of protein unfolding: T_m , ΔH^{cal} , ΔH^{VH} was used). All scans were performed in the temperature range from 283 K to 383 K. Scan rate was 90 K/h.

Results and Discussion

Thermal denaturation process of BSA (0.050mM) was studied under the low ionic strength conditions (deionised water) and with addition of 0.050mM, 0.150mM, 0.300mM, 0.450 and 20mM ZnCl₂, pH=6.2.

Obtained DSC curves showed that thermal denaturation of protein depends of ZnCl_2 concentration, what is evident from shapes of DSC curves , number of thermal transitions and calculated thermodynamical parameters: temperature midpoint T_m , calorimetric enthalpy (ΔH^{cal}) and Van't Hof enthalpy (ΔH^{VH}) (Figure 1.,Table 1.).

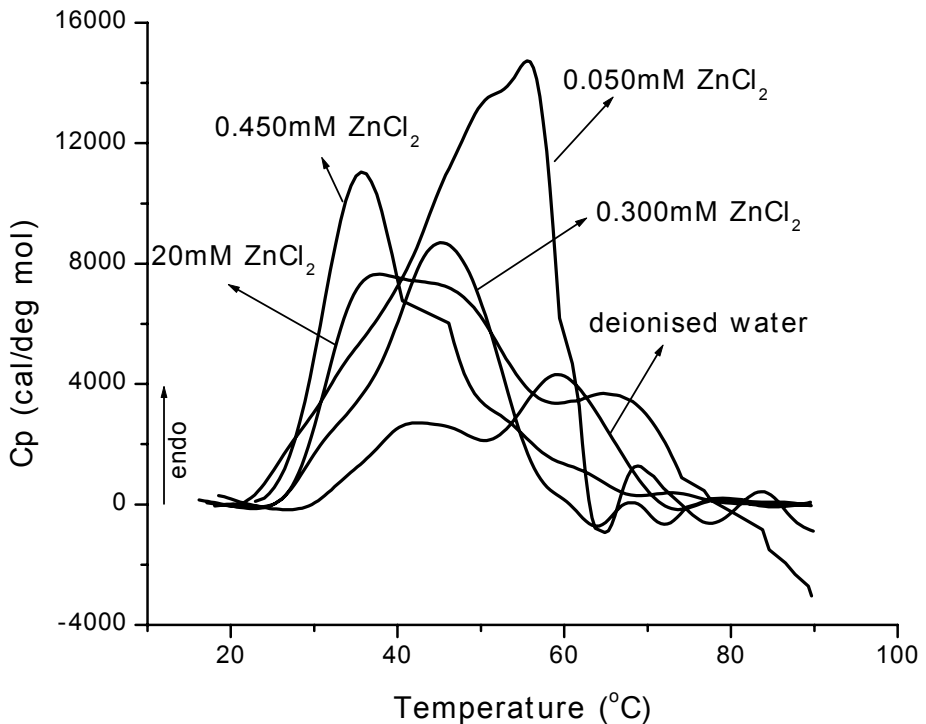


Figure 1. DSC curves of BSA in the presence of different ZnCl_2 concentrations in deionised water pH=6.2.

Table 1. Thermodynamical parameters of BSA (0.050mM) thermal denaturation in deionised water pH=6.2 and in presence of ZnCl₂ different concentrations, obtained from DSC curves.

ZnCl ₂ c(mM)	T _m (K)	ΔH ^{cal} (kJ/mol)	H ^{VH} (kJ/mol)	H ^{cal} /H ^{VH}	Protein:ZnCl ₂ molar ratio
	316.5	169.26	215.37	0.78	-
0	332.4	209.40	297.40	0.70	
	319.0	800.78	179.80	4.45	
0.050	328.6	430.08	436.50	0.98	1:1
	311.3	93.07	288.70	0.32	
0.150	319.7	529.94	344.30	1.53	1:3
	309.9	184.78	218.73	0.84	
0.300	319.4	425.71	277.81	1.5	1:6
	308.9	532.32	316.21	1.6	
0.450	323.8	217.65	299.39	0.72	1:9
	308.5	253.60	325.95	0.77	
20	318.5	319.31	243.56	1.3	1:400

During the thermal denaturation, in the presence of zinc(II), conformational changes in the protein structure were induced compared to denaturation of protein in deionised water. BSA is a globular protein composed of three structurally similar globular domains, each of which contains two subdomains (IA, IB, IIA IIB, IIIA and IIIB) [1, 2, 4]. Stewart et al. [1] identified a potential five coordinate Zn site at the interface of domains II and I.

Conclusion

It can be assumed that obtained differences in stability of protein structure were consequence of zinc/protein interaction. This interaction caused perturbation of protein domains undergoing thermal unfolding what can be seen from ΔH^{cal}/ΔH^{VH} ratio (Table 1).

Acknowledgment

The present investigations are partially supported by Ministry of Science Technologies and development of Serbia.

References

- [1] A.J. Stewart, C.A.Blindauer, S.Berezenko.D. Sleep, P. Sadler, PANAS, 2003, 100(7), 3701.
- [2] M. X. He, C. D.Carter, Nature, 1992, 385, 209.
- [3] M. Sokolowska, A. Krezel, M. Dyba, Z. Szewczuk, W. Bal, Eur. J. Biochem., 2002, 269, 1323.
- [4] M. Dockal, D.C. Carter, F. Ruker, JBC, 1999, 274(41), 19303.

ANTIBODY "OVERCHARGING" BY FLUOROCHROME DYE – FITC.

M. Petrović, N. Ilić and Lj. Sofronić-Milosavljević

*INEP, Institute for the Application of Nuclear Energy,
Banatska 31b, 11080 Zemun, Serbia and Montenegro*

Abstract

In this paper we presented methods for labeling of isolated sheep antihuman molecules IgG by fluorochrome dye (FITC) using two methods: standard and modified method (overcharging). Aim of this work was to examine the "overcharged" conjugate (contains high number of FITC dye molecules per antibody molecule) applicability for the detection of specific antibody presence in circulation of humans (using IFA methods), comparing with "standard" labeled conjugates. Parallel investigation of conjugates, was performed with in the immunoparasitological (*T.spiralis*, *T.gondii* and *B.burgdorferi*) test models. Quality of prepared conjugates was examined on the basis of "apple green" fluorescence intensity that was emitted from the antigen-antibody reaction site. Results of performed investigation suggested the advantage of "overcharged" conjugates in case when pathogens are isolated and applied in IFA test in its free form (like in IFA tests for anti: - *T.gondii*, or - *B.burgdorferi* antibody determination), while standard labeled conjugates are optimal for work when pathogens are present in infected host tissue (like applied IFA test for anti- *T.spiralis* antibody detection).

Introduction

The fluorescent antibody test, particularly the indirect method (IFA), has been widely applied in determination of human humoral immune response in health and disease. Preparative requirements and selected measurable chemical parameters for fluorescein-labeling of anti-human antibody determine the field of its applicability. Sensitivity of IFA method relies on the immunological parameters for quality determination of isolated antibodies. Namely, the total number of fluorochrome molecules per molecule of antibody, strongly influence the sensitivity of immunological reaction. Several sheep anti human IgG, purified from sera that were ranging in titer (represents the quality of antibody reactivity to related antigen, expressed as Becker units – B.u.) from: 1.25; 3.4; 6.0 to 10.3 B.u., were used for antibody labeling e.g. fluorescent conjugate production. The standard as well as modified "overcharging" method, were applied for conjugates production. Applicability of these conjugates was compared for specific antibody detection, in three different parasite model systems (*T.spiralis*, *T.gondii*, *B.Burgdorferi*).

Experimental

Anti sera. Sheep anti human IgG sera were used for our investigation. Titer of 4 prepared anti-sera was determined [1] and expressed in units as: 1.25 B.u (A); 3.4 B.u (B); 6.0 B.u (C) and 10.3 B.u (D).

Antibody purification and FITC labeling. IgG originating from the sera of immunized sheeps was purified by combination of 2 methods: desalting and ion exchange chromatography [2]. Purified immunoglobulins were labeled with fluorescein isothiocyanate (FITC, isomer I, Serva, Germany). The same quantity of immunoglobulin isolates (obtained from each of 4 anti-sera with different titer) were used for the preparation of conjugates. For FITC dye labeling the standard (1.8 mg of FITC per 100 mg of immunoglobulin) and modified - "overcharging" (10 times more FITC, for same quantity of immunoglobulin) methods were applied. Conjugation was performed at the rotation mixer. In aim of removing the excess of unbound dye, each sample was passed over Sephadex G-25 (m) (Pharmacia, Sweden) column. All labeling procedures were cared out at room temperatures (18°C – 22°C), but differ in time of incubation periods.

Conjugate performance. The conjugate FITC (F) and protein (P) concentrations were measured, range between them was calculated and expressed by the molar (F/P) ratio, all according to The and Feltkamp [3].

IFA test. All produced FITC labeled anti human IgG conjugates were tested for detection of antibody immune response in humans infected with macro (*T.spiralis*) [4] and micro parasites (*T.gondii*, *B.Burgdorferi*) [5].

Results and Discussion .

The purified IgG immunoglobulins from antisera with different titer, were labeled by standard and modified-"overcharging" procedures.

By applied procedures, conjugates were obtained after 15, 30, 60 90, 180 and 1200 minutes of dye-IgG reaction for standard labeling method. Modified method for conjugate labeling included one procedure more after 7.5 min.

The results of this investigation are presented at Figure 1.

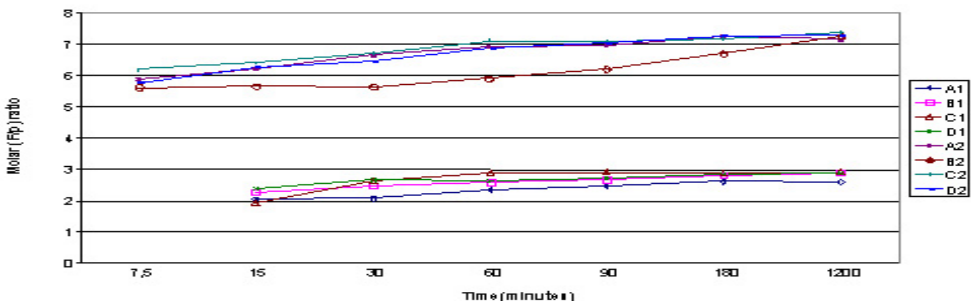


Figure 1. Molar (F/P) ratio in function of reaction time for IgG immunoglobulin labeling (isolated from sera with different B.u. and designated as A,B,C,D). Conjugates obtained by application of standard (A1,B1,C1,D1) or modified (A2,B2,C2,D2) labeling methods.

Different time intervals that were used for dye-protein interaction did not influence interaction obtained by particular labeling method.

Based on this result, we estimated the quality only of conjugates that were prepared by longest incubation time procedure (for each applied labeling method) by IFA in 3 parasite model systems. All conjugates had equal started concentration. Conjugates were tested in serial dilutions, from 1:4 to 1:1024, by application of one appropriate dilution of positive or negative control sera. The quality of each of those conjugates was judged by determination of its last dilution by which the positive fluorescent reaction was achieved with positive control sera application and with no staining on the pathogen or in surrounding tissue when negative control sera was used.

In *T. spiralis* model system: for standard labeling conjugates results were A1-1:32, B1-1:128, C1-1:256 and finally D1-1:512. Nonspecific reaction on parasite components was noticed only by application of the first conjugate dilution (1:4) except for D1, where this phenomenon wasn't observed. Conjugates prepared by modified labeling method, gave the following results: A2-1:64; B2-1:64; C2-1:256 and D2-1:512. Non-specific reaction on parasite components was similar, as in the case of standard conjugates but high background tissue staining was phenomenon that accompanied application of all investigated conjugate dilutions.

For IFA testing in the micro parasite system, *T. gondii* or *B. burgdorferi* was used as antigen substrate. In this model, applicability of C1 and C2 conjugates were investigated. Results in the *T. gondii* -model system were the following: C1-1:64 (non-specific reaction absent) and C2-1:256 (non-specific reaction was present only on the first conjugate dilution 1:4). Results in the *B. burgdorferi*- model system: C1-1:128 (non-specific reaction wasn't observed) and C2-1:256 (same results for non-specific reactions as in the case of C1). The intensity of fluorescence emission was stronger with C2 conjugate.

Conclusion

"Overcharged" conjugates, prepared with "high" number of FITC molecules per one IgG molecule, enabled better conditions for specific antibody detection in micro parasite model systems where isolated pathogens were used for antigen preparation in IFA. Conjugates made by classical labeling method are preferred to be used for specific antibody detection in such model system where the pathogen is located *in situ* e.g. when the sections of infected tissue were applied as antigen in IFA. In all circumstances the non-specific reaction can be avoided by choice of optimal working dilution of conjugate.

References :

- [1] W.Becker, Immunochemistry, 1969, 6, 539.
- [2] M.Petrović et al. Acta Veterinaria, Beograd, 1975, 25, 19.
- [3] The T.H, Feltkamp T.E.W, Immunology, 1970, 18, 865.
- [4] M.Petrović et al.Periodicum Biologorum, 1986, 88, 266.
- [5] R. Lalić, et al. Acta Veterinaria, Beograd, 1982, 32, 283.

COMPARISON OF EXPERIMENTAL AND CALCULATION PROCEDURES FOR ESTIMATION OF LIPOPHILICITY: NEW IDA DERIVATIVES

M. S.Jovanović¹, S.Vranješ¹, J. Brborić², S.Vladimirov² and M.Orlić¹

¹Laboratory for Radioisotopes, Vinča Institute of Nuclear Sciences, P.O.Box 522, 11001 Belgrade,

²Faculty of Pharmacy, P.O.Box 146, 11000 Belgrade, Serbia and Montenegro

Abstract

The lipophilicity expressed as the partition coefficient of newly synthesized IDA derivatives (DIETHYLIODIDA and DIIODIDA) and commercial IDA derivatives as well as their corresponding complexes with ^{99m}Tc was calculated using two computer programs: PACO and ChemOffice Ultra 2003 and determined experimentally by extraction method. The correlation between: log P calculated by two programs; ChemOffice program and experimental log P; and PACO program and experimental log P, is $r=0.76$, $r=0.81$ and $r=0.91$ respectively.

Introduction

The lipophilicity of compounds is one of the most important parameters in the relation between structure and biological activity. n-octanol/water partition coefficient P or its logarithm (log P) is important in predicting of transmembrane transport properties, protein binding and receptor affinity. Lipophilicity of complexes ^{99m}Tc and iminodiacetic acid (IDA) derivatives, radiopharmaceuticals for hepatobiliary scintigraphy, has major influence on biokinetics and competition with bilirubin of these compounds [1]. In order to select the most lipophilic ligands for synthesis, partition coefficients of 5 commercial IDA derivatives and 2 theoretically possible 4-iodo- 2,6-diethyl (DIETHYLIODIDA) and 2,4-diiodo-6-methyl (DIIODIDA) IDA derivatives were calculated using two computer programs. After the synthesis [2], in order to estimate the hepatobiliary properties of chosen compounds, lipophilicity of the corresponding complexes of newly synthesized ligands with ^{99m}Tc and, up to now, the best clinical verified commercial radiopharmaceutical ^{99m}Tc-3-bromo-2,4,6-trimethyl (BROMIDA) IDA derivative was determined experimentally by extraction method for the system n-octanol/water. The correlation between calculation and experimental procedures was considered.

Experimental

DIETHYLIODIDA and DIIODIDA were synthesized [2] and labeled with 18 MBq Na ^{99m}TcO₄ by standard tin (II) chloride method. BROMIDA lyophilized kit (N.C.S.R."Demokritos"Greece) was labeled with 10 MBq Na ^{99m}TcO₄. The radiochemical purity was determined by TLC method on SA and SG strips with 2 mol/dm³ NaCl and 80 % CH₃OH as mobile phases, respectively (> 97%).

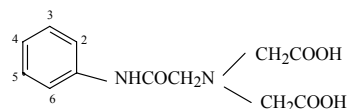
Partition coefficients of ^{99m}Tc-complexes were determined experimentally by extraction method with n-octanol. 1 ml of ^{99m}Tc-BROMIDA and 0.5 ml of both ^{99m}Tc-DIETHYLIODIDA and ^{99m}Tc-DIIODIDA (pH=5.8) were extracted by varying vol-

ume of n-octanol (0.5 ml-2 ml) at 21 °C for 30-180 min. After stirring, to assure distribution between the two solvent phases, the tubes were centrifuged at 3000 rpm for 5 min to separate two phases. Organic phase was carefully and entirely removed. The radioactivity of 0.1 ml of both organic and aqueous phases was measured.

Results and Discussion

Among different calculation methods for estimating octanol-water partition coefficient (log P) for chemical structures, the best accuracy was obtained by fragmental method [3]. In this paper log P values for 7 IDA derivatives were calculated by two programs based on fragmental method: PACO (Version 2.9, Chemodata 1990) and ChemOffice Ultra (Version 7.0.1, 2003). The calculation procedure applied in PACO is based on contribution of substructures with 2 and 3 atoms for which log P contributions have been determined using experimental log P for about 1000 molecules. In ChemOffice log P is calculated by Crippen's fragmentation [4]. Obtained results are presented in Table 1. The correlation between log P values calculated by these programs is $r=0.76$.

TABLE 1. Calculated Partition coefficients (log P) of some IDA derivatives



IDA DERIVATIVE	PACO	ChemOffice
2,6-dimethyl	0.32	0.26
2,6-diethyl	1.01	1.10
2,6-diisopropyl	1.94	1.76
3-iodo-2,6-diethyl	1.16	2.46
3-bromo-2,4,6-trimethyl (BROMIDA)	1.78	1.58
2,4-diiodo-6-methyl (DIIODIDA)	3.47	2.49
4-iodo-2,6-diethyl (DIETHYLIODIDA)	3.80	2.47

Experimentally determined log P for ^{99m}Tc -DIIODIDA, ^{99m}Tc -DIETHYLIODIDA and ^{99m}Tc -BROMIDA were calculated by [5]: $\log P = \log (A_0 / A_w)$
 A_0 - activity of 0.1 ml of organic phase after extraction expressed as cpm
 A_w - activity of 0.1 ml of water phase after extraction expressed as cpm

The partition coefficients of ^{99m}Tc -DIIODIDA, ^{99m}Tc -DIETHYLIODIDA and ^{99m}Tc -BROMIDA for different time intervals and different volumes of n-octanol are shown in Table 2. Equilibrium between organic and water phases was achieved after 1h of extraction with 1ml of n-octanol for ^{99m}Tc -DIIODIDA and after 2h with 0.75ml of n-octanol for ^{99m}Tc -DIETHYLIODIDA. Equilibrium for ^{99m}Tc -BROMIDA was achieved after 2h with 2ml of n-octanol. Log P values, determined upon described conditions are: 0.53 for ^{99m}Tc -DIIODIDA, 1.22 for ^{99m}Tc -DIETHYLIODIDA and -0.04 for ^{99m}Tc -BROMIDA. It is expected that newly synthesized compounds, because of higher lipophilicity, have better hepatobiliary properties in regard to commercial BROMIDA.

Table 2. Partition coefficients (log P) of ^{99m}Tc -BROMIDA (I), ^{99m}Tc -DIIODIDA (II) and ^{99m}Tc -DIETHYLIODIDA (III) (n=5)

n-octanol (ml)	Radiopharmaceutical	Time of extraction (min)							
		30		60		120		180	
		logP	SD	logP	SD	logP	SD	logP	SD
0.50	II	0.13	0.0058	0.28	0.0171	0.37	0.0365		
	III	0.31	0.0233	0.80	0.0272	0.94	0.0878		
0.75	II	0.12	0.0058	0.34	0.0404	0.49	0.0058		
	III	0.77	0.0162	0.98	0.0411	1.22	0.0424		
1.00	I	-0.70	0.0535	-0.63	0.0171	-0.58	0.0458		
	II	0.16	0.0245	0.53	0.0150	0.55	0.0155	0.53	0.0189
	III	0.79	0.0100	1.00	0.0490	1.21	0.0100	1.24	0.0512
1.50	I	-0.51	0.0785	-0.40	0.0556	-0.18	0.0206		
2.00	I	-0.28	0.0311	-0.26	0.0359	-0.04	0.0100	-0.04	0.0171

There is good correlation ($r = 0.91$) between calculated log P values of IDA derivatives by PACO program and experimental log P values of corresponding ^{99m}Tc -complexes. Poor correlation ($r=0.81$) between ChemOffice Ultra 2003 program and experimental log P is obtained. Numerical values of log P are significantly different for all three methods, but the highest values of log P were obtained by calculation with PACO program. Numerical values of log P for DIIODIDA and DIETHYLIODIDA calculated by ChemOffice Ultra 2003 program are almost the same while experimentally obtained values of log P for corresponding ^{99m}Tc -complexes are significantly different. Log P values of these compounds calculated by PACO program are different and these results have the same trend as experimentally obtained.

Conclusion

The application of computer programs for calculation of partition coefficient (log P) is more simple and faster than its determination by experimental method. The data calculated by PACO program show acceptable correlation with experimental results for IDA derivatives. The prediction of lipoflicity of IDA derivatives is very useful for the selection for synthesis and the estimation of hepatobiliary properties of newly synthesized IDA derivatives.

References

- [1] M. S. Jovanović, J. Brborić, S. Vladimirov, Lj. Šturkova, J. Radioanal. Nucl. Chem., 2000, 245, 555.
- [2] J. Brborić, S. Vladimirov, M. S. Jovanović, N. Dogović, Monatshefte für Chemie (2004) in press.
- [3] A. A. Petrauskas, E. A. Kolovanov, Perspectives in Drug Discovery and Design, 2000, 19, 99.
- [4] A. K. Ghose, G. M. Crippen, J. Chem. Inf. Comput. Sci., 1987, 27, 21.
- [5] S. S. Zoghbi, R. M. Baldwin, J. Seibyl, D. S. Charney, R. B. Innis, XIIth International Symposium on Radiopharmaceutical Chemistry, Sweden, Book of Abstracts, 1997, 136.

SONOLYTIC DEGRADATION OF OVOMUCIN BASED PROTEIN MATRIX OF HEN EGG WHITE

D. Filipović and M. B. Radojčić

*Laboratory of Molecular Biology and Endocrinology
VINČA Institute of Nuclear Sciences,
P.O.Box 522, 11001 Belgrade, Serbia and Montenegro*

Abstract

Sonication of ovomucin based protein matrix of the thick fraction of egg white with the therapeutic ultrasound of 23 kHz frequency and 5 μ m amplitude causes irreversible decrease of its viscosity down to the limit value of 2.1 mPa·s. The ultrasound treatment does not affect structure of proteins with lower molecular mass ($M_m < 270,000$ g/mol), such as ovalbumin, conalbumin and ovoglobulins, which reside within the protein matrix, but it leads to the fragmentation of ovomucin fibers ($M_m > 3 \times 10^6$ g/mol) which form the thick egg white matrix. The results suggest that in analogy with avian egg white matrix, sonication-induced changes in mammalian mucin matrix of joints and tendons may constitute the therapeutical action of ultrasound.

Introduction

Ultrasound ($\nu=0.75$ -3MHz) is used for physical therapy of damaged ligaments, joint capsules, or tendons and for emulsification of cataracts and repair of soft tissue injuries [1]. Its beneficial effect is taught to be based on the local increase in tissue temperature. Many of the treated tissues are composed of ductular and tubular structures lined with epithelial cells embedded in extra cellular jelly-like protein matrix composed of mucins [2]. The molar mass (M_m) of mucins is *cca* 10 - 15×10^6 g/mol, and they compose surfactants, molecular sieves, or supportive and protective matrix structures. Although not precisely defined, the changes in mucin matrix are taught to play important part in ultrasound therapy [3]. Mammalian mucins are not easily available in high quantities, but their avian complement ovomucin ($M_m \cong 3 \times 10^6$ g/mol) is easily obtained from the thick fraction of hen's egg white. Egg white ovomucin forms fibrillar matrix ($M_m \cong 40 \times 10^6$ g/mol) encompassing other egg white globular proteins [4]. Sonochemistry postulates the existence of a critical molar mass (M_{mc}), termed lower molar mass limit (LMmL), according to which the molecules whose M_m is below LMmL remain unaffected by ultrasound of certain frequency. Using synthetic polymeres the M_{mc} of 274,000 g/mol was determined for $\nu=23$ kHz, $A=5\mu$ m laboratory ultrasound [5]. As M_m of ovomucin monomer, as well as M_m of ovomucin matrix are above M_{mc} , it is of interest to characterized its changes induced by the treatment with $\nu=23$ kHz, $A=5\mu$ m laboratory ultrasound.

Experimental

Fresh Brown Leghorn (*Gallus gallus*) farm hen's eggs were used as a source ovomucine based matrix. The thick fraction of egg white was separated by filtration on a Büchner funnel, placed in a treatment tube and sonified for 20-300 s (in 20s or 40-60s pulses followed by 30 or 60 min breaks) using Soniprep 150 apparatus ($v=23$ kHz, $A=5\mu\text{m}$). The viscosity was measured by an Ostwald viscometer at 20.0°C . After 300 s treatment samples (1 ml) were dissolved in 0.1M Tris-HCl pH 6.8 containing 4% SDS, 5% β -mercaptoethanol, 6M urea, 20% glycerol and 0.1% brom-phenol-blue (1:1= vol: vol), boiled 2 min at 100°C and analysed by 10% SDS-polyacrylamide gel electrophoresis (SDS-PAGE). The gel was calibrated using chicken muscle myosin heavy chain ($M_m=223,000\text{g/mol}$) and ovalbumin ($M_m=43,500\text{g/mol}$) as standards. A linear relationship between $\log M_m$ and protein mobility was established, and used to estimate the M_m of egg white protein peaks. Resolved proteins were stained by 0.125 % Commasie Brilliant Blue and scanned by UltraScan-XL densitometer. The quantification was performed by the comparison of the respective integral area of control and treated sample. The experimental error of the measurements was $\leq 8\%$.

Results and Discussion

The viscosity measurements of the thick egg white ovomucin matrix treated with $v=23\text{kHz}$, $A=5\mu\text{m}$ ultrasound for various time periods, showed an abrupt decrease in viscosity to 2.61 ± 0.09 mPas (mean \pm SEM, $n=5$) during the first 60s of ultrasonification. Prolonged ultrasound treatment ($>60\text{s}$) lead to further decrease in viscosity which was much slower and which finally reached a minimum value of 2.08 ± 0.03 mPas after 120s ultrasonication (*Figure 1*). Densitometric scan of SDS-PAGE separated proteins (*Figure 2*) indicated *cca* 26% decrease in ovomucin matrix proteins, corresponded to $M_m > 40 \times 10^6$ at the entrance of the stacking gel, indicating partial disruption of the matrix upon 300 s ultrasound treatment. The decrease in ovomucin monomer peak ($M_m = 3 \times 10^6$ g/mol) with mobility between 0.01 and 0.03 was *cca* 14%. The other thick egg white matrix proteins with $M_m < M_{mc}$ (274,000 g/mol): conalbumin ($M_m = 78,000$ g/mol), avidin ($M_m = 64,000$ g/mol), ovalbumin ($M_m = 43,500$ g/mol), and ovomucoid ($M_m = 28,000$ g/mol) were not fragmented (*Figure 2*) after 300 s ultrasound treatment. The ovalbumin peak was even somewhat increased (*cca* 9%), which was interpreted as a release of this most abundant protein (68% of total egg white proteins) upon disruption of ovomucin matrix. The ultrasound generated ovomucin fragments $< 10,000\text{g/mol}$ were not detectable under these experimental conditions.

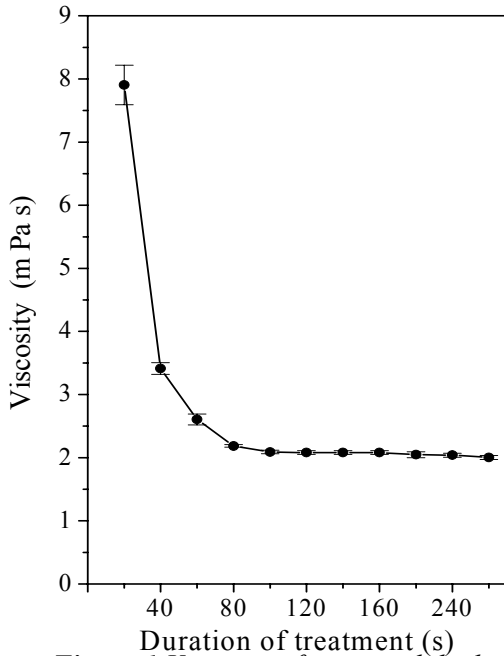


Figure 1 Viscosity of sonicated thick egg white ovomucin matrix

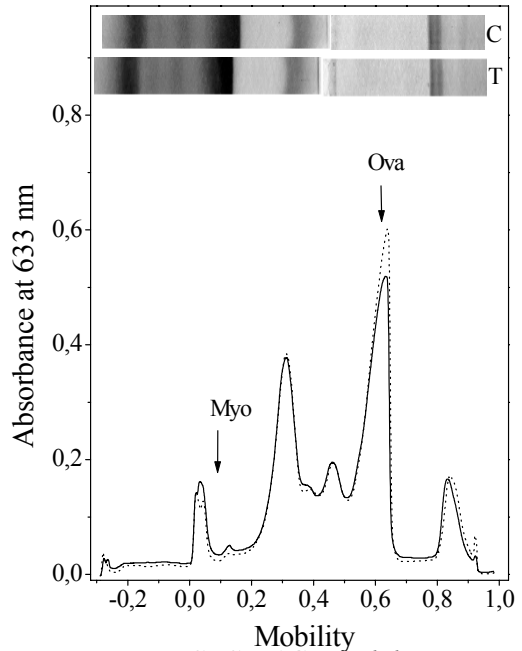


Figure 2 SDS-PAGE and densitogram of thick egg white proteins: C-control; T-sonicated

Conclusions

The results indicated that ovomucin matrix of the thick fraction of egg white is partly disrupted after treatment with $v=23\text{kHz}$, $A=5\mu\text{m}$ laboratory ultrasound. They confirmed that CMm hypothesis is valid for the natural mucin based structures, such as hen thick egg white matrix. In analogy with the avian matrix, sonolytic treatment of mammalian mucous tissues may also cause partial disruption of their matrix. The resulting changes in protein structure and in the related viscosity of extracellular tissue milieu may constitute the beneficial therapeutic action of ultrasound.

References

- [1] M.Dyson, In: *Biological effects of Ultrasound* (Ed. Nyborg and Ziskin) Churchill-Livingston, New York, 1986, 121-33.
- [2] W.L.terHaar, In: *Physics in Medicine and Biology*, Encyclopedia. (Ed. McAinsh) Pergamon Press, Oxford, 1986, 843-6.
- [3] M.C.Rose, W.A.Voter, C.F.Brown, B.Kaufman, *Biochem.J.* 1984, 222, 371-7.
- [4] M.Vučković, M.Radojčić, B.H.Milosavljević, *J.Serbian Chem.Soc.* 2000, **65**, 157-66.
- [5] D.Filipović, M.Radojčić, B.H.Milosavljević, *J.Serb.Chem.Soc.* 2000, **65**, 123-30.

FLUOROPHORE BASED ON (*E*)-4-ARYL-4-OXO-2-BUTENOIC ACIDS

B. M. Kolarić¹, B. J. Drakulić², I. O. Juranić³

¹Max-Planck Institute für Molekulare Physiologie, Dortmund, Germany; ²Department of Chemistry-Institute for Chemistry, Technology and Metallurgy, Belgrade, Serbia and Montenegro; ³Faculty for Chemistry, University of Belgrade, Belgrade, Serbia and Montenegro

Abstract

In this manuscript synthesis and properties of six alkyl-, halo- and nitro-phenyl substituted (*E*)-4-phenyl-4-oxo-2-butenoic acids are described. Since aroylacrylic acids show biological activity their fluorescent analogues offer possibility to investigate mechanism and kinetics of their interactions within the cell, without additional modification of molecule [e.g. fluorescent labeling].

Introduction

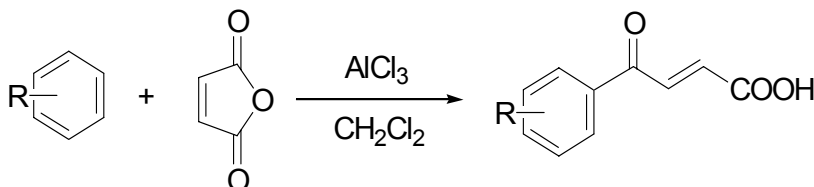
(*E*)-4-Aryl-4-oxo-2-butenoic acids exert antibacterial [1], antiviral [2] and antiproliferative action [3]. Ketovinyl fragment -C-(O)-C=C- as a part of (*E*)-4-aryl-4-oxo-2-butenoic acids is Michael acceptor suitable for addition of nucleophiles, thiol and amino group of biomolecules. It is suggested that biological activity of aroylacrylic acids could be attributed to this type of action.

On the other side (*E*)-4-Aryl-4-oxo-2-butenoic acids are convenient for the fluorescent investigation due to the presence of the system of conjugated double bonds, from a phenyl ring to the carboxylic group.

The aim of our research is to use the fluorescent properties of (*E*)-4-aryl-4-oxo-2-butenoic acids for monitoring biological tests. It is important to noticed that, for good monitoring fluorescence, emission should be between 450-620 nm in order to distinguished emission of probe from autofluorescence of the cell [4].

Experimental

Title compounds were prepared by the modification of Friedel-Crafts reaction (*Scheme 1*). Aromatic substrates were added to the solution of maleic anhydride and anhydrous aluminium-chloride (molar ratio 1:2) in methylene chloride at the room temperature. The structures of acids were confirmed by microanalysis, ¹H NMR, ¹³C NMR and IR spectrometry. Crystal structure of (*E*)-4-phenyl-4-oxo-2-butenoic acid was determinate as well [5].



R- = H- (1), 2,5-di-*i*-Pr- (2), 3-NO₂-4-Me- (3), 2-Cl-4-Me- (4), 2,4-di-Cl- (5), 4-Br- (6)

Scheme 1.

Fluorescence spectra were recorded on *Spex Fluoromax-3* spectro-fluorometer (Jobin Yvon, Edison, NJ, USA) in a 150 μl quartz cuvette (Hellma).

Result and Discussion

All title compounds were investigated under the same condition. Emission and excitation spectra were recorded from CHCl_3 solution at concentration of $2 \cdot 10^{-5}$ M at 25 °C. Excitation spectra show maxima between 340-440 nm. It is possible to assume that this peak is caused by charge transfer between electron donor-acceptor pair *via* conjugate unit [6,7]. Intensity of this peak is much more higher, related to the peak between 260-320 nm which correspond to absorption of phenyl moiety. Since absorption of the charge transfer is dominant, molecules were excited with the wavelength of the CT maxima and corresponding emission were recorded. In *Table 1* emission and excitation maxima are summarized.

Table 1. Fluorescence and excitation maxima (nm)

Compounds N ^o	Emission max.	Excitation max.	Stokes shift
1	400	270	130
2	450	430	20
3	470	425	40
4	470	410	60
5	490	425	65
6	470	420	50

Emission and excitation spectra of compounds **2** and **6** are presented in Figure 1.

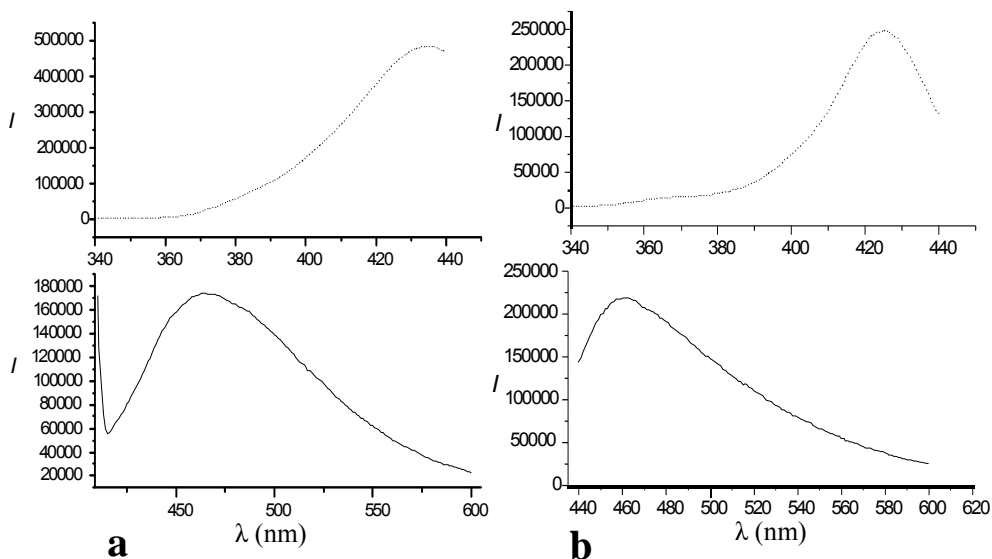


Figure 1. Excitation (···) and emission (—) spectra of compounds **2** (a) and **6** (b)

Results clearly show that halogenation and nitration of aryl moiety cause shift of fluorescence into red region (bathochromic shift). Generally bathochromic shift is caused by additional stabilization of polar excited state (S^1) in comparison to the ground state. Similar shifting of fluorescence emission due to halogenation of molecules was recently published for different compounds [8]. Stokes shifts (*Table 1*) represent difference between absorption and emission maximum and is a measure of change in geometry between excited and ground states between which transitions occurs. Substitution of phenyl moiety increases Stokes shift due to stabilization of excited states.

Presented synthetic approach offer possibility for designing a small fluorophore, which can be used for monitoring different biological processes. One of the most interesting outcomes of this research is to introduce these molecules as non-natural analogue of amino acid into peptide chain *via* solid phase method. Kinetics and dynamics of these non-natural peptides or proteins could be monitored by fluorescence techniques.

References:

- [1] K. Bowden, A. Del Pozzo, C.K Duah., J.Chem.Res., 1990, (S) 377, (M) 2801 and cited references.
- [2] I.L. Pinto, R.L. Jarvest, B. Clarke, C.E. Dabrowski, A. Fenwick, M.M. Gorczyca, L.J. Jennings, P. Lavery, E.J. Sternberg, D.G. Tew, A. West, Bioorg.Med.Chem.Lett., 1999, 9, 449.
- [3] Z. Juranić, Lj. Stevović, B. Drakulić, T. Stanojković, S. Radulović, I. Juranić, J.Serb. Chem. Soc., 1999, 64, 505.
- [4] B.J. Drakulić, G.A. Bogdanović, S.B. Novaković, I.O. Juranić, 41. Conference of Serbian Chemical Society, Belgrade 2003. Book of abstarcts, OH-5, p. 191.
- [5] A. Diaspro (Ed.) Confocal and Two Photon Microscopy: Foundations, Applications and Advances, Wiley-Liss Inc., New York, 2002.
- [6] M. Hesse; H. Meier; B. Zeeh, Spectroscopic Methods in Organic Chemistry, Georg Thieme Verlag-Stuttgart-New York; 1997, 1-17.
- [7] G. Angelovski, B.Costisella, B.Kolaric, M.Engelhard, Peilbracht submitted to J. Org. Chem.
- [8] B.R. Renikuntla, H.C.Rose, J. Eldo, A.S. Waggoner, B.A. Armuitage, Organic Letters, 2004, 6(6), 909.

PHOTOLYTIC DEGRADATION OF CHLORPYRIFOS INDUCED BY AN ARTIFICIAL LIGHT SOURCE

N. Abazović, J.J. Čomor and M.I. Čomor

Vinča Institute of Nuclear Sciences, P.O. Box 522, 11001 Belgrade, Serbia and Montenegro

Abstract

Chlorpyrifos dissolved in methanol was illuminated by the Xe polychromatic light source, which is commonly used as artificial solar radiation source. Photolytic degradation of the parent compound was followed by UV/Vis spectrophotometry and GC/MS technique. GC/MS measurements indicated that very few pyridine containing intermediates are formed during the degradation process. After 2 hours of illumination almost no chlorpyrifos could be observed and significant mineralization (formation of carbon dioxide, water, alkyl phosphates and sulfates) was achieved.

Introduction

Organophosphate esters are an important class of pesticides. The pathways of their decomposition such as hydrolysis, photolytic oxidation, microbial transformations and other biological processes have been intensively investigated recently [1]. The photodecomposition of organophosphorous pesticides and other man-made pollutants in environment occurs in both direct and indirect photochemical processes. Direct photolysis involves direct absorption of light by pollutants followed by chemical reactions, while indirect photolysis may be initiated by natural substances or solvents.

Chlorpyrifos, O,O-diethyl(O-3,5,6-trichloropyrid-2-yl)phosphorothioate (trade names Dursban, Lorsban), belongs to organophosphate pesticides. It is widely used in a variety of agricultural and urban pest control scenarios. It is used at the rate of over 50,000 kg per year in Europe and in amounts exceeding 5 million kg per year in US agriculture [2]. Chlorpyrifos is a broadly active insecticide, effective by ingestion and contact, being absorbed through skin, gut and pulmonary membranes. It is strongly adsorbed by soil and sediment, the extent being greater with organic soil and sandy loams due to liophylic nature of chlorpyrifos [3]

In this work the products of photolytic degradation of chlorpyrifos by UV/Vis spectrophotometry and GC/MS technique, using a Xe lamp as light source, were studied. The goal was to determine if any pyridine and chlorine containing products are formed during direct photolysis of chlorpyrifos.

Experimental

All chemicals used in the experiments were of reagent grade and were used without further purification. Chlorpyrifos was purchased from Sigma-Aldrich. Methanol used as a solvent was HPLC grade produced by JTBaker. All experiments were performed at $21 \pm 1^\circ\text{C}$

Photodegradation procedure

Experiments have been carried out in a 1 cm × 1 cm quartz cuvette using an Osram XBO 150 W Xenon lamp. The absorbed light intensity was 8.73×10^{-5} ein·min⁻¹·ml⁻¹, for 200–400 nm illumination measured with monochloroacetic acid actinometry. Methanol solutions containing 0.1 mM (35 ppm) of chlorpyrifos were used for all photodegradation experiments.

Analytical procedure

Absorption spectra were recorded on a Perkin-Elmer Lambda 5 UV/Vis spectrophotometer.

A HP 5890 series II+ gas chromatograph (Hewlett Packard) equipped with a HP 5891 mass spectrometer (Hewlett Packard) and J&W DB-5MS capillary column (30 m, 0.25 mm, 0.25 μm) was used for measurements. The temperature program started at 50 °C for 1 min, then increased at 10 °C·min⁻¹ to 300 °C. The injector was operated in split mode at 250 °C. Helium was used as carrier gas at flow rate of 1 ml·min⁻¹.

Results and Discussion

The changes of the absorption spectra of chlorpyrifos during the illumination are shown in Fig 1. Chlorpyrifos has three distinct absorption peaks at 206, 230 and 288 nm. It can be seen that the change in the absorbance during illumination is the most significant at 288 nm; after 120 min of illumination the absorbance is almost zero. The absorbance at 208 and 230 nm is significantly higher than zero even after 4 hours of illumination. This indicates that some intermediates and/or degradation products formed during photolysis also absorb in this region.

GC/MS technique was used to determine which products are formed during illumination. Chromatogram of the starting solution of chlorpyrifos as well as chroma-

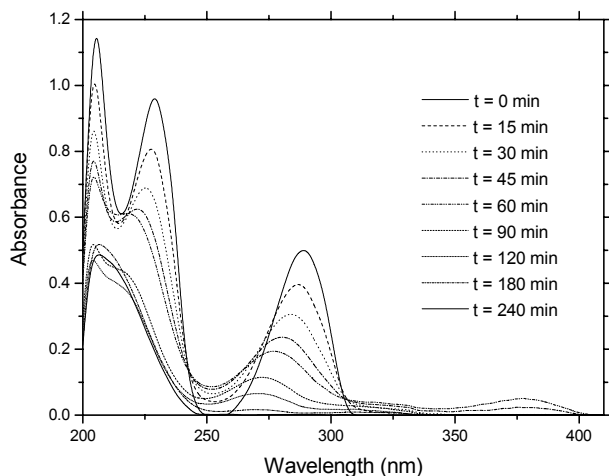


Figure 1. Absorption spectra of chlorpyrifos solutions illuminated for the indicated time by the Xe light source.

tograms of the solutions after designated time of illumination are shown in Fig. 2. Peak 1 corresponds to chlorpyrifos. Its intensity decreases with increasing of illumination time; after 120 min of illumination it could be hardly detected - almost all chlorpyrifos was degraded. The peak of the major intermediate degradation product is marked with number 2. It corresponds to O-(3,6-dichloro-2-pyridyl)-O,O-diethylphosphorothioate according to MS spectra. Its concentration increases until

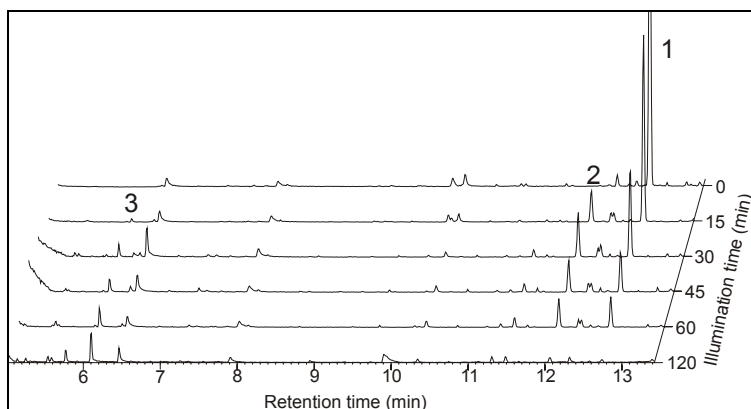


Figure 2. Chromatograms of chlorpyrifos solutions illuminated for the indicated time by the Xe light source.

60 minutes of illumination and then starts to decrease. After 2 hours of illumination it could hardly be detected just like chlorpyrifos. On the other hand some O,O-diethyl-O-methylphosphorothioate could be detected ($t_r = 6.45$ min) even before illumination and additional amounts are formed during illumination. Also, there are several alkylphosphates detected at retention times ≤ 6.1 min (marked with number 3 in Fig. 2) suggesting the nature of the final degradation products. These findings are somewhat different than the literature [2, 4] where the major degradation products were identified as 3,5,6-trichloropyridin-2-ol (TCP) and O,O-diethyl-O-methylphosphorothioate, and as a secondary product 3,5,6-trichloro-2-methoxypyridine (TMP). We could not detect any TCP or TMP in the illuminated solutions. According to our results, photolytic degradation pathway of chlorpyrifos, using Xe lamp as a light source, has only one major intermediate product: O-(3,6-dichloro-2-pyridyl)-O,O-diethylphosphorothioate which is further degraded to smaller molecules.

References

- [1] K. D. Racke, Degradation of Organophosphorus Insecticides in Environmental Matrices, eds. J. E. Chambers, P.E. Levi, Academic Press, Inc. 1992.
- [2] D. Simon, S. Helliwell, K. Robards, *Anal. Chem. Acta* 1998, 360, 1.
- [3] M.S. Sharom, J.R.W. Miles C.R. Harris, F.L. McEwen, *Water Res.* 1980, 14, 1095.
- [4] A.W. Abu-Qare, M. B. Abou-Donia, *J. Chrom. B*, 2001, 757, 295.

THE RADIOPROTECTIVE PROPERTIES OF POLYPHENOLS ON HUMAN LYMPHOCYTES

A. Leskovac¹, T. Momić¹, T. Janković², G. Joksić¹

¹Laboratory of Physical Chemistry, Vinča Institute of Nuclear Sciences, POB 522, 11001 Belgrade,

²Faculty of Chemistry, University of Belgrade, Studentski trg 16, 11000 Belgrade,
Serbia and Montenegro

Abstract

The aim of this study was to evaluate radioprotective properties of medical plants *Gentianella austriaca* and *Gentianella dinarica*. For this purpose human lymphocytes were irradiated using ⁶⁰Co γ rays and treated with different fractions of plant extracts, afterwards micronuclei (MN) and malondialdehyde (MDA) were measured. Polyphenols, fractions isolated from those plants have shown the protective effects, seen as significantly reduced incidence of micronuclei which was followed with reduced level of malondialdehyde. The results obtained in this study indicate that polyphenols isolated from *Gentianella austriaca* and *Gentianella dinarica* possess radioprotective properties possibly through reduction of the lipid peroxidation.

Introduction

Ionizing radiation induces chromosomal aberrations very efficiently. Main types of lesions that are induced in the DNA by ionizing radiation are single- and double strand breaks, base damages and DNA-protein cross-links. Injury to living cells is to large extent due to oxidative stress induced by ionizing radiation. Reactive oxygen species (ROS) and free radicals induced by partial reduction of oxygen (O₂) react with cellular macromolecules as lipids, proteins, and nucleic acids and damage them [1]. The most often assay used in genotoxicity testing is the induction of chromosomal aberrations. Instead, the in vitro micronucleus test is also suitable for evaluation of the genotoxicity [2]. Major biomarkers of oxidative damage to living cells are lipid peroxidation (LPO) products, such as malondialdehyde (MDA) as well as activity of myeloperoxidase and catalase.

The most important compounds present in plants, which are of considerable pharmacological significance, are the polyphenols. Polyphenols are very effective scavengers for free radicals and thus probably act to prevent oxidative damage [3].

The aim of this study was to evaluate the radioprotective effects of natural polyphenols, isolated from medical plants *Gentianella austriaca* (fractions 1, 2 and 3) and *Gentianella dinarica* (fractions 1, 2 and 3) on harvested human lymphocytes. Incidence of radiation-induced micronuclei and level of MDA was analyzed using cytochalasin block micronucleus (CBMN) test and thiobarbituric acid (TBA) test, respectively.

Experimental

Preparation of plant extracts: *Gentianella austriaca* and *Gentianella dinarica* were examined. The plant flowers were air dried and ground separately in a mixer. The finally powdered material was subjected to separate extractions with 70% ethanol. After removal of the ethanol under reduced pressure, the aqueous phase was evaporated to dryness, which was further separated onto different fractions.

Irradiation: Aliquots of heparinized whole blood were placed in sterile plastic test tubes in a 15 x 15cm Plexiglas container, and irradiated using ^{60}Co γ ray source, dose of 2 Gy. Irradiated samples were set up in cultures 1 hour after irradiation.

Micronucleus analysis: The assay is carried out on cultures of PHA-stimulated blood lymphocytes. Whole blood (0.5 ml) was added to 5 ml of Karyomax medium (Invitrogen-Gibco). One hour after stimulation 100 μl of water-soluble fractions of plant extracts were added to the cultures. Preparation of cultures for MN scoring was proceed according to method of Fenech [4].

MDA measurement: After 72 hours of incubation, parallel cultures were separated on Lymphoprep, lymphocytes were collected by centrifugation, washed in physiological saline, and were prepared for measurement MDA. The lipid peroxidation was indexed by measuring the MDA production, spectrophotometrically at 532 nm, using the 2- thiobarbituric acid (TBA) test [5]. Protein concentration was determined according to Lowry [6].

Results and Discussion

The purpose of this study was to assess the radioprotective properties of natural polyphenols, isolated from medical plants *Gentianella austriaca* (fractions 1, 2 and 3) and *Gentianella dinarica* (fractions 1, 2 and 3).

The results demonstrated that fractions of extracts isolated from *Gentianella* species significantly modulate the level of radiation-induced micronuclei and considerable change MDA production. As provided in Fig. 1A, the polyphenols from *G. austriaca*, particularly fractions 1 and 2 display the best radioprotective effects: the yield of radiation-induced micronuclei is reduced for 40,20% and 44,97%, respectively. The same fractions decrease MDA production for 15,97% and 25,62%, respectively. The similar decreases have shown fractions 1 and 2 from *G. dinarica*, (Fig. 1B). The yield of micronuclei is reduced for 27,78 % and 16,98%, respectively and the MDA production was reduced for 35,56% and 7,76%, respectively. On the opposite fraction 3 *G. austriaca* (Fig. 1A) and fraction 3 from *G. dinarica* (Fig. 1B), have shown insignificant increase of the yield of radiation-induced micronuclei which was followed with slight enhancement of MDA production. Statistical analysis demonstrated high positive, statistical significant correlation between incidence of micronuclei and MDA ($r = 0.93$, $p < 0.05$).

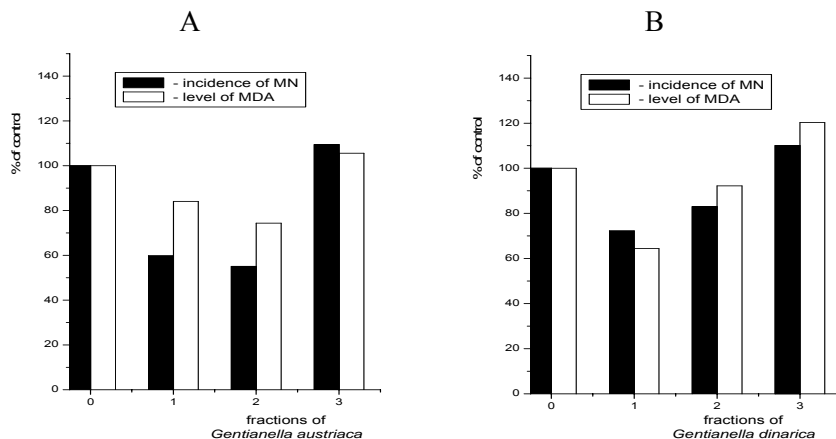


Figure 1. Incidence of micronuclei and level of MDA in human lymphocytes treated with extracts of A) *Gentianella austriaca* (fractions 1, 2 and 3) and B) *Gentianella dinarica* (fractions 1, 2 and 3)

Conclusion

This study indicates that polyphenols isolated from *Gentianella austriaca* and *Gentianella dinarica* possess radioprotective properties. The natural polyphenols obtained from *Gentianella* species are protectors against cellular damages and their benefit for human health should be examined further.

Acknowledgement

Financial support was provided by the MSTD of the Republic of Serbia, Grant No. 1991.

References

- [1] H. Sies, *Angew Chem Int Ed Engl.*, 1986, 25, 1058.
- [2] L.L. De Zwart, J.H.N Meerman, J.N.M. Commandeur, N.P.E. Vermeulen, *Free Radic Biol Med.*, 1999, 26, 202.
- [3] B.Z.L. Vijayalaxmi, T.S. Deahl, M.L. Meltz, *Mutat Res.*, 1995, 348, 45.
- [4] M. Fenech, *Mutat Res.*, 1993, 285, 35.
- [5] O.L. Aruoma, B. Halliwell, M.J. Laughton, G.J. Quinland, J.M.C. Gutteridge, *Biochem J*, 1989, 258, 617.
- [6] O.H. Lowry, N.J. Rosebrough, A.L. Farr, R.J. Randall, *J Biol Chem.*, 1951, 193, 265.

CHANGES OF *c-myc* EXPRESSION IN B16 MELANOMA CELLS INDUCED BY 8-CHLOROADENOSINE-3', 5'-MONOPHOSPHATE AND TIAZOFURIN

L. Korićanac, D.V. Todorović, N. Popović, A. Ristić-Fira

Vinča Institute of Nuclear Sciences, P.O.Box 522, 11001 Belgrade, Serbia and Montenegro

Abstract

The aim of this study was to investigate the *in vitro* effects of 8-chloroadenosine 3', 5'-monophosphate (8-Cl-cAMP) and tiazofurin (TR) on the expression of *c-myc* gene in B16/F10 and B16/C3 mouse melanoma cells. Exponentially growing cells were treated with 8-Cl-cAMP or TR (5 μ mol - 25 μ mol) for 6h and 24h. The level of *c-myc* expression, estimated by RT-PCR, did not significantly change in B16/F10 cells after treatment with 8-Cl-cAMP or TR. Similar results were obtained in B16/C3 cells after treatment with 8-Cl-cAMP. The level of *c-myc* expression has shown a significant increase in B16/C3 cells after treatment with TR. Further studies of these agents will lead to better understanding of molecular mechanisms of their action.

Introduction

Disseminated malignant melanoma is among tumours resistant to radiation and chemotherapy. Drug resistance is caused by a deregulation of process of cell death. A more complete understanding of molecular mechanisms involved in the control of cell survival and death could potentially lead to the discovery of new drugs with the ability to interfere with specific cellular targets and finally more efficient therapeutic approaches for the treatment of melanoma [1, 2].

8-Cl-cAMP and tiazofurin are novel antineoplastic agents with selective effects on different tumour cells. 8-Cl-cAMP is a site-specific cAMP analogue that selectively modulates two isoforms of cAMP-dependent protein kinase A (PKA-I and PKA-II) [3]. Tiazofurin (2- β -D-ribofuranosyl-thiazole-4-carboxamide) is an inhibitor of inosine 5'-monophosphate dehydrogenase (IMPDH) type II, a rate-limiting enzyme in the synthesis of GTP and dGTP [4].

Materials and Methods

Mouse melanoma cells, B16/F10 and B16/C3, were maintained as a monolayer culture in RPMI 1640 medium supplemented with 10 % fetal calf serum, under standard conditions (37°C, 5%CO₂).

Total cellular RNA was isolated from B16 melanoma cells (1x10⁶) using Qiagen RNeasy Total RNA Preparation kit according to the manufacturer's instructions. For cDNA synthesis 1 μ g of total RNA was reverse transcribed in 5 x RT buffer in the presence of 0.5 μ M Oligo(dT)₁₆, 50 μ mol/L of each dNTPs, 0.4 U/ μ L RNase inhibitor (Perkin-Elmer), 5 U/ μ L murine leukemia virus reverse transcriptase (MuLV

RT) in a final volume of 10 μL . The reverse transcription reaction (RT) was performed at 42°C for 1h and stopped at 95°C for 5 min. For the amplification of samples in polymerase chain reaction (PCR), appropriate amounts of cDNA samples, representing 200 ng of total RNA were mixed with PCR buffer, 1.5 mM MgCl_2 , 200 $\mu\text{mol/L}$ of each dNTPs, 0.25 $\mu\text{mol/L}$ of each *c-myc* and GAPDH primer, 0.05 U/ μL Taq polymerase in a total volume of 25 μL . The samples were denatured at 94°C for 5 min. The amplification cycle parameters were 94°C for 30", 62°C for 30" and 72°C for 30" (35 cycles) followed by 72°C for 5 min. PCR-amplified products were analyzed on a 2% agarose gel. Quantification was performed using a Multi-Analyst/PC Software Image Analysis System (BioRad, Gel Doc 1000). The relative mRNA level of *c-myc* gene was normalized to the corresponding GAPDH mRNA level in individual samples and the respective mRNA changes were determined relative to the untreated samples. Primer sequences for *c-myc* were: upstream 5' CAA GAG GCG AAC ACA CAA CGT CT and downstream 3' AAC TGT TCT CGT CGT TTC CGC AA. The size of PCR product was 218 bp.

Results and discussion

Previous results have shown that 8-Cl-cAMP and TR significantly inhibit B16/F10 and B16/C3 cell growth. The growth inhibition is connected with the changes in cell cycle distribution in B16/F10 cells. The growth inhibition detected in B16/C3 cells is related to the induction of apoptosis [5]. Considering previous results and literature data concerning gene expression connected to apoptosis and proliferation, the effects of 8-Cl-cAMP and TR on *c-myc* expression were examined. Literature data indicated that *c-myc* plays an important role in melanoma pathogenesis and may, therefore, provide a potential target for treatment [6].

Exponentially growing B16 mouse melanoma cells were treated with increasing concentrations of 8-Cl-cAMP or TR (5 $\mu\text{mol/L}$, 10 $\mu\text{mol/L}$, 25 $\mu\text{mol/L}$) for 6h or 24h. In order to modify the method for the detection and quantification of low abundance *c-myc* proto-oncogene mRNA, simultaneously with abundant GAPDH mRNA, various experimental conditions for RT-PCR were tested and optimized. Optimal concentrations of "primers" were established for GAPDH (0.25 $\mu\text{mol/L}$) and *c-myc* (0.25 $\mu\text{mol/L}$). Aliquots of cDNAs representing 200ng of total cellular RNA were used in the assay to co-amplify *c-myc* and GAPDH mRNAs. To estimate changes of *c-myc* expression, densitometric analysis of the agarose gels were performed. The obtained results have shown that in B16/F10 cells, 6h or 24h after treatment with 8-Cl-cAMP the level of *c-myc* expression did not significantly change (**1A**). Treatment of B16/C3 cells with 8-Cl-cAMP in the duration of 6h did not cause significant changes in *c-myc* expression. Twenty four hours after treatment with 8-Cl-cAMP, the level of *c-myc* expression did not significantly increase in B16/C3 cells treated with 5 $\mu\text{mol/L}$ 8-Cl-cAMP and 10 $\mu\text{mol/L}$ 8-Cl-cAMP, but *c-myc* expression did significantly increase in the samples treated with 25 $\mu\text{mol/L}$ 8-Cl-cAMP ($p < 0.05$) (**1B**). The expression of *c-myc* did not significantly change in B16/F10 mouse melanoma cells 6h or 24h after treatment with tiazofurin (**1C**). In B16/C3 mouse melanoma cells only 24h after the

same treatment, the level of *c-myc* expression increased significantly in all analyzed samples (**1D**).

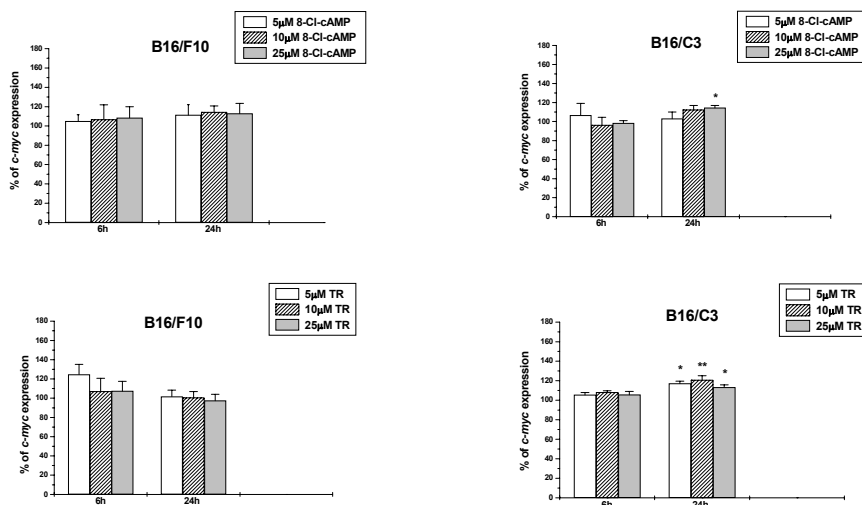


Figure 1. Level of *c-myc* mRNA expression after treatment of B16/F10 (A, B) or B16/C3 (C, D) melanoma cells with different concentrations of 8-Cl-cAMP or tiazofurin (TR) for either 6h or 24h. The densitometric analysis of *c-myc* normalized to GAPDH. Results are expressed as percent change relative to control levels set at 100%. Data represent the means \pm S.E.M. from a minimum of 3 independent assays. (M-PCR marker, 1-control, 2-5 μ mol/L, 3-10 μ mol/L, 4-25 μ mol/L).

The duration of the mouse melanoma cells treatment with 8-Cl-cAMP or TR do not influence significant changes in the level of *c-myc* expression.

Conclusion

8-Cl-cAMP and tiazofurin did not change the level of *c-myc* expression in B16/F10 melanoma cells, as well as in B16/C3 cells 6h after treatment. Also, 8-Cl-cAMP (25 μ mol/L) and tiazofurin (5 μ mol/L, 10 μ mol/L, 25 μ mol/L) significantly increased *c-myc* expression, 24h after treatment.

Acknowledgments: This work was supported by grant N^o 1956 from the Ministry of Science and Environmental Protection, Republic of Serbia.

References:

- [1] Grossman D., *et al.*, J. Invest. Dermatol., 1999, 113 (6), 1076.
- [2] Satyamoorthy K., *et al.*, Trends in Mol. Med., 2001, 7 (5), 191.
- [3] Noguchi K., *et al.*, European J. Canc., 1998, 34 (8), 1260.
- [4] Weber G., *et al.*, Anticancer Res., 1996, 16, 3313.
- [5] Korićanac L., *et al.*, Signal Transd., Proceedings, 2004, 139.
- [6] Chana J.S., *et al.*, British J. Plastic Surg., 2002, 55, 623.

**Radiochemistry
Nuclear Chemistry**

(F)

MEMBRANE METHODS FOR PROCESSING OF LIQUID RADIOACTIVE WASTE

G. Zakrzewska-Trznadel

Institute of Nuclear Chemistry and Technology, Dorodna 16, 03-195 Warsaw, Poland

Abstract

The possibility of application of membrane processes for liquid low level radioactive wastes (LLLRW) processing have been investigated at Department of Nuclear Methods in Process Engineering, Institute of Nuclear Chemistry and Technology (INCT), Warsaw.

Such membrane processes as ultrafiltration, "seeded" ultrafiltration and reverse osmosis were studied in laboratory and pilot scale. Pilot plant experiments show many advantages of membrane methods over some other processes used for radioactive wastes processing. Reverse osmosis method was implemented at Institute of Atomic Energy in Swierk (Warsaw), where liquid radioactive wastes from all of Poland are collected and processed before final storage and disposal. The membrane installation is composed of three stages of reverse osmosis and was included into the existing system of liquid low and intermediate level radioactive wastes purification.

Another method for liquid radioactive wastes treatment employing hydrophobic polymer membrane was developed at INCT. The process called membrane distillation after laboratory study was tested in pilot plant, processing 50 dm³/h of radioactive effluents. The pilot plant experiments show membrane distillation allows complete removal of radioactive compounds from liquid radioactive waste in one stage and does not need additional processes to ensure sufficient purity of water discharged to the environment.

Introduction

Radioactive wastes are dangerous to human life and natural environment. This is why research on new methods of effective waste neutralisation is being carried out in many countries. Nuclear reactors, isotope laboratories, and nuclear medicine centres produce a wide range of liquid radioactive wastes. Liquid low-level radioactive waste appears as a result of decontamination of rooms, laboratory glass as well as remains of solutions used in experiments, production and distribution of radioisotopes, and as effluents from laundries washing contaminated clothes. Two main aims are to be reached in decontamination process of radioactive effluent: elimination of radioisotopes from the waste and volume reduction of the concentrate. The next step before safe disposal is a fossilisation in glass, asphalt or concrete.

Different methods and multistage processes are employed to reduce the concentration of radionuclides in regenerated water to the level permitted by sanitary standards for communal sewage or industrial water. The purification of radioactive waste in solution can be performed by many methods including chemical precipita-

tion, sedimentation, ion exchange, thermal evaporation, as well as membrane permeation.

Membrane permeation is fairly recent technology, even though the history of membranes itself dates over hundred years back. This field has been developed very rapidly in several branches of science and technology. Membranes are used for separation of multi-component liquid and gaseous mixtures, for communal and industrial sewage purification, for desalination of seawater and production of high-purity water for special applications and water recycling in chemical processes. Membrane processes have been already applied in nuclear technology and nuclear power industry for such purposes:

- uranium ore enrichment,
- recovery of nuclear fuel,
- capture and separation of volatile, radioactive products of nuclear reactions,
- purification of reactor water and boric acid recovery,
- separation of stable isotopes,
- radioactive waste concentration.

Membrane processes were employed in nuclear power plants for the laundry wastes and mixed laboratory wastes purification, and for cleanup of boric acid solutions for recycle. Mixed aqueous waste processing plant is operated at the Chalk River Laboratory of Atomic Energy of Canada Ltd [1, 2].

Ultrafiltration is used in two stages in the Enhanced Actinide Removal Plant at Sellafield [3]. In Hungary, at the Paks Nuclear Power Plant, an ultrafiltration plant is applied for cleaning and recycling contaminated boric acid solutions. At Harwell pilot plant using ultrafiltration to separate floc and liquid good decontamination and high volume reduction (about 200) is being achieved [3]. The application of ultrafiltration to low level wastes arising from a fuel fabrication plant is being examined at Nukem, Hanau [4]. The seeded ultrafiltration procedure is being developed in Cadarache Nuclear Research Centre [5] and in Harwell [6]. Other membrane processes including electroosmosis and electrodialysis are under examination [7, 8]. Electrodialysis has been examined at Japan Atomic Energy Research Institute for the removal of radioactive ions from low and intermediate level radioactive liquid waste using inactive coexisting salts as ionic carriers of radioactive ions [8]. Another example of electrodialysis applied in nuclear industry is recovery of NaOH and H₂SO₄ from the secondary liquid waste from the regeneration of ion exchange columns installed in LWR, carried out by the Chubu Electric Power Co., Ltd. (Japan) in the system of two-compartment cells in bipolar mode [9].

The liquid low-level radioactive waste from all of Poland are collected and processed in ZUOP-IAEA (Institute of Atomic Energy) in Świerk, Warsaw. They are different with regard to radioisotope content, specific activity and chemical composition. They are mainly low and medium-level wastes containing first of all γ and β emitters and very small amount of actinides with specific activity below 10^7 kBq/m³.

Results and Discussion

Reverse osmosis

Laboratory and pilot plant experiments carried out at INCT showed reverse osmosis can be applied for the treatment of liquid low level radioactive wastes from Polish nuclear laboratories. However, to reach high decontamination the process should be arranged as a multistage operation.

The RO method was implemented at Institute of Atomic Energy in Świerk, where the wastes collected from all users of nuclear materials in Poland have to be treated before safe disposal. Last time the technology based on chemical precipitation and sorption on non-organic sorbents was replaced by a new evaporator integrated with membrane installation. Two installations can operate simultaneously or separately. The membrane plant can be used for initial concentration of the waste before an evaporator or for final cleaning of the distillate, depending on actual needs. However, evaporation is a very efficient cleaning process, it is high energy consuming. The application of the membranes at the beginning of cleaning cycle reduces significantly the energy consumption. The need of additional distillate purification is connected with entrainment of radionuclides with droplets or with the presence of some volatile radioactive compounds.

Membrane installation, capacity of $\sim 1 \text{ m}^3/\text{h}$ of permeate is composed of three stages of reverse osmosis preceded by pre-treatment with polypropylene depth filters. The first two stages are used for purification; the third one for final concentration of retentate. Two types of spiral wound RO modules were used in the installation: *SU-720R* and *SU-810 (TORAY)*. Both types of modules work under pressure of 20 bar and with high salt rejection, higher than 99%. The membrane was manufactured from cross-linked fully aromatic polyamide composite. Two *Model SU-720R* modules connected in series placed in one housing form the first stage of reverse osmosis. The second stage is the same as the first one: two modules in one housing. The third stage is composed of two housings in parallel, two *Model SU-810 (TORAY)* modules in each vessel.

Liquid radioactive waste is directed from the waste storage tank to the 8m^2 -feed reservoir. After pre-treatment on polypropylene depth filters and antiscalant injection the wastes are introduced into the first stage of RO. The retentate from this stage is concentrated in the third RO unit. This concentrated solution can be directly fossilised if the concentration of the total solute is appropriate ($\sim 250 \text{ g}/\text{dm}^3$). If the concentration is not sufficient, the further treatment takes place in the evaporator. Permeate from the first and third stages is directed to the permeate reservoir before the second RO unit. The product from the membrane installation (permeate from the second stage) is of radiochemical purity and after control of specific activity and salinity can be discharged to the communal sewage.

The laboratory experiments showed an influence of the total concentration of ballast salts on decontamination factor for some radioisotopes. As the concentration of total solute in permeate from the first and third stages is very low a decrease of reten-

tion of radionuclides was observed. To improve the efficiency of radioisotopes removal additional salt injection takes place before the second stage.

The characteristic of the streams, which have to exit RO plant, is presented in Table 1. The concentration of salt in permeate is lower than 0.1 g/dm^3 . The concentration of some specific elements as heavy metals, have to be in conformity with the limits of impurities for communal sewage. Total specific activity for β and γ emitters is lower than 10 kBq/m^3 , while for α emitters less than 1 kBq/m^3 (the obligatory limits for liquid waste). The total salt concentration in retentate is limited by ability of binding the solution with the concrete and the specific activity by nuclear safety regulations. The results of the example experiment with radioactive liquid waste is shown in Fig.1.

Table 1. Characteristic of the streams after RO installation.

Retentate:	
Total concentration [g/dm^3]	250
Specific activity	10^7 kBq/m^3 (0.3 Ci/m^3)
Permeate:	
Total concentration [g/dm^3]	0.1
Specific activity	$0.01 \text{ ALI}_p/\text{m}^3$ or $<10 \text{ kBq/m}^3$ (β and γ) and $<1 \text{ kBq/m}^3$ (α)

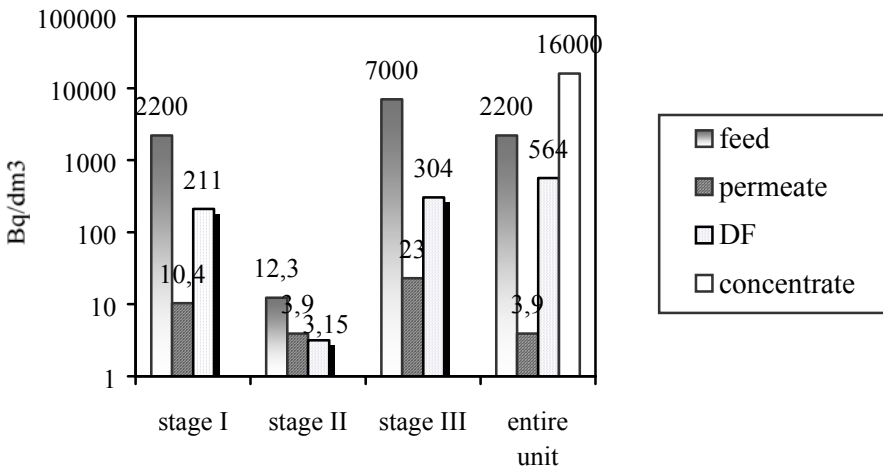


Fig.1. Removal of radioactive compounds; experiments with 3-stage RO plant.

Seeded ultrafiltration

The seeded ultrafiltration is a process of binding macromolecular ligands with ions, which are difficult to retain by UF membranes. Ultrafiltration membranes that were

permeable to the small ions retain the macromolecules or particles formed in the process of complexation or simply adsorption. The selection of appropriate complexant is the main problem of seeded ultrafiltration.

Many different complexants and adsorbers were examined in INCT laboratory. As ligands attaching ions of Cr, Co and Cs, polyethyleneimine (PEI), microcrystalline chitosan (MCH), polyacrylic acid (PAA), polyvinylpyrrolidone (PVP) and suspension of cupric hexacyanoferrate (CuFC) were used. It was found out that the best conditions of binding Cr^{3+} and Co^{2+} ions with PEI macromolecules occur at pH=4 to 6. The most effective adsorption of ions Cs^+ by CuFC was found at pH=9.5 to 10.5 (Figure 2).

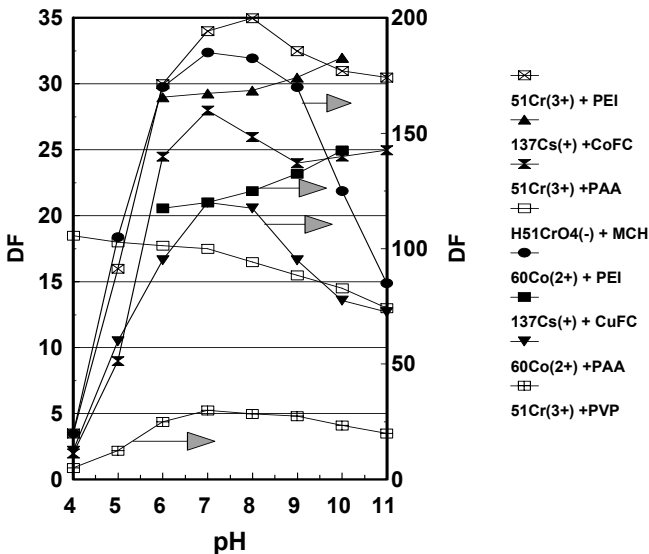


Figure 2. Decontamination factor vs. pH for small ions combined with macromolecules.

Ceramic membranes, made from alumina, titania and zirconia, for filtration of radioactive solutions were tested. They were MEMBRALOX[®] tubes, 250 mm long and 7/10 mm diameter with the membrane sintered inside the tube and CeRAM *IN-SIDE*[®] three-channel monoliths. The pore size of ceramic barriers was in 1kD-100nm range. The experiments were performed with non-active and with radioactive model solutions, as well. Since the aim of the work was to remove the ions, the membranes in UF/NF range were not sufficient to achieve high decontamination factors and the process has to be enhanced by chemical complexation or adsorption. The experiments showed the significant increase of retention factors and decontamination factors while the macromolecular compounds were added. Further tests were done with pilot plant equipped with Sunflower *CeRAM INSIDE*[®] (23-8-1178) ceramic module, 0.35m² filtration area.

Membrane Distillation

The facility used in experiments consisted of spiral-wound module, equipped with PTFE membrane, effective surface area 4 m². The installation enabled the recovery of the part of heat by two installed heat exchangers.

The experiments were conducted in temperature range 35-80 °C at feed inlet, and 5-30 °C at distillate inlet, and with feed and distillate flow rates up to 1500 dm³/h. Under these conditions permeate stream was 10-50 dm³/h (60-300 dm³/m²day). During experiment run the activity of distillate was stable on the level of natural background radioactivity and the concentration of radioactive compounds took place in retentate. Retention of radioactive ions in retentate was almost complete (decontamination factor $\rightarrow \infty$, Table 2). Most of radionuclides were not detected in distillate; only trace amounts of Co-60 and Cs-137 were present.

Table 2. Radiochemical composition of the waste sample used in experiments and effluent after membrane distillation plant.

Radionuclide	Activity of the feed [Bq/ dm ³]	Activity of the effluent [Bq/ dm ³]	Decontamination factor (DF)
⁶⁰ Co	4.51 E+03	1.04 E+00	4336.5
⁶⁵ Zn	3.39 E+03	not detected	$\rightarrow \infty$
^{114m} In	8.62 E+01	not detected	$\rightarrow \infty$
^{110m} Ag	1.04 E+01	not detected	$\rightarrow \infty$
¹³³ Ba	2.99 E+03	not detected	$\rightarrow \infty$
¹³⁴ Cs	7.84 E+00	not detected	$\rightarrow \infty$
¹³⁷ Cs	2.95 E+01	6.73 E-01	43.8
¹⁴⁰ La	<6.53 E-01	not detected	$\rightarrow \infty$
¹⁷⁰ Tm	5.26 E+02	not detected	$\rightarrow \infty$
¹⁹² Ir	3.73 E+01	not detected	$\rightarrow \infty$

The experiments have proved the statement that membrane distillation can be applied for liquid low level radioactive waste treatment. In one stage installation the membrane retains all radionuclides and decontamination factors are higher than those obtained by other membrane methods that were tested. The distillate obtained in the process was pure water, which could be re-utilised or safely discharged into the environment. The process avoids various problems inherent with normal evaporation such as corrosion, scaling or foaming. The entrainment of droplets is not possible because the membrane separates two phases. Operation at low evaporation temperature can decrease the volatility of some volatile nuclides present in the waste. The process is especially economic for the plants, which can utilise waste heat, e.g. plants operating in power and nuclear industry.

Conclusions

Membrane technology can be easily employed for hazardous effluents treatment. It can be applied in nuclear centres processing low and intermediate level liquid radioactive wastes. All the methods reported in the paper have many advantages and can be used in purification cycle of liquid radioactive wastes. Some of them are good pre-treatment methods; the other can be used separately as final cleaning steps, or can be integrated with some other processes. Membrane methods can supplement or replace techniques of distillation, extraction, adsorption, ion exchange, etc.

References

- [1] S. K. Sen Gupta, J. A. Slade, W. S. Tulk, Liquid Radwaste Processing with Crossflow Microfiltration and Spiral Wound Reverse Osmosis, AECL-11270, Feb. 1995, Chalk River, Ontario.
- [2] S. K. Sen Gupta, L. P. Buckley, S. Rimpelainen, A. Y. Tremblay, Liquid Radwaste Processing with Spiral Wound Reverse Osmosis, WM '96 Conference, Tuscon, Arizona 1996, Feb. 25-29.
- [3] *Advances in Technologies for Treatment of Low and Intermediate Level Radioactive Liquid Wastes*, Technical Report Series No.370, IAEA, Vienna, 1994.
- [4] Commission of the European Communities, research and development on radioactive Waste management and Storage, 3rd Annual Progress Report 1982 of the European Community Programme 1980-1984, Harwood Academic Publishers, New York, 1982.
- [5] R. Barnier, S. Caminade, L. Loudenot, M. Maurel, F. Courtois, Ultrafiltration treatment of laundry liquid wastes from a nuclear research centre, Conf. on Waste Management, Kyoto, 1989.
- [6] E. W. Hooper, Sellers R. M., Activity Removal from Liquid Streams by Seeded Ultrafiltration, Waste Management '91, Proc. Symp. University of Arizona, Tucson, 1991, 1, 749.
- [7] A. D. Turner, A. R. Junkison, N. J. Bridger, Electrical Processes for Liquid Waste Treatment, Management of Low and Intermediate Level Radioactive Wastes 1988, Proc. of an International Symp. On Management of Low and Intermediate Level Radioactive Wastes, Stockholm, 16-20 May 1988, vol. 2, p.75.
- [8] S. Sugimoto, Removal of radioactive ions from nuclear waste solutions by electrodialysis, J. Nucl. Sci. Technol. 1987, 15, 753.
- [9] M. Miyagawa, T. Mizutani, M. Miki, I. Ohuchi, Volume reduction system of radioactive waste by electrodialysis, Karyoku Genshiryoku Hatsuden 1979, 30, 351.

RADIOBIOLOGICAL STUDIES ON THE 62 MeV THERAPEUTIC PROTON BEAM AT LNS CATANIA:

I. SURVIVAL OF HTB140 MELANOMA CELLS

I. Petrović, D.V. Todorović, L. Valastro¹, P. Cirrone¹, G. Cuttone¹, A. Ristić-Fira

Vinca Institute of Nuclear Sciences, P.O.Box 522, 11001 Belgrade, SCG

¹Istituto Nazionale di Fisica Nucleare, LNS, Catania, Italy

Abstract

The aim of this study was to determine the initial inactivation of cells induced by high-energy proton beam designed for the treatment of eye melanoma. Exponentially growing HTB140 cells were exposed to an unmodulated 62 MeV proton beam delivered over the single dose range from 8 Gy to 24 Gy. Position of samples was in the zone of the Bragg peak, having high LET values. Surviving fractions were evaluated at 6, 24 and 48 h post-irradiation. The survival curves exhibited a well-known shoulder, decreasing for doses higher than 8 Gy. Therefore, a significant dose dependent early cell inactivation after single delivery of 16 Gy to 24 Gy to the cell monolayer was observed. With the increase of the post-irradiation incubation time, a better killing effect, as the consequence of clonogenic survival, was detected.

Introduction

In the past decades, therapeutic proton beams were successfully used in treating several tumour types [1]. The physical properties of protons, especially its Bragg peak, are used to target a large radiation dose precisely in the tumour. When charged particles enter the patient, their specific energy per unit of length deposited along the track (LET, linear energy transfer) increases with decreasing particle velocity. This gives rise to a sharp maximum in ionization near the end of the range at the position of Bragg peak [2, 3]. It is known that the effectiveness of protons on cell survival strongly depends on LET, therefore reaching its maximum in the Bragg peak [4]. Studies on cell inactivation have been performed on different mammalian cells, irradiated with low energy, monoenergetic beams, showing a significant increase in cell killing with LET [2, 5, 6]. Several studies have been reported on the effects of proton beams with energy less than 100 MeV that are used for the treatment of eye melanoma [7].

Materials and Methods

Human melanoma HTB140 cells (5×10^4 /ml) were maintained as a monolayer in RPMI 1640 tissue culture medium, 10 % foetal calf serum under standard conditions (37 °C, 5 % CO₂). The plating efficiency (PE) for HTB140 cells was approximately 70%, and the doubling time (Td), evaluated from the growth curve, was $24 \pm 2,7$ h. The thickness of the cell monolayer was between 3-6µm. Irradiations with high energy monoenergetic protons were carried out at the CATANA treatment facility at INFN, LNS - Catania. Exponentially growing cell monolayers were irradiated within the

Bragg peak of the 62 MeV protons obtained by a superconducting cyclotron. Single doses delivered to the cells were 8, 12, 16, 20 and 24 Gy with the dose rate of 15 Gy/min. The viability of cells was measured at different time points by MTT assay (Roche) based on the ability of viable cells to reduce 3-(4,5-dimethylthiazol-2-yl)-2,5-diphenyltetrazolium bromide into blue-purple formazan crystals. The absorbance was measured using a microplate reader (Wallac, VICTOR2 1420 Multilabel counter, LKB) at a test wavelength of 550nm and a reference wavelength of 690nm. For cell survival assay, irradiated exponentially growing cells were seeded (7×10^3 cells/ml) and incubated for 6, 24 and 48 h, when cells were fixed with methanol and stained with 10 % Giemsa. Colonies with more than 50 cells were scored as survivors. The Student t-Test was used for statistical analysis (level of significance, $P < 0.05$).

Results and Discussion

We have examined early effects of high-energy proton irradiation on human melanoma cells *in vitro*. Figure 1 shows the 62 MeV proton depth-dose distribution measured by inserting thin Perspex plates in front of a plane-parallel PTW 34045 Markus ionization chamber, calibrated according to IAEA TRS 398 [8]. The arrow indicates the irradiation position of the cells, within the Bragg peak, obtained by inserting 25 mm thick Perspex plates just before the Petri dish. This gave the corresponding relative dose of $90.4\% \pm 4\%$. The level of early cell growth inactivation, estimated at 48 h post-irradiation, has shown a dose dependent increase, reaching values from 55.16% to 58.97% for irradiation with 16 Gy and 20 Gy respectively (MTT assay).

To quantify the dose response in exponentially growing cultures, the surviving fraction of HTB140 cells from an average of three duplicate experiments were fitted to a linear - quadratic equation [3]. For the generation of cell survival curves, possible differences in response were further investigated after giving high single doses similar to those delivered in the radiotherapy of ocular melanoma. The survival curves of HTB140 cells exhibited a shoulder at lower doses and an exponential decrease for doses higher than 8 Gy (Fig. 2). The width of the shoulder and the initial slope of the survival curves generated at 24 and 48 h of post-irradiation time, were not significantly different. At 6 h of post-irradiation incubation mean values for cell-surviving fraction, for all doses applied, were $50.01\% \pm 0.11$, with no significant difference regarding the increase of the delivered dose. At 24 h post-irradiation, the shape of the fitted curve showed the decrease of the survival fraction with the increase of the dose, having the high S.D. values for the irradiation with 24 Gy. This could be explained by the fact that heterogeneous cell cultures, having melanoma cells in different stages of differentiation, were irradiated in our experiments. The survival curve generated after 48 h post-irradiation, has shown almost the same shape as the survival obtained at 24 h post-irradiation, with significantly lower S.D. values. The present shape of the dose-response curve is consistent with the results already reported [3, 5]. Some differences in the detected cell sensitivity might be a consequence of the nature of cell damage induced by high-LET radiation, cell-repair capacity and other cell parameters involved in the different metabolic processes.

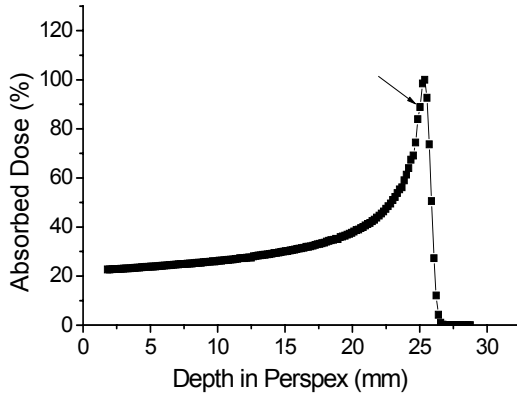


Fig. 1 Measured dose in Perspex vs. depth for the 62 MeV proton beam produced at the LNS, INFN, Catania. Arrow indicates position of cell irradiation.

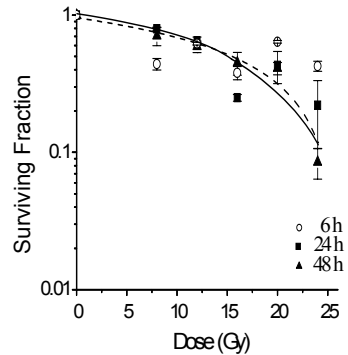


Fig. 2 Survival fraction of HTB140 cells exposed to 62 MeV protons at 25 mm in Perspex.

Conclusions

The data obtained on human melanoma cells irradiated within the Bragg peak of an unmodulated 62 MeV proton beam pointed out a significant dose dependent early cell inactivation. With the increase of the post-irradiation incubation time, a better killing effect, as the consequence of clonogenic survival, was detected.

This study is part of an overall effort to understand the mechanisms involved in cell survival after irradiation with high-LET charged particles of human cells with different radiosensitivity. All the knowledge gained through these investigations is aimed to improve the efficiency of the therapeutic approach to cure different malignant diseases.

References:

- [1] U. Amaldi, *Tumori*, 1998, 84, 188.
- [2] W.T. Chu, *et al.*, *Rev. Sci. Instr.*, 1993, 64, 2055.
- [3] M. Belli, *et al.*, *Int. J. Radiat. Biol.*, 2000, 76(6), 831.
- [4] J. Gueulette, *et al.*, *Radiat. Res.*, 1996, 145, 70.
- [5] D. Bettega, *et al.*, *Int. J. Radiat. Res.*, 2000, 76 (10), 1297.
- [6] A. Ristić-Fira, *et al.*, *J. Exp. Clin. Canc. Res.*, 2001, 20 (1), 525.
- [7] A. Courdi, *et al.*, *Int. J. Radiat. Biol. Phys.*, 1999, 45 (1), 5.
- [8] IAEA TRS 398, 2000, 135.

RADIOBIOLOGICAL STUDIES ON THE 62 MeV THERAPEUTIC PROTON BEAM AT LNS CATANIA: II. FACS ANALYSES OF HTB140 MELANOMA CELLS

A. Ristić-Fira, D.V. Todorović, L. Valastro¹, P. Cirrone¹, G. Cuttone¹ and I. Petrović

Vinca Institute of Nuclear Sciences, P.O.Box 522, 11001 Belgrade, SCG

¹*Istituto Nazionale di Fisica Nucleare, LNS, Catania, Italy*

Abstract

The objective of this study was to determine whether apoptosis and cell cycle redistribution were influenced by high-LET irradiation. Exponentially growing HTB140 cells were exposed to an unmodulated 62 MeV proton beam, within the Bragg peak, delivered over the single dose range from 8 Gy to 24 Gy. At 6 h post-irradiation, there was a low level of early apoptosis. At 48 h irradiated cells were more damaged, showing the increase in number of apoptotic nuclei. The dose dependent cell cycle phase distribution was detected at 48 h post-irradiation. The cell population exhibited phase redistribution toward G2/M phase.

Introduction

The basic task of the cell cycle is to provide a faithful DNA replication during S phase and equal distribution to two daughter cells during M phase. The process of malignant transformation includes deregulation of normal cell cycle controls. Most commonly seen cell cycle perturbation, in irradiated tumour cells, is a delay in the transition from G2 to M [1]. The ability of radiation to induce apoptosis is detected in many cell types. However, there are cells that are resistant to radiation induced apoptosis, and they die by radiation induced necrosis or enter a terminal cell cycle arrest [2]. Malignant melanoma has been increasingly analyzed in recent years. Knowing that some forms of melanoma (uveal melanoma) are successfully cured using proton irradiation [3, 4], there is a great interest to investigate the effects of protons on different human melanoma cell lines. The effects of irradiation within the Bragg peak of an unmodulated 62 MeV proton beam on HTB140 cells regarding the induction of apoptosis and cell cycle phase redistribution are given in this study.

Materials and methods

Human HTB140 melanoma cells were maintained and irradiated under the same conditions already described elsewhere [5]. Exponentially growing cells were irradiated within the Bragg peak of an unmodulated 62 MeV proton beam, delivering to the cells doses from 8 to 24 Gy, at the dose rate of 15 Gy/min. To analyse the cell cycle and apoptosis, 1×10^6 cells were used. Assays were performed with Annexin-V-Fluos kit (Roche), according to the manufacturer's protocol. Propidium iodide (PI) was added prior to FACS analyzes (Becton Dickenson, Heidelberg, Germany). Apoptotic population was calculated using CellQuest computer program (Becton Dickenson, Heidelberg, Germany). DNA was extracted from irradiated cells at 6 and 48 hours

postirradiation [6] and analyzed electrophoretically on 2 % agarose gel (Gibco BRL) with ethidium bromide (1 $\mu\text{g}/\text{ml}$). DNA profiles were analyzed on Gel doc 1000 (Bio-Rad). The Student t-Test was used for statistical analysis. The level of significance was set at $P < 0.05$. Results are presented as the Mean \pm S.D.

Results and Discussion

The ability of proton radiation with respect to the induction of apoptosis in the HTB140 cells was examined. The gel electrophoretic analyses of DNA samples, isolated from control and irradiated HTB63 cells, 6 and 48 hours post-irradiation, have shown ladder pattern, a typical DNA fragmentation characteristic for apoptotic cells (data not presented). Table I contains data obtained by FACS analyses for the proportion of cells in apoptosis as a function of dose and time. At 6 hours post-irradiation there was a moderate level of apoptosis, not more than 10% of apoptotic cells for irradiation with 16 Gy. At 48 hours post-irradiation, the highest number of detected apoptosis was 17.71% for the irradiation with 8 Gy, while the number of apoptosis after irradiation with 16 Gy did not exceed 12.11%. Corresponding apoptotic indexes for 6 hours post-irradiation incubation ranged from 2.91 to 3.96 and for 48 hours post-irradiation from 1.76 to 3.15, as shown in Table I.

Table I Radiation-Induced Apoptosis in HTB140 Cells

Post-irradiation time	Dose (Gy)	Apoptosis (%)	Apoptotic index
6 hours	0	2.66 ± 0.85	1
	8	9.77 ± 0.47	3.84 ± 1.04
	12	8.96 ± 1.49	3.37 ± 0.05
	16	10.30 ± 1.98	3.96 ± 0.52
	20	7.47 ± 0.81	2.91 ± 0.62
	24	8.64 ± 3.05	3.23 ± 0.11
48 hours	0	5.98 ± 2.71	1
	8	17.71 ± 3.52	3.15 ± 0.83
	12	15.39 ± 4.09	2.69 ± 0.54
	16	12.11 ± 2.81	2.13 ± 0.49
	20	11.52 ± 2.57	2.04 ± 0.48
	24	10.24 ± 3.45	1.76 ± 0.21

The detected apoptosis, induced in HTB140 cells by proton-beam radiation was almost immediate, appearing at about 6 hours after irradiation. It appears that these cells enter directly into programmed cell death, without a lag typical of those described for intact cell cycle checkpoint processes, which allow cells to repair damage prior to undergoing division [7].

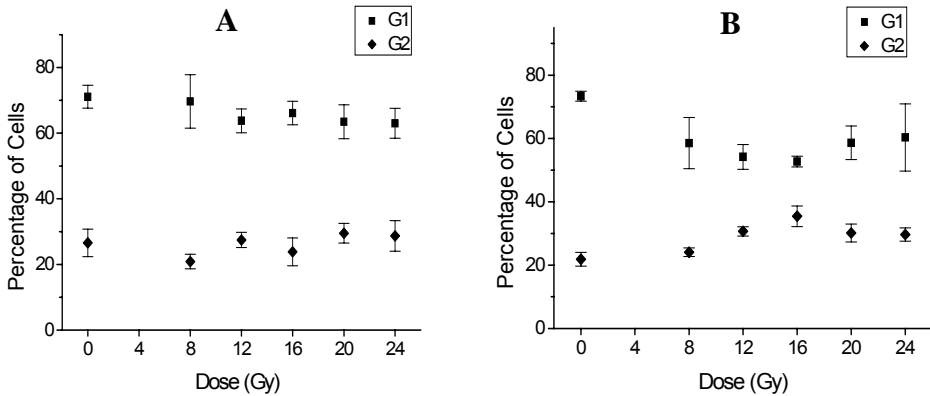


Fig. 1 The effects of proton irradiation on cell cycle phase redistribution in HTB140 cells at 6h post-irradiation (panel A) and 48h post-irradiation (panel B).

The cell cycle phase distribution of control HTB140 cells is approximately 71.09 % in G1 phase, 8.17 % in S phase and 26.56 % in G2/M phase. Cultured cells were exposed to ionizing radiation and sampled at 6 and 48 hours post-irradiation. With the increase of the dose, at 48 hours post-irradiation, the cell population exhibited phase redistribution toward G2/M phase. After single exposure to 12 and 16 Gy, the number of cells in G2/M phase ranged from 30.67 % to 35.44% respectively. Data from two duplicate experiments are represented in Fig. 2. The cell cycle redistribution, evaluated in irradiated cells at 6 (panel A) and 48 hours (panel B) post-irradiation, was not significantly different. These data are in agreement with literature data reported for other cell lines [7].

Conclusions

The results of these experiments indicate that cell cycle phase redistribution in HTB140 cells was dependent on dose but not on the duration of post-irradiation incubation. The position of cells in cell cycle at the time of irradiation did not influence the results obtained.

References:

- [1] G. Iliakis, *Sem. Oncol.*, 1997, 24, 602.
- [2] K.R. Blank *et al.*, *Int. J. Radiat. Biol.*, 1997, 71, 455.
- [3] A. Courdi *et al.*, *Int. J. Radiat. Oncol. Biol. Phys.*, 1999, 45 (1), 5.
- [4] D. Bettega *et al.*, *Int. J. Radiat. Biol.*, 2000, 76(10), 1297.
- [5] I. Petrovic *et al.*, same issue.
- [6] D.K. Armstrong *et al.*, *Cancer. Res.*, 1992, 52, 3418.
- [7] L.M. Green *et al.*, *Radiat. Res.* 2001, 155, 32.

HPLC ANALYSIS OF TECHNETIUM(I)-99m LABELLED C₆₀(OH)₂₂

T.Maksin, D.Janković¹ and A.Đorđević²

¹ The Vinča Institute of Nuclear Sciences, Laboratory for Radioisotopes POB 522, 11001 Belgrade,

² University of Novi Sad, Faculty of Natural Sciences and Mathematics,
Trg Dositeja Obradovica 3, Novi Sad, Serbia and Montenegro

Abstract

Fullerenols, water-soluble polihydroxylated fullerenes, are very important kinds of fullerene derivatives because it is suitable for biological study. In order to get convenient substance for studies (*in vivo* and *in vitro*) we investigate possibilities of labeling fullereneol. The HPLC results performed by isocratic HPLC, confirmed that hydrophilic organometallic [^{99m}Tc(CO)₃(H₂O)₃]⁺ precursor allows forming of ^{99m}Tc(I) complexes with fullereneol.

Introduction

Fullerenes have some potential effects, e.g. specific cleavage of DNA, antiviral activity, inhibition of HIV protease and photodynamic therapy [1], so it has become a challenging research field at present. Fullereneols, water-soluble polihydroxylated fullerenes, are very important kinds of fullerene derivatives because they are suitable for biological study. The biological behaviour of fullereneol derivatives shows their considerable potential for medical application.

Radiolabelled fullereneol is suitable for many different investigations (radiochemical purity, pharmacokinetics and biodistribution). Technetium-99m is still the radionuclide of choice because of his ideal physical properties (T_{1/2}=6.02h, E_γ=141keV) for many applications in nuclear medicine. For radiopharmaceuticals preparation it was often used like technetium pertechnetate (TcO₄⁻), which have to be reduced in lower oxidation state. Besides this labelling approach, it is possible to use hydrophilic organometallic [^{99m}Tc(CO)₃(H₂O)₃]⁺ precursor to form Tc(I) radiopharmaceuticals based on the tricarbonyltechnetium (I) core [2].

Experimental

[^{99m}Tc(CO)₃(H₂O)₃]⁺ ion was prepared by addition of 1 ml of ^{99m}Tc-pertechnetate (20 – 100 mCi ^{99m}TcO₄⁻ eluted in saline from ^{99m}Tc-generator, Vinča Institute) to a penicillin vial with lyophilized form of 7.15 mg sodium carbonate, 4.5 mg sodium boranocarbonate, 2.85 mg sodium tetraborate. The samples of fullereneol, produced at the University of Novi Sad [3] were prepared by dissolving in water appropriate amount of substances for obtaining solution with 1.5 mg fullereneol/ml. The pH of solutions was adjusted at about 9.0 and 5.5. ^{99m}Tc-carbonyl fullereneol complexes were prepared by addition of 0.5ml of fullereneol solutions to a proper volume of [^{99m}Tc(CO)₃(H₂O)₃]⁺ precursor with appropriate pH values to get fullereneol: carbonyl ratio 1:1; 1:3 and 1:9. The vials were heated for 30 min in boiling water bath.

The quality control of the obtained $[\text{}^{99\text{m}}\text{Tc}(\text{CO})_3(\text{H}_2\text{O})_3]^+$ precursor (pH = 10 - 11) was performed by the gradient HPLC (Liquid Chromatograph, Hewlett Packard 1050, S/N with UV and Ray test gamma flow detector) on RP C18 column (250 x 4.6 x 5 mm). The solutions of 0.05 M triethylammonium phosphate (TEAP) of pH = 2.25 and methanol were used as mobile phases. The labelling efficiency for $^{99\text{m}}\text{Tc}$ -carbonyl tagged fullereneol was determined in isocratic HPLC with 90 % TEAP : 9 % H_2O : 1 % CH_3OH , pH = 2.25 as mobile phase (flow rate 0.7 ml / min) at room temperature.

Results and Discussion

In this paper the results of the conditions and possibilities investigation of water soluble fullereneol $\text{C}_{60}(\text{OH})_{22}$ labelling with $[\text{}^{99\text{m}}\text{Tc}(\text{CO})_3(\text{H}_2\text{O})_3]^+$ as precursor for $^{99\text{m}}\text{Tc}(\text{I})$ were presented.

For determination of radiochemical purity of all $^{99\text{m}}\text{Tc}$ -labelled compounds the standard paper (Whatman No1) and instant thin layer chromatography (ITLC-SG) with two solvents (acetone and saline) were used.

The same chromatographic methods for investigation of $^{99\text{m}}\text{Tc}(\text{CO})_3\text{-}[\text{C}_{60}(\text{OH})_{22}]$ labelling yields were used. The obtained results have shown that applied chromatographic methods could not separate labelled fullereneol from radiochemical impurities like $[\text{}^{99\text{m}}\text{Tc}(\text{CO})_3(\text{H}_2\text{O})_3]^+$ precursor or free $^{99\text{m}}\text{TcO}_4^-$.

The quality control performed by HPLC method show good separation impurities from radiolabelled fullereneol. The results of $^{99\text{m}}\text{Tc}$ -carbonyl tagged of fullereneol, as well as $[\text{}^{99\text{m}}\text{Tc}(\text{CO})_3(\text{H}_2\text{O})_3]^+$ precursor, obtained with heating of the samples in boiling water for 30 min, were presented as HPLC chromatograms, in Fig. 1 and Fig. 2 respectively.

The retention time values (R_t) for $[\text{}^{99\text{m}}\text{Tc}(\text{CO})_3(\text{H}_2\text{O})_3]^+$ and $^{99\text{m}}\text{TcO}_4^-$, obtained by gradient HPLC with 0.05 M triethylammonium phosphate (TEAP) of pH = 2.25 and methanol as mobile phases (flow rate 0.7 ml/min, room temperature) were 4.736 min and 12.624 min respectively. HPLC quality control results of $[\text{}^{99\text{m}}\text{Tc}(\text{CO})_3(\text{H}_2\text{O})_3]^+$ precursor have shown that the radiochemical purity of precursor was higher than 95 %. The HPLC results performed by isocratic HPLC with 90% TEAP, 9 % H_2O and 1% CH_3OH as eluense, with flow 0.7 ml/min, confirmed that hydrophilic organometallic $[\text{}^{99\text{m}}\text{Tc}(\text{CO})_3(\text{H}_2\text{O})_3]^+$ precursor allows forming of $\text{Tc}(\text{I})$ complexes with fullereneol. The retention time value (R_t) for $^{99\text{m}}\text{Tc}(\text{CO})_3\text{-fullereneol}$ (pH around 9.0, carbonyl : fullereneol = 1 : 1 v/v), was 15.923. The labelling yield was 95.35%, with 4.65% of free, not bound $[\text{}^{99\text{m}}\text{Tc}(\text{CO})_3]^+$ as radiochemical impurities. If the labelling was performed at pH around 5.5, better results were obtained for samples with carbonyl : fullereneol = 3 : 1 v/v then 9 : 1 v/v. If ration was 9 : 1 v/v, the labelling yield was about 20%, but if ration was 3 : 1 v/v the labelling yield was more then 65%.

The lipophilicity measurements for $^{99\text{m}}\text{Tc}(\text{I})$ -labelled fullereneol were done by solvent extraction method with n-octane equilibrated with 0.15 mol dm^{-3} phosphate buffers (pH=3.5-7.5) at room temperature. The fullereneol labelled by $[\text{}^{99\text{m}}\text{Tc}(\text{CO})_3(\text{H}_2\text{O})_3]^+$ precursor gave compound with hydrophilic character.

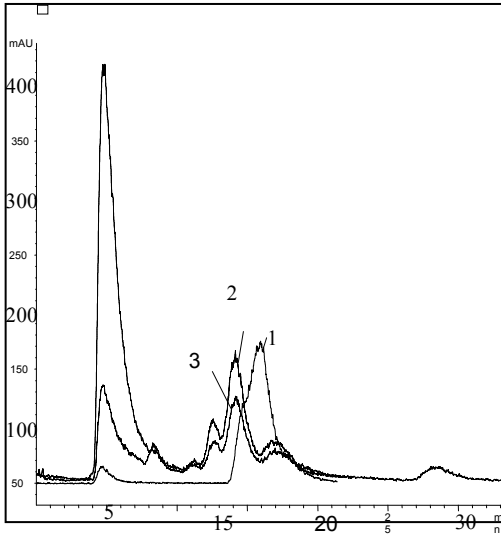


Figure 1. HPLC chromatogram : fullereneol :
Tc(I) = 1:1v/v (1); 1:3 (2) and 1:9 (3);

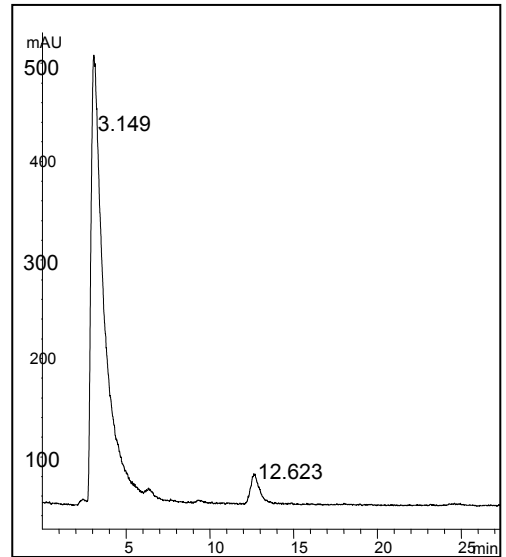


Figure 2. HPLC chromatogram of
[^{99m}Tc(CO)₃(H₂O)₃]⁺ precursor

Conclusion

The obtained results have shown that applied standard paper (Whatman No1) and instant thin layer chromatography (ITLC-SG) methods with two solvents (acetone and saline) could not separate labelled fullereneol from radiochemical impurities. The quality control performed by HPLC method shows good separation impurities from radio-labelled fullereneol. The labelling yield was more than 95%.

References

- [1] Mather. S.J., Textbook of Radiopharmacy: Theory and Practice, ed.C.B.Sampson, Gordon and Breach, Singapore p.87.
- [2] Alberto R, Schibili R, Waibel R, Abram U, Schubiger AP. Coord Chem Rev, 1999, 190-192, 901.
- [3] A.Đorđević and all., Fullerenes Sciences & Technology, 1998, 6(4), 689.

THE "ORGANOMETTALIC APPROACH" TO LABELLING OF AMINO ACIDS WITH $[\text{}^{99\text{m}}\text{Tc}(\text{CO})_3(\text{H}_2\text{O})_3]^+$

D. Đokić and D. Janković

*The Vinča Institute of Nuclear Sciences, Laboratory for radioisotopes,
P.O. Box 522, 11001 Belgrade, Serbia and Montenegro*

Abstract

The possibilities for $^{99\text{m}}\text{Tc}$ -labelling of some amino acids with $^{99\text{m}}\text{Tc}$, by use of "organomettalic approach" of labelling with $[\text{}^{99\text{m}}\text{Tc}(\text{CO})_3(\text{H}_2\text{O})_3]^+$ precursor, were investigated. HPLC results have shown the coordination of $^{99\text{m}}\text{Tc}(\text{I})$ precursor with examined amino acids. The best results were obtained at $\text{pH} \approx 7.5$ with heating.

Introduction

Recent approaches to development of new radiopharmaceuticals for diagnosis are centred on the use of $^{99\text{m}}\text{Tc}$ -labelled peptides. Possible targets for their labelling are amino acids: tyrosine, lysine and histidine. Labelled artificial amino acids has more advantages, as they enter into cells *via* single mechanisms and increased uptake into malignity cells in comparison with normal cells. The labelled amino acids with $^{99\text{m}}\text{Tc}$ are expected to facilitate research on tumours and cerebral function as well as to make possible the research of membrane transport of amino acids [1, 2].

As technetium-99m has ideal physical properties for many applications in nuclear medicine, it is still the radionuclide of choice. For radiopharmaceuticals preparation it was often used like technetium pertechnetate ($^{99\text{m}}\text{TcO}_4^-$), which had to be reduced in lower oxidation state. Besides this direct labelling approach, the use of bi-functional chelating agent (BFCA) has been more fruitful [2]. Nowadays, hydrophilic organometallic $[\text{}^{99\text{m}}\text{Tc}(\text{CO})_3(\text{H}_2\text{O})_3]^+$ precursor allows the forming of Tc (I) radiopharmaceuticals based on the tricarbonyltechnetium(I) core [3-5]. Three molecules of water are labile coordinated to Tc(I) and could be readily exchanged with different mono-, bi- and tridentate ligands. This way of labelling is known as "organomettalic approach" of labelling [6]. In this paper HPLC results of complexation of the amino acids with $[\text{}^{99\text{m}}\text{Tc}(\text{CO})_3(\text{H}_2\text{O})_3]^+$ were presented.

Experimental

Amino acids tyrosine, lysine, histidine, leucine, valine, asparagine and glutamic acid were labelled with technetium-99m by use of $[\text{}^{99\text{m}}\text{Tc}(\text{CO})_3(\text{H}_2\text{O})_3]^+$ precursor.

$[\text{}^{99\text{m}}\text{Tc}(\text{CO})_3(\text{H}_2\text{O})_3]^+$ ion was prepared by addition of 1 ml of $^{99\text{m}}\text{Tc}$ -pertechnetate (20-30 mCi $^{99\text{m}}\text{TcO}_4^-$ elute in 0.9 % NaCl, from $^{99\text{m}}\text{Tc}$ -generator, Vinča Institute) to a penicillin vial with lyophilised form of 7.15 mg sodium carbonate, 4.5 mg sodium boranocarbonate, 2.85 mg sodium tetraborate and 8.5 mg sodium tartarate (IsoLinkTM, Mallinckrodt Medical B.V., The Netherlands). After heating for 30 min in boiling water bath and cooling, pH of solution was adjusted to desired value with 1 mol dm⁻³ HCl.

^{99m}Tc -carbonyl targeted amino acids were prepared by addition of 0.1 ml of investigated amino acid solutions ($10^{-3} \text{ mol dm}^{-3}$) to 0.9 ml of $[\text{}^{99m}\text{Tc}(\text{CO})_3(\text{H}_2\text{O})_3]^+$ precursor. The samples were labelled with $^{99m}\text{Tc}(\text{I})$, without and with heating (30 min in boiling water bath). The dependence of pH on labelling efficiency was investigated too.

The quality control of the obtained $[\text{}^{99m}\text{Tc}(\text{CO})_3(\text{H}_2\text{O})_3]^+$ precursor (pH=10-11) was performed by gradient HPLC (Liquid Chromatograph, Hewlett Packard 1050, S/N with UV and Raytest gamma flow detector) and RP C18 column (250x4.6 mm). The solutions of 0.05 mol dm^{-3} triethylammonium phosphate (TEAP) with pH=2.25 and methanol were used like mobile phases. All other investigations were performed as isocratic HPLC with 90 % TEAP : 1 % CH_3OH : 9 % H_2O , pH=3.0 as mobile phase and flow rate 0.7 ml/min.

Results and Discussion

HPLC quality control results of $[\text{}^{99m}\text{Tc}(\text{CO})_3(\text{H}_2\text{O})_3]^+$ precursor have shown that the radiochemical purity of precursor was higher than 95 %. The retention time values (R_t) for $[\text{}^{99m}\text{Tc}(\text{CO})_3(\text{H}_2\text{O})_3]^+$ and $^{99m}\text{TcO}_4^-$, obtained with 20 % TEAP and 80 % H_2O as eluense, with flow 0.7 ml/min, were 3.078 min and 12.624 min, respectively.

The values of retention times together with the labelling yield for each of Tc-carbonyl coordinated amino acid were presented in Table 1.

Table 1. Retention times and labelling yield of Tc-carbonyl coordinated amino acid

Ligands \ ^{99m}Tc -species	$[\text{}^{99m}\text{Tc}(\text{CO})_3]$		$[\text{}^{99m}\text{Tc}(\text{CO})_3\text{-L}]$		$^{99m}\text{TcO}_4^-$	
	R_t (min)	Yield (%)	R_t (min)	Yield (%)	R_t (min)	Yield (%)
$[\text{}^{99m}\text{Tc}(\text{CO})_3]$	3.978	95.8	-	-	12.623	4.2
Tyrosin	3.401	39.9	5.171	60.1	-	-
Lysine	3.401	19.3	5.697	80.7	-	-
Histidine	-	0	23.056	100	-	-
Leucine	5.112	30.1	13.846	69.9	-	-
Valine	4.987	65.1	14.337	34.9	-	-
Asparagine	-	0	13.168	100	-	-
Glutamic acid	5.012	27.9	13.846	72.1	-	-

The quality control results of $[\text{}^{99\text{m}}\text{Tc}(\text{CO})_3(\text{H}_2\text{O})_3]^+$ precursor and $^{99\text{m}}\text{Tc}$ -carbonyl tagged amino acids, obtained with heating of the samples ($75\text{ }^\circ\text{C}$) and $\text{pH}\approx 7.5$, were presented as HPLC chromatograms, in Fig. 1 and Fig. 2.

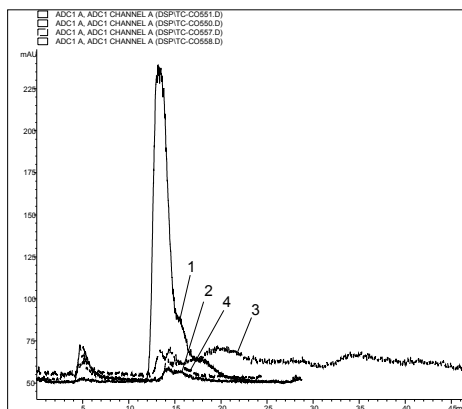


Fig. 1. HPLC chromatograms of Tc-carbonyl coordinated amino acid: asparagin (1), valin (2), leucin (3) and glutamic acid (4)

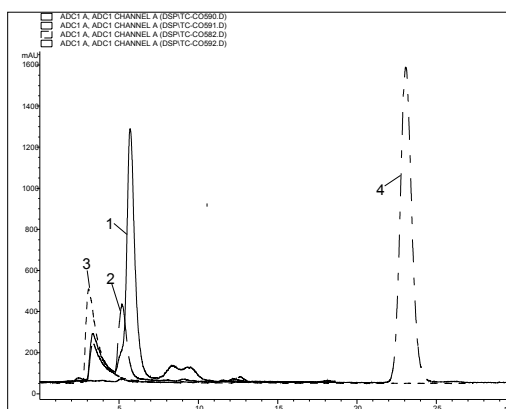


Fig. 2. HPLC chromatograms of Tc-carbonyl coordinated amino acid: lysine (1), tyrosine (2), $[\text{}^{99\text{m}}\text{Tc}(\text{CO})_3(\text{H}_2\text{O})_3]^+$ precursor (3) and histidin (4)

Conclusion

The HPLC results performed by isocratic HPLC, pointed at complexation of amino acids with $[\text{}^{99\text{m}}\text{Tc}(\text{CO})_3(\text{H}_2\text{O})_3]^+$. The best labelling yield was obtained at $\text{pH}\approx 7.5$, when the samples of amino acids together with $^{99\text{m}}\text{Tc}(\text{I})$ carbonyl precursor were heated in water boiling bath for thirty minutes.

Acknowledgment

This paper has been financially supported from Ministry of Sciences, Technologies and Development of Serbia, under Project OI 1980.

$[\text{}^{99\text{m}}\text{Tc}(\text{CO})_3(\text{H}_2\text{O})_3]^+$ precursor (IsoLinkTM) was obtained from Tyco Healthcare, Mallinckrodt Medical B.V., The Netherlands.

References

- [1] S.M. Okarvi, Nucl. Med. Comm., 1999, 20, 1093.
- [2] W.C. Eckelman, Eur. J. Nucl. Med., 1995, 22, 249.
- [3] R. Alberto, R. Schibli, A. Egli, A.P. Schubiger, J. Amer. Chem. Soc., 1998, 120, 7987.
- [4] R. Alberto, R. Schibli, R. Waibel, U. Abram, A.P. Schubiger, Coord. Chem. Rev., 1999, 190-192, 901.
- [5] R. Schibli, A.P. Schubiger, Eur. J. Nucl. Med., 2002, 29, 1529.
- [6] M. Salmán, M. Gunn, A. Gorfí, S. Top, G. Jaouen, Bioconjugate Chem., 1993, 4, 425.

COMPARISON OF TRAINING ALGORITHMS IN NEURAL NETWORK MODELING OF GAMMA SPECTROMETRIC UNCERTAINTY

S. Dragović¹, S. Stanković¹ and A. Onjia²

¹ *Institute for the Application of Nuclear Energy – INEP, Banatska 31b,
11080 Belgrade, Serbia and Montenegro*

² *Vinča Institute of Nuclear Sciences, P.O. Box 522, 11001 Belgrade,
Serbia and Montenegro*

Abstract

A three-layer feed-forward artificial neural network with six different algorithms applied on different training sets was used to model uncertainties of activity levels of eight radionuclides (²²⁶Ra, ²³⁸U, ²³⁵U, ⁴⁰K, ²³²Th, ¹³⁴Cs, ¹³⁷Cs and ⁷Be) in soil samples as a function of measurement time. The performance of applied neural network architecture is found to be very good, with correlation (R^2) values between measured and predicted uncertainties ranging from 0.9291 for ⁷Be to 0.9915 for ¹³⁷Cs.

Introduction

Artificial neural networks (ANNs) are data processing systems that simulate biological neural networks. They consist of a large number of simple, highly interconnected processing elements. Many models of ANNs have different approaches both in architecture and in training algorithms. There is always one input and one output layer and there should be at least one hidden layer. Each layer of nodes receives its input from the previous layer or from network input [1].

In gamma spectrometry, ANNs were used for automatic identification of radioactive isotopes from their spectra [2] as well as for quantitative spectrometry analysis [3]. In the present study an ANN was employed and optimized to model the measurement uncertainties of activities of radionuclides detected by gamma spectrometry with six different training algorithms applied on different training sets.

Experimental

The measurements were performed using HPGe gamma spectrometer ORTEC-AMETEK (34% relative efficiency and 1.65 keV FWHM for ⁶⁰Co at 1.33 MeV; 8192 channels). The soil samples were measured in 1L Marinelli beakers for 17 hours. The obtained spectra were recorded after each hour. As the average difference between uncertainty data obtained for three soil samples from the same location was within 2 %, a simple arithmetic mean value for each radionuclide was used. The uncertainties of activity measurements of radionuclides detected in soil samples (²²⁶Ra, ²³⁸U, ²³⁵U, ⁴⁰K, ²³²Th, ¹³⁴Cs, ¹³⁷Cs and ⁷Be) were analyzed.

The ANN systems were simulated using MS-Windows based software, QwikNet Version 2.23 [4]. The training set consisted of uncertainties of activity measurements of radionuclides obtained after 2, 5 and 10 hours. Neural network models were tested to predict uncertainties of radionuclide activities for 14 times of meas-

urement, which were not used for the network training. Six different training algorithms are tested and compared, in order to find the one with possible least root mean square error: online backpropagation (OBP), online backpropagation randomized (OBPR), batch backpropagation (BB), delta-bar-delta (DBD), resilient propagation (RP) and quick propagation (QP) [4]. The influence of training set selection was also investigated. The 17 objects were divided into the training and test set in six different ways.

Results and Discussion

A three-layer (input, hidden and output) feed-forward neural network with sigmoidal transfer function was used to model measurement uncertainties. The RMS used as the error function is computed as: $RMS = (\sum_{i=1}^n (d_i - o_i) / n)^{1/2} / x$, where d_i is the desired output (experimental values) in the training or testing set, o_i the actual output (ANN predicted values) in the training or testing set, n the number of data in the training or testing set, and x is the average value of desired output in the training or testing set. The RMS errors for predictions on the test set applying different training algorithms are presented in Table 1.

Table 1. RMS errors of test set predictions obtained with six training algorithms

Number of objects in the training/test set	RMS error					
	OBP	OBPR	BBP	DBD	RP	QP
13/4	0.0035	0.0032	0.0037	0.0061	0.0048	0.0046
11/6	0.0048	0.0045	0.0051	0.0073	0.0061	0.0058
9/8	0.0062	0.0051	0.0068	0.0088	0.0075	0.0074
7/10	0.0079	0.0064	0.0083	0.0107	0.0089	0.0090
5/12	0.0094	0.0088	0.0096	0.0128	0.0091	0.0103
3/14	0.0102	0.0098	0.0104	0.0144	0.0106	0.0120

The trend that can be seen is increase of RMS error with decreasing the number of objects in the training set. This is understandable since using more data in the training set the modeling area is more evenly covered. Further it can be seen that OBPR training algorithm gives the lowest RMS errors.

In order to examine the predictive power of the neural network model experimental and predicted standard uncertainties of measurement were compared. The obtained results for the model with lowest RMS error (OBPR) applied on training set with 3 objects are shown in Fig 1.

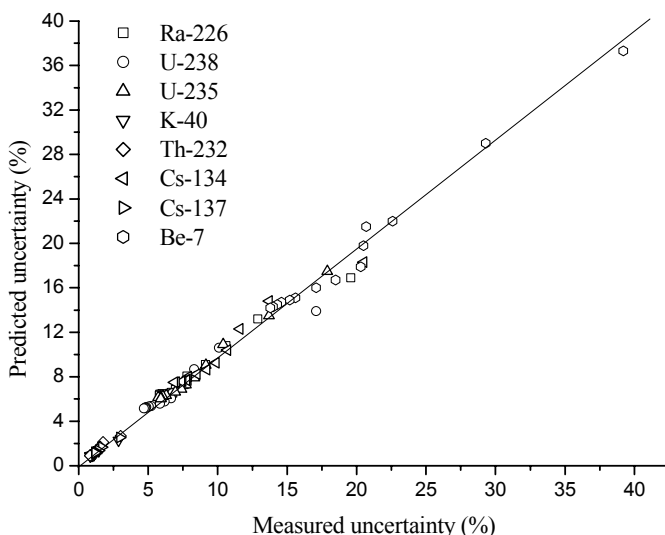


Figure 1. Measured versus predicted uncertainties of activities of eight radionuclides for 14 time of measurement using neural network OBPR model

The correlation coefficients were in range of 0.9291 for ^7Be to 0.9915 for ^{137}Cs . From these results it is obvious that the proposed neural network model generalizes data well and it can be used for uncertainty modeling in gamma spectrometry.

Conclusion

All six ANN training algorithms (OBP, OBPR, BB, DBD, RP, QP), studied in this work, showed very good performance in prediction of gamma spectrometric uncertainties. The lowest RMS testing error obtained for OBPR ranged from 0.0032 to 0.0098. An increase of RMS error was observed with decreasing the size of the ANN training set.

References

- [1] M. Gevrey, I. Dimopoulos, S. Lek, *Ecol. Model.*, 2003, 160, 249.
- [2] E. Yoshida, K. Shizuma, S. Endo, T. Oka, *Nucl. Instr. Meth. Phys. Res. A*, 2002, 484, 557.
- [3] V. Pilato, F. Tola, J.M. Martinez, M. Huver, *Nucl. Instr. Meth. Phys. Res. A*, 1999, 422, 423.
- [4] QwikNet Version 2.23, Craig Jensen, Redmond, USA, 1999.

GAMMA-RADIATION-INDUCED DAMAGE OF PROTEINS IN THE THICK FRACTION OF EGG WHITE

M. Vučković and M. B. Radojčić

*Laboratory of Molecular Biology and Endocrinology, VINČA Institute of Nuclear Sciences,
P.O.Box 522, 11000 Belgrade, Serbia and Montenegro*

Abstract

The ^{60}Co gamma-ray irradiation of ovomucin based protein network of the thick fraction of egg white in the absence of oxygen causes both protein cross linking and protein fragmentation. Protein fragmentation in the absence of oxygen is interpreted as a consequence of decreased diffusion of protein radicals within the protein network. Both protein cross linking and fragmentation, are dose dependent processes, with fragmentation prevailing below 10-15 kGy, and cross linking prevailing at the radiation doses >15 kGy. The radiolytic behaviour of the thick fraction of egg white, suggests that gamma irradiation of similar mucine containing structures might also result in accumulation of structurally altered and conceivably non-functional proteins *in vivo*.

Introduction

Due to its well-defined structure egg white represents a convenient model for investigation of radiation-induced damage of complex protein systems. Egg white is composed of the thin and the thick fraction. The thin fraction is a true solution of several proteins: ovalbumin, conalbumin, ovoglobulin and lysozyme. The thick fraction is composed of highly glycosylated, hydrated proteins ovomucine and ovomucoid which form a matrix encompassing other egg white proteins in a form of monomers, agglomerates or conglomerates [1]. Upon irradiation the proteins of the thin fraction, saturated with N_2O , undergo the reaction of cross-linking, but interestingly enough the scissoring reaction was also observed in the absence of oxygen [2]. This observation was in contrast with the results of the radiolytic behaviour of purified ovalbumin in N_2O saturated solution, when only cross-linking was observed [3,4]. The radiation-induced protein scissoring in the absence of oxygen was interpreted as a consequence of the thin fraction complexity, compared to the simple, one-component solution. In this paper we report the results of the study of radiation-chemical behaviour of the thick fraction matrix of egg white as an even more complex protein system.

Experimental

Fresh Brown Leghorn (*Gallus gallus*) farm hen's eggs were used as a source of thick fraction of egg white. It was separated by Buchner funnel filtration, saturated with either N_2O or Ar, sealed in ampoules and irradiated at a gamma source of ^{60}Co . The dose rate was 51.5 Gy/min is determined by Fricke dosimetry. The viscosity of egg white was measured by Ostwald viscometer at 20.0 °C (n=5). Protein analysis was performed by Sephadex G-200 gel filtration and SDS-polyacrylamide gel electrophoresis (SDS-PAGE). The Sephadex G-200 column was calibrated by Blue Dextran

2000 (molar mass $M_m=2,000,000$ g/mol,) and cytochrom C ($M_m=13,370$ g/mol, $R_s=1.79$ nm). For SDS-PAGE calibration was performed by chicken muscle myosin heavy chain ($M_m=223,000$ g/mol) and ovalbumin ($M_m=43,500$ g/mol). The quantification of protein products was performed after gel scanning with Pharmacia-LKB UltraScan-XL densitometer. The experimental error of these measurements was less than 8%.

Results and Discussion

The Sephadex G-200 chromatography of the thick fraction proteins showed that at the radiation dose of 1.5 kGy most of egg white matrix was decomposed and major proteins: conalbumin ($M_m=87,000$ g/mol), ovoglobulins G_2 and G_3 and ovalbumin ($M_m=43,500$ g/mol) co eluted with ovalbumin (*Figure 1*).

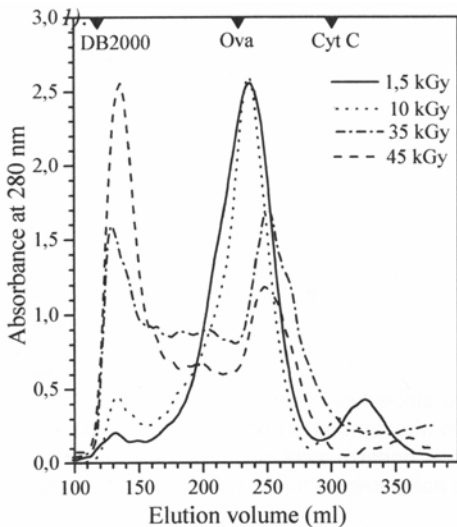


Figure 1. Sephadex G-200 chromatography of irradiated egg white proteins; R_s markers are indicated by arrows.

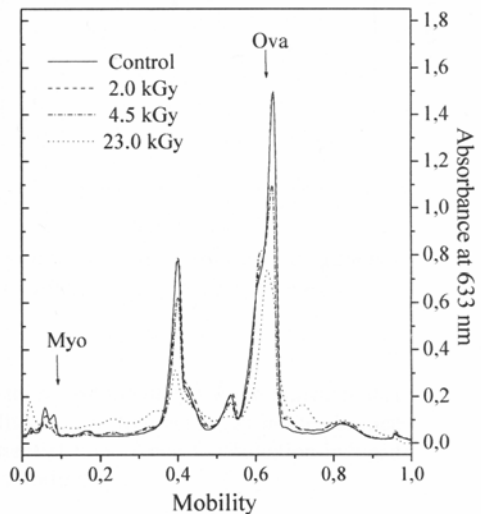


Figure 2. SDS-PAGE of gamma-irradiated egg white proteins. M_m markers are indicated by arrows.

Protein cross linking was also observed, thus that at 45 kGy the dominant protein peak contained products with $M_m > 250,000$ g/mol (*Figure 1*). The SDS-PAGE analysis (*Figure 2*) confirmed that both protein fragmentation and cross linking of the thick fraction occurred upon irradiation. The former reaction was dominant at the lower radiation doses (10-15 kGy), while the later was prevailing above 15 kGy (*Figure 3*). The results suggested that while the egg white proteins were tightly bound inside the protein matrix, the diffusion of radiation generated protein radicals was slower and protein fragmentation was more likely to occur. With the increase in the radiation dose, S-S bridges and other matrix stabilizing bonds were disrupted, the diffusion of released protein radicals became faster and the cross linking reaction prevailed. These

results correlated well with viscosity measurements of the irradiated thick fraction, which showed more abrupt decrease when samples were saturated with Ar, *i.e.* when S-S bridges holding the matrix were broken, compared with of N₂O saturated samples (Figure 4).

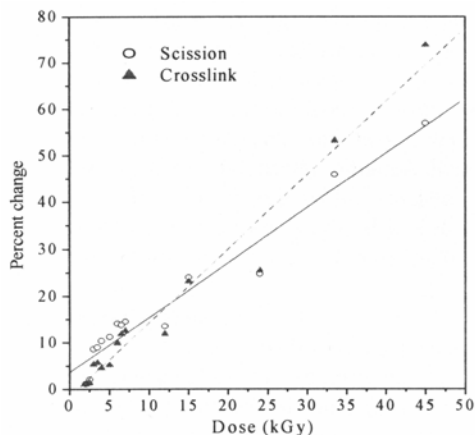


Figure 3. The percent of cross linked and fragmented thick fraction proteins

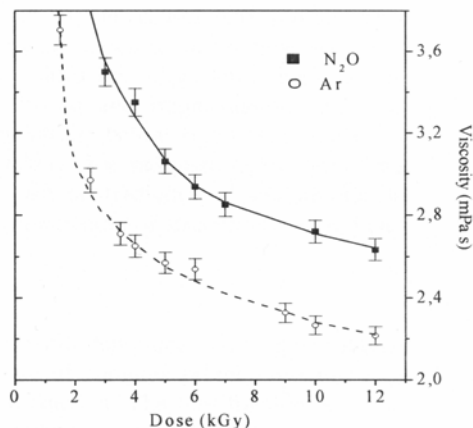


Figure 4. The viscosity of gamma-irradiated thick fraction proteins

Conclusions

The radiation-chemical behaviour of the thick fraction of egg white indicates that in the complex protein matrix both protein cross linking and fragmentation in the absence of oxygen take place. The later reaction is of potential importance for radiation-induced reactions *in vivo*, *i.e.* for radiation protection and radiotherapy.

References

- [1] M.Vučković, M.Radojčić, B.H.Milosavljević, J. Serbian Chem.Soc. 2000, 65,157.
- [2] Lj.Josimović, M.Radojčić, B.H.Milosavljević, Radiat. Phys. Chem. 1996, 47, 445.
- [3] K.J.A. Davies, J. Biol. Chem. 1987, 262, 9895.
- [4] Z.Tuce, E.Janata, M.Radojčić, B.H.Milosavljević, Radiat.Phys.Chem. 2001, 62, 325.

GAMMA-RADIATION-INDUCED DAMAGE OF CHICKEN MYOSIN AND ACTIN

A. Nićiforović and M. B.Radojčić

*Laboratory of Molecular Biology and Endocrinology
VINČA Institute of Nuclear Sciences, P.O.Box 522
11000 Belgrade, Serbia and Montenegro*

Abstract

The single ^{60}Co gamma radiation-induced damage of purified chicken myosin and actin in N_2O saturated solution is dose dependent protein cross-linking. The differences in myosin and actin conformation and Mm do not influence the type of radiation-induced damage, but they influence the extent of radiation-induced damage, judged by the lower cross linking of fibrillar myosin compared to actin. The radiolytic behavior of myosin and actin in purified forms is different from their radiolysis in intact muscle, according to the absence of protein fragmentation in the former. The results confirm that industrially sterilized meat may contain significant amount (25-35%) of structurally altered proteins.

Introduction

Biological decontamination from pathogenic organisms in meat industry is commonly performed by irradiation with 4-7 kGy of x- or gamma-rays [1]. Although it is claimed that after irradiation organoleptic characteristics of meat are not significantly changed, marked structural changes of meat proteins were detected in irradiated frozen chicken muscle [2]. The dominant damage was protein fragmentation. Due to the complexity of muscle, the damage was difficult to ascribe to any individual muscle protein. In this paper purified chicken muscle proteins: fibrillar myosin and globular actin were irradiated with 1-3 kGy in N_2O saturated solutions. Radiation-induced products were resolved by SDS-polyacrylamide gel electrophoresis (SDS-PAGE) and quantified after densitometric scanning. The type and the extent of radiation damage of myosin and actin inducing changes in their molar mass (Mm) were determined. The results were compared with gamma-radiation-induced changes in Mm of another purified globular chicken protein, ovalbumin, which was previously thoroughly characterized [3] and herein used as a reference.

Experimental

Purified chicken muscle myosin (Sigma M-7266, Mm 520 000 g/mol) and actin (Mm 42 000 g/mol) were dialysed against 100 mM Na-phosphate buffer pH 7.4, saturated with N_2O , sealed in micro capillaries and irradiated with Co-60 gamma-rays for various time intervals. The dose rate was 47.8 Gy/min as determined by Fricke dosimetry. After irradiation samples were mixed with equal volume of 125 mM Tris-HCl pH 6.8 containing 2% SDS, 10% glycerol and 0.002% brom-phenol-blue, either

with or without 5% β -mercaptoethanol, boiled for 2 minutes and analyzed by SDS-PAGE. The gel consisted of 5% or 15% polyacrylamide resolving part, for analysis of myosin or actin, respectively. The protein bands were visualized by Coomassie Brilliant Blue and scanned using UltraScan XL scanning densitometer. Molar mass (Mm) of each component was determined after calibration with SeeBlue™ standards (Novex, San Diego). Densitometric scans were processed by PC UltraScan and Microcal Origin 4.0 software, and quantification of radiation products was performed by comparison of respective integral area of control and irradiated samples. The experimental error was estimated to be $\leq 8\%$.

Results and Discussion

In contrast with the results of gamma-radiation-induced effects in frozen (partially anoxic) chicken muscle proteins, where protein fragmentation was the dominant protein damage [2], the major damage of purified myosin and actin in N_2O saturated solution, was protein cross linking or agglomeration (*Figure 1 a,b*). The protein fragmentation was negligible. The Mm of cross linked myosin products exceeded 250 000 g/mol, so they mostly appeared in front of 5% resolving gel (mobility *cca* 0), and were partially unable to penetrate the stacking gel (not shown). The amount of cross linked myosin was proportional to the radiation dose (*Figure 1a*): *cca* 11% of cross linked myosin was observed after irradiation with 1Gy, while 20% and 27% of the protein was cross linked after 2- and 3 Gy, respectively (*Table 1*).

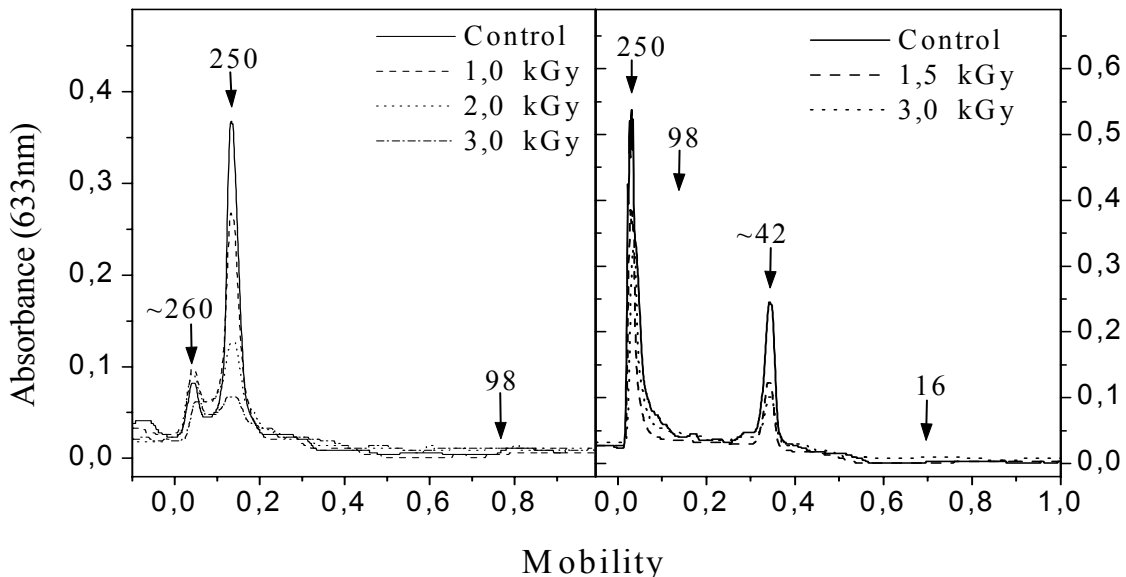


Figure 1. The densitometric scan of irradiated chicken muscle myosin (a, left) and actin (b, right). Mobility of Mm standards is indicated by arrows

Cross-linked actin products (*Figure 1b*) had $M_w > 98\,000$ g/mol and were unable to enter 15% resolving gel. They were found together with cross-linked myosin in the stacking gel (mobility 0.01-0.03). The actin cross linking was also dose dependent, yielding 24% and 36% of cross linked products after irradiation with 1.5- and 3 Gy, respectively (*Table 1*). The radiation damage of purified myosin and actin suggested that protein conformation (fibrillar vs. globular) and size (250 000 g/mol vs. 42 000 g/mol) did not influence significantly the type of radiation-induced damage. However, the extent of radiation-induced cross-linking (for protein concentration in the μM range) was significantly different (*Table 1*). Thus, for the radiation dose of 3 Gy, the cross linking was highest for ovalbumin (~77%), less pronounced for actin (~46%) and the least for myosin (~27%).

Table 1 The extent of the radiation-induced cross-linking of myosin, actin and ovalbumin (mean \pm SEM, n=3) as a function of gamma-radiation dose

Radiation dose (kGy)	Protein agglomerates (%)		
	Myosin	Actin	Ovalbumin
1	11.4 \pm 0.8	-	56.2 \pm 0.6
1.5	-	23.8 \pm 1.4	-
2	20.6 \pm 0.5	-	67.3 \pm 0.7
3	26.8 \pm 1.1	36.1 \pm 0.5	77.1 \pm 0.6

Conclusions

The major damage of chicken muscle proteins myosin and actin, induced by Co-60 gamma-radiation under anaerobic conditions, is protein cross-linking. The protein conformation and/or size do not influence the type, but influences the extent of the radiation-induced protein damage. The extent of cross linking is dose dependent and is more pronounced in the case of actin, but is less pronounced for both muscle proteins compared with the globular protein ovalbumin under the same experimental conditions. The radiation-induced crosslinking of proteins also occurs under aerobic conditions and may influence the digestibility of meat after the routine industrial radiation-sterilization.

References

- [1] Irradiation in the Production, Processing and Handling of Food, 21 CFR Part 179, USA-Federal Register 1997, 62, 64107.
- [2] A.Ničiforović, M.B.Radojčić, B.H.Milosavljević, Radiat.Phys.Chem. 1999, 55, 731.
- [3] Z.Tuce, E.Janata, M.B.Radojčić, B.H.Milosavljević, Radiat.Phys.Chem. 2001, 62, 325.

GAMMA SPECTROMETRIC ANALYSIS OF FUR

G. Pantelić¹, M. B. Rajković² and D. Tošković³

¹ *Clinical Center of Serbia, Institute of Occupational and Radiological Health "Dr Dragomir Karajović", Belgrade,* ² *Institute of Food Technology and Biochemistry, Faculty of Agriculture, Zemun, University of Belgrade, Serbia&Montenegro*

³ *Faculty of Technology, University of Serbian Sarajevo, Bosnia&Hertzevovina*

Abstract

The analysis of heavy metals content in fur, taken from water-supply system of the town of Belgrade, showed the presence of radioactive elements of uranium and strontium. Gammaspectrometre analysis indicates that the largest contribution has isotope ²³⁸U (< 10 Bq/kg) while the found presence of strontium isotopes ⁹⁰Sr is 0.72 ± 0.11 Bq/kg.

Because of that, the aim of this paper was to analyse if the presence of uranium and strontium in fur can influence on the quality of drinking water and also to influence on the evaluation of drinking water suitability from radiological aspect.

Introduction

The analysis of heavy metals content in fur, taken from water-supply system of the town of Belgrade, showed the presence of naturally occurring terrestrial radionuclides (⁴⁰K, the members of the U and Th series) and radioactive element ⁹⁰Sr [1]. Specific activity of ⁹⁰Sr in drinking water decreased from 1986 [2] and it's presence is not in significant amounts in which it could significant induce aggravation of the health of drinking water consumer. In spite of its low concentration uranium is more dangerous because of its chemical toxicity and its radioactivity.

The aim of this paper was to analyse if the presence of uranium in fur can indicate the quality of drinking water.

Pursuant to recommendations of the World Health Organization and International Commission for Radiological Protection on Drinking Waters Quality, new legal regulations have been passed in our country [3].

Experimental

During the investigation fur formed by precipitation on heater of a house boiler, during a time period of 6 months has been used. The fur originated from water present in water-supply system of Belgrade (Pančevo, Krnjača).

Gamma-spectrometry was carried out on pure germanium detector manufactured by EG&G "ORTEC", placed in vertical cryostat and protected with 10 cm of lead, relative efficiency of 25 % and energy resolution of 1.85 keV (1332.5 keV ⁶⁰Co). Detector is connected with multichannel analyzer (8192 channels) produced by the same manufacturer and with adequate computer facilities. Energetic calibration, as well as calibration of detector efficiency is performed by means of Amersham radioactive

standard. The time of measurement for a single sample was 200000 s, while it was 250000 s for basic radiation. Total photon counting rate in energetic range of 50-3000 keV was 1.0 impulse/sec

Gamma-spectrometric analysis of the fur was carried out so that the sample has been previously dried at 105°C (24 hours) in order to remove the moisture and reduce measurements to dry substance. Boiler fur was packed in small plastic vessels and hermetically closed to retain evolved radon.

Radiochemical method of ^{90}Sr separation is based on oxalate isolation of Ca and Sr, ignition to oxides and usage of aluminum as ^{90}Y carrier. The equilibrium is achieved in 18 days, and after that time ^{90}Y is isolated on $\text{Al}(\text{OH})_3$ carrier, which is then ignited to oxide that is subsequently measured by α - β anti-coincidence counter. The size of planchete is 2.3 cm in diameter. The performance of counter is 24% and is determined by ^{90}Sr standard [4].

Results and Discussion

The measurement time for each spectrum was about 55 hours, and all measurements were repeated after 20 days to obtain radioactive equilibrium of the evolved radon, and resulting spectrum is presented in Fig.1.

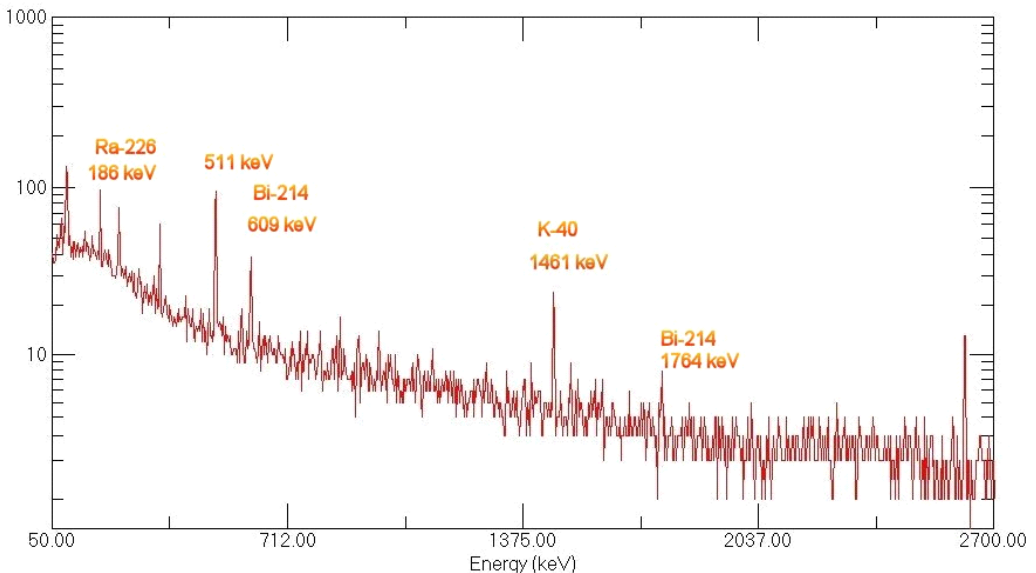


Figure 1. Boiler fur sample spectrum

The results of measurement of gamma-emitter activity concentration in the fur sample (in Bq/kg) are presented in Table 1. Since the activities of gamma emitters are given in Bq/kg and 1 dm³ water gives 0.2 of fur, over 2.000 dm³ of water is needed for observation of calculated activity. That means that in a house boiler, of 80 dm³ volume this mass of fur can hardly arise.

The measured activity that comes from isotope ^{90}Sr is 0.72 ± 0.11 Bq/kg.

Table 1. Specific activity of different radionuclides in the fur (in Bq/kg)

^{238}U	^{235}U	^{226}Ra	^{232}Th	^{40}K	^{134}Cs	^{137}Cs
< 10	< 0.3	4.6±1.3	1.8±0.5	2.06±0.22	< 0.2	< 0.3

The crystal structure of fur under electronic microscope indicates that fur is made from calcium carbonate which means *calcite* which is confirmed by making picture with diffract meter [5]. On the basis of the presented diffractogram, it is not possible to establish the presence of other compounds, although an irregular and widened form of the reflection at 0.7 nm indicates presence of other substances, but at very low concentrations, which can not be determined by this method. This extended peak indicates the presence of amorphous substances of organic and inorganic origin (and if inorganic, the most frequent of them is *limonite*).

Conclusion

The analysis of fur extracted from drinking water in a house boiler indicates that it consists mainly of calcium carbonate (*calcite*), which is confirmed by the electron microscope analysis.

^{238}U and ^{235}U specific activities in fur were below detection limit (less than 1 ppm). The presence of strontium is not confirmed by the examination on atomic absorption spectrophotometer (AAS).

Gamma-spectrometric analysis indicates that the largest contribution to fur activity comes from natural radionuclides ^{40}K , ^{232}Th and ^{226}Ra .

Acknowledgements. The work from our laboratory was supported by the Ministry for Science, Technology and Development of Serbia (Project 1941).

References

- [1] M. B. Rajković, M. Stojanović, *Ekologija*, 2001, 36(1), 71.
- [2] G. Pantelić: "Zračenje oko nas", Seminar Zdravlje i bezbednost na radu u procesnim industrijama, Beograd, 1996, 16.
- [3] Službeni list SRJ, Beograd, br 9, 19 Februar 1999.
- [4] M. H. Francois, Dosage du Sr-90 et de Y-90 dans les eaux naturelles chargees, Rapport CEA No.1965; 1961.
- [5] M.B.Rajković, M.D.Stojanović, G.K.Pantelić and D.Tošković, *Acta Periodica Technologica*, 2004 (in press).

TRICARBONYL TECHNETIUM(I) COMPLEXES WITH DIFFERENT PHOSPHATE LIGANDS

Lj. Lj. Stamenković and D. Đ. Đokić

*The Vinča Institute of Nuclear Sciences, Laboratory for Radioisotopes
POB 522, 11001 Belgrade, Serbia and Montenegro*

Abstract

The possibilities for labelling of different phosphate ligands with technetium-99m through $[^{99m}\text{Tc}(\text{CO})_3(\text{H}_2\text{O})_3]^+$ precursor were investigated. The HPLC results have shown that hydrophilic organometallic $[^{99m}\text{Tc}(\text{CO})_3(\text{H}_2\text{O})_3]^+$ precursor allows forming of Tc (I) complexes with different phosphate ligands, based on the tricarbonyltechnetium (I) core.

Introduction

In everyday nuclear medicine practice there are different phosphate ligands labeled with technetium pertechnetate ($^{99m}\text{TcO}_4^-$) eluted from $^{99}\text{Mo}/^{99m}\text{Tc}$ generator, where oxidation state of technetium in complexes isn't determined [1]. Tricarbonyl agent $[^{99m}\text{Tc}(\text{CO})_3(\text{H}_2\text{O})_3]^+$, with oxidation state of technetium +1, has proved as an excellent agent for labeling different kind of ligands [2,3]. $[^{99m}\text{Tc}(\text{CO})_3(\text{H}_2\text{O})_3]^+$ precursor could be formed in high yield directly from $^{99m}\text{TcO}_4^-$. As the coordination of three water molecules are labile, they could be exchanged readily with a variety of mono-, bi- and tridentate ligands forming complexes. Phosphate ligands used in this study were: 3,3-diphosphono-1,2-propanedicarboxylic acid (DPD), imido-diphosphate (IDP), pyrophosphate (PyP) and 1-hydroxyetan-1,1-diphosphonic acid (HEDP).

Experimental

$[^{99m}\text{Tc}(\text{CO})_3(\text{H}_2\text{O})_3]^+$ was prepared from carbonyl labelling agent Isolink™ (Mallinckrodt Medical B.V.) or carbonyl precursor prepared in NCRS "Democritos", according the instructions for use. Before use the basic solution was neutralised. At first, phosphate solutions DPD, IDP, PYP and HEDP with concentration 10^{-3} mol dm⁻³ were prepared. Each of these solutions were distributed into thee equal portions and pH was adjusted to 2.5, 5.5 or 7.5. Neutralised precursor was added to the solution in volumetric ration: phosphate (DPD, IDP, PYP or HEDP): $[^{99m}\text{Tc}(\text{CO})_3(\text{H}_2\text{O})_3]^+$ =1:1; 1:2; 1:5 or 1:9. All mixtures were heated at 75°C for 30 minutes, because there was no reaction between phosphate ligands and Tc(I)-carbonyl without heating.

Reaction products, prepared from different solutions of ligand and Tc-carbonyl, were analysed by Liquid Chromatograph, Hewllet Packard 1050 S/N with UV and Raytest gamma flow detector RP and Alltech C18 column (250x4.6 mm). Flow was 0.7 ml/min. Runs were isocratic. Mobile phase was 90 % 0.05 mol dm⁻³ TEAP:9 % water:1 % methanol.

Results and Discussion

A great number of ^{99m}Tc -phosphate compounds, made by adding $^{99m}\text{TcO}_4^-$ to a kit, have been applied for bone imaging. There are a lot of literature data about forming mixed-metal complexes containing Tc(III), Tc(IV), Tc(V) and Sn(II) in undetermined proportions. The subject of this paper was labelling of some phosphate ligands with $[\text{}^{99m}\text{Tc}(\text{CO})_3(\text{H}_2\text{O})_3]^+$, where oxidation state of technetium was +1.

The HPLC results performed by isocratic HPLC, pointed at complexation of phosphate ligands with $[\text{}^{99m}\text{Tc}(\text{CO})_3(\text{H}_2\text{O})_3]^+$. The influence of molar ratio on labelling yield was presented in Fig.1. as HPLC chromatograms for Tc-carbonyl coordinated DPD, for three different ratios. These results pointed at the highest labelling yeald for ration: DPD: $[\text{}^{99m}\text{Tc}(\text{CO})_3(\text{H}_2\text{O})_3]^+=1:9$.

The quality control results of ^{99m}Tc -carbonyl tagged phosphate ligands, obtained with hitting of the samples ($75\text{ }^\circ\text{C}$) and for $\text{pH}\cong 7.5$, were presented as HPLC chromatograms in Fig. 2.

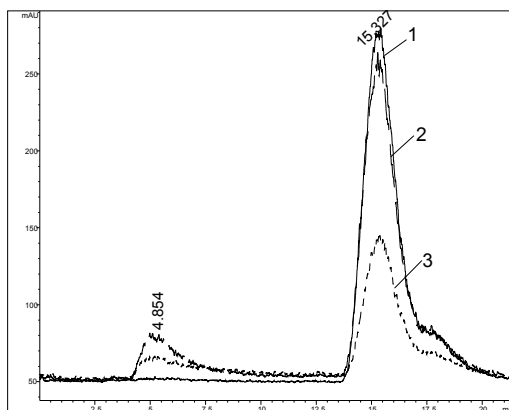


Fig. 1. HPLC radiochromatograms of $^{99m}\text{Tc}(\text{CO})_3$ -DPD, with different DPD : $[\text{}^{99m}\text{Tc}(\text{CO})_3(\text{H}_2\text{O})_3]^+$ ratios: 1:9 (1); 1:5 (2) and 1:2 (3) ($\text{pH}=7.5$, with heating)

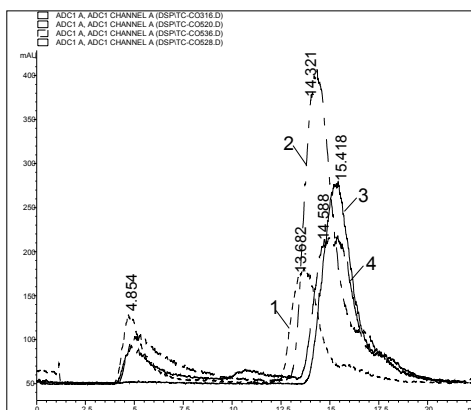


Fig. 2. HPLC radiochromatograms of different phosphate ligands labelled with $^{99m}\text{Tc}(\text{CO})_3$, at $\text{pH}=7.5$: IDP (1), PYP (2), DPD (3), HEDP (4)

The values of retention times, together with the labelling yield for each of Tc-carbonyl coordinated phosphate ligands, were presented in Table 1. Phosphate ligands have shown different bonding to tricarbonyl Tc(I) precursor, so obtained phosphate complexes have different retention times.

Table 1. Dependence of retention times and labelling yield for phosphate ligands coordinated to $[^{99m}\text{Tc}(\text{CO})_3]^+$ on pH

Ligand (L)	pH	5.5		7.5		
		^{99m}Tc -species	t_r (min)	Yield (%)	t_r (min)	Yield (%)
DPD	$[^{99m}\text{Tc}(\text{CO})_3(\text{H}_2\text{O})_3]^+$		4.8	31.7	4.8	0
	$^{99m}\text{Tc}(\text{CO})_3\text{-L}$		15.4	68.3	15.3	100
	$^{99m}\text{TcO}_4^-$		10.7	0	10.7	0
IDP	$[^{99m}\text{Tc}(\text{CO})_3(\text{H}_2\text{O})_3]^+$		4.7	58.8	4.7	31.0
	$^{99m}\text{Tc}(\text{CO})_3\text{-L}$		13.7	41.2	13.6	69.0
	$^{99m}\text{TcO}_4^-$		10.7	0	10.7	0
HEDP	$[^{99m}\text{Tc}(\text{CO})_3(\text{H}_2\text{O})_3]^+$		4.8	19.6	4.8	16.0
	$^{99m}\text{Tc}(\text{CO})_3\text{-L}$		14.7	39.5	14.6	42.0
			15.4	21.0	15.4	36.2
	$^{99m}\text{TcO}_4^-$		10.7	19.9	10.7	5.8
PYP	$[^{99m}\text{Tc}(\text{CO})_3(\text{H}_2\text{O})_3]^+$		4.8	64.1	4.8	15.4
	$^{99m}\text{Tc}(\text{CO})_3\text{-L}$		14.5	35.9	14.3	84.6
	$^{99m}\text{TcO}_4^-$		10.7	0	10.7	0

Conclusion

These investigations have shown that complexation of phosphate ligands with $[^{99m}\text{Tc}(\text{CO})_3(\text{H}_2\text{O})_3]^+$ precursor were depended on labelling conditions like volumetric ratio, pH of solution or heating of samples. It was not possible without heating. If the samples of phosphate ligands together with $^{99m}\text{Tc}(\text{I})$ precursor were heated in water boiling bath for thirty minutes, higher labelling yield was obtained at pH=7.5 than at pH=5.5, but there was no labelling at pH=2.5. The best results were obtained for molar ratio 1:9. Among investigated phosphate compounds, DPD was the best labelled ligand.

Acknowledgment

This paper has been financially supported from Ministry of Sciences, Technologies and Development of Serbia, under Project OI 1980.

$[^{99m}\text{Tc}(\text{CO})_3(\text{H}_2\text{O})_3]^+$ precursor (IsoLinkTM) was obtained from Tyco Healthcare, Mallinckrodt Medical B.V., The Netherlands.

References

- [1] B.G. Saha, Fundamentals of Nuclear Pharmacy, Springer-Verlag, New York, 1979.
- [2] R. Alberto, R. Schibli, A. Egli, A.P. Schubiger, J. Amer. Chem. Soc., 1998, 120, 7987.
- [3] R. Schibli, A.P. Schubiger, Eur. J. Nucl. Med., 2002, 29, 1529.

CALCIUM (Ca^{2+}) CONTENT IN THE LOWER JAWS OF RATS IRRADIATED IN THE HEAD REGION WITH X-RAYS

M. A. Demajo, D.S. Đorđević¹, I. S. Đujić¹

Institute of Nuclear Sciences "Vinča", P.O.Box 522, 11001 Belgrade,

¹*Institute of Chemistry, Technology and Metallurgy, Njegoševa 12, 11000 Belgrade, Serbia and Montenegro*

Abstract

Irradiating the head region of 8-day-old rats with a dose of 8.64Gy of X-rays, at the age of 42 days, results in stunting of lower jaw growth as illustrated by measuring the length and height of the jaws. This irradiation dose also has as a consequence an increased content of Ca^{2+} in the bone tissue of the lower jaw (270.36 ± 27.97 mmol/kg bone tissue) when compared to the corresponding non-irradiated controls (188.58 ± 19.26 mmol/kg bone tissue, $p < 0.05$) and rats irradiated with a dose of 3.84Gy of X-rays (143.99 ± 15.29 mmol/kg bone tissue, $p < 0.01$).

Introduction

It has been shown that in clinical radiotherapy, when the head region is in the field of radiation exposure, unwanted side effects may occur including adverse effects on the developing dentition [1]. Studies on rats serving as mammalian model systems, have also demonstrated that ionizing radiation affects the development of dentition in these animals by breaking the continuity of the incisor and stunting the full development of the third molar [2]. Changes in the content of magnesium [3] and selenium [4] was observed in the lower jaws of adult rats when their head region was irradiated with X-rays at the age of 8 days. Since calcium, together with magnesium and phosphorus is the main macro element constituting the skeletal tissue in the mammalian body, the object of this study was to measure the content of Ca^{2+} in the bone tissue of lower rat jaws after irradiating the head region of these animals with X-rays at the age of 8 days.

Materials and Methods

In the experiments, female rats of the Wistar strain were used. The heads of 8-day-old rats were exposed to a single dose of 3.84 Gy or 8.64 Gy of X-rays from a Siemens instrument (dose rate: 0.71355 Gy/min), details of the irradiation procedure and post-irradiation care of the animals is described elsewhere [3]. Non-irradiated animals of the same age served as controls. At the age of 42 days, all animals were sacrificed, the lower jaws removed and cleaned of surrounding tissue. Morphometric measurements were performed with a caliper. The jaw length (sagittal dimension) was defined as the distance between the incisival edge and *angulus-mandibulae*. The height was defined as the vertical distance between the position of the third molar and lower mandibular edge. Calcium in the previously mechanically ground jaws and ashed was measured by atomic absorption spectrometry (AAS). The Ca^{2+} content was

expressed as mmol/kg of rat jaw bone tissue. The results are expressed as the Mean \pm S.E.M. ANOVA was used followed by the Scheffe test to determine the statistical differences between the groups. The level of significance was set at $p < 0.05$.

Results and Discussion

As demonstrated in Table 1., the values for the length and height of jaws from rats irradiated with 8.64Gy of X-rays are significantly lower when comparing these morphometric parameters with those of non-irradiated controls and rats irradiated with 3.84Gy of X -rays.

Table 1. Morphometric measurements of the length and height of lower jaws in non-irradiated control and X-irradiated rats

Animals	length of jaw in mm.	height of jaw in mm.	statistical difference between the groups
1.Controls non-irradiated	23.60 \pm 0.15 (16)	4.44 \pm 0.11 (17)	1-2. $p > 0.1$ not significant
2.Irradiated-3.84Gy	23.63 \pm 0.32 (11)	4.52 \pm 0.10 (11)	2-3. $p < 0.001$ significant
3.Irradiated-8.64Gy	18.47 \pm 1.73 (8)	3.75 \pm 0.08 (8)	1-3. $p < 0.001$ significant

Mean \pm S.E.M.; ()-number of animals; p-statistical significance.

As illustrated in Fig. 1, the content of Ca^{2+} in the bone tissue of the lower jaw of non-irradiated control rats is 188.58 \pm 19.26 mmol/kg bone tissue. In rats irradiated with a dose of 3.84Gy, Ca^{2+} content is 143.99 \pm 15.29 mmol/kg bone tissue. The bone tissue of rats irradiated with a dose of 8.64Gy of X-rays, shows a significant increase of Ca^{2+} content (270.36 \pm 27.97 mmol/kg bone tissue) as compared to the intact controls ($p < 0.05$) and rats irradiated with a dose of 3.84Gy ($p < 0.01$). This accumulation of Ca^{2+} in the lower jaw of rats irradiated with 8.64Gy is similar to the accumulation shown previously in the case of magnesium [3] and may be also explained by the stunted jaw growth and lowered activity of the pituitary gland [5].

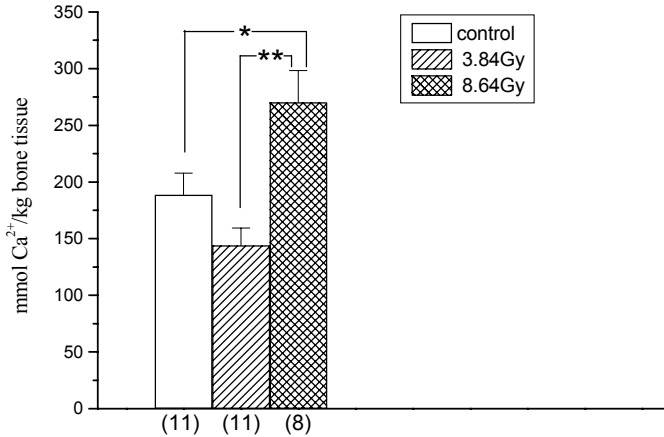


Figure 1. Ca²⁺ content in the bone tissue of rat lower jaws.
()-No of animals; *p<0.05, **p<0.01

Conclusion

Irradiating the head region of 8 day-old-rats with 8.64Gy of X-rays, at the age of 42 days, results in the stunting of jaw growth and a significant increase of Ca²⁺ content in the lower jaw bone tissue. This effect of the high irradiation dose applied may result not only from the direct action of X-rays on the bone tissue itself, but also as a result of damage to the pituitary gland which was in the field of irradiation.

Acknowledgement

This study was supported by the Serbian Ministry of Science and Environmental Protection, project No. 1956.

References

- [1] S.Doline *et al.*, J. Pediatr. Opthamol. Strab., 1980, 17, 109.
- [2] O.Karađžov *et al.*, Strahlentherapie, 1985, 161, 448.
- [3] M.Demajo *et al.*, Serb. Acad. Sci. & Arts, 1999, Sci. Meetings, Vol.XCII, No.1, 103.
- [4] M.Demajo *et al.*, J.Environ.Pathol.Toxicol.Oncol., 1998, 17, 301.
- [5] M.Demajo *et al.*, Jugoslov.Med.Biohem, 2003, 22, 11.

Materials Science

(G)

Ceramic microstructure induced by molecular precursors. The case of Boron Nitride: Adaptation of the precursor to the best properties for high technology applications.

Bernard Bonnetot and Sylvain Jacques.

*Laboratoire des Multimatériaux et Interfaces, University LYON I, UMR CNRS
5615, 69622 Villeurbanne Cedex, France.*

Abstract.

The vapour pressure and the boron/nitrogen ratio have been shown to be important factors for applications of BN in the electronics industry, and the more interesting precursors for the preparation of suitable BN materials seem to be aminoboranes. Thin layers of BN have been prepared from tris-dimethylaminoborane (TDMAB) and tested as high-gap semiconductors. Aminoboranes are also interesting for applications as fibre coatings in ceramic-ceramic composites: e.g. coatings of Hi-Nicalon fibres have been obtained from TDMAB but also using asymmetrical aminoborane. Aminoboranes have also been used in the sintering of Si_3N_4 -BN ceramics. Ground boron nitride is very difficult to sinter and the addition of tris-methylaminoborane (TMAB) enhances the compaction of the composites by about 10 %. The polymers obtained from aminoboranes were shown to be inefficient for the preparation of BN fibres. For this purpose, borazines and aminoborazines are more machinable. Micro-structured thin and long BN fibres were successfully prepared from poly-trimethylamino-borazine polymers (*p*MAB), although the ceramic yield of the polymer was lower than 60%. Attempts to enhance this ceramic yield using borazine were not successful. The use of poly-aminoboranes led to hollow fibres due to leaking of volatile by-products. A similar behavior was found for micro-structured BN powder. The obtained structure was related to the reactivity of the precursors, and nano-crystalline powders were prepared.

Introduction.

Boron nitride (BN) is one of the most studied non oxide ceramics, attracting a lot of interest due to its specific properties. Boron nitride is a white artificial ceramic described for the first time in the mid-1920s. It was obtained through high temperature reaction of boron with nitrogen [1] or from boron oxide and ammonia [2]. Boron nitride was expected to present a molecular analogy with carbon because the boron-nitrogen couple and the carbon-carbon bond present the same number of electrons. The analogy of C-C and B-N has been widely studied and discussed [3].

Several reviews [4-6] have been published dealing with the elaboration of boron nitride from molecular precursors for special applications. Some of the results gathered have given new outlooks into the possibilities of classical well-known molecules when subjected to clever ceramisation conditions.

The precursors of boron nitrides, apart from the gaseous mixture BX_3/NH_3 , consist of two main families of compounds: aminoboranes and borazines. Aminoboranes are small molecules composed from one boron atom surrounded by three amino group derivatives, as shown on Figure 1. The properties of the aminoborane are induced by the nature of the amino group and the nitrogen atom substituents. If large alkyl groups are grafted on the nitrogen atom, the vapour pressure of the compound becomes lower, but the chemical reactions of substitution by ammonia are favoured. If a substituent is a hydrogen atom, polymerisation can be induced, leading to larger molecules of the borazine group.

Borazines are benzene-like molecules in which $C=C$ groups are replaced by $B=N$ groups, as shown on Figure 2. If the boron and nitrogen atoms are only bonded to hydrogen, the obtained borazine has formula $B_3N_3H_6$ and properties quite similar to benzene C_6H_6 .

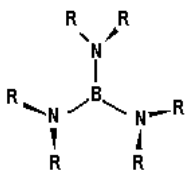


Figure 1 : Aminoborane structure

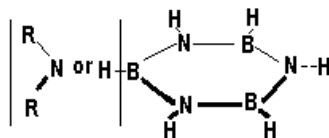


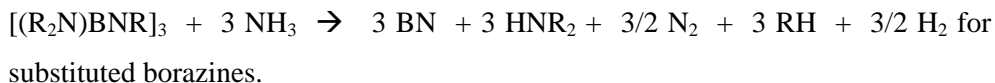
Figure 2 : Borazine structure.

The hydrogen atoms bonded to boron or nitrogen can be substituted, leading to a very large number of compounds with very different physical and chemical properties depending on the nature of the substituted atom on the borazine framework and on the substituent. Absolute rules relating the properties of the substituted borazine to the substituent have not been clearly established; moreover, some substituting groups can allow the formation of polymers.

The number, the nature and the properties of the precursors which can be prepared is virtually infinite. The choice of a precursor among this large number of possibilities is not obvious, and sometimes several precursors have been tested in order to choose the most convenient one after experimentation.

In all cases, the role of ammonia during the ceramisation is very important. In fact ammonia is a harder base than all the amino groups used as substituents on the precursor. A reaction takes place between the precursor and ammonia, leading to a drastic lowering of the carbon content of the deposited substrate. Using polymeric precursors, the reaction of decarbonation is slower and the ceramisation rate must be very slow.

The reactions leading to BN synthesis can be summarised as follows:



The experimental conditions for these reactions could be very different depending on the apparatus and on the intended applications.

The description of the precursors, their utilisation and the results obtained in our laboratory will be presented. Different possible ways in which the properties of the precursor can be adapted to the conditions will be related.

Boron Nitride coatings

The preparation of thin coatings covers a very large domain of applications.

Electronic devices [7].

If the coatings are intended for micro-electronics, the deposition must be realised from non corrosive species under conditions as soft as possible. Thin layers of BN have been deposited onto Si(0 0 1) substrates in a T-shape quartz reactor using only hydrogen as a carrier gas and TDMAB as molecular precursor. The precursor feed was 1 to 5×10^{-5} mol.mn⁻¹, and the apparatus was kept under atmospheric pressure. The thickness of the film varied from 5 to 70 nm for deposition temperatures between 700 and 1000°C during runs of 2 to 3 hours. The BN growth rate is given on Figure 3, and the surface morphology studied using AFM on Figure 4.

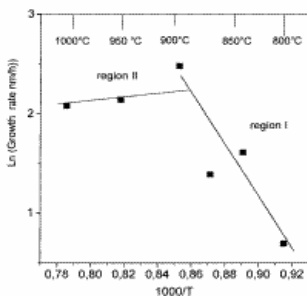


Figure 3 : BN growth rate as a function of the temperature.

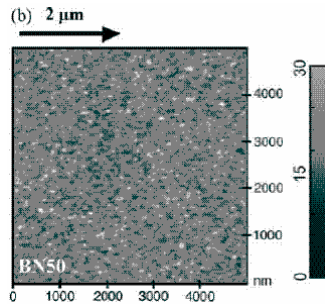


Figure 4 : AFM surface morphology Of the sample obtained at 900°C

BN coating of fibres for ceramic-ceramic composites [8].

Ceramic-ceramic composites composed of high modulus fibres, such as SiC Hi-Nicalon fibres, and a ceramic matrix, usually SiC, are promising high technology materials but they are brittle. To bring robustness to the composite, a thin film of material called "interphase" is added between the fibre and the matrix. The best results were obtained using lamellar interphases such as pyrolytic carbon. Unfortunately the resistance of the composite to high temperatures is drastically lowered by the carbon combustion. BN is also a good candidate, but the coatings obtained from corrosive precursors like the BF₃/NH₃ mixture affect the properties of the fibres. BN interphases of about 150 nm thickness have been obtained using Low Pressure CVD (at 20 hPa) in a horizontal hot-wall reactor at 1100°C during 90 s. TDMAB vapour was carried by hydrogen, and ammonia was added in order

to remove the carbon moieties. The composites were obtained by imbedding the coated fibres into a SiC matrix obtained by low pressure deposition at 950°C from a CH₃SiCl₃/H₂ gas mixture. The SiC/BN/SiC mini composites were tensile tested at room temperature with unload-reload cycles using a machine equipped with a 2 kN load cell. The samples exhibited high resistance and very low brittleness. When cracks appeared, TEM was used to characterise the influence of the interphase. Figures 5 and 6 show a crack deviation by the interphase and the partial debonding of the matrix and fibre.

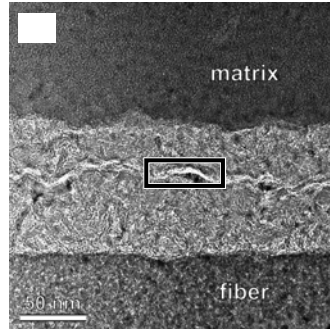
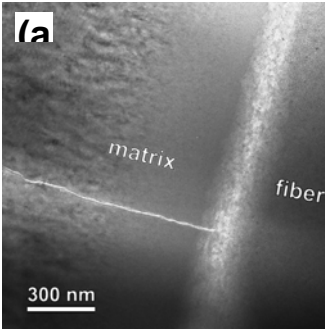


Figure 5 : Crack deviation by the interphase. Figure 6 : Matrix debonding.

Carbon protection by thick coatings. [9]

Another coating application is the oxidation protection of carbon substrates, usually graphite. For large substrates, the CVD technique becomes too difficult to handle, and coating is performed using dip-coating. This has been realised using aminoborazine precursors. Trimethylaminoborazine was polymerised in order to obtain a very mobile liquid phase, into which graphite pieces were dipped. The thermal treatment was carried out under pure ammonia up to 1100°C, followed by annealing up to 1500°C under nitrogen. Figure 7 shows a micrograph of a sample in which the BN/C interface composition was measured, showing a penetration of the nitride into the carbon. This was related to the precursor composition containing a large amount of hydrocarbon moieties, allowing a good wetting of the graphite.

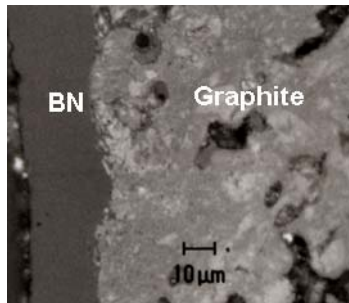


Figure 7 : thick coatings obtained from poly aminoboranes over graphite.

Boron Nitride fibres.

BN long and thin fibres [10].

Long and thin BN fibres have been obtained from poly-methyl-aminoborazine. This precursor has no substituent on the cycle nitrogen atoms, and on the boron atoms of the cycle, easily polymerised methylamino groups, evolving methylamine and yielding a polymer where the borazine cycles are bonded through amino bridges. The spinning of the polymer was realised at about 180°C and, from the extruded 200 µm fibre, an appropriate stretching led to a crude 20 µm polymeric fibre rolled onto a 10 cm diameter graphite spool. The ceramisation into carbon-free BN was achieved through a two-step thermal and chemical treatment, first up to 650°C under a pure ammonia atmosphere followed secondly by a heating up to 1100°C under nitrogen. To stabilise and crystallise the fibres, an annealing up to 1800°C was performed under a nitrogen atmosphere. Long and thin fibres (about 200 m long for a monofilament of 10 µm of diameter) are usually obtained with a 1.5 GPa resistance at room temperature. Figure 8 shows a TEM picture of an obtained fibre, showing clearly crystallised micro-domains.

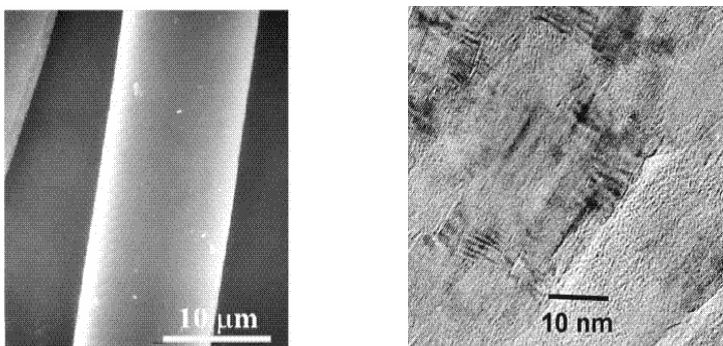


Figure 8 : SEM and TEM photographs of a BN fibre

BN fibres obtained from other precursors.

Mixture of borazine and aminoborane precursors. [11]

To enhance the ceramic yield of the MAB derivative precursor, attempts have been made to obtain a highly condensed precursor by reaction of borazine with aminoborane in various proportions. Few of the obtained compounds could be spun, and only a 90 wt% MAB / 10 wt% borazine mixture reacting for 15 hours at 75°C led to a polymer which could be extruded and stretched. The fibres obtained do not have good mechanical properties, and the stretching of the fibre to get 20 µm crude fibres led to numerous breaks in the thread. When ceramised, the surface of the fibres became irregular, and BN whiskers could be seen at the surface (Figure 9). This was related to the ceramisation of the polymer, as studied using TGA, where a very long plateau could be characterised, corresponding to partial decomposition of the polymer into borazine which transformed into BN outside of the fibre.



Figure 8 : Fibres obtained from the Precursor mix MAB / borazine.

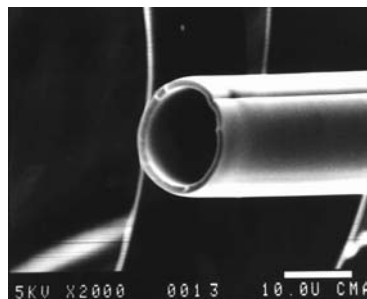


Figure 9 : fibre obtained from a poly-aminoborane precursor

Poly-aminoborane precursor [12]

Polymerisation of triisopropylaminoborane made it possible to obtain a spinnable polymer, leading under very easy conditions to 20 μm crude fibres. During the ceramisation, hollow and very brittle fibres were obtained (Figure 10). This was related to the ability of the precursor to lead to BN if ceramised very slowly at low temperature, or to a volatile borazine at higher temperature, leading to these strange fibres. The skin thickness was related to the duration of the low temperature ammonia treatment.

Boron Nitride powders.

The aim of this work was to prepare high surface area BN powders to be used as thermally conducting catalyst support. In fact, when BN is ground, the powders obtained present low surface area because hexagonal BN form platelets which are resistant to grinding. Three different precursors were tested, and the crystallinity and surface area of the resulting powders could be related to the nature of the precursor [13].

MAB precursor : Polyaminoborazines lead to low surface area powders, showing large pores surrounded by a glassy skin as shown in Figure 11. This was related to the good ability of aminoborazine polymers to remain waxy up to high temperatures, building a hard BN skin surrounding a nano-porous body..

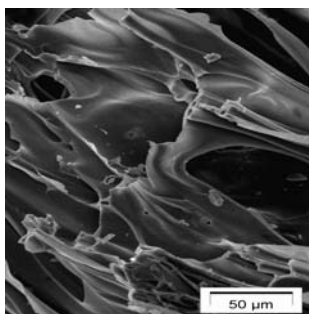


Figure 10 : BN foam obtained from polyMAB precursor.

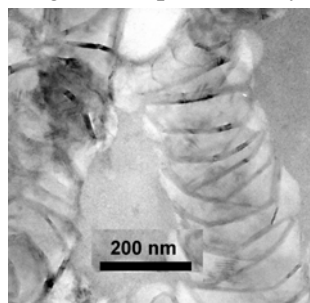


Figure 11 : TEM micrograph of BN Powders obtained from polyborazine.

Polyborazine precursor : Using polyborazine as precursor, fine powders were obtained but with a poor yield because ammonia leads to a partial decomposition of the precursor into smaller volatile molecules. The crystallinity of the obtained BN is much higher than using other precursors, and the microstructure determined using TEM observations consists of highly crystallised zones and some poorly organised parts, as shown in Figure 12.

Polyhaloborazine precursor : The last type of precursor tested is polyhaloborazine derived from trichloroborazine [CIBNH]₃. This substituted borazine reacts with ammonia, leading to a solid complex 6NH₃-[CIBNH]₃ which decomposes into BN and NH₄Cl. The powders obtained above 600°C are only composed of BN. However an annealing up to 1800°C is required to stabilise the BN powder. The obtained powder presents a surface area of about 200 m².g⁻¹, and it has been shown to be very stable to moisture and oxidation. SEM and TEM micrographies show a granular ball structure as evidenced using SEM (Figure 13), and a nanostructure of organised BN planes as characterised by TEM (Figure 14).

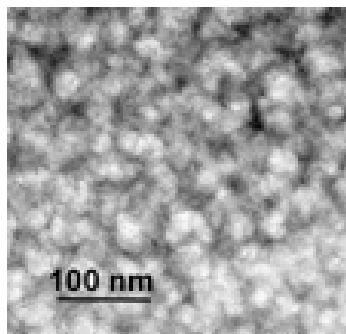
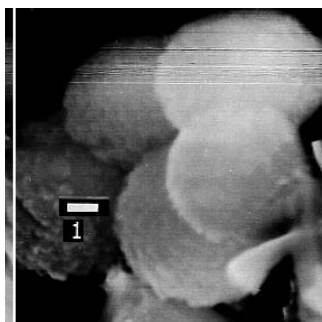


Figure 12 : SEM micrography of BN powders obtained from haloborazines

Figure 13 : TEM micrography of BN powders obtained from haloborazines

For catalytic application, the powders obtained from polyhaloborazine were the more promising and the synthesis from trichloroborazine is quiet easy. Sufficient amount of BN powder can be prepared to permit palladium deposition and catalytic tests [14].

Conclusions

The preparation of boron nitride for high technology application could be realised using appropriated molecular precursors. In fact each application requires special properties as vapour pressure, reactivity, physical properties which can be improved by smart substitutions on the precursor molecular framework. The precursors must be adapted to the purpose and the technical conditions of the utilisation. It is also possible to favour properties of the obtained nitride by a judicious choice of an appropriated precursor.

Literature

- [1] R. Lorenz, J. Woolcock, *Z. Anorg. Chem.*, 1928, 176, 289.
- [2] E. Podszus, *Z. Anorg. Chem.*, 1933, 211, 41.
- [3] Gmelins Handbuch der Anorg. Chem., Num. 13, Verlag Chemie GMBH Weinheim/Bergstrasse, 1954.
- [4] R. Reidel, *Naturwissenschaften*, 1995, 82, 12.
- [5] R.T. Paine and C.K. Narula, *Chem. Rev.*, 1990, 30, 71.
- [6] R.T. Paine, and L.G. Sneddon, *Chemtech.*, 1994, 7, 29.
- [7] Dumont Herve; Bayle, Beatrice; Bonnetot, Bernard; Bouix, Jean. *Mat. Research Bull.* 2002, 37, 1565. Dumont, H.; Bayle, B.; Bonnetot, B. *Physica Status Solidi C: Conferences and Critical Reviews*, 2003, 7, 2470.
- [8] S. Jacques, B. Bonnetot, M-P. Berthet and H. Vincent, *Proc. 28th International Cocoa Beach Conference & Exposition on Advanced Ceramics & Composites, Fla, USA, January 25-30, 2004*, (in press)
- [9] Cornu, David; Miele, Philippe; Toury, Berangere; Bonnetot, Bernard; Mongeot, Henri; Bouix, Jean, *Journal of Materials Chemistry*, 1999, 9, 2605. Bonnetot, B.; Guilhon, F.; Viala, J. C.; Mongeot, H. *Chemistry of Materials*, 1995, 7(2), 299.
- [10] Vincent, H.; Chassagneux, F.; Vincent, C.; Bonnetot, B.; Berthet, M. P.; Vuillermoz, A.; Bouix, J. *Materials Sci. & Engineering, A*, 2002, A340, 181.
- [11] Duriez, Christophe; Framery, Eric; Toury, Berangere; Toutois, Pascaline; Miele, Philippe; Vaultier, Michel; Bonnetot, Bernard. *Journal of Organometallic Chemistry* 2002, 657, 107.
- [12] Cornu, David; Miele, Philippe; Faure, Rene; Bonnetot, Bernard; Mongeot, Henri; Bouix, Jean. *Journal of Materials Chemistry* 1999, 9, 757. Miele, P.; Cornu, D.; Toury, B.; Toutois, P.; Bonnetot, B.; Bouix, J.; Mongeot, H. *Special Publication - Royal Society of Chemistry*, 2000, 253, 84.
- [13] Perdigon-Melon, Jose Antonio; Auroux, Aline; Guimon, Claude; Bonnetot, Bernard. *Journal of Solid State Chemistry*, 2004, 177, 609. Perdigon-Melon, Jose Antonio; Auroux, Aline; Cornu, David; Miele, Philippe; Toury, Berangere; Bonnetot, Bernard. *Journal of Organometallic Chemistry*, 2002, 657, 98.
- [14] Perdigon-Melon, Jose Antonio; Auroux, Aline; Guil, Jose Maria; Bonnetot, Bernard. *Studies in Surface Science and Catalysis*, 2002, 143, 227.

THE BASIS OF PHYSICAL CHEMISTRY, PROPERTIES OF TWO-DIMENSIONAL SOLIDS

T. M. Nenadović and M. T. Nenadović

Institute of Nuclear Sciences "Vinca", Belgrade, Serbia

Abstract

Advanced surfaces provide opportunities to develop new surface materials and surface technology. The recent development of hyperfine surface structure - clean surface, thin films and nanophase structures – as well as sophisticated analytical tools, opened up atomic/molecular studies of surface phenomena and new application.

Introduction

Today materials science is an interdisciplinary science. It include physical, chemical and engineering processes from microscopic to atomic levels. Sophisticated analytical instruments and theoretical understanding of materials has shown three important points: a.- material has a structure (a particular arrangement of internal components), b.- material have a range of properties (characteristic responses to external stimuli) and c.- by processing through nonequilibrium state it is possible to change a materials properties.

The physical chemistry is the border line subject between pure physics, chemistry and material science. Since the first scientific journal on the subject (*Zeitschrift fur Phsicalische Chemie*, 1887) it start to be an interdisciplinary science applicblle to the problems of physics, chemistry and material science. For all of these sciences, surface properties remain the most interesting subject of research and applications.

Surface science does not have such a long history as material science[1]. The birth of surface science can be the fact studied in 18th century by B. Franklin – the spontaneous spreading of oil on water. The use of surface chemical processes (catalysis, J. Dobereiner, G. Kirchhof, J. Berzelius) began in the early years of the 19th century. The studies of tribology, coincide with the industrial revolution when moving parts became prevalent. (Some understanding appears at 16th century - Leonardo da Vinci). The existence of polyatomic or polymolecular aggregates- colloids – was described by T. Graham, in 1861.

Thin solid films on surface were first obtained by electrolysis and chemical reactions. The first evaporated thin films/coatings were obtained by M. Faraday in 1857, when he exploded the metal wires in inert atmosphere. Crooks discovered the possibility of sputter-deposition of thin metal films in glow-discharge tube. In 1903 A. Wehneld discovered that poorly emitted metal cathodes when coated with barium or other alkaline earth oxides produce current million times greater than uncoated metal. In 1914 I. Langmuir and W. Roger showed that tungsten wire containing a little

thorium – after a heat treatment – could emit a current 10^5 times higher than pure tungsten at the same temperature.

The scientific curiosity in the properties of **two-dimensional solids** has led to the development of different types of surface materials. Recent development of hyperfine surface structures - **clean surfaces, thin films and nanophase structures** - opened atomic/molecular studies of surface phenomena and new applications[2].

Clean surface

In characterization of solids, the most important area of interest is to define the state of the surface – a **market discontinuity** from one material to another. At the beginning, surfaces are modeled as *sharp discontinuities*. In 1866, H. Sorby found that the *crystalline structure* of fractured surface depends on chemical composition and thermal treatment. *Terrace model* (1950) revealed that the surface is rough. *Clean surface* has been studied from 1960 when ultrahigh vacuum system and new experimental technique, made possible the molecular and atomic level investigation. Low energy incident beams provide a unique opportunity for investigation of physics and chemistry with surfaces. Such experiments bridge the gap between chemisorption and adsorption ($E < 5\text{eV}$) and sputtering and implantation ($E > 100\text{eV}$). Depending on the energy of incoming particles or chemical environment the surface atoms move/adjust their position on the bulk. In characterisation of any real surface the **surface depth** is defined by the choice of characterization method – from one atomic layer to few microns[3].

Surface materials can be divided in *two groups*: those that utilize **external surface** and **microporous materials** where most of the surface resides in internal pores. Surface atom concentration may vary depending on the crystal structure and crystal face also. The *concentration of atoms/molecules* at solid surface can be estimated from the bulk density. For a bulk density of water/ice of 1g/cm^3 , the molecular density is $5 \cdot 10^{22} \text{ mol/cm}^3$. The surface concentration assuming cube-like packing $C = \rho^{2/3} \approx 10^{15} \text{ mol/cm}$ [4].

Clean surfaces are fastly covered with particles from surrounding atmosphere. From the kinetic theory of gasses, the flux F of atoms/molecules striking the surface of unit area at ambient pressure P is given by:

$$F = \frac{N_A \cdot P}{2\pi MRT} \quad F(\text{at/cm}^2/\text{s}) = \frac{3.51 \times 10^{22} \cdot P(\text{Torr})}{[M(\text{g/mol})]^{1/2}}$$

where: M is the average molar mass of gaseous species, T – temperature in Kelvin, N_A – Avogadro's number and R – gas constant. Using the value for nitrogen molecule for which $M = 28 \text{ g/mol}$, room temperature $T = 300 \text{ K}$ and Avogadro's number $N_A = 6,02 \cdot 10^{23} \text{ molecules/mol}$ one obtains $F = 10^{15} \text{ molecules/cm}^2/\text{s}$. To keep the surface clean for 1s or 1h the flux of incident particles (atoms/molecules) must be less than 10^{15} or $10^{12} \text{ particles/cm}^2/\text{s}$. At UHV conditions ($1,33 \times 10^{-7} \text{ Pa}$) it takes 10^3 seconds before a surface is covered completely with the particles from ambient forming an interface.

The *residence time* of an adsorbed atom on the substrate is given by $\tau = \tau_0 \exp(\Delta H_{ad} / RT)$

where τ_0 is correlated with surface atom vibration times (10^{-12} s). The surface concentration σ at/cm² of adsorbed particles on clean surface: $\sigma = F\tau$, where F is the incident flux.

Microporous materials have very large internal surface area. Crystalline alumina silicate (zeolites) have ordered cages of molecular dimensions where molecules can adsorb. Graphite and coal have porous structure with pore diameters $10^2 - 10^3$ nm and very large surface area (100-400 m²/g of solid). Bones of mammals (made of calcium apatite) have highly porous structure with pore diameters of 10 nm.

For theoretical considerations when the surface is covered with 10^{15} atoms/cm² we usually say that the surface is covered with **monoatomic layer**. However, it is not the case. The atoms of the deposited layer are never distributed as a monoatomic layer. They diffuse and form three dimensional nucleus and clusters. Particles of finite size are described as *dispersion* D ($D = N_s/N_{tot}$ number of surface atoms/total number of atoms, Fig.1). Only for small nucleus D is unity, while for cluster D decreases with the number of atoms.

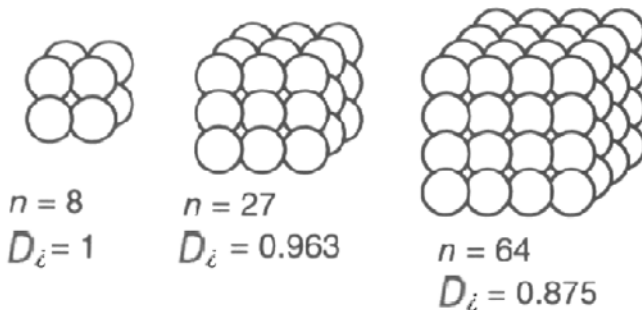


Fig.1. Number of atoms in the cluster (cubic crystal).

Finally, we must point-out that surface structure differs from the bulk structure. Three phenomena occur at clean surfaces: relaxation, reconstruction and modification [5].

Relaxation. By relaxation of metal surfaces, the first layer of atoms moves inward and leads to a shortened interlayer spacing between the first and second layer of the surface (Fig.2). On rough surfaces, the atoms relax in order to smooth irregularity. At ionic crystals, two ions move in a way that the positive and negative ions are almost coplanar.

Reconstruction. The atoms at the surface move not only perpendicular but also in the parallel direction. This often leads to new unit cells. Surface structure of Pt, Au and Ir (100) that should have square unit cells reconstruct to form hexagonal surface unit cells.

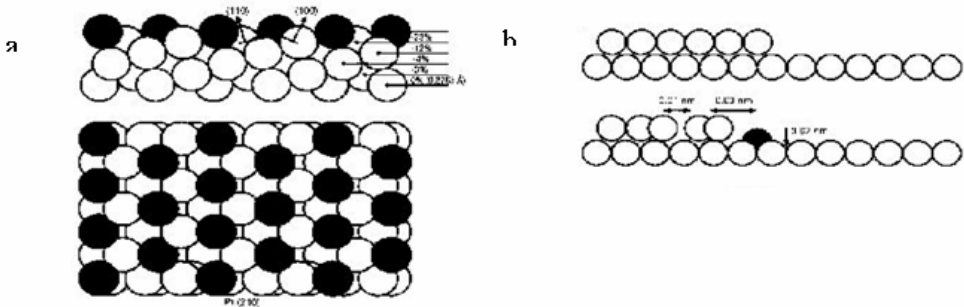


Fig. 2 (a and b). a- Relaxation at the clean crystal surface Pt (210), b- Restructuring at a step site; each atom attempts to optimize its coordination.

Modification. When energetic particles strike a solid surface, many kinds of interactions occur: desorption from surface, deposition of beam particles, the emission from solids, projectile implantation and momentum transfer to the target atoms[6]. All these processes are energy dependent and lead to a relocation of target atoms (Fig.3).

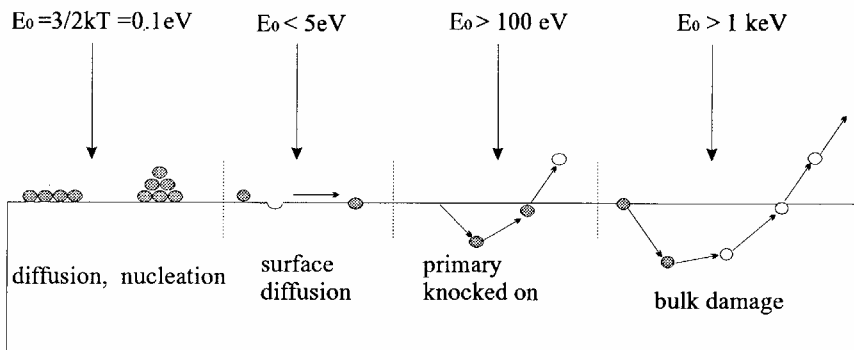


Fig.3. Simplified comparison of the incident particle path for: a and b – low energy beam, c- medium energy beam and d- high energy beam activated reaction.

Hyperthermal particles arriving at the surface dissipate their energy within a small area. Adsorbed particles can migrate over the surface and then aggregate. For higher energies, beam surface modification processes are important. Penetration depth of the beam particles into material allows modification of the materials due to requirements.

Chemical sputtering with small energies is observed, when the impinging particles react with target atoms producing a volatile chemical compound.

Physical sputtering occurs at incident energies of few hundred eV and higher [7]. Low-energy beams, with the incident energy E_k of the order of a few tens eV, can be used for direct film deposition on surfaces if two conditions are satisfied: 1. the

atom/ion sticking probability is higher than the sputtering probability, and 2. the reaction product is not volatile.

Surface modification technique has been applied mostly in semiconductor technology. Implantation of Y into the near-surface region improves the mechanical properties and the resistance to oxidation of stainless steel; implantation of N₂ reduced the coefficient of friction and increases the hardness of surface. The ion beam processing can alter biomaterial characteristics also (surgical implants).

Thin films

Thin film studies have advanced many new area of research. A number of methods have been developed—physical and chemical vapor depositions, electroplating and spraying—to prepare thin films/coatings of different types of materials. *Properties* of deposit depend on starting material, method used, vacuum, deposition condition, properties of the substrate and final thickness. The fundamental relationships between processing parameters and microstructure, as well as between microstructure and thin film/coating properties are important to determine the system quality and actual applications.

Physical and chemical vapor depositions are the most commonly used methods for deposition of different type and structure of thin films. Since the gaseous material-evaporated and sputtered- are very sensitive to the presence of impurities it is necessary to work at high vacuum condition to obtain high-quality thin films/coatings.

The *deposition* of thin films/coatings in vacuum consists of *several steps*: transitions of solid or liquid phase in the gaseous phase; transport of gaseous material from vapor source to substrate at low pressure; condensation of vapor phase on the appropriated substrate.

The first *characterization of thin film* structural characteristics includes the analysis of homogeneity as a function of thickness of deposited material[8]. Four stages characterizing the distribution of condensed material are mostly evident. The first stage (up to 10 nm for Au) consists of three-dimensional islands. By further deposition the islands grow, the nuclei coalescence and empty channels (with 5-20 nm) randomly distributed on the substrate are formed. If the thickness is higher than 30 nm (for Au, depend on materials T_m) a thin film is continuously deposited on the substrate. Microstructure, sizes, shapes and orientation of crystal grains and morphology of the surface material are strictly thin film phenomena, depending on deposition parameters and substrate properties (Fig. 4).

Depending on the physico-chemical properties of the substrate and the deposition parameters, various type of growth can occur: island growth (Volmer – Weber mechanism); layer growth (Frank – Van der Merwe); and island - layer growth (Stranski – Krastanov). The microstructure of coatings may vary from defect free single crystals (on single crystal substrate) to highly columnar and faceted structure.

The major application of thin film components is in integrated thin-film networks. Circuits consisting of thin film resistors (NiCr), capacitors (Ta₂O₅), contacts (Al, TiPd, Au), and interconnections are produced for different purposes

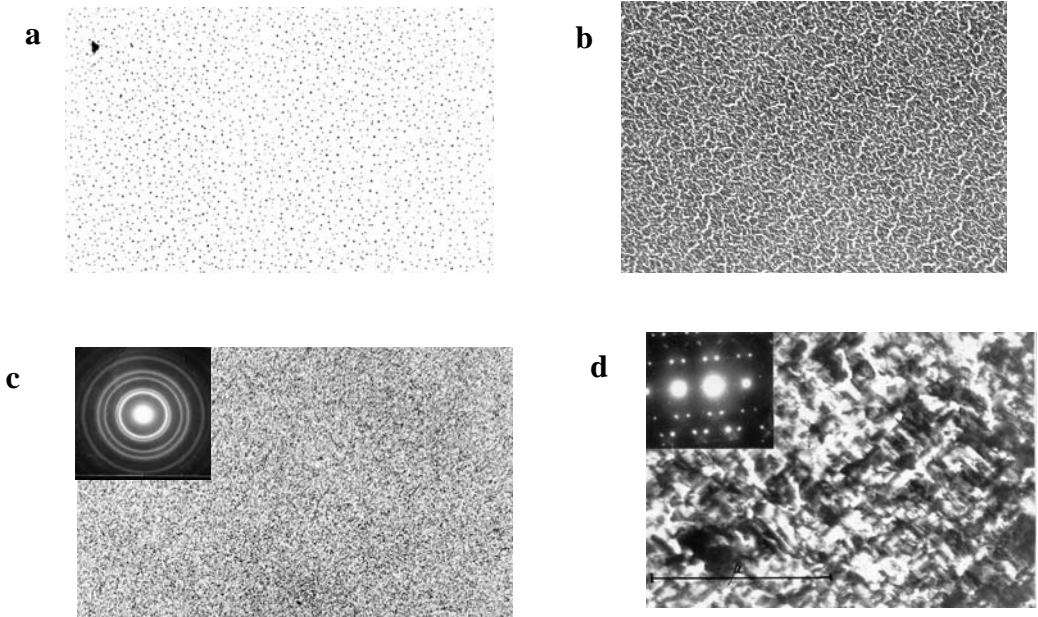


Fig.4 (a – d). Steps of the thin film/coating growth presented schematically: a-formation and coalescence of islands, b-the large islands growth, c-the channels and holes, d-continuous film/coating.

A large variety of deposited thin films/coatings grown by PVD technique has the high level of application: optically functional thin films (mirrors and lenses), energy transmission thin films/coatings (solar absorbers architectural glass), electrically and magnetically functional thin films (active devices, photovoltaic solar cells) mechanically functional coatings (hard, tribological, lubricant), chemically functional coatings (corrosion protective, thermal barrier) and decorative coatings (jewellery, toys, papers). The most frequently investigated mechanical properties of thin films/coatings are their adhesion to substrates, mechanical stresses and their tensile properties.

Nanophase structures

The properties of material are not determined only by chemical composition, alloying, cold working, annealing or deposition method. Ordered array of atoms and idealized structures can not explain all observed material properties. *Unique properties are based on deviation from ideal crystal structure.* It was found that fine grain size, presence of crystal of second phase or repetitive structure of deposited thin films improve material properties. The interface between individual grains, different phases or deposited layers, act as barriers to the motion of dislocation and are mainly responsible for plastic deformation of crystalline solids. Fine grain material is harder and stronger because surface/interface atoms are not bonded to the

maximum number of neighbors and are in higher energy state than interior atoms. The dependence of yield stress σ on the grain size varies approximately according the relation:

$$\sigma = \sigma_0 + kd^{-1/2},$$

where σ_0 is applied stress, k and d are constant for particular material.

The necessity for more efficient uses of materials invites a close look at **nanophase structure** of materials. Nanoparticles represent surfaces in three dimensions. The explosion of scientific and industrial interest in these materials arises from their properties.

Fine grain size – less than 10 μm to few nm – are produced by many methods: superplastic forming (from prealloyed fine powders), hot isostatic pressing (explosion), mechanical alloying (welding in a high-speed ball mill), rapid solidification (splat cooling and laser-glazing) and some other techniques.

Nanostructured materials may be defined as materials whose structural elements have dimensions in the range from 1 nm to 100 nm [9]. *Nanocrystal* is a fragment comprising between a few and few tens of atoms. The cluster synthesis can be done by: gas-phase synthesis (clusters are formed in the gas phase and then deposited - Ag cluster on graphite); self-assembled clusters on surfaces, Stranski – Krastanov and Wolmer – Weber growth (GaAsAl sandwich, vertical InAs nanocluster on GaAs) and colloidal synthesis of nanoclusters (Au and Ag colloids, cluster-cluster and cluster-surface interaction). The advances in nanocrystal synthesis have been made in: development of techniques for obtaining nanocluster of various compositions, passivation of cluster surface and for their assembly into well-ordered nanostructured solids.

The **properties of nanophase materials** depend not only on crystal size, but also on crystal surfaces and grain boundary characteristics. In this region dislocation change the direction of motion and the slip planes must overcome this discontinuity. The critical stress σ_c required to move a dislocation across the interface is given by: $\sigma_c = (E_A - E_B) / (E_A + E_B)$.

There is repulsive forces that increase as dislocations in a layer with smaller modulus (the ratio stress to strain) E_B approach the interface with the layers with larger modulus E_A .

It has been suggested that a high strength material could be obtained by deposition of layered structure of two materials with the same crystal structure [10]. Soon after, by deposition of two thin films TiN/NbN with nanometric thickness, superlattice structure of high hardness was obtained. **Superhard superlattices** are characterized by bilayer repeat period λ (Fig.5.). The material is scientifically and technologically very interesting. Hardness of TiN/NbN with $\lambda = 4,6$ nm is almost equal with highest hardness cubic BN (50 GPa). The structure of deposited TiN/NbN is easily produced by sputtering.

Two hardest known materials diamond ((80 – 100 GPa) and BN (50 GPa) have many applications (tribology, protection of engine components and cutting tools). However, diamond is etched by O_2 in air at high temperature. Sintetizing of cubic BN is difficult. New methods (three-dimensional surface science) provide opportunities to replace naturel materials with manmade materials.

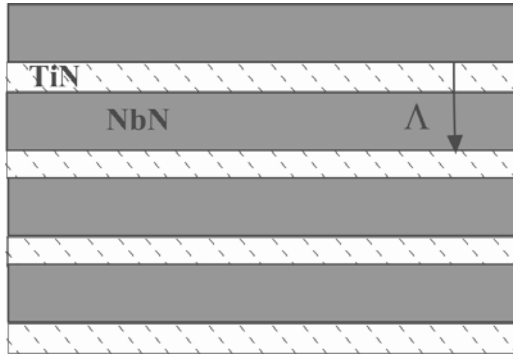


Fig. 5. Cross-section through a single-crystal superhard superlattice TiN/NbN with bilayer repeat period $\lambda = 5$ nm.

Comparing with crystalline material of the same composition, nanophase structures have lower density about 10 – 25%. The crystallites of nanophase materials have polygonal or lens shaped structure and their physical characteristics can be easily calculated: constituent volume $V = \pi d^3/6$, surface area $P = \pi d^2$, mass $m = \pi d^2 \rho/6$, molar mass $M = N_a \pi d^2 \rho/6$ and molar volume $V_m = MV/M$.

Conclusion

Hyperfine surface structure stands as a critical element in the resolution of the problem of the finiteness of resources, the scarcity of strategic materials and competitiveness in the market. The obtained results in advanced surfaces and materials are the basis of research into smart structures and intelligent material systems. No results have been published yet on smart and intelligent functional system, although some components of such system have been demonstrated. A complete smart material system would contain: sensor, actuators, signal processors, communication network and energy source. Many technological problems need to be overcome before applications reach the market.

References

- [1] Y. Quere, *Physique des Materiaux*, Elipses, Paris, 1988.
- [2] T. Nenadovic, *Oplemenjeni materijali*, BIGS-Galaksija, Beograd, 2001.
- [3] J. Hudson, *Surface Science*, Butterworth, Boston, 1992.
- [4] T. Nenadovic, *Materials and Technology*, 2002, 36, 91-100.
- [5] G. Samorjai, *Introduction to Surface Chemistry*, J. Wiley, New York, 1994.
- [6] T. Nenadovic, B. Gakovic, B. Todorovic, T. Jokic, *Nucl. Instr. Methods*, 1996, 115, 523.
- [7] T.M. Nenadovic, *Fizika*, 1989, 21, 392.
- [8] T. Nenadovic et al., *Bulletin T. CXV Ac. Serbe Sci.*, 1998, 37, 49.
- [9] P. Moriarty, *Rep. Prog. Physics*, 2001, 64, 297.
- [10] A. Madan et al., *Phys. Rev. Letters*, 1997, 78, 1743.

REACTIONS RESPONSIBLE FOR MASS LOSS DURING PRESSURE LESS SINTERING OF Si₃N₄ CERAMICS WITH LiYO₂ ADDITIVE

B. Matović, A. Vučković, D. Bucevac and S. Bošković

INN Vinča, Material Science Lab. 11001 Belgrade

Abstract

The reactions were investigated with emphasis on the mass loss during pressureless sintering of Si₃N₄ ceramics without powder bed. A Si₃N₄ powder compacts with LiYO₂ additive were heat-treated at different temperatures under the pressure of N₂ of 0.1 MPa. The mass loss increased with increasing temperature as well as with increasing additive content. It is expected that the major mass loss should be caused by volatilisation of lithia due to its high vapour pressure. However, the results of the chemical analysis of the samples are in contradiction with this assumption.

Introduction

Since silicon nitride is a covalently bonded solid compound, the self-diffusivities of Si and N in pure Si₃N₄ are very small [1], therefore it cannot be sintered to full density without additives which form liquid phase upon firing [2]. Thus, liquid-phase sintering is the only method applied for densification of Si₃N₄ ceramics. However, during sintering loss of mass occurs, which is common phenomenon with Si₃N₄ [3]. Si₃N₄ is not getting melt; it decomposes under 0.1 MPa N₂ at 1880° C. The reaction during decomposition according to the formula [4]:



is of increasing importance above 1500° C. In addition, it should be born in mind that sintering additives, which form silicate or oxinitride liquid during the sintering evaporate, as well [5]. The mass loss leads unavoidably to composition change. Moreover, it disturbs the consolidation, causes creation of pores and hence degrades the mechanical properties of the ceramics [6]. For these reasons it is very important to decrease mass loss as much as possible.

The objective of the present work is to examine the mass loss during the pressureless sintering of Si₃N₄ ceramics with LiYO₂ additive.

Experimental

The starting powders were commercial Si₃N₄ (Silzot HQ) and homemade LiYO₂ powder. Si₃N₄ powders with 5, 10, 15 and 20 wt% LiYO₂ were prepared. Sintering was accomplished in a graphite-heated furnace (FCT, Germany) under 0.1 MPa nitrogen atmosphere, in the temperature range from 1550° to 1700°C, with a heating rate of 10 K/min. Chemical analysis by inductively coupled plasma-optical emission spectrometry (ICP-OES, Spectro, Germany) was used to quantify

the Li content of samples after various heat treatments. Mass loss (Δm) of the specimens was calculated according to the following formula: $\Delta m = [(m_G - m_S) \div m_G] \cdot 100$, where m_G = mass of the green body.

Results and Discussion

The mass loss upon sintering with different amounts of LiYO_2 additive is shown in Fig. 1. The loss increased with increasing temperature, as well as with increasing additive content. Larger amount of additive means the larger amount of the liquid phase which in turn, leads to more intensive evaporation. At 1550°C total amount of additive is converted into liquid forming Si-Li-Y-O-N melt. It can be assumed that the vaporization of liquid originates from the vaporization of each of its constituents. Also, reactions between Si_3N_4 and the glassy phases are responsible for the instability of Si_3N_4 ceramics at elevated temperatures. However, Y_2O_3 is stable based on thermodynamic calculations [7]. In contrast, the high vapour pressure of lithia causes its easy evaporation as mentioned earlier.

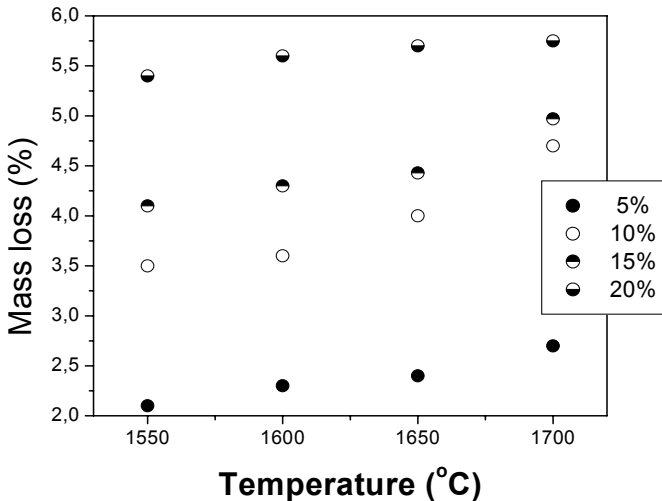
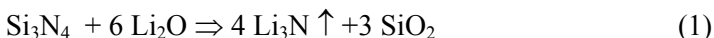


Fig. 1. Mass loss as a function of temperature for Si_3N_4 compacts with different amounts of LiYO_2 additive during sintering with a holding time of 5 min.

It is expected on the basis of the vapour pressure data for Li_2O [8] that lithia should volatilise completely at higher temperatures. However, the results of the chemical analysis of the samples are in contradiction with this assumption (Fig.2). With increasing the LiYO_2 additive the Li_2O content decreases significantly with temperature. However, Li_2O is still present after long annealing times, at all sintering temperatures.

It is known that lithia reacts with Si_3N_4 to give a very volatile lithium nitride (Li_3N) according to the reaction [9]:



The silica formed in reaction (1) combines with unreacted Si_3N_4 [10] according to the reaction (2)



This reaction is well known from thermodynamics and experimental work on the Si-N-O system [11].

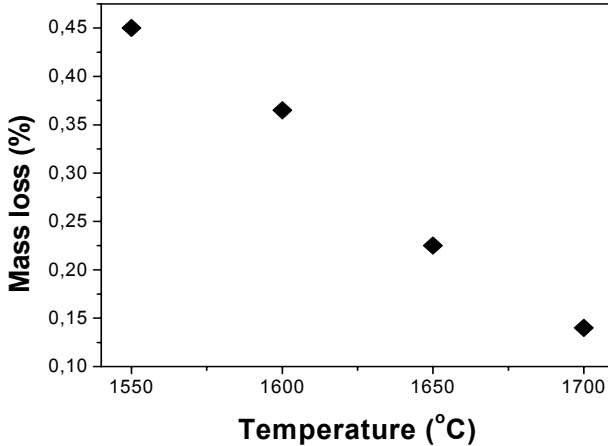


Fig. 2. Mass loss of lithium in Si_3N_4 samples sintered at various temperatures; annealing time is 4 h.

Conclusion

On the basis of the experimental results, it is to be concluded that the major part of the mass loss of the Si_3N_4 ceramics during sintering is a consequence of interaction of silicon nitride with silica, according to the reaction (2).

Acknowledgement

We acknowledge the support of MNTR of Serbia.

References

- [1] F. Riley, *J. Am. Ceram. Soc.*, 2000, 83, 245.
- [2] G. Petzow and M. Herrmann, in *Structure and Bonding*, Springer-Verlag, Berlin, 2002, 102, 51.
- [3] S. Wada, *J. Ceram. Soc. Jpn.*, 2001, 109, 803.
- [4] F. F. Lange, *J. Am. Ceram. Soc.*, 1982, 65, C120-21.
- [5] G. Ziegler, J. Heinrich, G. Wötting, *J. Mater. Sci.*, 1987, 22, 3041.
- [6] K. Yokoyama, S. Wada, *J. Ceram. Soc. Jpn.*, 2000, 108, 230.
- [7] K. Yokoyama, S. Wada, *J. Ceram. Soc. Jpn.*, 2000, 108, 6.
- [8] Y. Zou, A. Petric, *J. Phys. Chem. Solids*, 1994, 55, 493.
- [9] S. Jana, D. Tompson and K. Jack, in *Nitrogen Ceramics*, Noordhoff, 1976, 405-414.
- [10] O. Gob, M. Herrmann, S. Siegel and P. Obenaus, *Key. Eng. Mater.*, 1997, 132, 751.
- [11] P. Rocabois, C. Chatillon and C. Bernard, *J. Am. Ceram. Soc.*, 1996, 79, 1351.

SYNTHESIS AND PROPERTIES OF NANOSIZED Fe/TiO₂ AND FeM/TiO₂ (M=Pd, Pt) SYSTEMS. PART 1: PREPARATION AND PHASE ANALYSIS

Z. Cherkezova-Zheleva*, M. Shopska, B. Kunev, I. Mitov, G. Kadinov, L. Petrov

*Institute of Catalysis, Bulgarian Academy of Sciences, Acad. G. Bonchev St.,
Block 11, 1113 Sofia, Bulgaria*

Abstract

Samples of mono- (Fe) and bimetallic (Fe-Pd and Fe-Pt) catalysts were prepared by incipient wetness impregnation of TiO₂ support (anatase). The phase composition was studied by MS and XRD. The preparation procedure resulted in the formation of bidisperse (ultradisperse and highdisperse) hematite-like α -Fe₂O₃ supported particles. Their size is lower than 3-4 nm or about 10-20 nm.

Introduction

Complete oxidation of hydrocarbons is of great importance for the environmental protection. Investigation of transition metal–noble metal supported catalysts is a question of theoretical and practical interest, because of the expected synergetic effect between the components and improvement of their catalytic performance in hydrocarbon oxidation due to formation of nanosize metal/metal oxide supported particles. It was found, that the formation of highly active sites is associated with the formation of highly dispersed iron oxide on TiO₂ because of strong iron-support interaction [1]. The aim of the present study was to prepare nanosize mono- and bimetallic supported on TiO₂ catalysts and to investigate their phase composition and dispersity.

Experimental

The catalysts were prepared by incipient wetness impregnation of the TiO₂ (anatase) with solutions of Fe(NO₃)₃·9H₂O and Pd(NO₃)₂·2H₂O or (NH₃)₄PtCl₂·H₂O. The samples were dried at 343 K in vacuum, heated 3 hours at 493 K in vacuum and calcined in air 3 hours at 713 K. The metal loading was 8 wt.% Fe and 0.7 wt.% noble metal. The samples were studied by Moessbauer spectroscopy on Wissenschaftliche Elektronik GmbH instrument (constant acceleration mode, ⁵⁷Co/Cr, α -Fe standard). The parameters of hyperfine interactions were determined by computer fitting: isomer shift (IS), quadrupole splitting (QS), hyperfine magnetic field (H_{eff}) as well as line widths (FW) and relative weights of components (G). X-ray diffraction pattern (XRD) is obtained on TUR M62 apparatus, HZG-4 goniometer, CoK _{α} radiation and Fe filter. Data base (PDF, JCPDS, Philadelphia PA, USA, 1997) was used for the phase identification.

Results and Discussion

Moessbauer spectra (MS) of the bimetallic samples are represented in Figs. 1–4. Spectra of the monometallic samples are not shown because they are almost identical

with those of FePt samples, obtained at the same conditions (the difference between the relative weights of the components was about 10 %).

All spectra consist of quadrupole doublet or a doublet and a sextet. The doublet part of the spectra was computer processed according to the "core-shell" model – Dbl 1 and Dbl 2 and their parameters could be assigned to ultradisperse α -Fe₂O₃ particles (D<10 nm) with superparamagnetic (SPM) behavior [2, 3].

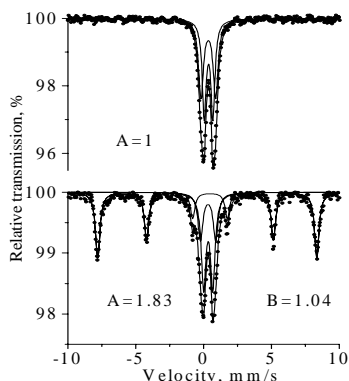


Figure 1. Moessbauer spectra of FePt/TiO₂ heated at 493 K before (top) and after catalytic test* (bottom).

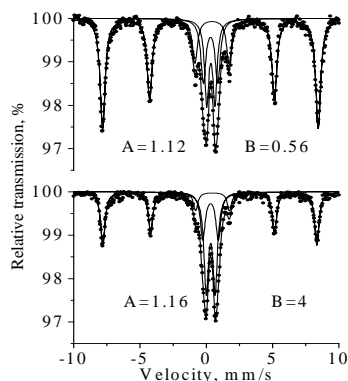


Figure 2. Moessbauer spectra of FePt/TiO₂ calcined at 713 K before (top) and after catalytic test* (bottom).

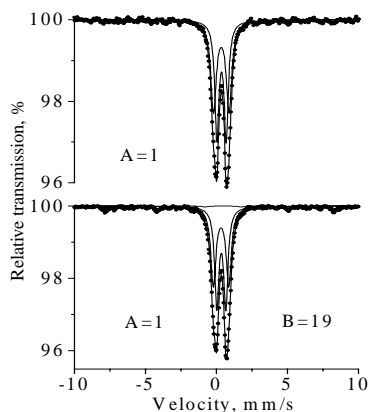


Figure 3. Moessbauer spectra of FePd/TiO₂ heated at 493 K before (top) and after catalytic test* (bottom).

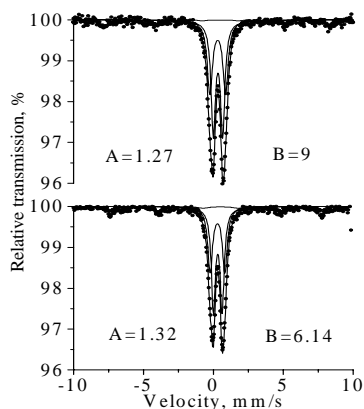


Figure 4. Moessbauer spectra of FePd/TiO₂ sample calcined at 713 K before (top) and after catalytic test* (bottom).

*The catalytic test is discussed in Part 2 of this study, presented at this Conference.

The IS = 0.32–0.36 mm/s are typical for the high spin Fe³⁺ ions in an octahedral oxygen coordination. The doublet (Dbl 1) with lowest QS = 0.62–0.67 mm/s belongs to iron ions from the core of the particles. The doublet (Dbl 2) with larger QS = 1.05–1.17 mm/s can be assigned to interface ferric ions. The lower symmetry in the environment of “surface” iron ions results in a change in the electric field gradient. The

ratio of the relative weight corresponding to the “outer” and “inner” iron ions is about $A = 1$ before high temperature calcination and, consequently, particle size is below 3–4 nm [3]. After calcination at 713 K and catalytic test, the ratio increases to $A = 1.5$ – 1.8 , i.e. the amount of “inner” iron ions and particle size increase. The appearance of sextet component with $IS = 0.37$ mm/s, $QS = -0.11$ mm/s and $H_{\text{eff}} = 492$ – 506 kOe shows some agglomeration of $\alpha\text{-Fe}_2\text{O}_3$ particles after thermal treatment and catalytic test. These values are lower than $H_{\text{eff}} = 515$ kOe (for bulk hematite) and impose that these particles are still of high dispersion. The B-value on Figs. 1–4 represents the ratio $G_{\text{DbI}}/G_{\text{Sxt}}$, i.e. the ratio ultradisperse/highdisperse iron oxide particles.

The spectra of FePd samples are not significantly changed after the thermal treatment and catalytic test. The core-shell ratio is close to $A = 1$ and the relative weight of sextet component is below 5%.

The relatively narrow spectral lines of all components show nearly bidisperse particle size distribution. This mode of distribution could be explained with presence of hematite-like ultradisperse particles in the pores and on the surface. The latter part could agglomerate with the increase in temperature. The hematite-like particles in Fe and FePt samples are both in the pores and on the surface of the support TiO_2 , whereas in FePd sample they are predominantly in the pores. This is due to the strong influence of the Pd particle as a result of different used noble metal precursor salts. The noble metal disturbs the contact interaction between hematite particles. In result the crystallite size of Fe(M) samples decrease in the following order: FePt sample > Fe sample > FePd sample.

X-ray diffraction pattern of all prepared samples showed the characteristic pattern of the support only. The supported metal-oxide phase is either amorphous, or have very small crystallite size.

Conclusions

Bidisperse hematite-like particles, supported on TiO_2 (anatase) are synthesized. The crystallites are ultradisperse, with particle size about 3–4 nm and highdisperse, with a size about 10–20 nm. The different ratio between these two particle size phases can be ascribed to the presence of noble metal (Pt and Pt) and /or to the different noble metal precursor salts, which are used for the synthesis.

Acknowledgments

The authors are grateful to the National Science Fund at the Ministry of Education and Science of Bulgaria for the support (Project MU-1301/2003).

References

- [1] G. Pecchi, P. Reyes et al., *J. Sol-Gel Sci. Technol.*, 2003, 27, 205.
- [2] A. Van der Kraan, *Phys. Status Solidi*, 1973, 18, 215.
- [3] J. Niemantsverdriet, A. Van der Kraan, *J. Phys. Chem.*, 1985, 89, 67.
- [4] L. Signorini, L. Pasquini et al., *Phys. Review*, 2003, 68, 195423.

**SYNTHESIS AND PROPERTIES OF NANOSIZED
Fe/TiO₂ AND FeM/TiO₂ (M=Pd, Pt) SYSTEMS.
PART 2: TEMPERATURE-PROGRAMMED REDUCTION
AND CATALYTIC ACTIVITY IN BENZENE OXIDATION**

M. Shopska*, Z. Cherkezova-Zheleva, I. Shtereva, B. Kunev, G. Kadinov,
I. Mitov and L. Petrov

*Institute of Catalysis, Bulgarian Academy of Sciences,
Acad. G. Bonchev St., Block 11, 1113 Sofia, Bulgaria*

Abstract

Fe/TiO₂ and Fe(Pt,Pd)/TiO₂, containing nanosize particles of iron oxide were characterised by TPR and catalytic activity in C₆H₆ oxidation. The catalysts performance is explained as due to the noble metal stabilised by the iron oxide.

Introduction

Noble metals are widely used as catalysts for complete oxidation of hydrocarbons. Catalysts based on transition metal oxides are less efficient, as far as oxidation of aromatics is aimed, but resistant toward deactivation at high temperatures. The nanosized materials exhibit different physical and chemical properties in comparison with bulk substances. Higher catalytic activity and selectivity in hydrocarbon oxidation are expected from such metal/metal oxide supported particles. It was found that the most active sites are associated with existence of relatively high iron dispersion because of strong iron-support interaction [1–3]. One can expect that the additional improvement of catalytic performance could be obtained by using TiO₂ as a carrier. The aim of the present study was to investigate the composition and catalytic properties in benzene oxidation of mono (Fe) and bimetallic (FePd, FePt) supported on TiO₂ catalysts, containing nanosize particles.

Experimental

The catalysts (8 wt.% Fe and 0.7 wt.% Pt or Pd) were prepared by incipient wetness impregnation of TiO₂ (anatase), drying at 343 K in vacuum, heating 3 hours at 493 K in vacuum and calcination 3 hours at 713 K in air [4]. Temperature-programmed reduction (TPR) was carried out in a quartz reactor as described in Ref. [4]. The catalytic activity of the heated and calcined samples was studied in a flow type glass reactor at atmospheric pressure in the temperature range 373–773 K with a reaction mixture C₆H₆/N₂/air = 1/13/92 at a total flow rate of 133 ml/min and catalyst loading 140 mg. Reaction products were analysed by a gas chromatograph Varian Model 3700 equipped with TCD and FID and 2 m column with Porapak Q. Nitrogen was used as carrier gas, whereas benzene was utilised for oxidation and calibration.

Results and Discussion

Three main peaks were observed in the TPR patterns of the heated samples at

$T \approx 560$ (540 K with FePt, 440 K with FePd), 740 and 870 K (Fig. 1). The reduction of Fe_2O_3 supported on titania in the same temperature range has been reported in Refs. [1–3]. Hydrogen consumption at temperatures below 573 K is assigned to the process $\text{Fe}_2\text{O}_3 \rightarrow \text{Fe}_3\text{O}_4$. The peaks at 740 and 870 K are, likely, result of further reduction following the scheme $\text{Fe}_3\text{O}_4 \rightarrow \text{FeO} \rightarrow \text{Fe}$. A strong promoting effect of Pd is clearly seen at the first reduction step of the bimetallic FePd sample. Pt also stimulates the reduction of iron oxide, but to a lesser extent. TPR shows the highest H_2 consumption for Pd containing sample. However, the consumption of all samples is less than the stoichiometry required for complete reduction of Fe^{3+} to Fe^0 . Accordingly, formation of mixed hardly reducible Fe-Ti-O compound(s) during the preparation of the catalyst is quite possible.

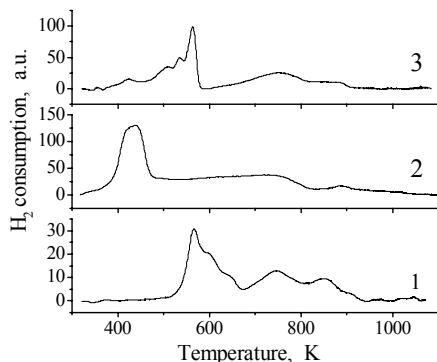


Figure 1. TPR of heated catalysts:

- 1- 8%Fe/TiO₂ ;
- 2- (8%Fe+0.7%Pd)/TiO₂
- 3- (8%Fe+0.7%Pt)/TiO₂

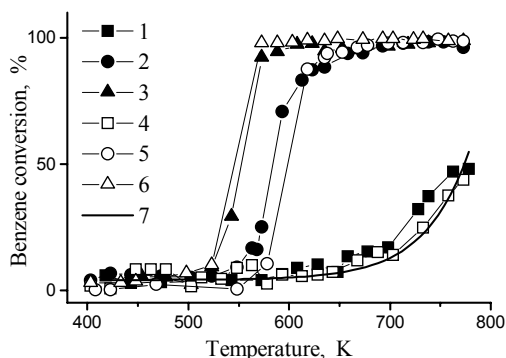


Figure 2. C₆H₆ conversion registered with heated (1, 2, 3) and calcined (4, 5, 6) samples: 1,4 - 8%Fe/TiO₂; 2,5 - (8%Fe+0.7%Pd)/TiO₂; 3,6 - (8%Fe+0.7%Pt)/TiO₂; 7 - 8%Fe/TiO₂ mechanical mixture

The results for C₆H₆ oxidation are shown in Fig. 2. A low catalytic activity was observed for the catalysts containing iron oxide only. The FePt/TiO₂ catalysts exhibited the best performance attaining total benzene conversion at about 573 K. Palladium containing catalysts exhibited slightly lower activity. As it is seen, the calcination at 713 K of the samples did not affect significantly the performance of both mono- and bimetallic catalysts.

The benzene conversion over Fe/TiO₂ catalysts and a mechanical mixture of Fe₂O₃ and TiO₂ with the same composition can be compared in Fig. 2. The activity of the samples was very low (less than 10% at temperatures below 700 K) and it was practically the same for the calcined sample and the mechanical mixture. In Part 1 of the present study [5] it was shown that the iron oxide particles both in the heated and in the calcined catalyst were finely dispersed. Assuming that the particles in the mechanical mixture are an order of magnitude larger in size, one can conclude that the catalytic activity in benzene oxidation for the Pd(Pt)+Fe₂O₃/TiO₂ is due to the noble metal only. However, higher dispersion of iron oxide in the heated sample results in a

slightly higher activity. Most probably, the role of iron oxide(s) particles in the bi-metallic catalysts was to stabilise the noble metal dispersion.

The slightly better performance of calcined FePt/TiO₂ could be explained considering the processes of thermal decomposition of the [Pt(NH₃)₄]²⁺ ion. It is partially decomposed below 573 K with release of NH₃ accompanied by evolution of small amounts of H₂ and N₂ and autoreduction of Pt²⁺ to Pt⁰ [6, 7]. Thus, in the sample heated at 493 K, a small amount of metallic Pt is present. The calcination at 713 K results in further decomposition of the platinum complex, reduction of Pt²⁺ to Pt⁰ and surface oxidation of the existing and newly formed platinum particles (the so-called "redispersion" [8]). Thus, the calcined FePt/TiO₂ catalyst manifests slightly higher metal surface and higher catalytic activity in C₆H₆ oxidation.

During the preparation of FePd/TiO₂ (drying at 343 K and heating at 493 K in vacuum) complete destruction of the palladium salt to Pd occurs [9]. The activity of Fe(Pd)/TiO₂ samples was practically unaffected by calcination. However, the latter procedure leads to a slight increase of the "ignition temperature". Since the metallic Pd is thermally stable on calcination at T < 873 K, this result could be explained by negligible agglomeration both of metal (Pd) and iron oxide particles as it was found with Moessbauer spectroscopy in Part 1 [5].

Acknowledgement

The authors are grateful to the National Science Fund at the Ministry of Education and Science of Bulgaria for the support (Project MU-1301/2003).

References

- [1] G. Pecchi, P. Reyes, T. Lopez, R. Gomez, A. Moreno, J. L. G. Fierro, *J. Chem. Technol. Biootechnol.*, 2002, 77, 944.
- [2] G. Pecchi, P. Reyes, T. Lopez, R. Gomez, A. Moreno, J. L. G. Fierro, A. Martinez-Arias, *J. Sol-Gel Sci. Technol.*, 2003, 27, 205.
- [3] G. Pecchi, P. Reyes, R. Zamora, *React. Kinet. Catal. Lett.*, 2003, 80, 375.
- [4] Z. Cherkezova-Zheleva, M. Shopska, B. Kunev, I. Shtereva, G. Kadinov, I. Mitov, L. Petrov, in: *Nanoscience and Nanotechnology*, 17-18 November 2003, Sofia (in press).
- [5] Z. Cherkezova-Zheleva, M. Shopska, B. Kunev, I. Mitov, G. Kadinov, L. Petrov, (present volume, p. 478).
- [6] L. R. Raddi de Araujo, M. Schmal, *Appl. Catal. A: General*, 2000, 203, 275.
- [7] J. Novakova, L. Kubelkova, L. Brabec, Z. Basti, *Zeolites*, 1996, 16, 173.
- [8] I. Sushumna, E. Ruckenstein, *J. Catal.*, 1987, 108, 77.
- [9] A. Lapidus, V. Maltzev, E. Shpiro, *Izv. Akad. Nauk SSSR, Ser. Khim.*, 1977, 11, 2424.

SYNTHESIS AND CHARACTERIZATION OF POLYVINYL ALCOHOL / LEAD SULFIDE NANOCOMPOSITE

J. Kuljanin, M. I. Čomor and V. Đoković

Institute of Nuclear Sciences Vinča, P.O. Box 522, 11001 Belgrade, Serbia and Montenegro

Abstract

The nanocomposite consisting of lead sulfide (PbS) nanoparticles (NPs) with average diameter of 2.6 nm and polyvinyl alcohol (PVA) were synthesized using colloidal chemistry methods. The PbS/PVA nanocomposites were characterized using optical, structural and thermal techniques. The presence of the PbS NPs in the PVA matrix induced the increase of the crystallization temperature and enthalpy of crystallization.

Introduction

The usage of nanoparticles (NPs) as polymer fillers relates to the strong current interest in development and application of new materials [1, 2]. Resulting properties of nanocomposites are, most of the time, simple combination of the properties of inorganic and organic components, although the appearance of completely novel characteristics sometimes can take place due to synergistic effect.

Lead sulfide (PbS) is a narrow band gap semiconductor ($E_g = 0.41$ eV) with large exciton Bohr radius (18 nm). Thus, when crystallite size is smaller than the Bohr radius, a large blue shift of the absorption onset can be expected due to size quantization effect. Since optical properties of PbS can be tuned into the spectral region important for many technology applications many methods have been developed to fabricate PbS NPs in micelles [3], polymers [4], monolayer surfaces [5], zeolites [6] and glasses [7].

Polyvinyl alcohol (PVA) is a hydrophilic polymer frequently used as a matrix for variety of NPs [8]. In most cases, due to optical clarity, PVA has been used just as a host medium to enable investigation of optical properties of NPs. In this work we attempt to use the PVA as a stabilizer for growth of the PbS NPs. The PVA was chosen because uniform and optically transparent films can be easily prepared from this material. In addition, thermal properties of the PVA were investigated after incorporation of the PbS NPs.

Experimental

Preparation of the PbS/PVA nanocomposite

The colloidal solutions consisting of the PbS NPs were synthesized by controlled precipitation of PbS in the presence of the PVA (MW = 72,000) using slightly modified method already described elsewhere [9, 10]. In order to prepare the PbS/PVA nanocomposite solvent was evaporated at ambient conditions without the presence of light. Final concentration of the PbS NPs in nanocomposite films was 4.6 mass%. The neat PVA films, without the PbS NPs, were prepared on the same man-

ner. All chemicals used were of the highest purity available (Merck or Fluka). Solutions were prepared using triply distilled water.

Characterization

Spectrophotometric measurements of the PbS/PVA nanocomposite films, the neat PVA films as well as colloids consisting of the PbS NPs were measured using Perkin-Elmer Lambda 5 UV-VIS spectrophotometer.

The X-ray diffraction (XRD) measurements of the PbS/PVA nanocomposites were performed on Philips PW1710 diffractometer.

The differential scanning calorimetry (DSC) measurements of the neat PVA and the PbS/PVA nanocomposite were performed under a nitrogen atmosphere on a Perkin-Elmer DSC-2 instrument in the temperature range from 25°C to 250°C. The heating rate was 20°C/min. In order to insure the same thermal history of the samples, prior to measurements they were heated up to 250°C (above the glass transition temperature) and then cooled down (heating and cooling rates were 20°C/min).

Results and discussion

Large blue shift of the absorption onset of the PbS NPs incorporated in the PVA can be attributed to size quantization effect. Well defined bands peaking at 2.11 and 3.31 eV can be observed indicating narrow size distribution of the PbS NPs. The size of the PbS NPs was estimated to be 2.6 nm based on the position of the excitonic peaks and the transmission electron microscopy data [7]. To the best of our knowledge, usage of the PVA as a stabilizer leads to the formation of the smallest PbS NPs in solution.

XRD spectrum of the PbS/PVA nanocomposite indicates that the PbS NPs are in a cubic phase. The PbS XRD peaks are very broad due to small size of the particles. We use Scherrer diffraction formula relating diffraction angular width (β) to the domain size (D). We found a 3 nm PbS diameter, and this result is in reasonable good agreement with the PbS diameter estimated from the spectral shift ($D = 2.6$ nm).

Table 1. Melting (T_m) and crystallization (T_c) temperatures as well as melting (ΔH_m) and crystallization (ΔH_c) enthalpies of the neat PVA and the PbS/PVA nanocomposite with 4.6 mass% of inorganic phase.

PbS/PVA (mass% of PbS)	T_m (°C)	ΔH_m (J/g)	T_c (°C)	ΔH_c (J/g)
0	230.0	22.9	191.3	-17.8
4.6	231.0	26.3	203.9	-21.3

The DSC heating and cooling curves of the neat PVA and the PbS/PVA nanocomposite are obtained. The results are presented in Table 1. In the lower temperature region DSC measurements indicated that incorporation of the PbS NPs did not induce change of the glass transition temperature of the PVA (75 °C). The change of the glass transition temperature can be considered as a measure of polymer immobilization upon incorporation of NPs. On the other hand, incorporation of the PbS NPs affected

the crystallization temperature of the PVA matrix (see Table 1). The crystallization temperature of the PbS/PVA nanocomposite is about 10 °C higher compared to the neat PVA. It seems that the PbS NPs act as a nucleation centers at which crystal chain-packing starts. The increase in crystallization temperature is followed by the change of the distribution of lamellae thickness, which is manifested by broadening of crystallization peak. Also, the slight increase of melting temperature as well as the increase of enthalpies of melting and crystallization was observed after incorporation of the PbS NPs in the PVA matrix (Table 1).

References

- [1] D.Y. Godovsky, *Advan. Polym. Sci.*, 2000, 165, 153.
- [2] W. Caseri, *Macromol. Rapid Commun.*, 2000, 21, 705.
- [3] A.J.I. Ward, E.C. O'Sullivan, J-C. Rang, J. Nedeljković, R.C. Patel, *J. Colloid Interface Sci.*, 1993, 161, 316.
- [4] Y. Zhou, H. Itoh, T. Uemura, K. Naka, Y. Chujo, *Langmuir*, 2002, 18, 5287.
- [5] X.K. Zhao, S.Q. Xu, J.H. Fendler, *Langmuir*, 1991, 7, 520.
- [6] M. Mukherjee, A. Datta, D. Chakravorty, *Appl. Phys. Lett.*, 1994, 64, 1159.
- [7] T. Okuno, A.A. Lipovskii, T. Ogawa, I. Amagai, Y. Masumoto, *J. Lumin.*, 2000, 87-89, 491.
- [8] Z.H. Mbhele, M.G. Salemane, C.G.C.E. van Sittert, J.M. Nedeljković, V. Djoković, A.S. Luyt, *Chem. Mater.*, 2003, 15, 5019.
- [9] M.T. Nenadović, M.I. Čomor, V. Vasić, O.I. Mičić, *J. Phys. Chem.*, 1990, 94, 6390.
- [10] J.M. Nedeljković, R.C. Patel, P. Kaufman, C. Joyce-Pruden, N. O'Leary, *J. Chem. Educ.*, 1993, 70, 342.

SYNTHESIS OF BCP AND BCP/PLGA BIOMATERIALS BY ULTRASONIC SPRAY PYROLYSIS

M. Radić¹, N. Ignjatović¹, D. Jugović¹, Z. Nedić², M. Mitrić³ and M. Miljković⁴

¹*Institute of Technical Sciences of the Serbian Academy of Sciences and Arts, Belgrade;*

²*Faculty of Physical Chemistry, Belgrade;* ³*The Vinča Institute of Nuclear Sciences, Laboratory for Theoretical and Condensed Matter Physics, Belgrade;* ⁴*Faculty of Medicine, Laboratory for Electron Microscopy, Nis;*

Abstract

The most significant mass part of the bony tissue consists of calcium phosphate ceramics. This paper describes method of obtaining fine particles of biphasic calcium phosphate (BCP) as well as fine particles of biphasic calcium phosphate covered by polymer, poly-lactide-co-glycolide (BCP/PLGA), by ultrasonic spray pyrolysis. Methods used for characterization of obtained particles of BCP and BCP/PLGA are Infrared Spectroscopy (IR) and Scanning Electron Microscopy (SEM) techniques.

Introduction

Materials which have structure and characteristics similar to the natural bone are called bioceramic materials [1,2]. For the reparation and replacement of the bony tissue we use calcium phosphate whose characteristics are being improved with polymer. We used spray pyrolysis [3,4,5] for obtaining fine particle of BCP which are at the later stage covered by polymer, poly-lactide-co-glycolide. All samples of obtained particles of BCP and BCP/PLGA are characterized by Infrared Spectroscopy (IR) and Scanning Electron Microscopy (SEM) techniques.

Experimental Procedure

Biphasic calcium phosphate was made by precipitation from $\text{Ca}(\text{NO}_3)_2 \cdot 4\text{H}_2\text{O}$ and $(\text{NH}_4)_3\text{PO}_4$ in the alkali environment. After 24h the suspension is filtered through Bihner's hopper with vacuum. The obtained gel (≈ 40 g) is dissolved in 500 ml of water and that makes precursor solution for the spray pyrolysis. The concentration of precursor solution is 0,002 M. Spray pyrolysis is performed at $T=400^\circ\text{C}$ with air as carrier gas. The flow of the gas is 60 l/h and the frequency of the ultrasonic atomizer is $\nu=1,7$ MHz. Fine biphasic calcium phosphate particles obtained by spray pyrolysis are covered with the polymer by being added in to the solution of poly-lactide-co-glycolide (PLGA) in chloroform ($\approx 0,3\%$) and then at the later stage methanol is added into the obtained polymer solution at the appropriate ratio. The solution after that is precipitated.

All samples are characterized by IR and SEM techniques. The IR measurements were performed on Perkin-Elmer 983G Infrared Spectrophotometer, using the KBr pellet technique, in the frequency interval of $250\text{-}4000\text{ cm}^{-1}$.

The morphology of obtained particles BCP and BCP/PLGA were examined by scanning electron microscope (SEM) JEOL JSM-5300. The powder samples for SEM analysis were coated with gold using the PVD process.

Results and Discussion

All typical bands for BCP are shown in the IR spectrogram in Fig 1. The bands that correspond to the wave numbers 1093 and 1037, and 606 and 568 cm^{-1} , belong to the ν_4 and ν_3 asymmetrically stretching vibrations for the phosphate group. The symmetrical stretching modes (ν_1 and ν_2) of PO_4^{3-} ion were also found at around 957 and 468 cm^{-1} . The liberation and stretching modes of the OH^- were detected at around 630 cm^{-1} and 1612 cm^{-1} , respectively, while the band on 3400-3700 cm^{-1} belongs to the OH^- group of the water molecule.

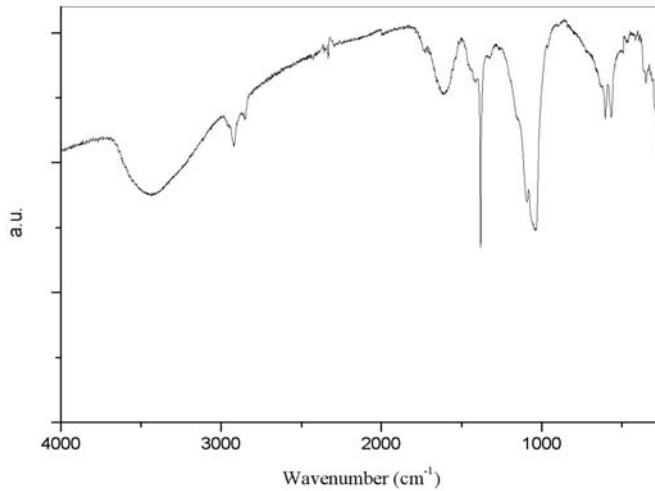


Figure 1. The IR spectra of the obtained biphasic calcium phosphate particles by the spray pyrolysis method

Figure 2 shows the morphology of the BCP particles obtained by spray pyrolysis.

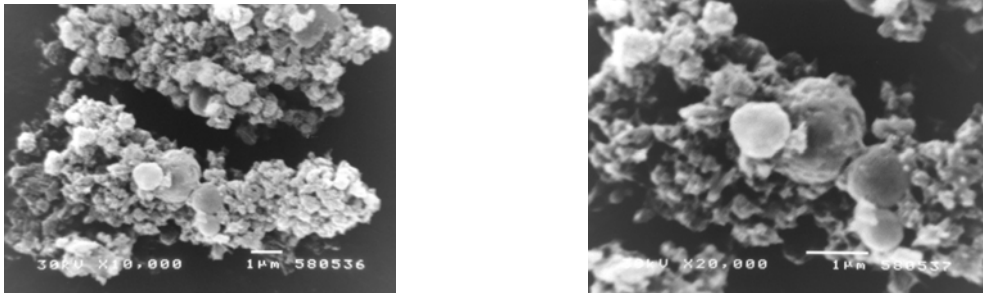


Figure 2. Solid particles of biphasic calcium phosphate produced at 400 °C by spray pyrolysis

Scanning Electron Microscopy (SEM) of the obtained powder shows that powder particles, based on biphasic calcium phosphate, obtained with spray pyrolysis, have spherical shape. However, it also shows that powder contains the particles of the irregular shape. The surfaces of the particles are not smooth. They represent aggregation of the particles, which are in submicron range.



Figure 3. SEM micrographs of particles of biphasic calcium phosphate covered by polymer poly-lactide-co-glycolide

SEM micrographs of the BCP/PLGA show characteristic details of the agglomerates and particle gathering.

Conclusion

The spray pyrolysis method is used to synthesize the particles of BCP, which are afterward covered with polymer PLGA thus obtaining the composite material BCP/PLGA. The particles have specific morphology characteristics which are determined with the parameters of the spray pyrolysis process. The particles have spherical and irregular shape with rougher surface.

Acknowledgements

The Ministry of Science, Technologies and Development of Republic of Serbia provided financial support under grant no. 1243.

References

- [1] Park J., Lakes R.S., "Biomaterials – an Introduction", Plenum Press, New York, 1979.
- [2] Hench L.L., "Bioceramics", Journal of American Ceramic Society, 1998, 81, 1705.
- [3] O. Milošević, D. Uskoković, Synthesis of advanced powders by the reaction spray pyrolysis, New materials 1994, 3, 3.
- [4] G.L. Messing, S.C. Zgang and G.V. Jayanthi, J.Am.Ceram.Soc 1993, 76, 2707.
- [5] A. Gurav, T. Kodas, T. Pluym, Y. Xiong, Aerosol Processing of Materials, Aerosol Science and Technology 1993, 19, 411.

LOW- TEMPERATURE SYNTHESIS OF SILICALITE-1 WITH PRECIPITATED SILICA AS RAW MATERIAL

O. Kovačević¹, B. Kovačević¹, N.L. Lazić¹, Z. Filipović-Rojka¹, K. Anđelković²
and Ž.Lj. Tešić²

¹ *Institute of General and Physical Chemistry, Studentski trg 12-16, P.O. Box 551, 11000 Belgrade,*

² *Faculty of Chemistry, Studentski trg 12-16, P.O. Box 158, 11000 Belgrade, Serbia and Montenegro*

Abstract

Precipitated silica is convenient raw material in the synthesis of the silicalite-1. In low-temperature synthesis, in the systems without stirring, with precipitated silica as raw material, a sample obtained for 92 h of crystallization depicted that silicalite-1 (MFI) of high crystallinity is appeared in the form of the shelly agglomerates immersed in the suspension, which is on the beginning of the crystallization. As crystallization succeeds, the crystallinity of the dispersed particle in suspension increases and shelly agglomerates enlarge on the bottom of the reactor. The final product is the silicalite-1 phase of high crystallinity.

Introduction

E.M. Flanigen et al [1] were reported the synthesis, crystal structure and properties of silicalite-1. The crystal lattice of silicalite-1 is isostructural with ZSM-5 (MFI framework). In the recent years many efforts have been made in the study of the synthesis, characterization and application of this type of zeolite. Recently, Q. Li et al [2, 3] used one- and two-stage varying-temperature synthesis method to explore the effect of silica source, including tetraethoxysilane and colloidal silica sols, on the dynamics of nucleation and crystallization of TPA-silicalite-1. We were used precipitated silica as raw material, in systems without stirring during one-step low-temperature crystallization. Precipitated silica is solid amorphous silica, which is widely used in industrial applications [4]. The crystallisation of silicalite-1 was followed by i.r. spectroscopy [6-8]. Under this condition silicalite-1 is appeared in the form of the shelly agglomerates and in the form of the dispersed particles in the suspension. The subject of our future interest will be the control of shelly agglomerates rising.

Experimental

The initial materials for synthesis were precipitated silica (87.20 % SiO₂, T.G. "Birač", Zvornik), sodium hydroxide ("Zorka", Šabac), sulphuric acid ("Zorka", Šabac), tetrapropylammonium bromide (Merck) and distilled water. The reactants were mixed with constant vigorous stirring to get a homogenous gel-mix, with a composition of 0.1 TPABr : SiO₂ : 27.13 H₂O and 0.1 OH/SiO₂. Crystallization runs were carried out under autogeneous pressure in systems without stirring in screw-top polypropylene bottles that were placed in a oven at 86 ± 2 °C. To interrupt process of crystal-

lization the reactor was quenched in cold water, the solid phase was filtered off, washed with distilled water and dried in a static – air oven below 60 °C.

The infrared spectra were recorded on a Carl-Zeiss SPECORD 75IR Spectrometer using the KBr pellet technique.

Results and Discussion

During the crystallisation the silicalite-1 is appeared in the form of the easy breakable shelly agglomerates and in the form of the dispersed particles in the suspension and have been investigated as separate sample denoted as G for shelly agglomerates or S for suspension. The shelly agglomerates are similar to the ZSM-5 zeolite films, as reported by T. Sano et al. [5].

The mid i.r. spectra (1500-400 cm^{-1}) of the both samples, G and S, that have been obtained for 92 h and 135 h of crystallization, together with spectrum of precipitated silica, which is raw material in the synthesis, are shown in Figure 1.

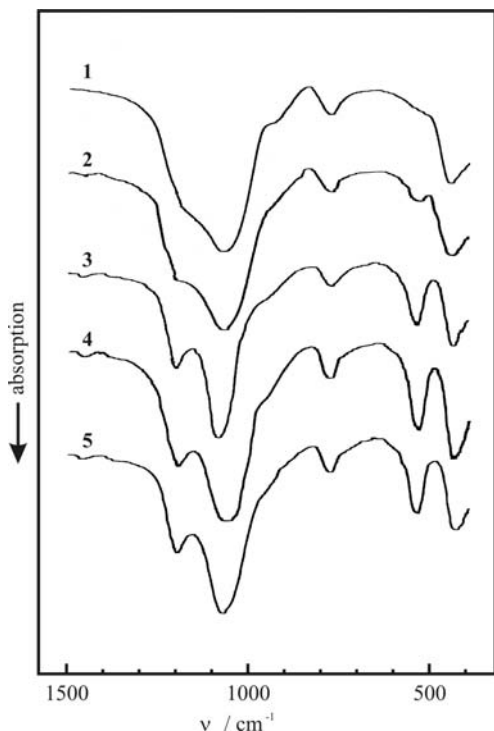


Figure 1. Infrared spectra of precipitated silica (1) and products from low-temperature synthesis of silicalite-1: suspension - 92 h of crystallization (2), shelly agglomerates - 92 h of crystallization (3), suspension - 135 h of crystallization (4), shelly agglomerates - 135 h of crystallization (5)

The spectrum of the particles dispersed in the suspension for 92 h of crystallization, depicted in Figure 1-2, shows the similarity to the spectrum of precipitated silica (Fig. 1-1) and the appearing of the weak absorption bands of the characteristic silicalite-1 (MFI) vibration [6-8] on the position of 1220 cm^{-1} and 550 cm^{-1} . The spectrum of the shelly agglomerates, obtained as a part of the sample for 92 h of crystallization, depicted on Fig. 1-3, shows that crystallization product is silicalite-1 of high crystallinity [6-8]. The spectra of the dispersed particles (Fig. 1-4) and the shelly

agglomerates (Fig. 1-5) for the 135 h of crystallization are very similar and represent spectrum of silicalite-1 of high crystallinity [6-8].

The samples that have been obtained for 92 h of crystallization correspond to the end of induction period and the beginning of the silicalite-1 crystals growth. As crystallization succeeds, two effects are dominant: 1) i.r. spectra of the samples show that the crystallinity of the dispersed particle in suspension increases and overtakes high crystallinity at the end of this period and 2) shelly agglomerates enlarge on the bottom of the reactor. I.r. spectra of shelly agglomerates for different time of crystallization are similar to spectra depicted in Fig. 1-3 and 1-5 and reveal that shelly agglomerates for different time of crystallization are composed of silicalite-1 of high crystallinity.

The characterization of the products of this type of synthesis in more details (XRD, Coulter Counter and SEM) will be the subject of a following paper.

References

- [1] E.M. Flanigen, J.M. Bennett, R.W. Grose, J.P. Cohen, R.L. Patton, R.M. Kirchner and J.V. Smith, *Nature*, 1978, 271, 512.
- [2] Q. Li, D. Creaser and J. Sterte, *Microporous and Mesoporous Materials*, 1999, 31, 141.
- [3] Q. Li, B. Mihailova, D. Creaser and J. Sterte, *Microporous and Mesoporous Materials*, 2000, 40, 53.
- [4] N.L. Lazic, M. Sc. Thesis, University of Belgrad, Belgrade, Serbia and Montenegro
- [5] T. Sano, Y. Kiyozumi, F. Mizukami, H. Takaya, T. Mouri and M. Watanabe, *Zeolites*, 1992, 12, 131.
- [6] G. Coudurier, C. Naccache and J.C. Vedrine, *J. Chem. Soc., Chem. Commun.*, 1982, 1413.
- [7] J.C. Jansen, F.J. van der Gaag and H. van Bekkum, *Zeolites*, 1984, 4, 369.
- [8] A. Miecznikowski and J. Hanuza, *Zeolites*, 1987, 7, 249.

NEW BIOCOMPOSITE FILLER BIPHASIC CALCIUM PHOSPHATE/POLY-DL-LACTIDE-CO-GLYCOLIDE FOR RECONSTRUCTION OF HARD BONE TISSUE

N. Ignjatović¹, P. Ninkov², D. Krnojelac³ and D. Uskoković¹

¹*Institute of Technical Sciences of the Serbian Academy of Sciences and Arts, Belgrade*

²*Faculty of Medicine, Clinic of Stomatology, University of Novi Sad, Novi Sad*

³*Faculty of Medicine, University of Novi Sad, Novi Sad, Serbia and Montenegro*

Abstrakt

Biphasic calcium phosphate-poly-DL-lactide-co-glycolide composite biomaterial was synthesised in the form suitable for reconstruction of bone defects. The composite used as filler was obtained by precipitation in solvent-non-solvent systems. The material, calcium phosphate granules covered by polymer, was characterised by wide-angle X-ray structural analysis, scanning electron microscopy, infrared spectroscopy and differential scanning calorimetry. Reparation of bone tissue damaged by osteoporosis was investigated *in vivo* on rats. The method applied enabled production of granules of calcium phosphate-poly-DL-lactide-co-glycolide composite biomaterial of average diameter 150-200µm. Histological analysis confirmed recuperation of the alveolar bone, which osteoporosis-induced defects were repaired using composite biomaterial.

Introduction

Composite biomaterials have enormous potential for natural bone tissue reparation, filling and augmentation. Calcium hydroxyapatite/polymer composite biomaterials belong to this group of composites and due to their osteoconductive and biocompatible properties they can be successfully implemented in bone tissue reparation [1-3]. The structure and properties of this kind of composites depend on the polymer molecular weight, crystalline/amorphous ratio, porosity, etc. [4, 5]. Mixed with calcium phosphates, DLPLG polymer realizes more intensive activity of alkaline phosphatase, which is important for differentiation of osteoblasts that dictate regeneration processes within the organism. Addition of biphasic calcium phosphate (BCP) to polymers can largely increase the polymer bioactivity, while BCP itself can be an exceptional carrier of growth factors, which facilitates its wider application in medicine and stomatology. In this paper we report on a new biphasic calciumphosphate/poly-DL-lactide-co-glicolide (BCP/DLPLG) composite biomaterial synthesized in the form of granules of desired shape and dimensions. Possible differences between BCP/DLPLG and pure BCP implementation were examined in *in vivo* conditions.

Materials and Methods

A calcium phosphate gel was produced by precipitation of calcium nitrate and ammonium phosphate [1, 2]. Poly-DL-lactide-co-glicolide (DLPLG) (Sigma Chemical Company, USA) was used as a polymer component. The granules of calcium phos-

phate/DLPLG composite biomaterial, sizes 0.15-0.20 mm, were sterilized by γ rays (25kGy) before use. Composite biomaterials were characterized by wide angle X-ray structural analysis (WAXS), scanning electron microscopy (SEM), infrared spectroscopy (IR) and differential scanning calorimetry (DSC). *In vivo* research was carried out on female rats of Pauster type, age 12 weeks. Animals were divided into two experimental groups. The first group was implanted with BCP/DLPLG and the second with BCP. Animals were sacrificed after 12 weeks. Extracted alveolar bone was decalcinated and treated with the standard procedure of making paraffin cuts.

Results and Discussion

After production of powder and granules of calcium phosphate according to the previously given procedure, phosphate phase was analysed by WAXS. As evident from results of WAXS, the obtained calcium phosphate powder is highly crystalline. The most intense peaks at $2\theta=29^\circ$ (2 1 0) and 31.8° (2 1 1) originate from calcium hydroxyapatite (HAp) and that at $2\theta=31^\circ$ (0 2 10) from β -calciumphosphate (β -TCP). Mass content of HAp and β -TCP, 80% and 20%, respectively, were calculated according to WAXS results. Thereby, this calcium phosphate is also called biphasic calcium phosphate (BCP) and is used for the BCP/DLPLG composite biomaterial production. BCP granules are coated with polymer and their average diameter is 0.15-0.20 mm, as indicated by SEM results. Bands originating from BCP and DLPLG can be seen in the spectrum. BCP is identified within the spectrum by a doublet with maxima at 1052 and 1087 cm^{-1} , which are the most intense and originate from phosphate groups, and by a triplet with maxima at somewhat lower frequencies of 571 and 602, arising from the PO_4^{3-} group vibrations, and at 632 cm^{-1} , assigned to the hydroxyl group vibrations appearing also at 3567 cm^{-1} . DLPLG is characterized by an absorption band at 1756 cm^{-1} corresponding to the C=O group vibrations and two smaller maxima at 2996 and 2944 cm^{-1} ascribed to C-H group vibrations. According to DSC analysis, all transformations occurring in the temperature range from 305 to 480 K are connected with the polymer, while BCP is stable. The only noticeable transformation is characterized by a glass transition peak at the glass transition temperature (T_g) 324.4 K. Non-existence of phase transition, characteristic of melting, indicates amorphousness of the polymer. Analysis of histological preparations of both materials after 12 weeks of implantation does not indicate the presence of cellular infiltration around the implanted materials as occurrence following the presence of foreign tissue. Deposits of BCP/DLPLG composite material, between which there is a mature bone tissue in direct contact with implanted material without interposed connective tissue, are noticeable in figure 1. When pure BCP is used, there are no signs of ossification between BCP particles in histological preparations.

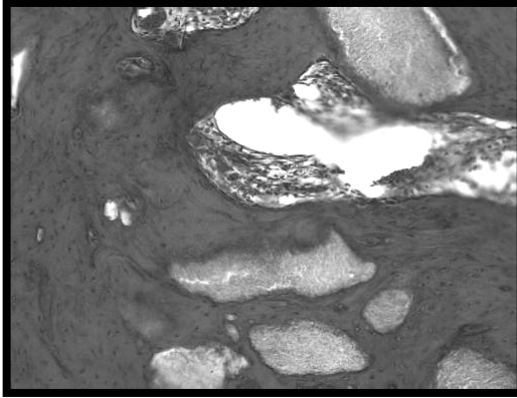


Figure 1. Histological finding of implanted composite material BCP/DLPLG in rat's lower jaw after 12 weeks. He (40x6,2)

Conclusion

BCP/DLPLG composite biomaterial was synthesized in the shape of spherical granules, 150-200 μm in diameter; each BCP particle is coated with amorphous DLPLG polymer. The composite is suitable for application as filler in reparation of bone tissue. Calcium phosphate present in the composite is in the form of biphasic calcium phosphate consisting of 80% calcium hydroxyapatite and 20% tricalciumphosphate.

Comparative analysis of histological characteristics of both materials, after 12 weeks of implantation into the rats' lower jaw, establishes that both materials are biocompatible. However, there is a big difference in qualitative content of host's tissue between the implanted materials. The basic characteristic of the tissue around and between the BCP/DLPLG particles is the presence of a mature bone tissue with all its usual characteristics, while around the particles of pure BCP, connective tissue is without present signs of ossification.

References

- [1] N. Ignjatović, S.Tomić, M. Dakić, M. Miljković, M. Plavšić and D. Uskoković, *Biomaterials*, 1999, 20, 809.
- [2] N. Ignjatović, M. Plavšić, M. Miljković, Lj. Živković and D. Uskoković, *Journals of Microscopy*, 1999, 196, 243.
- [3] N. Ignjatović, M. Plavšić and D. Uskoković, *Adv. Eng. Mater.*, 2000, 2, 511.
- [4] N. Ignjatović, K. Delijić, M. Vukčević, D. Uskoković, *Z. Metallkunde* 92, 2001, 2, 145.
- [5] N. Ignjatović, E. Suljovrujić, J. Budimski, I. Krakovsky, D. Uskoković, *Journal of Biomedical Materials Research Part B: Applied Biomaterials*, (2004) in print

COMPOSITES BASED ON BENTONITE CLAYS AND NONWOVEN TEXTILES

A. Milutinović-Nikolić¹, S. Lukić², J. Krstić¹, Z. Vuković¹ and M.V. Stanković¹

¹*Institute of Chemistry, Technology and Metallurgy, Department of Catalysis and Chemical Engineering, Belgrade, Serbia and Montenegro*

²*Faculty of Technology and Metallurgy, Belgrade, Serbia and Montenegro*

Abstract

The novel composite material based on bentonite clay and hemp-nonwoven textiles was synthesized. The influence of bentonite grain size and filtration flow rate on composite Pb²⁺ removal efficiency was studied. The composites proved irreversible capability of highly efficient Pb²⁺ removal within investigated conditions. The obtained results confirmed that removal efficiency increases with decrease of bentonite particle size and decrease of filtration flow rate.

Introduction

The specially designed composite geotextiles are gaining importance in environmental protection as filters, bio-barriers and geosynthetic clay liners (GCL). GCLs are made by bonding bentonite granules between layers of geotextiles. The bonding can be performed by sandwiching the bentonite between two nonwovens and then needling the layers or by the use of water-based adhesive to bond bentonite between the two geotextiles [1,2].

The GCLs act as barriers, while bentonite component of GCLs provides adsorption of pollutants. The polypropylene (PP) fibers are the most commonly used for production of nonwoven component of GCLs. Bio-based fibers are seldom used in geotextiles mainly for temporary or short term applications although they have advantage being recyclable and biodegradable [3].

The part of results obtained during the investigation of synthesis of composites based on bentonite clays and hemp-nonwovens are presented. The main goal of this work was to study the influence of bentonite grain size on capability of composite to remove Pb²⁺ from solutions simulating atmospherical pollution.

Experimental

Hemp from Bački Brestovac, Serbia was previously chemically modified in order to obtain fine fibers used in synthesis of composite. Needle-punched polypropylene (PP) nonwoven "INTEX", Mladenovac, Serbia ($m_A = 40 \text{ g/m}^2$) was used for thermal bonding of hemp fibers. The textile material was formed by alternating layers of hemp and nonwoven PP. Both lower and upper nonwoven part of composite had only 30 mass % of PP. The bentonite layer was embedded between two nonwovens. Those layers were then pressed in die on elevated temperature to form composite. Bentonite layer consisted of chemically, physically, morphologically and texturally characterized bentonite powder from coal mine "Bogovina", Serbia [4]. Composites consisted of

powders having different particle size distribution. One composite contained clay particles ground to pass 74 μm sieve (sample A), while the other composite consisted of coarser particles in interval 74-500 μm (sample B). In both composites the mass ratio between textile and bentonite part of composite was 1:2. For comparison purposes the sample solely made of textile components hemp and PP was made.

By using the obtained materials the efficiency of Pb^{2+} ion removal from solutions was measured. The 10 ppm Pb^{2+} solution was filtrated through investigated samples. The filtration area was constant for all experiments. The investigation process consists of four filtrations with different precisely controlled flow rates and one rinsing cycle. Different flow rates were implied in order to investigate the influence of contact time on sorptional properties of composite. The Pb^{2+} content in filtrate was measured by dropping mercury electrode using polarograph 757 VA Computerance-Metrohm in presence of acetate buffer.

Results and Discussion

The various parameters affecting the efficiency of heavy metal removal by investigated composites is possible to divide in two groups. First consisting of composite properties and second of investigation - filtration conditions. The type, amount and ratio of individual constituents of composite, quality of each constituent (particle size, specific surface area of bentonite, fineness of hemp fibers, pore size of nonwoven PP etc.) synthesis conditions, composite history, humidity and pH are among the most important parameters of first group. The investigation conditions include concentration of Pb^{2+} ions, composite: solution mass ratio, flow rate- contact time, temperature, solution pH etc. [5]

Fig 1. shows the influence of flow rate on efficiency of Pb^{2+} removal of both investigated composites.

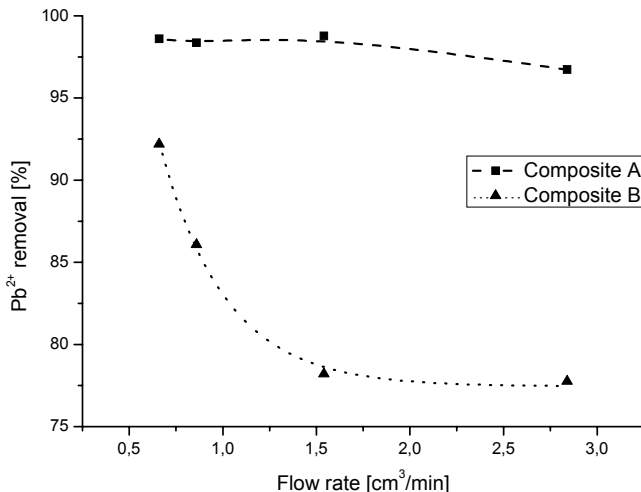


Figure 1. The influence of flow rate on Pb^{2+} removal

Both investigated composites were highly efficient in removal of Pb^{2+} ions from its solution. The results presented in Fig. 1 clearly indicate that the composite A, con-

taining finer bentonite particles $< 74 \mu\text{m}$ shows greater adsorption properties than composite B. The composite A shows exquisite adsorption properties being capable to remove 96.7% Pb^{2+} at the highest investigated flow rate.

It was established that the degree of Pb^{2+} ion removal by composite B exponentially decreases with flow rate. The results obtained for composite A are somewhat different. With the increase of flow rate the removal efficiency slightly decreases not showing any particular regularity. It can be assumed that some of previously mentioned parameters have as much importance for composite A efficiency as flow rate. For example the pore size of nonwoven PP gain on importance for composite with finer bentonite fraction since each subsequent filtration cycle might be performed with somewhat smaller quantity of the finest bentonite fraction of composite due to rinsing.

Difference between solely textile material and both investigated composites is particularly proved when their behavior was tested by rinsing with distilled water. After rinsing of both composites the adsorbed Pb^{2+} remain completely within bentonite layer, while solely textile material partially releases previously absorbed ions. The composites proved irreversible capability of Pb^{2+} removal within investigated conditions.

Conclusion

The investigated bentonite/nonwoven composite materials showed great efficiency in irreversible removal of Pb^{2+} ions from solution. Composite containing finer bentonite fraction $< 74 \mu\text{m}$ showed better adsorption properties than composite with coarser bentonite fraction. Composite with finer bentonite fraction showed very high Pb^{2+} removal efficiency adsorbing 96.7-98.8 % of Pb^{2+} ions depending on flow rate and filtration cycle.

The investigation confirmed that synthesized composite exhibits quality necessary to perform ecological function of the agrotexile composite, protecting the soil from heavy metal pollution. The investigations are still in progress.

Acknowledgements

This work was supported by the Ministry of Science & Environmental Protection of R. Serbia (Projects MHT.2.09.0022.B and MHT.2.10.0221).

References

- [1] M. L. Marienfeld, Tappi Journal, 1995, 78(9), 143.
- [2] H. Y. Jo, T. Katsumi, C. H. Benson, T. B. Edil, J. Geotech. Geoenviron., July 2001, 557.
- [3] B. English, Proc. "Research in industrial application of non food crops, I: plant fibres", Copenhagen, Denmark, 1995.
- [4] Lj. Rožić, T. Novaković, M. Anić, Z. Vuković, D Jovanović: Proc. 6th Inter. Conf. Fund. App. Phys. Chem., Belgrade, Serbia, 2002, 520.
- [5] H. B. Bradl, J. Colloid Interface Sci., 2004, in press.

THE EFFECT OF SILVER CONTENT ON THE CIS-TRANS ISOMERIZATION SELECTIVITY DURING HYDROGENATION OF SOYBEAN OIL OVER SILVER-PROMOTED Ni/DIATOMITE CATALYSTS

M.V. Stanković, B. Marković, A. Šućurović and D. Jovanović

*IChTM Department of Catalysis and Chemical Engineering,
Njegoševa 12, 11000, Belgrade, Serbia and Montenegro*

Abstract

The effect of silver content in silver-promoted Ni/Diatomite catalyst on the cis-trans isomerization selectivity in the process of soybean oil hydrogenation was studied. Precursors of silver-promoted Ni/Diatomite catalyst were prepared by coprecipitation. The silver content in obtained catalyst varied in the range from 0.1 to 4.0 wt %. Catalytic test was performed in a three-phase semi batch reactor at 160°C and pressure of hydrogen 0.16 MPa. Samples were characterized by atomic absorption spectrometry (AAS), nitrogen adsorption at -196°C (BET), mercury porosimetry, and FT-IR spectrometry. The results obtained suggest that formation of trans fatty acids (TFA) during soybean oil hydrogenation depend on the silver content. A correlation between the silver content and the cis-trans isomerization selectivity was established. The results also reveal that, this effect was in a good correlation with the textural characteristics of the prepared samples.

Introduction

Reduced Ni/Diatomite is a classic vegetable oil hydrogenation catalyst used in industrial conditions at $393 < T < 453$ K and $0.1 < P_{H_2} < 1.0$ MPa [1]. In these conditions, polyunsaturated fatty acids are hydrogenated preferentially compared to monounsaturated species. This selectivity increases with the increase of temperature and decreases with hydrogen pressure; unfortunately, this also applies to the production of TFA. The selectivity in hydrogenation could be greatly improved by using a promoted nickel catalysts [2, 3], with aim to suppress cis-trans isomerization reaction during hydrogenation vegetable oils. If the factor contributing to this complex hydrogenation process can be understood, then the industry would benefit because margarine and vegetable shortening would contain less undesired TFA.

In the present paper, the silver promotion of Ni/Diatomite was performed in order to improve cis-trans isomerization selectivity during hydrogenation of soybean oil. The research was focused on the effect of silver content in promoted catalyst samples on the cis-trans isomerization selectivity.

Experimental

Precursors of silver-promoted Ni/Diatomite catalysts have been prepared by coprecipitation from mixed solution of $Ni(NO_3)_2 \cdot 6H_2O$ and $AgNO_3$ using solution of Na_2CO_3 . The amount of mixed salt solution of nickel and silver were chosen in order

to achieve desired composition of silver in the final catalyst (0.1-4.0 wt %), while the Diatomite/Ni weight ratio was 1.17. The co-precipitation was performed at 90°C with stirring and controlled pH at pH 9.2±0.05. After the co-precipitation was completed, the resultant precipitates were filtered, washed, and reduced at 430°C in a stream of gas mixture (50% H₂/50% N₂). In order to reduce pyrophority of the reduced metal nickel, passivisation was performed with the mixture of 350 ppm O₂ in nitrogen at ambient temperature. Impregnation of passivated catalyst samples were made with pure paraffin oil.

Catalyst samples were tested in the process of soybean oil hydrogenation using a three-phase semi batch reactor operating under 0.16 MPa P_{H₂} and 160°C. Each experiment was performed with 5 dm³ of soybean oil, 0.1 wt% of catalyst, and stirring rate of 750 r.p.m. The change in the TFA composition of the soybean oil during hydrogenation with a certain catalyst sample was determined by means of a series of hydrogenations, interrupted at various intervals of time. After each interval, the content of TFA was determined by IR [4].

The nickel and silver content of the catalyst samples were determined on a Varian AA1275 atomic absorption spectrophotometer. Adsorption and desorption isotherms for nitrogen were obtained at -196°C using a Thermo Finnigan Sorptomatic 1990. Specific surface (S_{BET}) values were obtained using the Brunauer-Emmet-Teller (BET) equation [5]; mean pore size distributions were those of the Barrett-Joyner-Halenda (BJH) method [6], with the desorption branch being analyzed. Pore volume was determined by mercury porosimetry (Carlo Erba Porosimeter 2000 series). The IR spectra were obtained on a Perkin Elmer FT-IR spectrometer 1725 X.

Results and Discussion

Textural characteristics of the prepared silver-promoted Ni/Diatomite catalyst samples are summarized in Table 1.

Table 1. Textural characteristics of the prepared Ag-Ni/Diatomite catalyst samples

Sample	Silver wt %	S _{BET} m ² /g	Pore volume cm ³ /g	B.J.H. Pore size median pore diameter/nm
0.1Ag-Ni/Diatomite	0.1	41.4	0.630	71
1.0Ag-Ni/Diatomite	1.0	60.4	0.539	30
4.0Ag-Ni/Diatomite	4.0	109.9	0.455	11

From data presented in Table 1, it can be observed that the specific surface area (S_{BET}) is affected by the silver content. The increase in S_{BET} with the increase of silver content can be explained by the development of surface of silver within the diatomite support and possible metal-support interaction [7]. On the other hand, pore volume and median pore diameter decreased with the increase of silver content.

Results of the catalytic test are shown in Table 2. The formation of TFA is controlled by the silver content; increased amount of silver promoter decrease the cis-trans selectivity. The explanation that selectivity and cis-trans isomerisation are controlled by the silver content may be results of several factors among the most important are: (i) surface reaction of hydrogenation of oil are favoured on the samples with better

textural performances (Table 1); (ii) hydrogen spillover mechanism in the presence of silver particles [8].

The data obtained for refractive index and solid fat content are in accordance with the TFA content (Table 2).

Table 2. Characteristics of hydrogenated soybean oil vs x%Ag-Ni/Diatomite catalyst

Sample	Time min	Refractive index ^a n_D^{20}	SFC ^b (AOCS)			Total TFA %
			20°C	30°C	35°C	
0.1Ag-Ni/Diatomite	55	1.4620	0.75	0.78	0.55	45.2
	115	1.4612	1.45	0.93	0.55	70.5
	155	1.4608	2.07	1.12	0.59	79.2
	195	1.4606	2.53	1.17	0.61	81.1
1.0Ag-Ni/Diatomite	55	1.4615	0.70	0.63	0.22	12.9
	115	1.4613	1.32	0.53	0.77	41.2
	155	1.4609	2.01	0.93	0.71	60.9
	195	1.4605	2.94	0.54	0.74	66.4
4.0Ag-Ni/Diatomite	55	1.4609	2.67	0.60	0.71	5.0
	115	1.4590	21.17	1.91	0.46	20.0
	155	1.4578	32.99	5.13	0.67	33.8
	195	1.4573	36.32	6.37	0.96	39.5

^aRefractive index determined by Abbe refract meter; ^bSolid Fat Content determined by NMR

Conclusion

The whole set of measurement carried out has shown that silver content in silver-promoted Ni/Diatomite catalyst could control product distribution in the process of soybean oil hydrogenation.

Selectivity of silver-promoted Ni/Diatomite catalyst samples to the formation of TFA decrease in the in the following order:

4.0 Ag-Ni/Diatomite < 1.0 Ag-Ni/Diatomite < 0.1 Ag-Ni/Diatomite.

Acknowledgement

This work was supported by the Ministry of Science and Environmental Protection of Republic of Serbia (Project-MHT.2.09.0022.B).

References

- [1] J. W. E. Coenen, J. Am. Oil Chem. Soc., 1976, 53, 382.
- [2] H. Li, H. Li, J. F. Deng, Catal. Today, 2002, 74, 53.
- [3] M. P. Gonzales-Markos, J. I. Gutiérrez-Ortiz, C. Conzález-Ortiz de Elguea, J. I. Alvarez, J. R. González-Velasko, Canadian J. Chem. Eng. 1998, 76, 927.
- [4] R. R. Allen, J. Am. Oil Chem. Soc., 1969, 46, 552.
- [5] S. Brunauer, P. H. Emmett, E. Teller, J. Am. Chem. Soc. 1938, 60, 309.
- [6] E. P Barrett, L. G. Joyner, P. P. Halenda, J. Am. Chem. Soc. 1951, 73, 373.
- [7] R. Lamber, N. Jaeger, G. Schulz-Ejkloff, Surf. Sci. 1990, 227, 268.
- [8] G. M. Pajonk, S.J. Teichner in Catalytic Hydrogenation, L. Červený (ed.), Elsevier, Amsterdam, 1986, 284.

THE INFLUENCE OF THE STRUCTURAL RELAXATION ON CHANGE OF FREE ELECTRON DENSITY OF $\text{Co}_{70}\text{Fe}_5\text{Si}_{10}\text{B}_{15}$ AMORPHOUS ALLOY

A. Maričić^a, D. Minić^b, B. Jordović^a and M.M. Ristić^c

^aTechnical Faculty Čačak, Čačak, Serbia,

^bFaculty of Physical Chemistry, University of Belgrade, Belgrade, Serbia,

^cSerbian Academy of Sciences and Arts, Belgrade, Serbia

Abstract

In this study we present the results on structural relaxation of $\text{Co}_{70}\text{Fe}_5\text{Si}_{10}\text{B}_{15}$ amorphous alloy investigated by measurements of thermo-electromotive force (TEMF) during an isothermal annealing (600 s duration). The activation energies of structural relaxation $E=224$ kJ/mol rate constants $k_1=6.66 \cdot 10^{-5} \text{ s}^{-1}$, $k_2=33 \cdot 10^{-5} \text{ s}^{-1}$ and $k_3=76 \cdot 10^{-5} \text{ s}^{-1}$ at temperatures T_1 , T_2 and T_3 , respectively, have been determined for process.

Introduction

The process of crystallization is usually studied under conditions of non-isothermal heating at constant rate and under conditions of isothermal heating at temperatures some lower than temperatures of crystallization. Kinetic features of amorphous alloys show correlation between the physical nature of the anomalous behavior of electronic states density at the Fermi level, thermal conductivity, heat capacitance and electrical resistivity on the one hand and structural inhomogeneities in these materials on the other. At temperatures up to 100 °C lower than the crystallization temperature, two competitive processes take place during annealing of amorphous alloys: on the one hand, free volume decreases, which lowers the rate of diffusion mass transport, and on the other hand, arranging processes bring the alloy closer to the crystallized state increasing its readiness for crystallization¹⁻³

Experimental

A thirty-micrometer-thick ribbon of the $\text{Co}_{70}\text{Fe}_{53}\text{Si}_{10}\text{B}_{15}$ amorphous alloy was used as a sample in our research. The mechanical junction of the investigated alloy and copper conductor was constructed for measuring TEMF. The measurements of TEMF and temperature dependence of the electric resistance were performed using double-channel voltage signals recorder with sensitivity of 1 μV . All measurements were done in the argon atmosphere.

Results and Discussion

According to DSC thermogram, Fig. 1, the alloy crystallizes in two stages, at temperatures $T_1=460.0\text{K}$ for first stage and at $T_2=540\text{K}$ for the second one.

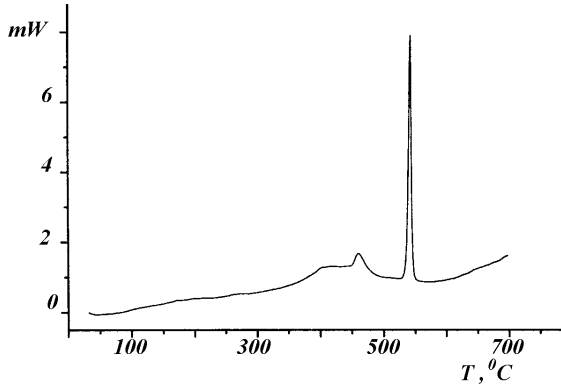


Figure 1. DSC curve; heating rate 10 K/min

The process of structural relaxation was investigated by measuring of thermo electromotive force (TEMS) constructed by mechanical junction of the copper conductor and investigated amorphous alloy (AL) under non-isothermal and isothermal conditions. Isothermal measurements were performed at temperatures $T_1=430\text{K}$, $T_2=460\text{K}$, $T_3=480\text{K}$ during 600 s. It was found that after each annealing the change of temperature coefficient of TEMS which is function of difference of electron density at Fermi level occurs:

$$\alpha = \frac{h^2}{2me} \left(\frac{3}{8\pi} \right)^{2/3} \left(N_{(E_F)_1}^{2/3} - N_{(E_F)_2}^{2/3} \right)$$

where h is Planck's constant, m_e is weight of electron, $N_{(E_F)_1}$ is electron density at Fermi level of copper and $N_{(E_F)_2}$ is electron density at Fermi level of amorphous alloy. During annealing electron density of copper does not change, so the change of temperature coefficient of TEMS is caused by the change of electron density of amorphous part of thermocouple. From the change of the TEMF temperature coefficient, after each isothermal annealing, relative change of electronic state density at Fermi level of amorphous alloy was determined:

$$\Delta N_{21}/N_2 = 2.36\% ; \Delta N_{22}/N_2 = 3.21\% ; \Delta N_{23}/N_2 = 9.80\% .$$

Experimentally obtained isothermal dependencies of the TEMF of the Cu-Al amorphous alloy thermocouple on time at given temperatures are linear and can be given as:

$$\varepsilon = \varepsilon_0 - k\tau$$

where ε is the TEMS at any moment during isothermal annealing, k – is a structural relaxation rate constant at a certain temperature and ε_0 – is TEMS at the annealing temperature for the initial moment of time τ . This value is proportional to the temperature of isothermal annealing and inversely proportional to the sample-heating rate to the given temperature.

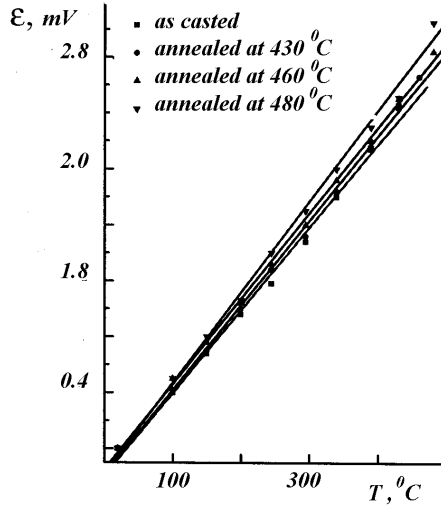


Figure 2. TEMF dependence on temperature alloys: as casted; annealed at 430K, annealed at 460K and annealed at 480K

From the line slopes $\Delta\varepsilon/\Delta\tau$ structural relaxation rate constants $k_1=6.66\cdot 10^{-5}\text{s}^{-1}$, $k_2=3310^{-5}\text{s}^{-1}$ and $k_3=76\cdot 10^{-5}\text{s}^{-1}$ for relaxation process were determined at temperatures $T_1=430\text{K}$, $T_2=460\text{K}$, $T_3=480\text{K}$, respectively.

From the slopes of linear dependencies $\ln k$ vs. $10^3/T$ the value of activation energy $E_a=224\text{kJ/mol}$ were determined.

The results on the measuring of the change of relative magnetic permeability before and after the annealing show that after structural relaxation magnetic properties have changed, being in direct correlation with the change of electronic state density at the Fermi level.

Conclusion

$\text{Co}_{70}\text{Fe}_5\text{Si}_{10}\text{B}_{15}$ amorphous alloy retains its amorphous structure up to 400°C . During the isothermal annealing, TEMF increases at temperatures about 50 to 100°C lower than the crystallization temperature. The electronic state density at the Fermi level increases after each isothermal annealing. The changes of electron density at the Fermi level during structural relaxation cause changes of its electrical and magnetic properties. Direct proportionality between the increase of electronic state density and electrical conductivity has been determined. The dependence of the magnetic properties on electronic state density is considerably more complex.

References

- [1] L.A.Jacobson, J.McKittrik, Rapid Solidification Processing, Elsevier, 1994.
- [2] A.P. Spak., V.L. Karbovskij, A.N. Jaresko, Metalofizika i noveisje tehnologij, 1994, 16 (3), 32.

ZEOLITE MODIFICATION BY INCORPORATION OF PALLADIUM CLUSTERS

S.Mentus¹, Z.Mojović² and Z.Tešić³

¹*Faculty of Physical Chemistry, Belgrade University, Studentski Trg 12, Belgrade,*

²*ICHM-Center of Catalysis and Chemical Engineering, Njegoševa 12, Belgrade*

³*Faculty of Chemistry, Belgrade University, Studentski Trg 12, Belgrade*

Abstract

Nanodispersed palladium clusters were incorporated into 13X zeolite cavities by impregnation/thermal degradation method. Procedure was repeated until Pt/13X mass ratio of 0.162 was obtained. Modified zeolite samples were characterized by x-ray diffractometry. This material, with 10% wt of black carbon added, was applied to a rotating glassy carbon disc electrode and was used to study electrochemical water splitting in slightly acidic aqueous solution, 2.5 mM H₂SO₄ + 1M Na₂SO₄.

Introduction

Electrocatalysis by precious metals dispersed on high surface area have been object of many studies. Zeolites, with their specific surface area of several hundred square meters, represent the ideal support for dispersed metal clusters. Negative charge of zeolite structure is usually compensated by alkali cations which may be replaced by transition metal ions through ion exchange, which are later transformed by reduction into metal nanoclusters inside zeolite cages.[1]. The catalytic effectiveness of such systems in numerous chemical reactions is well known. [2,3]

Haruta et al. [4] used impregnation / thermal degradation method to apply nanosized gold cluster on aluminosilicate surface.

In this paper, the technique of zeolite impregnation by acetylacetonate solution in acetone was used for palladium incorporation. [5] Zeolite modified by incorporated palladium clusters is used as electrode material for electrolytic water splitting.

Experimental

Palladium acetylacetonate was dissolved in acetone and zeolite 13X was soaked by the solution, dried to evaporate acetone and heated to 350^oC in order to decompose the complex compounds and desorb the decomposition products. In this way nanodispersed palladium clusters were introduced in zeolite cages. Procedure was repeated until Pd/zeolite weight ratio 0.162 was reached.

XRD of original and modified zeolites were taken on a Philips PW 1710 diffractometer and CuK α radiation being used.

Modified zeolite was homogenously dispersed in poly(vinylidene fluoride) (PVDF) solution (5%) in N-methyl pyrrolidone, by means of ultrasonic bath. 10 wt.% carbon black Vulcan XC72 (Carbot Corp.) was added to this suspension, in order to improve the electrical contact between zeolite particles and glassy carbon support. Thin layer of this suspension was applied on rotating glassy carbon disc. After solvent evaporation a thin film of modified zeolite in a polymer binder matrix remained. Electrolytic water

splitting from dilute acid solutions 2.5 mM H₂SO₄ + 1M Na₂SO₄ was carried out by use of rotating disc technique.

Results and Discussion

The diffractograms of pure 13X zeolite and palladium modified zeolite 13X-Pd as well as the 13X-Pd which was synthesized in air and then annealed under hydrogen atmosphere are presented in Fig. 1. The comparison of diffractograms indicates that by modification the original crystal structure of zeolite was not destroyed since all diffraction lines characteristic of original zeolite appear with same intensity ratios in the diffractograms of modified zeolite. Diffractogram of 13X-Pd indicates presence of PdO only, although Pd was expected, based on TGA.[6]. After annealing under hydrogen atmosphere, PdO lines are shifted to the ones which correspond to crystalline Pd. Appearance of oxide during the decomposition in air is probably consequence of high reactivity of nanodispersed Pd.

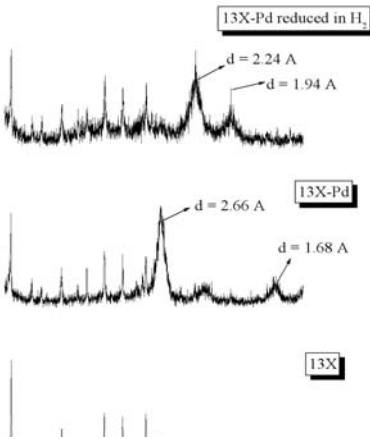


Figure 1. Comparative X-ray diffractograms of zeolite 13X, 13X-Pd synthesized in air, before and after annealing under hydrogen atmosphere

The cyclovoltammogram of 13X(Pd) (with 10% carbon black added), in dilute sulphuric acid, in the voltage region characteristic of water splitting, is presented in Fig 2. The materials shows high interfacial capacitance. Consequently, the polarization rates equal to, or lower than, 2 mVs⁻¹ were required to minimize the capacitance current. For the sake of comparison, the voltammogram obtained on smooth platinum disc under identical conditions was plotted in the same figure.

Palladium oxide reduction takes place around the potential of 0.2 V. Peaks of hydrogen adsorption/desorption, preceding hydrogen evolution, are much more pronounced on zeolitic sample then on smooth platinum. Hydrogen evolution on 13X(Pd) which involves protons from sulphuric acid starts at about -0.4 V. At potentials around -0.6 V limiting current appeared, followed by an additional current jump at potential below -0.9 V, due to the H₂ evolution. High anodic peak is registered probably as consequence of oxidation of Pd hydride, which can be quickly formed at room temperature on thin Pd foils [7]. Nanocluster form is even more favorable in that sense.

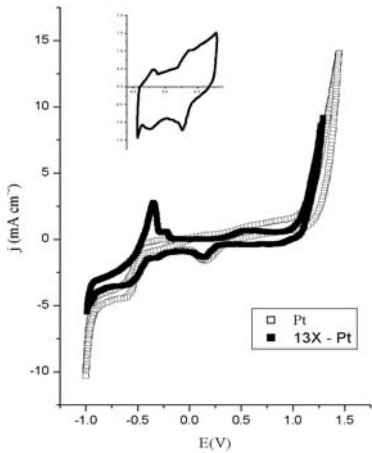


Figure 2. The voltammogram of 13X – Pd electrode in 2.5 mM H₂SO₄ recorded at polarization rate 2 mV/s and at rotation rate 10 cps, in comparison to the voltammogram of smooth Pt. The inserted picture presents the voltammogram of palladium modified zeolite electrode, recorded at scan rate of 10 mV/s, within limited voltage region characteristic of hydrogen adsorption and desorption.

The inserted picture in Fig 2 presents the voltammogram of 13X(Pd), recorded at an enhanced scan rate of 10 mVs⁻¹, within a limited voltage region characteristic of hydrogen adsorption and desorption. This voltammogram was corrected for the background charging capacitance current in

order to calculate surface coverage with adsorbed hydrogen, amounting to 2.9 mC cm⁻²

Conclusion

Modification of 13X zeolite by impregnation/thermal degradation method results in nanostructured metal deposits into zeolite cavities. XRD analysis evidence that the metal incorporation do not destroy the original crystal structure of zeolite. Palladium incorporated in zeolite in air atmosphere appears in the form of oxide, which can be easily reduced to metal state. If used as electrode material with 10 wt.% carbon black added, in comparison to smooth platinum, it displays lower overvoltage for water electrolysis. Accessible surface of palladium clusters within zeolite cavities corresponds to 2.9 mC cm⁻² of adsorbed hydrogen.

Acknowledgment

The work was supported by Ministry of Science, Technology and Development of Republic Serbia, contract No 1399 (S.M.), contract No MHT.2.09.0022.B (Z.M.) and contract No 1713 (Z.T)

References

- [1] D.W.Breck, *Zeolite Molecular Sieves: Structure, Chemistry and Use*, New York, 1974
- [2] T.V.Choudhary, C.Sivadinarayana, C.C.Chusuei, A.Klinghoffer, D.W.Goodman, *J.Catalysis*, 2001, 199, 9.
- [3] T.F.Garetto, E.Rincon, C.R.Apestequia, *Appl.Catalysis B* 2004, 48, 167.
- [4] M.Okumura, T.Tanaka, A.Ueda, M.Haruta, *Solid State Ionics*, 1997, 95, 143.
- [5] S.Mentus, Z.Mojović, N.Cvjetičanin, Z.Tešić, *Fuell Cells – From Fundamentals to Systems*, 2003, 3, 1.
- [6] Z.Mojović, S.Mentus, N.Cvjetičanin and Z.Tešić, Introduction of Pt and Pd nano-clusters in zeolite cavities by thermal degradation of acetylacetonates, *Materials Science Forum*, 2003, 453-454, 257.
- [7] A.Czerwinski, I.Kietszryn, M.Grden, *J.Electroanal.Chem.*, 2000, 492, 128.

IN SITU XRPD AND DSC STUDY OF ORDER-DISORDER PHASE TRANSITION IN NANOSIZE LI-FERRITE

M. Vučinić-Vasić¹, B. Antić², A. S. Nikolić³, A. Kremenović⁴, S. Rakić⁵,
J. Blanuša², N. Cvjetičanin⁶ and A. Kapor⁵

¹ Faculty of Technical Sciences, University of Novi Sad, Trg D. Obradovica 6, Novi Sad, ² Institute of Nuclear Sciences "Vinca", Laboratory of Solid State Physics, P. O. Box 522, Belgrade, ³ Faculty of Chemistry, Department for Inorganic Chemistry, University of Belgrade, P. O. Box 158, Belgrade, ⁴ Faculty of Mining and Geology, Laboratory for Crystallography, University of Belgrade, P. O. Box 162, Belgrade, ⁵ Institute of Physics, University of Novi Sad, Trg D. Obradovica 4, Novi Sad, ⁶ Faculty of Physical Chemistry, University of Belgrade, P. O. Box 137, Belgrade, Serbia and Montenegro

Abstract

An order-disorder phase transition of nanosize Li-ferrite ($\text{Li}_{0.50}\text{Fe}_{2.50}\text{O}_4$) was studied by DSC measurements and *in situ* XRPD technique. The phase transition temperature is found to be 762 °C (DSC) and (745±5) °C (XRPD).

Introduction

The cubic nanosize spinel ferrites are well known, important materials for applications. Also, nanometer scale ferrites are under current interest in basic researches, as convenient systems for studies of nanomagnetism.

Ferrites with spinel structure have a general formula AB_2X_4 with cations occupying two sites, tetrahedral 8a (A site) and octahedral 16d (B site) in the space group (S.G.) $\text{Fd}\bar{3}\text{m}$. Some spinels possess ordered structure with possible cation ordering at tetrahedral or/and octahedral sites [1]. The order-disorder phase transitions ($\text{P4}_3\text{32} \leftrightarrow \text{Fd}\bar{3}\text{m}$) of $\text{Li}_{0.50}\text{Fe}_{2.50}\text{O}_4$ spinel take place at $T=735\text{-}755$ °C [2]. In our previously paper we have reported synthesis and structural characterisation of three phases Li-ferrite sample [3]. The obtained sample is composed of three phases that are determined by standard Rietveld procedure: $\text{Li}_{0.5}\text{Fe}_{2.5}\text{O}_4$ (S.G. $\text{P4}_3\text{32}$), $\text{Li}_{1.16}\text{Fe}_3\text{O}_4$ (S.G. $\text{Fd}\bar{3}\text{m}$) and LiFeO_2 (S.G. $\text{Fm}\bar{3}\text{m}$). Particle size of ~ 50 nm of as prepared sample has been determined from scanning electron microscopy (SEM) [3].

The aims of this work have been to study (i) order-disorder phase transition and (ii) thermal expansion of nanosize Li-ferrites, obtained from acetylacetonato complexes by *in situ* XRPD and DSC measurements.

Experimental Details

The high temperature XRPD measurements were performed in an Anton Paar HTK-2 furnace in 2θ range from 10° to 90° with step of 0.02° and exposition of 4s per step. Differential scanning calorimetry (DSC) measurements were done in air at V3.7A TA instrument in the temperature range 20-1000 °C.

Results and Discussion

The refinement of high temperature XRPD data was performed with the Fullprof computer program [4]. The $\text{Li}_{0.5}\text{Fe}_{2.5}\text{O}_4$ was refined in S.G. $P4_32$ up to 740°C , while above this temperature it was refined in S.G. $\text{Fd}\bar{3}m$. Presence and disappearing of ordered phase reflections, (110), (210), (211) was used to choose one of the space groups and to determine temperature of phase transition. Observed $T_C = (745 \pm 5)^\circ\text{C}$ is close to the one found for bulk $\text{Li}_{0.5}\text{Fe}_{2.5}\text{O}_4$ [5]. Figure 1 shows the temperature dependence of lattice parameter of nanosize Li-ferrites. The corresponding linear coefficients of the thermal expansion (α) are given at the end of Table 1.

During the refinement procedure occupation numbers in $\text{Li}_{1.16}\text{Fe}_3\text{O}_4$ were varied separately, thus allowing changes in stoichiometry. Percentage of each phase in sample is given in Table 1 together with occupation numbers (N) of Fe in spatial position 4b and 16d. At elevated temperatures Fe ions migrate from 12d to 4b sites (Li vice versa), which induce change in crystal symmetry ($P4_32 \leftrightarrow \text{Fd}\bar{3}m$). With heating we have shown that percentage of $\text{Li}_{0.5}\text{Fe}_{2.5}\text{O}_4$ decreases, while the one of LiFeO_2 increases, Table 1. Coefficients of thermal expansion of ordered phase ($P4_32$) and disordered ($\text{Fd}\bar{3}m$) are close to the one in ref. [5].

Also, we have used DSC measurement to find phase transition temperatures in sample. Figure 2 shows the phase transformation temperatures during the sample heating at a heating rate of $20^\circ\text{C}/\text{min}$. The critical temperature $T_C' = 633^\circ\text{C}$ corresponds to the magnetic phase transition of $\text{Li}_{0.5}\text{Fe}_{2.5}\text{O}_4$ (ferrimagnetic \leftrightarrow paramagnetic). The second critical temperature at $T_C'' = 762^\circ\text{C}$ corresponds to an order-disorder phase transition of Li-ferrite.

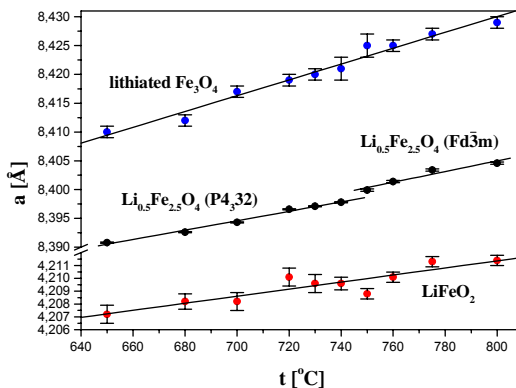


Figure 1. Temperature dependence of lattice parameter of nanosize Li-ferrites

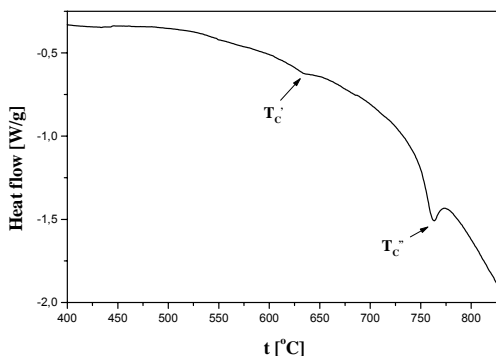


Figure 2. DSC curve of nanosize Li-ferrites

Table 1. Results of temperature monitoring of order-disorder phase transition in nanosize Li-ferrites

T [°C]	Li_{0.5}Fe_{2.5}O₄			lithiated Fe₃O₄	LiFeO₂	
	%	P4 ₃₂ N(Fe _{4b})	Fd $\bar{3}$ m N(Fe _{16d})	formula unit	%	%
650	83(2)	0.07(1)	-	Li _{1.23} Fe ₃ O ₄	9(2)	8(1)
680	79(2)	0.09(1)	-	Li _{1.16} Fe _{3.13} O ₄	10(1)	11(2)
700	76(2)	0.15(1)	-	Li _{1.07} Fe _{3.13} O ₄	12(1)	12(1)
720	74(2)	0.16(1)	-	Li _{1.12} Fe _{3.25} O ₄	12(1)	14(2)
730	75(2)	0.26(1)	-	Li _{1.18} Fe _{3.10} O ₄	9(1)	16(2)
740	77(2)	0.43(1)	-	Li _{1.25} Fe _{2.96} O ₄	6(1)	17(1)
750	69(2)	-	1.5(fix)	Li _{1.20} Fe _{3.07} O ₄	8(2)	23(2)
760	70(2)	-	1.5(fix)	Li _{1.24} Fe _{3.19} O ₄	10(2)	20(2)
775	73(2)	-	1.5(fix)	Li _{1.33} Fe _{3.23} O ₄	10(1)	17(1)
800	67(2)	-	1.5(fix)	Li _{1.25} Fe _{3.04} O ₄	10(2)	23(2)
$\alpha \cdot 10^{-6}$ [1/°C]		0.98(5)	1.1(2)	16.5(9)		0.67(9)

References

- [1] C. Hass: J. Phys. Chem. Solids 1965, 26, 125.
- [2] M. Guillot: Magnetic Properties of Ferrites, in Electronic and Magnetic Properties of Metals and Ceramics, ed. K. H. J. Buschow (VCH Germany 1994).
- [3] M. Vučinić-Vasić, B. Antić, J. Blanuša, S. Rakić, A. Kremenović, A. S. Nikolić and A. Kapor, submitted to Applied Physics A.
- [4] J. Rodriguez-Carvajal, FullProf computer program, 1998,
<ftp://charybde.saclay.cea.fr/pub/divers/fullprof.98/windows/winfp98.zip>.
- [5] M. Brunel and F. Bergevin: C. R. Acad. Sc. Paris, 1964, 258, 5628.

MECHANICALLY ACTIVATED CERIA

S. Zec and S. Bošković

*Institute of Nuclear Science Vinča, Materials Science Laboratory,
11001 Belgrade, POB 522, Serbia and Montenegro*

Abstract

The reduction of commercial and mechanically activated CeO_2 powder at $1200\text{ }^\circ\text{C}$ in an argon atmosphere was examined by XRD. Mechanical activation of oxide powder was performed by milling in a vibratory mill for different lengths of time. During 30 min of milling it came to the greatest change in crystallite size, as well as of lattice distortion of CeO_2 while after 60 min of activation effect of milling on the CeO_2 properties was negligible. Fired CeO_2 was partly reduced but firing of 60 min milled CeO_2 produced only CeO_{2-x} with lattice parameter $a = 0,550\text{ nm}$.

Introduction

Studying of ceria - CeO_2 , has been intensified recently, due to its wide range of applications[1]. CeO_2 is important in a various fields of technology including optoelectronics, microelectronics, catalysis, solid oxide fuel cells, corrosion protection, ceramics sintering etc. The main attention is paid to the oxygen transport ability of ceria as a result of the presence of oxygen vacancies, due to different cerium ion valent states, tetravalent and trivalent, in non-stoichiometric CeO_{2-x} ($0 < x < 0.3$). Defect fluorite structure is formed due to the presence of oxygen vacancies [2]. Different procedures (chemical processes, solid solutions, etc.) were applied with the aim to obtain ultrafine ceria powders and to improve the degree of the ceria reduction [3]. As no evidence of the influence of mechanical activation on the formation of CeO_{2-x} was found in the literature we have investigated in the present paper the reduction of mechanically activated ceria.

Experiment

Commercial oxide powder CeO_2 (Aldrich, purity 99,9 %, particle size $< 5\text{ }\mu\text{m}$) was mechanically activated in vibratory mill, Pulverisette 9(Fritsch), made of tungsten carbide (WC). Oxide powder batch of 10 g were milled 2, 15, 30, 45, 60, 90 and 120 min applying the vibration speed of 1450 rpm. The activated mixture and non-activated oxide powder were pressed into pellets (diameter 10 mm) under 35 MPa. Pellets were fired in an Astro furnace in the flowing argon atmosphere at $1200\text{ }^\circ\text{C}$, 1 hour. Cooling of pellets were done under argon together with furnace down to the room temperature. X-ray powder diffraction (XRD) analysis was performed by Siemens D500 diffractometer using Ni-filtered $\text{CuK}\alpha$ radiation and scanning speed of $0.02\text{ }^\circ/2\theta/\text{s}$. XRD data were processed with Diffracplus software while the lattice parameters were refined by Wincell program. Crystallite size (D) and lattice distortion

(ϵ) were determined on the base of FWHM (full width at half maximum) of diffraction peaks using Cauchy expression [4].

Results and Discussion

Lattice parameter change as a function of milling time of the cubic CeO_2 unit cell was not observed. Rapid decrease in CeO_2 crystallite size up to 34 nm in comparison with 140 nm measured in non-activated oxide powder occurred in the first 2 min of milling. During 30 min of milling the greatest change of crystallite size as well as lattice distortion of CeO_2 (Fig. 1) was observed, due to its particles fragmentation and lattice defects formation. After 60 min of activation, effect of milling on the CeO_2 crystallographic properties was negligible. CeO_2 fired 1 h at 1200 °C in argon was partly reduced, so that two phases were present according to the related XRD pattern (Fig. 2a), CeO_2 phase with lattice parameter $a = 0,541$ nm and smaller quantity of the second one, non-stoichiometric CeO_{2-x} with lattice parameter $a = 0,548$ nm. Firing of 60 min milled CeO_2 for 1 h at 1200 °C produced only CeO_{2-x} (Fig. 2b), which lattice parameter $a = 0,550$ nm corresponding to the expansion of the unit cell of 1.8% compared to the unreduced cell.

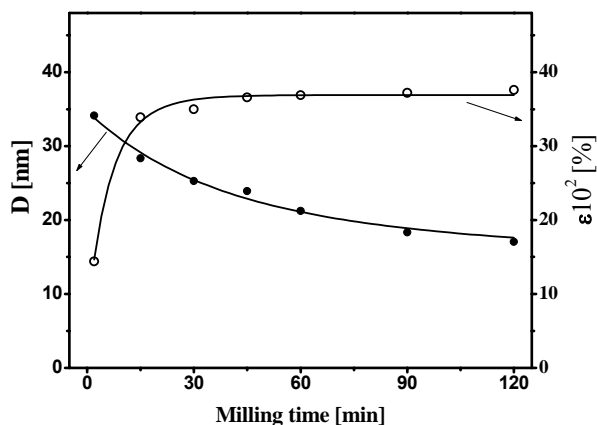


Fig. 1 CeO_2 crystallites size (D) and lattice distortion (ϵ) as a function of milling time

These results designate that activation of CeO_2 by milling accelerates its reduction process and makes it more effective on heating. Through the particles fragmentation, crystallite size decrease and the lattice defects got introduced. Mechanical activation affects also the surface structure of the CeO_2 powder because in the activated ceria heated at 1200 °C mobility of oxygen ions was higher, release of oxygen from the crystal lattice was easier and followed by oxygen vacancies formation as well as reduction of the part of tetravalent cerium into trivalent. Therefore, the mechanical activation can be applied as prosperous procedure in the redox reaction of ceria.

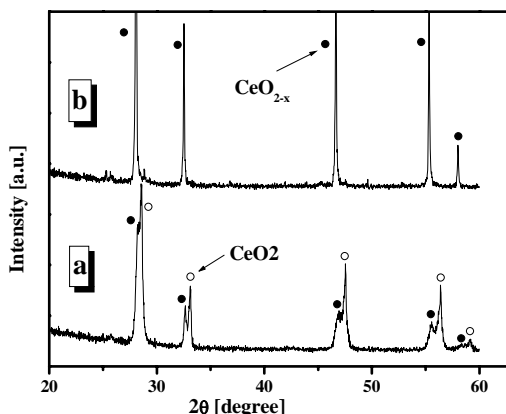


Fig. 2 XRD patterns of a) non-activated and b) 60 min activated CeO_2 fired at 1200 °C in argon.

Conclusion

The major change in crystallite size and lattice distortion of the CeO_2 powder occurred within 60 min of milling in a vibratory mill while the lattice parameter of CeO_2 was not affected by milling. Ceria fired 1 h at 1200 °C in argon was partly reduced into non-stoichiometric CeO_{2-x} with lattice parameter $a = 0,548$ nm but firing of 60 min milled ceria for 1 h at 1200 °C produced only CeO_{2-x} with lattice parameter $a = 0,550$ nm. Activation of CeO_2 by milling accelerates its reduction process and makes it more effective upon heating. In the mechanically activated ceria mobility of oxygen ions is higher and the release of oxygen atoms was followed by reduction of the part of tetravalent into trivalent cerium ions, and consequently by oxygen vacancies formation.

Acknowledgment

This work was supported with the Ministry of Science and Environment protection of the Government of the Republic Serbia, project No. 1947.

References:

- [1] A. Trovarelli, M. Boaro, E. Rocchini, C. Leitenburg, G. Dolcetti, J. Alloy and Compo., 2001, 323-324, 584.
- [2] A. Gotte, K. Hermansson, M. Baudin, Surface Science, 2004, 552, 273.
- [3] Y. Zhou, M. N. Rahaman, Acta Mater., 1997, 45, 3635.
- [4] B. Lönnberg, J. Mater. Sci., 1994, 29, 3224.

DTA STUDY OF THE PARTICLE SIZE EFFECT ON THE CRYSTALLIZATION MECHANISM OF SILICATE GLASS POWDER DOPED WITH FLUORINE ANIONS

M. B. Tošić, V. D. Živanović and J.D. Nikolić,

*Institute for Technology of Nuclear and Other Mineral Raw Minerals,
86 Franchet d' Esperey, Belgrade, Serbia and Montenegro*

Abstract

This paper presents the results of DTA study of the particle size effect on the mechanism of crystallization of silicate glass powder doped with F⁻ anions. The results show the complex crystallization behaviour. Increasing of F⁻ anion content in the silicate glass powder has effect on the change of the phase composition for the surface crystallization mechanism and has not effect for the volume crystallization mechanism.

Introduction

Previous investigations of crystallization in glasses showed that the particle size of the powder glass has an influence on the mechanism of its crystallization [1]. If the surface and volume crystallization mechanisms compete in the same glass, one usually is being dominant [2]. The aim of this study was to investigate the influence of particle size on the mechanism of crystallization of silicate glass powder by DTA method. For this study the glass samples with initial composition: 53.5SiO₂ · 11.5Al₂O₃ · 12 CaO · 16.5MgO · 6.5K₂O (mol%) were chosen . This composition was doped with fluorine anions in quantity which made the content of anion F⁻ in glasses of : 0.5; 1.5 and 2.0 mol%.

Experimental

The raw materials used are reagent grade Al₂O₃, MgO, CaO, CaF₂, K₂CO₃, and high-purity quartz (>99.5% SiO₂). The appropriate batch composition was melted at 1520 °C for 1 h in Pt crucible. The melts were cast on a steel plate and cooled in air. Powder X-ray diffraction analysis (XRD) confirmed that the quenched melts were vitreous. The glass samples were transparent, without visible residual gas bubbles. In order to investigate the dominant crystallization mechanism, powder samples of the following granulations were prepared: <0.038; 0.038-0.053; 0.053-0.1; 0.1-0.212; 0.212-0.3; 0.3-0.4; 0.4-0.63; 0.63-0.7 and 0.7-1.0 mm. In the experiments, a constant weight (100 mg) of the samples were heated at a heating rate of v=10 °C/min. The series of experiments were performed using a Netzch STA 409 EP device, with Al₂O₃ powder as the reference material.

Results and Discussion

Surface and volume crystallization mechanisms compete in the same glass, one usually being dominant. For assessment of the surface and bulk crystallization, the

method proposed by C.S.Ray *et al.*[3] is suggested. According to this method, the ratio $T_p^2/(\Delta T)_p$ is plotted as a function of particle size, where is T_p the temperature of the DTA peak and $(\Delta T)_p$ is the width at half the peak maximum. The parameter $T_p^2/(\Delta T)_p$ is related to the crystal growth dimension n , according to the following relation[4]

$$n = \frac{2.5 \cdot R}{E_a} \cdot \frac{T_p^2}{(\Delta T)_p} \tag{1}$$

Here, R is the gas constant and E_a the effective activation energy for the glass-to-crystal transformation. Assuming E_a to be independent of particle size and temperature (at least in the temperature regime of the DTA scans), the ratio $T_p^2/(\Delta T)_p$ was used as a qualitative measure for evaluating the crystallization mechanism of glass powders. If surface crystallization continues to dominate with increasing particle size, $T_p^2/(\Delta T)_p$ should be the same for all particle sizes. Crystal growth on volume nuclei results in a three-dimensional crystallization process. For dominant volume crystallization, therefore, $T_p^2/(\Delta T)_p$ should increase with increasing particle size.

Figure 1 shows a comparative presentation of the change in $T_p^2/(\Delta T)_p$ with the average particle size for this three different glasses

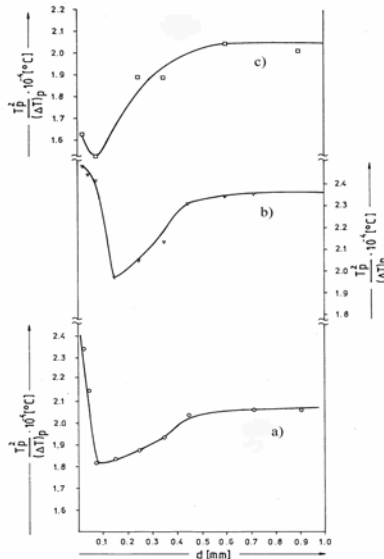


Figure 1 $T_p^2/(\Delta T)_p$ vs. particle size for glasses with F^- content of :
 a) 0.5, b) 1.5 and c) 2.0 mol %.

As can be seen from this figure, complex curves of similar shape with three distinguishable regions were obtained. For average particles size <0.075 mm (smallest granulations), in the total number of present nuclei, the number of surface with respect to internal nuclei is dominant. Due to that, the surface crystallization is dominant

in these particles. The ratio $T_p^2/(\Delta T)_p$ should have a constant value for the dominant surface nucleation. In this case, a limited number of measurements were performed (for two or three particles sizes) and the experimental errors were presented, so that this is insufficient for a reliable conclusion regarding to behaviour of $T_p^2/(\Delta T)_p$.

In the range of glass particle sizes from 0.075-0.150 mm, the number of surface nuclei is reduced to such an extent that it is equalized with the number of volume nuclei. The total number of the present nuclei is smallest and $T_p^2/(\Delta T)_p$ display minima, which is in agreement with Equation (1). With increasing of F^- content in glass, the minima shifts toward to the larger particle size.

In the range of 0.15-0.6 mm with the increase of particle size the ratio of volume to surface grows as well, the number of internal nuclei increases with respect to the number of surface nuclei. Due to that, the change in the mechanism of crystallization from surface towards volume glass crystallization occurs. The values of parameter $T_p^2/(\Delta T)_p$ extending to the point where the curves nearly reach their asymptotic values, which is also in agreement with Equation (1). Increasing of F^- content in glass, this range of particle size is propagating.

For average particle sizes of >0.6 mm, internal nuclei is dominant and the volume glass crystallization occurs. The parameter $T_p^2/(\Delta T)_p$ have constant values.

XRD patterns show that the samples in the range of particle sizes <0.075 mm with low content of F^- anion consist of leucite and diopside and the sample with higher content (2 mol%) of F^- anion is characterized by the appearance of leucite, diopside and phlogopite. In the range >0.15 mm all samples consist of three phases (leucite, diopside and phlogopite).

Conclusion

This analysis shows that increase of F^- anion content in silicate glass powder has effect on the change of the phase composition for the surface crystallization mechanism. Also, it is extending the range of the particle size in which the mechanism of crystallization is changing from surface towards volume glass crystallization. Increasing of F^- anion content has not effect on the volume crystallization mechanism of silicate glass powder.

References:

- [1] M.C. Weinberg, *J.Non-Cryst.Solids*, 1991, 127, 151.
- [2] C.S.Ray, D.E.Day, *J.Am.Ceram.Soc.*, 1990, 73, 439.
- [3] C.S. Ray, Q. Yang, Haung, D.E. Day, *J.Am.Ceram.Soc.*, 1996, 79, 3155.
- [4] J.A. Augis, J.E. Bennet, *J.Thermal.Anal.*, 1978, 13, 283.

STRUCTURAL AND ELECTRICAL PROPERTIES OF TUNGSTEN - TITANIUM SPUTTERED COATINGS

S. Petrović, B. Gaković, M. Radović Z. Rakočević and T. Nenadović

Institute of Nuclear Sciences "Vinča", P.O.B. 522, Belgrade, SCG

Abstract

Correlation of structural and electrical properties of W-Ti thin films deposited by sputtered were studies. The results have shown that changes of grain size are in agreement with the sheet resistance behavior as a function of the thin films thickness. The characteristic change of grain size and sheet resistance are obtained in thickness interval between 100 – 150 nm

Introduction

Thin films and coatings of the system W-Ti have been developed as an alternative to titanium – based coatings, which are considered for applications as protective coatings. Beside very high hardness and adhesion, these thin films/coatings should be thermally stable and oxidation resistant[1]. Thin films of tungsten with specific properties, can be used in very important fields: protective materials[2], microeletronic and gas sensors [3].

For deposition coatings, the sputtering method is especially interesting because the composition and the properties of thin films can be controlled by sputtering conditions. In this work, we have studied structural and electrical properties of sputtering deposited thin films of alloy. These features of deposits have been observed as a function of the deposits thicknesses.

Experimental

The thin films have been deposited by d.c. sputtering of a tungsten – titanium (90%W – 10%Ti w.t.) alloy target by Ar^+ ions. Acceleration voltage ($U = 1.5 \text{ kV}$) and current on target ($I = 0.7 \text{ A}$) were maintained constant during the deposition. The base pressure in the chamber was $p = 1 \cdot 10^{-3} \text{ Pa}$ and the partial pressure of argon in the chamber was $p_{\text{Ar}} = 1 \cdot 10^{-1} \text{ Pa}$.

The phase composition and crystalline structure of W-Ti deposits were determined by x-ray diffraction method (Cu $K\alpha$ emission). Angles 2θ , in the range from 30° to 80° . The crystalline size was determined by FWHM from corresponding peak and for crystalline spheric sharpe [4].

The sheet resistance of the deposited W-Ti thin films onto the silicon substrate was determined by the standard four-point probe method.

Results and Discussion

The thin films of W-Ti alloy were deposited on single crystal silicon orientation (100). The x-ray diffractograms of the as – deposited layer, thickness $d = 900 \text{ nm}$ is presented in Fig. 1a and it has shown only diffraction lines, which corresponded to

the bcc α - tungsten phase. The diffractograms of W-Ti thin films showed the (110) preferred growth orientation, although the presence of (211) diffraction line was also detected.

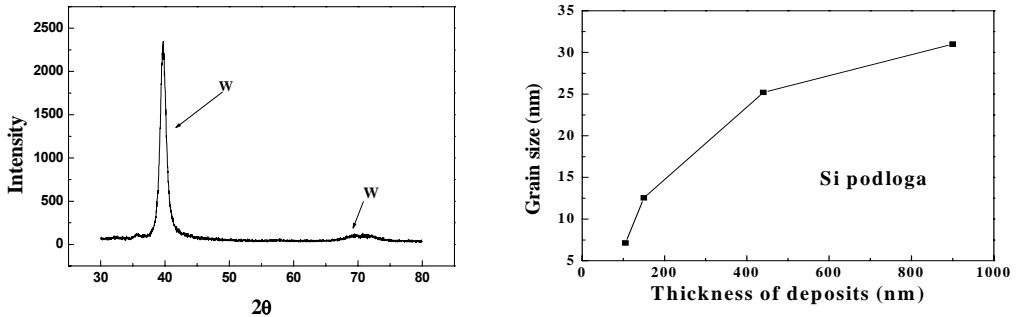


Fig. 1. Structural properties of W-Ti deposits on Si: a) XRD diffractograms and b) the grain size in a function of thickness of deposits.

The value of lattice parameters of the W-Ti layer for thickness of $d = 900$ nm $a = 0.3223$ nm. In comparison obtained values for the lattice parameters with a value of α - tungsten which amounted $a = 0.3165$ nm, the addition of the titanium to the W alloy, resulted in an expanded α - tungsten lattice.

The grain size have shown growth with increase of the thickness of W-Ti films on Si substrate, as presented in Fig. 1b. In chosen interval thickness, the grain size increases and reaches values about 31 nm. The obtained values of grain size characterize the preferential growth of the crystallites in the layer plane.

Electrical properties of deposited W-Ti are determined with sheet resistance and resistivity, which are presented on diagrams on Fig. 2(a and b). The sheet resistance of W-Ti films as a function of film thickness, in range 10 to 900 nm is presented in Fig. 2a. The values of sheet resistance were high for a low thickness and amounted about $80 \Omega/\text{sq}$. By further increase of the thickness deposit, the sheet resistance decreases and at above 400 nm, approaches value for bulk material. The conduction mechanism of the deposits change also, from thermally activated tunneling for low thickness to metallic conduction when the deposit thickness increases [5].

The W-Ti film resistivity as a function of film thickness in a range from 10 to 900 nm, is presented in Fig. 2b. The results have shown that for thickness smaller than 400 nm, the resistivity depends on film thickness. For W-Ti deposits, thickness greater than 400 nm, resistivity has a value of $119 \mu\Omega\text{m}$. In small thickness region, significant maximum of resistivity at 100 nm appeared. The obtained results are in agreement with the grain size behavior as a function of the film thickness (Fig 1b). For thickness of 100 nm rapid increase of the grain size is obtained. He obtained resistivity value at used experimental conditions is higher than the bulk resistivity of tungsten, as a consequence of electron scattering at alloying elements – titanium.

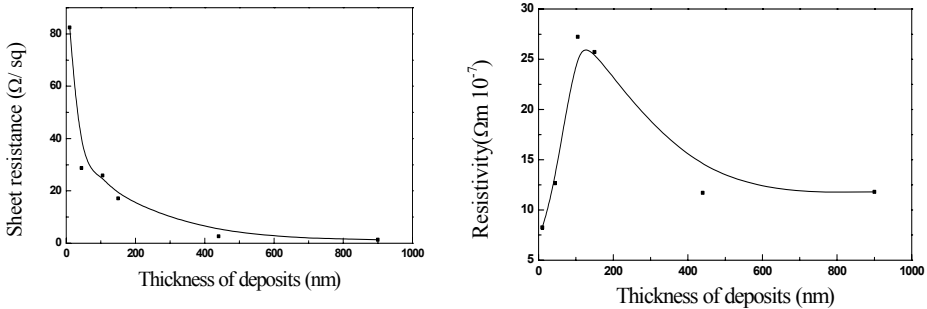


Figure 2. Electrical properties of W-Ti deposits on silicon substrate as: a) sheet resistance and b) resistivity as a function of thickness deposits

Conclusion

The properties of W-Ti thin films deposited by sputtering onto silicon are presented. At chosen experimental conditions, W-Ti deposits had a fine grain structure at the same time as crystal structure of W-Ti deposits corresponded to structure of α -tungsten with bcc lattice. The presence of titanium lead to extended crystal lattice of α -tungsten.

The electrical properties are thickness dependent. By increasing the thickness the sheet resistance rapidly decreases reaching constant value of $2\Omega/\text{sq}$ at the thickness 400 nm and higher. High resistivity of W/Ti deposits from $119\ \mu\Omega\text{m}$, are consequence electron scattering at alloying elements and other factors.

References

- [1] T. Nenadović, Material Science Forum 1996, 214, 163
- [2] C. Louro and A. Cavaleiro, J. Electrochem. Soc., 1997, 144(1), 259.
- [3] J. M. Oparowski, R. D. Sisson, Thin Solid Films, 1987, 153, 313.
- [4] B.D. Cullity, Elements of X-ray Diffraction, 2nd ed. Addison-Wesley, Ma, 1978.
- [5] I.M. Rycroft, B.L. Evans, Thin Solid Films 1996, 290-291, 283

TEXTURAL PROPERTIES AND SURFACE FRACTAL DIMENSION OF ACID-ACTIVATED BENTONITE CLAYS

Z. Vuković, A. Milutinović-Nikolić, J. Krstić and D. Jovanović,

*IChTM-Center for Catalysis and Chemical Engineering,
Njegoševa 12, Beograd, Serbia and Montenegro*

Abstract

The bentonite powder < 0.074 mm, was acid activated with HCl of different concentrations. The N_2 physisorption was used to estimate textural properties. The results proved that by acid activation the specific surface area, total pore volume significantly increase while the increase of surface fractal dimension is low.

Introduction

Clay minerals are used extensively as bleaching agent for mineral and vegetable oils, catalyst supports and cracking catalysts in the petroleum industry. Activation with hot mineral acids strongly increases the adsorptive, bleaching and catalytic power and increases the specific surface area. During acid treatment of bentonite exchangeable cations (K^+ , Na^+ and Ca^{2+}) are replaced with H^+ in the interlamellar space while part of Al^{3+} , Fe^{3+} and Mg^{2+} ions are leached from the octahedral sheets of the lattice structure. These changes result in increase of amorphous structure and improvement of porosity [1, 2].

In the present paper the influence of acid treatment on the textural properties and surface fractal dimension is presented.

Experimental

Bentonite from coal mine "Bogovina", Serbia was used as the raw material. The chemical composition of raw sample (B0) dried at $110^\circ C$ was: SiO_2 57.51, Al_2O_3 17.13, Fe_2O_3 7.67, MgO 2.35, CaO 1.81, Na_2O 0.75, K_2O 1.18, CO_2 0.5 and ignition loss (mainly structural water) 11.10 mass %.. The XRD confirmed smectite as the main constituent of investigated clay with some impurities of quartz, calcite, feldspar and illite.

The raw material was ground to pass 0.074 mm sieve. This fraction was used for acid activation. The samples were chemically activated with solutions of HCl of nominal concentrations: 1.5 (B1) and 3.0 (B2) $mol\ dm^{-3}$. The mass ratio between acid solution and mass of clay was 4:1. Activation of the bentonite clay samples was carried out at $90^\circ C$ for 2 h. After filtration and rinsing with hot distilled water the activated bentonite clay samples were dried to constant mass at $110^\circ C$.

Nitrogen adsorption-desorption isotherms were determined on Sorptomatic 1990 Thermo Finningen at $196^\circ C$. Samples were outgassed at $180^\circ C$, during 10 h. The specific surface area of samples S_{BET} , was determined by the BET method, using data up to $P/P_0 < 0.35$. Total pore volume was calculated according to Gurvitch method for $P/P_0 = 0.98$ [3].

The surface fractal dimension D , was estimated through the nitrogen isotherms. The equation (1) first presented by Avnir and Jaroniec is used to provide reliably information about geometric heterogeneity of the surface [4,5].

$$\frac{N}{N_m} = K \left(\ln \frac{P_0}{P} \right)^{D-3} \quad (1)$$

where N/N_m represent relative adsorption (the surface fractional coverage), K is characteristic constant, P and P_0 are the equilibrium and saturation pressures of the adsorbate, D is the fractal dimension of the accessible surface.

Results and Discussion

Fig. 1 shows the nitrogen adsorption-desorption isotherms measured on examined samples.

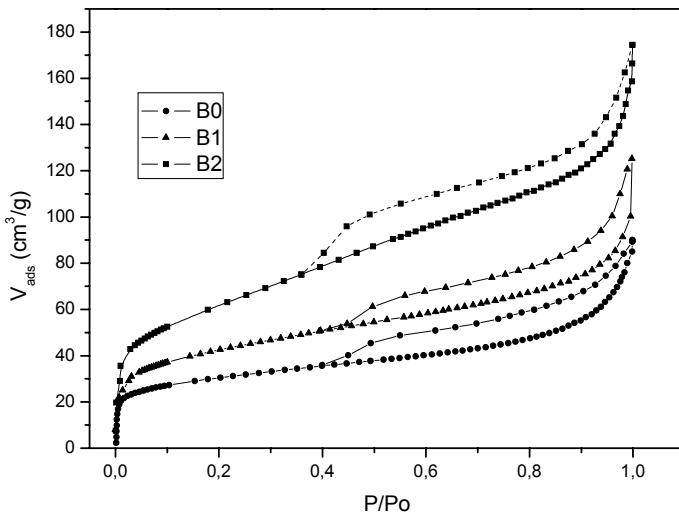


Fig.1. Nitrogen adsorption-desorption isotherms of raw and acid activated bentonites

All the adsorption isotherms are of the Type II isotherms according to IUPAC classification. These isotherms have reversible part at low relative pressures and hysteresis loops of the H3 type at higher relative pressures, indicating presence of slit shape pores [3]. Aggregates with plate-like particles like bentonites with this type of isotherms exhibit capillary condensation and therefore equation (1) is appropriate for investigated materials.

Fig. 1 shows that activated samples are able to adsorb more N_2 than the raw sample. The adsorption increases with the increase of concentration of HCl used for acid activation due to textural changes. Some textural properties of investigated samples are given in Table 1.

Table 1. The influence of acid activation on specific surface area, total pore volume and surface fractal dimension

Sample	Specific surface area (m ² /g)	Total pore volume (cm ³ /g)	Surface fractal dimension (D)
B0	96	0.11	2.797
B1	149	0.14	2.828
B2	220	0.24	2.834

The specific surface area, total pore volume and surface fractal dimension (D), are higher for activated bentonites compared to raw clay and increase with the increase of acid concentration. Usually, the surface fractal dimension is between 2 and 3. A surface having D=2 is regular and smooth and extremely irregular at D=3. A higher D values suggests a greater roughness. Fractal dimension D of raw bentonite is relatively high indicating its significant surface heterogeneity (surface roughness). According to D values the influence of acid treatment on surface roughness is slight, while the increase of specific surface area and total pore volume is significant. In raw bentonite samples the larger ions screen some smectite surface rugosity, becoming inaccessible for the nitrogen molecule and decreasing the BET surface area. The acid activation enables the exchange of cations with small H⁺ leading in the increase in specific surface area and the total pore volume by eliminating the screening effect.

Conclusion

According to experimental results the acid activation acts predominantly on inner surface of bentonite grains eliminating the screening effect, producing bentonites with highly developed porosity essential for adsorption capacity of the investigated bentonite. At the same time surface roughness is only slightly affected by acid activation since the fractal dimension is almost constant.

Acknowledgements

This work was supported by the Serbian Ministry of Science, Environmental Protection through the Project (MHT.2.09.0022.B).

References

- [1] Francisco R. Valenzuela Díaz and Pérsio de Souza Santos, *Quim. Nova*, 2001, 24(3), 345.
- [2] U. Flessner, D.J. Jones, J. Rozière, J. Zajac, L. Storaro, M. Lenarda, M. Pavan, A. Jiménez-López, E. Rodríguez-Castellon, M. Trombetta, G. Busca, *J. Mol.Catal. A-Chem.*, 2001, 168, 247.
- [3] F. Rouquerol, J. Rouquerol, K. Sing, *Adsorption by Powders and Porous Solids*, Academic Press, London, 1999.
- [4] Y. F. Xu, De'an Sun, Yangping Yao: *Chaos Soliton Fract.*, 2004, 19, 347.
- [5] Fu-Chuang Huang, Jiunn-Fwu Lee, Chung-Kung Lee, Wen-Ni Tseng and Lain-Chuen Juang: *J.Colloid Interf. Sci.*, 2002, 256, 360.

SYNTHESIS OF $\text{LiCr}_x\text{Mn}_{2-x}\text{O}_4$ ($x \sim 0.18$) BY GLYCINE-NITRATE METHOD

I. Stojković¹, D. Jugović², M. Mitrić³, N. Pavlović⁴ and N. Cvjetičanin¹

¹Faculty of Physical Chemistry, University of Belgrade, Studentski Trg 12-16, P.O. Box 137, Belgrade, ²Institute of Technical Sciences, Serbian Academy of Sciences, Knez Mihajlova 35/IV, Belgrade, ³The Vinča Institute of Nuclear Sciences, Laboratory for Theoretical and Condensed Matter Physics, P.O. Box 522, Belgrade, ⁴The Military Technical Institute of the SCG Army, Katanićeva 15, Belgrade, Serbia and Montenegro

Abstract

$\text{LiCr}_{0.18}\text{Mn}_{1.82}\text{O}_4$ spinel has been successfully synthesized by glycine-nitrate method. As a cathode material for lithium batteries it shows initial discharge capacity of 107.1 mAh/g and capacity retention of 93.3% after ten cycles.

Introduction

LiMn_2O_4 is a promising cathode material for ion-lithium batteries because it delivers high voltage, good capacity and it is a low cost and non toxic material. Unfortunately LiMn_2O_4 spinel shows considerable decrease in capacity during electrochemical charging-discharging on the 4V plateau. Recently several dominant modes of capacity fade have been proposed: Mn-dissolution and concomitant Li-for-Mn ion exchange at the end-of-discharge, and development of microstrain between two cubic phases formed during cycling [1,2]. The largest improvement in preventing capacity fade has been achieved by substitution of some manganese by other metal cations. These more robust spinels have higher average oxidation state of remaining manganese ($>3.5+$). This leads to a lower theoretical capacity because of the lower number of lithium ions that can be extracted from the spinel structure before all manganese is oxidized. Not only the choice of M^{2+} metal cation type but also its amount "x", is important for obtaining $\text{LiM}_x\text{Mn}_{2-x}\text{O}_4$ cathode material with adequate initial capacity and high capacity retention. Cr^{3+} is among the cations whose substitution for manganese gives best performance increase especially for $x = 0.175$ [1,3,4]

$\text{LiM}_x\text{Mn}_{2-x}\text{O}_4$ spinels are usually prepared by time and energy consuming solid state reaction, starting from carbonates and/or oxides [1-3,5]. In this work we tried to synthesize $\text{LiCr}_x\text{Mn}_{2-x}\text{O}_4$ ($x \sim 0.18$) powder material by rapid glycine-nitrate method developed before for synthesis of $\text{YBa}_2\text{Cu}_3\text{O}_{7-x}$ ceramics [6].

Experimental

1 M aqueous solutions of LiNO_3 , $\text{Mn}(\text{NO}_3)_2 \cdot 4\text{H}_2\text{O}$ and $\text{Cr}(\text{NO}_3)_3 \cdot 9\text{H}_2\text{O}$ were prepared from p.a. chemicals. They were mixed in appropriate ratio so the total volume was 30-40 ml. Glycine was added in the mixture either as a solid or as a water solution. Its role was to serve both as a fuel for combustion and as a complex ant to prevent inhomogeneous precipitation of individual components prior to combustion. Amount of glycine was such to make glycine-to-nitrate molar ratio equal to 1.2. Precursor solution was placed in a covered glass beaker and heated in an oven at 200°C

until spontaneous ignition occurred. Ash resulting from combustion was heated at 800°C for 4 hours.

The XRPD experiments were done with the $\text{CuK}\alpha_{1,2}$ radiations in 15-70° 2 θ range with the 0.05° step and 2 seconds exposition time.

Electrochemical experiments were performed in a cell filled with argon. Electrolyte was 1 M LiClO_4 in PC and EC mixture (1:1 mole ratio). Before dissolving p.a. LiClO_4 was dried under vacuum at 120-140°C for at least 2 hours. PC and EC were distilled twice under vacuum, and both times middle $\frac{2}{3}$ fraction was collected. Working electrode was made from synthesized material, "Vulcan" carbon black and PVDF mixed in 90:5:5 weight percent ratio and deposited on platinum foil from slurry prepared in N-Methyl-2-Pyrrolidone. Active cathode material weighted 3.9 mg and was spread over 1.7 cm² of Pt-foil surface area. Two glass tubes filled with lithium metal were used as double counter electrode.

Results and Discussion

All reflections of obtained XRPD pattern correspond to pure spinel phase. Small shifts in 2 θ values exist for all reflections comparing to LiMn_2O_4 diffraction pattern. Lattice parameter $a = 8.223 \text{ \AA}$ has a lower value than for LiMn_2O_4 ($a = 8.241-8.249 \text{ \AA}$) [1,2,7]. This lattice contraction indicates that chromium-ion is incorporated into spinel manganese oxide [8] and a more complex oxide $\text{LiCr}_{0.18}\text{Mn}_{1.82}\text{O}_4$ is formed.

For potential application the most important thing is to have acceptable electrochemical behavior of obtained cathode material. So we checked cycling characteristics of $\text{LiCr}_{0.18}\text{Mn}_{1.82}\text{O}_4$ by charging electrochemical cell to 4.3 V and discharging to 3.3 V. Quite high current rate C/3 has been chosen. Current density was 112 $\mu\text{A}/\text{cm}^2$. Ten cycles have been recorded. Fig.1 shows relationship between discharge capacity and cycle number for our $\text{LiCr}_{0.18}\text{Mn}_{1.82}\text{O}_4$ comparing to LiMn_2O_4 prepared by solid state reaction and cycled at C/15 current rate [1]. Discharge capacity of $\text{LiCr}_{0.18}\text{Mn}_{1.82}\text{O}_4$ synthesized by glycine-nitrate method changes from 107.1 in the first to 99.9 mAh/g in the tenth cycle. LiMn_2O_4 [1] although cycled with five times lower current rate decreases a discharge capacity from 108.6 to 73.3 mAh/g in the first ten cycles. The capacity retention of $\text{LiCr}_{0.18}\text{Mn}_{1.82}\text{O}_4$ is 93.3% comparing to that of only 67.5% for LiMn_2O_4 . As a conclusion it may be said that $\text{LiCr}_{0.18}\text{Mn}_{1.82}\text{O}_4$ is successfully synthesized by a rapid combustion method delivering very good cyclability as a cathode material for lithium batteries.

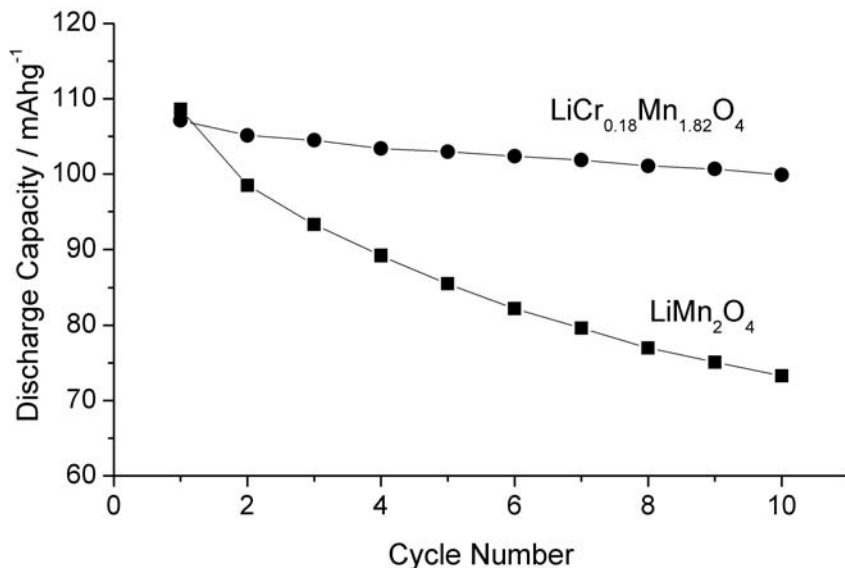


Figure 1. Discharge capacity of $\text{LiCr}_{0.18}\text{Mn}_{1.82}\text{O}_4$ (glycine-nitrate method) and LiMn_2O_4 (solid state reaction [1]) versus cycle number.

References

- [1] M. C. Tucker, J.A. Reimer, E.J. Cairns, *J. Electrochem. Soc.*, 2002, 149(5), A574.
- [2] Y. Shin, A. Manthiram, *J. Electrochem. Soc.*, 2004, 151(2), A204.
- [3] C. Sigala, D. Guyomard, Verbaere, Y. Piffard, M. Tournoux, *Solid State Ionics*, 1995, 81, 167.
- [4] C-H. Lu, Y. Lin, H-C. Wang, *J. Mater. Sci. Lett.*, 2003, 22, 615.
- [5] R. Koksang, J. Barker, H. Shi, M. Y. Saïdi, *Solid State Ionics*, 1996, 84, 1.
- [6] L. R. Pederson, G. D. Maupin, W. J. Weber, D. J. McReady, R. W. Stephens, *Mat. Lett.*, 1991, 10, 437.
- [7] D. Jugović, M. Mitrić, N. Cvjetičanin, M. Miljković, V. Jakanović, D. Uskoković, *Mater. Sci. Forum*, 2004, 453-454, 387.
- [8] M. C. Tucker, J.A. Reimer, E.J. Cairns, *J. Electrochem. Soc.*, 2001, 148(8), A951.

STRUCTURE AND DIELECTRIC CHARACTERISTICS OF $\text{BaTi}_{1-x}\text{Sn}_x\text{O}_3$ CERAMIC POWDERS

S. Marković¹, N. Cvjetičanin², M. Mitrić³ and D. Uskoković¹

¹*Institute of Technical Science of the Serbian Academy of Sciences and Arts, Knez Mihailova 35/IV, Belgrade 11001*, ²*Faculty of Physical Chemistry, Studentski Trg 12-16, P.O. Box 137, Belgrade*,

³*Institute of Nuclear Sciences "Vinča", Belgrade, Serbia and Montenegro*

Abstract

$\text{BaTi}_{1-x}\text{Sn}_x\text{O}_3$ (BTS) ceramic powders, with different tin content ($x = 0-1$) were prepared. The BTS powders were calcined at 1370 °C for 4 hours. The structure of these powders was characterized by XRPD method, tetragonal and cubic crystal structures were noticed. Powders were pressed in pellets and sintered at 1370 °C for 1 hour. The dielectric properties of BTS ceramics were measured and the results were reported.

Introduction

Barium titanate, well known perovskite-type oxide [1,2], is an attractive material for industrial applications including multilayer capacitors, pyroelectric detectors, ferroelectric memory, and positive temperature coefficient sensors. Two crystalline phases of BaTiO_3 are especially important for applications in the microelectronic industry. The tetragonal phase is used in a broad area of electronic devices because of ferroelectric properties, and the cubic form, although not ferroelectric, has a high dielectric constant that makes it suitable for capacitors. The interest in barium titanate is mainly due to the easy modification of its electric properties by the selection of an adequate dopant cation and due to its stability at high temperature [3]. For barium titanate piezoceramic, Sn is one of very interesting dopant cations [4].

In this paper, we present the results of investigation of structural and dielectric properties of $\text{BaTi}_{1-x}\text{Sn}_x\text{O}_3$ (BTS) ceramic powders.

Experimental procedure

Mixture of BaCO_3 , TiO_2 and SnO_2 powders (BTS mixture), was homogenized by steering in ethanol for 1 hour and calcined at 1370 °C for 4 hours. BTS samples with $\text{BaTi}_{1-x}\text{Sn}_x\text{O}_3$ stoichiometry ($x = 0-1$) were obtained. All XRPD measurements were performed at room temperature on Philips PW-1050 automatic diffractometer using CuK_α radiation. Thermal characteristics of BTS ceramic powders were studied by SETARAM DSC 111 instrument.

The BTS powders were pressed uniaxially into pellets of the dimension $\phi=8$ mm and $h=2$ mm. Pellets were sintered at 1370 °C in air for 1 hour. Green parts were 3.9 g/cm³ in density, however, after sintering, because of shrinkage; every pellet was 4.6 g/cm³ in density. The density of sintered ceramics has been determined by Archimedes's method.

BTS ceramics have been electrically studied as a function of composition i.e. concentration of Sn. The electrical measurements were performed using a Wayne Kerr

Universal Bridge B224 (internal frequency 1000 Hz). Electrical characterizations have been performed on air. All dielectric measurements were done in cooling, from 160 to 20 °C. The relative permittivity (ϵ_r) and dielectric loss ($\tan\delta$) were calculated.

Results and Discussion

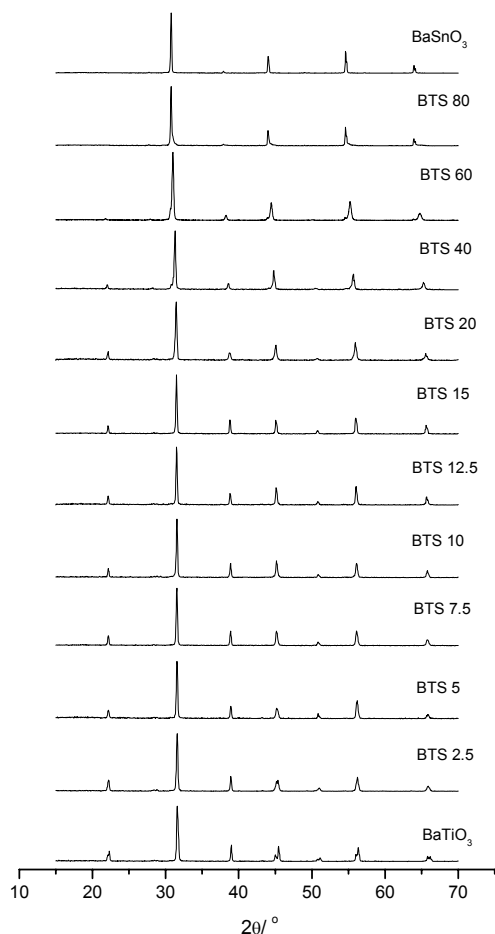


Figure 1 shows XRPD patterns of $\text{BaTi}_{1-x}\text{Sn}_x\text{O}_3$ samples (BTS, $x=0-1$), calcined at 1370 °C for 4 hours. It is known from literature that when BaTiO_3 transforms from cubic to tetragonal the (002) peak splits into the (002) and (200) peaks at near $45^\circ 2\theta$. For pure barium titanate, phase transformation from tetragonal to cubic structure is at near 125 °C. Increasing of Sn content in BTS powders decrease temperature of phase transformation, and in our case BTS sample with ~15 mol% of Sn have cubic structure at room temperature. As we expected, XRPD patterns confirmed that BTS samples with more than 15 mol% of Sn have cubic crystal structure at room temperature, too.

Figure 1. XRD patterns of BTS powders calcined at 1370 °C for 4 hours.

The temperature dependence of relative permittivity ϵ_r for BTS samples sintered in air is shown in Fig. 2.

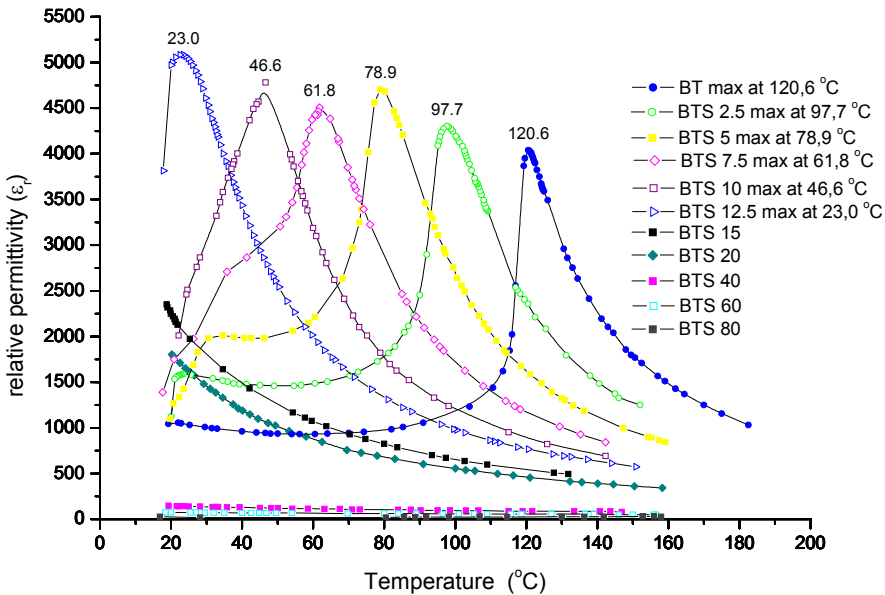


Figure 2 The temperature dependence of relative permittivity ϵ_r as a function of Sn concentration in BTS samples sintered at 1370 °C for 1 hour.

The correlation between relative permittivity and samples crystal structure is noticed. This correlation is in agreement with Curie's Principle, which states that crystal structure must be a subgroup of Curie's symmetry group ∞m , polar vector symmetry group that represents electric polarization. This means that system which possesses dielectric moment must reduce cubic structure to lower crystal structure that belongs to one of the 20 classes with polar axes. Hence, samples with 0-12.5 mol% of tin have phase transition from cubic to tetragonal crystal structure, and high relative permittivity (ϵ_r). In the case of BTS samples with cubic crystal structure ($x = 0.20-1$) there is no phase transition in temperature interval 160-20 °C, and their relative permittivity is small.

Acknowledgments

The Ministry of Science, Technologies and Development of Republic of Serbia provided financial support under grant no. 1431.

References

- [1] L.E. Cross, Am. Ceram. Soc. Bull., 1984, 63, 586.
- [2] F.S. Galasso, "Structure, Properties and Preparation of Perovskite-Type Compounds", Pergamon Press, New York, 1969.
- [3] J. Cerda, J. Arbiol, G. Dezangau, R. Diaz, J.R. Morante, Sensors and Actuators B, 2002, 84, 21.
- [4] U. Straube, H.T. Langhammer, H.P. Abicht, H. Beige, J. Eur. Ceram. Soc., 1999, 19, 1171.

DETERMINATION OF KINETIC PARAMETERS FOR THERMAL DECOMPOSITION OF SODIUM BICARBONATE USING THE SINGLE-HEATING-RATE INTEGRAL METHODS

B. Janković

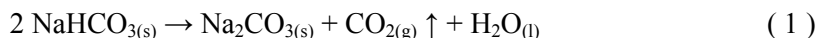
*Faculty of Physical Chemistry, University of Belgrade,
Studentski trg 12-16, P.O. Box 137, 11001 Belgrade, Serbia and Montenegro*

Abstract

The decomposition process of the sodium bicarbonate was investigated by single-heating-rate integral methods. Based on the original TG curves taken from A. Ortega [1] work, degree conversions at different temperatures and heating rates was determined. The activation energies and pre-exponential factors are determined by application of Coats-Redfern and Horowitz-Metzger methods. With increasing heating rate activation energies and pre-exponential factors moves to higher values. Horowitz-Metzger method give for 10% higher values of kinetic parameters at same heating rate. At the lower heating rates, kinetic parameters are in a good agreement with results obtained by isoconversional method.

Introduction

The decomposition reaction for sodium bicarbonate is represented by the equation [2]:



in the range of 360-480 K.

The thermal decomposition process, was investigated using the original TG-analysis data at different heating rates from reference [1]. A.Ortega [1] was calculate the activation energy (E) of decomposition process using the isoconversional method [3,4]. This method yielding the same activation energy of 93.9 kJ/mol. Activation energy is dependent neither on the heating rate nor on the degree of conversion [1]. In this paper, were determined the kinetic parameters of thermal decomposition of sodium bicarbonate using the two integral methods based on the single TG curve. Results obtained by this two methods are compared with results obtained by isoconversional method, which applied A. Ortega [1] at four experimental TG curves.

Results and Discussion

Figure 1 shows the series of curves a degree conversion versus temperature, at different heating rates for the thermal decomposition of sodium bicarbonate.

All curves shown in Figure1 are symmetrical in shape and shift to higher temperatures with increased heating rate. Increase of heating rate, shifts the initial decomposition temperature from 356 to 383 K and the final decomposition temperature from 445 to 483 K.

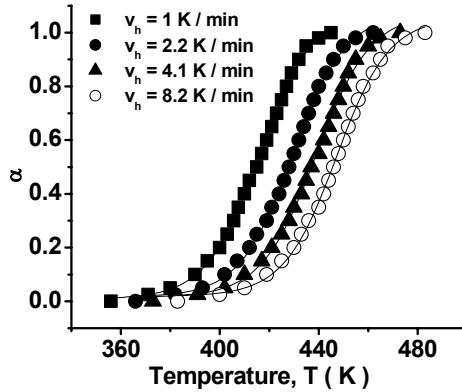


Figure 1. Curves of degree conversion (α) versus temperature T at different heating rates for thermal decomposition of sodium bicarbonate

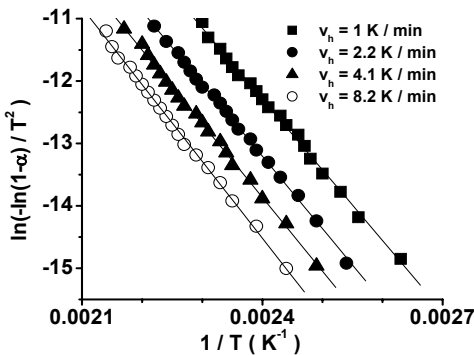


Figure 2. A plots $\ln(-\ln(1-\alpha)/T^2)$ versus $1/T$ (Coats-Redfern method)

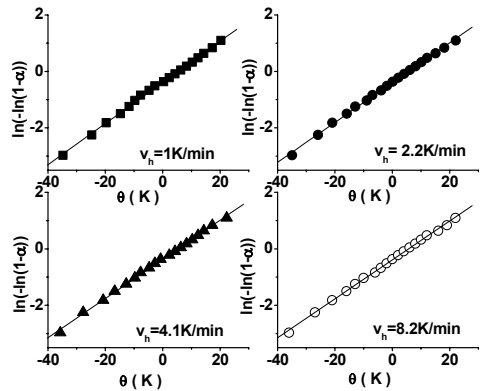


Figure 3. A plots $\ln(-\ln(1-\alpha))$ versus θ , where $\theta = T - T_s$, (Horowitz-Metzger method)

Figure 2 shows a plots $\ln(-\ln(1-\alpha)/T^2)$ versus $1/T$ obtained by Coats-Redfern [5,6] method and Figure 3 shows a plots $\ln(-\ln(1-\alpha))$ versus θ (where T_s is characteristic temperature) obtained by Horowitz-Metzger [7] method, at different heating rates. Table 1 summarizes the activation energies, pre-exponential factors, reaction order (n), conversion range and correlation coefficients (r) at four heating rates for both methods. It is obvious that for the same conversion degree with increasing heating rate, both the activation energies and pre-exponential factors tend to higher values. Horowitz-Metzger method give for about 10% higher activation energy values than

other method, at same heating rate. This is due to the fact that in equation developed by Coats-Redfern, when evaluating the result of the integral of the expression $[\exp(-E/RT)]$, a recurrent series is used that is truncated when arriving at the second term. On the other hand, Horowitz-Metzger method is based on the development of the asymptotic expansion of $[\exp(-E/RT)]$ before integration, other values are taken into account. These values increase the result of the integral. Activation energy values are in a good correlation with value of 93.9 kJ/mol obtained by A. Ortega [2], especially at lower heating rates.

Table 1. Kinetic parameters of thermal decomposition of sodium bicarbonate determined by different methods

Method	v_h (K / min)	n	α	A (min^{-1})	E (kJ / mol)	r
Horowitz- Metzger	1	1	0.05-0.98	9.72×10^{11}	104.2	0.999
	2.2	1	0.05-0.98	2.06×10^{12}	107.5	0.999
	4.1	1	0.05-0.98	4.38×10^{12}	110.5	0.999
	8.2	1	0.05-0.98	1.31×10^{13}	114.1	0.999
Coats- Redfern	1	1	0.05-0.98	3.59×10^{10}	94.4	0.998
	2.2	1	0.05-0.98	6.10×10^{10}	96.6	0.999
	4.1	1	0.05-0.98	9.13×10^{10}	98.1	0.999
	8.2	1	0.05-0.98	3.33×10^{11}	102.3	0.999

Conclusion

The decomposition process were investigated by TG analysis at different heating rates. It's used a single-heating-rate methods for determining kinetic parameters of sodium bicarbonate decomposition process. All obtained values for kinetic parameters are in a good agreement with values obtained by isoconversional method, thus confirming that the thermal decomposition of sodium bicarbonate fits a first-order kinetic model. Furthermore, the single-heating rate methods are in advantage of concern to isoconversional method, because that require only single TG-curve for kinetic parameters determining.

References

- [1] A. Ortega, *Thermochim. Acta.*, 1996, 284, 379.
- [2] P.K. Heda, K.S. Alexander, *Thermochim. Acta.*, 1999, 340-341, 165.
- [3] T. Ozawa, *Bull. Chem. Soc. Jpn.*, 1965, 38, 1881.
- [4] J. H. Flynn, L. A. Wall, *Polym. Lett.*, 1966, 4, 191.
- [5] A.W. Coats, J.P. Redfern, *Nature.*, 1964, 201, 68.
- [6] A.W. Coats, J.P. Redfern, *J. Polym. Sci. Polym. Lett. Ed.*, 1965, 3, 917
- [7] H.H. Horowitz, G. Metzger, *Anal. Chem.*, 1963, 35, 1464.

Solid State Physical Chemistry

(H)

COUPLED PLASMA AND ELASTIC WAVES IN SEMICONDUCTOR

D. M. Todorović

*Center for Multidisciplinary Studies, University of Belgrade
Serbia & Montenegro*

Abstract

The system of coupled plasma and elastic wave (plasmaelastic wave) equations were analyzed. The solution of the coupled system of plasma and elastic equations were given for a typical PA configuration. A quantitative analysis of the coupling effects was given. Analysis shows that the modified plasmaelastic waves, in comparison with uncoupled plasma and elastic waves, show the attenuation and disperse phenomena.

Introduction

The photoacoustic (PA) and photothermal (PT) science and technology have extensively developed new methods in investigation of semiconductors and microelectronic structures during the last ten years [1], [2]. The PA and PT techniques were recently established as diagnostic methods with good sensitivity to the dynamics of photoexcited carriers [3]. The plasma waves, generated by the absorbed intensity-modulated laser beam, can play the dominant role in the PA and PT experiments for most semiconductor materials. Semiconductor materials show a mechanical strain when electron-hole plasma is generated. The photoexcited carriers produce periodic elastic deformation in the sample - electronic deformation (ED) [4]. This mechanism of elastic wave generation is the specialty of semiconductors. The ED mechanism is based on the fact that photogenerated plasma in the semiconductor causes a deformation of the crystal lattice, i.e. the deformation of the potential of the conduction and valence bands in the semiconductor. The electronic strain in turn may produce plasma waves in the semiconductor in a manner analogous to thermal wave generation by local periodic elastic deformation.

Photogeneration and transport of carriers in semiconductor is conventional modeled as the carrier-diffusion wave, i.e. with the parabolic partial differential equations. In this work the diffusion - type carrier wave equations (parabolic type) were transformed in hyperbolic type. Then the governing field equations in this dynamic coupled theory are wave-type (hyperbolic) equations of carrier distribution and elastic displacements. The concept was introduced in analogy of generalized thermoelasticity proposed by Lord and Shulman in [5], in which, in comparison to the classical theory, a single relaxation time into consideration was introduced. This theory shows that the plasmaelastic disturbance propagates as a wave with a finite speed equal to or less than the speed c defined by the relation $\tau = c/v$.

Many authors analyzed the partially system of plasma and elastic equations. The ED effect in semiconductors, i.e. partially coupled plasma and elastic waves, had been studied previously by Stearns and Kino [4]. Further, Avanesyan, Gusev and Zheludov [6] analyzed generation of deformation waves in silicon. The thermoelastic and ED effects contribution to the PA signals were experimentally and theoretically analyzed in recently published papers by Todorović et al [7,8,9].

Coupled Plasma and Elastic Fields

The coupled plasma, $n(\mathbf{r}, t)$, and elastic displacement, $\mathbf{u}(\mathbf{r}, t)$, transport equations in a vector form, for an elastic medium with isotropic and homogeneous electronic, thermal and elastic properties, are

$$\left(\frac{\partial}{\partial t} + t_o \frac{\partial^2}{\partial t^2} \right) n(\mathbf{r}, t) = D_E \nabla^2 n(\mathbf{r}, t) - \frac{n(\mathbf{r}, t) - n_o}{\tau} + \gamma_u \nabla \frac{\partial \mathbf{u}(\mathbf{r}, t)}{\partial t} + G(\mathbf{r}, t) \quad (1)$$

$$\rho \frac{\partial^2 \mathbf{u}(\mathbf{r}, t)}{\partial t^2} = \mu \nabla^2 \mathbf{u}(\mathbf{r}, t) + (\lambda + \mu) \nabla (\nabla \times \mathbf{u}(\mathbf{r}, t)) - \delta_n \nabla n(\mathbf{r}, t) \quad (2)$$

where D_E is the carrier diffusion coefficient, τ is the photogenerated carrier lifetime, E_G is the energy gap of the semiconductor, n_o is the equilibrium carrier concentration, γ_u is the elastic coupling factor, μ, λ are the Lamé elastic constants, \mathbf{r} is the position-vector, t is the time, ρ is the density, $G(\mathbf{r}, t)$ is the carrier photogeneration 'source' term, δ_n is the difference of deformation potential of conduction and valence band. The phenomena described by the system of equations (1)-(2) can be indicate as coupled dynamic generalized plasmaelastic problem. The first equation represents the hyperbolic plasma equation where it is assuming for the speed of carrier transport, c_E , that identical to the longitudinal wave velocity/pulse speed c_l . The plasma relaxation time $t_o = D_E/c_l^2$, where D_E is the carrier diffusivity. The third term in the elastic equation (2) represent the 'source' term and describe the influence of the plasma waves on the elastic wave.

If we take in consideration the one-dimension (1-D) case, using $\mathbf{r} = (0, 0, z)$ and $\mathbf{u} = (u, 0, 0)$, the dimensionless coupled dynamic equations of carrier density and elastic displacement are

$$\left[\frac{\partial^2}{\partial z^2} - \left(\frac{\partial}{\partial t} + t_o \frac{\partial^2}{\partial t^2} - \frac{1}{\tau} \right) \right] \Delta n - \varepsilon \left(\frac{\partial}{\partial t} + t_o \frac{\partial^2}{\partial t^2} \right) \left(\frac{\partial u}{\partial z} \right) = -G \quad (3)$$

$$- \frac{\partial \Delta n}{\partial z} + \left(\frac{\partial^2}{\partial z^2} - \frac{\partial^2}{\partial t^2} \right) u = 0 \quad (4)$$

where $c_l^2 = \frac{(\lambda + 2\mu)}{\rho}$, $\omega_E = \frac{c_l^2}{D_E}$, $\varepsilon = \frac{\delta_n^2 n}{\rho c_l^2 \omega_E}$, and the dimensionless quantities

$\mathbf{r}' = \omega_E \mathbf{r} / c_l$; $t' = \omega_E t$; $\mathbf{u}' = \rho \omega_E c_l \mathbf{u} / (\delta_n n_o)$; $n' = n / n_o$; $k' = c_l k / \omega_E$.

Here ω_E is the characteristic frequency of the medium, k the wave number, c_l is the longitudinal wave velocities in the medium and ε is the PE coupling factor.

The dimensionless solution of the system (3)-(4) can have the form

$$\Delta n = N^o \exp(kz + i\omega t), \quad u = u^o \exp(kz + i\omega t), \quad (5)$$

where N^o and u^o are dimensionless carrier density and displacement wave amplitude. Generally, in equations (5) the values k and ω can be complex constants. If the value ω is the real constant then we have *the wave of determined frequency*. On the other hand, if the value k is the real constant then we have *the wave of determined wavelength*. For our analysis of possible attention are the waves of determined frequencies.

It can be obtain the secular equation

$$k^4 + k^2 \left[\omega^2 - \chi(1 + \varepsilon) + \frac{1}{\tau} \right] - \omega^2 \left(\chi - \frac{1}{\tau} \right) = 0, \quad \chi = i\omega - t_o \omega^2 \quad (6)$$

In low frequency range ($\omega \ll 1$), the approximated values roots of secular equation have the form

$$k_{1,2} = \mp \left(\sigma_1 + i \frac{\omega}{v_1} \right), \quad k_{3,4} = \mp \left(\sigma_2 + i \frac{\omega}{v_2} \right), \quad (7)$$

where v_j and σ_j are the corresponding real parameters.

The solution for coupled dynamic plasmaelastic problem has the form

$$\Delta n = N_+^{\circ} \exp \left[-\sigma_1 z + i\omega \left(t - \frac{z}{v_1} \right) \right] + N_-^{\circ} \exp \left[\sigma_1 z + i\omega \left(t + \frac{z}{v_1} \right) \right] + \quad (8)$$

$$N_u \times \left\{ u_+^{\circ} \exp \left[-\sigma_2 z + i\omega \left(t - \frac{z}{v_2} \right) \right] - u_-^{\circ} \exp \left[\sigma_2 z + i\omega \left(t + \frac{z}{v_2} \right) \right] \right\},$$

$$u = u_+^{\circ} \exp \left[-\sigma_2 z + i\omega \left(t - \frac{z}{v_2} \right) \right] + u_-^{\circ} \exp \left[\sigma_2 z + i\omega \left(t + \frac{z}{v_2} \right) \right] + \quad (9)$$

$$U_N \times \left\{ N_+^{\circ} \exp \left[-\sigma_1 z + i\omega \left(t - \frac{z}{v_1} \right) \right] - N_-^{\circ} \exp \left[\sigma_1 z + i\omega \left(t + \frac{z}{v_1} \right) \right] \right\},$$

where $N_u(\omega)$ and $U_N(\omega)$ are corresponding complex parameters. The solutions (8) and (9) define the thermoelastic waves which consist of *modified plasma wave* ($j=1$) and *modified elastic waves* ($j=2$).

Conclusion

The system of coupled plasma and elastic wave equations in semiconductors are analyzed. The treatment considers a semiconductor elastic medium with isotropic and homogeneous elastic properties. The solution of the coupled system of plasma and elastic equations was given. A quantitative analysis of the coupling effects was given. Analysis in 1D case shows that the modified waves, in comparison with uncoupled plasma and elastic waves, show the attenuation and disperse phenomena. The attenuation factors and phase velocities are different functions of frequency ω . Another characteristics in the coupled case, that the elastic wave is followed by plasma wave and vice versa.

References

- [1] D.Almond, P.Patel, Photothermal Science and Techniques, Chap&Hall, London, 1996.
- [2] A.Mandelis and K.H.Michaelian, Eds, Photoacoustic and Photothermal Science and Engineering, Special Section of Opt. Eng., 1997, 36(2).
- [3] Semiconductors and Electronic Materials, Eds. A.Mandelis and P.Hess, Series: Progress in Photothermal and Photoacoustic Science and Technology, Opt.Eng.Press, NY, 2000.
- [4] R.G.Stearns, G.S.Kino, Appl. Phys. Lett., 1985, 47, 1048.
- [5] H.W.Lord,] H.W.Lord, Y. Shulman, J. Mech.Phys.Solids, 1967, 15, 229.
- [6] S.M.Avanasyan, V.E.Gusev, N.I.Zheludov, Appl. Phys. A, 1986, 40, 163.
- [7] D.M.Todorović, P.Nikolić, A.Bojičić, K.Radulović, Phys.Rev.B, 1997, 55, 15631.
- [8] D.M.Todorović, P.M.Nikolić, A.I.Bojičić, J.Appl.Phys., 1999, 85(11), 7716.
- [9] D.M.Todorović, Rev.Sci.Instrum., 2003, 74(1), 582.

SURFACE CHARACTERISTICS OF OXIDE POWDERS STUDIED BY IN SITU ELECTRICAL CONDUCTIVITY MEASUREMENTS

G.Postole¹, M.Caldararu^{1*}, M.Carata¹, C.Hornoiu¹, C.Munteanu¹
and B.Grzybowska²

¹*Institute of Physical Chemistry "I.G.Murgulescu" of the Romanian Academy,
Spl. Independentei 202, 060041 Bucharest, Romania,*

²*Institute of Catalysis and Surface Chemistry of the Polish Academy of Sciences,
ul Niezapominajek 1, Krakow, Poland*

Abstract

Ac in situ electrical conductivity was used to study the influence of iron and tungsten doping on adsorption properties of titania (anatase) in presence of dry or humid oxygen, in conditions which mimic the catalytic experiment by using the differential steps technique. Doping with tungsten favors surface reduction, while doping with iron promotes deeper oxidation of the surface.

Introduction

The correlation between the electrical properties of oxides and their adsorption behavior was frequently studied, with the aim of using the semiconductor properties to control the rate of adsorption/catalytic reactions or the sensitivity of catalytic sensors [1]. Doping with aliovalent cations is frequently used for modifying the electrical properties of semiconductor surfaces.

The measured conductivity can be expressed by the relation:

$$\sigma_t = \sigma_i + \sigma_e$$

with σ_i ionic (cation or anion) conductivity, and σ_e represents electron (or hole) conductivity. The electrical response of polycrystalline oxides is determined by the transport of carriers over the barriers at the contacts between the adjacent grains. The relative distribution of various types of carriers in intergrain area depends on the temperature range/conditions of experiment. In oxygen - rich atmosphere, chemisorbed oxygen species act as traps for the bulk electrons on the surface of n-type oxides. At the same time, water chemisorption (competing with oxygen on the same adsorption sites [2]) increases the population of surface OH groups and thus the contribution of proton conductivity (by "vehicle" or by Grothuss mechanism). Weak (physical) adsorption of water in intergrain area decreases the height of intergrain barriers due to its higher dielectric constant [3, 4]. The presence of foreign cations as dopants will influence these phenomena in a rather unpredictable manner so their effect must be studied in conditions of the real experiment. This paper aims to study the influence of Fe²⁺ and W⁶⁺ doping on the surface behavior of TiO₂ (anatase) during dry and humid oxygen adsorption, by using the response of ac electrical conductivity measured *in situ*.

Experimental

Samples of TiO_2 (Tioxide, $48 \text{ m}^2/\text{g}$) and the same material doped with $1 \text{ wt}\% \text{Fe}^{2+}$ (surface area $38.9 \text{ m}^2/\text{g}$) and $5 \text{ mol}\% \text{W}^{6+}$ ($38.6 \text{ m}^2/\text{g}$) were studied. The initial TiO_2 sample was calcined at $750 \text{ }^\circ\text{C}$ to mimic the thermal history of doped samples. The surface area of this sample decreased to $22.5 \text{ m}^2/\text{g}$; thus, the presence of dopants hindered the sintering. Changes of the surface conductance G of 1.5 cm^3 of nonpressed powder (fraction between 0.25 and 0.5 mm) were measured in gas flow, by using the differential step technique [3] and a special cell for *in situ* measurements on powders [2]. A precision RLC bridge (TESLA BM 484) measuring the admittance at 1592 Hz allowed to follow simultaneously the evolution of parallel conductance (G_p) and capacitance (C_p) of the cell with powder filling the space between the cylindrical concentric electrodes. The method consists essentially of measuring the same batch of powder thermally cycled between 20 - $400 \text{ }^\circ\text{C}$ in various atmospheres coupled with simultaneous monitoring of the composition of the effluent by gas chromatography. The overall flow-rate in all cases was $69.3 \text{ cm}^3/\text{min}$. Cycles succession was: DAR 1-3, DO, HO (where DAR, DO and HO abbreviate dry argon, dry and humid oxygen, respectively). DAR-3 cycle was taken as a reference.. G values obtained were used to calculate the conductivity σ , by taking into account the cylindrical geometry of the powder sample and the conductivity of the empty cell.

Results and Discussion

The results obtained on heating the Fe-doped and respectively W-doped titania in comparison with those on basic TiO_2 are presented in Figures 1 and 2.

Figure 1. Comparison of variation of σ (nS/m) during heating for Fe/ TiO_2 and TiO_2 samples

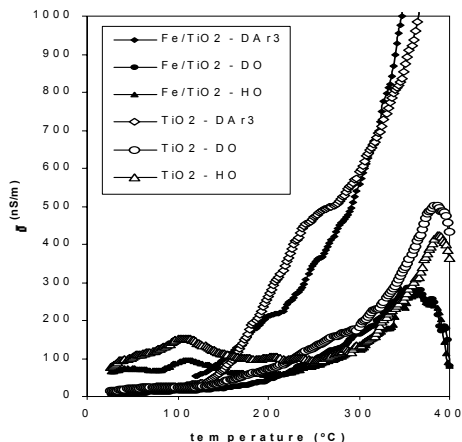


Figure 1

Figure 2. Comparison of variation of σ (nS/m) during heating for W/ TiO_2 and TiO_2 sample

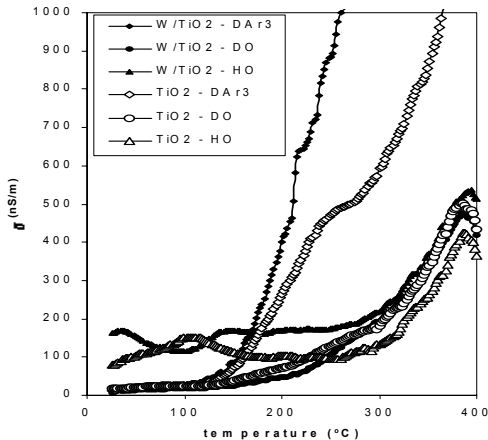


Figure 2

Doping TiO_2 with Fe^{2+} does not change essentially the behavior of conductivity in dry inert (a weak reducing agent). The lower rate of increase of conductivity on heating in DO flow indicates that part of electronic carriers are trapped by oxygen ad-

sorption (as O_2^- , O^- and O^{2-} species) [3], more extensive for Fe-doped powder in comparison with TiO_2 . The sharp decrease of conductivity above 390 °C (for TiO_2) and 365 (for Fe/ TiO_2) indicates extensive lattice oxidation above these temperatures; thus the rate of oxygen adsorption is much higher than the supply of oxygen vacancies on the surface (by migration from the bulk and/or by surface dehydroxylation); trapping of the electronic charge carriers by adsorbed oxygen is dominant. Obviously, the presence of iron promotes the oxygen adsorption and also shifts the temperature for the onset of extensive oxidation to lower values. Higher values of σ were measured for TiO_2 in presence of humid oxygen at low temperature in comparison with values in DAR or DO. The peak around 100 °C belongs to physically adsorbed water, acting as a proton vehicle; as the number of molecularly adsorbed water diminishes by desorption on heating, thus this temperature can be taken as a limit of thermal stability of physically adsorbed water on the surface [3,5]. The amount of physically adsorbed water is lower for Fe/ TiO_2 compound. The effect of water diminishes in both cases above 250 °C, when apparently oxygen adsorption prevails.

A different behavior was in evidence for W/ TiO_2 , with respect to TiO_2 showing a much higher conductivity in DAR, in comparison with TiO_2 , indicating a much higher reducibility, while in dry oxygen both samples show identical σ values. In HO, the conductivity was much higher for W/ TiO_2 sample than for TiO_2 up to 300 °C, and only slightly higher above. The extensive oxidation occurs in all cases at 390 °C.

An evaluation of the oxygen coverage from electrical conductivity data (by taken the conductivity of surface in DAR-3 cycle as a reference for the zero oxygen coverage) indicates that while the oxygen coverage of Fe-doped compound is much higher at low temperature (up to 200 °C and above 330 °C) with respect to TiO_2 (e.g 0.42 versus 0.75 at 150 °C), the difference is smaller, but at constantly higher values for W/ TiO_2 in the whole temperature range sample (0.42 versus 0.70 at 150 °C).

Conclusions

the oxygen adsorption ability of titania surface is increased by doping with Fe or W. Doping influences also TiO_2 behavior in presence of moisture

References

- [1] M. Madou and S.R. Morrison, "Chemical sensing with solid state devices", Academic Press, 1989.
- [2] M. Caldararu, D. Sprinceana, V.T. Popa and N.I. Ionescu, Sensors and Actuators B, 1996, 30, 35
- [3] M. Caldararu, G. Postole, C. Hornoiu, V. Bratan, M. Dragan and N.I. Ionescu, Appl. Surf. Sci., 2001, 181(3-4), 255.
- [4] A. Bielanski and J. Haber, Oxygen in Catalysis, Marcel Dekker, New York, 1990.
- [5] M. Caldararu, G. Postole, M. Carata, C. Hornoiu, N.I. Ionescu, T. Jouhakova, A. Redey, Appl. Surf. Sci, 2003, 207, 318.

CRYSTAL AND ABSOLUTE STRUCTURE OF THE AQUADICHLORO(PYRIDOXAL THIOSEMICARBAZONE) IRON(III) CHLORIDE

G. A. Bogdanović¹, V. S. Jevtović², V. M. Leovac²

¹ *Vinča Institute of Nuclear Sciences, Laboratory of Theoretical Physics and Condensed Matter Physics, P.O.Box 522, 11001 Belgrade,*

² *Institute of Chemistry, Faculty of Sciences, University of Novi Sad, Trg Dositeja Obradovića 3, 21000 Novi Sad, Serbia and Montenegro*

Abstract

A new Fe(III) complex of pyridoxal thiosemicarbazone (H₂L) has been characterized by single-crystal X-ray analysis. The Fe atom in the title complex, [Fe(H₂L)Cl₂(H₂O)]Cl, has a distorted octahedral configuration formed by NSO₂Cl₂ donor set. Six-membered chelate ring significantly deviates from planar form. The crystal structure is stabilized by weak intermolecular C-H... π interaction directed towards the center of the pyridine ring.

Introduction

Transition metal complexes of thiosemicarbazones of different denticity are great interest because of their chemical, structural and pharmacological properties [1,2]. Tridentate (ONS) pyridoxal thiosemicarbazone H₂L (Fig.1) is an interesting ligand which can be easily prepared by reacting of pyridoxal, e.g. 3-hydroxy-2-hydroxymethyl-2-methylpyridine-4-carbaldehyde (one of the forms of vitamine B₆) with thiosemicarbazide [3]. With this ligand a substantial number of metal complexes has been synthesized [4], among them some Fe(III) complexes. Namely, the synthesis, spectroscopic and voltammetric characteristics of Fe(III) complexes, including other with pyridoxal Schiff bases derivatives, of the formulas Fe(H₂L)Cl₃·H₂O and [Fe(HL)₂]Cl were described in [5]. Besides, the crystal structure of the square pyramidal [Fe(HL)Cl₂] complexes was referred in [6]. This work reports the crystal and molecular structures of octahedral [Fe(H₂L)Cl₂(H₂O)]Cl complex determined by X-ray structural analysis.

Experimental

Black monocrystals of the title complex were obtained by the reaction of a warm dilute EtOH solution of the protonated form of the ligand H₂L·HCl·H₂O (5), and FeCl₃·6H₂O in a 1:1,2 molar ratio, respectively.

The X-ray data were collected on an Enraf-Nonius CAD-4 diffractometer by using graphite-monochromated MoK α (0.71073 Å) radiation at 293(2) K. Cell constants and orientation matrix were obtained from 24 centered reflections (13.17° to 16.70° θ range) corresponded to a orthorhombic cell whose parameters are: a = 7.304(2) Å, b = 8.401(2) Å, c = 25.359(7) Å, $\alpha = \beta = \gamma = 90^\circ$, V = 1556.2(7) Å³. A total of 2743 reflections (1.61° to 25.97° θ range) were collected by using $\omega/2\theta$ scans. The data were corrected for Lorentz and polarization effects. A gaussian-type absorp-

tion correction based on the crystal morphology was successfully applied ($T_{\min} = 0.5930$, $T_{\max} = 0.8507$). The positions of Fe and Cl atoms were solved by the heavy-atom method in the $P2_12_12_1$ space group. The rest of non-hydrogen atoms was determined by difference Fourier methods and refined anisotropically (together with Fe and Cl atoms) on the F^2 by full-matrix least-square method to $R1 = 0.0281$ and $Rw = 0.0805$ for 218 refined parameters and 2258 reflections with $I > 2\sigma(I)$. The final difference map was with the largest residual peak and hole of 0.348 and $-0.300 \text{ e.}\text{\AA}^{-3}$ respectively.

All of seven H atoms bonded to N and O were determined by difference Fourier method. Their positions and isotropic temperature parameters were freely refined. The rest of H atoms, bonded to carbon atoms, were placed geometrically and refined with a riding model, and with U_{iso} constrained to U_{eq} of the carrier atom. Crystallographic data: formula $\text{C}_9\text{H}_{14}\text{Cl}_3\text{SN}_4\text{O}_3\text{Fe}$, orthorhombic, space group $P2_12_12_1$, $Z = 4$, $D_c = 1.795 \text{ g/cm}^3$, $\mu = 1.631 \text{ mm}^{-1}$, crystal size = 0.42 x 0.36 x 0.10 mm.

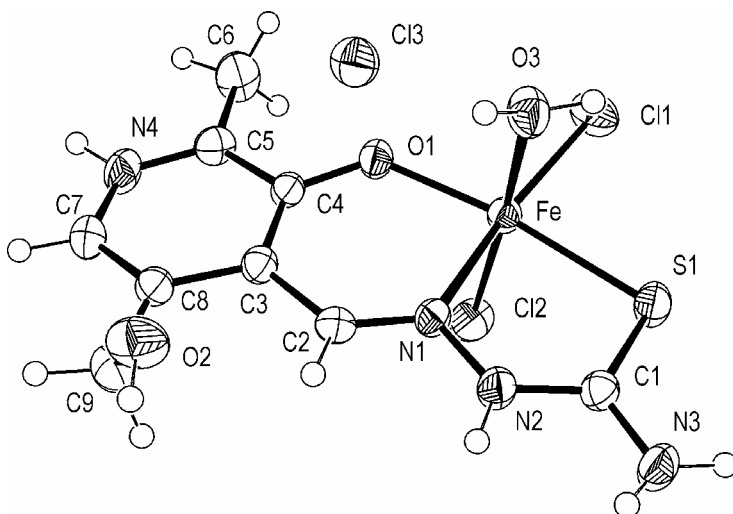


Fig. 1. Perspective view of the crystal structure of $[\text{Fe}(\text{H}_2\text{L})\text{Cl}_2(\text{H}_2\text{O})]\text{Cl}$ complex showing 50% probability displacement ellipsoids and the atom-numbering scheme.

Result and Discussion

Absolute structure of $[\text{Fe}(\text{H}_2\text{L})\text{Cl}_2(\text{H}_2\text{O})]\text{Cl}$ complex has been correctly assigned what was confirmed by the Flack absolute structure parameter $x = -0.01(3)$. The Fe(III) is sited in an octahedral environment. The equatorial plane is formed by a tridentate coordination of the H_2L ligand and one Cl atom, while the next Cl atom and one water molecule are in axial positions (Fig. 1). The Fe-Cl2 bond distance [2.2990(13) Å] is longer than it is for the Fe-Cl1 bond [2.2740(13) Å]. Coordination geometry is significantly deformed, for instance, the Fe atom is displaced by 0.167(1) Å from the N1/S1/Cl1/O1 coordination plane toward the apical Cl2 atom. The Cl1-Fe-Cl2 coordination angle is $97.73(5)^\circ$ what is much higher than 90° .

The six-membered chelate ring adopts non-planar form with total puckering amplitude of 0.202(3) Å. It is a surprise regarding that tridentate thiosemicarbazide-based ligands usually form planar chelate rings. In the present case of [Fe(H₂L)Cl₂(H₂O)]Cl complex six-membered chelate ring is mainly distorted around Fe-O1 bond (The N1-Fe-O1-C4 torsion angle is 23°). This structural behavior has important consequences in the conformation of complex cation presented by existing absolute structure. Thus the interplanar angle between mean plane of N1S1Cl1O1 and mean plane of pyridine ring is 11.1(2)°. In that way the C5 atom is displaced by 0.552(7) Å from equatorial coordination plane.

The crystal packing consists of 2D-layers parallel to (001) crystallographic plane. Within the layers neighboring molecules form weak intermolecular interactions and hydrogen bonds. The Cl3 anions are located between 2D-layers interconnected them by hydrogen bonds which are the strongest among those indicated in the present crystal structure. The C6-methyl group form weak intermolecular C-H... π interaction directed towards the center of the pyridine ring. The same type of C-H... π interaction was observed in the crystal structure of Cu(II) with pyridoxal isothiosemicarbazone [7].

References

- [1] J. S. Casas, M. Garcia-Tasende, J. Sordo, *Coord. Chem. Rev.*, 2000, 209, 197 and refs. therein.
- [2] D. X. West, S. B. Padhye, P. B. Sonowane, *Struct. Bond.*, 1991, 76, 1.
- [3] M. B. Ferrari, G. G. Fava, E. Leporati, C. Pellizzi, P. Tarasconi, G. Tosi, *J. Chem. Soc. Dalton Trans.*, 1986, 2455.
- [4] J. S. Casas, E. E. Castellano, M. C. R. Arguelles, A. Sanchez, J. Sordo, J. Z. Schpector, *Inorg. Chim. Acta*, 1997, 260, 183 and refs. therein.
- [5] V. S. Jevtovic, Lj. S. Jovanovic, V. M. Leovac, L. J. Bjelica, *J. Serb. Chem. Soc.*, 2003, 68, 929.
- [6] M. B. Ferrari, G. G. Fava, C. Pellizzi, P. Tarasconi, *J. Chem. Soc. Dalton Trans.*, (1992) 2153.
- [7] V. M. Leovac, V. S. Jevtovic, G. A. Bogdanovic, *Acta Cryst.*, 2002, C58, 514.

CRYSTAL STRUCTURE REDETERMINATION AND ATOMIC CHARGES OF AMMONIUM DECAVANADATE HEXAHYDRATE BASED ON A LOW TEMPERATURE X-RAY EXPERIMENT

N. Bošnjaković-Pavlović^{1,2}, N. E. Ghermani^{2,3}, A. Spasojević-de Biré²
G. A. Bogdanović⁴ and U. Mioč¹

¹ Faculty of Physical Chemistry, University of Belgrade, P.O. Box 137, Belgrade, Serbia-Montenegro

² Laboratoire SPMS UMR CNRS 8580, Ecole Centrale Paris, 1,

Grande Voie des Vignes, 92295 Châtenay-Malabry, France

³ Laboratoire de Physique Pharmaceutique UMR CNRS 8612, Faculté de Pharmacie 5, Rue Jean-Baptiste Clément, 92296 Châtenay-Malabry cedex, France

⁴ Laboratory of Theoretical Physics and Condensed Matter Physics, VINČA Institute of Nuclear Sciences, P.O. Box 522, Belgrade, Serbia-Montenegro

Abstract

The X-ray structure of ammonium decavanadate hexahydrate, $(\text{NH}_4)_6\text{V}_{10}\text{O}_{28}\cdot 6\text{H}_2\text{O}$, was redetermined at low temperature (100 K) in order to locate the hydrogen sites. A kappa refinement was performed to estimate the experimental atomic charges. Comparisons with previous theoretical calculation results were discussed.

Introduction

The decavanadates belong to wide family of the polyoxometalate complex compounds [1]. Since that vanadium is important in biological systems as a trace element, decavanadates are investigated as potential drugs, for example, in virology [1]. The previous room temperature crystallographic study [2] of ammonium decavanadate hexahydrate, $(\text{NH}_4)_6\text{V}_{10}\text{O}_{28}\cdot 6\text{H}_2\text{O}$, left open questions with the respect to the hydrogen atom positions and hydrogen bonding system in this compound. Regarding that hydrogen bonds can play very significant role in the intermolecular interactions we performed a low-temperature single-crystal X-ray experiment with a goal to obtain relevant crystallographic results. In this work we report significantly improved crystal structure of ammonium decavanadate hexahydrate and experimental atomic charges in this compound.

Experimental

The title compound was prepared by dissolving NH_4VO_3 (0.4 g, 3.42 mmol) in distilled water (20 ml) as described in reference [3] to obtain decavanadate anions.

Single crystal X-ray data collection was performed at 100 K on a Bruker-SMART three-circle diffractometer equipped with a CCD area detector using monochromated $\text{MoK}\alpha$ radiation ($\lambda = 0.71073 \text{ \AA}$). A total of 42599 reflections were collected in the θ range 1.23 to 38.10°. The Lorentz-polarization correction and the integration of the diffracted intensities were performed using SAINT software package. An empirical absorption correction was applied using the SADABS computer program.

The structure was solved by the heavy atom method and difference Fourier methods and refined on the F^2 by full-matrix least-square method to $R1 = 0.0633$ and $Rw = 0.1166$ for 451 refined parameters and 12342 unique reflections with $I > 2\sigma(I)$. Almost all hydrogen atoms were found from difference Fourier maps. Their positions were refined as a riding and with U_{iso} constrained to U_{eq} of the carrier atom. The rest of H atoms were determined after geometrical consideration and they refined in the same way. Crystallographic data: formula $N_6H_{36}O_{34}V_{10}$, triclinic, space group $P\bar{1}$, $a = 10.1421(2) \text{ \AA}$, $b = 10.2376(2) \text{ \AA}$, $c = 16.6452(3) \text{ \AA}$, $\alpha = 83.817(1)$, $\beta = 87.239(2)$, $\gamma = 71.017(1)^\circ$, $V = 1624.6(2) \text{ \AA}^3$, $Z = 2$, $D_c = 2.399 \text{ g/cm}^3$, $\mu = 2.862 \text{ mm}^{-1}$.

The atomic fractional coordinates were transferred to the input file of the full-matrix least-square MOLLY program [4] allowing both structural and kappa refinements [5]. In this latter model, the atomic electron density is expressed as

$$\rho_{at}(\mathbf{r}) = \rho_{core}(\mathbf{r}) + P_{val} \kappa^3 \rho_{val}(\kappa\mathbf{r})$$

where ρ_{core} and ρ_{val} are Hartree-Fock free atomic core and valence spherical electron densities, respectively. The refined parameters are the valence population P_{val} yielding the atomic charge and the contraction ($\kappa > 1$) or expansion ($\kappa < 1$) coefficients. During the kappa refinements, the formal charges of $[V_{10}O_{28}]^{6-}$ and $(NH_4)^+$ were always imposed as constraints in the least-squares procedure. The final R(F) residual factor for kappa-refinement was 5.15% [$wR(F) = 4.97\%$].

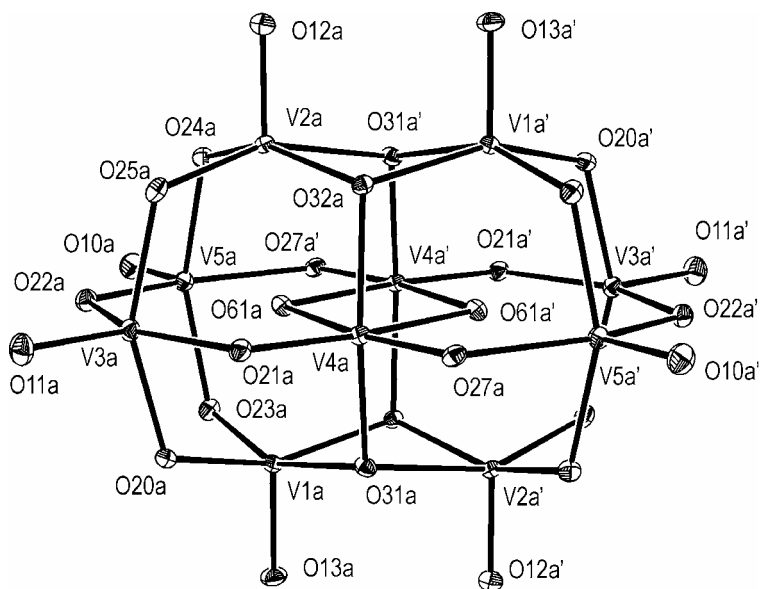


Figure 1. Perspective view of decavanadate polyanion **a** showing the labeling scheme.

Results and Discussion

The title compound crystallizes in $P\bar{1}$ triclinic space group with two independent halves of decavanadate anions (labelled hereafter **a** and **b**), six NH_4^+ cations and six water molecules in the asymmetric unit. The vanadium atoms are in distorted octahedrons where V-O bond lengths are in the range of 1.600(3) to 2.318(2) Å and internal O-V-O angles from 74.3(1) to 106.9(1)°. It was established that three water molecules labelled O91, O93, O95 in the previous X-ray study [2] were in fact ammonium cations. Decavanadate polyanions **a** and **b** are oriented in a such way that the crystal lattice can be described with a primitive cell of decavanadate **a** having one decavanadate **b** in its center. The NH_4^+ counterions and water molecules are distributed in the empty space of the anion compact lattice. It is worthy of note that the decavanadate **a** equally interacts with seven NH_4^+ cations and seven water molecules. Conversely, the decavanadate **b** is closely surrounded by eleven counterions and by only two aqua ligands.

The kappa refinement gave an average positive charge for the V atoms of +1.6 *e* and a common κ parameter value of 1.2 (contracted electron density). In the two polyanions, the internal V4**a** and V4**b** (Fig. 1) have the highest charges, +2.0(1) and +1.9(1) *e*, respectively. In comparison, a vanadium charge equal to +2.0(1) *e* was reported for an isolated decavanadate anion (in an ideal D_{2h} symmetry) from theoretical calculations [6]. The decavanadate oxygen atom electron densities are slightly expanded ($\kappa \leq 1.0$). The corresponding experimental charges are found distributed in large intervals: from -0.5(1) to -1.2(1) *e* for **a**, and from -0.3(1) to -1.4(1) *e* for **b**. The Mulliken population analysis for an isolated polyanion restricts, in *ab initio* theoretical calculations, the oxygen atom net charges to the range from -0.7 to -1.3 *e* [6].

References

- [1] M.T. Pope, A. Müller, polyoxometalates: From Platonic Solids to Anti-Retroviral Activity, Kulwer, Dordrecht, 1994.
- [2] C. Eglmeier, K.J. Range, S. Afr. J. Chem., 1993, 46(1/2), 7.
- [3] B. Chinea, D. Dakternieks, A. Duthie, C.A. Ghilardi, P. Gili, A. Mederos, S. Midollini, A. Orlandini, Inorg. Chim. Acta, 2000, 298, 172.
- [4] N.K. Hansen, P. Coppens, Acta Crystallogr., 1978, A34, 909.
- [5] P. Coppens, T.N. Guru, P. Leung, E.D. Stevens, P. Becker, Y.W. Yang, Acta Crystallogr., 1979, A35, 63.
- [6] J.Y. Kempf, M.M. Rohmer, J.M. Poblet, C. Bo, M. Benard, J. Am. Chem. Soc., 1992, 114, 1136.

IR, NMR AND XRPD INVESTIGATION OF RINGS EVOLUTION IN ALUMINOSILICATE STRUCTURES

S. Marković¹, V. Dondur², R. Dimitrijević³ and S. Macura⁴

¹*Institute of Technical Science of the Serbian Academy of Sciences and Arts, Knez Mihailova 35/IV, Belgrade,* ²*Faculty of Physical Chemistry, Studentski Trg 12-16, P.O. Box 137,* ³*Faculty of Mining and Geology, Department of Crystallography, Džušina 7, Belgrade, Serbia and Montenegro* ⁴*Department of Biochemistry, Mayo Foundation, Rochester, Minnesota, USA*

Abstract

In this paper we present the results of an investigation of phase transformation of zeolite NaP in temperature interval from room temperature up to 1400 °C. It has been found that crystal structure of NaP zeolite collapsed at 590 °C. Furthermore, with prolonged heating nepheline phase has formed at 900 °C. This phase was stable up to 1200 °C where it was transformed to glass. The disconnection of single four rings (S4R) secondary building units in NaP structure, the forming of amorphous precursor and the crystallization of nepheline phase, built from single six rings (S6R), were studied. Investigated phases were characterized by XRPD, IR, NMR and DSC methods.

Introduction

The mechanism of transformation, transition temperatures and structure of formed phases are very important for practical application of zeolite as precursor in the ceramic or ceramic composite materials [1-4]. The mechanism of thermally induced transformation strongly depends on extra framework cations and type of used zeolite.

Forming of rings i.e. secondary building units, and their ordering in framework aluminosilicate structures is not investigated enough. Besides theoretical studies based on Ab Initio and Monte Carlo simulations, forming and ordering of rings in framework aluminosilicate structures could be investigated by experimental techniques such as IR, Raman and NMR spectroscopy. A disordering and breaking of rings, their reconnection and reordering can be studied during phase transitions of structurally known precursors.

In this paper, breaking of S4R secondary building units in zeolite NaP, forming of amorphous precursor, and crystallization of nepheline phase made from S6R is studied.

Experimental procedure

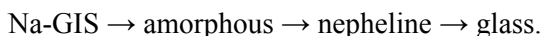
The sodium form of synthetic zeolite P (Si/Al = 1.5, produced in our laboratory) was used as starting material. Samples for further analysis were obtained by thermal treatment of zeolite NaP in temperature range from 500 up to 1400 °C, in 20 °C intervals. The samples were heated at constant temperature (1 to 4 hours, ± 2 °C) using Carbolite CTF 15/75 electric furnace.

After the samples had been cooled, all XRPD, IR and NMR measurements were performed at room temperature. The XRPD patterns were obtained on Philips PW-1710 automatic diffractometer, using Cu tube operating at 40 kV and 35 mA. The

IR measurements were performed at Perkin-Elmer 983 spectrophotometer using the KBr pellet technique, in the frequency interval 300-1400 cm^{-1} . MAS NMR spectra were obtained on a Bruker AMX300 spectrophotometer. ^{29}Si spectra were recorded at 59.61 MHz, using a WB-7BL (7 mm) probe and a MAS rate 3.0 KHz, with a single (7 μs , $\pi/2$) pulse acquisition. The ^{29}Si chemical shifts are reported relative to tetramethylsilane (TMS), using the previously calibrated signal from Na-LTA zeolite as a secondary reference. DSC experiments were performed on TA SDT 2960 instrument, between 25 and 1300 $^{\circ}\text{C}$ under nitrogen flow, against an aluminum oxide reference. The heating rate was 20 $^{\circ}\text{min}^{-1}$.

Results and Discussion

XRPD analysis of phases obtained by thermal treatment of NaP zeolite indicates three phase transformations in the temperature range from 500 to 1400 $^{\circ}\text{C}$. At 590 $^{\circ}\text{C}$, the first indications of partial collapse of NaP structure are evident in XRPD patterns, and phase obtained at 780 $^{\circ}\text{C}$ is completely amorphous. At 850 $^{\circ}\text{C}$, low-crystalline nepheline phase starts to grow. The pure nepheline structure with hexagonal symmetry was formed after the sample was heated for 4 hours at 900 $^{\circ}\text{C}$. This phase is stable up to 1200 $^{\circ}\text{C}$ when glass transformation was noticed. According to the obtained results following conversion scheme is recognized:



The results of XRPD measurements have been confirmed by DSC method. In Table 1 all examined samples, condition of their preparation and some structural characteristics are listed.

Table 1 List of examined samples and condition of their preparation

Sample	SBU* rings	Condition of samples treatment		Symmetry
		T ($^{\circ}\text{C}$)	t (h)	
NaP	S4R, S8R			Cubic
Amorphous phase	/	780	1	/
Amorphous phase	/	800	1	/
Amorphous and traces of nepheline	S6R*	850	4	/
Nepheline	S6R	900	4	Hexagonal
Nepheline	S6R	1100	4	Hexagonal

*S6R in traces

Due to XRPD and DSC results, it is evident that NaP zeolite gradually collapsed in the temperature region from 590 to 800 °C. According to IR results (Fig. 1) it is assumed that during heating, Si-O-Si and Si-O-Al bonds, making S4R and S8R secondary building units, are broken (bands at 603 and 675 cm^{-1} disappeared, Fig. 1b). At higher temperature the bonds are reestablished and six membered rings (S6R) are built (band at 517 cm^{-1} is appeared, Fig. 1d).

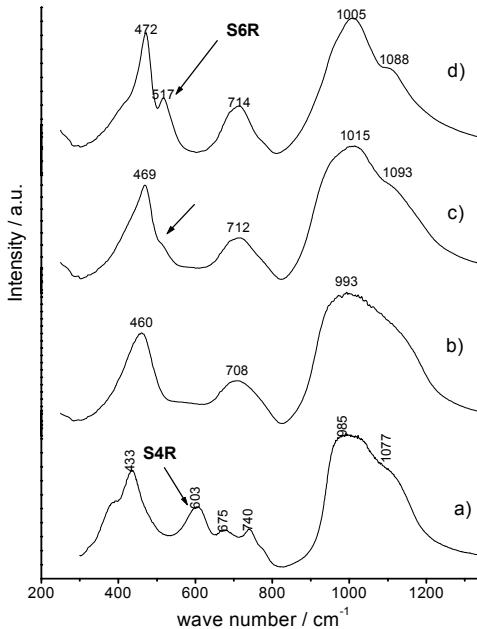


Fig. 1 IR spectra of: a) zeolite NaP at room temperature; b) amorphous phases obtained at 800 °C, 1 h; c) amorphous phases with traces of nepheline structure at 850 °C, 4 h and d) nepheline phases obtained at 1100 °C, 4 h.

Because starting zeolite NaP has Si/Al ratio 1.5 and disordered S4R (2Si2Al, 3Si1Al and 4Si) it was assumed that S6R in formed nepheline phase should have disordered structure, too. This assumption was confirmed by ^{29}Si MAS NMR spectroscopy. It was noticed that single six membered rings with atom combinations 3Si3Al, 4Si2Al, 5Si1Al and 6Si exist.

Acknowledgments

The Ministry of Science, Technologies and Development of Republic of Serbia provided financial support under grant no. 1243.

References

- [1] A. Kremenovic, Ph. Colomban, B. Piriou, D. Massiot, P. Florian, *J. Phys. Chem. Solids*, 2003, 64, 2253.
- [2] A. Kremenovic, P. Norby, R. Dimitrijevic, V. Dondur, *Phase Trans.*, 1999, 68(4), 587.
- [3] C. Ferone, G. Dell'Agli, M.C. Mascolo, M. Pansini, *Chem. Mater.*, 2002, 14(2), 797.
- [4] S. Boskovic, D. Kosanovic, V. Dondur, R. Dimitrijevic, *Ceram. Inter.*, 2000, 26, 33.

AN EFFECTIVE MEDIUM APPROACH TO ANALYSIS OF NANOSCALE DISORDER IN PHOTONIC BANDGAP MATERIALS

Z. Jakšić, M. Maksimović and D. Vasiljević-Radović

*IHTM - Institute of Microelectronic Technologies and Single Crystals,
Belgrade, Serbia and Montenegro*

Abstract

We investigated the influence of technologically-introduced nanoscale disorder to the macroscopic optical parameters of rf-sputtered 1D silicon-silica photonic crystals. We used atomic force microscopy to examine the spatial noise on the interfaces between layers and entered thus obtained profiles of surface roughness into an effective medium model. We further utilized these results to calculate the modified spectral reflection and transmission of the samples by the transfer matrix method. The approach is applicable to other mesoscopic and to subwavelength nanooptical structures.

Introduction

The technologies of microfabrication and nanofabrication enable the production of different ordered structures for mesoscopic and subwavelength optics, e.g. photonic bandgap materials (photonic crystals) [1], metamaterials [2], etc. The dimensions of the features are of the order of tens to hundreds of nm, with a detail accuracy of about 2-4 nm or better. These requirements push the available technologies to their limits and the possibilities of deviations from the designed dimensions are high. Yet the papers dealing with technologically induced disorder on nanooptical devices are scarce. Some of the papers deal generally with light propagation in disordered media [3]. Most are dedicated to photonic crystals. Some analyze the randomness of lattice constant [4], others consider the deviations of the unit cell shape and dimensions [5]. The paper [6] deals with fabrication-induced holographic noise.

The aim of this paper is to apply the effective medium theory to approximate the disordered part in the case of 1D photonic crystals and to use the transfer matrix technique to calculate thus introduced losses to the signal. We obtain the data on the disorder nature itself experimentally by the atomic force microscopy (AFM). In this way a connection between nanoscale "noise" and macroscopic optical parameters is established.

Approach and Results

We analyzed deviations of the surface of our structure from the designed value, i.e. the spatial "white noise", since it is the most often encountered deviation in the practice, albeit the least researched. We start our investigation of a 1D stack of alternately deposited Si and SiO₂ strata from a single interface between strata, Fig. 1.

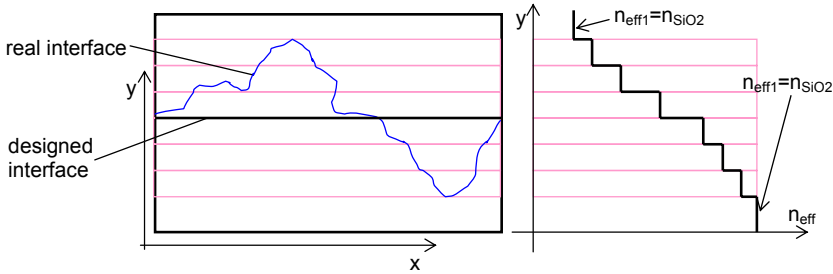


Figure 1. An interface between strata in a 1D photonic crystal. a) spatial noise profile; b) equivalent representation by effective index

We divided the interface into a finite number of sublayers (a larger number means a higher accuracy). We replaced each sublayer by a homogeneous layer with the identical thickness, but with an effective value of refractive index. Thus the "noisy" interface is represented as an additional layer with antireflective (AR) properties. This effective AR layer decreases reflection, but does not improve transmission, since it scatters the light off normal incidence, causing leakage. We calculated the effective index values using the Bruggeman model [7].

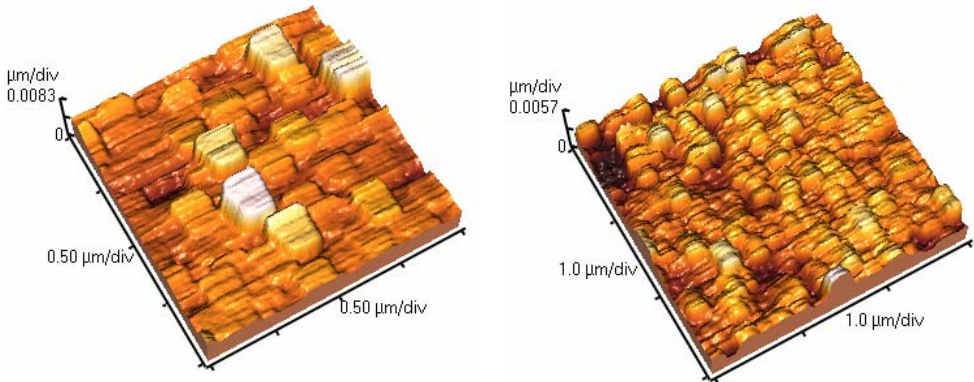


Figure 2. Surface morphology of Si strata in two samples of 1D Si-SiO₂ photonic crystals. Left: 2x2 μm, right: 3x3 μm. Thickness variation (min. to max.) 5.7 and 8.3 nm

We applied the approach to our 1D photonic crystals rf sputtered on single crystal silicon substrate. The samples had 10 layer pairs, $d_{\text{SiO}_2}=0.63 \mu\text{m}$ and $d_{\text{Si}}=0.27 \mu\text{m}$, the middle Si layer replaced with an acceptor defect, $d_{\text{def}}=0.17 \mu\text{m}$. The AFM pictures of the surfaces of typical layers are shown in Fig. 2.

Fig. 3a shows the AFM surface profiles (3 per each sample). We divided each to 3 sublayers (3 nm each) to determine the effective medium profile. Fig. 3b shows measured spectral transmissions in different points of the samples measured on an FTIR spectrophotometer (solid) and calculated by transfer matrix method (TMM) for the ideal case (dashed) and with surface roughness taken into account (dotted). The expected qualitative behavior is observed.

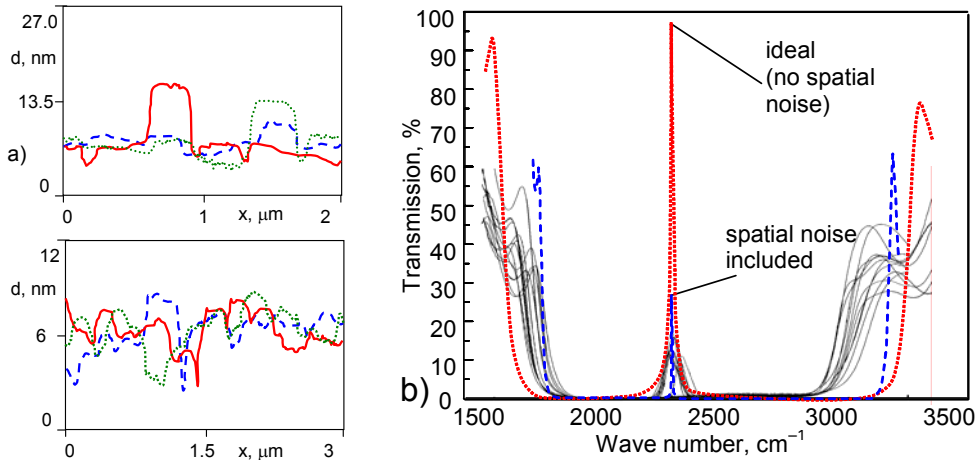


Figure 3. a) AFM-measured interface profiles of two different samples; b) spectral transmission of the samples. Solid: measured; dotted: no roughness, calculated by TMM; dashed: roughness included, calculated by TMM.

Conclusion

We investigated the connection between nanoscale disorder (as determined by the AFM) and spectral characteristics of 1D photonic crystals (calculated by effective medium theory and TMM). Our results show that a surface roughness of about 4-6 nm results in a transmission drop of 20 to 40 %. In this way the accuracy of nanofabrication determines the attainable transmission and reflection. The approach is general and is applicable to other mesoscopic and subwavelength structures.

References

- [1] E. Yablonovitch, Phys. Rev. Lett., 1987, 58, 2059.
- [2] J. B. Pendry, Phys. Rev. Lett., 2000, 85, 3966.
- [3] A. Lagendijk, B.A. van Tiggelen, Phys. Rep., 1996, 270, 143.
- [4] L. Businaro, Ph.D. Thesis, Universita degli studi di Catania, 2003.
- [5] H. Y. Ryu, J. K. Hwang, Y. H. Lee, Phys Rev B, 1999, 59, 5463.
- [6] Z. Jakšić et al, Proc. 23rd MIEL 2002, 2, Niš, May 12-15, 293.
- [7] W.Theiß, Surf. Sci. Rep. 1997, 29, 91.

OPTICAL TRANSMISSION OF PHASE-COMPENSATED 1D PHOTONIC CRYSTALS INCORPORATING NEGATIVE-INDEX MATERIAL AND AMPLIFYING MEDIUM

M. Maksimović and Z. Jakšić

*IHTM - Institute of Microelectronic Technologies and Single Crystals,
Belgrade, Serbia and Montenegro*

Abstract

We present an analysis of a 1D photonic crystal-based subwavelength resonant cavity composed of alternate layers of negative refractive index metamaterial and conventional dielectric. We studied phase compensation in such a structure for the case of lossy material. Optical amplification is utilized for the compensation of absorption in metamaterial. Macroscopic optical properties of the structure are calculated and analyzed.

Introduction

Metamaterials ("left-handed materials", LHM) are artificial composites with simultaneously negative permittivity and permeability, thus characterized by a negative refractive index [1]. In such materials evanescent waves are amplified [2] and light propagates in the direction opposite to the energy flow. The Poynting vector is antiparallel to the wave vector at the interface between conventional material and metamaterial [3]. The application of photonic crystal principles to the LHM promises the fabrication of left-handed materials with operating frequencies reaching THz and even the optical range [4]. The use of nanostructured metallic inclusions with dimensions 10 nm to 100 nm for localized modes in photonic crystals allows to engineer negative permittivity in the infrared [5]. Such structures are difficult but not impossible to produce by the state-of-the-art nanofabrication [5]. The use of phase compensation for the enhancement of metamaterial properties was described in [6], and the behavior of lossy LHM was investigated in [7]. A compact thin subwavelength resonant cavity based on phase compensation in metamaterials for 1D case is described in paper [8] and further studied in [9].

This paper analyzes the optical behavior of a phase-compensated 1D photonic crystal resonant cavity which simultaneously incorporates positive- and negative-refractive index media. We utilized optical amplification to compensate losses in the metamaterial part. We utilized the transfer matrix technique to calculate the transmission.

Calculation and Results

We consider a resonator structure composed of alternating layers of conventional dielectric (RHM, $n_1 > 0$) and of metamaterial with negative permittivity and permeability (LHM, $n_2 < 0$). Perfect reflectors are at the both open surfaces of the structure. The fields in the cavity can be described as sum of forward and backward

waves. A wave through the structure is characterized by its wave vector $\vec{k}_i = \vec{k}_0 n_i$ in the material i , $i=1,2$ (\vec{k}_0 is wave vector in free space, n_i is refractive index). The phase at the end of the second slab is $\phi = \vec{k}_1 d_1 + \vec{k}_2 d_2 = \vec{k}_o (n_1 d_1 + n_2 d_2)$, therefore $\phi = k_o (n_1 d_1 - |n_2| d_2)$. If we choose $n_1/|n_2|=d_2/d_1$ the total phase difference between the front and the back of a two-layer structure becomes zero. For materials with complex refractive index $N_i=n_i-ik_i$ the condition for phase compensation is $\phi = k_o (n_1 d_1 - |n_2| d_2) - i(k_1 d_1 + k_2 d_2) = 0$. If the first material is RHM with gain and the second is LHM with losses, the overall phase compensation conditions are

$$\frac{n_1}{|n_2|} = \frac{d_2}{d_1}, \quad \frac{k_1}{|k_2|} = \frac{d_2}{d_1}. \quad (1)$$

The boundary conditions in the cavity impose that fields are equal to zero for a structure thickness equal to 0 and to d_1+d_2 and that tangential components of the fields are continuous at the boundary between two layers a thickness equal to d_1 . Utilizing these boundary conditions we derive the following dispersion relation for the RHM-LHM structure

$$\left(\frac{\Gamma_2}{\mu_2} \right) \tan(\Gamma_1 d_1) + \left(\frac{\Gamma_1}{\mu_1} \right) \tan(\Gamma_2 d_2) = 0, \quad (2)$$

The above relation does not put any constraint on the sum of the individual layer thickness, but it rather deals with their ratio as shown in the relation. The above relation implies that one can have a subwavelength resonant cavity for a given frequency. However, there is no explicit frequency dependence in (2) and the system is thus not frequency selective [4].

Assume that the considered two-layer structure is surrounded by air ($n=1$). The transmission properties of the structure can be calculated by the transfer matrix method (e.g. [10]). We consider a RHM-LHM structure with 2, 6 and 10 layer pairs. For RHM $N_1=1.5$ and for the LHM $N_2=-0.5$ ($\epsilon_2=-0.5$, $\mu_2=-0.5$). We chose $d_1=\lambda_0/10$, $d_2=2\lambda_0/10$.

Fig. 1a) shows transmission for the described 1D photonic crystal structures. Losses are represented by $k_2=-0.01$. It is clear that in the presence of losses the transmission is reduced, but for sufficiently low losses there is still a transmission resonance in the subwavelength range. This effect of reduction of the transmission response is greater when the light is incident on the LHM layer.

As losses could be compensated by introducing optical amplification, Fig. 1 b) shows the transmission when the RHM is amplifying and the LHM is lossy. The amplifying process is introduced in the RHM by taking positive imaginary part of refractive index, set to the equal absolute value as the losses in the metamaterial. As expected, this leads to an increase of the transmission. The effect is greater when light is incident on the conventional (optically amplifying) layer.

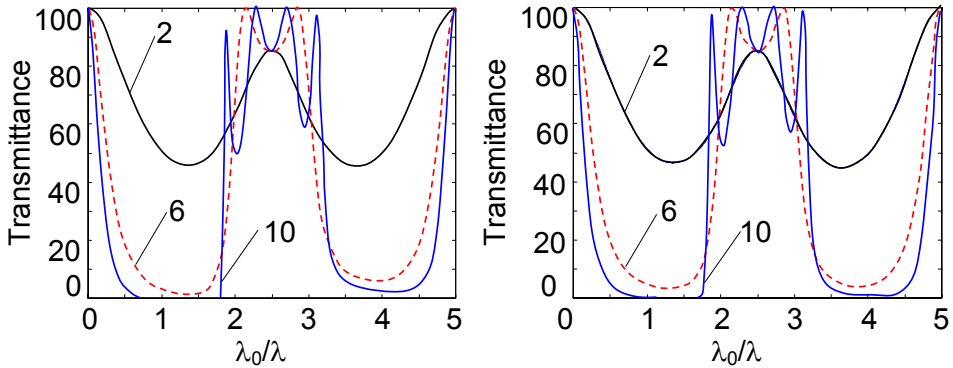


Fig. 1 Transmission for a multilayer structure with lossy LHM for 2, 6 and 10 layers, $k=0.01$. a) conventional RHM (no gain); b) amplifying RHM (with gain)

Conclusions

We analyzed a 1D photonic crystal structure consisting of alternate layers of negative-refractive index material and of conventional positive-index dielectric. Losses can be compensated by introducing optical gain in the RHM part of the structure, which is a technologically feasible solution. In an RHM-LHM subwavelength resonant cavity with loss and gain regions it is possible to obtain true resonant effect because of the frequency selectivity of the gain region. Let us assume that gain is provided by semiconductor quantum dots embedded in conventional material. Because of strong frequency localization of the amplifying process in the subwavelength resonator the frequency selectivity is fully provided. The phase- and loss-compensated LHM structures can be utilized for the amplification of evanescent waves and thus for near-field lensing with subwavelength resolutions.

References

- [1] V.G. Veselago, *Sov.Phys.Usp.*, 1968, 10, 509.
- [2] J. B. Pendry, *Phys. Rev. Lett.*, 2000, 85, 3966.
- [3] R. Ziolkowski, E. Heyman, *Phys. Rev E*, 2001, 64, 056625.
- [4] M. Notomi, *Opt. Quant. Electronics*, 2002, 34.
- [5] S O'Brien, J. B. Pendry, *J. Phys. C*, 2002, 14, 6383.
- [6] S. Ramakrishna, J. B. Pendry, *Phys. Rev. B*, 2003, 67, 201101-1-4.
- [7] T. J. Cui et al, *Physics Letters A*, 2004, 323, 484.
- [8] N. Engheta, *IEEE Ant. Wireless Prop. Lett.*, 2002 1, 10.
- [9] S. A. Tretyakov et al., *Microw. Opt. Technol. Lett.*, 2003, 38, 153.
- [10] H. Cory, C. Zach, *Microw. Opt.Tech. Lett.*, 2004, 40, 460.

ON THE TREATMENT OF FAU TYPE ZEOLITE BY CITRIC ACID AND AMMONIUM CITRATE

V. Rakić¹, Lj. Damjanović², V. Dondur² and R. Dimitrijević³

¹Faculty of Agriculture, Nemanjina 6 Zemun, ²Faculty of Physical Chemistry, Studentski trg 12,

³Faculty of Mining and Geology, Djušina 1, Beograd, Serbia and Montenegro

Abstract

In this work, dealumination of Y type zeolite performed by ammonium citrate and citric acid was studied. The obtained samples of dealuminated zeolite were characterized by XRPD method and temperature programmed desorption (TPD) technique. The obtained results indicate the influence of dealumination treatment on the amount and strength of active sites in the investigated samples.

Introduction

Dealuminated faujasite type zeolites exhibit a higher thermal and hydrothermal stability and higher catalytic activity than those of the aluminium-rich as synthesized zeolite Y (Si/Al = 2.5). Therefore, dealumination procedures have gained growing attention. Highly dealuminated Y zeolites often used as adsorbents, solid acid catalysts or supports are commonly obtained by leaching with strong inorganic acids [1], or by treating with SiCl₄ [2]. However, we have shown in our previous work [3] that only a slight dealumination performed with Na₂H₂EDTA or H₄EDTA (Si/Al = 4.5) has a strong influence on the sites active in the adsorption of CO_x, very important atmospheric pollutants. Recently, the influence of citric acid treatment on the surface properties of zeolite beta has been proven [4]. Therefore, in this work we investigated the dealumination of Y zeolite performed by treatment with citric acid and ammonium salt of citric acid.

Experimental

The dealuminated samples of Y zeolite were prepared from parent SK-40, Na₅₄(AlO₂)₅₆(SiO₂)₁₃₆ (Union Carbide). NH₄⁺ forms were obtained by ion-exchange procedure in aqueous solutions of NH₄Cl performed at 100°C. The obtained NH₄Y zeolite was treated with aqueous ammonium citrate solutions (0.01M) different period of time, at room temperature. These samples were denoted as Y*D, where * denotes the number of performed procedures. Additionally, parent NH₄Y was treated with 0.02 M citric acid at room temperature. Thus obtained samples are denoted as YD*. Subsequent to the treatment, all the samples were washed with deionised water and dried at 110°C.

XRPD analysis was done in the case of all investigated samples, in order to check whether FAU type structure was preserved after above described treatments or not. XRPD pattern were obtained Philips PW-1710 automatic diffractometer.

Temperature programmed heating of NH₄ forms of zeolites was carried out on a flow-type apparatus: differential scanning calorimeter (DSC 111, Setaram) coupled

with mass spectrometer (Thermostar, Pfeiffer). Temperature programmed desorption profiles of masses corresponding to ammonia ($m/e = 17, 16$ and 15) and water ($m/e = 18, 17$ and 16) were collected with a heating rate of 5 K min^{-1} . Helium with a flow rate of $\approx 10 \text{ cm}^3/\text{min}$ was used as a carrier gas.

Results and Discussions

XRPD analysis confirmed that a structure of Y zeolite was preserved in the case of the sample treated with ammonium acetate. However, a collapse of a zeolite structure was noticed in the case of the samples treated with citric acid.

Table 1 compiles the results of chemical and XRPD analysis, and the enthalpies calculated from DSC curves, for all investigated samples.

Table 1. Results obtained for the treated samples

Sample	Treated with	Si/Al	Crystal structure	ΔH_1 , J/g	High temperature peak at	ΔH_2 , J/g
NH ₄ Y	/	2.5	parent	575	635°C	38.3
NH ₄ Y1D	Citrate*	3.7	preserved	576	642°C	28.6
NH ₄ Y2D	Citrate*	4.6	preserved	498	655°C	21.0
NH ₄ YD1	Citric acid	4.8	30-40% preserved	480	/	/
NH ₄ YD2	Citric acid	>5	collapsed	422	/	/

* - ammonium citrate ($(\text{NH}_4)_3\text{C}_6\text{H}_5\text{O}_7$; ΔH_1 – endothermic effect in the region room temperature - 500°C; ΔH_2 – endothermic effect above 500°C

TPD spectra of ammonia and water were monitored in the course of deammoniation procedure. High-temperature desorption processes of mass 18 are noticed above 600°C, they are assigned to the dehydroxylation. It is known from the literature that the intensity of the dehydroxylation process can be correlated with the number of Brønsted acid sites [5]. The results obtained in this work clearly show that, after Y zeolite was treated with ammonium citrate, the intensities of dehydroxylation peaks are diminished. Additionally, it is evident from the Figure that high-desorption process of water is shifted to higher temperature with increasing Si/Al ratio, id. est., with increasing dealumination. It is worth to notice that high-temperature desorption process of water was not found for the samples treated with citric acid.

TPD profiles recorded for the masses corresponding to ammonia indicate the influence of chemical treatment with ammonium citrate, also (Figure 1).

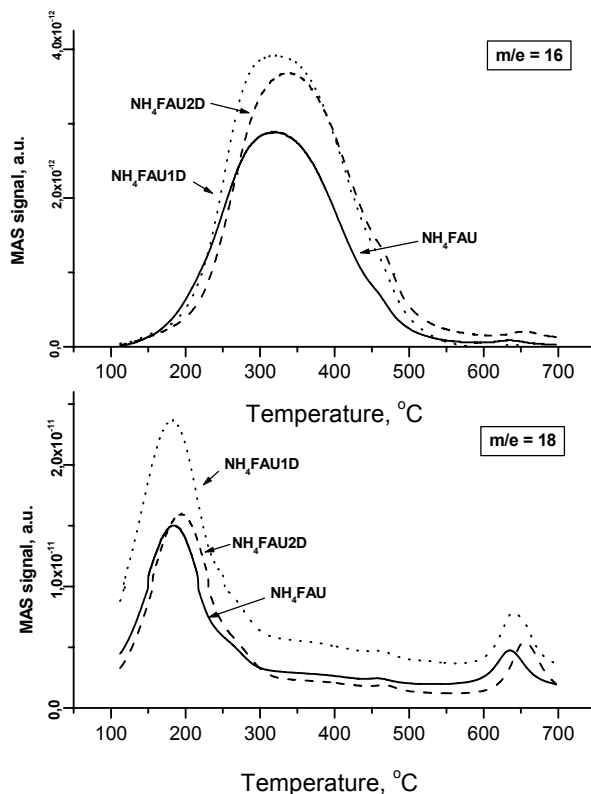


Figure 1. TPD spectra of water ($m/e = 18$) and ammonia ($m/e = 16$)

Conclusion

It is noticeable from the results presented here that, as a result of treatment with citric acid, the structure of Y zeolite collapsed. As a result of treatment with ammonium citrate, the extraction of aluminum from the zeolite network happened. Thus, it was shown that this “soft” method could be applied in order to achieve the desired Si/Al ratio. The influence of dealumination on the population of the strongest sites is recognized.

References

- [1] G.T.Kerr, J. Phys. Chem., 1968, 72, 2594.
- [2] H.Miessner, H.Kosslick, U.Lohse, B.Parlitz and V.A. Tuan, J. Phys. Chem., 1993, 97, 9741.
- [3] X. Zaiku, C.Qingling, Z. Chengfang, B. Jiaqing and C. Yuhua, J. Phys. Chem. B, 2000, 104, 2853.
- [4] V.M.Rakić, V.T.Dondur, R.V.Hercigonja and V.Andrić, J. Therm. Anal. Calor. 2003, 72, 761.
- [5] H.G.Karge, V. Dondur and J. Weitkamp, J. Phys. Chem., 1991, 95, 283.

INFLUENCE OF SILICA SOURCE ON THE NaA ZEOLITE CRYSTALLIZATION

Z. Miladinović and J. Zakrzewska

Institute of General and Physical Chemistry, Studentski trg 12-16, 11000 Belgrade, Yugoslavia

Abstract

^{29}Si and ^{27}Al NMR spectroscopy was used for investigation of properties and influence of different composition of silica solution on course of zeolite synthesis. Observed differences in 'crystallization curves' are consequence of different mechanism of nucleation.

Introduction

It is well known that the course of crystallization depends considerably on many factors, which may be collectively recognized as 'synthesis condition'. One such parameter is the silica source.

Freund [1] and Hamilton at al. [2] tried to explain the effect of silica source on the course of zeolite crystallization, by the presence of different amounts of anion impurities in different silica solution, which can act as a nucleation center of zeolite.

Rate of dissolution/depolymerization and hydrolysis, respectively, of the silica source was identified as a critical factor that determines the pathway of crystallization and structural and particulate properties of crystallized zeolite [3]. Subotic at al. [4] have showed that degree of silica polycondensation (DPS) can influence the distribution of Na, Al, and Si between the solid and the liquid phases of the hydrogel.

Engelhardt at al. [5,6] have investigated properties of silica solution by using ^{29}Si NMR spectroscopy, and influence of silica composition on the crystallization of the zeolite NaA. By using two different type of silica solution, with different molar ratio of Si/Na, with same batch composition for synthesis: $2\text{SiO}_2:\text{Al}_2\text{O}_3: 3.4\text{Na}_2\text{O}: 170\text{H}_2\text{O}$, they observed different chemical composition of initial aluminosilicate gels and different rates of crystallization.

Experimental

Sodium silicate solution were prepared by dilution of water-glass solution (Galenika; 8.88% Na_2O , 25.80% SiO_2) with sodium hydroxide solution of appropriate concentration for preparing silicate solutions with molar ratio $\text{SiO}_2/\text{Na}_2\text{O} = 3.0, 2.2, 1.6$. Each sample of silicate solution was analyzed by ^{29}Si NMR spectroscopy. Sodium aluminate solutions were prepared to obtain appropriate batch composition for synthesis: $2.54\text{SiO}_2:\text{Al}_2\text{O}_3:3.76\text{Na}_2\text{O}:120\text{H}_2\text{O}$. ^{27}Al NMR spectra were obtained from zeolite suspension taken from reactor after mixing and stirring aluminate and silicate component for about 2 min. All spectra were recorded on Bruker MSL 400 spectrometer.

Results

The ^{29}Si NMR spectra of silica solution for different molar ratio $\text{SiO}_2/\text{Na}_2\text{O}=3.0, 2.2, 1.6$ are presented in Fig. 1.

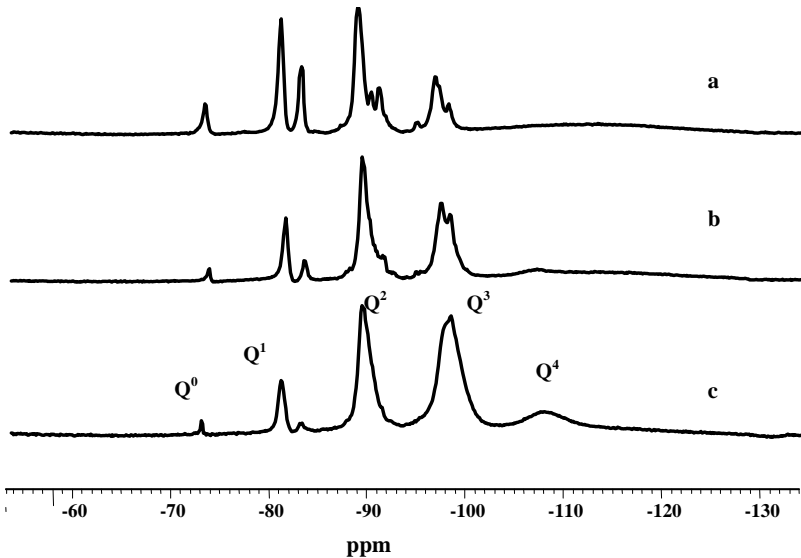


Figure 1. ^{29}Si NMR spectra of silica solutions a) $\text{SiO}_2/\text{Na}_2\text{O}=1.6$; b) $\text{SiO}_2/\text{Na}_2\text{O}=2.2$; c) $\text{SiO}_2/\text{Na}_2\text{O}=3.0$;

Five groups of lines present in each spectrum correspond to different degree of silica polycondensation. Characteristic ranges of ^{29}Si chemical shifts have been observed for different types of silicate structural units Q^n (Q represents a silicon atom bonded to four oxygen atoms and n is the number of $\equiv\text{Si}-\text{O}-\text{Si}\equiv$ bridges attached [5]). As can be seen from Fig. 1, the degree of polycondensation decreases with decreasing $\text{SiO}_2/\text{Na}_2\text{O}$ ratio.

^{27}Al NMR spectroscopy was used for monitoring the crystallization process [7]. The changes of intensity of the line at 79 ppm, obtained during synthesis, are presented in Fig. 2. The curves represent synthesis using different starting silica solutions for the same batch composition. The differences in starting plateau and slope of these curves can be explained by differences in mechanism and rate of nucleation process [3].

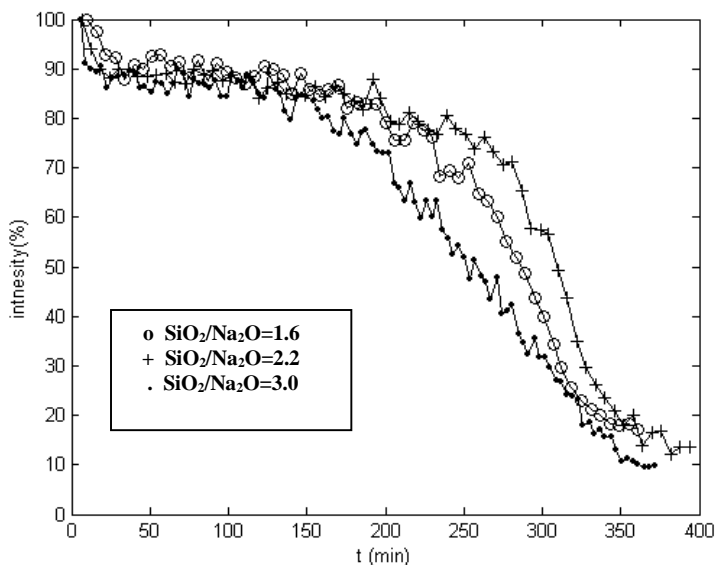


Figure 2. The dependency of ^{27}Al NMR line intensity on crystallization time for different silica solution used in synthesis.

Conclusion

^{29}Si NMR spectroscopy is a powerful tool for the study of the silicate anion species and structural units present in silicate solution. Being simpler and providing more structural information are main advantages compared to classical method for DPS analysis (with molybdc acid). Analysis of kinetic aspect and shape of curves obtained from ^{27}Al NMR spectra can give information about nucleation process of zeolite crystallization.

References

- [1] E.F. Freund, *J.Cryst.Growth*, 1976, 34, 11.
- [2] K.E.Hamilton, E.N.Coker, A.Sacco,Jr., A.G.Dixon, and R.W.Thompson, *Zeolites*, 1993, 13, 645.
- [3] I.Krznarić, T.Antonić, J.Bronić, B.Subotić, R.W.Thompson, *Croat.Chem.Acta*, 2003, 76, 7.
- [4] T.Antonić, B.Subotić, V.Kaučić and R.W. Thompson, *Stud.Surf.Sci.Catal.*, 1999, 125, 13.
- [5] G. Engelhardt, D. Hoebbel, *J. Chem. Soc., Chem. Commun.*, 1984, 514.
- [6] G.Engelhardt, B.Fahlke, M.Magi, and E.Lippmaa, *Zeolites*, 1985, 5, 49.
- [7] Z.Miladinović, J.Zakrzewska, *Proceedings of the 6th International Conference on Fundamental and Applied Aspect of Physical Chemistry*, 2002, 487.

TWO METHODS FOR FLY ASH CONVERSION INTO NaP1 ZEOLITE

D. Vučinić, I. Miljanović and A. Rosić

Faculty of Mining and Geology, 11000 Belgrade, Serbia and Montenegro

Abstract

Two methods have been applied for the NaP1 zeolite synthesis using a fly ash as raw material. One method consists of conventional hydrothermal treatment of bulk fly ash sample mixed with NaOH solution at 90 °C in open system (atmospheric pressure). The other comprises a combination of alkaline fusion of fly ash with NaOH at 550 °C prior to a hydrothermal reaction at 90 °C, where the fusion product is mixed with water.

Introduction

Fly ash is composed primarily of aluminosilicate glass, mullite ($\text{Al}_6\text{Si}_2\text{O}_{13}$) and quartz (SiO_2), hence it provides a ready source of Al and Si, which are necessary for zeolite synthesis. A number of hydrothermal activation processes have been proposed for the conversion of fly ash into zeolites [1-4]. Also, some authors found that the fusion process of sodium hydroxide with fly ash prior to hydrothermal reaction can dissolve more silicates and aluminosilicates from a fly ash, thereby increasing the yield of zeolites [5-7].

In the present study the objective was to compare the fusion and hydrothermal methods for producing NaP1 zeolite.

Experimental

Fly ash produced during the combustion of coal (lignite) from "Kolubara" deposit, near Belgrade, was obtained from "Nikola Tesla-B" power station, using electrostatic precipitators.

The chemical composition and the grain size distribution of raw material were detected on the representative sample of a fly ash [7]. Analysis by X-ray diffraction (XRD) revealed the major inorganic phases in fly ash, using a Philips PW 1710 automated power diffractometer with monochromatic CuK_α radiation and an automatic divergence slot.

In the first, bulk fly ash sample without prior treatment was used for the zeolite synthesis by conventional hydrothermal reaction. The activation of fly ash was performed by means of NaOH solution in open system (atmospheric pressure) at 90 °C, for 5h, stirring at 300 min^{-1} . Fusion method comprises two stages. Firstly, a fly ash was mixed and ground with NaOH to obtain a homogenous mixture which was then heated in a nickel crucible in air at 550 °C for 3h. Secondly, the fusion product was ground and dissolved in distilled water, followed by aging with stirring 1 day at room temperature and then used for hydrothermal reaction at 90°C, for 5h, stirring at 300 min^{-1} . In the both case a mass ratio of a fly ash and NaOH was 1:1.2, and the mole

ratio $\text{Na}_2\text{O}:\text{H}_2\text{O}=1:25$. At the end of the process the solid was separated by filtration, washed several times with distilled water and then dried overnight at $105\text{ }^\circ\text{C}$. The samples were stored in a dessicator over a saturated ammonium chloride solution for two weeks before XRD analyses.

Results and Discussion

The chemical analysis of raw material showed it to be a high-silica ash with the mole ratio of $\text{SiO}_2:\text{Al}_2\text{O}_3=3.97:1$ [4, 7]. According to the grain size distribution the average size of particles was about 0.115 mm (the content of size class $-0.589+0\text{ mm}$ was about 99%), [7]. Analysis by X-Ray diffraction revealed that the major crystalline phases in the fly ash were quartz, mullite and hematite together with the amorphous component based on an aluminosilicate glass (Fig. 1).

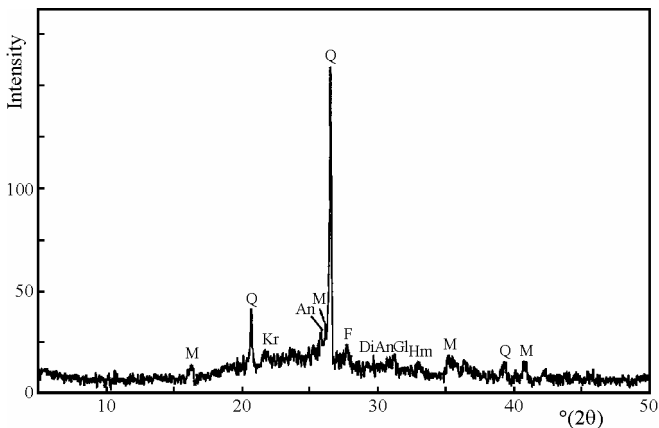


Figure 1 X-Ray diffraction pattern of fly ash (Q-quartz, M-mullite, Hm-hematite, F-feldspars, Kr-cristobalite, Di-diopside, Gl-gehlenite, An-anhydrite)

Bulk fly ash sample was hydrothermal activated under defined experimental conditions and the XRD pattern of obtained sample was shown in Fig.2. The crystalline phases identified in this sample were quartz and mullite, which were also present in the unmodified fly ash. This means that under the given experimental conditions these phases were not digested. Besides the residual ash phases new peaks are present in the XRD pattern that match a high silica variety of a NaP zeolite phase called NaP1, for which the ideal unit cell content is $\text{Na}_6[(\text{AlO}_2)_6(\text{SiO}_2)_{10}]x12\text{H}_2\text{O}$ the best [8,9]. Similar results were obtained by Woolard et al. for hydrothermal fly ash modification at room temperature using NaOH solution of concentrations from 1M to 3M [2]. Also, Moreno et al. identified NaP1 in fly ash treated at low temperature ($t < 150^\circ\text{C}$) and reagent concentrations from 0.5M to 1.0M NaOH [3].

The XRD pattern of fused fly ash (fig.3, curve a) showed the formation of sodium silicate, indicating that fusion is very effective in extracting the silicon species in the fly ash. From the disappearance of quartz and mullite peaks, it is deduced that both minerals in the fly ash have reacted with NaOH. After 1 day of aging the fused fly ash in water no crystalline phase was found (curve b). All sodium silicate was dis-

solved in water. When the fused fly ash solution was hydrothermal treated a pure NaP1 zeolite was identified (curve c).

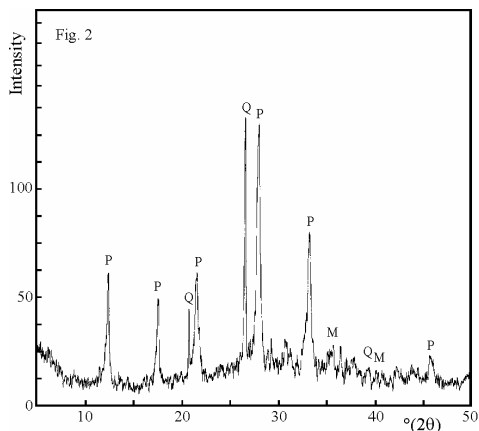


Figure 2 X-Ray diffraction pattern of zeolitized fly ash (P-NaP1 zeolite)

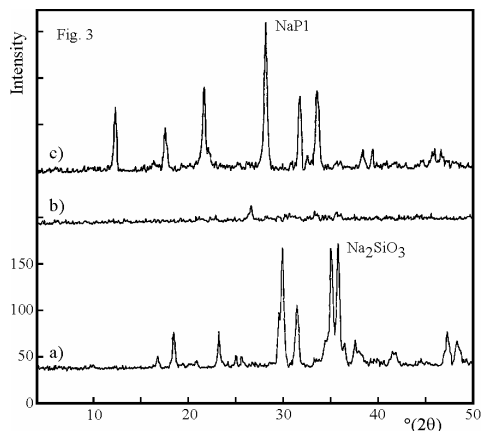


Figure 3 X-Ray diffraction patterns of: a) fused fly ash (sodium silicate); b) the sediment of fused fly ash after 1 day in water; c) zeolitized fused fly ash (NaP1 zeolite)

Conclusion

Two methods (hydrothermal and fusion) have been converted a fly ash from "Nikola Tesla-B" power station into NaP1 zeolite. In the hydrothermal process, under the given experimental conditions, the product is zeolitic material (NaP1, quartz, mullite). The fusion method results a pure NaP1 zeolite.

References

- [1] X.Querol, F.Plana, A.Alastuey, A.Lopez-Soler, Fuel, 1997, 76, 793.
- [2] C.D. Woolard, K. Petrus, M. van der Horst, ISSN 0378-4738=Water SA, 2000, 26, 531.
- [3] N.Moreno, X.Querol, C.Ayora, A.Alastuey C.Fernandez-Pereira, M. Janssen-Jurcovicova, J.Environ.Eng., 2001, 127, 994.
- [4] D.Vučinić, I.Miljanović, A.Rosić, P.Lazić, J.Serb.Chem.Soc.,2003, 68, 471.
- [5] H.L. Chang, W.H. Shih, Ind.Eng.Chem.Res., 1998, 37, 71.
- [6] A.Molina, C.Poole, Minerals Eng., 2004, 17, 167.
- [7] D.Vučinić, I. Miljanović, A.Rosić, R.Tomanec, 6th Int.Conf.Environmental and Mineral Processing, Ostrava, 2002, 231.
- [8] B.R.Albert, A.K. Cheetham, J.A. Stuart, C.J. Adams, Microporous and Mesoporous Materials, 1998, 21, 133.
- [9] JCPDS 39-0219

COMPUTER SIMULATION OF LIQUID PHASE SINTERING FOR POROUS STRUCTURE

Z. S. Nikolić

*Faculty of Electronic Engineering, Department of Microelectronics
University of Nish, 18000 Nish, PO Box 73, Serbia*

Abstract

The microstructure during liquid phase sintering may change either by growing of larger particles during Ostwald ripening process or by shape accommodation. In this study, two-dimensional numerical method for simulation of liquid phase sintering of porous structure based on numerical models for solution-precipitation and grain coarsening was considered.

Introduction

The main characteristic of liquid phase sintering is that the composition of the powder and the firing temperature must be chosen such that a small amount of liquid forms between the grains. This process is especially important for systems that are difficult to densify by solid state sintering or when the use of solid state sintering requires high sintering temperatures.

In recent years, a range of computer simulation models has been developed with the aim of simulating the detailed evolution of microstructure during grain growth. Recently the results of a computer simulation of boundary migration during liquid phase sintering have been reported [1]. This paper describes the two-dimensional (2-D) simulation of the solid/liquid interface during liquid phase sintering of porous structure.

Topology of model system

Let there is a mixture of two powders: a major component that forms the particulate solid, and an additive phase as a liquid-producing component. It will be assumed that the liquid wets and spreads to cover the solid particle surfaces, so that a liquid layer will separate them. A model system of S contours of solid phase and P contours of pore phase in the liquid will be located within the smallest enclosing square box, and not allowing the particles and pores to lie outside the square box. A time-dependent microstructure will be mapped onto a 2-D by three discrete matrices: two real matrices for the concentration and the flux, and the integer matrix $\|e_{ij}\|_{n \times m}$, where the value of the element e_{ij} indicates the phase present at the point (i, j) , so that $e_{ij} < 0$ for pores $(-1, -2, \dots, -P)$, $e_{ij} = 0$ for liquid phase, and $e_{ij} > 0$ for solid phase $(1, 2, \dots, S)$.

Modeling of Solution-precipitation

The solution-precipitation process is characterized by dissolution of smaller solid grains at solid/liquid interface (thermodynamically unstable), dissolved atoms diffuse through the liquid, and precipitate on the larger grains. We will assume a system con-

sisting of a dispersion of spherical particles with different radii in a liquid in which the solid phase has some solubility. Thus, the concentration of the dissolved solid around a particle of radius r is given by the Gibbs-Thomson equation [2], so that the concentration at an interface with high curvature will be above that at an interface with low curvature. Therefore a higher concentration around a smaller particle gives rise to a net flux of matter from the smaller to the larger one.

Grain coarsening is a typical multibody free boundary problem in which the domains alter their morphologies in response to the diffusion field. After solution-precipitation, the particles grow in supersaturated liquid phase, and after the supersaturation becomes small, large particles start to grow at the expense of small particles. The tendency for particles to grow or to shrink depends on the size of particles relative to a critical particle radius for which $dr/dt = 0$. This value depends on type of process growth control [3].

Pore filling process will be considered similarly as Park *et al.* [4] developed models for liquid flow into isolated pores. It was assumed that the spherical pores exist within solid-liquid system in which the grain shape is in equilibrium with the liquid menisci. In the initial stage the pores are stable and individual liquid menisci are maintained between grains around the pores. During sintering when the grain growth reaches a critical point meniscus radius becomes equal to the radius of pore. As the grains grow beyond the critical point pores start to decrease. The balance of the liquid pressure between menisci at the pore and those at the surface is now broken and liquid can flow rapidly into the pore. Our model assumes that for each pore there is a critical grain size required for filling.

Simulation Method

We will assume that mass diffusion outside the particles is the only mass transfer process. Thus diffusion through the liquid phase is defined by the partial differential equation of the parabolic type $\partial C/\partial t = D_L \cdot \nabla^2 C$. For the computation of time-dependent concentration of liquid phase finite-difference technique will be used within an experimental region of a rectangular shape that is partitioned into subregions by a mesh with the grid spacings Δx and Δy for two distance coordinates x and y , respectively.

Results and Discussion

We will use the present numerical model for the study a sintering of the W-Ni system. For this system, the same data as in [5] will be used. An initial model system, shown on Fig. 1, was applied: average particle radius $37.20 \mu\text{m}$, average pore radius $12.5 \mu\text{m}$, the experimental region $600 \mu\text{m} \times 600 \mu\text{m}$.

Smaller contours have higher concentration levels, and dissolve in the liquid matrix. Dissolved atoms diffuse through the liquid layer or through the liquid matrix, and precipitate on the larger contours. The smaller contours tend to be preferentially located near the large contours. Hence they give way to new packing of small and large contours. Large contours always grow, resulting in the surrounding contours being

small. Further morphological changes may occur by large contours growing during contour coarsening.

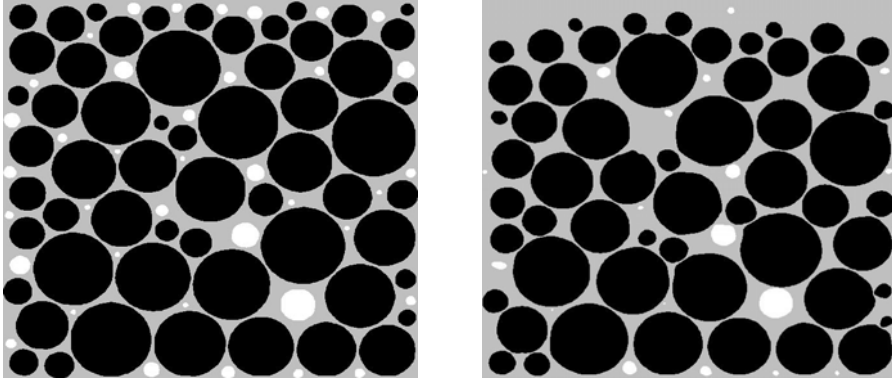


Fig.1 Computed microstructures at the beginning and after 35 min. (Colored regions: black - solid phase, white - pores, gray - liquid phase).

From this examination it can be concluded that contours principally assume a rounded shape because the amount of liquid is fairly large. However, in a late stage of liquid phase sintering, it can be assumed that some of the contour contacts can be approximately flattened, as it has been observed in Ref. [6].

Acknowledgements

The present work was performed under the project *Synthesis of Functional Materials According Tetrad "Synthesis - Structure - Properties - Application"* supported financially by the Ministry for Science, Technologies and Development of Republic Serbia, Yugoslavia.

References

- [1] Nikolic Z.S., Journal of Materials Science 1999, 34(4), 783.
- [2] Nikolic Z.S., Sci. of Sintering, Special Issue, 1996, 28, 55.
- [3] Fischmeister H. and Grimvall G., in Sintering and Related Phenomena, edited by G. C. Kuczynski, Plenum Press, New York, 1973, 119.
- [4] Hyo-Hoon Park, Seong-Jai Cho, Duk N. Yoon, Met. Trans. A, 1984, 15A, 1075.
- [5] Nikolic Z.S. and Spriggs R.M., Sci. of Sintering, 1994, 26, 1.
- [6] Oh-Hun Kwon and Messing G.L., J. Am. Ceram. Soc., 1990, 73, 275.

SIMULATION OF RAPID SOLIDIFICATION OF ALUMINA ON A METALLIC SUBSTRATE

Z. S. Nikolic¹, M. Yoshimura² and S. Araki²

¹*Faculty of Electronic Engineering, Department of Microelectronics
University of Nis, 18000 Nis, PO Box 73, Serbia*

²*Materials and Structure Laboratory, Center for Materials Design
Tokyo Institute of Technology, Yokohama 226-8503, Japan*

Abstract

In this paper the numerical method for computation of temperature distribution in a sample and in a substrate, as well as phase change and solid-liquid interface position during rapid solidification was considered.

Introduction

The fabrication of oxide eutectics by more rapid solidification techniques has yielded moderate success, producing partially amorphous or inhomogeneous samples, because it is difficult to maintain a homogeneous heat transfer at high cooling rates.

In this paper a numerical model is adopted to analyze heat transfer process during rapid solidification of sample melted in Arc-image furnace [1,2]. Numerical solution of this complex problem enabled us to calculate the temperature distribution in both sample and substrate, including the phase change phenomena.

Rapid Solidification Method

A detailed description of this method has been given elsewhere [3,4] and only a brief summary will be presented here. Pellet of the mixed powders with the eutectic composition is placed on a copper plate that is cooled by water and melted in air in an arc-image furnace by the radiation of a Xe lamp. The spherical arc-melted specimen is quenched by rapidly moving the copper plate from the focal point.

There are two major mechanisms controlling the rapid solidification - the external extraction of heat through convective and/or radiative heat transfer and the internal heat conduction combined with solidification. This radially symmetric heat-conduction model problem can be solved numerically if we assume that the molten sample with the uniformly distributed initial temperature is subjected to convective and radiative cooling on its surface. In this analysis solidification of undercooled sample is addressed allowing for a nonuniform temperature distribution inside the sample, and symmetric about the growth axis (which coincides with direction the copper plate - top of the sample), because the solidification starts at some discrete points on the contact surface. It also means that the problem becomes two-dimensional (multi-dimensional effects are believed to be small for cooling and solidification processes).

The governing heat conduction equations for solidifying sample on the substrate, assuming spherical symmetry, can be written as

$$\frac{1}{r^2} \frac{\partial}{\partial r} \left(r^2 \frac{\partial T_i}{\partial r} \right) + \frac{1}{r^2} \frac{\partial^2 T_i}{\partial \theta^2} = \kappa_i \frac{\partial T_i}{\partial t} \quad \left(\kappa_i = \frac{\rho_i c_i}{\lambda_i} \right), \quad (1)$$

where λ is the thermal conductivity, ρ is the density, C is the specific heat capacity, and the subscript $i = 1, 2, 3$ stands for the liquid (melt), solid and substrate, respectively. For solution the heat conduction equations (1) we will specify the initial temperature as T_0 in the sample and T_s in the substrate, and the boundary condition at the sample surface as

$$-\lambda_i \frac{\partial T_i}{\partial r} = h_c (T_i - T_a) + \varepsilon_i \sigma (T_i^4 - T_a^4) \quad (i = 1, 2),$$

where h_c is the convective heat transfer coefficient, ε_i is the surface emissivity, and σ is the Stefan-Boltzmann constant.

The finite difference method is used to solve iteratively the governing Eqs. (1). The formulation and numerical solution procedure used in this model is described elsewhere in detail [5]. Assuming that the sample is much smaller than the substrate and that the substrate will be permanently cooled by water during solidification, boundary condition for rectangular substrate will be $T(t) = T_s$ at all boundary point except on the interface between sample and substrate.

We will assume that solidification begins on the sample surface across the contact interface with the colder substrate when the sample surface temperature reaches the equilibrium melting temperature. During this process interface starts to change from the initial liquid-solid contact to a solid-solid contact.

Results and Discussion

The heat conduction equations in both the sample and the substrate are used together with the solid-liquid interface energy balance condition [6]. Given the alumina sample of diameter 4 mm that was placed onto cold Cu substrate of diameter 50 mm radius, the initial melt temperature (melting temperature + 50 K) and initial substrate temperature (308 K) as well as the corresponding material properties [7], the model can calculate the time-dependent temperature distribution in the sample and in the substrate. Figure 1(a) shows the position and shape of the solid-liquid interface as the solidification process progresses. It can be seen that at the very beginning of the solidification a solid "shell" will be partly form. Figure 1(b) shows the temperature profiles in the sample for solidification time 0.1 s. It can be seen transition from flat to circular profile in vertical direction around the sample center as a consequence of undercooling from the substrate. The isotherms in the sample are almost parallel to each other except at the interface area where the initial temperature distribution will be consequence of high temperature gradient between the sample and the substrate before solidification and during the early period of solidification. During medium stage up to the end of solidification the temperature profiles will be characterized by a concentric pattern, as a consequence of uniform temperature distribution within the substrate.

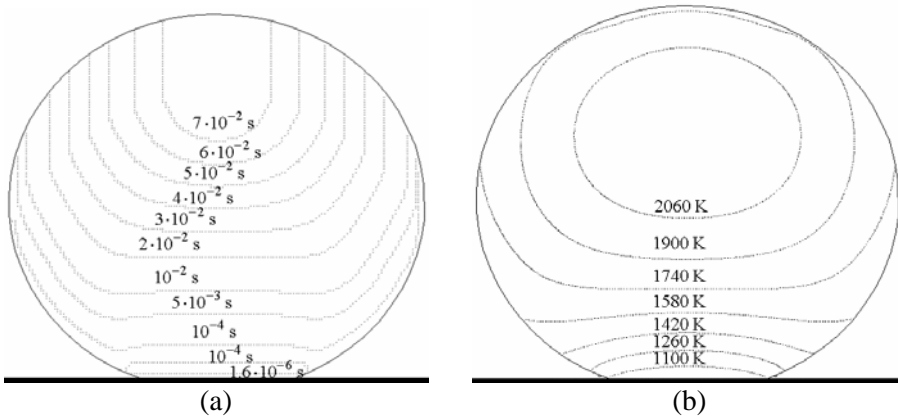


Figure 1. Computer simulation of rapid solidification. a) Interface liquid-solid positions during solidification. b) Temperature profiles after 0.1 s.

Conclusion

In this paper we have proposed computer-based method for simulation of rapid solidification of spherical sample placed on the water-cooled substrate. In that sense we defined a heat conduction model with a moving interface liquid-solid during solidification. This model we applied for prediction of solidification of alumina on copper plate through the computation time dependencies such as temperature distribution, position of interface solid-liquid, solid and liquid fraction, sample cooling rate etc. This model can be also used as predictive model for solidification process control of rapidly solidified sample for achieving desired sample microstructures and properties.

References

- [1] T.S. Laszlo, *Image Furnace Techniques*, Technique of Inorganic Chemistry, Interscience Publishers, New York, 1965, **5**.
- [2] M. Yoshimura, J. Coutures and M. Foex, *J. Mater. Sci.*, 1977, **12**, 415.
- [3] J.M. Calderon-Moreno and M. Yoshimura, *Scripta Mat.*, 2001, **44**, 2153.
- [4] M. Yoshimura and S. Somiya, *Proc. Intern. Conf. on Rapidly Quenched Metals*, Eds. T. Masumoto and K. Suzuki, 1982, p. 23.
- [5] J. Crank, *The Mathematics of Diffusion*, Oxford University Press, London, 1956.
- [6] F.P. Incropera and D.P. DeWitt, *Introduction to Heat Transfer*, John Wiley & Sons, New York, 2002.
- [7] NIST Property Data Summaries for Advanced Materials, *Ceramics WebBook* (<http://www.ceramics.nist.gov/srd/summary/advmatdb.htm>).

3-D SIMULATION OF REARRANGEMENT DURING LIQUID PHASE SINTERING

Z. S. Nikolić

*Faculty of Electronic Engineering, Department of Microelectronics
University of Nish, 18000 Nish, PO Box 73, Serbia*

Abstract

In this paper the numerical method for three-dimensional analysis of rearrangement during liquid phase sintering using multi-particle model was considered. The computed microstructures have shown that rearrangement is essentially governed by geometrical factors.

Introduction

Liquid phase sintering (LPS) is viewed in terms of three overlapping stages: particle rearrangement, solution-precipitation, and coarsening. During the first stage rearrangement of the solid phase takes place causing rapid densification. If there is good wetting between liquid and solid phase, solid particles can rearrange themselves under the action of surface tension forces, producing more stable packing.

This paper outlines a computer-based method for three-dimensional (3-D) study of rearrangement during LPS. The method can be applied for analysis the effects of the liquid bridge volume, contact angle, initial particle distance (representing the green density) and particle size on densification by rearrangement.

Modeling the rearrangement

Our model will be based on the capillary force definition [1]. Since the meniscus is dependent on the surface tension-to-viscosity ratio and the capillary force is a function of surface tension, in order to draw a simple law from the behavior of a model system we will assume that the velocity of the topological change of two particle model due to the capillary action is proportional to the capillary force, $v \approx \chi F$. For constant sintering temperature parameter χ will be approximately constant. Now the value of reducing interparticle distance can be obtained by relation $\Delta D \sim \chi F \Delta t$, where Δt is time increment.

For 3-D model generation we will use the method of revolution [2], by which a surface of revolution can be formed by the rotation of a planar curve about an axis in the plane of the curve and not cutting the curve. Method for 3-D visualization of the rearrangement of the model of two spherical particles connecting by liquid bridge is given elsewhere [1,3].

We will simulate the rearrangement of multi-particle system by using multi-particle model of spherical particles of radii 100 μm and 125 μm (bimodal distribution, average radius 109 μm) with 194 liquid bridges generated by random (Fig. 1(a)). Our theoretical investigation has to involve a network of capillary forces [4], which is

especially for 3-D case extremely complex because of randomly selected elementary unit rearrangement. The network is made up of a unique, interconnected set of closed polygons. Each particle in the network has to have the information about the nearest neighbor. For computation of the balance forces it is very important that the network should be fully connected, i.e. there must be at least one link per vertex (particle center). During the sintering each bridging link length will be updated. In some special cases some link lengths can be shortened so that they cannot connect corresponding particles and such links possess closure errors which produce the essential topological constraint. Such closure will be accommodated either as to retain the originally closed and connected polygon topology or will be restored with some change in polygon shape with requirement that closed polygons in the network must remain closed.

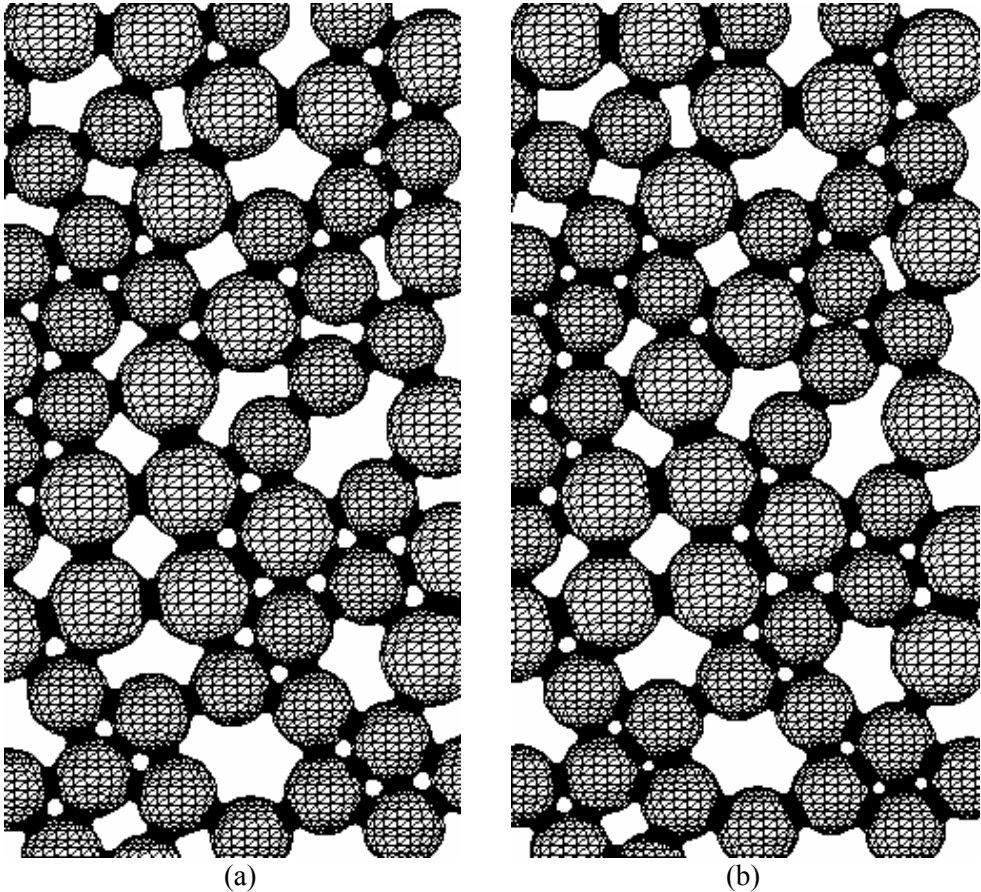


Fig. 1 Computed 3-D model rearrangement. (a) Initial geometry.
(b) After 150 iteration.

During the rearrangement the model system responds as a viscous solid to the capillary action. The rearrangement of particles is a consequence of attractive capillary force action resulting from the liquid wetting the particles. As soon as the liquid bridge

is formed, the capillary force acts in direction to change the liquid bridge with no solid contact (solid-liquid-solid contact) to direct contact (solid-solid contact in liquid). The capillary force tends to pull the neighboring particles together, up to the zero particle separation. With the increase of time, more and more bridge contacts turn to zero separation (direct contacts) if they are not constrained by the neighboring particles during their relative motion (Fig. 1(b)). Therefore it decreases the distance between the particles and causes densification. At the end of the initial stage, most of the contacts will become direct contacts. Such conclusion agrees with experimental observation on metallographic section made by Huppmann and Riegger [5] which showed that after sintering the tungsten particles have direct contacts as a consequence of positive capillary force acting between two adjacent tungsten particles connected by a bridge of liquid.

Conclusion

During rearrangement model responds as a viscous solid to the capillary action and the rearrangement of particles is a consequence of attraction resulting from the liquid wetting the particles. The force tends to pull the adjacent particles together, up to the zero particle separation. Therefore it decreases the distance between the particles and causes densification. Our theoretical investigation has shown that rearrangement is essentially governed by geometrical factors and nearest neighbor interaction.

Acknowledgements

The present work was performed under the project (No 1832) *Synthesis of Functional Materials According Tetrad "Synthesis-Structure-Properties-Application"* supported financially by the Ministry for Science, Technologies and Development of Republic Serbia.

References

- [1] Z.S. Nikolic, Proceeding of the X WRTCS, Science of Sintering: Current Problems and New Trends, Serbian Academy of Sciences and Arts, Belgrade, 2003, 13.
- [2] CRC Standard Mathematical Tables and Formulas, Dan Zwillinger (ed.), 30th Edition, CRC Press, Boca Raton, 1995.
- [3] Z.S. Nikolic, Proceedings of the 6th International Conference on Fundamental and Applied Aspects of Physical Chemistry, Vol. II, Belgrade, 2002, 502.
- [4] Z.S. Nikolic and G. Tomandl, 2nd Intern. Conference on Materials Processing for Properties and Performance, D8-13-O09, Yokohama, Japan, 2003, 256.
- [5] W.J. Huppmann and H. Riegger, Acta Metall. 1975, 23, 965.

Macromolecular Physical Chemistry

(I)

THEORY OF GELATION IN POLYCONDENSATION PROCESSES

S.I.Kuchanov

*Polymers & Crystals Chair, Physics Department,
Lomonosov Moscow State University, Vorobjevi Gori, 119992 Moscow, Russia*

Abstract

Key concepts of contemporary theory of the formation of polymer networks (chemical gels) in the course of the processes of branched polycondensation are briefly discussed.

Introduction

Polycondensation is one of the most widespread methods of polymer manufacturing. If among the initial monomers are those containing more than two functional groups (e.g. glycerin), branched polymer molecules will be formed in the course of the synthesis differing in number of monomeric units involved and in the pattern of their arrangement (configuration). The measurement of the viscosity of a reaction system in this case shows that it gradually enhances with time to diverge abruptly thereafter. Just at this moment, known as the gel point, a giant molecule of macroscopic size (whose radius of gyration is comparable with the size of the reactor) appears for the first time. The weight of this gel molecule increases then due to the addition of the sol molecules right up to complete exhaustion of the latter. Under a theoretical description of the gelation phenomenon problems of two kinds are generally encountered [1], [2]. The solution of the first of them suggests finding the evolution of the distribution of sol molecules for number of the constituent monomeric units. The other group of the problems deals with the calculation of the elasticity properties of the polymer network of a gel formed by fixed instant of time.

Theoretical Approaches

The solution of the aforementioned problems implies the recourse to both *kinetic* and *statistical* approaches [1], [3]. The first of them consists in deriving and solving the material balance equations for the concentrations of all molecules with given number of their units. Under the second approach the fraction of molecules with given configuration among all those remaining in a reaction system is supposed to be calculated. This fraction is identified with the probability for a randomly chosen molecule to have corresponding configuration. Mathematically speaking this procedure means the construction of the probability measure on the set of possible configurations of polymer molecules.

The statistical method is traditionally used in the theory of gelation. In the framework of this method the probability measure on the set of macromolecules in a reaction system and that on the set of the realizations of a stochastic processes are pre-

sumed to be identical. The main advantage of the statistical method is its ability to exhaustively describe in a considerably simple way the configurational structure of both sol and gel in terms of some probability parameters. Under the most general version of this method the realization of a stochastic process characterized by small number of parameters is put in correspondence to every polymer molecule.

However, it should be stressed that the matter of the choice of the stochastic process producing the probability measure on the set of the macromolecules may not be settled in principle in the framework of the statistical method itself. To cope with this task recourse should be made to the kinetic method which simultaneously permits to express the probability parameters of this stochastic process through the rate constants of the reactions between functional groups and concentrations of initial monomers. Using the kinetic method as applied to polymer systems one should find the solution of the set of infinite number of material balance equations in correspondence with the number of the components of a reaction system. Remarkably, however, it has been possible to find exact analytical solutions of this infinite set of nonlinear ordinary differential equations for several kinetic models extensively employed nowadays in polymer chemistry [1], [3].

Kinetic Models

The most frequently used among them is the so called ideal polycondensation model assuming that finite size molecules are free of cyclization reactions and besides the Flory principle holds. According to this fundamental principle the reactivity of any functional group of a particular type does not depend on which molecule this group belongs to as well as on its locus in a molecule. There is a considerable body of evidence reported in literature testifying to the fact that the ideal model despite its simplicity provides an adequate treatment of experimental data on gelation in appreciable number of real polymer processes. Nevertheless such processes are known where the ideality condition is deliberately violated. Possible deviations from the Flory principle may be caused by short-range and long-range effects [3]. Among the first of them are the so called substitution effects induced by steric, induction, catalytic or some other types of the influence of the reacted functional groups on the reactivity of their neighboring unreacted groups. The long-range effects are due to possible impact of the solvent on the spatial conformational structure of macromolecules and, consequently, on the reactivity of their functional groups at the expense of the change of the local environment of each of them. In this case the reactivity of the groups is governed along with chemical reasons also by physical ones which can markedly affect the probability for the reacting groups to converge. Evidently, the account of the long-range effects in the theory of branched polycondensation is substantially more complicated than that of the short-range effects because polymer molecules are considered in these two cases as abstract molecular graphs and graphs embedded in three-dimensional Euclidean space, respectively [2].

Results Obtained

By now the theory of chemical gelation in polycondensation systems describable by the ideal model may be considered as completed [3], [4]. Here general equations are derived enabling one to calculate apart from the gel-point also any statistical characteristics of the configurational structure of sol molecules as well as to find the parameters of the polymer network of a gel characterizing its elasticity properties. Among such parameters the most important are the number of elastically active chains per one monomeric unit, their number-average length and the cyclic rank of the molecular graph of the polymer network in hand. All aforementioned characteristics may be readily calculated for the process of polycondensation of any set of monomers, each containing arbitrary numbers of different type functional groups. The rate constants of the elementary reactions between these groups as well as molar fractions of the initial monomers constitute a complete set of parameters of the ideal polycondensation model. The simplicity of this model explains its popularity in macromolecular chemistry.

As for the models allowing for the short-range effects, general algorithms of the theoretical description of the gelation phenomenon in polycondensation systems have also been developed [4], [5]. The success achieved here is due to the recourse to the Flory principle in its extended formulation [1], [3], [5] rather than in the traditional one. By the extended Flory principle the reactivity of a functional group can depend on the microstructure of the neighboring fragments of a macromolecule and change together with it during the process. Far more less impressive are advances in the theory of gelation where the long-range effects play a crucial role. Their accurate account calls for the usage of physico-chemical models based on the consideration of the conformation-configuration structure of the molecule as a whole rather its local fragments. A considerable progress in the solution of models of such a kind is hardly conceivable without invoking the recent achievements of the statistical physics of polymers.

References

- [1] S.I. Kuchanov, *Methods of Kinetic Calculations in Polymer Chemistry*, Chimia Publ., Moscow, 1978 (in Russian).
- [2] S.I.Kuchanov, S.V.Korolev, S.V.Panyukov, *Graphs in Chemical Physics of Polymers*, Adv. Chem. Phys., 1988, 72, 115.
- [3] S.Kuchanov, *Principles of Quantitative Description of Chemical Structure of Synthetic Polymers*, Adv. Polym. Sci., 2000, 152, 157.
- [4] S.I.Kuchanov, H.Slot, A.Stroeks, *Development of Quantitative Theory of Polycondensation*, Progr. Polym. Sci., 2004, 29(6), 513.
- [5] S.Kuchanov, T.Zharnikov, *J. Stat. Phys.*, 2003, 111(5/6), 1273.

ANALYSIS OF THE SOLUBILITY BEHAVIOR OF IRRADIATED POLY(VINYL ALCOHOL-CO-ETHYLENE)

B. H. Milosavljević

*Radiation Laboratory, University of Notre Dame
Notre Dame, IN 46556-5674, USA*

Abstract

The previously measured sol phase vs. dose relation corresponding to the radiation induced cross-linking of the co-polymer of polyethylene-polyvinyl alcohol, PVA-co-PE, (Nucl. Instrum. Meth B., 2003, **208**, 185-190) was analyzed using the Charlesby-Pinner theoretical model. The analysis produced the gel dose of 700 kGy for dry PVA-co-PE irradiated in vacuum. Water embedded in the PVA-co-PE matrix markedly affects the radiolysis; the 10% hydration reduces the gel dose about three times. The corresponding $s + s^{1/2}$ vs. $1/D$ plot was found to be convex downwards indicating the initial polydispersity < 2 . Better fit was achieved using the version modified by Charlesby and Rosiak. The virtual dose obtained ($D_v = -225$ kGy) indicates that the initial molecular weight distribution is relatively narrow and a dose of 225 kGy is required for the sample to reach $M_w/M_n = 2$.

Introduction

Poly(ethylene-co-vinyl alcohol), PVA-co-PE, is one of the commercially important polymeric materials (over 4500 patents related to PVA-co-PE illustrate the high industrial interest in it) as it combines the useful rheological properties of polyethylene, PE, with the low gas permeability of poly(vinyl alcohol), PVA. For example, oxygen permeability of PVA/PE-44 (44 mol% ethylene) in the dry state is approximately three orders of magnitude less than that of PE [1]. However, PVA-co-PE is hygroscopic and the absorbed water lowers its glass transition temperature; consequently, PVA-co-PE loses much of its ability to inhibit oxygen diffusion, which is undesirable from the aspect of food packaging. Much like PE, PVA-co-PE can be crosslinked by ionizing radiation and provides a pathway to reduce the hygroscopicity. However, early studies were somewhat discouraging as they reported a very low crosslinking efficiency [2]. Our recent study [3] showed that the 10% of water embedded in the PVA-co-PE polymer matrix significantly enhances the crosslinking, but the effect observed was not quantitatively analyzed.

The present work reports the analysis of the sol phase vs. dose data for PVA-co-PE using the Charlesby-Pinner model. The DSC data corresponding to dry and hydrated PVA-co-PE are also presented and discussed.

Results and Discussion

Figure 1 shows the sol phase vs. reciprocal dose plot for the PVA-co-PE (44 mol% ethylene) radiolysis (the sol phase is defined as the ratio of the polymer dissolved after solvent extraction to that before extraction). The data presented were taken from Ref [3].

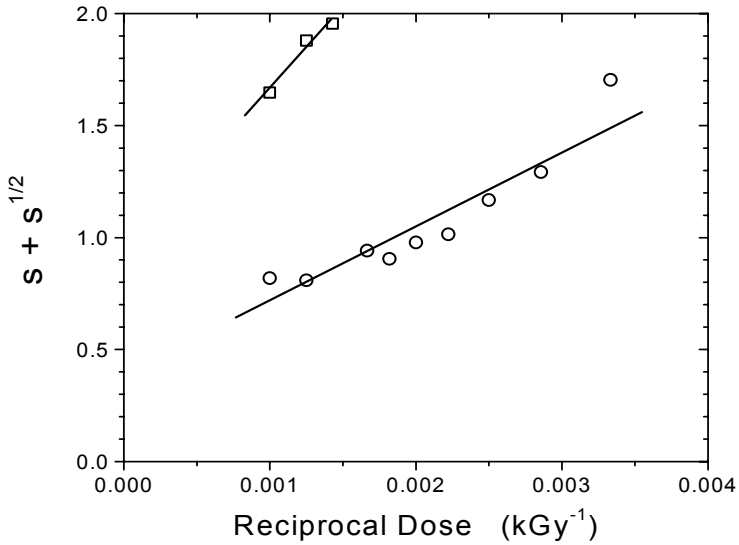


Figure 1. Sol phase vs. reciprocal dose plot for PVA-co-PE radiolysis. Solid lines represent the best fits by the Charlesby-Pinner equation. Dry sample (squares): $p_0/q_0 = 0.93$, $D_g = 680$ kGy. Hydrated sample (circles): $p_0/q_0 = 0.33$, $D_g = 210$ kGy

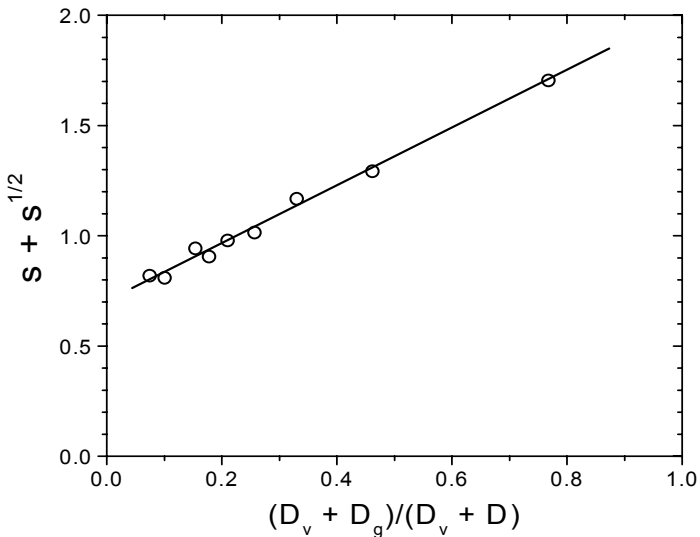


Figure 2. Charlesby-Rosiak plot for the hydrated sample. Parameters obtained: $p_0/q_0 = 0.70$, $D_g = 280$ kGy, $D_v = -225$ kGy

The best fit by the Charlesby-Pinner equation resulted in the gel dose of ~700 kGy and the degradation/crosslinking ratio, q_0/p_0 , of 0.9, both indicative of relatively inefficient crosslinking in the dry sample. The 10% hydration significantly decreases the radiolytic parameters ($D_g = 210$ and $q_0/p_0 = 0.33$) giving rise to the crosslinking efficiency close to the one measured in crystalline polyethylene [3]. However, one can observe that the $s + s^{1/2}$ versus $1/D$ plot (Figure 1) is convex downwards (linear fit correlation coefficient = 0.85) indicating departure from the random molecular weight distribution ($M_w/M_n = 2$) assumed in the Charlesby-Pinner formula. Therefore, the improved version of the Charlesby-Pinner relation modified by Charlesby and Rosiak [6] was used (Figure 2). The fit (linear fit correlation coefficient = 0.98) provided the virtual dose, $D_v = -225$ kGy. The negative value obtained means the initial molecular weight distribution is relatively narrow and the dose of 225 kGy is required for the sample to reach $M_w/M_n = 2$.

In order to further elucidate the effect of water on the crosslinking efficiency in PVA-co-PE, DCS experiments were performed (thermograms not shown). The results obtained show that the 10% hydration decreases the glass transition point from 55 °C to 17 °C, the latter temperature being 8 °C lower than the temperature at which the irradiation was performed. This indicates that the hydration effect on the crosslinking is rather physical than chemical in its nature, *i.e.*, it arises from the increased mobility of species in PVA-co-PE, but not from the water radiolysis contribution to the overall chemistry underlying the crosslinking.

Conclusions

The remarkable result that water vastly improves the efficiency of radiation-induced crosslinking in PVA-co-PE was analyzed (and quantified) using both the Charlesby-Pinner theoretical model and its improved version by Charlesby and Rosiak. The analysis produced the gel dose of 700 kGy for dry PVA-co-PE irradiated in vacuum; the 10% hydration reduces the degradation – crosslinking ratio, p_0/q_0 from 0.9 to 0.3 which in turn decreases the gel dose about three times. The corresponding $s + s^{1/2}$ vs. $1/D$ plot was found to be convex downwards indicating the initial polydispersity < 2 . The modified Charlesby-Rosiak model provided the virtual dose, $D_v = -225$ kGy for the hydrated sample indicating that the initial molecular weight distribution is relatively narrow and the dose of 225 kGy is required for the sample to reach $M_w/M_n = 2$. The effect of water on the crosslinking efficiency was attributed to increased mobility of species in PVA-co-PE in 10% water.

Literature cited

- [1] W. E. Brown, *Plastics in Food Packaging*; Marcel Dekker Inc., New York, 1992.
- [2] G. Spadaro, E. Calderaro and D. Acierno, *Colloid & Polym. Sci.*, 1983, 261, 231.
- [3] B. H. Milosavljevic and J. K. Thomas, *Nucl. Instrum. Meth. B.*, 2003, 208, 185.
- [4] A. Charlesby and S. H. Pinner, *Proc. Roy. Soc. (London)*, 1959, A249, 367.
- [5] E. J. Lawton, J. S. Balwit and R. S. Powell, *J. Polym. Sci.*, 1958, 32, 275.
- [6] J. Oleiniczak, J. Rosiak and A. Charlesby, *Radiat. Phys. Chem.*, 1991, 37, 499.

SWELLING BEHAVIOR OF 2-HYDROXYETHYL METHACRYLATE BASED HYDROGELS

S. Lj. Tomić , T. M. Manić and J. M. Filipović

Faculty of Technology and Metallurgy, Belgrade University, Belgrade, Serbia and Montenegro

Abstract

In this study, various copolymeric hydrogels based on poly(2-hydroxyethyl methacrylate)s with different types of poly(alkylene glycol) acrylate and small fraction of itaconic acid were synthesized. Dynamic swelling was monitored in phosphate buffers of pH 2.20, 3.85, 4.50, 5.45 and 6.80 at 20 °C. Characteristic parameters of hydrogels: swelling ratio (q), kinetic constant (k) and diffusional exponent (n) were determined. We have demonstrated that the water uptake of pHEMA gels is governed by the type and the chain lengths of poly(alkylene glycol) acrylate components and by the external pH. There is a sharp increase of q_e values at pH 4.50, probably due to the ionisation of IA. At pH around 5.00 there is a sudden change in swelling, probably due to the transformation from the unswollen to the swollen state of the HEMA component.

Introduction

Hydrogels are two- (or multi-) component three-dimensional polymer networks which can adsorb large amounts of water at equilibrium, depending on the properties of the polymer used, as well as on the nature and density of the crosslinks [1]. Poly(2-hydroxyethyl methacrylate) (PHEMA) hydrogels have good chemical and thermal stability which makes them suitable materials for pharmaceutical applications. The controlled release of drugs from a PHEMA network is strongly affected by its water swelling capacity. Therefore, the swelling changes induced by external conditions (pH, temperature, ionic strength) are of a special importance for controlled release drug delivery systems.

In this study, four types of hydrogels based on 2-hydroxyethyl methacrylate and different poly(alkylene glycol) acrylates and methacrylates, with a small percent of itaconic acid, were prepared by solution copolymerization. The swelling behavior and kinetic parameters of these hydrogels as a function of poly(alkylene glycol) acrylate type and pH of swelling medium are reported.

Experimental

Materials. 2-hydroxyethyl methacrylate (HEMA) (Fluka), itaconic acid (IA) (Aldrich), and poly(alkylene glycol) acrylates, i.e. short chains-Bisomers (BIS) (Laporte Chemical) were used as monomers. The structure of Bisomers are given in Figure 1. Ethylene glycol dimethacrylate, (EGDMA) (Aldrich) crosslinking agent, and potassium persulfate (Fluka) initiator and tetramethylethylene diamine (TEMED) (Aldrich) activator were used in all polymerizations. Distilled water was used as a solvent.

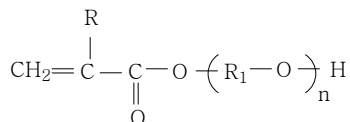


Figure 1. General formula for Bisomers used (R = H or CH₃; R₁ = ethylene or propylene groups, n is the number of groups)

The samples were designated according to the bisomer used as:

Bis1 - (EG₆-PG₃)-MA, Bis2 - (EG₆)-A, Bis3 - (PG₅)-MA, Bis4 - (EG₃-PG₆)-MA

Preparation of hydrogels. Gels were prepared by radical crosslinking polymerization at 60 °C for 24 h. The mixture of monomers were degassed prior to polymerization. The monomer ratio was HEMA/BIS/IA=50/48/2 wt/wt, and the monomer to water ratio was 10/90 (wt/wt). 1, 1 and 2 wt% of initiator, activator and crosslinker were added to the feed mixture, respectively. The hydrogels were treated in water, in order to remove the unreacted chemicals and dried at room temperature to constant weight.

Swelling studies. Dynamic swelling experiments were monitored in phosphate buffers of pH 2.20, 3.85, 4.50, 5.45 and 6.80 at 20 °C. The swelling ratio (q) was calculated using the equation: $q = (\text{weight of swollen disc})/(\text{weight of dry disc})$ (1).

Results and Discussion

The equilibrium swelling ratio (q_e) of all Bisomers in different buffer solutions are given in Figure 2. Kinetic parameters were calculated from the first part of the swelling curve using the following equation: $M_t/M_\infty = kt^n$ (2), where M_t and M_∞ are water absorbed at time t and at equilibrium, respectively, k is a kinetic constant and n is the diffusional exponent. In the case of cylindrical geometry, the water diffusion mechanism is Fickian for $n = 0.5$. For $0.5 < n < 1.0$ the diffusion mechanism is non-Fickian, and both diffusion and polymer relaxation control the overall rate of water transport. The values of q_e , n and k are reported in Table 1 for Bis2. Similar trends in swelling behavior and for k and n values were obtained for Bis1, Bis3 and Bis4.

Table 1. q_e , k and n values for Bis2.

pH	q_e	k	n
2.20	5.97	0.471	0.482
3.85	6.90	0.488	0.400
4.50	9.79	0.643	0.503
5.45	6.73	0.275	0.583
6.80	7.52	0.207	0.719

The water transport mechanism is Fickian in the pH range of 2.20-4.50, but in the pH range of 5.45-6.80 the non-Fickian (anomalous) water transport mechanism is observed.

For all samples there is a sharp increase of q_e values at pH 4.50, which is most pronounced for Bis4, probably due to the ionisation of IA. At pH around 5.00 there is a sudden change in swelling, probably due to the transformation from the unswollen to the swollen state of the HEMA component [3].

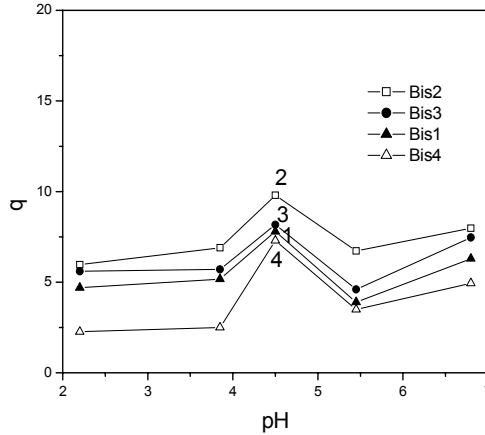


Figure 2. The swelling ratio versus pH

Conclusion

HEMA/Bis/IA gels with different types of poly(alkylene glycol) acrylates were examined. On the basis of equilibrium and dynamic swelling data we have demonstrated that the water uptake of gels is governed by the type and the chain lengths of poly(alkylene glycol) acrylate component and by the external pH. These hydrogels are good candidates for controlled release drug delivery systems.

References

- [1] A.S. Hoffman, *Adv Drug Deliv. Rev.*, 2002, 54, 3.
- [2] L. Ferreira, M.M. Vidal, M.H. Gil, *Int. J. Pharm.*, 2000, 194, 169.
- [3] S.K. Dee, N.R. Aluru, B. Johnson, W.C. Crone, D.J. Beebe, J. Moore, J. *Microelectromech. Syst.*, 2002, 11, 544.

USE OF REFLECTANCE SPECTROPHOTOMETRIC METHOD FOR THE DETERMINATION OF COLOUR OF ORGANIC COATING WITH TiO₂ PIGMENT

M. Miljković, M. Purenović and A. Zarubica

*Faculty of Mathematics and Natural Sciences, Department of Chemistry,
University of Nis, Visegradska 33, 18000 Nis, Serbia and Montenegro,*

Abstract

In this experiment the passive anticorrosive protection of metal sample was performed using organic coating based on polyurethane with TiO₂ pigment and determination of coat of paint colour by reflectance spectrophotometric method. The obtained results show the example of new use of the mentioned method, which can be applied for numerous colours determinations of different final products and quality control.

Introduction

Metal protection is performed using different methods: passive, active and active-passive ones. Passive protection based on organic coatings is the most common and often the most acceptable economically.

The basic components of organic coatings are: pigments, inhibitors, extenders, binders, solvents, thinners, plasticizers, driers and hardeners. The role of pigments is to increase the protective features of paints, their chemical and thermal durability; to hinder the photodegradation of paints; to improve the mechanical features of coatings and to make the coating coloured and opaque [1].

The determination of colours and differences appearing under the different influences cannot be evaluated visually with precision. However there exists a reliable method, i.e. reflectance spectrophotometry for the evaluation and optimal formulation of the stated differences, as well as all colour features. This method, supported by Ciba CGREC software, offers the possibility of improving and facilitating reproducibility in production, and also control of the final products based on the pigment formulations for all intended industries, as well as those using pigments [2].

Numerous systems exist for the systematization of colours. Among them the CIE chromatic system is the most important one. This system is scientifically recognized as the basis for numerical and metric evaluation of colours and the calculation of differences between them.

The system of coordinates designated as L*, a* and b* was recommended by CIE (International Committee of Illumination) in 1976. One colour is completely determined by three coordinates: L*, a* and b* or L*, C* and H* [3].

L* is the vertical coordinate of a three-dimensional system of colours which has values from 0 (black) to 100 (for white);

a* is the horizontal coordinate the values of which range from -80 (green) to +80 (red);

b^* is the horizontal coordinate the values of which range from -80 (blue) to +80 (yellow).

The angle H^* , the colour hue, is expressed in degrees ($H^* = 0$ corresponds to red, $H^* = 90$ to yellow, $H^* = 180$ to green, $H^* = 270$ to blue);

C^* the colour saturation, represents the mentioned colour distance from a non-multicolored point, which corresponds to $a^* = b^* = 0$ [3].

Experiment

Polyurethane coatings are produced on the basis of polyurethane resins of high-quality and stable pigments and extenders, as monocomponent or two-component systems. Apart from the fact that they can be without solvents and non-toxic, polyurethane coatings are characterized by excellent physico-mechanical and aesthetic characteristics such as extraordinary high and stable gloss, retention of paint colour, considerable film hardness and elasticity, impact and abrasion resistance.

The polyurethane protection system is recommended in all cases where aesthetic appearance, chemical and mechanical resistance, duration and protection stability are required. This protection system is especially suitable for the protection of passenger railroad vehicles, road cars, plants in the chemical industry, machines and tools exposed to strong corrosive agents effects. The polyurethane protection system gives excellent results when it is applied on aluminum and other non-ferrous metals and alloys. It is also used in the food industry.

In this experiment, the passive anticorrosive protection of steel plate sample was performed using polyurethane coating with TiO_2 pigment. The experimental procedure consisted of the following phases:

- sample surface preparation (degreasing, removal of corrosion products and old coatings, sandblasting),
- application of paint,
- sample drying,
- metric characterization of the tested sample by means of the
- reflectance-spectrophotometric method.

The coat of paint on the basis of polyurethane was made of two components. The first one of: binder (Macrynal SM 518), pigment (titanium (IV)-oxide), solvents (butyl acetate, xylene) and additives. The second one of: cross linker (Basonate HB 175).

Metric characterization was done by reflectance spectrophotometer "Update Color Eye 3000". Reflectance spectra, CIELAB coordinates, tristimulus values, constants of colour intensities were recorded. The values were determined for three light sources such as daylight, incandescent and fluorescent light. The measurement geometry was: $d / 8^\circ$. The computer was with one place.

Results and Discussion

The three used light sources are designated in the results:

1. daylight (D65/10)
2. incandescent (A-10)
3. fluorescent light (TL 84/10).

Reflectance factors and colour intensity constants were scanned at every 20 nm in the wavelength range from 400 to 700 nm.

Some of the results are shown in Tables 1. and 2.

Table 1. Tristimulus values of colour of polyurethane coating with TiO₂ pigment

		X	Y	Z	x	y
D65-	10°	80.19	85.31	92.19	0.3112	0.3310
A-	10°	93.56	84.88	30.39	0.4480	0.4064
TL84-	10°	87.84	85.06	56.85	0.3823	0.3702

Table 2. CIELAB coordinates of colour of polyurethane coating with TiO₂ pigment

		L	A	B	C	H
D65-	10°	94.02	-1.35	-0.45	1.43	198.42
A-	10°	93.83	-1.30	-1.08	1.69	219.64
TL84-	10°	93.91	-0.91	-1.15	1.47	231.66

The obtained results (Table 1., 2.) show the example of new use of the reflectance spectrophotometric method for the determination and evaluation of organic coating colour.

Conclusion

Reflectance spectrophotometry supports numerous spectrophotometers of different producers. The spectrophotometer "Update Color Eye 3000" is the integral part of a system the parts of which are a computer and its metric programs. The metric programs include: a program for guidance of the spectrophotometer and for memorizing the measured reflectance values on a magnetic plate, a program for the calculation of colour coordinates, colour intensities and differences, metamerism indices, whiteness levels, etc. These can be applied for numerous colours determinations of different final products and quality control.

References

- [1] The Society of Dyers and Colorists-American Association of Textile Chemists and Colorists, Colour Index, Third Edition, Volume 4, 1971.
- [2] S.D. Senker, T. A. Potter, J. Coat. Technol., 1991, 63, 19.
- [3] P.B. Jacobs, P.C. Yu, J. Coat. Technol., 1993, 65, 45.

SCALING OF POLYMER NANO -PARTICLE CLUSTERS AND ABILITY FOR HYDRODYNAMIC AGGREGATION

M B. Plavšić, I. Pajić-Lijaković and B. Bugarski

Faculty of Technology and Metallurgy, Belgrade

Abstract

Hydrodynamic aggregation ability is interpreted in terms of interface particle fraction of total number of cluster particles. The structural factor and fractal dimension are estimated for a series of clusters, generated on two dimensional lattice using Monte Carlo methods, with proper account of number and position of embedded particles. Results indicate that scaling prefactor here assigned as structural factor is much more sensitive to interface particle fraction changes than cluster fractal dimension.

Introduction

A number of papers have interpreted the viscoelastic properties of aggregating colloids and polymer dispersions in terms of the fractal concept (1-3). Although differing in details, the models all depend on the key assumption that the aggregated structure transmits stress through the chains of the elastic back-bone. These chains can be either connected into a space filling network (1-3) or confined to the internal volume of the aggregated clusters. Cluster mass scales as a power of its geometrical size. For any cluster of radius R containing N primary particles of radius a , the mass-radius relation is:

$$N = k_0 [z] \left(\frac{R}{a} \right)^{D_f} \quad (1)$$

where D_f is fractal dimension and k_0 structural factor (scaling prefactor) [4] The prefactor is usually taken as a constant close to unity [1,2]. But, generally scaling prefactor should take account on local properties of the system [5]. According to Mandelbrot prefactor can be understood as a measure of cluster lecnarity and can be correlated with primary particle coordination numbers z [6]

. The first step in understanding the aggregation cluster structure in flow field is to analyze the ability for hydrodynamic aggregation. [7] This ability depends on the cluster interfaces. In this paper we interpret the cluster interface as the fraction of primary particles relative to total number of particles which build up the interface of cluster. The particles which are the constituents of the cluster interface have the coordination number lower than others. But, maximal coordination number of particles depends on the dimensionality of space in the model considered. For two-dimension simulation maximal coordination number of particles is supposed to be four. It is now interesting to analyze in such simple and obvious presentation the correlation between the fractal dimension and structural factor with the interface fraction of particles.

Description of Simulation

The two-dimensional lattice Monte Carlo simulation included the diffusion limited particle-cluster aggregation in the course of cluster growth. The structure of clusters is largely determined by the fluctuations represented by the individual random walks of the incoming particles[4]. To simulate experimental situations with varying degree of randomness it is necessary to control the amount of fluctuations present in the aggregation process. The effects of surface tension and flow field action were included into simulation procedure by varying the particle sticking probability[4]. The series of generated aggregates have $3000 < N < 5000$ primary particles.

Results and Discussion

The fractal dimension and structural factor of generated clusters are between $1.574 < D_f < 1.818$, $2.694 > k_0 > 1.252$ respectively. The influence of cluster compactness on fractal dimension and structural factor is illustrated in Figure 1. The cluster with obvious high compactness has the lowest fractal dimension $D_f = 1.574$ and structural factor $k_0 = 2.694$ as shown in Figure 1(a). The cluster with the highest fractal dimension $D_f = 1.818$ and structural factor $k_0 = 1.252$ is shown in Figure 1 (b) has much lower compactness.

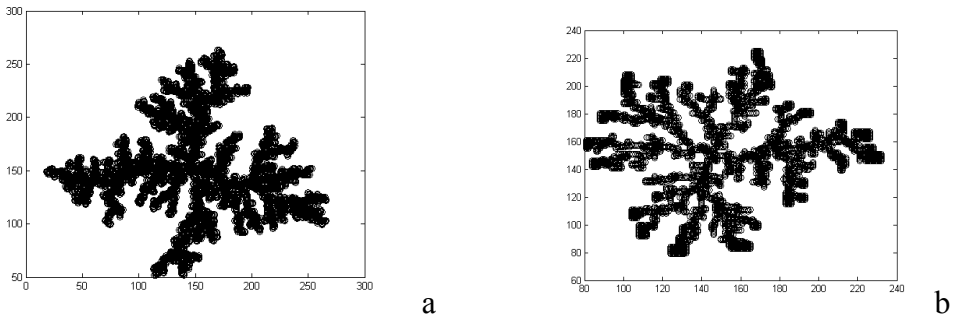


Figure 1. Illustration of cluster compactness relations with fractal dimensions

Fractal dimension and structural factor for various clusters related to the fraction of interface particles, X , are shown in Figure 2. Two regimes are established. For fractal dimension between $1.1797 < D_f < 1.818$ and structural factor between $1.290 > k_0 > 1.252$ fraction of interface particles is 0.90 (regime I). For fractal dimension between $1.574 < D_f < 1.774$ and structural factor between $2.694 > k_0 > 1.357$ fraction of interface particles is 0.96 (regime II).

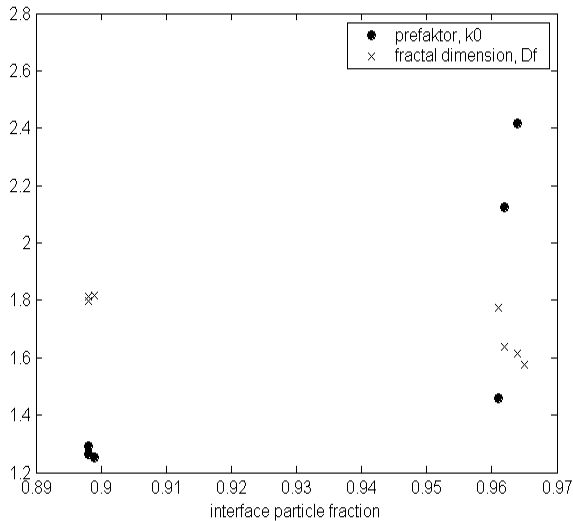


Figure 2. Fractal dimension and structural factor as function of fraction of interface particles

Conclusions

The fractal dimension and structural factor are correlated with the fraction of cluster interface particles. Higher ability for hydrodynamic aggregation corresponds to higher fraction of interface particles, and higher fractal dimension. At the same time higher cluster compactness corresponds to lower fractal dimension and higher structural factor.

References

- [1] R. De Rooij, A.A. Potanin, Van den Ende, J. Mellema, J. Chem. Phys., 1993, 99, 9213.
- [2] A.A. Potanin, R., De Rooij, D. Van den Ende and J. Mellema, J. Chem. Phys., 1995, 102, 5845.
- [3] L. Gmachowski, J. Coll. Int. Sci., 1996, 178, 80.
- [4] M.B. Plavsic et al. the previous papers in the same Proceeding
- [5] P.G.de Gennes Scaling Concept in Polymer Physics Cornell Univ. Press Ithaca New York, 1979.
- [6] B.B. Mandelbrot, The Fractal Geometry in Nature, W.H., Freeman, New York, 1983.
- [7] D. Avnir ed. The Fractal Approach to Heterogeneous Chemistry, John Wiley, New York, 1989.

FLUCTUATION OF MASS AS MEASURE OF POLYMER CLUSTER LACUNARITY AND HYDRODYNAMIC PERMEABILITY

M. B. Plavšić, I. Pajić-Lijaković and B. Bugarski

Faculty of Technology and Metallurgy, Belgrade

Abstract

The structural factor and fractal dimension as cluster morphology parameters are considered in terms of distance fluctuations of particle building the cluster, from the center of mass. The clusters generated by Monte Carlo methods. The effects of surface tension and flow field action are included into simulation procedure. The structural factor and fractal dimension dependence on the sum of averaged fluctuations of primary particle radius from cluster center are investigated. Structural factor is much more sensitive to averaged fluctuation changes than fractal dimension.

Introduction

Aggregation phenomena are of central interest in biology, immunology and polymer and colloid science with important implications for technological problems [1,2]. The structure of formed clusters is fractal, which means that the cluster mass scales as a power of its size as described in [3]. For any cluster of radius R containing N primary particles of radius a , the mass-radius relation, fractal dimension D_f and k_0 structural factor (prefactor), can be determined. Quantification of cluster morphology by fractal dimension and structural factor has the major impact on hydrodynamic study of aggregate permeability [1,2]. Much effort has been spent in studying the fractal dimension, which is of great importance in ramified cluster morphology. A less well-studied parameter is the structural factor k_0 . So far, there is no general agreement as to the value of k_0 , which is essential to fully characterize the morphology, nor have there been any systematic studies regarding the dependence of k_0 on the aggregation process [2]. Structural factor k_0 can be considered as the measure of fluctuations of primary particle radius from the center of mass [4]. When the fluctuations are small, the cluster is said to have low "lacunarity" [4]. The lower the lacunarity the more Euclidian-like is the cluster. The sum of averaged fluctuations of primary particle radius from the center of mass is interpreted as:

$$\langle f \rangle = \frac{1}{N} \sum_{i=1}^N \left(\frac{r_i}{R_g} - 1 \right)^2 \quad (1)$$

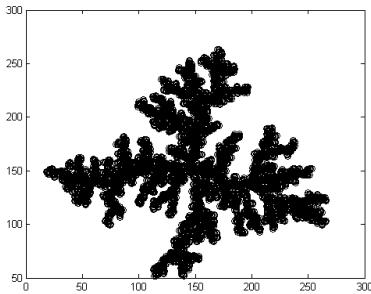
where r_i is the radius of primary particle from cluster center of mass, R_g is the radius of gyration, $R_g = \left(\frac{1}{N} \sum_{i=1}^N r_i^2 \right)^{1/2}$. In this paper we investigate the structural factor dependence on the sum of averaged fluctuations of primary particle radius from center of mass generated using two-dimensional simulation.

Description of Simulation

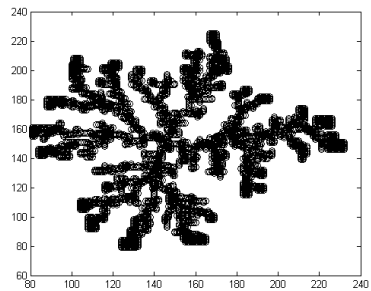
The two-dimensional lattice simulation includes diffusion limited particle-cluster aggregation. The structure of clusters is largely determined by the fluctuations represented by the individual random walks of the incoming particles. To simulate experimental situations with varying degree of randomness it is necessary to control the amount of fluctuations present in the aggregation process. The effects of surface tension and flow field action were included into simulation procedure varying the particle sticking probability. The series of generated clusters have $3000 < N < 5000$ primary particles.

Results and Discussion

The fractal dimension and structural factor of generated clusters are between $1.574 < D_f < 1.818$, $2.694 > k_0 > 1.252$, respectively. The cluster with the lowest fractal dimension $D_f = 1.574$ and structural factor $k_0 = 2.694$ is shown in Figure 1(a). The cluster with the highest fractal dimension $D_f = 1.818$ and structural factor $k_0 = 1.252$ is shown in Figure 1 (b).



a



b

Figure 1. a) Fractal dimension is $D_f = 1.574$ and structural factor is $k_0 = 2.694$,
b) Fractal dimension is $D_f = 1.818$, and structural factor is $k_0 = 1.252$.

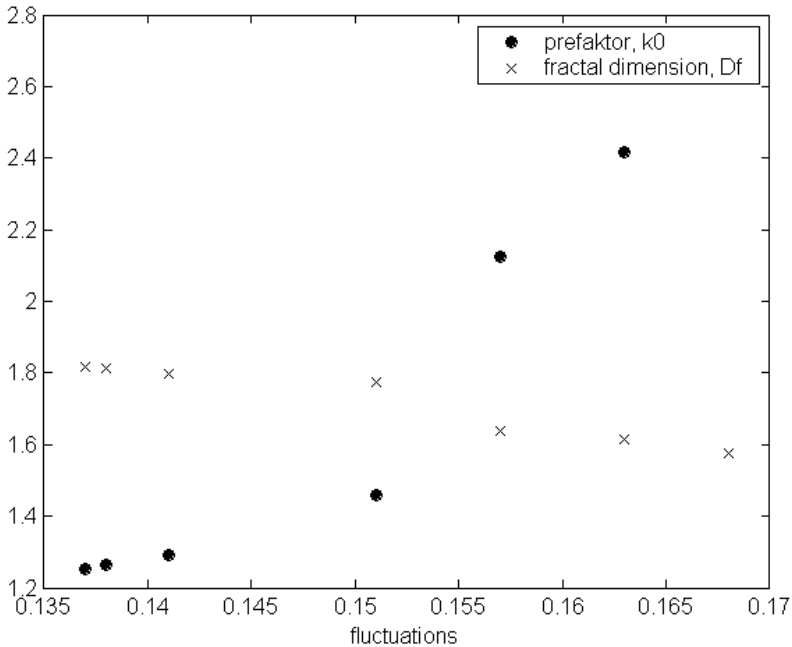


Figure 2. Fractal dimension and structural factor as function of averaged sum of fluctuations of primary particles radius from cluster center of mass.

The sum of fluctuations of primary particle radius as a measure of cluster leucarity and hydrodynamic permeability as represented in Fig2, increase when fractal dimension increases and structural factor decreases. Changes of sum fluctuations for 18 % correspond to changes of fractal dimension for 13 % and structural factor for 54 %. Structural factor is much more sensitive to averaged fluctuation changes then fractal dimension.

Conclusions

According to our numerical results and literature data the sum of fluctuations of primary particle can be used for explanation of physical mining of structural factor. Determination of structural factor as well as the fractal dimension is necessary for analyzing cluster morphology changes in flow field. Hydrodynamic permeability of cluster is interpreted in term of sum of fluctuations of primary particle radius from cluster center of mass. Structural factor is much more sensitive to changes of hydrodynamic permeability of cluster then fractal dimension.

References

- [1] C.M. Sorensen and G.C. Roberts, *J. Coll. Int. Sci*, 1997, 186, 447.
- [2] L. Gmachowski, *J. Coll. Int. Sci*, 1996, 178, 80.
- [3] see Eq.1. in previous contribution of the same authors in this Proceeding
- [4] B.B. Mandelbrot, "The fractal geometry in nature", W.H., Freeman, New York, 1983.

STRUCTURAL FACTOR AND HYDRODYNAMIC PROPERTIES OF POLYMER PARTICLE CLUSTERS

M.B. Plavšić, I. Pajić-Lijaković, Z. Todosijević and B. Bugarski

Faculty of Technology and Metallurgy, Belgrade

Abstract

The structural factor and fractal dimension as cluster morphology parameters are determined for series of clusters generated using Monte Carlo methods. For clusters obtained, accessibility of their surface for fluid molecules is studied by simulation of Brownian motion of fluid molecules on the lattice. Results indicate possibility of distinguishing two zone types in external cluster areas: passive and active zones. Cluster compactness is correlated with fraction of passive part in external area of cluster. The higher number of fluid particles in external area relative to total number of cluster particles corresponds to the lower fraction of passive part in external area. The results indicate that structural factor is much more sensitive to changes of cluster compactness than fractal dimension.

Introduction

The theory of hydrodynamic interactions between suspended particles and the surrounding fluid phase plays a fundamental role in understanding phenomena in a wide variety of systems such as colloids, aerosols and polymer dispersions [1-3]. Their cluster structure is fractal and can be interpreted as different arrangements of particles in contacts. For example, a proper account of hydrodynamic forces is required for prediction of transport properties, such as viscosity of dispersions and sedimentation velocity of aggregated particles. The cluster mass scales as a power of its geometrical size [2]. For any cluster of external radius R containing N primary particles of radius a , the mass-radius relation is:

$$N = k_0 \left(\frac{R}{a} \right)^{D_f} \quad (1)$$

where D_f is fractal dimension and k_0 structural factor (scaling prefactor) [4]. External radius of a cluster determines the cluster zones. Cluster zones include the internal and external ones. The internal zone consists of primary particles and inter-particle gaps. The inter-particle distance is here usually small, compared to the primary particle size. The external area of cluster consists of active and passive parts depending on global cluster shape. The passive part of external zone is mainly filled by primary particles with small free space between them and low accessibility for fluid particles coming from outside of the cluster. But, how to quantify the description of the active and passive parts of external area? It can be done combining numerical experiments and fractal geometry. For that purpose we made a series of fluid particle dynamic simulations in the vicinity of clusters of known fractal geometry

Description of Simulation

The accessibility of cluster surface points for i -th fluid particle, at the distance r on cluster interfaces from the center of mass of the existing N -th particle cluster, is estimated as a fraction of successful events of attachment. We generate fluid particles which start Brownian walk on the two dimensional lattice and determine the fraction of fluid particles which come into the cluster area. The part of external area of cluster covered by fluid particles represents the active part. It is interest to correlate the structural factor with the number of fluid particles in external area relative to total number of cluster particles. Structure of clusters highly correlated with the fluctuations represented by the individual random walks of the incoming particles. The effects of surface tension and flow field action were included into simulation[4]

Results and Discussion

The fractal dimension and structural factor of generated clusters are $1.574 < D_f < 1.774$, $2.694 > k_0 > 1.357$, respectively. The cluster with the highest fractal dimension $D_f = 1.774$ and structural factor $k_0 = 1.357$ with attached fluid particles is shown in Figure 1 (a). The cluster with the lowest fractal dimension $D_f = 1.574$ and structural factor $k_0 = 2.694$ with attached fluid particles is shown in Figure 1(b).

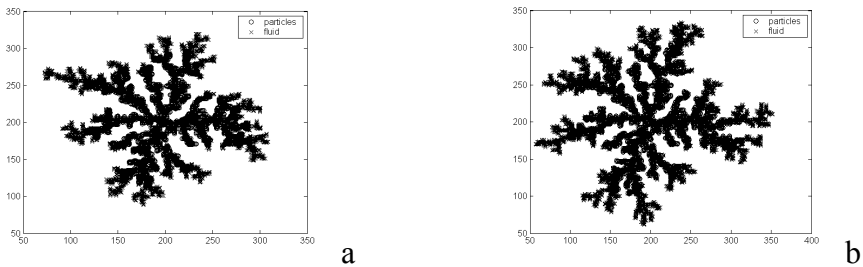


Figure 1. a) Fractal dimension structural factor are 1.574 and 2.694.
b) Fractal dimension and structural factor are 1.774 and 1.357.

Fractal dimension and structural factor for various clusters related to the number of fluid particles in external zone, Y are shown in Figure 2.

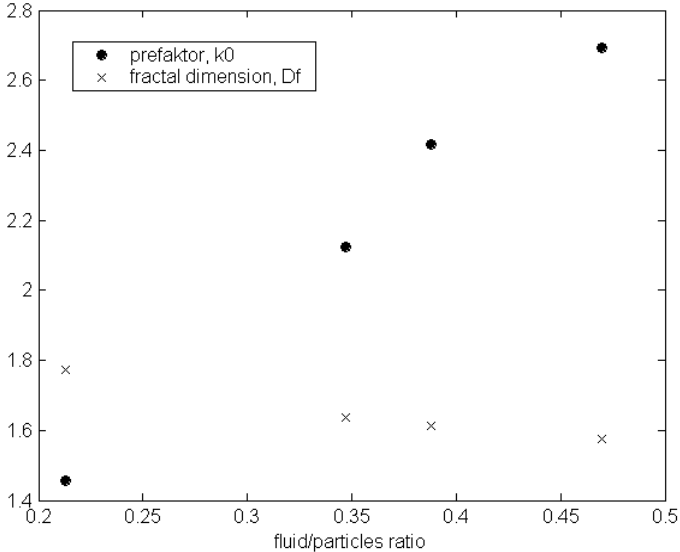


Figure 2. Fractal dimension and structural factor as function of the fluid particles in external area relative to total number of cluster particles

The higher number of fluid particles in external area corresponds to higher fraction of active part and smaller compactness of cluster. Compactness of cluster is quantified by fractal dimension and structure factor.

Conclusions

The cluster compactness is correlated with the fraction of passive part in external area of cluster. Lower cluster compactness corresponds to lower fraction of passive part in the external area. The fraction of passive part in is correlated with the number of fluid particles in external area relative to total number of cluster particles. Cluster morphology is quantified with fractal dimension and structural factor. The results of two-dimensional simulation show that structural factor is much more sensitive to changes of cluster compactness than fractal dimension.

References

- [1] C.M. Sorensen, G.C. Roberts, *J. Coll. Int. Sci.*, 1997, 186, 447.
- [2] L. Gmachowski, *J. Coll. Int. Sci.*, 1996, 178, 80.
- [3] M. Plische, Z., Racz, *Fractals in Physics*, 1986, 217.
- [4] for more detailed discussion of prefaktor issue see contributions of the same authors M.B. Plavsic et al. that follows this contribution in the Proceeding
- [5] B. Mandelbrot, "The fractal geometry in nature", W.H., Freeman, New York, 1983.

CATIONIC POLYMERS AS RHEOLOGY MODIFIERS: PROPERTIES OF POLYGEL K-SERIES

S. Blagojević and M. Ilić

Institute of General and Physical Chemistry, POB 551, Belgrade, SCG

Abstract

In this paper we present a recently developed class of cationic rheology modifiers for application in formulations as fabric softeners, toilet bowl cleaners and lime scale removers.

Introduction

The thickening of some detergent formulation is still, a not yet solved problem, mainly due to the fact that the most common thickeners are anionic ones and are not compatible with cationic and/or acidic solutions [1]. The polyelectrolyte of the synthetic polymer (Polygel K, 3V-Sigma, Italy) allows achievement of good thickening performance and storage stability of both quaternary ammonium derivate containing formulations and acidic products [2]. The evolution of the household cleaning products has been driven by several changes in lifestyle. In particular, more convenient, efficient, easy to be used products have been recently requested and the answer to these needs has been the proliferation of a range of special products [3].

Results and Discussion

Cationic thickening agent properties were determined by measuring viscosity.

Table 1 Viscosity (mPas) of polymer dispersion (Brookfield RV 20 rpm 25C pH 4)

% Dispersion	Viscosity	Spindle	Type of Polygel
0.2	1580	4	K-100
0.3	550	4	K-200
0.5	5500	5	K-100
0.5	1200	5	K-200
1.0	14000	6	K-100
1.0	2200	6	K-200

Polygel K-100 and K-200 gel formation exhibit typical viscoelastic behavior as shown in Fig.1 (a and b). Gel viscosity is also dependent on the Polygel concentration and the dispersion pH value (Fig 2).

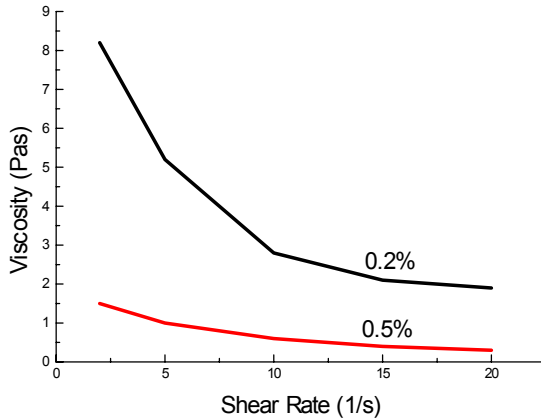


Fig 1a. Viscosity vs. Shear Rate for Polygel K-100

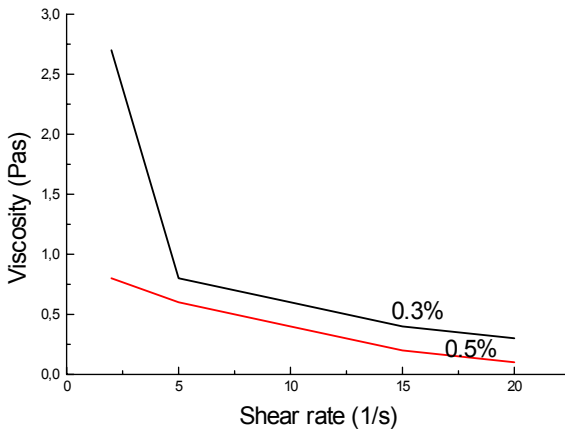


Fig 1b. Viscosity vs. Shear Rate for Polygel K-200

Polymers K-100 and K-200 are viscoelastic. There is a "viscous" element in their behavior which causes the time-dependent deformations. This is due to the fact that applied forces cause bonds in polymer chains rotate around an axis to unfold the chain, and this takes time. Under these conditions, polymers undergo conformational changes and the Hooke-type elastic element of the polymer's behavior (i.e., the spring-like response) plays only a minor part in the deformation mechanism. However, if the load is applied vary rapidly; the chains do not have sufficient time to react. Instead of rotating, the bonds within a chain only have time to stretch and bend. Conformational changes will not take place and, consequently, the polymer appears more elastic and much less flexible.

This dependence of deformation behavior on the duration of the applied load, or strain rate, (i.e., how fast deformations take place) is referred to as viscoelasticity.

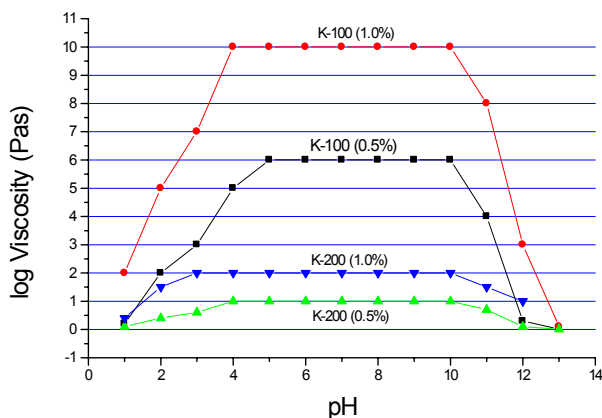


Fig 2. Viscosity vs. pH for Polygel K-100 and K-200

Conclusion

We presented a class of cationic polyelectrolyte with a trade name Polygel K Series. They have been specifically developed to thicken cationic and/or acid solutions present in the detergent field. The most common areas of application of these synthetic polymers are disinfectant bathroom cleaners and fabric softeners. The main benefits of giving a certain viscosity to these products are to improve the aesthetic characteristic and provide a noticeable cling effect on vertical hard surfaces. These cationic polymers are able to increase the viscosity of the medium by several orders of magnitude even if they are used at low amounts. In addition, they can provide good stability performance of the finished products even to concentrated formulations and after prolonged storage period at high temperature.

Acknowledgment:

We gratefully acknowledge for the financial support in grant no. 1448 of the Ministry for Science, Technology and Development of the Republic of Serbia.

References

- [1] M.Schick, Surfactants Science Series, Nonionic Surfactants, Dekker, 1990.
- [2] 3V Detergent division, Technical Report No. 23 Edition 1st, 1999.
- [3] W.Baschong, SOFW-Journal, 2002, 128, vol 5, 10-14.

THE CHARACTERIZATION OF POROUS STRUCTURE OF CHELATING POLY(GMA-CO-EGDMA) COPOLYMER

A.B. Nastasović¹, Z. Vuković² and T. Novaković²

¹*Institute for Chemistry, Technology and Metallurgy, Center for Chemistry, Njegoševa 12, Beograd,*

²*Institute for Chemistry, Technology and Metallurgy, Center for Catalysis and Chemical Engineering, Njegoševa 12, Beograd, Serbia and Montenegro*

Abstract

The influence of the functionalization with ethylenediamine and metal chelation on the porous structure of macroporous crosslinked poly(glycidylmethacrylate-co-ethyleneglycoldimethacrylate) was investigated. The chelation with Au(III) has much more pronounced effect on the porosity parameters of macroporous copolymer compared with chelation with Cu(II).

Introduction

Chelating polymers have been used as polymer-supported metal catalysts for a wide range of reactions, including olefin hydrogenation, oligomeration, hydroformylation, oxidation, etc [1]. Besides a few constraints, chelated polymers have many advantages, like good activity, selectivity and reproducibility, combined with the easy separation and recovery. Macroporous hydrophilic copolymers based on glycidyl methacrylate, GMA, produced by radical suspension copolymerization in the shape of regular beads of the required size, are versatile starting materials for the synthesis of polymer-supported metal catalysts [2]. Namely, these copolymers can be functionalized to give ligands for attaching transitional metal complexes through coordination bonds. [3]. In this study, the effect of the functionalization and metal chelation on the porous structure of the macroporous poly(glycidyl methacrylate-co-ethylene glycol dimethacrylate), PGME and copolymer modified with ethylene diamine, EDA, PGME-en, will be presented.

Experimental

Macroporous crosslinked poly(glycidyl methacrylate-co-ethylene glycol dimethacrylate), PGME, was synthesized by suspension copolymerization [4]. After reaction, the copolymer particles were washed with water and ethanol, kept in ethanol for 12 h, and dried in vacuum at 40 °C. For further investigations, the fraction with a particle size of 150-500 μm was used. The sample was modified with tenfold excess of ethylene diamine, in toluene at 70 °C for 7h, and labeled as PGME-en (the additional label -en designates functionalization with ethylene diamine). The Cu(II) ions were immobilized on PGME-en by contacting 0.2 g of modified copolymer with 25 ml of CuCl₂ solution (0.05 M) and 25 ml of NaOAc/HOAc (pH 5.0) solution. The Au(III) ions were immobilized on PGME-en by contacting 0.2 g of modified copolymer with 25 ml of HAuCl₄ (0.01 M). The metal-chelated samples were labeled as PGME-en/Cu and PGME-en/Au.

Nitrogen adsorption isotherms were determined on Sorptomatic 1990 Thermo Finnigen at 77 K. The specific surface area of samples, total pore volume and pore size distribution were calculated from these isotherms. The amount of Cu(II) and Au(III) ions sorbed per unit mass of the modified copolymer sample (sorption capacity, Q , mmol/g) was calculated from the metal concentration in filtrate solution by Atomic Absorption Spectrometry (AAS, SpektrAA Varian Instruments).

Results and Discussion

As the catalyzed reactions take place at the easily accessible active sites on the internal surfaces of the macroporous structure, important feature of polymer-supported catalysts is an optimized porous structure [1]. The porosity parameters (specific pore volume, V_s , specific surface area, S_{BET} , and pore diameter which corresponds to half of the pore volume, $d_{V/2}$) for PGME, PGME-en and samples chelated with Cu(II) and Au(III), PGME-en/Cu(II) and PGME-en/Au(III) were calculated from the adsorption isotherm data and given in Table 1.

Table 1. Porosity parameters (specific pore volume, V_s , specific surface area, S_{BET} , and pore diameter which corresponds to the half of the pore volume, $d_{V/2}$) for PGME, PGME-en, PGME-en/Cu(II) and PGME-en/Au(III).

	$S_{s, BET}, m^2 g^{-1}$	$V_s, cm^3 g^{-1}$	$d_{V/2}, nm$
PGME	47.6	0.61	53.0
PGME-en	69.2	1.18	42.0
PGME-en/Cu(II)	65.8	0.93	36.3
PGME-en/Au(III)	59.4	0.61	50.9

The porous structure of macroporous copolymers can be controlled by the type and amount of the inert component and the type and the amount of crosslinking monomer in the reaction mixture [4]. Our results show that functionalization and metal immobilization can also alter the porosity of macroporous copolymers. Reaction of PGME with EDA caused a substantial modification of porosity and formation of smaller mesopores. The specific surface area increases 44% (from 47.6 to 69.2 m^2/g), the value of the $d_{V/2}$ decreases from 53 to 42 nm, and the cumulative pore volume increases from 0.61 to 1.18 $cm^3 g^{-1}$. The changes in porous structure of the PGME-en/Cu(II) and PGME-en/Au(III) can be ascribed to the formation of the crosslinks between polymer and metal species through coordination bonds. The metal-chelating with Cu(II) causes a slight decrease of S_{BET} , V_s and $d_{V/2}$, compared with PGME-en. However, sample with immobilized Au(III), PGME-en/Au has noticeable decreased pore volume and specific pore volume. Bearing in mind the lower amount of Au(III) immobilized on PGME-en (0.6 $mmol g^{-1}$) than Cu(II) (1.2 $mmol g^{-1}$), the influence of chelated Au(III) on the porosity parameters of chelated copolymer is much more pronounced.

Surface areas and pore size distributions were calculated from the corresponding nitrogen adsorption-desorption isotherms at 77 K. For the sake of illustration, BET isotherm ($p/p_0 < 0.35$) of PGME-en is given in Fig. 1. None of the isotherms show enhanced nitrogen uptake or hysteresis in the low pressure range, which indicates the absence of microporosity [5].

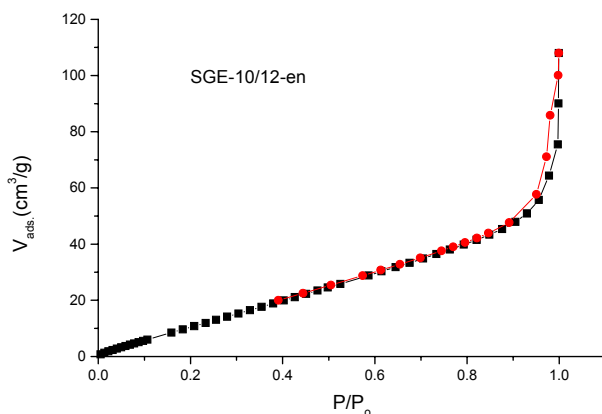


Fig. 1. The pore size distribution of PGME-en, by the BET method.

Conclusion

The functionalization with ethylenediamine and metal chelation modifies the porous structure of macroporous PGME. The chelation with Au(III) has much more pronounced effect on the porosity parameters of macroporous copolymer compared with chelation with Cu(II).

Acknowledgement: This work was supported by the Serbian Ministry of Science, Serbian Ministry of Science and Environmental Protection (Projects No. 1948. and 0022.B).

References

- [1] A. J. Pardey, M. FernandezFernandez, J. Alvarez, C. Urbina, D. Moronta, V. Leon, C. Longo, P. J. Baricelli, S.A. Moya, *J. Mol. Catalysis A: Chemical*, 2000, 164, 225.
- [2] F. Švec, *Angew. Makromol. Chem.*, 1986, 144, 39.
- [3] P. M. van Berkel, P. D. Verweij, W. L. Driessen, J. Reedijk, D. C. Sherrington, *Eur. Polym. J.*, 1992, 28(7) 747.
- [4] S. M. Jovanović, A. Nastasović, N. N. Jovanović, K. Jeremić, *Materials Science Forum*, 1996, 214, 155
- [5] B. Paredes, S. Gonzales, M. Rendueles, M.A. Villa-Garcia, *Acta Materialia*, 2003, 51, 6189.

UV-VISIBLE SPECTROSCOPICAL STUDY OF 1-AMINO-2-NAPHTHOL-4-SULFONIC ACID ELECTROPOLYMERIZATION

G. Ćirić-Marjanović¹ and B. Marjanović²

¹Faculty of Physical Chemistry, Studentski trg 12-16, 11001 Belgrade,

²Centrohem, Karadjordjeva 129, 22300 Stara Pazova, Serbia and Montenegro

Abstract

Electrochemical polymerization of 1-amino-2-naphthol-4-sulfonic acid was for the first time performed by electrolysis of its sodium salt aqueous solution at a controlled potential of 1.0 V (vs. SCE). The obtained polymerization products were soluble in water. Polymerization reaction was followed by UV-Visible spectroscopy using the solutions got from the reaction system. After application of the electrode potential new absorbance bands of formed polymeric products appeared at 475 nm and 640 nm. Their intensities continuously increase during the electropolymerization reaction.

Introduction

In our previous works related to the electrochemical polymerization of 1-naphthylamine [1] and 2-methyl-1-naphthylamine [2], [3], it has been shown that various carbon sites on the naphthalene rings can take part to the linkages between repeated units during the polymerization. These results differ from those in earlier works of other authors which have insisted on aromatic amines polymerization *via para*- position to the amino group. In connection with this, to the best of our knowledge, the possibility of the polymerization of aromatic amine class of compounds which have a substituent in *para*-position was not previously reported. That was one reason for our investigation of the electropolymerization of 1-amino-2-naphthol-4-sulfonic acid (ANSA), the naphthylamine type compound which have a substituent in the *para*- position. We proved by gel permeation chromatography, that the polymerization of ANSA occurs in spite of the fact that *para* position is occupied. In this work, we present the study of ANSA electropolymerization reaction by UV-visible spectroscopy.

Experimental

ANSA (Lachema, p.a.) was used without further purification. It was transformed in its sodium salt whose 0.084 M aqueous solution was used for electropolymerization. Electropolymerization was performed by the electrolysis at a controlled potential 1.0 V for 10 hrs in a thermostated three-electrode cell at 45 °C, by using a PAR model 273 potentiostat/galvanostat. The working electrode was a platinum plate of 1.6 cm² working area. Saturated calomel electrode (SCE) was used as reference electrode, and the counter electrode was a platinum foil. UV-visible spectra of the ANSA-Na salt solution as well as of the poly(ANSA-Na salt) solutions got from the reaction system were taken out on an Carl Zeiss Jena Specord UV-VIS spectrophotometer. Concentration of the solutions used for UV-visible spectroscopy was 1.0 x 10⁻⁴ M.

Results and Discussion

During the electrolysis the colour of the ANSA-Na salt solution changed from orange-red to violet-black gradually with the reaction continuing. UV-visible spectroscopy was suitable for following of the polymerization reaction because of the fact that obtained polymerization products were soluble in the water as a solvent. The UV-visible spectra of the solutions got from the reaction system at different reaction times are shown at Fig. 1. It can be seen from this picture that the monomer aqueous solution has low absorption without obvious bands in the wavelength region 400-800 nm, in the spectrum recorded before the start of the electrolysis. After application of 1.0 V potential on the working electrode, two new absorbance bands appeared at 475 nm and 640 nm, and a continuous growth of their intensities was observed during the electropolymerization. The band at 475 nm can be attributed to the formation of partly oxidized form of polymeric products, while the band appearing around 640 nm could be associated with the fully oxidized (bipolaronic) polymeric form [4], Fig.2. The appearance of the band at ~ 340 nm for the solution during the electrolysis is attributable to the $\pi \rightarrow \pi^*$ transition of the benzenoid moiety in the polymeric structure [5].

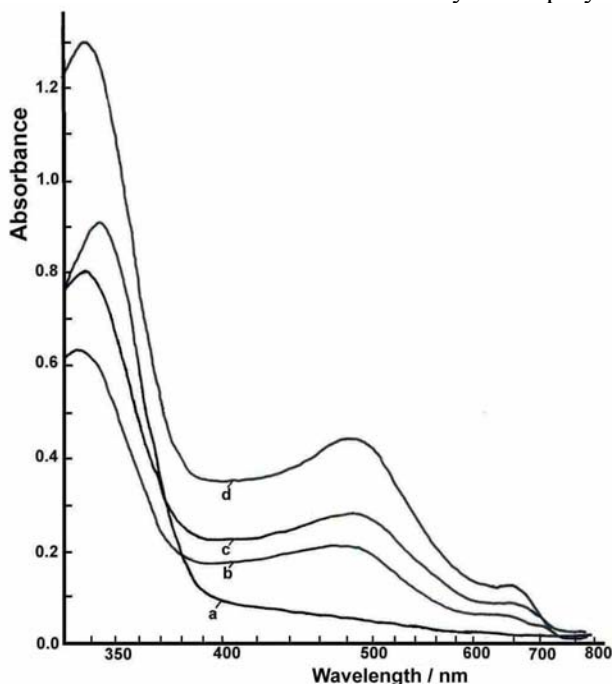


Figure 1. UV-visible absorption spectra of the aqueous solution of ANSA-Na salt before and during the electropolymerization reaction:
curve a - before the start of the electropolymerization;
curve b - at 372 min of the electropolymerization;
curve c - at 510 min of the electropolymerization;
curve d - at 577 min of the electropolymerization.

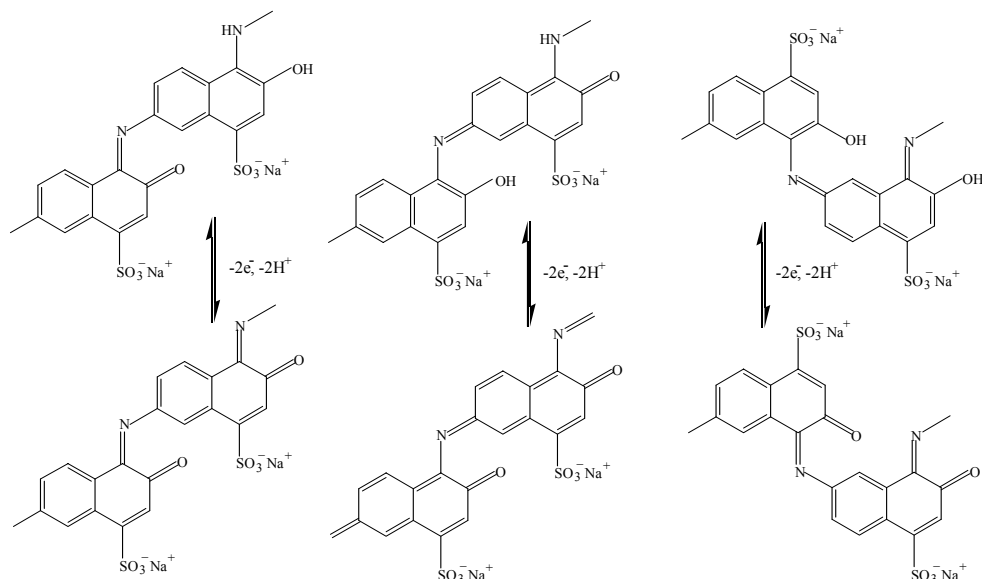


Figure 2. Proposed structures of half-oxidized and fully-oxidized N1-C6 and N1-C7 coupled ANSA-Na salt dimer units.

Conclusion

Electropolymerization of 1-amino-2-naphthol-4-sulfonic acid (ANSA) sodium salt aqueous solution is studied by UV-visible spectroscopy. Obtained polymeric products showed new absorption bands at 475 nm and 640 nm, which are attributed to the partly oxidized and fully oxidized forms of poly(ANSA), respectively. UV-visible spectroscopy is found as suitable method for controlling ANSA polymerization rate by following mentioned bands intensities growth during the electropolymerization.

References

- [1] G. Ćirić-Marjanović, B. Marjanović, V. Stamenković, Ž. Vitnik, V. Antić, I. Juranić, J. Serb. Chem. Soc., 2002, 67(12), 867.
- [2] G. Ćirić-Marjanović, N. Cvjetičanin, S. Mentus, J. Budinski-Simendić, I. Krakovsky, Polym. Bull., 2003, 50, 319.
- [3] G. Ćirić-Marjanović, N. Cvjetičanin, S. Mentus, Spectrosc. Lett., 2003, 36(1&2), 151.
- [4] C.-Y. Chung, T.-C. Wen, A. Gopalan, Spectrochim. Acta, Part A, 2004, 60, 585.
- [5] Y. Şahin, K. Pekmez, A. Yıldız, Synth. Met., 2002, 129, 107.

THE SYNTHESIS AND CHARACTERIZATION OF TELECHELIC DIISOCYANATES AS END-REACTIVE NETWORK PRECURSOR

J. Budinski-Simendić¹, R. Ž. Radičević¹, M. Špirkova², K. Dušek²
and M. Ilavský^{2,3}

¹ *University of Novi Sad, Faculty of Technology, Serbia and Monte Negro*

² *Institute for Macromolecular chemistry, Academy of Sciences, Czech Republic*

³ *Faculty of Mathematics and Physics, Charles University, Prague, Czech Republic*

Abstract

In this work the telechelic diisocyanates based on α,ω -dihydroxypoly(oxypropylene) and 2,4-tolylenediisocyanate as end-reactive precursor chain intended for poly(urethane-isocyanurate) network preparation has been studied. The size-exclusion chromatography was used for the estimation of molar mass distributions, the amount of unreacted isocyanates in network precursor, and the substitution effect on 2,4-TDI (from the amount of free isocyanate).

Introduction

Since properties of a polymer networks prepared by end-linking of telechelic diisocyanates largely depend on precursor chain distributions and the amount of free isocyanates in prepolymer, it is important to have access to appropriate analysis methods for its determination. Distribution analysis can only be performed after separation of the chemical inhomogeneous polymer mixture into its components, since any bulk technique will only provide an average value of a specific compositional feature. In this respect, the analysis of molar mass distributions by size-exclusion chromatography (SEC) is well known [1]. Recently more precise methods for the kinetic study of the diisocyanate reactivity using HPLC, SEC, UV and fluorescence spectroscopy have been proposed [2]. In the case of telechelic diisocyanates based on 2,4-tolylenediisocyanate (2,4-TDI) and long size diols due to the negative substitution effect (FSSE) on the diisocyanate the presence of dimers or trimers in end-reactive precursor chains is expectable. Thus the aim of this work was to prepare precursor chains based on long size diols and 2,4-TDI intended for network formation by cyclotrimerization and to estimate its molar mass distributions. The SEC method was used for the estimation of the substitution effect on 2,4-TDI (FSSE) from the amount of unreacted isocyanates.

Experimental

Diisocyanate 2,4-TDI (Fluka) was used as received. Its purity was checked prior to use. Diol component was α,ω -dihydroxypoly(oxypropylene) (PPG 425, PPG 725, PPG 2000, PPG 3000 Aldrich) and PPG 1200 Union Carbide). The reaction was carried out in the bulk, at 60 °C, reaction times between 24 h and 48 h (estimated earlier) [3]. The reaction vessel was stirred under nitrogen. Diols were reacted with a stoichiometric excess of isocyanates (OH/NCO= $r=0.5$). At complete conversion, all of the hydroxyl groups were consumed to form urethane groups. Each urethane forming reaction consumed an isocyanate, but since the isocyanates are in excess, at com-

plete conversion the conversion of NCO groups was equal to 0.5. The conversion of isocyanate during reaction was determined by reaction of the remaining NCO with a known excess of dibutylamine. The amount of remaining dibutylamine was then titrated with HCl. A small amount of the network precursor was either titrated or stirred with dry methanol (MeOH) to cap any unreacted NCO at ends. The end-capped telechelic diisocyanate was recovered via evaporation. SEC measurements were done by a Du Pont 830 chromatograph equipped with five Waters μ styragel columns (pore size 100 μ m; 500 μ m; 1000 μ m) and UV detector. Tetrahydrofuran was used as the mobile phase. A calibration curve of log (Mw) vs. elution volume was constructed by combining the peak molecular weight (Mp) of standards with curve fitting of the SEC traces.

Results and Discussion

The dominant structure in prepared network precursor is shown in the figure 1. Due to the negative substitution effect on 2,4-TDI as it was expected the existence of small amount of dimer, trimer and free 2,4-TDI is estimated by SEC measurements. SEC traces of MeOH end-capped telechelics based on PPG 1200 are shown in the figure 2. Values for Mn, Mw and MMDs were calculated based on experimentally determined values of FSSE on 2,4-TDI ($\rho_{\text{FSSE}}=3$) using the data for the amount of free 2,4-TDI (Table 1).

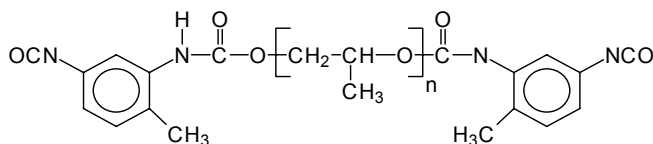


Figure 1. The dominant structure in network precursor (telechelic diisocyanate) prepared from 2,4-TDI and α,ω -dihydroxypoly(oxypropylene).

Table 1. Data for diol characteristics, the determined amount of free 2,4-TDI in telechelic diisocyanates based on different diols, and calculated data for molar mass distributions based on estimated values of FSSE on 2,4-TDI

PPG	425	725	1200	2000	3000
Mn of diol (VPO)	425	730	1230	1900	2490
Diol functionality f_n	2.0	1.95	1.94	1.92	1.86
Water content in diol (ppm)	16	61	83	51	69
The amount of free 2,4-TDI (mol %)	19.1	15.4	13.3	13.9	18.9
Calculated value of Mn	771	1106	1564	2234	2808
Calculated value for Mw	1179	1798	2616	3826	4788
MMDs (Mw/Mn)	1.53	1.63	1.67	1.71	1.70

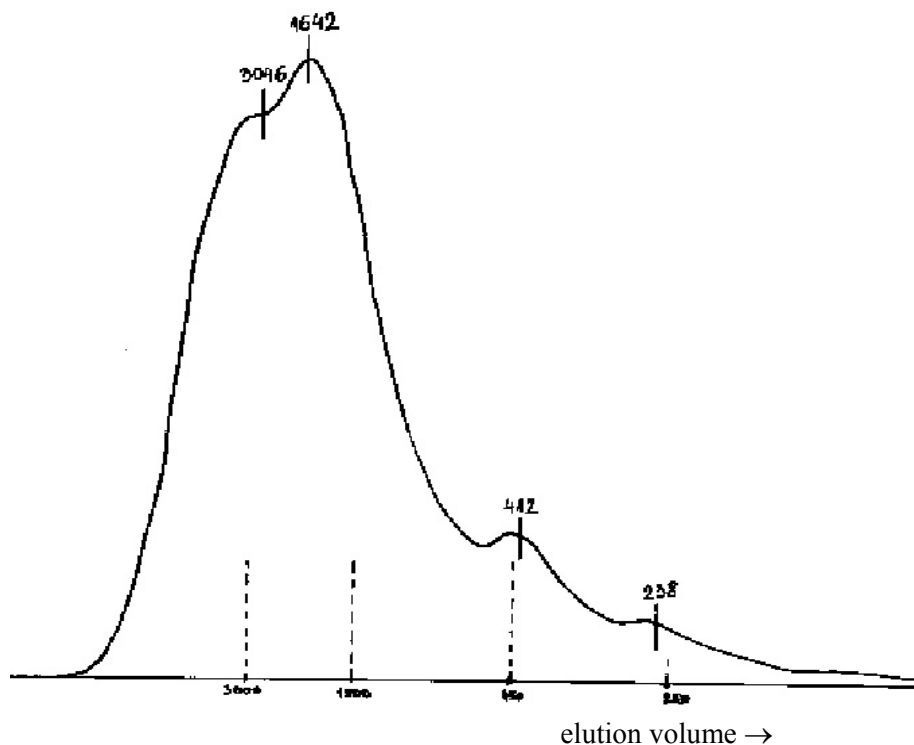


Figure 2. Size-exclusion chromatography measurement of telechelic diisocyanate (MeOH end-capped) based on 2,4-TDI and poly(oxypropylene)diol (PPG 1200). The peak positions of some polystyrene standards are noticed.

Conclusion

End reactive telechelic diisocyanates based on long size diols and 2,4-TDI intended for network formation by catalytic cyclotrimerization were prepared. As it was expected due to the negative substitution effect on 2,4-TDI, the existence of dimer, trimer and free 2,4-TDI in network precursor was estimated by size-exclusion chromatography. Calculated data for molar mass distributions (MMDs) based on the estimated values of negative substitution effect on 2,4-TDI ($\rho_{\text{FSSE}}=3$) are in the range from 1.53 to 1.71.

Acknowledgements

This work was performed on project No. 1948 financed by the Ministry for Science, Technology and Development of the Republic of Serbia.

References

- [1] M.G. Styring, A.E. Hamielec, "Determination of molecular weight distribution by gel permeation chromatography." (ed. R. Cooper), New York: Wiley Publications, 1989.
- [2] A.A. Caraculacu, S. Coseri, Progress in Polymer Science, 2001, 26, 799.
- [3] M. Špirkova, J. Budinski-Simendić, M. Ilavsky, P. Špacek, K. Dušek, Polym.Bull. 1993, 31, 83.

STUDY OF AUTOACCELERATION IN FREE RADICAL POLYMERIZATION OF STYRENE - EFFECT ON THE MOLECULAR WEIGHT DISTRIBUTION OF POLYSTYRENE

R. Ž. Radičević, D. M. Stoiljković and J. K. Budinski-Simendić

*University in Novi Sad, Faculty of Technology, 21000 Novi Sad,
Bulevar Cara Lazara 1, Serbia and Montenegro*

Abstract

In this paper are reported the study of autoacceleration in free radical polymerization of styrene by analysis of the molecular weight distribution (MWD) of polystyrene. Polymerization of styrene was performed in DSC under isothermal conditions, in the temperature range 70-90 °C. MWD of polystyrenes were determined by gel permeation chromatography (GPC). By two-peak deconvolution of GPC curves it is possible to separate the fraction of polystyrene obtained before and after onset of the gel effect.

Introduction

The gel effect is a phenomenon that often occurs during free radical polymerization of vinyl monomers as the result of autoacceleration of the polymerization rate. Relatively few studies reported in the literature have attempted to use MWD for kinetic analysis [1-3]. The technique of deconvolution of MWD curves at different conversions can be an attractive means of analysis of the effect of the gel effect on MWD of the polymer and also a means of determining the effect of kinetic factors on the conversion: it can therefore give useful information for building a model for prediction of MWD [4]. Several approaches for analysis of polymer molecular weight distributions have recently been presented. Teymour and Campbeell [5] describe a dynamic model of MWD based on sol-gel theory. The single peaks were represented by a logarithmic normal distribution instead of the theoretical Flory or Poisson distribution [6]. A two-peak deconvolution technique was used by Machio et al. [4] in a study of the free radical polymerization of methyl methacrylate. This method enables deconvolution of MWD curves by means of two characteristic unimodal distributions weighted with the conversion. The first peak, located at low molecular weight, characterises the polymer formed during the first part of the polymerization, when the reaction is under chemical control; the second peak, at higher molecular weight, represents the contribution of the polymer fraction which has been formed under diffusion control [4].

The aim of this work was the study of the autoacceleration effect, in free radical polymerization of styrene, on the molecular weight distributions of synthesized polystyrenes.

Experimental

Styrene was freed of inhibitor and distilled under nitrogen and reduced pressure. Initiator, 2,2'-azobis(isobutyronitrile), was recrystallized from methanol. Free radical polymerization of styrene in bulk was performed in a Du Pont model DSC 910 differential scanning calorimeter, under isothermal conditions, in the temperature range 70-90 °C. The initiator concentration was 1 % (w/w). The MWD of polystyrenes were measured by gel permeation chromatography (GPC Analyst, Labio, Prague), on a single 600 mm×7.5 mm PL gel column of porosity 500 Å. THF was used as mobile phase at a flow rate of 1 mlmin⁻¹. A RIDK-102 differential refractometer (Laboratorni Pstroje, Prague) was used for detection of polystyrenes and GPC instrument was connected to a computer for digital collection of data. Obtained data were processed by use of the software package Origin 5.0 (for graphic elaboration).

Results and Discussion

Differential MWD curves of polystyrenes (PS) were obtained by computer processing of GPC chromatograms. Fig. 1 shows that the MWD of polystyrene synthesized at 80 °C is bimodal. The same MWD were observed for PS samples synthesized at 70 °C and 90 °C.

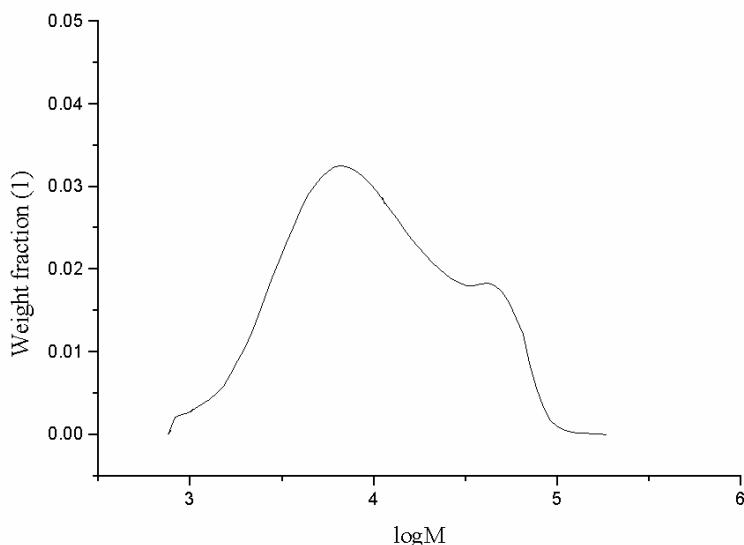


Figure 1. MWD of polystyrene synthesized at 80°C; 1 % w/w AIBN

The first peak, located at low molecular weight, characterises the polymer formed before the onset of autoacceleration; the second peak, at higher molecular weight, represents the contribution of the polymer fraction which has been formed after the onset of autoacceleration. By two-peak deconvolution of MWD curves the fractions of polymer of low molecular weight LMW, (first peak, Fig. 1) and high molecular weight, HMW (second peak, Fig. 1) were obtained:

at 70 °C, 67.9 % HMW and 32.1 % LMW

at 80 °C, 48.3 % HMW and 51.7 % LMW

at 90 °C, 17.2 % HMW and 82.8 % LMW

The amount of high molecular weight fraction in the PS sample decreases as the polymerization temperature is increased from 70 °C to 90 °C. Because the theory of the polymerization of organized monomers [7,8] suggests that the organization of monomers decreases with increasing temperature it can be expected that the fraction of polymerized disordered phase of monomer (low molecular weight) is the highest at 90 °C. Our results confirm this prediction.

Conclusion

In this paper the results about the investigation of autoacceleration effect, in free radical polymerization of styrene, on MWD of polystyrene are presented. MWD curves of synthesized PS samples are bimodal. By two-peak deconvolution of those curves the fractions of PS before and after gel effect were calculated. Obtained results can be explained by the theory of the organized monomers.

Acknowledgements

This work was performed on project no. 1948 financed by the Ministry for Science, Technology and Development of the Republic of Serbia

References:

- [1] J. A. May, W. B. Smith, *J. Phys. Chem.*, 1968, 72, 216.
- [2] W. B. Smith, J. A. May, C. W. Kim, *J. Polym. Sci. Part A*, 1966, 4, 365.
- [3] S. T. Balke, A. E. Hamielec, *J. Appl. Polym. Sci.*, 1973, 17, 905.
- [4] G. Machio, A. Visco, A. Scali, *Proc. First Eur. Congr. Chemical Engineering*, 1997, Florence, Italy, pp 167.
- [5] F. Teymour, J. D. Campbell, *Macromolecules*, 1994, 27, 2460.
- [6] V. Kissin, *Makromol. Chem. Makromol. Symp.*, 1993, 66, 82.
- [7] A. V. Kargin, A. V. Kabanov, V. P. Zubov, *Vysokomol. Soed.*, 1960, 2, 303.
- [8] R. Radičević, Lj. Korugić, D. Stoiljković, S. Jovanović, *J. Serb. Chem. Soc.*, 1995, 60, 347.

HYDROGELS OF N-ISOPROPYLACRYLAMIDE, ACRYLAMIDE AND ITACONIC ACID

M. Kalagasidis-Krušić and J. Filipović

*Faculty of Technology and Metallurgy, University of Belgrade,
Karnegijeva 4, 11 000 Belgrade, Serbia and Montenegro*

Abstract

The present work reports on the swelling behavior of copolymer hydrogels of poly(N-isopropylacrylamide-co-itaconic acid) (PNIPAM/IA) and poly(acrylamide-co-itaconic acid) (PAAm/IA) as a response to changes of external media. Small quantities of IA were used in order to impart pH-sensitive swelling behavior to the non-ionic NIPAM and PAAm gels. The PNIPAM/IA gels are pH and temperature sensitive system, owing to the lower critical solution temperature (LCST) of PNIPAM.

Introduction

Hydrogels are insoluble crosslinked polymer networks, composed of homo- or copolymers, capable of imbibing a large amount of water. A special class of hydrogels, called 'intelligent' or stimuli-responsive hydrogels change their structure and physical properties in response to physical or chemical stimuli. They have a great potential for pharmaceutical and biomedical applications. Among them, pH and temperature-sensitive polymer hydrogels are the most studied ones [1].

The present work reports on the swelling properties of the copolymer hydrogels based on N-isopropylacrylamide and itaconic acid, as well as of those based on acrylamide and itaconic acid, as a response to the changes of the external stimuli.

Experimental

The copolymer hydrogel NIPAM/IA was obtained by radical crosslinking copolymerization at 25°C during 7 days (in N₂ atmosphere). Ten wt % of the monomers were dissolved in water with the redox couple potassium persulphate (PPS) and N,N,N',N'-Tetramethylenediamine (TEMED) (1.0 wt %) and a crosslinking agent N,N'-methylenebisacrylamide (MBA) (2.0 wt %) with respect to the monomers. The AAm/IA hydrogel was synthesized by radical crosslinking copolymerization at 60°C during 24 h (in N₂ atmosphere) with the redox couple PPS/PPyS (potassium pyrosulphate) (1.0 wt %) and MBA (2.0 wt %) with respect to the monomers. The reaction mixtures were placed between two glass plates sealed with a rubber spacer. After completion of the reaction, the gels were cut into discs and immersed in water to remove the unreacted monomers. The discs were dried at room temperature to obtain dry samples (1 mm thick and 5 mm in diameter).

The swelling behavior of copolymer hydrogels were studied as a function of pH (pH 2.2; 4.5 and 6.8) at 20°C. The progress of the swelling process was monitored gravimetrically and the degree of swelling was calculated using the equation: $q = W_t/W_0$, where W_0 is the weight of the xerogel at time 0 and W_t is the weight of the swollen hydrogel at time t [1].

Results and Discussion

In contrast to non-ionic NIPAM and PAAm gels, where the change of the swelling degree, q , with pH is negligible, the swelling of ionic copolymer hydrogels NIPAM/IA and PAAm/IA is much higher and strongly pH dependent. At low pH the itaconic acid COOH groups are not ionized, so the swelling ratio is low and intermolecular complexation due to hydrogen bonding occurs, acting as physical crosslinks. As the degree of ionization increases, above the nominal pK_a values of IA (3.85; 5.44 [2]), the increased hydrophilicity of COO^- results in greater swelling (Figure 1).

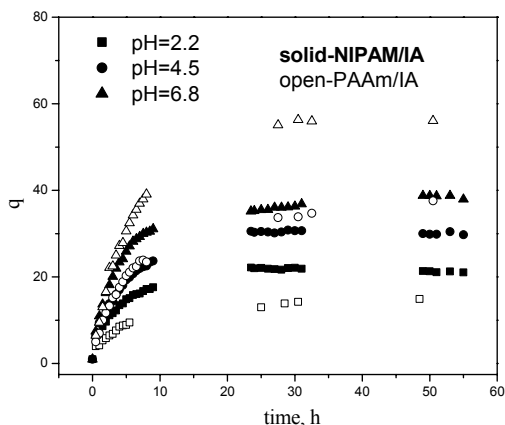


Figure 1. Degree of swelling vs. time for NIPAM/IA and PAAm/IA hydrogels at 20 °C

A pH sensitive hydrogels are interesting for the colon-specific delivery of drugs. For that purpose the swelling in the stomach, where the pH is low, should be negligible, while at the higher pH, which is the case in the colon, high swelling degree is needed in order to release the drug to that specific site. This was not completely achieved using PAAm/IA system, because the swelling was high in acidic buffers used, but replacing AAm with NIPAM gave satisfactory results.

At 37 °C NIPAM is above its phase transition temperature and in the collapsed state, so its swelling degree is low at pH=2.2, while its swelling is higher at pH=6.8 owing to the ionization of itaconic acid (Figure 2). For that reason, hydrogel, which is practically not swelling at the body temperature in acidic solutions and swollen at pH neutral media (pH=6.8), was designed for the possible use in the colon-specific drug delivery applications.

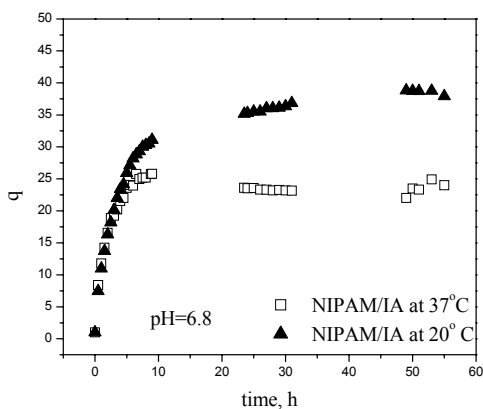


Figure 2. Degree of swelling vs. time for NIPAM/IA gels at 20 and 37 °C at pH=6.8.

Conclusion

Small quantities of IA and NIPAM were used to achieve pH- and temperature-sensitive swelling behavior for NIPAM/IA hydrogel. This gel practically does not swell at low pH at body temperature and is highly swollen at pH neutral media, which is very interesting for the colon-specific drug delivery.

Acknowledgments

The authors acknowledge funding from the Ministry of Sciences, Technologies and Development of the Republic of Serbia, Fundamental Science Project No. 1948, 'The Synthesis, Modification and Characterization of Synthetic and natural Polymeric Materials'.

References

- [1] N. A. Peppas, P. Bures, W. Leobandung, H. Ichikawa, *Europ.J. Pharm. Biopharm.*, 2000, 50, 27.
- [2] Wheast RC, editor. *Handbook of Chemistry and Physics*, 53 edn. Cleveland, Ohio, 1975.

THE VISCOMETRIC INVESTIGATION OF POLY(ITACONIC ACID) IN SOLUTION

S. J. Veličković, Đ. Anđelkoski, M. Kalagasidis Krušić and I.G. Popović

Faculty of Technology and Metallurgy, Karnegijeva 4, 11000 Belgrade

Abstract

In this paper seven different equations were used to fit the viscometric data of poly(itaconic acid) (PIA), which was synthesized in solution under various conditions in the presence and absence of dimethyl aminoethanol (DMEA). The viscometric data were obtained in the following solvents: water, methanol and their mixtures. The samples synthesized in the presence of the amine were insoluble in methanol. The Fedors equation most accurately described the dilute solution properties of PIA, while the other equations could be used to some extent. The solubility parameter of PIA according to the Fedors equation was estimated to be $42 \text{ (J/m}^3\text{)}^{1/2}$.

Introduction

Poly(itaconic acid) (PIA) is a water-soluble polymer with two carboxyl groups in each monomer unit that is commercially used as a "superabsorbent"[1]. The solution behaviour of water-soluble polymers can be studied from viscometric data using various equations[2,3], seven of which were used in this study. The equations that were applied are listed in the following table:

Huggins	$\frac{\eta_{sp}}{c} = [\eta] + k_H \cdot [\eta]^2 \cdot c = [\eta] + b \cdot c; \quad b = k_H \cdot [\eta]^2$
Schultz Blaschke	$\frac{\eta_{sp}}{c} = [\eta] + k_{SB} \cdot [\eta] \cdot \eta_{sp}$
Kraemer	$\frac{\ln \eta_{rel}}{c} = [\eta] - k_k \cdot [\eta]^2 \cdot c$
Fedors	$\frac{1}{2 \cdot (\eta_{rel}^{1/2} - 1)} = \frac{1}{[\eta]} \left(\frac{1}{c} - \frac{1}{C_m} \right)$
Fuoss	$\frac{c}{\eta_{sp}} = A \cdot \sqrt{c} + \frac{1}{c}$
Martin- Staudinger- Heauer	$\log \left(\frac{\eta_{sp}}{c} \right) = \log [\eta] + k_m \cdot [\eta] \cdot c$
Rao	$\frac{1}{2 \cdot (\eta_{rel}^{1/2} - 1)} = \frac{1}{[\eta]} \cdot \frac{1}{c} - \frac{k_r - 1}{2.5}$

where η_{sp} is the specific viscosity, c – the concentration, g/dl, k – a constant corresponding to the denoted equation, $[\eta]$ – the limiting viscosity number (LVN), dl/g, C_m – the polymer concentration parameter, η_{rel} – the relative viscosity.

Experimental

Poly(itaconic acid) (PIA) was synthesized by four different procedures (in water using the initiator/activator system potassium pyrosulfate (PP)/dimethyl aminoethanol (DMEA), and in dioxane using AIBN as the initiator). The details of the synthesis are given in the following table:

Sample	Solvent	Initiator, conc.	Amine	Ratio I/A, molar	Temperature, °C	Time, h
◇	0.1M aq HCl	PP, 5 mass%	DMEA	1:1	40	96
○	0.1 M aq HCl	PP, 5 mass%	DMEA	62.5:1	40	96
□	Water	PP, 5 mass%	DMEA	1:1	40	96
△	Dioxane	AIBN 1.4 mass%	-	-	40	504

De-aerated monomer solutions were polymerized in sealed ampoules. The obtained polymers were precipitated twice from isopropanol. The viscosities were measured in pure methanol and water and in their mixtures (13:2 and 1:1 by volume), using an Ubbelohde viscometer at 25°C.

Results and Discussion

The PIA samples synthesized with equal amounts of amine and initiator were insoluble in methanol, but were soluble in the mixtures of water and methanol and pure water. All the other samples were soluble in all the solvents applied. The linear regression coefficients showed that the best fit was obtained when the Fedors equation was applied, the lowest value of the coefficient being 0.982. The values of the LVN, using that equation, and the values of the Fedors constant are given as a function of the solvent composition in Figure 1.

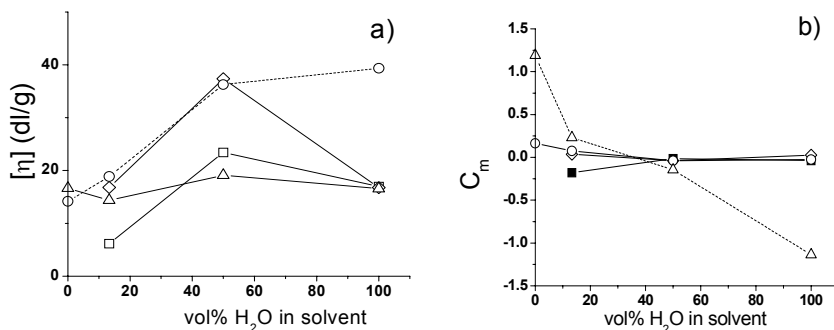


Figure 1. The dependence of the LVN (a) and the polymer concentration parameter C_m^E (b), based on the Fedors equation, on the amount of water in the methanol/water solvent (vol %)

It may be seen that the viscosity number is the highest for the equimolar mixture of methanol and water in three of the four samples. The increased LVN may be attributed to better solvatization, i.e. to stronger interactions between the polymer and the solvent. Such behaviour might imply that in this type of mixture the hydrophilic parts of the polymer interact with water, while the hydrophobic main chain interacts with methanol, resulting in the strongest interactions with the solvent.

The polymer concentration parameter C_m is considered to decrease with increasing interactions between the polymer chains[4]. While that increase is significant in the dioxane-polymerized sample, it is negligible in the case of amine-activated polymers. While the dioxane-synthesized sample probably exhibits clustering of the hydrophilic groups with decreasing hydrophilicity of the solvent system, this might not be the case in the amine-activated samples. The amine, which is known to be retained in the polymer to a certain extent when present in the polymerization of itaconic acid even after thorough purification[5], may prevent carboxyl group interactions by forming complexes with them[6], and maintain the Fedors concentration parameter relatively constant in the whole solvent range.

The data obtained were also used to estimate the solubility parameter of the polymer, δ_p . In all the samples the value of δ_p was about $42 \text{ (J/m}^3)^{1/2}$. A more detailed investigation of the solubility parameter of PIA is currently in progress.

Conclusions

This investigation has shown that the Fedors equation gives the most accurate description of the behaviour of PIA in solution. The other equations applied also gave satisfactory results for most of the samples. It was also shown that water-based polymerizations afforded somewhat different products in terms of solution behaviour than the dioxane-based one.

Acknowledgement

The authors acknowledge funding from the Ministry of Sciences, Technologies and Development of the Republic of Serbia, Fundamental Science Project No. 1948, 'The Synthesis, Modification and Characterization of Synthetic and natural Polymeric Materials'.

References

- [1] Technical Report of Platform Chemicals, June 25 2002, Agriculture and Agri-Food Canada, Government of Canada, Ottawa, 2002.
- [2] M.V.S. Rao, *Polymer*, 1993, 34, 592.
- [3] S. Dragan, M. Mihai, L. Ghimici, *Eur. Polym. J.*, 2003, 39, 1847.
- [4] J. Ba, B. Liang, P. Cui, H. Dai, R. Huang, *Polymer*, 2003, 44, 1281.
- [5] R. Devasia, C.P. Reghunadhan Nair, K.N. Ninan, *Eur Polym. J.*, 2003, 39, 537.
- [6] E Tsuchida, *JMS-Pure Appl Chem.*, 1994, A31, 1.

OXIDATIVE CHEMICAL POLYMERIZATION OF *o*-TOLIDINE

G. Ćirić-Marjanović¹, B. Marjanović², and P. Holler³

¹*Faculty of Physical Chemistry, Studentski trg 12-16, 11001 Belgrade, Serbia and Montenegro*

²*Centrohem, Karadjordjeva 129, 22300 Stara Pazova, Serbia and Montenegro*

³*Institute of Macromolecular Chemistry, Heyrovský Sq. 2, Prague, Czech Republic*

Abstract

The *o*-tolidine was polymerized by chemical oxidation in an acidic water solution using ammonium persulphate oxidant, at +5.5 °C. Polymerization was proved by gel-permeation chromatography of the obtained product using N-methyl-2-pyrrolidone as a mobile phase. Poly(*o*-tolidine) has the weight-average and number-average molecular weights of 3610 g/mol and 2400 g/mol, respectively. Molecular weight values was found to be up to ~13000 g/mol.

Introduction

In last two decades electroconductive polymers based on aromatic amines have attracted considerable interest particularly as new electronic materials, [1], [2]. The *o*-tolidine belongs to the class of aromatic amines with occupied *para*-position to the amino group. To the best of our knowledge, such compounds generally were not studied as monomers for homopolymers, but only rarely as a copolymer units [3]. It was expectable that *para*-position is the most favourable, and in many cases exclusive position for linkages between repeated units. On contrary to this expectations, in our previous works we showed that different carbon sites than *para*-position on the aromatic rings can take important part in the oxidative polymerization process. Thus, regarding mentioned fundamental aspect as well as practical aspect of obtaining new conjugated polymeric materials, it would be interesting to prove the polymerization of *o*-tolidine. In the present paper, we report the preparation of poly(*o*-tolidine) by oxidative chemical polymerization and its characterization by gel permeation chromatography (GPC).

Experimental

The *o*-tolidine (Centrohem) and (NH₄)₂S₂O₈ (Centrohem) were used without further purification. Poly (*o*-tolidine) was synthesized chemically using the solution of 5 mmol of *o*-tolidine in a 225 ml of aqueous 1M HCl, placed in a cooling bath maintained at +5.5 °C. Polymerization was performed by slowly addition of an oxidant solution (2.9 g of ammonium persulphate in 60 ml of aqueous 1.0 M HCl, at +5.5 °C) to the monomer solution. This reaction mixture was left stirring for 2 hrs in a cooling bath at +5.5 °C, and then it was left at room temperature overnight. The precipitated dark-brown polymer was filtered and washed 3 times with the portions of 50 ml aqueous 0.2 M HCl, and then dried under vacuum for 2 hrs at 70 °C. Molecular weights of poly(*o*-tolidine) were assessed with gel permeation chromatography using 500 x 8

mm Labio GM 1000 column operating with N-methyl-2-pyrrolidone and calibrated with polystyrene standards, using toluene as an internal standard. Spectrophotometric detection at a wavelength of 436 nm was carried out. Poly(*o*-tolidine) samples for GPC measurements were prepared by dissolving 10 mg of polymeric sample in 5 ml N-methylpyrrolidone containing 100 mg triethanolamine for deprotonation of poly(*o*-tolidine) *i.e.* to improve solubility of polymer. Mobile phase N-methyl-2-pyrrolidone was contained 0.5 % LiBr to prevent aggregation. Flow rate was 1 ml/min. GPC data were treated by CSW1.7 software and GPC for Win.

Results and Discussion

The gel permeation chromatogram and corresponding molecular weight distribution of poly(*o*-tolidine) sample synthesized by described procedure are shown in Fig. 1.

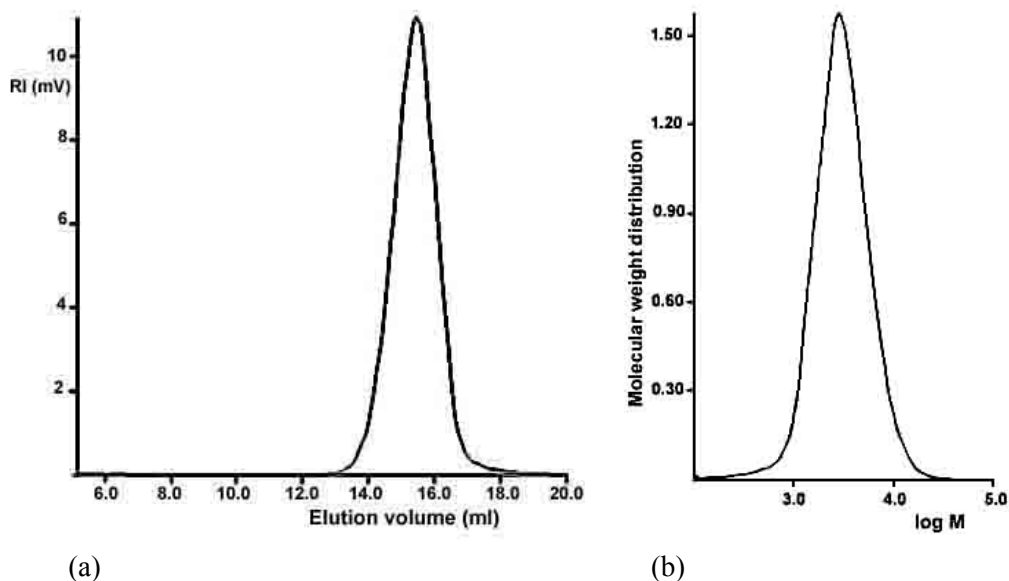


Figure 1. (a) Gel permeation chromatogram and (b) molecular weight distribution of poly(*o*-tolidine) determined by gel permeation chromatography in N-methyl-2-pyrrolidone.

The weight-average and number-average molecular weights, M_w and M_n , of poly(*o*-tolidine) were calculated to amount 3610 g/mol and 2400 g/mol, respectively. Polydispersity index expressed as the ratio M_w / M_n was 1.5 and the peak molecular weight value, M_p , was 2760 g/mol. Molecular weight values was found to be up to ~13000 g/mol.

Proposed polymerization mechanism of the *o*-tolidine is given considering delocalization of electron spin density in the radical-cation of the *o*-tolidine, and on the basis of steric hindrance, inductive and resonance effects of amino and methyl groups

(Fig. 2). N-C coupling mode is shown. Hydrazo and azo dimer units as a result of N-N coupling mode are also possible.

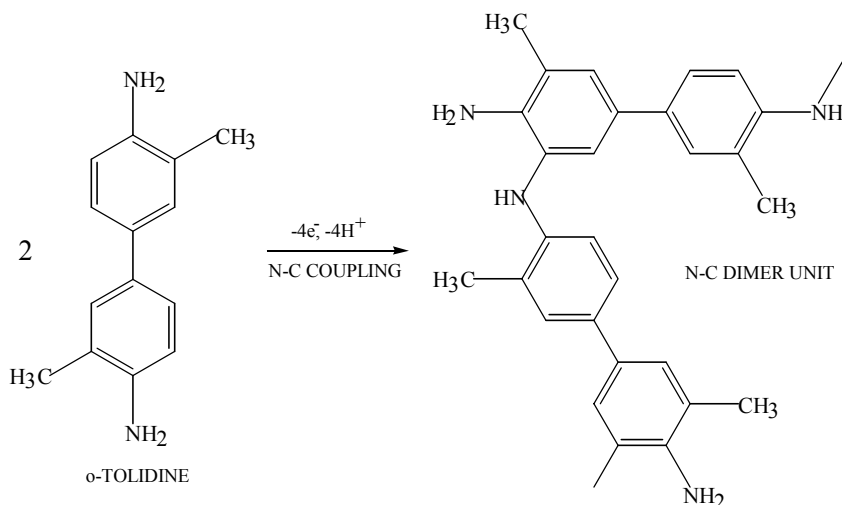


Figure 2. N-C oxidative coupling of the *o*-tolidine.

Conclusion

The chemical oxidation of *o*-tolidine in an acidic aqueous solution, using ammonium persulphate as an oxidant, leads to the polymeric product. Gel permeation chromatography of poly(*o*-tolidine) detected the chains with molecular weight values up to ~13000 g/mol, affirming our expectation that homopolymer of *o*-tolidine, which has occupied *para*-position to the amino group, can be formed.

References

- [1] G. Ćirić-Marjanović, N. Cvjetičanin, S. Mentus, J. Budinski-Simendić and I. Krakovsky, *Polym. Bull.*, 2003, 50, 319.
- [2] G. Ćirić-Marjanović, I. Krakovsky and J. Budinski-Simendić, *Mat. Sci. Forum*, 2004, 453/454, 139.
- [3] O. Aksimentyeva, *Mol. Cryst. Liq. Cryst.*, 1998, 324, 125.

INFLUENCE OF THE CROSS-LINK DENSITY ON THE SWELLING KINETICS OF PAA HYDROGELS IN WATER

J.Jovanović¹, B.Adnadević², V.Randelović³ and D.Uskoković¹

¹*Institute of Technical Science of the Serbian Academy of Science and Arts, Knez Mihailova 35, 11000 Beograd,* ²*Faculty of Physical Chemistry, Studentski trg 16, 11000 Beograd,* ³*Faculty of Chemistry, Studentski trg 12, 11000 Beograd, Serbia and Montenegro*

Abstract

Samples of SAP-PAA hydrogels were synthesised with different crosslink densities. Effect of crosslink densities on swelling behaviour in distilled water at 25° was investigated. With the increase of the cross-link density the swelling rate constant also increased, but both the equilibrium swelling degree and time for linear SD decreased. It was found that water diffusion into SAP-PAA hydrogels is independent on crosslink density and follows the so called non-Fickian diffusions.

Introduction

Hydrogels are three-dimensional cross linked polymeric structures that are able to swell in the aqueous environment. Due to characteristic properties such as swellability in water, hydrophilicity, biocompatibility, and lack of toxicity, hydrogels have been utilized in a wide range of applications. The most important types of hydrogels based on synthetic polymers are those of poly(acrylamide) and poly(acrylic acid), either based on cross-linked homopolymers or combined with other comonomer units, or in the form of interpenetrating networks. Hydrogels of acrylic polymers and copolymers of acrylic acid and several acrylamides have been reported as hydrogels with adjustable swelling kinetics that showed special properties such as super-absorbent hydrogels [1]. It has been shown that the presence of polyacrylic segments in hydrogels, significantly increases their ability of water uptake [2]. Although, the relationship between the degree of swelling and the cross-link density is well established [3], there have been no systematic investigations concerning the influence of hydrogel structure and the degree of cross-linking on their swelling behaviour [3]. The aim of this study was to investigate the effect of crosslink density on the physical-chemical characteristics, primarily swelling behavior and swelling kinetics of synthesized hydrogels based on poly(acrylic acid) in the sodium salts form (PAA-Na⁺).

Experimental

Materials: Acrylic acid, sodium persulfate, sodium thiosulfate, N,N'-methylenebisacrylamide (NMBA) and ethylenediaminetetraacetic acid (EDTA), p.a. purity, were purchased from Merck-Darmstadt, Germany. Hydrogen peroxide, 30%, and sodium carbonate were purchased from Zorka-Šabac, Serbia and Montenegro. All chemicals used were reagent grade and used as purchased without further purification. The water used in all the experiments, was doubly distilled. *Synthesis of SAP-PAA hydrogels:* The procedure for the preparation of super-absorbing cross-linked poly(acrylic acid)

hydrogels was based on the simultaneous radical polymerization of acrylic acid and cross-linking of the formed poly(acrylic acid) according to procedure described previously [4]. The reaction process was carried out in nitrogen atmosphere, varying cross-linker (NMBA) concentrations under constant all the other reaction parameters. *Methods of physical-chemical characterization:* Density determination: The apparent density of the synthesized samples was determined according to a procedure described in the literature, using n-hexane as the non-solvent [5]. Swelling experiments: Dried hydrogels (xerogels) were left to swell in distilled water at temperature 25° to determine the parameters of swelling and diffusion. Swollen gels which were removed from the water bath at regular intervals were dried superficially with filter paper, weighed and placed in the bath. The swelling degree (SD), defined by equation (1) as the difference between the mass of the swollen sample (m_t) at time (t) and the dry mass (m_o) divided by the mass of the dry sample:

$$SD (\%) = (m_t - m_o) \cdot 100 / m_o \quad (1)$$

was determined as a function of time. At least three swelling measurements were performed for each sample and the average values were reported. The time for initial swelling, t_{in} : is time for initial swelling stage of linear SD changes. Determination of swelling kinetics parameters: Swelling kinetics parameter determination was based on equation (2) [6]:

$$\ln(SD_{eq} / (SD_{eq} - SD)) = kt \quad (2)$$

where: SD_{eq} is equilibrium swelling degree, SD is swelling degree at time t , and k is the swelling rate constant. Determination of water diffusion parameters: Kinetics parameters of water diffusion into hydrogels were determined according to equation (3) [7]:

$$F = m_t / m_{eq} = k_D t^n \quad (3)$$

where F denotes the amount of solvent fraction at time t , m_{eq} is mass of the swollen sample at swelling equilibrium, k_D is the diffusion rate constant which related to the structure of the network and the exponential n is a parameter indicative of the type of diffusion. The equation is applied up to 60% of swelling.

Results and Discussion

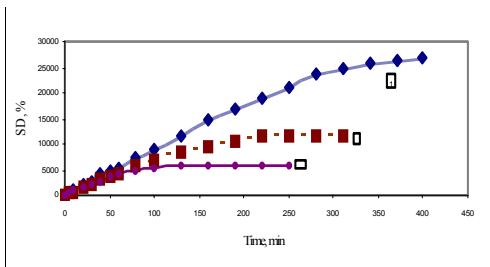


Figure 1. Isotherms of SD changes in water at 25° for investigated SAP-PAA

Figure 1 presented isotherms of SD changes as a time function for the examined SAP-PAA hydrogels in distilled water at 25°. For all the obtained results, existence of two characteristic ranges is specified.

Table 1 presents determined values for apparent densities, swelling parameters: SD_{eq} and t_{in} values, and kinetic swelling parameters: swelling rate constant (k , min^{-1}) and diffusional parameters for water diffusion: diffusion exponent (n) and diffusion rate constant ($\ln k_D$) for examined SAP-PAA samples in distilled water at 25°C. Based on the obtained results shown at Table 1, it can be concluded that the increase of the crosslinker concentration in reaction mixture leads to an increase in apparent densities of the obtained hydrogels. With the increase the cross-link

density, also increase the swelling rate constant (k), but both equilibrium swelling degree (SD_{eq}) and the initial time of swelling (t_{in}) decrease. Unregardless to the crosslink density of the investigated SAP-PAA hydrogels, water diffusion into them is independent on crosslink density and always follows the so called non-Fickian diffusions ($n > 0.5$) and diffusion kinetics is determined by intractions of water molecules with active sites (carboxylate groups) of the hydrogel.

Table 1. Influence of cross-link density on swelling parameters

Sample	SAP-PAA		Swelling		Sweling kinetic	Diffusion	
	NMBA, % _{mol}	Density, g/cm ³	t_{in} , min	SD_{eq} , %	k , min ⁻¹	n	$\ln k_D$
1	0.25	1.81	290	26690	0.0056	0.9	4.9578
2	0.42	1.91	160	11600	0.0123	0.98	4.3366
3	0.68	2.09	80	8620	0.0374	0.95	5.2699
4	0.85	2.15	50	5850	0.0395	0.92	4.575

Conclusions

Samples of SAP-PAA hydrogels were synthesised with different crosslink densities. With the increasae of the cross-link density also increase the swelling rate constant (k), but equilibrium swelling degree (SD_{eq}) decrease as well as the initial time of swelling (t_{in}). It was found that cross-link density don't influence the type of water diffusion into investigated SAP-PAA hydrogels and follows the so called non-Fickian diffusions and that diffusion kinetics is determined by interactions of water molecules with active sites of the hydrogels.

Aknowledgements

These investigations were partly supported by the Republic Ministry of Science, Technologies and Development by projects 1948.

Literature

- [1] C.Elvira, J.F.Mano, J.S.Roman, *Biomaterials*, 2002, 23, 1955.
- [2] S.J.Kim, K.J.Lee, S.I.Kim, *React&Funct.Polym.*, 2003, 55(1), 69.
- [3] P.Flory, J.Rehner, *J.Phys.Chem.*, 1943, 11, 512.
- [4] J.Jovanovic, B.Adnadjevic, S.Ostojic, M.Kicanovic, *Mater. Sci.Forum*, 0000, 2004.
- [5] F.A. Dorkoosh, et.all., *Polymer*, 2000, 41, 8213.
- [6] I. Katime, et.all., *Polymer International*, 1996, 40, 281.
- [7] D. Sareydin, Y.Caldiran, *Pol.Bull.*, 2001, 46, 91.

PROPERTIES OF ELASTOMERIC MATERIALS BASED ON POLYCHLOROPRENE/CHLOROSULFONATED POLYETHYLENE RUBBER BLENDS

G. S. Marković¹, M. Marinović-Cincović², H. Valentova³,
M. Ilavsky³ and J. Budinski-Simendić⁴

¹*Tigar, Pirot, Serbia and Montenegro,*

²*Institute of Nuclear Science VINČA, Belgrade, Serbia and Montenegro,*

³*Sant Charles University, Macromolecular Physics Department, Prague,*

⁴*Faculty of Technology, Novi Sad, Serbia and Montenegro*

Abstract

In this work the elastomeres based on polychloroprene/chlorosulphonated polyethylene rubber blends (CR/CSM) intended for rubber-metal bonding has been studied. The rheographs and curing characteristics of blends reinforced by active precipitated silica and diatomaceous earth were obtained using a Monsanto rheometer. Crosslinking has been performed by sulphur at 160 °C up to optimum cure time. Temperature dependence of storage modulus (E'), $\tan\delta$ and glass transition temperature were determined by mechanical spectroscopy. Adhesion strength has been measured by two methods. It was concluded that a adhesion strength value can be increased by using nano fillers as reinforcing agents

Introduction

The rubber products have to meet a set of properties and process requirements, which could be opposing in nature [1]. Since different elastomers have different types of responses to stress, blending of selected rubbers has been practiced to meet the need for contradicting sets of properties [2]. Reinforcement of an elastomer by filler is associated with a strong interaction between the filler surface and macromolecules of rubber. Although a comprehensive understanding of the exact nature of rubber reinforcement is still lacking, the elastomer-filler attachments appear to be both physical and chemical depending on physico-chemical character of the filler surface, and the chemical nature of the elastomer. In many applications, rubber is bonded to rigid substrates such as metal to provide a means of attachment [3]. Various test methods have been developed to evaluate bond strength. Most of these methods involve measuring the tensile force needed to break a standard test piece of arbitrary shape and size. The main goal of this work was to study the influence of reinforcing fillers on adhesion strength of elastomeric materials based on polychloroprene/chlorosulphonated polyethylene rubber blends (CR/CSM) filled either by active precipitated silica or by diatomaceous earth

Experimental

Macromolecules used for network preparation: chloroprene rubber (CR), [poly(2-chloro-1,3-butadiene)], chlorosulfonated polyethylene rubber (CSM) (rubber-like thermoset material based on high molecular weight of polyethylene with sulphonil chloride). Reinforcing fillers: active precipitated silica - Ultrasil VN₃, BET 160-200 (N₂) m²/g, with nominal particle size 15 nm notated as SiO₂(15nm), and diatomaceous earth, CELITE 281 with nominal particle size 28 μm notated as SiO₂(28μm). The compounds were prepared on a laboratory mixing roll mill by a speed ratio of the rollers $n_1/n_2=28/22$, at roller temperature of 40-50 °C (during ca. 20 minutes) and molded into 2 mm thick slabs for determination of mechanical properties. Crosslinking procedure has been performed at 160 °C up to optimum cure time (t_{c90}) which has been estimated by the rheograph. Temperature dependence of storage modulus (E') and $\tan \delta$ were determined from -50 °C to 150 °C by mechanical spectroscopy (rheometrix). Glass transitions were determined from the position of maximum $\tan \delta$. Adhesion strength was determined by measuring the shear force needed to break a standard test piece and by peel test which measures the force of separation at a constant peel rate (5 mm/min), the peel angle was equal to 180°. The test were carried out at the room temperature.

Results and discussion

The curing characteristics of all compounds determined by Monsanto Rheometer and are summarised in Table 1. Temperature dependences of $\tan \delta$ for all elastomeric materials determined in the temperature interval from -50 °C to 150 °C by mechanical spectroscopy are shown in the figure 1. The values of the crosslink densities were evaluated from the storage modulus (E') at 70 °C and summarised in the table 2. . The adhesion strength data are given in the table 2. It is obvious that in metal-elastomer bonded systems based on CR/CSM rubber blend, the adhesion strength value can be increased by using nano fillers as reinforcing filler.

Table 1. The curing characteristics for crosslinking systems based on pure rubbers and its blends reinforced with two types of filler

Crosslinkin system	MU(1+4) at 373K	t_{s2} (min)	Rmax (dNm)	Rmin (dNm)	t_{c90} (min)
CSM rubber	33	6.52	32	3	50.15
CR rubber	31	2.21	24	3	21.09
CR/CSM rubber blend (50/50)	38	3.48	28	5	25.32
Rubber blend filled with nano silica: CR/CSM/SiO ₂ (15nm)	62	4.27	57	14	28.04
Rubber blend filled with diatomaceous earth: CR/CSM/SiO ₂ (28μm)	37	2.31	37	8	43.33

Table 2. Properties of elastomeric materials based on CR/CSM rubber blend: glass transition (T_g), modulus (E'), shear adhesion strength (AS), peel adhesion strength (PAS), crosslink density (ν)

Elastomeric material	T_g °C	E' at 70°C, Pa	AS MPa	PAS MPa	ν , Mol.m ⁻³
Crosslinked CR/CSM rubber blend (50/50)	-38	1.43E+6	1.1	5.6	70
CR/CSM/SiO ₂ (28 μ m)	-45	2.98E+6	2.0	6.3	356
CR/CSM/SiO ₂ (15nm)	-40	1.62E+7	2.1	7.5	1933

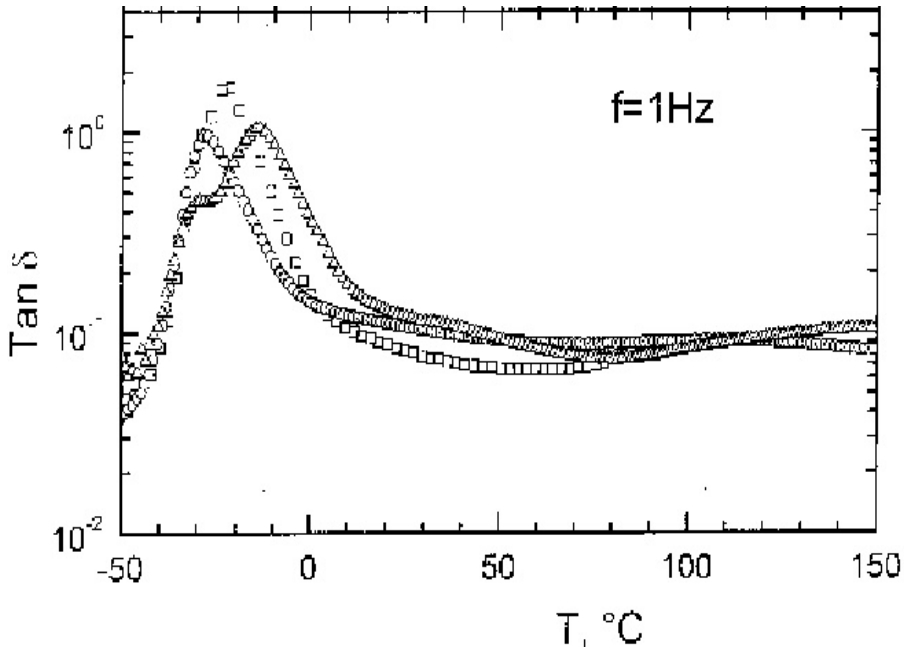


Figure 1. Temperature dependence of $\tan \delta$ estimated by mechanical spectroscopy for elastomeric materials based on CR/CSM rubber blends: unfilled (\square), filled with nano particles of silica (O), filled with diatomaceous earth (Δ).

Conclusion

In metal-elastomer bonded systems based on CR/CSM rubber blend, the adhesion strength value can be increased by using nano fillers as reinforcing agents.

References

- [1] D.C. Leicht, O.H. Yeoh, A.N. Gent, J. Padovan, R.L. Mullen. Rubber Chemistry and Technology, 2003, 76, 160.
- [2] D. Mangaraj, Rubber Chemistry and Technology, 2002, 75, 365.
- [3] R.S. Rajeev, S.K De. Rubber Chemistry and Technology, 2002, 75, 475.

Environmental Protection

(J)

PARTITION OF SEMIVOLATILE ORGANIC COMPOUNDS IN THE ATMOSPHERE OF ATHENS, GREECE

I. E. Sitaras and P. A. Siskos

Environmental Analysis Group, Laboratory of Analytical Chemistry, Department of Chemistry, National and Kapodistrian University of Athens, Panepistimioupoli, 15771 Zografos, Athens, Greece.

Introduction

Gas/particle partitioning of semivolatile organic compounds (SOCs) in the atmosphere is a decisive atmospheric process concerning their fate and distribution in the environment. SOC's exhibit different reactivity, rate of deposition and wash-out efficiency according to their physical phase. The partitioning of a given compound between the particulate and the gas-phase depends on the ambient temperature, the nature of the aerosol, the interactions being established between the compound and the aerosol and the overall behavior of the compound in the environment [Bidleman, 1988].

The explanation of SOC's partitioning was initially based on the adsorption of semivolatile organic compounds on the particle surface [Pankow, 1987] and the absorption into the organic phase of the aerosols [Pankow, 1994]. The sub-cooled saturation vapor pressure P°_L was used as descriptor of the sorption process for both adsorption and absorption. More recently, the octanol-air partition coefficient K_{OA} was used to describe the gas-particle partitioning to organic aerosols [Finizio et al, 1997]. The physicochemical properties of aerosol (composition, size), the interactions of aerosol with other environmental compartments and the mechanism by which the partitioning is taking place, are under discussion [Simcik et al, 1998]

The present work has been focused on the gas/particle partitioning of the twelve PAHs among the 16 PAHs proposed by EPA, four n-alkanes (C18-C21) and 7 PCBs congeners (CB28, CB52, CB101, CB118, CB153, CB138, CB180) in three sites: an urban, a semi-urban and an industrial site, located in Athens basin. The gas/particle partitioning of PAHs was studied through (a) the temperature dependence of gas phase concentration in order to investigate the significance of local emissions (b) the temperature dependence of the partition constant, from which seasonal variation in aerosol properties is emerged (c) the description based on the vapor pressure approach according to the Pankow's model (d) the description based on the K_{OA} approach.

Experimental

Sampling: sampling was performed at three sites: 1) on the roof of the building of Ministry of Environment, 21 m above the street level (Pattision street) in the Athens center, a site influenced by a heavy traffic emissions, 2) on the roof of the building of Institute of agricultural research (7 m) in Lykovrisi, an Athens suburb influenced by highway vehicle emissions and residential activities and 3) in a building located at the landfill of western Athens (4 m) influenced by the industrial zone of Athens as well as by an occasional fire episodes at the landfill. Sampling was carried out using a high

volume sampler equipped with holders for a glass fiber filter, GFF (25 cm x 20 cm) and polyurethane foam sheet, PUF (25 cm x 20 cm x 5 cm).

Sample preparation: GFFs and PUFs were Soxhlet extracted with dichloromethane and cyclohexane respectively and a liquid chromatography procedure on an alumina-silica gel column was followed to provide a non polar fraction eluted by pentane, containing PCBs and n-alkanes and a semi-polar fraction eluted by 30% dichloromethane in cyclohexane. PCBs were determined by GC-ECD and PAHs and n-alkanes were determined by GC-FID

Quality Assurance: Compound identification was verified by analysis in two different chromatographic systems and standard addition of the studied compounds in selected samples. Analysis of the urban dust organics SRM1649a (NIST, USA) gave 68-138% for PAHs and 86-110% for PCBs of the certified values respectively. LODs were calculated as three times the standard deviation of blank samples and were found to be 0.14-1.84 ng m⁻³ for PAHs in GFF, 0.12-4.33 ng m⁻³ for PAHs in PUF, 0.12-1.17 ng m⁻³ for n-alkanes in GFF, 3.55-7.76 ng m⁻³ for n-alkanes in PUF, 0.05-1.55 pg m⁻³ for PCBs in GFF and 0.59-46 pg m⁻³ for PCBs in the PUF, all calculated for a sampling volume of 385 m³. Sampling experiments showed that loss of gas phase compounds due to PUF breakthrough in the studied range of volatility was less than 72 % at 20 °C for a sampling volume of 200 m³.

Results And Discussion

Mean concentrations of SOCs

PAHs: PAHs were ranged in particle phase between 17,6 - 243 ng m⁻³ at the urban site, 37,5 - 112 ng m⁻³ in the semi-urban site and 1,8 - 1235 ng m⁻³ at the landfill site. PAHs concentrations in the gas phase were significantly higher and ranged between 24,9 - 847 ng m⁻³ at the urban site, 36,8 - 448 ng m⁻³ at the semi-urban site and 9,7 - 4328 ng m⁻³ at the landfill site. Diagnostic ratios of PAHs indicate that traffic originated emissions to be responsible for the PAHs levels at the urban and semi-urban site and industrial emissions by combustion of heavier fractions of oil and occasional fire episodes at the landfill are responsible for the elevated PAHs levels at the landfill site.

n-alkanes: The concentrations of n-alkanes C18-C36 to the particle phase were ranged between 58,4-1640 ng m⁻³ at the urban site and 198-964 ng m⁻³ at the semi-urban site. The average value of Carbon Preference Index (CPI) was found to be 1,04 at the urban site and 1,11 at the semi-urban site, while the mean % percentage contribution of biogenic alkanes was 8,7 and 9,7% respectively. Seasonal and wind direction variation of CPI and biogenic alkanes showed that n-alkanes from biogenic sources were increased during fall and winter as well as when north winds transfer particulate matter from remote areas. Anthropogenic sources (combustion of fossil fuels) were the more important sources of n-alkanes as it can be seen by their profile in the particle phase.

PCBs: The total concentration of the 7 congeners in the particle phase was ranged between 0,26-112 pg m⁻³ at the urban site, 7,5 to 43,6 pg m⁻³ to the semi-urban site and

1,40 – 315 pg m^{-3} at the landfill site. Their total concentration in the gas phase was ranged between 50,7 -674 pg m^{-3} at the urban site, 32,6 to 818 pg m^{-3} at the sub-urban site and 21,9-1835 pg m^{-3} at the landfill site. PCBs at the urban and the semi-urban site were found to be increased in the case of south and west winds blowing from the industrial reasons, while in the landfill site PCBs concentrations were found to be increased during and after a major fire episode.

Temperature dependence of gas phase concentration of SOCs

The temperature dependence of gas phase concentration of SOCs expressed as partial pressure can provide information about the magnitude of local emissions, processes like volatility from surfaces, soil, vegetation or other matrices and/or transport from other areas [Hoff et al, 1998]. The regression data for the relation $\ln P = mT^{-1} + b$ [1] (P in Atm, T in K) are presented in **Table 1** for 37 samples taken at the urban site for the period January to December 2000. Values of m and b are similar to those obtained in other studies [Sofuoglou et al, 2001] and in a limited sampling campaign for PAHs in the same site during 1998 [Sitaras et al 2004]. It can be suggested by the determined values of slopes that for some PAHs, n-alkanes and PCBs gas phase data can be classified to groups of three wind directions or two wind sectors representing air masses with different origin. SOCs situated to the middle of the examined volatility range (PHE to PYR, C20, C21 and CB153) showed different behavior according to wind direction. Statistically insignificant regression or shallower slopes indicate the influence of local emissions directly to gas phase as well as processes by which SOCs are transported directly to gas phase from other matrices [Hoff et al, 1998].

Temperature dependence of gas-particle partition

Yamasaki suggested (1982) the use of temperature dependent thermodynamic partition constant K ($\mu\text{g m}^{-3}$) described by $K = [A]/([F]/[\text{TSP}])$ [2] where [F] and [A] are particle and gas phase concentrations of the SOCs (ng m^{-3}) and [TSP] is the particle concentration ($\mu\text{g m}^{-3}$). Yamasaki assumed that adsorption of the gas on the particle surface follows a Langmuir isotherm: $\log K = m_Y T^{-1} + b_Y$ [3], where m_Y and b_Y are constants for the individual compounds and m_Y seemed to be related to the heat of sublimation of the individual compound. (Pankow, 1987) proposed the use of a more convenient and intuitive form of partition constant K_p ($\text{m}^3 \mu\text{g}^{-1}$) $K_p = ([F]/[\text{TSP}])/[A]$ [4]. Pankow also proved that m_Y depends on the enthalpy of desorption and b_Y on the specific area of the TSP and the molecular weight of the compound. The partition constants K_p of SOCs have been calculated according to equation [4] in order to examine their temperature dependence. The logarithm of partition constant K_p has been correlated to the inverse absolute temperature T (K^{-1}). Samples were divided in three different wind sectors (south sector, north sector and west sector). Plots of $\log K_p$ vs $1/T$ for PCBs had steeper slopes for south sector indicating adsorption from gas phase to particles while slopes for the plots of n-alkanes and PAHs were shallower for south sector indicating that the gas phase of these SOCs was more than the equilibrium predicts probably influenced by direct emission of vehicles. West sector plots lack of linearity indicating

loss of equilibrium due to atmospheric reactions taking place in the gas and particle phase.

Table 1. Regression parameters for the equation $\ln P = mT^{-1} + b$ for 37 samples taken in an urban site in Athens center for the period January-December 2000, where N is the number of available samples included in the regression. Classification of samples according to the three main wind directions.

SOC	Classification	m	b	r ²	N	p
ACF	All samples	-7296	-1,35	0,31	37	<0,01
ACE	All samples				36	NS
FLU	All samples	-6175	-5,44	0,26	36	<0,01
PHE	South wind	-5328	-8,5	0,49	15	<0,01
	West wind	-7255	-1,14	0,29	12	<0,05
	North wind	-2881	16,5	0,32	11	<0,05
ANT	All samples				37	NS
FLA	South wind				17	NS
	West wind				12	NS
	North wind	-3774	-14,7	0,39	11	<0,05
PYR	South wind				17	NS
	West wind				12	NS
	North wind	-4026	-14,8	0,42	10	<0,05
CHR	All samples	-4201	-14,0	0,26	34	<0,01
BbkFLA	All samples	-6879	-5,30	0,52	19	<0,01
BaP	All samples	-5383	-10,5	0,46	12	<0,01
C18	All samples	-5298	-6,8	0,43	33	<0,01
C19	All samples	-4888	-8,8	0,34	34	<0,01
C20	South Wind				16	NS
	North and West winds	-4039	-12,2	0,36	19	<0,01
C21	South Wind	4943	-43,2	0,30	16	0,05
	North and West winds	-4814	-9,6	0,22	18	0,05
CB28	All samples	-5474	-7,3	0,40	14	<0,05
CB52	All samples	-8012	1,12	0,26	16	<0,05
CB101	All samples	-6924	-3,4	0,72	19	<0,01
CB118	All samples	-3906	-14,1	0,57	14	<0,05
CB153	South and West winds	-2862	-17,1	0,25	12	<0,01
	North winds				5	NS
CB138	All samples	-9291	-4,1	0,34	12	<0,05
CB180	All samples	-7606	-2,2	0,44	14	<0,05

NS: non significant

Dependence of partition constant on vapor pressure and octanol-air partition coefficient

The gas-particle partitioning of SOC was studied by correlating the partition constant (K_p) to the sub-cooled liquid saturation vapor pressure (P_L^o), calculated for each SOC by theoretical models [Paasivirta et al, 1998] and to the octanol air partition coefficient (K_{OA}) for several SOCs, which K_{OA} was known. Regression data for the vapor pressure approach in the form of: $\log K_p = m_r \log P_L^o + b_r$ [5] are presented in **Table 2**, for the K_{OA} approach in the form of $\log K_p = m_{OA} \log K_{OA} + b_{OA}$ [6] are presented in **Table 3**. Slopes m_r should be taking the value of -1 according to the theory [Pankow 1987]. As it can be seen m_r are taking greater values and the m_{OA} values seem to follow this tendency having an average value equal to the absolute value of m_r . Similar values of m_r and m_{OA} were found in other studies too [Lohmann et al 2000, Simsik et al 1998 Finizio et al 1997].. Comparison with the data obtained in the same site during the limited sampling campaign for volatile PAHs of 19 samples during the period December 1997 and July 1998 [Sitaras et al 2004; Sitaras et al 2002; Sitaras and Siskos 2000] shows similar m_r , b_r , m_{OA} , b_{OA} values but it must be taken into consideration that more SOCs are included in regressions presented in this study and samples are well distributed concerning seasonal and meteorological variation. It can be noted that the variation in m_r is less than the variation in m_{OA} but still the values of K_{OA} for several compounds are not known (volatile PAHs as acenaphthylene, acenaphthene and non-volatile PAHs like benzo[a]anthracene, chrysene, benzo[b and k]fluoranthene, benzo[a]pyrene). As a result of this lack of data, m_r contains more information concerning the partition.

Table 2. Regression parameters for the equation $\log K_p = m_r \log P_L^o + b_r$ for 37 samples in an urban site in Athens center for the period January-December 2000, where N is the number of SOCs included in the regression (PAHs, n-alkanes and PCBs). All the regressions are statistically significant at $p < 0,05$

Parameter	$x \pm s$	Maximum-Minimum	
m_r	$-0,36 \pm 0,09$	-0,09	-0,47
b_r	$-3,77 \pm 0,44$	-2,07	-4,03
r^2		0,88	0,18
N		20	9

Table 3. Regression parameters for the equation $\log K_p = m_{OA} \log K_{OA} + b_{OA}$ for 30 samples in an urban site in Athens center for the period January-December 2000, where N is the number of SOCs included in the regression (PAHs, n-alkanes and PCBs). All the regressions are statistically significant at $p < 0,05$.

Parameter	$x \pm s$	Minimum-Maximum	
m_{OA}	$0,41 \pm 0,25$	0,16	1,31
b_{OA}	$-6,22 \pm 2,14$	-14,14	3,62
r^2		0,24	0,94
N		4	16

Conclusions

Partition of SOCs can be described with the vapor pressure approach as well as with the octanol-air partition coefficient approach for the Athens data. Using one of the two descriptors the partition behavior of the three classes of compounds (PAHs, n-alkanes, PCBs) can be described as one group of compounds. The use of K_{OA} although is limited because K_{OA} values cannot be calculated for all the compounds studied. The partition behavior of SOCs in Athens basin showed differences caused by either different emission processes or variation in the meteorological conditions as it was shown by the temperature dependence of gas phase concentration and the gas particle partition constant.

References

- [1] Bidleman TF, Atmospheric Processes, Environ Sci Technol 1988, 22, 361.
- [2] Finizio A et al, Octanol-Air Partition Coefficient as a Predictor of Partitioning of Semi-Volatile Organic Chemicals to aerosols, Atmos Environ 1997, 31(15), 2289.
- [3] Hoff RM, Brice KA, Halsall CJ. Nonlinearity in the slopes of Clausius Clapeyron plots for SVOCs; Environ.Sci.Technol 1998, 32, 1793.
- [4] Lohmann R. et al, A Comparative Study of the Gas/Particle Partitioning of PCDD/Fs, PCBs and PAHs, Environ.Sci.Technol. 2000, 34, 4943.
- [5] Paasavirta J, Sinkkonen S, Mikkelsen P, Rantio T, Wania F. Estimation of vapor pressures, solubilities and Henry law's constants of selected POPs as functions of temperature. Chemosphere 1999, 39, 811.
- [6] Pankow JF. Review and comparative analysis of the theories on partitioning between the gas and aerosol particulate phases in the atmosphere. Atmos Environ 1987, 21, 11, 2275.
- [7] Pankow JF, An Absorption Model of Gas-Partitioning of Organic Compounds in the Atmosphere, Atm Environ 1994, 28, 185.
- [8] Simcik M et al, Gas-Particle Partitioning of PCBs and PAHs in the Chicago Urban and Adjacent Coastal Atmosphere: States of Equilibrium, Environ Sci Technol 1998, 32, 251.
- [9] Sitaras IE, Siskos PA, Physicochemical Characterization of Organic Aerosols in Athens Atmosphere, Physical Chemistry 2000, Proceedings of the 5th International Conference of Fundamental and Applied Aspects of Physical Chemistry, September 2000, Belgrade, Yugoslavia.
- [10] Sitaras IE, Maurovouniotis V, Misailidou E, Siskos PA, Octanol-Air Partition Coefficient as a Descriptor of Partitioning of Semivolatile Organic Compounds on Urban Aerosols, 8th FECS Conference 2002, Environmental Science and Pollution Research, Special Issue 3 2002, 41.
- [11] Sitaras, I.E., Bakeas, E.B., Siskos, P.A., Gas/particle partitioning of seven volatile polycyclic aromatic hydrocarbons in a heavy traffic urban area, Science of the Total Environment, 2004, 327, 249.
- [12] Sofuoglou A et al, Temperature dependence of gas phase PAHs and organochlorine pesticide concentration in Chicago air, Atmos Environ 2001, 35, 6503.
- [13] Yamasaki H, Kazuhiro K, Hiroko M, Effects of ambient temperature on aspects of air-borne polycyclic aromatic hydrocarbons, Environ.Sci.Technol. 1982, 16(4), 189.

POWER PLANT FLY ASH-SOURCE OF TRACE ELEMENTS IN AMBIENT AIR

J. Jekić, M. Grbavčić and Z. Stoimirović

*Institute for Technology of Nuclear and Other Mineral Raw Materials,
86 Franchet d'Esperey St., 11 000 Belgrade, Serbia and Montenegro*

Abstract

Fossil fuels are widely used in modern power stations to produce electricity. Besides energy, a variety of by-products are also obtained. Coal-fired electric generating stations produce large amount of coal combustion products (CCP), such as fly ash, bottom ash, flue gases desulfurization sludge, and so on. Only part of these products is used in different applications. The rest of CCP is landfilled where it is exposed to different influences-hence, some relatively non-soluble elements can become soluble (and pollute surface and ground waters); some particles can be blow by wind (far from source) and become a part of ambient air in some surrounding settlements; this also refers to surrounding soil.

This paper presents results of air quality monitoring (AQM) which was conducted at three different locations (two in urban and one in rural area). One of these locations is in surrounding of Power plant *Nikola Tesla A, Obrenovac*. Amounts of total suspended particles (TSP) and trace elements (such as Mn, Cr, Cd, Ni, Pb, Zn) were measured and compared. Results of this investigation are presented and discussed in this paper.

Introduction

One of the most versatile and therefore desirable forms of energy is electricity. For example, electricity accounts for more than one third of the total energy consumption in the US and more than half of the Nation's electricity is produced by burning coal [1]. Combustion of coal in power generating plants produces a number of residues (bottom ash, boiler slag, fly ash, flue gas desulfurization sludge, and non-captured particles). The relative amount of each residue depends on the power plant configuration and on the emission control devices available. Fly ash is collected by means of electrostatic precipitation and constitutes about 70% of the total amount of residue generated in coal-fired power plants. Trace metals, though present as a relatively small fraction in fly ash, are of special interest, due to their cumulative build up, long life, and high toxicity to man, plants, and animals through air, water, and soil intake [2]. Since many trace elements existing in fly ash can leach out and contaminate soils as well as surface and groundwater resources, but become a part of surrounding air, the study of them has been regarded as important in connection with protection of the environment.

Results and Discussion

Air quality monitoring was conducted at three different locations for two months period (March-April 2004). These locations are settled in urban (Obrenovac

and Belgrade city) and rural area. The amount of TSP was measured according to the ASTM 1739 standard method. The amount of trace metals from non-soluble part of TSP was measured according to the standard atomic absorption spectroscopy methods. The metal content in all samples was determined by using a Perkin Elmer Analyst (model 300). The results of TSP concentrations are presented at Figure 1.

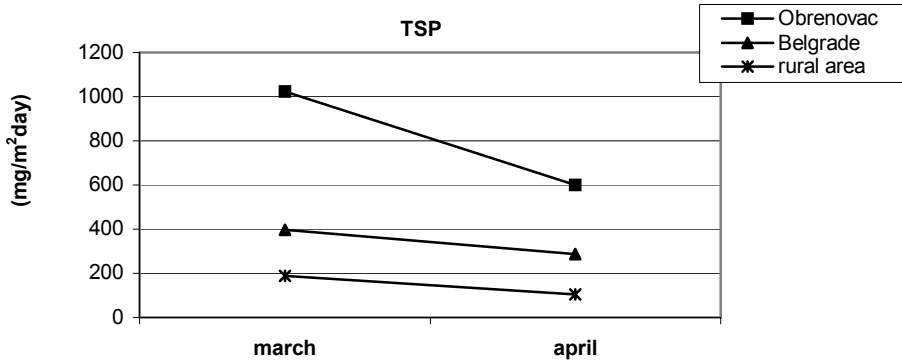


Figure 1. Concentration of TSP at three different locations

As it can be seen from this figure, the TSP concentration is greatest at Obrenovac sampling site than at other two sites. This value is also higher than value given as maximum allowed concentration in ambient air (which is 450 mg/m²/day for this kind of pollutant). We speculate that this is because of short distance (1200m SW) between sampling site-Obrenovac and Power plant *Nikola Tesla A*. The results of TSP and trace metals (obtained for two months period) are given in Table 1 and Table 2.

Table 1. Values of investigated parameters in March

Location	TSP (mg/m ² day)	Mn (mg/m ² day)	Cr (μg/m ² day)	Cd (μg/m ² day)	Zn (μg/m ² day)	Ni (μg/m ² day)	Pb (μg/m ² day)
Obrenovac	1023.50	1.24	78.18	2.5	319.43	258.89	168.02
Belgrade	397.69	0.13	30.06	0.68	148.34	32.64	323.03
rural area	187.56	0.062	10.65	-	53.41	17.45	37.84

Table 2. Values of investigated parameters in April

Location	TSP (mg/m ² dan)	Mn (mg/m ² day)	Cr (μg/m ² day)	Cd (μg/m ² day)	Zn (μg/m ² day)	Ni (μg/m ² day)	Pb (μg/m ² day)
Obrenovac	600.64	0.57	62.31	1.5	258.76	192.31	154.78
Belgrade	287.21	0.101	22.74	0.41	108.73	44.78	221.40
rural area	103.54	0.025	10.97	-	49.36	18.69	40.54

Since the concentration of investigated parameters was significantly higher at Obrenovac sampling site compared to the other two locations, we decided to do some further analyses, and try to determine the connection between *Nikola Tesla A* and ambient air quality in Obrenovac. For this purpose, fly ash samples from plant landfill were collected. Each sample was composite of four samples taken from active cassette. Particle size distribution was determined using coulter multisizer. These results are presented in Table 3 and Table 4.

Table 3. Values of trace metals in ash samples taken from the active cassette

Sample	Mn (%)	Cr (ppm)	Cd (ppm)	Zn (ppm)	Ni (ppm)	Pb (ppm)
1	0.072	120	2,5	62	150	50
2	0.092	135	2,5	88	180	60

Table 4. Granulometric composition of ash samples taken from the active cassette

Sample	+37 µm	-37+30 µm	-30+20 µm	-20+15 µm	-15+10 µm	-10+5 µm	-5+2 µm	-2+0 µm
1	90.50 %	1.85 %	3.27 %	1.46 %	1.28 %	1.16 %	0.47 %	0.01 %
2	37.50 %	4.19 %	14.25 %	11.50 %	13.06 %	14.08 %	5.33 %	0.09 %

Conclusion

As it can be seen from results presented in this paper, there is a significant affect of power plant Nikola Tesla A on ambient air quality in Obrenovac city. The production of fly ash will increase in the future, but fly ash can either be considered as a burdensome waste and source of other pollution, if landfilled, or a tremendous resource for a wide range of uses (e.g. cement industry, road base, minning applications, etc.).

References

- [1] B. R. Stewart, R. S. Kalyoncu, Materials Flow in the Production and Use of Coal Combustion Process, Paper #46, 1999 International Ash Utilization Symposium, Center for Applied Energy Research at the University of Kentucky
- [2] K. Fytianos, B. Tsaniklidi, E. Voudrias, Leachability of Heavy Metals in Greek Fly Ash from Coal Combustion, Environment International, 1998, 24, 477.
- [3] R. Davison, D. Natusch, J. Wallace, C. Evans, Trace element in fly-ash. Dependence of concentration on particle size, Environ. Sci. Technol. 1974, 8, 1107.

ATMOSPHERIC DEPOSITION OF HEAVY METALS IN BELGRADE URBAN AREA

M.D. Tasić¹, Z.R. Mijić¹, S.F. Rajšić¹, D.S. Đorđević², D.J. Radmanović³,
V.T. Novaković¹ and M.N. Tomašević¹

¹*Environmental Physics Laboratory, Institute of Physics, Pregrevica 118, Belgrade*

²*IHTM, Center of Chemistry, Njegoševa 12, 11000 Belgrade*

³*Faculty of Chemistry, POB 158, Belgrade*

Abstract

The primary objective of the present study was to assess anthropogenic impacts of heavy metals to the environment by determination of total atmospheric deposition of heavy metals. Samples of atmospheric deposits were collected from June 2002 to August 2003 at three urban locations in Belgrade using bulk deposition samplers, and were analyzed for heavy metal concentrations. Based upon these results, the study attempted to examine elemental associations in atmospheric deposition and to indicate the potential sources of heavy metal contaminants in the region. Various sources were identified by a principal component analysis as resuspended soil particles, oil combustion, emissions from industrial activities and traffic.

Introduction

Heavy metals in the atmosphere are derived from a variety of sources including the Earth's crust, the oceans, volcanic activities, the biosphere, and a number of anthropogenic processes (i.e. fossil fuel burning, waste incineration, various industrial activities). Direct collection of atmospheric deposition using bulk sampling devices offers a practical approach to monitor atmospheric heavy metal deposition providing valuable information on the influences of atmospheric inputs of heavy metals on the surface environment.

The primary objectives of the present study was to evaluate atmospheric deposition of heavy metals, to examine elemental associations and to indicate the main sources of heavy metals in the city. This study is the part of the integrated monitoring project aimed to estimate the quality of urban air in which suspended particulate matter [1], plants material [2], soil samples, and total monthly atmospheric deposits have been sampling and analyzing on first priority metals .

Experimental

Total monthly atmospheric deposits have been sampling since June 2002 at Student Square, Botanic Garden and Autokomanda site in the urban area of Belgrade. The deposit gauge was an open polypropylene cylinder with an collecting area of about 380 cm² and a height of 40 cm fixed in a basket on a pole 2 m above the ground and it was filled with 20 ml of 10M HNO₃. Samples were evaporated to dryness, digested with 50 ml 0.1M HNO₃ on ultrasonic bath, the digested solution was filtered through an 0,45 μm porosity filters and analyzed by atomic absorption spectrometry using Spectra AA 55 Varian. [3].

Results and Discussion

A total of 44 atmospheric deposits were collected from June 2002 to August 2003 and mean daily atmospheric depositions of heavy metals are presented in Table 1.

Table 1. Average daily atmospheric deposition of heavy metals ($\mu\text{g m}^{-2} \text{day}^{-1}$) in the Belgrade urban area

	Cd	Cr	As	Ni	V	Zn	Cu	Pb
Student Square	0,55	0,62	1,15	4,51	10,49	65,09	249,00	44,37
Botanic Garden	0,62	1,69	4,52	7,01	14,82	109,83	71,81	83,21
Autokomanda	0,63	2,59	12,95	19,70	72,11	180,39	66,35	107,85

High total deposition values of Pb, V and Zn have been observed in samples at Autokomanda site (Table 1) what have been expected due to traffic oriented point. High depositions of Cu in samples at Student Square, comparing to other locations and other heavy metals indicate the possible local source influence.

The principal component analysis (PCA) with Varimax rotation [4] was applied to the atmospheric deposition data to find the groups of elements with similar behaviour for the identification of the sources of atmospheric deposition. The number of significant principal components was selected on the basis of the Kaiser criterion with eigenvalue higher than 1. The rotated component matrixes of the PCA of the atmospheric deposition of heavy elements and major elements are presented in Table 2. The PCA results show that three factors explained 82.5% of the total variance of the atmospheric deposit data.

The first factor shows high loading for Mn, Zn, Cr, Al and Cd and moderate for Fe and As, identifying particles emitted from industrial activities and soil. It was documented in some other studies [4] that, in some cases, it is difficult to separate industrial source from earth crustal source due to soil particles that are always present and mixed with other particles in air.

The results for Factor 1 show that the influences of several sources of heavy elements are not well separated in this factor; for example, Zn may be a marker of crude and fuel oil burning, but can be also emitted from tires, while Cr normally originate from the metallurgical industry while Mn and Al are known as crustal elements.

The second factor presents a high loading for V, Ni, As and Fe indicating the heavy oil combustion sources related to municipal district heating power plants, local heating facilities and industrial power plants using heavy oil and coal.

Table 2. Varimax rotated factor loadings of atmospheric deposition elements concentration data

Element	Factor 1	Factor 2	Factor 3	Communality
Fe	0,465	0,623	0,377	0,75
Cd	0,714	0,412	0,008	0,69
Pb	0,114	0,235	0,749	0,63
Cu	-0,216	0,009	-0,784	0,66
Ni	0,276	0,930	0,007	0,95
Zn	0,814	0,328	0,367	0,91
Cr	0,828	0,361	0,299	0,91
Mn	0,961	0,003	0,008	0,93
Al	0,844	0,284	0,173	0,82
V	0,107	0,979	0,009	0,98
As	0,404	0,816	0,171	0,86
Variance	6,46	1,59	1,01	
Variance %	58,8	14,5	9,2	
Origin	Industrial and re-suspended dust		Traffic	

The third factor has high loading for Pb and was assigned to emissions related to local traffic, hence Pb concentrations may be attributed to still common use of leaded gasoline in Belgrade.

The PCA results presented in Table 2 also have shown that all elements except Cu have positive loadings. Atmospheric deposition of Cu was neither significantly associated with other metals nor strongly dominated by one of the three PCs what is not easy to explain.

Conclusion

The results of PCA indicated three main sources of heavy metal atmospheric deposition in Belgrade urban area: mixture of industrial and resuspended soil and road dust; emission from heating facilities and traffic emission. The highest values of atmospheric deposition were measured at Autokomanda site (except for Cu), very close to the busy road.

Acknowledgement

The authors appreciate receiving financial support from the Ministry of Science and Technology of the Republic of Serbia (Contract No 1449).

References

- [1] S.Rajšić, M.Tasić, V.Novaković, M.Tomašević, *Env.Sci&PollRes.*, 2004, 11(3), 141.
- [2] M.Tomašević, S. Rajšić, D. Đorđević, M.Tasić, J. Krstić, V. Novaković, *Envir. Chem. Lett*, 2004, Online first - DOI: 10.1007/s10311-004-0081-8.
- [3] EU, Ambient air pollution by As, Cd and Ni compounds, Position Paper, 2000.
- [4] C.S.C.Wang, X.D.Li, G.Zhang, S.H.Qi, X.Z.Peng, *Atm. Env.*, 2003, 37, 767.

PARTICULATE MATTER MASS CONCENTRATIONS IN THE AMBIENT AIR OF BELGRADE

M.D.Tasić, Z.R.Mijić, S.F.Rajšić, V.T.Novaković and M.N.Tomašević
Environmental Physics Laboratory, Institute of Physics, Pregrevica 118, Belgrade

Abstract

In order to assess the level of mass concentrations of ambient suspended particles PM₁₀ and PM_{2.5}, pilot study was performed in the urban area of Belgrade. The PM mass concentrations were high (average value being 72 μg m⁻³) in comparison to other European cities and more than 68% of daily samples exceeded the limit value of 50 μg m⁻³. Analysis of the PM₁₀ mass concentrations indicated seasonal variation. Frequency distribution of PM mass concentrations and wind speed was best represented by log-normal distribution. Physical and chemical characterization of suspended particulate matter was accomplished by electron microscopy methods.

Introduction

Airborne particulate matter PM₁₀ and PM_{2.5} (less than 10 μm and 2.5 μm in size) in the last decades have attracted much attention due to their adverse impact on human health by inducing chronic respiratory illness, cancer and premature death [1, 2]. These findings have underlined the importance of ambient particles, explicitly, mass concentration measurements, physico-chemical characteristics, as well as their spatial and temporal variation, especially in cities with large populations. European Commission Directive [3] establishes an annual limit for average PM₁₀ value of 40 μg m⁻³, and a daily limit value of 50 μg m⁻³ to be met by 2005. In this paper annual average and daily PM mass concentration values were assessed to compare them to the corresponding EU standards.

Experimental

During the period of June 2002 to June 2003, sampling of PM₁₀ and PM_{2.5}, was carried out at three sites in the urban area of Belgrade. Suspended particles were collected 24^h on Pure Teflon filters, Whatman Ø 47 mm, using the low volume air sampler Mini-Vol Airmetrics Co., Inc., (5 l min⁻¹ flow rate). Filters were equilibrated for 48^h at the temperature T=20°C and humidity RH around 50% and weighed in clean room Class 100. The morphology, size distribution and semi-quantitative chemical composition of the suspended particles were examined by a scanning electron microscope.

Results and Discussion

Daily mass concentrations of 105 PM₁₀ (coarse particles) and 49 PM_{2.5} (fine particles) were determined. The mean values and basic statistical parameters are presented in Table I. On average, a seasonal variation was found: mean 24 hours PM₁₀ mass concentrations were 96 μg m⁻³ and 64 μg m⁻³ in winter (heating season) and summer

respectively. The mean 24 hours PM_{10} concentration value, over whole measuring period was $72 \mu\text{g m}^{-3}$, more than 68% of days had concentrations above limit value of $50 \mu\text{g m}^{-3}$.

During the high pollution episode, between 9 and 12 July 2002, calm and stable atmospheric conditions occurred: wind speed was $< 2 \text{ m s}^{-1}$, no rain was recorded, daily temperatures were $> 30^\circ\text{C}$, so intensive photochemical reactions resulted in the secondary fine ($PM_{2.5} / PM_{10} = 0,96$) particles.

Table I. Statistical parameters of daily PM mass concentrations ($\mu\text{g m}^{-3}$) in Belgrade from June 2002 to June 2003

	Period	N	X_A	S.D	X_G	Max	Min	Med.	98 th Percentile
PM_{10}	Summer	80	64	28	58	164	12	60	134
	Winter	25	96	73	78	362	21	83	284
	Whole period	105	72	45	62	362	12	63	188
$PM_{2.5}$	Summer	17	35	16	30	78	3	36	68
	Winter	32	75	61	60	333	12	56	227
	Whole period	49	61	53	47	333	3	44	169

X_A – Arithmetic mean; S.D.– Standard arithmetic deviation; X_G –Geometric mean.

During the simultaneous measurements of PM_{10} and $PM_{2.5}$ particles in November and December, PM_{10} and $PM_{2.5}$ concentrations data were very well correlated (Pearson's coefficient $R=0.99$), which indicated the same source for fine and coarse particles. The mass percentage of $PM_{2.5}$ was 85% of PM_{10} and it was the period with the highest PM mass concentrations up to $362 \mu\text{g m}^{-3}$ for PM_{10} and $333 \mu\text{g m}^{-3}$ for $PM_{2.5}$ particles. The high pollution episode was mainly due to the lasting of the persistent stable conditions for many days.

Three theoretical distributions (log-normal, Weibull, gamma) were selected to fit the PM_{10} , $PM_{2.5}$ and wind speed distributions [4, 5]. It was found that the log-normal distribution was the most appropriate one to represent the actual air pollution data and wind distribution. The fitted results of log-normal distributions for PM_{10} and $PM_{2.5}$ mass concentrations and wind speed are presented in Fig. 1. Suspended particles analyzed by SEM were classified into several classes. The majority were typical fly-ash particles, produced in combustion processes, containing Si, Ni, V, Pb, Zn and Fe. Particles with high Pb contents were observed indicating the traffic as the significant pollution source. Gypsum (containing Ca and S) as spherical agglomerates or irregular shape; Si-rich aluminosilicates as mineral dust (irregular shapes) and Fe-rich clusters, usually spherical in shape were also obtained.

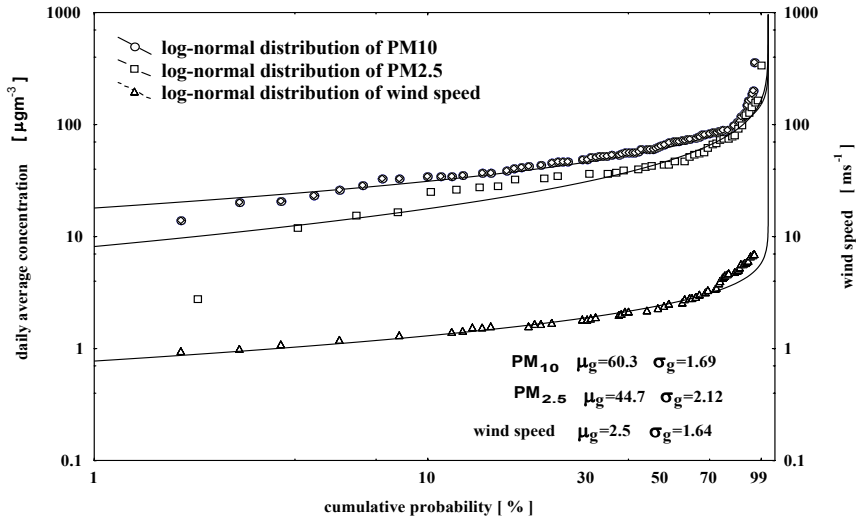


Figure 1. The fitted results of log-normal distributions for PM_{10} , $PM_{2.5}$ and wind speed; μ_g -geometric mean; σ_g - standard geometric deviation (shape factor).

Conclusion

Gravimetric analyses of 154 PM samples were performed in Belgrade. 68% of samples exceeded the level of $50 \mu\text{g m}^{-3}$ (EU standard). Strong seasonal modulation existed, possibly attributed to the higher traffic density and combustion of fossil fuels for heating during winter, as well as to the prevailed meteorological conditions. During the exceptional high pollution days, both in the summer and winter periods, high production of secondary aerosols occurred, (increase of $PM_{2.5}$ in respect to PM_{10}). The results could be used in the future to assess the effectiveness of the implemented emission control strategy.

Acknowledgement

The authors appreciate receiving financial support from the Ministry of Science and Technology of the Republic of Serbia.

References

- [1] J. Schwartz, D.W. Dockery, L.M. J. Neas, *Air Waste Manage. Assoc.*, 1996, 46, 927.
- [2] D.W C. Dockery, C.A. Pope, *Ann. Rev. of Public Health*, 1994, 15, 107.
- [3] EU Commission. Council Directive 1999/30/EC.
- [4] D. Mage, W. Ott, *Atmos. Environ.*, 1984, 18, 163.
- [5] H. Lu, G. Fang, *Sci. Total Environ.*, 2002, 298, 119.

ANALYSIS OF AIR POLLUTION AND WIND EPISODIC MEASUREMENTS IN KOSJERIC (Serbia)

P. Gburčik¹, D. Marković², V. Gburčik³

¹*Center for Multidisciplinary Studies, Belgrade, Serbia and Montenegro,*

²*Faculty of Physical Chemistry, Belgrade, Serbia and Montenegro,*

³*NGO Green Limes, Belgrade, Serbia and Montenegro*

Abstract

Parallel measurements of air quality and meteorological parameters were conducted during two episodes, with the use of three air pollution devices and an automatic meteorological station. The experiment brought better understanding of the atmospheric circulation and air pollution conditions in the investigated region.

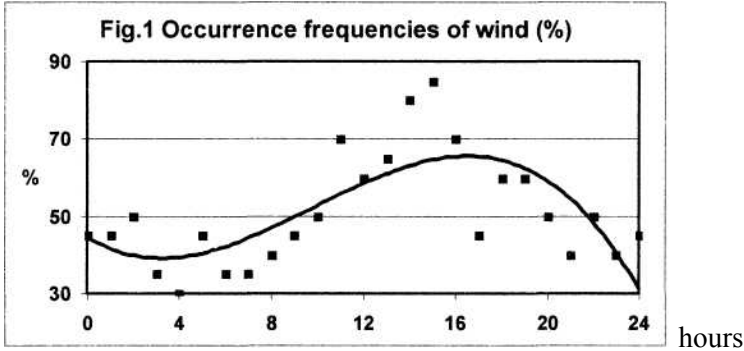
Introduction

The object of this investigation was the control of the air quality in Kosjeric, a small town in Central Serbia. In the neighborhood of the town is a cement factory and the investigation should help to decide whether the activities of this factory contribute significantly to the air quality in the town. Air pollution (concentration of particulate matters in the air, as well as the content of heavy metals in the particels), was measured daily during two episodes, at three locations in the town. The samples were 24-hour values of concentration. Total suspended particles (TSP) were collected by using a low-volume air sampler (16.2 l min⁻¹ flow rate) and particle mass was determined gravimetrically. Relevant meteorological elements were measured parallel to air quality, with an automatic station positioned at the roof of the municipality hall. Special attention was dedicated to the wind direction data. The hourly values of these data made it possible to deduce some conclusions about the wind regime and trajectories of particulate matters.

Results and Discussion

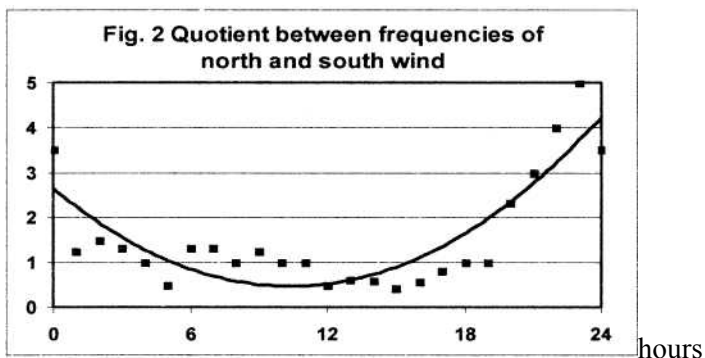
Wind regime in Kosjeric. The topography of the region Kosjeric may be described as a rather narrow valley of the mountain river Skrapez, oriented from NW to SE. Upstream of the town, at the distance of about 2km is located the cement factory. The climate of Kosjeric is influenced by the surrounding topography. The prevailing winds are canalized along the river. Easterly and westerly winds are almost absent. For this reason, all directions with the northern component were grouped in the sector N and all directions with the southern component were grouped in the sector S. In this way were obtained frequencies of downstream directions (N) and upstream frequencies (S) [1,2]. The real situation was simplified (modelled), as if there exist only north and south winds. Meteorological elements were measured with an automatic station, positioned at the roof of the municipality hall. The main meteorological elements were obtained in hourly intervals. Special attention was dedicated to the wind direction data. The meteorological station, as well as all air pollution measurement instruments was

active in the course of two episodes. The first episode lasted from 27 November 2003 to 18 December 2003, and the second one from 9 February 2004 to 23 February 2004. In spite of the relatively short measuring periods, it was possible to obtain the structure of the daily wind direction changes.



From the Fig.1. may be concluded that the windiest time during the day is in the afternoon, with the maximum around 16 hours. This time of maximal frequency was obtained by the polinomial analyzis, although separate measurements, represented by points at the graph show different values. Appearance of the wind of any direction is an important fact because the transport of air pollution occurs mainly in the downwind direction. During the calms the dispersion of the air pollution occurs uniformly in all directions. Since the wind direction changes in the course of the day, the air pollution transport must also have its daily course [3]. The change of the direction of air pollution transport means that the same pollution may come back to a location. This is a sign of poor ventilation in spite of the present wind. Consequently very high TSP concentration has been found in 24-hour samples. Average daily concentrations were more than $800 \mu\text{g m}^{-3}$ during the first episode. The reason for such a finding is not only the cement factory emission but also this exceptional wind behaviour.

The Fig.2. presents the quotient between the frequencies of winds from the north sector and the frequencies of winds from the south sector (Q). This quotient oscillates in individual situations between 5 and 0,5. Values greater than 1 mean that N is more frequent. Values less than 1 mean that S is more frequent. In some situations N was (during the night) five time more frequent than S, but during the daytime S was often two times more frequent. Here is also important to pay more attention to the line that represents the most probable values, obtained by polinomial analysis, than to individual values which may demonstrate large dispersion.



Conclusion

General ventilation conditions are better in the daytime. The winds from the south sector are more frequent in the daytime, while the winds from the north sector are more frequent during the night. In this way the air pollution is transported by day to the north and by night to the south. So the same air pollution is transported upstream or downstream.

References

- [1] P. Gburčik, *Clim.Modell.*, 1985,.Rep. WMO/TD, 63, 8.12-8.16.
- [2] P. & V. Gburčik, *Proc. IAUC/WMO*, 2003, ICUC5, O_6.1, 1-4
- [3] EEA, *Towards a local sustainability profile: EU common indicators*, 2001

SELECTIVE REDUCTION OF PAH CONTENT IN CIGARETTE TOBACCO SMOKE BY CATALITIC CRACKING PROCES

V. Radojičić¹, M. Nikolić¹, B. Adnađević² and A. Jovanović³

¹*Faculty of Agriculture, 11080 Belgrade-Zemun, SCG*

²*Department of Physical Chemistry, University of Belgrade, POB 137, 11001 Belgrade, SCG*

³*Institute for Health Protection, Belgrade, SCG*

Abstract

The possibility of TAR (dry particulate matter without nicotine) content reduction and selective reduction of PAH (polynuclear aromatic hydrocarbons) content by using zeolite catalysts has been examined.

The smoke condensate, extracted from Cambridge filter with methanol, has been analyzed by GC-MS.

The obtained results are confirming the possibility of effective and selective catalytic reduction of PAH in tobacco cigarette smoke. The determined reduction degree for TAR was 0,3 - 0,8 and the PAH reduction degree was 24 - 73.

Introduction

In the total amount of cigarette smoke the part of TPM is around 8%. Less than 1% of that are PAH compounds [2]. Distributed in between the streams, as the coefficient of SS/MS is 2 - 20 [4]. Among 4863 substances identified in cigarette smoke, 755 are in the class of PAH [3,7].

The content of PAH in the smoke varies with many factors: type of cigarette, cigarette design and burning conditions. The most important factors are type of tobacco and temperature of combustion zone [6].

According to a recently published researches of American Health Foundations [2], the quantity of PAH in the smoke of American blended cigarette is in the range of 62 to 193 ng/cig. Reported quantity of total PAH in the flue-cured cigarettes is at the level of 12,641 µg/cig [5]. There is no any report on a level of PAH in the smoke of domestic cigarettes.

Decreasing of the PAH content in the cigarette smoke anticipate the decrease of the TAR contents, too. For the TAR decrease the method of nonselective filtration are used mostly [1]. As the selective filtration regarding particulate PAH compounds on zeolites has been confirmed [5], the possibility of selective PAH reduction in the smoke of cigarette by catalytic cracking on zeolite catalysts and adsorption on a silica adsorbent has been examined.

Experiment

On the Department of Physical Chemistry, University of Belgrade, zeolite catalysts-type Y (under the mark 2 and 3), pentasil type (mark 1) and silica adsorbent (mark 4), have been synthesized.

Catalysts have been applied as a powder on the cut tobacco blend in a quantity of 3%. After the equalization of the blend, the cigarettes were made on the ciga-

rette making machine type MOLINS-9. For the experiment only the cigarettes with the weight of $970\text{mg} \pm 0,5$ have been used.

The cigarettes were smoked on the BORGVALDTH RM 20/CSR under the standard conditions: puffing 2s, smoldering 58s, buff lent 23 mm, puffing volume of 35ml/s.

The smoke condensate was extracted from Cambridge filter with methanol. GC-MS analyses (equipment Gas Chromatograph 6890 Network GC System with mass detector 5973 Network Mass Selective Detector) were as follows:

- $2\mu\text{l}$ methanol solution injected, using Pulsed Splitless injecting regime at pulse drop from 30psi.
- Column capillary Model No. Agilent 19091S-433 HP-5MS, $0,25\text{mm} \times 30\text{mm} \times 25\mu\text{m}$, was used.
- Temperature of injector $250\text{ }^\circ\text{C}$; temperature program, from $50\text{ }^\circ\text{C}$ (4min), $8\text{ }^\circ\text{C}/\text{min}$ to $310\text{ }^\circ\text{C}$ (5min); 1ml/min He flow.

Degree of reduction

$$\text{DR} = \frac{C_0 - C_i}{C_0} \times 100$$

where is:

C_0 - content of component in the smoke of non-modified cigarettes

C_i - content of component in the smoke of cigarettes with zeolite catalysts.

Results

In the table 1. TAR content and PAH content in the smoke of experiment cigarettes are presentment.

Table 1. The content of total PAH and total TAR in cigarette tobacco smoke

	0	1	2	3	4
PAH ($\mu\text{g}/\text{cig}$)	0,7039	0,1881	0,5181	0,5351	0,7037
DR (%)		73,3	26,4	23,9	0
TAR (mg/cig)	11,89	11,79	11,85	11,80	14,01
DR (%)		0,8	0,3	0,7	+17,8

0 – non-modified cigarette (control), 1 – cigarette with pentasil type zeolite catalyst, 2 - cigarette with Y type zeolite catalyst, 3 – cigarette with ultra-stable Y type zeolite catalyst, 4 – silica adsorbent.

According to obtain results the following conclusion could be drawn:

- The PAH content could be reduced by used of zeolite catalysts from 24 - 73%.
- The TAR content could be reduced from 0,3 to 0,8%, and
- The use of silica adsorbent causes a slight increase in TAR and no any changes in PAH content in the cigarettes tobacco smoke.

Selectivity of zeolite acting regarding particulate PAH compound is shown in table 2.

Table 2. Selectivity of zeolite acting regarding particulate PAH compound

PAH $\mu\text{g}/\text{cig}$	0	1	DR%	2	DR%	3	DR%	4	DR%
Naphthalene	0,1178	0,1015	13,8	0,0780	33,7	0,0963	18,3	0,1283	+8,9
Acenaphthylene	0,2305	/	100	0,1490	35,4	/	100	0,1875	18,6
Anthracene	0,0238	0,0218	22,9	0,0398	+40,6	0,0260	8	/	100
Fluorene	0,0235	0,0088	62,5	0,0820	+245	0,0920	+291	0,1055	+349
Fluoranthene	0,1810	/	100	0,0945	47,8	0,1490	17,7	0,1608	11,2
Acenaphthene	0,0305	0,0790	+159	0,0565	+82,5	0,0873	+186	0,0943	+209
Phenanthrene	0,0968	0,0683	29,4	0,0183	81	0,0845	12,7	0,0273	71,8

Pentasil type of zeolite catalyst (sample 1) has been the most selective on acenaphthylene and fluoranthene. Zeolite ultra-stable catalyst (sample 3) has been the most selective on acenaphthylene, too, while Y zeolite type (sample 2) has shown the high selectivity for fluoranthene.

Conclusion

The obtained results are confirming the possibility of effective and selective catalytic reduction of PAH in tobacco cigarette smoke. The changes noticed in catalytic activity and selective ability of catalysts are the consequence of the different structure characteristic, force and force distribution of active catalysts centers of particulars catalyst in reactions of Polycyclic Aromatic Hydrocarbons cracking.

References

- [1] D.W. Eaher, *Rec.Adv.Tob.Sci.*, 1990, 16, 103.
- [2] D. Hoffmann and I.Hoffmann, American Health Foundation, *Tabakforschung International*, 1998, 18(1), 49.
- [3] R.W. Jenkins and Mc Rae D.D., *Rec.Adv.Tob.Sci.*, 1996, 22, 337.
- [4] C. Liang and J.F. Pankow, *Environ. Sci. Technol.*, 1999, 33, 189.
- [5] W.M. Meier, K. Siegmann, *Microporous and Mesoporous Materials*, 1999, 33, 307.
- [6] M. Muramatsu, *Sci. Papers Central Res.Inst.Japan, Tob.*, 1981, 123, 9.
- [7] Mc Rae D.D., *Rec.Adv.Tob.Sci.*, 1990, 16, 233.
- [8] E.L. Wynder and D. Hoffmann, *Tobacco and Tobacco Smoke*, Academic Press INC. New York and London, 1967.

CONTRIBUTION OF EMISSION SOURCES ON METALS CONTENT IN THE AIRBORNE PARTICLES USING PCA

D. S. Đorđević¹, A. J. Mihajlidi-Zelić² and D. J. Radmanović²

¹*ICHtM – Center of Chemistry, Njegoševa 12, Belgrade, Serbia and Montenegro*

²*Department of Chemistry, University of Belgrade, Belgrade, Serbia and Montenegro*

Abstract

Natural aerosol sources in the investigated receptor region are: sea spray, windborn dust, volcanic eruptions in south Italy, desert dust, etc. In the investigated region there are some anthropogenic sources. High temperature sources are emitting aerosol and heavy metals from Ironworks Nikšić, CFPP in Pljevlje etc. Using PCA contributions of various emission sources to the content of metals in the atmospheric aerosol were differentiated. Systematic measurements of metal concentrations in the atmospheric particles on model receptor were made from 1995 to 2000.

Introduction

The topic of this paper is heavy metals in atmospheric particles at the south Adriatic Sea coast as a model receptor. The chosen receptor is located in the eastern part of the town Herceg-Novı (18°33'N, 42°27'E) and it is under influence of various aerosol emission sources, natural and anthropogenic origin. From these emission sources particles can be transported through the atmosphere to the south Adriatic Sea coast [1].

Experiment

At the chosen receptor 24-h samples of the Total Suspended Particles (TSP) were taken each sixth day. Samples of TSP were collected on a boron-silicate fiber glass filters (Schleicher & Schuell) using a High volume sampling system. Filters with collected deposits and blanks were digested with concentrated Supra pure HF (50 %) i HNO₃ (> 69.5 %) in covered PTFE vessels at 130 °C. Concentration of metals were determined using AAS [2]. Obtained concentrations of metals in air were processed by Principal Component Analysis (PCA), for differentiation of the contribution of various emission sources [3].

In the part of the receptor the concentration of some chemical species is:

$$c_i = \sum_{j=1}^m f_{ij} a_{ij} s_j \quad i = 1, 2, \dots, n$$

$f_{ij} a_{ij}$ is a fraction of the species i in particles from the source j , and s_j is total contribution of particles from the source j .

Concentration is a linear combination of all emission sources contributions and fraction of the species i . The problem is mathematically unsolvable because of the infinite number of possible solutions. Using multivariate PCA by SPSS 10 statistical program the principal contributions to the content of elements in the atmospheric particles can be differentiated by analysis of Eigenvalues *varimax* of rotated Eigenvec-

tors. Eigenvectors are in connection with emission sources and represented by Components.

Results and Discussion

The primary data base is results of the individual metal concentrations (ng m^{-3}) in atmospheric aerosol, which are in this paper expressed as average values and standard deviation ($x_{av.} \pm \text{SD}$), of the following elements: Cd (0.3 ± 0.3), Co (0.8 ± 0.5), Cr (2.6 ± 1.7), Cu (4.8 ± 4.7), Hg (2.88 ± 3.34), Fe (502 ± 405), Mn (8.3 ± 9.2), Ni (4.4 ± 9.2), Pb (50 ± 46), Se (0.14 ± 0.63) and Ti (58.8 ± 48.8). Applying the PCA 11 components was obtained. The components which represent contributions of various emission sources are shown in Table 1.

Table 1. Calculated Eigenvalues, relevant Components and rotated values

Comp	Initial Eigenvalues			Extraction Sums of Squared Loadings			Rotation Sums of Squared Loadings		
	Total	% of Var.	Cumul. %	Total	% of Var.	Cumul. %	Total	% of Var.	Cumul. %
1	3.15	28.59	28.59	3.15	28.59	28.59	2.86	25.99	25.99
2	1.34	12.17	40.76	1.34	12.17	40.76	1.36	12.33	38.33
3	1.24	11.29	52.06	1.24	11.29	52.06	1.31	11.87	50.20
4	1.09	9.88	61.93	1.09	9.88	61.93	1.29	11.74	61.93
5	0.93	8.46	70.39						
6	0.85	7.68	78.08						
7	0.78	7.06	85.14						
8	0.65	5.95	91.09						
9	0.50	4.53	95.62						
10	0.29	2.64	98.26						
11	0.19	1.74	100.00						

The first four components with Eigenvalue larger than 1 represents dominant influences. Total contribution of the first four components is 62 % (Tab. 1). The first four components are shown on Fig. 1. Association Fe-Mn-Ti, shown on Fig. 1a), points out to the existence of the common emission source of these elements. Ratio $\text{Mn/Fe} = 1.7 \times 10^{-2}$ and $\text{Ti/Fe} = 1.2 \times 10^{-1}$ in atmospheric aerosol, corresponds to their ratio in the surface layer of the local soil: $\text{Mn/Fe} = 4.3 \times 10^{-2}$ and $\text{Ti/Fe} = 1.7 \times 10^{-1}$. This indicates that local resuspension is the source of these elements [4]. On the Fig. 1a), on the vertical axis F1 the association Pb-Cu can be seen, indicating the traffic as emission source. Association Ni-Cr can be noticed on the axis F2, Fig. 1b); association Cd-Se on the axis F3, Fig. 1c), and on the axis F4, Fig. 1d) association Hg-Co.

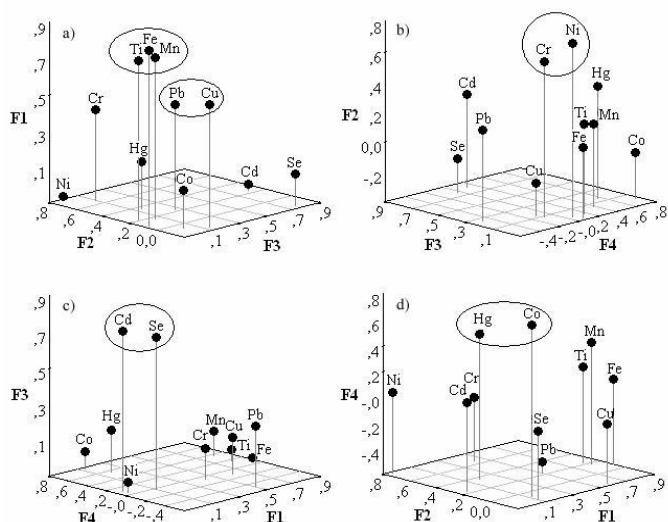


Figure 1. Eigenvalues rotated Eigenvectors (vertical axis is relevant component)

Conclusion

Using PCA, contribution of local emission sources - F1 (resuspension, traffic) is differentiated from other sources (F2, F3 and F4) in the region. This implies that investigated elements have different genesis and atmospheric transport to the model receptor.

Acknowledgement

The authors gratitude the Ministry of Science and Environment of the Republic of Serbia for financial support (Contract No 1449).

References

- [1] D. Đorđević, D. Radmanović, A. Mihajlić-Zelić, M. Ilić, P. Pfenndt, Z. Vukmirović, P. Polić, Principal associations of trace elements in the long-term sampled airborne particulate matter, *Environmental Chemistry Letters*, (2004), in press.
- [2] WMO, Guidelines for Air Quality, Chapter 5. Ambient air quality monitoring and assessment, Geneva, 2000.
- [3] J.H. Seinfeld, S.N. Pandis, Atmospheric Chemistry and Physics from Air Pollution to Climate Change, John Wiley & Sons, New York 1998.
- [4] D.A. Braaten, U.K.T. Paw, R.H. Shaw, Particle resuspension in a turbulent boundary layer - observed and modelled. *Journal of Aerosol Science* 1990, 21, 613.

NEW METHOD OF CATALYTIC REMOVAL OF ZINC FROM MODEL WATERY SOLUTIONS BY MICRO ALLOYED ALUMINIUM BASED COMPOSITE

M. Miljković, M. Purenović, V. Mitić and A. Zarubica

*Faculty of Mathematics and Natural Sciences, Department of Chemistry,
University of Nis, Visegradska 33, 18000 Nis, Serbia and Montenegro,*

Abstract

In this experiment it is studied a new method of catalytic removal of zinc from simulated wastewaters (model watery solutions ZnCl_2 and ZnSO_4) by a composite material based on steel and microalloyed aluminium. The obtained results show that concentration of Zn^{2+} ions is decreased for more than 130 times at first 90 min of treatment, getting into the MAC area.

Introduction

Water is necessary for the existence on the earth. It is indispensable for vital biochemical processes in every organism. Besides that, it has a great significance in industries and everyday life (as solvent, industrial raw material, heat conductor, hygienic means...). The main sources of water pollution are: household wastewaters, wastewaters of cities, industrial and agricultural ones. Industrial wastewaters containing zinc originate from metal industries (plating operations), galvanization, cellulose and paper industry, pharmaceutical industry etc. The maximal allowed concentration (MAC) of zinc is 5 mg dm^{-3} for potable water, so wastewater containing higher concentration have to be refined before discharge. A few methods of removal of zinc from wastewaters are in current use, such as: chemical precipitation with disposal of the resultant sludge that may be recovered. This recovery process and finer refinement include ion exchange methods on zeolites and ion-exchange resins [1].

This experiment scope involves study of a new method of catalytic removal of zinc from simulated wastewaters (model watery solutions ZnCl_2 and ZnSO_4) by a composite material based on steel and microalloyed aluminium, which has roles of a catalyst and a coagulant at the same time. The catalyst based on the new composite material is a metal wire with a steel net plated with active contact mass of microalloyed aluminium PAL-3 quality by molten metal metallization [2]. Microalloyed aluminium is prepared by microalloying aluminium of 99.8 % purity, with: Sn, Ga and Bi. Real structure is determined by flame atomic absorption spectrophotometry on Varian AAS Spectra A-20. Obtained microalloyed aluminium has: 0.105 % Sn, 0.098 % Ga and 0.040 % Bi. The aluminium oxide layer that protects metal against corrosion becomes porous and permeable for different ions, because of numerous defects in crystal lattice, caused with microalloying process. The microalloyed elements form interstitials, vacancies and irregularities of charge distribution in the metal structure. These defects initiate decrease of energy barrier for transport of Al^{3+} and O^{2-} ions. The catalyst surface is amorphous, scales-like; with very spread real area according to geometric one and active due to a presence of deposited metal ions. Steel base, amor-

phous surface of microalloyed aluminium and a huge number of micro-galvanic cells, as well as, macro-galvanic cell Fe-Al_{microalloy} present dipolar electrode systems. Potential of the system Fe / microalloyed Al / Me / H₂O realizes potential of maximal adsorption of ions, neutral molecules and water. Partial anodic and cathodic processes take place on the local micro-cathodes and micro-anodes with previous adsorption of reactive molecules on the surface. Stationary potential of micro-galvanic cell steel-microalloyed aluminium is about -1.15 V/SCE to -1.25 V/SCE (saturated calomel electrode) that enables high electrochemical activity to the catalyst.

Experiment

This experiment procedure comprised the following steps:

- preparation of model watery solutions of ZnCl₂ and ZnSO₄,
- treatment of model solutions with catalytic composite wires,
- sampling of solution probes on every 30 min and finally after 24 h treatment,
- determination of concentration of Zn²⁺ ions by AAS method, assessment of changes in concentration of Zn²⁺ ions during the treatment time.

It was prepared model watery solutions of ZnCl₂ and ZnSO₄ (working volume 0.5 dm³), concentrations of Zn²⁺ ions 2-50 mg·dm⁻³. pH values of model solutions were regulated to 4.5 with diluted HCl, because of avoidance of hydrolysis and formation of colloidal deposits. Higher pH values (≈ 5.1-5.2) would lead to Zn(OH)₂ precipitation and loss of Zn²⁺ ions. Adjusted samples of model solutions were put in plastic baths and zero probes were taken before the catalytic treatment. Catalytic composite wires were activated in saturated NaCl solution (the activation time was 15-30 min). After that, composite wires were immersed in samples solutions and the moment of immersion was the start of treatment. During the catalytic treatment, probes were sampled on every 30 min to 150 minutes and finally after 24 h treatment. Model solutions samples were stirred with a magnetic stirrer (300 rpm, 5 min before sampling). Test tubes with samples probes were centrifuged (3000 rpm, 15 min) removing Zn(OH)₂ deposit. Concentrations of Zn²⁺ ions were determined by flame atomic absorption spectrophotometry (Pye Unicam Sp-9).

Results and Discussion

The results are shown in Table 1.

Table 1. The results of change in concentration of Zn²⁺ ions during the treatment

c (Zn ²⁺) (mg·dm ⁻³)	T (min)
362.50	0
282.50	30
212.50	60
165.00	90
131.20	120
85.00	150
2.75	1440

On the basis of the obtained results (Table 1.), it can be seen that the use of the new catalytic composite material gives the possibility of Zn^{2+} ions concentration reduce to the MAC. This concentration decreased for more than 130 times at first 90 min of treatment, getting into the MAC area. Also, it is registered small rate of Zn^{2+} ions concentration reduction with time, from 90 to 200 min of treatment, and a rapid one to the end. Other experiment results show that the rate of microalloyed aluminium dissolution decreased with pH increase. This is the second reason for adjusting the pH of model watery solutions to 4.5.

The effects of the composite are based on its spontaneous reaction with water. Because of high difference in the stationary potential of steel and electrochemically active aluminium, it is occurred spontaneous polarization of cathodes and anodes, i.e. cathodic and anodic processes. Cations and anions are adsorbed on the local anodic and cathodic regions of the catalyst wire. Some appropriate oxidation-reduction processes that are followed with arising of Al^{3+} ions, water reduction and formation of voluminous, colloidal deposit of $Al(OH)_3$, are performed on the local anodic and cathodic regions. Colloidal deposit of $Al(OH)_3$ has very spread surface, which coprecipitate a part of pollutants from water or the products of their chemical degradation. Every particle that arrives to the composite surface may become participant of numerous physicochemical processes.

Conclusion

This refining process is performed using of the new modern catalytic treatment reducing concentration of Zn^{2+} ions on the satisfied level in simulated wastewaters samples. Known zinc removal processes form new, often undesirable pollutants. Used composite wire can be applied for removal of numerous ionic and colloidal impurities. Further investigations and wastewaters refining may be improved by preparation of a new composite wire with enough spread active surfaces and using of flowing catalytic reactors, which will enable more intensive removal of Zn^{2+} ions for a shorter treatment time.

References

- [1] V.A. Crowle, Effluent Treatment and Materials Recovery from the Metal Finishing Industry Using the Integrated Method of Treatment, *Water Poll Cont.*, London, 1972, 636-645.
- [2] M.L. Purenovic, *Yu - Patent P - 669/92* (1992).

CONTENTS DETERMINATION OF METAL IN COMBINED WATER SOLUTIONS USING EDXRF (SOFTWARE PACKAGE ESP)

D. Grandić-Aleksić¹, N. Pavlović¹ and D. Minić²

¹*NIS Factory of Lubricants FAM, Jastrebačka 14, 37000 Kruševac, Serbia and Montenegro*

²*Faculty of Physical Chemistry, Studentski trg 12, 11001 Belgrade, Serbia and Montenegro*

Abstract

This work is a presentation of an investigation of metal contents in water solutions by using EDXRF (Energetic Dispersion X-Ray Fluorescence). The spectra of the combined solutions were shown the possibility of detection for certain elements present in the solutions. Differences of peak intensities that present a basis for determining the contents of the elements can also be seen. The results of the investigation are given tabularly and graphically.

Introduction

In this work we present an investigation of metal contents in water solutions by using EDXRF. A software package ESP (**E**nvironmental **S**oftware **P**ackage) was delivered with the device type OXFORD XR 400 and it presents a combination of more methods with different parameters such as the voltage (25 kV, 35 kV, 50 kV), the filters (THIN filter, Cu filter or without a filter) in an inert helium atmosphere. The software estimates the results in such a way that the results are taken from the lower energies for the light elements and from the higher energies for the heavy elements. The aim of the work is to check the applicability of the ESP method for the quoted sample type.

Experimental

The spectra of combined water metal solutions were registered by varying the voltage (25 kV, 35 kV, 50 kV) using filter changers (THIN filter, Cu filter or without a filter) in an inert He atmosphere on a device type OXFORD XR 400. The solutions were prepared by dissolving p.a. chemicals (MERCK) in distilled water that contain 10 metals (Ca, Cr, Mn, Fe, Co, Ni, Cu, Zn, Hg i Pb). The concentration of elements was estimated on the basis of the mass fraction of element in the compound and on the degree of dilution (table 1). The concentration of elements is in the range from 0 do 400 ppm.

Results and Discussion

The spectra of the combined solution are shown on Figure 1. On the basis of the spectral lines (peaks) energy we can identify the presents elements, [1,2], and according to the intensity of a peak, their concentration [3].

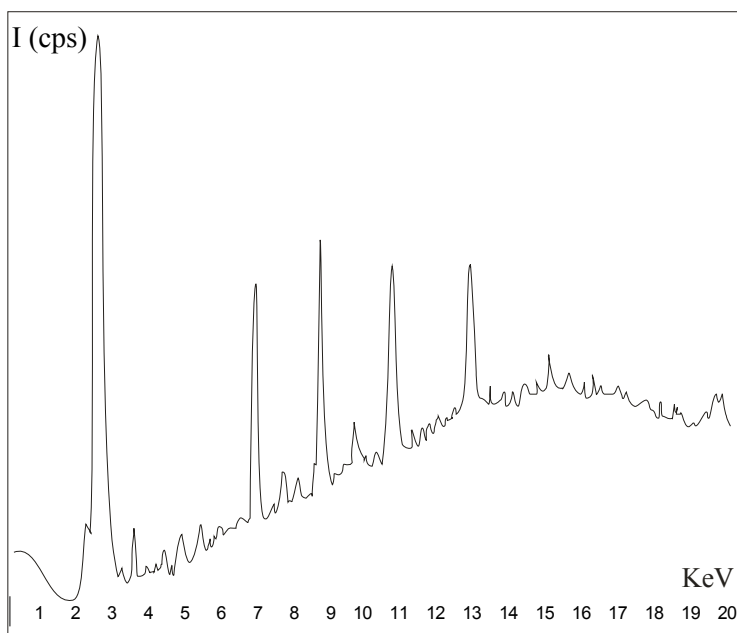


Figure 1. Spectra of the combined element solution

The concentration of each element ($C_{\text{calculated}}$) was estimated according to the mass fraction of element in the compound and to the degree of dilution [4]. The concentration of each element (C_{found}) was obtained according to the results of measurement by the method ESP (table 1).

Table 1. Results of the investigation for the combined solutions by the method ESP

No. Element	20	24	25	26	27	29	30	80	82	
	Ca	Cr	Mn	Fe	Co	Cu	Zn	Hg	Pb	
R6	$C_{\text{calculated}}$	151.5	50.0	8.5		128.8		126.7	402.7	
	C_{found}	120.0	62.6	10.3	< 6	106.5	32.2	110.7	< 5	454.7
	%	79.2	125.2	121.8		82.7		87.3		112.9
R9	$C_{\text{calculated}}$		187.1	12.4	195.5	57.0		27.1	384.1	
	C_{found}		170.8	< 11	191.8	50.5	29.2	24.9	< 5	401.7
	%		91.3		98.1	88.6		91.9		104.6
R13	$C_{\text{calculated}}$		66.4	19.3	156.4	34.6		37.5	33.6	79.5
	C_{found}		52.5	< 10	137.7	27.4	30.5	31.3	31.0	69.4
	%		79.0		88.0	79.3		83.5	92.3	87.3

The spectra of combined solutions show the possibility of detection for the certain elements present in the solutions. Differences of peak intensities can also be seen. They present a basis for determining the contents of the elements.

The results of the investigation are given tabulary and graphically. The relation of the obtained results (C_{found}) on the real concentrations of elements in the solutions ($C_{\text{calculated}}$) can be seen in a graph (Figure 2). It is also shown proportionally in the table 1.

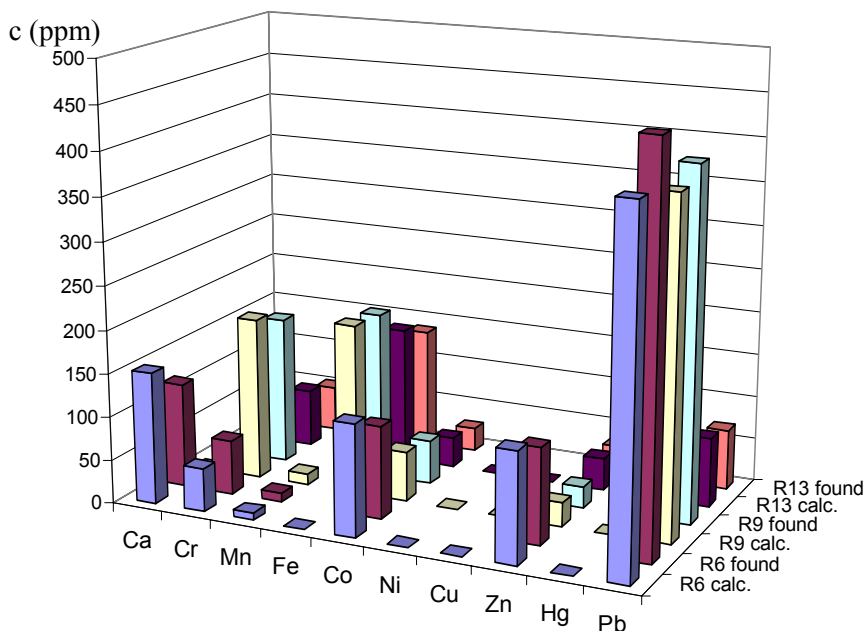


Figure 2. Graphic survey of the investigation results

Conclusion

The combined method ESP is used for the qualitative and semi quantitative analysis. The results of the investigation show that in a range of concentration from 10 to 400 ppm we obtain values lower from the expected ($C_{\text{calculated}}$). It can be explained by the matrix effect (the influence of other elements).

Acknowledgement

This work was supported by *NIS* Factory of Lubricants *FAM*, Kruševac.

References

- [1] A. A. Jovanović, *Atomska spektroskopija – spektrohemijski aspekt*, Fakultet za fizičku hemiju, Beograd, 1999.
- [2] J. A. Bearden, *X-Ray Wavelengths*, *Review of Modern Physics*, 1967, 86-89.
- [3] *OXFORD ESP Manual*, Oxford Instruments, 1991.
- [4] *ASTM D 4307 Standard Practice for Preparation of Liquid Blends for Use as Analytical Standards*, 1988.

CONTENTS DETERMINATION OF Mn, Fe, AND Ni IN WATER BY ENERGETIC DISPERSION X-RAY SPECTROMETER

D. Grandić-Aleksić and N. Pavlović

¹NIS Factory of Lubricants FAM, Jastrebačka 14, 37000 Kruševac, Serbia and Montenegro

Abstract

In this work the investigation of metal contents in water solutions was shown by using EDXRF (Energetic Dispersion X-Ray Fluorescence). On the basis of obtained spectra, of the investigation results and of the formulae of the calibration curves, it can be concluded that appropriate results can be obtained. The increase of sensitivity was confirmed with the increase of atomic number (the growth of the curve slope factor). The degree of correlation (R^2) for all the three lines is close to one which shows a good match of measuring points with the obtained calibration curves.

Introduction

In this work we present an investigation of metal contents of Mn, Fe and Ni in water solutions by using EDXRF.

A qualitative analysis was made by identification of spectrum lines (peaks) on the basis of literature (table) [1,2]. A quantitative analysis was made by using the method FPT25LIQ (Fundamental Parameter Test for Liquide - software package).

Experimental

Primary solutions were prepared by dissolving p.a. chemicals $MnCl_2$, $FeCl_3$ and $NiSO_4$ (MERCK) in distilled water. Spectra were made on a device type OXFORD XR 400. Quantitative analysis was made by using the method FPT25LIQ with control parameters $U=25$ KV, $I=100$ A i t=150 sec. Three series of single liquids samples were investigated, and calibration curves were made for each elements [3].

Results and Discussion

Table 1 shows the energies of single transitions for each element in KeV. The spectra of primary solutions (Figure 1) shows that the received peaks energy of each element corresponds to literature facts [1,2] by which the qualitative analysis was made.

The quantitative analysis was made by using the method FPT25LIQ. The series of single liquid samples were prepared diluting primary liquid samples by distilled water [4]. The concentrations of elements were precised on the basis of mass fractions of an element in a compound and on the degree of the dilution (table 2). Parallely to the concentrations, there are also given the values of the peak intensities of the present elements in cps (count per second) for every examined solution.

Table 1: Elements radiation energies

	Mn (Z-25)	Fe (Z-26)	Ni (Z-28)
K _a (keV)	5.90	6.40	7.48
K _b (keV)	6.49	7.06	8.26
L _a (keV)	0.64	0.71	0.85
L _b (keV)	0.65	0.72	0.87

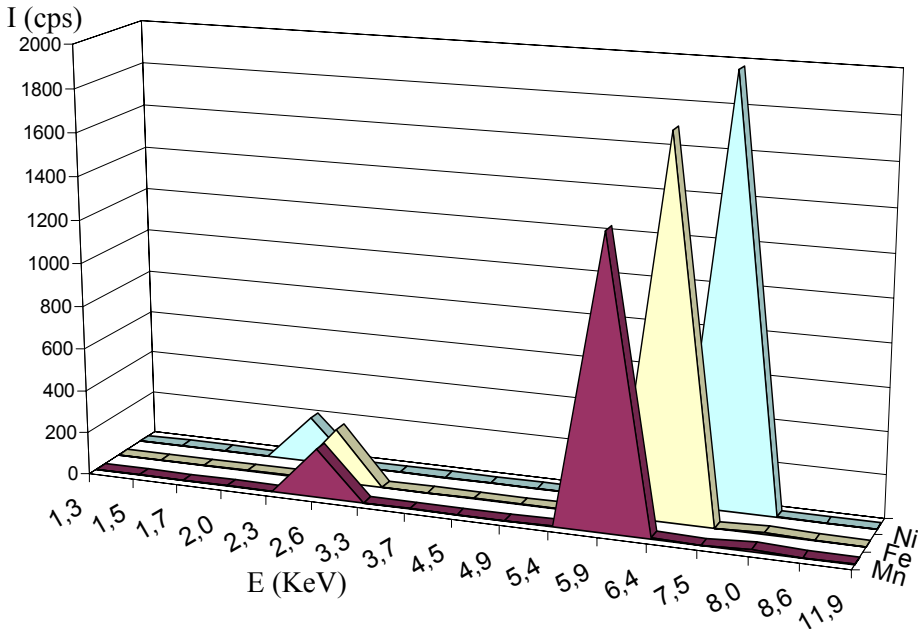


Figure1. Primary solution elements spectra

Table 2: Concentration of the elements and peak intensities with RSD (relative standard deviation)

% RSD	% Mn	I (cps)	% RSD	% Fe	I (cps)	% RSD	% Ni	I (cps)
0,68	0,2788	535,3	0,69	0,0416	144,5	0,59	0,0381	171,4
1,82	0,0562	114,8	1,78	0,0210	72,8	1,71	0,0206	91,4
2,92	0,0283	59,6	3,04	0,0069	22,2	2,74	0,0071	34,6
7,52	0,0093	19,0	8,38	0,0049	18,6	6,08	0,0042	23,4
10,99	0,0056	12,3	9,70	0,0030	10,7	8,67	0,0030	16,1
15,91	0,0041	8,3	16,35	0,0021	7,5	12,02	0,0021	12,1
17,07	0,0032	7,8	23,27	0,0000	2,8	15,81	0,0000	0,6

On the basis of the obtained results the calibration curves (Eqs. 1, 2 and 3) were formed (Figure 2) for each element [5]:

$$\text{Mn} \quad y = 1914 x + 2,76 \quad R^2 = 0,9998 \quad (1)$$

$$\text{Fe} \quad y = 2890 x + 7,12 \quad R^2 = 0,9993 \quad (2)$$

$$\text{Ni} \quad y = 4293 x + 4,36 \quad R^2 = 0,9994 \quad (3)$$

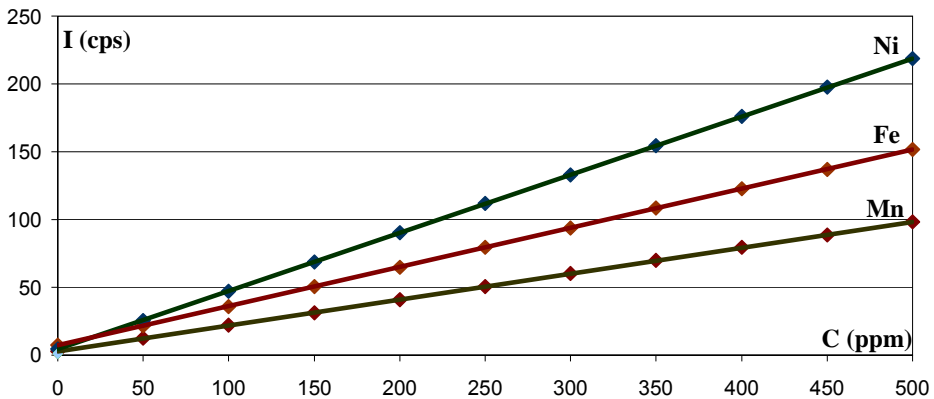


Figure 2. Calibration curves for Mn, Fe and Ni

Conclusion

On the basis of the obtained spectra, of the investigation results and of the calibration curves formulae, it can be concluded that on the device type OXFORD XR 400 using the method FPT 25 LIQ appropriate results can be obtained. With the increase of atomic number (the growth of the curve slope factor), the increase of sensitivity was confirmed. The degree of correlation for all the three lines is close to one which shows a good match of measuring points with the obtained calibration curves.

Acknowledgement

This work was supported by NIS Factory of Lubricants FAM, Kruševac

References

- [1] A. A. Jovanović, *Atomska spektroskopija – spektrohemijski aspekt*, Fakultet za fizičku hemiju, Beograd, 1999.
- [2] J. A. Bearden, *X-Ray Wavelengths*, *Review of Modern Physics*, 1967, pp 86-89.
- [3] OXFORD XRF User Handbook XA-1503, Oxford Instruments, 1991.
- [4] ASTM D 4307 Standard Practice for Preparation of Liquid Blends for Use as Analytical Standards, 1988.
- [5] J. Driscoll, *Determination of ppb levels of metals in water by XRF*, 2001.

CHEMICAL CHARACTERIZATION OF POTABLE MINERAL WATERS

D. Golobočanin, A. Žujić and N. Miljević

Vinča Institute of Nuclear Sciences, POB 522, 11001 Belgrade, Serbia & Montenegro

Abstract

This article discusses chemical characteristics of Serbian natural mineral waters in comparison to worldwide-recognized waters. The attempt has been made to range mineral waters in respect to the calculated statistical line of mineralization. A moving average method was adopted for the calculation of statistical representative points for the main ions content of mineral waters. Proposed mode for characterization specifies the pathway from low to high mineralized water accompanied with the changes in water chemical composition.

Introduction

In the Food Safety Act 1990 [1] water is included as a food where it is used as a drink or as a food ingredient. Generally, mineral water contains at least 250 mg/L total dissolved solids (TDS), comes from a source tapped at one or more boreholes or springs, and originates from a geologically and physically protected underground water source. Records of mineral water exploitation in Serbia date as far back as in 1719 and the sale of bottled water has continuously increased and reached up 388.202.000 liters in 2002.

Due to surface speciation and dissolution kinetics in aqueous solutions, waters are not necessarily uniform throughout a particular geological formation, but often the waters of a particular district have much resemblance to each other. It is not known with any certainty the depth from which various mineral waters proceed, nor the various distances from the surface at which they take up their different mineral constituents from neighboring rocks. The aim of this paper was to find the pattern for the most frequent cation and anion combinations in mineral waters as the result from the rock formations, through which the water flowed.

Results and Discussion

Most of Serbian waters occur predominantly in geological setting of crystalline schists of different degree of metamorphism [2]. They are highly saturated with CO₂ likely of magmatic origin. Main features of potable waters are in a wide range of pH values (6.5 - 8.5) and TDS (52 - 2800) mg/L as the dry residues at 180°C what is commonly considered satisfactory [3]. The characteristic (pH, bicarbonate, and concentration of bioelements Na, Ca, K, Mg, F, Cl, and SO₄) of mineral waters of Serbian origin exhibit frequency distributions similar to 1500 waters of worldwide recognized supply. The presence of dominant ions (bicarbonate and carbonate) and cations (Na and Mg) is obvious indicating the lime rock water-bearing layers. Usually, the fluoride

concentration is low except in some case when it reaches up to 6 mg/L (*Aqua Heba*). Our mineral waters are pretty drinkable because of depleted sulfate concentration that makes bitter taste. As the consequence, a very poor content of important bioelement selenium, which follows sulfur chemistry, was noted.

In the present study we calculated the statistical line of mineralization, SLM, (how much minerals the water carries) as the average of 1500 mineral waters of the world sorted by TDS. A moving average method was applied for the calculation of statistical representative point for the main ions content of mineral waters

$$\overline{X}_j = \sum_{i=100j}^{i=100j+99} \frac{x_i}{100}, j = 0,1,2,\dots,N$$

where x_i is a concentration of ionic species and \overline{X}_j determines the point on SLM as the mean value of 100 analyzed waters. SLM represents the global most probable anion-cation ratio for particular mineralization. It is shown together with available Serbian potable waters in Piper diagram [4] (Fig. 1) where mole equivalent fraction of anions (Cl^- , SO_4^{2-} , HCO_3^- , and CO_2^{2-}) and cations (Na^+ , Ca^{2+} , K^+ , and Mg^{2+}) are presented on the trigonal coordinate axes. The thickness of crosshatched line corresponds to magnitude of mineralization. In addition, the mean value of mineralization for both 1500 worldwide waters and for 15 Serbian commercially available waters is drawn. Most of our bottled mineral waters are close to SLM except *Mivela* water due to its relative high content of Mg in respect to Ca.

Conclusion

In spite of the differences, the Serbian waters are mostly typified by their HCO_3^- , Na, and Mg content. We followed the general rule for classification of water under the head of its predominant elements. The proposed mode uses TDS as a guideline for understanding the relative cation-anion content for the particular water. The calculated statistical line of mineralization specifies the pathway from low to high-mineralized water accompanied with the changes in chemical composition.

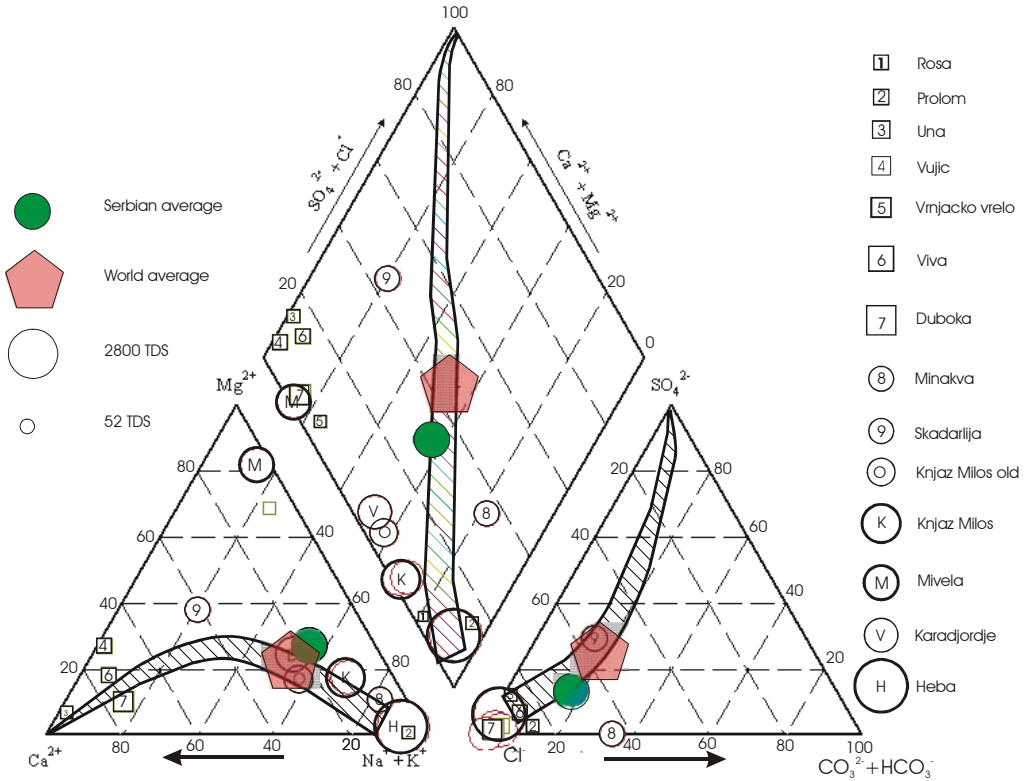


Figure 1. Piper diagram for the considered mineral waters

References

[1] Food Standard Agency, The Food Safety Act 1990 and You, London, UK, 1990.
 [2] D. Protić, Mineral and Thermal Waters of Serbia. (In Serbian), Geoinstitut, Belgrade, 1995.
 [3] World Health Organization (1996) Guidelines for drinking-water quality, 2nd edn. 2. Health criteria and other supporting information. Geneva
 [4] R.B.Winston, Graphical User Interface for MODFLOW, Version 4: U.S. Geological Survey Open-File Report 00-315, 27 p., 2000.

RADIONUCLIDES IN SOME SPRING MINERAL WATERS IN SERBIA

J. D. Joksić and M. B. Radenković

*Vinča Institute of Nuclear Sciences, Radiation and Environmental Protection Laboratory,
11001 Belgrade, P.O.B. 522, Serbia & Montenegro*

Abstract

Radiochemical analyses of some natural mineral bottled waters from different location in Serbia were investigated. Concentrations of all present naturally occurring radionuclides, ^{238}U , ^{234}U , ^{232}Th , ^{230}Th , ^{228}Th , ^{228}Ra and ^{226}Ra and $^{234}\text{U}/^{238}\text{U}$, $^{226}\text{Ra}/^{230}\text{Th}$, $^{228}\text{Th}/^{232}\text{Th}$, and $^{228}\text{Ra}/^{228}\text{Th}$ activity ratios were calculated and discussed. Uranium series disequilibria in the hydrosphere occur due to geochemical differentiation processes resulting with different mobility of the radionuclides from the same series. We have investigated radioactive disequilibrium in the spring waters Crni Guber, Čibutkovic and Studenica, originated from metamorphic rock area. High content of radium isotopes (^{226}Ra , ^{228}Ra) in analysed natural spring waters indicates contribution from other non-water sources, probably environmental sediment.

Introduction

Consumption of spring mineral water is continuously increasing during last few decades. Waters coming from deeply located sources in the earth crust may transport natural radioactive isotopes (including radium isotopes) under certain geological conditions. Two of them (^{226}Ra , ^{228}Ra) are of real menace from radiological point of view, because when disintegrating they create series of daughter alpha and beta radioactive elements. Permanent consumption of mineral water with higher concentration of radium isotopes might be dangerous for human health. Increased contents of ^{226}Ra were observed in some mineral waters, used as drinking waters in France where the highest concentration was 2.7 Bq/l, Portugal 2.2 Bq/l, Germany 1.8 Bq/l, Brazil 3.5 Bq/l [1]. Activity concentrations for drinking water, recommended by WHO, are 0.1 Bq/l for gross *alpha* and 1 Bq/l for gross *beta* activity. These recommendations must be applied to routine operational conditions of existing or new water supplies. For natural spring water we have to measure naturally occurring radionuclide ^{40}K , which makes up about 0.01 % of natural potassium (WHO, 1996).

We have investigated several natural spring waters. In these spring waters gross *alpha* and gross *beta* activity exceed recommended values of 0.1 Bq/l and 1 Bq/l, respectively, for drinking and mineral water. These are carbon acid waters with similar chemical composite and same pH value (6.5).

Experimental

Alpha spectrometry procedure for uranium and thorium isotopes included: sampling, preliminary samples treatment, ion-exchange chemical separation, ion-exchange purification of separated elements, thin-layer source preparation and alpha spectrometry measurements.[3]

After collection water samples have been acidified, evaporated and ashed at 550°C. ^{232}U and ^{229}Th have been added in a quantity of about 0.1 Bq as a tracer to each sample, for radiochemical yield recoveries.

Radiochemical separation and purification was done on ion-exchange resin DOWEX 1x8, 100-200 mesh. Electroplating of purified fractions, was used to make thin-layer radioactive sources. After electrodeposition, a thorium source was covered by vinyl-foil. Samples have been concentrated by evaporating 10 l water to 450 ml for gamma analysis. After preparation, samples have been sealed in the acrylic containers for 4 weeks to reach radioequilibrium between ^{228}Ra and ^{228}Ac and ^{226}Ra and ^{222}Rn .

Low-level activity measurements have been done by the use of Canberra 2004 alpha-spectrometry counting system, including vacuum chamber (20 mbar), PIPS-detector (300 mm² surface), with: counting efficiency 15%, at 25mm distance; multichannel energy scale 9.1 keV/ch, resolution 24 keV for ^{241}Am .

The counting time required had to be a few days, that is long enough to ensure an accurate result.

The gamma activity of the samples has been counted using high purity Ge detector, with counting relative efficiency 23 %.

Results and Discussion

Spring water Crni Guber exhibits a disequilibrium mostly in the ^{232}Th series (Table 1.). The ^{226}Ra content, that should be in equilibrium with ^{238}U , exceeds the value expected for the equilibrium. The equilibrium means that neither gain nor loss of any parent or daughter in a decay chain are not possible. The ^{230}Th isotope was not found in this sample. However, the ^{226}Ra and ^{228}Ra activities found in this sample are much higher than those of their parents, because of the same chemical behaviour of different isotopes of an element. In the ^{232}Th series the $^{228}\text{Th}/^{228}\text{Ra}$ disequilibrium is much higher than expected from present ^{232}Th . High ^{228}Th content may derive from ^{228}Ra . Since chemical properties of uranium and radium are quite different, mobility of the parent and product isotopes are different in most chemical environments. ^{232}Th is insoluble in water environments. However, its daughter nuclide ^{228}Ra is much more soluble. The $^{228}\text{Th}/^{232}\text{Th}$ and $^{228}\text{Ra}/^{228}\text{Th}$ ratios are 126.7 and 7.7.

Table 1: Radioactivity ratios of $^{234}\text{U}/^{238}\text{U}$, $^{228}\text{Th}/^{232}\text{Th}$, $^{226}\text{Ra}/^{230}\text{Th}$ and $^{228}\text{Ra}/^{228}\text{Th}$ in mineral waters

	$^{234}\text{U}/^{238}\text{U}$	$^{228}\text{Th}/^{232}\text{Th}$	$^{226}\text{Ra}/^{230}\text{Th}$	$^{228}\text{Ra}/^{228}\text{Th}$
Crni Guber	1.24	126.7	/	7.7
Čibutkovic	0.95	54.3	38.5	12.4
Studnica	1.24	13.6	50000	/

In the Čibutkovic spring water a disequilibrium has been found, both in the ^{238}U and ^{232}Th series. The ^{226}Ra content, that should be related to the ^{238}U one, exceeds very much the equilibrium value. The ^{228}Th , ^{228}Ac and ^{228}Ra concentrations are much higher than expected from present ^{232}Th amount. In the decay process from ^{232}Th to

^{228}Th , the ^{228}Ra radionuclide ($t_{1/2} = 5.75$ y) is in the middle. Since chemical properties of radium and thorium are different, high ^{228}Th content may derive from ^{228}Ra content. The $^{228}\text{Th}/^{232}\text{Th}$, $^{226}\text{Ra}/^{230}\text{Th}$ and $^{228}\text{Ra}/^{228}\text{Th}$ ratios are 54.3, 38.5 and 12.4, respectively.

The results obtained here show that the rise in the activity level corresponds to the ^{226}Ra isotope, for the Studenica water, since the $^{226}\text{Ra}/^{230}\text{Th}$ ratio was found to be 50000. Corresponding ratio for the Čibutkovića water is 38.5. The ^{228}Ra isotope was not found in this water, so because of that the $^{228}\text{Ra}/^{228}\text{Th}$ ratio was missed. For comparison, the least $^{228}\text{Th}/^{232}\text{Th}$ ratio (of only 13.6) was found in the Studenica water.

Conclusion

The uranium series disequilibria can occur due to geochemical differentiation processes resulting with different mobility of the radionuclides from the same series. High content of radium isotopes (^{226}Ra , ^{228}Ra) in analysed natural spring waters indicates contribution from other non-water sources, probably environmental sediment.

References

- [1] A.Hetman, J.Dorda, W.Zipper *Nukleonika*, 1998, 43(4), 481-488.
- [2] WHO, Guidelines for drinking water quality, 2nd Edition 1996, Vol. 1,2.
- [3] M.Radenković, D. Vuković, V.Šipka, D.Todorović, *J.Radioanal.Nucl.Chem.*, 1996, 208(2), 467-475.

THE EFFECT OF SIMULATED ACID RAIN ON ^{137}Cs DESORPTION IN *CETRARIA ISLANDICA*

A. Čučulović¹, S. Stanković¹, Š. S. Miljanić², D. Milivojević¹
and D. Veselinović²

¹INEP-Institute for the Application of Nuclear Energy,
11080 Zemun, Banatska 31b, Serbia & Montenegro

²University of Belgrade, Faculty of Physical Chemistry,
11001 Belgrade, P.O. Box 137, Serbia & Montenegro

Abstract

Radiocesium desorption from the lichen *Cetraria islandica* by simulated acid rain of different pH values (2.00 - 3.75) was examined in this work. Before treatment with acid solutions the pH value of the thallus was 4.56, which confirmed that the lichen was growing in an acid medium. After five extractions with distilled water (pH 6.48) 57.2% of the initial radiocesium was desorbed. The extraction efficiency for radiocesium by acid extraction solutions (A, B, C), after five steps, was in the range from 39.5 to 69.5% of the initial radioactivity. The most effective desorption of $^{137}\text{Cs}^+$ was achieved with acid solution (C); pH 2.87 (69.5%). The results obtained indicated that solutions imitating acid rain can isolate $^{137}\text{Cs}^+$ without destruction of the basic structure of lichen, which can then be used as food or animal feed and also in the pharmaceutical industry.

Introduction

The urban emission of atmospheric pollutants, such as SO_2 , NO_2 and NH_3 , gives rise to precipitation of so-called acid rain, which is a mixture of H_2SO_4 , HNO_3 and $(\text{NH}_4)_2\text{SO}_4$. Lichens lack both stomata and a cuticular layer and therefore absorb gases over the entire surface and their cells are directly exposed to rain. This makes lichens more sensitive to acid rain. However, the lichen upper cortex, formed of fungal hyphae, plays an important role in the interaction with the environment (1). The use of lichens as a biomonitor of atmospheric pollution by radionuclides, especially by radiocesium-137 from the Chernobyl accident (1986), has been widely discussed by numerous authors, but the exact mechanism of cesium accumulation has not been determined yet. Buck and Brown (2) showed that lichen cell walls bound very little K^+ , which was the main cation in the cytoplasm. In the thallus of the lichen *Parmotrema tinctorum* Beckett found that K^+ was intercellular and apoplasmic or associated with the cell wall (3). We suppose that intracellular cesium transport is based on a potassium transport system, including ion diffusion, ion exchange and active ion uptake. In this work we attempted to investigate whether ^{137}Cs could be isolated with acid solutions as simulated acid rain without destruction of the lichen cellular structure, which would imply that the whole amount of ^{137}Cs in the plant is ion-exchangeable.

Materials and Methods

Dry samples of the lichen *C. islandica* (specific activity 1376 Bq/kg, 10g d.w) were treated (occasionally mixing during 24 hours) with 200 mL distilled water or solutions of acids and salts simulating acid rain: **A**: H₂SO₄, **B**: H₂SO₄-HNO₃ and **C**: H₂SO₄-HNO₃-(NH₄)₂SO₄ solutions. These solutions **A** and **B** were prepared by adding corresponding solutions in the distilled water to the pH values: 2.00; 2.58; 2.87; 3.28 and 3.75. Initial solutions were concentrated H₂SO₄ and (1:1) mixture of concentrated H₂SO₄ and HNO₃. Solution **C** was prepared by adding 1g of (NH₄)₂SO₄ in 100 mL of solution **B**. After this pH values was corrected using H₂SO₄. After each extraction step (five) the mixtures were filtered and the samples were dried at room temperature. Their masses were measured as well as their specific radioactivities using a gamma spectrometer (ORTEC-AMETEK, 8192 channels). The resolution was 1.65 keV; the energy used was 1.33 MeV and the efficiency was 34%. for 1.33 MeV (⁶⁰Co). To determine pH levels, 100 mg of lichen thallus was homogenized in liquid nitrogen and 4 mL of deionized H₂O. After centrifugation at 100g for 10 min, the pH value of the supernatant was read on a pH meter (MA 5730 Iskra).

Results and Discussion

High levels of SO₂ and NO_x may reduce the pH of the lichen thallus. Therefore, measurement of lichen thallus pH can supply information about the state of pollution of a site. The pH of untreated *C. islandica* thallus was found to be 4.85, which indicates that it is a species tolerant to an acid environment. Gauslaa reported that *Lobaria pulmonaria* is endangered in some sites subject to acid rain and pH 5 has been indicated as a threshold value below which lichen is unable to survive (4). After five successive extraction steps with acid solutions (**A**, **B**, **C**) the pH of lichen thallus ranged from 2.58 (pH 2.00 -**C**) to 4.68 (pH 3.75 -**B**). The extent of ¹³⁷Cs extraction from the lichen is shown in Table 1.

Table 1. Efficiency of ¹³⁷Cs extraction (%) from the lichen *Cetraria islandica* with acid extraction solutions after five steps

pH	Distilled water	Extraction solutions		
		A	B	C
2.00		57.9	63.5	66.5
2.57		63.0	59.6	66.7
2.87		51.7	45.0	69.5
3.28		52.3	44.3	63.2
3.75		39.5	45.4	61.7
6.48	57.2			

Five successive steps with distilled water extracted 57.2% of the initial ¹³⁷Cs⁺ in *C. islandica*. With the acid solutions **A**, **B**, **C** the amount of extracted ¹³⁷Cs⁺ ranged from 39.5% (pH 3.75; solution **A**) of the initial radiocesium in *C. islandica* to 69.5% (pH 2.87; solution **C**). In general, the greatest ¹³⁷Cs⁺ desorption from lichen was

achieved using solution **C**. Thus, radiocesium desorption from lichens with distilled water and acid solutions **A** and **B** was less successful than with solution **C** at all pH values examined. Moreover, acid solutions **A** and **B** (pH: 2.87; 3.28 and 3.75) extracted less $^{137}\text{Cs}^+$ than distilled water.

Sulphuric and nitric acids destroy cell membranes and strip all other potentially competitive cations ($^{137}\text{Cs}^+$) from both the extracellular and intracellular exchange sites, the substituted hydrogen ions apparently acting as a highly competitive cation against subsequent ammonium binding. Ammonia has more clear alkaline properties than water. Many acids that release few protons in aqueous solutions can easily do so in liquid ammonia. The ammonium ion has a similar radius to that of the K^+ -ion, which means that potassium, ammonium and finally cesium salts are similar. Once ammonium has been adsorbed on to wall sites in an exchangeable form, it appears relatively labile.

The final mass of the lichens was only slightly decreased after this procedure (approximately 5%), indicating that the desorption was achieved without significant destruction of plant structure.

Conclusion

In this work we have shown that acid solution **C**: $\text{H}_2\text{SO}_4\text{-HNO}_3\text{-(NH}_4)_2\text{SO}_4$ pH 2.87, which simulated acid rain, was able to extract more $^{137}\text{Cs}^+$ from *C. islandica* than the other solutions tested.

References

- [1] T. Hallingbäck, O. Kellner, *New Phytologist*, 1992, 120, 99.
- [2] G. W. Buck, D. H. Brown, 1994, 44, 265.
- [3] R. P. Beckett, *The Lichenologist*, 1996, 28(3), 257.
- [4] Y. Gauslaa, *The Lichenologist*, 1985, 17, 117.

LEVELS OF SELENIUM IN THE RAT PINEAL GLAND: THE EFFECTS OF SELENIUM SUPPLEMENTATION

M. A. Demajo, O. N. Jozanov-Stankov and I. S. Đujić¹

Institute of Nuclear Sciences "Vinča", P.O.Box 522, 11001 Belgrade,

¹*Institute of Chemistry, Technology and Metallurgy,
Njegoševa 12, 11000 Belgrade, Serbia and Montenegro*

Abstract

Levels of selenium (Se) were measured in the pineal glands of rats aged 4, 5, 8 and 12 months and the following corresponding levels of Se were determined: 1.058 nmol/gland, 0.63 nmol/gland, 0.58 nmol/gland and 0.43 nmol/gland. In the rat pineal glands obtained from rats which drank water containing Se coupled to brewers yeast (average daily intake of Se per animal was 0.5 µg) the following increased levels of Se were determined: 0.87 nmol/gland, 0.72 nmol/gland and 0.59 nmol/gland at the ages of 5, 8 and 12 months respectively. Since Se participates in the antioxidative defense of the mammalian organism, the increased levels of Se in the pineal glands of rats supplemented with Se in drinking water, may be of physiological benefit during ageing.

Introduction

The pineal gland is a neuroendocrine organ of a multitarget regulative role, inhibitory rather than stimulatory. It is instrumental in the coordination and synchronization of homeostasis and behaviour under physiological and stress-inducing microambient influences. Melatonin is the chief secretory product of the pineal gland and has a role as a free radical scavenger and antioxidant [1]. Since selenium (Se) is known to be part of the "antioxidant defense system" [2], the purpose of this study was to analyse the content of Se in the rat pineal gland and to study the effects of Se supplementation *via* drinking water.

Materials and Methods

Male rats of a Wistar strain aged 3 months were used and maintained under standard conditions. At this age, one group of animals started receiving continuously pure brewery yeast dissolved in drinking water (Y: control animals), while the second group of animals received Se enriched yeast also in drinking water (SeY group). The SeY emulsion in water provided on average a daily intake of 0.5 µg Se/animal. Both groups of animals were subsequently sacrificed between 9:00 and 12:00 hrs. at the ages of 4, 5, 8 and 12 months. Se in the excised and consequently ashed pineal glands was measured by gaseous hydride generation atomic spectrometry, using a Perkin Elmer 5000 atomic absorption spectrometer equipped with MHS-10 vapour generator accessory. As the pineal glands are very small, 4-8 glands were pooled. The results are expressed as nmol/gland of Se. The comparison between SeY and Y groups are expressed as the % of increase of Se in respect to the Y control group, its value taken as 100%. The origin 5.0 graphic programme was used to integrate the surface below the

line connecting the Se concentrations during the whole time period the animals were investigated (between 4-12 months of age).

Results and Discussion

At the age of 4 months, the level of Se in the pineal gland was the highest in the Y group (1.058 nmol/gland). With increased age, Se levels fell gradually from 0.63 nmol/gland at 5 months to 0.58 nmol/gland and 0.43 nmol/gland at the ages of 8 and 12 months respectively (Fig.1).

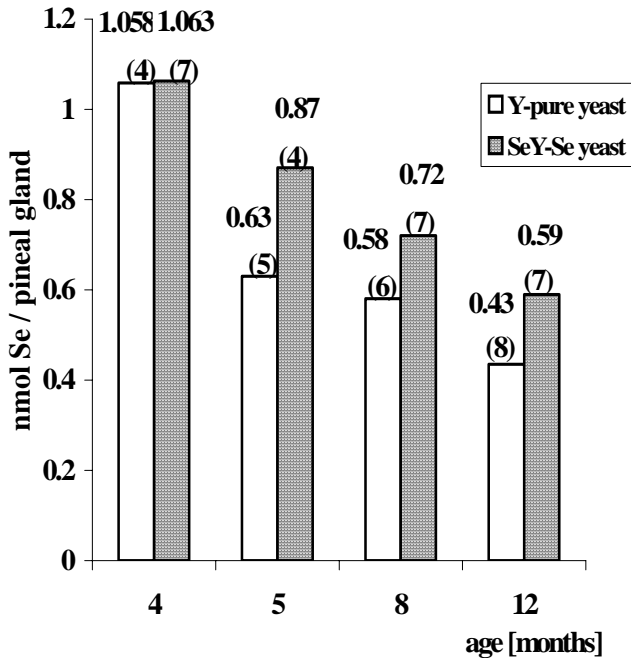


Figure 1. Changes of Se levels in the rat pineal glands at various ages. (n)-number of pineal glands pooled.

In the SeY supplemented rats, the pineal gland Se level was 1.063 nmol/gland at 4 months, gradually falling to 0.87 nmol/gland, 0.72 nmol/gland and 0.59 nmol/gland at the ages of 5, 8 and 12 months respectively (Fig. 1). Starting from the age of 5 months, the pineal gland Se concentrations from the SeY supplemented rats were higher by 38.16%, 25.04% and 35.17% at the ages of 5, 8 and 12 months respectively, when compared to the Se concentrations in the corresponding ages of the Y control group. The differences in the integrated surfaces of the age variables were not markedly different between the Y group (4.68) and the Se supplemented animals (5.98). This may result from the fact that at the age of 4 months, both groups of animals had similar levels of Se in the pineal gland.

There is not much data in the literature concerning the presence of microelements in the pineal gland, especially under different physiological conditions. By electron probe X-ray microanalysis [3], it has been shown that the rat pineal gland contains a range of elements: S, Ca, Al, Si, P, Fe, Na, Mg, Cl, K, Ti, Cr, Mn, Ni, Cu and Zn. We detected the presence of Se in the rat pineal gland. Our study also shows that Se levels increase in the rat pineal gland when the animals consume Se through drinking water. Considering that melatonin plays a role as an antioxidant [4] and that Se is involved in the antioxidant defense system [2], [5], the increased Se levels in the pineal glands from rats supplemented with Se in drinking water may be beneficial, especially with progressing age.

Conclusion

From our present study, it may be concluded that Se is a microelement present in the rat pineal gland. The levels of Se change in the pineal gland with age. Consuming Se coupled to yeast in drinking water, its levels increase in the rat pineal gland.

Acknowledgement

This study was supported by the Serbian Ministry of Science and Environmental Protection, Project No. 544.

References

- [1] R.Reiter *et al.*, Life Sci., 1997, 60, 2255.
- [2] Y. Xia *et al.*, J.Nutr.Biochem., 1992, 3, 202.
- [3] W.Humbert *et al.* J.Pineal Res., 1996, 20, 39.
- [4] R. Reiter *et al.* J. Pineal Res., 1995, 18, 1.
- [5] O. Jozanov-Stankov *et al.*, J.Env.Pathol.Tox.Oncol., 1998, 17, 251.

THE CORRELATION OF THE VALUES OF PLANT-AVAILABLE Cd IN THE SOIL AND AMOUNTS IN THE PLANT PARTS OF WHEAT

D.Veselinović², D.Marković² and A.Savin¹

¹"Eko-Lab", Industrijska zona bb, 11000 P. Skela, Belgrade,

²Faculty of Physical Chemistry,

11001 Belgrade, 12-16 Studentski Trg, P.O.Box. 137, Serbia and Montenegro

Abstract

The plant-available amount of Cd in the soil determined by using extraction solutions [1,2,3]: **1)** 0.5 M Na₂EDTA, pH=5.2; **2)** 1 M KCl, pH=7; **3)** 0.1 M KCl, 0.05 M Na₂EDTA, pH=6.2; **4)** 2 % CH₃COOH, pH=2.5; and **5)** 1 M CH₃COONH₄, pH=4.8. In the experiments chernozem from the Middle Banat are used. It is concluded that the amount of Cd in the stalks depended on the plant-available amount of Cd in the soil.

Introduction

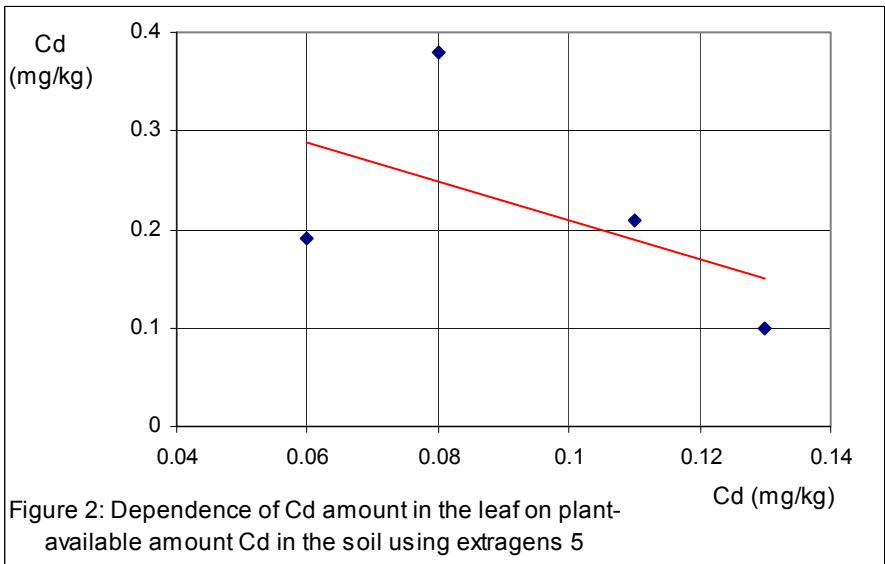
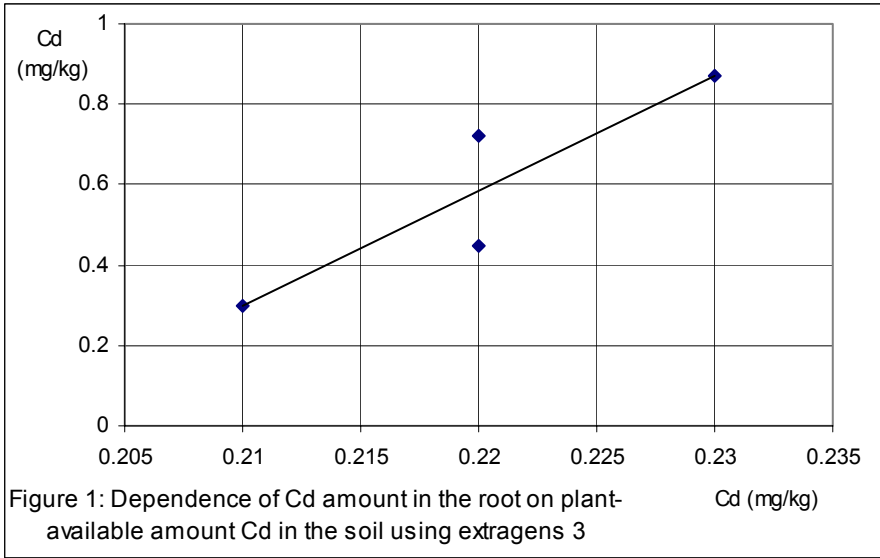
The sampling took place on the parcel of the village of Farkaždin in the Middle Banat in the period between 20 December 2000 and 5 July 2001 (the sampling took place four times). The sampling of the plant and soil material took place simultaneously. In each period 4-5 samples took places. Each samples has been analysed 3 times.

The sampling was carried out by a sound (depth 0-30 cm). The samples were air-dried, grinded and sieved in the laboratory. [4]

The plant material was deconstructed with HNO₃ and HClO₄ and the Cd concentrations in solutions was determined by atomic absorption spectrophotometry.[2]

Results and Discussion

Obtained data have been presented on the graphs, as a dependence of plant parts Cd contents on plant-available contents of useful metals. Characteristical graphs are given in the Figure 1 and 2.



Correlation factors of linear dependence of Cd amount in plant parts on plant-available amount of Cd in the soil has been determined. The obtained correlation factors of linear dependence of amount Cd plant parts on plant-available amount of Cd in the soil are given in the Table I.

Table I. Correlation factors of linear dependence of Cd amount in plant parts on plant-available amount of Cd in the soil

	Cd (t)	Cd (1)	Cd (2)	Cd (3)	Cd (4)	Cd (5)
Cd(in root)	+0.84	+0.58	+0.34	+0.90	+0.71	+0.66
Cd (in stalks)	+0.95	+0.83	+0.74	+0.95	+0.99	+0.94
Cd (in leaf)	-0.57	-0.46	-0.64	-0.31	-0.72	-0.52

Conclusion

On the basis of the obtained data it is concluded that exist the linear dependence of amount Cd in the stalks on total and plant-available amount of Cd in the soil for ever extragens except for 1M KCl, pH=7. Correlation of Cd amounts in a leaf on Cd amounts in the soil is not exist. It is concluded that not exist linear correlation of amount Cd in the root and Cd amounts in the soil when using extragens: 0.5 M Na₂EDTA, pH=5.2, 1 M KCl, pH=7 and 2% CH₃COOH, pH=2.5.

References:

- [1] P.R. Hesse, "A Textbook of Soil Chemical Analysis", John Murray Ltd, 1971, p: 371-377, 388.
- [2] Dr R. Kastori, "Uloga elemenata u ishrani biljaka", Matica Srpska – Odeljenje za prirodne nauke, Novi Sad, 1983.
- [3] D.Veselinovic, A.Savin, M.Gojkov, S. Filip, M.Milovac, 2nd International Conference of the chemical Societies of the South-Eastern European Countries on Chemical Sciences for Suitainable Development, Book of Abstract, Vol. I, 2000.
- [4] N. Vučić, Water, Air and Thermal Regime of Soil (in Serbian), Vojvodina Academy of Sciences, Novi Sad, 1987, p:15-35

TRACE AND MINOR ELEMENTS DETERMINATION IN SOME HERBAL DRUGS BY FAAS

S. Ražić^a, S. Đogo^a, L. Slavković^b and A. Popović^c

^aFaculty of Pharmacy, P.O.Box 146, University of Belgrade, 11001 Belgrade, Serbia

^bThe Vinča Institute of Nuclear Sciences, P.O. Box 522, 11001 Belgrade, Serbia

^cFaculty of Chemistry, P.O.Box 158, University of Belgrade, 11001 Belgrade, Serbia

Abstract

In this paper trace (Cu and Zn) and minor (Mn and Fe) elements in some herbal drugs originating from the plants of the family *Asteraceae* were determined by flame atomic absorption spectrometry. Chamomillae flos, Milefolii herba and Absinthii herba were analyzed taking into account their importance in phytotherapy in different diseases and disorders and the essentiality of mentioned elements for plants life cycle. Validation of proposed method was performed by using CRM, NIST 1573a.

Introduction

Herbal drugs, originating from the plants of the family *Asteraceae*, also present in a few European pharmacopeias, are of special importance in phytotherapy widely and usually used in supportive therapy for certain digestive and skin disorders. There are many literature data regarding to the numerous active compounds (essential oils, sesquiterpene lactones, alkalamides, tannins, flavonoides, sterols, biogene amines etc.) and effectiveness but there is a lack of valid information concerning trace and minor elements determination. Copper, Zn, Mn and Fe are essential for normal growth of plants, their protection against plant viruses, immunity and the completion of the life cycle [1]. Therefore this paper is dedicated to the determination of total element content in samples.

Experimental

Solutions and reagents Standard solutions were prepared by dilution of stock solutions (1000mg/L) with 1M HCl. HCl and HNO₃ were purchased from Merck and were of reagent grade quality. For preparation of the solutions double distilled water was used.

Sample preparation Accurately weighted samples (~ 1 g each) were slightly heated on a hot plate at 100 - 120 °C, for 15 min, then placed into a furnace and further heated at 500 °C for 2 hours. After cooling, 10 drops of double distilled water and then 4.0 mL of 8M HNO₃ were added into each sample, slightly heated on the hot plate to dryness then placed in the furnace at 500 °C, for 1 hour. After cooling, 10mL of 6M HCl was added in each sample and the contents were quantitatively transferred into 50mL volumetric flasks.

Instrumentation Samples were analyzed for Cu, Zn, Fe and Mn by flame atomic absorption spectrometry using Perkin-Elmer Model 5000. The operating parameters and

the analyte characteristics are given in Table 1. The signals were measured with deuterium background correction at optimal flame (air-acetylene) heights.

Table 1. Operating conditions and analyte characteristics

Element	λ [nm]	Slit [nm]	Flame type	Sensitivity [$\mu\text{g/ml}$]	Linear range [$\mu\text{g/ml}$]
Cu	324.7	0.7	A-Ac	0.030	5.0
Zn	213.9	0.7	A-Ac	0.011	1.0
Mn	279.5	0.2	A-Ac	0.030	2.0
Fe	248.3	0.2	A-Ac	0.040	5.0

Results and Discussion

The composition of environmental samples varies from purely inorganic to purely organic, but generally there are an intermediate combination of these extremes. Such examples are plants. Sample preparation i.e. total mineralization and dissolution, as the most critical points, cannot be achieved in one step using single reagent, but often several steps and several reagents are necessary. Among dry ashing and wet digestion procedures [2-4] there are many advantages and disadvantages as well. First procedure, applied in this work has the biggest advantage due to the possibility of ashing large sample amount and dissolving the resulting ash in a small volume of acid allowing the preconcentration of trace elements in the final solution. Temperature used in the preparation procedure is very important and 450 - 550⁰C can be tolerated even for volatile elements. Increasing of temperature must be very slow to avoid any local hot spots or self-ignition of the sample and much loss as well [2].

FAAS offers a detection power ranging between $\mu\text{g/l}$ and mg/l depending on the element considered and also enables cost-benefit analysis [4]. For elements determination an external calibration method was applied and the result of regression and correlation analysis are presented in Table 2.

Table 2. Statistical analysis of the experimental data (x – concentration, mg/L , y – absorbance, Sa, Sb and $S_{y/x}$ – standard error of intercept, slope and calibration line)

Element	Calibration line	r	Sa	Sb	$S_{y/x}$
Cu	$y = 0.00071 + 0.04160x$	0.99995	0.00128	0.00041	0.00146
Zn	$y = 0.00311 + 0.12916x$	0.99882	0.00252	0.00444	0.00334
Mn	$y = 0.00017 + 0.03950x$	0.99997	0.00037	0.00029	0.00041
Fe	$y = 0.00370 + 0.02538x$	0.99908	0.00437	0.00077	0.00579

The validity of whole analytical procedure is also controlled by using certified reference material (NIST 1573a - Tomato leaves) in order to ensure that there was (or no) contamination and/or losses. The analytical results are shown Table 3.

Table 3. Results [mg/kg] for certified reference material NIST 1573a (Tomato leaves)

Element	Found ^a	Recommended value ^a	% Recovery
Cu	4.26±0.29	4.70±0.14	90.64
Zn	29.42±0.64	30.9±0.7	95.21
Mn	246.18±1.72	246±8	100.07
Fe	338.98±0.56	368±7	92.11

^a Mean ± standard deviation

It can be noticed that Mn was fully recovered; Zn has good recovery as well. Poorer recoveries for Fe and Cu respectively, are possible consequence of the influence of the particular plant matrix, probably in relation to the binding of analytes with the invisible fine particles of insoluble residue.

The whole procedure was applied for determination of Cu, Zn, Mn and Fe in herbal drugs and obtained results, expressed on a dry weight basis, are shown in Table 4.

Table 4. Concentration of elements [mg/kg] in analyzed herbal drugs

Plant	Herbal drug	Cu ^a	Zn ^a	Mn ^a	Fe ^a
Matricaria chamomilla	Chamomillae flos	10.89±0.58	29.16±0.64	48.98±2.76	253.27±0.02
Achillea millefolium	Milefolii herba	7.53±0.30	18.84±0.32	60.92±2.62	103.12±1.50
Artemisia absinthium	Absinthii herba	12.25±0.01	31.70±0.96	36.20±0.38	172.55±0.16

^a Mean ± standard deviation

The concentration of measured elements decreases as follow: Fe>Mn>Zn>Cu. The differences in concentrations of those elements are attributed to the differences in botanical structure of particular part and their mobility within the plant [1].

Conclusion

Chamomillae flos, Milefolii herba and Absinthii herba, as herbal drugs of special importance in phytopharmacy were the subject of this work. Copper, Zn, Mn and Fe were determined by applying FAAS after the appropriate sample preparation procedure. Validation of the whole procedure was performed by using certified reference material NIST 1573a – Tomato leaves.

References

- [1] S. Ražić, A. Onjia, B. Potkonjak, J. Pharm. Biomed. Anal., 2003, 33, 845.
- [2] M. Hoenig, A. de Kersabiec, Spectrochim. Acta Part B, 1996, 51, 1297.
- [3] M. Hoenig, H. Baeten, S. Vanhentenrijk, E. Vassileva, Ph. Quevauviller, Anal. Chim. Acta, 1998, 358, 85.
- [4] M. Hoenig, Talanta, 2001, 54, 1021.

CONVERSION OF PULLULAN INTO KETO-ALDEHYDO POLYMER

D. Jakovljević¹, M. M. Vrvic^{1,2}, M. Radulović¹
and M. Hranisavljević-Jakovljević²

¹Department of Chemistry, Institute of Chemistry, Technology and Metallurgy, 11001 Belgrade, Njegoševa 12, ²Faculty of Chemistry, University of Belgrade, 11001 Belgrade, Studentski trg 16, P.O. Box 158, Serbia and Montenegro

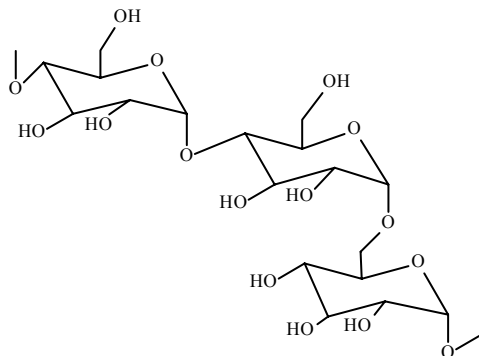
Abstract

The conversion of some hydroxyl groups of pullulan to aldehyde and ketone groups in reaction with methyl sulfoxide-acetic anhydride was investigated. Accompanying the oxidation was the formation of O-(methylthio)methylpullulan at a degree of substitution about equal to, or smaller than, the degree of substitution for the carbonyl group, depending on the reaction conditions.

Introduction

Chemically modified polysaccharides are used in medicine, biotechnology, and food and cosmetic industry, in particular, to develop new and improve the existing drugs. One of methods for activation of neutral polysaccharides is oxidation with reagent dimethyl sulfoxide-acetic anhydride allowing introduction of a required amount of carbonyl groups into the polymer. This reagent has been extensively employed in prior studies as a selective oxidant for the introducing carbonyl groups into carbohydrate chains [1].

In this work we used extracellular microbial polysaccharides pullulan which is produced by the yeast-like fungus *Aureobasidium pullulans*. This polysaccharide can be described as a linear α -D-glucan (Scheme 1) comprising a regular repeating trisaccharide residue that can be presented in a number of ways, e.g., maltotriosyl residues terminally linked by (1 \rightarrow 6) bonds, 6²- α -D-glucosylmaltose linked by (1 \rightarrow 4) bonds, etc. [2].



Scheme 1.

Occasionally, maltotriosyl residues are replaced by maltotetraosyl or α -(1 \rightarrow 4)-linked glucose units that are 10 or even more in length, in an apparently random fashion [3,4]. Pullulan used in this work is produced by the *A. pullulans*, strain CH-1 (IChTM, Collection of Microorganisms) [5].

In this work, observations on the reaction oxidation of pullulan by reagent dimethyl sulfoxide-acetic anhydride are presented.

Results and Discussion

The oxidation of pullulan was performed with dimethyl sulfoxide-acetic anhydride at room temperature. The ratio of these reagents to pullulan was 12 ml dimethyl sulfoxide and 8 ml acetic anhydride per 1 g of pullulan. In addition to the oxidation of pullulan by this reagent, a significant proportion of (methylthio)methyl ether (Pull-OCH₂SMe) was also formed, as indicated by the sulfur content of the product. The total content of carbonyl group (aldehyde + ketone) is reflected by the increase in nitrogen content, by elemental analysis, after reaction of the respective samples of oxidized pullulan with hydroxylamine reagent. The content of sulfur is also obtained from elemental analysis. The effect of reaction time on the oxidation and (methylthio)methylation of pullulan with this reagent is presented in Table 1.

Table 1. Effect of reaction time on the oxidation and (methylthio)methylation of pullulan

Reaction time (days)	N _{oxime} ^a (%)	Carbonyl groups (miliequivalents per D-glucose residue) ^b	S ^c (%)	(Methylthio)methyl-groups (miliequivalents per D-glucose residue)
0.3	1.18	136	2.18	110
1	1.82	210	2.63	132
3	3.81	440	6.04	207
5	5.94	687	7.30	356
8	6.18	715	7.62	369
11	6.35	734	7.77	393

^a Calculated from % N determined by elemental analysis after complete conversion into the polyoxime

^b Monomeric unit i.e. anhydroglucoside unit

^c Calculated from % S found by elemental analysis

FT-IR spectrum (conventional potassium bromide pellet technique) of pullulan displayed bands at 940, 850 and 767 cm⁻¹ indicating α -glucosidic linkages. FT-IR spectrum after treatment with reagent dimethyl sulfoxide-acetic anhydride clearly showed carbonyl absorption at \sim 1725 cm⁻¹. Further evidence that aldehyde or ketone groups had been generated along the pullulan chain was the reaction of the treated pullulan with hydroxylamine.

Table 1. shows the effect of varying reaction times on the distribution of product. The increase of this parameter lead to significant increase in carbonyl groups, with undesired formation of the (methylthio)methyl ether. Reaction temperature was

25 °C. The levels of oxidation and (methylthio)methyl ether formation are about the same at reaction times up ~1 day, after which the former reaction predominates. The presence (methylthio)methyl groups is undesirable, as a subsidiary reaction. However, it has been found that the (methylthio)methyl group can be removed by acid hydrolysis under conditions that not affect on the carbonyl content. For example, on boiling with 3.3M acetic acid, a sample of pullulan that had been treated with reagent dimethyl sulfoxide-acetic anhydride underwent an 85% diminution in the sulfur content, with no loss in carbonyl groups.

Conclusion

On the basis of the presented results, it may be concluded that the product obtained by treating pullulan with reagent dimethyl sulfoxide-acetic anhydride (under mild conditions) contains carbonyl and (methylthio)methyl ether groups. The carbonyl groups which generated along the pullulan chain were confirmed by spectral data from the FT-IR spectra of treated pullulan as well as by conversion into the polyoxime. The (methylthio)methyl ether groups can be removed by hydrolysis with weak acid, yielding an oxypullulan having a carbonyl content of 0.1 to 0.7 per D-glucose residue.

References

- [1] R. F. Butterworth and S. Hanessian, *Synthesis*, 1971, 70.
- [2] H. Bender and K. Wallenfels, *Biochem. Z.*, 1961, 334, 79.
- [3] G. Carolan, B. J. Catley and F.J. Mc Dougal, *Carbohydr. Res.* 1983, 114, 237.
- [4] D. D. McIntyre and H. J. Vogel, *Starch* 1993, 45, 406.
- [5] D. Jakovljević, M. M. Vrvić, M. Radulović, M. Hranisavljević-Jakovljević, J. *Serb. Chem. Soc.* 2001, 66, 377.

THE REACTIVITY OF FLY ASH OF INTEREST FOR ITS SOLIDIFICATION

S. Marinković*, B. Simonović**, D. Arandelović** and A. Kostić-Pulek*

*Faculty of Mining and Geology, Dušina 7, 11001 Belgrade,

**Holding Institute of General and Physical Chemistry, Studentski Trg 12, 11000 Belgrade,
Serbia and Montenegro

Abstract

This study has investigated the possibility of solidification of fly ash from the Serbian lignite power plant Nicola Tesla in the presence of additives (FGD gypsum and lime). Results showed that a satisfactory solidification of fly ash can be attained by simultaneous use of FGD gypsum (15 %) and lime (5 %), at different water/solid ratio (1, 0.78 and 0.75).

Introduction

In 1960, the definition of a pozzolan was extended to cover fly ash. A pozzolan is a silicious or silicious and aluminous material which in the presence of water reacts with $\text{Ca}(\text{OH})_2$ to form cementitious compounds. The pozzolanic reactivity of fly ashes depends very much on their chemical and mineralogical composition. High calcium fly ashes can form cementitious products without any supplementary activator [1]. Low calcium fly ashes have relatively low reactivity. Thus different approaches are used to accelerate the hydration reactions of these fly ashes. Sulphate activation is based on the ability of sulphates to react with aluminium oxide in the glass phase of fly ash to produce ettringite- $[\text{Ca}_3\text{Al}(\text{OH})_6]_2(\text{SO}_4)_3 \cdot 26\text{H}_2\text{O}$ [2]. Lime may react with amorphous silica of the ash to produce hydrated calcium silicates ($\text{C} - \text{S} - \text{H}$; $\text{C} = \text{CaO}$, $\text{S} = \text{SiO}_2$, $\text{H} = \text{H}_2\text{O}$) [3].

The amount of fly ashes, from power stations, which is utilized in recycling is always smaller than that produced. Therefore, the disposal of fly ashes is necessity. Disposal of fly ashes poses serious environmental problems because of the possibility for the contaminants in these materials to leach toward surroundings or ground water. To minimize these risks a treatment that has found extensive application is the solidification of fly ashes by means of ettringite or/and hydrated calcium silicates formation [4]. The aim of the present study was to test the possibility of solidification of fly ash from the Serbian lignite power plant Nicola Tesla in the presence of two additives: flue gas desulphurization (FGD) gypsum and lime. FGD gypsum is also a waste from power plants.

Experimental

Fly ash from the Serbian lignite power plant – Nicola Tesla, FGD gypsum from the Bohemian lignite power plant – Hvaletice (no Serbian plants have a FGD system installed yet) and lime from a mineral source (Serbia) were used in this study. The fly ash was characterized by determining its chemical composition and its minera-

logical composition by means of X – ray diffraction analysis (XRD) The lime and FGD gypsum were investigated by classical quantitative chemical analysis and qualitative IR analysis (a Perkin Elmer 782 spectrophotometer).

The mixtures were prepared at room temperature. The ratio of fly ash – FGD gypsum – lime was kept constant (8 : 1.5 : 0.5), but the content of water (W) was various (water/solid -W/S ratio: 1, 0.78 and 0.75) in them. The so-prepared samples were placed in cylindrical moulds (height – 36 mm and diameter – 38 mm) and cured 30 days in ambient air. Subsequently, the samples were tested for their compressive strength in accordance with Yugoslav standard. Also, the samples were examined by means of X – ray diffraction analysis (XRD), differential thermal analysis (DTA) and thermogravimetric analysis (TGA). A Philips PW 1710 diffractometer ($\text{CuK}\alpha$ radiation) was used for the XRD. The DTA and TGA examination were performed on a STA 1000 simultaneous differential thermal and thermogravimetric analyzer (air atmosphere, heating rate of 10 °C/min).

Results and Discussion

On the basis of the chemical analysis of the fly ash used in this work (CaO - 6.64%, SiO_2 – 52.27%), it could be concluded that it was low calcium fly ash. Also, the mineralogical composition of the fly ash (determined by XRD) was typical for ashes with low calcium content (quartz – the major crystalline phase and a significant amount of amorphous aluminosilicates – glass). On the basis of the chemical analysis of FGD gypsum, it was apparent that it was essentially a pure substance (about 5 % of impurities). IR analysis confirmed the presence of some carbonates, as impurities, in the FGD gypsum. The chemical analysis of the lime suggested that it contained a relatively low amount of impurities (95.23 % CaO). CaO and $\text{Ca}(\text{OH})_2$ in the lime are confirmed by IR analysis .

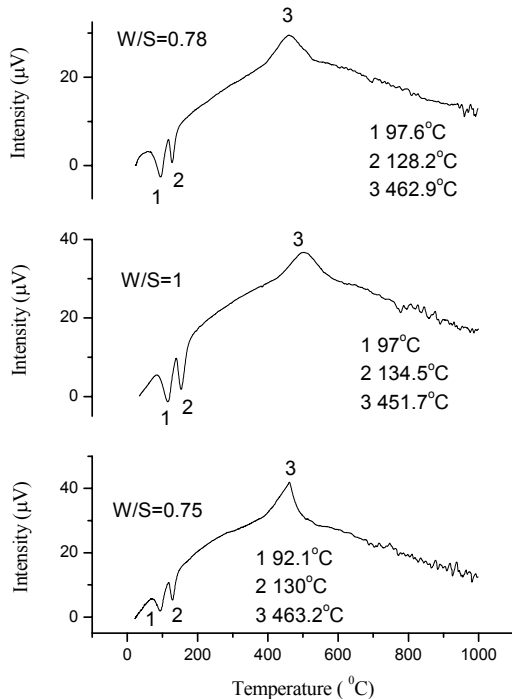


Figure 1. DTA curves of samples

The DTA curves of the samples (Figure 1) with the different water/solid ratio (1, 0.78 and 0.75) show two endothermic peaks (not very different in terms of their intensity) and one exothermic peak. The first endothermic peak is due to ettringite and the second one to gypsum (Fig.1). The exothermic peaks in the three DTA curves in Figure 1 appear from the burning of residual particles of coal, or carbon particles from the fly ash.

The thermogravimetric analysis results and the compressive strength of samples (after 30 days) are presented in Table 1. The mass losses of water during the dehydration of ettringite and non-reacted gypsum and the amount of ettringite and gypsum (calculated by means of mass losses) are shown in the mentioned table.

Table 1. Thermogravimetric analysis and compressive strength of samples

Sample (W/S)	%H ₂ O/[Ca ₃ Al(OH) ₆] ₂ (SO ₄) ₃ ·26H ₂ O	%H ₂ O/CaSO ₄ ·2H ₂ O	Compressive strength(MPa)
1. (1)	4.33/11.60	2.85/13.62	0.35
2.(0.78)	4.46/11.95	2.38/11.38	0.88
3.(0.75)	3.99/10.69	2.80/13.38	0.97

The XRD patterns of all three samples (W/S = 1, W/S = 0.78 and W/S = 0.75) had peaks of the same crystalline phases: ettringite (0.9800, 0.5600, 0.3500 nm), gypsum (0.76300, 0.4283, 0.3065 nm) and quartz (0.3350,0.2450, 0.2290nm). The results of the XRD analysis showed the presence of quartz which is inherent to fly ash, gypsum which did not react and ettringite – new crystals resulting by mutual reactions of CaO and Ca(OH)₂ from lime, FGD gypsum, aluminates from amorphous phases of fly ash and water.

Conclusion

On the basis of the above mentioned results, it can be concluded:

1. In all samples prepared in this work (W/S ratios: 1, 0.78 and 0.75) ettringite ([Ca₃Al(OH)₆]₂(SO₄)₃·26H₂O) was formed.
2. The amount of ettringite and non-reacted gypsum (CaSO₄·2H₂O) in these samples were not very different.
3. There is a indirect correlation between the W/S ratio and the compressive strength of samples (the greater the W/S ratio is, the smaller is the compressive strength).

The present study showed that fly ash from the Serbian power plant – Nicola Tesla reacted well with FGD gypsum and lime. Mixtures of the same composition (fly ash – FGD gypsum - lime = 8 : 1.5 : 0.5) and different quantity of water (water solid ratio: 1, 0.78 and 0.5) satisfied the compressive strength stipulated for the solidification of fly ash, as it suggested in literature[5].

References

- [1] T. Sebok, J. Simonik, K. Kulisek, Cem. Conc.Res., 2001, 31, 1101.
- [2] C. S. Poon, S. C. Kou, L. Lam, Cem. Concr. Res., 2001, 31, 873.
- [3] J. Scarano, G. Belz, G. Dinelli, Annal. Chim., 1998, 88, 211.
- [4] R. Ibanez, A. Andres, J. Irabien, I. Ortiz, J. Envir. Eng., 1998, 124, 43.
- [5] J. Solem-Tishmach, G. McCarthy, Cem. Conc. Res., 1995, 25, 658.

COPPER REMOVAL FROM CONTAMINATED WATER USING *MEDICAGO SATIVA*

T. Jovanović, A. Ćosović and V. Adamović

*Institute for Technology of Nuclear and other Mineral Raw Materials,
86 Franchet d'Esperey St., 11 000 Belgrade, Serbia and Montenegro*

Abstract

This study examined the ability of *Medicago sativa* to remove soluble copper under various laboratory conditions. It represents an effort to obtain preliminary data for the use of domestic species of *M. sativa* biomass as biofilter. Batch laboratory experiments were performed to study the effects of pH and to determine the optimal binding time for copper(II) adsorption by *M. sativa* shoots and sprouting seeds. All copper concentrations were determined by AAS (atomic absorption spectroscopy). Binding ability of shoots and sprouting seeds was compared. Both biomasses showed the ability to bind an appreciable amount of copper(II) from aqueous solutions.

Introduction

The use of biological materials for biosorption of toxic metal ions may be a cost-effective alternative technique for the treatment of industrial effluents [1]. In fact, many studies have been performed with bacteria, algae, and fungi to determine the abilities of these biomasses to adsorb metal ions [2]. More recently, plants have been of interest for their unique ability to bind heavy metals and phytoremediate contaminated areas [3]. Lujan et al. [2] found that metal binding by higher plant tissues was pH dependent. Therefore, plant tissues may be a good source of biological materials for the biosorption of toxic metal ions from aqueous industrial waste effluents. *Medicago sativa* may be a good source of plant tissues because it has been found to tolerate heavy metals and grow well in contaminated soils [2].

Methodology

Medicago sativa were collected from field studies conducted at Čortanovci. The plants were removed from the soil. The roots and shoots were separated and shoots were used for experiments. Sprouting seeds used in experiment were grown in laboratory conditions. The biomass was dried and ground. Samples were sieved through a 100-mesh sieve to give a uniform particle size. Biomass was washed with 0.01 M hydrochloric acid (HCl) to remove any debris that might interact with metal ions. Washings were collected and dried. Four biomass samples were resuspended in 25 ml of 0.01 M HCl with tissue concentration of approximately 5 mg/ml of solution (one for each pH value). The pH was adjusted to 2.0, 4.0, 5.0 and 6.0 using dilute sodium hydroxide (NaOH) and allowed to equilibrate. The suspensions were centrifuged at 2500 rpm for 5 min and supernatants were examined to determine if soluble materials in solution could be responsible for copper binding. A solution of 0.1 mM copper sulfate (CuSO_4) was prepared and the pH adjusted to 2.0, 4.0, 5.0 and 6.0 using dilute

sulfuric acid (H_2SO_4) and allowed to equilibrate. At each pH 25 ml of the copper solution were added to the respective pH biomass pellet, and to the separated supernatant solutions. All the tubes were equilibrated on a rocker for 1 h, except tubes for time dependency study, which were removed at the appropriate time intervals. The samples were then centrifuged at 3000 rpm for 5 min and the supernatants were separated from the pellets. Copper concentrations were determined by AAS Perkin Elmer Analyst 300.

Results and Discussion

As can be seen in Fig. 1, the binding of copper ions by the *Medicago sativa* biomass is pH dependent, with a maximum binding observed between pH 5.0 and 6.0. Experiments indicated that sprouting seeds bind more copper ions from solution, than shoots and seem to be less pH dependent. This can possibly be attributed to different chemical composition.

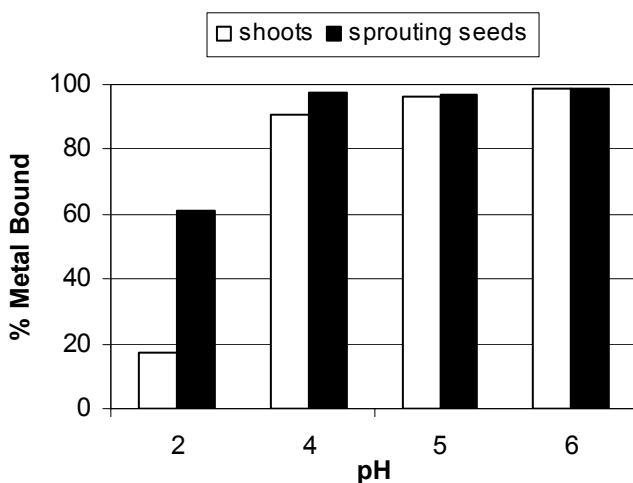


Figure 1. Effects of pH on copper binding by shoots and sprouting seeds

This trend in pH dependent binding suggests that carboxyl groups may play a role in the copper binding by the biomass. The acid dissociation constants for various carboxyl groups have been reported to be around 3-4. Free carboxyl groups are protonated at pHs lower than 3 and reduce any metal binding. At pHs greater than 4, the carboxyl groups are deprotonated and attract positively charged copper ions. Metal ions bind to the carboxyl groups through an ion-exchange type mechanism [4]. Figure 2. demonstrates the percent of copper ions removed from solution by *M. sativa* shoots and sprouting seeds when exposed to 0.1mM copper solution at pH 5 over a 60 min period. It can be seen that the mechanism for copper ion binding occurs in less than 5 min. Even after 1h of reaction, relatively the same amount of copper was bound. This shows that the binding of copper is relatively stable.

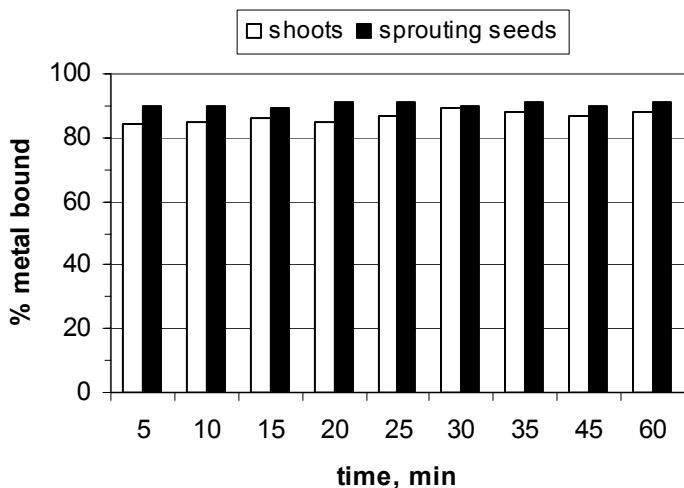


Figure 2. Time-dependency studies for copper binding by shoots and sprouting seeds

Conclusion

Medicago sativa shoots showed ability for high removal of copper ions from water solution which is in consistency with reported data. Sprouting seeds proved to be more efficient and less pH dependent. Both biomasses showed that the binding of copper is relatively stable and that copper ion binding occurs in less than 5 min. Obtained data will be used for the future development of an innovative, environmental friendly technology for removal or recovery of heavy metal contaminants from polluted ground waters. Experiments under flow and multi metal ion conditions are being conducted.

References

- [1] R. M. Atlas, Chem. Eng. News 3 (1995), 32.
- [2] J. L. Gardea-Torresdey, K. J. Tiemann, G. Gamez, K. Dokken, J. Hazard. Mater., 1999, B69, 41.
- [3] D. E. Salt, R. D. Smith, I. Raskin, Annu. Rev. Plant Physiol. Plant Mol. Biol. 1998, 49, 643.
- [4] J. L. Gardea-Torresdey, K. J. Tiemann, J. H. Gonzalez, J. A. Henning, M. S. Townsend, J. Hazard. Mater., 1996, 48, 181.

FENITROTHION - ADSORPTION AND DEGRADATION ON SYNTHETIC AND NATURAL ZEOLITE

V. Jovanović¹, V. Dondur¹, M. Damjanović² and M. Tomašević-Čanović³

¹*Faculty of Physical Chemistry, Beograd, Serbia and Montenegro*

²*Galenika Fitofarmacija, Beograd, Serbia and Montenegro*

³*Institute for the Technology of Nuclear and Other Mineral Raw Materials, Beograd, Serbia and Montenegro*

Abstract

The adsorption of insecticide fenitrothion on synthetic and natural zeolite has been studied by HPLC and UV/VIS spectroscopy. Zeolite's surface performed by modification cationic surfactants was also investigated. This paper shows that synthetic and natural zeolites can be used as efficient adsorbents for organophosphorous insecticides similar to fenitrothion.

Introduction

Insecticides are widely used for protection of herbs. Most of these insecticides are directly discharged into environment after usage, causing significant environmental problems. Therefore eliminating pesticide's molecules and determining their concentrations in environmental waters is of great importance. The photocatalytic degradation, thermal degradation, hydrolysis and photolysis in water are efficient methods [1], but these processes last a long time. However, adsorption of these molecules is a very fast process which can have environmental significance

Zeolites are hydrated aluminosilicate minerals characterized by cage - like structures, high internal and external surface areas, and high cationic exchange capacities. When appropriately modified with cationic surfactants, zeolites become excellent adsorbents for some anions, cations and nonpolar organic species [2]. Cationic surfactants may be used to enhance zeolite's adsorption of environmental contaminants like pesticide molecules. In this work we present a study of the insecticide fenitrothion (*O*, *O*-dimethyl-*O*-3-m-4-nitro-phenyl phosphorothioate) sorption on synthetic (CaY) and natural (clinoptilolite (Cli)) zeolite. Quantity of adsorbed fenitrothion on zeolites was determined by high pressure liquid chromatography (HPLC) and UV/VIS spectroscopy.

Experimental

Materials CaY zeolite used in this work was prepared from synthetic NaY (SK-40, Union Carbide, Si/Al = 2, 45) by aqueous cation exchange. Natural clinoptilolite was obtained from the deposit Zlatokop, Serbia, purity degree was higher than 90%, with pyrite, quartz and feldspar as the major impurities. This clinoptilolite is predominantly of the calcium type with a cation exchange capacity (CEC) of 1420 mmol M+/kg, and an external cation exchange capacity (ECEC) of 190 mmolM+/kg. The ECEC value refers to exchangeable cations at the external zeolite surface. The SMZ were prepared

by the adsorption of alkyl ammonium salt (stearyldimethylbenzyl ammonium chloride) on CaY and on clinoptilolite as described in [3].

Methods Zeolites suspensions in water (10 mg-200 mg in 10 ml of water) were treated with 30 μ l fenitrothion solution. The suspensions were mixed for two hours on a magnetic stirrer at 25° C. The amounts of fenitrothion adsorbed were calculated from the differences between the amount of fenitrothion added and that remaining in the final equilibrium solution. The insecticide fenitrothion (95% purity) was purchased as pesticide standard. UV/VIS-CINTRA spectrophotometer was used to record absorbance curves. Technical grade samples of fenitrothion were analyzed by HPLC on a reverse phase mode (RP-18 column) with UV detection (267 nm). The mobile phase contained acetonitrile-water (6:4). The HPLC system was mainly composed of a pump (LC 1150 HPLC), a sample injector (Rheodyne Model 7125, sample size 200 /zl-5 ml) and a UV detector (LC 1200 UV/VIS).

Results and Discussion

Fenitrothion adsorption on CaY and clinoptilolite is studied by the UV/VIS spectroscopy. The obtained spectra are shown in Figure1.

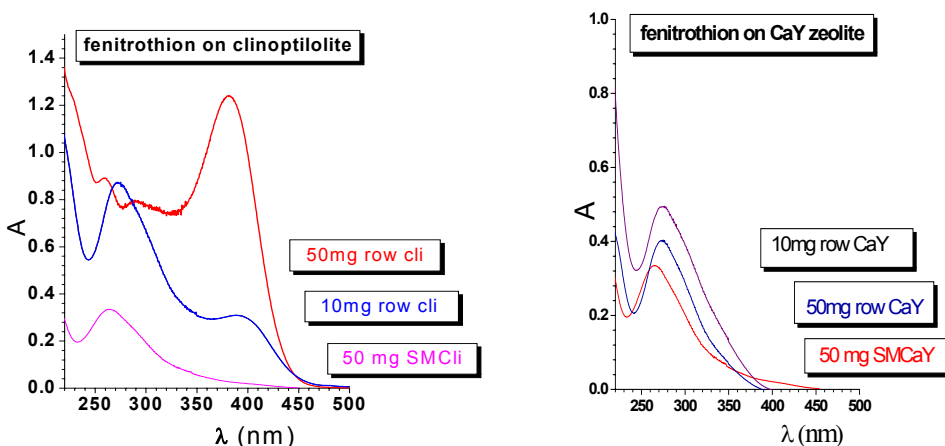


Figure 1. UV/VIS spectra recorded during fenitrothion adsorption on row and zeolite modified with cationic surfactant: a) clinoptilolite b) CaY

Two distinct absorption maxima are evident in the UV spectra of the in fenitrothion collected after adsorption on clinoptilolite in the range from 220 to 500 nm . The absorption maximum at the lower wavelength (227 nm) can be assigned to the aromatic group of the original compound and that the one at the higher wavelength (400nm) is a new signal which appears after adsorption.

Intensity of the maximum at 400 nm increases with increase of zeolite concentration as well as with increase of basicity of the environment. Adsorption is more efficient on the organomodified clinoptilolite and in that case signal at 400 nm corre-

spodentic to.. Maximum at 400 nm in the UV spectra shown in Fig. 1.a might be result of the degradation of fenitrothion.

As it can be seen from HPLC chromatographs of pesticide solution after adsorption, shown in Fig.2, more then 95% of fenitrothion were adsorbed on zeolites (CaY and Clinoptilolite).

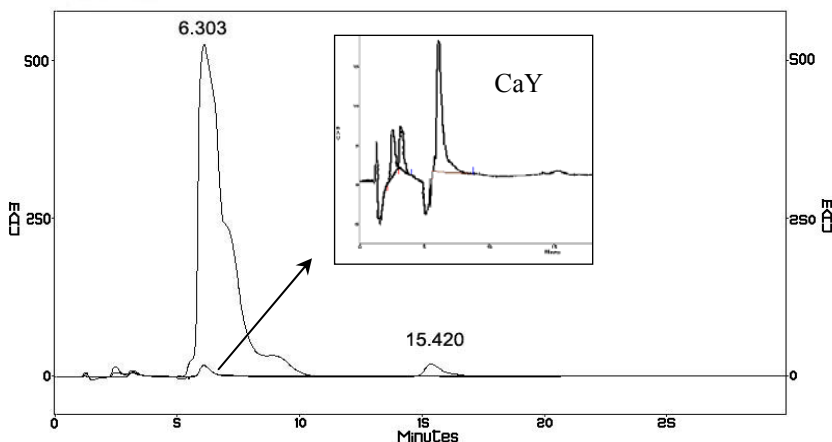


Figure 2. HPLC chromatogram of standard fenitrothion ($3\mu\text{l}/\text{cm}^3$) and sample solution CaY

Presented results indicate possible degradation of fenitrothion on row zeolite sample, while is the case of SMC only it's adsorbed takes place. The results obtained for CaY indicate only the adsorption of fenitrothion.

Conclusion

The obtained results show that synthetic and natural zeolite can be used as efficient fenitrothion adsorbents. Adsorption of fenitrothion on natural zeolites is accompanied by possible degradation of this insectide. The fenitrothion adsorption measurements showed that the most efficient adsorbent for fenitrothion were the zeolites modified with cationic surfactant. There is a great potential in application of the adsorption process for removal of pesticides from environmental waters.

References

- [1] Ioannis K. Konstantinou, Triantafyllos A. Albanis, *Appl. Catal. B: Envir.*, 2003, 42, 319.
- [2] Sullivan, E.J., R.S. Bowman, and I.A. Legiec. *J. Environ. Qual.*, 2003, 32, 2387.
- [3] A. Vujaković, A. Daković, J. Lemić, A. Radosavljević-Mihajlović and M. Tomašević-Čanović, *J.Serb.Chem.Soc*, 2003, 68, 833.

PHOTOCHEMICAL DEGRADATION OF DIGOXIN TESTED BY Na,K-ATPase ACTIVITY

K. Krinulović, V. Vasić, U. Černigoj* and M. Franko*

Vinča Institute of Nuclear Sciences, P.O.Box 522, 11001 Belgrade, Serbia & Montenegro

**Nova Gorica Polytechnic, Laboratory of Environmental Research,
P.O.B. 301, SI-5001 Nova Gorica, Slovenia*

Abstract

The photochemical degradation of digoxin aqueous solution was obtained by Xe-lamp irradiation. The concentrations of digoxin in irradiated solutions were detected by measurements of Na,K-ATPase activity and by HPLC analysis. The excellent agreement using two independent methods for determination of digoxin concentration in the irradiated samples was achieved.

Introduction

Na,K-ATPase is transmembrane enzyme, which utilize energy liberated from ATP hydrolysis for active transport of monovalent cations across the membranes [1,2]. Digoxin, cardiac glycoside most frequently used to improve cardiac contractility in the treatment of congestive heart failure, acts through the inhibition of Na,K-ATPase [3]. The exposure to light of a great number of organic compounds results in photolytic degradation, leading to their decomposition or to the formation of other toxic compounds. There is lack of data concerning the photochemical degradation of digitalis cardiac glycosides. However, digoxin is known as stable when keeping in the dark and well-closed containers, but it undergoes to the acid catalysed hydrolysis in water solutions [4]. Since digoxin belongs to the group of the specific Na,K-ATPase inhibitors, the aim of this work was to investigate the possibility of the use of Na,K-ATPase assay for the determination of its concentration after the photochemical treatment.

Experimental

Chemicals. All chemicals were of analytical grade. Na,K-ATPase from porcine cerebral cortex was purchased from Sigma Co. Digoxin was obtained from "Zdravlje", Leskovac. Digoxin was irradiated by using Xe lamp of 125 W. The sample was illuminated with light from 220 to 1100 nm, but only the light between 220 and 300 nm was consumed by the molecule.

ATPase assay. Na,K-ATPase activity was determined in 200 μ l of the standard incubation medium [4], 2 mg/ml protein and 20 μ l of the irradiated digoxin solution. The reaction was started by the addition of ATP at 37 °C. The inorganic orthophosphate (P_i) liberated from the hydrolysis of ATP was measured using modified spectrophotometric procedure [4]. The enzymatic activity in the presence of digoxin was calculated as the percentage of the control value of the standard incubation mixture, without the inhibitor.

Apparatus. HPLC measurements were carried out on a system Hewlett Pacard Series 1100, according to the procedure *Jedlička et al.* [5].

Results and Discussion

Detection of digoxin concentration by Na,K-ATPase assay. Aqueous solution containing 1×10^{-3} M digoxin and 30% ethanol was irradiated by Xe-lamp for 2.5, 5.0, 7.5, 10.0, 20.0, 40.0 min. The irradiated samples were diluted in the concentration range from 1×10^{-9} M to 1×10^{-4} M, related to the concentration of the unirradiated sample. The influence of the various irradiation times on digoxin induced inhibition of Na, K-ATPase activity was followed in the above mentioned concentration range as described in *Experimental*. The concentration dependent inhibition curve representing Na,K-ATPase activity vs. digoxin concentration in the unirradiated sample served as the calibration graph for determination of digoxin concentration in irradiated sample. The inhibition curves (activity vs. the added digoxin concentration before the photochemical treatment) for various irradiation times are presented in Figure 1. The results show that the increasing of the irradiation time decreased the digoxin-induced inhibition. The concentration of digoxin in irradiated solutions was extrapolated from the concentration dependent inhibition curve of the unirradiated sample and the results are given in Table 1.

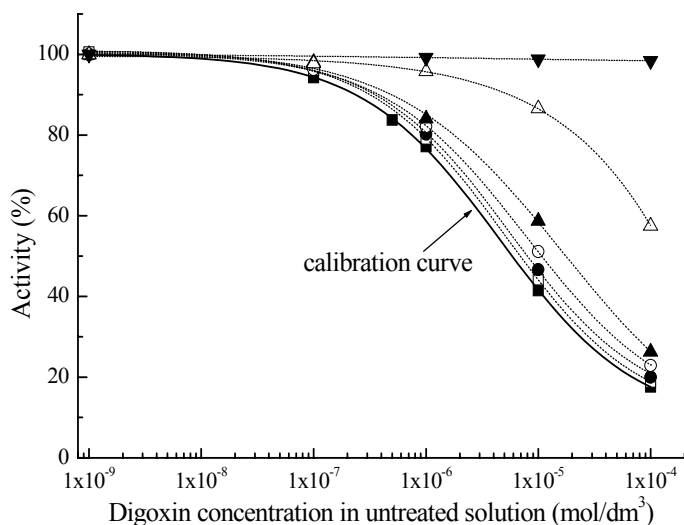


Figure 1. Digoxin-induced inhibition of Na,K-ATPase: unirradiated solution of digoxin (■), solutions of digoxin irradiated for 2.5 min. (□), 5.0 min. (●), 7.5 min. (○), 10.0 min. (▲), 20.0 min. (△) and 40.0 min. (▼)

HPLC analysis of irradiated samples. For the comparison, the concentrations of digoxin in irradiated samples were determined by HPLC. It is worthy to notice, that the other degradation products, except the reduced digoxin concentration, were not detected by HPLC analysis. The digoxin concentrations obtained by HPLC analysis are also presented in Table 1, together with the calculated efficiency of degradation. By the applied irradiation energy, over 96% degradation efficiency was achieved already 20 min following the irradiation, since after 40 min irradiation the degradation was complete.

Table 1. Comparison of concentrations of digoxin determined by HPLC and ATPase assay in the irradiated samples

Time of irradiation (min.)	digoxin concentration (mol/dm ³)		Efficiency of irradiation (%)
	determined by HPLC	determined by ATPase assay	
0	1.00 x10 ⁻³	1.00x10 ⁻³	0.0
2.5	8.83 x10 ⁻⁴	8.70x10 ⁻⁴	11.7
5.0	7.23 x10 ⁻⁴	7.32x10 ⁻⁴	27.7
7.5	5.41 x10 ⁻⁴	5.44x10 ⁻⁴	45.9
10.0	3.26 x10 ⁻⁴	3.48x10 ⁻⁴	67.4
20.0	3.76 x10 ⁻⁵	3.87x10 ⁻⁵	96.2
40.0	0	1.24 x10 ⁻⁹	100.0

Conclusion

The determination of digoxin concentration by standard analysis (HPLC) and by the measurement of Na,K-ATPase activity showed the excellent agreement. The measurement of digoxin induced inhibition of Na,K-ATPase activity was considered to be a good test for the determination of the degree of degradation after the photochemical treatment. Moreover, the change of Na,K-ATPase activity can indicate the toxicity of photochemically irradiated digoxin and its degradation products.

References

- [1] P.L. Jorgensen, P.A. Pedersen, *Biochim. Biophys. Acta*, 2001, 1505, 57.
- [2] L.A. Vasilites, W. Schwartz, *Biochim. Biophys. Acta*, 1993, 1154, 201.
- [3] C.P. Melero, M. Maderade, A. San Feliciano, *Molecules*, 2000, 5, 51.
- [4] V. Vasić, D. Jovanović, D. Krstić, G. Nikezić, A. Horvat, Lj. Vujisić, N. Nedeljković, *Toxicol.Let.* 1999, 110, 95.
- [5] A. Jedlička, T. Grafnetterova, V. Miller, *J. Pharm. Biomed. Anal.*, 2003, 33 109.

EFFICIENCY OF IRON(III)OXIDE IN PHOTOCATALYTIC DEGRADATION OF THE FUNGICIDE METALAXYL

A. Topalov¹, S. Korom¹, D. Molnár-Gábor¹ and M. Čomor²

¹*Department of Chemistry, Faculty of Sciences, University of Novi Sad, Trg D. Obradovića 3, 21000 Novi Sad, Serbia and Montenegro*

²*Vinča Institute of Nuclear Sciences, 11001 Belgrade, P.O. Box 522, Serbia and Montenegro*

Abstract

On the basis of quantitative ¹H NMR results we concluded that the photocatalytic degradation of the fungicide metalaxyl in the presence of Fe₂O₃ as photocatalyst, in the initial period, follows the first-order kinetics with reaction rate 4.4 times slower than with the TiO₂ as photocatalyst.

Introduction

In this study photocatalytic capability of Fe₂O₃ was tested because this material can harvest a greater portion of the solar spectrum, compared to TiO₂. Colloidal solutions consisting of Fe₂O₃ nanoparticles were used for photodegradation of metalaxyl (*N*-(2,6-dimethylphenyl)-*N*-(methoxy-acetyl)-*D,L*-alanine methyl ester, C₁₅H₂₁NO₄) as a model compound of organic waste photodegradable substance in water. The objective was to study the photocatalytic activity of Fe₂O₃ nanoparticles towards the degradation of the mentioned compound in water and to compare it with the literature data [1].

Experimental

The fungicide metalaxyl, 93% purity, was obtained from “Župa”, Kruševac (Serbia and Montenegro). The commercial product was purified by a conventional recrystallization method from water-ethanol (1:1) solution and its purity was confirmed by NMR spectroscopy (Bruker AC-250).

Colloidal Fe₂O₃ nanoparticles were synthesized at Institute of Nuclear Sciences “Vinča” Belgrade, by controlled acidic (HCl) hydrolysis of FeCl₃ (p.a., Merck) at temperature ~ 85 °C for 24h. The elimination of chloride ions was obtained by dialysis with triply distilled water [2]. Characterization of synthesized Fe₂O₃ was determined by X-ray diffraction (Philips PW 1710 diffractometer), spectrophotometrically (Perkin-Elmer Lambda 5 spectrophotometer) as well as by BET-surface area method (Micromeritics Instrument Corporation ASP 2000.V1.03). All the experiments were carried out using 1.6 mg cm⁻³ colloidal solution of Fe₂O₃.

The photochemical cell (sample volume 20.0 cm³) was made of Pyrex glass with a plain window (on which the light beam was focused), equipped with a magnetic stirring bar, a water circulating jacket, and two openings: for taking of ¹H NMR sample and O₂ stream. Colloids of Fe₂O₃ containing metalaxyl (2.7 mmol dm⁻³) were sonicated for 10 minutes before illumination, to make the Fe₂O₃ particles uniform. The

illumination process was carried out at temperature of 40 ± 1 °C. Colloids were illuminated with a simulated solar light (150 W halogen lamp, Osram).

Samples for quantitative ^1H NMR measurements (0.5 cm^3) were evaporated to dryness after filtration. After that, the ^1H NMR spectral profiles of only the parent compound were monitored on a Bruker DRX-500 instrument dissolving the evaporated samples in 0.5 cm^3 of D_2O with addition of sodium salt of 3-trimethylsilyl-1-propane sulfonic acid (DSS) as internal standard.

Results and Discussion

The X-ray and spectrophotometrical analysis showed that Fe_2O_3 nanoparticles have corundum crystal structure with energy band gap 2.2 eV (light of wavelengths $\lambda \leq 563.6\text{ nm}$) and a primary particle size of $\sim 5\text{ nm}$. By using of BET method it was determined that the surface area is $121.11 \pm 0.76\text{ m}^2\text{ g}^{-1}$.

The photoexcitation of Fe_2O_3 taking place under irradiation with the light of energy greater than its band gap, generates an electron-hole pair, creating the possibility for both reduction and oxidation processes to occur at the surface of the semiconductor. Although a number of possible decomposition pathways can be envisioned, the formation and subsequent reactions of hydroxyl radicals, being a very strong oxidizing agent (standard redox potential +2.8 V), generated from the oxidation of water molecules are generally accepted as the predominant degradation pathways of organic substrates in oxygenated aqueous solutions.

The photoassisted oxidative degradation of metalaxyl was followed by recording temporal ^1H NMR spectra (Fig. 1) of the parent compound (δ (ppm)): 0.97 (a, 3H, *d*, CH_3); 2.07 and 2.35 (b/c, 6H, *m*, $2 \times \text{CH}_3$); 3.21 (d, 3H, *s*, OCH_3); 3.62 (e, 2H, *m*, CH_2); 3.74 (f, 3H, *s*, OCH_3); 4.51 (g, 1H, *q*, CH) and 7.09-7.32 (h, 3H, *m*, aromat. H). The signal of the methine proton was partially overlapped by HDO signal from D_2O . Since, in this case, the spectra of illuminated and evaporated samples (subsequently dissolved in D_2O) were recorded, only the signals of the parent compound, and not of the intermediates, could be observed. The percentage of degradation was calculated on the basis of comparing the integrated surface value of the fungicide and the standard signals present in spectra. The apparent first-order reaction constant determined for 16 h of irradiation, pertaining solely to the degradation of the initial compound was $k_{ap} = 6.62 \cdot 10^{-4}\text{ min}^{-1}$ ($r = 0.9975$).

It can be concluded that decomposition of metalaxyl during initial illumination time in the presence of synthesized nanosized Fe_2O_3 occurred about 4.4 times slower in comparison to TiO_2 (Degussa P-25) [1] indicating that semiconductor studied in this work is less efficient.

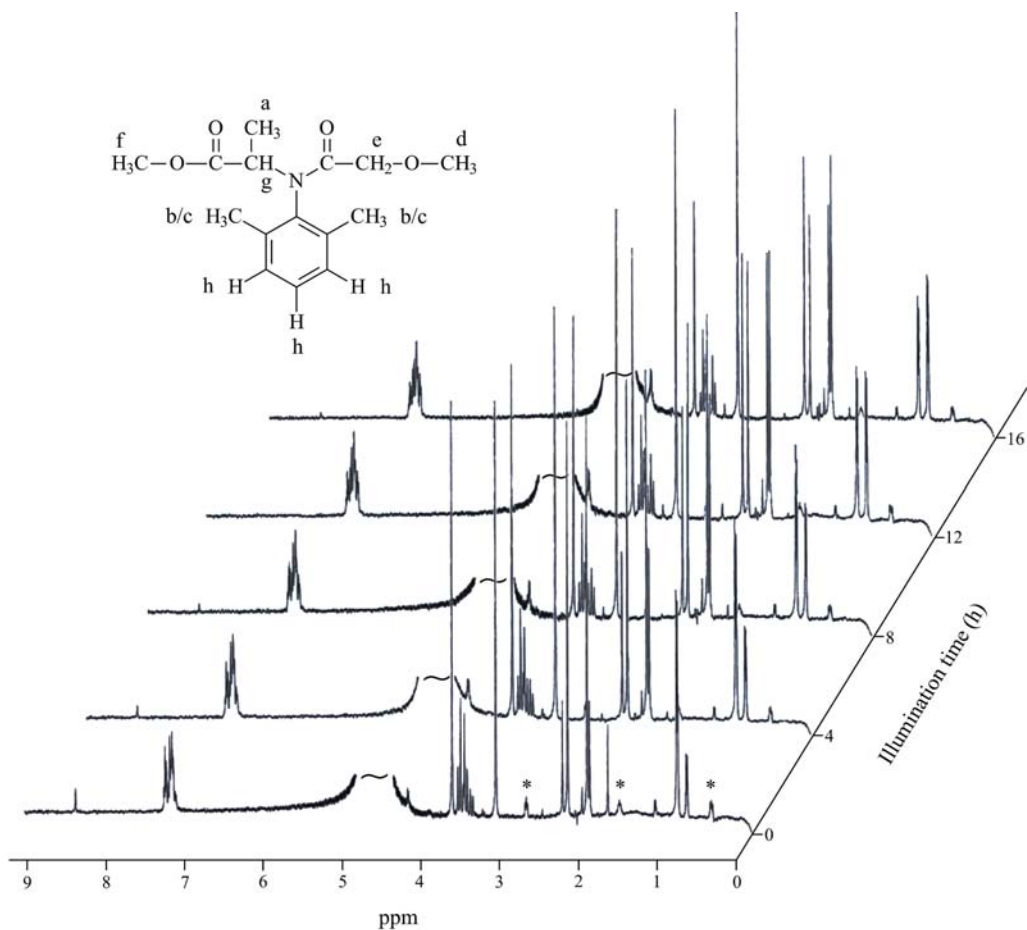


Figure 1. Temporal ^1H NMR spectral profiles of only parent substance during the metalaxyl (2.7 mmol dm^{-3}) photodegradation by using Fe_2O_3 ; * – signals of internal standard.

References

- [1] A. Topalov, D. Molnár-Gábor, J. Csanádi, *Wat. Res.*, 1999, 33, 1371.
- [2] E. Matijević, P. Scheiner, *J. Colloid Interface Sci.*, 1978, 63, 509.

THE INFLUENCE OF BACTERIZATION OF MAIZE SEEDS IN FUNCTION OF ENVIRONMENT PROTECTION

G. Cvijanović¹, N. Milošević² and D. Cvijanović³

¹Maize Research Institute, Slobodana Bajića 1, 11185 Zemun Polje, SCG

²Institute of Field and Vegetable Crops, Maksima Gorkog 30, 21000 Novi Sad, SCG

³Institute of Agriculture in Economics, Bulevar Kralja Aleksandra 80, 11000 Belgrade, SCG

Abstract

In the system of the safe food production the biological nitrogen fixation is a process of atmospheric nitrogen transformation to form accessible for plants by microorganisms – diazotrophs. The aim of experiment was to study influence of the maize seed inoculation with different diazotroph species and their mixtures, together with different fertilization regimes on the maize yield and parameters of soil biogenity (the sum of bacteria and *Azotobacter*). The seed bacterization, substituted some quantities of mineral nitrogen from fertilizers in equilibrium maintaining of soil with increase of the yield.

Introduction

In the system of the safe food production the biological nitrogen fixation is a safe process in transforming of atmospheric N to the forms accessible for the plants by microorganisms – diazotrophs. Such production characterises attained savings of expensive mineral fertilizers and conservation of soil biogenity, so the soil is able to regenerates in shorter time for next cycle of production, than in conventional fertilizer application.

The incorporation of diazotrophs in soil increases nitrogen content 20-70%. Additionally, they increase quality and quantity of yield [1,2] together with protection of pathogens [3].

The aim of experiment was to study influence of the maize seed inoculation with different diazotroph species and their mixtures, together with different fertilization regimes on the maize yield and parameters of soil biogenity.

Material and Methods

The trial was set up on the field of Maize Research Institute in Zemun Polje. Effectiveness of bacterization was studied on ZP SC 677, with liquid inoculums of selected high-effective species of azotrophs and their mixtures: **1-***Azotobacter chroococcum* 84; **2-** *Azospirillum lipoferum* 2; **3-** *Klebsiella planticola* 4; **4-** 1+2+3+*Bacillus megaterium*+*Azotobacter vinelandi*+*Bacillus subtilis*; **5-** 1+3+*Bacillus megaterium*+*Azotobacter vinelandi*+*Bacillus subtilis*. In experiment five doses of fertilizer were applied: no fertilizer, 30, 60, 90 and 120 kg N ha⁻¹. The seeds were bacterized before sowing.

The soil biogenity was tested through the number of microorganisms *via* standard used microbiological methods: total number of microorganisms (10⁻⁷/1 g of soil) on agarised soil extracts [4], number of *Azotobacter* on substratum of Fjodor

by "fertile drops" method (10^{-1} /1 g of soil). To express the total number of microorganisms was used the Index Level (I.N.), as percentage level of comparison to control.

Results and Discussion

The variants of seed bacterization had different effect on soil biogenity parameters (Tab. 1): They have shifted microorganisms *in situ* in course of increasing total number (609 I.N.), especially in combination 4 with 90 kg N ha⁻¹ doze. The similarly trend of number increasing was observed in *Azotobacter*, the microorganism with high importance to N utilization by root.

Tab. 1 The influence of bacterization on the parameters of soil biogenity

Combination		K	1	2	3	4	5	Average	
Fertil. (kgN.ha ⁻¹)								I.N.	
UB	0	84	533	165	117	112	161	218	258
	30	243	327	320	692	795	446	427	175
	60	418	306	231	766	423	451	435	104
	90	49	365	221	171	452	284	299	609
	120	39	21	37	35	27	34	31	78
Average		167	310	195	356	362	275	-	-
AZ	0	15	18	6	12	43	12	18	121
	30	25	50	43	12	31	35	34	136
	60	30	44	50	61	60	55	54	180
	90	22	60	61	37	24	24	40	182
	120	19	12	15	12	19	33	19	101
Average		22	37	35	27	35	32	-	-

K-Control; UB-Sum of microorganisms 10^{-7} ha⁻¹; AZ-Number of azotobacter 10^{-1} .ha⁻¹; I.N.-Index Level

Tab. 2 The influence of bacterization on the maize yield (kg.ha⁻¹)

Combination	K	1	2	3	4	5	Average	
Fertilization kgN.ha ⁻¹	t.ha ⁻¹	I.N.						
0	5,05	5,51	4,59	5,44	5,04	7,10	5,53	109
30	6,96	7,20	7,71	6,71	7,42	7,25	7,25	104
60	10,26	10,88	11,46	11,67	12,36	10,90	11,45	111
90	10,96	11,39	11,37	11,92	12,18	12,07	11,78	107
120	11,58	11,56	12,26	11,45	12,16	10,79	11,64	101
Average	8,96	9,31	9,48	9,44	9,83	9,62	-	-

Based on the attained results, the individual species (variants 1 and 2) increased number of microorganisms [5-8] especially of *Azotobacter* in combination with 60 kg N ha⁻¹ (180 I.N.) and 90 kg N ha⁻¹ (182 I.N.) [2,9,10]. Opposite to upper, the increased doses of N fertilizer reduced total soil biogenity [11].

Besides, the seed bacterization increased the maize yield: the variant 4 released the highest yield in combination with 60 kg N ha⁻¹, but the doze of 90 kg N ha⁻¹ took the highest yield in all variants of bacterization.

The application of N mineral fertilizer raises nitrate level in plants could influence harmful effect on human health. Despite of specific influence of maize plants on the diazotrophs, there is necessity for further investigations and selection of compatible species able to reduce oscillations of soil biogenity and recover soil equilibrium.

Conclusion

The bacterization of maize seeds increased numbers of microorganisms, parameters of soil biogenity and maize yield. The best e3ffectivines was observed in doze of 60 and 90 kg N ha⁻¹.

Based on obtained results it could be concluded that seed bacterization by diazotrophs could substitute some quantities of mineral nitrogen from fertilizers in the aim of equilibrium maintaining to the soil, with increasing of the yield.

References

- [1] Govedarica, M. Contemporary Agriculture, 1992, 40, 87. (In Serbian)
- [2] Cvijanović, G., Govedarica, M., Milošević, N., Jovanović, Ž. Book of articles Eco-conference, 2000, Safe food, Novi Sad, 2000, 365. (In Serbian)
- [3] Burns, R.G. Environmental Activites (eds Huang P. M., Bertelin, J., Bolag, J. M., Page, A. L.) CRC Press. Inc. 1995, 145.
- [4] Pochon, J., Tardiecx Tehnickues d analyse en microbiologique du Soil edit de la tourele, Paris, 1962.
- [5] Hajnal, T. Magistrate thesis, Agricultural Faculty, Novi Sad, 2002 (In Serbian)
- [6] O'Hara, G.W., Davey, M.R., Lucas, L., A. Can. J. Microbiol., 1981, 27, 871.
- [7] Govedarica, M., Jeličić, Z., Jarak, M., Milošević, N., Pavlović, M. Book of Articles from IX Council of Agronomists and Technologists, 14-16.02., Smederevo 1994, 44-47.
- [8] Govedarica, M., Jeličić, Z., Jarak, M., Milošević, N., Pavlović, M. Book of Articles from XI Council of Agronomists and Technologists, 13-16.02. Aranđelovac, 1997, 69-77.
- [9] Pavlenko, V.; F. Struktura i funkcii mikrobnih saobšćestv počve a sazičnoj antropogenoj nagruzkoj. Kiev, 1982, 180-184
- [10] Đukić, D., Mandić, L. The mineral nutrition as a factor of regulation in number of microorganisms and enzymic activity in the eutheric cambisol under weath, Yugoslavian Society of Soil Research, Novi Sad, 1987, 411 (In Serbian)
- [11] Asmus, F. Soily studies about humus VIIth Inter. Sym., Prague, 1980, 14-16.

APPLICATION OF FRACTIONAL EXTRACTION METHOD FOR DETERMINATION OF URANIUM ORIGIN IN BOILER FUR

M. B. Rajković¹ and M. Stojanović²

¹*Institute of Food Technology and Biochemistry, Faculty of Agriculture, Zemun, University of Belgrade,* ²*Institute for Technology of Nuclear and Other Mineral Raw Materials (ITNMS), Belgrade, Serbia&Montenegro*

Abstract

Method of fractional extraction showed its total appliance to determination of uranium origin in sediments (solid substance). On the basis of the results of fractional extraction, it can be concluded that the content of uranium in fur, which means in drinking water, represent potentially available and mobile fractions of uranium (94.20 wt.%) which indicates its anthropogenic origin.

Introduction

The concept of fractional extraction from sediment, in the case of our analyses it is fur, is based on the opinion that uranium with a solid substance could form connections of different strength and that connections could be gradually parted, by the activities of reagents of growing intensity during what the separated phases of extraction are defined according to their function or the type of connection in that substance [1].

By the analysis of fur, which is received by substance from drinking water in a house boiler, it was determined the presence of heavy metals and uranium [2].

The aim of this paper is qualitative determination of different forms of uranium by the method of fractional extraction in order to determine its origin in drinking water as the degree of adsorption by human beings.

Experimental

For the investigation, fur has been used, formed by precipitation on heater of a house boiler, during a time period of 6 months. The fur originated from water present in water-supply system of the town of Belgrade – town of Pančevo-Krnjača. After that, dry remnant has been determined by heating 1.0 dm³ of drinking water to boiling and evaporating to dry remnant.

Boiler fur were analysed using scanning electron microscopy SEM, JSM-840A, JEOL, Tokyo, Japan. Composition of the fur was determined on atomic absorption spectrophotometer AAS Perkin Elmer 703.

Quantitative uranium content has been determined by fluorimetric method. Decrease of fluorescence intensity is reduced to the lowest possible degree by the techniques of "standard addition" after uranium extraction with synergistic mixture TOPO in ethyl-acetate. Fluorescence intensity is determined by Fluorimeter 26-000 Jarrel Ash Division, Fisher Scientific Company, Waltham, 1978.

Fractional extraction is based on the theory that metals with solid phase form connections of different strength and that connections could be gradually parted by the

activities of reagents of growing intensity: *first fraction*, the solution of calcium chloride of 0.1 mol/dm^3 concentration (pH 7.0 value) is used for extraction of water-soluble and changeably adsorbed forms of metals, *second fraction*, the solution of acetic acid of 0.1 mol/dm^3 concentration (pH 5.0 value) is used for extraction of specifically adsorbed metals and metals connected with carbonates, *third fraction*, hydroxylamine hydrochloride in 25 wt.% solution of acetic acid (pH 3.0 value) is used for extraction of metals connected with manganese and iron oxides, *forth fraction*, nitric acid of 0.02 mol/dm^3 concentration in 30 wt.% solution of hydrogen peroxide is used for metals connected with organic matter. Structurally connected forms of metals in silicates (*fifth fraction*) are determined from the difference of total content of uranium and the content of the uranium from the first four fractions [1].

Results and Discussion

The results of the analysis of the fur on atomic absorption spectrophotometer are given as (in wt.%): calcium (as CaO) 48.85, magnesium (as MgO) 4.24, sodium (as Na₂O) 0.034, potassium (as K₂O) 0.012, iron (as Fe₂O₃) 4.02, manganese (as MnO) 0.031, silicon (as SiO₂) 0.10, aluminium (as Al₂O₃) less of 0.02, uranium 1 ppm, while sum loss from baking at 1,000°C is 42.67 wt.%.

SEM photograph of boiler fur obtained on scanning electron microscope is presented on Fig. 1.



Figure 1. SEM Photograph of crystalline structure of boiler fur (x1,100)

The picture of crystal structure of fur under an electronic microscope shows that fur is made from calcium carbonate, actually *calcite* which crystallize hexagonally, which is confirmed by making picture with diffract meter [2].

The results of the fractional extraction method usage for determination of different form of uranium connections in fur are shown in Table 1.

According to the received results it could be seen that the largest part of uranium is in the third fraction which clearly indicates that such solutions have great affinity towards uranium, and also indicates on its antropogenic origin.

Table 1. Content of uranium in boiler fur obtained from drinking water

No.	Uranium	U, ppm	% of U _{Total} *
1.	Total content of uranium in fur	1.1	100
2.	Water-soluble and measurably adsorbed	0.02	1.85
3.	Specifically adsorbed and connected with carbonates	0.09	8.33
4.	Connected with manganese and iron oxides	0.95	87.96
5.	Connected with organic matter	< 0.01	0.93
6.	Structurally connected in silicates	< 0.01	0.93

* Content, in %, individual fractions in total content of uranium in fur

On the basis of the results of fractional extraction, it can be concluded that the content of uranium in fur, which means in drinking water, represent potentially available and mobile fractions of uranium (94.20 wt.%) which indicates its anthropogenic origin.

Conclusion

The analysis of fur received from drinking water in house boiler, indicates that it consists mainly of calcium carbonate, *calcite*, which is confirmed by the picture under an electronic microscope. The rest of the elements, are represented in allowed concentrations except manganese, which is near the limit, and especially iron which is almost 20 times more (actually 18.73) than is permitted. That indicates to old installations but also that water in these sewers is rich with iron.

By the method of fractional extraction it is ratify that uranium is mostly connected with iron and manganese oxides (87.96 wt.%) which is total amount of 99.99 wt.% represents a form potentially available to human organism.

Acknowledgements

The work was supported by grant number 1941 from Ministry of Science, Technology and Development, Republic of Serbia.

References

- [1] A. Tessier, P. G. C. Campell, M. Bisson, *Anal.Chem.*, 1979, 51(7), 844.
- [2] M. B. Rajković, M. Stojanović, *Ekologija*, 2001, 36(1), 71.

MINERAL CONTENT OF WHEY CONCENTRATES AND ISOLATES

M. D. Pavlović, Z. I. Filipović, M. Ž. Živić and S. Ž. Gorjanović,
S. T. Hranisavljević and M. T. Dojčinović

Institute for General and Physical chemistry, P.O. Box. 551, Belgrade, Serbia and Montenegro

Abstract

Whey, the waste from dairy industry could be processed into high valuable food and pharmaceutical products. Low-temperature regime of whey concentration and fractionation, based on vacuum concentration and diafiltration, preserves whey proteins undenaturated and natural balance of whey minerals, with high K and Ca content. We have obtained components of functional food, based on native whey proteins and minerals, with potential benefits in prevention of cardiovascular and cancer diseases.

Introduction

Serbian dairies, poorly process whey, a by-product of cheese production, which is emitted into river systems. The most profitable solution of the ecological problem is processing of whey into food and pharmaceutical products. Whey concentrates and isolates (lactose, proteins, minerals and vitamins) could be obtained with low-temperature procedures of whey fractioning with satisfactory degree of microbiological purity and maximal preservation of whey protein physico-chemical and bioregulatory properties. The medicinal effects of undenaturated whey proteins, obtained with low-temperature regimes, are described for stimulating antioxidant and immunoregulatory activities in cancer treatment [1], hormonal effect in osteoporosis [2] and hypertension. Hypertension is also regulated by the high content of K, and relatively high content of Ca and Mg in whey [3].

Experimental

Sweet or acid cheese whey were obtained from Dairy Industry "Imlek" (Padinska Skela, SCG) and "Odžaci" (Odžaci, SCG) and pasteurised at 63°C. The milk or whey was cooled at 5°C, and concentrated on circulatory vacuum evaporator at 20°C. The whey concentrate was, then, used as the base for different foodstuff, or further processed. Row lactose of nutritional quality was obtained on filter-centrifuge or vacuum filter from whey concentrate (45-65% dry weight, d.w.), after storage on 4°C for 24 h, and processed by precrystalization and purified into lactose of pharmaceutical quality. Lactose, remaining in the filtrate (diluted to 20% d.w.) was separated from whey proteins by ultra filtration (U.F.) and diafiltration (D.F.). We applied polysulfonic 5000 D membrane. The processing solution was heated at 50°C. The U.F. and D.F. processing conditions considered an average transmembrane pressure of 1 bar and permeate flow rate of 10 ml/min with distilled water as diafiltration medium. Mineral content was determined by ion chromatography (Dionex, Sumyvale, USA). The samples for ion-chromatography were prepared in microwave oven on constant temperature ("Ethos", Milestone, E.U.). Whey protein content was determined by Kjeldahl and Lowry methods. We followed thermal stability (enthalpy of protein unfolding, ΔH^{cal} , and temperature of denaturation, T_m) in whey or whey protein concentrates, using the differential scanning calorimetry (DSC) method, [4]. All

DSC scans were carried out on MicroCal MC-2 Scanning Calorimeter, MicroCal Inc. Northampton, MA, USA.

Results and discussion

Under the pilot scale conditions we have obtained several whey products from waste whey: concentrated whey (30-60 % d.w.), whey paste (over 60% of d.w., 8-10% protein in d.w.), filtrate of concentrated whey after lactose separation (28-40% d.w., 17-40% protein in d.w.) whey protein concentrates purified by ultra filtration and diafiltration, (35-85% of protein in d.w.) lactose of nutritional quality (84% lactose in first crystallisation, 73-78% d.w., 1.5-3.3% protein in d.w.) and complex of minerals and vitamins, lactose and peptones in the permeate obtained after ultrafiltration of whey concentrate or crude whey. From DSC data obtained it can be assumed that thermal denaturation process of whey proteins during the concentration steps did not significantly differ regarding T_m and ΔH^{cal} , meaning that proteins did not suffer denaturation, what was also proven by second scans (DSC scans of denaturated whey proteins) (data not shown). Ion-chromatography data of main whey cations in vacuum-concentrated sweet whey, corresponds to literature data [5]. Concentrated sweet whey fractions: row lactose and whey filtrate (after lactose separation) have different distribution of main cations; Na and K concentrate in the filtrate. In acid whey, the Ca, also, concentrate in the filtrate, as expected, for Ca is more abundant in acid whey. After ultrafiltration of whey filtrate, the cations remain mostly in permeate, with the Na:K ratio similar to that of unconcentrated whey (approximately 1:2.5 - 1:4). Subsequent diafiltration fraction, retentate (protein concentrate fraction) is depleted of minerals, especially Na and K, Table.1.

Whey concentrates or whey protein concentrates were used as a source of protein for emulsions: in combination with vegetable oil (egg less mayonnaise, salad dressings or fruit creams) and for baked goods. Whey concentrate was mixed with different grain flours or dried vegetables and dried using fluid-bed dryer to obtain instant flours and additives for soups and whey filtrate permeate as salt replacement with high K vs. Na content. High K concentration in whey is supposed to be responsible for lowering blood pressure in experimental animals on moderate Na diet. Mg and Ca have also beneficial effects in hypertension. [3]. Besides, Ca, decrease accumulation of body fat and accelerates weight and fat loss during energy restriction.

Conclusion

Whey, a by-product of cheese industry could be processed into food and pharmaceutical products. We have shown that low-temperature regime of whey concentration and fractionation, based on vacuum concentration and diafiltration, preserves natural balance of whey minerals, especially high K content and undenaturated whey proteins with potentially high bioregulatory effects. Functional food products, based on native whey proteins, lactose of nutritional quality and complex of minerals and vitamins for salt replacement have been also obtained.

Table 1: Mineral content of vacuum-concentrated sweet and acid whey and whey fractions. The concentration of total protein content and main cations (Na, K, Ca and Mg) is expressed as percent of dry weight (d.w.).

Sample	d.w. (%)	Prot. (%)	Na (%)	K (%)	Ca (%)	Mg (%)
Sweet whey "Imlek"						
Whey (conc.10x)	61.7	11.6	0.61	2.69	0.40	0.10
Row lactose (centrifuged)	76.0	1.8	0.19	0.72	0.35	0.03
Whey filtrate after lactose separation	29.0	16.9	1.46	5.09	0.20	0.26
Retentate of whey diafiltration after lactose separation (R1)	10.4	51.9	0.23	0.36	0.07	0.86
Permeate of ultrafiltration of R1	7.7	0.5	1.18	4.23	0.20	0.16
Sweet whey "Odžaci"						
Whey (conc.)	27.0	17.6	0.87	2.19	0.34	0.10
Row lactose (not centrifuged)	59.0	2.0	0.60	1.68	0.26	0.07
Whey filtrate after lactose separation	34.1	40.0	1.92	4.38	0.13	0.19
Retentate of whey diafiltration after lactose separation (R1)	8.4	54.7	0.16	0.38	0.17	0.02
Permeate of ultrafiltration of R1	11.5	2.0	1.03	2.31	0.00	0.13
Acid whey "Odžaci"						
Whey (conc.)	35.9	14.8	0.67	2.08	1.05	0.15
Row lactose (centrifuged)	78.6	1.8	0.34	0.80	0.36	0.05
Retentate of whey diafiltration after lactose separation (R1)	5.1	48.0	0.32	0.60	0.26	0.03
Permeate of ultrafiltration of R1	12.9	2.2	0.81	2.94	0.65	0.00
Retentate of (unconcentrated) whey diafiltration	8.5	71.5	0.05	0.25	0.168	0.02
Permeate after ultrafiltration of whey (unconcentrated)	4.8	1.45	0.65	7.13	2.200	0.17

References

- [1] R. S. Kennedy, G. P. Konok, G. Bounous, S. Baruchel, T. D. Lee, *Anticancer Res*, 1995, 15 (6B), 2643.
- [2] Y. Takada, S. Aoe, M. Kumegawa, *Biochem. Biophys. Res. Commun.*, 1996, 223, 445.
- [3] X.Wu, J-P. Tolvanen, N. Hutri-Kahonen, M. Kahonen, H. Makynen, R. Korpela, H. Ruskoaho, K. Karjala, I. Porsti, *Cardiovascular Res.*, 1988, 40, 364.
- [4] P. L. Privalov, *Pure & Appl. Chem.*, 1980, 52, 479.
- [5] S. Damodaran & A. Paraf, edn. Marcell Dekker, Inc., New York Basel, 1997.

LOW CONCENTRATION VOLATILE ORGANIC POLLUTANTS REMOVAL IN COMBINED SORBENT/CATALYTIC REACTOR SYSTEM

Ž. Grbavčić¹, D. Ranković² and Z. Arsenijević³

¹*Faculty of Technology and Metallurgy, University of Belgrade, Karnegijeva 4, Belgrade,*

²*Faculty of Physical Chemistry, University of Belgrade, Studentski trg 12, Belgrade,*

³*ICHTM-Center for Catalysis and Chemical Engineering, Njegoševa 12, Belgrade, SCG*

Abstract

Removal of low VOCs concentrations in combined adsorber-desorber-catalytic reactor system using modified spouted bed with draft tube loaded with sorbent was investigated. Experiments were conducted on pilot unit of 3,5 m³/h nominal capacity. The sorbent was activated carbon, type K81/B - Traylor Corporation, Krusevac. A sphere shaped commercial Pt/Al₂O₃ catalyst with "egg-shell" macro-distribution was used for the investigation of xylene deep oxidation. Within this paper the investigations of xylene vapors removal, as typical pollutant in production of liquid pesticides, in combined adsorber/desorber/catalytic reactor system is presented.

Introduction

The removal of volatile organic compounds (VOCs) from numerous emission sources is of crucial importance due to more rigorous demands on air quality. Different technologies can be used to treat the VOCs from effluent gases: absorption, physical adsorption, open flame combustion, thermal and catalytic incineration. Their appropriateness for the specific process depends on several factors such as efficiency, energy consumption, secondary pollution, capital investments etc. The distinctive features of the catalytic combustion are high efficiency and selectivity toward benign products, low energy consumption and absence of secondary pollution. The supported noble catalysts are widely used for catalytic incineration due to their low ignition temperatures and high thermal and chemical stability.[1], [3]

In our combined system adsorption and desorption are applied in the spouted bed with draft tube (SBDT) unit. The annular zone, loaded with sorbent, was divided in adsorption and desorption section. Draft tube enabled sorbent recirculation between sections. Combustion of desorbed gases to the CO₂ and water vapor are realized in additive catalytic reactor. This integrated device provided low concentrations VOCs removal with reduced energy consumption. Within this paper, investigations of xylenes removal in adsorber/desorber/catalytic reactor system are presented.

Experimental

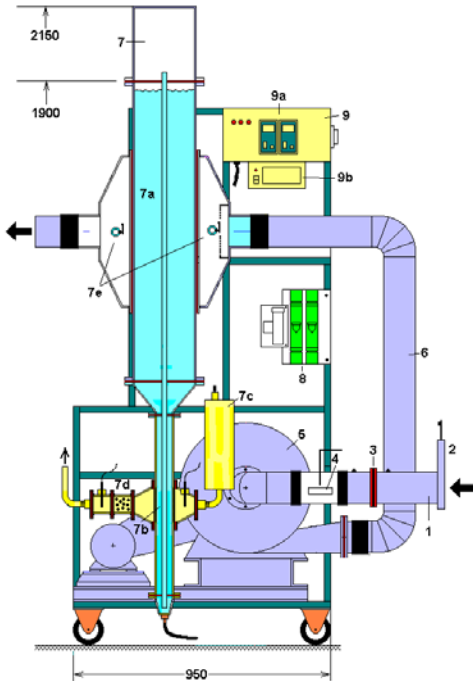


Figure 1. Pilot plant, nominal capacity of 3.5 m³/h waste gases

1- suction piping, 2- air flowrate regulation valve, 3- orificemeter for air flow, 4- evaporator, 5- blower, 6- repressing piping, 7- column with draft tube riser, 8- air flowrate indicator, 9- control panel (9a- temperature indicators, 9b- pulse mode programmer for sorbent transport)

Experimental investigations of xylenes removal from mixtures with air were performed on pilot unit of 3,5 m³/h nominal capacity, presented on Fig.1. The plant was developed in cooperation of IChTM and Faculty of Technology and Metallurgy in order to test wide range of pollutants under real industrial conditions. [2]

The adjusted amount of xylene vapors are generated in evaporator (4) and mixed with suction air in defined ratio. Gas mixture of known xylene concentration is introduced into adsorption zone (7a). Adsorption zone volume is 0,000942 m³ and available adsorption area is 0,0032 m². This zone is loaded with 0,531 kg of activated carbon, since its bulk density is 564,4 kg/m³ follows that. According to the sorbent capacity, the amount of VOCs than can be adsorbed is 0,531 kg. The flowrate of inlet gas mixture is 3,5 m³/h and corresponding superficial gas velocity is 0,3 m/s. The desorption zone is loaded with 0,182 kg of active carbon and zone volume is 0,006272 m². Available desorption area is 0,006272 m². The air flow of 3,8 m³/h is introduced

into desorption zone (7b) and corresponding superficial gas velocity is 0,17 m/s. This flowrate served as a heating medium and desired desorption temperature was achieved by electric heater (7c). Desorbed products are introduced in fixed bed catalytic reactor (7d) loaded with 0,169 kg of Pt/Al₂O₃ catalyst. The reactor volume is 0,00019 m³. Draft tube riser 16 mm in diameter and 1,23 m in height, placed in the center of the bed, enabled recirculation of activated carbon through both zones. The pulse sorbent transport from the desorption zone bottom to the top of the adsorption zone was attained by compressed air flow through the nozzle at the column bottom. In pulse mode there was periodical circulation of sorbent by means of electromagnetic valve and programmer for pulse introduction of compressed air (9b). During sorbent circulation air flow was 6 m³/h. The pulse duration was 6 seconds, while the pause between pulses was 4 minutes. The amount of transported active carbon in one pulse is 30,5 g that corresponds to bed height of 17,2 mm in desorption part. During pulse the sorbent mass flowrate through the transport tube was 5,08 g.

Temperatures at the desorption zone inlet and at the catalytic reactor inlet and outlet were continuously registered by NiCr-Ni thermocouples. Gas chromatograph equipped with FID detector was used for analyzing the xylene concentrations from the adsorption zone inlet and outlet, the desorption zone outlet and the catalytic reactor outlet. The xylene concentration in inlet air was maintained at $4,5 \text{ g/m}^3$.

Results and Discussion

Toward gas chromatograph analysis follows that the adsorption efficiency is above 99%. After the steady state operation was established in the system, at the desorption zone outlet was detected xylene concentration of $28,1 \text{ g/m}^3$. Inlet air temperature in the desorption zone was set up to the $150 \text{ }^\circ\text{C}$ that is required for xylene desorption. Under the same conditions the xylene concentration at the catalytic reactor outlet was $0,09 \text{ g/m}^3$. To incinerate desorbed xylene on the catalyst it was necessary to maintain the inlet temperature above the ignition point ($200 \text{ }^\circ\text{C}$) by electrical heater. The detected average temperature rise of $200 \text{ }^\circ\text{C}$ in the catalyst bed is the consequence of released heat of xylene catalytic combustion.

Conclusion

Adsorption, desorption and catalytic incineration were successfully integrated in proposed system. The overall system efficiency is above 99%. Our investigations point out that SBDT reactor is particularly suitable for the low VOCs concentrations. In comparison with conventional catalytic systems significant energy savings are achieved in the SBDT system. The system operation is flexible according to the inlet VOCs concentration variations by pulse/pause ratio adjustment. During experimental work the catalyst deactivation was not detected. Due to less grinding effects and lower pressure gradients, the coarser fractions of active carbon are more appropriate for industrial application. This system is applicable for various VOCs removal.

References

- [1] Boer J.H., The Dynamical Character of Adsorption, Oxford University Press, London, 1967.
- [2] Levenspiel O., Osnovi teorije i projektovanja hemijskih reaktora, Prevod sa engleskog, TMF, Beograd, 1992.
- [3] Ruthven D., Principles of Adsorption and Adsorption Processes, John Wiley & Sons, 1984.

MIGRATION OF DEPLETED URANIUM CONTAMINATION THROUGH THE SOIL

M. Radenković, D. Todorović and J. Joksić

*Radiation and Environmental Protection Department, Institute of Nuclear Sciences VINČA,
P.O.Box 522, Belgrade, Serbia and Montenegro*

Abstract

Military use of ammunition with depleted uranium at South Serbia, caused contamination of the environment. Surface soil and soil profile around projectile with depleted uranium were analyzed three years later by high resolution alpha/gamma spectrometry. It was found that activity levels in the soil layer next to the penetrator changes to 1% of initial value at 15 cm distance. This value is about double background uranium level of the soil at the Bratoselece location.

Introduction

In a few NATO air strikes in May and June 1999, about 1300 projectiles each containing 300g of depleted uranium, have been fired into the 5400m² area at Bratoselece, South Serbia. [1] No widespread contamination over the surface soil was found at the location but localized points of concentrated contamination around the projectiles. Three years later the clean-up action was undertaken and hot spots investigated. Isotopes ²³⁸U, ²³⁵U, ²³⁶U, ²³⁴U, ^{239,240}Pu and ²²⁶Ra are determined in the soil samples by high-resolution alpha and gamma spectrometry methods. This study should provide insight into the migration of contamination through the non-surface soil and to quantify contaminated soil to be removed from the environment within clean up.

Materials and Methods

Surface soil samples (0-15cm) and soil layers along the downward and sideward profiles were taken around depleted uranium penetrator, found at 50 cm depth. Homogenized samples are analyzed by alpha and/or gamma spectrometry.

For gamma spectrometry, samples were sealed for one month to reach the radioactive equilibrium. Measurements are performed with HP Ge detector with relative efficiency of 23%. The energies 1000 keV and 768 keV of ^{234m}Pa were used to determine ²³⁸U in samples with high activities and energy 63 keV of ²³⁴Th for low level activities. Low-level activities of ²³⁵U were determined with 143 keV and 186 keV (common with ²²⁶Ra). Isotope ²²⁶Ra was determined from energies of its daughters ²¹⁴Pb and ²¹⁴Bi (295, 351, 609, 1120, 1764 keV).

For alpha spectrometry method, the prior radiochemical procedure was performed. [2] Uranium and plutonium isotopes were extracted from the soil matrix and separated from each other by procedure based on the ion exchange at Dowex 1x8 anion resin. About 0.1 Bq of ²³²U and ²³⁶Pu tracer solutions were added to samples to obtain the chemical yield. After radiochemical separation, the thin-layer alpha radioactive sources were prepared by Talvitie's electrodeposition procedure at stainless still discs.

[3] The alpha spectra were obtained using vacuum chambers with PIPS detectors of 100 and 300 mm² surfaces and efficiencies 7% and 15% respectively for ²⁴¹Am.

Results and Discussion

Activities of analyzed soil samples are between: ²³⁸U (kBq/kg)=263.40±26.34; ²³⁵U (Bq/kg)=2174±370; ²²⁶Ra (Bq/kg)=255±4, just next to penetrator and ²³⁸U (kBq/kg)=0.16±0.06; ²³⁵U (Bq/kg)=1.2±0.2; ²²⁶Ra (Bq/kg)=151±26, at 10 cm downwards. The activities ratio ²³⁵U/²³⁸U is within interval 0.008-0.003 Bq/Bq. Activity levels at 15cm distance at the side are: ²³⁸U (kBq/kg)=0.10±0.04; ²³⁵U (Bq/kg)=0.40±0.07 and ²²⁶Ra (Bq/kg)=141±20. The mean content of ²³²Th in the samples was about 72±12 Bq/kg.

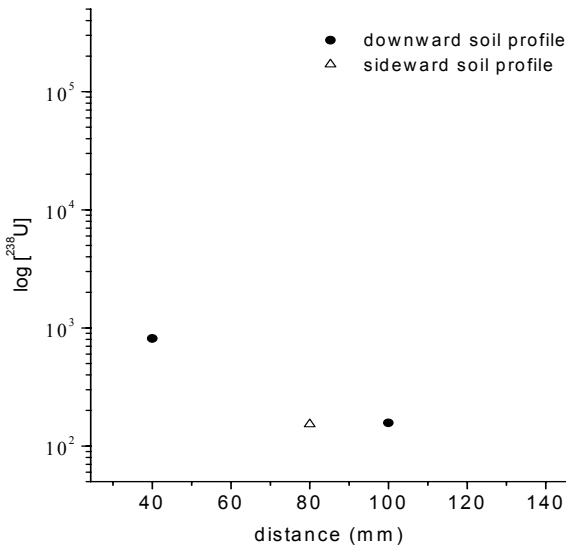


Figure 1. Content of ²³⁸U in the layers of the profiles around DU penetrator

Results have shown high DU contamination in the very vicinity of the penetrator and rapid devolution with the distance through the soil layers both downward and sideward of its centerline. According to the obtained results, the distance of about 15 cm is enough to decrease DU contamination level to 1% of the initial value. The contamination gradient is almost uniform in two studied directions around the projectile. (Fig. 1) Alpha spectrometry analysis of surface samples had shown the natural occurring ²³⁸U values to be 50-70 Bq/kg at the investigated location, known as granite petrology region. The traces of transuranic isotopes ²³⁶U, ^{239,240}Pu and ²³⁷Np were found earlier [4] in the penetrator, indicating that “dirty” uranium was a part of depleted uranium ammunition used at the site, but there was no detectable transuranic isotopes in the analyzed soil samples.

Uranium mobility through the soil depends on the present chemical forms of uranium under certain geochemical and weathering conditions at the location. Physical-chemical behavior of uranium oxides will be affected by the change of temperature, pH, surrounding soil composition, etc. Devolution of uranium activity with the distance could be explained as the summa of successive adsorption-desorption steps of depleted uranium through the soil.

Conclusion

Three years after contamination of the Bratoselce site, depleted uranium originated from the projectile penetrators have migrated through the deeper layers of soil reaching the double background concentration value at a distance of about 15 cm. The adsorption/desorption processes under physical-chemical changes in the environment are responsible for migration kinetics.

References

- [1] UNEP, Depleted Uranium in Serbia and Montenegro, Geneva: UNEP (2002).
- [2] M.Radenković, D.Vuković, V.Šipka, D.Todorović, J.Radioanal.Nucl.Chem., 1996, 208/2, 467.
- [3] N.A.Talvitie, Anal. Chem., 1972, 44, 280.
- [4] V.Šipka, M.Radenković, D.Paligorić, J.Djurić, Proceedings of XXI Symposium of YRPA, Belgrade, 2001, 69.

INVESTIGATION OF HEAVY METALS IN ROAD DUST AND SOIL SAMPLES IN TOURIST AREA BUDVA

J. Krstić¹, S. Petrović¹ and N. Vukelić²

¹*Institute of Chemistry, Technology and Metallurgy, Department of Catalysis and Chemical Engineering, Belgrade, Serbia and Montenegro*

²*Faculty of Physical Chemistry, University of Belgrade, Serbia and Montenegro*

Abstract

The concentration of heavy metals in street dust (9 samples) and soil (10 samples) that had been taken in Budva, the south of the Adriatic Sea, was determined by method of flame atomic absorption spectrometry after wet digestion. The mean concentration levels of Pb, Cu, V, Zn, Ni, Co in street dust samples versus soil samples were 253 vs. 67; 50 vs. 23; 29 vs. 31; 34 vs. 39; 187 vs. 122; 59 vs. 59; and 15 vs. 18 mg/kg respectively. The results showed extremely high value of Pb, which is related to a very intensive traffic in tourist season.

Introduction

Heavy metals are chemical elements, which are common for all kinds of soils. When the soil has very high content of such chemical elements, the term “heavy metal pollution” is used. These high contents may be of geogenic or atmospheric nature. Traffic and industry are two main anthropogenic factors. The determination of accumulated heavy metals in street dust and soil is very important in environmental monitoring [1].

Experimental

Budva is a small town on the south of the Adriatic Sea. During three summer months, it



represents a resort of tourist interest and the main destination of the majority of the visitors to Montenegro. This is clearly noticeable based on the data on contribution of Budva in total production of tourist waste of Montenegro in this three-month period, which amounts 81%. The majority of tourists come to holiday by cars, and regarding the applied circular traffic system in this town, it was interesting to test the content of heavy metals.

Figure 1. Map of Budva (a) dark circles—street dust (b) light circles—soil

Table 1. Concentration of heavy metals on different locations in road dust (bold) and soil samples nonbold

Loc. No.	Heavy metal concentration as mg/kg						
	Pb	Cu	Cr	V	Zn	Ni	Co
1	33	20,7	75,8	64	79	67	39
2	61	35,9	33,1	43	138	105	19
3	67	21,1	27,0	14	303	51	10
4	263	30,8	24,6	21	332	62	11
5	59	22,3	36,1	85	128	72	21
6	256	32,9	22,9	21	140	67	13
7	113	11,2	30,8	32	87	54	14
8	97	17,6	27,1	21	113	54	16
9	194	141,1	36,2	47	303	64	18
10	301	38,0	30,2	43	66	56	13
11	72	33,9	17,4	44	111	39	15
12	135	16,9	30,6	39	103	65	14
13	295	79,8	30,5	44	255	54	14
14	298	35,8	21,4	43	143	52	17
15	80	30,2	22,1	43	97	67	19
16	247	39,2	30,3	21	172	47	13
17	43	19,0	17,8	19	83	43	13
18	46	21,0	23,6	23	81	39	11
19	289	38,4	36,3	27	165	59	19

Street dust samples are among the important materials that should be tested during the investigation of environmental pollution originating from traffic [1]. Numerous investigations have shown the relation between heavy metal content in street dust and soil in highly urban areas that are burdened by heavy traffic [1,2]. The paper works, which shows the effects of traffic to the content of heavy metals in small areas, especially in the areas of intensive tourism, have not been found in literature. In August 2003, nine samples of street dust and ten samples of soil were taken in resort Budva in a manner as shown in Fig. 1. The dark

circles with white numbers designate the location of street dust sampling, while the light ones with dark numbers represent locations of soil sampling. There are no reference values for this type of soil, except [3]. Therefore, it was necessary to perform sampling from the locations for which, due to low traffic in their surrounding, a low level of heavy metals concentrations could be expected. For this purpose, the locations 1, 16 and 17 were selected. All soil samples were taken from the surface layer 15 cm deep. Both types of samples were sieved by use of sieve <0,5 mm mesh. After grinding in mortar, further they were dried at 110°C for 12 hours. 1 g of sample was destructed by wet acid procedure. All measurements were performed by use of Perkin Elmer 6500 atomic absorption spectrometry at prescribed wavelengths in air/acetylene or N₂O/acetylene flame.

Results and Discussion

All soil samples were dark red in colour. At the depth of 30 to 40 cm under the surface layer, a brown-yellow layer appeared of which chemical composition was essentially differed from the surface one. This is especially important, because wrong sampling, regarding that Budva is a zone of intensive construction works, could lead to inadequate conclusions. According to the location of sampling, the results may be divided into three groups. In the first group are the results obtained from the analysis of soil from the locations with low intensity traffic (samples 1, 17 and 18), The second group

of the results originates from soil sampling on the edge of major traffic arteries in Budva. Finally, in the third group are the results of street dust. Average content of heavy metals in the first group is the lowest. There is a slight deviation in content of Cr and Co. Average content of lead in these three groups is approximately given in ratio 5:8:30. This is far relative to zinc 8:12:19 or copper 2:2:5. Maximum measured concentrations are in the third group (Pb 301 mg/kg, Zn 332 mg/kg, and Cu 141,1 mg/kg). Such high concentration values of lead are characteristic for urban areas with a high number of passenger cars using lead petrol. Without doubting anthropogenic effect, it can be clearly concluded that increased content of Pb in street dust originate directly from tourist traffic. As there had been no rain at the sampling locations for almost 90 days, it could be said that obtained results represented total contribution of tourist, transit, and local traffic during three summer months, because migration of heavy metals in these conditions was very difficult. The content of heavy metals, primarily lead, can be found mostly in big cities with more intensive traffic and industrial activities. Some results could be compared, for instance, with those typically measured for Belgrade or Singapore [1].

Conclusion

The justification of street dust and soil analysis in order to establish the content of heavy metals in a small town exposed to intensive tourism was demonstrated. Considerably increased content of heavy metals, primarily Pb, in street dust was proved. The trend of increase of heavy metals in soil, which is in vicinity of Budva town major line of communication, was noticed. Combined measures, like construction of parking lot with the prohibition of use of motor vehicles in the part near Slovenska Plaza, redirection of traffic around the town, introducing of mandatory use of leadless petrol on the territory of Montenegro as whole during tourist season, would be necessary as to prevent noticed unwanted trends..

References

- [1] C. Y. Zhou, M. K. Wong,, L.L. Koh, Y. C. Wee, "Soil lead and other metal levels in industrial, residential and nature reserve areas in Singapore", *Environ. Monit. Assess.* 1997, 44, 605.
- [2] O. J. Ogunsola, A.F.Asubiojo, H.B. Akeredolu, F. A. AkanleH. Y. N.M.Spyrou, "Traffic pollution-preliminary elemental characterization of roadside dust in Lagos Nigeria" *Sci Total Environ.* 1994, 147, 175.
- [3] D. Đorđević, PhD Thesis, Faculty of Chemistry, University of Belgrade, 2004.

SOLIDIFICATION/STABILIZATION AS A METHOD FOR HAZARDOUS WASTE TREATMENT

M.R. Ilić¹ and S. Miletić²

¹*Institute for General and Physical Chemistry, Studentski trg 12/V, 11000 Belgrade*

²*Galenika – Fitofarmacija, Batajnicki drum b.b., 11000 Zemun*

Abstract

The process of solidification/stabilization is a widely accepted treatment/disposal process for a broad range of wastes, particularly those classified as toxic or hazardous, which are not suited for normal methods of disposal and where special treatment is necessitated. Portland cement is a material found to be most useful for solidification/stabilization purposes due to its ability for heavy metals fixation and immobilization. For the immobilization of waste containing high concentrations of heavy metals, as in the case of the galvanization process, solidification is a very acceptable treatment. Various types of cement and pozzolanas (e.g., coal burning fly ash, lime, blast-furnace slag and similar materials) are mostly used as the stabilizing matrix. Those stabilization techniques are used for the immobilization of inorganic or organic waste. The end product of the treatment, usually after sufficient curing, is solid monolithic material which, depending on characteristics of leaching, can be usefully applied or disposed of in a safe way.

Introduction

The goal of this paper was to find out a way to stabilize sludge containing mainly cadmium. Portland cement and Portland cement with addition 30% of fly ash were added as binders for immobilization of Cd^{2+} ions [1].

Experimental

Portland cement and Portland cement with 30% fly ash addition were used as matrix. Chemical composition, physico-chemical and mechanical properties of cements were determined. The samples 1x1x6 cm were prepared by mixing cement with wastewater containing 50 000 mg/l Cd^{2+} . The next samples were prepared:

- Cement paste 10: Portland cement (OPC) + distilled water
- Cement paste 15: OPC + 50000 mg/l Cd^{2+}
- Cement paste 20: Portland fly ash cement (PPC) + distilled water
- Cement paste 25: PPC + 50000 mg/l Cd^{2+}

Those samples were immersed in the aggressive acid solution (pH=4) and deionized water as reference. The temperatures of acid solution and deionized water were 20°C and 50°C. Flexural strength of samples was determined at the beginning and after 56 days in aggressive solution. After 1, 3, 7, 14, 28, 35, 42, 49 and 56 days the concentration of cadmium ions in leachate solutions was determined by atomic absorption spectrometry [2].

Results and Discussion

Both cements, Table 1, compile with the requirements of the Yugoslav standard JUS B.C1.011, concerning chemical composition. Portland fly ash cement PPC has the expected higher insoluble residue and the loss on ignition regarding Portland cement OPC because of the fly ash addition. Other constituents were not significantly changed with the fly ash addition.

Table 1. Chemical composition of Portland cement and Portland fly ash cement

Chemical composition, % mass	Cement	
	OPC	PPC
SiO ₂	20.20	19.98
Al ₂ O ₃	5.10	5.61
Fe ₂ O ₃	2.39	2.39
CaO	62.80	55.23
Insoluble residue	0.65	6.85
Moisture at 105 °C	0.90	1.40
LOI	1.79	2.91
Free CaO	0.93	1.24
CaO in CaSO ₄	3.48	1.67
SO ₃ in CaSO ₄	2.55	2.39
MgO	3.02	3.62
Alkalies as Na ₂ O	0.36	0.32
K ₂ O	0.74	0.70
Cl ⁻	0.00	0.00

Fly ash addition was obviously, increasing the demand for the water for the standard consistence and prolonging the setting time, but has no influence on the other cement characteristics. All characteristics were in the compliance with the Yugoslav standard JUS B.C1.011.

Figs. 1 and 2. shows cadmium leaching results from the prepared samples. There was the deviation of decreasing of cadmium concentration in the media during time. This means that in the static conditions cadmium diffusion to solution mechanism was not prevailing, but the adsorption/diffusion/solution mechanism was present [3]. This means that the cadmium leached produced insoluble compounds in the solution which adsorbed at the cement paste [4,5]. In any case, cadmium leaching was below 0.005 mg/l, which shown that the cadmium was successfully immobilized in the cement matrix.

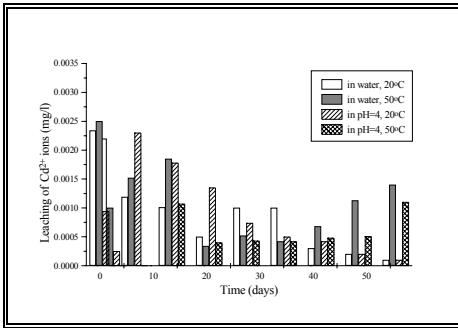


Figure 1. Leaching of cadmium in OPC samples

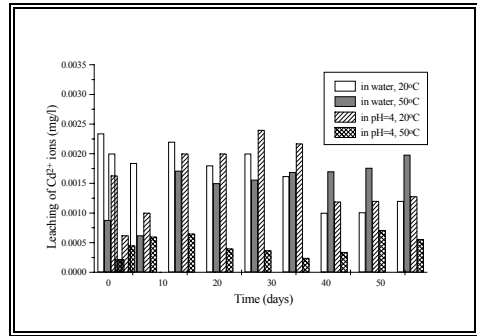


Figure 2. Leaching of cadmium in PPC samples

Conclusion

Successful stabilization/solidification of cadmium in the concentration 50,000 mg/l of Cd^{2+} , in the cement matrix is obtained. Low concentrations during leaching pointed out that the heavy metal containing waste could be successfully stabilized and immobilized on this way and landfilled, or safely utilized as the building material.

Both Portland cement and Portland cement with the addition of 30 % of fly ash enabled good immobilization, but Portland cement showed somewhat better results.

The presence of cadmium in the cement matrix with those concentrations didn't lead to decreasing of samples strengths. The leachability of cadmium is continuous as the pH decreases from 9.5 to lower values during the batch leaching steps, and confirms a simple insoluble hydroxide stabilization mechanism and pH-controlled dissolution.

References

- [1] Davis M, Cornwell D., *Introd to envir eng*, 3rd edn. McGraw-Hill, 1986.
- [2] Barlishen KD, Baetz BW *Waste Man & Res.*, 1996, 14, 71.
- [3] Owens JW, Stewart S *Magazine of Conc Res.*, 1996, 48, 37.
- [4] Roy A, Cartledge FK *J Haz Mat.*, 1997, 52, 151.
- [5] Van der Sloot HA, Heasman L, Quevauviller Ph, *Harmonization of leaching/extraction tests. Studies in Environmental science 70*, Elsevier Science, 1997.

Phase Boundaries

(K)

CHARACTERIZATION AND EFFICIENCY EVALUATION OF WATER SELECTIVE MEMBRANES WITH HYDROPHOBIC SURFACES

P. Bankovic¹, N. R. Demarquette¹ and M. L. P. da Silva

*1: Metallurgical and Materials Engineering Department, University of São Paulo
Av. Prof. Mello Moraes 2463, São Paulo, Brazil*

Abstract

In this work, selective membranes for water and hydrophobic liquids obtained by Plasma Enhanced Chemical Vapor Deposition (PECVD) of Hexamethyldisilazane (HMDS) or double layers of HMDS and n-hexane on porous substrates using a capacitive plasma reactor were investigated. The porous substrates used were paper filter, diatomite and polyester textiles. The films were characterized by X-ray Photoelectron Spectroscopy (XPS), Fourier Transform Infrared Spectroscopy (FTIR), Cobb and contact angle measurements. Mechanical resistance of the films was tested using conductivity tests. Their efficiency to separate hydrocarbon compounds from water was evaluated through filtration experiments and Karl Fischer titration tests. XPS analysis showed that Si, N, C and O were present at the surface of the HMDS film, while only C was present in the double layer film spectra. C-H_n, CH₂, Si-H, Si-CH₃, N-H, Si-CH₂-Si, Si-N-Si and Si-C bonds were identified in both types of the films by FTIR. The average contact angles formed by drops of water on the film surface ranged from 135° to 155°. Water adsorption decreased after treatment from average values ranging from 300 to 9000g m⁻² to values ranging from 0 to 20g m⁻². Conductivity of a water dissolved electrolyte through a hydrophobic surface membrane barrier doesn't change once the membrane has been folded. From 90 to 1000ppm (depending on the reagent used) of water remained in the hydrocarbon compound after filtration.

Introduction

Separation of various hydrophobic liquids, such as different types of oil, diesel and others, from water is of great importance in different fields such as, for example, petroleum, pharmaceutical, cosmetics and nutritional oil industries. Porous materials such as paper filter, diatomite and polyester textiles are possible candidates for making water selective filtering membrane if their surface is turned hydrophobic. Until now, surface hydrophobicity has been achieved by surface modification using solvents and organic reagents, mostly using wax emulsions, quaternary ammonium salts and hydrophobic resin finishes, all of which could cause environmental problems [1]. Plasma enhanced chemical vapor deposition (PECVD) of organo-silicon compounds such as hexamethyldisilazane (HMDS) is a powerful tool for making treated surfaces hydrophobic [2]. Organic silicon compounds can be used in plasma depositions in order to obtain hydrophobic surfaces. In a previous work conducted in our laboratories, it was shown that it is possible to produce hydrophobic paper by depositing a film of HMDS or a double-layered of HMDS and n-hexane without altering the porosity of the sub-

strate [3]. The modified paper was tested successfully as a selective membrane for hydrocarbon compounds and water. Due to the low mechanical resistance of paper, there was a need for an alternative material to be used as a substrate, therefore, the films of HMDS and double layers of HMDS and n-hexane were deposited on different porous substrates such as diatomite or polyester textiles, characterized and the efficiency of the obtained membranes was determined.

Results and Discussion

Table 1 shows the elemental composition of the HMDS and double layer films examined by XPS. It can be seen that the main peaks are obtained for Si, C, N and O, but once the n-hexane film has been deposited, the species originating from HMDS (Si and N) are not present within the thickness of the surface that can be analyzed by XPS (typically 5-10Å).

Table 1 – XPS results for the HMDS and double layer films on silicon wafers

Peak	Intensity [%]	
	HMDS film	HMDS/n-hexane film
O 1s	11.5	10.0
N 1s	9.5	/
C 1s	48.9	89.7
Si 2s	6.5	/
Si 2p	23.5	0.3

Infrared spectra were recorded for silicon wafers coated with HMDS or double-layered HMDS with n-hexane films. In the case of both HMDS and double layer film, C-H_n, CH₂, Si-H, Si-CH₃, N-H, Si-CH₂-Si, Si-N-Si and Si-C bonds can be identified. From XPS and FTIR results can be concluded that the surface of the double layer films is in a C-H_n form which explains its hydrophobicity.

The average contact angles formed by a sessile drop of water on the treated surfaces were between 135° and 155° showing that all treated surfaces are hydrophobic. Cobb values are presented in Table 2. It can be seen that the quantity of water absorbed by the sample decreases dramatically once the hydrophobic films have been deposited.

Table 2 – Cobb values obtained for paper, diatomite and polymer textile samples

Substrate	Cobb (g m ⁻²)		
	Not treated	HMDS film	HMDS + n-hexane film
Filter paper	334.0	14.5	19.4
Diatomite	9443.0	18.0	0.5*
Polyester Y6007N	1709.0	1.0	2.5
Polyester Y6010	1953.5	0.5	6.0
Polyester Y6007 Primatex	1081.5	2.0	2.5

*Fine particles lifted from the surface during the measurement which caused mass decrease

Average conductivity values obtained using non-treated, coated and coated and folded paper filters, were 624, 402 and 412 μ S respectively, showing that treated papers act as a barrier for electrolyte solutions and that there isn't a significant change in conductivity values once the membranes have been folded, which means that the films are probably not being damaged when folded.

Karl-Fischer titration results for hydrophobic liquids separated from water were from 90 to 1000ppm showing that the efficiency of the membranes is high. The efficiency of the membranes does not depend on the type of substrate used but it decreases with the increasing miscibility between water and the used reagents.

Conclusions

It has been shown that deposition of HMDS and double layer HMDS and n-hexane films by PECVD is an efficient method for treating surfaces in order to make them hydrophobic. These treatments result in a high concentration of CH_n at the treated surfaces. It has been proved that CH_n are the only species present within a 5-10Å thickness from the surface layer of the double layer film. These surface treatments can be used successfully to obtain selective membrane to separate H_2O from hydrophobic organic compounds.

References

- [1] A. M. Schwartz, *Advances in Textile Processing*, 1961, 1, 263.
- [2] I. H. Tan, M. L. da Silva, N. R. Demarquette, *J. of Materials Chemistry*, 2001, 11, 1019.
- [3] M. L. P. da Silva, N. R. Demarquette, I. H. Tan, *Cellulose*, 2003, 10, 171.

ADSORPTION ISOTHERMS OF CHLOROFORM ON MACROPOROUS COPOLYMERS DETERMINED BY INVERSE GAS CHROMATOGRAPHY

A.B. Nastasović¹, S.K. Milonjić² and S.M. Jovanović³

¹*Institute IChTM - Center for Chemistry, Technology and Metallurgy, Center for Chemistry,
Njegoševa 12, 11001 Belgrade, Serbia and Montenegro,*

²*Vinča Institute of Nuclear Sciences, P.O. Box 522, 11001 Belgrade, Serbia and Montenegro*

³*Faculty of Technology and Metallurgy, Karnegijeva 4, 11001 Belgrade, Serbia and Montenegro*

Abstract

The inverse gas chromatography (IGC) under finite surface coverage conditions was used for the determination of adsorption isotherms of chloroform on macroporous crosslinked poly(glycidyl methacrylate-co-ethylene glycol dimethacrylate), PGME and copolymer modified with ethylene diamine, EDA, PGME-en. The specific surface areas of initial and modified copolymer samples calculated from IGC data are in fair agreement with those determined by the BET method from the low-temperature nitrogen adsorption isotherms.

Introduction

Nowadays, most adsorption methods for cleaning, extracting and concentrating pollutants from gaseous environmental samples utilize macroporous polymeric adsorbents [1,2]. Among them, macroporous hydrophilic copolymer adsorbents based on glycidyl methacrylate, GMA, produced by radical suspension copolymerization in the shape of regular beads of required size and porosity are particularly attractive, due to possibility of chemical modification of epoxy groups [3]. In this paper, the adsorption isotherms determined from chromatographic peaks of chloroform obtained by inverse gas chromatography (IGC) under finite surface coverage were used for estimation of the surface area of macroporous poly(glycidyl methacrylate-co-ethylene glycol dimethacrylate), PGME and copolymer modified with ethylene diamine, EDA, PGME-en. The specific surface areas of initial and modified copolymer samples were compared with values determined by the BET method from the low-temperature nitrogen adsorption isotherms (77 K).

Experimental

Macroporous crosslinked poly(glycidyl methacrylate-co-ethylene glycol dimethacrylate), PGME, was synthesized by a radical suspension copolymerization, described elsewhere [4]. After reaction, the copolymer particles were washed with water and ethanol, kept in ethanol for 12 h, and dried in vacuum at 40 °C. The samples were purified by extraction in a Soxhlet apparatus with ethanol, and modified with tenfold excess of ethylene diamine, in toluene at 70 °C for 7h. The modified copolymer was labeled as PGME-en (the additional label -en designates modification

with ethylene diamine). The sorption properties of copolymer samples were examined using a Hewlett-Packard 5890II gas chromatograph, with a flame ionization detector (FID) maintained at 250 °C, the injector at 220 °C. Varian Star 4.5 software was applied to collect the data. Dry nitrogen was used as a carrier gas, at a flow rate in the range 24-28 cm³ min⁻¹. Methane was used for determination of the dead volume. A stainless steel column (50 cm long, 2.2 mm I.D.) was cleaned with both polar (C₂H₅OH) and nonpolar (C₆H₁₄) solvent, than packed with initial and modified copolymer sample (fraction with particle size of 150-500 μm). After each packing, the column was conditioned overnight in a stream of nitrogen (flow rate 5 cm³ min⁻¹) at 363 K. The appropriate amounts of analytical grade chloroform were injected in the column. Relevant IGC results from the retention data collected were calculated by a Mathcad program developed for the purpose.

Results and Discussion

The fronts of all peaks obtained by IGC were vertical and sharp suggesting that the predominant factor governing the bandwidth was isotherm curvature, typical for finite coverage conditions. Peak deformation due to high concentration of the injected organic compound was the basis for the determination of the gas adsorption isotherms on PGME and PGME-en. The adsorption isotherms for the chloroform on PGME and copolymer modified with ethylene diamine, PGME-en were obtained in the range 333-363 K, as described in the literature [5]. From the $\alpha(p)$ - (p) data, the adsorption isotherms were drawn (Fig. 1) and the related parameters were evaluated.

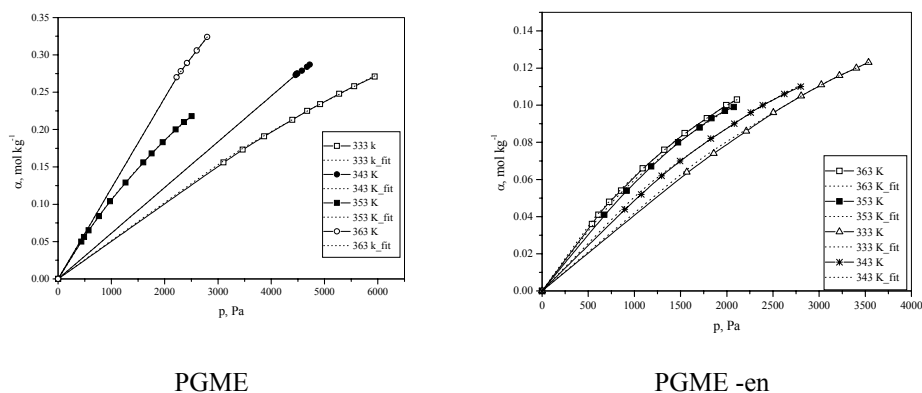


Figure 1. Adsorption isotherms of chloroform on PGME and PGME-en at indicated temperatures (dotted line represent BET fits).

The specific surface areas of the copolymer samples calculated from the IGC data, with values determined by the BET method from the low-temperature nitrogen adsorption isotherms (77 K) are shown in Table 1. The specific surface area for chloroform calculated from IGC data for PGME and PGME-en are in fair agreement with those determined by the BET method from the low-temperature nitrogen

adsorption isotherms. The accuracy of the IGC determination of the specific surface areas depends on the used adsorbate, porous structure of the material, as well as the adsorbate-adsorbent interactions.

Table 1. Specific surface areas, S_a , of PGME and PGME-en samples calculated from IGC data (temperature range 333-363 K) and from low-temperature nitrogen isotherms (77 K).

Adsorbate	$S_a, m^2/g$	
	PGME	PGME-en
CHCl ₃	30.8	47.4
N ₂	27.6	48.6

Conclusion

The adsorption isotherms of chloroform on PGME and PGME-en were determined by inverse gas chromatography (IGC) under finite surface coverage. The values of the specific areas for chloroform calculated from IGC data are in fair agreement with those determined by the BET method from the low-temperature nitrogen adsorption isotherms.

Acknowledgement

This study was financially supported by the Serbian Ministry of Science and Environmental Protection (Projects No. 1948. and 1978.). The authors thank Novartis Pharma AG (Basel, Switzerland) for their donation of the HP5890II gas chromatograph used in this work.

References

- [1] V.V. Podlesnyuk, J.Hradil, E.Kralova, *Reactive and Functional Polymers*, 1999, 42(3), 181.
- [2] A.W. Trochimeczuk, S. Aoki, K.Yamabe, A.Jio, *Eur. Polymer J.*, 2002, 38, 941.
- [3] J. Hradil, F. Švec, *J. of Chromatogr.*, 1984, 287, 67.
- [4] S. Jovanović, A. Nastasović, N. Jovanović, K. Jeremić, Z. Savić, *Angew. Makromol. Chem.*, 1994, 219, 161.
- [5] J.R. Conder, C.L. Young, *Physicochemical Measurements in Gas Chromatography*, New York, Wiley, 1979.

ADSORPTION OF FUMONISIN B₁ ON ORGANOZEOLITE

A. Daković¹, M. Tomašević-Čanović¹, G. Rottinghaus², S. Matijašević¹
and A. Radosavljević-Mihajlović¹

¹Institute for Technology of Nuclear and Other Mineral Raw Materials, P. O. Box 390,
11 000 Belgrade, Serbia and Montenegro

²Vet. Med. Diag. Lab., College of Veterinary Medicine, University of Missouri, Columbia, MO 65211,
USA

Abstract

In vitro results of adsorption of fumonisin B₁ (FB₁) on unmodified clinoptilolite and organozeolites are presented in this paper. The organozeolites were obtained via ion exchange of inorganic cations in clinoptilolite with different amounts of octadecyldimethylbenzyl ammonium ions (ODMBA). The adsorption of FB₁ on unmodified clinoptilolite was 90.3% at pH 3, 2.05 at pH 7 and 6.20% at pH 9. The presence of organic cation at the zeolitic surface increased adsorption of FB₁ at pH 3 as well as at pH 9. It was determined that, at low surface concentration of ODMBA, adsorption of FB₁ was pH dependent while, at higher level of ODMBA, the adsorption of this toxin was pH independent.

Introduction

Fumonisin is a group of mycotoxins widely distributed in corn products. These include fumonisin A₁, A₂, B₁, B₂, B₃ and B₄, with fumonisin B₁ (FB₁) being the major metabolite. FB₁ is toxic to the central nervous system, liver, pancreas, kidney and lung in a number of animal species [1]. Structural formulae of fumonisin B₁ is presented on Figure 1.

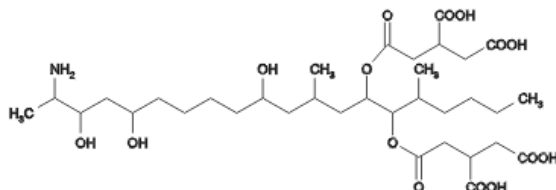


Figure 1. Structural formulae of fumonisin B₁

One approach of protecting animals against harmful effects of mycotoxins present in animal feed is utilization of adsorbents (alumosilicates, e. g. bentonite - montmorillonite and natural zeolite – clinoptilolite) in diet. In inorganic forms, they adsorb efficiently only aflatoxins *in vitro* and *in vivo*. The hydrophilic surfaces of alumosilicates are poor adsorbents of hydrophobic molecules, like are the most of mycotoxins. The new approach to increase the adsorption of low polar molecules is the chemical treatment of alumosilicates with long chain organic cations – surfactants. In our previous paper, it was shown that surface modification of clinoptilolite with surfactants greatly improved adsorption of zearalenone and ochratoxin A, *in vitro* [2].

In this paper, the *in vitro* results of FB₁ adsorption on clinoptilolite modified with different amounts of ODMBA ions are presented.

Experimental

The starting material was clinoptilolite rich tuff from Zlatokop deposit (Vranje, Serbia). The basic characteristics of this tuff were: content of clinoptilolite > 85%, cation exchange capacity (CEC) – 139 meq/100g, external cation exchange capacity (ECEC) – 10 meq/100g, dominant cation in exchangeable position - calcium.

Surfactant ODMBA-Cl was used for preparation of organozeolites. Aqueous solutions, containing ODMBA-Cl at concentrations to satisfy percentage of 20%, 50%, or 100% of ECEC of starting zeolitic tuff, were used for obtaining organozeolites. The obtained surfactant modified zeolites were denoted as OZ-2, OZ-5 and OZ-10.

In order to investigate FB₁ adsorption on natural zeolitic tuff and organozeolites, to each centrifuge tube, 100 mg of each adsorbent and 10 ml of FB₁ buffer solution were added at concentration of 2 ppm. FB₁ concentrations in buffer solutions without and with mineral adsorbents were determined by HPLC [3].

Results and Discussion

Organozeolites were obtained by ion exchange of inorganic cations in zeolitic tuff with ODMBA. Measurement of content of Ca²⁺, Mg²⁺ and Na⁺ in supernatants after ODMBA sorption confirmed that quantitative ion exchange was occurred.

The results of FB₁ adsorption on zeolitic tuff and OZ-2, OZ-5 and OZ-10 at different pHs are presented in Table 1. Percent of FB₁ bound is calculated from the difference between the initial and final concentration of mycotoxin in aqueous supernatant. As can be seen from Table 1, FB₁ adsorption on the zeolitic tuff was 90.3% at pH 3, 2.0% at pH 7 and 6.2% at pH 9. From Figure 1, it can be concluded that FB₁ is complex organic molecule with calboxylic and hydroxylic functional groups which suggest that exist in solution in different forms at different pHs. The data for the dissociation constants of FB₁ was not found in literature. Because unmodified zeolite has no affinity for anions, the obtained results suggest that FB₁ exist in anionic form at pH 7 and 9. In addition, FB₁ is also hydrophobic molecule and can be adsorbed on the hydrophobic surface of the organozeolites. From the results in Table 1, it can be seen that presence of ODMBA at zeolitic surface increased the adsorption of FB₁. The adsorption of FB₁, on OZ-2, with low amount of ODMBA, was 97.5% at pH 3 and about 82% at pH 7 and 9. Li et al (2000) showed that organozeolite treated to monolayer coverage (up to ECEC) had fewer sorption sites for phenolate anion, so the sorption became less as the phenol speciation shifted toward phenolate at higher pH values [4]. The lower adsorption on OZ-2 at pH 7 and 9 also indicate that FB₁ may exist in solution in anionic form at pH 7 and 9.

Table 1. The adsorption of FB₁ on zeolitic tuff and organozeolites at different pHs

	FB ₁ adsorbed, %		
	pH 3	pH 7	pH 9
Zeolitic tuff	90.3	2.0	6.2
OZ-2	97.5	82.4	82.8
OZ-5	97.5	95.0	96.6
OZ-10	98.0	95.2	95.7

However, further addition of ODMBA (50% of ECEC) led to additional adsorption of this toxin at pH 7 and 9. In OZ-10, in which all inorganic cations at zeolitic surface were replaced with ODMBA (monolayer coverage), the adsorption of FB₁ was 98.0%, 95.2% and 95.7% at pH 3, 7 and 9, respectively. The higher adsorption of FB₁ on OZ-5 and OZ-10, at pH 7 and 9, suggests that, even at the monolayer coverage, the part of sorbed ODMBA was present in the form of admicelles with Cl⁻ counterions providing sites for the additional anion adsorption. Results indicate that the surfactant treatment level plays a role in FB₁ adsorption on organozeolites. Further research will continue to investigate the hypothesis of FB₁ adsorption to organic cations in organozeolites.

Conclusions

The surface modification of zeolitic tuff with ODMBA resulted in preparation of organozeolites. The presence of surfactant at zeolitic surface greatly improved *in vitro* adsorption of fumonisin B1 at pH 3 as well as at pH 9. At low surface coverage with ODMBA, FB₁ adsorption was pH dependent, while in organozeolites with amount of ODMBA 50% and 100% of ECEC, the adsorption of FB₁ was pH independent. The small amount of surfactant required for the obtaining the organozeolite may lead to the practical application of this material.

References

- [1] IARC *Monographs On Evaluation Of Carcinogenic Risks To Humans*, Some naturally occurring substances: Food items and constituents, heterocyclic aromatic amines and mycotoxins, IARC, Lyon, France, 1993, 56, 445.
- [2] M. Tomašević-Čanović, A. Daković, G. Rottinghaus, S. Matijašević, M. Đuričić, *Micro-porous and Mesoporous Materials*, 2003, 61, 173.
- [3] D. Ledoux, G. Rottinghaus, *Biotechnology in the Feed Industry*, Proceedings of Alltech 15th Annual Symposium, 1999, 1.
- [4] Z. Li, T. Burt, R. S. Bowman, *Environ. Sci. Technol.* 2000, 34, 3756.

INFLUENCE OF THE ENERGETIC HETEROGENEITY OF ADSORBENTS BASED ON SiO₂ ON CHOLESTEROL ADSORPTION

B. Adnađević¹ and J. Jovanović²

¹ *Department of Physical Chemistry, University of Belgrade, POB 137, 11001 Belgrade,*

² *Institute of Technical Science of the Serbian Academy of Science and Arts, Knez Mihailova 35,
11000 Belgrade, Serbia and Montenegro*

Abstract

The influence of the energetic heterogeneity of structurally different adsorbents based on SiO₂ (pyrogenic SiO₂, precipitated SiO₂, silica gel) on the adsorption of cholesterol dissolved in toluene was investigated. Adsorption isotherms for the adsorption of cholesterol dissolved in toluene on structurally different SiO₂ types were determined. A theoretical model for cholesterol adsorption on adsorbents based on SiO₂ was developed. Based on that model, the existence of two well-dislocated centers, with different strength and concentration was established on all the examined adsorbents. Parameters of the density function of energy distribution on the dominant center were determined. The influence of the strength and width of the dominant adsorption center distribution on the saturation adsorption capacity of the adsorbents was established.

Introduction

Cholesterol is one of the most abundant steroids. It is assumed that cholesterol is responsible for many diseases caused by poor blood circulation, because he precipitated on arteries causing arteriosclerosis and heart illnesses [1]. Various processes are applied intend to reduce cholesterol content in food. Among them are enzymatic conversion of cholesterol to non-absorbable steroids, distillation with water vapor, complex formation and adsorption [2] Adsorption process is used as method for direct reduction of lipids content, as well as lipoproteins, low density lipoprotein from whole blood [3] Bearing in mind both adsorbents' and cholesterol's structures and knowing that cholesterol has hydroxyl group available for interacting, with high degree of certainty one can claim (expected) that material based on SiO₂ (silica gel, precipitated SiO₂, pyrogenic SiO₂) could be convenient adsorbents for cholesterol content reduction from food or blood.

So in this work, adsorption isotherms for cholesterol dissolved in toluene, on silica based adsorbents with different structural characteristics (silica gel, precipitated SiO₂, pyrogenic SiO₂) were examined.

Experimental

Materials: For this investigations following materials were used: *cholesterol*, p.a. purity, obtained from ICN-Galenika, Serbia and Montenegro; *toluene*, p.a. purity, purchased from Merck-Germany; *Silica gel*, obtained from Magmasil, Serbia and Montenegro (denoted as *SG*), samples of *precipitated SiO₂*: Vulkasil-S and Vulkasil-

C, both produced by Bayer, Germany, denoted as **VS** and **VC** with respect) and *pyrogenic SiO₂*, Aerosil-200, produced by Degussa, Germany (denoted as **AS**).

Determination of cholesterol's adsorptions isotherms: The adsorption isotherms at temperature T=298K were determined from the concentration change before and after adsorption.

The measured quantity of thermally activated powdered precipitated SiO₂ (under the following conditions: T=463K, air atmosphere, t=8 h), has been added to a predetermined volume of cholesterol solution in toluene (concentrations 1-15g/dm³). The adsorption system has been homogenized by stirring (stirring velocity 500 rpm) and left for 8 hours to achieve the adsorption equilibrium. After the adsorption, the adsorption system was centrifuged to separate the precipitated cholesterol from the mother liquor, and the amount of adsorbed cholesterol (a) was determined according to eq. (1):

$$a_{(mg/g)} = \frac{(C_o - C_i) \cdot V}{m} \quad (1)$$

where: C_o is the cholesterol concentration before adsorption (mg/ml), C_i is the equilibrium concentration of cholesterol in the mother liquor after the adsorption (mg/ml), V is the starting volume (ml) of the cholesterol toluene solution. The concentration of cholesterol in solution, before and after the adsorption, was determined photometrically using the Liebermann-Burchard reagent [4]. The results were calculated as a mean value of three measurements.

Results and Discussion

The adsorption isotherms for cholesterol adsorption from toluene solution on the examined adsorbents are given on Figure 1.

Assuming that adsorptions isotherms of cholesterol can be described by equation (2):

$$\theta = \sum_{i=1} \alpha_i \theta_i \quad (2)$$

where:

θ is the degree of coverness of the adsorption centers, and $\theta_i = a_i/a_{i\max}$ where

a_i - adsorption coefficient for i -center and

$a_{i\max}$ - saturation adsorption capacity for i -center and

α_i - relative concentration of the i -center in distribution function (discrete distribution function of adsorption centers)

Values for coefficients for adsorptions centers (a_i) and relative concentrations of adsorptions centers distributions (α_i) are determined and given in Table 1.

Presented results suggest that for all the examined adsorbents is characteristic existence of two well-dislocated with adsorption coefficients which are in functional relationship with the structure of the investigated adsorbents. Because the obtained adsorption isotherm can be described also with a Freundlich model to which, is added exponential function of the energy distribution of the adsorption centers is added (equation 3):

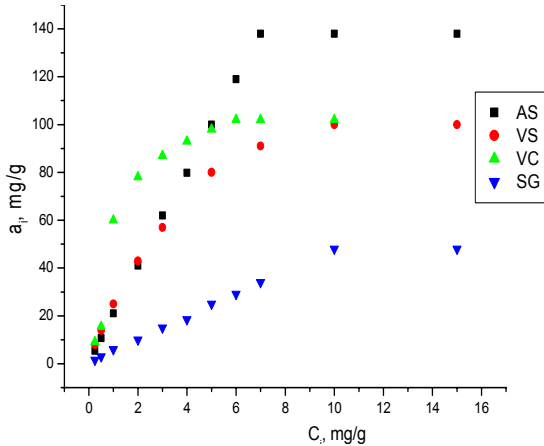


Fig 1. Cholestetrol adsorption isotherms

Table 1. Coefficients for adsorptions centers (a_i) and relative concentrations of their distributions(α_i)

Adsorbent	$\alpha_1, \%$	a_1	$\alpha_2, \%$
AS	95	0.24	5
VS	91	0.33	9
VC	95	0.28	5
SG	98	0.11	2

$$\rho(Q) = \beta \exp(-mQ) \tag{3}$$

where:

Q is adsorption center energy and (β and m) are distribution parameters of the adsorption center, determined distribution parameters for the dominant adsorption center are presented on Table 2.

Table 2. Entropy coefficient (b_0) and distribution parameters for the examined adsorbents

Adsorbent	$m \cdot 10^4, \text{ mol/J}$	$b_0, \text{ s}^{-1}$	$\beta, \text{ kJ/mol}$
AS	2.7	$4.1 \cdot 10^{-10}$	11.1
VS	2.3	$4.4 \cdot 10^{-12}$	25.1
VC	3.1	$3.6 \cdot 10^{-9}$	25.7
SG	3.7	$1.6 \cdot 10^{-8}$	31.4

Based on the presented results, it can be concluded that for adsorbents with so called low-structure (SG) is characteristic maximal strength of the dominant adsorption center

and maximal distribution dispersion, i.e. minimal value of saturation adsorption center (a_{\max}), while for aerogel, which is adsorbent with high structure, is attributable minimal strengthens of the dominant adsorption center and the smallest distribution, i.e. maximal value of saturation adsorption center (a_{\max}).

Acknowledgements These investigations were partly supported by the Republic Ministry of Science, Technologies and Development by project 1448.

Literature

[1] G.R.Thompson, Atherosclerosis, 2003, 66-71.
 [2] A.Kos, J.Bertrandt, A.Tutog, Atherosclerosis, 2000, 31-64.
 [3] R.L. Bradley, Removal of cholesterol from milk fat using supercritical carbon dioxide, J. Dairy Sci., 1989, 72, 2834.
 [4] T.C. Huang, C.P. Chen, V. Wefler and A. Raftery, Analytical Chem., 1961, 10, 1405.

INTERACTION OF SODIUM DODECILSULPHATE (SDS) WITH CALCIUM BENTONITE: ADSORPTION ISOTHERMS

M. Ilic, V. Pavelkić, S. Blagojević, S. Zlatanović and Z. Filipović-Rojka

*Institute of General and Physical Chemistry,
Studentski trg 12-16, Belgrade, Serbia and Montenegro*

Abstract

The interaction of dodecylsulfate anions DS^- with Ca bentonite and Na montmorillonite were investigated. Na montmorillonite do not adsorb DS^- and on Ca bentonite is DS^- precipitated as $Ca(DS)_2$.

Introduction

Surfactant belongs to the most produced organic compounds. Although the major part is degraded in sewage plants, a big amount gets into soil and into the aquatic environment. By adsorption onto colloidal particles they alter the properties of the mineral interface, an effect, which is very important to adsorption processes of environmental contaminants and their mobility. For this reason it is important to understand the binding mechanisms of surfactant at the interface between water and soil minerals. It is known, that cationic surfactants are predominantly adsorbed by ion exchange [1]. Here we are report about the interaction of an important anionic surfactant sodium dodecylsulfate (SDS) at concentration below and above its critical micelle concentration (CMC) with Ca bentonite and Na montmorillonite and the influence of competing anions (NO_3^- , SO_4^{2-} , HPO_4^{2-}) and pH value.

Experimental

Ca-bentonite (Suedchemie AG, Germany) was used without further purification (suspension 30 gdm^{-3}). The BET surfaces $73 \text{ m}^2 \text{ g}^{-1}$ and the cation exchange capacity (c.e.c) is $0.90 \cdot 10^{-3} \text{ eqv.g}^{-1}$. The c.e.c. was determined by the NH_4^+ technique. Na-montmorillonite (suspension 15 gdm^{-3}) was produced by purification (sedimentation), ion exchange (NaCl) and dialysis from Ca-bentonite. Its BET surface is $89 \text{ m}^2 \text{ g}^{-1}$ and the c.e.c is $0.98 \cdot 10^{-3} \text{ eqv.g}^{-1}$. Na-dodecylsulfate (SDS) (>99% pure) was supplied by Fluka AG. The adsorption isotherms have been recorded by the bath equilibrium technique, the suspensions were equilibrated for 24h at 25C. Analysis was performed by 2-phase titration (hyamine, NaDS). X-ray diffractograms were recorded with a XRD-9000 diffractometer from Seiffert (Germany).

Results and Discussion

Figure 1 shows the specific surface excess $n^{(v)}_{DS}$ as a function of the equilibrium concentration $m_{eq,DS}$ for Ca-bentonite and Na-montmorillonite.

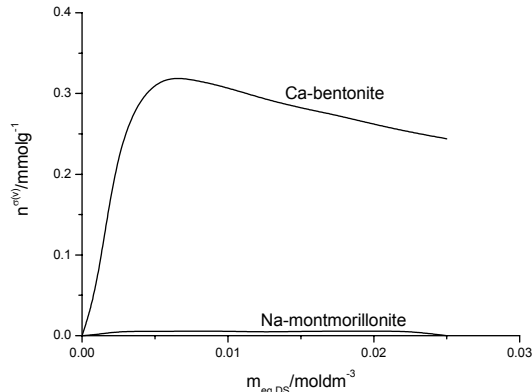


Figure 1. Adsorption of SDS at Ca-bentonite and Na-montmorillonite

At Ca-bentonite a maximum is obtained with $n^{\sigma(v)}_{\max} = 3,4 \cdot 10^{-4} \text{ mol g}^{-1}$. Above the maximum in Fig. 1 when the CMC of SDS is reached the precipitate will be solubilised in the micellar phase. The surface excess increases until the CMC. The drop of the isotherm beyond the maximum (the surface excess decreases) can be made clear due to the solubilisation of $\text{Ca}(\text{DS})_2$ in the micellar phase [2,3]. No adsorption is observed at Na-montmorillonite. This excludes the possible binding of DS^- by anion exchange at the edges. The reason is the anion exclusion effect [4,5] from the negatively charged surface of the montmorillonite. This result coincides with reported in the literature [6]. The precipitation process can also be investigated by x-ray diffractometry. Fig. 3 shows a x-ray diffractograms of DS precipitated at Ca-bentonite and pure $\text{Ca}(\text{DS})_2$.

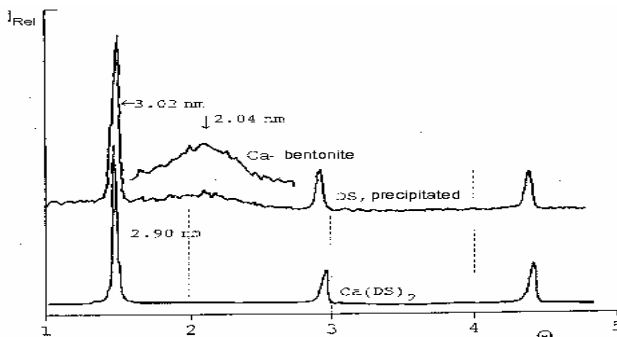


Figure 2. X-ray diffractograms of: Ca-bentonite; $\text{Ca}(\text{SD})_2$ as precipitate; $\text{Ca}(\text{SD})_2$ as solution

The broad reflection centered at $2\theta = 2.84$ corresponds to the basal spacing of the bentonite $d_{001} = 2.04 \text{ nm}$ and the sharp reflections at $2\theta = 1.48$; 2.94 and 4.41 are assigned to the d_{002} and d_{003} values of the $\text{Ca}(\text{DS})_2$ precipitate. A swelling of Ca-bentonite is not observable. The basal spacing of the montmorillonite did not increase, the anionic surfactants are not intercalated into the interlayer space. The adsorption is a

surface precipitation of Ca-bentonite. This view is supported in two arguments. Firstly, no adsorption of DS^- is observed at Na-montmorillonite (Fig.1.). Secondly, assuming an area per DS^- ion of $65 \text{ m}^2\text{g}^{-1}$ at $n_{\text{max}}^{\sigma(v)}=3.5 \cdot 10^{-4} \text{ molg}^{-1}$ is calculated for the formation of a belayed. This value agrees very well with the total outer surface (BET, $7.3 \text{ m}^2\text{g}^{-1}$) of the Ca-bentonite.

The observation that the adsorption of DS^- is independent on salt added (Table 1) is not in contradiction to this view. The adsorption of DS^- is a nearly independent on pH.

Table1. Adsorption maximum of SDS ($n_{\text{max}}^{\sigma(v)}/\text{molg}^{-1}$) at Ca-bentonite as function salt added

Nitrate	Sulphate	Phosphate
$3.5 \cdot 10^{-4}$	$3.4 \cdot 10^{-4}$	$3.4 \cdot 10^{-4}$

Conclusion

The adsorption of SDS at Ca-bentonite, Na- montmorillonite has been investigated. The adsorption process is a precipitation with Ca^{2+} . No intercalation into the interlayer space is observed, the interlayer distance is not increased. The adsorption is more or less independent on inorganic anions and pH.

References

- [1] K Jasmund, G.Lagaly (1993) Tone und Tonminerale, Steinkopff, Darmstadt
- [2] S.E.Friberg, D.W.Osborne, Colloids and Surfaces, 1984, 12, 357.
- [3] N.Kallay, E. Matijevic, J Coll. Interf. Sci., 1985, 106, 452.
- [4] Adamson AW Physical Chemistry of Surfaces, Wiley, New York, 1990.
- [5] Miller SE, Low PF, Langmuir, 1990, 6,572.
- [6] T. Permien, G. Lagaly, Clays Clay Min., 1995, 43, 229.

INFLUENCE OF HEATING OF KAOLIN, BENTONITE AND ZEOLITE ON ADSORPTION PROPERTIES AND CEC

T. Stanić, J. Lemic and M. Đuričić

*Institute for Technology of Nuclear and other Raw Mineral Materials,
11000 Belgrade, Franše d'Eperea 86, Serbia and Montenegro*

Abstract

Aluminosilicate minerals – kaolin, bentonite and zeolite have active centres on the surface, and for this reason they have good adsorption characteristics. These characteristics are related to the exchangeable cations surrounded by the layers of hydrated water. These minerals were treated in the temperature range from 300 to 700 °C and the changes of basic characteristics, such as CEC, adsorption coefficient of methylene blue and adsorption of water, were observed. By increasing of the heating temperature these adsorption characteristics decrease.

Introduction

Kaolin, bentonite and zeolite are aluminosilicates, whose natural and modified forms are used in different industrial branches and in environmental protection.

Kaolin has a 1:1-layer silicate structure with small number of exchangeable sites on the surface. Adsorption properties have an effective role in scavenging inorganic and organic pollutants from water. Kaolin may be effective in removing a basic dye like methylene blue [1].

Bentonite has a 2:1-layer silicate structure and large cation exchange capacity (CEC). Interlayered cations are easily exchangeable, producing a swelling and, as a result, the opening of layer that permits the interchange with bigger cations.

Zeolites are crystalline hydrated aluminosilicates of the alkalis and alkaline earths, and possess cavities occupied by the relatively large cations. They are widely used because of their properties which include molecular sieving, adsorbing and CEC. Surfactant-modified zeolites are good adsorbents for inorganic and organic molecules.

Thermal treatment of these minerals up to temperatures at which their structure is not decomposed, adsorption capacity increases.

Materials and Methods

Kaolin (Šabac), bentonite (Šipovo) and zeolite (Roumania) were thermally treated in a temperature range from 300 to 700 °C. The cation exchange capacity (CEC) of kaolins, bentonites and zeolites were determined by standard method of ionic exchange with NH_4Cl [2]. Adsorption coefficient of methylene blue was determined by Standard method [3]. Thermally treated minerals were held in the atmosphere of relative humidity of 100% for 24h, and then the adsorption of water was determined. The Netzsch STA 409 instrument was used for DTA analyses in air atmosphere, with constant heating rate of 10 °C/min, up to 800 °C.

Results and Discussions

Thermal treatment of kaolin, bentonite and zeolite causes the change of CEC and adsorption coefficient of methylene blue (A).

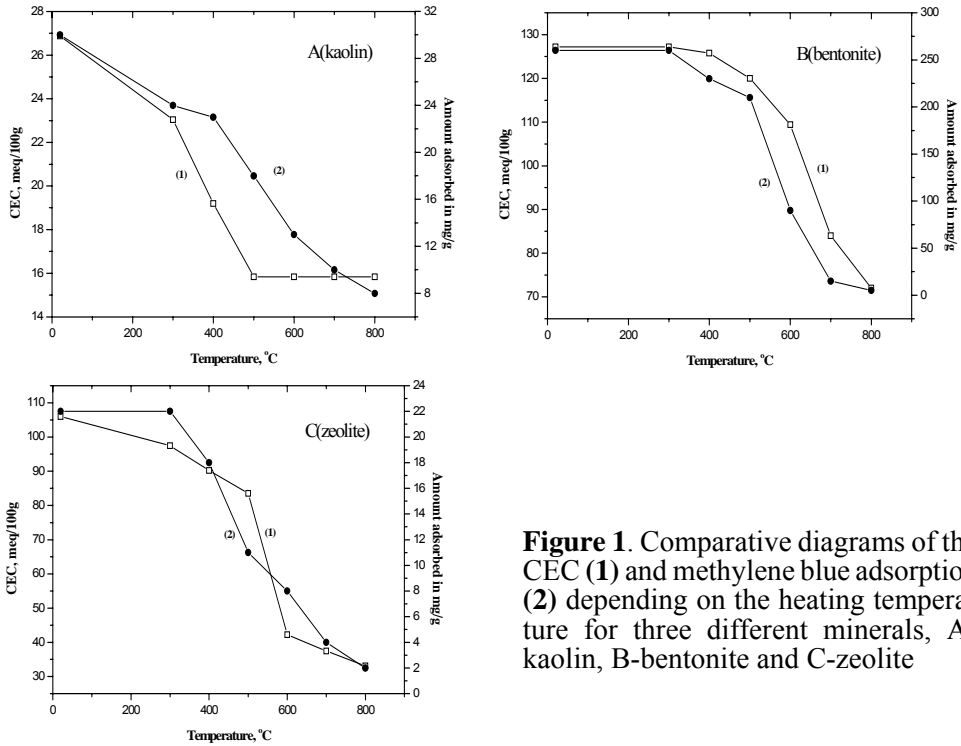


Figure 1. Comparative diagrams of the CEC (1) and methylene blue adsorption (2) depending on the heating temperature for three different minerals, A-kaolin, B-bentonite and C-zeolite

Adsorptive properties (CEC and A) rapidly decrease in the temperature range higher than 500 °C, because of transformation of kaolin in metakaolin (Fig. 1A).

Bentonite has better adsorptive characteristics regarding to the values of CEC and A than kaolin. Crystal structure of bentonite, likewise kaolin, has been changed above the temperature of 500 °C and a process of amorphization took place, which caused the decreasing of the number of active centers (Fig. 1B), which follow lower values of CEC and A.

The decreasing of the number of active centers up to 500 °C for zeolite is progressive, contrary to bentonite and kaoline. The destroying of the structure of zeolite above the temperature of 500 °C[4] causes the reducing of adsorptive properties (Fig.1C).

Reversibility of water adsorption after thermal treatment of minerals, are shown in Fig.2.

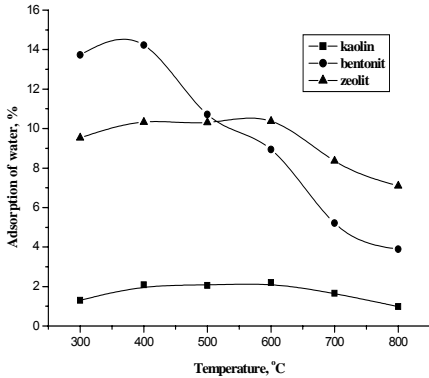


Figure 2. Water adsorption as a function of the temperature heating for three different minerals

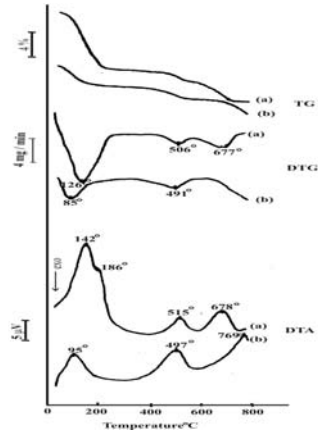


Figure 3. TG, DTG and DTA curves of bentonite: (a) raw and (b) thermally treated at 700 °C

As it can be seen from Figure 2, kaolin adsorbs small amounts of water because of its structure, and thermal treatment has not influence on water adsorption. Thermal treatment of bentonite changes water adsorption, especially above 400 °C. Displacing of hydration water layer, at lower temperatures (300–400 °C), gives the possibility of the adsorption of low polar organic compounds increment. Decrease of the water adsorption at higher temperatures indicates the structure changes. These changes can be seen on Fig.3, where TG/DTG/DTA diagrams are presented.

The changes of water adsorption during the heating of zeolite are different than bentonite. The zeolite structure is stable up to 600 °C, and water adsorption decreases. In the same time the CEC decreases during the heating above 500 °C.

Conclusions

Knowing the kaolin, bentonite and zeolite properties changes during the thermal treatment is the base for the processes of further preparation and application. Thermal treatment of kaolin, bentonite and zeolite influences on the water adsorption, CEC and coefficient of methylene blue adsorption. Changes caused by thermal treatment at lower temperatures correlate to hydration water around the active centers. In that way, active centers become more available for surface modification with organic compounds. The mineral structure becomes destroyed at higher temperatures, and this process is usually irreversible or very slow reversible.

Reference

- [1] D. Ghosh, K.G. Bhattacharyya, *Applied Clay Science*, 2002, 20, 295.
- [2] M. Tomašević-Čanović, J. Kačanik, L. Mihovilović, XXXI Savetovanje hemičara SR Srbije, Beograd, 1989.
- [3] ГОСТ 2128.3-75.
- [4] G.E. Christidis, D. Moraetis et al, *Applied Clay Science*, 2003, 24, 79.

SORPTION OF Ni^{2+} BY DIFFERENT SYNTHETIC HYDROXYAPATITE

I. Smičiklas, A. Onjia and S. Raičević

The "Vinča" Institute of Nuclear Sciences, P.O.Box 522, 11001 Belgrade, Serbia and Montenegro

Abstract

Two hydroxyapatite (HAP) samples of different crystallinity were studied as a nickel immobilization matrix. Sorption isotherms were obtained by batch equilibration method, in the concentration range $1 \cdot 10^{-4} - 8 \cdot 10^{-3} \text{ mol/dm}^3$. Low crystalline sample has sorption capacity of 0.212 mmol/g, and due to its higher specific surface area and lower Ca/P ratio it was found to be better sorbent for Ni^{2+} than crystalline HAP (0.092 mmol/g).

Introduction

Nickel is a member of group VIII of the periodic table, similar to iron in its physical properties. The earth's crust contains 0.008% nickel [1]. Due to natural geochemical activity and weathering, nickel occurs naturally in all soils, sediments and waters. Nickel has large industrial importance, and its salts in small amounts are essential to many life forms, including humans. In large amounts, however, they can be extremely toxic. The physico-chemical properties of the receiving environment (pH, redox potential, hardness, complexing and precipitating agents, ionic strength, other cations, temperature, solid organic and inorganic matter, cation exchange capacity) control the fate and bioavailability of nickel [2]. HAP, $\text{Ca}_{10}(\text{PO}_4)_6(\text{OH})_2$, is a naturally occurring mineral, also known as a good matrix for heavy metal and radionuclide immobilization by means of ion exchange, sorption and precipitation processes [3].

Experimental

Ni^{2+} immobilization by highly crystalline synthetic HAPc, obtained by neutralization method [4] and by commercial product from Bio-Rad Laboratories was investigated. Sorption isotherms were obtained by batch method. HAP samples were equilibrated with $\text{Ni}(\text{NO}_3)_2$ solutions (solid to liquid ratio 1:200) for 24 h, at room temperature ($20 \pm 1^\circ\text{C}$). Initial concentrations of Ni^{2+} were in the range $1 \cdot 10^{-4} - 8 \cdot 10^{-3} \text{ mol/dm}^3$, and ionic strength for all solutions was added to 0.1 mol/dm³, by KNO_3 addition. After filtration, final pH values were measured and remainder concentrations of Ni^{2+} in solutions were determined by AAS.

Results and Discussion

Sorbate samples were characterized by standard physico-chemical analyses. HAPc and Bio-Rad commercial product have crystal structure of HAP, but different fraction of crystalline phase (0.90 and 0.28), Ca/P ratio (1.70 ± 0.02 and 1.53 ± 0.02) and specific surface area (24 and $63 \text{ m}^2/\text{g}$). Point of zero charge (pH_{PZC}) obtained by batch

method, using $0.1 \text{ mol/dm}^3 \text{ KNO}_3$ as an inert electrolyte, was 6.6, for both HAP samples. Batch test results for Ni^{2+} sorption on two HAP samples are presented in Figure 1.

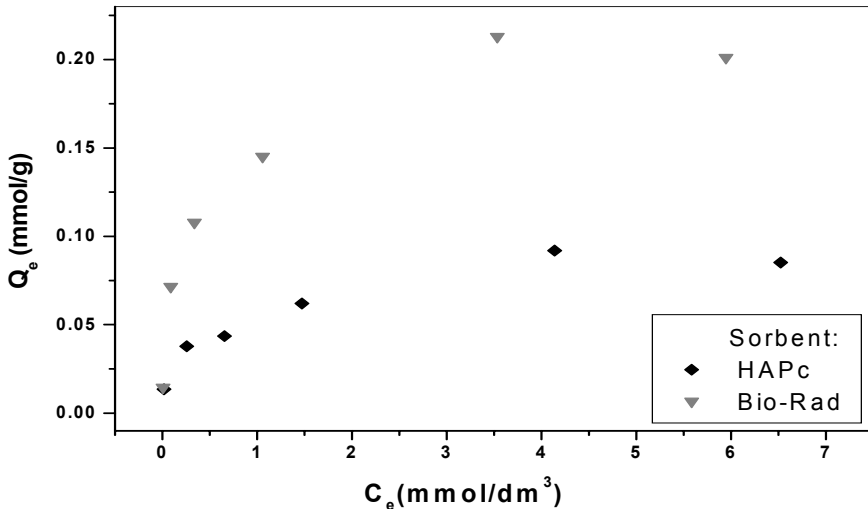


Figure 1. Sorption isotherms for Ni^{2+} on HAPc and Bio-Rad samples.

The increase in the initial metal concentration resulted in an increase in the Ni^{2+} sorption, until equilibrium was reached. Experimental results were found to be well represented by linear form of Langmuir adsorption isotherm:

$$C_e/Q_e = 1/X_m K + 1/X_m \cdot C_e$$

where Q_e (mmol/g) and C_e (mmol/dm³) presents the equilibrium concentration of sorbate in solid and liquid phase, K (dm³/mmol) is the Langmuir constant related to the energy of adsorption and X_m (mmol/g) is the maximum sorption capacity. Results of linear fit are summarized in Table 1.

Table 1. Linear form of Langmuir isotherms for Ni sorption on HAP samples.

Sorbent	Linear form of Langmuir Isotherm	X_m (mmol/g)	K (dm ³ /mmol)	R
HAPc	$C_s/Q_s = 4.55 + 10.80C_e$	0.092	2.371	0.993
Bio-Rad	$C_s/Q_s = 1.11 + 4.71C_e$	0.212	4.245	0.997

Bio-Rad sample is approximately two times better sorbent for Ni^{2+} , than crystalline HAPc (0.212 versus 0.092 mmol/g). It can be correlated to its lower crystallinity, higher specific surface area, and lower Ca/P ratio. Sorption is followed by pH changes (Table 2.)

Table 2. Initial pH and pH values after equilibration with HAPc and Bio-Rad sample.

Initial Ni ²⁺ conc. (mol/dm ³)	pH _{initial}	pH _{final} HAPc	pH _{final} Bio-Rad
1.10-4	6.17	6.65	6.63
5.10-4	6.00	6.36	6.38
1.10-3	5.92	6.38	6.21
2.10-3	5.88	6.30	6.12
5.10-3	5.87	6.26	5.91
8.10-3	5.86	6.00	5.85

Final pH increases comparing to initial pH, as a result of HAP amphoteric surface and buffer capacity. On the other hand, as the initial concentration of Ni increases, as well as the amount of sorbed Ni, the final pH decreases. This effect is more pronounced for Bio-Rad sample. The decrease of final pH comparing to pH_{PZC} (6.6) suggests specific cation sorption.

Sorption capacity of HAP towards Ni²⁺ is generally lower in respect to other heavy metals, such as Pb, Cd, Zn and Cu [5]. Maximum sorption capacity obtained for Bio-Rad HAP is similar to capacity of spent animal bones [6].

Conclusion

Bioavailability of nickel is correlated with toxicological effects of hydrated Ni²⁺ ion. HAP addition decreases concentration of chemically labile and bioavailable Ni²⁺ ion from aqueous solutions, by sorption processes. Low crystalline synthetic HAP, which is more similar to natural occurring apatites, have significantly higher sorption capacity than highly crystalline and pure sample.

References

- [1] J.M. Duke, Nickel in the Environment, ed. by J. Nriagu, John Wiley & Sons, New York, 1980.
- [2] E. Nieboer, G.G. Fletcher, I. Thomassen, J. Environ. Monit., 1999, 1, 1.
- [3] T.S.B. Narasaraaju, D.E. Phebe, J. Mater. Sci., 1996, 31, 1.
- [4] I.D. Smičiklas, S.K. Milonjić, P. Pfendt, S. Raičević, Sep. Purif. Technol., 2000, 18, 185.
- [5] S. Al-Asheh, F. Banat, F. Mohai, Chemosphere, 1999, 39, 2087.
- [6] F. M. Rivera, M. Fedoroff, Enciclopedia of Surface and Colloid Science, Marcel Dekker, Inc., New York, 2002, 1-28.

DETERMINATION OF THE POINT OF ZERO CHARGE OF ALUMINA BY BATCH EQUILIBRATION METHOD

Ž. N. Todorović and S. K. Milonjić

Vinča Institute of Nuclear Sciences, P.O.Box 522, Belgrade, Serbia&Montenegro

Abstract

In this work we present the points of zero charge, pH_{pzc} , of five commercial alumina samples, of an alumina/solution ratio of 0.100g/25 ml, obtained by batch equilibration method. As an inert electrolyte, KNO_3 of 0.001 - 0.1 mol dm^{-3} concentration was used. The obtained points of zero charge values are about 7 and they are independent of KNO_3 concentration, except the sample labeled as ICN (Alumina B). In this case, the increase in electrolyte concentration (from 0.001 to 0.1 mol dm^{-3}) leads to a decrease in pH_{pzc} (from 7.5 to 6.7) indicating specific sorption of K^+ ions on the sample.

Introduction

The point of zero charge of a solid, pH_{pzc} , represents the suspension pH value at which an immersed solid surface has zero net charge or the amounts of positive and negative charges are equal. The isoelectric point, pH_{iep} , is defined as the pH at which the ζ -potential = 0. If there is no specific adsorption of ions on the oxide surface, these two points will be equal. Specific adsorption of cations shifts pH_{pzc} and pH_{iep} towards lower and higher pH values and the specific adsorption of anions shifts these two points to the opposite directions [1,2].

The point of zero charge can be determined by several methods. The most widely used are the batch equilibration method described by one of the authors [3], acid-base potentiometric titration [4], mass titration [5], electrophoresis, and electroosmosis method [6].

In this work, we present the results of the point of zero charge, pH_{pzc} , of alumina obtained by batch equilibration method, for five commercial alumina samples.

Experimental

Five commercial alumina samples were investigated and the results are given in Table 1. All alumina samples were used as received, purity more than 99.5%. All other chemicals were of analytical reagent grade.

The pH_{pzc} were investigated in aqueous KNO_3 (as an indifferent electrolyte) solutions, concentrations 0.1-0.001 mol dm^{-3} . Samples of alumina

Table 1. The point of zero charge of studied alumina samples

No	Al_2O_3 samples different producers	pH_{pzc}
1	Merck	7.0
2	Kemika	6.6
3	ICN(Alumina B)	6.7-7.5
4	ICN (Adsorbentien)	6.8
5	Alcoa A16	6.9

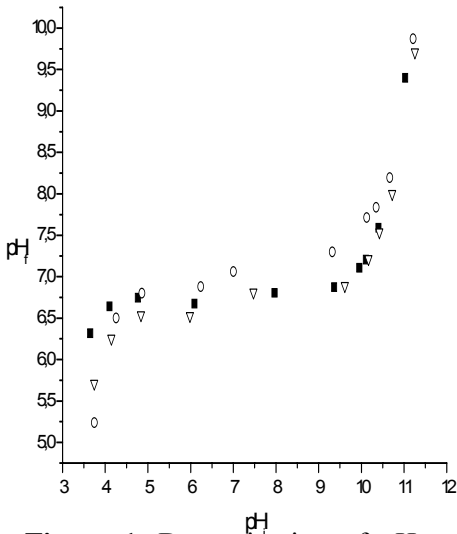


Figure 1. Determination of pH_{pzc} of ICN (Adsorbentien) alumina sample in KNO_3 solutions of \circ -0.001, Δ -0.01 and \blacksquare -0.1 mol dm^{-3} concentrations (pH_i -initial value, pH_f -final value)

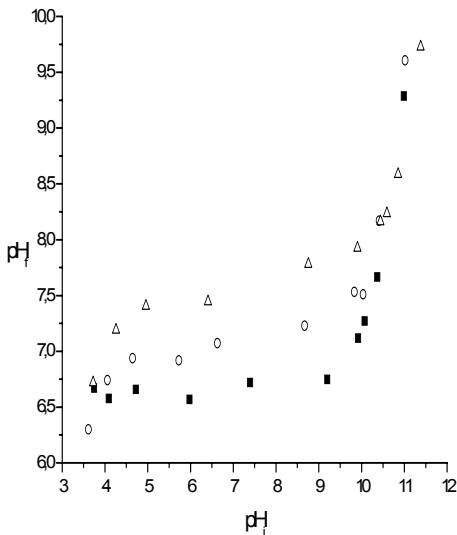


Figure 2. Determination of pH_{pzc} of ICN (Alumina B) alumina sample in KNO_3 solutions of Δ -0.001, \circ -0.01, and \blacksquare -0.1 mol dm^{-3} concentrations.

(0.100 g) with 25 ml of 0.1, 0.01 or 0.001 mol dm^{-3} KNO_3 solution of different pH values were shaken in PVC vials for 24 h. Initial pH values were obtained by adding a small amount of HNO_3 or KOH solution (0.1 mol dm^{-3}), keeping the ionic strength constant. The amount of H^+ or OH^- ions adsorbed by alumina was calculated from the difference between the initial and the final concentration of H^+ or OH^- ions. A Beckman pH-meter was used to determine the concentration of H^+ or OH^- .

Results and Discussion

Experimental results obtained for pH_{pzc} of ICN (Adsorbentien) alumina sample are illustrated in Figure 1. As can be seen, the final pH (pH_f) is presented as a function of initial pH values (pH_i) of the solution, for three different KNO_3 concentrations. pH_f are pH values of filtered solutions after equilibration. The point of zero charge, pH_{pzc} , represents the pH_f level where a common plateau is obtained. The pH_{pzc} value for this alumina sample is 6.8.

Table 1 presents the pH_{pzc} values obtained for all investigated alumina samples. They are all close to 7.

pH_{pzc} of alumina is very sensitive to surface treatment, synthesis process, presence of impurities, etc. A literature review showed that the measured pH_{pzc} vary significantly from 5 to 9.4 [7]. As found in our previous study [8], the point of zero charge of alumina depends on the solid/liquid ratio. Increase in alumina/solution ratio (up to 2.00g/25ml) leads to an increase in pH_{pzc} value. All results presented in this work were obtained for the solid/liquid ratio 0.100g alumina/25 ml KNO_3 .

Also, determination of pH_{pzc} in KNO_3 solutions of different concentrations gave the same results. It means that pH_{pzc} is independent of the ionic strength of KNO_3 solutions. The same results were obtained for other investigated samples, except ICN

(Alumina B). The pH_{pzc} of this sample is dependent on KNO_3 concentration (KNO_3 is not an indifferent electrolyte). An increase in electrolyte concentration decreases the pH_{pzc} , and leads to the specific sorption of K^+ -ions on the sample (Figure 2). pH_{pzc} is 7.5, 7.0 and 6.7 for KNO_3 concentration of 0.001, 0.01 and 0.1 mol dm^{-3} , respectively.

Conclusion

The points of zero charge of five commercial aluminas are determined by the batch equilibration method in KNO_3 solutions. For solid/liquid ratio of 0.100g/25ml, the obtained pH_{pzc} values are around 7. KNO_3 is an indifferent electrolyte for all used commercial samples except ICN (Alumina B). In this sample, K^+ -ions are specifically sorbed on the alumina surface.

Acknowledgements

The research reported in this paper was supported by the Ministry of Science and Environment Protection of the Republic of Serbia (Project 1978).

Reference

- [1] N. Kallay, V. Hlady, J. Jednaček-Bišćan, S. Milonjić, Investigation of Surfaces and Interfaces-Part A. Physical Methods of Chemistry Series, B.W. Rosites, R.C. Beatzold, editors, 2nd ed., Vol.IXA, A. Wiley-Interscience, New York, 1993.
- [2] S.K. Milonjić, Ph. D. Thesis, University of Belgrade, Belgrade, Serbia&Montenegro, 1981.
- [3] S. K.Milonjić, A.Lj. Ruvarac M.V. Šušić, *Thermochimica Acta*, 1975, 11, 261.
- [4] G. A. Parks, P.L. de Bruyn, *J. Phys. Chem.*, 1962, 66, 967.
- [5] J. S. Noh, J. A Schwarz, *J. Colloid Interface Sci.*, 1989, 130, 157.
- [6] H. Sadek, A.K. Helmy, V.M. Sabet, Th.F. Tadros, *J. Electroanal. Chem.* 1970, 27, 257.
- [7] M. Kosmulski, *J.of Coll.Interf. Sci.* 2002,253,77-87.
- [8] Ž.N. Todorović,S.K. Milonjić, S.P. Zec, V.T. Dondur,*Mat. Sci.Forum*, 2004, 453/454, 361.

RP-HPLC DETERMINATION OF RUTIN IN SOLID PHARMACEUTICAL DOSAGE FORMS

V. Kuntić, N. Pejić, B. Ivković¹, S. Mičić, Z. Vujić¹ and D. Malešev

*Institute of Physical Chemistry, Faculty of Pharmacy,
Vojvode Stepe 450, Belgrade, Serbia and Montenegro*

¹ *Institute of Pharmaceutical Chemistry and Drug Analysis, Faculty of Pharmacy,
Vojvode Stepe 450, Belgrade, Serbia and Montenegro*

Abstract

In this study, the analytical method for rutin determination from pharmaceutical formulations was developed. The commercial preparation of rutin available on our market: Rutinion[®] forte, GinkoMax[®] tablets and Veneton[®] capsules were investigated by reverse-phase high-performance liquid chromatography. A successful resolution was obtained from 50% methanol as mobile phase. The method was tested for precision, sensitivity and reproducibility. The low value of standard deviation, RSD less than 3% and recovery lying in stated range, indicate good application of method.

Introduction

Rutin (3,3',4',5,7-Pentahydroxyflavone-3-rhamnoglucoside) belongs to the group of flavonoids, very important plant phenolic compounds, occurring in various kinds of foods (fruits and vegetables) and beverages (coffee, beer, tea, fruit juices). Among other flavonoid derivatives, which all display a remarkable array of biological and pharmacological activities (antioxidative, antiinflammatory, antimicrobial, anticancerogeneous, *etc*) [1], rutin has the most potent therapeutic action. Since it increases the strength of the capillaries and regulates their permeability, helping hemorrhages and ruptures in the capillaries and the connective tissues, rutin is mostly applied as a drug for curing blood vessel diseases. Various pharmaceutical preparations consisting rutin alone or in combination with other substances are available on our market. Therefore, a sensitive analytical method for quantitative determination of rutin in dosage form is required.

So far, HPLC [2-4] with various detections modes were the most common and widely spread techniques that have been utilized for separation, identification and quantitation of rutin from plant extracts, food and plant based beverages, as well as from body fluids, but there are no data about its determination from pharmaceutical formulations. Here, we proposed rutin determination from dosage forms by reverse-phase HPLC.

Experimental

Reagents

Methanol (gradient grade), Absolute Ethanol, and phosphoric acid (analytical reagent grade) were purchased from Merck (Darmstadt). Rutin was available from Fluka (Buchs), Rutinion[®] forte tablets from biomo Natur-Medizin, GmbH, Veneton[®] cap-

sules from Diethparm, Kirchberg, and GinkoMax[®] tablets were available from ESI s.p.a, Italy.

Reversed-phase high performance liquid chromatography

Isocratic HPLC was performed with a Hewlett Packard (Beaverton, OR) chromatograph equipped with high-pressure pumps, a Rheodyne model injector (sample loop 20 μ L) USA, and a Hewlett-Packard (HP) 1100A UV detector attached with IBM PC Pentium Vectra XA computer and Chem Station software package. Rutin was separated on a Supelcosyl C8 reverse-phase analytical column (250 \times 46 mm, i.d., 5- μ m particle size) which was maintained at 40°C. The mobile phase was 50 % methanol (pH=2.8 was adjusted with phosphoric acid) at flow rate of 1mL/min The injection volume was 20 μ L and absorbance was monitored at 360 nm.

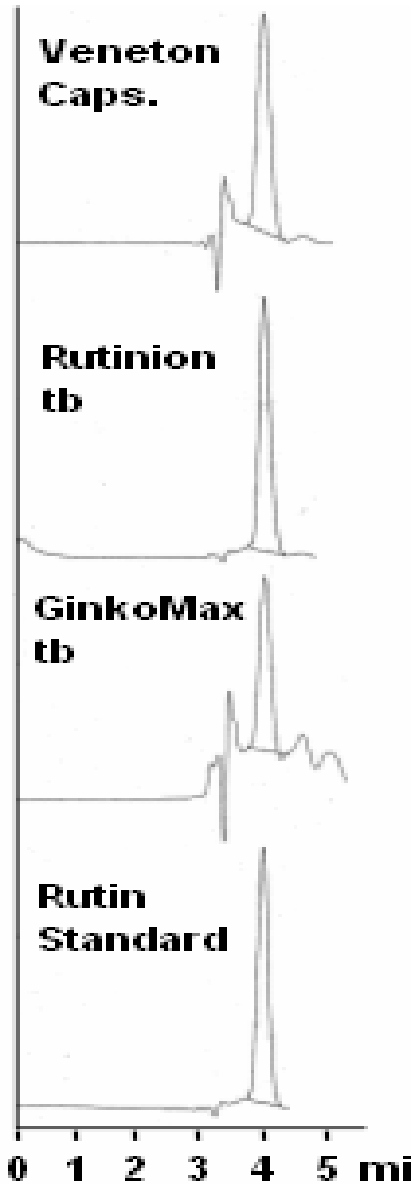
General procedure

Standard stock solution of rutin was prepared by dissolving rutin in absolute ethanol to obtain the concentration of 1mg/mL and diluting with mobile phase in 1:20 ratio. The samples solutions were prepared dissolving an amount equivalent to the average weight of one tablet in absolute ethanol, sonicating for 15 min at room temperature and filtered through filter paper Whattman N^o 1. Ethanolic solutions of samples were diluted with mobile phase in 1:10 ratio.

Results and Discussion

RP-HPLC with UV detection was used for analysis of rutin in solid pharmaceutical dosage forms. In order to determine the optimum set of operating conditions variety parameters have been changed: composition of mobile phase, the percentage of methanol, pH, variety of acids (phosphoric, acetate) and flow rate (changed from 0,5 to 1.5 mL/min). The chromatograms obtained at selected conditions are shown in the picture.

The selectivity of method was determined by injected blank samples and standard solutions. No interfering peak was detected at retention time of the drug. The method was tested for precision and the obtained RSD value confirmed satisfactory repeatability of the system. The accuracy of the method was determined by analysis of three different concentrations of Rutinion[®] forte tablets, Veneton[®] capsules and GinkoMax[®] tablets (80, 100 and 120 %). The low values obtained for the SD showed the accuracy and reproducibility of the method.



Conclusion

The optimum set of operating conditions variety parameters have been chosen from rutin determination from dosage forms by RP-HPLC. Under selected conditions, obtained results confirmed that proposed method was accurate, precise and could be used for the determination of rutin in pharmaceutical formulations.

References

- [1] D.W. Lamson, M.S.Brignall, *Altern Med Rev.*, 2000, 5(3), 196.
- [2] J.P.Leite, L.Rastrelli, G. Romussi, A.B.Oliveira, J.H.Y.Vilegas, C.Pizza, *J. Agric. Food. Chem.*, 2001, 49(8), 3796.
- [3] G.Stecher, C.W.Huck, M.Popp, G.K.Bonn, *Fresenius J Anal Chem.*, 2001, 371(1), 73.
- [4] O.Tokusoglu, M.K.Unal, Z.Yildirim *Acta Chromatographica*, 2003, 13, 196.

SEPARATION OF RHENIUM(VII) FROM TUNGSTEN(VI)

J. Vučina¹, D. Lukić¹, M. Stoiljković², M. Milošević³ and M. Orlić¹

¹Laboratory for Radioisotopes

²Department of Physical Chemistry

³Centre for Nuclear Technologies and Research

Vinča Institute of Nuclear Sciences, 11001 Belgrade, P.O. Box 522, Serbia and Montenegro

Abstract

Examined were the conditions for an effective separation of tungsten(VI) and rhenium(VII) on alumina if the solution of $0.20 \text{ mol dm}^{-3} \text{ NaCl}$, $\text{pH}=2-6$, is used as the aqueous phase. Under the given experimental conditions alumina was found to be much better adsorbent for tungsten than for rhenium. The breakthrough and saturation capacities of alumina at $\text{pH} = 2$ are 24 and 78 mg W/g Al_2O_3 , respectively. With the increase of pH these values decrease. So, at $\text{pH} = 6$ they are only 4 and 13 mg W/g Al_2O_3 , respectively. The elution volume for rhenium for the given column dimensions and the quantity of the adsorbent, is about 16 ml. These results were confirmed by the experiments of the radiochemical separations. Tungsten-187 remains firmly bound to alumina. The radionuclidic purity of the eluted $^{186,188}\text{Re}$ at $\text{pH} = 2$ is very high.

Introduction

Therapy in nuclear medicine gained a renewed interest and investigations are devoted to the introduction of new radionuclides. Particular emphasis is given to ^{188}Re which is the decay product of its parent ^{188}W ($T_{1/2}=69 \text{ d}$) formed in nuclear reactor during the irradiation of tungsten targets. However, the isolation of rhenium from tungsten is not easy. Many efforts are devoted to the development of an efficient routine separation procedure based on alumina as the adsorbent [1,2].

Experimental

Sodium tungstate ($\text{Na}_2\text{WO}_4 \cdot 2\text{H}_2\text{O}$, p.a., Fluka) and potassium perrhenate (KReO_4 , p.a., Aldrich) were commercially purchased. Alumina for column chromatography (Alumina N- Super I, ICN Biomedicals), grain size 40-140 μm , is used without any pretreatment.

The concentrations of tungsten and rhenium in the solutions were determined by the direct current argon arc plasma atomic emission spectroscopy (DCP-AES) with aerosol supply [3].

The column experiments were performed for the system: alumina- $0.20 \text{ mol dm}^{-3} \text{ NaCl}$. The breakthrough and saturation capacities of alumina for W(VI) were determined in the glass column (8 mm diameter 40 mm length) containing 1 g of Al_2O_3 . The concentration of tungsten was $5.4 \times 10^{-3} \text{ mol dm}^{-3}$ in $0.20 \text{ mol dm}^{-3} \text{ NaCl}$, $\text{pH} = 2-6 (\pm 0.2)$. The flow rate was $2.5 \text{ ml min}^{-1} \text{ cm}^{-2}$. According to the previous results [2] the capacity of alumina for rhenium is low. Therefore its breakthrough and saturation capacities were not determined.

The elution volumes of rhenium were determined in the glass column (10 mm diameter; 100 mm length) containing 3.5 g Al_2O_3 . After sorption of 1 ml of rhenium solution ($9 \times 10^{-3} \text{ mol dm}^{-3}$ in 0.2 mol dm^{-3} NaCl), rhenium was eluted by 0.20 mol dm^{-3} NaCl, $\text{pH} = 2-6$, (± 0.2). The flow rate of the eluence solution was $1.5 \text{ ml min}^{-1} \text{ cm}^{-2}$. The elution volumes for tungsten were not determined.

For the irradiations the samples containing 50 mg of KReO_4 and H_2WO_4 , respectively, were used. The irradiations were performed in the thermal core No. 114 of zero power heavy water reactor RB (Vinča Institute of Nuclear Sciences) at fission power equal 40 W (neutron flux $3.6 \times 10^8 \text{ n cm}^{-2} \text{ s}^{-1}$) for 60 minutes [4]. The gamma activities of the irradiated samples were measured by using Canberra XtRa (Extended Range) coaxial Ge-detector in the Canberra 777 ultra low-background shield and the ISOCS (In Situ Object Counting System) Calibration Software [5]. Neutron activation of tungsten ^{186}W gives ^{187}W ($T_{1/2} = 23.8 \text{ h}$) while the products of the reaction $^{\text{nat}}\text{Re}(n,\gamma)$ are ^{186}Re ($T_{1/2} = 90.6 \text{ h}$) and ^{188}Re ($T_{1/2} = 16.9 \text{ h}$).

After irradiation, Re samples were dissolved in water and diluted to 5 ml by 0.20 mol dm^{-3} NaCl ($\text{pH} = 2$). Tungsten samples were dissolved in 1 mol dm^{-3} NaOH and the excess alkali was neutralized by HF. Finally they were diluted to 10 ml by 0.20 mol dm^{-3} NaCl ($\text{pH} = 2$). Both solutions were mixed and passed through alumina column (10 mm diameter, 100 mm length) containing 6 g Al_2O_3 . The elutions were performed by 0.20 mol dm^{-3} NaCl ($\text{pH} = 2$), flow rate 1 ml min^{-1} .

Results and Discussion

The breakthrough and saturation capacities of alumina for tungstate anion and the elution volumes of inactive rhenium and $^{186,188}\text{Re}$ are shown in Table I. Data in Table I present the adsorption characteristics of alumina when the aqueous phase is 0.20 mol dm^{-3} NaCl. It can be seen that they depend on pH. Both the breakthrough and saturation capacities decrease with the increase of pH.

The results for the elution volumes of inactive rhenium and $^{186,188}\text{Re}$ refer to the applied experimental conditions. It can be concluded that they do not depend on pH. For inactive rhenium the value is about 15 ml 0.20 mol dm^{-3} NaCl throughout the examined pH range. These results were tested also with the solutions containing ^{187}W , ^{186}Re and ^{188}Re . The radiochemical separation of rhenium and tungsten radioisotopes was achieved on alumina column containing 6 g Al_2O_3 . Under the given experimental conditions W is efficiently adsorbed and its elution volumes are high. In 100 ml of the eluence passed through the column only the peaks belonging to rhenium radioisotopes were observed. For the elution of rhenium activity ($^{186}\text{Re} + ^{188}\text{Re}$) 23 ml of the eluence was needed. Since no activity of ^{187}W was detected, the radionuclidic purity of the eluted rhenium is very high.

Table I. Breakthrough and saturation capacities of alumina for tungsten and elution volumes of inactive rhenium and $^{186,188}\text{Re}$

Column: 8 mm diameter, 40 mm length; bed: 1 g Al_2O_3 N Super I (ICN Biomedicals)

Rhenium elution volume-Column: 10 mm diameter, 100 mm length; bed: 3.5 g Al_2O_3 N Super I (ICN Biomedicals)

$^{186,188}\text{Re}$ elution volume-Column: 10 mm diameter, 100 mm length; bed: 6 g Al_2O_3 N Super I (ICN Biomedicals)

PH of 0.20 mol dm^{-3} NaCl	Breakthrough capacity (mg W/g Al_2O_3)	Saturation capacity (mg W/g Al_2O_3)	Elution volume of ReO_4^- (ml)	Elution volume of $^{186,188}\text{ReO}_4^-$ (ml)
6	4	13	15	-
4	17	26	15	-
2	24	78	16	23

Conclusion

Sorption studies for WO_4^{2-} and ReO_4^- were carried out by using alumina and aqueous solution of 0.20 mol dm^{-3} NaCl. Our experiments confirm that alumina is, under examined experimental conditions, much better adsorbent for tungstate than for perrhenate anions. The breakthrough and saturation capacities of alumina for tungsten are relatively high. For the given column dimensions and the quantity of alumina used in the experiments, it was found that rhenium can be separated with a relatively low volume of NaCl solution. These results were tested by using the solutions containing ^{187}W , ^{186}Re and ^{188}Re . The radiochemical separations confirm that tungsten is strongly adsorbed on alumina. The radionuclidic purity of separated $^{186,188}\text{Re}$ is very high.

Acknowledgement

This work has been financially supported by Ministry of Science, Technologies and Development of Republic of Serbia under Project No.1980

References:

- [1] N.Botros, M.El-Garhy, S.Abdulla, H.F.Ally, *Isotopenpraxis*, 1986, 22, 368.
- [2] C.Klofutar, F.Krašovec, A.Kodre, *J.Radioanal.Chem.*, 1970, 5, 3.
- [3] FM.Marinković, T.J.Vickers, *Appl.Spectrosc.*, 1971, 25, 319.
- [4] M.J.Milošević, V.Ljubenov, Report Vinča NTI-109, Vinča Institute of Nuclear Sciences (March 2003).
- [5] R.Vekataraman, F.Bronson, V.Abashkevich, B.M.Young, M.Field, *Nuclear Instruments and Methods in Physics Research, Section A: Accelerators, Spectrometers, Detectors and Associate Equipment*, 1999, 422, 450.

REMOVAL OF ARSENATE BY CATIONIC SURFACTANT AND IRON HYDROXIDE-LOADED NATURAL CLINOPTILOLITE

M.Tomašević-Čanović¹, T.Stanić¹, A.Živanović² and J. Lemic¹

¹ Institute for Technology of Nuclear and other Raw Mineral Materials, 11000 Belgrade, Serbia and Montenegro, ²VMA, Institute for Hygiene, 11000 Beograd, Crnotravska 17

Abstract

Arsenic in drinking water is of major concern to many of water utilities in the world. Numerous studies have examined the removal of arsenic through treatment processes such as coagulation-precipitation, reverse osmosis, ion exchange and using different adsorbents. In this study describes the efficiency of arsenate adsorption on different form modified natural clinoptilolite.

Introduction

Arsenic, a potential carcinogenic element is present in natural water as a result of natural and anthropogenic activities. The investigation of arsenic-contaminated water can cause deleterious effects on the human body, and these effects are well documented. The World Health Organization standard for arsenic stands at $10\mu\text{g}/\text{dm}^3$. The current maximum contaminant level for arsenic in drinking water is $50\mu\text{g}/\text{dm}^3$ in U.S., whereas the maximum acceptable concentration for arsenic is $25\mu\text{g}/\text{dm}^3$ in Canada. The U.S.Environmental Protection Agency has proposed to reduce the maximum level of As to $5\mu\text{g}/\text{dm}^3$. In European Community is aiming at a standard in the range of 2 to $20\mu\text{g}/\text{dm}^3$ [1] In Japan Effluent Standard is $10\mu\text{g}/\text{dm}^3$ [2]

Removal of As is one of the most important areas of waster water treatment. Various treatment methods such as adsorption, ion exchange, ultra filtration, reverse osmosis coagulation-precipitation, etc. Adsorption technique is generally considered to be a promising method and has been studied for As removal [3,4,5]. Zeolite has high internal and external surface areas and high internal and external cation exchange capacities suitable for surface modification by cationic surfactants. Various types of efficacy adsorbent for remove As from water on the basis modification of zeolite were developed [2,3,4,5,6]In present work, describes the efficiency of arsenate adsorption on different form modified natural clinoptilolite.

Materials and Methods

Samples were prepared by different treatment and modification natural clinoptilolite rich tuff Zlatokop deposited (Serbia). Starting zeolite was different particle size; for modification it's used different amines, primary and quaternary, separately or in the combination with acid pretreatment. Summary of various samples of clinoptilolite prepared and corresponding modifier, are given in Table 1.The all amines supplied by Akzo Chem. Analytical-reagent grade chemicals were used for the preparation all solution. As was determined by AAS. *Batch procedure* – 100ml water containing $100\mu\text{g As}/\text{dm}^3$ mixed with 1g of an adsorbent on magnetic stirrer for 60 minute. The samples were then filtrated and non-adsorbed As was determined in supernatant.

Table 1. Clinoptilolite samples used for adsorption of arsenate in water

Sample No	Natural CLI, mm	HCl	Amine	Iron-coated
1	-0.2 + 0.0	2M	-	-
2	-0.2 + 0.0	2M	stearyl	-
3	-0.2 + 0.0	-	hexadecyltrimethyl	-
4	-0.2 + 0.0	-	ditalowdimethyl	-
5	-0.2 + 0.0	-	-	3 mg/g
6	-0.8 + 0.4	2M	Soyabean	-
7	-0.2 + 0 (400°)	-	stearyl	-
8	-0.8 + 0.4	-	soyabean	-
9	-0.2 + 0.0	-	stearyl	-
10	-0.2 + 0.0	-	cholestyramine	-
11	-0.2 + 0.0	-	ditalowdimethyl+chol.	-
12	-0.8 + 0.4	-	stearyldimethylbenzyl	-
13	-0.8 + 0.4	-	stearyldimethylbenzyl	3 mg/g
14	-0.2 + 0.0	-	stearyldimethylbenzyl	3 mg/g
15	-0.2 + 0.0	-	stearyldimethylbenzyl	2 mg/g
16	-2.0 + 1.0	-	ditalowdimethyl	2 mg/g

Results and Discussion

The results of arsenate removal from water solution ($100\mu\text{g}/\text{dm}^3$), with corresponding samples different modified clinoptilolite, are summarized in Table 2.

The adsorption of arsenate on examined samples is greatly affected by the modifier-zeolite interaction. In terms of arsenate adsorption ability, the examined adsorbents may be divided into three groups: (a) strong arsenate adsorbents based on the zeolite coated with ferric hydroxide, before (Sample 5) or after modification with long-chained primary or quaternary amine (Samples: 13, 14, 15 and 16); (b) –samples good arsenate adsorbents obtained long-chained amine (Samples: 2, 10 and 11) and (c) –samples with less or more but not sufficient, adsorption arsenate (Samples: 1, 3, 4, 6, 7, 8, 9 and 12).

Table 2. Adsorption of As on different samples

Sample	As -added	As-in super- natant	% A	Sample	As-added	As-in super- natant	% A
1	100 $\mu\text{g}/\text{l}$	92.1 $\mu\text{g}/\text{l}$	7.9	9	100 $\mu\text{g}/\text{l}$	57.0	43.0
2	100 $\mu\text{g}/\text{l}$	4.4	95.6	10	100 $\mu\text{g}/\text{l}$	3.5	96.5
3	100 $\mu\text{g}/\text{l}$	84.9	15.1	11	100 $\mu\text{g}/\text{l}$	<3.0	> 97
4	100 $\mu\text{g}/\text{l}$	70.2	29.8	12	100 $\mu\text{g}/\text{l}$	21.5	78.5
5	100 $\mu\text{g}/\text{l}$	<3.0	>97.0	13	100 $\mu\text{g}/\text{l}$	<3.0	> 97
6	100 $\mu\text{g}/\text{l}$	11.2	88.8	14	100 $\mu\text{g}/\text{l}$	<3.0	> 97
7	100 $\mu\text{g}/\text{l}$	28.5	71.5	15	100 $\mu\text{g}/\text{l}$	<3.0	> 97
8	100 $\mu\text{g}/\text{l}$	63.9	36.1	16	100 $\mu\text{g}/\text{l}$	<3.0	> 97

Sorption of arsenate using Sample 5 (iron-loaded zeolite) and Sample 14 (amine modified and iron loaded zeolite), were done for different starting concentration of As- 0.1- 10.0 mg As/ dm^3 , mixing 100 ml arsenate solution with 1g adsorbent for 30 min. In Figure 1 are

given curve adsorption of As versus added concentration As in Table 2. Adsorption of As on different samples mg/dm^3 .

The high adsorption was obtained with both samples. At equilibrium concentration below 1.0 mg As/l over 98% of arsenate were removed by the both samples. Sample 14 removed more than 95% up to 3.0 mg As/l . At higher arsenate concentration, the adsorption efficiency was lower.

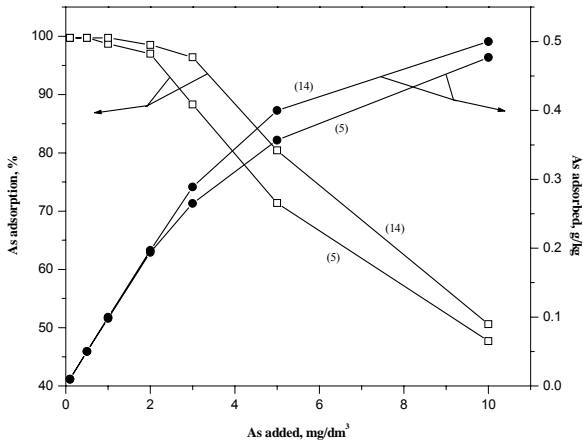


Figure 1. Arsenate adsorption on iron-loaded zeolite (sample 5), and surface-amine modified and iron-loaded zeolite (sample 14), open symbols-adsorption in %, solid symbols adsorption As in g/kg adsorbent

Conclusion

The obtained results showed that efficient arsenate adsorbents were prepared by appropriate modifications and iron loaded of natural clinoptilolite tuff. Considerable higher increase of adsorption characteristics, for adsorption of arsenate, was observed with iron-loaded clinoptilolite before surfactant-modified clinoptilolite. Simultaneously, such adsorbents may also adsorb certain nonpolar organic compounds and other inorganic anions.

References

- [1] O.S. Thirunavukkarasu, T. Viraraghavan, K.S. Subramanian, *Water Quality Research Journal of Canada*, 2001, 36(1), 55.
- [2] Y. Xu, T. Nakajima, A. Ohki, *Journal of Hazardous Materials*, 2002, B92, 275.
- [3] Z. Li, I. Anghel, R.S. Bowman, *J. Dispersion Science and Technology*, 1998, 19(6&7), 843.
- [4] Z. Li, R.S. Bowman, *Wat. Res.*, 2001, 35(16), 3771.
- [5] E. Chmielewska, K. Jesenak, K. Gaplovska, *Collect. Czech. Chem. Commun*, 2003, 68, 823.
- [6] Y. Xu, A. Ohki, S. Maeda, *Shemistry Letters*, 1998, 1015.

Complex Compounds

(L)

STRUCTURAL STUDIES OF METAL ION COMPLEXES OF THE ANTICANCER DRUG BLEOMYCIN USING NMR IN COMBINATION WITH MOLECULAR DYNAMICS SIMULATIONS.

A. Papakyriakou and N. Katsaros

Institute of Physical Chemistry, NCSR "Demokritos", 15310 Ag. Paraskevi, Attikis, Greece

Introduction

Bleomycins are a group of antibiotics with clinical use as anticancer drugs.^[1-3] The commercial preparation, Bleocin or Blenoxane, consists predominantly of bleomycins A2 and B2. Their efficacy is mainly attributed to their ability to mediate cleavage of the DNA backbone by attacking at the deoxyribose 4'-H and causing single and double strand cleavage and base release. A number of putative pathways have been proposed to initiate the DNA oxidation. The drug is activated in the presence of iron and oxygen species as cofactors. Other metals can also facilitate DNA cleavage by bleomycin in vitro, even though their reactions are less well-characterized [1, 2].

Results and Discussion

The solution structure of three complexes of the anticancer drug bleomycin (BLM) has been carried out using high-field NMR methods in combination with molecular dynamics simulations. The stability of Ga(III)-BLM has allowed us to assign all the exchangeable amine and amide protons for the first time, which in turn was proven to be a valuable piece of information for its solution structure [3]. NMR data were used as constraints in conjunction with simulated annealing molecular dynamics calculations. The NMR structure revealed that Ga(III)-BLM shares a similar structure with Co(III)-BLM complexes. By virtue of the fact that Ga(III) adducts are used as a probe for the biologically relevant Fe(III) compounds, their binding mode with BLM is proposed to be similar. Additionally, its interaction with the self-complementary oligonucleotide d(CCAGGCCTGG)₂ was investigated by means of NMR. Our data, in comparison with those obtained for Co(III)-BLM, indicate that the drug binds strongly via intercalation of the bithiazole moiety between the central d(-CC-) step and that the pyrimidine ring of BLM might be involved in the formation of a base-triple-like interaction with the adjacent (G•C) base pair (Figure 1).

Employing the same methods, we have also determined the solution structure of In(III)-BLM, which is successfully applied as radioactive imaging agent. NMR studies were performed both at pH 3.3 and 6.8 with the aim to investigate possible structural changes that could occur upon preparation of the kit for clinical use (low pH) and administration of the radioactive complex (neutral pH). Our data indicate that In(III)-BLM has a similar structure with that of Ga(III)-BLM, which is not dependent on the pH of the solutions [4].

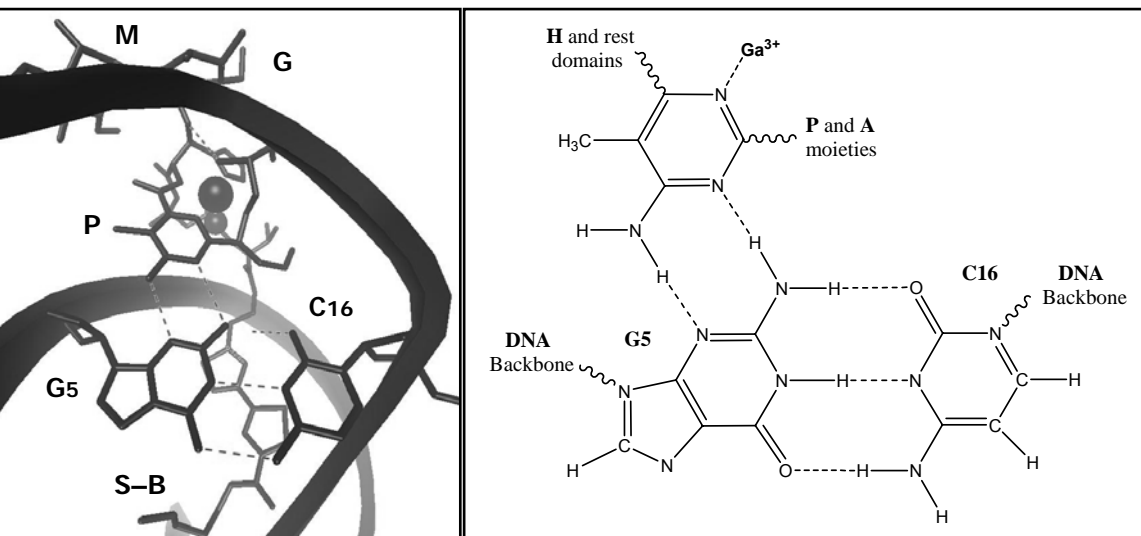


Figure 1. Model of the interaction between Ga(III)-BLM A2 and $d(\text{CCAGGCCTGG})_2$ and schematic representation of the base-triple-like interaction between the pyrimidine ring of the complex and the (C•G) base pair.

Finally, the interaction of Pd(II) ions with BLM was studied in solutions with high ionic strength [5]. In this way, it was found that one major species is present, which was characterized using NMR and molecular modeling. Experimental data indicate that BLM binds to Pd(II) via the four common nitrogen donor atoms. The NMR structure exhibits that the drug is folded around the coordination sphere, a fact that was attributed to intramolecular hydrogen bonding interactions, either directly or mediated by solvent molecules and chlorine anions [6]. The kinetically more inert Pt(II) ions result in the formation of several species when interacting with BLM, but on the other hand, their similarity with Pd(II) supports the suggestion that both metals form the same adducts with BLM. The force field AMBER(96) has been used throughout the molecular dynamics calculations, which was carefully parameterized in order to accurately represent the above compounds. All atom-centered point charges were derived from the electrostatic potential of BLM molecular fragments, which were calculated at the HF/6-31G* level of theory.

Conclusions

NMR in combination with molecular modeling is a powerful tool in the investigation of the solution structures of metal ion complexes and their interactions with DNA. Detailed structural information can elucidate molecular mechanism that are responsible for their biological activity.

References

- [1] R. M. Burger, *Chem. Rev.* 1998, 98, 1153.
- [2] C. A. Claussen and E. C. Long, *Chem. Rev.* 1999, 99, 2797.
- [3] A. Papakyriakou, B. Mouzopoulou and N. Katsaros, *J. Biol. Inorg. Chem.* 2003, 8, 549.
- [4] A. Papakyriakou and N. Katsaros, *Eur. J. Inorg. Chem.* 2003, 16, 3001.
- [5] A. Papakyriakou, I. Bratsos and N. Katsaros, *J. Serb. Chem. Soc.* 2003, 68, 337.
- [6] A. Papakyriakou, I. Bratsos, M. Katsarou and N. Katsaros, 2004, submitted.

METAL LIGAND AROMATIC CATION- π INTERACTIONS IN CRYSTAL STRUCTURES OF COMPLEXES WITH ACETYLACETONATO LIGAND

D. N. Sredojević, M. K. Milčić,^a N. Juranić,^b and S. D. Zarić^a,

^a *Department of Chemistry, University of Belgrade, Studentski trg 16,
P.O. Box 158, 11001 Belgrade, Serbia and Montenegro*

^b *Departments of ¹Biochemistry and Molecular Biology, Mayo College of Medicine,
Mayo Clinic and Foundation, Rochester, Minnesota, 55905 U.S.A*

Abstract

The cation- π interactions is recognized as an important noncovalent bonding force in a wide range of molecular systems. Metal-ligand aromatic cation- π (MLAC- π) interactions are interactions of cation- π type between cationic or neutral complexes of transition metal and aromatic group. In this paper is shown that MLAC- π interactions exist in crystal structures of complexes with acetylacetonato ligand. Hydrogen atom from acetylacetonato ligand is involved in interactions with aromatic ring. Geometrical parameters indicates that this interactions are similar to earlier described MLAC- π interactions.

Introduction

The cation- π interactions is recognized as an important noncovalent bonding force in a wide range of molecular systems. The gas-phase studies of these complexes established that cation binds strongly to simple aromatic systems. High-level theoretical studies on ion-molecule systems have shown an excellent agreement between calculated and experimental bonding energies.

It has been documented that cation- π interactions are important for molecular recognition in many biological systems. Investigation of cation- π interactions in proteins [1a] and peptides [1b] show that cation- π pairs contribute as much to protein stability as more conventional interactions [1c].

Cation- π interaction between a cationic metal complex and π systems were predicted by the density functional theory (DFT) calculations [2]. It was shown that cationic metal complex interacts strongly with the π -system of benzene, acetylene and ethylene. Based on these calculations it was proposed that the cation- π interactions may exist when ligands coordinated to metal can get in contact with π -system. These type of interactions are called metal ligand aromatic cation- π (MLAC- π) interactions.

MLAC- π interactions in metalloproteins were found in crystal structures of metalloproteins from the Protein Data Bank (PDB). These interactions play a role in stability and conformation of metalloproteins, and in some cases may also be directly involved in the mechanism of enzymatic reactions that occur at the metal center [3].

MLAC- π interactions were found as intramolecular interactions in transition metal complexes [4]. By searching crystal structures of metal complexes from the

Cambridge Structural Database (CSD), it was shown that there are a number of complexes where ligands coordinated to the metal interact with an aromatic group that is part of an organic ligand in the same complex. By DFT calculations on model system of Co(III) complexes with total charge +1 it was evaluated that the interaction energies in these model systems is about 4 kcal/mol.

Until now we were investigating only MLAC- π interactions with hydrogen atom bounded on ligating atom, i.e., it was two bonds between M and H. In this work we are investigating MLAC- π interactions in systems where there are four bonds between M and H. However, π -delocalization in the acetylacetonate ligand may enable a distant metal influence.

Results and Discussion

System that we are investigating comprises crystal structures of transition metal complexes with acetylacetonato ligand. By coordination, molecule of acetylacetonone losses one hydrogen from C_α carbon atom and becomes negatively charged acetylacetonato ligand. Other hydrogen atom bound to the C_α carbon is partially positive and should be able to form MLAC- π interactions with nearby aromatic groups.

We searched CSD for structures in which distance between hydrogen atom bound to the C_α carbon of acetylacetonato ligand and center of phenyl ring is shorter than 3.5 Å. Also, angle between C-H vector and center of the ring (angle α), was constrained in the range 150°-180°. Angle between H-atom, centroid of the ring, and one of C-atoms from phenyl ring (angle β) was constrained between 50° and 120° (Figure 1).

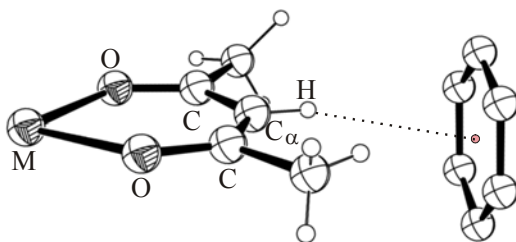


Fig. 1. MLAC- π interaction between acetylacetonato ligand and aromatic molecule. Coordinates are taken from structure ACTBPD.

Searching crystal structures of transition metal complexes from CSD with these parameters we found 42 structures. All of these structures have intermolecular MLAC- π interactions. Some geometrical parameters for the MLAC- π interaction in crystal structures of metal complexes with acetylacetonato ligand are shown in Table 1. We noticed that distances between H atom and center of phenyl ring are very similar to the corresponding distances found previously [4], where there were only two bonds between H and M. Hence, the strength of MLAC- π interactions of acetylacetonato ligand is comparable with the strength of these interactions with ammine or aqua ligands.

Table 1. Some geometrical parameters for the MLAC- π interaction in crystal structures of metal complexes with acetylacetonato ligand.

	Refcode	metal	H \cdots center of ring	α	β
1	ACTBPD	Pd(II)	3.155	164.549	111.866
2	ACXMPD	Pd(II)	3.016	169.817	85.981
3	COWREL	Ru(II)	3.037	159.593	106.466
4	DORVAH	Rh(I)	2.963	154.041	86.883
5	LOPGIG	Zr	3.157	178.625	96.453
6	MANSOJ	Ru(II)	3.158	169.301	92.193
7	NIFNAR	Ru(II)	2.988	157.038	96.459
8	PIPTEZ	Ru(II)	2.996	162.348	91.387
9	YIPSUL	Rh(III)	3.256	172.054	102.081
10	WANYUF	Pt(II)	2.903	161.456	86.857
11	YODTEQ	Cr(III)	3.414	161.972	98.842

Conclusion

This study shows that acidic hydrogen atom from acetylacetonato ligand can be involved in the intermolecular MLAC- π interactions with aromatic groups. Searching Cambridge Structural database we found 42 structures with unusually short distances between hydrogen atom from acetylacetonato ligand and aromatic group. Geometrical data for this interactions are similar to the previously found MLAC- π interactions, indicating that strength of these interactions are comparable.

References

- [1] a) J.P. Gallivan, D. A. Dougherty, Proc. Natl. Acad. Sci, USA, 2000, 96, 9459;
 b) T. P. Burghardt, N. Juranić, S. Macura, K. Ajtai, Biopolimers, 63, 2002, 261;
 c) C. J. Ma, D. A. Dougherty, Chem. Rev., 1999, 97, 1303.
- [2] S. D. Zarić, Chem. Phys. Lett., 1999, 311, 77.
- [3] S.D. Zarić, D. Popović, E.W. Knapp, Chem. Eur. J., 2000, 6, 3935.
- [4] M. Milčić, S.D.Zarić, Eur. J. Inorg. Chem., 2001, 2143.

C – H... π INTERACTIONS IN THE METAL-PORPHYRIN COMPLEXES WITH CHELATE RING AS THE H ACCEPTOR

V. B. Medaković,^a M. K. Milčić,^a and S. D. Zarić^a

^a *Department of Chemistry, University of Belgrade, Studentski trg 16,
P.O. Box 158, 11001 Belgrade, Serbia and Montenegro*

^b *Vinča" Institute of Nuclear Sciences, Laboratory of Theoretical Physics and Condensed Matter
Physics, 11001, Belgrade, P. O. Box 522, Serbia and Montenegro*

Abstract

Specific C – H... π interactions with the π -system of porphyrinato chelate ring were found in crystal structures of transition metal complexes from the CSD and statistical analysis of geometrical parameters for intramolecular and intermolecular interactions was done. DFT calculations on a model system show that energy of the interaction is 1.58 kcal/mol and that the strongest interaction occurs when the distance between hydrogen atom and the center of the chelate ring is 2.6 Å. This prediction is in good agreement with the distances for intermolecular interactions found in the crystal structures. In many cases the intramolecular interaction distances are much shorter than 2.6 Å, and these short distances appear to be caused by geometrical constraints. The C – H... π interactions with chelate ring of porphyrinato ligand can be important in biomolecules with porphyrin as they can influence the structure, contribute to the stability and play some role in function of biomolecules.

Introduction

Noncovalent interactions of π -systems have been extensively studied in recent years, and their importance has been shown in different molecular systems from molecular biology to crystal engineering. X – H... π interactions in metal complexes including organometallics, have been found by searching databases of crystal structures, and investigated by both quantum chemical calculations and spectroscopic methods. C – H... π interactions are the weakest among the X – H... π interactions. However, C – H groups are very abundant and these interactions appear frequently, hence they are important for molecular recognition.

Recently, a few studies of noncovalent interactions with chelate ring as a π -system were published [1-3]. In our previous study structural and computational evidence was given for a particular type of C – H... π interaction where the hydrogen atom interacts with a chelate ring [1]. The Cambridge Structural Database (CSD) was screened in order to find C – H... π interactions with a six-membered chelate ring with delocalized bonds. It was shown that there is large number of structures with short distances between the interacting hydrogen atom and the center of the chelate ring (< 3.0 Å) and with C – H line almost perpendicular to the center of the chelate ring. Calculations of these interactions by density functional theory (DFT) show energies of interaction of about 1 kcal/mol [1]. The calculated energies and observed geometries are

comparable to those of $C - H \cdots \pi$ interactions where the proton acceptor is an organic aromatic ring.

Porphyrin molecule and derivatives of porphyrine possess four pyrrole rings with delocalized π -systems. When porphyrin is coordinated as a tetradentate ligand to a metal, additional rings with delocalized π -bonds are formed four six-membered chelate rings. These chelate ring π -systems of the coordinated porphyrin can be involved in $C - H \cdots \pi$ interactions.

Here, we present the first results and analysis on $C - H \cdots \pi$ interactions in porphyrinato complexes where the π -systems of the six-membered chelate rings have role of a π -systems.

Results and Discussion

The structures of metal complexes with coordinated derivatives of porphyrin were screened using the same geometric criteria as in the previous work [1] described briefly below. We searched CSD for structures with hydrogen atom to center of the six-membered ring (Ω) distances shorter than 3.0 Å, and with a $X-H \cdots \Omega$ axis in a narrow cone perpendicular to the ring ($\alpha > 110^\circ$, $\beta < 16^\circ$) (Fig. 1).

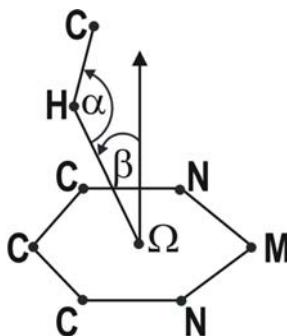


Figure 1. Geometrical parameters for the $C - H \cdots \pi$ interaction with the chelate ring of the porphyrinato ligand.

In searching crystal structures of transition metal complexes from the Cambridge Structural Database (CSD) for specific $C - H \cdots \pi$ interactions, interactions between $C - H$ groups and the π -system of porphyrinato chelate rings in metal complexes, we found 655 such interactions. Among them, 411 are intermolecular and 244 are intramolecular. As can be anticipated from steric considerations, intermolecular $C - H \cdots \pi$ interactions are possible only in metal complexes with a vacant axial position. For intermolecular interactions, most of the examples are found for complexes with Zn (122), Ni (74), Fe (69) and Cu (36), while for intramolecular $C - H \cdots \pi$ interactions, most of the examples are found for complexes with Fe (116), Zn (37) and Ru (33). The differences in the distributions of geometrical parameters for intramolecular and intermolecular interactions can be explained by geometrical constrains in the in-

tramolecular interactions, where in most of these cases the hydrogen atom that interacts with the chelate ring is part of the axial ligand.

The calculations have been done using DFT method (B3LYP). Calculations were performed with GAUSSIAN98 program. The LANL2DZ basis set was chosen for the copper atom and 6-31G** basis sets were chosen for the carbon, nitrogen and hydrogen atoms. The bonding energies were calculated as the difference between the energy of the [Cu(por)] – C₂H₂ system and the sum of the energies of the [Cu(por)] complex and acetylene. Single point calculations have been done for different H...Ω distances from 1.8 – 3.4 Å. For distances below 2.0 Å, the interaction is repulsive. At a distance of 2.3 Å, the interaction energy is greater than 1 kcal/mol. The minimum occurs at 2.6 Å, and the energy of interaction for this structure is 1.58 kcal/mol. The minimum is shallow and the interaction energy is greater than 1.5 kcal/mol for the range of 2.4 – 2.9 Å, while it is greater than 1 kcal/mol to 3.4 Å. Hence, there is attractive interaction even at the distances longer than 3.0 Å. The calculated energies for the interaction at different distances is in good agreement with the distances for the intermolecular interactions found in the crystal structures.

Conclusion

The study shows that chelate rings of coordinated porphyrin can be hydrogen acceptors in C – H...π interactions. In searching crystal structures of transition metal complexes with porphyrin from the CSD, 655 C – H...π interactions (411 intermolecular and 244 intramolecular) were found. Statistical analysis show that there are different distributions of geometrical parameters for intramolecular or intermolecular interactions, caused by geometrical constrains for the intramolecular interactions. DFT calculations on a model system show that energy of the interaction is 1.58 kcal/mol and that the strongest interaction occurs when the distance between hydrogen atom and the center of the chelate ring is 2.6 Å. This prediction is in good agreement with the distances for intermolecular interactions found in the crystal structures. In many cases the intramolecular interaction distances are much shorter than 2.6 Å, and these short distances appear to be caused by geometrical constrains.

The C – H...π interactions with chelate ring of porphyrinato ligand can be important in biomolecules with porphyrin as they can influence the structure, contribute to the stability and play some role in function of biomolecules.

References

- [1] G. A. Bogdanović, A. S. Bire, S. D. Zarić, *Eur. J. Inorg. Chem.*, 2002, 1599.
- [2] Z. D. Tomić, V. M. Leovac, S. V. Pokorni, D. Zobel, S. D. Zarić, *Eur. J. Inorg. Chem.*, 2003, 1222.
- [3] Z. D. Tomić, S. Novaković, S. D. Zarić, *Eur. J. Inorg. Chem.*, 2004, in press.

UNUSUAL CATION- π INTERACTION: CATION- π INTERACTION WITH CHELATE RING AS π -SYSTEM

M. K. Milčić, and V. B. Medaković

*^a Department of Chemistry, University of Belgrade, Studentski trg 16,
P.O. Box 158, 11001 Belgrade, Serbia and Montenegro*

Abstract

By searching Cambridge Structural Database we found transition metal complexes with cation- π interactions between helat ring and alkali metal cations. We found 13 structures with this type of interactions, but only four of them are with porphyrine ligand. Distance between alkali metal cation and center of chelaten ring are similar to distances between alkali metal cation and center of the phenyl group. DFT calculations on model system have shown that interaction energies are 31.83 kcal/mol for sodium and 23.19 kcal/mol for potassium cation. These energies are similar with energies calculated for cation- π interactions with organic aromatic molecules. This shows that properties of chelat ring are similar to properties of organic aromatic molecules.

Introduction

Importance of noncovalent interactions of π systems has been shown in different molecular systems from molecular biology to crystal engineering. Noncovalent interactions involving metal atoms has gained particular attention with the recognition that metal atoms can bind to the phenyl ring, and the explanation of this in terms of cation- π interaction. Cationic metal complexes are involved in similar metal-ligand aromatic cation- π interactions, where ligands coordinated to the metal interact with π system. These can be considered also as a type of X-H $\cdots\pi$ hydrogen bonds [1,2].

Recently, a few studies of noncovalent interactions with chelate ring as a π system were published. In our previous studies it was shown that chelate rings with delocalized π -bonds can be involved in C-H $\cdots\pi$ interaction with organic moiety and in stacking interactions with phenyl ring [3-5].

These recent results show that chelate rings with delocalized π bonds can be involved in noncovalent interactions as π systems. Hence, one can assume that chelate rings can be also involved in cation- π interactions with simple metal cations. On other hand, since member of the chelate ring is metal atom with partial positive charge, and in these interactions two positively charged metal atoms would be very close, one can assume that these interactions hardly can occur. It was shown that by analysing crystal structures from data banks it is possible to elucidate facts about intermolecular and intramolecular interactions. In order to find out if cation- π interactions with chelate rings exist in crystal structures we searched Cambridge Structural Database (CSD). In this work we present results of searching CSD and results of DFT calculation on these

interactions. To the best of our knowledge this is the first study on cation- π interactions with chelate ring.

Results and Discussion

Crystal structures of metal complexes with five and six membered chelate ring and alkali metal ion as contraion were extracted from CSD. The structures of these metal complexes were screened for intermolecular cation- π interactions between chelate ring and alkali metal ion using geometric criteria. We searched for structures, where the distance between the alkali metal ion and the center of the chelate ring is less than 3.7 \AA , angle α is between 70 and 110 degrees and angle β less than 25 degrees (Figure 1).

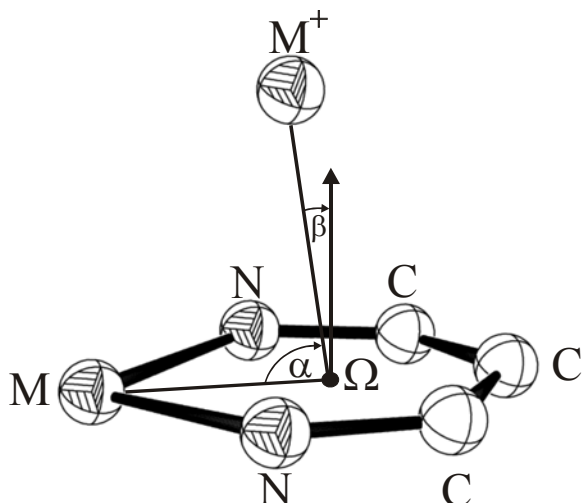


Fig. 1. Geometrical parameters for the cation- π interaction with the chelate ring of the porphyrinato ligand. Coordinates are taken from the structure FAGCIZ in the Cambridge Structural Database (CSD).

By searching CSD we found 13 structures with this type interactions. Four of them are structures with chelate ring of porphyrin ligand. In all cases cation is situated almost over the center of the chelate ring, in most cases angle β is less than 13° . The distance between the center of the ring and the cation are similar to the distances for phenyl ring that are found in the crystal structures from CSD.

There is only one example of interaction with Li^+ cation, where cation is situated between two six membered chelate rings of two porphyrin rings, with the $\text{M}^+-\Omega$ distances of 1.861 and 1.837 \AA . The shortest $\text{Na}^+-\Omega$ distance is 2.410 \AA , while the longest one is 3.666 \AA . However, most of them are around 2.5 \AA . For K^+ cation the

distances are between 2.714 and 3.317 Å. It is interesting that K⁺-Ω distances are mainly shorter for the interactions with five membered chelate ring.

The DFT calculation of interactions of metal cation with the chelate ring was done for a few model systems, where chelate ring was ring from porphyrin coordinated to the copper (II). Calculations were performed with GAUSSIAN98 program. The LANL2DZ basis set was chosen for the copper atom and 6-31G** basis sets were chosen for the carbon, nitrogen, hydrogen and alkali metal atoms. The bonding energies were calculated as the difference between the energy of the [Cu(por)] - M⁺ system and the sum of the energies of the [Cu(por)] complex and alkali metal ion. We put K⁺ and Na⁺ cations over the center of the chelate ring, and calculated interacting energy by DFT method. The calculated energy for interactions of Na⁺ cation at Na⁺-Ω distance of 2.410 Å, was 31.83 kcal/mol, while the calculated energy for interactions of K⁺ cation at K⁺-Ω distance of 3.00 Å was 23.19 kcal/mol. These energies are comparable with the energies calculated and experimentally obtained for interactions of Na⁺ and K⁺ with benzene.

Conclusion

These results show that chelate rings can act as a π system in cation-π interactions. Searching Cambridge Structural Database we found 13 structures with cation-π interactions where chelate ring is π system. DFT calculations show that there is no difference in energy between cation-π interactions with phenyl ring and with chelate ring, indicating that chelate rings have similar properties to phenyl ring.

References

- [1] S.D. Zarić, D. Popović, E.W. Knapp, *Chem. Eur. J.*, 2000, 6, 3935.
- [2] M. Milčić, S.D.Zarić, *Eur. J. Inorg. Chem.*, 2001, 2143.
- [3] G.A.Bogdanović, V.B.Medaković, M.K.Milčić, S.D. Zarić, *Int. J. Mol. Sci.*, 2004, 5, 174.
- [4] Z. D. Tomić, V. M. Leovac, S. V. Pokorni, D. Zobel, S. D. Zarić, *Eur. J. Inorg. Chem.*, 2003, 1222.
- [5] Z. D. Tomić, S. Novaković, S. D. Zarić, *Eur. J. Inorg. Chem.*, 2004, in press.

COMPARISON OF TWO VIEWS REGARDING THE NATURE OF THE X-H...PHENYL INTERACTION

Z. D. Tomić, S. Novaković and S. D. Zarić^a

Institute of Nuclear Sciences "Vinča", P.O. Box 522, 11001 Belgrade,

^aDepartment of Chemistry, University of Belgrade, Studentski trg 16, PO Box 158, 11001 Belgrade, Serbia and Montenegro

Abstract

There are two approaches in the analysis of the nature of the X-H...phenyl interactions. One is based on the assumption that atoms, bonds and the π plane belonging to the phenyl ring, are the points which can be involved in the interaction. The other states that center of the phenyl ring is the point acceptor. In this paper we compare two views using the directionality of the X-H vector and length/angle correlations relative to both assumed point acceptors. The results suggest that on the basis of this methodology there is no clear answer regarding the nature of the acceptor site in the phenyl ring.

Introduction

The study of weak interactions is a topic of great current interest, determined by their potential role in the crystal engineering, supramolecular assemblies, and protein ligand interactions. One of the interesting findings was that X-H... π interactions where X = O, N, C and π is a phenyl ring, can be considered as weak hydrogen-bonding interactions where the π system acts as a hydrogen-bond acceptor [1]. The question which originate from the observation that aromatic ring can accept hydrogen bond was: how to define point acceptor in a multiatom fragment such this? There are two views on this question and both has been used for specifying the criteria used in the analysis of crystallographic data. One is based on the assumption that the element of the aromatic ring (ie. mean plane of the ring, the closest carbon and the closest C-C bond) which is closest to hydrogen is point acceptor in the fragment X-H... π (π designate phenyl ring in the following text) and geometrical parameters of the interacting fragment are calculated relative to that point [2]. The other approach use the center of the ring as the reference point [3]. The former approach is essentially based on observation that hydrogen atoms are concentrated in certain regions around the phenyl ring, hence they represent areas where interaction exists. The latter approach is based on carbon-center of the ring distances and inverse length-angle correlation of the respective points [4]. However the position of H atom near the center of the ring does not necessarily mean that X-H bond is directed to the center and not for instance to the atom or some other of the ring elements. Having in mind that H bonds have directional properties we wanted to include the angle to any of the assumed acceptors in the analysis of the geometry of the X-H... π fragments. To our knowledge there is no comparison of the two views regarding the point of interaction, using the directionality of the X-H vector, relative to the assumed point acceptor, as parameter. The Cambridge Structural Database was searched to extract all structures satisfying the follow-

ing criteria: intermolecular contacts from H to any of the possible point of interaction in the aromatic ring shorter than 3.05, crystallographic R factor < 0.05, no polymers, no disorder. X-H distances were normalized. The limit for interactions was set at 3.05 based on the sum of the van der Waals radii. The possible point acceptors whose positions has been used for length / angle calculations are: center of the ring, closest point on the mean plane of the ring, closest phenyl carbon, closest point on the C-C bond. Definitions of parameters used in the analysis are given in the Fig. 3. The HCEN and XHCEN are H...center distance and the X-H...center angle, while DMIN and ANGIN are distance and angle assuming the closest point (instead of the center) being the point acceptor. The picture depicts only the center and the closest atom as the assumed acceptors.

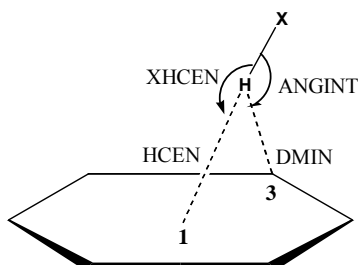


Figure 3. Definition of parameters used in analysis assuming that point acceptor could be center, or the closest atom of the aromatic ring.

Results and Discussion:

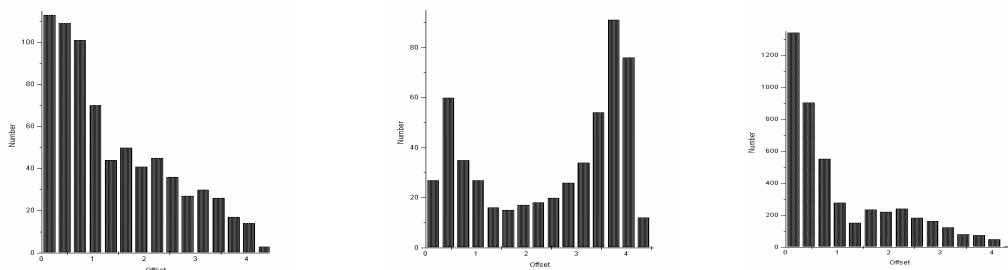


Figure 4. Corrected histograms of offsets r for a) N-H...Ph (1021 fragments), b) O-H...Ph (1326 fragments), c) C-H...Ph (4971 fragments)

Area corrected histograms showing distribution of r values for N-H... π , O-H... π and C-H... π fragments are given in Fig 4. Angles to the assumed point acceptor (XHCEN or ANGIN, Fig. 3) has been set to minimum 110° . Besides the expected concentration of H atom in the region near the center of the ring the significant number of H atoms can be found out of the ring area, at r 1.2-2.5 for N, 3.5-4 for O

and 1.5-2.5 for C. This is particularly obvious for the O-H... π fragments. Such distribution suggests that interactions other than H...center of ring can also influence the distribution of X-H fragments. It is worth to mention here that it was proposed¹³ that ring hydrogen can form C-H...O hydrogen bond. In order to analyze the data presented in the histograms with respect to the directionality of the X-H vector relative to proposed acceptor sites the correlation coefficients between the H-point acceptor distance and X-H...point acceptor angle was calculated. To ensure availability of both assumed point acceptors only data satisfying the following criteria has been used: $h_{cen} \leq 3.05$, $x_{hcn} \geq 110$, $angint \geq 110$. The correlation coefficients are given in Tab. 2.

	R max = 1,2					
	O-H...Ph	N-H...Ph	C-H...Ph	O-H...Ph	N-H...Ph	C-H...Ph
dmin/angint	-0.70	-0.52	-0.45	-0.75	-0.53	-0.46
hcn/xhcn	-0.38	-0.28	-0.33	-0.64	-0.35	-0.37
No. of data	103	259	1195	74	192	1101

The correlation between DMIN / ANGINT is found to be somewhat greater than for HCEN / XHCEN. To check these relations in the region encompassing only the area in the ring we have calculated the correlation coefficients for above set with restrictions that r value is set up to maximum $r=1.2$. The calculated correlations coefficients are given in the last three columns of Tab. 3. These results suggest that on the basis of length/angle correlation the possibility for other elements of the ring to be the point acceptors cannot be excluded, at least if we use only length / angle correlation as criteria for determine the point acceptor in the ring. However it must be noted that the observation that strongest hydrogen bond interaction is associated with the more linear donor-H...acceptor angle has been studied using the "classical" examples with the one-atom acceptor. It remain us with the question how appropriate is to use concept of directionality of the hydrogen bonds with the multiatom acceptor.

References

- [1] T. Takagi, A. Tanaka, S. Matsuo, H. Maozaki, M. Tani, H. Fujiwara, Y. Sasaki, J. Chem. Soc. Perkin Trans., 1987, 1015.
- [2] Y. Umezawa, S. Tsuboyama, H. Takahashi, J. Uzawa, M. Nishio, Bioorg. Med. Chem., 1999, 7, 2021.
- [3] D. Braga, F. Grepioni and E. Tedesco, Organometallics, 1998, 17, 2669.
- [4] G. R. Desiraju and T. Steiner, The Weak Hydrogen Bond in Structural Chemistry and Biology, Oxford University Press, 1999.

ORIENTATION OF AXIALLY COORDINATED PYRIDINES IN CRYSTAL STRUCTURES OF PORPHYRINATO COMPLEXES

A. A. Rakić^a, V. B. Medaković^b and Đ. Cvijović^a,

^a Faculty of Physical Chemistry, University of Belgrade, Studentski trg 12-16,

P.O. Box 137, 11001 Belgrade, Serbia and Montenegro

^b Department of Chemistry, University of Belgrade, Studentski trg 16,

P.O. Box 158, 11001 Belgrade, Serbia and Montenegro

Abstract

In order to investigate the influence of bulky substituents from porphyrin ring on the orientation of axially coordinated ligands Cambridge Structural Database (CSD) was screened. It was found that mutual orientation of axially coordinated pyridines depends on the substituents on porphyrin ring, but it doesn't depend on substituents. All found crystal structures with mesityl groups contain Fe ion. In complexes with Fe(III), axially coordinated pyridines are mutually orthogonal and porphyrin ring is ruffled. Porphyrinato complexes with Fe(III) ion contains mutually parallel pyridines and porphyrinato ring is planar. Since there are different orientations in complexes with Fe(III) and Fe(II) it could be assumed that in these complexes mutual orientations of pyridines are not only consequence of steric interactions of mesityl groups.

Introduction

Heme-proteins have many different biological functions and there are very important and interesting questions about the role of the protein in modulating the properties of the iron-porphyrin cofactor.

In heme-proteins, there is the protein environment, which can have an influence on the orientation of the axial ligands. The major factors determining conformations of imidazole axially coordinated to heme in heme-proteins have been found by analyzing crystal structures of heme-proteins [1]. It was shown that there are two main factors that determine the orientations of imidazole ligated to heme. These are the interactions of imidazole with the propionic acid side chains of heme and with the histidine backbone. Generally the NH-group of imidazole is oriented towards the propionic groups of the heme.

Quantum chemical calculations on porphyrinato complexes of iron with axially coordinated imidazoles and pyridines show that there is difference in behavior of these two complexes [2,3]. Axially coordinated ligands (imidazol or pyridine) can be in mutually parallel or orthogonal orientation. Iron(III) complex with mutual orthogonal orientation of pyridines has more ruffled porphyrin ring than complex with imidazoles. Also, for complex with pyridines orthogonal orientation of pyridines is by 16 kcal/mol more stable than parallel orientation [3], while in complex with imidazoles there is no difference in stability for orthogonal and parallel orientation [2]. The as-

sumption was made that these differences are consequence of steric interactions of α -hydrogen atoms of pyridine with chelate ring from equatorial porphyrin.

In the model systems there are bulky substituents on porphyrin ring, which can have influence on orientations of axially coordinated imidazoles. In order to investigate the influence of bulky substituents from porphyrin ring on orientation of axially coordinated ligands Cambridge Structural Database (CSD) was screened.

Results and Discussion

Crystal structures of all metal-porphyrinato complexes with two axially coordinated pyridines were obtained from metalloporphyrines in the CSD. Screening the CSD provided fifty structures containing Fe (twenty structures), Ca, Mo, Mg, Ru, Ni, Ti, Zn, Co, Cu, Os.

There is large number of crystal structures containing mesityl and ethyl groups as substituents of porphyrin ring, and these structures were studied in more detail. We noticed that the bulky substituents on porphyrin ring have influence on mutual orientation of axially coordinated pyridines. At the same time, in this structures, the mutual orientation of pyridines does not depend on substituents on pyridine.

In the case when eight ethyl groups are bonded to the porphyrin, all the structures have parallel mutual orientations of axially coordinated pyridines, and the pyridines are situated between M-N_{eq} bonds. It could be assumed that some kind of steric interactions are responsible for this orientations. In these structures porphyrin ring is planar. In Figure 1 the geometry of the crystal structure with eight ethyl side chains is shown.

In case of the crystal structures with mesityl rings as substituents on porphyrin, we found only complexes with Fe. There are different orientations of coordinated pyridines in Fe(III) and Fe(II) complexes. In complexes with Fe(III) pyridines are nearly orthogonal and porphyrin ring is not planar. We found the crystal structures with two different types of distortion. In case where pyridines are situated between M-N_{eq} bonds porphyrin ring is in ruffled conformation. The saddled conformations are found in the structures with normal pyridines situated along M-N_{eq} bonds.

In the three structures with Fe(II) ion pyridines are parallel and porphyrin ring is planar. Since there are different orientations in complexes with Fe(III) and Fe(II) it could be assumed that in these complexes mutual orientations of pyridines are not only consequence of steric interactions of mesityl groups.

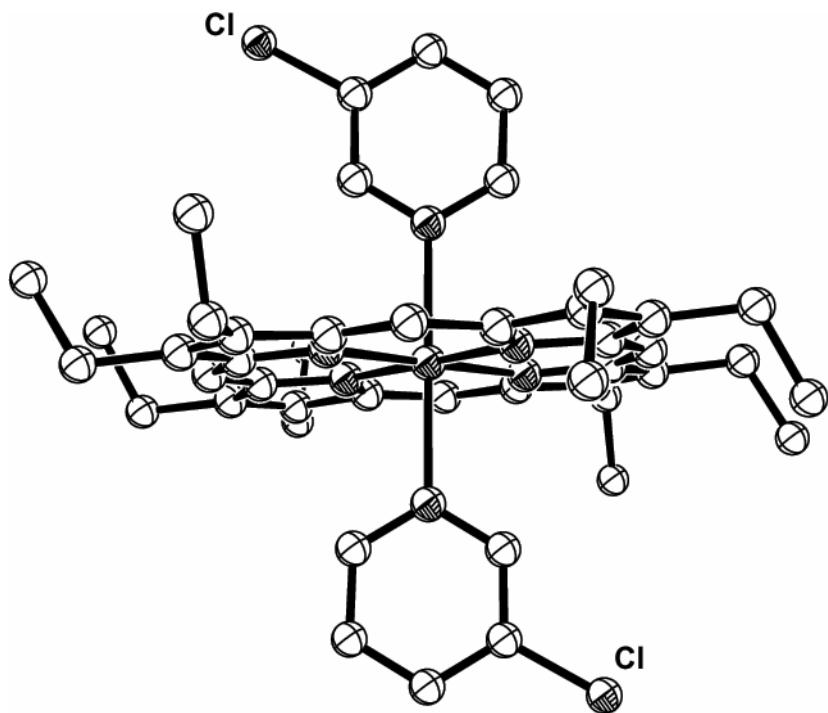


Fig. 1. ORTEP diagrams showing the arrangement of the ethyl groups and the axial ligands in the crystal structure of CPOEFE.

Conclusion

In order to investigate the influence of bulky substituents from porphyrin ring on orientation of axially coordinated ligands Cambridge Structural Database (CSD) was screened. The substituents on porphyrin ring have influence on mutual orientation of axially coordinated pyridines, however, this orientation does not depend on substituents on pyridine. In case of the crystal structures with mesityl rings as substituents on porphyrin, we found only complexes with Fe. In complexes with Fe(III) pyridines are nearly orthogonal and porphyrin ring is not planar. We found the crystal structures with two different types of distortion. In the three structures with Fe(II) ion pyridines are parallel and porphyrin ring is planar. Since there are different orientations in complexes with Fe(III) and Fe(II) it could be assumed that in these complexes mutual orientations of pyridines are not only consequence of steric interactions of mesityl groups.

References

- [1] S. D. Zarić, D. M. Popović, E. W. Knapp, *Biochemistry*, 2001, 40, 7914.
- [2] V. B. Medaković, S. D. Zarić, *Inorg. Chem. Acta*, 2003, 349, 1.
- [3] A. Ghosh, D. F. Bocian, *J. Phys. Chem.*, 1996, 100, 6363.

COPPER(II) COMPLEXES OF REDUCED LOW-MOLECULAR DEXTRAN: AN ESR STUDY

G. M. Nikolić¹, Lj. Ilić², M. Cakić³, G. S. Nikolić³, R.S. Nikolić⁴ and Ž. Mitić¹

¹*Faculty of Medicine, Bulevar dr Zorana Djindjića 81, 18000 Niš,*

²*Pharmaceutical and Chemical Industry "Zdravlje-Pharmaco", Vljakova 199, 16000 Leskovac,*

³*Faculty of Technology, Bulevar Oslobođenja 124, 16000 Leskovac,*

⁴*Faculty of Sciences and Mathematics, Višegradska 33, 18000 Niš, Serbia and Montenegro*

Abstract

Stable complexes of Cu(II) with reduced low molecular dextran (average molar mass 5000 g mol⁻¹) were synthesized. Depending on the synthesis conditions (pH, time, temperature) the Cu content of complexes varied from 7 to 19% as determined by the AAS method. Room temperature ESR spectra of powder samples were recorded at X-band. Analysis of ESR spectral parameters (A_{II} , g_{II} , g_{\perp}) revealed that Cu(II) ions in our complexes had tetragonal coordination with oxygen ligands. Appearance of ESR spectra and spectral parameters of complexes synthesized at pH 10 and 12 were very similar to the ESR spectra of Cu(II) complexes with cellulose and carboxymethyl-dextran obtained at high pH values.

Introduction

Metal complexes of various oligo- and polysaccharides are the subject of intensive research mainly because of its possible application in human and veterinary medicine [1]. Copper(II) complexes are of special importance since they could be used for the treatment of sideropenic anemia. In this paper we present the results of electron spin resonance (ESR) study of copper(II) complexes with reduced low-molecular dextran (RLMD).

Experimental

Low-molecular dextran (LMD, $M_w = 5000$ g mol⁻¹) was obtained from "Zdravlje-Pharmaco" pharmaceutical company (Leskovac, Serbia). All the others chemicals (CuCl₂·2H₂O, HCl, NaOH) were of reagent grade and were used as received.

The reduction of dextran was performed with NaBH₄ (p.a. Merck, Darmstadt, Germany) with subsequent purification on ion-exchange columns filled with Amberlite IR-120 and Amberlite IRA-410 resins. The reduced group content in the final product was measured by the Somogyi method [2] and found to be below 0.1 %.

The synthesis of the complexes was performed at the pH values ranging from 7.0 to 12.0 by boiling the reactant solution containing reduced low-molecular dextran and CuCl₂. Green solution of the complex was filtrated and complex precipitated by the addition of 96% ethanol. Unbounded ions were removed by dialysis.

Copper(II) content of the complexes was measured by the atomic absorption spectrometry (AAS) on the Philips Pye Unicam SP9 spectrometer.

For the ESR measurements an X-band Bruker ESP 300 spectrometer was employed. ESR spectra of powder samples in quartz tubes (3 mm i.d.) were recorded at room temperature.

Results and Discussion

ESR spectrum of complex containing 6.97 % of copper synthesized at pH 12.0 is shown in figure 1.

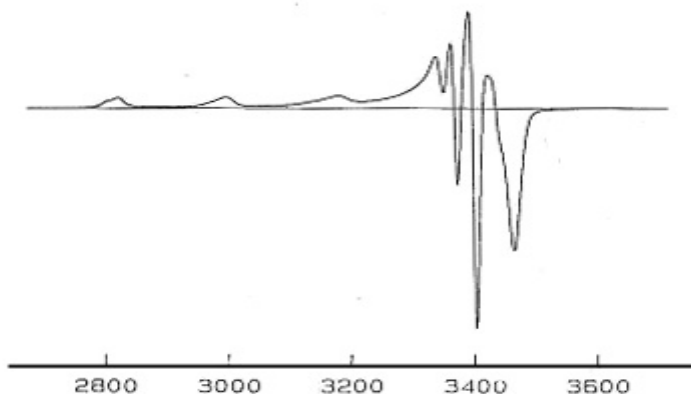


Figure 1. ESR spectrum of copper(II) complex with RLMD at pH=12, %Cu = 6.97.

ESR parameters of spectrum in figure 1 ($A_{||} = 187 \times 10^{-4} \text{ cm}^{-1}$, $g_{||} = 2.23$ and $g_{\perp} = 2.03$) were close to the values for the frozen Cu(II)-ethylene glycol complex thus indicating the square-planar coordination of Cu(II) ion with four oxygen atoms [3]. Appearance and ESR parameters for the spectra of complexes obtained at pH 10 and 12 were very similar to the ESR spectra of some Cu(II) ion complexes with cellulose and carboxymethyldextran obtained at high pH values [4,5]. Although the Cu(II) content of complexes synthesized at lower pH values was much higher (up to 18.95% for the complex synthesized at pH 7.5) ESR signal of these complexes was lacking due to the strong spin-spin interactions of neighboring Cu(II) ions [6].

Acknowledgement

This study was supported by the Ministry of Science, Technologies and Development of the Republic of Serbia, for the scientific research under the Project *MHT.02.11.0029B*.

References

- [1] B. Gyuresik, L. Nagy, *Coord. Chem. Rev.*, 2000, 203, 81.
- [2] M. Somogyi, *J. Biol. Chem.*, 1945, 160, 61.
- [3] Y-Y. H. Chao, D. R. Kearns, *J. Phys. Chem.*, 1977, 81, 866.
- [4] S. I. Ajiboye and D. R. Brown, *J. Chem. Soc. Faraday Trans.*, 1990, 86, 65.
- [5] A. Bartkowiak, J. Jezierska, T. Spsychaj, *Polym. Bull.*, 1998, 41, 199.
- [6] Ž. Mitić, G. Nikolić, M. Cakić, Lj. Ilić, XVII Ulusal Kimya Kongresi, Istanbul, 2003, 206.

INFLUENCE OF MAGNETIC FIELD ON THE REDUCTION OF 4,8-DIAZA-3,6,6,9-TETRAMETHYL UNDECANE-3,8-DIENE- 2,10-DIONE DIOXIME

N. Nikolić¹, D. Veselinović² and J. Vučina¹

¹ Vinča Institute of Nuclear Sciences, Laboratory for Radioisotopes, Belgrade, P.O. Box 522,

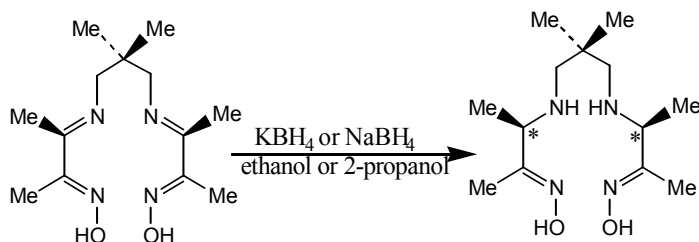
² Faculty of Physical Chemistry, University of Belgrade, P.O. Box 137, Serbia and Montenegro

Abstract

The influence of the magnetic field with the magnetic induction up to 1,35T on the reduction of 4,8-diaza-3,6,6,9-tetramethylundecane-3,8-diene-2,10-dione dioxime (DI) in anhydrous protic solvents (anhydrous ethanol and 2-propanol) was defined. As the reductants NaBH₄ and KBH₄ were used.

Introduction

It is well known that magnetic fields affect water solutions and biological systems, as well as that the magnetic treated water influences the processes in it. However, there are no data on the influence of magnetic fields on chemical reactions, especially those in non-aqueous solutions. The reduction of the two imines groups in DI with NaBH₄ (or KBH₄) in protic solvent (anhydrous ethanol or 2-propanol) provides 4,8-diaza-3,6,6,9-tetramethylundecane-2,10-dione dioxime (HM-PAO) as an equal mixture of the *meso*- and *d,l*-diastereoisomers. In our previous work CLEC (Chiral Ligand Exchange Chromatography) method for resolution of the isomers of HM-PAO is described [1]. So, the reaction of reduction can be followed via the quantities of the starting substance and final products.



Results and Discussion

Instrumentation: The analyses were carried out on the Hewlett-Packard HPLC system Model HP 1050 with HP 1100 UV-Visible variable wavelength detector. The separations were performed on the analytical column LiChroCart Superspher 100-RP-18 (125mm x 4mm ID), particle size 5µm (Merck). The magnetic fields were produced by the electromagnets on the Faculty of Physical Chemistry [2] and in the Vinča Institute, providing the magnetic induction up to 1.5 and 1.4 T, respectively.

Chemicals: The substance 4,8-diaza-3,6,6,9-tetramethylundecane-3,8-diene-2,10-dione dioxime was synthesized and characterized according to the method of Canning and Nowotnik [3]. The chiral selector *N,N*-dimethyl-*l*-phenylalanine (*l*-DM-PhA) 99% (Aldrich) and p.a. grade chemicals (Merck) were used.

Procedure: The mobile phase contained 0.7 mM Cu(II) and 2.8 mM *l*-DM-PhA in pH range 4.1–4.2 (adjusted by acetic acid) and up to 0.8 mM triethylamine. The presaturation procedure for an analytical column (RP-18) and the mobile phase preparation were reported previously [1]. The injection volume was 5 μ l, UV detector was set at 225 nm, the flow rate of the eluent was 0.5 ml min⁻¹ and the column temperature was 30°C. Aliquots (50 μ l) of the reaction mixtures were diluted with 1 ml of the mobile phase and analyzed. The experiments were performed at room temperature. The reaction mixtures were exposed to the magnetic fields (1-24 h) and analyzed on the same day. The elution order of DI and HM-PAO isomers was previously determined [1]. The reduction reactions were followed **with (Analyze)** and **without (Blank)** magnetic field.

Results: The reduction of 0.0227g DI with 0.0035g NaBH₄ (❶) is presented on the Figs 1 and 2, while the reduction of 0.0227g DI with 0.0045g KBH₄ (❷) is presented on the Figs 3 and 4, both in 2ml of anhydrous ethanol. The samples for reduction ❶ and ❷ were taken after 30 minutes and 3.5 hours, respectively.

Elution order of DI and HM-PAO isomers was previously determined [1], so the peak (1) with retention time $t_r=15.4$ min belongs to *l*-isomer, the peak (2) with retention time $t_r=16.8$ min belongs to *meso*-isomer, the peak (3) with retention time $t_r=20.8$ min belongs to the starting DI and the peak (4) with retention time $t_r=26.5$ min belongs to *d*-isomer of HM-PAO.

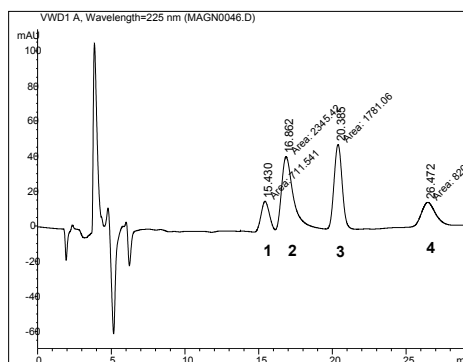


Figure 1. The reduction ❶ (Analyze)

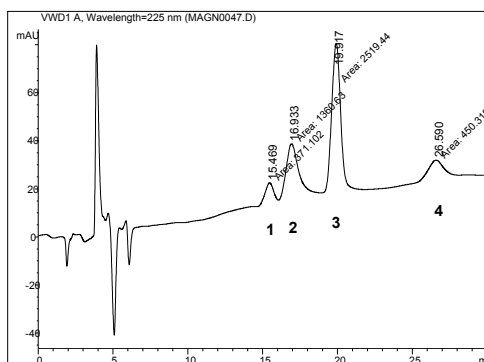


Figure 2. The reduction ❶ (Blank)

The samples of the reductions ❶ and ❷ were exposed to the magnetic fields with magnetic induction of the 1.35 T.

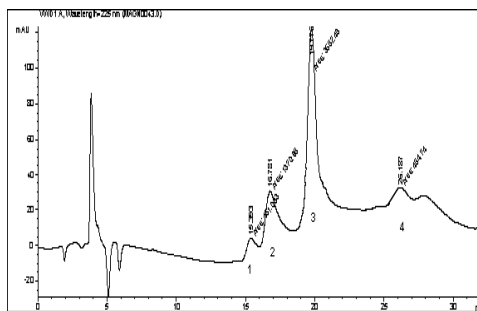
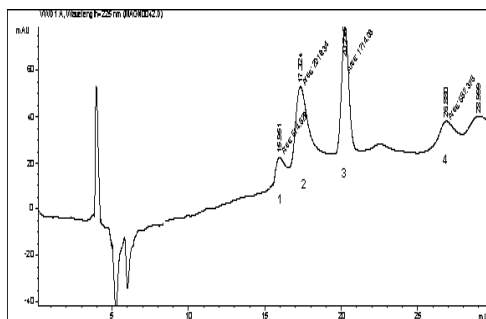


Figure 3. The reduction **②** (**Analyze**) **Figure 4.** The reduction **②** (**Blank**)

As it can be seen in the chromatograms in the reduction **①** the content of the starting DI (peak 3) is much lower in the **Analyze** than in the **Blank** samples, while the content of the final product, HM-PAO isomers, is higher. This indicates that the reduction in the magnetic field is faster. Similar effect is obtained in the reduction **②**, but after a longer period of time. So, it can be concluded that the reduction **①** is significantly faster than the reduction **②**. In the samples taken after 3.5 h, the content of *meso*-isomer of HM-PAO in the **Analyze** samples is higher (for 3.2-3.5 %, mean value of three experiments), which indicates also the effect of the magnetic field at HM-PAO isomers content. It should be mentioned that the effect of the magnetic field disappeared if the samples were left in the mobile phase for more than 24 h. The contents of the HM-PAO in the **Analyze** and the **Blank** samples are the same.

Conclusion

The influence of the magnetic field is observed in the both investigated reduction reactions. The reduction reactions in the magnetic fields are found to be faster. There some indications that the magnetic field influences also the content of the HM-PAO isomers in the reaction mixture. According to the present experience, the effect of the magnetic field on chemical reactions in non-aqueous environment, could be explained by its influence on the molecules of the substance and solvent, especially if the solvent is included in the reaction process. Further investigations are in progress.

References

- [1] N. Nikolić, D. Veselinović, J. Vučina, H. Lingeman, K. Karljiković-Rajić, J. Pharm. Biomed. Anal., 2003, 32, 1159.
- [2] D. Veselinović, D. Ilić, M. Vukić, Book of Abstracts of the Third Yugoslav Simposium "Chemistry and Environment", Vrnjačka Banja 1998, p. 339.
- [3] R. Neirinckx, L. Canning, I. Piper, D. Nowotnik, R. Pickett, R. Holmes, W. Volkert, A. Foster, P. Weisner, J. Marriott, S. Chaplin, J. Nucl. Med., 1987, 28, 191.

THE SUPRAMOLECULAR ARRANGEMENT IN THE Ni(II) COMPLEXES OF ISOTHIOSEMICARBAZIDE

S. B. Novaković^a, G. A. Bogdanović^a, V. M. Leovac^c

^a *VINČA Institute of Nuclear Sciences, Laboratory of Theoretical Physics and Condensed Matter Physics, PO Box 522, 11001 Belgrade, Serbia and Montenegro*

^b *Department of Chemistry, Faculty of Sciences, University of Novi Sad, Trg Dositeja Obradovića 3, 21000 Novi Sad, Serbia and Montenegro*

Abstract

The molecules of two complexes $[\text{Ni}(\text{ITSC})_2(\text{H}_2\text{O})_2](\text{tere}) \cdot 2\text{H}_2\text{O}$ and $[\text{Ni}(\text{ITSC})_2(\text{NO}_3)_2]$ (ITSC = S-methylisothiosemicarbazide; tere = terephthalate) tend to associate through the hydrogen bonding interactions into the characteristic 2D blocks separated by the S-methyl moieties. The different coordination mode of the isothiosemicarbazide comparing to thiosemicarbazide (TSC) prevents the formation of the complementary hydrogen bonds with dicarboxylate important for self-assembly of TSC complexes, however in these ITSC the terephthalate anion has role in connection of the blocks and transformation of the 2D into the 3D supramolecular structure. The similar crystal arrangement is found in two earlier reported complexes of Ni(II) with ITSC.

Introduction

Thiosemicarbazide-based ligands and their metal complexes have attracted much attention mainly because of their wide-ranging biological activities, however some of the recent investigations in the field of supramolecular chemistry have been shown that bis(thiosemicarbazide) metal complexes should be also considered as potential building blocks for supramolecular structures [1-4]. In this kind of structures beside thiosemicarbazide (TSC) complex cation some dicarboxylate is present as a counter ion. Since TSC, $\text{N}^1\text{H}_2\text{-N}^2\text{H-C}^3(\text{S})\text{-N}^4\text{H}_2$, behaves as a bidentate ligand coordinated through terminal N^1 and S atoms its remaining N atoms, hydrazine N^2 and thioamide N^4 , form the hydrogen bonding donor pair, suitably oriented for interaction with hydrogen bonding acceptor pair i.e. oxygen atoms of dicarboxylate anion. This complementary hydrogen bonding could be considered as a starting interaction in the processes of self-assembly of bis(TSC) metal complexes with dicarboxylate. In contrast to TSC, S-methylisothiosemicarbazide, $\text{N}^1\text{H}_2\text{-N}^2\text{H-C}^3(\text{S-CH}_3)\text{-N}^4\text{H}_2$, (ITSC) coordinates through terminal N atoms, i.e. it involves N^4 instead of alkylated S atom [5]. This different coordination mode separates the N atoms and excludes the formation of complementary hydrogen bonds with dicarboxylates. Despite to this fact, we found that bis(ITSC) nickel complex with terephthalate exhibit interesting structural features which also deserve investigation from the aspects of supramolecular chemistry. In this work we analyze the supramolecular arrangement of two ITSC complexes, the octahedral $[\text{Ni}(\text{ITSC})_2(\text{NO}_3)_2]$ (**1**) and the product of its reaction with sodium terephthalate, the octahedral $[\text{Ni}(\text{ITSC})_2(\text{H}_2\text{O})_2](\text{tere}) \cdot 2\text{H}_2\text{O}$ (**2**). The crystal structures of these com-

plexes were determined by X-ray analysis. In addition the Cambridge Structural Database (CSD) was searched for other Ni(II) complexes containing this ligand and their structural arrangements compared with those found in complexes **1** and **2**.

Results and Discussion

In the crystal packing of **1** each molecule forms twelve intermolecular hydrogen bonds with four neighboring molecules. Heaving in mind the size of the molecule this is a considerable number of hydrogen interactions. The important fact is that the equatorial part of the molecule contains eight available hydrogen atoms bonded to the nitrogen atoms, while negatively charged axial ligand, poses three oxygen atoms and acts as a strong proton acceptor. The axial ligand of each molecule serves as an acceptor for two hydrogen donors, the hydrazine (N^1) and the thioamide (N^4) atoms, from its neighbor placed in the position: $x+1, y, z$. In this manner the molecules of complex are connected into the chain extended along the a axis. The additional hydrogen interaction between nitrate group and remaining, N^2 -H donor connects these chains into the compact 2D block (A region) in which S-methyl groups of all molecules take the orientation toward the bordering surfaces of the block (Figure 1. (left)). There are no further hydrogen interactions between these molecule aggregates. Since the region with S-methyl groups (B region) represents the weak connection between the blocks, in the case of $[Ni(ITSC)_2(NO_3)_2]$ we can only speak about 2D supramolecular structure. It is interesting to note that the earlier reported octahedral complex $[Ni(ITSC)_2(NO_2)_2]$ [6] shows similar structural behavior. Namely, the molecules of this complex are also organized into the 2D blocks separated by their S-methyl moieties.

In the crystal packing of **2**, each molecule forms six intermolecular hydrogen interactions. The replacement of the axial nitrate ligand with the molecule of water decrease the number of the hydrogen bonding acceptors, however introduction of the crystal water molecules partly compensate this lack and the molecules are again aggregated into the 2D blocks (A) separated by their S-methyl moieties (B). The important structural difference comparing to above described complex is the incorporation of the terephthalate anion in the B region. The symmetrically disposed COO^- groups of anion bind to the neighboring A blocks through two strong hydrogen bonds transforming the 2D structure of $[Ni(ITSC)_2(H_2O)_2](tere) \cdot 2H_2O$ into 3D supramolecular structure (Figure 1. (right)). The similar structural behavior we also found in the earlier reported square-planar $[Ni(ITSC)_2]Br_2$. In this case the molecules within the block A are mutually interconnected by hydrogen bonds with Br anions. The rest of the Br anions are located in the crystallographically different positions within a B block and form the hydrogen bonds with the complex molecules of the neighboring A blocks.

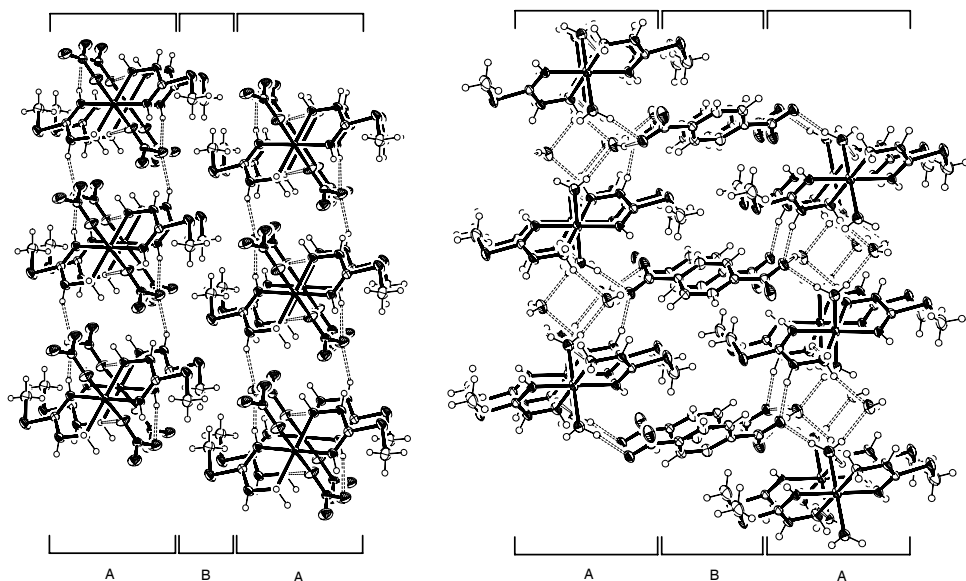


Figure 1. Formation of 2D supramolecular blocks (A region) separated by S-methyl groups (B region) in the crystal packing of complexes **1** (left) and **2** (right).

Conclusion

The Ni(II) complexes of ITSC show an interesting structural arrangement. Their extensive hydrogen interactions aggregate the molecules into the characteristic 2D supramolecular blocks which are separated by S-methyl groups. The dicarboxylate anions introduced to the structure take the place between the S-methyl moieties and bind the neighboring blocks transforming the 2D into the 3D supramolecular structure. The similar behavior in the structural arrangement we also found in two additional, earlier published crystal structures.

References

- [1] J.E.V. Babb, A.D. Burrows, R.W. Harrington, M.F. Mahon, *Polyhedron*, 2003, 22, 673.
- [2] A.D. Burrows, R.W. Harrington, M.F. Mahon, S.J. Teat, *Cryst. Eng. Comm.*, 2002, 22, 539.
- [3] A.D. Burrows, S. Menzer, D.M.P. Mingos, A.J.P. White, D.J. Williams, *J. Chem. Soc., Dalton Trans.*, 1997, 4237.
- [4] A.D. Burrows, R.W. Harrington, M.F. Mahon, *Eur. J. Inorg. Chem.*, 2003, 766-
- [5] G.A. Bogdanović, V.M. Leovac, S.B. Novaković, V.I. Češljević, A. Spasojević-de Bire, *Acta Cryst.*, 2001, C57, 1138.
- [6] P.N. Bouroush, M.D. Revenko, Yu.A. Simonov, N.V. Gerbeleu, A.A. Dvorkin, T.I. Malinovskii, *Dokl. Akad. Nauk SSSR*, 1987, 293, 119.
- [7] D.Z. Obadović, V. Divjaković, V.M. Leovac, *Polyhedron*, 1997, 16, 695.

ACTIVITY OF SOME PLATINUM(II/IV) COMPLEXES WITH EDDA-TYPE LIGANDS AGAINST HeLa CELL LINE

G. N. Kaluderović^a, V. M. Đinović^a, Z. Juranić^b, T. Stanojković^b and T. J. Sabo^a

^aFaculty of Chemistry, University of Belgrade, P.O. Box 158, 11001 Belgrade,

^bInstitute of Oncology and Radiology, 11000 Belgrade, Serbia & Montenegro

Abstract

This paper reports syntheses and characterization of dichloro(ethylenediamine-*N,N'*-di-3-propanoic acid)platinum(II) and iodo(ethylenediamine-*N,N'*-di-3-propanoic acid)platinum(II) complexes, with the formulae [Pt(H₂eddp)Cl₂] and [Pt(Heddp)I], respectively. The complexes have characterized by elemental analysis and infrared spectroscopy. In the aim to assess the selectivity in the antitumor action of these complexes, as well, as *trans*-dichloro(ethylenediamine-*N,N'*-di-3-propanoato)platinum(IV), *trans*-dibromo-(ethylenediamine-*N,N'*-di-3-propanoato)platinum(IV), *trans*-dichloro(propylenediamine-*N,N'*-diacetato)platinum(IV) and *trans*-dibromo(propylenediamine-*N,N'*-diacetato)platinum(IV), the antiproliferative action of these compounds have determined to human adenocarcinoma HeLa cells.

Introduction

The thousands of platinum complexes have been synthesized not only in order to investigate their physico-chemical properties but, also, to identify novel platinum compounds with improved properties in comparison to the parent drug cisplatin [1-2]. Platinum(IV) complexes are more inert than platinum(II) and this property may allow for oral administration [3]. Cytotoxicity of platinum(IV) complexes with ethylenediamine-*N,N'*-di-3-propanoato (eddp) and chloro or bromo ligands, *trans*-[Pt(eddp)Cl₂] [4] and *trans*-[Pt(eddp)Br₂], are recently investigated [5]. These two complexes showed low activity against the A2780 and A2780cisR cells. Several new complexes have been synthesized and tested against two tumor model systems, with the hope of discovering new drugs.

The present work struggles with platinum complexes varying in the chelating aminocarboxylato and diamine backbone, halogeno ligands and oxidation states. These complexes have been designed, synthesized and further investigated to establish how the size of the aminocarboxylato and diamine rings and oxidation state affect in vitro antiproliferative activity against human adenocarcinoma HeLa cells.

Experimental

Materials and measurements

Potassium tetrachloroplatinate(II), potassium iodide were obtained by Merck and used without further purification. Infrared spectra were recorded on a Perkin-Elmer FTIR 31725-X spectrophotometer using the KBr pellet technique. Elemental analyses for C, H, and N were done on a Vario III CHNOS Elemental Analyzer, Ele-

mental Analysensysteme GmbH. The complexes *trans*-[Pt(eddp)Cl₂] (3), *trans*-[Pt(eddp)Br₂] (4), *trans*-[Pt(pdda)Cl₂] (5) and *trans*-[Pt(eddp)Br₂] (6) were prepared according to the previous methods [4-7].

Preparation of [Pt(H₂eddp)Cl₂](1)

K₂[PtCl₄] (0.200g; 0.482mmol) was dissolved in (10.00 ml) water at 90°C. The H₂eddp·2HCl (0.133g; 0.482mmol) was then added. This solution has stirred for 4h, in which period LiOH (9.02 ml; 0.107M; 0.964mmol) have added. The solution was then filtered and evaporated on a steam bath to small volume. After few days yellow power was obtained, filtered off and air dried. Yield: 0.153g (67.80%). Elemental analysis: Calc.: C, 20.43; H, 3.43; N, 5.96. Found: C, 20.47; H, 3.67; N, 5.80%.

Preparation of [Pt(Heddp)I](2)

K₂[PtCl₄] (0.200g; 0.482mmol) was dissolved in (10.00 ml) water at room temperature. The KI (0.320g; 1.928mmol) was then added. This solution has stirred for 10 minutes. After that period H₂eddp·2HCl (0.133g; 0.482mmol) was added and stirred for 2h, in which period LiOH (2.49 ml; 0.107M; 0.266mmol) have added in small portions. The solution was then filtered and evaporated on a steam bath to small volume. After few days dark power was obtained, filtered off and air dried. Yield: 0.110g (43.47%). Elemental analysis: Calc.: C, 18.26; H, 2.87; N, 5.32. Found: C, 18.46; H, 3.16; N, 5.32.

Results and Discussion

Synthesis and chemical characterization

The platinum(II) with eddp, chloro and iodo ligands, from this paper, represents examples of two unusual coordination of this potential tetradentate linear flexible ligand. Namely, in the case of [Pt(H₂eddp)Cl₂] eddp is coordinated as bidentate ligand and in the case of [Pt(Heddp)I] as tridentate.

In the IR spectra of the [Pt(H₂eddp)Cl₂] complex the characteristic COOH asymmetric stretching bands were found at 1702 and 1721 cm⁻¹. This is in a good agreement with COOH asymmetric stretching bands of the free ligand [8]. While, in the [Pt(Heddp)I] complex one band is found at 1722, like free ligand, and the other at 1644 cm⁻¹, which is characteristic for coordinated COO group [9]. The COO symmetric stretching bands appears at 1377 and 1375 cm⁻¹ for [Pt(H₂eddp)Cl₂] and [Pt(Heddp)I] complexes, respectively.

In vitro cytotoxicities

The values for IC₅₀ (μM) for the 72h of action of investigated compounds on HeLa cells determined by MTT test are presented in Table 1.

Table 1.

Complex	(1)	(2)	(3)	(4)	(5)	(6)
IC ₅₀ (μM)±SD	165,05±6,35	194,00±3,00	179,50±7,50	143,00±2.95	175*	149*

* n=1

Complex (1) showed higher activity than (2) and (3) because he have two chloro ligands in *cis* position. Substitutions of chloro ligands, from complex (3), with bromo, complex (4), increased cytotoxic activity. The same trend was noticed for compounds (5) and (6), *i. e.*, substitutions of chloro ligands, in complex (5), with bromo ligands in complex (6), increased cytotoxic activity.

Conclusion

The two new complexes of platinum (II) were synthesized and characterized with elemental analysis and infrared spectroscopy. In complex (1) the eddp ligand expressed bidentate coordination, while in complex (2) tridentate coordination which are unusual coordination of announced potentially tetradentate ligand. Cytotoxicity has been determined against Hela cell line. The most active compounds are with bromo ligands in complexes (4) and (6). Therefore all complexes have showed low cytotoxicity.

Acknowledgements

The authors are grateful to the Ministry of Science, Technology and Development of the Republic of Serbia for financial support (Projects #1253 and #1614).

References

- [1] E. Wong, C.M. Giandomenico, *Chem. Rev.*, 1999, 99, 2451.
- [2] G. Natile, M. Coluccia, *Coord. Chem. Rev.*, 2001, 383, 216.
- [3] T.W. Hambley, A.R. Battle, G.B. Decon, E.T. Lawrenz, G.D. Fallon, B.M. Gatehouse, L.K. Webster, S. Rainone, *J. Inorg. Biochem.*, 1999, 77, 3.
- [4] G.N. Kaluderović, G.A. Bogdanović, T.J. Sabo, *J. Coord. Chem.* 2002, 55, 817.
- [5] T.J. Sabo, G.N. Kaluderović, D. Poleti, Lj. Karanović, A. Boccarelli, F. Cannito, G. Natile, *J. Inorg. Biochem.*, 2004, in press.
- [6] V.M. Đinović, G.A. Bogdanović, T.J. Sabo, *J. Coord. Chem.*, 2004, in press.
- [7] G.A. Bogdanović, V.M. Đinović, T.J. Sabo, A. Spasojević-de Biré, IX Conference of the Serbian Crystallographic Society, Belgrade, 2001, pp. 20.
- [8] T.J. Sabo, S.R. Grgurić, S.R. Trifunović, *Synth. React. Inorg. Met.-Org. Chem.*, 2002, 32, 1661.
- [9] G.N. Kaluderović, T.J. Sabo, *Polyhedron*, 2002, 21, 2277.

SYNTHESIS AND CHARACTERIZATION OF TWO NOVEL MIXED LIGAND COMPLEXES WITH N-CARBOBENZYLOXYGLYCINE AND 2,2'-BIPYRIDINE

Z. M. Miodragović¹, B. Krajčinović², S. Anđelić¹, I. Hodžić¹
and Đ. U. Miodragović¹

¹*Faculty of Chemistry, University of Belgrade, Studentski trg 12-16, Belgrade,*

²*Institute of Chemistry, Technology and Metalurgy, Njegoševa 12, Belgrade, Serbia and Montenegro*

Abstract

Two novel mixed ligand complexes containing N-carbobezyloxyglycinate and 2,2'-bipyridine as ligands, and Zn(II) or Cd(II) as central metal ions, are synthesized. The isolated complexes are characterized by means of elemental analysis, IR and ¹H and ¹³C NMR spectroscopy, and their structures are proposed. In the case of both isolated compounds two N-carbobezyloxyglycinate anions are coordinated engaging two O atoms of the carboxylate group in a chelating bidentate or bridging manner. The 2,2'-bipyridine is coordinated as bidentate *via* two N atoms. The investigation of anti-tumor activity of obtained complexes is in progress.

Introduction

Metal complexes are very attractive for drug design, because of possibilities of encoding various thermodynamic, as well as kinetic molecular informations, which than have to be read out and processed at the site of action [1]. The investigation of complexes of metal ions with amino acids or peptide is of interest due to their presence in biological systems, and to the possibility to be used as models of recognition for peptides [2]. The interest for study of N-protected amino acids (in which protecting group is an acetyl, benzyl or carbobezyloxy group) is the fact that they are the simplest systems containing a peptide linkage. Investigation of metal complexes with such ligands could provide the informations about behavior of protein like molecules as ligating groups toward metal ions. In these complexes the N-protected aminocarboxylates are invariably coordinated through the carboxylate group. Because of the week coordination ability of COO⁻ group they must easily react with strong donor molecules like 2,2'-bipyridine (**bipy**) for instance. As a consequence deprotonation of amidic nitrogen followed by coordination geometry change may occur, depending of central metal ion, pH, and the acidity of N-protecting group [3]. The additional ligand **bipy**, accomplishing π back donation causes rearrangement of electron density with lowering the pK_a value of peptide NH [4]. At the other hand, glycine applied directly or used in very large amounts exhibit anticonvulsive activity in some extent [5]. Among a relative large number of N-protected derivatives of glycine, only N-carbobezyloxyglycine (**NCBZ-gly**) and its methyl-ester exhibit remarkable anticonvulsive activity. In spite of that, only two papers describing complexes with **NCBZ-gly** as ligand are reported [6,7]. The scope of this report is the synthesis of two new ternary complexes of Zn(II) or Cd(II) with **NCBZ-gly** and **bipy**.

Results and Discussion

Complexes $[\text{Zn}(\text{NCBZ-gly})_2(\text{bipy})]\text{H}_2\text{O}$ and $[\text{Cd}(\text{NCBZ-gly})_2(\text{bipy})]\text{H}_2\text{O}$ are obtained by the reaction of **bipy** and starting complex $[\text{Zn}(\text{NCBZ-gly})_2]\text{H}_2\text{O}$ or $[\text{Cd}(\text{NCBZ-gly})_2(\text{H}_2\text{O})_2] \cdot 0.5\text{H}_2\text{O}$ in 1:1 molar ratio. Both of the isolated complexes are white, air stable substances, soluble in ethanol, methanol, acetone, acetonitrile, chloroform, dichloromethane, DMSO, and THF, and insoluble in water, ether, toluene, n-butanol and n-hexane. The results of elemental analysis are presented in Table 1, and are in accordance with neutral complexes. The value of λ_M in methanol solution for complex $[\text{Cd}(\text{NCBZ-gly})_2(\text{bipy})]\text{H}_2\text{O}$ ($c=10^{-3} \text{ mol dm}^{-3}$) is $48,1 \Omega^{-1} \text{ cm}^2 \text{ mol}^{-1}$, and also suggests a nonelectrolyte type of complex.

Table 1. The yields and results of elemental analysis of the isolated complexes

Complex		% C	% H	% N	Yield (%)
$[\text{Zn}(\text{NCBZ-gly})_2(\text{bipy})]\text{H}_2\text{O}$ (1)	Calcd. for $\text{ZnC}_{30}\text{H}_{30}\text{O}_9\text{N}_4$	54.93	4.577	8.544	60
	Found	54.63	4.523	8.497	
$[\text{Cd}(\text{NCBZ-gly})_2(\text{bipy})]\text{H}_2\text{O}$ (2)	Calcd. for $\text{CdC}_{30}\text{H}_{30}\text{O}_9\text{N}_4$	51.25	4.271	7.937	78
	Found	51.44	4.130	8.010	

In the IR spectra (KBr technique) of obtained complexes and metal free ligands **NCBZ-gly**, sodium salt of **NCBZ-gly** (**NaNCBZ-gly**) and **bipy** the expected bands are found. The positions of selected characteristic bands are presented in Table 2. On the basis of these data, following could be proposed: a) each carboxylic group participates in coordination engaging both O atoms as ligators in a chelate bidentate or bridging manner; b) in the case of cadmium(II) complex the amide N atom is not included in coordination; in the case of Zn(II) complex, however, this possibility could not be excluded, or this group perhaps takes part in a relative strong H-bond formation. The reliability of these conclusions is diminished to some extent by the fact that many IR bands in $1550\text{-}400 \text{ cm}^{-1}$ range, arising from **bipy** overlap with those of **NCBZ-gly**.

The ^1H and ^{13}C NMR spectra of complex (1), as well as uncoordinated ligands **NCBZ-gly** and **bipy** are recorded. The lack of a signal arising from carboxylic group proton in ^1H spectrum is evidence that carboxylic group is deprotonated and takes part in coordination. That supposition is supported by the fact that in ^{13}C NMR spectrum of complex only signal shifted toward higher δ values in comparison with the spectrum of noncoordinated ligand is that one assigned to carboxylic C atom.

Table 2. The positions of selected IR bands (cm^{-1}) and corresponding $\Delta\nu^*$ values

Compound	$\nu(\text{NH})$	AmideI	$\nu_a(\text{OCO})$	AmideII	$\nu_s(\text{OCO})$	$\nu_a(\text{OCO})$ ester	$\Delta\nu$
Complex (1)	3326 s	1696 s	1603 s	1541 s	1405 m	1252 m	191
Complex (2)	3360 m	1688 s	1596 s	1527 m	1411 m	1250 m	185
NaNCBZ-gly	3344 m	1687 s	1605 s	1528 w	1407 m	1254 m	198

* $\Delta\nu = \nu_a(\text{OCO}) - \nu_s(\text{OCO})$; s = strong, m=medium, w=weak.

Conclusions

Two new ternary complexes of Cd(II) or Zn(II) with **NCBZ-gly** and **bipy** are synthesized and characterized. The composition of the complexes is defined on the basis of results of elemental analysis and molar conductivity measurements. The mode of coordination of **NCBZ-gly** ligand through deprotonated carboxylate group is established on the basis of IR, ^1H and ^{13}C NMR data. The attempts to obtain monocrystals, as well as the study of anticancer activity of isolated complexes are in progress.

Acknowledgements

These investigations are financially supported by the Ministry of Science and Technology of the Republic of Serbia (Projects 1318 and 1354).

References

- [1] X. Liang, J.A. Parkinson, M. Weishaupl, R.O. Gould, S.J. Paisey, H. Park, T.M. Hunter, C.A. Blindauer, S. Parsons and P.J. Sadler, *J. Am. Chem. Soc.*, 2002, 124, 9105.
- [2] M.C. Capllonch, A. Garcia-Raso, A. Terron, M.C. Apella, E. Espinosa and E. Molins, *J. Inorg. Biochem.*, 2001, 85(2-3), 173.
- [3] M. Saladini, D. Iacopino and L. Menabue, *J. Inorg. Biochem.*, 2000, 78(4), 355.
- [4] A. Anagnostopoulos and S. Hadjispyrou, *J. Inorg. Biochem.*, 1995, 57, 279.
- [5] D.M. Lambert, *Bull. Acad. Med. Belg.*, 1995, 150, 294.
- [6] L. Antolini, L. Manabue, G. Pellacani and M. Saladini, *J. Chem. Soc. Dalton Trans.*, 1984, 2325.
- [7] L. Antolini, L. Manabue, G. Pellacani, M. Saladini, M. Sola, L. Battaglia and A. Bonamarti Corradi, *J. Chem. Soc. Dalton Trans.*, 1984, 2319.

THE FIRST COMPLEXES WITH N-CARBOBENZYLOXY-L-PHENYLALANINATO LIGAND

Đ. U. Miodragović, B. Stojadinović, Z. M. Miodragović, I. Hodžić, M. Vitorović
and K. Anđelković

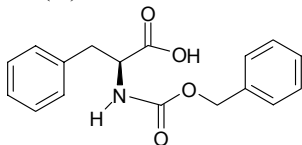
*Faculty of Chemistry, University of Belgrade, P. O. Box 158, 11000 Belgrade,
Serbia and Montenegro*

Abstract

In this paper we have synthesized a first complexes with N-CBZ-L-phe ligand exploring Co(II) and Cd(II)-ions. Complex of Co(II) is octahedral with N-CBZ-L-phe ligand coordinated as bidentate trough carboxylic group. Complex of Cd(II) is tetrahedral with N-CBZ-L-phe ligand coordinated trough amide nitrogen and carboxylic oxygen.

Introduction

Derivates of N-carbobenzyloxy-L-phenylalanine (N-CBZ-L-pheH, Scheme 1) have shown a significant activity *in vitro* [1,2]. Of the N-CBZ-L-phenylalanine derivates, N-carbobenzyloxy-L-phenylalanine cyanomethyl ester was one of the most active agents against Erlich ascites cell proliferation. This derivate was also the most active against carrageenan-induced inflammation [1]. In the literature there are no data concerning of complexes with N-carbobenzyloxy-L-phenylalanine or its derivates. Because of that, in this paper we have synthesized first complexes with N-CBZ-L-phe ligand exploring Co(II) and Cd(II)-ions.



Scheme 1. N-CBZ-L-phenylalanine

Experimental

Synthesis of the diaquabis(N-carbobenzyloxy-L-phenylalaninato) cobalt(II) complex

In 5 cm³ of ethanol-water solution (1:1) was dissolved 0.20 g (0.70 mmol) of N-CBZ-L-PheH and 0.08 g (0.35 mmol) of CoCl₂·6 H₂O. The pH value of the reaction mixture was justified at 6 by means of NaOH solution, and mixture was heated on the water bath to 45 °C and stirred for 1 hour. After that, obtained suspension was filtered out, and the pink crude product dried in the air.

Yield: 12.90 %. Elemental analysis: Calculated: % N 4.05, %C 58.99, % H 5.26%. Found: % N 4.04, % C 58.45, % H 5.07.

Synthesis of the bis(*N*-carbobenzyloxy-*L*-phenylalaninato)cadmium(II) complex

The bis(*N*-carbobenzyloxy-*L*-phenylalaninato)cadmium(II) complex was obtained by procedure described in 2.1., using 0.08 g (0.35 mmol) CdCl₂·2.5 H₂O. Yield: 35.8 %. Elemental analysis: Calculated: % N 3.90, %C 56.82, % H 4.59 %. Found: % N 3.97, % C 56.86, % H 4.79.

Results and Discussion

Diaquabis(*N*-carbobenzyloxy-*L*-phenylalaninato)cobalt(II) complex

Results of the elemental analysis (2.1.) are in agreement with octahedral complex of the [Co(N-CBZ-*L*-phe)₂(H₂O)₂] composition. The complex is characterized also by means of IR and UV/VIS spectroscopy.

On the basis in differences in asymmetric and symmetric carboxylate stretching vibration ($\Delta\nu$, Table 1) in IR spectra of complex ($\Delta\nu = 186 \text{ cm}^{-1}$) and in ligand sodium salt ($\Delta\nu = 191 \text{ cm}^{-1}$) it is concluded that *N*-CBZ-*L*-phe is coordinated to the Co(II) ion as bidentate, through oxygen atoms of carboxylic group. Vibration frequencies of N-H band in complex is at 3401 cm^{-1} , and in ligand sodium salt at 3393 cm^{-1} , respectively, what indicates that amide nitrogen don't take part in coordination.

UV/VIS spectrum of complex obtained exhibit one asymmetric maximum at 560.8 nm, what is agreement with Co^{II}O₆ complex chromophore.

On the basis all aforesaid, it is proposed that complex of Co(II) adopt the geometry presented in Figure 1.

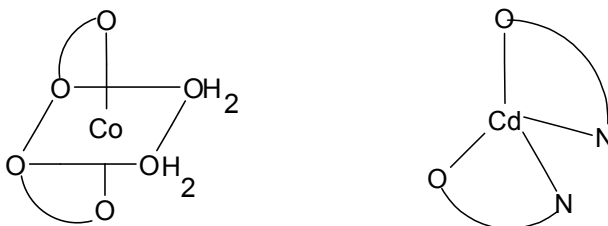


Figure 1. Proposed geometry for the [Co(N-CBZ-*L*-phe)₂(H₂O)₂] complex (left) and [Cd(N-CBZ-*L*-phe)₂] · 0.5 H₂O complex (right).

Table 1. Frequencies of selected stretching vibration in IR spectra of NaN-CBZ-*L*-phe, [Cd(N-CBZ-*L*-phe)₂] (**1**) and [Co(N-CBZ-*L*-phe)₂(H₂O)₂] (**2**) complexes

	ν_{NH}	Amid.I	$\nu_{\text{as}}(\text{OCO})$	Amid.II	$\nu_{\text{s}}(\text{OCO})$	$\nu_{\text{as}}(\text{OCO})$ ester	$\Delta\nu$
NaN-CBZ- <i>L</i> -phe	3393	1685	1596	1531	1405	1248	191
Complex 1	3338	1696	1636	1564	1413	1245	223
Complex 2	3401	1698	1597		1411	1257	186

Bis(N-carbobenzyloxy-L-phenylalaninato)cadmium(II) complex

Results of elemental analysis are in agreement with complex of $[\text{Cd}(\text{N-CBZ-L-phe})_2] \cdot 0.5 \text{H}_2\text{O}$ composition.

The data obtained on the basis of IR spectra (Table 1) pointed out on the possibility of coordination through amide nitrogen. Namely, frequencies of stretching vibration of N-H band are at 3338 cm^{-1} in complex, and at 3393 cm^{-1} in ligand sodium salt, respectively. The differences in frequencies of stretching asymmetric and symmetric vibration of COO^- group in complex ($\Delta\nu = 233 \text{ cm}^{-1}$) and in salt ($\Delta\nu = 191 \text{ cm}^{-1}$) indicate on monodentate type of carboxylic group coordination.

^1H NMR spectrum of complex has shown that both N-CBZ-L-phe ligands have identical environments in DMSO-d_6 solution. The absence of signal of carboxylic proton in ^1H NMR spectrum of Cd(II) complex is in agreement with coordination through carboxylic group.

On the basis all results it is proposed that complex of Cd(II) adopt tetrahedral geometry (Figure 1).

Conclusion

Derivates of N-carbobenzyloxy-L-phenylalanine have shown a significant activity *in vitro* [1,2]. In this paper we have synthesized a complexes of Co(II) and Cd(II) with N-CBZ-L-phe ligand. Complex of Co(II) is octahedral with N-CBZ-L-phe ligand coordinated as bidentate trough carboxylic group. Complex of Cd(II) is tetrahedral with N-CBZ-L-phe ligand coordinated trough amide nitrogen and carboxylic oxygen. The complexes are interesting as simple model systems that contain peptide bond. Investigations of anticancer activity of these complexes are in progress.

References

- [1] Sajadi Z., Almahmood M., Loeffler L. J., Hall I. H., Journal of Medicinal Chemistry, 1979, 22, 1419.
- [2] Kaiser A., Koch W., Scheer M., Woelcke U., Ger. Offen., 1972, 31.

HPLC AND SPECTROPHOTOMETRIC INVESTIGATION OF THE FORMATION OF Sn(II)-p-AMINOHIPPURIC ACID COMPLEX IN PERCHLORATE MEDIUM

D. Janković and D. Đokić

*The Vinča Institute of Nuclear Sciences, Laboratory of Radioisotopes,
PO Box 522, 11001 Belgrade, Serbia and Montenegro*

Abstract

The complex equilibrium in tin(II)-p-aminohippuric acid (PAH) solutions in perchlorate medium was investigated. HPLC, spectrophotometric and pH-metric methods were used. The experimental results have shown that weak mononuclear complex of the general composition PAH/Sn(II)=1/1 was formed.

Introduction

o-Iodohippuric acid labelled with isotope ^{131}I (OIH) has been used in clinical evaluation of renal tubular function. The greatest disadvantage of OIH is relatively high-absorbed radiation dose of ^{131}I to the patient, even at low diagnostic doses. In order to replace it, numerous chelate reagents labelled with technetium-99m ($^{99\text{m}}\text{Tc}$), were developed, but none of these radiopharmaceuticals could completely replace OIH. Therefore, we attempted to label p-aminohippuric acid ($\text{H}_2\text{NC}_6\text{H}_4\text{CONHCH}_2\text{COOH}$, PAH), "gold standard" for renal tubular function diagnostic, with $^{99\text{m}}\text{Tc}$ using Sn(II) chloride method [1]. In this process, Sn(II)-ion reduces technetium from non-reactive, +7 (in $^{99\text{m}}\text{TcO}_4^-$) in lower +3, +4 or +5 oxidation states. However, the possibility of interaction between some ligand and Sn(II)-ion existed too [2-4]. In this paper the possibility for formation of Sn(II)-PAH complexes were studied.

Experimental

All chemicals used in our experiments were of analytical purity grade (p.a. Merck). The stock solution of PAH and was prepared by dissolving of the measured amount of pure acid in doubly distilled water. The stock solution of $\text{SnCl}_2 \cdot 2\text{H}_2\text{O}$ was prepared by dissolving of the measured amount of the pure salt in concentrated HCl and then diluting it with doubly distilled water until the definite volume.

HPLC analysis was performed by isocratic HPLC. All measurements were made on Liquid Chromatograph, Hewlett Packard 1050, S/N with UV and Raytest gamma flow detector RP and C18 column (250x4.6 mm). The different methanol/water mixtures prepared from HPLC grade water, were used like mobile phases. UV spectra of 10 μl PAH (1×10^{-4} mol dm^{-3}) as well as PAH-Sn(II) mixture with different molar ratios: 1/1; 1/10, and 1/25, $\text{pH} \approx 3$, were obtained at wavelength of 220 nm and 295 K.

All spectrophotometric measurements were performed using Uvicon 810/820 (Kontron Instruments, Austria) spectrophotometer. The absorbency of solutions was measured in wavelength range 190 nm to 350 nm, in 10-mm quartz cells. UV spectra of PAH (4×10^{-6} mol dm^{-3} - 2×10^{-4} mol dm^{-3} , $\text{pH} \approx 3$) and Sn(II) (4×10^{-6} mol dm^{-3}) in 0.1 mol dm^{-3} NaClO_4 ionic medium, were recorded using 0.1 mol dm^{-3} NaClO_4 in doubly

distilled water as a reagent blank. UV spectra of the mixtures of PAH and Sn(II) in 0.1 mol dm⁻³ NaClO₄ ionic medium, in concentration ratios: [Sn]/[PAH]=1/1; 1/2; 1/5; 1/10; pH≈3, were recorded too, using corresponding Sn-free solution as a reagent blank.

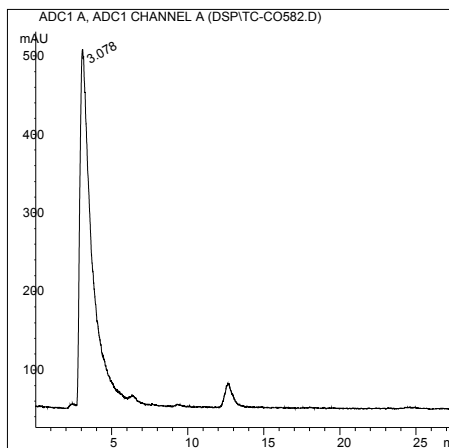


Figure 1a) HPLC chromatograms of PAH obtained with 10 %CH₃OH:90 % H₂O as mobile phase (0.7 ml/min)

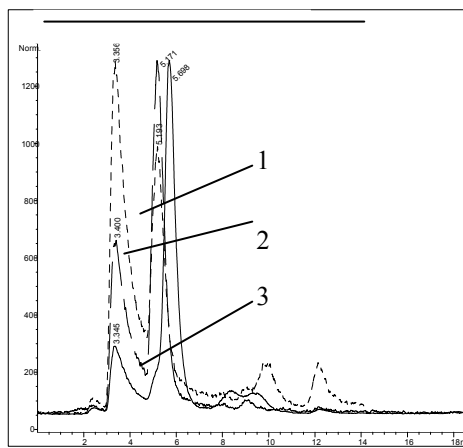


Figure 1b) HPLC chromatograms of PAH/Sn(II) with different molar ratios: 1/1 (1); 1/10 (2), and 1/25 (3)

Results and Discussion

UV spectra of PAH obtained with at 220 nm point to a peak with retention time 3.078 min and some impurity at ~12.7 min. The HPLC chromatograms for PAH/Sn(II) solutions, exhibit two well separated peaks for each chromatogram: peak at 3.345-3.400 min for PAH and peak at 5.171-5.698 min for PAH-Sn(II) complexes. The position and intensity of these peaks vary upon changing the concentration ratio of PAH and Sn(II). The best results were for concentration ratio PAH/Sn(II)=1/1 where peak for Sn(II)-PAH complex was the highest.

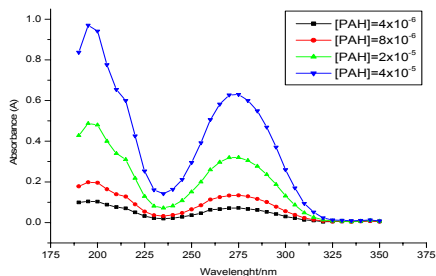


Figure 2. UV spectra of PAH (4×10^{-6} mol dm⁻³- 2×10^{-4} mol dm⁻³) in 0.1 mol dm⁻³ NaClO₄, pH≈3

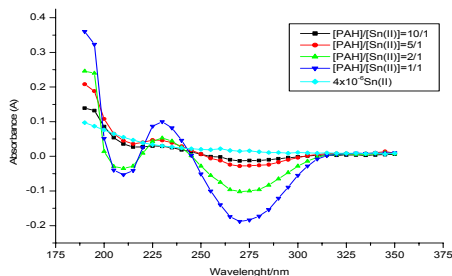


Figure 3. UV spectra of Sn(II)-PAH solutions in 0.1 mol dm⁻³ NaClO₄: [PAH]/[Sn]=10/1; 5/1; 2/1; 1/1

Spectrophotometric measurements were performed with the aim to examine the possibility of complex formation in PAH-Sn(II) solutions and the nature of complexes. UV spectra made on the series of PAH with different concentration, in 0.1 mol dm^{-3} NaClO_4^- ionic medium, have shown two peaks: at 200 nm and 275 nm. UV spectra of Sn(II)-PAH-solutions showed the disappearance of a peak at 275 nm and a new peak at 228 nm. The appearance of a new peak at 228 nm confirmed the complexation between Sn(II)-ion and PAH in investigated conditions. The negative absorbance of the spectra at wavelength 275 nm were consequence of the use of PAH solutions with the same concentration as a reagent blank. The highest absorbance possessed the spectrum of PAH/Sn(II) solution with concentration ratio 1/1.

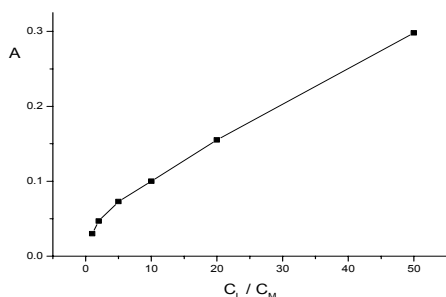


Figure 4. Dependence of absorbency on molar ratio metal and ligand

The UV spectra obtained with different concentrations of PAH and constant concentration of Sn (II) made possible the application of the molar-ratio method. (Fig 4.). From the form of the curve it could be concluded that one weak complex with high degree of dissociation was obtained

The application of Bent-French method at this low stable complex enable the calculation not only the stoichiometric coefficients p and q , but also the stability constant $\beta_{p,q,r}$ of complexes, forming in reaction:



In the case $q=0$, pure [Sn-PAH] complexes was formed, while for $q<0$ mixed complex $[\text{Sn}_p(\text{OH})_q(\text{PAH})_r]$. If $\log A$ is presented as a function of $\log C_M$, the number of metal or ligand ion, as well as stability constant could be obtained. The slope of the curve on the graph have shown that the mononuclear complex of the general composition PAH/Sn(II)=1/1 was formed.

Acknowledgment

This paper is supported by a joint grant from Serbian Ministry of Sciences, Technologies and Development (Project OI 1980).

References

- [1] D.Đokić, D.Janković, T.Maksin, E.Jakšić, S.Beatović, R.Han, Nuc. Med. Commun., 1999, 20 (12), 1133.
- [2] D.Đokić, B.Zmbova, D.Veselinović, P.Đurđević, J.Serb.Chem.Soc., 1991, 56, 661.
- [3] P.Đurđević, D.Đokić, J.Inorg.Biochem., 1996, 62, 17.
- [4] P.Đurđević, T.Maksin, D.Veselinović, J.Label. Comp. Radiopharm., 1994, 34, 475.

THERMAL ANALYSIS OF ALUMINIUM-HISTIDINE COMPLEX

M. Cvijović¹, M. Kićanović² and P. Đurđević³

¹The Copper Mill, Sevojno, 31000 Užice, ²Institute of General and Applied Physical Chemistry, 11000 Belgrade, ³Faculty of Science, 34000 Kragujevac

Abstract

The complex [Al(HHis)His]Cl₂ was synthesized and characterised by elemental DSC and TGA analysis. The histidine ligands in the complex are bound to aluminium with different strength.

Introduction

Aluminium ion belongs to the class of “hard” metal ions showing the highest affinity toward “hard” donor atoms. One of the strongest binder of Al³⁺ ion is negatively charged oxygen atom, O²⁻. Thus, alcoxides, phenolates, catecholates, etc form unusually stable complexes with aluminium ion. The carboxylate group is medium strong binder of Al³⁺ ion, though complexes with glutamate, aspartate and succinate ion possess appreciably high stability. Complexes of aluminium with essential amino acid –L-histidine, were studied very scarcely, so far. To reveal binding mode and binding strength of histidine to aluminium ion, in this work we studied the thermal properties of the previously [1] synthesized complex between Al³⁺ and histidine.

Experimental

The DSC and TGA thermograms of the synthesized complexes were taken on Du Pont Instruments model 910 DSC, and Du Pont model 951 TGA Analyser, respectively. Instrument calibration was performed with standard indium sample of known melting temperature and enthalpy. 10-15 mg of the samples were weighted into Al pans. The inert atmosphere was maintained by nitrogen flow with flow rate of 35 cm³/min.

Results and Discussion

First DSC-gram of pure histidine was taken. Only melting at 284.3 °C is seen in the thermogram. The decomposition takes place at appreciably higher temperatures (> 300 °C) but are not well defined. In Fig. 1 the DSC-gram of the complex is given. Five different, well defined thermal processes are seen in different temperature intervals. The first process between 20 and 100 °C shows broad peak with mass loss of about 4.5%. This peak may be attributed to water loss. Since the peak is broad and centered at relatively low temperature range it means that water molecules are loosely bound in complex. Thus, the first process is probably loss of adsorbed water. It may also arise from traces of hydrated aluminium hydroxides.

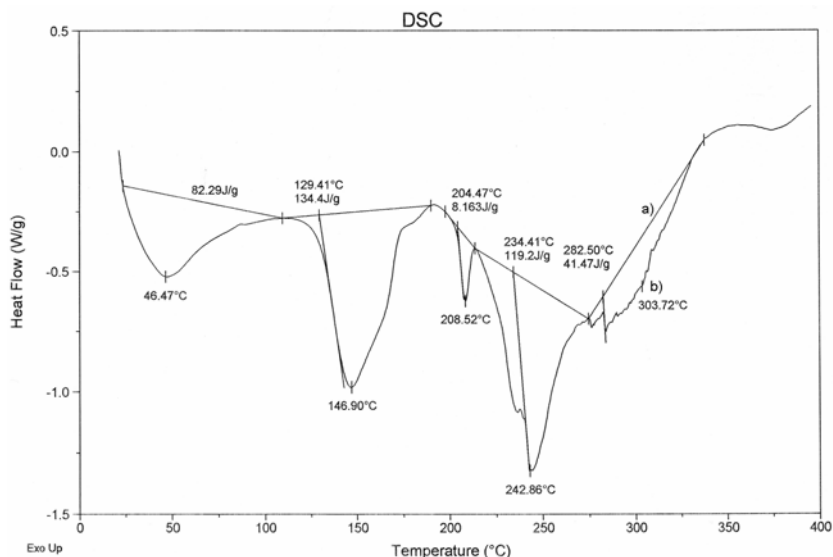


Figure 1: DSC-gram of Al-His complex

Second thermal process extending from 100 to 190°C is well defined with rather sharp peak. This process may be attributed to chemical decomposition of the one or both bonded histidine molecules. Most probably, judging by the temperature interval, it represents loss of the chloride perhaps in the form of HCl. This process is continued farther up to 275 °C. The stoichiometric composition of the complex indicates that one of protons is located on imidazole nitrogen. This proton is considerably weaker bound than the one located on ammonium group. (For the imidazole proton $pK_a = 6.3$ and for ammonium $pK_a = 9.1$). Thus upon heating this proton splits first while more strongly bound proton splits later at higher temperatures. Further thermal decompositions proceed at higher temperature ranges. Loss of mass corresponds to decarboxylation and deamination of the histidine molecules. These processes proceed stepwise i.e., more loosely bound histidine decomposes first while more strongly bound shows decarboxylation at slightly higher temperatures. Irregular shape of fourth process at about 300 °C and the fact that in this temperature range the same process is seen in thermogram of pure histidine supports the above discussion.

In Fig. 2 the TGA (a) and DTA (b) thermograms of the complex are shown. Five different thermal processes taking place in different temperature ranges, may be observed as in DSC-gram. All the observed processes are accompanied with the mass loss which means that they represent the chemical decomposition of the complex. The processes above 300 °C coincide with these in pure histidine and since histidine decomposes by decarboxylation and deamination it means that high temperature processes in the complex involve the decomposition of ligated histidine molecules.

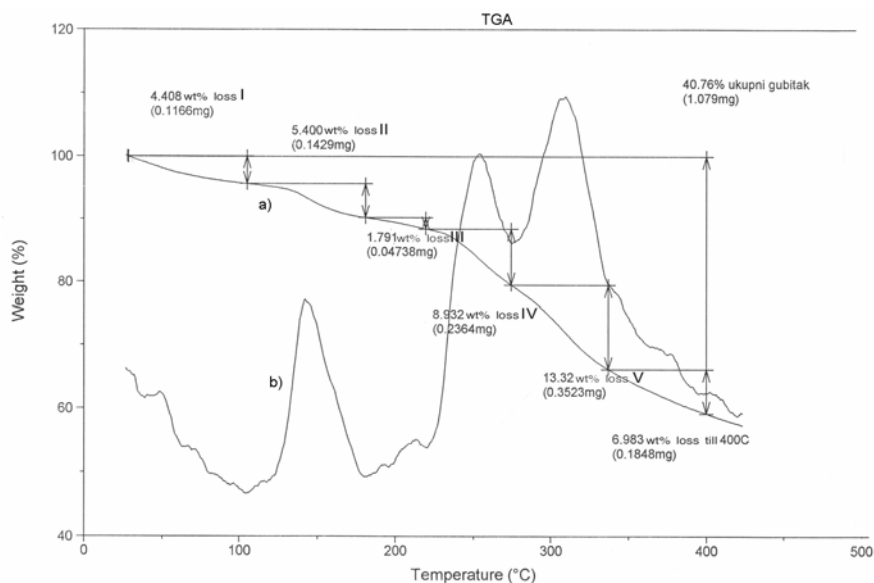


Figure 2: TGA and DTA of the complex

The observed thermal transitions are summarized bellow:

Temperature interval	Experimental mass loss	Calculated mass loss	Leaving group
(20-105)°	4.4 %	4.41 %	H ₂ O
(105-185)°	5.4 %	-	-
(185-220)°	1.79 %	-	-
(220-275)°	8.93 %	9.85 %	HCl
(275-330)°	13.32 %	13.75 %	CO ₂
(335-400)°	6.98 %	6.16 %	NH ₃

Conclusion

Five stages of histidine – Al complexes decomposition can be observed from the TGA and DSC curves. On the basis of the obtained results and literature data on similar compounds [2,3] we conclude that both amino and carboxylate groups are bonded to aluminium ie histidine acts as a bidentate ligand. The two ligands however, are bonded to aluminium with different strength.

References

- [1] M.Cvijović, Z.Tomić, M.Mitrović, P.Đurđević, II InternationSymposium: Light Metals and Composite Materials, Belgrade, 2004, 115.
- [2] S.Materazzi and R.Curini, *Thermochim.Acta*, 1996, 275, 93.
- [3] A.Onofrio, *Thermochim. Acta*, 2004, 413, 47.

NEW Cu(II) AND Co(II) COMPLEXES WITH FULLY N-(2-PYRIDYLMETHYL) FUNCTIONALISED CYCLAM (tpmc) AND MULTIDONOR CARBOXYLATO LIGANDS

M. Antonijević-Nikolić¹, S. B. Tanasković² and G. Vučković³

¹High school for Chemistry and Technology, 15000 Šabac; ²Faculty of Pharmacy, University of Belgrade, Vojvode Stepe 450; ³Faculty of Chemistry, University of Belgrade, P.O.Box 158, 11001 Belgrade, Serbia and Montenegro

Abstract

Three new complexes: $[\text{Cu}_4(\text{pm})(\text{tpmc})_2] \cdot 8\text{H}_2\text{O}$ (A); $[\text{Cu}_4(\text{succ})(\text{tpmc})_2](\text{ClO}_4)_6 \cdot 2\text{H}_2\text{O}$ (B) and $[\text{Co}_2(\text{succ})\text{tpmc}](\text{ClO}_4)_2 \cdot \text{H}_2\text{O}$ (C) (tpmc = *N,N',N'',N'''*-tetrakis(2-pyridyl methyl)-1,4,8,11-tetraazacyclotetradecane; pmH₄ = pyromellitic acid; succH₂ = succinic acid) formulas of which are proposed on the basis of elemental analyses were prepared under controlled experimental conditions. Complex A is the first neutral complex with tpmc. Magnetic moment (at room t°), IR spectra and in the case of B and C conductivities and electronic absorption spectra are discussed and compared with previously described complexes having analogous ligands.

Introduction

Polyaza macrocyclic compounds bearing pyridylmethyl pendant arms and their metal complexes were intensively studied [1]. Among them is fully N-substituted cyclam with 2-pyridylmethyl groups (tpmc). Its Cu(II) and Co(II) complexes containing additional multidonor carboxylato ligands have different geometries, unusual spectral and redox properties, and in some cases catalytic or microbiological activity [2-4]. Here we described preparation and some physico-chemical properties of two new Cu (II) and one Co (II) tpmc complexes with succinato or pyromellitato ligands.

Results and Discussion

Preparation

Cu(II) and Co(II) perchlorates, tpmc and $[\text{Cu}_2\text{tpmc}](\text{ClO}_4)_4$ were prepared according to the procedures given in [2] **Caution!** Perchlorate metal salts with organic ligands are potentially explosive and should be stored and handled with extreme care!!!

A) was obtained by reaction of $\text{Cu}(\text{NO}_3)_2 \cdot 3\text{H}_2\text{O}$, tpmc and pyromellitic acid (neutralized previously to pH 6.0 with NaOH) (molar ratio 2:1:1.5) in MeOH-H₂O. Mixture was stirred and refluxed (~80°C) 3h, concentrated to 1/2 of initial volume and left in refrigeration overnight. Microcrystalline blue product was separated by suction, dried, powdered, washed with ethanol, cold water and dried at room t°C. Yield 79.7 %. Anal. Found C 48.30; H 5.43; N 9.99; Cu 11.39 %. Calcd. for $\text{C}_{44}\text{H}_{62}\text{O}_{16}\text{N}_8\text{Cu}_2$ (FW = 1086.04) C 48.66; H 5.77; N 10.32; Cu 10.69 %. Product was insoluble in common solvents. By heating its colour change: at ~110°C to turquoise, above ~190°C into deep green, and from 210°C - 250°C became brown suggesting liberation of lattice

water, and some decomposition of the ligand(s) and/or complex. $\mu_{\text{eff}}(\text{room } t^{\circ}) = 2.07 \mu_{\text{B}} / \text{Cu (II)}$ (corresponds to one unpaired electron).

B) $[\text{Cu}_2\text{tpmc}](\text{ClO}_4)_4$ and succinic acid (neutralized previously to pH 5.5 with NaOH) in molar ratio 1:2 were dissolved in MeCN- H_2O , stirred and refluxed under the same conditions like A). Blue crystals were properly washed with cold water. Yield 78.0%. Anal. Found C 40.51; H 4.52; N 10.70 %. Calcd. for $\text{C}_{72}\text{H}_{96}\text{O}_{30}\text{N}_{16}\text{Cl}_6\text{Cu}_4$ (FW = 2132.67) C 40.55; H 5.54; N 10.51 %. Solubility: well in MeCN, sparingly in H_2O , MeOH, insoluble in EtOH. $\Lambda_{\text{M}}^{230^{\circ}\text{C}}$ (in MeCN) = $630 \text{ S cm}^2 \text{ mol}^{-1}$ (electrolyte type 1: 6); $\mu_{\text{eff}}(\text{room } t^{\circ}) = 1.47 \mu_{\text{B}} / \text{Cu (II)}$ (considerably lower than spin-only value)

C) $\text{Co}(\text{ClO}_4)_2 \cdot 6\text{H}_2\text{O}$ and succinic acid (neutralized to pH 5.5 with NaOH) in min amount of water were dissolved and refluxed 1/2h ($\sim 80^{\circ}\text{C}$), then tpmc suspension in MeCN was added (molar ratio 2:1,5:1) and heating was prolonged for 1.5 h with stirring. Further procedure was the same as for B). Purple flaky compound was obtained. Yield 80.2%. Anal. Found C 44.94; H 4.79; N 10.96 %. Calcd. for $\text{C}_{38}\text{H}_{50}\text{O}_{13}\text{N}_8\text{Cl}_2\text{Co}_2$ (FW = 1015.57) C 44.94; H 4.96; N 11.03 %. Solubility: well in MeCN, less soluble in N,N-DMF and DMSO, insoluble in water, EtOH and MeOH. $\Lambda_{\text{M}}^{230^{\circ}\text{C}}$ (in MeCN) = $290 \text{ S cm}^2 \text{ mol}^{-1}$ (electrolyte type 1:2); $\mu_{\text{eff}}(\text{room } t^{\circ}) = 4.95 \mu_{\text{B}} / \text{Co (II)}$ (high-spin Co(II))

Table I - VIS spectral data (in MeCN)

Complex	reference	λ_{max} [nm], (ϵ) [$\text{dm}^3 \text{ mol}^{-1} \text{ cm}^{-1}$]
$[\text{Cu}_2(\text{ox})\text{tpmc}]^{2+}$	2 a	732(252)
$[\text{Cu}_4(\text{mal})(\text{tpmc})_2]^{6+}$	2 a	648(799)
$[\text{Cu}_4(\text{succ})(\text{tpmc})_2]^{6+}$	this work	655 (654)
$[\text{Co}_2(\text{ox})\text{tpmc}]^{2+}$	3	534sh (61); 507 (86); 478 (68)
$[\text{Co}_2(\text{mal})\text{tpmc}]^{2+}$	2 a	550 (95); 533 (97); 514sh (95); 427 (86)
$[\text{Co}_2(\text{succ})\text{tpmc}]^{2+}$	this work	570 sh (47); 527 (101); 475 sh (68)

Cu(II) complex with succ^{2-} is tetranuclear, while Co(II) complex is binuclear, as a consequence of the: inductive effect of the neighbour carboxylato groups, the steric hindrance of ligands, more pronounced tendency of Co(II) to form 6-coordination than Cu(II), radii of the metal etc. VIS electronic spectral data are given in Table I and compared with some earlier described ones. There is a bathochromic shift in the case of Cu(II) complex with succ^{2-} in comparison with mal^{2-} one, and quite different position of the λ_{max} of the corresponding ox^{2-} complex, due to its binuclear structure. In the case of $[\text{Co}_2(\text{ox})\text{tpmc}]^{2+}$ complex, X-ray analysis showed unusual way of μ -bonded ox^{2-} using three O and one rested uncoordinated. Each Co(II) was 6-coordinated. As for the mal^{2-} and succ^{2-} complex there is possibility for the similar coordination mode - as bis bidentate, and bridged, although in the case of such type of

ligands a great number of stereochemistries is found depending of the rest of the molecule, metallic center, H-bonds, etc. As for the complex Cu (II) with pm^4 the geometry is not easy to predict due to its insolubility and scarce information. It is possible that pm^4 ligand bridges Cu(II) atoms and the rest of O atoms are involved in H-bonds with water molecules (inside and outside of coordination sphere). IR spectra of the mentioned complexes and free ligands were the useful tool for the prediction of the composition as well as the proposition of more favourable coordination modes supposed.

Conclusion

First neutral metal complex with four N-functionalized 2-pyridylmethyl groups on cyclam ring (tpmc) and piromellitato ligand pm^4 , $[Cu_2(pm)tpmc]$, and two cationic Cu(II) and Co(II) complexes with tpmc and succinato ligand, $[Cu_4(succ)(tpmc)_2]6+$ and $[Co_2(succ)tpmc]^{2+}$ as perchlorate salts were isolated in pure solid state. Some of their physico-chemical characteristics are given and discussed.

References

- [1] S-G Kang and S-J Kim, Bull. Korean.Chem.Soc., 2003, 24, 269. and references cited therein.
- [2] a) Z.M.Miodragović, G.Vučković, S.P. Sovilj, D.Manjlović, M.J. Malinar, J.Serb.Chem.Soc.,1998, 63, 781.; b) G. A. Bogdanović, Z. M. Miodragović, G.Vučković, R.Marković A. Spasojević-de Biré, Synth. React. Inorg. Met.-Org. Chem., 2001, 31, 1189.
- [3] S.P.Sovilj, G.Vučković, K.B.Babić-Samardžija, N.Matsumoto, V.J.Jovanović, J.Mroziński, Synth.React.Inorg.Met.-Org.Chem., 1999, 29, 785.
- [4] G.Vučković, M. Antonijević, D. Poleti, J.Serb.Chem.Soc., 2002, 67, 677.

**INADEQUACY OF THE USE OF THE MTT-ASSAY
IN THE EXAMINATION OF CYTOTOXIC ACTIVITY
OF PLANAR PENTADENTATE LIGAND
2', 2'''-(2,6-PYRIDINDIYLDIETHYLIDYNE) DIOXAMOHYDRAZIDE
DIHYDRATE (H₂L·2H₂O) AND ITS COORDINATION METAL
COMPLEXES**

M. J. Lazić¹, K. K. Anđelković², D. M. Sladić², Ž. Lj Tešić² and S. S. Radulović^{1*}

¹Laboratory for Experimental Pharmacology, Institute for Oncology and Radiology of Serbia,
Belgrade, Serbia and Montenegro

²Faculty of Chemistry, University of Belgrade, Belgrade, Serbia and Montenegro

Abstract

In this study we have investigated, for the first time to our knowledge, the antineoplastic activity of a planar pentadentate ligand (H₂L·2H₂O = 2', 2'''-(2,6-pyridindiyldiethylidyne)dioxamohydrazide dihydrate) and some of its coordination metal complexes [Cu(L)(H₂O)]·H₂O, [Cu(HL)(H₂O)]ClO₄, [Co(L)(H₂O)₂]·6H₂O, [Co(H₂L)(H₂O)(MeOH)](ClO₄)₂ and [Fe(L)(H₂O)₂]ClO₄·3H₂O, as well as of inorganic salts CuCl₂·2H₂O, CoCl₂·6H₂O and FeCl₃·6H₂O of corresponding metal ions.

The antiproliferative activity of these compounds was examined in a human melanoma cell line FemX with exposure time of 48 hours by performing two cytotoxicity tests: 3-(4,5-dimethylthiazol-2-yl)-2,5-diphenyltetrazolium bromide (MTT) assay and sulforhodamine B (SRB) assay.

Among these substances, the ligand H₂L·2H₂O expressed the greatest antineoplastic activity IC₅₀ = 45.40 μM, while the IC₅₀ of others could not be determined by SRB assay in the examined range of concentrations due to their low activity. FeCl₃·6H₂O showed stimulatory activity.

We have found remarkable discrepancies between the results obtained by MTT assay and SRB assay that influence IC₅₀ value as well as other measures of cytotoxicity, which led to the conclusion of uncertainty of using the MTT assay in evaluation of antineoplastic activity of organometallic complexes and inorganic metal salts.

Introduction

The role and the importance of metal ions in biological systems for the maintenance of normal physiological functions is well known. In addition to that, it was found that metal ions may exhibit antitumour effect.

The aim of this investigation was to evaluate, for the first time, antiproliferative activity of the polydentate ligand (H₂L·2H₂O) and its metal coordination complexes with copper(II), cobalt(II), and iron(III) in which the polydentate ligand (H₂L·2H₂O) is coordinated in its fully protonated (H₂L) form in [Co(H₂L)(H₂O)(MeOH)](ClO₄)₂, singly-deprotonated (HL⁻) form in [Cu(HL)(H₂O)]ClO₄ and doubly-deprotonated (L²⁻) form in

[Cu(L)(H₂O)]·H₂O, [Co(L)(H₂O)₂]·6H₂O and [Fe(L)(H₂O)₂]ClO₄·3H₂O complexes(1-5). For comparison the activity of inorganic salts of corresponding metals, CoCl₂·6H₂O, CuCl₂·2H₂O and FeCl₃·6H₂O was also evaluated.

Materials and Methods

The antiproliferative effects of these compounds were evaluated by two cytotoxic assays MTT(6) and SRB(7) in human melanoma cell line FemX with exposure time of 48 hours in order to examine whether the obtained results are dependent on the type of the assay. The antiproliferative activity is expressed as IC₅₀ value (i.e. the concentration of test agent that reduces cell survival to 50% of that in the control).

Results and Discussion

Among these substances, the ligand H₂L·2H₂O expressed the greatest antineoplastic activity, revealed IC₅₀ = 45.40 μM, measured by SRB assay, but did not reach any IC₅₀ value by MTT assay in the tested concentration range. FeCl₃·6H₂O exhibited weak stimulatory effect in the whole examined concentration range. At the FeCl₃·6H₂O concentration of 100 μM, the proliferation of FemX cells was 20% greater in comparison to the control growth. MTT assay of compounds [Cu(HL)(H₂O)]ClO₄, [Fe(L)(H₂O)₂]ClO₄·3H₂O, CoCl₂·6H₂O, CuCl₂·2H₂O indicated that their IC₅₀ values were 93 μM, 90 μM, 80 μM and 34 μM, respectively. On the contrary, by performing SRB assay none of these compounds induced 50% growth inhibition. In the case of FeCl₃·6H₂O, the survival curves obtained by MTT and SRB assay are in agreement, but there are remarkable discrepancies in the survival curves obtained by MTT and SRB assays for all other examined compounds. These discrepancies influence not only IC₅₀ value but also the other measures of antiproliferative activity such as PG (%) values of compounds at maximum examined concentration.

The discrepancies of the survival curves obtained by MTT and SRB assays were previously noticed by other authors (8, 9) but it was led to general conclusion that these discrepancies did not significantly influence IC₅₀ values (8, 9). On the contrary, our findings showed that MTT assay may influence the most common measure of cytotoxicity IC₅₀ as well as the other measures of cytotoxicity such as PG(%) at maximum examined compound concentration.

Conclusion

The observed disagreements between MTT and SRB assays imply caution in interpreting results obtained by MTT assay, especially in the case where the results of the MTT assay are not compared to the results of some other cytotoxic assays such as SRB assay, for the same compounds.

References

- [1] K. Andjelković, I. Ivanović, B. V. Prelesnik, V. M. Leovac, D. Poleti, *Polyhedron*, 1996, 15, 4361.
- [2] I. Ivanović-Burmazović, A. Bacchi, G. Pelizzi, V. M. Leovac, K. Andjelković, *Polyhedron*, 1998, 18, 119.
- [3] K. Anđelković, I. Ivanović, S. R. Niketić, B. Prelesnik, V. M. Leovac, *Polyhedron*, 1997, 16, 4221.
- [4] I. Ivanović, K. Andjelković, V. Beljanski, B. V. Prelesnik, V. M. Leovac, M. Momirović, *J. Coord. Chem.*, 1997, 42, 335.
- [5] K. Andjelković, A. Bacchi, G. Pelizzi, D. Jeremić, I. Ivanović-Burmazović, *J. Coord. Chem.*, 2002, 55, 1385.
- [6] H. Tada, O. Shiho, K-I Kuroshima, M. Koyama, and K. Tsukamoto, *J. Immunol. Methods*, 1997, 93, 157.
- [7] P. Skehan, R. Storeng, D. Scudiero, A. Monks, J. McMahon, D. Vistica, J. W. Warren, H. Bokesch, S. Kenney, M. R. Boyd, *J. Natl. Cancer Inst.*, 1990, 82, 1107.
- [8] L. V. Rubinstein, R. H. Shoemaker, K. D. Paull, R. M. Simon, S. Tosini, P. Skehan, D. A. Scudiero, A. Monks, M. R. Boyd, *J. Natl. Cancer Inst.*, 1990, 82, 1113.
- [9] Y. P. Keepers, P. E. Pizao, G. J. Peters, J. Van Ark-Otte, B. Winograd, H. M. Pinedo, *Eur J. Cancer*, 1991, 27, 897.

SPECTROPHOTOMETRIC STUDY OF SOLUTION EQUILIBRIA BETWEEN Al^{3+} ION AND L-HISTIDINE

M. Cvijović¹, V. Pavelkić², N. Miljević², D. Stanisavljev³ and P. Đurđević⁴

¹The Copper Mill, Sevojno, 31000 Užice, ²Institute of Nuclear Sciences, Laboratory of Physical Chemistry, Vinca, 11000 Belgrade, ³Faculty of Physical Chemistry, 11000 Belgrade, ⁴Faculty of Science, 34000 Kragujevac

Abstract

Aluminium(III) ion and L-histidine (HHis) react in water solution to yield two mononuclear binary complexes $[Al(HHis)]^{3+}$ and $[Al(HHis)His]^{2+}$. The over-all stability constants for these complexes were calculated by non-linear least-squares treatment of the spectrophotometric data and found to be: $\log \beta_{1,1,1} = 13.12 \pm 0.04$, $\log \beta_{1,2,1} = 20.9 \pm 0.1$, respectively. Indices refer to stoichiometric coefficients in complexation equilibrium: $p Al + q His + r H \rightarrow [Al_pHis_qH_r]$. The possible structures of the complexes in solution, are discussed.

Introduction

Aluminium is detrimental and toxic element. In human organism it may enter from the environment, the diet or medication. Its toxic effects are mainly exerted on brain, bone and muscle tissues. L-histidine is most metabolically active amino acid and is constituent of active site of many enzymes, proteins, oligopeptides, hemoglobin and mioglobin. Toxic effects of aluminum may arise from blocking enzyme function or modification of conformation of protein chain. Explanation of these interactions at molecular level requires the knowledge of binding properties of amino acids toward Al^{3+} ion. Hence in this report we studied the complexation behaviour of histidine with respect to Al^{3+} ion in water solution at 0.1 mol/L ionic strength adjusted with LiCl.

Experimental

The UV spectra were taken on Beckman model 5260 and GBC Cintra 40 double beam spectrophotometers. The matching pair of quartz cells were used for blank and specimen. The concentration ratios of aluminium to histidine were 1:3, 1:5 and 1:8, with the total aluminium concentration ranging from 3 to 10 mmol/L. The pH of the solutions was adjusted with standard HCl or NaOH and was varied in the interval 4.0 – 6.0. The spectra were taken in the wavelength interval 240 – 350 nm.

Results and Discussion

L-histidine shows UV absorption in far UV region of electromagnetic spectrum with a maximum at 211 nm.

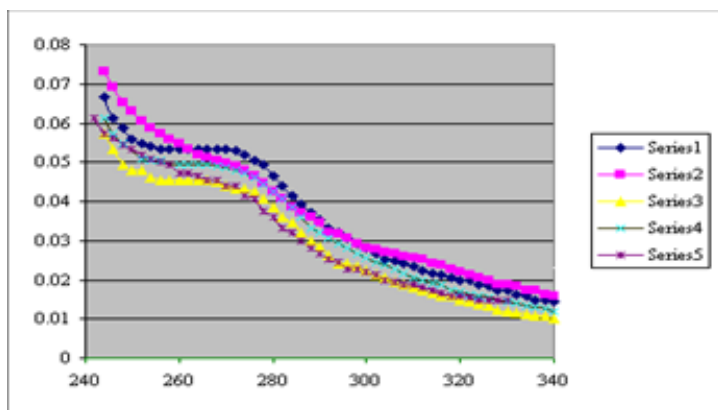


Figure 1. UVspectra of His+Al³⁺ solutions. $C_{\text{His}} = 30 \text{ mmol/dm}^3$, $C_{\text{Al}} = 3.6 \text{ mmol/dm}^3$. (1) pH= 5.10; (2) 5.24; (3) 5.54 (4) 5.63, (5) 6.0

The absorption band is symmetrical and approaches zero at wavelengths higher than 240 nm. In the presence of Al³⁺ ion the tail extending into wavelengths higher than 240 nm exhibits appreciably higher absorption than pure histidine. Raising of absorption is observable after 2-3 days of ageing of the solution. Thus, the spectra of all solutions were taken 72 h after the preparation. The obtained spectra (Fig. 1) show monotonous decrease in absorbance with increasing the wavelength. The plateau appears between 250 and 275 nm. Its position is pH dependent. The dependence of the intensity and position of the spectral bands on pH indicates the presence of several absorbing complexes in solution. In order to evaluate spectrophotometric data, the Squad [2] program was used. In Squad calculations the protonation constants of histidine and stability constants of aluminium hydrolytic complexes were taken from our previous work [1] and were not optimized while these of Al³⁺ with histidine and their molar absorptivities were varied until minimum value of the sum, S and standard deviations of the fit, SD, were obtained. During the calculations various models were tested. The finally obtained results of calculation are given in table 2.

Table 1. Calculated stability constants of Al³⁺ - His complexes. Data for protonation constants of His and hydrolytic complexes of aluminum are from ref. [1].

Species	$\log \beta_{p,q,r} \pm \sigma$
Al(HHis)(His) ²⁺	20.9 ± 0.1
Al(HHis) ³⁺	13.12 ± 0.04
Al(His) ²⁺	6.98 ± 0.15
Statistical parameters of the fit	S=2·10 ⁻³ , SD=1.0·10 ⁻³

The distribution diagram of the Al³⁺ - L-histidine complexes in solution is shown in Figure 2.

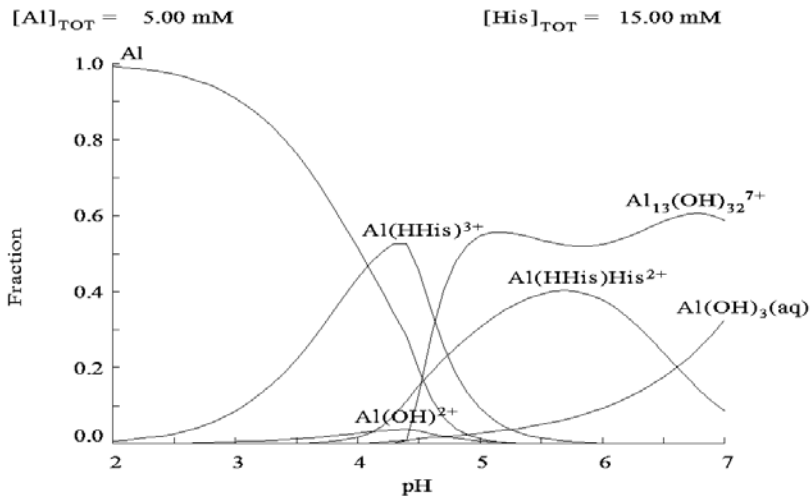


Figure 2. The distribution diagram of Histidine- Al^{3+} complexes

The distribution diagram of pure hydrolytic species [] indicates that in the pH interval 4.0 – 4.5 most important reactive species of aluminium is monohydroxo complex $Al(OH)^{2+}$ so that the probable mechanism of the formation of binary ligand complexes should be:



Bearing in mind the concentrations of the reactive species in the pH region in which $Al(His)$ complex is formed, it seems reasonable to suppose that the actual composition of the complex is $Al(OH)(HHis)$, i.e. that one of coordinated water molecules to aluminium is protolyzed and ammonium group of histidine does not dissociate.

References

- [1] P.Đurđević,R.Jelić,D.Dzajević,M.Cvijović,Metal Based Drugs, 2002, 8, 235.
- [2] D.J.Legget, Squad Stability quotients from absorbance data. In D.J.Legget (ed) Computational Methods for the Determination of Formation Constants, Plenum Press, N.Y., 1985. pp 159-220

SYNTHESIS AND CHARACTERIZATION OF COBALT(II) AND ZINC(II) COMPLEXES WITH N-1-SUBSTITUTED 2-METHYLBENZIMIDAZOLES

S. O. Podunavac-Kuzmanović¹ and G. S. Četković¹

¹ Faculty of Technology, Bulevar Cara Lazara 1, 21000 Novi Sad, Yugoslavia

Abstract

Complexes of 1-benzoyl-2-methylbenzimidazole(L¹) and 1-(4-chloro-benzoyl)-2-methylbenzimidazole(L²) with chlorides of cobalt(II) and zinc(II) were synthesized. All the complexes are characterized by data of elemental analysis (metal), IR spectra, magnetic conductivity and molar susceptibility measurements. The molar ratio metal:ligand in the reaction of the complex formation was 1:2. It should be noticed, that the reaction of both the metal salts yielded bis(ligand) complexes of the general formula M(L)₂Cl₂ (M=Co or Zn). Co(II) complexes behave as 1:1 types of electrolytes, whilst Zn(II) complexes are 1:2 electrolytes. Co(II) complexes have an octahedral stereochemistry, whilst Zn(II) complexes have tetrahedral configuration. In all the complexes ligand is bidentate coordinated by participation of pyridine nitrogen and carbonyl oxygen.

Introduction

Benzimidazole and its derivatives are interesting heterocycles because of their presence in many various medicaments. It has been found that they possess antibacterial, antifungal, antihistaminic, cytostatic, local analgesic, hypotensive, antiinflammatory and anti-HIV activity [1-3]. However, in the last time possible therapeutical properties of the metal complexes have been examined. It was found that the complexes of transition metal salts with benzimidazole derivatives showed a larger antimicrobial activity than only ligands [4].

The coordination chemistry of benzimidazole and its derivatives has received considerable attention because of their biological significance and interesting spectral, magnetic and structural aspects. In view of previous observations [5-7] that the presence of metal ions considerably enhances the biological activity of organic molecules, we report the synthesis and study of cobalt(II) and zinc(II) complexes with 1-benzoyl-2-methylbenzimidazole(L¹) and 1-(4-chlorobenzoyl)-2-methylbenzimidazole (L²).

Experimental

Complexes were synthesized according to a next procedure: a solution of 1.25 mmol of metal salts in 5 cm³ EtOH was added into a solution of 2.5 mmol of the ligand in 5 cm³ EtOH. The resulting mixture was boiled under reflux on a water bath for about 2h and then cooled. The complexes which separated from the reactions were

removed by filtration, washed with EtOH and dried *in vacuo* over CaCl₂. The yield of the complexes varied in the range of 40-45%.

The metal content was determined by a chelatometric titration with EDTA. Molar conductivities of freshly prepared 1×10^{-3} mol dm⁻³ solutions were measured on a Jenway 4010 conductivity meter. The infrared spectra (KBr pellets) were recorded on an Infrared 457 Perkin-Elmer spectrophotometer.

Results and Discussion

The elemental analyses of complexes, magnetic moments and molar conductance data are summarized in **Table 1**. All the complexes are nearly insoluble in most common organic solvents, highly soluble in DMF and less soluble in MeOH and EtOH.

An indication of the most probable stereochemistry of the synthesized cobalt(II) complexes is given by their magnetic moments. Both the cobalt(II) complexes exhibit μ_{eff} values which fall in the range expected for the octahedral cobalt(II). The molar conductances of cobalt complexes in DMF solutions fall in the range of 65-90 Scm²mol⁻¹. These values are characteristic for 1:1 types of electrolytes, which indicates a partial substitution of the coordinated chloride with solvent molecules [8]. Zinc(II) complexes are diamagnetic, as well as its complexes are tetrahedral. The molar conductivities of zinc(II) complexes in DMF solutions indicate 1:2 type of electrolyte [8].

Table 1. Some physical characteristics and analytical data of the complexes

Complex	Colour	μ_{eff} (μ_{B})	λ_{M}	Metal % Found(Calcd.)
Co(L ¹) ₂ Cl ₂	violet	4.89	84.5	10.60 (10.71)
Co(L ²) ₂ Cl ₂	violet	4.92	87.1	9.52 (9.62)
Zn(L ¹) ₂ Cl ₂	white	diam.	124.3	9.68 (9.76)
Zn(L ²) ₂ Cl ₂	white	diam.	127.1	8.51 (8.76)

The infrared spectra of the ligands exhibit band at 1671-1660cm⁻¹ assigned to the $\nu(\text{C}=\text{O})$ vibrations and a band at 1630cm⁻¹ assigned to the $\nu(\text{C}=\text{N})$ vibrations in the benzimidazole ring, respectively [9]. The infrared spectra of the investigated complexes are similar to those of the corresponding ligands. The $\nu(\text{C}=\text{O})$ absorption is shifted to lower frequencies compared to the free ligands in all the complexes. This suggests coordination of the carbonyl oxygen. The $\nu(\text{C}=\text{N})$ of the benzimidazole ring is lowered by about 15-25 cm⁻¹ from the free ligand positions. These shifts of $\nu(\text{C}=\text{N})$ band in the IR spectra of the complexes as compared to its value in the free ligand, suggests coordination through the pyridine nitrogen of the benzimidazole to the metal ion [9].

Conclusions

The formula of the synthesized complexes with 1-benzoyl-2-methylbenzimidazole(L¹) and 1-(4-chloro-benzoyl)-2-methylbenzimidazole(L²) was M(L)₂Cl₂ (M=Co or Zn). Both the metals form bis-ligand complexes bidentate coordinated by participation of sp²-hybridized nitrogen and carbonyl oxygen. The molar ratio metal:ligand in the reaction of the complex formation was 1:2. The molar conductances of Co(II) complexes indicate 1:1 types of electrolytes, whilst Zn(II) complexes are 1:2 electrolytes. Both the cobalt(II) complexes exhibit μ_{eff} values which fall in the range expected for the octahedral cobalt(II), whilst Zn(II) complexes are diamagnetic, as well as its complexes are tetrahedral.

Acknowledgment

These results are the part of the project "*Physico-chemical, structural and biological investigations of complex compounds*", supported by the Ministry for Science, Technologies and Development of the Republic of Serbia.

References

- [1] T. Harada, I. Koyama, M. Tuncbilek, K. Sato, T. Komoda, *Comp. Biochem. Physiol. PT B*, 2000, 127, 193.
- [2] H. Goker, G. Ayhankilcilgil, M. Tuncbilek, C. Kus, R. Ertan, E. Kendi, S. Oybey, M. Fort, C. Garcia, A.J. Farre, *Heterocycles*, 1999, 51, 2561.
- [3] A. Chimirri, S. Grasso, P. Monforte, A. Rao, M. Zappala, A.M. Monforte, C. Pannecouque, M. Witvrouw, J. Balzarini, E. Declercq, *Antivir. Chem. Chemother.*, 1999, 10, 211.
- [4] S.O. Podunavac-Kuzmanović, G.S. Četković, V.M. Leovac, S.L. Markov, J.J. Rogan, *Acta Periodica Technologica*, 2001, 32, 145.
- [5] S.O. Podunavac-Kuzmanović, V.M. Leovac, N.U. Perišić-Janjić, J.J. Rogan, J. Balaž, *J. Serb. Chem. Soc.*, 1999, 64, 381.
- [6] N.U. Perišić-Janjić, S.O. Podunavac-Kuzmanović, J.S. Balaž, Đ.S. Vlaović, *Acta Periodica Technologica*, 1998-1999, 29-30, 173.
- [7] S.O. Podunavac-Kuzmanović, Lj.S. Vojinović, *Acta Periodica Technologica*, 2003, 34, 119.
- [8] W.J. Geary, *Coord.Chem.Rev.* 1971, 7, 81.
- [9] K.Nakamoto: *Infrared and Raman Spectra of Inorganic and Coordination Compounds*, Wiley, New York (1986) 324.

SYNTHESIS AND PHYSICO-CHEMICAL PROPERTIES OF IRON(II), NICKEL(II) AND COPPER(II) COMPLEXES WITH 1-BENZOYL-2-AMINOBENZIMIDAZOLE

S. O. Podunavac-Kuzmanović¹, Lj. S. Vojinović²

¹ Faculty of Technology, Bulevar Cara Lazara 1, 21000 Novi Sad, Yugoslavia

² Faculty of Sciences, Trg Dositeja Obradovića 3, , 21000 Novi Sad, Yugoslavia

Abstract

The synthesis of iron(II), nickel(II) and copper(II) complexes with 1-benzoyl-2-aminobenzimidazole (L) was described. The molar ratio ligand:metal in the reaction of the warm ethanolic solutions of ligand and metal chlorides was 2:1. The formula of the synthesized complexes was $M(L)_2Cl_2$ ($M=Fe, Ni$ or Cu). All the metals form bis-ligand complexes bidentate coordinated by participation on sp^2 -hybridized nitrogen and carbonyl oxygen. Synthesized copper(II) complexes have a square-planar configuration, while the nickel(II) and iron(II) complexes have octahedral geometry. All the complexes are characterized by data of elemental analysis, IR spectra, magnetic conductivity and molar susceptibility measurements.

Introduction

Benzimidazole derivatives with substituents such as methyl and amino in different positions have been found to possess inhibitory effect on the development of several yeasts and bacteria. Various benzimidazoles are effective inhibitors of the growth of lactobacilli, vaccinia virus, influenza virus and HIV-virus. Many different benzimidazoles have such activities as analgetics, anticarcinogens, sedatives, etc [1-3].

As an extension of our previous studies [4-6], in this paper we report the synthesis and some physico-chemical characteristics for complexes of 1-benzoyl-2-aminobenzimidazole (L) with iron(II), nickel(II) and copper(II).

Experimental

Complexes were synthesized according to a next procedure: a solution of 2.5 mmol of metal salts in 10 cm^3 EtOH was added into a solution of 5 mmol of the ligand in 10 cm^3 EtOH. The resulting mixture was boiled under reflux on a water bath for about 2h and then cooled. The complexes which separated from the reactions were removed by filtration, washed with EtOH and dried *in vacuo* over $CaCl_2$. The yield of the complexes varied in the range of 45-50%.

The metal content was determined by a chelatometric titration with EDTA. Molar conductivities of freshly prepared $1 \times 10^{-3}\text{ mol dm}^{-3}$ solutions were measured on a Jenway 4010 conductivity meter. The infrared spectra (KBr pellets) were recorded on an Infrared 457 Perkin-Elmer spectrophotometer.

Results and Discussion

The elemental analyses of complexes, magnetic moments and molar conductance data are summarized in **Table 1**. All the complexes are nearly insoluble in most common organic solvents, highly soluble in DMF and less soluble in MeOH and EtOH.

The magnetic moment value (Table 1) of the iron(II) complex is in the expected range for octahedral stereochemistry. The room temperature effective magnetic moment of the nickel(II) complex is in the range which also support their octahedral geometry, whilst the μ_{eff} value for Cu (II) complex supports square-planar geometry.

The molar conductance value of iron(II) complex compared with the values of non-electrolytes are increased. The same value is considerably less compared with the molar conductances of the 1:1 type electrolytes ($\lambda_{\text{M}}=65\text{-}90 \text{ Scm}^2\text{mol}^{-1}$) [7], which indicates the partial substitution of coordinated anions with solvent molecules. The molar conductances of nickel(II) complex in DMF solution fall in the range of 65-90 $\text{Scm}^2\text{mol}^{-1}$ which is characteristic for 1:1 types of electrolytes. It indicates a partial substitution of the coordinated chloride with solvent molecules [7]. The molar conductivity of copper(II) complex indicate 1:2 type of electrolyte [7].

Table 1. Some physical characteristics and analytical data of the complexes

Complex	Colour	$\mu_{\text{eff}}(\mu_{\text{B}})$	λ_{M}	Metal % Found(Calcd.)
Fe(L) ₂ Cl ₂	red	5.30	48.0	9.12 (9.29)
Ni(L) ₂ Cl ₂	blue-green	3.11	75.7	9.65 (9.72)
Cu(L) ₂ Cl ₂	light brown	1.79	127.1	8.84 (8.91)

The infrared spectra of the ligand exhibit band at 3450-3330 cm^{-1} and ca. 1650 cm^{-1} , assigned to $\nu(\text{NH}_2)$ and $\delta(\text{NH}_2)$ of the benzimidazole ring, respectively [8]. The band appearing at about 1671-1660 cm^{-1} may be assigned to the $\nu(\text{C}=\text{O})$ vibrations and a band at 1630 cm^{-1} assigned to the $\nu(\text{C}=\text{N})$ vibrations in the benzimidazole ring, respectively [8]. The infrared spectra of the investigated complexes are similar to those of the corresponding ligands. The $\nu(\text{C}=\text{O})$ absorption is shifted to lower frequencies compared to the free ligands in all the complexes. This suggests coordination of the carbonyl oxygen. The $\nu(\text{C}=\text{N})$ of the benzimidazole ring is lowered by about 5-15 cm^{-1} from the free ligand positions. These shifts of $\nu(\text{C}=\text{N})$ band in the IR spectra of the complexes as compared to its value in the free ligand, suggests coordination through the pyridine nitrogen of the benzimidazole to the metal ion [8].

Conclusions

Iron(II), nickel(II) and copper(II) with 1-benzoyl-2-aminobenzimidazole (L) formed complexes of the general formula $\text{M}(\text{L})_2\text{Cl}_2$ ($\text{M}=\text{Fe}, \text{Ni}$ or Cu). The magnetic moment values (Table 1) of the Fe(II) and Ni (II) complexes is in the expected range for octahedral stereochemistry, whilst the μ_{eff} value for Cu (II) complex supports

square-planar geometry. The molar conductance value of iron(II) complex compared with the values of non-electrolytes are increased, but less compared with the molar conductances of the 1:1 type electrolytes which indicates the partial substitution of coordinated anions with solvent molecules. The molar conductance of nickel(II) complex in DMF solution is characteristic for 1:1 types of electrolytes which also indicates a partial substitution of the coordinated chloride with solvent molecules. The molar conductivity of copper(II) complex indicate 1:2 type of electrolyte. All the metals form bis-ligand complexes bidentate coordinated by participation of pyridine nitrogen and carbonyl oxygen.

Acknowledgment

These results are the part of the project "*Physico-chemical, structural and biological investigations of complex compounds*", supported by the Ministry for Science, Technologies and Development of the Republic of Serbia.

References

- [1] H. Kucukbay, R. Durmaz, E. Orhan, S. Gunal, *Il Farmaco*, 2003, 58, 431.
- [2] H. Goker, G. Ayhankilcilgil, M. Tuncbilek, C. Kus, R. Ertan, E. Kendi, S. Oybey, M. Fort, C. Garcia, A.J. Farre, *Heterocycles*, 1999, 51, 2561.
- [3] L. Gata, F. Perna, N. Figura, C. Ricci, J. Holton, M. Miglioli, D. Vaira, *J. Antimicrob. Chemother.*, 2003, 51, 439.
- [4] S.O. Podunavac-Kuzmanović, V.M. Leovac, N.U. Perišić-Janjić, J.J. Rogan, J. Balaž, *J. Serb. Chem. Soc.*, 1999, 64, 381.
- [5] N.U. Perišić-Janjić, S.O. Podunavac-Kuzmanović, J.S. Balaž, Đ.S. Vlaović, *Acta Periodica Technologica*, 1998-1999, 29-30, 173.
- [6] S.O. Podunavac-Kuzmanović, Lj.S. Vojinović, *Acta Periodica Technologica*, 2003, 34, 119.
- [7] W.J. Geary, *Coord.Chem.Rev.* 1971, 7, 81.
- [8] K.Nakamoto: *Infrared and Raman Spectra of Inorganic and Coordination Compounds*, Wiley, New York (1986) 324.

COMPLEXES OF 1-(4-CHLOROBENZOYL)- 2-AMINOBENZIMIDAZOLE WITH DIFFERENT METAL IONS

S. O. Podunavac-Kuzmanović¹, Lj. S. Vojinović²

¹ Faculty of Technology, Bulevar Cara Lazara 1, 21000 Novi Sad, Yugoslavia

² Faculty of Sciences, Trg Dositeja Obradovića 3, , 21000 Novi Sad, Yugoslavia

Abstract

The synthesis of copper(II), zinc(II), cobalt(II), nickel(II) and iron(II) complexes with 1-(4-chlorobenzoyl)-2-aminobenzimidazole (L) was described. The molar ratio ligand:metal in the reaction of the the warm ethanolic solutions of ligand and metal chlorides was 2:1. The formula of the synthesized complexes was $M(L)_2Cl_2 \cdot nH_2O$ ($M=Cu, Zn, Co, Ni$ or Fe ; $n=0$ or 2). All the complexes are characterized by data of elemental analysis, IR spectra, magnetic conductivity and molar susceptibility measurements. Synthesized copper(II) complexes have a square-planar configuration, the cobalt(II), nickel(II) and iron(II) complexes have octahedral geometry, whilst zinc(II) is tetrahedral. All the metals form bis-ligand complexes bidentate coordinated by participation on pyridine nitrogen and carbonyl oxygen.

Introduction

The antimicrobial activities of imidazoles and benzimidazoles have long been established. Derivatives of these compounds are known for their antibacterial, antiviral and fungicidal activities [1-3]. These groups of molecules are of wide interest because of their diverse biological activity and clinical applications. This ring system is present in numerous antiparasitic, antihelmintic and anti-inflammatory drugs. They are also inhibitors of photosynthesis, and some exhibit appreciable herbicidal activity.

We have recently reported isolation, characterization and antimicrobial activities of different metal complexes with benzimidazole derivatives [4-6]. As an extension of our previous studies, the objective of the present work was to synthesize and study physico-chemical characteristics of 1-(4-chlorobenzoyl)-2-aminobenzimidazole complexes with chlorides of copper(II), zinc(II), cobalt(II), nickel(II) and iron(II).

Experimental

Complexes were synthesized according to a next procedure: a solution of 5 mmol of metal salts in 20 cm^3 EtOH was added into a solution of 10 mmol of the ligand in 20 cm^3 EtOH. The resulting mixture was boiled under reflux on a water bath for about 2h and then cooled. The complexes which separated from the reactions were removed by filtration, washed with EtOH and dried *in vacuo* over $CaCl_2$. The yield of the complexes varied in the range of 45-50%.

The metal content was determined by a chelatometric titration with EDTA. Molar conductivities of freshly prepared 1×10^{-3} mol dm^{-3} solutions were measured on a

Jenway 4010 conductivity meter. The infrared spectra (KBr pellets) were recorded on an Infrared 457 Perkin-Elmer spectrophotometer.

Results and Discussion

The elemental analyses of complexes, magnetic moments and molar conductance data are summarized in **Table 1**.

The molar conductances of cobalt(II) and nickel(II) complexes in DMF solution fall in the range of 65-90 $\text{Scm}^2\text{mol}^{-1}$ which is characteristic for 1:1 types of electrolytes. It indicates a partial substitution of the coordinated chloride with solvent molecules [7]. The molar conductivities of zinc(II) and copper(II) complexes indicate 1:2 type of electrolytes [7], whilst that value of iron(II) complex compared with the values of non-electrolytes are increased. The same value is considerably less compared with the molar conductances of the 1:1 type electrolytes ($\lambda_M=65-90 \text{ Scm}^2\text{mol}^{-1}$), which indicates the partial substitution of coordinated anions with solvent molecules.

The magnetic moment values (Table 1) of the cobalt(II), nickel(II) and iron(II) complexes are in the expected range for octahedral stereochemistry. The room temperature effective magnetic moment of the copper(II) complex is in the range which support its square-planar configuration, whilst the Zn (II) complex is diamagnetic and has tetrahedral geometry.

Table 1. Some physical characteristics and analytical data of the complexes

Complex	Colour	$\mu_{\text{eff}}(\mu_B)$	λ_M	Metal % Found(Calcd.)
$\text{Cu(L)}_2\text{Cl}_2 \cdot 2\text{H}_2\text{O}$	brown	1.79	135.5	8.84 (8.91)
$\text{Zn(L)}_2\text{Cl}_2$	white	diam.	134.2	9.58 (9.62)
$\text{Co(L)}_2\text{Cl}_2$	violet	4.92	89.1	8.59 (8.76)
$\text{Ni(L)}_2\text{Cl}_2$	dark green	3.12	83.5	8.60 (8.72)
$\text{Fe(L)}_2\text{Cl}_2$	dark red	5.29	53	8.17 (8.34)

The infrared spectra of the ligand exhibit band at 3450-3330 cm^{-1} and ca. 1650 cm^{-1} , assigned to $\nu(\text{NH}_2)$ and $\delta(\text{NH}_2)$ of the benzimidazole ring, respectively [8]. The band appearing at about 1671-1660 cm^{-1} may be assigned to the $\nu(\text{C}=\text{O})$ vibrations and a band at 1630 cm^{-1} assigned to the $\nu(\text{C}=\text{N})$ vibrations in the benzimidazole ring, respectively [8]. The infrared spectra of the investigated complexes are similar to those of the corresponding ligands. The $\nu(\text{C}=\text{O})$ absorption is shifted to lower frequencies compared to the free ligands in all the complexes. This suggests coordination of the carbonyl oxygen. The $\nu(\text{C}=\text{N})$ of the benzimidazole ring is lowered by about 5-15 cm^{-1} from the free ligand positions. These shifts of $\nu(\text{C}=\text{N})$ band in the IR spectra of the complexes as compared to its value in the free ligand, suggests coordination through the pyridine nitrogen of the benzimidazole to the metal ion [8].

Conclusions

Copper(II), zinc(II), cobalt(II), nickel(II) and iron(II) react with 1-(4-chlorobenzoyl)-2-aminobenzimidazole (L) and form complexes of the general formula $M(L)_2Cl_2 \cdot nH_2O$ ($M=Cu, Zn, Co, Ni$ or Fe ; $n=0$ or 2). The magnetic moment values of the cobalt(II), nickel(II) and iron(II) complexes are in the expected range for octahedral stereochemistry. The μ_{eff} of the copper(II) complex is in the range which support its square-planar configuration, whilst the Zn (II) complex is diamagnetic and has tetrahedral geometry. The molar conductivities of zinc(II) and copper(II) complexes indicate 1:2 type of electrolytes, whilst these values of cobalt(II) and nickel(II) complexes are characteristic for 1:1 types of electrolytes. In the case of iron(II) complex coordinated anions are partial substituted with solvent molecules. All the metals form bis-ligand complexes bidentate coordinated by participation of pyridine nitrogen and carbonyl oxygen.

Acknowledgment

These results are the part of the project "*Physico-chemical, structural and biological investigations of complex compounds*", supported by the Ministry for Science, Technologies and Development of the Republic of Serbia.

References

- [1] H. Kucukbay, R. Durmaz, E. Orhan, S. Gunal, *Il Farmaco*, 2003, 58, 431-437.
- [2] A. Akbay, I. Oren, O. Temiz-Arpaci, E. Aki-Sener, I. Yalcin, *Arzneim.-Forsch./Drug Res.*, 2003, 53, 266.
- [3] L. Gata, F. Perna, N. Figura, C. Ricci, J. Holton, M. Miglioli, D. Vaira, *J. Antimicrob. Chemother.*, 2003, 51, 439.
- [4] S.O. Podunavac-Kuzmanović, V.M. Leovac, N.U. Perišić-Janjić, J.J. Rogan, J. Balaž, *J. Serb. Chem. Soc.*, 1999, 64, 381.
- [5] N.U. Perišić-Janjić, S.O. Podunavac-Kuzmanović, J.S. Balaž, Đ.S. Vlaović, *Acta Periodica Technologica*, 1998-1999, 29-30, 173.
- [6] S.O. Podunavac-Kuzmanović, Lj.S. Vojinović, *Acta Periodica Technologica*, 2003, 34, 119.
- [7] W.J. Geary, *Coord.Chem.Rev.* 1971, 7, 81.
- [8] K.Nakamoto: *Infrared and Raman Spectra of Inorganic and Coordination Compounds*, Wiley, New York (1986) 324.

General Physical Chemistry

(M)

THE SYNTHESIS OF ORGANIC MOLECULES IN A LASER PLASMA SIMILAR TO THE PLASMA THAT EMERGES IN HYPERVELOCITY COLLISIONS OF MATTER

G. Managadze¹, W. Brinckerhoff², A. Chumikov¹, N. Managadze¹

¹Space Research Institute (IKI), Moscow, Russia

²Applied Physics Laboratory, The Johns Hopkins University, Laurel, Maryland, USA

Abstract

Ions of organic molecules and polymers as well as multiply ionized hydrocarbons were synthesized and detected with a time-of-flight (TOF) mass analyzer in laboratory experiments simulating with a laser the plasma processes that accompany a hypervelocity micrometeorite impact on the target surface. A hypervelocity impact (HVI) of micrometeorites moving at velocities of 80 km s^{-1} on a inorganic target was simulated with a Q-switched laser. The laser provided a power density (W) of 10^9 – $10^{11} \text{ W cm}^{-2}$ in a spot with an impact diameter (\emptyset) of 30–150 μm for a pulse duration of 7–10 ns and a laser plasma electron density of 10^5 – 10^6 K . The ions of organic compounds are shown to be synthesized mostly during the free expansion of a hot laser plasma at the stage of its cooling and recombination if, initially, the plasma was completely atomized and ionized. Molecular ions have high yields only for a carbon target. The results obtained indicate that organic or other polyatomic compounds can be abiogenically synthesized in intense hypervelocity meteorite impacts on the Earth's surface at the early stage of its formation during meteorite showers and in hypervelocity collisions of dust particles in interstellar molecular clouds.

Introduction

When the impact velocity reaches a critical value V_{cr} of 15–20 km s^{-1} [1], a plasma cloud or a plasma torch is generated in the collision area of the bodies [2]. This requires that the impinging body–target interaction time scale, t_{int} , be shorter than the time scale of heat outflow from the impact area, t_h . An energy that exceeds the binding energy of the atoms in matter and their ionization energy is rapidly absorbed under these conditions. As a result, the impinging body and part of the target turn into a hot plasma. Depending on the physical parameters of the interacting bodies at impact velocities of $V_{\text{sh}} > V_{\text{cr}}$, the generated plasma reaches a temperature of 30–50 eV and is usually completely atomized and ionized at the initial stage. At the stage of adiabatic expansion, the plasma cools down and recombines, and the degree of ionization decreases by a factor of approximately 100. The ion composition of such a plasma corresponds to the elemental composition of the interacting bodies. However, polyatomic ions can also be synthesized in such a plasma during its expansion [3]. Here, our goal is to study this phenomenon or, more specifically, the synthesis of molecular ions during the expansion of a impact plasma. A HVI is the most characteristic phenomenon for the processes in space, e.g. the surfaces of atmosphereless cosmic bodies in the Solar system (SS) are continuously subjected to HIV of particles with masses from 10^{-15} to 10^{-12} g .

Micrometeorites with $\varnothing < 1 \mu\text{m}$, are accelerated by light pressure to $V \sim 50 \text{ km s}^{-1}$. Such an impact plays an important role in the formation of the regolith surface layer on atmosphereless objects [4]. During the so-called meteorite shower period 4.5–3.5 Gyr ago, the Earth's surface was subjected to intense impacts. The presumed impact energy flux was large, comparable to the volcanic heat, about $10^{22} \text{ eV m}^{-2}$ per year [5] at collision velocities from 11 to 70 km s^{-1} . Interestingly, life on Earth originated precisely during this period [6, 7]. HVI is a common phenomenon in nature virtually at all evolutionary stages of the Universe, from the formation of novae and planetary systems to their death [8–10].

Formulation of the Problem

The physical processes of impact interactions in laboratory conditions are studied using microparticle (MP) accelerators, capable to accelerate particles with masses of 10^{-11} – 10^{-17} g to the velocities of 30 – 100 km s^{-1} [11]. In the experiments, apart from other results, it was shown that MP mass composition could be determined from the spectrum of the impact-produced plasma ions. Special-purpose mass spectrometers were developed to study the MP mass and isotopic compositions in space “in situ” experiments; the impact plasma generated during a HVI of a micrometeorite or a dust particle on the target served as the source of ions in these instruments [12]. MP composition in the gas–dust cloud of Halley's comet was first defined by the PUMA and PIA dust-impact instruments on the Vega and Giotto missions [13–15]. The MP collision velocities in these studies reached 80 km s^{-1} , which provided conditions of $V_{\text{sh}} > V_{\text{cr}}$ and $t_{\text{int}} < t_h$.

The most promising experimental direction is associated with laboratory simulations of a HVI using a Q-switched laser [16,17], and is based on its capabilities to generate a light pulse of duration $t_l \sim 1$ – 10 ns and to provide a W of up to $10^{13} \text{ W}\cdot\text{cm}^{-2}$ in 10^2 – $10^3 \mu\text{m}$ \varnothing spot. The processes that arise in kinematic and laser impacts can much differ in simulations of this class [17]. But the processes after the plasma generation (adiabatic expansion, cooling, and recombination), must be similar [3]. Our choice of parameters for the laser simulations of impact processes is based on the results obtained in “in situ” dust-impact experiments on the Vega mission [12–14]. According to which, at a impact velocity of $\sim 80 \text{ km s}^{-1}$ for MPs with $\varnothing \sim 0.01$ – $1 \mu\text{m}$ and masses of 10^{-18} – 10^{-12} g , the ionization multiplicity of the plasma ions was $\alpha \sim 1$ and their energy was $E \sim 50$ – 70 eV .

The plasma nature of these ions was confirmed in direct numerical simulations [18] of the mass spectrometric cometary dust measurements made with the PUMA-1 and PUMA-2 instruments. The dependence of the ionization multiplicity and the ion energy on the W for a laser plasma has been adequately studied, e.g. as W increases from 10^9 to $10^{11} \text{ W cm}^{-2}$, the ionization multiplicity for Al increases from 1 to 5 and the particle energy increases from $\sim 100 \text{ eV}$ to 2 keV . Consequently, the energy contribution to the plasma generation can be accurately determined from these parameters. Therefore, a similarity of the physical processes during the plasma expansion should be ensured when choosing the laser parameters. The laser must ensure: 1) the plasma generation, 2) identical parameters of the laser and impact plasmas, i.e. the ionization

multiplicity and the ion energy, and, 3) equal numbers of produced ions or equal plasma-generation volumes for these processes.

First condition constrains the plasma generation time t_i : $t < t_i < t_h$. For a laser with tl in the range 0.1-10 ns, this condition is satisfied with a comfortable margin. For identical plasma parameters, the identical energy contributions must be ensured: at a $W \sim 10^9 \text{ W cm}^{-2}$, the plasma ions will be singly ionized with mean energy $\sim 50\text{--}70 \text{ eV}$, in close agreement with the impact plasma parameters. By varying the W and the laser crater \emptyset , we can reproduce the basic parameters for a given MP \emptyset and velocity [19,20]. The identity of the ion-generation processes in the laser and impact plasmas is evidenced by the fact that such a plasma is used as the source of ions for TOF mass spectrometers, laser [21] and dust-impact [12] ones. The synthesis of molecules or molecular ions during the expansion and cooling of a impact plasma [22, 23] is of great interest in analyzing the synthesis of organic materials at the early evolutionary stage of the Earth, the falling of meteorites, and hypervelocity collisions of dust particles in molecular, interstellar, and gas-dust clouds because of their similarity.

Description of the Experiment

As a basic instrument for our laser simulations of an impact we used the LASMA TOF laser mass reflectron, which is described in [21, 22–26]. Considering the special role of carbon in the organic molecules synthesis [6, 7] and its ability to combine into polyatomic structures, we have used carbon-rich materials (including specially purified carbon) as the target, which also increased the yield probability of the synthesized organic molecules. Singly ionized molecules of methane, acetylene, ethylene, propylene, allene, and carbon polymer $C_N H_M$ -type structures containing from 1 to 40 C atoms and from 1 to 4 H atoms were detected and identified in the highly reproducible mass spectra Fig. 1.

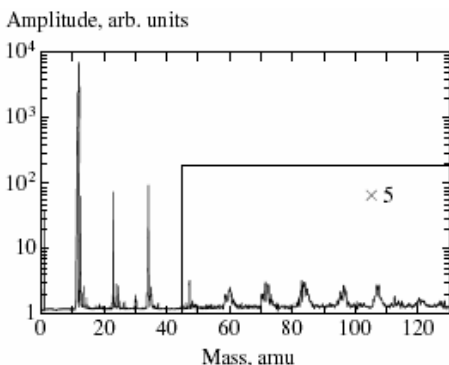


Fig. 1 The mass spectrum of polyatomic ions for a carbon

Subsequently, such hydrocarbon structures and polyatomic molecules were also obtained with other carbon containing materials: industrial carbon, sinking oil fraction, and bitumen. To synthesize more complex organic molecules containing the basic gas-forming elements H, C, N, and O, we carried out a series of experiments in which pure inorganic materials containing these elements were mixed with a carbon powder. The NH_4NO_3 , $\text{Ni}(\text{NO}_3)_2$, Ti_2O_3 , and NaNO_3 materials were

used in order to synthesize and detect the organic molecules that could be used in the natural synthesis of amino acids or biopolymers. To detect molecular peaks, we examined those areas of the mass scale where there were no peaks from the elements or where atypical strong violations of the isotopic ratios were observed (Fig. 2).

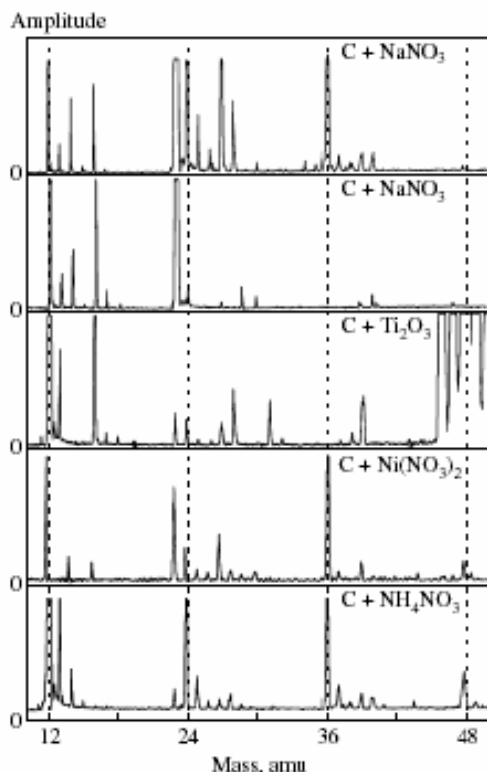


Fig. 2 The mass spectra for the targets containing a mixture of a carbon powder with the various salts and oxides.

C powders as well as W and C powders. In these mixtures, the synthesis of polyatomic molecules containing Si and C or W and C at the powder mixing stage can be ruled out. We detected the mass peaks of polyatomic ions shown in Fig. 3 that correspond Sim^+ to up to $m = 11$ and, $SimCn^+$, $SimCnHp^+$ where m was varied from 1 to 7 and n and p were varied from 1 to 3. Ions WC, WC_2 , WC_3 , and W_2C were also obtained in this series of experiments. The presence of these ions can be explained only by their synthesis in a plasma.

Thus, our laser simulations of a HVI showed that organic compounds could be synthesized from inorganic materials. For most of the experiments $W \sim 10^9 \text{ W cm}^{-2}$ for a laser spot $\varnothing \sim 30\text{--}50 \mu\text{m}$. Hence, the parameters of the generated plasma were identical to those of the impact plasma at a MP velocity of 80 km s^{-1} and a \varnothing of $5\text{--}10 \mu\text{m}$.

In this series of experiments, together with the peaks of the atomic ions of H, C, N, O, Na, Ti, Ni and the above C_N -type carbon structures, we obtained the mass peaks corresponding to the NH_3 , OH^+ or NH^+ , H_2O^+ or NH_4^+ , H_3O^+ , CO^+ , N_2^+ molecular ions using the amino acids that were synthesized in the laboratory for the first time [29, 30]. The combination of these materials with hydrocarbons could primarily provide the synthesis of organic materials whose mass peaks were also observed experimentally: CH_2NH^+ ($m = 29$), H_2CO^+ ($m = 30$), $C_2H_2O^+$ ($m = 42$), $HNCO^+$ ($m = 43$), $NHCHO^+$ ($m = 44$), and $CH_2O_2^+$ ($m = 46$). We cannot rule out the possibility that some of these mass peaks also include the N_2O^+ , NO_2^+ , CO^+ materials of the same mass whose contributions could not be determined here. To confirm the plasma nature of the polyatomic ions, we carried out an experiment in which a laser acted on a mixture of Si and

Amplitude, arb. units.

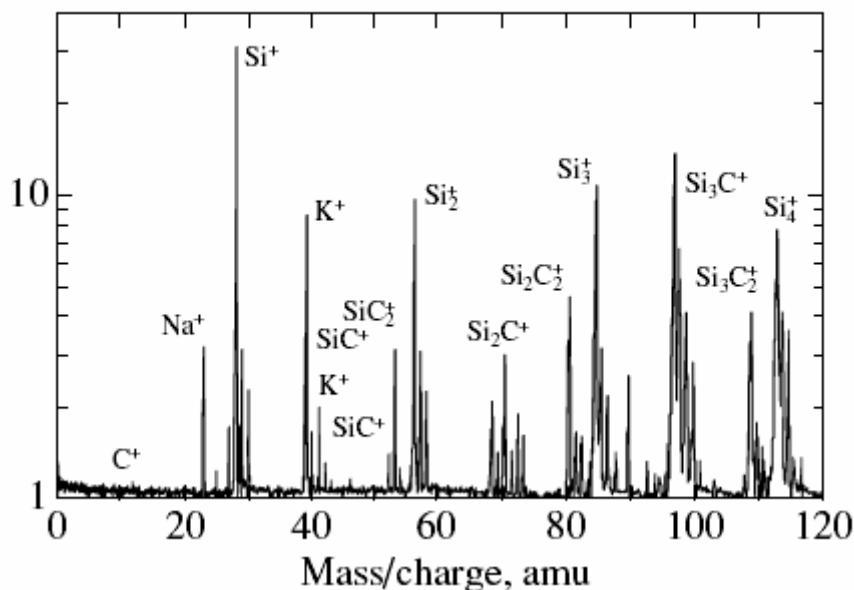


Fig. 3 The mass spectrum for polyatomic ions of a mechanical mixture of C and Si powders.

Discussion

Let us consider the most important results and compare them with the data obtained by other authors. In [31,32], the laser-produced fullerenes and metallofullerenes were controlled with a mass spectrometer. However, the experiments with two-component powders most clearly show the plasma nature of the produced molecular ions. In this case, the plasma torch is the most likely area of the combination of the components to form more complex two-component molecules.

Therefore, it follows from our results and the results of other authors that laser simulations of HVIs allow the impact-plasma processes, including the plasma expansion, to be reproduced, and molecular ions can be synthesized in such a hot, nonequilibrium medium. Below, we use the results of our simulations to consider the two most important processes associated with the synthesis of organic molecules on Earth at the early stage of its formation and in interstellar gas-dust clouds. Let us first consider the possible abiogenic synthesis of organic compounds on Earth in impacts during meteorite showers. In work [5] is presented data on the energy sources for the chemical evolution at the early stage of the Earth's formation, where meteorite impacts flux is estimated to be $\sim 10^{22}$ eV m⁻² year⁻¹. This value is comparable to an analogous value for an X-ray contribution and the input of cosmic rays, which were recognized to be highly efficient energy sources for the formation of organic compounds.

Let us consider an alternative possibility of the impact synthesis of molecules, including organic molecules in the interstellar medium. In recent years, organic compounds, among which HCN, CH₂NH, and CH₃NH known as the source material for the formation of amino acids [7], have been discovered and identified in molecular gas–dust clouds by radioastronomical methods. Two processes are currently believed to be responsible for the formation of molecules: chemical association reactions in a gaseous medium and particle surface reactions in clouds [9]. Although the collisions of dust particles are a major mechanism of their destruction [10], and about 10% of the dust particles can be destroyed [34] during a HVI, molecules and polyatomic ions can be synthesized in these processes. We compared the chemical composition of the polyatomic ions produced in our simulations with that of the molecules and polyatomic ions detected in interstellar gas–dust clouds and considered only molecules containing C, N, O, H, and Si, ~45% of the obtained by us ions were also observed as ions and molecules in molecular clouds [38].

These results led to the assumptions: 1) the material from which the planets were formed could initially be enriched in the organic molecules synthesized through HVIs. It may well be that the SS was also formed from matter enriched in organic material; 2) organic materials could also be intensely synthesized in HVIs on Earth at the early stage of its evolution and be accumulated on the surface, being shielded from the decomposition under radiation by the layer of rock ejected from an impact crater. Consequently, the synthesis of organic materials could begin much earlier, even before the appearance of a dense atmosphere and liquid water.

Currently, an important and independent experimental confirmation of our concept has been found [39]. The mass spectra of the dust-impact experiments revealed hitherto noninterpreted mass peaks of the rhodium carbide dimmer obtained during the impact of a carbon-containing MP moving at a velocity of about 16 km s⁻¹ on a target of pure rhodium. Analysis of published papers suggests that no experimental or theoretical studies of the synthesis of organic materials in the plasma of a HVI had been carried out previously. Such studies have been performed only in terms of laser simulations of this process in [3, 22, 23, 40] and in this paper.

References

- [1] Ya. B. Zel'dovich and Yu. P. Razer, *Physics of Impact Waves and High-Temperature Hydrodynamic Phenomena*, 1966.
- [2] J.F. Friichtenicht and J.C. Slattery, *Ionization Associated with Hypervelocity Impact*, NASA TN D-2091, 1963.
- [3] G. G. Managadze, Preprint No. PR-2037, IKI RAN (Space Research Inst., RAS, Moscow), 2001.
- [4] R. Z. Sagdeev, G. G. Managadze, A. V. Tur, and V. V. Yanovskioe, in *Proceedings of International Conference on the FOBOS Project*, 1986, 129.
- [5] K. Kobayashi and T. Saito, in *The Role of Radiation in the Origin and Evolution of the Life*, 2000, 25.
- [6] H. J. Goldschmidt and T. Owen, *The Search for Life in the Universe*, 1983.

- [7] S. Miller and L. Orgel, *The Origins of Life on Earth*, 1974.
- [8] L. Spitzer, Jr., *Physical Processes in Interstellar Medium*, 1981.
- [9] N. G. Bochkarev, *Fundamentals of Physics of the Interstellar Medium*, 1992.
- [10] A.M. Tielens, C.F. McKee, G.G. Seab, and D.J. Hollnbach, *Astrophys. J.* 1994, 431, 321.
- [11] E.M. Drobyshchevski, B.G. Zhukov, V.A. Sakharov, et al., *Int. J. Impact Eng.* 1995, 17, 285.
- [12] J. Kissel, R. Z. Sagdeev, J. L. Bertaux, et al., *Nature*, 1986, 321 (6067), 280.
- [13] D. A. Mendis, in *Exploration of Halley's Comet*, 1988, 939.
- [14] R. Reinhard, in *Exploration of Halley's Comet*, 1988, 950.
- [15] R. Z. Sagdeev, J. Kissel, E. N. Evlanov, et al., *Astron. Astrophys.* 1987, 187, 179.
- [16] K. Hornung, Yu. G. Malama, and K. Thoma, *Adv. Space Res.* 1996, 17 (12), 77.
- [17] V. V. Kostin, V. E. Fortov, I. K. Krasnyuk, et al., *Teplofiz. Vys. Temp.* 1997, 35, 962.
- [18] E.N. Avronin, N.N. Anuchina, V.V. Gadzhieva, et al., *Fiz. Goreniya Vzryva* 1996, 32, 117.
- [19] G. G. Managadze and I. M. Podgornyi, *Geomagn. Aeron.* 1968, 8, 609.
- [20] G. G. Managadze and I. M. Podgornyi, *Dokl. Akad. Nauk SSSR* 1968, 180, 1333
- [21] G. G. Managadze and I. Y. Shutyaev, in *Laser Ionization Mass Analysis*, Chem. Anal. Ser., 1993, 124, 505
- [22] G.G. Managadze, W.B. Brinckerhoff, A.E. Chumikov Molecular synthesis in hypervelocity impact plasmas on the primitive Earth and in interstellar clouds, *Geoph. Res. Lett.*, 2003, 30(5), 1247.
- [23] G.G. Managadze. The Synthesis of organic molecules in a laser plasma similar to the plasma that emerges in hypervelocity collisions of matter at the early evolutionary stages of the Earth and in interstellar clouds, *J. Exper. & Teoret. Phys.*, 2003, 97(1), 49.
- [24] G. G. Managadze and N. G. Managadze, *Zh. Tekh. Fiz.* 1999, 69(10), 138 [*Tech. Phys.* 1999, 44, 1253].
- [25] G. G. Managadze and N. G. Managadze, Preprint No. Pr- 1962, IKI RAN (Space Res. Inst, RAS), Moscow, 1997, 22.
- [26] W.B. Brinckerhoff, G.G. Managadze, R.W. McEntire, et al., *Rev. Sci. Instr.* 2000, 71, 536.
- [27] G. G. Managadze, RF Patent No.1732396 (1992), *Invention Bulletin*, 1992, 17.
- [28] G.G. Managadze and N.G. Managadze, RF Patent No.2096861, *Invent. Bulletin* 1997, 32.
- [29] H. C. Urey, *Proc. Natl. Acad. Sci. USA* 1952, 38, 351.
- [30]. S.L. Miller, in *Mineral Deposits and Involution of the Biosphere*, 1982, 155.
- [31] R. Zhang, Y. Achiba, J. K. Fisher, et al., *J. Phys. Chem.*, 1999, 103, 9450.
- [32] L. Laska, J. Krasa, L. Juha, et al., *Carbon*, 1996, 34, 363.
- [33] C. Sagan and B. N. Khare, *Science*, 1971, 173, 417.
- [34] L. M. Mukhin, *Nature*, 1974, 251, 50.
- [35] T. Matsu and Y. Abe, *Nature*, 1986, 319, 303.
- [36] S. L. Miller and H. C. Urey, *Science*, 1959, 130, 245.
- [37] A. Bar-Nun, N. Bar-Nun, S. H. Bauer, and C. Sagan, *Science*, 1970, 168, 470.
- [38] V. S. Strel'nitskioe, in *Small Soviet Encyclopedia: Physics of Space*, 1989, 415.
- [39] M. Stubig, R. Srama, E. Grun, and G. Schafer, in *Proc. of 27th Gen. Assem. of the European Geophysical Society, Nice 2002*, Abstract EGS02-A-01364, 274.
- [40] G. G. Managadze, *Geophys. Res. Abstr.*, 2001, 3, 7595.

INTRAMOLECULAR INTERACTIONS BETWEEN NON-BONDED ATOMS IN THIAZOLIDINE DERIVATIVES AND CHEMICAL REACTIVITY

R. Marković,^{1,2,*} A. Rašović² and S. Jovetić³

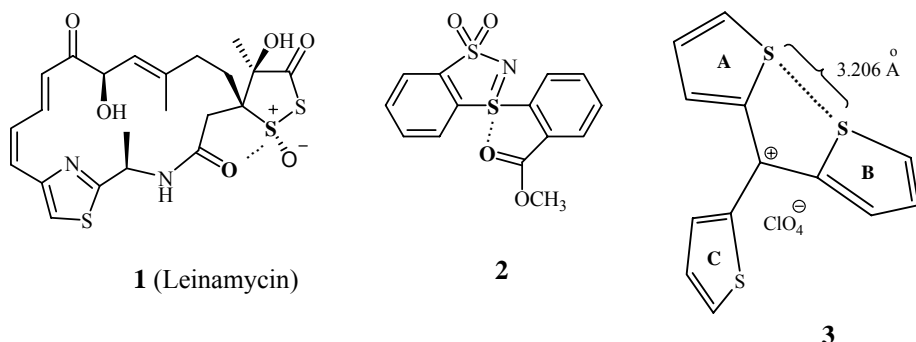
¹Faculty of Chemistry, University of Belgrade, P.O.Box 158, Belgrade,

²Center for Chemistry, ICTM, P.O.Box 815, Belgrade,

³Department of Chemistry, Faculty of Sciences, University of Novi Sad, Trg D. Obradovića 3, 21000 Novi Sad, Serbia and Montenegro

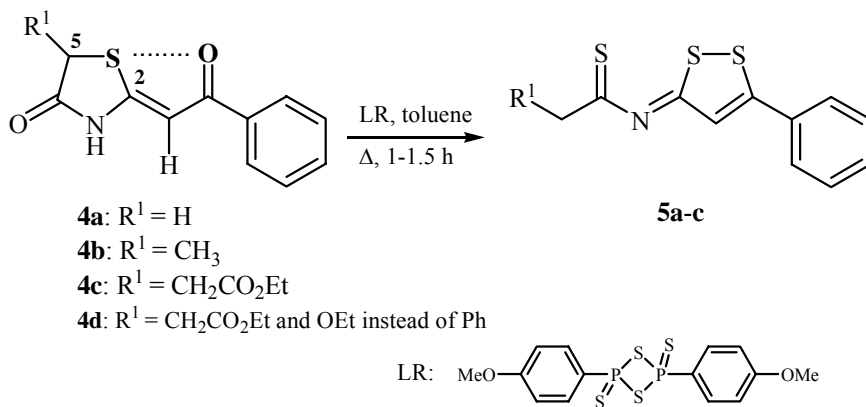
Introduction

An intramolecular sulfur-oxygen non-bonded interaction has attracted much interest over the years on account of controlling the structural and spectroscopic properties of organosulfur compounds, as well as their chemical reactivity. As amply documented by the series of papers [1-7], the intramolecular S...O distance in a large number of compounds, exemplified by structures **1-2**, is much shorter, being even as low as 2.03 Å, than the sum of their van der Waals radii (3.22 Å). Therefore, attractive through-space non-bonded S...O interaction forces S atom in antibiotic Leinamycin (**1**) to adopt a distorted trigonal bipyramidal geometry (S...O distance: 2.810 Å) [1]. In the cyclic *N*-sulfonyl sulfilimine **2** the close S(IV)...O (carbonyl) distance (2.68 Å) influences its conformation, having almost linear N=S(IV)...O array (171°) [2]. With emphasis on the sulfur-sulfur interaction, structure **3** depicts the non-equivalence of the three thiophene rings **A**, **B** and **C** and consequently tris(2-thienyl)methyl perchlorate crystallizes as a statistically disordered racemate [3]. Again the distance indicated in tris(2-thienyl)methyl cation **3** between the sulfur atoms in the rings **A** and **B** is 0.4 Å shorter than the sum of the van der Waals radii of sulfur.



The rationale for the presence of the three non-identical heterocyclic rings and therefore the formation of the stable asymmetric molecule **3** is attributed to a delocalization over a conjugated polymethine unit possessing 12 electrons distributed over 11 atoms, and attractive intramolecular S...S interaction.

These observations initiated our experimental study on the chemical reactivity of (*Z*)-2-alkylidene-4-oxothiazolidines **4** (Scheme 1) to assess the influence of close contacts involving indicated the non-bonded sulfur and oxygen atoms on the course of the reactions of **4** with Lawesson's reagent [LR: 2,4-bis(4-methoxyphenyl)-1,2,3,4-dithiadiphosphetane 2,4-disulfide]. Thus, in this paper we describe the remarkable effect which heteroatoms, i.e., sulfur and oxygen lying in the 1,5-positions, exert on an efficient ring opening-closing rearrangement of cyclic β -enamino ketones **4** to highly functionalized 1,2-dithioles **5**.



Scheme 1

Experimental

(*Z*)-2-Alkylidene-4-oxothiazolidines **4a-c** and rearranged products **5a-c** were synthesized according to the general procedures reported previously [8-10]. For typical model compounds **4d** and **5c** the following data are pertinent.

Ethyl (*Z*)-(5-ethoxycarbonylmethyl-4-oxothiazolidin-2-ylidene)ethanoate (4d**)** was obtained as a white solid in 54% yield (3.47 g) from 4.98 g (24.2 mmol) of diethyl mercaptosuccinate and 2.74 g (24.2 mmol) of ethyl cyanoacetate: mp 105-106 °C; IR (KBr): ν_{\max} 3188, 3122, 3079, 2985, 1739, 1722, 1691, 1605, 1474, 1380, 1298, 1196, 1144, 1093, 1029, 817, 725, 676 cm^{-1} ; 1H NMR (200 MHz, $CDCl_3$): δ 1.28 (6 H, t, 2 CH_3 , $J = 7.2$ Hz), 2.93 (1 H, dd, H_A , $J_{AB} = 17.3$ Hz, $J_{AX} = 8.5$ Hz), 3.13 (1 H, dd, H_B , $J_{AB} = 17.3$ Hz, $J_{BX} = 4.1$ Hz), 4.19 (4 H, q, 2 CH_2O , $J = 7.2$ Hz), C(5)-H signal buried below the quartet centered at δ 4.19, 5.59 (1 H, s, =CH(2')), 9.35 (1 H, s, NH); ^{13}C NMR (50.3 MHz, $DMSO-d_6$): δ 14.16, 14.54, 36.50, 42.61, 59.29, 60.87, 88.86, 157.84, 167.24, 170.42, 175.41; Mass spectrum (EI) m/z (rel. intensity): 273 (M^+ , 11), 227 (46), 182 (22), 154 (100), 127 (14), 87 (15), 68 (15), 55 (21). Analytically pure sample was obtained by crystallization of the isolated solid from a 4:1 ethanol/water solvent mixture. Anal. Calcd for $C_{11}H_{15}NO_5S$: C, 48.30; H, 5.52; N, 5.12; S, 11.73. Found: C, 48.12; H, 5.35; N, 5.36; S, 11.95;

Ethyl 3-(5-phenyl-[1,2]dithiol-3-ylideneethiocarbamoyl)propanoate 5c

From **4c** (52 mg, 0.17 mmol) in toluene (4 mL) and LR (70 mg, 0.17 mmol) after column chromatography (toluene/EtOAc 3:1 to 1:1) the 1,2-dithiole **5c** was isolated; yield 53 mg (92 %); mp 65 °C. IR (KBr): ν_{\max} 1730, 1512, 1483, 1450, 1426, 1401, 1375, 1305, 1177, 1157, 1107, 1049, 1015, 945, 867, 830, 760, 687 cm^{-1} ; ^1H NMR (CDCl_3): δ 1.26 (3H, t, $J=7.2$ Hz, CH_3), 2.92 (2H, t, $J=7.3$ Hz, $\text{CH}_2\text{-CO}$), 3.40 (2H, t, $J=7.3$ Hz, $\text{CH}_2\text{-CS}$), 4.17 (2H, q, $J=7.0$ Hz, $\text{CH}_2\text{-O}$), 7.41-7.53 (3H, m, *m*- and *p*-Ph), δ 7.78-7.87 (2H, m, *o*-Ph), 8.37 (1H, s, =CH); ^{13}C NMR (CDCl_3): δ 14.7 (CH_3), 32.9 ($\text{CH}_2\text{-CO}$), 37.5 ($\text{CH}_2\text{-CS}$), 60.6 ($\text{CH}_2\text{-O}$), 126.4 (=CH), 127.4 (*o*-Ph), 129.1 (*m*-Ph), 131.1 (*p*-Ph), 136.0 ($\text{C}_{\text{ipso}}\text{-Ph}$), 172.2 (CO_{ester}), 177.5 ($\text{C}=\text{C-S}$), 187.4 ($\text{N}=\text{C-S}$), 201.9 ($\text{C}=\text{S}$); MS (EI): m/z (rel.intensity): 337 (M^+ , 38), 304 (65), 277 (7), 264 (8), 236 (100), 211 (15), 194 (10), 178 (20), 145 (38), 117 (73), 102 (33), 71 (45), 55 (65); UV (DMSO): λ_{\max} (ϵ) 332.6 nm (15.990) and 446.1 nm (12.720). Anal. calcd for $\text{C}_{15}\text{H}_{15}\text{N O}_2\text{S}_3$: C, 53.39; H, 4.48; N, 4.15; S, 28.50; Found: C, 53.15; H, 4.45; N, 4.24; S, 27.97.

Results and Discussion

A complete understanding of the structures and physicochemical properties of thiazolidines **4** is necessary in order to get the insight into their reactivity toward LR and other reagents. In preceding papers [8-10] we reported the preparation of stereodefined (*Z*)-5-substituted thiazolidinone derivatives **4** and new derivatives thereof, which have been of considerable interest due to (i) their possible biological activity [11], (ii) utility as organic intermediates for the synthesis of push-pull polyenes [12], and (iii) their role as an excellent model to study the hydrogen bonding interactions found in structurally related biochemical systems [13].

Figure 1 shows a perspective view of the solid-state structure for a model compound **4d** of the thiazolidine series **4** as obtained by the X-ray diffraction [9]. The tautomeric enamine form was definitively determined by location and refinement of the NH hydrogen. The central thiazolidinone ring is planar (mean deviation from planarity = 0.014 Å, maximum deviation 0.023 Å). The molecular packing is controlled by intermolecular hydrogen bonds between the NH group and the C4 carbonyl of an adjacent molecule related by a crystallographic two-fold screw axis [$\text{H3}\cdots\text{O41} = 2.00(3)$ Å; $\text{N3}\cdots\text{O41} = 2.765(2)$ Å; $\text{N3-H}\cdots\text{O41} = 165(2)^\circ$]. The X-ray analysis of derivative **4d** proved the *Z*-configuration of the double bond. The C2 side chain is also essentially coplanar with the five-membered ring which brings O21 into close proximity with the sulfur atom ($\text{O21}\cdots\text{S1} = 2.873(2)$ Å). This distance is less than the sum of the van der Waals radii (3.22 Å), but greater than that previously observed in similar thiazolidinones. In other words, thiazolidine derivatives **4** containing the $\text{S-C}(\text{sp}^2)\text{-C}(\text{sp}^2)\text{-C}(\text{sp}^2)=\text{O}$ moiety with the *cis*-configuration of the C-C double bond, exhibit typical 1,5-intramolecular $\text{S}\cdots\text{O}$ interaction.

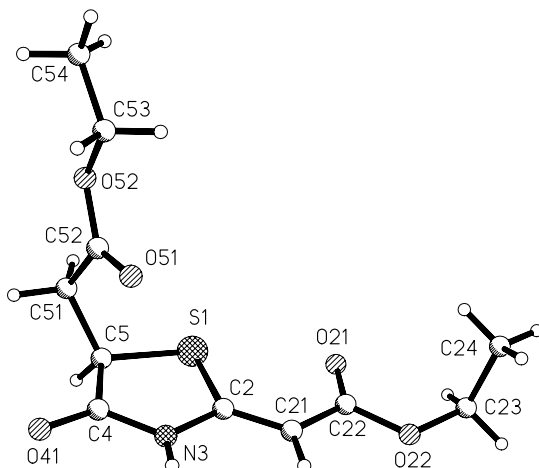
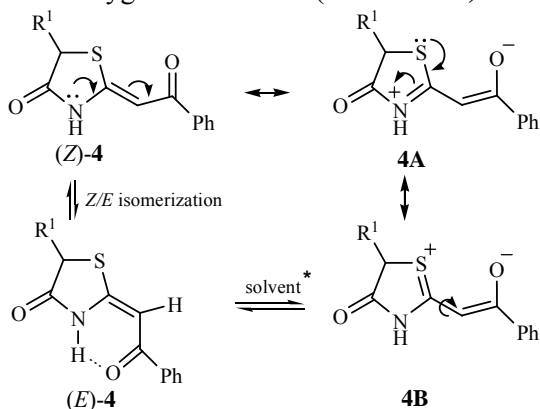


Figure 1. Perspective view of ethyl (*Z*)-(5-ethoxycarbonylmethyl-4-oxothiazolidin-2-ylidene)ethanoate (**4d**), showing the crystallographic numbering scheme.

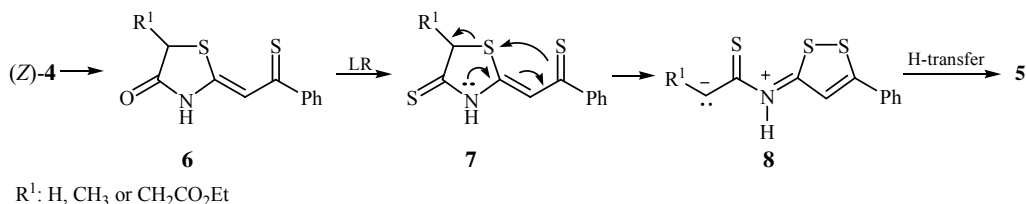
As Csizmadia and Kucsmán demonstrated [7], the stability of the numerous molecular arrangements of such type with short $S\cdots O$ distances, is additionally enhanced by the contribution of charged species. The directed n, π -conjugation of the push-pull unit consisting of two electron donors (NH and -S-), the intervening $C=C$ bond, and an electron acceptor ($C=O$), is outlined in Scheme 2, implicating, among other properties of thiazolidines **4** (reduced double bond character of the exocyclic $C=C$ bond, the *Z/E* isomerization, inter- and intramolecular and hydrogen bonding etc.), the strong electrostatic sulfur-oxygen interactions (structure **4B**).



* (*Z*)-**4** major form in polar solvents (DMSO, acetone, EtOH)
 (*E*)-**4** major form in nonpolar solvents (CHCl₃, toluene)

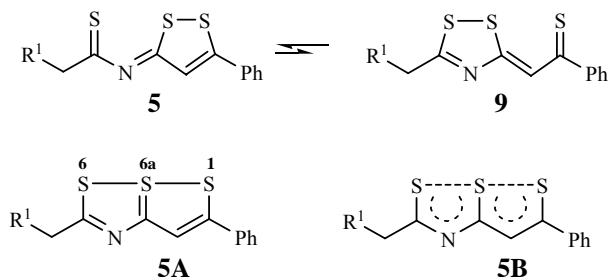
Scheme 2

The formation of sole product **5** from (*Z*)-**4** and LR occurs in a highly regioselective fashion. The plausible mechanism is as follows (Scheme 3). First, the reaction of (*Z*)-configured thiazolidine **4** with LR generates a key intermediate **7** via the transient thioxo derivative **6**. The latter was isolated in 40% yield as a main product in a separate reaction performed under far milder conditions [14]. Based on the results from the X-ray structure analysis of the model compound **4d** we may assume that if the carbonyl oxygen is replaced by a sulfur atom, then the non-bonded S...S distance in the intermediate **7** should stay close to the original value of 2.873(2) Å for the S...O distance. The distance is approximately 0.75 Å shorter than the corresponding van der Waals distance. The significant shortening of the non-bonded distance promotes close 1,5-contact between the two sulfur atoms. Subsequently, through-bond S-S interaction initiates an intramolecular rearrangement by concerted thioxothiazolidine ring opening-1,2-dithiole closing process and H-transfer (steps **7**→**8**→**5**).



Scheme 3

The MS, UV, ^1H and ^{13}C NMR spectroscopic data are in good agreement with the 1,2-dithiole structures **5a-c**. However, as discussed in a comprehensive review by N. Lozac'H [15], compounds of that type could exist in a solution as a non-degenerate valence tautomers **5** and **9** in a fast equilibrium, or as a 1,6,6a λ^4 -trithiaazapentalenes **5A** containing an internal hypervalent sulfur atom [16]. Formula **5B**, depicting partial bonding between the sulfur atoms, is another acceptable representation of this trisulfur bicyclic ring system [16-19].



A single-crystal X-ray analysis confirmed the azapentalene structure (formulae **5A** or **5B**; $\text{R}^1 = \text{CH}_2\text{CO}_2\text{Et}$) for the product **5c** obtained by the ring opening-closing of **4c** with Lawesson's reagent (Fig. 2).

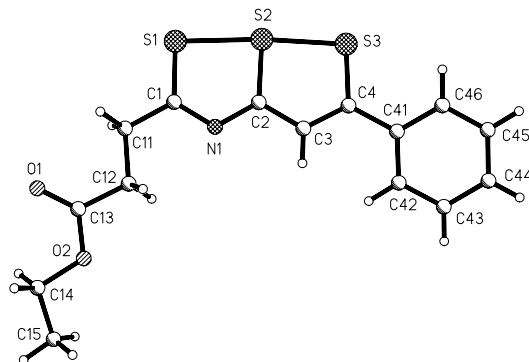


Figure 2. Solid-state structure for compound **5c** as established by X-ray diffraction with atom numbering-scheme for non-hydrogen atoms. Selected bond lengths: S(1)-S(2) 2.3623(7), S(2)-S(3) 2.2905(7), S(1)-C(1) 1.7003(16), S(2)-C(2) 1.7567(16), S(3)-C(4) 1.7047(17), N(1)-C(1) 1.314(2), N(1)-C(2) 1.351(2), C(2)-C(3) 1.398(2), C(3)-C(4) 1.370(2), C(4)-C(41) 1.478(3) Å. Bond angles: S(3)-S(2)-S(1) 175.44(2), C(2)-S(2)-S(3) 89.13(6), C(2)-S(2)-S(1) 86.66(6), C(4)-S(3)-S(2) 95.07(6), N(1)-C(1)-S(1) 121.50(13), C(11)-C(1)-S(1) 119.03(12), N(1)-C(2)-S(2) 122.25(13), C(3)-C(2)-S(2) 118.38(13), C(4)-C(3)-C(2) 121.55(15), C(3)-C(4)-S(3) 115.86(13)°.

From the data above it is apparent that, in addition to the nearly linear S(1)-S(2)-S(3) array (175°), the two S-S bonds, being 2.36 and 2.29 Å, respectively, are not of exactly equal length as the structures of the two fused rings differ. The computed sulfur-sulfur single bond length in a *cis* planar disulphide group is 2.08 Å [15] and accordingly, the order of this bond is 1. Based on a correlation between the bond order and bond length, obviously the assumed bond order in the solid state structure **5A** and in analogous trithiapentalenes is lower than 1 [15-19].

Conclusion

In summary, it appears from this investigation that X-ray diffraction data correspond to azapentalene-type structure **5A** ($R^1 = \text{CH}_2\text{CO}_2\text{Et}$) with central hypervalent sulfur atom, whereas the spectroscopic data for the rearranged product in solution support the existence of **5A** and the dominating 1,2-dithiole type structure **5c** which are in a continuous equilibrium. The potential of the directional non-bonded interactions to induce incipient stage of chemical reactions, has also been demonstrated for the parent thiazolidine system undergoing the rearrangement in the presence of Lawesson's reagent.

References

- [1] S. Wu and A. Greer, *J. Org. Chem.*, 2000, 65, 4883.
- [2] J. Rábai, I. Kapovits, I. Jalsovszky, Gy. Argay, V. Fülöp, A. Kálmán and T. Koritsánszky, *J. Mol. Struct.*, 1996, 382, 13.

- [3] T. Varea, M. Medio-Simón, B. Abarca, R. Ballesteros, G. Asensio, S. García-Granda, E. Pérez-Carreño and F. Gómez-Beltrán, *Chem. Commun.*, 1993, 1476.
- [4] I. P. Csonka, G. Vass, L. Szepes, D. Szabó and I. Kapovits, *J. Mol. Struct. (Theochem)*, 1998, 455, 141.
- [5] G. D. Markham and C. W. Bock, *J. Mol. Struct. (Theochem)*, 1997, 418, 139.
- [6] D. Britton and J. D. Dunitz, *Helvetica Chimica Acta*, 1980, 63, 1068.
- [7] J. G. Ángyán, R. A. Poirier, Á Kucsman and I. G. Csizmadia, *J. Am. Chem. Soc.*, 1987, 109, 2237 and references cited therein.
- [8] R. Marković, M. Baranac and S. Jovetić, *Tetrahedron Letters*, 2003, 44, 7087.
- [9] R. Marković, M. Baranac, Z. Džambaski, M. Stojanović and P. Steel, *Tetrahedron*, 2003, 59, 7803.
- [10] R. Marković and M. Baranac, *Heterocycles*, 1998, 48, 893.
- [11] S. P. Singh, S. S. Parmar, K. Raman and V. I. Stenberg, *Chem. Rev.*, 1981, 81, 175.
- [12] R. Marković, M. Baranac and Z. Džambaski, *Heterocycles*, 2004, 63, 851.
- [13] R. Marković, A. Shirazi, M. Baranac, Z. Džambaski and D. Minić, *J. Phys. Org. Chem.*, 2004, 17, 118.
- [14] R. Marković, A. Rašović and S. Jovetić, Manuscript in preparation.
- [15] N. Lozac'H, *Comprehensive Heterocyclic Chemistry*; editor K. T. Potts; Pergamon: Oxford, 1984, 6, 1049.
- [16] M. Yokoyama, T. Shiraishi, H. Hatanaka and K. Ogata, *Chem. Commun.*, 1985, 1704.
- [17] K. T. Potts, S. A. Nye and K. A. Smith, *J. Org. Chem.*, 1992, 57, 3895.
- [18] C. Th. Pedersen and C. Lohse, *J. Chem. Soc., Perkin Trans.* 1977, 1, 994.
- [19] A. Hordvik, E. Sletten and J. Sletten, *Acta Chem. Scand.*, 1969, 23, 1377.

DECOHERENCE: THE OCCURRENCE AND CONTROL

M. Dugić

Department of Physics, Faculty of Science, Kragujevac, Serbia and Montenegro

Abstract

We briefly outline the fundamentals of the decoherence theory along with the interest in the theory in the different areas of modern science. An emphasis has been placed on the subtleties of the occurrence of the decoherence process (effect), and particularly on the task of avoiding decoherence. This way emerges a need for the cross-disciplinary research work on both theoretical and experimental issues of the decoherence theory.

Introduction

The so-called *decoherence process (effect)* is a quantum mechanical process that refers to the *open quantum systems*, which are in interaction with their environments. In contrast to the isolated quantum systems, whose dynamics is governed by the Schrodinger law, the open systems experience the stochastic (non-unitary), effectively irreversible dynamics. Typically, the decoherence effect occurs in the very short time intervals. It is therefore not for surprise that significant progress in the field falls within the last 20 years approximately [1-12]. Decoherence theory is at the heart of modern quantum mechanics of open systems that deals with the complex (e.g., many particle) systems bearing variety of methods and approaches in describing the dynamics of the open quantum systems. The lack of the general law governing dynamics of the open systems exhibits the difficulties of both physical and mathematical nature in this regard.

In this paper, we put an emphasis on the *subtleties* concerning the occurrence of decoherence, and particularly to the issue of *avoiding decoherence*.

What is “decoherence”?

In order to build some intuition, we omit the technical details and we make use of an illustration.

In Fig. 1a, we give the typical plot of the interference experiment, e.g. of the famous Young two-slit interference experiment in optics. The plot is characterized by the sharp contrast of the neighbor (local) maximums and minimums. Physically, this plot refers to a unique wave process (“wave”) in front of the screen. In Fig. 1b, we describe the same situation yet assuming existence of *external action* on the electromagnetic (EM) field in front of the screen. *Due to the external action*, the interference pattern is *lost*--as obvious from the loss of the contrast in Fig. 1b; by I , we denote the light intensity on the screen.

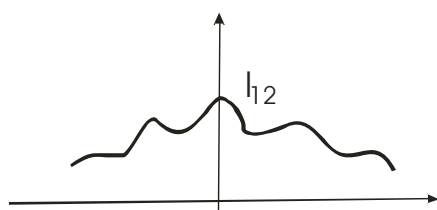


Fig. 1a

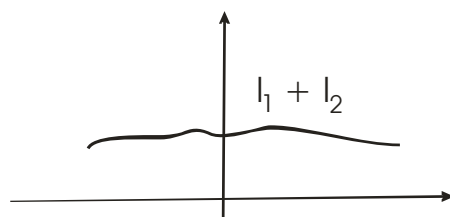


Fig. 1b

Physically, and *in analogy with the decoherence process*, the transition from Fig. 1a to Fig. 1b gives rise to the following change of the EM field in front of the screen: the initial (unique) wave *has split into*, e.g., the two, *mutually distinguishable* and *objectively present* (non-interfering), *simultaneously propagating* waves in front of the screen. In other words: the *implicitly present* (mutually interfering) waves (Fig. 1a) *objectively appear* (Fig. 1b) due to the *external action* (influence) exerted on the system (EM field in front of the screen).

This effect is similar to the process of quantum measurement that--based on distinguishability of the outcomes--*breaks initial coherence* in the system (*DE*coheres the system). Nowadays, we understand that the decoherence process is responsible also for the effect of quantum measurement [1]. Furthermore, we learned that the *environment* (that is responsible for the “external action” on the (open) system) acts on the system very much like the “measurement instrument” acts on the object of quantum measurement. This striking effect of the loss of coherence (loss of interference in Fig. 1b) bears some even more interesting consequences.

As long as the external action is present, the effect of the loss of coherence (loss of interference as in Fig. 1b) is *objectively present* in the system of interest, with only *tiny probability* of re-establishing the initial coherence (of the initial interference in Fig. 1a). This *robustness of the decoherence effect* (i.e. of the loss of coherence) *reduces the dynamics* of the (open) system into a proper physical-states subspaces that may be described as the “*environment-induced super-selection rules*” [2, 7, 12, 13]. As a consequence, appearance of coherence in the (open) system’s state is *quickly destroyed* by the influence of the environment.

In the terms of Fig. 1 (cf. Appendix A), the external action induces appearance of the (semi-classical) trajectories of the photons--very much like the appearance (from “nowhere”) of a quantum particle’s trajectory in the Wilson chamber. The absence of the external action would give rise to *re-establishing of coherence* (of the interference as in Fig. 1a) as well as of the validity of the Schrodinger law for the system.

What is the decoherence theory useful for?

In this section, we briefly outline the main interest in the decoherence theory.

- *Academic interest.* In his famous lectures, Richard Feynman expressed his sentiment about the “puzzles of quantum mechanics”: *I may say that nobody understands quantum mechanics* [14]. Understanding physics means both interpretation of the physical phenomena as well as expressing oneself when discussing the physical issues. In this regard, the decoherence theory *sharpens* some “puzzles” thus allowing us to be free to claim, e.g., that:

speaking of the definite position and/or momentum of the electron in the hydrogen atom does not make sense.

‘So much about understanding’--one might say. However, this assertion perfectly fits with the Copenhagen school of quantum mechanics [15]: a phenomenon is not phenomenon unless it’s recorded a phenomenon. With such positive (provable) statements under our belts, it is easier to proceed in making a consistent interpretation of quantum mechanics.

- *Some fundamental issues.* The “environment-induced super-selection rules” seem perfectly suited for the purposes of dealing with the problem of the “transition from quantum to classical” [1-8, 12, 13]. Actually, the objective presence of certain qualities of physical systems is exactly what is expected from the macroscopic (classical physics) systems. For instance, the *coherent superpositions* of the different positions of the center-of-mass of a macroscopic body has never been observed--which is the ultimate origin of the *classical-physics determinism and causality*. In this context, the nontrivial observations concerning the quantum measurement as well as ergodicity of the open systems are expected, too, along with the fundamental physical origin of the macroscopic (phenomenological) irreversibility (as well as of the “arrow of time”) [16-18].

As an immediate consequence, one may pose the following question: whether or not avoiding (or at least suppressing, e.g. delaying) the effect of decoherence might help in observing the quantum mechanical behavior of the macroscopic bodies--e.g. quantum mechanically to *teleport* a macroscopic object? It’s really hard to predict the progress of the theory in this regard.

- *Some cross-disciplinary interest.* Decoherence theory investigates the “border territory” between the “quantum” and “classical“. Some *mesoscopic systems* (the atoms-, or molecules- clusters, complex molecules, macromolecules) naturally fall within this “territory”. There already exist some results in this regard concerning, e.g., the molecules’ chirality [19], the macromolecules’ conformations [20], as well as the short-living entangled states in the condensed matter chemistry [21].

On the other side, manipulating the *individual* quantum systems is the “philosopher’s stone” of the emerging fields of *nanotechnology* as well as of the so-called *quantum technology* [22, 23] (and references therein). Finally, investigating decoherence in depth is expected significantly to improve the methods of combating decoherence in

the context of the *quantum information and computation theory*--therein, the quantum coherence is the ultimate information resource [24, 25].

On the occurrence and control of decoherence

The early papers on decoherence (e.g., [1, 2, 4, 5]) point out the fundamental observations on the occurrence of the decoherence effect. However, partly influenced by the quantum measurement theory [26-28], occasionally there appear some non-critical statements producing even some prejudice about the occurrence of decoherence. Some of the recent results challenge this prejudice yet leaving much research work to be done.

Without any details, we emphasize the following (seemingly plausible), non-critically adopted statements in this regard. Usually, it is taken for granted that the decoherence process bears *ubiquitariness*--the effect is supposed to occur virtually independently on the conditions describing the open system and its environment. Then naturally appear the expectations that decoherence is an *unavoidable* as well as *uncontrollable* process--interaction in the composite system is assumed (in general) uncontrollably to occur and therefore unavoidably to produce decoherence. In analogy with the quantum measurement process it is almost generally assumed that the occurrence of decoherence *requires the macroscopic environment*, as well as the *strong interaction* of the (open) system with its environment.

As we show in the sequel, none of these (seemingly plausible) statements should be literally understood.

- *The necessary conditions for the occurrence of decoherence.* It can be shown [13] that the occurrence of decoherence requires rather specific coupling (interaction) in the composite system "system + environment". Actually, in the macroscopic context of the theory [2, 6, 7, 12, 13], the interaction in the composite system should fulfill certain requirements in order to allow the occurrence of decoherence. Thus, one may conclude that the decoherence effect does *not bear ubiquitariness*.

- *Macromolecules spatial interference.* The beautiful experiments on the macromolecules' spatial interference [29, 30] point out another subtlety of the occurrence of decoherence. Actually, naively, one would expect the decoherence of the macromolecules spatial positions and consequently the lack of the spatial interference. This expectation comes from the fact that even the *single molecules* interact with the thermal radiation, which now may play the role of the molecules environment. However, the interference has been observed! The point here is in the fact that decoherence refers to the spatial distances that are by many orders of magnitude larger than the molecule's diameter. The same applies to the constant d of the diffraction grating, thus allowing the grating to recognize the molecules as the quantum systems. This lesson is fundamental for speculating about the limits of the quantum mechanical behavior of the meso-, macro- objects. It seems that the quest in this regard is in its early stage.

- *The short-living entanglement.* The experiments as well as the theoretical explanation of the anomalous neutron scattering [21] offer another lesson for us. First, it is a beautiful justification of the fundamental interpretation of “entangled states” [27]: the subsystems of a complex quantum system in entangled state do not have the states of their own. Consequently, the standard statistical methods (that assume the definite states of the subsystems--here: of the target protons) simply do not apply--the neutrons do not recognize the single protons, which are mutually entangled. Second, these experiments point out that the decoherence effect *need not be so fast*. This opens another possible route to investigating quantum behavior of the complex systems--“simply” by delaying decoherence.

- *Mesoscopic environment.* The early models of the famous Stern-Gerlach experiment pointed out a fascinating observation: the role of the “measurement instrument” is played by the atom’s center-of-mass system, which, in turn, consists of less than 10^2 particles [31]. In other words: the decoherence underlying this effect [1] is caused by the micro/meso- scopic environment of the number of particles of the order of 10^2 ! A recent analysis [32] of a similar experimental situation justifies this observation as well as offers a proposal for the possible experimental test in this regard. The lesson is rather simple: *either* our understanding of the Stern-Gerlach experiment fails, *or a small environment* is capable of producing decoherence.

- *Avoiding decoherence.* The so called “decoherence-induced suppression of decoherence (DISD)” method offers a model for *avoiding decoherence* [33]. The method employs external control of the open system’s environment (the bath, B), so effectively giving rise to the unitary (Schrodinger-like) dynamics of the open system (S), for the price of renormalization of the system’s Hamiltonian. Actually, in principle, one may design the interaction of B with an external system (directly controlled by experimenter), which effectively plays the role of B ’s environment (E). If the interaction of B and E dominates the composite system’s ($S + B + E$ ’s) dynamics, then for the relatively *long time interval*, the dynamics of S is unitary--as if S were an isolated quantum system! Physically, the interaction of B and E induces *controlled decoherence* of the states of B , effectively freezing the B ’s dynamics for the virtually arbitrarily long time interval. However, for the literally arbitrarily long time intervals, there occur entanglement between S and E that may induce decoherence of S , despite the fact that these two subsystems are not in the direct mutual interaction. Fortunately enough, formation of entanglement in the system $S + E$ becomes effective only after the very long time intervals thus giving rise to every subsystem (S, B, E) to bear its *own quantum state* in this period of time.

To this end, the two remarks are in order.

First, *prima facie*, it might seem that decoherence is still present, although only delayed--not avoided. In respond to this objection, we emphasize: for the open systems dynamics, everything is a matter of the “interplay between the time axes” for the different processes. For instance, in the situation in which the position of a body of the

mass 1g decoheres in the interval of the order of 10^{-23} s, a single electron *experiences decoherence* in 10^4 s—the later is usually considered as the *absence of decoherence* [3]. Second, the DISD method naturally and straightforwardly model *suppression of entanglement* in a composite system. This effect is considered fundamental for the task of deducing the fundamental physical background of the micro-particles' individuality (e.g. of the ions in a solution) [34] (and references therein). The model [34] offers a basis for the final solution of this fundamental issue of the kinetic theory. Therefore, the DISD method offers a *clue* for dealing with the task of the *decoherence control*, which is a remote goal of the theory, yet.

Conclusion

Recent progress in the decoherence theory highlights how subtle the issue of the occurrence of decoherence actually is. E.g. the decoherence effect does not bear ubiquity, while *not* requiring the macroscopic environment (which should induce the decoherence effect). Finally, a proper control of the (open) system's bath might give rise to (effectively) avoiding decoherence, thus saving the purely quantum behavior of the open systems (e.g. of the individual micro-particles in a solution) for (almost) arbitrarily long time interval. Future progress along these lines requires the cross-disciplinary research on the different kinds of the physical/chemical systems.

References

The Internet resources on decoherence:

- <http://www.decoherence.de>

- <http://physics.kg.ac.yu/Prezentacija/Prezentacije%20zaposlenih/Miroljub%20Dugic/DECOHERENCE/default.htm>

- [1] W.H. Zurek, Phys. Rev. D, 1981, 24, 1516.
- [2] W.H. Zurek, Phys. Rev. D, 1982, 26, 1862.
- [3] W.H. Zurek, Phys. Today, October 1991, 44, 36.
- [4] E. Joos and H. D. Zeh, Z. Phys. B, 1985, 59, 223.
- [5] A.O. Caldeira and A.J. Leggett, Ann. Phys. (NY), 1983, 149, 374.
- [6] D. Giulini et al, 1996, "Decoherence and the Appearance of a Classical World in Quantum Theory", Springer, Berlin.
- [7] M. Dugić, 2004, „Decoherence in the Classical Limit of Quantum Mechanics“ (in Serbian), in press.
- [8] R. Omnes, 1994, "The Interpretation of Quantum Mechanics", Princeton University Press, Princeton.
- [9] M.H. Devoret, J.M. Martinis and J. Clarke, Phys. Rev. Lett., 1985, 55, 1908.
- [10] M. Brune et al, Phys. Rev. Lett., 1996, 77, 4887.
- [11] H. Amann et al, Phys. Rev. Lett., 1998, 80, 4111.
- [12] W.H. Zurek, Prog. Theor. Phys., 1993, 89, 281.
- [13] M. Dugić, Physica Scripta, 1997, 56, 560.
- [14] R. P. Feynman, 1965, Lecture Notes at Cornell University, "The Character of Physical Law".

- [15] N. Bohr, 1961, "Atomic Physics and Human Knowledge", Science Edition, New York.
- [16] P. Grigolini, 1993, "Quantum Mechanical Irreversibility and Measurement", World Scientific, Singapore.
- [17] Cvitanović et al (Eds.), 1991, "Quantum Chaos-Quantum Measurement", Kluwer Academic Publ., Dordrecht.
- [18] H. D. Zeh, 1999, "The Physical Basis of The Direction of Time", Springer-Verlag, 3rd Edition, Berlin.
- [19] G. Jona-Lasino and P. Clavie, Prog. Theor. Phys., Suppl., 1986, 86, 54.
- [20] D. Raković, M. Dugić, M. Plavšić, Materials Science Forum, 2004, 453-454, 521.
- [21] C. A. Chatzidimitriou-Dreismann et al, Phys. Rev. Lett., 1997, 79, 2839.
- [22] G. Milburn, 1997, "Schrodinger's Machines: The Quantum Technology Reshaping Everyday Life", W.H. Freeman & Co., New York.
- [23] M. Dugić, "Quantum Technologies: Quantum Mechanics as Applied Physics", Proceedings of the Scientific Meeting "Applied Physics in Serbia-APS", S. Koićki, N. Konjević, Z. Lj. Petrović and Đ. Bek-Uzarov (Eds.), 27-29 May 2002, Beograd, Jugoslavija, pp. 285.
- [24] M. A. Nielsen and I. L. Chuang, 2000, "Quantum Computation and Quantum Information", Cambridge University Press, Cambridge, UK.
- [25] Китаев А., Шень А., Вьялый, 1999, "Классические и квантовые вычисления", МЦНМО, ЧаРо, Москва.
- [26] J. von Neumann, 1955, "Mathematical Foundations of Quantum Mechanics", Princeton University Press, Princeton.
- [27] B. d'Espagnat, 1976, "Conceptual Foundations of Quantum Mechanics", 2nd ed., Addison/Wesley, Perseus.
- [28] J.A. Wheeler and W.H. Zurek, (Eds.), 1983, "Quantum Theory of Measurement", Princeton University Press, Princeton.
- [29] M. Arndt et al, Nature, 1999, 401, 680.
- [30] L. Hackermüller et al, Phys. Rev. Lett., 2003, 91, 90408.
- [31] D. Bohm, 1951, "Quantum Theory", Prentice-Hall, Englewood Cliffs, New Jersey.
- [32] M. Dugić, European Physical Journal D, 2004, in press.
- [33] M. Dugić, Quantum Computers & Computing, 2000, 1, 102.
- [34] M. Dugić, Europhys. Lett., 2002, 60, 7.

Appendix A

The physical situations referring to Figs. 1a,b are illustrated below.

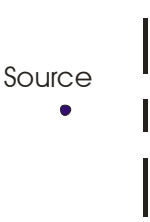


Fig. A1

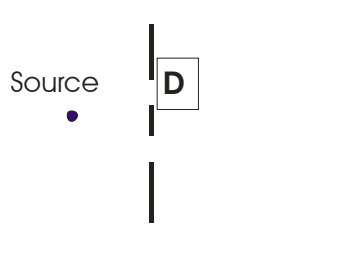


Fig. A2

Fig. A1 refers to Fig. 1a, while Fig. A2 refers to Fig. 1b. Figs. A1,2 represent the sketches of the Young two-slit interference experiment. In Fig. A2, there is the *detector* (of photons' trajectory), **D**, which is described as the “*external action*” in the body text. Detecting the photon's trajectory gives rise to its passage *either* through the slit 1, *or* through the slit 2 on the first screen of the setup. This detection (or, in the macroscopic limit, measurement of the light intensity *on* the slits) *destroys the interference pattern*, thus producing, in an ensemble of photons, the loss of the contrast as in Fig. 1b. Denoting the passage of a *single photon* through the upper slit (slit 1) by the wave function $\psi_1(x)$, and analogously for the lower slit (slit 2) by $\psi_2(x)$, one may write:

$$I_{12}(x) = |\psi_1(x) + \psi_2(x)|^2 \neq |\psi_1(x)|^2 + |\psi_2(x)|^2 = I_1(x) + I_2(x) \quad (\text{A.1})$$

while, of course:

$$\int I_{12}(x) dx = \int (I_1(x) + I_2(x)) dx = I_{\text{Source}} \cdot \quad (\text{A.2})$$

DETERMINATION OF SETSCHENOW SALTING-OUT CONSTANTS OF CATECHOL BY LIQUID-LIQUID EXTRACTION

G.M. Nikolić¹, R.S. Nikolić² and J.M. Perović²

¹ Department of Chemistry, Faculty of Medicine, Bulevar dr Zorana Đinđića 81, 18000 Niš,

² Department of Chemistry, Faculty of Science, Višegradska 33, 18000 Niš, Serbia and Montenegro

Abstract

Salting-out constant values of catechol for various inorganic salts were determined by the liquid-liquid extraction from aqueous solutions with diethyl ether. Among the chloride salts investigated in this study the highest salting-out constant value was obtained for MgCl₂. This result implies that MgCl₂ may be used instead of most commonly used NaCl for the salting-out extraction of catechol in various analytical procedures in order to improve the sensitivity of its determination. Beside the possible practical applications, the results of this study are also important for better understanding of the salting-out phenomena which is currently an area of very intensive research because of the needs of the pharmaceutical industry.

Introduction

It is well known that organic compounds are generally less soluble in aqueous salt solutions than in pure water, the so-called salting-out phenomenon. This effect is used, for example, to facilitate the separation of organic compounds from aqueous solutions and to precipitate proteins.

An empirical equation to describe this effect was derived by Setschenow over a century ago [1].

$$\log(S/S_0) = k_s C_s$$

In this equation S_0 and S are the solubilities of the solute in water and salt solutions respectively, k_s is the Setschenow or the salting-out constant and C_s is the molar concentration (mol dm⁻³) of the salt solution. However, in some cases when the aqueous solubility of the organic compounds is very low (or very high) the determination of salting-out constants by the solubility measurements is not convenient.

Another way of salting-out constants determination is by the liquid-liquid extraction of organic solutes from aqueous salt solutions in which case the following equation applies:

$$\log(D/D_0) = k_s C_s$$

where D_0 and D are the distribution ratios of organic solute between a water immiscible organic solvent and water or aqueous salt solutions.

In this paper we present the results of salting-out constants determination of catechol (1,2 benzenediol) for some of the most common inorganic salts by the liquid-liquid extraction from aqueous solutions with diethyl ether.

Experimental

All the chemicals used in this work were of analytical grade purity and have been used without further purification. Catechol stock solutions (1 g dm^{-3}) were prepared by dissolving exactly weighted amount of catechol in distilled water and pH of the solution was adjusted to 2 by the addition of HCl. The stock solution of catechol (2 cm^3) was diluted to 20 cm^3 with water and/or aqueous salt solution of known concentration and then extracted with 10 cm^3 of diethyl ether. The absorbance of aqueous phase was measured at 290 nm and the D value of catechol was calculated according to the equation [2]:

$$D = \frac{A_0 - A}{A} \frac{V_{aq}}{V_{org}}$$

where A_0 and A are the absorbances of the aqueous phase before and after extraction, and V_{aq} and V_{org} are the volumes of aqueous and organic phase respectively.

SPECORD UV/VIS spectrophotometer (Carl Zeiss, Jena) was employed for absorbance measurements.

Results and Discussion

All the salts used in this study greatly enhanced the extraction efficacy of catechol with diethyl ether (D_0). The dependence of $\log(D/D_0)$ on the concentration of various aqueous salt solutions is shown in Figure 1.

Salting-out constants of catechol obtained in this work for NaCl (0.163) and KCl (0.126) were close to the values obtained by the extraction of catechol with *n*-hexanol (0.158 and 0.128 respectively) [3]. The highest salting-out constant for MgCl_2 (0.381) among the chloride salts investigated in this study implied that this salt might be much better salting-out agent for catechol extraction in various analytical applications instead of commonly used NaCl [4].

The much higher value of catechol salting-out constant obtained for $(\text{NH}_4)_2\text{SO}_4$ (0.281) in comparison to NH_4Cl (0.078) was indicative of higher salting-out efficiency of sulfate anion in comparison to chloride anion. However, the D values obtained for the diethyl ether extraction of catechol from 0.5 mol dm^{-3} aqueous solutions of MgCl_2 and MgSO_4 were almost the same (9.8) which indicated that more experimental data are needed to clarify this issue.

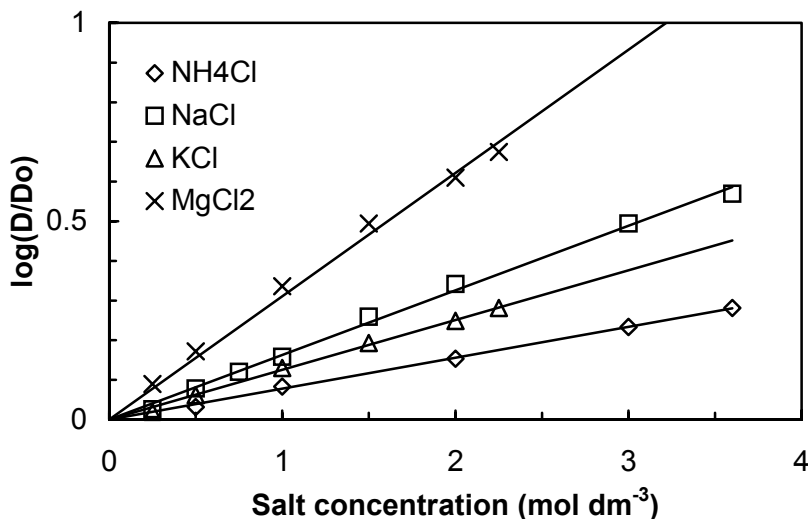


Figure 1. Dependence of the $\log(D/D_0)$ for the catechol extraction with diethyl ether on the concentration of various salt solutions.

Conclusion

Since catechol in urine may be used as a biological marker for benzene exposure, our results could be used for improving the sensitivity of various analytical procedures for its determination where an extraction step is usually included [4,5]. The results of this study may also be valuable regarding the fact that salting-out phenomenon is currently an intensive area of research especially because of the needs of pharmaceutical industry [6].

References

- [1] Setschenow J.Z., *Z. Physik. Chem.*, 1889, 4, 117.
- [2] I. Kojima, S.S. Davies, *Int. J. Pharm.*, 1984, 20, 247.
- [3] Ya.I. Korenman, T.N. Ermolaeva, *Zh. Prikl. Khim.*, 1989, 62, 114.
- [4] B.L. Lee, H.Y. Ong, C.Y. Shi, C.N. Ong, *J. Chromatogr.*, 1993, 619, 259.
- [5] G.M. Nikolić, P.I. Premović, M.Ž. Abramović, B.Lj. Milić, J.M. Čanadanović-Brunet, *Eur. J. Clin. Chem. Clin. Biochem.*, 1995, 33, A80.
- [6] N. Ni, S.H. Yalkowsky, *Int. J. Pharm.*, 2003, 254, 167.

SIMPLE UNBIASED ENERGY MINIMIZATION FOR LENNARD-JONES CLUSTERS

D. Jovanović and Đ. Cvijović

*Faculty of Physical Chemistry, University of Belgrade,
Studentski trg 12-16, 11000 Belgrade, Serbia and Montenegro*

Abstract

We reproduce the lowest known structures for the Lennard-Jones clusters containing from 5 up to 75 atoms by using a very simple global optimization technique. We show that this technique easily overcomes so-called the first and the second “hurdle”, i.e. correctly finds global minima for clusters with 38 and 75 atoms.

Introduction

The Lennard-Jones (LJ) cluster is a classical system consisting of N identical atoms interacting by a pairwise LJ potential and its potential energy is given by [1]:

$$U(r_1, r_2, \dots, r_N) = 4\varepsilon \sum_{i=1}^N \sum_{j=i+1}^{N-1} \left[\left(\frac{\sigma}{r_{ij}} \right)^{12} - \left(\frac{\sigma}{r_{ij}} \right)^6 \right] \quad (1)$$

Here, N is the number of atoms, r_{ij} is the distance between atoms i and j , while ε and $2^{1/6}\sigma$ are the pair well depth and the equilibrium pair separation, respectively. This is a very simple, yet reasonably accurate mathematical model of low temperature clusters of heavy rare gas atoms such as argon, krypton or xenon. The LJ cluster structure determination involves the minimization of the potential energy $U(\mathbf{r}_1, \mathbf{r}_2, \dots, \mathbf{r}_N)$ (equation 1), which is a function of the positions of the particles \mathbf{r}_i , $i = 1, \dots, N$. Through the combined efforts of many workers, likely candidates for the global minima of LJ_N clusters have been found up to $N = 147$.

From the point of view of optimization methods, the LJ cluster structure determination is an excellent test for local and global unconstrained optimizations methods; it is one of the simplest models, yet one of the most difficult, as it has been shown that the number of local minima grows at least exponentially with N .

Methods

Many methods have been applied to the optimization of LJ clusters, such as simulated annealing, genetic algorithm, basin-hopping, lattice methods, smoothing and hyper-surface deformation techniques. Some of them are general purpose methods and can be used in other global optimization (GO) problems, but many are specific to the LJ clusters. Most of the global minima were first found by Northby

using method which is specific to the LJ clusters. However, nowadays, it is preferred to use unbiased, more general GO methods. Moreover, it is customary to test new and improved existing GO methods by determination of global minima for LJ clusters [1].

Results and Discussion

In this work, we have used the very simple GO technique for finding global minimum. It is based on multistart method and is, in principal, designed as a general purpose technique [2]. Our aim is to reproduce the lowest known structures for the LJ_N clusters in the range $5 \leq N \leq 75$ atoms.

Our results are in complete agreement with known results which are earlier obtained by various techniques. As an illustration, in Table 1, we give some of our values of energy LJ_N .

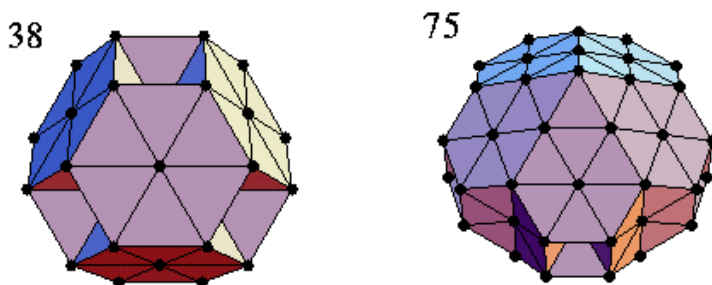


Figure 1. Global minimum structure for the LJ clusters with 38 and with 75 atoms. LJ_{38} and LJ_{75} exhibit shown equilibrium structures for -173.928403 eV and -397.492331 eV .

It is well-known that it is very difficult to correctly determine the structure of LJ_{38} [3, 4]. This is so-called “the first hurdle” that any optimization method should aspire to overcome. Part of the problem is that this cluster does not exhibit icosahedral symmetry. In our numerical experiments we successfully found that the lowest energy structure for LJ_{38} is a face-centered-cubic truncated octahedron as is shown in Figure 1.

Table 1. Global minima for some LJ clusters

N	Point Group	Energy/ϵ (our values)	Energy/ϵ (literature)
38	O _h	-173.928403	-173.928427
50	C _s	-244.549918	-244.549926
51	C _{2v}	-251.181701	-251.253964
52	C _{3v}	-258.156366	-258.229991
53	C _{2v}	-265.203010	-265.203016
54	C _{5v}	-272.208616	-272.208631
55	I _h	-279.248453	-279.248470
56	C _{3v}	-283.643101	-283.643105
57	C _s	-288.342590	-288.342625
58	C _{3v}	-294.378083	-294.378148
59	C _{2v}	-299.738044	-299.738070
60	C _s	-305.875453	-305.875476

The second “hurdle” is the location of the Marks decahedron for LJ₇₅ which is more serious problem and this is shown by number of failed trials in the structure determination.

In conclusion, we have used the LJ optimization problem to test new numerical technique. Apart from correctly reproducing seventy known cluster structures, we have shown that employed technique is very efficient and robust and can easily be used in other global optimization tasks.

References

- [1] Dragana Jovanović, Diploma Project, Faculty of Physical Chemistry, University of Belgrade, 2003.
- [2] M. Locatelli and F. Schoen, *Comput. Optim. Appl.*, 2002, 21, 55.
- [3] D. J. Wales and J. P. K. Doye, *J. Phys. Chem. A*, 1997, 101, 5111.
- [4] R. H. Leary, *J. Glob. Optim.*, 1997, 11, 35.

PREDICTION OF MIXED OXIDES FORMATION IN MOLTEN ALKALINE NITRATE EUTECTIC

C. Matei^{1,2}, P. Marote², D. Berger¹, C. Nitulescu¹, F. Papa³ and J.P. Deloume²

¹"Politehnica" University Bucharest, Department of Inorganic Chemistry,
1 Polizu street, 011061, Bucharest, Romania

²Université Claude Bernard Lyon 1, LACE, Bd. du 11 novembre, 69622, Villeurbanne, France

³Romanian Academy, Institute of Physical Chemistry,
202 Splaiul Independentei, 77208 Bucharest, Romania

Abstract

In order to obtain the best experimental conditions for mixed oxides preparation in molten NaNO_3 - KNO_3 eutectic, this paper presents and discusses the thermogravimetric data of nine hydrated salts decomposed in molten alkaline nitrate eutectic.

Introduction

Various oxides powders (titania, zirconia and ceria) having a submicronic homogeneous chemical composition were recently prepared by reaction of transition metal salts with alkali metal nitrates or nitrites [1,2]. In our previous papers we report the obtaining of CuFe_2O_4 [3], La_2CuO_4 [4] and LaNiO_3 [5] from simple systems. In his papers, D. H. Kerridge proves that the anhydrous salt of a transitional metal in molten alkali metal nitrates or nitrites generate, in most of the cases, an oxide of the metal as the last stable compound. In this paper we compare the thermogravimetric data of nine hydrated salts ($\text{FeCl}_3 \cdot 6\text{H}_2\text{O}$; $\text{Fe}(\text{NO}_3)_2 \cdot 9\text{H}_2\text{O}$; $\text{FeSO}_4 \cdot 7\text{H}_2\text{O}$ $\text{CuCl}_2 \cdot 2\text{H}_2\text{O}$; $\text{Cu}(\text{NO}_3)_2 \cdot 3\text{H}_2\text{O}$; $\text{CuSO}_4 \cdot 5\text{H}_2\text{O}$; $\text{NiCl}_2 \cdot 6\text{H}_2\text{O}$; $\text{Ni}(\text{NO}_3)_2 \cdot 6\text{H}_2\text{O}$; $\text{NiSO}_4 \cdot 7\text{H}_2\text{O}$) in NaNO_3 – KNO_3 molten eutectic in order to obtain the optimal system and the temperature range for their mixed oxides or solid solutions formation.

Experimental

The samples were prepared from pure iron(II), copper(II) and nickel(II) salts. The NaNO_3 – KNO_3 mixture has been prepared as previously described [3] and the compounds were added to the alkali metal mixture in proportion corresponding to a 0.2 mol/kg concentration. Thermal analyses were performed on a thermobalance at a heating rate of $10^\circ\text{C}/\text{min}$ up to 500°C in a 5 ml silica crucible.

Results and Discussions

In the first step of decomposition in NaNO_3 - KNO_3 eutectic, $\text{FeCl}_3 \cdot 6\text{H}_2\text{O}$ and $\text{Fe}(\text{NO}_3)_2 \cdot 9\text{H}_2\text{O}$ form oxysalts (at 110 - 120°C) but at higher temperatures (270°C , 370°C and 380°C respectively) all studied iron(III) salts form Fe_2O_3 (Fig. 1a.).

Contrary to the behaviour of iron salts in alkali nitrate eutectic, nickel(II) salts decompose without oxysalts formation and give NiO (Fig. 1b.).

After the loss of water, $\text{CuCl}_2 \cdot 2\text{H}_2\text{O}$ form a black powder, identified by RX analysis as CuO . $\text{Cu}(\text{NO}_3)_2 \cdot 3\text{H}_2\text{O}$ decomposes to form CuO as final product through

some copper(II) nitro-hydroxide intermediaries (Fig. 1c.). In molten eutectic, hydrated copper sulfate forms an intermediary and CuO over 450°C.

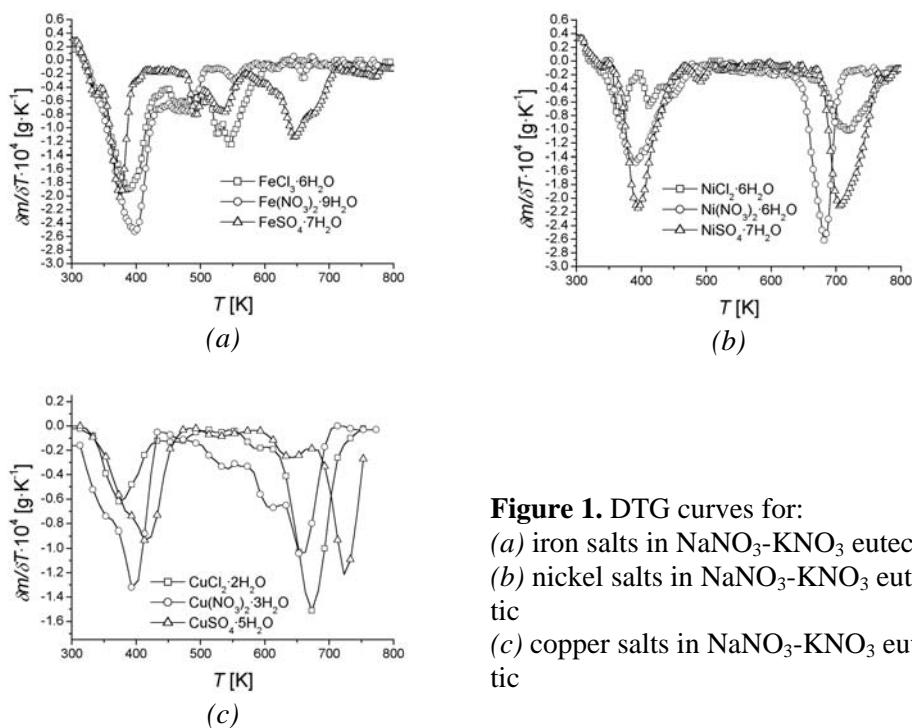


Figure 1. DTG curves for:
 (a) iron salts in NaNO₃-KNO₃ eutectic
 (b) nickel salts in NaNO₃-KNO₃ eutectic
 (c) copper salts in NaNO₃-KNO₃ eutectic

Conclusions

In molten NaNO₃-KNO₃ eutectic, all studied salts (Fe(NO₃)₃·9H₂O, FeSO₄·7H₂O, FeCl₃·6H₂O, CuCl₂·2H₂O, Cu(NO₃)₂·3H₂O, CuSO₄·5H₂O, NiCl₂·6H₂O, Ni(NO₃)₂·6H₂O, NiSO₄·7H₂O) by decomposition, form the corresponding oxide. Considering that in molten salts, a pure ionic medium, the obtaining of mixed oxide is possible starting with the lowest temperature of both oxides formation, we synthesised our results in Table I. We may conclude that in molten NaNO₃-KNO₃ eutectic any combination of two hydrated salts (from those nine studied salts), at the right temperature, could form a mixture of oxides, but very probably a mixed oxide or a solid solution. At least in two cases (the systems Fe(NO₃)₃·9H₂O - Cu(NO₃)₂·3H₂O - NaNO₃-KNO₃ and FeSO₄·7H₂O - CuSO₄·5H₂O - NaNO₃-KNO₃), our suppositions are correct and the CuFe₂O₄ formation was confirmed by XRD patterns and FTIR analysis [4].

Table I. The lowest temperatures of simultaneous formation of oxides in molten $\text{NaNO}_3\text{-KNO}_3$ eutectic.

<i>Couples</i>	<i>Analysed system</i>	<i>Temperature</i> [°C]	
Fe-Cu	$\text{FeCl}_3 \cdot 6\text{H}_2\text{O}$	$\text{CuCl}_2 \cdot 2\text{H}_2\text{O}$	300
		$\text{Cu}(\text{NO}_3)_2 \cdot 3\text{H}_2\text{O}$	360
		$\text{CuSO}_4 \cdot 5\text{H}_2\text{O}$	400
	$\text{Fe}(\text{NO}_3)_3 \cdot 9\text{H}_2\text{O}$	$\text{CuCl}_2 \cdot 2\text{H}_2\text{O}$	309
		$\text{Cu}(\text{NO}_3)_2 \cdot 3\text{H}_2\text{O}$	360
		$\text{CuSO}_4 \cdot 5\text{H}_2\text{O}$	400
	$\text{FeSO}_4 \cdot 7\text{H}_2\text{O}$	$\text{CuCl}_2 \cdot 2\text{H}_2\text{O}$	300
		$\text{Cu}(\text{NO}_3)_2 \cdot 3\text{H}_2\text{O}$	360
		$\text{CuSO}_4 \cdot 5\text{H}_2\text{O}$	400
Ni-Cu	$\text{NiCl}_2 \cdot 6\text{H}_2\text{O}$	$\text{CuCl}_2 \cdot 2\text{H}_2\text{O}$	394
		$\text{Cu}(\text{NO}_3)_2 \cdot 3\text{H}_2\text{O}$	394
		$\text{CuSO}_4 \cdot 5\text{H}_2\text{O}$	400
	$\text{NiSO}_4 \cdot 7\text{H}_2\text{O}$	$\text{CuCl}_2 \cdot 2\text{H}_2\text{O}$	392
		$\text{Cu}(\text{NO}_3)_2 \cdot 3\text{H}_2\text{O}$	392
		$\text{CuSO}_4 \cdot 5\text{H}_2\text{O}$	400
	$\text{Ni}(\text{NO}_3)_2 \cdot 6\text{H}_2\text{O}$	$\text{CuCl}_2 \cdot 2\text{H}_2\text{O}$	300
		$\text{Cu}(\text{NO}_3)_2 \cdot 3\text{H}_2\text{O}$	360
		$\text{CuSO}_4 \cdot 5\text{H}_2\text{O}$	400
Fe-Ni	$\text{FeCl}_3 \cdot 6\text{H}_2\text{O}$	$\text{NiCl}_2 \cdot 6\text{H}_2\text{O}$	394
		$\text{NiSO}_4 \cdot 7\text{H}_2\text{O}$	392
		$\text{Ni}(\text{NO}_3)_2 \cdot 6\text{H}_2\text{O}$	283
	$\text{Fe}(\text{NO}_3)_3 \cdot 9\text{H}_2\text{O}$	$\text{NiCl}_2 \cdot 6\text{H}_2\text{O}$	394
		$\text{NiSO}_4 \cdot 7\text{H}_2\text{O}$	392
		$\text{Ni}(\text{NO}_3)_2 \cdot 6\text{H}_2\text{O}$	309
	$\text{FeSO}_4 \cdot 7\text{H}_2\text{O}$	$\text{NiCl}_2 \cdot 6\text{H}_2\text{O}$	394
		$\text{NiSO}_4 \cdot 7\text{H}_2\text{O}$	392
		$\text{Ni}(\text{NO}_3)_2 \cdot 6\text{H}_2\text{O}$	297

References

- [1] J.P. Deloume, , B. Durand, Molten Salt Forum, 1998, 5/6, 485.
- [2] B. Durand, Ceramic Powders, 1983, 413.
- [3] Matei, C., Jitaru, I., Andronescu, E., Novac, A., Advances in Molten Salt, 1999, 400.
- [4] C. Matei, I. Jitaru, E. Andronescu, A. Novac, Advances in Molten Salt, 1999, 242.
- [5] C. Matei, I. Jitaru, J.P. Deloume, Progress in Molten Salt Chemistry, 2000, 1 331.

DETERMINATION OF THE IONIZATION CONSTANTS OF 2,4-DIIODO-6-METHYLPHENYL CARBAMOYLMETHYL IMINODIACETIC ACID

J. Brborić¹, M. Jovanović² and S. Vladimirov¹

¹*Faculty of Pharmacy, P.O.Box 146, 11000 Belgrade, Serbia and Montenegro*

²*Institute of Nuclear Science Vinča, 11000 Belgrade, Serbia and Montenegro*

Abstract

The ionization constants of 2,4-diiodo-6-methylphenylcarbamoymethyl iminodiacetic acid were determined: pK_1 1.3 (the first carboxylic group), pK_2 2.52 (the second carboxylic group), pK_3 5.86 (amino group) and pK_4 10.85 (amide group). The determination were performed at 25°C.

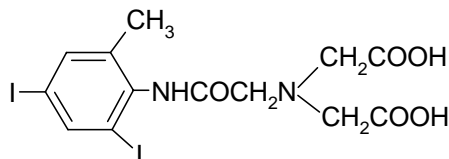
Introduction

The analogues of iminodiacetic acid (IDA) labeled with technetium-99m are used as diagnostic radiopharmaceutical for hepatobiliary imaging. In order to develop a radiopharmaceutical with better hepatobiliary properties and larger tolerance on bilirubin, a new ligand for complexation of technetium-99m, 2,4-diiodo-6-methyl phenylcarbamoymethyl iminodiacetic acid (DIIODIDA) was synthesized [1].

The data of acid-base equilibria of DIIODIDA are important for determination of complex formation conditions. Considering the fact that DIIODIDA is newly synthesized compound it was of interest to determine its ionization constants.

Results and Discussion

In molecule of DIIODIDA there are three acidic centers (two carboxylic groups and amide group) and one basic center (amino group).



The neutral form of DIIODIDA (H_3A) is rearranged spontaneously to the zwitter ion (H_3A^\pm) due to the protolysis of the first carboxylic group and proton acceptance of the amino group. The protolysis of the second carboxylic group, amino and amide group results in H_2A^- , HA^{2-} and A^{3-} forms. The form H_4A^+ exists in more acidic media. The corresponding ionization constants are as follows:

$$K_1 = \frac{[H_3A^\pm][H^+]}{[H_4A^+]} \quad (1) \quad K_2 = \frac{[H_2A^-][H^+]}{[H_3A^\pm]} \quad (2)$$

$$K_3 = \frac{[HA^{2-}][H^+]}{[H_2A^-]} \quad (3) \quad K_4 = \frac{[A^{3-}][H^+]}{[HA^{2-}]} \quad (4)$$

The ionization constants K_2 , K_3 and K_4 were determined potentiometrically by application of the formation function method (\bar{n}_H) [2]:

$$\bar{n}_H = \frac{\sum_1^n n[H_n A]}{\sum_0^n [H_n A]} \quad (5)$$

(The charges in equation (5) were omitted due to simplicity)

The function \bar{n}_H was calculated from experimental data of potentiometric titration of DIIODIDA with standard solutions of HCl (K_2) and NaOH (K_3 and K_4):

$$\bar{n}_H = \frac{3c_{\text{DIODIDA}} + c_{\text{HCl}} - c_{\text{NaOH}} - [H^+] + [OH^-]}{c_{\text{DIODIDA}}} \quad (6)$$

where c_{DIODIDA} , c_{HCl} and c_{NaOH} correspond to the stoichiometric concentration of DIIODIDA, HCl and NaOH; $[H^+]$ is the equilibrium concentration of protons obtained from pH measurements ($\text{p}c_H = -\log[H_3O^+] = \text{pH} - 0.05$) [3]; $[OH^-]$ is concentration of hydroxyl ions.

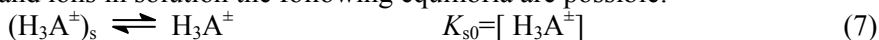
The ionization constants are determined in separated pH ranges where only one acid-base pair is dominant. The calculation of ionization constants was performed using equations which correspond to monoprotic acids. pH intervals for determination of ionization constants as well as obtained values are presented in Table I.

Table I. Stoichiometric equilibrium constants determined in homogeneous and heterogeneous systems of DIIODIDA; $t = 25^\circ\text{C}$.

Constants	pH range of determination	Acid-base pair	$\text{p}K \pm \text{sd}$
$\text{p}K_1$	0 - 1.0	$\text{H}_4\text{A}^+ - \text{H}_3\text{A}^\pm$	$1.3 \pm 0.4^*$
$\text{p}K_2$	2.3 - 3.5	$\text{H}_3\text{A}^\pm - \text{H}_2\text{A}^-$	2.52 ± 0.02
$\text{p}K_3$	4.7 - 6.8	$\text{H}_2\text{A}^- - \text{HA}^{2-}$	5.86 ± 0.01
$\text{p}K_4$	9.2 - 11.0	$\text{HA}^{2-} - \text{A}^{3-}$	10.85 ± 0.01
$\text{p}K_{s0}$	0 - 1.0		5.0 ± 0.4
$\text{p}K_{s1}$	0 - 1.0		3.69 ± 0.04

*The great value of Sd for $\text{p}K_1$ could be explained by unsatisfactory reliable determination of $\text{p}K$ in very acid medium ($\text{pH} < 1$)

The acid-base process were the first carboxylic group of DIIODIDA participates was performed in range $\text{pH} < 2$. As DIIODIDA in this pH range is slightly soluble in water (zwitter-ion), the constant K_1 could not be determined using pH-metrical titrations. This constant was determined indirectly, on the basis of equilibrium constants obtained in heterogeneous system. In aqueous solution at $\text{pH} < 1$ between solid phase, $(\text{H}_3\text{A}^\pm)_s$, and ions in solution the following equilibria are possible:



The constant K_1 can be directly calculated from the equation:

$$K_1 = \frac{K_{s0}}{K_{s1}} \quad (9)$$

Stoichiometric equilibrium constants K_{s0} and K_{s1} were determined spectrophotometrically using method of solubility [3]. The solubility (S) of DIIODIDA at $\text{pH} < 1$ was calculated by equation:

$$S = \text{H}_3\text{A}^+ + \text{H}_4\text{A}^+ = K_{s0} + K_{s1} [\text{H}^+] \quad (10)$$

Applying the experimentally determined solubility of DIIODIDA in solutions of HCl (0.1-1M; pC_H 0-1) and using the equation (10), the constants K_{s0} and K_{s1} were calculated from intercept and slope of linear dependence. The constant K_1 was calculated by applying equation (9).

The corresponding distribution diagram of DIIODIDA, obtained from experimental data of pK_a values, is presented in Figure 1.

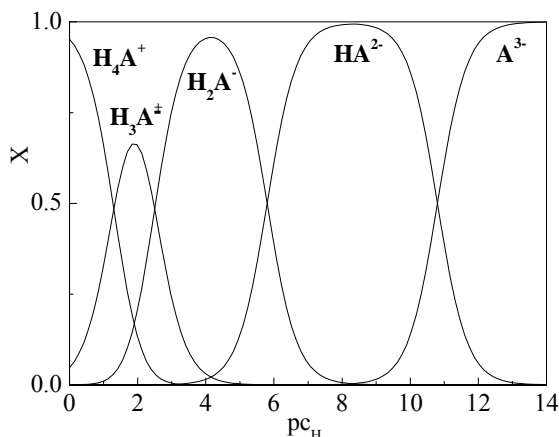


Figure 1. Distribution diagram of DIIODIDA in function of pC_H

Acknowledgments

The authors would like to express their gratitude to prof. Dr. G. Popović for the assistance given them during the work on this subject.

These results are the part of Project N°1980, partly financially supported by Serbian Ministry of Science and Technologies.

References

- [1] J.S. Brborić, S. Vladimirov, M.S. Jovanović, and N. Dogović, *Monatsh. Chem.*, 2004 (Published Online May 21, 2004)
- [2] H. Rossotti, *The Study of Ionic Equilibria*, Longman, New York, 1978.
- [3] L.B. Pfenndt, D.M. Sladić, T.J. Janjić, G.V. Popović, *Analyst*, 1990, **115**, 383.

DERIVATIVE SPECTROPHOTOMETRIC DETERMINATION OF PARTITION COEFFICIENT OF HYDROCHLOROTHIAZIDE BETWEEN CETYLTRIMETHYLAMMONIUM BROMIDE MICELLES AND WATER

O. Čudina^a, K. Karljiković-Rajić^b, I. Ruvarac-Bugarčić^c and I. Janković^c

^a Institute of Pharmaceutical Chemistry and Drug Analysis, Faculty of Pharmacy,

^b Institute of Analytical Chemistry, Faculty of Pharmacy, Vojvode Stepe 450, P.O. Box 146, 11000 Belgrade, Serbia and Montenegro, ^c Laboratory for Radiation Chemistry and Physics, Vinča Institute of Nuclear Sciences, P.O. Box 522, 11001 Belgrade, Serbia and Montenegro

Abstract

The interaction of hydrochlorothiazide (HCT), benzothiadiazine diuretic, with cationic surfactant cetyltrimethylammonium bromide (CTAB) was studied as a model system for drug/membrane interactions. From the dependence of first order derivative amplitude $^1D_{250.1}$ on CTAB concentration, by using mathematical models based on the partition of the drug between micellar and aqueous pseudo-phase, CTAB/water partition coefficient K_p was calculated.

Introduction

Drug interactions with heterogeneous media (micelles, lipid bilayer vesicles, biomembranes) induce changes in some physicochemical properties of the drugs (solubility, spectroscopic and acid-base properties) [1]. By monitoring these changes it is possible to quantify the degree of drug/micelle interaction which is expressed as micelle/water partition coefficient, K_p . The elucidation of K_p is important for the understanding of interactions with biomembranes and for the quantitative structure-activity relationship of drugs, as well as for the use of surfactants in HPLC or MEKC in drug quality control.

In this work, the effect of cationic micelles of cetyltrimethylammonium bromide, CTAB, on the spectroscopic properties of benzothiadiazine diuretic hydrochlorothiazide (6-chloro-3,4-dihydro-2H-1,2,4-benzothiadiazine-7-sulfonamide-1,1-dioxide), HCT is described. The derivative spectrophotometry was used to quantify the partition coefficient of HCT by applying the mathematical model [2] that considers partitioning of the drug between CTAB micellar and aqueous pseudo-phase.

Experimental

Spectrophotometric measurements used to calculate derivative spectra were performed on a GBC Cintra 20 spectrophotometer with 1.0 cm quartz cuvettes. The optimized operating conditions were: wavelength range 230 – 260 nm; slit width 1.0 cm; scan speed 100 nm min⁻¹; data interval 0.32 nm. The first-order derivative spectra were calculated using Savitzky-Golay algorithm with smoothing of 7 points. Stock solutions of 10 mM hydrochlorothiazide (Gödecke GmbH, Freiburg, Germany) were prepared by dissolving the compound in methanol.

Results and Discussion

The absorption spectra of HCT at pH=5 and pH=10.5, both in aqueous and CTAB micellar solutions, were measured. The effect of cationic micelles on the absorption spectrum of HCT is observed only in basic solutions. Hence it was concluded that electrostatic interaction between positively charged micelle surface and HCT dianion (pK_a^{HCT} are 7.0 and 9.2 [3]) is crucial for the micelle/drug binding.

The first order derivative spectra calculated from the absorption spectra of 0.42 mM HCT at pH=10.5 in the wavelength spectral range from 230 nm to 260 nm as a function of various concentrations of CTAB ($c_{\text{CTAB}}=0.1-2$ mM) are depicted in Figure 1. It is evident that a hypsochromic shift exists as a consequence of HCT binding to CTAB micelles, i. e. the drug exists in two states, free and micelle-bound, that have different derivative spectra. Two characteristic wavelengths are 250.1 nm and 242.1 nm being zero-crossing points of free and micelle-bound HCT, respectively. Hence, the concentration of free and/or micelle-bound HCT can be calculated from the values of ${}^1D_{242.1}$ and ${}^1D_{250.1}$, respectively, since the derivative intensity is proportional to solute concentration ${}^1D_{\lambda} = E_{\lambda} \cdot c$. From the calibration curves of ${}^1D_{242.1}$ and ${}^1D_{250.1}$ versus c_{HCT} (concentration range 0.02 – 0.5 mM) measured in aqueous and micellar solutions ($c_{\text{CTAB}}=3$ mM) respectively, the molar derivative intensity for free HCT $E_{242.1}^w = -185.4 \pm 1.5 \text{ M}^{-1} \text{ cm}^{-1}$ ($r=0.999$) and micelle-bound HCT $E_{250.1}^m = 143.7 \pm 1.8 \text{ M}^{-1} \text{ cm}^{-1}$ ($r=0.999$) were obtained.

The addition of increasing concentrations of CTAB to the aqueous solutions of HCT resulted in the corresponding hyperbolic binding isotherm (${}^1D_{\lambda}$ vs. c_{CTAB} , inset of Fig. 1), representing the disappearance of free HCT (${}^1D_{242.1}$) and the formation of micelle-bound HCT (${}^1D_{250.1}$). The values of ${}^1D_{242.1}$ and ${}^1D_{250.1}$ are constant in the concentration range of $c_{\text{CTAB}}=0-0.2$ mM assuming that it is the premicellar region, i. e. $\text{CMC}_{\text{CTAB}} = 0.2$ mM under experimental conditions used.

The partition coefficient K_p defined as the ratio of the mole fractions of HCT in micellar and aqueous phase was determined from ${}^1D_{250.1}$ values by using the equation [2]

$$\frac{1}{{}^1D_{250.1}} = \frac{1}{{}^1D_{250.1}^{\infty}} + \frac{1}{K_c \cdot {}^1D_{250.1}^{\infty} \cdot (c_{\text{HCT}} + c_{\text{CTAB}} - \text{CMC})}$$

where ${}^1D_{250.1}^{\infty}$ is derivative intensity at infinite concentration of CTAB and $K_c = K_p / n_w$ ($n_w = 55.5$ M is the molarity of water). By measuring ${}^1D_{250.1}$ in five series ($n=5$) containing HCT ($c = 0.42$ mM) and increasing concentrations of CTAB (0.1-2.0 mM) and plotting $1/{}^1D_{250.1}$ versus $1/(c_{\text{HCT}} + c_{\text{CTAB}} - \text{CMC})$ the values obtained for partition coefficients were $K_c = 985 \pm 100 \text{ M}^{-1}$ and $K_p = 54668 \pm 5550$.

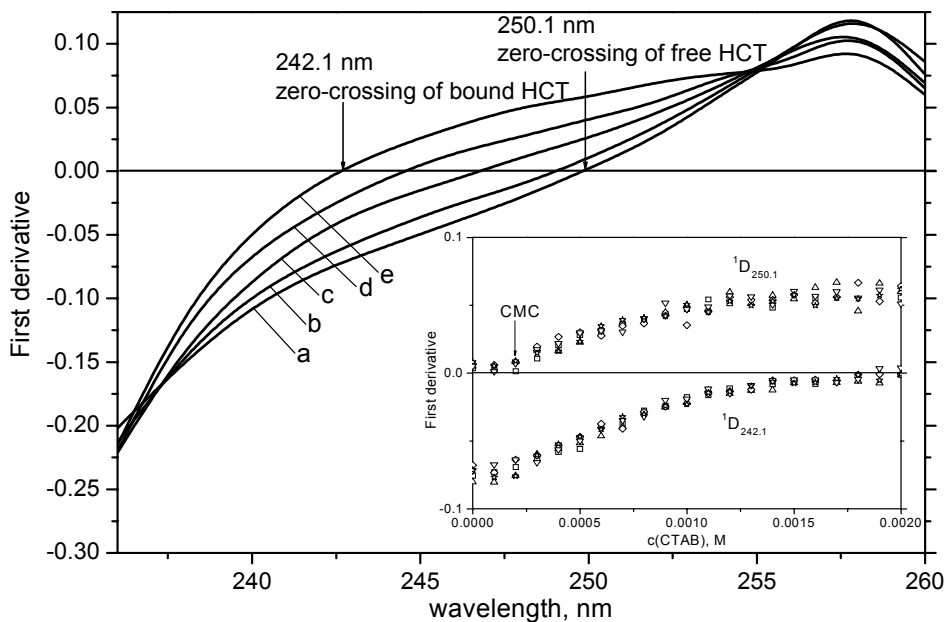


Figure 1. First order derivative spectra of 0.42 mM HCT at pH=10.5 containing various amounts of CTAB (mM): a) 0; b) 0.3; c) 0.6; d) 0.9; e) 2.0.

Inset: First order derivative intensity at 242.1 nm and 250.1 nm of 0.42 mM HCT as a function of CTAB concentration.

References

- [1] S. Schreier, S. V. P. Malheiros, E. de Paula, *Biochim. Biophys. Acta*, 2000, 1508, 210.
- [2] H. Kawamura, M. Manabe, Y. Miyamoto, Y. Fujita, S. Tokunaga, *J. Phys. Chem.*, 1989, 93, 5536.
- [3] C. C. Hansch in: *Comprehensive Medicinal Chemistry*, Vol.6, R. G. Sammes, J. B. Taylor (Eds.), Pergamon Press, Oxford, 1990.

ANALYTICAL METHOD TRANSFER PROCESS IN PHYSICO-CHEMICAL LABORATORIES FOR TRIXIFEN SUGAR COATED TABLETS

G. N. Kaluđerović¹, M. Dašić¹, T. Geđa¹, Z. Todorović¹ and S. D. Petrović^{1,2}

¹*Hemofarm koncern, Beogradski put bb, 26300 Vršac,*

²*Faculty of Technology, University of Belgrade,
Karnegijeva 6, 11000 Belgrade, Serbia and Montenegro*

Abstract

Analytical method transfer process between Physico-Chemical Laboratory Hemofarm, as the transferring, and Laboratory Hemofarm Banja Luka, as the receiving laboratory, of the subject drug was carried out successfully. Identification and assay of thioridazine hydrochloride and related substances as well as dissolution tests were performed and presented in this work. A routine spectrophotometric method was applied in these investigations. The receiving laboratory showed great confidence that it can routinely utilise new method.

Introduction

Analytical method transfer process represents a means of transferring information and demonstrating equivalent method performance in both the transferring and the receiving laboratory [1]. A successful method transfer based upon meeting pre-defined acceptance criteria will ensure that the receiving laboratory is able to apply validated methodology using available personnel and equipment. Any testing performed during analytical method transfer must be performed by the staff that has been fully trained in all aspects of the relevant techniques. This training should be preceded by a full knowledge transfer and must be documented in accordance with internal procedures. Training procedures are critical for providing confidence that the receiving laboratory can routinely utilise new methods [2].

The analytical method transfer process for Trixifen 25 mg sugar coated tablets is presented in this work. By comparing the results of Physico-Chemical Laboratory Hemofarm, as the transferring, and Laboratory Hemofarm Banja Luka, as the receiving laboratory, the latter showed great confidence that it can routinely utilise new method.

Experimental

Identification of active component, thioridazine hydrochloride, was performed as described in HFG 0191 procedure [3]. Electron absorption spectra were recorded on UV/Vis Beckman DU Series 600 in both laboratories. Dissolution tests were performed on Erweka DT 70 and Erweka DT 800 in the transferring and the receiving laboratory, respectively. Working standard Control No. 0291103 was used for dissolution test and assay. Trixifen sugar coated tablets 25 mg, obtained from Hemofarm Group, with Control No. 0460803, 0471103 and 0411202, were used for this analytical method transfer process.

Results and Discussion

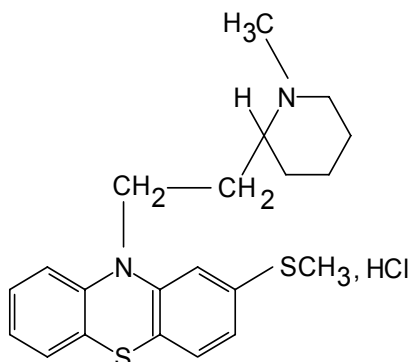


Figure 1. Structural formula of thioridazine hydrochloride

Identification tests were performed on the tablets with the Control No. 0460803 in both laboratories. As a result, both of them confirmed the presence of the active compound, thioridazine hydrochloride (Fig. 1.), using electron absorption spectra as identification method. These spectra showed the band characteristic for thioridazine hydrochloride at 264 nm (Fig. 2.).

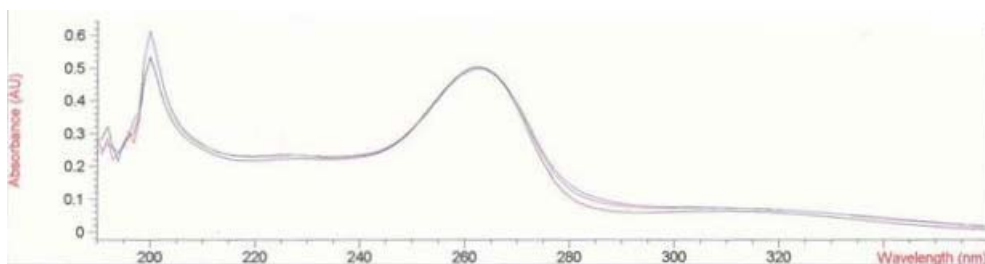


Figure 2. Electron absorption spectrum of thioridazine hydrochloride

Assay was carried out in both transferring and receiving laboratory. Namely, six test solutions were prepared from the tablets with the Control No. 0460803 and four test solutions from the tablets with the Control No. 0471103 and 0411202, as described in TPAM-0191 [4]. The results obtained by spectrophotometric measurements are shown in the Table 1. The value of a well-transferred analytical method must range between 99-101% [4]. Our results confirm this fact and they are complying with the proposed value for the acceptance of analytical method transfer process for assay. The related substances were detected in neither laboratory.

Table 1. Results obtained from assay tests

Control No.	Transferring laboratory (mg/tbl)	Receiving laboratory (mg/tbl)	Average (mg/tbl)	Compliance %
0460803	22.91	22.58	23.75	99.28-100.72
0471103	22.64	22.66	22.65	99.96-100.04
0411202	23.39	23.81	23.60	99.12-100.88

Dissolution test is also complying. The proposed deviation of the receiving laboratory from the transferring laboratory is 5.0% [4]. Our result showed -4.17% deviation from the transferring laboratory results on Control No.0460803 (Table 2.).

Table 2. Results of dissolution tests

No	Transferring laboratory (%)	Receiving laboratory (%)	Deviation - receiving vs. transferring lab.
1.	94.22	93.51	
2.	97.05	92.11	
3.	94.74	91.82	
4.	90.04	90.42	
5.	98.32	91.73	
6.	100.26	89.88	
7.	101.13	95.92	
8.	100.10	89.99	
9.	93.18	93.95	
10.	94.40	95.05	
11.	98.99	93.03	
12.	93.35	92.10	
average	96.31	92.46	-4.17 %

Conclusion

The receiving laboratory, using electron absorption method for analytical method transfer process, showed great confidence that it can routinely utilise method for Trixifen 25 mg sugar coated tablets.

References

- [1] Analytical Method Transfer, GlaxoSmithKline, CAP051/02, pp 1-33.
- [2] Analytical Method Transfer, Hemofarm Group, OP0221044, edition A/0, pp 3-5.
- [3] Analytical Method, Trixifen Sugar Coated Tablets 25 mg, HFG 0191, Hemofarm Group, edition A/3, pp 7.
- [4] Transfer Protocol of Analytical Method, TPAM-0191, Hemofarm Group.

SALTING-OUT THIN-LAYER CHROMATOGRAPHY (SOTLC) OF SOME AMINOCARBOXYLATO Co(III) COMPLEXES ON MODIFIED SILICA GEL

V. Živković-Radovanović and G. Vučković

Faculty of Chemistry, Belgrade, Studentski trg 16, P.O.Box 158

Abstract

15 mixed aminocarboxylato Co(III) complexes divided into 4 groups according to their composition and structure were chromatographed using ammonium sulphate solutions of 8 different concentrations on silica gel impregnated with polyethylene glycol (PEG) (average relative molecular mass 4000 or 5500). Comparison of the chromatographic parameters showed that such modifications of silica gel gives practically new sorbents of enhanced hydrophobic properties.

Introduction

Earlier investigations of the chromatographic behaviour of the mentioned complexes by SOTLC on non-impregnated sorbents: silica gel, polyacrylonitrile sorbent (PANS) and cellulose showed great influence of the sorbent nature on separation [1]. Many regularities that could be used for estimation of optimal separation conditions were established [2]. The same complexes were separated on silica gel impregnated with PEG-s of lower average relative molecular masses (400, 1000 and 1540, respectively) [3], which are commercially used as stationary phase in gas chromatography [4]. In continuation, the influence of greater PEG molecular masses impregnature on behaviour of the same series of complexes in SOTLC was studied.

Results and Discussion

The hR_F -values obtained are given in Table I. The salting-out effect, i.e. enhanced retention with increase of the salt concentration in the solvent system was found in all investigated cases, which is in accordance with previously obtained results [1,3]. In addition, on both impregnature applied, the reverse-phase order of complexes within a series, as well as a stronger retention of complexes containing normal hydrocarbon chains compared with isomers having branched aminocarboxylato ligands was found. This could be explained by the mechanism of non-specific hydrophobic interactions caused with greater contact hydrophobic surfaces of sorbent [5].

The salting-out effect is greater when silica gel is impregnated with PEG of greater average molecular mass, as was observed earlier with others PEG-s [3] due to the enhanced non-specific hydrophobic interactions. Namely, the impregnatures were applied in the same molar concentration to the sorbent, thus its contact hydrophobic surface is proportional to the average relative molecular mass of the PEG used.

Table I. R_F -values ($R_F \times 100$) of the investigated complexes obtained on silica gel impregnated with polyethylene glycol of average molecular mass A: 4000 or B: 5500.

α	Complex ^a	n^b	GlyH	Ammonium sulphate content [mol%]							
				0,92	1,88	2,89	3,97	5,12	6,36	7,70	9,15
1	$(+)^{589}$ - <i>cis</i> (NO ₂), <i>trans</i> (N)- [Co(S-Ala) ₂ (NO ₂) ₂]	4	A	84	78	72	62	52	44	35	25
			B	81	74	68	54	45	33	25	15
2	(S-Abu) ₂	6	AB	82	70	61	47	36	18	13	6
				77	61	53	40	27	14	8	4
3	(S-Nval) ₂	8	AB	70	56	42	24	13	6	3	1
				68	49	38	20	10	4	1	0
4	(S-Nleu) ₂	10	AB	62	46	27	14	6	2	0	0
				60	40	22	10	3	1	0	0
5	(Aibu) ₂	6	AB	82	70	62	49	38	25	17	10
				79	69	54	43	28	19	9	5
6	(S-Val) ₂	8	AB	72	59	48	29	20	8	4	2
				71	56	40	23	11	6	3	0
7	(S-Leu) ₂	10	AB	68	50	32	18	10	3	0	0
				64	44	27	13	5	2	0	0
8	(S-Ile) ₂	10	AB	70	52	34	19	11	4	0	0
				66	46	28	14	6	2	0	0
9	<i>mer</i> -[CoGly(NO ₂) ₃ NH ₃]	1	AB	92	90	85	82	78	70	62	49
				88	83	77	70	62	48	38	28
10	$(-)^{589}$ - <i>mer</i> - [Co(S-Ala)(NO ₂) ₃ NH ₃]	2	AB	90	87	81	76	64	54	48	32
				86	80	71	60	49	35	24	16
11	(S-Abu)	3	AB	88	81	74	65	52	41	31	18
				85	76	64	52	38	22	16	8
12	(S-Nval)	4	AB	83	74	62	54	40	24	15	7
				82	71	57	42	28	14	6	3
13	<i>cis</i> (NO ₂), <i>trans</i> (NH ₂ ,NH ₃)- [CoGly(NO ₂) ₂ (NH ₃) ₂]	1	AB	96	95	94	93	92	90	87	84
				95	94	93	91	89	87	83	78
14	$(+)^{589}$ - <i>cis</i> (NO ₂), <i>trans</i> (NH ₂ ,NH ₃)- [Co(S-Ala)(NO ₂) ₂ (NH ₃) ₂]	2	AB	93	91	90	88	83	80	72	68
				92	90	88	85	80	72	68	59
15	(S-Abu)	3	AB	89	85	81	77	70	65	55	46
				88	84	79	74	68	62	53	41

^a GlyH = glycine; S-AlaH = S-alanine; S-AbuH = S-aminobutyric acid; S-NvaH = S-norvaline; S-NleH = S-norleucine; AibuH = isoaminobutyric acid; S-ValH = S-valine; S-leuH = S-leucine; S-IleH = S-isoleucine; ref. for syntheses cited in [1]

^b n = Number of C- atoms in hydrocarbon part of the complex

^c Impregnatures were applied in concentration of $1,56 \times 10^{-3}$ mol/100 g of the sorbent

On both silica gel modifications the Linear dependence Rule is valid [6], i.e. the R_M -value is a positive linear function of mol % of ammonium sulphate in the solvent system. The positive linear dependence between R_M -values (obtained with ammonium sulphate of the corresponding mol%) and number of C-atoms in aminocarboxylato hydrocarbon part within the same group of complexes is also found. Besides, a positive linear correlation between the separation factors (α) of complexes of the same

group and mol% of the salt in the solvent system was found. As regularities previously found on non-impregnated sorbents [1,2] are also valid for studied impregnated silica gel, a new sorbents of enhanced hydrophobic properties are proposed.

The quality of the separation of *bis*(aminocarboxylato) complexes increased with increasing of the hydrophobic properties of impregnated sorbents using salt content higher than 5,12 mol%. Another advantage is successful mutual separation of the complexes containing glycinate ligand which was not the case on non-impregnated silica gel.

Conclusion

New sorbents of enhanced hydrophobic properties usable in SOTLC were obtained by impregnation of silica gel with different polyethylene glycols.

References

- [1] T.J.Janjić, V.Živković and M.B.Ćelap, *Chromatographia*, 1994, 38, 447 and references cited therein.
- [2] T.J.Janjić, V.Živković and M.B.Ćelap, *J.Serb.Chem.Soc.*, 1997, 62, 1.
- [3] V.Živković-Radovanović and G.Vučković, The XLII Meeting of the Serbian Chemical Society, Novi Sad, 2004, AH-16, p.26.
- [4] a) C.F.Poole et al., *J.Chromatogr.A*, 2000, 898, 211; b) I.A.Bardina et al., *Zhurnal Fizicheskoi Khimii*, 2001, 75, 510.
- [5] a) C.Horvath et al., *J.Chromatogr.*, 1976, 125, 129; b) A.R.Timerbaev and O.M.Petrukhin, *Zhidkostnaya Adsorbtionaya Khromatografiya Khelatov*, Nauka, Moskva, 1989, p.68.
- [6] T.J.Janjić, V.Živković and M.B.Ćelap, *Chromatographia*, 1994, 38, 355.

POTENTIOMETRIC STUDY OF HYDROLYSIS OF ALUMINIUM(III) ION IN MICELLAR AND MIXED WATER-DIOXANE MEDIA

R. M. Jelić, Lj. G. Joksović and P. T. Đurđević

Faculty of Science, Institute of Chemistry, P.O.Box 60, 34000 Kragujevac, SCG

Abstract

Hydrolytic equilibria of aluminium(III) ion were studied in the presence of surfactant, sodium n-dodecylsulphate (SDS) and separately, in mixed water-dioxane medium at 298 K, by glass electrode potentiometric measurements. The ionic strength of the solutions was 0.1 mol/dm³ (LiCl). The total concentration of aluminium(III) ion used was 2.50 mmol/dm³ while that of SDS was varied from 2.5 to 12.5 mmol/dm³. The content of dioxane was from 30% to 50% vol.%. The general least-squares treatment of the data indicates the formation of mononuclear complexes (1,-1), (1,-2) and (1,-3) in all studied systems. Only to fit the data in the presence of 2.5 mmol/dm³ SDS it was necessary to include the polynuclear hydrolytic complexes (2,-4), (3,-4) and (13,-32). The dioxane influence the hydrolysis only slightly in terms of the stability constants of the hydrolytic complexes, while much higher values for the stability constants of corresponding hydrolytic species were obtained in the presence of SDS in comparison with these in pure 0.1 mol/dm³ LiCl medium.

Introduction

The effect of surface active substances (SAA) on hydrolysis of aluminium(III) ion has been studied very little[1]. The effect of SAA on hydrolysis of Al³⁺ ion may be expected to depend on many factors such as, nature of SAA molecule, type and concentration of the ionic medium, pH and the presence of other organic molecules in solution[2].

In this work we used anionic surface active substances (SDS) and dioxane as modifiers of the pure ionic medium, to investigate the hydrolytic behavior of aluminium(III) ion. These the data may be useful in the water purification technology. Aluminium salts have traditionally been used as both, primary coagulants and flocculating agents in the treatment of water[3]. Aluminium sulfate or chloride is added to water in the process of purification with subsequent formation of colloidal Al(OH)₃. The formation of aluminium hydroxide and its adsorbing properties would depend on the presence of natural SAA (humic and fulvic acids) and other organic material[4] in treated water. In this work, to better understand the coagulation behavior of Al(OH)₃ in waters, SDS and dioxane were used to mimic the effect of humic acids and organic pollutants on hydrolysis of Al³⁺ ion.

Experimental

The potentiometric measurements were carried out using a Tacussel Isis 20000 pH meter equipped with a combination glass electrode (Ingold). The electrode was calibrated with standard Beckman pH 4.01 and 7.00 buffers. Metrohm Dosimat model 665 automatic burette was used to deliver the titrant, standard NaOH (0.1000 mol/dm^3). The temperature of the solutions was maintained at $25.0 \pm 0.1^\circ\text{C}$ by circulating thermostatically controlled water through the jacket of the titration vessel. All the measurements were carried out under a nitrogen atmosphere.

Results and Discussions

The emf data of the hydrolysis of $2.50 \text{ mmol/dm}^3 \text{ Al}^{3+}$ ion in $0.1 \text{ mol/dm}^3 \text{ LiCl}$ medium, in the presence of SDS and in mixed water-dioxane medium are given in Figure 1 as a dependence of the hydroxide number of aluminium(III) on the free hydrogen ion concentration, $-\log h$ (pH).

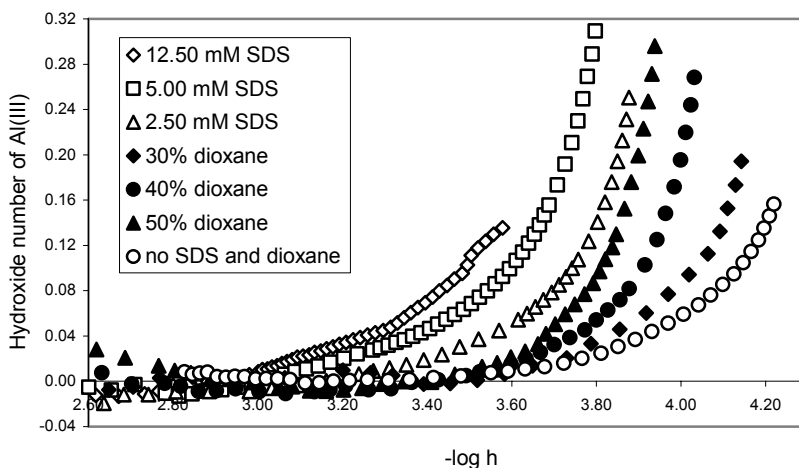


Figure 1. Hydrolysis of aluminium(III) ion in the presence of SDS and in mixed water-dioxane medium. The concentration of Al^{3+} ion was 2.50 mmol/dm^3

The composition of the hydrolytic complexes and their stability constants were determined by non-linear least-squares treatment of the experimental data.

The final results of calculations are given in Table 1 together with the calculated statistical parameters, χ^2 and s (Pearson's test and standard error, respectively).

Table 1. Stability constants of hydrolytic complexes formed in 0.1 mol/dm³ LiCl ionic medium, at 298 K in the presence of SDS and dioxane

Species	$-\log \beta_{p,q}$						
	mmol/dm ³ SDS + 0,1 mol/dm ³ LiCl				% dioxane + 0,1 mol/dm ³ LiCl		
	0.00	2.50	5.00	12.5	30	40	50
(1, -1)	5.15(0.01)	4.70(0.01)	4.54(0.02)	4.45(0.03)	4.85(0.02)	4.50(0.05)	4.52(0.02)
(1, -2)	9.53(0.01)	8.67(0.01)	8.44(0.01)	8.33(0.07)	9.40(0.07)	9.10(0.06)	8.95(0.01)
(1, -3)	14.18(0.10)	12.72(0.16)	12.60(0.04)	12.42(0.06)	13.97(0.09)	13.52(0.08)	13.27(0.04)
(2, -4)	15.44(0.03)	14.14(0.01)	13.65(0.01)	13.45(0.04)	-	-	-
(3, -4)	13.44(0.01)	-	-	-	-	-	-
(13, -32)	105.79(0.14)	93.37(0.13)	-	-	-	-	-
χ^2	12.36	14.12	10.25	10.89	12.89	11.89	13.25
S	1.11	0.50	0.57	0.50	1.58	1.87	1.57

As seen from the Table 1 in the presence of SDS aluminium(III) ion produces only mononuclear complexes (1,-1), (1,-2) and (1,-3) for the concentration of SDS higher than 2.5 mmol/dm³. At the lowest concentration of SDS (2.5 mmol/dm³) the polynuclear hydrolytic complexes (2,-4) and (13,-32) are formed. The stability constants of the complexes increase with increasing the concentration of the SDS. The SDS creates the micellar medium which surrounds the small hydrolytic species in early phase of their formation and hinders their hydration thus preventing further polymerization of these species[5]. The absence polynuclear hydrolytic complexes at higher the concentrations of SDS may be explained by the formation of stable species between SDS and mononuclear hydrolytic complexes.

In the presence of dioxane aluminium(III) ion forms only mononuclear complexes (1,-1), (1,-2) and (1,-3). The explication can be given by considering the formation of the binary aggregate of dioxane and water molecules[6]. The formation of these aggregates increases the activity of water molecules because the water-dioxane bond is weaker than Cl⁻ water bond and as a result the hydrolyses of the aluminium(III) ion shifts to lower pH values (Figure 1).

References

- [1] S. B. Savvin, R. K. Tshernova, S. N. Shtykov, *Analiticheskie Reagenty. Poverhnostnoaktivnye veschestva*, Nauka, Moskva, 1991.
- [2] M. J. Rosen, *Surfactants and Interfacial Phenomena*, 2nd Edition, J. Wiley and Sons. New York, 1989.
- [3] F.N.Kemmer, *Nalco Water Handbook*, 2nd ed., McGraw-Hill, NewYork, 1988.
- [4] J. Y. Bottero, J. L. Berisllon, *Aluminium and Iron(III) Chemistry: Some implications for organic substances removal in I. H. Suffet, P. MacCarthy (Eds.) Aquatic Humic Substances-Influence on Fate and Treatment of Pollutants, Advances in Chemistry Series 219, American Chemical Society, Washington, 1989, 425.*
- [5] J. Boisvert, T.C. To, A. Berrak and C. Jolicoeur. *Water Res.*, 1997, **31**, 1939.
- [6] T. Takamuku, A. Yamaguchi, D. Matsuo, M. Tabata, T. Yamaguchi, T. Otomo and T. Adachi, *J. Phys. Chem. B*, 2001, 105, 41.

NEURAL NETWORK PREDICTION OF THE GAS CHROMATOGRAPHIC SEPARATION OF POLYCYCLIC AROMATIC HYDROCARBONS

S. Sremac¹, Ž. Todorović¹, A. Popović² and A. Onjia¹

¹The Vinča Institute of Nuclear Sciences, P.O. Box 522, 11001 Belgrade, Serbia

²Faculty of Chemistry, Studentski trg 12-16, 11000 Belgrade, Serbia

Abstract

This paper describes the application of artificial neural networks (ANNs) method to the modeling of 13 polycyclic aromatic hydrocarbons (PAHs) retentions in temperature - programmed gas chromatography. The ANN method used resulted in relatively good agreement ($RMS_{\text{testing}} = 0.018$) between the measured and the predicted retention times for 13 PAHs. Somewhat higher discrepancy in prediction was observed for the late - eluted PAHs at lower temperature ramps.

Introduction

The programmed-temperature gas chromatography (GC) is one of the widely used techniques to determine polycyclic aromatic hydrocarbons (PAHs) in the environment. Some PAHs have very similar physico-chemical properties that may cause overlapping of their GC peaks. In order to optimize GC separation of PAHs, the retention behavior of each PAH has to be investigated. Of several systematic approaches to GC retention modeling, artificial neural networks (ANNs) offer the possibility to model the retention with no prior knowledge of the separation mechanism. The theory behind ANNs and their use in chromatography have been reported elsewhere [1-5]. In this work, the effect of changing of GC temperature program (initial temperature and linear temperature ramp) on the retention times of 13 PAHs has been studied by means of ANNs.

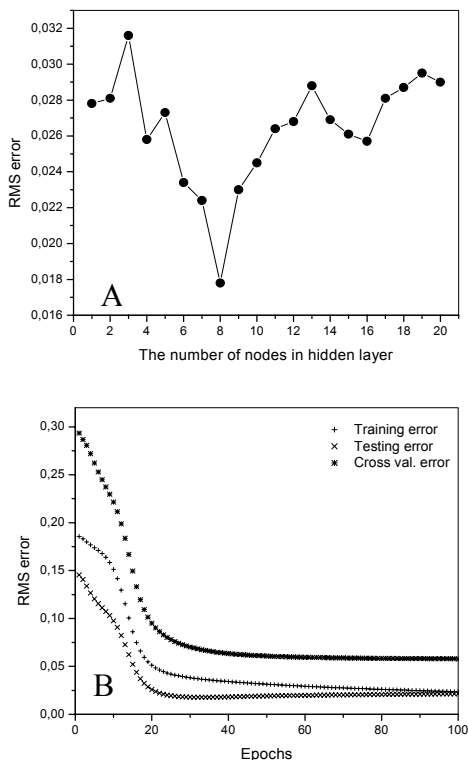


Fig. 1. RMS error vs. (A) hidden node number; (B) training epochs.

Experimental

All measurements were performed using a Spectra-physics model 7100 gas chromatograph with a flame ionization detector (FID). Commercially supplied PAH standards from Macharey-Nagel were used to prepare 20.0 ppm PAH solution in toluene. A 1.0 μL aliquot was injected into an Ultra[®]-1 (cross linked methyl silicone) capillary column (50 m x 0.32 mm, 0.52 μm df). As the final column temperature, 290 °C were selected, while the initial temperature and linear temperature ramp varied in the range 40 - 100 °C and 3 - 15 °C/min, respectively. The FID operated at 330 °C and a carrier (N_2) flow rate of 2.0 ml/min was used.

The retention time for each PAH was measured in duplicate using 9 combinations of initial temperature and temperature ramp. This data set was used to train, while unseen 4 temperature - ramp combinations were used to test ANN. The ANN systems were simulated using a QwikNet ANN simulator.

Table 1. ANN predicted (A) and measured (B) GC retention times (min) of PAHs.

PAH	Ramp. (°C/min)	6.0	6.0	12	12
	T _{init} (°C)	55	85	55	85
Naphthalene	A	17.48	14.40	12.10	11.16
	B	18.58	13.88	12.95	10.49
Acenaphthylene	A	25.16	20.95	16.14	15.09
	B	25.53	20.57	16.72	14.21
Acenaphthene	A	26.43	21.83	16.28	15.25
	B	26.38	21.41	17.17	14.65
Fluorene	A	29.29	23.97	17.48	16.39
	B	28.69	23.70	18.34	15.83
Phenanthrene	A	34.10	28.27	20.14	19.06
	B	32.94	27.94	20.70	18.18
Anthracene	A	34.60	28.13	20.27	19.00
	B	33.17	28.17	20.82	18.31
Fluoranthene	A	39.43	33.19	24.42	23.04
	B	38.40	33.40	24.04	21.53
Pyrene	A	41.71	33.93	24.53	23.10
	B	39.37	34.37	24.77	22.25
Benzo(a)anthracene	A	49.64	40.95	30.00	28.43
	B	45.77	40.78	30.12	27.61
Chrysene	A	49.34	41.11	30.29	28.75
	B	45.98	40.98	30.33	27.81
Benzo(b)fluoranthene	A	58.94	50.75	38.16	36.88
	B	54.58	49.60	38.40	34.67
Benzo(k)fluoranthene	A	59.39	50.38	38.58	36.98
	B	54.83	49.85	38.61	35.10
Benzo(a)pyrene	A	62.41	53.04	41.45	39.76
	B	57.81	52.84	41.55	37.99

Results and Discussion

The topological structure of the ANN employed in this study consists of three layers: input layer with 2 nodes (initial temperature and temperature ramp), output layer with 13 nodes (PAH retention times), and hidden layer with the number of nodes to be optimized. To find the best ANN parameters, a trial and error approach has been used. Root mean square (RMS) error function employed was computed with the following formula:

$$\text{RMS} = \left[\sum_{i=1}^n (d_i - o_i) / n \right]^{1/2} / x$$

here d_i is the desired output, o_i the actual output, n the number of retention time data, and x is the average value of desired output in the testing set.

Details on applied ANN algorithm and training method were given previously [1]

Fig. 1A shows a curve of RMS error versus the number of hidden layer nodes. The

optimum number of hidden layer nodes was found to be 8. To illustrate the learning process, the curves of RMS error values of the training, cross-validation, and testing set versus the learning epochs, when the number of hidden layer nodes is 8, were shown in Fig. 1B. The minimum average RMS error value for the testing set was 0,018.

The trained ANN was used to predict the retention data for 13 PAHs at 4 temperature programs not included in the ANN training set. This gave a total of $4 \times 13 = 52$ predicted retention times for the ANN, as shown in Table 1.

If the values of the retention times for the late-eluting PAHs at the lower temperature ramps are excluded, the remaining predicted values in Table 1 are in relatively good agreement with the experimental ones. The higher difference between the ANN predicted and experimentally derived retention times for highly retained PAHs can be ascribed to the problem that these PAHs, in fact, are still in the column upon reaching the final temperature. This phenomenon, of elution at the holding at the final temperature (290 °C), diminishes the role of GC temperature ramp and causes a wrong input to the ANN model.

Conclusion

ANNs can be applied to predict the retention behaviour of PAHs in temperature-programmed GC. Two parameters, initial temperature and linear temperature ramp, were chosen, in this work, as input descriptors. The retention time values predicted using the ANN method are satisfactorily close to experimental results. Somewhat higher discrepancy between ANN calculated and measured retention times of late eluting PAHs arised from the limitation of reaching the upper column temperature (hold temperature) of the linear temperature ramp before all PAHs are eluted.

Acknowledgment

The authors gratefully acknowledge financial support by the Ministry of Science and Environmental Protection of the Republic of Serbia (Projects No. 1978).

References

- [1] A. Onjia, W. Maenhaut, 6th Int. Conf. Fundam. Appl. Aspects Phys. Chem., Belgrade, 26-28th Sept. 2002, Proc., Vol. 2, p. 679.
- [2] T. Vasiljević, A. Onjia, Đ. Čokeša, M. Laušević, Talanta, in press.
- [3] S. Agatonović-Kuštrin, M. Zečević, Lj. Živanović, I. Tucker, Anal. Chim. Acta, 1998, 364, 265.
- [4] R. Zhang, A. Yan, M. Liu, H. Liu, Z. Hu, Chem. Intel. Lab. Sys., 1999, 45, 113.
- [5] M.H. Fatemi, J. Chromatogr. A, 2002, 955, 273.

Education

(N)

NOVEL EXPERIMENTS IN CHEMISTRY: METHODS TO DEMONSTRATE WHAT CANNOT BE DEMONSTRATED ORDINARILY

V. M. Petruševski,

*Department of Chemistry, Faculty of Sciences,
Sts. Cyril & Methodius University,
Skopje, Republic of Macedonia*

Abstract

Sciences rely on experiments, hence when teaching sciences demonstrations are among the first things the instructor should think of. Consequently, demonstrations are very important in all areas of chemistry, including physical chemistry. There are phenomena, however, that are not easy to demonstrate: chemical waves and transport phenomena (diffusion, osmosis, etc.) are usually time consuming, while demonstrations are supposed to be short (few minutes preferably). Dangerous experiments (e.g. those including a high risk of explosion) are, on the other hand, something instructors often try to avoid. Finally, spectral and structural properties usually require very expensive equipment that is not readily available. Some ideas are offered for effective demonstrations of many of the mentioned phenomena.

Introduction

The importance of demonstration experiments (demonstrations) in the process of teaching the Sciences has often been stressed. The particular importance of the chemical demonstrations has been elaborated many times [1–4]. Indeed, given the possibility to ‘activate’ each and every of our senses [5], carefully chosen demonstrations together with experienced instructor make chemistry teaching to be exciting and fun.

Since there are excellent books on chemical demonstrations and chemistry experiments in general (like those mentioned above [1–4]), at first sight it may seem that the instructor can easily choose one book and just repeat what other authors recommend. This misconception puts the instructor in a rather passive position. As a result he/she soon becomes unmotivated and reluctant to perform demonstrations.

Motivation, one has to say, is a symmetric relation [6]. Unmotivated instructors (i.e. teachers, professors etc.) produce unmotivated students. And unmotivated students will eventually end their studies as unmotivated, non-enthusiastic, and lazy... student teachers! Then the process starts all over again...

Of course, this must be prevented. A point of importance will be elaborated.

First of all, when it comes to demonstrations, it is imperative to realize that nothing has been said once and for all! Even more: every instructor is supposed to show initiative and invention in the course of performing a demonstration on the lecture bench. We shall simply postulate that one must be prepared for making modifica-

tions of well-known demonstrations, or even for thinking of novel ones. There are several reasons for this assertion:

- Modifications might appear to be inevitable (e.g. due to a lack of chemical)
- There is a need for more effective demonstration
- One might look for a safer demonstration
- A well-known phenomenon lacks suitable demonstration
- In order to offer an explanation for a phenomenon
- For checking a phenomenon assumed to be possible/feasible
-

In all of the above-mentioned examples a certain extent of originality is needed.

During the years of teaching lecture experiments and demonstrations (for students that will graduate as high school chemistry teachers), we prepared and published a number of modified and novel effective demonstrations [7–21]. We shall describe few of them, in order to picture the possible ways of giving contributions to this wide and very important area of chemistry education.

Marathon experiments: the fast motion technique

According to Fowles [1] there are several *classes* of chemistry experiments: (a) *casuals* or *ad hoc* experiments (short, almost unplanned experiments); (b) *marathons* (long-period experiments); (c) *majors* (or complex, elaborate experiments), and (d) *serials* (a series of several simple experiments). An extension of this classification with *moderate experiments* was proposed [5].

Understandably, marathons are the real problem, if the idea is to present them as chemical demonstrations. Namely, the duration of a chemical demonstration is rather short (5–10 minutes in most cases; the upper time limit is 20 minutes). Now imagine one intends to demonstrate a chemical wave (like the diffusion-reaction wave in the system KI–HgCl₂–gelatin [22], or the wave in arsenite–iodate system [23]). At least several days are needed for the former one; few hours for the latter. For example, the ‘time sections’ of the reaction presented in Fig. 1 (the test-tube contains a mixture of KH₂AsO₃, KIO₃, KHSO₄ and water), showing the propagation of a chemical wave in the arsenite–iodate system, covered a period of almost two hours [15]. Naturally, no demonstration could last that long.

Quite soon we discovered [19] a chemical wave in the system hypochlorite–iodide–water studied in gel media. This one is based on two succeeding reactions: oxidation of iodide to iodine, and further oxidation of the iodine to iodate. Similarly as in the case of the waves in arsenite–iodate system, iodine survives at the boundary surface between the hypochlorite solution and the iodide containing gel. Again, it takes a couple of hours for only partial completion of the reaction (cf. Fig. 2). Ordinary lecture demonstration is out of question.



Figure 1. Propagation of chemical wave in the arsenite-iodate system (the iodine ring slowly moves downwards).

Let us just mention in passing that both mentioned demonstrations of chemical waves (and also the wave in the system KI-HgCl_2 -gelatin [22]) are of the so-called ‘pencil-and-eraser’ type [19]. The motion of the iodine ring (or iodine disk) resembles the motion of tied pencil and eraser over a piece of paper (only a small dot or a dash will ‘survive’).

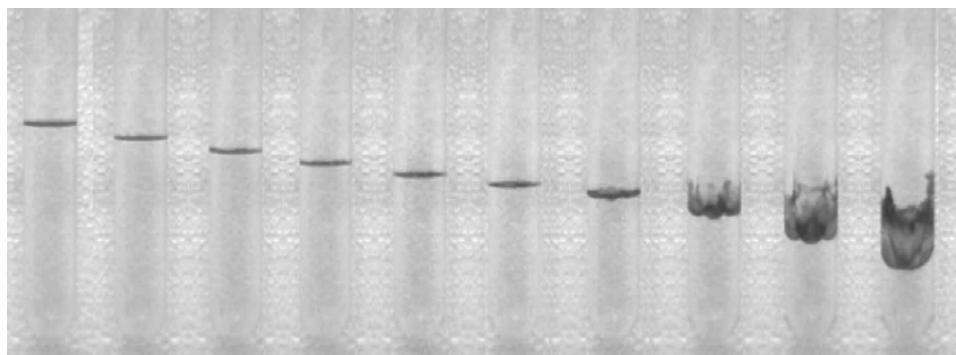


Figure 2. Propagation of chemical wave in the system hypochlorite-iodide-water (wave dispersion in the 3 rightmost tubes occurs due to hypochlorite depletion).

If one chooses examples of diffusion (of 2 liquids or a liquid and a solid etc.) it is becoming even worse (i.e. it could take many weeks before the phenomenon would cease seemingly). Consequently, one can safely conclude that all these phenomena cannot be demonstrated.

Few years ago we came across the lucky idea for ‘accelerating’ the above phenomena [15]. The propagation of the chemical wave in the arsenite-iodate system

(that originally took 3 hours) was photographed every 30 seconds. The collected photos were linked to give a unique 40 s movie, which could be used as an attractive demonstration of the otherwise overlong process. Exactly the same procedure was used for the other wave (the wave in the system hypochlorite–iodide–water [19]).

Once the trick was discovered (using this *fast-motion technique* applied above), it was relatively easy to make movies presenting diffusion (between potassium permanganate and water, bromine vapour and air, and nitrogen dioxide and air [21]). Further, it was shown for the first time [20] that effusion in liquids is feasible and can be easily demonstrated using the same equipment that one uses in the demonstration of gaseous effusion (cf. Fig. 3).

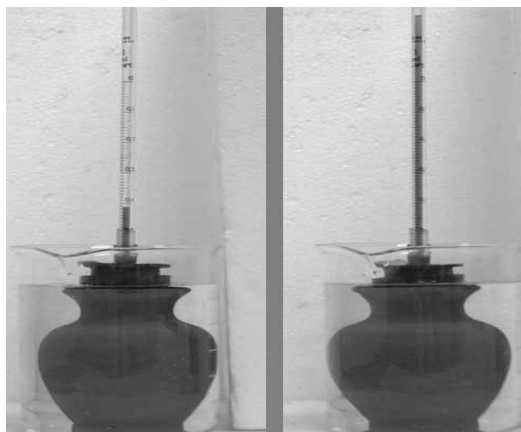


Figure 3. Water (in the beaker) effuses slowly through the porous walls in the cup filled with coloured glycerol. Start (left) and end (right, after 3 hours).

Video-clips were prepared of all above-mentioned long-lasting experiments.

Performing dangerous experiments: the safety spoon

The reaction of sodium and water has for many years been one of the favourite demonstrations of instructors, especially if performed using a Petrie dish on an overhead [24]. From a physicochemical point of view it might be interesting as a vigorous, highly exothermic reaction. In practically all manuals, the authors insist that only a small piece of sodium be used (size of a rice-grain). Large pieces are hazardous due to possible explosion. Further, the reaction of potassium and bromine is a spectacular demonstration, but it is always followed by a loud explosion and, it must be added, a serious risk for the instructor since there is not enough time to step aside, after the piece of potassium is dropped in the bromine.

We developed several versions of a device called *safety spoon* [16]. The schematic view of the safety spoon is presented in Fig. 4. All versions of the spoon are based on some kind of a remote control device (radio controlled, or controlled by a long cable, or activated by a laser pointer).

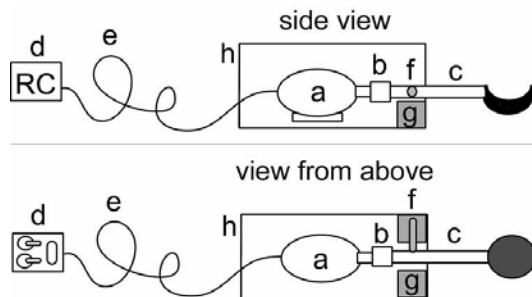


Figure 4. Construction of the safety spoon: electromotor (a); rubber connector (b); glass spoon (c); remote control (d); connection cable (e); brake (f); sponge (g); housing (h).

The use of the safety spoon gives the opportunity to perform both mentioned dangerous demonstrations with a high degree of safety. The instructor may be at a safe distance (e.g. sitting together with the class), and then simply starts the demonstration by pressing the trigger. Video-clips were also prepared as an absolutely safe, as well as time saving alternative [16].

Crystals and quasicrystals: laser pointer demonstrations

When teaching topics like spectroscopy and structure, instructors often find it impossible to present a demonstration. True, the equipment (spectrometers, diffractometers etc.) is both very expensive and robust – certainly not the kind of equipment one would bring in the classroom to demonstrate a phenomenon. While this cannot be done, spectra can definitely be shown (e.g. using transparencies on an overhead). Much more than that could be added to a lecture, as will be elaborated shortly.

Often analogies and simulations work very well instead of ‘in vivo’ demonstration. Even if an X-ray goniometer is available, nothing can be seen in real time on the instrument. However, as pointed out by Lisensky et al. [25] there is one-to-one correspondence of plane crystals and 2D optical gratings. In this way, it was easy to prepare drawings (actually, computer printouts) of various plane lattices, photograph them with conventional photo-camera and use the negatives as diffraction gratings in conjunction with a laser pointer (cf. Fig. 5, [18]). Obviously, the gratings take the role of 2D single crystals, the laser pointer is the X-ray source, and the projection screen is the film (or the CCD camera) used in the X-ray experiment.

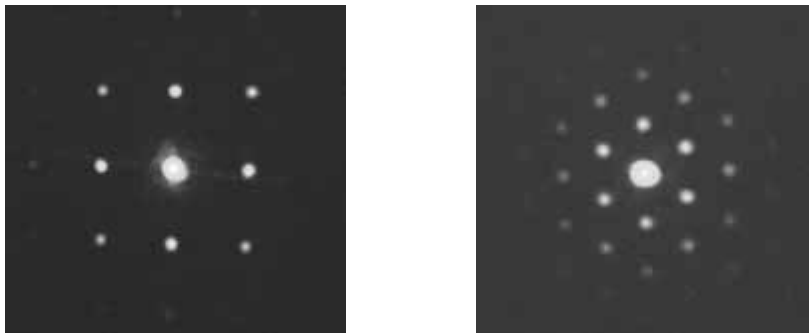


Figure 5. Diffraction patterns of 2D optical gratings, showing square (left) and hexagonal (right) lattice

Much in the same way, for graduates/postgraduates one could prepare ‘exotic’ gratings based on the Penrose or Amman tilings [25], and thus make an introduction to quasicrystals (i.e. aperiodic structures). Indeed, if the translational periodicity of the lattice is sacrificed, there is no restriction on the order of symmetry axes as has already been demonstrated (cf. Fig. 6 taken from [18]).

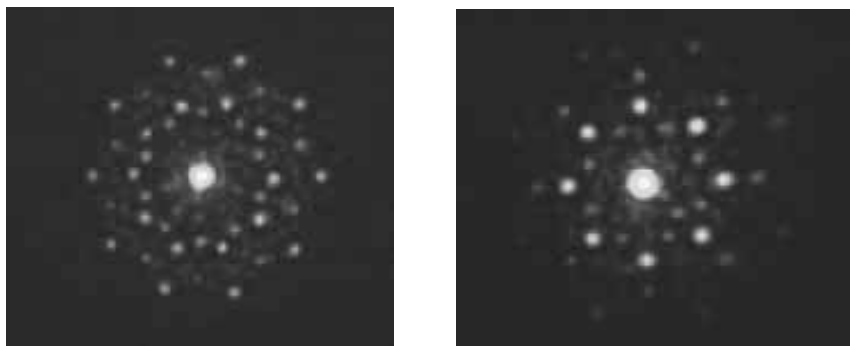


Figure 6. Diffraction patterns of 2D optical gratings, showing Penrose (left, decagonal) and Ammann (right, octagonal) lattices of aperiodic quasicrystals

Acknowledgement: The paper comprises the results of several papers published previously. I would like to sincerely thank all co-authors (M. Najdoski, M. Monković, S. Kalajdžievski and R. Aleksovska) for their invaluable contribution, and my professor and triple supervisor B. Šoptrajanov, who was spreading enthusiasm and was a constant driving force for the whole educational chemistry group.

References

- [1] G. Fowles, *Lecture Experiments in Chemistry*, Fifth Edition, G. Bell & Sons Ltd., London, 1959.
- [2] В. Н. Верховский, *Техника и методика хемијског експеримента у школи*, Књига II, Завод за издавање уџбеника СР Србије, Београд, 1965.
- [3] L. R. Summerlin, C. L. Borgford, B. J. Ealy, *Chemical Demonstrations: A sourcebook for Teachers*; American Chemical Society, Washington DC, 1987, Vol. 2.
- [4] B. Z. Shakhshiri, *Chemical Demonstrations: A Handbook for Teachers of Chemistry*; The Wisconsin University Press: Madison, WI, 1985, Vol. 2.
- [5] В. М. Петрушевски, М. Најдоски, *Експериментот во наставата по хемија I*, Магор, Скопје, 2000.
- [6] O. B. Popov, private communication.
- [7] V. M. Petruševski, M. Najdoski, Lj. Pejov, *Bull. Chem. Technol. Macedonia* 1998, 17, 53.
- [8] M. Najdoski, V. M. Petruševski, *Bull. Chem. Technol. Macedonia* 1998, 17, 61.
- [9] M. Najdoski, Lj. Pejov, V. M. Petruševski, *J. Chem. Educ.* 1999, 76, 360.
- [10] V. M. Petruševski, M. Najdoski, *Bull. Chem. Technol. Macedonia* 2000, 19, 85.
- [11] V. M. Petruševski, M. Ž. Najdoski, *Chem. Educator* 2000, 5, 193.
- [12] M. Najdoski, V. M. Petruševski, *J. Chem. Educ.* 2000, 77, 1447.
- [13] V. M. Petruševski, M. Ž. Najdoski, *Chem. Educator* 2001, 6, 91.
- [14] V. M. Petruševski, M. Z. Najdoski, *Chem. Educator* 2001, 6, 161.
- [15] M. Najdoski, R. Aleksovska, V. M. Petruševski, *Chem. Educator* 2001, 6, 319.
- [16] V. M. Petruševski, M. Ž. Najdoski, *Chem. Educator* 2002, 7, 81.
- [17] V. M. Petruševski, M. Ž. Najdoski, *Chem. Educator* 2002, 7, 220.
- [18] V. M. Petruševski, S. M. Kalajdzievski, M. Ž. Najdoski, *Chem. Educator* 2003, 8, 358.
- [19] V. M. Petruševski, M. Monković, M. Najdoski, *Chem. Educator* 2004, 9, 39.
- [20] V. M. Petruševski, M. Monković, M. Ž. Najdoski, *Chem. Educator*, submitted.
- [21] V. M. Petruševski, M. Monković, M. Ž. Najdoski, in preparation.
- [22] I. Das, A. Pusharna, A. Agrawal, *J. Phys. Chem.* 1989, 93, 7269.
- [23] I. R. Epstein, *J. Chem. Educ.* 1983, 60, 494.
- [24] DoChem 046. Sodium in water, http://dwb.unl.edu/Chemistry/DoChem/DoChem_046.html
- [25] G. C. Lisensky, T. F. Kelly, D. R. Neu, A. B. Ellis, *J. Chem. Educ.* 1991, 68, 91.
- [26] B. Grunbaum, G. C. Shepard, *Tilings and Patterns*, Freeman, New York, 1989, 520.

ROSALIND E. FRANKLIN IN BELGRADE

T. Halasi and R. Halasi

*Department of Chemistry, Faculty of Natural Sciences and Mathematics,
trg Dositeja Obradovića 3, Novi Sad, Serbia and Montenegro*

Abstract

In this paper is presented an interesting detail from the biography of Rosalind Ellias Franklin (1920-1958). She was excellent Physical-chemist, who visited the Serbian Chemical Society on May, 22nd, 1952. in Belgrade. On that occasion she held a lecture: *SOME ASPECTS OF THE ULTRA-FINE STRUCTURE OF COALS AND COKES*.

Rosalind E. Franklin developed the method for quantitative determination of structure of coal and cokes by XRD and found the correlation between the structure and the quality. It has great apply in industry. In same time worked on investigation of the double helix structure of DNA, together with known Nobel prize winners: Francis Harry Compton Crick, James Dewey Watson and Maurice Hugh Frederick Wilkins. But Rosalind E. Franklin was never mentioned because she died very young.

Introduction

The 1952 year is important for physical chemistry as the jubilee 200 years. Namely, Russian literate and artist Mihail Vasilevich Lomonosov worked on the Academy in Sankt Petersburg with his three students giving a course what He named *Course of Physical Chemistry* (orig. germ. *Lehrkursus der wahren Physikalische Chemie*)[1]. Lomonosov was inspired by Robert Boyle (1627-1691), who published *The Sceptic Chemist (1661)* and Benjamin Franklin (1706-1790), who published the *Declaration of the Independence*[2].

In XX century two women Rosalind E. Franklin and Dorothy Crowfoot-Hodgkin (1910-1991, Nobel prize win. 1964) worked on XRD, they have common trait to help Yugoslav scientist, as prof. Drago Grdenić etc [3,4]. Biography of Rosalind E. Franklin presented by the friend of Her, Anne Piper[5].

Biographical Notice of Rosalind E. Franklin

Rosalind Ellias Franklin was born in London June 25, 1920. in orthodox jewish family. Studied chemistry in Cambridge in Newnham College and graduated 1941. Through the World war II worked at British Coal Utilization Research Association, where started with coal structure study by means of XRD. She was devoted to this method till the end of Her career. Also worked on humanitarian activity in the frame of *German-jewish Committee for Refugees*. After the war 1947. she went to Paris, there worked in *Laboratory of Central des Services Chimiques des l'Etat*, where she defended Her PhD thesis in the class of prof. Mering.



Fig. 1. Rosalind Elias Franklin (June 7, 1920-April 16, 1958)

She was back in London 1951. and worked in *King's College* in the *Laboratory of Medical Research*. There started to work one structural problem of DNA by XRD method. She had a hard clash with Watson, who used Her X-ray diagrams of B-form of DNA of Mozaik virus of tobacco, where the double helix contour coming in sight. After all she went to Birkbeck College (1953) to prof. John Desmond Bernal (1901-1971). John Bernal was student of cristallography of William Lawrence Bragg (1890-1971). Rosalind as prof. Bernal was liberal socialist-humanist, although she was reserved and retiring person.

Rosalind E. Franklin in Belgrade

She held the lecture: *SOME ASPECT OF THE ULTRA-FINE STRUCTURE OF COALS AND COKES*, was published in *BULLETIN DE LA SOCIETE CHIMIQUE, BELGRADE, 1953*[6]. In her lecture in Belgrade she emphasised that the coal and the cokes are colloides in fine dispersed system where the properties depends on nature and whole surface. She cited D.H. Bangham with whom worked on carbonised coal, measuring dimensions of interior pores and active surfaces. The parametrers led to investigation of agregation of structural entiteties of different aged coals. She worked at the begining by methods of the classical physical-chemistry. After that used ultra microscopic and electronic microscopic methods which followed by XRD measurments[7-8]. Rosalind E. Franklin relied on H.L Riley's work[9], who concluded that coals contains graphitelike crystallites, which comes out on the base of XRD diffuse bands. In her paper[10] she critised the mentioned interpretation because with this can't be explained quantitatively the crystallite growth. The first quantitative

X-ray study was carried out by Biscoe and Warren. Rosalind E. Franklin also applied this method and showed that X-ray method can't easily be applied to coals. But the application to carbonised coals which is treated on higher temperature is good for much information because there were eliminated the noncarbon atoms except of hydrogen. On that way formed more regular layers of graphite, which could include also aromatic rings with high number of C-atoms. She explained this structures, by 5 parameters which came out from X-ray diagrams. This parameters are presented as: 1. L(mean diam. of layers), 2. M(mean num. of layers), 3. The proportion of disorder carbon, 4. The amount of truly graphite-like 3-dimensional order, 5. The mean particle diameters.

Rosalind E. Franklin found that coals treated on experimental temperature range 1000-3000°C contain graphitising and nongraphitising carbons. On the base of the values of L and M could be predicted the temperature of the crystallisation of the graphite in the carbonised coals. This observations could be applied to the carbonisation of coals. Rosalind E. Franklin found that the coking coals form compact structure, with oriented graphitising carbons. Rosalind E. Franklin this work presented in Belgrade which is an excellent example for history of applied physical chemistry!

Acknowledgment

The authors are thankful to Ministry of Sciences, Development and Technology of the Government of Republic of Serbia for support of the project „Education-stimulus for social and economic transformation of Serbia”, Code 1880.

Literature

- [1] Muratov M., M.V. Lomonosov, Prosveta, Beograd, 1948, 140.
- [2] Franklin B., Autobiography, Universal Library, spec. ed.
- [3] Kamenar B., Drago Grdenić, Croat. Chem. Acta, 1990, 63, C2.
- [4] Grdenić D. Mojih pedeset godina kemije, Kem. Ind., 2000, 49(7-8), 317.
- [5] Piper A., Light On A Dark Lady, Tibs, April 98, (268) vol. 23, p. 151-154.
- [6] Franklin R.E., Some Aspect of the Ultra Fine Structure of Coals And Cokes, Glasnik Hem. Društ. Beograd, 1953, 18(4), 203.
- [7] Franklin R.E., Trans. Far. Soc., 1949, 45, 274.
- [8] Bangham D.H., Franklin R.E., Maggs F.A.P. and Hist W., Fuel. 1949, 28, 231.
- [9] Franklin R.E., Fuel. 1948, 27, 46.
- [10] Franklin R.E., Proc. Roy. Soc. A., 1951, 209, 196.

Author Index

Abazović, N.	407	Caldararu, M.	538
Abbasov, V. M.	273	Caldeira, J.	338
Abu Rabi, A.	320	Carata, M.	538
Adamović, V.	688	Cebers, G.	350
Adnađević, B.	622, 649, 730	Cekić, B. Đ.	299
Aldrich, J. V.	350	Cekić, I.	60
Aleksić, M.	317	Cherkezova-Zheleva, Z.	478, 481
Andelić, S.	787	Chumikov, A.	819
Andelkoski, Đ.	616	Cirrone, P.	426, 429
Andelković, K. K.	490, 790, 802	Compton, R. G.	302
Anić, S.	39	Crisan, D.	279
Antić, B.	508	Cuttone, G.	426, 429
Antić-Jovanović, A.	104, 116, 143	Cvijanović, D.	700
Antonijević-Nikolić, M.	799	Cvijanović, G.	700
Antonović, D. G.	48	Cvijović, Đ.	772, 844
Araki, S.	568	Cvijović, M.	796, 805
Arandelović, D.	685	Cvjetičanin, N.	523, 526, 508
Arnaud-Neu, F.	66	Čakar, M.	45, 249
Arsenijević, Z.	709	Černigoj, U.	694
Auroux, A.	189	Čomor, J. J.	407
Azizov, R. E.	273	Čomor, M. I.	407, 484, 697
Bačić, G.	140, 359, 386	Čučulović, A.	670
Bakalkin, G.	331, 350	Čudina, O.	853
Bankovic, P.	721	Čupić, Ž.	222
Banks, C. E.	302	Četković, G. S.	808
Baranac, J.	119, 161	Čirić-Marjanović, G.	604, 619
Begović, N.	39	Ćosović, A.	688
Beljanski, M.	296, 362, 365	da Silva, M. L. P.	721
Berger, D.	216, 847	Daković, A.	727
Bijelić, G.	344	Daletou, M. K.	287
Blagojević S.	598, 733	Damjanović, Lj.	556
Blanco, C.	207	Damjanović, M. N.	155, 691
Blanco, C.	210, 213	Dašić, M.	164, 856
Blanuša, J.	508	Debeljković, D.	258, 261
Bogdanović, G. A.	541, 544, 781	Deloume, J. P.	847
Bogdanović, J.	347	Demajo, M. A.	374, 453, 673
Bojović, V.	116	Demarquette, N. R.	721
Bonnetot and, B.	459	Dimitrić-Marković, J.	119
Bošković, S.	475, 511	Dimitrijević, R.	547, 556
Bošnjaković-Pavlović, N.	544	Dobrescu, G.	216
Bowmaker, G. A.	146	Dojčinović, M. T.	706
Božin, D.	377	Dondur, V.	547, 556, 691
Božović, B.	54	Dragičević, V.	353
Brandl, W.	311, 314	Dragović, S.	438
Brborić, J.	398, 850	Dragutinović, V.	392
Brdarić, T.	119	Drakulić, B. J.	404
Brinckerhoff, W.	819	Drinić, G.	353
Bryliakov, K. P.	149, 255	Duban, E. A.	149
Bucevac, D.	475	Dugić, M.	833
Budinski-Simendić, J. K.	607, 625, 610	Dušek, K.	607
Bugarski, B.	589, 592, 595	Đerić, A.	152
Burić, N.	317	Đikanović, D.	347
Cakić, M.	775	Đinović, V. M.	784

Dogo, S.	679	Hubscher, V.	66
Đokić, D. Đ.	435, 450, 793	Hugonin, L.	350
Đoković, V.	484	Idakiev, V.	201
Đorđević, A.	432	Ignjatović, N.	487, 493
Đorđević, D. S.	640, 652, 453	Ilavsky, M.	607, 625
Đujić, I. S.	453	Ilić, Lj.	775
Đujić, I. S.	673	Ilić, M.	240, 598, 733
Đurđević, P. T.	796, 805, 862	Ilić, M. R.	886
Đuričić, M.	736	Ilić, N.	395
Edreva-Kardjieva, R.	279	Ilić, S.	125
Efremenko, E. N.	273	Ionescu, N. I.	216
Elokhin, V. I.	179	Ivanović, M.	353
Figueirinhas, J. L.	338	Ivković, B.	745
Filip-Cristea, C.	323	Jacques, S.	459
Filipović, D.	401	Jakovljević, D.	341, 682
Filipović, J.	143	Jakšić, Z.	550, 553
Filipović, J. M.	583, 613	Janković, B.	529
Filipović, Z. I.	706	Janković, D.	432, 435, 793
Filipović-Rojka, Z.	490, 733	Janković, I.	853
Franko, M.	87, 694	Janković, T.	410
Gabrovska, M.	279	Jekić, J.	637
Gajinov, S.	276	Jelić, R. M.	862
Gaković, B.	517	Jensen, A. A.	27
Gattás-Asfura, K. M.	3	Jeremić, M.	143, 347
Geda, T.	856	Jevtović, V. S.	541
Ghermani, N. E.	544	Jitaru, M.	323
Giba, Z.	140	Joksić, G.	356, 410
Gobor, L.	48, 158	Joksić, J. D.	667, 712
Godinho, M. H.	338	Joksović, Lj. G.	862
Golobočanin, D.	664	Jones, K. A.	14
González, F.	207, 210, 213	Jordović, B.	502
Gorjanović, S. Ž.	296, 380, 706	Jovanović, A.	649
Gourdoupi, N.	287	Jovanović, D.	219, 499, 520
Grahovac, Z. M.	243	Jovanović, D.	844
Grandić-Aleksić, D.	658, 661	Jovanović, J.	57, 622, 730
Gräslund, A.	350	Jovanović, M.	204
Grbavčić, M.	637	Jovanović, M.	258, 261
Grbavčić, Ž.	709	Jovanović, M.	850
Grbić, B.	225	Jovanović, M. S.	398
Grković-Popović, M.	270	Jovanović, O.	134
Grubišić, D.	140	Jovanović, S. M.	724
Grzybowska, B.	538	Jovanović, T.	167, 170
Halasi, R.	878	Jovanović, T.	688
Halasi, T.	878	Jovanović, V.	691
Hall, M. B.	20	Jovetić, S.	826
Hercigonja, R.	60, 276	Jozanov-Stankov, O. N.	673
Hildebrant, P.	74	Jugović, D.	487, 523
Hodžić, I.	787, 790	Juranić, I. O.	404
Holclajtner-Antunović, I.	107	Juranić, N.	14, 760
Holler, P.	619	Juranić, Z.	784
Hornoiu, C.	538	Kadinov, G.	228, 478, 481
Horvat, A.	368, 371, 374	Kalagasisdis-Krušić, M.	613, 616
Hranisavljević, S. T.	706	Kalauzi, A.	347
Hranisavljević-Jakovljević, M.	341, 682	Kallitsis, J. K.	287

Kaluđerović, G. N.	784, 856	Managadze, G.	819
Kapetanović, V.	317	Managadze, N.	819
Kapor, A.	508	Manić, T. M.	583
Karljiković-Rajić, K.	853	Manova, E.	204
Katsaros, N.	757	Maravić, D. S.	155
Kellenberger, A.	311, 314	Marčeta-Kaninski, M. P.	308
Khazaeli-Parsa, P.	66	Maričić, A.	502
Kićanović, M.	380, 389, 796	Marinković, A. D.	173
Kocić, G.	122	Marinković, M.	101, 110
Kojić, D.	234	Marinković, S.	685
Kolar-Anić, Lj.	39, 344	Marinova, Z.	350
Kolarić, B. M.	404	Marinović-Cincović, M.	625
Koltsov, N. I.	252	Marjanović, B.	604, 619
Konjević, R.	140	Marjanović, V.	51
Konova, P.	201	Marković, B.	219, 499
Konstantinović, S.	125, 128	Marković, D.	107
Korićanac, L.	413	Marković, D.	131
Korićanac, Z.	167, 170	Marković, D.	676
Korom, S.	697	Marković, G. S.	625
Kostić-Pulek, A.	685	Marković, R.	161, 826
Kovačević, B.	258, 261, 490	Marković, S.	270, 526, 547
Kovačević, O.	490	Marković, Z.	39
Krajčinović, B.	787	Marote, P.	847
Kremenović, A.	508	Matei, C.	847
Krinulović, K.	231, 237, 694	Matić, Lj.	204
Krmar, M.	113	Matijašević, S.	727
Krnojelac, D.	493	Matović, B.	475
Krstić, J.	496, 520, 715	Mayerand, C.	146
Krstić, V.	207, 210	Medaković, V. B.	763, 766, 772
Krstić, V.	213	Mentus, S.	305, 505, 302
Kuchanov, S. I.	577	Mićić, M.	347
Kukavica, B.	359	Mićić, S.	745
Kuljanin, J.	484	Mihajlići-Zelić, A. J.	652
Kunev, B.	204, 478, 481	Mijić, Z. R.	640, 643
Kuntić, V.	745	Mijjin, D. Ž.	173
Kuzmanović, M. M.	101, 104, 116	Miladinović, J.	51, 54
Lačnjevac, Č.	326	Miladinović, Z.	146, 559
Lazić, M. J.	802	Milčić, M. K.	760, 763, 766
Lazić, N. L.	490	Miletić, G. Ž.	246
Leblanc, R. M.	3	Miletić, S.	886
Lemic, J.	736, 751	Milivojević, D.	670
Leovac, V. M.	541, 781	Miljanić, Š. S.	308, 670, 883
Leskovac, A.	410	Miljanović, I.	562
Logar, M.	137	Miljević, N.	664, 805
Lončarević, D.	222	Miljković, M.	487, 586, 655
Lukić, D.	748	Milonjčić, S. K.	724, 742
Lukić, S.	496	Milosavljević, B. H.	580
Macura, S.	14, 547	Milošević, M.	368, 371, 374
Majkić, S.	158	Milošević, M.	748
Makhliis, T. A.	273	Milošević, N.	700
Maksić, A. D.	308	Milutinović-Nikolić, A.	496, 520
Maksimović, M.	550, 553	Minchev, Ch.	204
Maksin, T.	432	Minić, D.	161, 502, 658, 661
Malešev, D.	745	Mioč, U.	544

Miodragović, Đ. U.	787, 790	Pavelkić, V.	240, 733, 805
Miodragović, Z. M.	787, 790	Pavlović, A. N.	246
Mitić, N.	362, 365	Pavlović, M.	110, 380, 383
Mitić, S. S.	243, 246, 264	Pavlović, M. D.	706
Mitić, V. D.	655, 282	Pavlović, M. S.	101, 104
Mitić, Ž.	775	Pavlović, N.	523, 658, 661
Mitov, I.	204, 478, 481	Pavlović, R.	122
Mitrić, M.	487, 523, 526	Pavlović-Lažetić, G.	362, 365
Mojović, M.	140	Pecev, E. T.	243
Mojović, Z.	505	Pejić, N.	745
Molnár-Gábor, D.	697	Pérez, L. M.	20
Momić, T.	410	Perkins, W. J.	14
Munteanu, C.	538	Perović, J. M.	841
Murgida, D.	74	Pešić, D.	116
Nastasović, A. B.	341, 601, 724	Pesquera, C.	207, 210, 213
Naydenov, A.	201	Petković, J.	170
Nedeljković, J. S.	173	Petković, M.	270
Nedić, Z.	487	Petkovska, Lj. T.	155
Nenadović, M. T.	467	Petranović, N.	119
Nenadović, T. M.	467, 517	Petrov, L. A.	6, 478, 481
Nešković, O.	80, 152	Petrović, G.	134
Ničiforović, A.	444	Petrović, I.	426, 429
Nikolić, A. D.	48, 158	Petrović, J.	131
Nikolić, A. S.	508	Petrović, M.	395
Nikolić, G.	131	Petrović, S.	164
Nikolić, G. M.	122, 775, 841	Petrović, S.	368
Nikolić, G. S.	775	Petrović, S.	371, 374
Nikolić, J. D.	514	Petrović, S.	517
Nikolić, M.	649	Petrović, S.	715
Nikolić, M.	98	Petrović, S. D.	158, 173, 856
Nikolić, N.	778	Petruševski, V. M.	871
Nikolić, R. S.	122, 775, 841	Pezo, L.	258, 261
Nikolić, S. D.	282	Pfendt, L.	42
Nikolić, Z. S.	565, 568, 571	Plavšić, M. B.	589, 592, 595
Ninkov, P.	493	Plesu, N.	311, 314
Ninković, R.	51, 54	Podunavac-Kuzmanović, S. O.	808, 811, 814
Nitulescu, C.	847	Poharc-Logar, V.	137
Novaković, S. B.	769, 781	Popović, A.	679, 865
Novaković, T.	601	Popović, G.	42, 45, 317
Novaković, V. T.	640, 643	Popović, I. G.	616
Novović, I.	107	Popović, N.	413
Obradović, M. V.	264	Popović-Bijelić, A.	344
Onjia, A. E.	438, 739, 865	Postole, G.	538
Orlić, M.	398, 748	Potkonjak, N.	290, 293
Ostojić, S. B.	380, 389, 392	Pramanik, A.	331
Ostrovskii, N. M.	195	Purenović, M.	586, 655
Pajić, Z.	353	Rac, V.	276
Pajić-Lijaković, I.	589, 592, 595	Radak, B. B.	155
Paneva, D.	204	Radenković, M. B.	667, 712
Pantelić, G.	447	Radić, M.	487
Papa, F.	216, 847	Radić, N.	225
Papakyriakou, A.	757	Radičević, R. Ž.	607, 610
Parvulescu, V.	228	Radivojević, B.	164
Patmar, E. S.	252	Radmanović, D. J.	640, 652

Radojčić, M. B.	401, 441, 444	Stanisavljev, D.	805
Radojčić, V.	649	Stanković, M.	258, 261
Radosavljević-Mihajlović, A.	727	Stanković, V. M.	219, 496, 499
Radotić, K.	347	Stanković, S.	438, 670
Radovanović, B.	134	Stankov-Jovanović, V. P.	282
Radović, M.	517	Stanojković, T.	784
Radulović, M.	341, 682	Stoiljković, D. M.	610
Radulović, S. S.	802	Stoiljković, M.	104, 110, 748
Raičević, S.	739	Stoimirović, Z.	637
Rajić, N.	258, 261	Stojadinović, B.	790
Rajković, M. B.	326, 447, 703	Stojanović, M.	703
Rajšić, S. F.	640, 643	Stojčeva Radovanović, B.	125, 128
Rakić, A. A.	772	Stojić, D. Lj.	234, 299, 308
Rakić, S.	508	Stojković, I.	523
Rakić, V.	60, 276, 556	Streiff, J.	14
Rakočević, Z.	517	Su, B. L.	228
Randelović, V.	622	Sunarić, S.	122
Ranković, D.	709	Surcheva, S.	350
Rašović, A.	826	Sužnjević, D.	290, 293, 320
Ražić, S.	679	Šašić, S.	143
Rikić, D.	48	Šipka, V.	152
Ristić, M. M.	502	Šljukić, B. R.	302
Ristić-Fira, A.	413, 426, 429	Špirkova, M.	607
Rosić, A.	562	Šućurović, A.	219, 499
Rottinghaus, G.	727	Tabakova, T.	201
Ruvarac-Bugarčić, I.	853	Talsi, E. P.	149, 255
Sabo, T. J.	784	Tanasković, S. B.	799
Saiz, V.	207	Tančić, A. R.	92, 95, 98
Santos, C.	338	Tasić, M. D.	640, 643
Sanz, R.	210	Tenchev, K.	228
Savić, J.	63, 267, 323	Terenius, L.	331, 350
Savin, A.	676	Terlecka-Baricević, A.	204, 225
Savović, J. J.	101, 104, 110	Tešić, Z.	505
Shopska, M.	478, 481	Tešić, Ž. Lj.	490, 802
Shtereva, I.	481	Todorova, S.	228
Simić, N. D.	299, 308	Todorović, D.	413, 426, 429, 712
Simonović, B.	389, 392, 685	Todorović, D. M.	535
Siskos, P. A.	631	Todorović, M.	51, 54
Sitaras, I. E.	631	Todorović, S.	74
Sladić, D. M.	42, 802	Todorović, Z.	125, 856
Slavković, L.	679	Todorović, Ž. N.	742, 865
Smičiklas, I.	739	Todosijević, Z.	595
Sofronić-Milosavljević, Lj.	395	Tomašević, M. N.	640, 643
Somacescu, S.	228	Tomašević-Čanović, M.	691, 727, 751
Spasojević, I.	359	Tomić, S. Lj.	583
Spasojević-de Biré, A.	544	Tomić, Z. D.	769
Spasojević-Tišma, V.	240	Topalov, A.	697
Sredojević, D. N.	760	Tošić, M. B.	514
Sredojević, S.	353	Tosić, S. B.	264
Srejić, R.	386	Tošković, D.	326, 447
Sremac, S.	865	Tripković, M.	107
Stamatović, A.	71	Trtica, M. S.	883
Stamenković, Lj. Lj.	450	Tsoncheva, T.	204
Stanić, T.	736, 751	Uskoković, D.	493, 526, 622

Valastro, L.	426, 429	Vujić, Z.	745
Valentova, H.	625	Vukelić, N.	715
Varfolomejev, S. D.	273	Vukojević, V.	331, 344, 350
Vasić, V.	249, 323, 694	Vuković, Z.	496, 520, 601
Vasiljević-Radović, D.	550	Warner, D. O.	14
Vaszilcsin, N.	311, 314	Weijie, F.	350
Veličković, S.	152	Yakovleva, T.	331, 350
Veličković, S. J.	616	Yoshimura, M.	568
Veljković, M.	152	Zakrzewska, J.	359, 559
Veselinović, D.	670, 676, 778	Zakrzewska-Trznadel, G.	419
Vitorović, M.	790	Zarić, S. D.	760, 763, 769
Vladimirov, S.	398, 850	Zarubica, A.	586, 655
Vojić, M.	42	Zec, S.	511
Vojinović, Lj. S.	811, 814	Zlatanović, S.	733
Vranješ, S.	398	Živanović, A.	751
Vrvić, M. M.	341, 353, 682	Živanović, M.	240, 249
Vučina, J.	748, 778	Živanović, V. D.	514
Vučinić, D.	562	Živić, M. Ž.	380, 706
Vučinić-Vasić, M.	508	Živković-Radovanović, V.	859
Vučković, A.	475	Žujić, A.	664
Vučković, G.	799, 859	Žujović, Z. D.	146
Vučković, M.	441		

Participating Institutions

AD Chemical Industry HIPOL, Odžaci, Serbia & Montenegro	195
Azerbaijan NAS the Y.H. Mamedaliyev Institute of Petrochemical Processes, Baku, Azerbaijan	273
Boreskov Institute of Catalysis SB RAS, Prosp. Akad. Lavrentieva, 5, 630090, Novosibirsk, Russia	179
Centre for Multidisciplinary Studies, University of Belgrade, 29. Novembra 142, 11000 Beograd, Serbia	347, 359, 535
Centrohem, Karadorđeva 129, 22300 Stara Pazova, Serbia and Montenegro	604, 619
Charles University, Faculty of Mathematics and Physics, Prague, Czech Republic	607
Chuvash State University, Department of Physical Chemistry, Moskovskii prospect 15, 428015 Cheboksary, Russia	252
Clinical Center of Serbia, Institute of Occupational and Radiological Health "Dr Dragomir Karajović", Belgrade,	447
"Eko-Lab", Industrijska zona bb, 11000 P. Skela, Belgrade,	676
Fachhochschule Gelsenkirchen, Neidenburger Strasse 10, 45877 Gelsenkirchen, Germany,	311, 314
Faculty of Agriculture, University of Belgrade, Nemanjina 6, Zemun, Serbia and Montenegro	60, 276, 326, 556, 649,
Faculty of Biology, University of Belgrade, Belgrade, Serbia and Montenegro	140
Faculty of Chemistry, Belgrade University, Studentski Trg 12, P.O.Box 158, Belgrade, Serbia and Montenegro	42, 161, 282, 341, 353, 404, 410, 505, 622, 640, 652, 679, 760, 763, 766, 769, 772, 784, 787, 790, 799, 802, 818, 851, 857,
Faculty of Chemistry, Department for Inorganic Chemistry, University of Belgrade, P. O. Box 158, Belgrade,	508,
Faculty of Electronic Engineering, University of Nis, Department of Microelectronics, 18000 Nis, PO Box 73, Serbia	565, 568, 571,
Faculty of Mathematics and Natural Sciences, University of Nis, Department of Chemistry, Visegradska 33, 18000 Nis, Serbia and Montenegro	134, 243, 246, 282, 586, 655
Faculty of Mathematics, 11000, Belgrade	362, 365
Faculty of Mechanical Eng., 27. marta 80, Belgrade, Serbia and Montenegro	258, 261
Faculty of Medicine, Bulevar dr Zorana Djindjića 81, 18000 Niš,	487, 775
Faculty of Medicine, Clinic of Stomatology, University of Novi Sad, Novi Sad	493

Faculty of Medicine, Department of Biochemistry, Bulevar dr Zorana Đinđića 81, 18000 Niš, Serbia and Montenegro,	122
Faculty of Medicine, Department of Chemistry, Bulevar dr Zorana Đinđića 81, 18000 Niš, Serbia and Montenegro,	122, 833
Faculty of Medicine, University of Novi Sad, Novi Sad, Serbia and Montenegro	493
Faculty of Mining and Geology, University of Belgrade, Djušina 1, Beograd, Serbia and Montenegro	137, 508, 556, 562, 685,
Faculty of Mining and Geology, Department of Crystallography, Djušina 7, Belgrade, Serbia and Montenegro	547
Faculty of Natural Sciences and Mathematics, Department of Chemistry, trg Dositeja Obradovića 3, Novi Sad, Serbia and Montenegro	870
Faculty of Natural Sciences and Mathematics, University of Novi Sad, Trg Dositeja Obradovica 3, Novi Sad, Serbia and Montenegro	432
Faculty of Natural Sciences, Niš, Serbia and Montenegro	98
Faculty of Pharmacy, Institute of Pharmaceutical Chemistry and Drug Analysis, Vojvode Stepe 450, Belgrade, Serbia and Montenegro	745, 845
Faculty of Pharmacy, Institute of Physical Chemistry, Vojvode Stepe 450, Belgrade, Serbia and Montenegro	317, 745
Faculty of Pharmacy, Institute of Physics and Mathematics, Vojvode Stepe 450, P.O.Box 146, 11000 Belgrade	317
Faculty of Pharmacy, University of Belgrade, P.O.Box 146, Vojvode Stepe 450, 11001 Belgrade, Serbia and Montenegro	42, 45, 167, 170, 249, 317, 398, 679, 799, 842, 845
Faculty of Physics, 11001 Beograd, P.O.Box 368, SCG	71
Faculty of Physical Chemistry, Belgrade University, Studentski trg 12-16, 11000 Belgrade, Serbia and Montenegro	39, 57, 60, 101, 104, 107, 110, 116, 119, 140, 143, 152, 161, 170, 270, 276, 290, 293, 302, 344, 305, 308, 347, 359, 386, 487, 502, 505, 508, 523, 526, 529, 544, 547, 556, 604, 619, 622, 649, 658, 661, 670, 676, 691, 715, 730, 772, 778, 796, 805, 836, 883
Faculty of Science, Department of Chemistry, Cirila i Metodija 2, 18000, Nis, Serbia and Montenegro	125, 128
Faculty of Science, Department of Chemistry, Radoja Domanovica 12, P.O.Box 60, 34000 Kragujevac	39, 796, 805, 854
Faculty of Science, Department of Chemistry, Višegradska 33, 18000 Niš, Serbia and Montenegro	122, 833

Faculty of Science, Department of Physics, Kragujevac, Serbia and Montenegro	825
Faculty of Sciences and Mathematics, Višegradska 33, 18000 Niš, Serbia and Montenegro	264, 625, 775
Faculty of Sciences, Department of Chemistry, Sts. Cyril & Methodius University, Skopje, Republic of Macedonia	863
Faculty of Sciences, Department of Chemistry, University of Novi Sad, Trg D. Obradovića 3, 21000 Novi Sad, Serbia and Montenegro	48, 158, 541, 697, 781, 818,
Faculty of Technical Sciences, University of Novi Sad, Trg D. Obradovica 6, Novi Sad, Serbia and Montenegro	508
Faculty of Technology and Metallurgy, Belgrade University, Belgrade, Serbia and Montenegro	48, 51, 54, 158, 164, 173, 258, 261, 496, 583, 589, 592, 595, 613, 616, 724, 848,
Faculty of Technology, Novi Sad, Serbia and Montenegro	625
Faculty of Technology, University in Novi Sad, 21000 Novi Sad, Bulevar Cara Lazara 1, Serbia and Montenegro	610
Faculty of Technology, University of Nish, Bulevar Oslobođenja 124, 16000, Leskovac	125, 128, 131, 775
Faculty of Technology, University of Novi Sad, Serbia and Montenegro	607
Faculty of Technology, University of Serbian Sarajevo, Bosnia&Herzegovina and	326, 447
Force Technology, Søborg Gladsaxe Møllevej 15, DK-2860 Søborg, Denmark	27
Freie Universität, Institut für Chemie-Physikalische und Theoretische Chemie, Berlin	270
G. K. Borekov Institute of Catalysis, Siberian Branch of the Russian Academy of Sciences, 630090 Novosibirsk, Russian Federation.	149, 255
Galenika Fitofarmacija, Batajnički drum b.b., Zemun, Serbia & Montenegro	155, 691, 886
Hemofarm koncern, Beogradski put bb, 26300 Vršac, Serbia and Montenegro	164, 173, 848
High School for Chemistry and Technology, 15000 Šabac	799
High Technical School, 34 St. Sava square, 31000 Užice, SCG	51
Holding Institute of General and Physical Chemistry, P.O. Bo 551, Studentski trg 12/V, Belgrade,	39, 146, 240, 258, 261, 276, 290, 293, 296, 320, 344, 359, 362, 365, 380, 383, 389, 392, 490, 559, 598, 685, 706, 733, 796, 886
INEP, Institute for the Application of Nuclear Energy, Banatska 31b, 11080 Zemun, Serbia and Montenegro	395, 438, 670

Institut de Recherches sur la Catalyse, CNRS, 2 avenue Einstein, 69626 Villeurbanne Cedex, France	189
Institute for Chemistry, Technology and Metallurgy, Center for Catalysis and Chemical Engineering, Njegoševa 12, Beograd, Serbia and Montenegro	204, 219, 222, 225, 320, 496, 499, 505, 520, 601, 715,
Institute for Chemistry, Technology and Metallurgy, Center for Chemistry, P.O. Box 815, Belgrade, Serbia and Montenegro	161, 341, 404, 601, 640, 652, 682, 724, 818,
Institute for Chemistry, Technology and Metallurgy, Institute of Microelectronic Technologies and Single Crystals, Belgrade, Serbia and Montenegro	550, 553,
Institute for Chemistry, Technology and Metallurgy, Njegoševa 12, 11000 Belgrade, Serbia and Montenegro	453, 673
Institute for Health Protection, Belgrade, SCG	649
Institute for Macromolecular chemistry, Academy of Sciences, Czech Republic	607
Institute for Oncology and Radiology of Serbia, Laboratory for Experimental Pharmacology, Belgrade, Serbia and Montenegro	802
Institute Goša, Milana Rakića 35, 11000 Beograd	113
Institute of Agriculture in Economics, Bulevar Kralja Aleksandra 80, 11000 Belgrade, SCG	700
Institute of Biological Research "Siniša Stanković", Belgrade,	140
Institute of Catalysis and Surface Chemistry of the Polish Academy of Sciences, ul Niezapominajek 1, Krakow, Poland	538
Institute of Catalysis, Bulgarian Academy of Sciences, Acad. G. Bonchev St., Block 11, 1113 Sofia, Bulgaria	6, 201, 204, 228, 279, 478, 481,
Institute of Chemical Engineering and High Temperature Chemical Processes, ICE/HT-FORTH, P.O.Box 1414, 26500 Patras, Greece.	287
Institute of Field and Vegetable Crops, Maksima Gorkog 30, 21000 Novi Sad, SCG	353, 700
Institute of Food Technology and Biochemistry, Faculty of Agriculture, Zemun, University of Belgrade, Serbia&Montenegro	447, 703
Institute of General and Inorganic Chemistry, Bulgarian Academy of Sciences, 1113 Sofia, Bulgaria	201
Institute of Macromolecular Chemistry, Heyrovský Sq. 2, Prague, Czech Republic	619
Institute of Nuclear Chemistry and Technology, Dorodna 16, 03-195 Warsaw, Poland	419
Institute of Nuclear Science Vinča, Materials Science Laboratory, 11001 Belgrade, POB 522, Serbia and Montenegro	475, 511

Institute of Nuclear Science Vinča, P. O. Box 522, 11000 Belgrade, Serbia and Montenegro	80, 92, 95, 98, 152, 155, 231, 237, 249, 356, 377, 407, 413, 426, 429, 438, 453, 467, 484, 517, 526, 625, 664, 673, 679, 694, 697, 724, 739, 742, 748, 769, 842, 857, 883
Institute of Nuclear Sciences Vinča, Centre for Nuclear Technologies and Research, 11001 Belgrade, P.O.Box 522, Serbia and Montenegro	748
Institute of Nuclear Sciences Vinča, Department of Physical Chemistry, PO Box 522, 11001 Belgrade, Serbia and Montenegro,	63, 101, 104, 110, 234, 240, 267, 299, 308, 323, 410, 748, 805,
Institute of Nuclear Sciences Vinča, Laboratory for Radioisotopes, P.O.Box 522, 11001 Belgrade, Serbia and Montenegro	398, 432, 435, 450, 778, 748, 793,
Institute of Nuclear Sciences Vinča, Laboratory of Molecular Biology and Endocrinology, P.O. Box 522, 11001 Belgrade, Serbia and Montenegro	368, 371, 374, 401, 441, 444,
Institute of Nuclear Sciences Vinča, Laboratory of Physics, 11001-Belgrade, P.O. Box 522, Serbia and Montenegro	299
Institute of Nuclear Sciences Vinča, Laboratory of Theoretical Physics and Condensed Matter Physics, P.O.Box 522, 11001 Belgrade, Serbia and Montenegro	541, 487, 523, 544, 763, 781
Institute of Nuclear Sciences Vinča, Radiation and Environmental Protection Laboratory, 11001 Belgrade, P.O.B. 522, Serbia and Montenegro	667, 712,
Institute of Nuclear Sciences, Laboratory for Radiation Chemistry and Physics, Vinča P.O. Box 522, 11001 Belgrade, Serbia and Montenegro	845
Institute of Nuclear Sciences, Vinča, Laboratory of Solid State Physics, P. O. Box 522, Belgrade, Serbia and Montenegro	508,
Institute of Oncology and Radiology, 11000 Belgrade, Serbia and Montenegro	784,
Institute of Organic Chemistry, Bulgarian Academy of Sciences, 1113 Sofia, Bulgaria	204
Institute of Physical Chemistry "I.G.Murgulescu" of the Romanian Academy, Spl. Independentei 202, 060041 Bucharest, Romania,	538
Institute of Physical Chemistry, 202 Independentei Blvd., Bucharest, Romania	228
Institute of Physical Chemistry, NCSR "Demokritos", 15310 Ag. Paraskevi, Attikis, Greece	757
Institute of Physical Chemistry, Romanian Academy, Bucharest 77208, Romania	279
Institute of Physics, Environmental Physics Laboratory, Pregrevica 118, Belgrade	107, 640, 643

Institute of Physics, University of Novi Sad, Trg D. Obradovica 4, Novi Sad,	508
Institute of Technical Science of the Serbian Academy of Science and Arts, Knez Mihailova 35, 11000 Beograd, Serbia and Montenegro,	57, 270, 487, 493, 523, 547, 526, 622, 730,
Institute of Technology of Nuclear and other Mineral Raw Materials, 86 Franchet d'Esperey St., 11 000 Belgrade, Serbia and Montenegro	514, 637, 688, 691, 703, 727, 736, 751,
Instituto Superior de Ciências da Saúde – Sul, 2829-516 Caparica, Portugal	338
Islamic Azad University-North Tehran Branch, Chemistry Department, N°9, Darab-nia b.alley, Daftari-Sharghi alley, Shariati St., Tehran-IRAN	66
Istituto Nazionale di Fisica Nucleare, LNS, Catania, Italy	426, 429
Karolinska Institute, Department of Clinical Neuroscience, Stockholm, Sweden	331, 344, 350
Karolinska Institute, Department of Medical Biochemistry and Biophysics, Stockholm, Sweden	331
Laboratoire de Chimie-Physique, UMR 7512 (CNRS-ULP), 25, rue Becquerel 67087 Strasbourg Cedex 02, France	66
Laboratoire de Physique Pharmaceutique UMR CNRS 8612, Faculté de Pharmacie 5, Rue Jean-Baptiste Clément, 92296 Châtenay-Malabry cedex, France	544
Laboratoire SPMS UMR CNRS 8580, Ecole Centrale Paris, 1, Grande Voie des Vignes, 92295 Châtenay-Malabry, France	544
Lomonosov Moscow State University, Polymers & Crystals Chair, Physics Department, Vorobjevi Gori, 119992 Moscow, Russia	577
Maize Research Institute, Slobodana Bajića 1, 11185 Zemun Polje, SCG	353, 700
Max-Planck Institute für Molekulare Physiologie, Dortmund, Germany,	404
Mayo College of Medicine, Mayo Clinic and Foundation, Departments of Biochemistry and Molecular Biology, Rochester, Minnesota, 55905 U.S.A	760
Mayo College of Medicine, Mayo Clinic and Mayo Foundation, Departments of Anesthesiology and Biochemistry and Molecular Biology, Rochester, MN, USA	14
Mayo Foundation, Department of Biochemistry, Rochester, Minnesota, USA	547
Metallurgical and Materials Engineering Department, University of São Paulo, Av. Prof. Mello Moraes 2463, São Paulo, Brazil	721
Military Technical Institute of the SCG Army, Katanićeva 15, Belgrade, Serbia and Montenegro	523
Moscow State University M.V. Lomonosov, Chemical Faculty, Moscow, 119992, Russia,	273
MP Biomedicals, Inc., 15 Morgan, Irvine CA 92618-2005, USA	347
National and Kapodistrian University of Athens, Department of Chemistry, Laboratory of Analytical Chemistry, Environmental Analysis	631

Group, Panepistimioupoli, 15771 Zografos, Athens, Greece.	
NIS Factory of Lubricants FAM, Jastrebačka 14, 37000 Kruševac, Serbia and Montenegro	658, 661
Nova Gorica Polytechnic, Laboratory of Environmental Research, P.O.B. 301, SI-5001 Nova Gorica, Slovenia	87, 694
Oxford University, Physical and Theoretical Chemistry Laboratory, South Parks Road, Oxford OX1 3QZ, UK,	302
Pharmaceutical and Chemical Industry "Zdravlje-Pharmaco", Vljakova 199, 16000 Leskovac,	775
Romanian Academy, Institute of Physical Chemistry, 202 Splaiul Independentei, 77208 Bucharest, Romania	216, 839
Romanian Academy-Institute of Chemistry, Bd.Mihai Viteazul 24, 1900 Timisoara, Romania	311, 314
Sant Charles University, Macromolecular Physics Department, Prague, Czech Republic	625
Scientific Research Centre at the Oil Refinery Panchevo, Serbia and Montenegro	204
Serbian Academy of Sciences and Arts, Belgrade, Serbia	502
Space Research Institute (IKI), Moscow, Russia	811
Stockholm University, Department of Biochemistry and Biophysics, Stockholm, Sweden;	350
Technical Faculty Čačak, Čačak, Serbia,	502
Technische Universität Berlin, Max-Volmer-Laboratorium für Biophysikalische Chemie, Institut für Chemie, Strasse des 17. Juni 135, D-10623 Berlin, Germany.	74
Texas A&M University, Department of Chemistry, College Station, TX 77843-3255, U. S. A.	20
The Copper Mill, Sevojno, 31000 Užice,	796, 805
Tigar, Pirot, Serbia and Montenegro,	625
Tokyo Institute of Technology, Center for Materials Design, Materials and Structure Laboratory, Yokohama 226-8503, Japan	568
Trayal Corporation, Krusevac, Serbia and Montenegro	204
Universidad de Cantabria, Grupo de Química Inorgánica. Dept. de Ingeniería Química y Química Inorgánica, E.T.S.I.I. y T., E- 39005 Santander, Spain	207, 210, 213
Universidade de Lisboa, Departamento de Física, Instituto Superior Técnico, 1049-001 Lisboa, and Centro de Física da Matéria Condensada, Av. Professor Gama Pinto 2, 1649-003 Lisboa, Portugal.	338
Universidade Nova de Lisboa, Faculdade de Ciências e Tecnologia, Departamento de Ciência dos Materiais, and CENIMAT, 2829-516 Caparica, Portugal.	338

Universidade Nova de Lisboa, Faculdade de Ciências e Tecnologia, Requimte / Centro de Química Fina e Biotecnologia, 2829-516 Caparica, Portugal,	338
Universidade Nova de Lisboa, Instituto de Tecnologia Quimica e Biologica - Apartado 127, Laboratory for Raman Spectroscopy, 2781-901, Oeiras, Portugal	74
Universität Duisburg, Institut für Physikalische und Theoretische Chemie, 47048 Duisburg, Germany	146
Université Claude Bernard Lyon 1, LACE, Bd. du 11 novembre, 69622, Villeurbanne, France	839
University Babes-Bolyai, Faculty of Chemistry and Chemical Engineering, Associated Francophone Laboratory, 11 Arany Janos, 3400 Cluj-Napoca, Romania	323
University Bucharest "Politehnica", Department of Inorganic Chemistry, 1 Polizu street, 011061, Bucharest, Romania	216, 311, 314, 839
University Johns Hopkins, Applied Physics Laboratory, Laurel, Maryland, USA	811
University Lyon I, Laboratoire des Multimateriaux et Interfaces, UMR CNRS 5615, 69622 Villeurbanne Cedex, France.	459
University of Auckland, Department of Chemistry, Private Bag 92019, Auckland, New Zealand,	146
University of Kansas, School of Pharmacy, Department of Medicinal Chemistry, Lawrence, USA	350
University of Miami, Department of Chemistry, Coral Gables, FL 33146 USA	3
University of Missouri, College of Veterinary Medicine, Vet. Med. Diag. Lab., Columbia, MO 65211, USA	727
University of Namur (FUNDP), Laboratoire de Chimie des Matériaux Inorganiques, ISIS, 61 rue de Bruxelles, B-50 Namur, Belgium	228
University of Notre Dame, Radiation Laboratory, Notre Dame, IN 46556-5674, USA	580
University of Patras, Department of Chemistry, 26500 Patras, Greece,	287
VMA, Institute for Hygiene, 11000 Beograd, Crnotravska 17	751